

# PROCEEDINGS

## of the 3<sup>rd</sup> International Conference on Chemical Technology



April 13 - 15, 2015  
Mikulov, Czech Republic

[www.icct.cz](http://www.icct.cz)

## SPONSORS | EXHIBITORS



Unipetrol  
ORLEN GROUP

dekonta



TEVA



[www.BioTech.cz](http://www.BioTech.cz)



## MEDIA PARTNERS

Chemické listy

CHEMAGAZÍN

# **Proceedings of the 3<sup>rd</sup> International Conference on Chemical Technology**

1<sup>st</sup> edition, July 2015

## **EDITORS**

### **Petr Kalenda**

University of Pardubice  
Studentská 95  
532 10 Pardubice, Czech Republic

### **Jaromír Lubojacký**

Ixa Consulting  
Jistebník 242  
742 82 Jistebník, Czech Republic

**All communications submitted were duly reviewed by the scientific committee.**

## **PUBLISHED AND DISTRIBUTED BY**

Czech Society of Industrial Chemistry  
Novotného Lávká 5  
116 68 Prague, Czech Republic

in cooperation with  
Czech Chemical Society  
Novotného Lávká 5  
116 68 Prague, Czech Republic

## **PRINTED BY**

Ocean Design, Prague, Czech Republic

ISBN: 978-80-86238-79-1 (Print)  
ISBN: 978-80-86238-82-1 (Online)  
ISSN 2336-811X (Print)  
ISSN 2336-8128 (Online)

Copyright © 2015 Czech Society of Industrial Chemistry

## SCIENTIFIC COMMITTEE

Assoc. Prof. Jaromír Lederer, Ph.D., Litvínov, (president)  
Prof. Ing. Ján Šajbidor, DrSc. | FCHPT STU Bratislava  
Prof. Elena Korotkova | Tomsk Polytechnic University  
Prof. Dr. Fabio Fava | Department of Civil, Chemical, Environmental and Materials Engineering of the University of Bologna  
Dr. Martínez Agustín | Universidad Politécnica de Valencia  
Prof. Dimitry Murzin | Industrial Chemistry and Reaction Engineering, Åbo Akademi University, Turku, Finland  
Dipl. Ing. Jaromír Lubojacký, MBA, Ostrava (vice-president)  
Prof. Jiří Hanika, Ph.D., Prague (vice-president)  
Prof. Martin Bajus, Ph.D., Bratislava  
Prof. František Babinec, Ph.D., Brno  
Prof. Zdeněk Bělohav, Ph.D., Prague  
Prof. Dr. Karel Bouzek, Prague  
Assoc. Prof. Karel Ciahotný, Ph.D., Prague  
Prof. Jiří Drahoš, Ph.D., dr.h.c., CAS Prague  
Assoc. Prof. Tomáš Herink, Ph.D., Unipetrol RPA, Litvínov  
Prof. Ludovit Jelemenský, Ph.D., Bratislava  
Prof. Petr Kalenda, Ph.D., Pardubice  
Assoc. Prof. Milan Králik, Ph.D., Bratislava  
Prof. Dr. Bohumil Kratochvíl, Ph.D., Prague  
Prof. Ing. Petr Mikulášek, CSc. | FCHT Univerzity Pardubice  
Dipl. Ing. Jozef Mikulec, Ph.D., Bratislava  
Dipl. Ing. Ladislav Novák, Ph.D., Prague  
Assoc. Prof. Milan Olšovský, Ph.D., MSM Martin, s. r. o., Nováky  
Prof. Josef Pašek, Ph.D., Prague  
Assoc. Prof. Dr. Petra Patáková, Prague  
Dipl. Ing. Zbyněk Průša, Agrofert, Deza Valašské Meziříčí  
Assoc. Prof. Milan Pospíšil, Ph.D., Prague  
Prof. Jitka Ulrichová, Ph.D., UP Olomouc  
Dipl. Ing. Radomír Věk, Lovochemie Lovosice  
Prof. Kamil Wichterle, Ph.D., Ostrava  
Dipl. Ing. Miloslav Slezák, Ph.D., Pardubice

## PROGRAM COMMITTEE

Dipl. Ing. Jaromír Lubojacký, MBA, Ostrava (president)  
Assoc. Prof. Jaromír Lederer, Ph.D., Litvínov (vice-president)  
Prof. Jiří Hanika, Ph.D., Prague (vice-president)  
Prof. Ing. Zdeněk Bělohav, CSc., Prague  
Assoc. Prof. Karel Ciahotný, Ph.D., Prague  
Prof. Petr Kalenda, Ph.D., Pardubice  
Prof. Dr. Karel Bouzek, Prague  
Assoc. Prof. Dr. Petra Patáková, Prague  
Prof. Bohumil Kratochvíl, Ph.D., Prague  
Dipl. Ing. Miloslav Slezák, Ph.D., Pardubice  
Prof. František Babinec, Ph.D., RISCO Brno  
Prof. Dr. Dalibor Vojtěch, VŠCHT Praha  
Dipl. Ing. Petra Lovecká, Ph.D., VŠCHT Praha

## CONTENTS

### PETROCHEMICALS AND ORGANIC TECHNOLOGY

#### **HYDROGENATION OF C4 ALKENES**

Kolena J., Morávek P., Šťávoval G., Štěpánek K., Schöngut J., Růžicka M.

#### **VERIFICATION OF METHODOLOGY FOR ACCELERATED ACTIVITY TESTS OF HDS CATALYSTS**

Prokešová A., Tukač V., Zbuzek M., Černý R.

#### **NOVEL APPROACH FOR EVALUATION OF PRIMARY PRODUCT SELECTIVITY OF CO-PYROLYZED HYDROCARBONS BASED ON REGRESSION ANALYSIS**

Petrů J., Zámotný P., Kolena J.

#### **PRINS CYCLIZATION OF ISOVALERALDEHYDE AND ISOPRENOL**

Vyskočilová E., Krátká M., Červený L.

#### **MODIFICATION OF CARBON MATERIALS BY INORGANIC ACIDS**

Antoš P., Horová D., Čmelík J., Ryšánek P., Pospíšilová M.

#### **CONCEPTUAL DESIGN OF A DIMETHYL CARBONATE PRODUCTION AND SEPARATION PROCESS PLANT**

Labovský J., Danko M., Červeňanský I., Janošovský J., Labovská Z., Dudáš, J.

#### **CHEMICAL ENGINEERING SIMULATION ON PARALLEL COMPUTERS**

Labovský J., Danko M., Janošovský J., Labovská Z., Jelemenský Ľ.

#### **RUTHENIUM CATALYSTS FOR HYDROGENATION OF COUMARIN**

Bílková D., Stáně R., Červený L.

#### **HETEROGENEOUS BASIC CATALYSTS IN 2-BUTYLCINNAMYLALDEHYDE SYNTHESIS**

Vrbková E., Krupičková K., Vyskočilová E., Krupka J., Červený L.

#### **UTILIZATION OF OIL FRACTIONS FROM PYROLYSIS OF WASTE TIRES**

Šťávoval G., Soukupová L., Kolena J.

#### **A COMPARATIVE STUDY OF LIQUID- AND GAS-PHASE CYCLOPENTENE HYDRATION CATALYZED BY THE MCM-22 ZEOLITE**

Krupka J., Otmar J., Pawlesa J.

#### **HYDROCARBON CRACKING IN THE PRESENCE OF ALCOHOL: THEORETICAL STUDY**

Karaba A., Zámotný P., Lederer J.

### OIL, GAS, COAL, FUEL, BIOFUELS

#### **PILOT-SCALE POSTCOMBUSTION CO<sub>2</sub> CAPTURE USING ACTIVATED CARBON**

Smutná J., Štefanica J., Hájek P., Ciahotný K., Machač P.

#### **40<sup>TH</sup> ANNIVERSARY FROM COMMISSIONING OF THE NEW REFINERY KRALUPY N. VLT. – HOW IMPORTANT WAS FOR PROCESSING OF CRUDE OIL IN CR**

Kittel H., Krch J., Tlustý J.

#### **EFFICIENCY OF SUPERCRITICAL WATER GASIFICATION: PROCESS CONDITIONS**

Purkarová E., Šváb M., Ciahotný K.

**EXPERIMENTAL AND INDUSTRIAL DEACTIVATION OF HDS CATALYSTS IN THE PRODUCTION OF DIESEL FUEL**

Zbuzek M., Vráblik A., Černý R., Prokešová A., Veselý M., Tukač V.

**STABILIZATION OF ASPHALTENES IN FUEL OILS**

Vráblik A., Černý R.

**ULTRA PURIFICATION OF ENERGETIC GAS FROM BIOMASS GASIFICATION**

Machac P., Duong V. M.

**ANALYSIS OF OPTIMAL HYDROGEN-RICH REFINERY OFFGAS UTILIZATION**

Mierka O., Variny M.

**EXPLORING DIFFERENT POTENTIAL CZECH ELECTRICAL MIXES WITH ELEXTERN**

Wertz F., Karásková Nenadálová L., Kočí V.

**LIGNITE GASIFICATION – MATHEMATICAL MODELING OF SYNGAS EQUILIBRIUM COMPOSITION**

Bártová Š., Klajmon M., Kůs P., Stehlík K., Vonková K.

**DESIGN CALCULATIONS FOR ETHANOL – WATER MIXTURE SEPARATION USING IONIC LIQUID - BUTYL-3-METHYLIMIDAZOLIUM CHLORIDE**

E. Graczová, P. Steltenpohl

**ENVIRONMENTAL GAINS AND IMPACTS OF A CCS TECHNOLOGY – CASE STUDY OF POST-COMBUSTION CO<sub>2</sub> SEPARATION BY AMMONIA ABSORPTION**

Štefanica J., Smutná J., Kočí, V. , Machac P., Pilař L.

**INFLUENCE OF REACTION CONDITION ONTO HYDROTREATING OF RAPESEED OIL**

Kočetková D., Váchová V., Blažek J., Šimáček P., Staš M.

**SBA-5 AND BENTONITE BASED CATALYSTS USED FOR THE VISCOSITY REDUCTION OF A REB VACUUM RESIDUE USING A LOW-TEMPERATURE HYDROVISBREAKING PROCESS.**

Hidalgo J. M. , Vráblik A. , Jíša P. , Černý R. , Hamerníková J. , Yopez A. , Romero A. A.

**LOW-TEMPERATURE PROPERTIES OF DIESEL FUEL CONTAINING DIFFERENT FAME**

Vráblik A., Zbuzek M., Hamerníková J., Němec J., Černý R.

**ADDITIVES FOR IMPROVEMENT OF THERMAL STABILITY OF BITUMINOUS BINDERS**

Jíša P., Černý R.

**HYDROTREATING OF LIGHT CYCLE OIL**

Tomášek J., Blažek J., Zbuzková B., Matějovský L., Kočetková D.

**INCREASING SOLUBILITY AND DISSOLUTION RATE OF CANDESARTAN CILEXETIL**

Gruberová L., Kratochvíl B., Seilerová L.

**EFFECT OF β-CYCLODEXTRIN ON PHYSICAL PROPERTIES OF ORALLY DISINTEGRATING TABLETS CONTAINING CETIRIZINE DIHYDROCHLORIDE**

Škopková T., Krejzová E. , Bělohav Z.

**INORGANIC TECHNOLOGY**

**PREPARATION AND COLOR PROPERTIES OF PIGMENTS BASED ON YMnO<sub>3±δ</sub>**

Burkovičová A., Dohnalová Ž., Šulcová P.

#### **HYDROGELS BASED ON GLUCOMANNAN AND THEIR UTILIZATION IN AGRICULTURE**

Hermann P., Svoboda L., Bělina P.

#### **APPLICATION POSIBILITIES OF ZINC OXIDE NANOPARTICLES**

Švrček J., Bierská L., Souček M., Krýsa J.

#### **STRUCTURE AND PROPERTIES OF LEAD-YTTRIUM PHOSPHATE GLASSES**

Račický A., Mošner P., Koudelka L.

#### **MECHANOCHEMICAL PREPARATION OF ALUMINA-CERIA**

Jiráťová K., Spojakina A., Tyuliev G., Balabánová J., Kaluža L., Palcheva R.

#### **PYROCHLORES OF LANTHANIDES DOPED BY ZIRCONIA**

Hablovičová B., Šulcová P.

#### **THE INFLUENCE OF AMOUNT OF CHROMOPHORE ON THE COLOR PROPERTIES OF MALAYAITE PIGMENT**

Luxová J., Šinkovská M., Šulcová P.

#### **SYNTHESIS OF Mn/Mg FERRITES USING UNUSAL PREPARATION METHODS – COMPARATIVE STUDY**

Bělina P., Strouhal J., Pluhařová L., Šulcová P., Svoboda L.

#### **STUDY OF PROPERTIES OF MODIFIED COMMERCIAL HYDROGEL**

Šustek S., Svoboda L.

#### **THE EFFECT OF LANTHANIDES ON COLOUR PROPERTIES OF THE MIXED OXIDE PIGMENTS BASED ON Bi-Ce-Nb**

Těšitelová K., Šulcová P., Gorodylova N. O.

#### **THE EFFECT OF ADMIXTURES Ti a Zr ON THE COLOUR PROPERTIES OF CASSITERITE PIGMENTS DOPED BY Cr**

Karolová L., Trojan J., Trojan M., Luxová J.

### **MATERIAL ENGINEERING**

#### **CHEMICAL ASPECTS OF ANTIBALLISTIC CERMETS PREPARATION**

Brozek V., Kubatík F.T., Chraska T., Mušálek R., Janata M., Mastny L.

#### **SYNTHESIS AND APPLICATIONS OF INTERMETALLICS**

Novák P., Salvetr P., Kříž J., Marek I., Kubatík T.F.

#### **MECHANICAL AND CHEMICAL PROPERTIES OF PLASMA-SPRAYED BRONZE CuAlO COATING ON MAGNESIUM AND MAGNESIUM ALLOY AZ 9**

Kubatík F.T., Vilémová M., Mušálek R., Janata M.

#### **RESEARCH OF THE CHEMICAL PRE-TREATMENTS APPLIED ON THE SURFACE OF THE LOW CARBON UNALLOYED STEEL SHEET USING SEM AND EDS ANALYSIS**

Svobodová J., Weiss V., Cais J.

#### **RESEARCH AND EVALUATION OF CRYSTAL SEGREGATION DURING CASTING OF THE ALLOY Al-Zn-Cu-Mg**

Weiss V., Svobodová J., Cais J.

#### **THE INFLUENCE OF GERMANIUM ON THE PROPERTIES OF COMMERCIAL MAGNESIUM ALLOYS**

Šerák J., Kovalčík T., Vojtěch D., Novák P.

**INFLUENCE OF HEAT TREATMENT ON MICROSTRUCTURE AND MECHANICAL PROPERTIES OF AISi9CuMgNiMn ALLOY**

Cais J., Weiss V., Svobodová J.

**POLYMERS, COMPOSITES**

**OPTIONS FOR REDUCTION OF CONTENT OF ZnO IN RUBBER COMPOUNDS**

Božek M., Švrček J., Olšovský M.

**THE EFFECT OF PURE BIOFUELS ON PHYSICAL AND MECHANICAL PROPERTIES OF FLUORORUBBER BLENDS**

Dubovský M., Haninčík S., Olšovský M.

**INFLUENCE OF NITROGEN OXIDE ATMOSPHERE ESPECIALLY N<sub>2</sub>O<sub>4</sub> ON AGING PROCESSES OF POROUS LIGNOCELLULOSE MATERIALS**

Filipi M., Milichovský M., Mikala O.

**ALTERNATIVE SOURCE OF NATURAL RUBBER - TKS AND GUAYULE**

Brejcha J., Herzigová L.

**SIMULATION OF MECHANICAL PROPERTIES OF HETEROPHASE POLYPROPYLENE COPOLYMER**

Grůza J., Kratochvíla K.

**RHEOLOGICAL BEHAVIOUR OF PROPYLENE COPOLYMERS AND TERPOLYMERS**

Balgová V., Sadílek J.

**BIODEGRADABLE POLYPROPYLENE BLEND WITH CONTROLLED DEGRADATION**

Balgová V., Vrátničková Z., Babka M.

**WASHING OF SODA PULP FROM RAPESEED STRAW**

Potůček F., Hájková K.

**INFLUENCE OF CHEMI-MECHANICAL PULP ADDITION TO SECONDARY FIBRES UPON BENDING STIFFNESS**

Potůček F., Gurung B., Říhová M.

**CONDUCTIVE POLYMERS IN PROTECTIVE COATINGS**

Kalendová A., Hájková T.

**THE SATURATED VAPORS OF SELECTED COMPONENTS OF ESSENTIAL OILS AND ITS INFLUENCE ON THE PROPERTIES OF THE LIGNOCELLULOSE MATERIALS**

Mikala O., Gojný J., Milichovský M., Hájek M.

**INFLUENCE OF SELECTED DISINFECTANTS AND DEACIDIFICATION MEANS ON LIGNOCELLULOSIC MATERIALS**

Hájek M., Milichovský M., Filipi M., Mikala O.

**INFLUENCE OF SBR/BR BLENDS FORMULATION ON THE COURSE OF VULCANIZATION AND PROPERTIES OF THE VULCANIZATES**

Kadeřábková A., Ducháček V.

**WASTE PROCESSING, AIR AND WATER PROTECTION, TECHNOLOGIES FOR THE DECONTAMINATION OF SOILS**

**FEASIBILITY STUDY OF THE PARTICULATE MATTER FILTRATION FROM THE AIR STREAM IN GRANULATED FERTILIZER PRODUCTION**

Jecha D., Brummer V., Lestinsky P., Skryja P.

**A PRACTICAL APPROACH FOR PREDICTING A RIGHT GEOMETRY OF CYCLONE SEPARATORS**

Kušnierik O.

**SOIL DECONTAMINATION OF POPS BY THERMAL DESORPTION, APPLYING OF THERMAL DESORPTION FOR SOIL DECONTAMINATION PROCESS.**

Grof A., Uotilla J.

**EVALUATION OF UV, UV/H<sub>2</sub>O<sub>2</sub> AND UV/Na<sub>2</sub>S<sub>2</sub>O<sub>8</sub> SYSTEMS FOR THE TREATMENT OF INDUSTRIAL WATERS – ORGANICS DEGRADATION AND DISINFECTION**

Bártová Š., Šveda H., Kús P., Šmejdomá V., Říhová Ambrožová J., Vonková K.

**INFLUENCE OF PHOSPHORUS TO DENITRIFICATION WITH THIOBACILLUS DENITRIFICANS**

Blažková Z., Slebová E., Trousil V., Slezák M., Palarčík J., Čákl J.

**HOME WASTE TREATMENT PLANTS WITH ELECTROCHEMICAL CLEANING**

Dušek L.

**REDUCTION OF NEGATIVE IMPACTS OF INFRASTRUCTURE CONSTRUCTIONS ON THE SURFACE WATER QUALITY**

Hnátková T., Šereš M., Kriška M., Rozkošný M., Vymazal, J.

**SACRIFICIAL ANODES CATALYZING ELECTRO-FENTON OXIDATION OF WASTEWATER**

Kočanová V., Dušek L., Novotný L.

**METAMITRON DEGRADATION FROM MODEL WASTEWATER BY INDIRECT OXIDATION**

Tomić A., Dušek L., Palatý Z., Vojs M.

**DEVELOPMENT OF A PILOT PLANT FOR REDUCTION Hg EMISSION FROM LARGE POWER PLANT**

Pilař L., Vlček Z., Zseliga Z., Veselý V.

**NUMERICAL SIMULATION OF MIXED LAYER EVOLUTION CONSIDERING THE INFLUENCE OF BUOYANCY AND SHEAR PRODUCTION**

Duong V. M.

**LIFE CYCLE ASSESSMENT (LCA) METHOD IN NUCLEAR ENERGY FIELD: A CRITICAL OVERVIEW**

Zakuciová K., Kočí V.

**THE ROLE OF ADDITIVES IN HYDRODEHALOGENATION OF HALOGENATED ANILINES USING Al-Ni ALLOY**

Weidlich T., Opršal J., Beneš L., Vlček M.

**APPLICATION OF IONIC LIQUIDS FOR THE PRODUCTION OF BROMAMINE ACID**

Šimek M., Vyňuchal J., Weidlich T.

**OPTIMIZATION OF WALL TEMPERATURE IN VACUUM FILM EVAPORATOR**

Timár P., Stopka J., Báleš V., Timár P.Jr., Hanus K.

**HEAT TRANSFER COEFFICIENTS IN LIQUID FILM EVAPORATOR**

Stopka J., Timár P., Báleš V., Timár P. Jr.

**THE DEGRADATION OF RESIDUES OF DRUGS IN WASTEWATER USING PHOTOCATALYSIS WITH TITANIUM DIOXIDE**

Kořínková J., Bauerová D., Machalický O.

**ASSESSMENT OF SELECTED OPTIONS IN OPERATION OF WATER TREATMENT PLANT IN PILSEN BY MEANS LCA**

Klimtová M., Kočí V.

**DETERMINATION OF SORPTION CAPACITY OF ORGANIC VAPORS ON ACTIVATED MESOCARBONS**

Špitová B., Koutník I., Večeř M.

**BIOTIC METHODS FOR IDENTIFYING THE EFFECTS OF POLYPHENOLIC COMPOUNDS IN THE AQUATIC ENVIRONMENT**

Kobetičová K., Losonszky G., Pařízek O., Kočí V.

**QUARTZ CRYSTAL MICROBALANCE ODOR SENSOR OF VOLATILE AMINES BASED ON PHTHALOCYANINE FILM**

Seidl J., Jirešová J., Hofmann J., Smolná K.

**BIOTECHNOLOGY**

**PRESSURE HYDROLYSIS OF PROTEIN IN WASTE OF CHICKEN CARTILAGE AND FEATHERS IN THE PRESENCE OF CARBON DIOXIDE**

Hanika J., Šolcová O., Kaštánek P.

**UTILIZATION OF LIGNOCELLULOSIC SUBSTRATES BY CLOSTRIDIUM BACTERIA**

Kolek J., Patáková P.

**USING THE TYROSINASE FROM *AGARICUS BISPORUS* AND THE CYANIDE HYDRATASE FROM *ASPERGILLUS NIGER* K0 IN THE DEGRADATION OF PHENOL AND *o*-, *m*- AND *p*-CRESOL AND THE FREE CYANIDE FROM COKE PLANT WASTEWATER**

Chmátal M., Veselá A.B., Rinágelová A., Kaplan O., Martínková L.

**DOUBLE REACTOR MEMBRANE HYBRID SYSTEM FOR PHENYLACETIC ACID PRODUCTION**

M. Mihaľ, I. Červeňanský, J. Markoš

**IN VITRO ACTION OF BAICALEIN ON *CANDIDA ALBICANS*, *CANDIDA PARAPSILOSIS* AND *CANDIDA KRUSEI* GROWTH INHIBITION**

Kvasničková E., Masák J.

**EXTRACTION OF CAROTENOIDS FROM SELECTED PLANTS**

Rousková M., Maléterová Y., Hanika J., Šolcová O.

**ANTIMICROBIAL ACTIVITY OF COBALT BIS(DICARBOLLIDE) AMINODERIVATIVES**

Kvasničková E., Masák J., Šícha V.

**MODELING OF WHITE WINE FERMENTATION – PARAMETER SENSITIVITY STUDY**

Báleš V., Baláž J., Timár P. Jr., Timár P.

**PHARMACEUTICAL TECHNOLOGY**

**OPTIMIZING FLOW AND SEGREGATION PROPERTIES OF LACTOSE/MICROCRYSTALLINE CELLULOSE MIXTURE FOR TABLET COMPRESSION**

Zámstný P., Kreibichova B., Hofmanova D., Kulaviak L., Zelenkova K., Růžička M.

**A STUDY OF DISSOLUTION AND STABILITY KINETICS OF SOLID DOSAGE FORM PREPARED BY HOT-MELT EXTRUSION**

Patera J., Blažková K., Beneš M.

**EFFECT OF HYDROPHOBIC INCLUSIONS ON POLYMER SWELLING KINETICS STUDIED BY MAGNETIC RESONANCE IMAGING**

Gajdošová M., Pěček D., Sarvašová N., Štěpánek F.,

**SECURE MANAGEMENT PROCESSES, ACCIDENTS PREVENTION**

**UNWELCOME RESULTS OF SAFETY ANALYSES**

Ferjenčík M., Mašín J.

**ASPEN HYSYS MODELLING IN SAFETY ANALYSIS AUTOMATION**

Janošovský J., Labovský J., Jelemenský Ľ.

**IDENTIFICATION OF HAZARDS ASSOCIATED WITH OPERATION OF INDUSTRIAL CEMENTATION FURNACE**

Mukhametzianova L., Kotek L.

## **PETROCHEMICALS AND ORGANIC TECHNOLOGY**

### **HYDROGENATION OF C<sub>4</sub> ALKENES**

**Kolena J.**<sup>1</sup>, Morávek P.<sup>1</sup>, Šťávoval G.<sup>1</sup>, Štěpánek K.<sup>1</sup>, Schöngut J.<sup>2</sup>, Růžička M.<sup>2</sup>

<sup>1</sup>*Výzkumný Ústav Anorganické Chemie, UniCRE, Chempark Litvínov, Záluží – Litvínov, 436 70, Czech Republic, Tel.: 476 163 659, E-mail: jiri.kolena@vuanch.cz*

<sup>2</sup>*UNIPETROL RPA, Chempark Litvínov, Záluží – Litvínov, 436 70, Czech Republic*

#### **Introduction**

C<sub>4</sub> alkanes, mainly butane, are appreciated as excellent feedstock for the production of ethylene by steam cracking. Saturated C<sub>4</sub> mixture in which n-butane prevails can be industrially produced by total hydrogenation of the mixture of C<sub>4</sub> alkenes and alkanes, known as Rafinate 2 which is a residue after extracting of 1,3-butadiene and isobutene from pyrolysis C<sub>4</sub> fraction by standard chemical processes.

Hydrogenation of lower alkenes is a strongly exothermic process, quite simple by its chemical nature but rather complicated in terms of chemical engineering problems. Even measurement of kinetic data is not a facile problem. Maybe for this reason, there is a lack of industrially relevant data on hydrogenation kinetics in modern literature. Major part of the studies aimed at utilization of noble metals as catalysts, are based on mechanistic approach, trying to understand sorption phenomena on catalyst surface and describe the kinetics by means of Langmuir Hinshelwood type of kinetic equations [1]. Some kinetic measurements have been done with pure alkenes i.e. in non-competitive environment. It has been however discovered that relative reactivity of individual alkenes can change in the environment of competitive sorption [2]. It is therefore necessary to measure industrially relevant data with an alkenic mixture of real composition.

Though the gas-liquid-solid hydrogenation is the most frequently utilized industrial process, the gas phase hydrogenation can be an interesting alternative for lower alkenes, mainly C<sub>4</sub>, bringing some advantages over the liquid phase process. The gas-liquid-solid system is more complex in terms of kinetics and mass transfer as gas-solid, liquid-solid and gas-liquid-solid mass transfer mechanisms can take place. On the other hand, in the gas phase reaction, large excess of hydrogen is necessary to maintain hydrocarbons in gas phase on one hand and to prevent the system from unacceptable preheating on the other hand as hydrogen takes part of a coolant in this system. Measuring and evaluating of kinetic data is therefore not a facile problem.

As for catalyst, Pt or Pd, impregnated usually on silica or  $\gamma$ -alumina, are most frequently used systems [2,3,4]. Pt based catalysts are known as selective towards hydrogenation below 200 °C, the selectivity decrease being observable above this limit. It is also known from the literature [4] that the activity of Pt catalyst strongly depends on the reduction procedure so very careful in-situ reduction, with slow temperature increase and gradual raise of hydrogen concentration in reduction gas is recommended [4].

It is the main goal of this study to provide kinetic data of C<sub>4</sub> alkene mixture hydrogenation in gas phase, obtained with real, industrially utilizable, catalyst particles, which can be used for the process design.

#### **Experimental**

Hydrogenation of alkenes ranks among strongly exothermic reactions so that it is impossible to run it in isothermal regime even in intensively cooled, narrow tube, laboratory reactors. The temperature profile should be however carefully controlled, not to allow the temperature maximum in the reactor to exceed the limit above which some undesirable reactions, e.g. C-C bond hydrogenolysis, can take place. Optimally, the axial temperature profile should be flat, nearly isothermal. However, this can hardly be expected in real reactors.

A double tube reactor, heated/cooled by silicone oil, circulating between the tubes in countercurrent flow, the same system recently described in our previous study [5], was used for the data measurement. This type of arrangement guaranteed relatively flat axial temperature profile. Nevertheless, even in this arrangement, non-isothermal kinetic data were obtained and had to be processed.

The reaction products were analyzed by on-line gas chromatograph Shimadzu 2010, equipped with a temperature controlled, two valve dosing loop for gas sample injection. A 50 m capillary column HP PONA (Agilent), ID 0.2 mm, film thickness 0.5  $\mu$ m and He as carrier gas, were used. The inlet temperature was 250 °C, FID detector temperature 200 °C, the oven temperature program being as follows: 30 °C for 15 min isothermally, 10 °C/min up to 100 °C, then 20 °C/min up to 200 °C. Only hydrocarbons in the output stream were determined and quantified.

Rafinate 2, an industrially available mixture of predominantly linear C<sub>4</sub> alkenes and alkanes was used as the feedstock for the kinetic data measurement. Three samples of a bit different composition were used for the experiments. Their composition is summarized in Table I.

Table I: Composition of C<sub>4</sub> fraction (Rafinate 2) used as starting material for kinetic data measurement.

Composition [Vol,.%]	sample 1	sample 2	sample 3
isoutane	21.38	13.62	21.72
n-butane	18.39	15.68	18.83
propandiene	0.05	0.03	0.05
1-butene	33.63	39.92	32.97
trans-2-butene	14.05	15.22	14.27
isobutene	2.50	5.20	2.14
cis-2-butene	8.75	9.19	8.89
1,3-butadiene	0.00	0.08	0.00
methanol	1.25	1.06	1.13

An egg shell type of Pt/ $\gamma$ -alumina catalyst containing 0.56 wt. % of Pt was used for the kinetic tests. Other catalyst characteristics: catalyst surface 211 m<sup>2</sup>/g, the shell thickness 50  $\mu$ m. The catalyst was shaped to balls of 2-2.5 mm in diameter.

### Results and discussion

Experiments in wide range of experimental conditions were performed, at three different levels of reaction temperature (110, 120, 130 °C) and overall pressure. Though it is not that difficult to keep C<sub>4</sub> hydrocarbons in gaseous phase even at higher pressure, considerable excess of hydrogen was used to measure the data as close to supposed industrial conditions as possible. As proven recently[5], changes in H<sub>2</sub>/hydrocarbons molar ratio in the range of 5 to 9.5 have only negligible effect on the reaction kinetics, therefore all data of C<sub>4</sub> alkene hydrogenation were measured at the same ratio of H<sub>2</sub> to hydrocarbons (=6.5).

Axial temperature profiles at different values of time coordinate W/F are illustrated by Figure 1. It can be seen from the Figure 1, that hydrogenation is very fast, so the maximum of the temperature profile lies in the first half of the catalyst layer.

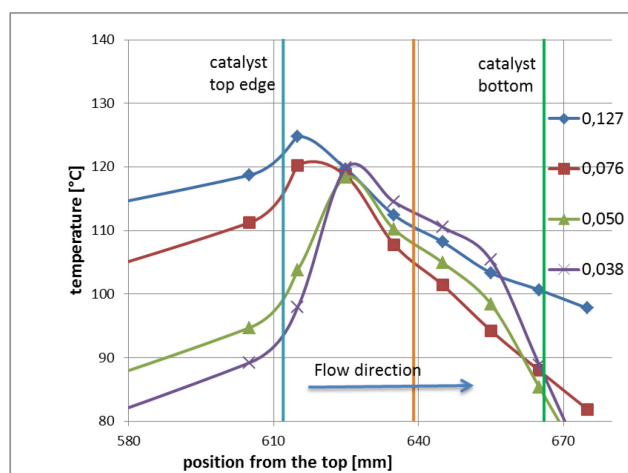


Figure 1: Axial temperature profiles at different values of W/F ratio in the interval of 0,038-0,128. Pressure 3.1 MPa, temperature 110°C, H<sub>2</sub>/CH=6,5.

An example of conversion curves i.e. dependencies of individual C<sub>4</sub> alkenes on time parameter W/F, is illustrated by Figure 2. As can be seen from Figure 2, 1-butene reacted faster than isomers with inner double bond that were present in the feedstock in comparable concentrations.

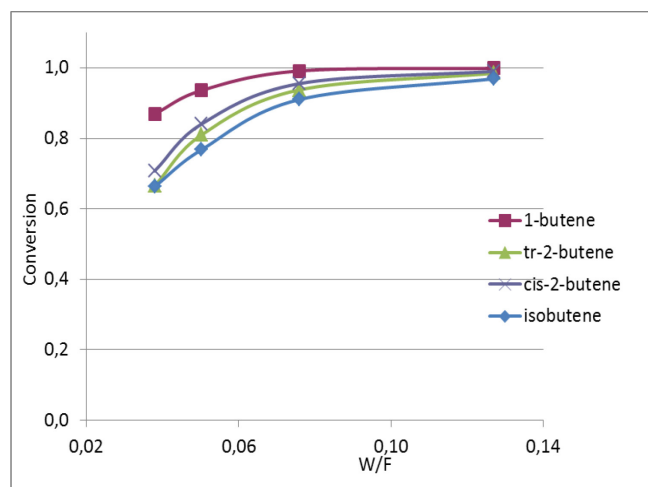


Figure 2: Plot of butenes conversions v.s. W/F coordinate. Pressure 3.1 MPa, temperature 110°C, H<sub>2</sub>/CH=6,5. Despite the fact that the data were measured in relatively narrow tube, cooled by liquid, strongly non-isothermal data were obtained (see Figure 1). The data were therefore treated with similar approach as in the previous study [5]. The tube non-isothermal reactor was modeled as a series of 10 isothermal reactors, equal in length and volume, but working at different temperatures, the working temperature of each reactor being calculated from a real, measured, temperature profile. The scheme of the model is shown in Figure 3.

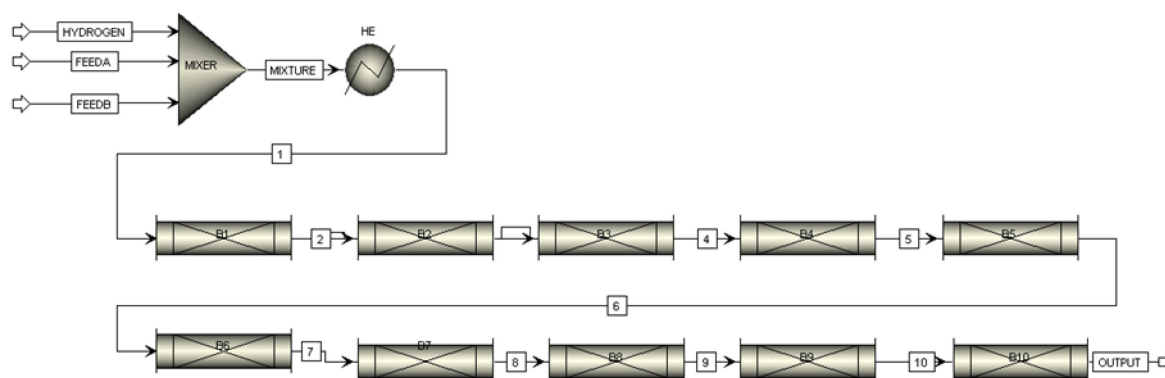


Figure 3: Scheme of simulation model used for Aspen Plus simulation.

It is necessary to know the input and output values of molar flow of all components to evaluate kinetic parameters. The components balances were calculated from following experimental data: C<sub>4</sub> fraction feed, H<sub>2</sub> input, output gas stream volume, relative output concentrations of hydrocarbons (relatively to hydrocarbon part of product) determined by GC. It was therefore necessary to calculate the output molar flows of all components. Following assumptions were taken for the molar balance to be calculated:

- C-C bond cleavage doesn't take place in the system
- No isomerization proceeds
- Input flow analyses are more accurate than those from the output GC analyzer.

Assumptions a) and b) were verified by detailed GC analyses of both liquid and gaseous products. Considering the assumptions, it is true that the sum of particular groups of hydrocarbons, i.e. nC<sub>4</sub>, iC<sub>4</sub>, is of the same value in input and output respectively. It is then possible to calculate relative proportion of individual hydrocarbons in each of the hydrocarbon groups. From the knowledge of relative proportion of hydrocarbon groups it is then possible to calculate the molar output of individual components. There are also some inert

compounds in the system, the input and output molar flows of which are equivalent. The molar output of hydrogen was calculated on the basis of reactions stoichiometry.

In the gas phase reaction of C<sub>4</sub> hydrocarbons, relatively large excess of hydrogen is necessary. It can be therefore expected that the reaction is formally of zero order to hydrogen. This assumption was verified by performing the experiment in wide range of H<sub>2</sub>/C<sub>4</sub> ratio. Assuming zero order to hydrogen, the kinetic constants of all reactions can be evaluated independently. For estimation of kinetic constants, first order to hydrocarbons was supposed. The first order reaction taking place in a plug-flow reactor can be (for component A) described by equation (1)

$$\frac{dc_A}{dz} = -\frac{S}{\dot{V}} \rho_b k_A c_A \quad (1)$$

Taking large excess of hydrogen into consideration, it can be seen realistic that there is a constant volume flow. At these conditions, molar flow of component A in the output from (i+1) section can be described by following equation (2):

$$N_{A,i+1} = \frac{N_{A,i}}{\exp\left[k_{A,i+1}(T_{i+1}) \frac{\rho_b V_{i+1}^R}{\dot{V}}\right]} \quad (2)$$

where

$$k_{A,i+1}(T_{i+1}) = A_A e^{\frac{-E_A}{RT_{i+1}}} \quad (3)$$

Reaction constants (k, E) were estimated by minimizing the sum of squares of deviations between calculated and experimental values of the reacting components molar flow values in the reactor output. This calculation was done by means of the Solver function in Excel program. The kinetic constants estimations obtained this way were used as the starting values for Aspen Plus simulation.

The Aspen Plus program makes it possible to calculate kinetic constants of defined reactions by means of a regression model which takes into account composition of input and output streams and their temperature and pressure values. The kinetic constants of all reactions were thus evaluated. All these constants were evaluated at the same time by a single run optimization. Pengov-Robinson equation of state was used for the calculation.

A mathematical model containing ten isothermal plug flow reactors was used to approximate the real experimental reactor - see Figure 3.

The kinetics constants for complete reaction scheme, evaluated by Aspen Plus simulation are listed in Table II. A comparison with previously obtained [5] kinetic constant for structurally similar C<sub>5</sub> alkenes is also shown in the same table (Table II).

Table II – Kinetic constants of the hydrogenation of alkenes contained in C<sub>4</sub> fraction in comparison with the kinetic constants of the reactions of structurally similar C<sub>5</sub> alkenes (data measured in the frame of previous study [5]).

Compound	A[m <sup>3</sup> /(kg . s)]	E [kJ/kmol]	Compound	A[m <sup>3</sup> /(kg . s)]	E [kJ/kmol]
1-butene	7.71 · 10 <sup>4</sup>	56505	1-pentene	3.26 · 10 <sup>5</sup>	64075
Trans-2-butene	2.06 · 10 <sup>3</sup>	47077	Trans-2-pentene	2.16 · 10 <sup>3</sup>	48929
2-methylpropene	7.74 · 10 <sup>4</sup>	59000	2-methyl-1-butene	1.01 · 10 <sup>4</sup>	55119
Cis-2-butene	2.03 · 10 <sup>2</sup>	39437	Cis-2-pentene	2.88 · 10 <sup>4</sup>	56968

It is apparent, that kinetic behavior of structurally similar C<sub>4</sub> and C<sub>5</sub> alkenes is very similar, the linear 1-alkenes being the only exception as different reactivity of 1-butene, in comparison with 1-pentene was observed.

### Conclusions

Concentration based kinetics of gas phase hydrogenation of C<sub>4</sub> alkenes in a real C<sub>4</sub> fraction (Rafinate II) from steam cracking was measured, at the conditions considered as suitable for an industrial process design. It is very important to have kinetic data obtained with a multicomponent mixture of alkenes, the composition of which is close to that of real potential industrial feedstock, for minimizing the effect of competitive adsorption on catalyst surface.

1<sup>st</sup> order reaction to alkene and zero order to hydrogen proved to be a relevant kinetic equation for main reactions description. A large set of non-isothermal experimental data was processed and kinetic constants (preexponential factor, energy of activation) for all reactions involved were evaluated in one go calculation by means of the Aspen Plus software. A good agreement between calculated and experimental data was achieved. As the experimental data were measured at conditions suitable for an industrial process, the kinetics can be considered utilizable for the industrial process design.

### Acknowledgement

*This publication is a result of the project no FR TI/253, supported by the Ministry of Industry and Trade of the Czech Republic, which is being carried out in the UniCRE centre whose infrastructure was supported by the European Regional Development Fund and the state budget of the Czech Republic.*

### Literature

1. Rogers G.B., Lih M.M., Hougen O.A.: *AIChE Journal* 12,369 (1966).
2. Coletto I., Roldán R.: *Catalysis Today* 149,275 (2010).
3. Ru 2 197 460 (2001).
4. Canning A., Jackson S., Monaghan A. and Wright T.: *Catalysis Today* 116, 22 (2006).
5. Kolena J., Morávek P., Šťávková G., Štěpánek K., Schöngut J., Růžička M.: *Kinetics of Gas Phase Hydrogenation of C5 alkenes; ICCT 2014.*

### Abbreviations

A	Pre-exponential factor
c	Concentration of reacting component
E	Activation energy
k	Reaction-rate constant
n	Reaction order
r	Reaction rate (in relation to catalyst mass)
N <sub>A</sub>	Molar flow of component A
R	Universal gas constant
$\dot{V}$	Volume flow
S	Reactor cross section area
V <sub>i</sub> <sup>R</sup>	Volume of part of the reactor supposed to be isothermal
z	Axial coordinate of the reactor
ρ <sub>b</sub>	Packing density of the catalyst

## VERIFICATION OF METHODOLOGY FOR ACCELERATED ACTIVITY TESTS OF HDS CATALYSTS

**Prokešová A.**<sup>1</sup>, Tukač V.<sup>1</sup>, Zbuzek M.<sup>2</sup>, Černý R.<sup>2</sup>

<sup>1</sup>University of Chemistry and Technology, Department of Organic Technology, Technická 5, 16628, Prague 6,

<sup>2</sup>Research Institute of Inorganic Chemistry (VÚAnCh), Department of Efficient Refining Technologies (UniCRE-EFFRET), Chempark Litvínov, 43670, Litvínov  
aneta.prokesova@vscht.cz

### Introduction

At present time, the sulphur content in diesel fuels is limited to 10 mg.kg<sup>-1</sup> by European Union directive 2009/30/EC. The deep hydrodesulphurization, and processing of more aromatic raw material leads to requirement of more stable and active catalysts.

Diesel fuel contains a large variety of sulphur compounds with different reactivity. The sulphur compounds presented in diesel fuels can be divided into two main groups. The first one contains thiophenes, the second one dibenzothiophenes, presented especially in alkylated molecules form<sup>1</sup>. Several studies have shown that the relative reactivity of different thiophenic sulphur compounds is significantly different, as might be expected<sup>2,3</sup>. Benzothiophenes and their derivatives are usually desulphurized at higher reaction rate than DBT and alkylated DBTs. Alkylated dibenzothiophene isomers containing alkyl groups close to the sulphur atom, e.g. 4-methyldibenzothiophene (4-MDBT), 4,6-dimethyldibenzothiophene (4,6-DMDBT), 4,6-diethyldibenzothiophene (4,6-DEDBT), are less reactive due to steric hindering<sup>4,5</sup>. Also, in the mixture of large amount of sulphur compounds, there is a competition on the catalyst surface active centres. More active sulphur compound, reacting preferentially, can influence HDS rate of less reactive sulphur compound<sup>6</sup>.

There is a continual development in refinery processes technologies. Using of an unusual raw material (e.g. light cycle oil, containing large amount of aromatic compound, which can be problematic under the standard hydrodesulfurization conditions) require development in the hydrotreating processing conditions and hydrotreating catalyst. A very important step in the preparation of a new catalyst is its pilot testing under the real reaction conditions.

The objective of this work was to verify the consecutive steps of the methodology for HDS catalyst activity testing via accelerated deactivation. It was necessary to evaluate the conditions of the elimination of external mass transfer in a pilot fixed-bed reactor. Also the influence of different compounds on activity was studied and finally, the accelerated deactivation test were approved to forecast the HDS catalyst life cycle.

### Material and method

The activity tests were carried out in the pilot scale trickle-bed reactor 30 mm I.D., WHSV 0.5 - 3 h<sup>-1</sup>, gas/liquid volumetric feed ratio 300, pressure 3 – 6 MPa and temperature 350 – 400 °C.

Elimination of the external effects of mass and heat transfer was made by the dilution of void space of fixed catalyst bed by inert silicon carbide particles. This arrangement allows the suppressing axial mixing deflection from a piston flow pattern, to create even fluid velocity distribution on the cross-section of the reactor bed and to accomplish the complete wetting of catalyst particles.

The accelerated deactivation test was applied to forecast HDS catalyst life cycle. The deactivation step consist in two hours injecting of light cycle oil, which contain higher amount of aromatics compound than atmospheric gas oil, and also more nitrogen compounds. The outlet concentration of sulphur in product before and after the deactivation step was evaluated. The hydrodesulfurization rate constant and the deactivation constant were calculated by the pseudo-first reaction order power kinetics by a linear regression.

The HDS kinetics experiments were carried out in autoclave with a commercial CoMo/Al<sub>2</sub>O<sub>3</sub> hydrotreating catalyst. Batch was composed of hydrogenated gas oil (GO) promoted by various sulphur species: 3-methylthiophene (3-MT), 3-methylbenzothiophene (3-MBT), 4-MDBT, 4,6-DMDBT and 4,6-DEDBT. The effects of pressure and temperature on the sulphur species removal reaction rate were also observed. Hydrogen partial pressure was constant during the reaction, set on 3 MPa, 4.5 MPa or 6 MPa and the reaction temperatures were ranging at 350°C, 365°C and 380°C.

During each experiment, both in trickle bed reactor and in autoclave, samples were regularly taken off and they were analyzed by gas chromatography to monitor sulphur concentrations during the experiment.

Data from the kinetics experiments were evaluated by two different ways – (i) modeling by Aspen Plus process simulation and (ii) using a nonlinear regression by Matlab software.

To compare the accelerated and standard process of deactivation, the samples of deactivated catalyst from an industrial hydrotreating unit were taken as well. The residual activity of these samples was measured in the

pilot scale trickle bed reactor under the same conditions as for the previous experiments but without application of any deactivation step.

### Results and discussion

The reaction rate constants of hydrodesulfurization reactions in a trickle bed reactor were evaluated by pseudo first order power-law kinetic.

$$\frac{dc_s}{d\left(\frac{W}{F}\right)} = -kc_s \quad (1)$$

where  $W/F$  is the overturn value of the weight hourly space velocity ( $1/WHSV$ ).

### Evaluation of reaction rate constants

The dependence of catalyst activity on reaction conditions was investigated. At first, the influence of reaction temperature was tested at constant hydrogen partial pressure (4.5 MPa) and weight hourly space velocity ( $WHSV = 1 \text{ h}^{-1}$ ) respectively.

Table I: Reaction rate constants at different reaction temperature

Catalyst		CoMo		
Temperature [°C]	350	360	365	
$c_s$ [mg/kg]	47.7	18.9	9.7	
Rate constant [ $\text{h}^{-1}$ ]	7.35	8.57	9.43	
Catalyst		NiW		
Temperature [°C]	350	360	377	
$c_s$ [mg/kg]	181.7	41.7	8.4	
Rate constant [ $\text{h}^{-1}$ ]	3.81	5.12	6.55	

The reaction rate constants increased with increasing reaction temperature. The required level of sulphur (10 mg/kg) in product was achieved at temperature 365 °C for CoMo catalyst, and at 377 °C for NiW catalyst, which was less active.

Next set of experiment was performed for different values of WHSV under constant reaction temperature 370°C and hydrogen partial pressure 4.5 MPa.

Table II: Reaction rate constants at different WHSV

Catalyst		CoMo			
WHSV [ $\text{h}^{-1}$ ]	1	2	3	4	
$c_s$ [mg/kg]	4.2	21.0	62.3	116.3	
Rate constant [ $\text{h}^{-1}$ ]	13.56	22.90	30.06	36.81	
Catalyst		NiW			
WHSV [ $\text{h}^{-1}$ ]	0.5	1.0	1.5	2.0	
$c_s$ [mg/kg]	3.8	14.8	31.8	74.8	
Rate constant [ $\text{h}^{-1}$ ]	4.66	8.10	11.13	13.31	

Again, the rate constants were increased with increasing WHSV, however, the reaction rate increase was not sufficient in relation to space velocity. When the velocity was more than  $1 \text{ h}^{-1}$ , the catalyst activity is not sufficient under this reaction temperature and hydrogen partial pressure.

The last dependency, the influence of hydrogen partial pressure was observed for NiW catalyst only. The reaction temperature of these experiments was set on 370 °C and WHSV was  $1 \text{ h}^{-1}$ .

Table III: Reaction rate constants at different hydrogen partial pressure

Catalyst		NiW		
$p$ [MPa]		3	4.5	6
$c_s$ ([g/kg]		52.9	16.7	8.2
Rate constant [ $\text{h}^{-1}$ ]		4.9	5.9	6.6

Higher hydrogen partial pressure had a positive influence on hydrodesulfurization activity.

### Comparison of deactivated catalysts

The activity of the fresh catalyst was compared with the activity of laboratory accelerated and industrially deactivated catalysts.

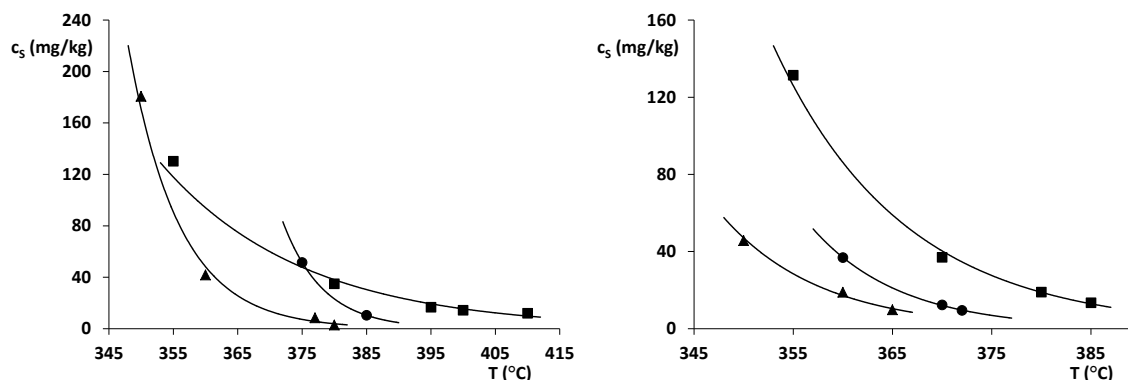


Figure 1: Comparison of activity of fresh (triangle), accelerated deactivated (circle) and industrially deactivated (square) catalysts. The left part is for NiW/Al<sub>2</sub>O<sub>3</sub>, the right for CoMo/Al<sub>2</sub>O<sub>3</sub>.

Table IV: Reaction rate constants

	Fresh catalyst		Accelerated deact.		Industrially deact.	
	CoMo	NiW	CoMo	NiW	CoMo	NiW
360 °C	8.68	5.01	7.73	3.36	6.56	4.38
370 °C	10.00	6.14	9.16	4.59	7.59	4.90
380 °C	11.29	7.24	10.54	5.78	8.58	5.34

NiW based catalyst is less active and more sensitive to deactivation. After the deactivation process the activity of this catalyst is less dependent on temperature. It is probably due to the different structure characteristic of NiW catalyst in comparison with CoMo catalyst. It caused formation of different and more stable carbon deposits.

The reaction rate decreases about 20.2 and 26.2 percent for accelerated, respectively industrially deactivated NiW catalyst, and about 6.6 and 24.0 percent for accelerated and industrially deactivated CoMo catalyst.

In the following table 5 the minimal reaction temperatures are mentioned at which the activity of the catalysts is adequate to sulphur content in product less than 10 mg/kg.

Table V: Reaction temperatures for 10 mg/kg

	NiW	CoMo
Fresh catalyst	371.3	364.9
Accelerated deact.	384.3	370.1
Industrially deact.	409.6	389.3

### Kinetics measurements

Mathematical modeling was accomplished by commercial Aspen Plus process simulator. Redlich-Kwong-Soave<sup>7</sup> equation of state was used for the description of non-ideal compounds behavior under high pressure. This method is recommended for hydrocarbon processes, including refinery and petrochemical applications and description of non-ideal system behavior.

Gas solubility in liquid is also taken into consideration and described by Henry's law. The reaction mixture evaporating was modelled on the basis of vapor-liquid equilibrium.

The rate equations are based on the power-law kinetics and the reaction rate constants were calculated by the first order reaction kinetics using Levenberg-Marquardt optimization method. The experimental data was applied as initial values. The activation energy was calculated by Arrhenius equation.

Because of hydrogenated gas oil composition complexity, a model mixture of hydrocarbons was defined using simulated distillation curve. The reaction pathway of sulphur removing depends on the type of sulphur compound. All alkylated benzothiophenes and dibenzothiophenes monoalkylated in position 4 were desulphurized without hydrocarbon ring saturating. In the case of dibenzothiophenes alkylated in position 4 and

6 saturation of hydrocarbon ring in first step, and after that sulphur atom was released as hydrogen sulfide. 3-methylthiophene is hydrogenated to 2-methylbutane.

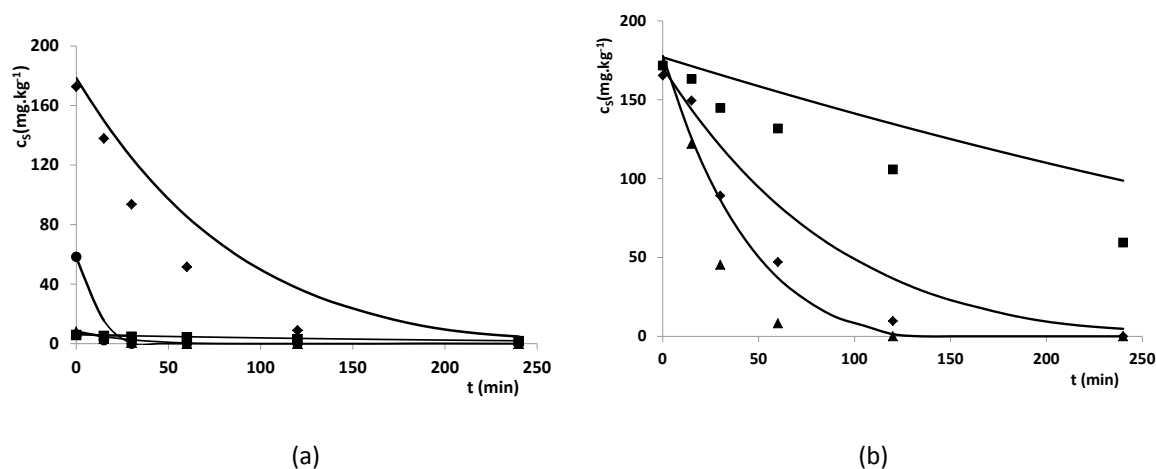


Figure 2: Sulphur concentration gradient in time on stream. (a) 350°C, 4.5 MPa, (b) 365°C, 4.5 MPa. Points – experimental data, line – data obtained by reaction model.

, The description of experimental data by mathematical model is not exactly identical in the case of presuming pseudo-first rate reaction kinetics (Figure 2). This deviation is more significant with the increasing compound concentration and increasing reaction rate.

The trend of increasing reaction rate with increasing temperature is described well, however not exactly, like the influence of hydrogen partial pressure. Including of hydrogen solubility in liquid is important for the precision of calculation. The modeling approach applied by Aspen Plus simulation, including hydrogen-liquid solubility, described experimental data much better in comparison with the model which do not employing this characteristic.

Table VI: Hydrodesulphurization rate constants of pseudo first reaction order; influence of temperature and hydrogen partial pressure. Data obtained from Aspen Plus process simulation

$p$ , [MPa]	4.5			3	6
	350	365	380	360	
$t$ , [°C]	$k$ , [ $m_L^6 / (kg_k kmol_{H_2} s)$ ]				
DBT	1.01E-04	1.61E-04	2.15E-04	3.17E-04	1.60E-04
4MDBT	3.06E-05	5.15E-05	5.73E-05	6.95E-05	5.02E-05
4,6-DMDBT	6.46E-06	6.79E-07	4.68E-06	2.96E-08	4.68E-06

Further, Matlab program was used to evaluate experimental data. The reaction rate constant and activation energy was determined for both pseudo-first reaction order and nth order. The catalyst amount, hydrogen pressure and volume difference was taken also into consideration.

$$-r.W = A.c_s - \frac{d(c_s V)}{dt} \quad (2)$$

and

$$r = k.P_{H_2}.c_s^n \quad (3)$$

where  $c$  is sulphur compound concentration,  $k$  reaction rate constant,  $W$  catalyst weight,  $P_{H_2}$  hydrogen pressure,  $n$  is reaction order with respect to sulphur compound and  $V$  actual liquid volume, which is defined as initial volume reduced by volume of samples taken from reaction mixture.

$$V = V_0 - A.t \quad (4)$$

By modifying equation (2) using equation (3) the term (5) is obtained

$$\frac{dc_s}{dt} = - \frac{k.c_s^n.W.P_{H_2}}{V} \quad (5)$$

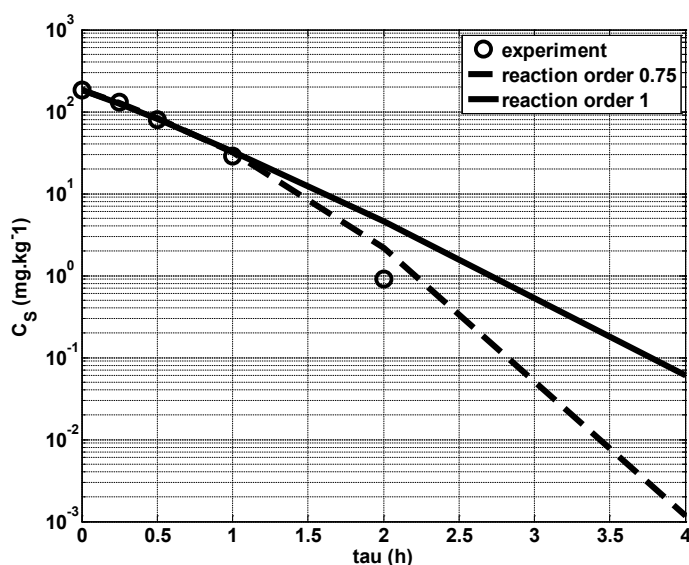


Figure 3: Description of experimental data using nonlinear regression in Matlab. 4-MDBT, 365°C, 6 MPa. Reaction order 0.75.

The real reaction order was different from order one (Figure 3). The reaction rate during the first hour of reaction corresponded with the first reaction order, after that the reaction rate increased and the reaction rate 0.75 was determined. In the concentration range important to technical ( $10^0$ - $10^4$  mg<sub>s</sub>/kg) the difference from first reaction order is negligible.

Together the expected trend is present, when the reaction rate constant increasing with increasing reaction temperature. One methyl substituent in position 4 caused inhibition of the reaction rate about three times in comparison with non-substituted DBT and one more substituent in 6 position inhibited the reaction rate almost ten times in comparison with monosubstituted DBT. Ethylene substituent in positions 4 and 6 slowed down the reaction rate by third.

Table VII: Hydrodesulphurization kinetic parameters of pseudo first reaction order; influence of reaction temperature evaluated by Matlab

p, [MPa]	4.5			E [kJ/mol]
	t, [°C]			
	350	365	380	
	k, [kg <sub>L</sub> /(kg <sub>k</sub> h.MPa)]			
DBT	26.00	34.07	44.09	84.7
4MDBT	8.22	12.03	17.31	83.9
4,6-DMDBT	0.84	1.41	2.32	113.3
4,6-DEDBT	0.55	0.88	1.38	151.3

The reaction order was evaluated by the equation (5) and the order of hydrodesulphurization was determined 0.75.

The activation energy showed good trend – increase with sulphur atom hindering and correspond with literature data<sup>8,9</sup>.

### Conclusion

The initial activity of CoMo/Al<sub>2</sub>O<sub>3</sub> and NiW/Al<sub>2</sub>O<sub>3</sub> hydrodesulfurization catalysts and influence of the reaction conditions on activity were investigated. These results were compared with the activity after the accelerated deactivation laboratory method and industrial deactivation. NiW catalyst is generally less active for hydrodesulfurization reactions, the activity decrease after the accelerated deactivation was 20.2 % and after the industrial deactivation 26.2%. The activity of CoMo catalyst decreased about 6.6% after the accelerated

deactivation and 24.0% after the industrial deactivation. The experimental data were used for prediction of the catalyst operation time.

The set of hydrodesulphurization experiments at three different temperatures and three different hydrogen partial pressures was performed. Experimental data were evaluated by nonlinear regression. Furthermore, two mathematical models were defined. The first one in Aspen Plus, using pseudo-first order reaction kinetic, including solubility of hydrogen in liquid. The second one in Matlab computing pseudo-first reaction order and reaction order 0.75. This model is describing research area more precisely. It is necessary to describe the influence of hydrogen partial pressure by gas-liquid solubility characteristics. The calculated activation energy corresponded with data in literature. Steric hindering effect of alkyl substituent on dibenzothiophene hydrodesulphurization was confirmed.

### **Acknowledgement**

*This publication is a result of the project no. FR-T13/084, supported by the Ministry of Industry and Trade of Czech Republic, which is being carried out in the UniCRE centre whose infrastructure was supported by the European Regional Development Fund and the state budget of the Czech Republic. Also financial support from specific university research (MSMT no. 20/2014) is acknowledged.*

### **Literature**

1. Depauw G.A., Froment G.F.: J. Chromatogr. A, 761, 231 (1997).
2. Shafi R., Hutchings G.J.: Catal. Today, 59, 423 (2000).
3. Stanislaus A., Marafi A., Rana M.S.: Catal. Today, 153, 1 (2010).
4. Ho T.C.: Catal. Today, 98, 3 (2004).
5. Choi K.-H., Sano Y., Korai Y., Mochida I.: Appl. Catal., B, 53, 275 (2004).
6. Lamure-Meille V., Schulz E., Lemaire M., Vrinat M.: Appl. Catal. A-Gen., 131, 143 (1995).
7. Soave G.: Chem. Eng Sci., 27, 1197 (1972).
8. Chen J., Yang H., Ring Z.: Catal. Today, 98, 227 (2004).
9. Varga Z., Hancsok J., Nagy G., Poelczmann G., Kallo D.: Top. Catal., 45, 203 (2007).

## NOVEL APPROACH FOR EVALUATION OF PRIMARY PRODUCT SELECTIVITY OF CO-PYROLYZED HYDROCARBONS BASED ON REGRESSION ANALYSIS

**Petrů J.**<sup>1,2</sup>, Zámstný P.<sup>1</sup>, Kolena J.<sup>2</sup>

<sup>1</sup>*Department of Organic Technology, Faculty of Chemical Technology, University of Chemistry and Technology Prague, Technická 5, 166 28 Prague 6, Czech Republic*

<sup>2</sup>*Research Institute of Inorganic Chemistry, a. s., Revoluční 1521/84, 400 01 Ústí nad Labem, Czech Republic  
jiri.petru@vscht.cz*

### Introduction

Production of short chain olefins by steam cracking is one of the most important processes in the petrochemical industry. Most often, very complex feedstocks are processed in steam cracking, such as naphtha or LPG, and even mixtures thereof. As the individual components in the feedstock interact, it is necessary to be focused not only on the pure components, but also on their mixtures, when studying steam cracking. The interaction between the components in the pyrolysed mixture has an impact on the change of conversion and selectivity.

Historically, the authors (e.g. <sup>1-4</sup>) were focused on the influence of co-pyrolysis on conversion of the present hydrocarbons in the feedstock. In these studies, the binary mixtures were tested, so that the change of conversion could be discussed from the point of view of inhibition or acceleration of the co-pyrolysed hydrocarbon decomposition. The most important fact is that, based on the pyrolysis of pure components, it is not possible to decide, if the particular component will behave as an accelerator or inhibitor, since the more reactive components must not necessarily accelerate the conversion of less reactive ones and vice versa. The acceleration or inhibition effect is given by the concentration and activity of radicals provided by the particular component in the mixture <sup>5,6</sup>.

Concurrently, the authors (e.g. <sup>7-10</sup>) were focused on the influence of co-pyrolysis on product selectivity of the present hydrocarbons in the mixture. However, the results of these authors differ. While Illes <sup>8</sup> claimed that neither conversion nor selectivity is influenced by co-pyrolysis, Murrata et al. <sup>9</sup> showed the conversion is influenced and the selectivity is changed only due to the change of conversion. Finally, Froment et al. <sup>10</sup> showed that both the selectivity and conversion is influenced by co-pyrolysis and he proposed the evaluation of selectivity based upon "global kinetics". Subsequently, authors express the change of selectivity due to interaction by using mathematical models. However, the problem of these models is that they include number of simplifications, which influence the reliability of their results. Moreover, the error of these models increases with the number of secondary reactions such as radical and molecular additions. These reactions are very significant in the thermal decomposition of unsaturated and short chain hydrocarbons, and thus the reliability of the models is the lowest for these hydrocarbons. At the same time it is obvious, these hydrocarbons will be influenced by co-pyrolysis the most.

Therefore, we intended to develop a general approach for evaluating the product selectivity of co-pyrolysed hydrocarbons, which would include the data from the pyrolysis of pure components and data from the co-pyrolysis of these components, without necessity to consider any simplifications. Moreover, in order to prevent the selectivity to be influenced by conversion we aimed at evaluating the primary selectivity, which is product selectivity close to zero conversion. At the same time, the evaluation of primary selectivity enables to compare particular hydrocarbons at the same conditions.

### Materials and Methods

In the present work, we used model mixture containing hexane and 1-butene for the development of the methodology. These hydrocarbons were selected intentionally as hexane represents a hydrocarbon which provides high concentration of active radicals to the system and 1-butene significantly supports addition reactions in the system. Hence, we assumed the selectivity of both hydrocarbons will be strongly influenced by co-pyrolysis.

#### *Mixture preparation*

The model mixtures were prepared in a gas sampling bag by hexane gasification in the presence of an inert gas at a laboratory temperature and subsequent addition of 1-butene to the sample bag. The mixture of butene and hexane were prepared in 3 concentrations containing approx. 25, 50 and 75 wt. % of 1-butene in hexane. The accurate concentration was determined by a gas chromatography (see below). The use of gas sampling bags enabled to keep the constant composition of the mixture through the experiments. Also it enabled to

keep constant partial pressure of the hydrocarbons in the mixture, which was necessary to prevent the change of the product selectivity, due to change of pressure. This was also controlled by analysis by gas chromatography.

#### *Experimental conditions*

The yields of pyrolysis products and the composition of the model mixtures were determined by the pyrolysis gas chromatography and ordinary gas chromatography respectively, which is described in detail in ref. <sup>11</sup>. At first, the composition of the tested mixtures was determined. Hereby, the temperature in the reactor was set to 400 °C. At this temperature, the sample is gasified for GC analysis, but pyrolysis reactions do not take place. The pyrolysis experiments were performed at 750 °C. Pressure in the reactor was 400 kPa. The residence time of the sample in the reactor was adjusted by the flow rate of the carrier gas, which was between 400 and 100 ml/min. At these conditions the conversions of the feedstocks were low, which enabled to evaluate the primary product selectivity.

#### *Single component primary product selectivity*

The evaluation of the selectivity was based on the method of Schneider and Frolich <sup>12</sup> and on the method of Starkbaumova et al. <sup>13</sup>. In the work of Schneider and Frolich, the molar selectivity on each product (moles of product formed per 100 moles of reactant decomposed) was plotted against the percent conversion. The primary selectivity was then obtained by extrapolation of the selectivities to zero. This method was further modified by Starbaumova et al., who showed the very low conversions were not suitable for the primary selectivity evaluation due to insufficient reliability of the measurement and on the other hand high conversions are not suitable as they are significantly influenced by secondary reactions. For this reason we kept the conversion between 5 and 40%.

We proposed the selectivity for single component can be calculated according to the equation:

$$S_i = \frac{w_i}{\zeta} \frac{M_r}{w_r} \frac{M_i}{M_i} \cdot 100 \% \quad (1)$$

where  $S_i$  is selectivity on  $i$ -th product,  $w_i$  is a mass fraction [wt. %] of the product in the outlet mixture,  $w_r$  is a concentration [wt. %] of a reactant in the feedstock (for single components equals 1),  $\zeta$  is the conversion of the reactant [%],  $M_r$  molecular weight of the reactant [ $\text{g}\cdot\text{mol}^{-1}$ ] and  $M_i$  molecular weight of the product [ $\text{g}\cdot\text{mol}^{-1}$ ].

Primary selectivity on a particular product  $S_i^0$  was then obtained as a selectivity limiting to zero conversion:

$$S_i^0 = \lim_{\zeta \rightarrow 0^+} \left( \frac{w_i}{\zeta} \frac{M_r}{w_r} \frac{M_i}{M_i} \cdot 100 \% \right) \quad (2)$$

which was performed by non-linear extrapolation.

#### *Binary mixture primary product selectivity*

The principle of the primary selectivity evaluation of binary mixtures was fundamentally the same as for the single component. However, it was necessary to determine, which part of the overall product yield was formed from each component in the mixture. This was based on the concept that if the co-pyrolyzed hydrocarbons do not interact, the overall product mass fraction can be expressed as a weighted sum of contributions at specified conversion of the present hydrocarbons in the mixture:

$$w_i = Y_{i,6} \zeta_6 w_6 + Y_{i,4} \zeta_4 (1 - w_6) \quad (3)$$

where  $Y_{i,6}$  and  $Y_{i,4}$  [wt. %] are the yields of the  $i$ -th product, which were obtained by pyrolysis of pure hexane and 1-butene respectively.  $\zeta_6$  and  $\zeta_4$  are the conversion of hexane and 1-butene respectively in the pyrolysis of binary mixture.  $w_6$  [wt. %] is the concentration of hexane in the feedstock.

However, if there is some interaction due to co-pyrolysis, the equation (3) must be expanded with increments  $\Delta Y_{i,6}$  and  $\Delta Y_{i,4}$  which characterize the influence of co-pyrolysis on hexane and 1-butene respectively:

$$w_i = (Y_{i,6} + \Delta Y_{i,6}) \zeta_6 w_6 + (Y_{i,4} + \Delta Y_{i,4}) \zeta_4 (1 - w_6) \quad (4)$$

These increments were obtained by regression analysis of experimental data, which was performed using ERA 3.0 software <sup>14</sup>. The increments were incorporated in p1 and p2 parameters, the values of which were obtained by regression analysis:

$$\Delta Y_{i,6} = (1 - w_6) p_1$$

$$\Delta Y_{i,4} = w_6 p_2$$

Finally, the contributions of hexane

$$w_{i,6} = (Y_{i,6} + \Delta Y_{i,6}) \zeta_6 w_6$$

and 1-butene

$$w_{i,4} = (Y_{i,4} + \Delta Y_{i,4}) \zeta_4 (1 - w_6)$$

were used in the equation (1) and the selectivity on a particular product from a particular component in the feedstock was determined. Further, the primary product selectivity from a particular component in the feedstock was determined by extrapolation of obtained selectivities to zero conversion.

## Results and Discussion

### Pyrolysis of pure components

At first it was necessary to find the product mass fraction in the outlet mixture obtained by pyrolysis of the pure components (table I).

Table I  
Main products of hexane and 1-butene pyrolysis

Product [wt. %]	Hexane Conversion [%]					1-Butene Conversion [%]				
	5.0	6.1	8.1	9.6	13.3	8.4	14.8	27.6	30.2	36.7
Methane	0.4	0.4	0.7	0.7	1.1	0.7	1.2	2.3	2.6	3.2
Ethylene	2.2	2.7	3.6	4.3	5.8	0.8	1.5	3.1	3.5	4.2
Propylene	1.2	1.4	1.9	2.3	3.1	1.9	3.6	7.0	7.9	9.7
Butadiene	0.0	0.0	0.0	0.0	0.1	2.5	4.3	7.6	8.4	9.4
$\Sigma$ C5	0.9	1.0	1.0	1.1	1.2	1.6	2.8	5.0	4.9	6.2

We found the yields of C5 hydrocarbons are significant even at low conversions of 1-butene. Mostly the C5 fraction contained unsaturated hydrocarbons, of which 2-pentene and 2-methyl-1-butene, which were formed by addition reaction, were the most significant. Hence, it is necessary to consider the addition products as the primary ones in the case of short olefins, such as butenes.

From the product mass fraction of the pure components pyrolysis it was possible to calculate their selectivities at particular conversion according to eq. 1 and by the extrapolation of the selectivities to zero conversion we obtained the primary selectivity (included in figure 2).

Subsequently, it was found the mass fraction depends linearly on the conversion at tested conditions. Hence, the yield of the product, which was obtained by pyrolysis of pure components ( $Y_{i,6}$  and  $Y_{i,4}$ ), was expressed by a linear function, which was used in the eq. 4 necessary for calculation the contribution of the reactants to the yield of the product in the pyrolysis of binary mixtures.

### Regression analysis

The data obtained from the pyrolysis of the pure components and binary mixtures were processed by regression analysis to estimate the values of parameters characterizing the co-pyrolysis effects (table II). The regression was performed over the whole data set; therefore, the obtained parameters are consistent within the whole scope of the study.

Table II  
Values of parameters and their confidence intervals obtained by regression analysis based on eq. 4

	$p_1$ effect on hexane	$p_{1,}$ confidence interval 95%	$p_2$ effect on butene	$p_{2,}$ confidence interval 95%
Methane	2.2	<0.0 ; 6.3>	2.5	<24.8 ; 38.5>
Ethylene	-22.4	<-12.8 ; -32.2>	31.5	<0.0 ; 5.0>
Propylene	14.3	<4.3 ; 24.2>	5.4	<-1.0 ; 12.2>
Butadiene	38.2	<26.6 ; 49.0>	-30.4	<-23.3 ; -36.3>
$\Sigma$ C5	-7.4	<-155.0 ; 0.0>	0.8	<0.0 ; 137.9>

The values of parameters in the table provide the information about the influence of co-pyrolysis on the product distribution of hexane and 1-butene. The larger being the deviation of the parameter from zero, the more significant is the effect of co-pyrolysis. Negative value of the parameter expresses the selectivity on a particular product is inhibited by co-pyrolysed hydrocarbon and, on the other hand, positive value expresses the selectivity on a particular product is supported.

The reliability of the obtained parameters can be assessed based on relatively narrow confidence intervals and by the comparison of the experimental data and data obtained from regression analysis, as the sum of contributions to the overall mass fraction of the particular product, which were obtained by regression analysis, must equal to that value found experimentally (Fig 1)

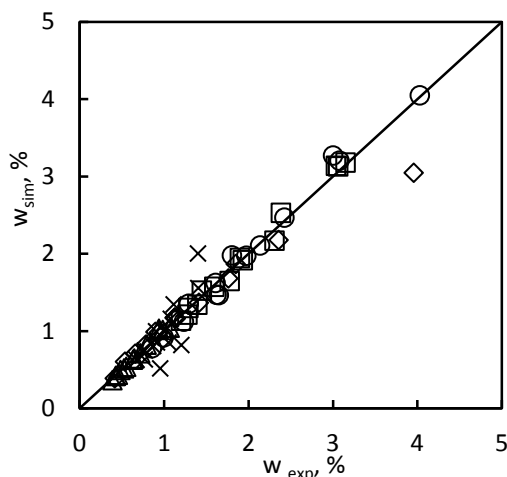


Figure 1. Mass fraction of  $\Delta$  methane,  $\circ$  ethylene,  $\square$  propylene,  $\diamond$  butadiene and  $\times$  C5 hydrocarbons found experimentally ( $w_{exp}$ ) and as a sum of contributions ( $w_{sim}$ ).

It is obvious the deviation of the experimental data and the calculated sum of contributions was minimal.

#### Primary product selectivity of binary mixtures

From the contributions of hexane and 1-butene to the overall mass fraction of the particular product, the selectivity could be calculated according to eq. 1 and by linear extrapolation to zero the primary selectivity could be obtained. Finally, for each product we obtained the dependence of its primary selectivity from 1-butene and from hexane on their ratio in the feed (Fig. 2).

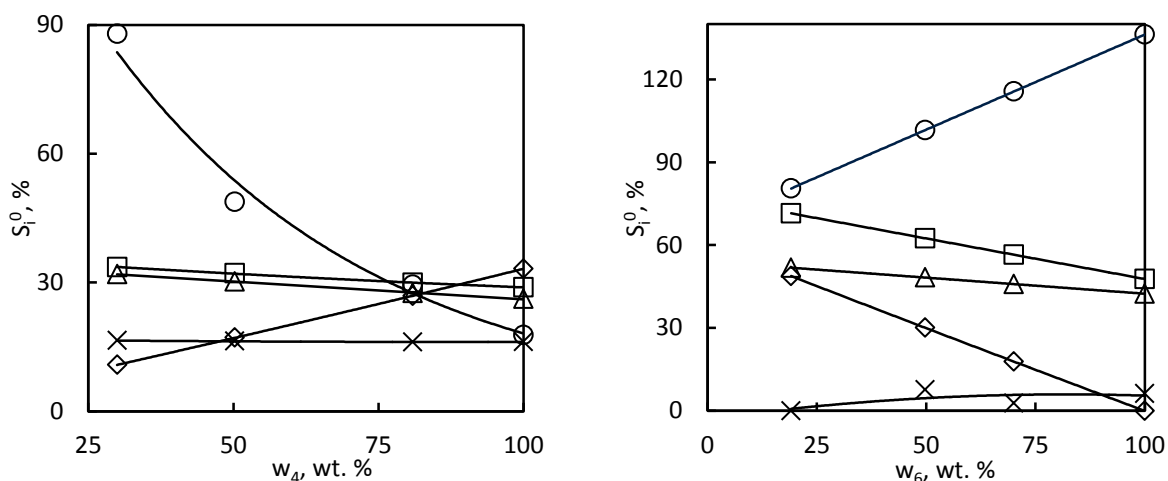


Figure 2. Primary selectivity of 1-butene (left) and hexane (right) on  $\Delta$  methane,  $\circ$  ethylene,  $\square$  propylene,  $\diamond$  butadiene and  $\times$  C5 hydrocarbons depending on the concentration of 1-butene ( $w_4$ ) and hexane ( $w_6$ ) in the feed.

From the table II and figure 2 is obvious that the particular product was not always formed from one of the co-pyrolysed hydrocarbons at the expense of the second one. This was the case of methane and propylene, where both parameters were positive and thus the selectivity on these products increased with decreasing content of 1-butene and hexane in the feedstock. On the other hand, selectivity on ethylene from 1-butene was supported by hexane, together with inhibiting the selectivity on ethylene from hexane due to 1-butene presence. Thus the primary selectivity on ethylene from 1-butene increased with decreasing content of 1-butene (Fig. 2 left) and at the same time selectivity on ethylene from hexane decreased with increasing content of 1-butene (Fig. 2 right). The trend of selectivity to 1,3-butadiene was just the opposite to that to ethylene.

The changes in the selectivities of the hydrocarbons in the feedstock are related to their behavior, when they are co-pyrolysed. For example hexane as donor of active radicals supports the scission of 1-butene, which results in the increase of the selectivity on ethylene from 1-butene. On the other hand, 1-butene captures the radicals, which discriminates the hexane scission. In addition to the decrease of the selectivity from hexane to ethylene, it means increasing manifestation of addition reactions, which is proved by increased selectivity on C5 hydrocarbons from 1-butene.

#### *Influence of co-pyrolysis on overall selectivity*

From the industrial perspective, it is not so important what is happening to the particular component in the feedstock, but how the overall selectivity is influenced by co-pyrolysis. This information was obtained from the sum of parameters for a particular product in table II and its deviation from zero. If the sum of parameters is positive, the particular product is formed in larger extent at co-pyrolysis than if the hydrocarbons were pyrolysed separately. The most influenced was the selectivity on propylene and on ethylene, which were both supported by co-pyrolysis. Also the selectivity on methane and butadiene was supported. On the other hand, selectivity on C5 was inhibited. To this corresponds also the graphical representation (Fig. 3), in which is the overall selectivity on the main products. Since it would not make much sense to express molar selectivity for a mixture, in this case we did not use primary molar selectivity discussed above, but the primary mass selectivity, which is basically the yield of the particular product (mass fraction related to conversion). The yield of the primary product was calculated equally as the primary selectivity discussed above with the difference that it was not expressed as moles of product formed per 100 moles of reactant decomposed. Then it was possible to calculate the overall primary yield, which was the weighted sum of the primary yields from hexane and from 1-butene. This overall primary yield is shown in figure 3.

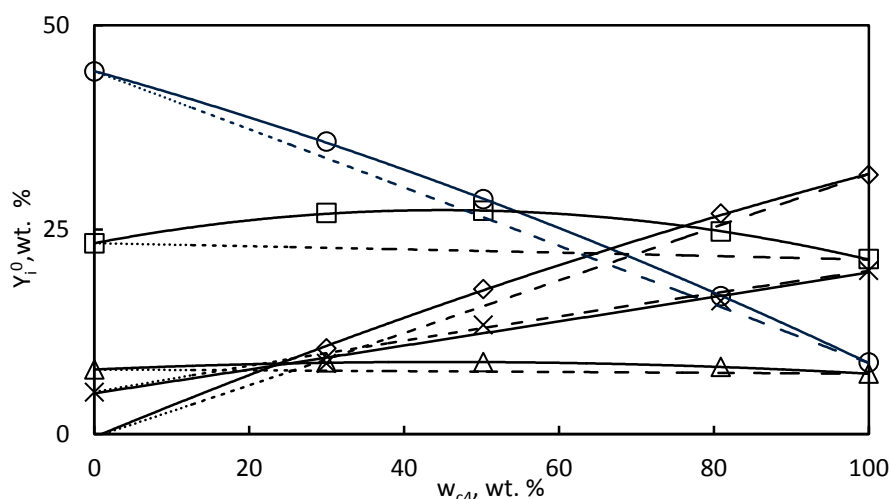


Figure 3. Dependence of primary yield of  $\Delta$  methane,  $\circ$  ethylene,  $\square$  propylene,  $\diamond$  butadiene and  $\times$  C5 hydrocarbons on the concentration of 1-butene in the feed in co-pyrolysis (solid line) and pyrolysis of reactants separately (dashed line).

The advantage of the graphical representation (Fig 3) is that it expresses the primary yield at different ratios of components in the feedstock. Hence it possible to find what will be the primary yield of a particular product at given composition of the feedstock and how significantly will it be influenced by co-pyrolysis at this composition. However, the most important was the fact that the yield of all important products in the co-pyrolysis of hexane and 1-butene was higher, than corresponding overall yields obtained, if hexane and 1-butene were pyrolysed separately. On the contrary, the yield of C5 hydrocarbons, which are undesirable, was lower. By this it was proved the great advantage of co-pyrolysis of these components in the industry.

#### **Conclusions**

In this paper we have shown an approach for evaluation of a selectivity, which was based on regression analysis. Based on this evaluation we were able to show the co-pyrolysis significantly influenced the selectivity of the components in the feedstock and also we were able to express the magnitude of this influence. Thanks to this approach, it is possible for example to decide if a particular hydrocarbon would rather be cracked or whether it rather participates in addition reactions in the presence of co-pyrolysed hydrocarbon and the

quantitative difference between these two processes may be estimated. Moreover, it was shown the selectivity is influenced by co-pyrolysis regardless of the conversion as the primary selectivity was evaluated. Hence, we propose this approach as a valuable tool for comparison of hydrocarbons in terms of the effect of co-pyrolysis.

#### **Acknowledgement**

Financial support from specific university research (MSMT No 20/2015).

#### **References**

1. Echols L. S., Pease R. N.: *J. Am. Chem. Soc.* **61**, 1024-1027 (1939).
2. Scott E. J. Y.: *Ind. Eng. Chem. Prod. Res. Dev.* **6**, 72-76 (1967).
3. Billaud F., Baronnet F., Niclaude M.: *Can. J. Chem.* **63**, 2869-2884 (1985).
4. Shevel'kova L., Gusel'nikov L., Bach G., Tsimmermann G.: *Usp. Khim.* **61**, 792-814 (1992).
5. Shevel'kova L. V., Vedeneeva L. M., Gusel'nikov L. E., Bach G., Zychlinski W., Zimmermann G.: *J. Anal. Appl. Pyrolysis* **17**, 201-215 (1990).
6. Petru J., Zamostny P., Kolena J., in *2st International Conference on Chemical Technology*, P37 (2014).
7. Illes V.: *Acta Chim. (Budapest)* **72**, 117-131 (1972).
8. Illes V.: *Acta Chim. (Budapest)* **72**, 133-146 (1972).
9. Murata M., Takeda N., Saito S.: *J. Chem. Eng. Jpn.* **7**, 286-294 (1974).
10. Froment G. F., Van De Steene B. O., Vanden Berghe P. J., Goossens A. G.: *AIChE Journal* **23**, 93-106 (1977).
11. Belohlav Z., Herink T., Lederer J., Marek J., Rachova N., Svoboda P., Zamostny P., Vojtova D.: *Pet. Chem.* **45**, 118-125 (2005).
12. Schneider V., Fronlich P. K.: *Ind. Eng. Chem.* **23**, 1405-1410 (1931).
13. Starkbaumová L., Bělohav Z., Katreniaková S., Zámstný P., in *CHISA 2006 - 17th International Congress of Chemical and Process Engineering*, P7.80 (2006).
14. Zamostny P., Belohlav Z.: *Comput. Chem. (Oxford, U. K.)* **23**, 479-485 (1999).

## PRINS CYCLIZATION OF ISOVALERALDEHYDE AND ISOPRENOL

**Vyskočilová E.**, Krátká M., Červený L.

University of Chemistry and Technology, Prague, Technická 5, 166 28, Prague, Czech Republic  
eliska.vyskocilova@vscht.cz

Prins cyclization, or condensation, is a reaction between aldehyde and unsaturated alcohol<sup>1,2</sup>. In a first step (Figure 1) hemiacetal **III** is formed that is dehydrated to carboxonium ion **IV**. This ion is stabilized by cyclization forming carbocation **V**, which reacts with nucleophile in the reaction media producing substituted tetrahydropyranol **VI** or dihydropyrans **VII**. One of important substituted tetrahydropyranol, which is prepared from isovaleraldehyde **I** and isoprenol **II**, is 2-isobutyl-4-methyl-tetrahydro-2H-pyran-4-ol, commercially called Florosa or Florol.

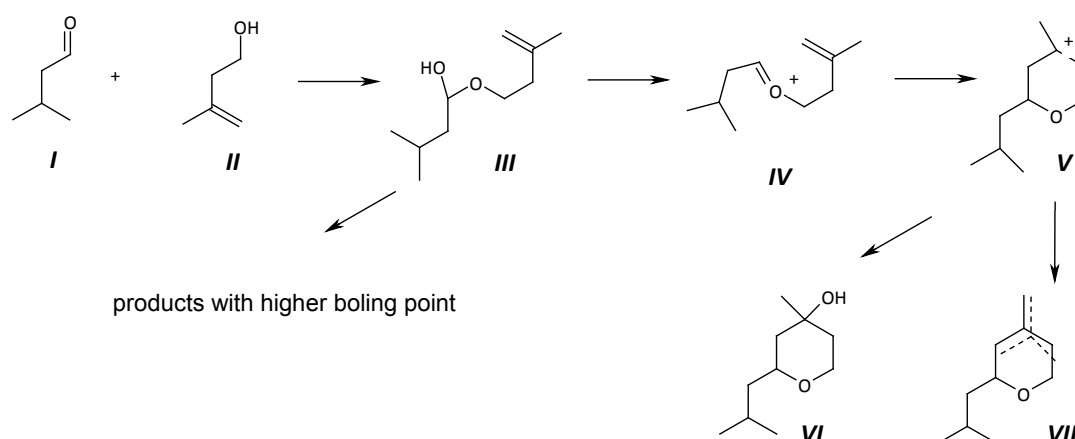


Figure 1: Mechanism of Florosa preparation (**I** – isovaleraldehyde, **II** – isoprenol, **III** – hemiacetal, **IV** – carboxonium ion, **V** – carbocation, **VI** – 2-isobutyl-4-methyl-tetrahydro-2H-pyran-4-ol, **VII** – 2-isobutyl-4-methyl-dihydropyrans)

This compound is used in a fragrance industry as an imitation of lily-of-the-valley scent and possible replacement of Lily aldehyde. The Prins cyclization is always acid catalyzed<sup>3</sup> and as a catalysts, Lewis<sup>4-7</sup> or Brønsted acids (inorganic<sup>1,8</sup>, organic<sup>9</sup>, ion exchangers<sup>10,11</sup>, may be used. In some cases heteropolyacids<sup>12</sup>, organometallic complexes<sup>13</sup> or heterogeneous aluminosilicates<sup>14</sup> are also used.

In this work we would like to show the comparison of Brønsted acids containing sulfo group (sulfuric, p-toluene sulfonic, p-dodecylbenzene sulfonic acid, Amberlyst 15), Lewis acids ( $\text{AlCl}_3$ ,  $\text{FeCl}_3$ ,  $\text{ZnCl}_2$ ,  $\text{FeCl}_3 \cdot 6\text{H}_2\text{O}$ ) and heteropolyacids (phosphotungstic and phosphomolybdic acid) in the preparation of Florosa.

In our previous work<sup>15</sup>, we already described the comparison of Brønsted acids containing sulfo group (sulfuric, p-toluene sulfonic, p-dodecylbenzene sulfonic acid, Amberlyst 15) in the studied reaction, together with the influence of water on the reaction rate and selectivity. The organic acid without addition of water were not a suitable catalysts and the best results were obtained using Amberlyst 15 and sulfuric acid – selectivity 68 % and ratio Florosa/dihydropyrans 3.5 (in the case of sulfuric acid). Water had a significant influence on the rate and selectivity especially in the case of organic acids. After optimization of the amount of water in the reaction, mechanism with the catalyst particle was designed (Figure 2) and was published elsewhere<sup>15</sup>.

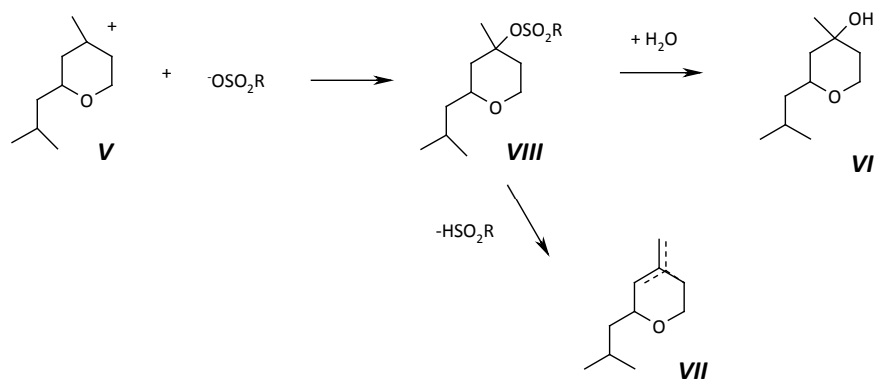


Figure 2: Possible inclusion of catalyst into the reaction<sup>15</sup>; R = -OH, -C<sub>6</sub>H<sub>5</sub>, -C<sub>18</sub>H<sub>29</sub>, copolymer styrene divinylbenzene (**V**- carbocation, **VI** - 2-isobutyl-4-methyl-tetrahydro-2H-pyran-4-ol, **VII** – 2-isobutyl-4-methyl-dihydropyranes, **VIII** – intermediate formed from carbocation and catalyst)

The optimization of reaction conditions using factorial design in the form central composite experiments was performed<sup>16</sup> using sulfuric acid and Amberlyst 15. After optimization the selectivity to Florosa was 96 % (florosa:dihydropyranes ratio 20) when using sulfuric acid as a catalyst (2.5 % concentration in water, 4 °C, ratio of the reactants 1:1) and 74 % when using Amberlyst 15 as a catalyst (10 mol.% of water, 30 °C ratio of the reactants 1:1).

Next teste catalysts were the Lewis acids, namely AlCl<sub>3</sub>, FeCl<sub>3</sub> and ZnCl<sub>2</sub>. These catalysts are known to be simply deactivated by water in the reaction mixture. The deactivation was visible especially in the case of aluminum chloride; in the reaction mixture high amount of unreacted hemiacetal was present. On the other side the amount of undesired dihydropyranes was significantly lower compared to the Broensted acids. This may be explained by the more simple hydrolysis of chlorinated intermediate (Figure 3) by water in the reaction mixture and more complicated evolution of hydrogen chloride from this intermediate.

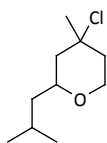


Figure 3: Chlorinated intermediate present (and detected) in the reaction mixture in the case when using Lewis acids as catalysts

The deactivation of the catalysts FeCl<sub>3</sub> and ZnCl<sub>2</sub> was not obvious from the measurement. This may be caused by the direct decomposition to hydrochloric acid that, under specific conditions, can also catalyze the Prins cyclization. The results of the Prins cyclization of isoprenol and isovaleraldehyde when using Lewis acids as catalysts are present in the Table I.

Table I

Results of the Prins cyclization of isoprenol and isovaleraldehyde using Lewis acids (3 h, molar ratio of the reactants 1:1, temperature 70 °C, amount of the catalyst 5wt.%)

Catalyst	Selectivity [%]	Florosa/ dihydropyranes [-]	Conversion (aldehyde) [%]	Concentration of hemiacetal [%]	Concentration of chlorinated product [%]
AlCl <sub>3</sub>	60	1.8	82	53	9.8
ZnCl <sub>2</sub>	61	5.7	79	40	9.3
FeCl <sub>3</sub>	67	7.1	91	18	14.3
FeCl <sub>3</sub> (40 °C, 24 h)	53	6.2	88	16.2	14.9
FeCl <sub>3</sub> + water (5 mol.%)	68	7.2	83	6.5	12.6
FeCl <sub>3</sub> * 6H <sub>2</sub> O	70	8.8	78	3.9	8.5

From the table I the deactivation of aluminum chloride is visible. Lot of hemiacetal was also present in the reaction mixture when using zinc chloride, but this was caused by the low activity of this catalyst because the reaction was terminated after 3 h and from the course it was obvious that the formation of substituted tetrahydropyranol and dihydropyrans still took place. The influence of reaction temperature was tested using ferric chloride and the reaction at 40 °C was performed, because lower temperature had a positive influence when using Broensted acids. When using ferric chloride at lower temperature the significant decrease of reaction rate (as it was expected) was observed. Due to the longer reaction time the dehydration of Florosa to undesired dihydropyrans was observed resulting in lower selectivity. With ferric chloride the highest amount of chlorinated product was obtained compared to the other Lewis acids. Due to the fact that this catalyst was not totally deactivated by water formed in the reaction mixture the addition of 5 mol.% of water was tested. The slight decrease of the conversion and the concentration of chlorinated product were observed under these conditions, but also decrease of the concentration of hemiacetal.

The best results (highest selectivity 70 %, highest ratio Florosa/dihydropyrans 8.8, lowest hemiacetal and chlorinated product concentration) were obtained surprisingly when using hexahydrate of ferric chloride. The explanation of this fact could be the decomposition of this catalyst under reaction conditions to hydrochloric acid and ferric oxides that did not neutralize the acid necessary for the cyclization. When using anhydrous ferric chloride, the decomposition of this catalyst to hydrochloric acid and ferric hydroxides was supposed. Formed hydroxides neutralized the acid and the reaction was stopped.

Other catalysts used for Prins cyclization are the heteropoly acids, namely phosphotungstic (HPW) acid and phosphomolybdic (HPMo) acid. The conditions offered in the literature describe the amount of catalyst in the reaction mixture 20 mol.% e.g. calculated on our conditions 0.5 g of catalyst on 0.2 g of organic phase (both substrates) and 2.5 ml of water. So large amount of catalyst was unacceptable for us and the optimization of reaction conditions leading to the significant decrease of catalyst amount was performed.

Reaction condition optimization is described elsewhere<sup>17</sup>, but the highest selectivity 93 % and ratio Florosa/dihydropyrans 16.5 was obtained using HPW as a catalyst. Moreover the heteropoly acids are often used supported on solid materials and may be possibly reused.

Table II offers the comparison of the catalyst tested for the Prins cyclization of isovaleraldehyde and isoprenol for the formation of 2-isobutyl-4-methyl-tetrahydro-2H-pyran-4-ol. In this table the most promising catalysts are depicted.

Table II

Comparison of the catalyst tested for the Prins cyclization; molar ratio of the isoprenol:isovaleraldehyde 1:1

Catalyst	Selectivity [%]	Florosa/dihydropyran [-]	Conversion (aldehyde) [%]	Catalyst amount [%]	Temperature [°C]	Amount of water added [mol.%]
Sulfuric acid (2.5 %)	96	22	75	8 mol.	4	50
Amberlyst 15	76	3	79	5 wt.	30	10
FeCl <sub>3</sub> *6H <sub>2</sub> O	70	9	78	5 wt.	70	0
HPW	93	16	96	0.8 mol.	80	30
HPMo	90	12	83	1.7 mol.	80	300

The highest selectivity was obtained using sulfuric acid and using this catalyst the experiment in larger scale was performed. The results were confirmed and after distillation Florosa of the 95.6 % purity was obtained. The problematic step in the purification was the separation of dihydropyrans from desired compound. Due to the availability and the price of this catalyst its use in the industry is now the more probable. The Amberlyst 15, even though that the lowest ratio Florosa/dihydropyrans was obtained, could be used because this heterogeneous catalyst may be repeatedly used without any treatment. Lewis acids were the worse catalysts for the Florosa preparation. Heteropoly acids are also promising catalysts for the preparation of desired compound, because the selectivity values obtained when using these catalysts were comparable with selectivity obtained when using sulfuric acid. The next step in our work will be the heterogenization of these catalysts and the use of their heterogenized forms in the studied Prins cyclization. The preliminary experiments are very promising.

## Literature

1. William P. H., Ballard S. A.: US 2 422 648, 1947.
2. Olier C., Kaafarani M., Gastaldi S., Bertrand M.P.: *Tetrahedron* **66**, 413 (2010).
3. Breugst M., Grée R., Houk K.N.: *J. Org. Chem.* **78**, 9892 (2013).
4. Chio F. K., Warne J., Gough D., Penny M., Green S., Coles S. J., Hursthouse M. B., Jones P.: *Tetrahedron* **67**, 5107 (2011).
5. Borkar P., Weghe P., Reddy B. V. S., Yadav J. S., Grée R.: *Chem. Commun.* **48**, 9316 (2012).
6. Yheng K., Liu X., Qin S., Xie M., Lin L., Hu Ch., Feng X.: *J. Am. Chem. Soc.* **134**, 17564 (2012).
7. Reddy K.R.K.K., Rosa I.M.L., Doriguetto A.C., Bastos E.L., Silva L.F. Jr.: *Molecules* **18**, 11100 (2013).
8. Yadav J. S., Reddy B. V. S., Reddy M. S., Niranjan N.: *J. Mol. Catal. A* **210** (1-2), 99 (2004).
9. Umeda A., Ataka Y., Tanaka S., Naito K., Mine K.: EP 149 3737 (2005).
10. More G. P., Rane M., Bhat S. V.: *Green Chem. Lett. Rev.* **5**, 13 (2012).
11. Gralla G., Beck K., Klos M., Griesbach U.: US 20110306779 (2011).
12. Li G., Gu Y., Ding Y., Yong Z., Hanpeng W., Jianming G., Qiang Y., Liang S. J.: *J. Mol. Catal. A* **218** (2), 147 (2004).
13. Tadpetch K., Rychnovsky S.: *Org. Lett.* **10**, 4839 (2008).
14. Telalović S., Ramanathan A., Fei Ng J., Maheswari R., Kwakernaak C., Soulimani F., Brouwer H.C., Chuah G.K., Weckhuzsen B.M., Hanefeld U.: *Chem. Eur. J.* **17**, 2077 (2011).
15. Vyskočilová E., Vrbková E., Paterová I., Červený L.: *Res. Chem. Intermed.*, In print DOI: 10.1007/s11164-015-2052-z
16. Vyskočilová E., Rezková L., Bělohav Z., Červený L.: prepared for publication (*React. Kinet. Mech. Catal.*)
17. Vyskočilová E., Krátká M., Červený L.: prepared for publication (*Appl. Catal. B*).

## MODIFICATION OF CARBON MATERIALS BY INORGANIC ACIDS

**Antoš P.**, Horová D., Čmelík J., Ryšánek P., Pospíšilová M.

*Výzkumný ústav anorganické chemie a. s., Revoluční 84, 400 01, Ústí nad Labem  
petr.antos@vuanch.cz*

### Abstract

Partial oxidation of hydrocarbons produced carbon black, which was depending on the used raw material contaminated with heavy metals. Cleaning of carbon black could be carried out with inorganic acids, which largely removes iron, nickel and vanadium. Acid treatment led to changes in surface characteristics of carbon black including the specific electrical conductivity.

### Introduction

The most important property of carbon black was the size of the primary particles and surface area. The particle size of carbon black was in the range 2-20 nm, the surface area of a particle from 800 to 1300 m<sup>2</sup>/g. An important characteristic was also the surface chemistry of carbon black. On the surface of carbon black were presented chemisorbed complexes containing oxygen, such as carboxylic, quinone or phenolic groups. Functional groups could significantly affect e.g. chemical reactivity, wettability, catalytic properties, electrical conductivity etc. The concentration, chemical origin and the physical distribution of surface groups depend on the nature of the raw materials, preparation method of carbon black and could be fundamentally modified by the type of surface treatment. Certain functional groups had acid-base character (carboxyl groups are weakly acidic, phenolic groups are very weak basis), some have redox properties (e.g. pair quinone-phenol) and others are neutral or non-reactive under normal conditions of pH (ketones, esters) - figure 1.

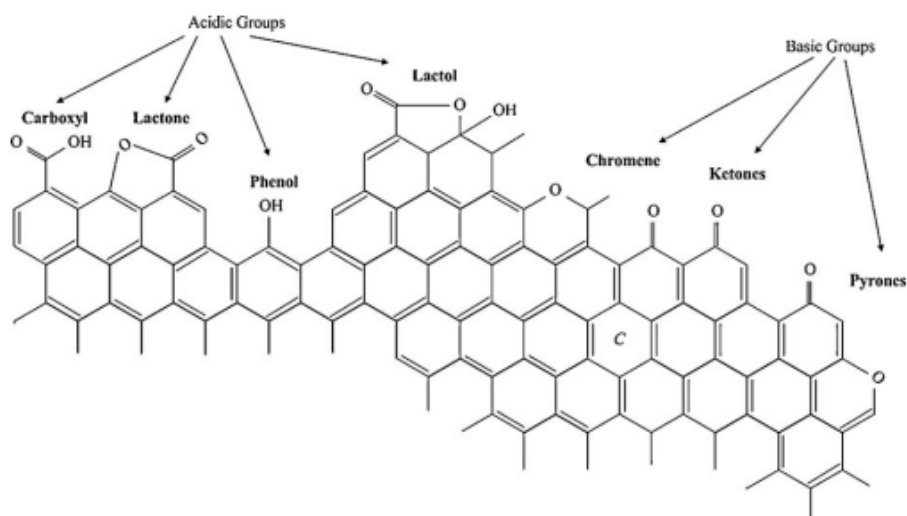


**Figure 1. Acidic and basic surface functional groups of carbon blacks<sup>8</sup>**

Carbon black contained certain amount of metals originating from raw material or from material of production equipment. For special applications of carbon black, such as adsorbents or catalysts was required minimum content of the metals. The presence of metal oxides, whether on the surface or in the internal structure of carbon black affected their basic characteristics. Reduction of metal content expanded the use of carbon black and had a positive effect on its market value. Reducing the content of metals in carbonaceous materials were often published in connection with an increase of market value of recycled materials e.g. carbon used as a filler in tires.

Removal of metals from carbonaceous materials could be achieved in various ways. The most of published processes for metal removing from carbon black was carried out in liquid phase. Used agents were chlorine gas in aqueous solution<sup>1</sup>, organic acid in the aqueous suspension<sup>2</sup>, inorganic acids<sup>3</sup>. In literature sources were also published dry methods of demetallization: under vacuum and heating to 900-3 500 °C with application of chlorine and inert gas flushing<sup>4</sup>. Extraction and separation of nickel and vanadium from fly ash was published by Al Ghouti<sup>5</sup>. In the first phase was removed nickel using NH<sub>4</sub>OH solution and precipitation in the form of

nickel sulfide NiS, in a second phase was from the fly ash without nickel extracted vanadium, using Na<sub>2</sub>CO<sub>3</sub> solution. Vanadium was extracted selectively from the other metal carbonates using triethylamine, again extracted with Na<sub>2</sub>CO<sub>3</sub> and finally precipitated in the form of NH<sub>4</sub>VO<sub>3</sub> using NH<sub>4</sub>Cl.

Demetallization of carbon black was tested using so called wet way, with the use of aqueous solutions of inorganic acids - HNO<sub>3</sub>, H<sub>2</sub>SO<sub>4</sub> and HCl.

## **Experimental**

### **Demetallization**

Demetallization tests were performed with sulfuric acid, hydrochloric acid and nitric acid. The untreated carbon black contained 0.16 wt. % Fe, 0.18 wt. % Ni and 0.37 wt. % V. The content of Fe, Ni and V in acids prior demetallization was in all cases below 1 mg / l, with the exception of the content of 1.7 mg / l Fe in 96% H<sub>2</sub>SO<sub>4</sub>. Demetallization procedure was as follows: Carbon black was mixed with an acid solution of a selected concentration in a weight ratio of carbon black:acid = 1:60. The resulting suspension was stirred on an overhead shaker. After the time of demetallization was added 250 ml of white spirit for separating the carbon black and the resulting suspension was filtered through a fritted funnel. Washing was performed with distilled water. The carbon black was dried in an oven at 80 °C for 8 hours and then dried at 105 °C.

Effect of carbon black treatment with mineral acids on its physical and chemical properties was investigated by determining the distribution of the proton affinity, FTIR and Raman spectroscopy, XRF, XRD, ICP-OES, and measuring the conductivity of the composite carbon black - polyethylene.

### **Distribution of the proton affinity (pK<sub>a</sub> spectra)**

Direct chemical method for the identification of surface functional groups of carbon black was based on acid-base behavior of carbon black in aqueous electrolyte solutions. Distribution of proton affinity of carbon materials (so. pK<sub>a</sub> spectra) was determined by measuring the pH of the carbon black suspension, after the addition of controlled quantities of strong acids or bases by potentiometric titration. The result of the measurement was PBI - proton binding isotherm that showed amount of a proton (H<sup>+</sup>) released or bounded by functional groups in equilibrium with a certain amount of carbon black, depending on the pH of the suspension. From a mathematical perspective, the PBI was an average property of reactive functional groups on the carbon black surface and was composed of the contributions of each individual group. The basic premise was that each group was characterized by a distinct dissociation constant. Surface groups that bounded or released protons at various pH values in accordance with their reactivity expressed by pK<sub>a</sub>. Major surface functional groups of carbon black were carboxyl (pK<sub>a</sub> 3-6), lactone (pK<sub>a</sub> 7-9) and phenolic (pK<sub>a</sub> 8-11).

Potentiometric titration was performed at a constant room temperature (ca. 25 °C) in the electrolyte solution (0.1 M NaNO<sub>3</sub>) with weighing 0.5 g<sup>7</sup> of carbon black. After equilibration, a solution of 0.1 M HNO<sub>3</sub> or 0.1 M NaOH was added to achieve pH 3.5 or 10.5. After equilibration (6 hours) was performed titration with acid or alkali. Throughout the titration reaction vessel was flushed with argon. The pK<sub>a</sub> values were determined from the course of the first and second derivative of PBI curves depending on pH (pK<sub>a</sub>).

### **FTIR spectroscopy**

Infrared Spectroscopy with Fourier transformation was difficult to apply for carbon materials, primarily due to significant infrared absorption of carbon. Infrared spectra were measured by Nicolet 380 FTIR spectrometer using a transmission technique with parameters of the device as follows: 64 scans and a resolution of 4 cm<sup>-1</sup>. Samples were measured in mixed KBr tablets, due to the high absorption of IR radiation by carbon black, optimal weight ratio for tablets was carbon black:KBr= 1:10 000. The total amount of material for one tablet was 100 mg.

### **Raman spectroscopy**

Raman spectroscopy gave a good picture of the presence of different modifications of carbon. The conductive form of carbon - graphite was characterized by the so-called. G band at 1582 cm<sup>-1</sup> (sp<sup>2</sup> hybridization), non-conductive form of carbon - diamond had a strong band at 1332 cm<sup>-1</sup> corresponding to sp<sup>3</sup> hybridization. Measurements were performed on a spectrometer DXR Raman Microscope. Individual measurements were performed by 1000 scans with an exposure time 2 s at a wavelength of laser source 633 nm.

### **X – ray diffraction and X – ray fluorescence analysis**

Diffraction phase analysis was performed on the X-ray diffractometer Philips MPD 1880 (crystal monochromator) under standard conditions. Diffraction data were analyzed using the programs X'Pert (X'Pert HighScore Plus software version 2.1b X'Pert Industry Software version 1.1 g).

X-ray spectral analysis was performed on the X-ray spectrometer Philips PW 1404 (wavelength dispersive device). Due to the high requirements on measurement accuracy (the contents of iron, vanadium and nickel), measurement was carried out using external standard.

#### Emission spectrometry with inductively coupled plasma (ICP-OES)

Determination of the metal content of carbon black was carried out after the decomposition of carbon black in concentrated sulfuric acid. The residue after the decomposition of H<sub>2</sub>SO<sub>4</sub> was extracted with hot hydrochloric acid and after dilution analyzed on a Perkin-Elmer device using optical emission spectrometry with inductively coupled plasma.

#### Electrical conductivity

Electrical conductivity was measured using a Brabender instrument in polyethylene with a weight concentration of carbon black 10%.

#### Results and discussion

Demetallization tests of carbon black with inorganic acids had shown that the use of HCl and HNO<sub>3</sub> could reduce the concentration of metals in the carbon black to the values for Fe 0.014 wt. %, Ni <0.008 wt.% and V <0.006 wt. %. Demetallization efficiency under different conditions was given in Table I.

Concentrations of the metals Fe, Ni, V, in the used acid after demetallization were in tens mg/kg, in the first washing water in singles of mg/kg. V and Ni concentrations in the washing water after the second and third wash received ICP detection limits (<0.0001 wt. % Ni, <0.0001 wt. % V).

**Table I**  
Efficiency (%) of demetallization using inorganic acids

	H <sub>2</sub> SO <sub>4</sub>			20% HCl			20% HNO <sub>3</sub>		40% HNO <sub>3</sub>	
	20% 5h	40% 5h	60% 5h	20°C 20 min	50°C 20 min	20°C 5 h	20 min	5 h	20 min	5 h
Iron	71.88	87.50	92.50	90.00	88.75	89.23	96.63	97.75	97.06	97.38
Nickel	51.67	71.67	97.22	85.56	91.67	87.78	98.83	98.72	98.50	98.67
Vanadium	85.41	91.89	98.11	95.14	97.03	98.35	99.05	98.78	99.16	99.24

An important factor of demetallization of carbon black was modification of their surface properties. Change of the properties of the dried carbon black after demetallization was assessed by measuring the electrical conductivity, the X-ray diffraction analysis, distribution of the proton affinity and infrared and Raman spectroscopy.

#### Electrical conductivity

Demetallization of carbon black by inorganic acids converted electrical conductivity of carbon black - see Table II. The product specification for the carbon black desired electrical value of the specific conductivity of at least 0.006 S.cm<sup>-1</sup>. Using hydrochloric acid reduced conductivity to about half compared to the original sample, but the conductivity was not below the threshold guaranteed by the manufacturer. When using HNO<sub>3</sub> conductivity of carbon black was significantly reduced and measured value was outside the range of the device. Carbon black treated by sulfuric acid had not been possible to test by this method because of non-standart behavior of carbon black during measurement.

**Table II**  
Electrical conductivity of carbon black

Sample	electrical conductivity (S.cm <sup>-1</sup> )
Carbon black - original	0.074
Carbon black - HCl	0.032
Carbon black - H <sub>2</sub> SO <sub>4</sub>	not measured
Carbon black - HNO <sub>3</sub>	<<0.006

#### X – ray diffraction analysis

From the nature of the diffraction diagrams it was evident that samples of carbon black modified by mineral acids were predominantly amorphous. Only one diffraction peak, corresponding to diffraction peak of carbon,

could be observed. Borah Dipu<sup>6</sup> described two broad peaks at an angle  $2\theta = 20 \sim 24^\circ$  and  $44^\circ$ . In the diffractogram of the untreated carbon black occurred only the first peak at  $24^\circ$  which moved due to the modification by mineral acids to lower angles ( $20^\circ$ ), at an angle of  $10^\circ$  appeared bland maximum that after the modification almost disappeared. Lattice constant  $L_c$  could be calculated according to Scherrer's equation  $L_c = K\lambda/\beta\cos\theta$ .  $K$  was a Scherrer constant (0.89),  $\lambda$  was the wavelength,  $\beta$  was the half width of the diffraction maximum, and  $\theta$  was the diffraction angle. The results were shown in Table III. It should be noted that the diffraction peak was very broad and its expansion was measured in software interleaving maximum, so that the values could not be sufficiently accurate. The values were significantly higher than that reported by Borah<sup>6</sup>.

**Table III**  
**Cristallite size**

Sample	$L_c$ (nm)	$L_c$ (nm) <sup>6</sup>
Carbon black - original	8.6	1.16
Carbon black - HCl	25.9	-
Carbon black - H <sub>2</sub> SO <sub>4</sub>	17.2	0.95
Carbon black - HNO <sub>3</sub>	6.0	1.49

### Infrared spectroscopy

In the IR spectra appeared bands of carbon dioxide (doublet at  $2300\text{-}2400\text{ cm}^{-1}$ ) which got into KBr tablets during their preparation, and molecular water (region  $1400\text{-}1700$  and  $3500\text{-}3800\text{ cm}^{-1}$ ), which was sorbed either on the surface of carbon black or to inner spaces.

IR spectra of the untreated carbon black were almost not different from the spectra of carbon black treated with acids, see Table IV. In area (A),  $3700\text{-}3600\text{ cm}^{-1}$  appeared broad band of molecular water, which was in the untreated carbon black represented by two wide featureless maxima. In all specimens appeared doublet with lower intensity (B) at wave numbers  $2925$  and  $2850\text{ cm}^{-1}$ , which were symmetrical and asymmetrical vibrations of CH<sub>3</sub> and CH<sub>2</sub> groups from the aliphatic hydrocarbon chains. The most intensive peak (C) was a doublet at wavenumbers  $2360$  and  $2340\text{ cm}^{-1}$  caused by absorption of carbon dioxide from the air. Other bands were from moderate to very bland with low intensity. At wave number of  $1740\text{ cm}^{-1}$  it was a vibration of a carbonyl group (D) (from ketones, aldehydes, lactones and carboxylic groups), and wave numbers (E) and (F) might be attributed to skeletal vibration of the carboxyl ion COO<sup>-</sup>, which was characterized by two maxima, the first in the  $1610\text{-}1550\text{ cm}^{-1}$  and the second in the  $1420\text{-}1300\text{ cm}^{-1}$ . In the area (E) were also the valence deformations of bond C = C ( $1575\text{-}1550\text{ cm}^{-1}$ ) of the aromatic ring. The peak at  $667\text{ cm}^{-1}$  (G) might be attributable to either the aromatic ring, possibly condensed, or to the vibration of -OH groups attached to the aromatic ring (i.e. phenols). Sulphates, respectively sulfo group -SOOH had a characteristic symmetrical and asymmetrical vibration at  $1260$  and  $802\text{ cm}^{-1}$ . Nitrates were characterized by symmetric vibration of -NO<sub>2</sub> group at  $1539\text{ cm}^{-1}$ . These bands were not observed in spectra of acid treated carbon black. Borah Dipu in his work<sup>6</sup> which referred to modification of carbon black by acids found the bands of nitro and sulfo groups, but he performed the modification with 20% acids (H<sub>2</sub>SO<sub>4</sub>, HNO<sub>3</sub> and their mixtrure) at  $110^\circ\text{ C}$  under reflux for 90 minutes. The reaction conditions were more drastic, and therefore it caused nitration and sulphonation of carbon black. Untreated carbon black had in the region below  $1500\text{ cm}^{-1}$ , a slightly different character of the spectrum, the band (F) was shifted to a higher wave number, this corresponded to a planar distortion of -OH group, not to the deformation of the carboxyl ion.

**Table IV**  
**Evaluation of IR spectra**

Wave number (cm <sup>-1</sup> )	H <sub>2</sub> O	-CH <sub>3</sub> , -CH <sub>2</sub>	CO <sub>2</sub>	C=O	COO <sup>-</sup> C=C	COO <sup>-</sup> -OH	Ph-OH
	<b>A</b>	<b>B</b>	<b>C</b>	<b>D</b>	<b>E</b>	<b>F</b>	<b>G</b>
Carbon black - original	3720; 3620	2925; 2855 d	2363; 2339 d s	1744 w	1536 w	1452 w	667 m
Carbon black - HCl	3700-3600 b	2923; 2855 d	2360; 2342 d s	1748 w	1557 w	1381 w	669 m
Carbon black - H <sub>2</sub> SO <sub>4</sub>	3700-3400 b	2922, 2849 d	2360; 2337 d s	1739 w	1550 w	1386 w	669 m
Carbon black - HNO <sub>3</sub>	3700-3600 b	2925; 2852 d	2360; 2342 d s	1740 w	1583 w	1384 w	667 m

Characterization of the band:

- b wide band (hydrogen bonds)
- w low intensity
- s high intensity
- m medium intensity
- d double band

### Raman spectroscopy

From the Raman spectra was obvious partial change of carbon modification in carbon black due to the process of modification by mineral acid. This caused the decrease of the ratio of intensity and area of a graphite band ( $sp^2$  hybridization –  $1582\text{ cm}^{-1}$ ) and the diamond band ( $sp^3$  hybridization -  $1332\text{ cm}^{-1}$ ) - see Table V. The increase of the percentage of less conductive modification corresponded to the results of electrical conductivity measurement.

Table V

#### Evaluation of Raman spectra

Sample	wavenumber $sp^2/sp^3$	intensity $sp^2/sp^3$	area $sp^2/sp^3$	ratio $sp^2/sp^3$
Carbon black - original	1591/1325	129.09/154.88	124.47/149.34	0.833
Carbon black - HCl	1593/1319	165.44/230.34	159.5/221.36	0.719
Carbon black - $H_2SO_4$	1592/1320	156.84/218.21	152.14/210.40	0.721
Carbon black - $HNO_3$	1589/1320	178.4/245.85	172.03/237.06	0.726

### Distribution of the proton affinity

From the distribution curve of proton affinity and both derivatives  $\Delta pH/\Delta V$  and  $\Delta(\Delta pH)/\Delta V^2$  were determined the  $pK_a$  values, which were shown in Table VI.

Table VI

#### Evaluation of distribution of proton affinity

Range of $pK_a$	$pK_a$ (carbon black - original)	$pK_a$ (carbon black - HCl)	$pK_a$ (carbon black - $H_2SO_4$ )	$pK_a$ (carbon black - $HNO_3$ )	functional groups
3 - 4	-	3.68	-	-	1; 2; 3
4 - 5	4.6	-	4.072	4.96	1; 2; 3; 4
5 - 6,5	5.17	-	-	6.43	3
6,5 - 7,5	6.02; 6.96	-	-	-	5
7,5 - 9	-	-	-	8.71	6; 7
9 - 10	-	-	-	9.66	7
10 - 11	-	-	-	-	7; 8; 9

Functional groups:

- 1 Amino groups on the aromatic ring
- 2 Imino groups on the aromatic ring
- 3 Karboxyl group on the aromatic ring
- 4 Karboxyl group on the aliphatic chain
- 5 Aromatic thiols
- 6 Lactones
- 7 Phenols
- 8 Aliphatic amines
- 9 Aliphatic thiols

Untreated carbon black were acidic, functional groups were mostly represented by -SH groups bonded to an aromatic ring ( $pK_a$  6.5-7.5). The acidic nature of carbon black was caused by carboxyl groups - COOH ( $pK_a$  4-6.5). The original carbon black contained about 0.5% sulfur, which was during the modification by acids displaced in the form of gaseous hydrogen sulfide. Thiols were not presented in the modified carbon black.

Modification by hydrochloric acid and sulfuric acid resulted in the disappearance of all the original functional groups on the carbon black surface. Residues of acids used for demetallization were presented by strongly

acidic groups with the  $pK_a$  of about 4. Treatment of carbon black by nitric acid was surprisingly not as drastic as by HCl and  $H_2SO_4$ . On the surface of the carbon black remained carboxyl groups on an aromatic ring, part of which was oxidized to phenols with  $pK_a$  approximately 10. Surface properties of carbon black treated with  $HNO_3$  was quite similar to the original sample, distribution of the proton affinities also indicated the presence of phenolic groups, which were formed by oxidation of originally presented phenolic groups.

### Conclusion

Inorganic acids treatment could remove a substantial part of the iron, nickel and vanadium from carbon black. Nevertheless this procedure influenced structural and surface properties of the carbon black. There was a change of crystallite size and a fundamental change in the distribution of proton-affinity on the surface of carbon black particles. Sulfuric acid and hydrochloric acid destroyed all original functional groups. Acid residue that remained absorbed on the surface of carbon black became functional. Nitric acid did not disrupt the functional surface to such an extent as sulfuric acid and hydrochloric acid, but a part of the functional groups were probably oxidized and formed the phenolic groups on the surface of carbon black. Testing of the electrical conductivity in the PE composite showed that the carbon black treated with mineral acids was less conductive, or did not conduct electric current at all.

### Acknowledgement

*This publication is a result of research project solved in a frame of UniCRE centre which infrastructure was supported by the European Regional Development Fund and the state budget of the Czech Republic. The publication was supported by institutional funds (Ministry of Industry and Trade of the Czech Republic).*

### Literature

1. Hoechst AG, CA 1142325, authors: Wolter M., Heymer G., Process for the removal of metals from carbon black, (1983).
2. Lion Corp. EP 2351798, authors: Inomata Kazuya, Unagami Runa, Method for producing high-purity carbon black, (2011).
3. Sotex AB, DE 2717303, authors: Nils R., Kuylenstierna U. V., Verfahren zur Wiedergewinnung von Metallen aus dem bei der Verbrennung von Oel entstehenden Russ, (1977).
4. China Rubber Group Carbon Black Res & Design Inst., CN 102702801, authors: Binghong Li, Zhi Zhang, Min Liu, Zhengping Fan, High purity carbon black and production method thereof, (2012).
5. Mohammad A. Al-Ghouti, Yahya S. Al-Degs, Ayoub Ghrair, Hani Khoury, Mahmoud Ziedan: Extraction and separation of vanadium and nickel from fly ash produced in heavy fuel power plant. Chemical Engineering Journal, Vol. 173, Issue 1, 191-197 (2011).
6. Dipu Borah, Shigeo Satokawa, Shigeru Kato, Toshinori Kojima: Applied Surface Science, 254, pp. 3049–3056, (2008).
7. Contescu C. I.: Selection and Characterization of Carbon Black and Surfactants for Development of Small Scale Uranium Oxide Carbide Kernels, Oak Ridge National Laboratory, ORNL/TM-2005/548, (2005).
8. Mohammad Saleh Shafeeyan, Wan Mohd Ashri Wan Daud, Amirhossein Houshmand, Ahmad Shamiri: A review on surface modification of activated carbon for carbon dioxide adsorption, Journal of Analytical and Applied Pyrolysis, 89, pp. 143-151, (2010).

## CONCEPTUAL DESIGN OF A DIMETHYL CARBONATE PRODUCTION AND SEPARATION PROCESS PLANT

Labovský J., Danko M., Červeňanský I., Janošovský J., Labovská Z., Dudáš, J.

*Institute of Chemical and Environmental Engineering, Faculty of Chemical and Food Technology, Slovak University of Technology, Radlinského 9, 812 37 Bratislava, Slovak Republic*

Dimethyl carbonate (DMC) has become a green and environmentally benign chemical due to its multiple reactivity and wide use in chemical industry. It has been used as a substitute to replace dimethyl sulfate and methyl halides in methylation reactions and as a carbonylation agent to substitute phosgene in the production of polycarbonates and urethane polymers. It is also valued as a non-aqueous electrolyte component in lithium rechargeable batteries.

The phosgene-free route for the synthesis of DMC has been widely studied by academic and industrial researchers, e.g. the oxidative carbonylation of methanol [1].

The presented work is focused on the conceptual design of a unit for DMC production. As DMC is obtained as a mixture with methanol, DMC purification is an indispensable step in DMC manufacturing. Under normal pressure, DMC and MeOH constitute an azeotrope; therefore, DMC/MeOH mixtures are difficult to separate. Despite the newly developed membrane separation or adsorption processes, proper design of the traditional DMC separation from the reaction mixture using a distillation tower considering the existence of the methanol-DMC azeotrope in large scale DMC production [2] is very important.

Conceptual design of DMC production is based on oxidative carbonylation of methanol with carbon monoxide and oxygen. This type of process was chosen because enough information on the reaction kinetics and thermodynamics is available. The primary target of the presented work was to design a production and separation unit allowing to produce 10 000 tons of DMC per year.

### Thermodynamic analysis

To describe the gas-liquid and liquid-liquid system, a UNIQUAC model with the Soave–Redlich–Kwong equation of state was used. The comparison of this model with experimental data can be found in [3], where the experimental data were also confronted with other types of equations of state. The mentioned model was used to perform thermodynamic analysis and, in a subsequent step, it was exported to the HYSYS environment. The T-xy diagram for the system DMC/water is depicted on figure 1.

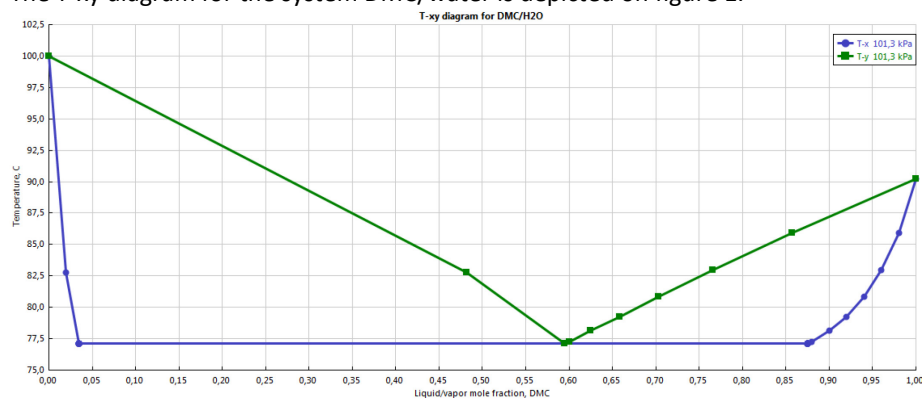


Fig. 1 T-xy diagram for the binary system DMC/water

Primary problem of the DMC separation is the presence of several azeotropes in the quaternary system DMC-water-formal-methanol. During the thermodynamic analysis, four azeotropes were identified and these are summarized in table 1.

Table I List of identified azeotropes present in the quaternary system

Temperature	Classification	Component 1	Component 2
64.10	Saddle	DMC: 0.0762	MEOH: 0.9238
77.12	Saddle	DMC: 0.5981	H <sub>2</sub> O: 0.4109
41.25	Saddle	MEOH: 0.1317	Formal: 0.6883
41.80	Saddle	H <sub>2</sub> O: 0.0241	Formal: 0.9759

From the separation point of view, homogeneity of the azeotrope methanol-formal, formed at 101 kPa and 41 °C, is very important. The mole fraction of formal at this point is 87 %. To eliminate the problem of separation it is necessary to increase the pressure to 1000 kPa, when equilibrium changes allow producing practically pure formal (from the column bottom) and the distillate can be recycled. This thermodynamic change is depicted in the following figures.

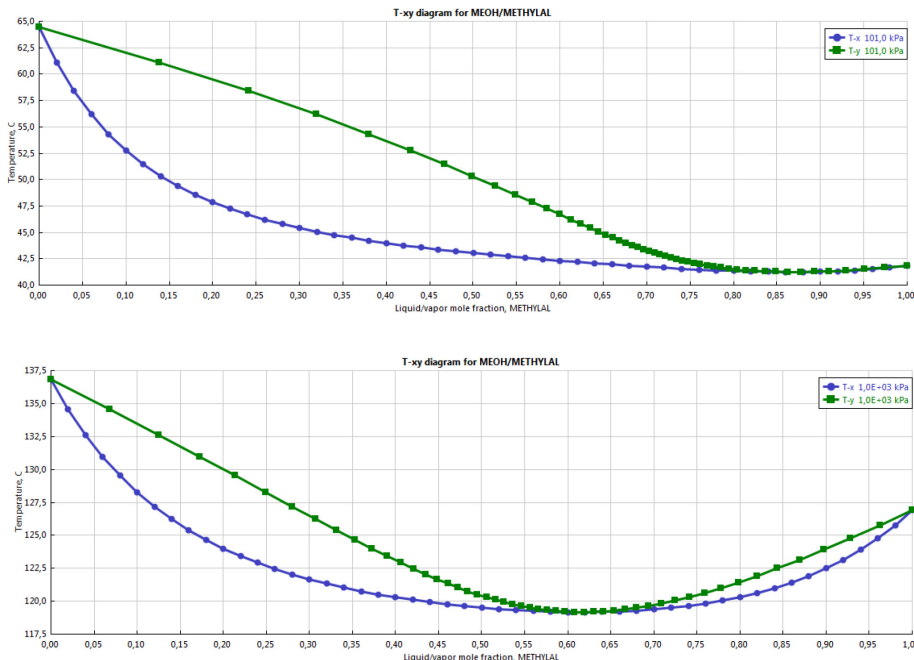
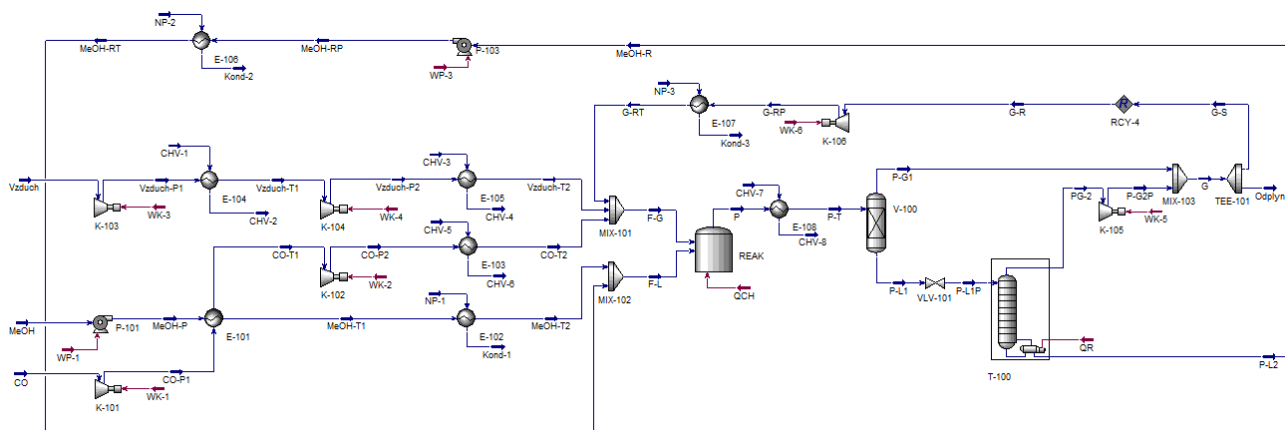


Fig. 2 T-xy diagram for the binary system methanol-formal at 100 kPa and 1000 kPa

### Description of production and separation process

Before the feed enters the reactor, temperature and pressure have to be adjusted. Fresh methanol flows from pump P-101 to heat exchanger E-101 at the pressure of 2000 kPa and it is partially preheated by carbon dioxide which exits compressor K-101. The heat exchanger is thus an intercooler in the two-stage compression of carbon monoxide using compressor K-101 and K-102 to achieve the required pressure of 2000 kPa. Methanol leaving this intercooler has to be heated to the final temperature of 130 °C in heat exchanger E-102. Carbon monoxide from the two-stage compression is cooled to 130 °C in heat exchanger E-103. Air, entering the process is also compressed in compressors K-103 and K-104, using intercooler E-104 and final cooler E-105. Fresh air and carbon monoxide are mixed with recycled gases G-RT and the mixtures enter the reactor. Fresh methanol is mixed (in MIX-102) with recycled methanol (MeOH-RT) from the separation part of the unit. Both feed streams (F-L and F-G) enter the reactor where DMC and formal (as byproduct) are produced.



**Fig. 3** Flow sheet of the basic units in the reaction part of the plant

In the separation part of the unit in the first phase, gaseous components are removed from the product stream leaving the reactor. The products are fed to heat exchange E-109, where the temperature decreases to 35 °C and are subsequently separated in phase separator V-100. The pressure of liquid stream P-L1 is reduced to 500 kPa and enters column T-100, which is used to separate the gasses (mainly CO<sub>2</sub>) from the liquid phase. Gaseous components from column T-100 are compressed (in K-105) to the pressure of 1900 kPa and mixed with gaseous stream (PG-1) from the phase separator V-100. The off-gasses are separated in TEE-101 and removed from the system to prevent the accumulation of nitrogen in the system. The major part of stream G is adjusted to the required pressure (in K-106) and temperature (E-107) and is recycled back to the reactor.

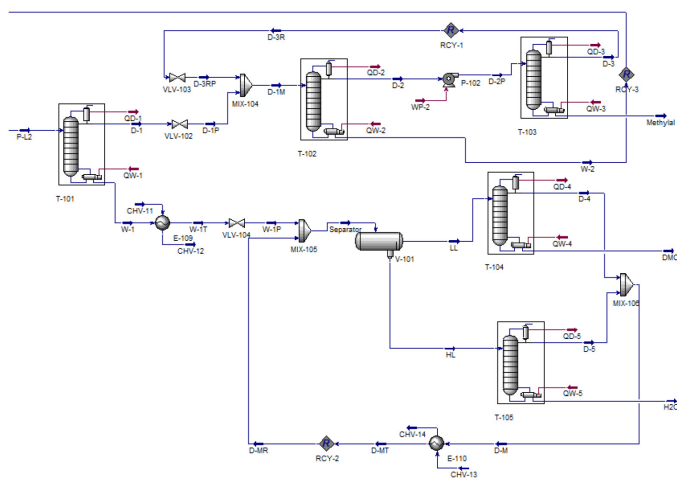


**Fig. 4** Flow sheet of the basic units of the separation part of the plant

In the second phase of the separation, the liquid streams are separated. The liquid outlet (P-L2) from column T-100 enters the main column for the separation of liquid components T-101. In this column, methanol and formal are separated from DMC and water. Methanol and formal leave the column in the distillate, water and DMC are mainly in the bottom outlet W-1. The distillate is reduced to the atmospheric pressure and is mixed with the recycled stream from methanol and formal separation (D-3RP) and enters column T-102. Bottom outlet from column T-102 is adjusted to the required pressure and temperature and is recycled back to the reactor. Distillate from column T-102 contains an azeotropic mixture of formal and methanol. This mixture is compressed to the pressure of 1000 kPa and enters column T-103, where pure formal is separated as the bottom product and the mixture of methanol and formal leaves the column in the distillate, which is reduced to the atmospheric pressure and returns back to column T-102. Bottom product from column T-101 is cooled (E-110) to 50 °C and the pressure is reduced to the atmospheric pressure. Consequently, this stream is mixed with the recycled stream which enters the three phase separator V-101. In separator V-101, the mixture of water and DMC is separated into light liquid phase (LL) which contains more DMC and heavy liquid phase which contains predominantly water. Stream LL enters column T-104, where DMC is obtained from the bottom

stream. Stream HL enters column T-105, where water with a small amount of methanol is obtained, DMC and water leave the column in distillate. Distillates D-4 and D-5 from columns T-104 and T-105 are mixed and cooled to 50 °C and subsequently recycled to the three phase separator.

### Conclusions

The main aim of the presented paper was to present a conceptual design of a technological unit for DMC production and purification. The conceptual design was oriented on minimization of the problems with low reaction conversion and to eliminate the problems of azeotropes formation during the separation process. The basic output from the economic analysis shows that the payback of the presented unit is approximately 5,5 years.

### Acknowledgement

*This work was supported by the Slovak Scientific Agency, Grant No. VEGA 1/0749/15*

### Literature

1. Liu, D.-H., He, J., Sun, L.-B., Liu, X.-Q., Zhong, Q., Cupric bromide-derived complex: An effective homogeneous catalyst for oxidative carbonylation of methanol to dimethyl carbonate, (2011), *J. Taiwan Inst. Chem. Eng.* 42: 616–621.
2. Keller, N., Rebmann, G., Keller, V., Catalysts, mechanisms and industrial processes for the dimethylcarbonate synthesis, (2010), *J. Mol. Catal. A Chem.* 317:1–18.
3. Santos, B. A. V., Silva, V., Loureiro, J.M., Barbosa, D., Rodrigues, A.E., Modeling of physical and chemical equilibrium for the direct synthesis of dimethyl carbonate at high pressure conditions, (2012), *Fluid Phase Equilib.* 336: 41–51.

## CHEMICAL ENGINEERING SIMULATION ON PARALLEL COMPUTERS

Labovský J., Danko M., Janošovský J., Labovská Z., Jelemenský Ľ.

*Institute of Chemical and Environmental Engineering, Faculty of Chemical and Food Technology, Slovak University of Technology, Radlinského 9, 812 37 Bratislava, Slovak Republic*

Many computational problems in science and engineering require the most powerful computers available today. The widespread deployment of multicore and many-core architectures has highlighted the need to exploit parallel computing techniques. High Performance Computing (HPC) is a collective term describing computational facilities that have the capacity to outperform the current high-end standalone machines. HPC facilities can vary from massively parallel processing supercomputers to clusters of commodity personal computers.

The main objective of the presented work was to highlight the advance of the high performance computing technology in chemical engineering. Several examples of the benefits of HPC are presented and their comparison with serial equivalents is provided.

### Introduction

Not long ago, parallel computers were associated with fairly large machines, most of them running Linux, dedicated to special computations requiring extreme performance, such as quantum mechanical calculations, computational fluid dynamics, molecular simulations, and chemical process optimization, among other applications relevant to chemical industries (Castierl et al. 2014). A considerable amount of work on better numerical methods development taking full advantage of parallel computations has been in progress. Large scale simulation of chemical processes is an application area where very large systems of coupled non-linear equations naturally occur (Smith and Dimenna, 2004).

This case study refers about global optimization method exploiting parallel computers, which was used to fit equation of state parameters. Sometimes, model developers wish to correlate experimental data as well as the possible ones, which means that the global minimum of the objective function is a desirable target. Locating the global minimum of complicated functions, with many state parameters or a massive number of experimental data points, demands large computational effort and time consuming calculations, often carried out using a single processor in a personal computer (PC). However, modern desktop, laptop, and tablet computers and even mobile phones have multiple processors. Recent Windows versions of software such as Mathematica and Matlab exploit such configurations to speed up the calculations. Nonetheless, many legacy sequential codes exist in languages such as Fortran and C. Their adaptation for maximum performance in parallel computers may require extensive reprogramming but substantial performance gains are possible in certain applications with only a few changes to the existing codes. This paper shows that EOS parameter fitting is one of such applications and compares two software utilizing the Simplex algorithm in parallel computers, applicable both in single multiprocessor PCs and in cluster supercomputers.

In the second presented case study, the benefits of parallelization of a large system of nonlinear equation were investigated. The main goal was to suggest a technique allowing utilization of existing codes, primarily designed for serial execution. As an example of this approach, a model of a distillation column for ammonia purification is presented.

### Case study – Global optimization

Fitting EOS parameters is a seemingly routine problem in chemical engineering praxis. Probably the most challenging task is related with multiple minima in objective functions, each given by a different parameter set. The most straightforward procedure is based on running local optimization algorithms several times from different initial estimates or using global optimization methods. It is important to underline that these local minima have very often similar values of the objective function but significantly different values of the EOF parameters. Another challenge of such approach is the selection of good starting points for the optimization and an efficient subsequent multiple optimization processes.

In the presented work, the optimization of parameters of NRTL equation for systems ethanol-benzene and diethylamine – ethanol was chosen as a case study. The objective function used in the presented case studies was in the form:

$$f = \sum_{k=1}^{n_{exp}} \left( (y_{exp} - y_{calc})^2 \right) + \sum_{k=1}^{n_{exp}} \left( \frac{(P_{exp} - P_{calc})^2}{P_{exp}^2} \right) \quad (1)$$

Comparison of the experimental and optimized data is depicted in Fig. 1.

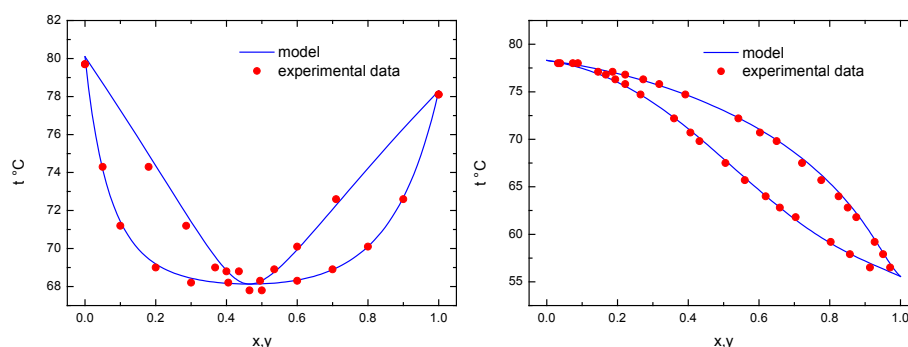


**Fig. 5. t -x,y diagrams for binary systems used in the case studies, ethanol-benzen (right), diethylamine-ethanol (left)**

The presented case studies were run on an 80 cores computer cluster. To highlight the benefits of parallelization, two different languages (platforms) were used. First chosen language was MATLAB, a programming language developed by MathWorks. Matlab is currently very popular in engineering and scientific disciplines, and is very often used as a teaching tool in many courses. An optional toolbox is the Parallel Computing Toolbox™, which allows solving computationally and data-intensive problems using multicore processors, GPUs, and computer clusters. High-level constructs—parallel for-loops, allows to parallelize applications without CUDA or MPI programming. The presented strategy is based on the parallel for loop that allows the code (objective function calculation) to be executed repeatedly. Basic quantitative parameter, which compares the efficiency of the parallel algorithms, is the speedup defined as a ratio between the base serial program's execution time and its parallel implementation execution time. Dependence of the execution time on the number of cluster cores and the speedup of the parallel code are depicted on the next series of figures (Fig. 2).

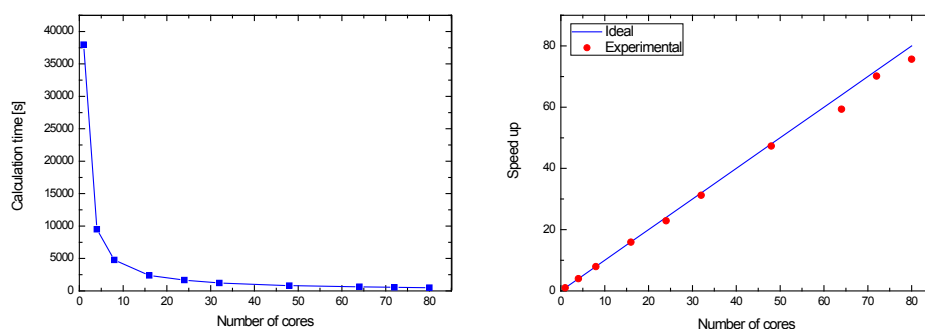


**Fig. 6. Execution time and speedup as a function of the number of cluster cores**

The second chosen platform was the .NET Framework and the programming language was C#. To parallelize the algorithm, the MPI.NET library was used. MPI.NET is a high-performance, easy-to-use implementation of the Message Passing Interface (MPI) for Microsoft's .NET environment. MPI is nowadays a standard for writing parallel programs running on a distributed memory system, such as a compute cluster. PI provides functions and subroutines to control parallel computations and pass information from one process to another. In a message-passing system, different concurrently-executing processes communicate by sending messages from one to another over a network. Unlike multi-threading, where different threads share the same program state, each of the MPI processes has its own, local program state that cannot be observed or modified by any other process except in response to a message. Therefore, the MPI processes themselves can be as distributed as the network permits, with different processes running on different machines or even different architectures. Speedup of the parallel version is depicted in Fig. 3.

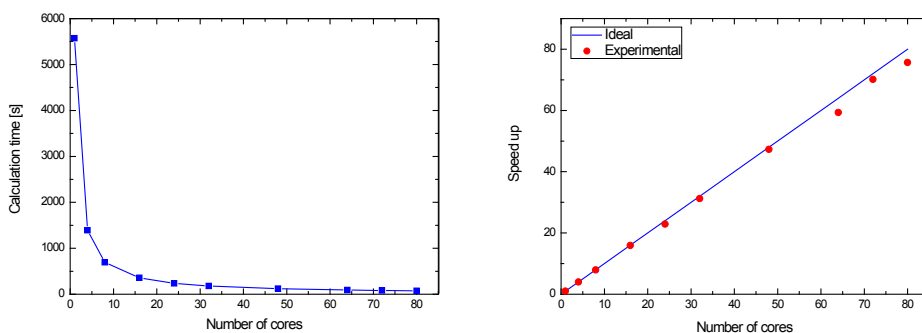


**Fig. 7. Execution time and speedup as a function of the number of cluster cores**

From Figs. 2 and 3 it is clear that the speed of the parallel optimization is quite linear and the capacity utilization of computer sources is higher than 90 % in both cases.

### Case study – Large system of nonlinear equations

The second case study was focused on parallelization of solving a large system of nonlinear equations. This problem occurs frequently in numerical methods in chemical engineering. To demonstrate the benefits of the parallelization, the standard algorithm for solving a system of nonlinear equations implemented in Matlab was modified.

The Newton's method is a basic general purpose approach for solving nonlinear equations. It creates a linear approximation to the nonlinear system based on a Jacobian matrix. In the general form of the Newton method, the iterations and phases of each step have to be performed one after another in order to preserve the correctness of the numerical algorithm. In general, the standard Newton's method comprises three basic steps:

1. estimation of the Jacobian – determined by backward differential formulas,
2. solution of a system of linear equation (very often large and sparse),
3. improvement of the previous estimate.

If the Jacobian is determined in each iteration, it is always the most time consuming part of the algorithm. On the other hand, parallelization of the estimation of the Jacobian is quite a trivial task as the columns of the Jacobi matrix can be process independently.

The most universal solver for a system of nonlinear equations presented in Matlab is the function *fsolve*. *Fsolve* uses a subspace trust-region method and is based on the interior-reflective Newton method. The default version of the algorithm uses sequential approach for the determination of the Jacobian. However, it allows overriding the estimation of the Jacobian via solver option settings. As our primary goal was to implement parallelization of the default version the solver (without significant modifications of the existing code), the sequential version of the Jacobian determination was replaced with a parallel version which is the most straightforward procedure. This approach allows utilizing the benefits of parallelization without modifying the existing users programs and default solver.

To demonstrate the simplicity and efficiency of the presented approach, a case study focused on the steady state simulation of a distillation column was prepared. The mathematical model was described by MESH equations. MESH being an acronym referring to the different types of equation: Material balances, vapor-liquid Equilibrium equations, mole fraction Summations and enthalpy (H) balances. The main idea is in the assumption that the vapor and liquid streams leaving an equilibrium stage are in complete equilibrium with each other and thermodynamic relations can be used to determine the equilibrium stage temperature and relate the concentrations in the equilibrium streams at a given pressure (Perry et al., 1997). A complete distillation column is considered as a sequence of these stages. A distillation column model is an ideal candidate for the presented case study, as it allows increasing the number of trays, which results in the increase of the number of nonlinear equation to be solved. Table 1. summarizes the execution times for four different numbers of trays. All execution times are in seconds.

Table 1. Execution time as a function of the number of equations and cores

Number of trays	Number of cores									
	1	2	4	8	16	24	48	64	72	80
50	13.9	8.3	6.2	4.3	3.2	3.1	3.1	3.5	3.8	3.5
250	219.2	111.6	61.0	34.5	19.7	15.7	10.5	9.9	9.5	9.6
1000	1590.0	798.8	428.3	221.4	119.8	83.8	52.4	41.2	38.7	35.5
2500	15329.6	7697.3	4097.5	2099.8	1065.8	750.7	401.7	324.0	292.3	269.2

For better visualization of the results, a speedup of the parallel code is depicted in Fig. 4. From the pictures it is clear that the parallel version of the algorithm is faster than its serial equivalent. On the other hand, in case of a 50 trays column (200 nonlinear equations) the benefits of parallelization are evident, in case of utilizing eight cores. Further increase in the core number did not provide a significant speedup increase. If the number of equations is higher, the capacity utilization increases radically. In case of the largest system investigated in the presented case study, the measured speedup was higher than 55.

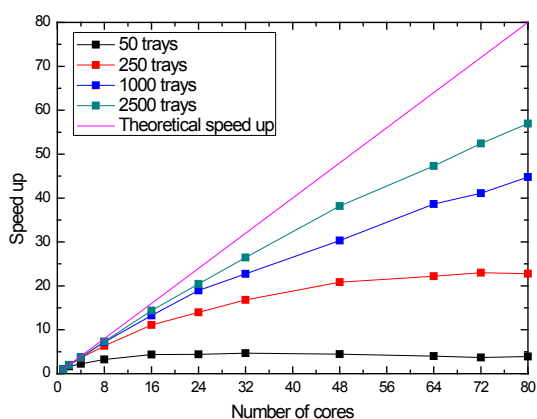


Fig. 8. Speedup of parallel code

#### Acknowledgement

This work was supported by the Slovak Scientific Agency, Grant No. VEGA 1/0749/15

#### Literature

- Castierl, M., Checonil R. F., Zuberl, A., Fitting equation of state parameters in parallel computers, 2014, *Brazilian Journal of Chemical Engineering* 31(4): 993-1002
- Perry, R. H., Green, D. W. & Maloney, J. O. *Perry's Chemical Engineers' Handbook*, McGraw-Hill, New York, 1997
- Smith, F.G., Dimenna, R.A., Simulation of a batch chemical process using parallel computing with PVM and Speedup, 2004, *Computers & Chemical Engineering* 28(9):1649-1659.

## RUTHENIUM CATALYSTS FOR HYDROGENATION OF COUMARIN

**Bílková D.**<sup>1</sup>, Stáně R.<sup>2</sup>, Červený L.<sup>1</sup>

<sup>1</sup>Department of Organic Technology, University of Chemistry and Technology Prague, Prague, Technická 5, 166 28, Prague 6, Czech Republic

<sup>2</sup>Glanzstoff-Bohemia s.r.o., Terezińska 60, 410 02, Lovosice, Czech Republic  
Dana.Bilkova@vscht.cz

### Abstract

Octahydrocoumarin,  $\delta$ -lactone, is a clear liquid with tonka beans and hay aroma that can replace toxic coumarin. Octahydrocoumarin is an industrially desirable synthetic fragrance (Food and Perfumery) which can be added for example to tobacco products to highlight the flavor and aroma of their smoke. Great advantage of the octahydrocoumarin is that it is not toxic to rodents. The aim of this work was to test various types of Ru-catalysts and study their deactivation in the octahydrocoumarin synthesis by hydrogenation of coumarin (Figure 1).

Several types of commercial Ru-catalysts (from Johnson Matthey: Type 97 Paste, Type 600 Paste, Type 603, Type 605 Paste, Type 619 Paste, Type 620 Paste; from Evonik Industries: Noblyst P3055, Noblyst P3060, Noblyst P3061; from Strem Chemicals: Escat 4401) was tested for hydrogenation of coumarin in methanol (3 : 2) at temperature of 130 °C and pressure of 10 MPa to obtain octahydrocoumarin with high selectivity. The highest selectivity of octahydrocoumarin 80% was achieved in the presence of catalyst Ru/C Type 605 from Johnson Matthey.

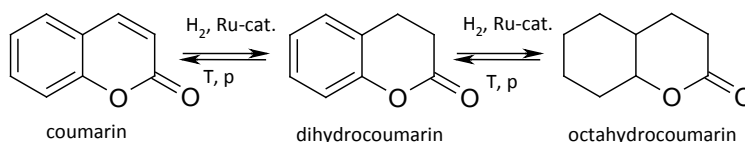


Figure 1. Hydrogenation of coumarin to octahydrocoumarin over Ru-catalyst

**Keywords** Coumarin, Hydrogenation, Ru supported catalysts, Dihydrocoumarin, Octahydrocoumarin

### Introduction

Coumarin (1,2-benzopyron, *o*-hydroxycinnamic acid lactone) is a white crystalline solid which is used in Food, Perfumery and medical industry<sup>1-3</sup>. For coumarin were found hepatotoxic properties in rodents and in large doses, coumarin may cause cytotoxicity in humans<sup>1,4</sup>. For these reasons, legislative measures on the amount of coumarin in food are introduced and looking for a suitable replacement.

Octahydrocoumarin is a clear liquid, which is not present in nature and is produced synthetically. It is similar in fragrance and flavor properties of coumarin or dihydrocoumarin. It is used primarily as an additive to the tobacco products<sup>5</sup>. Advantages of octahydrocoumarin are nontoxic and non-irritating properties.

Octahydrocoumarin can be synthesized by many ways<sup>6-14</sup>. Depending on the cooperation with Aroma Praha, a.s. it is desirable to find suitable conditions and catalyst for the preparation of octahydrocoumarin by coumarin hydrogenation. Hydrogenation of coumarin in the presence of various catalysts (Raney nickel, Adams catalyst, Ru/C) was investigated in several works<sup>15-19</sup>.

The aim of this study was to test various types of Ru-catalysts and study their deactivation in the octahydrocoumarin synthesis by hydrogenation of coumarin.

### Experimental

Hydrogenation of coumarin was carried out in a stainless steel autoclave with the volume of 60 ml under constant hydrogen pressure 10 MPa. Commercial Ru supported catalyst granted by Aroma Praha, a.s. (Table I) were tested for hydrogenation.

Table I  
Table of tested catalysts

Name	Producer	Support	Ru content [%]	Wetness [%]
Type 97 Paste	Johnson Matthey	active carbon	4.62	59.9
Type 600 Paste			4.90	49.9
Type 620 Paste			5.00	62.6
Type 605 Paste			4.89	52.3
Type 619 Paste			5.10	56.5
Type 603		graphite powder	1.40	-
Noblyst P3060	Evonik Industries	active carbon	5.00	58.5
Noblyst P3055			5.00	58.5
Noblyst P3061			aluminium oxide	5.00
Escat 4401	Strem Chemicals	active carbon	5.00	53.96

Coumarin (60 wt. %) in methanol solvent (40 wt. %) and the catalyst in the powder form (3 wt. % due to coumarin) were inserted into the autoclave. The reaction was carried out at the temperature of 403 K and hydrogen pressures equals 10 MPa.

The obtained samples were analysed using the gas chromatograph (SHIMADZU GC-2010 Plus) equipped with ZB-5 column (60 m, 0.32 mm diameter, 0.25  $\mu\text{m}$  film). The injector temperature was 523 K, the column temperature ramped from 283 K to 523 K at a rate of 10 K  $\text{min}^{-1}$ . Carrier gas rate was 471.8 ml  $\text{min}^{-1}$ . FID temperature was 523 K.

Identification of reaction mixture samples was performed on a gas chromatograph (SHIMADZU GC-2010 Plus) coupled with mass spectrometer (GCMS-QP 2010 Ultra) equipped with DB-1 column (50 m, 0.25 mm diameter, 0.5  $\mu\text{m}$  film). The injector temperature was 523 K, the column temperature ramped from 353 K to 523 K at a rate of 10 K  $\text{min}^{-1}$ . Carrier gas rate was 0.66 ml  $\text{min}^{-1}$ . Quadrupole detector temperature was 523 K.

### Result and Discussion

Hydrogenation of coumarin has been investigated using Ru/C catalysts (from Johnson Matthey: Type 97 Paste, Type 600 Paste, Type 603, Type 605 Paste, Type 619 Paste, Type 620 Paste; from Evonik Industries: Noblyst P3055, Noblyst P3060, Noblyst P3061; from Strem Chemicals: Escat 4401). The catalysts with the highest catalytic activity and their deactivation have been searched for. The concentration profiles of coumarin hydrogenation typical experiment are shown in Figure 2.

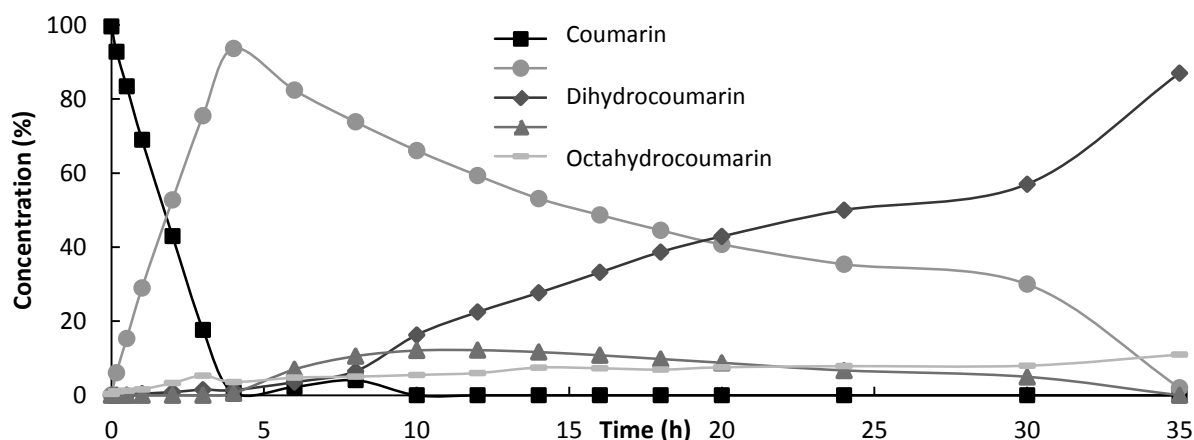


Figure 2. The concentration profiles of coumarin, dihydrocoumarin, octahydrocoumarin, methyl-3-(2-oxocyclohexyl)propionate and other products; conditions: 130  $^{\circ}\text{C}$ , 10 MPa, 60 wt. % of coumarin in methanol, 0.5 wt. % of Ru/C catalyst Johnson Matthey type 605

It was demonstrated that octahydrocoumarin can be prepared by hydrogenation of coumarin on ruthenium catalysts. From the achieved results and the available literature<sup>17-19</sup> was compiled simplified mechanism of coumarin hydrogenation on Ru/C (Figure 3).

The main products obtained were dihydrocoumarin (**II**, desired intermediate), formed by coumarin (**I**) hydrogenation, octahydrocoumarin (**III**, desired product) formed by dihydrocoumarin hydrogenation, methyl-3-(2-hydroxyphenyl)propionate (**VI**) and methyl-3-(2-hydroxycyclohexyl)propionate (**VIII**) formed by reaction of the appropriate lactone with methanol. A by-products (**IV**, methyl-3-(2-oxocyclohexyl)propionate; **V**, 3-(2-hydroxycyclohexyl)propanal; **VII**, 3-phenylpropionic acid; **IX**, 3-cyclohexylpropionic acid; **X**, methyl-3-cyclohexylpropionate) were also detected.

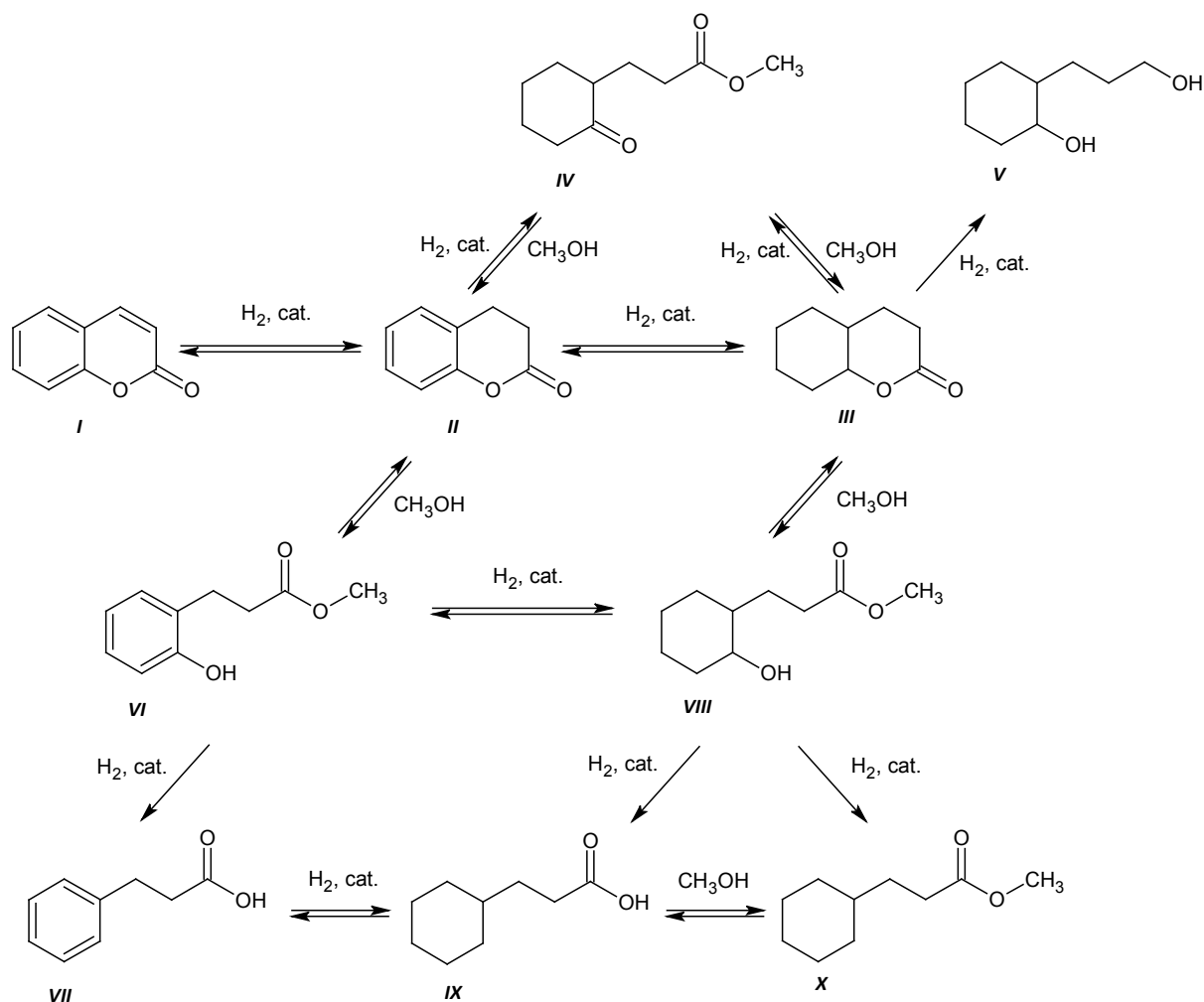


Figure 3. Coumarin hydrogenation mechanism, 130 °C, 10 MPa, Ru/C catalyst Johnson Matthey type 605, 30 h: **I** coumarin, **II** dihydrocoumarin, **III** octahydrocoumarin, **IV** methyl-3-(2-oxocyclohexyl)propionate, **V** 3-(2-hydroxycyclohexyl)propanal, **VI** methyl-3-(2-hydroxyphenyl)propionate, **VII** 3-phenylpropionic, **VIII** methyl-3-(2-hydroxycyclohexyl)propionate, **IX** 3-cyclohexylpropionic acid, **X** methyl-3-cyclohexylpropionate

#### Catalysts testing

Commercial Ru supported catalyst were granted by Aroma Praha, a.s. (Table I). Series hydrogenation of coumarin was performed on various types of Ru catalysts for comparison of their activity and selectivity (conditions: 25 ml autoclave, 60 wt. % of coumarin in methanol, 5 wt. % of Ru catalyst due to coumarin, 160 °C, 10 MPa). For selected catalyst (Ru/C Type 600 JM Paste, Ru/C Type 605 JM Paste, Ru/C Type 619 JM Paste, Ru/Al<sub>2</sub>O<sub>3</sub> Noblyst P3061) was achieved a high selectivity (over 75 %). The lowest selectivity of 55 % was observed in the presence of Ru/C JM Type 603. By-products content of coumarin hydrogenation by catalysts with high selectivity to octahydrocoumarin is shown in Figure 4.

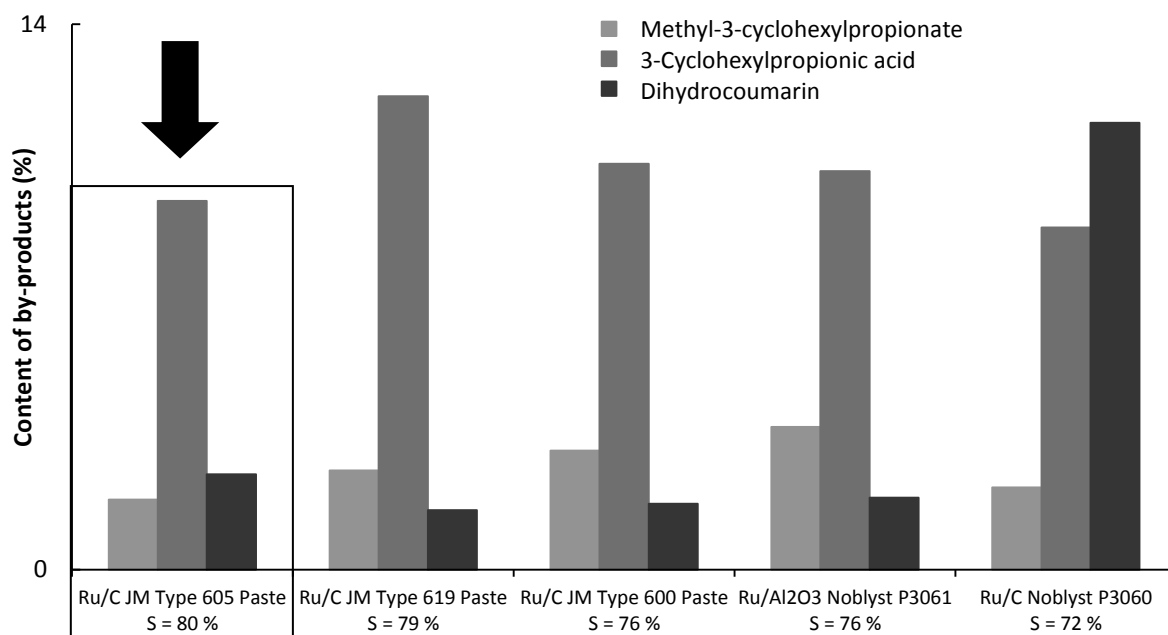


Figure 4. By-products content of coumarin hydrogenation by catalysts with high selectivity (S) to octahydrocoumarin; conditions: 130 °C, 10 MPa, 60 wt. % of coumarin in methanol, 0.5 wt. % of Ru/C catalyst

#### Catalysts deactivation

To investigate the degree of catalyst deactivation was chosen catalyst Johnson Matthey Type 605. First, the reaction was conducted with fresh catalyst (3 wt. % relative to coumarin) in a 160 ml autoclave at a temperature of 130 °C and a pressure of 10 MPa. The reactor was charged mixture of 60 wt. % coumarin in methanol. Progress of this reaction is shown in Figure 5a. The catalyst was then filtered off from the mixture in bench equipment company Aroma Praha, a.s. where the catalyst after separation was repeatedly washed with toluene. With this catalyst the reaction was conducted under the same conditions. The second reaction time was 17 h to achieve higher conversion of dihydrocoumarin. Progress of this reaction is shown in Figure 5b.

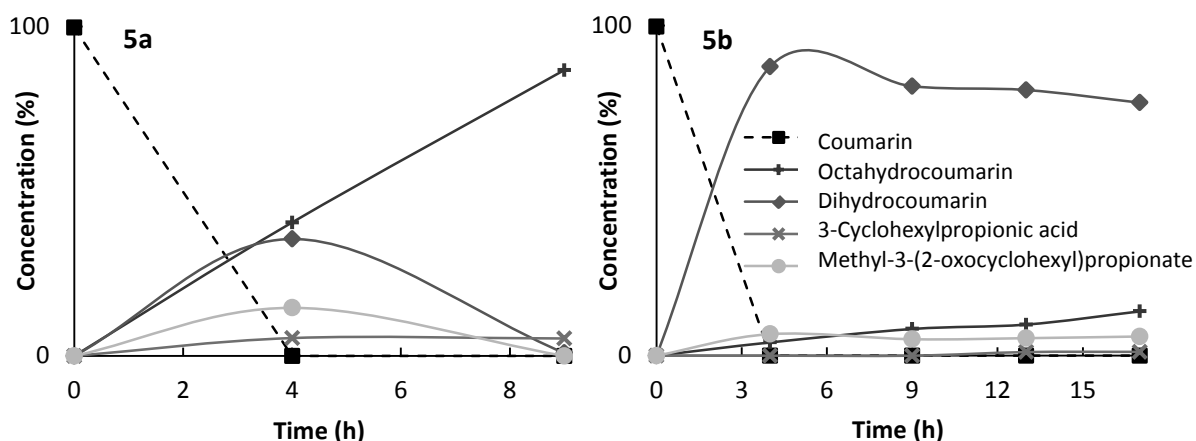


Figure 5. Hydrogenation of coumarin; conditions: 130 °C, 10 MPa, 60 wt. % of coumarin in methanol, 3 wt. % of Ru/C catalyst – 5a fresh catalyst, 5b reused catalyst

From Figure 5 it is obvious that the hydrogenation of coumarin to octahydrocoumarin proceeds with reused catalyst more slowly. The rate of hydrogenation of coumarin is comparable in both reactions. Hydrogenation of dihydrocoumarin to octahydrocoumarin shows a decrease in catalyst activity. With the decrease in reaction rate does not decrease the selectivity.

## Conclusions

The highest selectivity of octahydrocoumarin 80 % was achieved in the presence of catalyst Ru/C Type 605 from Johnson Matthey. This catalyst was tested for its deactivation. When the catalyst was reused for the hydrogenation of coumarin on octahydrocoumarin, the reaction proceeds much more slowly, but it has no effect on selectivity.

## Acknowledgment

*This work was supported by specific university research (MSMT No 20/2015).*

## Literature

1. Lake B. G.: Food Chem. Toxicol. 37, s 423-453 (1999).
2. VOSNAKI, E. Perfume Shrine. <http://perfumeshrine.blogspot.cz/2011/02/perfumery-materials-coumarin-tonka-bean.html> (accessed April 27, 2015).
3. Coumarin. <http://en.wikipedia.org/wiki/Coumarin> (accessed April 27, 2015).
4. Yourick J. J.; Bronaugh R. L.: J. Appl. Toxicol. 17, 3, s 153-158 (1997).
5. Vonášek F.; Trepková E.; Novotný L., v knize: *Látky vonné a chuťové*, SNTL/Alfa: Praha/Bratislava 1987.
6. Frank R. K., Pierle R. C.: J. Am. Chem. Soc. 73, s 723-730 (1951).
7. House H. O., Carlson R. G., Babad H. J.: Org. Chem., 28, 12, s. 3359-61 (1963).
8. Riehl T. F., Kennedey J. E.: Tobacco product. DE 2 023 914 A, 15 May 1970.
9. Aredova E. N., Krasutskii P. A.: Izv. Akad. Nauk SSSR. 4, s. 926-8 (1978).
10. Alekseeva N. A., Kolomeer G. G., Maksutova I. V., Minkovskij M. M., Filatova T. I.: Method of octahydrocoumarin synthesis. RU 2 059 632, 3 Juny 1992.
11. Sakai K., Nishida Y., Shirafuji T.: Process for producing octahydrocoumarin or derivative thereof. EP 0 533 378 A1, 4 September 1992.
12. Iwamoto K., Tanaka S.: A process for producing octahydrocoumarins and same as a product of such proces. EP 0 757 989 A1, 12 July 1996.
13. Wang X.: Jingxi Huagong. 26, 12, s. 1206-1210 (2009).
14. Chen X.: Xiangliao Xiangjing Huazhuangpin. 5, s 22-24 (2010).
15. Nakabayashi T.: Yakugaku Zasshi. 74, s 895-8 (1954).
16. Iwamoto K., Tanaka S.: A process for producing octahydrocoumarins and same as a product of such proces. EP 0 757 989 A1, 12 July 1996.
17. Adams T., Greer B., Doull J.: Food Chem. Toxicol. 36, s 249-278 (1998).
18. Pikna R. Hydrogenace kumarinu. Diploma thesis, VŠCHT Praha, 2012.
19. Bílková D. Technologie oktahydrokumarinu. Diploma thesis, VŠCHT Praha, 2013.

## HETEROGENEOUS BASIC CATALYSTS IN 2-BUTYLCINNAMYLALDEHYDE SYNTHESIS

**Vrbková E.**, Krupičková K., Vyskočilová E., Krupka J., Červený L.

*University of Chemistry and Technology, Technická 5, 166 28, Prague  
eva.vrbkova@vscht.cz*

### Introduction

Several fragrant substances with floral or fruity notes are synthesized using aldol condensation. These reactions are usually catalyzed by basic homogeneous catalysts (inorganic hydroxides). Such processes suffer from production of big amount of waste salts. The use of basic heterogeneous catalyst is widely studied because of the effort to decrease the amount of waste salts and for possibility of catalyst reuse. There are many types of heterogeneous basic catalysts as inorganic oxides, inorganic mixed oxides, materials modified using silanol grafting method, materials modified by inorganic alkaline media (potassium carbonate, potassium / sodium hydroxide, alkylammonium hydrochloride) and also materials modified by some more special metals as cesium or layered magnesium oxides<sup>1-5</sup>. In this work, several heterogeneous basic catalysts were tested in 2-butylcinnamyl aldehyde synthesis.

### Experimental

Cesium modification was performed by impregnation method<sup>3</sup>. Solid support (3 g) was stirred with solution of cesium acetate (0.864 g, Aldrich) in methanol (15 g, Penta) for 3 hours at 60 °C. After removing solvent under vacuum using rotary evaporator, resulted material was calcined (500 °C / 5 hours / air). Used amounts resulted in cesium concentration of 1.5 mmol/g of solid support.

Potassium modification was made by impregnation method<sup>1</sup>. Solid support (3 g) was stirred at room temperature with 10 wt.% water solution of potassium carbonate (Penta). Used amounts of potassium carbonate corresponded to a potassium concentration of 1.5 and 4.5 mmol/g of solid support.

Temperature programmed desorption (TPD) of CO<sub>2</sub> was carried out using Micromeritics Instrument, AutoChem II 2920. For evolved gas detection both a thermal conductivity detector (TCD) and quadrupole mass spectrometer (MKS Cirrus 2 Analyzer) with a capillary-coupling system were used. 0.1 g of catalyst sample was placed in a quartz U shaped tube. Prior to adsorption of CO<sub>2</sub>, the catalyst was heated under helium flow (30 mL/min) up to 500 °C and kept at 500 °C for 2 hours to remove water from sample and "clean" the catalyst surface. In the following step the sample was cooled down to adsorption temperature 40 °C. Measured pulses of carbon dioxide (pulse volume 0.5 mL) were injected into helium gas and carried through the catalyst sample until saturated adsorption. Then the sample was flushed with helium for 30 min to remove physisorbed carbon dioxide. Afterwards the linear temperature program (10 °C/min) was started and sample heated up to temperature of 900 °C. The desorbed amounts of carbon dioxide were determined by calibration of the intensity of 44 a.u. MS response.

Acido-basic titrations were performed according to described procedures<sup>6,7</sup> using different acido-basic indicators.

### Results and discussion

#### Catalyst basicity

Total amounts of desorbed CO<sub>2</sub> and benzoic acid amounts characterize material basicity. The most basic catalyst was: 4.5-K- Al<sub>2</sub>O<sub>3</sub> according to titration results and 1.5-K- Al<sub>2</sub>O<sub>3</sub> according to TPD results. This difference can be explained by pore blockage in the case of 4.5-K-Al<sub>2</sub>O<sub>3</sub> catalyst (S<sub>BET</sub> results, Table I), which could cause inaccessibility of some basic sites for CO<sub>2</sub> molecules during TPD measurement. On the other hand, titration was performed in solution and because of observed catalyst leaching (AAS results Table II), the majority of potassium was leached into solution where it was available for benzoic acid molecules.

Table I  
Titration and TPD results

Catalyst	$S_{\text{BET}}$ [m <sup>2</sup> /g]	Desorbed amount of CO <sub>2</sub> [mmol/g <sub>kat</sub> ]	Titrated benzoic acid amount [mmol/g <sub>material</sub> ]			
			Bromthymolblue	Phenolphthalein	Thymolphthalein	Alizarin yellow
CaO	3	-	0.04	-	-	-
MgO	45	106	0.14	-	-	-
MCM-41	495	-	-	-	-	-
Cs-MCM	94	26	0.15	-	-	-
HY	568	-	-	-	-	-
Cs-HY	452	-	-	-	-	-
NaY	673	-	-	-	-	-
Cs-NaY	148	256	-	-	-	-
USY	750	-	-	-	-	-
Cs-USY	193	13	0.09	-	-	-
Al <sub>2</sub> O <sub>3</sub>	298	-	-	-	-	-
1.5-K- Al <sub>2</sub> O <sub>3</sub>	250	469	1.02	0.20	-	-
4.5-K- Al <sub>2</sub> O <sub>3</sub>	93	289	1.29	1.66	1.29	1.48

Table II  
Metal leaching measured using AAS

Catalyst	Leached metal amount (%)
Cs-MCM	56.6
Cs-HY	30.3
Cs-NaY	9.8
1.5-K- Al <sub>2</sub> O <sub>3</sub>	80.3
4.5-K- Al <sub>2</sub> O <sub>3</sub>	93.0

The highest leaching was observed for 4.5-K- Al<sub>2</sub>O<sub>3</sub> and the lowest for Cs-NaY because of ion-exchange which was successfully performed during synthesis of Cs-NaY catalyst.

#### Reaction scheme

Aldol condensation of benzaldehyde (BA, Fig. 1) and hexanal (HX) provides two main products – desired 2-butylnminaldehyde (*I*, BCA) and undesired product of hexanal autocondensation – 2-butyloct-2-enal (*II*, BO). In some cases trimer of hexanal or products of subsequent aldol reaction and polymerization were also present in the reaction mixture. Reactions were base catalyzed, therefore in some cases products of Cannizzaro reaction – benzylalcohol and benzoic acid were detected in the reaction mixture in low concentration.

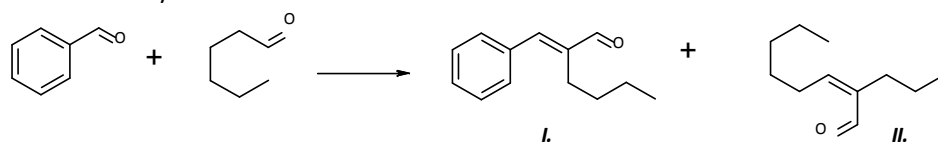


Figure 1. Reaction scheme

#### Reaction course

It is visible from Fig. 2 that after 5 hours of reaction the maximal conversion was obtained. Slight decrease in selectivity to 2-butyloct-2-enal was caused by increasing of high-boiling products origination (e. g. trimer of hexanal and polymerizations products).

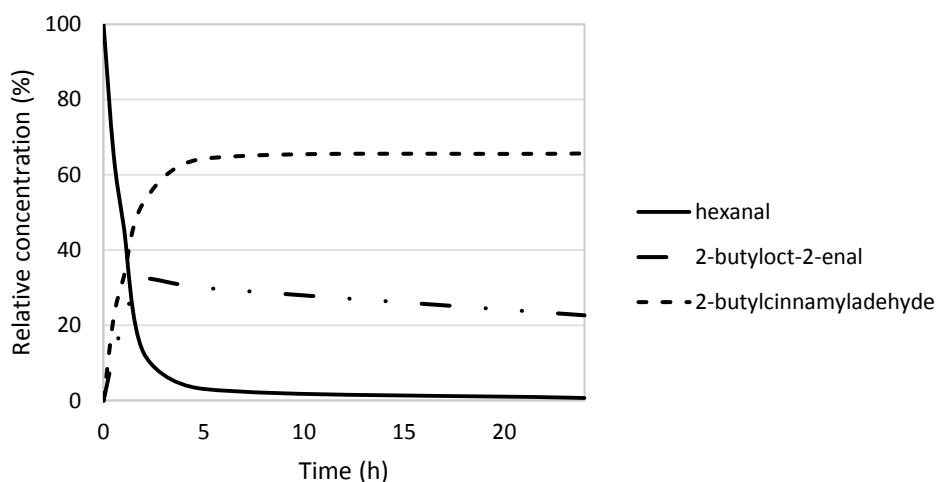


Figure 2. Reaction course (solvent DMF, 120 °C, 20 wt.% of catalyst MgO, HX:BZ = 1:2 (molar))

#### Influence of used catalyst

Reaction was performed under constant conditions (solvent DMF, temperature 120 °C, 20 wt.% of catalyst, molar ratio HX:BZ = 1:2). Several types of heterogeneous catalyst were used (Table III). The highest conversion was obtained using MgO and CaO (Table III, rows 1,2), but in the case of CaO a significant part of the products were high-boiling products. In case of non-modified Si and Al based catalysts (Table III, rows 3-6,11) aldol condensation also occurred. Modification of  $\gamma$ -Al<sub>2</sub>O<sub>3</sub> by potassium resulted in increase of hexanal conversion and in change of BCA:BO ratio in reaction mixture. Modification of materials by cesium (Table III, rows 7-10) caused preference of autocondensation products formation.

Table III

Reaction results using different catalysts (solvent DMF, 120 °C, 20 wt.% of catalyst, HX:BZ = 1:2 (molar), 5 h)

Row	Catalyst	Hexanal conversion [%]	Selectivity to 2-butyloct-2-enal [%]	Selectivity to 2-butylcinnamylaldehyde [%]	Others [%]
1	CaO	99	6	37	57
2	MgO	97	31	66	3
3	MCM-41	63	72	23	5
4	USY zeolite	65	54	19	27
5	HY zeolite	45	62	33	45
6	NaY zeolite	77	44	52	4
7	Cs-MCM-41	63	45	37	18
8	Cs-USY zeolite	63	75	25	0
9	Cs-HY zeolite	76	23	10	67
10	Cs-NaY zeolite	80	49	47	4
11	$\gamma$ -Al <sub>2</sub> O <sub>3</sub>	21	56	43	1
12	1.5-K- Al <sub>2</sub> O <sub>3</sub>	69	44	53	3
13	4.5-K- Al <sub>2</sub> O <sub>3</sub>	67	43	47	10

#### Influence of the reaction conditions

Hexanal conversion increased with increasing temperature. The significant increase was detected on the case of less active catalysts. Partly acidic properties may cause the increase of rate in under higher temperatures.

BCA:BO ratio in reaction mixture increased with increasing temperature using catalysts MgO and 1.5-K<sub>2</sub>CO<sub>3</sub>-Al<sub>2</sub>O<sub>3</sub>. Using Cs-MCM as catalyst, an opposite trend in BCA:BO ratio was observed together with increase of high-boiling products formation (Fig. 3). No straight trend in reaction result was observed using different amounts of catalyst (Table IV, rows 1-6) or reactant molar ratio (Table IV, rows 7-12). Use of different solvents (Table IV, rows 13-15) resulted into almost the same hexanal conversion, significantly higher BCA:BO ratio was observed in case of DMSO, but also the higher formation of higher boiling product.

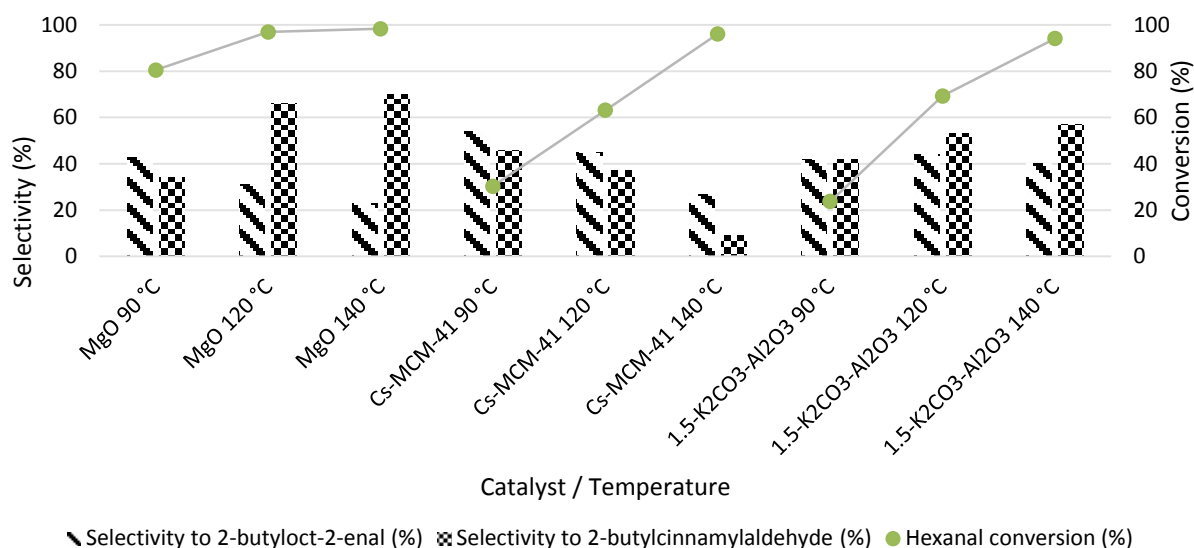


Figure 3. Influence of temperature (solvent DMF, 120 °C, 20 wt.% of catalyst MgO, HX:BZ = 1:2 (molar))

Table IV.

Reaction results changing selected reaction conditions (120 °C, 5 h; DMA = *N,N'*-dimethylacetamide)

Row	Catalyst	Catalyst amount [wt %]	Molar ratio HX:BZ	Solvent	Hexanal conversion [%]	Selectivity to 2-butyl-2-octenal [%]	Selectivity to 2-butylcinnamylaldehyde [%]	Other (%)
1	MgO	10	1:2	DMF	97	27	64	9
2	Cs-MCM	10	1:2	DMF	88	35	52	13
3	1.5-K- Al <sub>2</sub> O <sub>3</sub>	10	1:2	DMF	77	39	38	23
4	MgO	30	1:2	DMF	99	28	57	15
5	Cs-MCM	30	1:2	DMF	85	33	62	5
6	1.5-K- Al <sub>2</sub> O <sub>3</sub>	30	1:2	DMF	83	37	58	5
7	MgO	20	1:1,1	DMF	71	45	49	6
8	Cs-MCM	20	1:1,1	DMF	95	43	53	4
9	1.5-K-Al <sub>2</sub> O <sub>3</sub>	20	1:1,1	DMF	48	59	41	0
10	MgO	20	1:3	DMF	98	24	72	4
11	Cs-MCM	20	1:3	DMF	73	48	37	15
12	1.5-K-Al <sub>2</sub> O <sub>3</sub>	20	1:3	DMF	71	45	50	5
13	MgO	20	1:2	DMA	98	32	65	3
14	MgO	20	1:2	Toluene	99	23	73	4
15	MgO	20	1:2	DMSO	97	7	70	23

The reactions of benzaldehyde with pentanal (PE, Fig. 4) were made for comparison (Table V). It is worth to mention the boiling points of hexanal (131 °C) and pentanal (105 °C). Because of lower boiling point of pentanal, the decrease in reaction rate was observed, which was caused by pentanal reflux under reaction temperature, therefore lower relative concentration of linear aldehyde was present in reaction mixture during the reaction period. This caused slower reaction rate, but also remarkably suppressed undesired autocondensation comparing the reaction with hexanal. The higher reaction temperature in the case of hexanal would be desirable, but these reactions were not performed as it would require more tight laboratory equipment (e. g. autoclave).

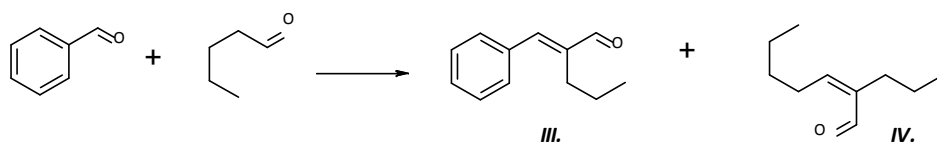


Figure 4. Aldol condensation of benzaldehyde and pentanal forming 2-propylcinnamylaldehyde (III) and 2-propylhept-2-enal (IV)

Table V

Reaction results of aldol condensation of benzaldehyde and pentanal using different catalysts (solvent DMF, 120 °C, 20 wt.% of catalyst, PE:BZ = 1:2 (molar), 24 h)

Row	Catalyst	Pentanal conversion (%)	Selectivity to 2-propylhept-2-enal (%)	Selectivity to 2-propylcinnamylaldehyde (%)	Others (%)
1	CaO	98	3	48	49
2	MgO	100	8	79	13
3	MCM-41	66	6	61	33
4	USY zeolite	69	1	67	32
5	HY zeolite	73	20	63	17
6	NaY zeolite	73	5	56	39
7	Cs-MCM-41	82	3	68	21
8	Cs-USY zeolite	61	2	74	24
9	Cs-HY zeolite	93	2	35	63
10	Cs-NaY zeolite	91	5	70	25
11	$\gamma$ -Al <sub>2</sub> O <sub>3</sub>	69	1	90	9
12	1.5-K-Al <sub>2</sub> O <sub>3</sub>	89	2	91	7
13	4.5-K-Al <sub>2</sub> O <sub>3</sub>	61	2	87	11

### Conclusion

Several catalysts modified by cesium and potassium were prepared. Prepared catalysts were used with other heterogeneous catalysts in aldol condensation of benzaldehyde and hexanal. Influence of catalyst type and amount, temperature, reactants ratio and solvent type were monitored. Comparison with reaction of pentanal and benzaldehyde was performed. Catalyst leaching was monitored using AAS.

The best obtained results in 2-butylcinnamylaldehyde synthesis (hexanal conversion 98 %, selectivity to 2-butylcinnamylaldehyde 70 %) were observed under following conditions: 140 °C, 20 wt.% of catalyst MgO, HX:BZ = 1:2 (molar), solvent DMF, 5 h. The best obtained results in 2-propylcinnamylaldehyde synthesis (pentanal conversion 89 %, selectivity to 2-propylcinnamylaldehyde 91 %) were observed under following conditions: 120 °C, 20 wt.% of catalyst 1.5-K-Al<sub>2</sub>O<sub>3</sub>, PE:BZ = 1:2 (molar), solvent DMF, 24 h.

The most basic catalyst was: 4.5-K- Al<sub>2</sub>O<sub>3</sub> according to titration results and 1.5-K- Al<sub>2</sub>O<sub>3</sub> according to TPD results.

### Acknowledgment

Financial support from specific university research (MSMT No 20/2015)

### Literature

1. Esmaili J., Ehsani Mr. R., J. Encapsulation Adsorpt. Sci. 3, 57 (2013).
2. Li X., Yu D., Zhang W., Li Z., Zhang X., Huang H., Appl. Catal., A 455, 1 (2013).
3. Bal R., Chaudhari K., Sivasanker S., Catal. Lett. 70, 75 (2000).
4. Minet J., Abramson S., Bresson B., Sanchez C., Montouillout V., Lequeux N., Chem. Mater., 16, 3955 (2004).
5. Xie Y., Sharma K. K., Anan A., Wang G., Biradar A. V., Asefa T., Journal of Catalysis 265(2), 131 (2009).
6. Tanae K., Yamaguchi K., J. Res. Inst. Catal., Hokkaido Univ. 11, 179 (1964).
7. Wenlei X., Hong P., Ligong C., J. Mol. Catal. A: Chem. 246, 24 (2006).

## UTILIZATION OF OIL FRACTIONS FROM PYROLYSIS OF WASTE TIRES

Šťávková G., Soukupová L., Kolena J.

*Výzkumný Ústav Anorganické Chemie, UniCRE, Chempark Litvínov, Záluží – Litvínov, 436 70, Česká Republika, Phone: 476 163 659, E-mail: gabriela.stavova@vuanch.cz, jiri.kolena@vuanch.cz*

### Introduction

The amount of waste tires worldwide keeps increasing every year becoming thus a significant environmental problem. The number of used tires is estimated in the range from about 55 000 to 70 000 t / year in the Czech Republic. About 20% of this amount is further processed, the rest being landfilled. Storing tires in landfills is not only demanding in terms of landfilling volume, but there are also problems with the tires behavior in the landfill body. There are only few possibilities of utilising the waste tires, which are economic and environmental-friendly at the same time. One of them is the vacuum pyrolysis which seems to be most promising way of the used tires disposal both from economic and from environmental point of view. This process converts waste tires mixture to carbon, oil, gas and metal scrap. From this products portfolio, mainly the pyrolysis oil has a high potential to become an interesting chemical intermediate. Its composition depends on the temperature in pyrolysis, but, with no regard to the pyrolysis conditions, there is always significant content of valuable aromatics, in particular benzene, toluene, xylenes, and naphthalene. The residue after the separation of BTX and naphthalene could be used as fuel component. But high content of sulfur compounds is the main disadvantage of the oil from the waste tires pyrolysis. These compounds have to be removed prior to further oil use.

### Literature study about the possibilities of utilization of oil products from waste tires pyrolysis

Generally, tires are composed of mixtures of natural and synthetic vulcanized rubber (about 50w.%), carbon black and other fillers (silica) ( about 26w.%) and the remaining part consists of other fibers (14w.%) admixture of antioxidants, plasticizers (5%) and steel wires (w.5%) [1].

As for elemental composition, tires contain big amount of carbon, nitrogen and sulphur which is appropriately reflected by the composition of the oil from tires pyrolysis. Water content in the rubber is another complication as it makes the thermal processing difficult, additional complication being the water content in pyrolysis oil [2].

In general, pyrolysis product consists of pyrolysis gas, oil and solid residue. The composition of each product phase depends first of all on pyrolysis temperature and the starting material composition. The gas phase contains predominantly hydrogen, methane, ethane, butadiene and H<sub>2</sub>S. As its heat of combustion is around 37 MJ/m<sup>3</sup>, it can be used as fuel in the pyrolysis itself [4].

The residue after pyrolysis contains besides carbon metals and their oxides. The amount of carbon initially increases with increasing pyrolysis temperature, but above 500 °C, carbonization is speeded up and the carbon amount starts increasing. Yield of hydrogen, unlike that of carbon, initially increases with the temperature increase and starts decreasing at higher temperature as a result of long chain hydrocarbons cleavage, the products of which (lower hydrocarbons) come into the gaseous phase [3].

Pyrolysis oil composition depends also, first of all, on the starting material character and pyrolysis temperature [5].

The pyrolysis oil from waste tires is a mixture of alkanes, alkenes and aromatics which contain 6-24 carbon atoms, the latest being the main oil components. The most significant components are aromatics, representing 53.4 to 74.8 mass %, they are formed by Diels-Alder reactions during pyrolysis. Benzene, toluene, xylenes, and styrene represent important monocyclic aromatics in the pyrolysis oil, naphthalene being the most important representative of polycyclic aromatic hydrocarbons. Additionally to hydrocarbons, there is relatively high content of nitrogen compounds (2.5 – 3.5 mass %) as well as oxygen components (2.3 – 4.8 mass %). Typically more than 30 % of hydrocarbons have boiling points between 70 and 210 °C so they can be used as gasoline components. Another 60 % of hydrocarbon boiling between 150 and 370 °C i.e. can be used as middle distillates components. [4,5,6,7]. However, high sulphur content (0.5 – 1.5 mass %) is a considerable obstacle for this way of utilization [5]. The amount of both Sulphur and nitrogen in the product is almost independent on the pyrolysis temperature. Sulphur has been disclosed as being present in the form of heterocyclic compounds like alkyl thiophenes e.g. 2-methylthiophene, 3-methylthiophene, 2-ethylthiophene, benzothiophene e.t.c. [8] Nitrogen is present in the form of amines, amides, nitriles, pyridine and its derivatives, pyrrole, quinoline and (mainly) indole [9].

## Experimental

### Methods of analyses

Density was determined by means of DMA 48 (Anton Paar) density meter. Sulphur content was determined by means of SW-Trace SN Cube device, while nitrogen content was measured by Total Nitrogen Analyzer TN-100 (Mitsubishi). Selective analyses by both of these Mitsubishi devices, is based on sample gasification and subsequent measurement of chemoluminescence (N) or UV fluorescence (S) respectively.

Simulated distillation of the samples was performed by HP 7890 GC equipped with FID detector and on-column injection.

The composition of particular distillation fractions was determined by GC/MS method with the use of Thermo Scientific, Trace ITQ 1100 device

### Fractionation of the oil from waste tires pyrolysis by distillation

The crude pyrolysis oil was separated to narrower fractions by a combination of atmospheric and vacuum distillation by means of a double mantle distillation column (vacuum in between the mantle walls). The atmospheric distillation continued up to 210 °C in reboiler as polymerization of some unsaturated compounds could have taken place above this temperature. Four distillation cuts had been obtained before the temperature limit was reached.

After interruption the distillation and cooling down the reboiler content, the distillation continued at decreased pressure, at the range of 12 to 2.6 kPa (90 to 9 mm Hg). 7 distillation fractions were obtained. Polymerization in reboiler was observed at the end of vacuum distillation at 210°C.

### Results and discussion

The oil from waste tires pyrolysis is very similar to the pyrolysis fuel oil from conventional steam cracker. It is apparent from Table I, in which its basic physical properties are compared with those of gasoline, diesel and typical oils from steam cracker (PGO, PFO)

Table I: Characteristic parameters of oil from pyrolysis of waste tires in comparison with the characteristics of the oils from steam cracking of hydrocarbons and automotive fuels.

	unit	PGO	PFO	Oil from waste tire	gasoline	diesel
density 20°C	kg/m <sup>3</sup>	920-985	1045-1150	900-915 (15°C)	720-775	80-845
flash point	°C	70-95	101-140	40-50	>55	-25
viscosity 100 °C	mm <sup>2</sup> /s		25-50			
sulfur	% hm.	max. 0,5	max. 1,0	1,5	<0,001	<0,001
water	% hm.	max. 0,1	max. 0,1			
<b>Distillation</b>						
IBP	°C	180-200	min. 200	85	30	198
50% vol.	°C	205-220	min. 300	225		279
FBP	°C	230-270	min. 300	550	215	360
calorific value	MJ/kg	40	40	38-42	46,4	43,8

By the combination of atmospheric and vacuum distillation, altogether 11 narrow fractions were obtained. Based on GC analyses, with respect to potential utilization, wider fractions were created by joining (mixing) some of original distillation cuts. By mixing cuts no 1 to 5, the fraction with boiling in the range of 48 to 152.1 was created. Its composition (see Table II) is quite similar to that of petrochemical BTX fraction. It can be therefore used as a source material for benzene production by hydrodealkylation, after the sulphur content is substantially decreased. Joined fraction 6-7 ranks among middle distillates by its boiling point range (152 – 216 °C). However, it contains relatively big amount of aromatics (see Table II) and its potential utilization is unclear at the moment. The distillate No.8 was naphthalene concentrate which can be used for naphthalene production by distillation or by crystallization. Higher fraction (joined distillates 9-11), with boiling point in the range of 240 to 299 °C, can hardly find utilization in petrochemical production but can be used as feedstock for hydrocracking.

Boiling point range and composition of joined distillation fractions are presented in Table II.

Table II: Composition of single fraction from atmospheric and vacuum distillation of pyrolysis oil from waste tires.

	<b>fraction 1-5</b>	<b>fraction 6-7</b>	<b>fraction 8</b>	<b>fraction 9-11</b>	<b>feedstock</b>
<b>weight [g]</b>	402.48	171.86	86.83	268.29	1513.55
<b>weight %</b>	26.59	11.35	5.74	17.73	100
<b>distill.range [°C]</b>	48.5-152.1	155.8-216	217.8-239	240-298.8	49 - 550
<b>compound [w.%]</b>					<b>w.% in feedstock</b>
<b>benzene</b>	17.46				4.64
<b>toluene</b>	28.32				7.53
<b>ethylbenzene</b>	6.14				1.63
<b>styrene</b>	2.84	0.98	0.92	0.41	0.99
<b>xylenes</b>	16.47	1.6	0.03		4.56
<b>ethylbenzenes</b>	0.31	0.51	0.02		0.14
<b>methylstyrenes</b>	0.23	9.79	0.6		1.21
<b>trimethylstyrenes</b>		14.18	0.03	0.14	1.64
<b>indane</b>		3.36	0.02		0.38
<b>indene</b>		0.87	0.78	0.22	0.18
<b>ethylstyrenes</b>			0.26		0.01
<b>dimethylstyrenes</b>		0.52	2.28	0.02	0.19
<b>methylindanes</b>		2.1	1.07		0.3
<b>methylindenes</b>		5.02	9.66	0.04	1.13
<b>1,2 dihydronaphtalene</b>		0.47	1.19		0.12
<b>naphtalene</b>		5.36	45.28	4.5	4
<b>dimethylindenes</b>			4.96	1.1	0.48
<b>2 methylnaphtalene</b>			1.57	10	1.86
<b>1 methylnaphtalene</b>			1.02	4.71	0.89
<b>trimethylindenes</b>				0.62	0.11
<b>biphenyle</b>				4.45	0.79
<b>2 ethylnaphtalene</b>				2.44	0.43
<b>1 ethylnaphtalene</b>				0.7	0.12
<b>2,6 dimethylnaphtalene</b>				3.26	0.58
<b>methylnaphtalenes</b>				3,33	0.59
<b>difenylmethane</b>				4,73	0.84
<b>acenaftylene</b>				0,87	0.16
<b>methylbiphenyle</b>				2,3	0.41
<b>others</b>	28,23	55,24	30,31	56,16	64.06

The oil from the pyrolysis of waste tires contains large amounts of sulfur. The main source of sulfur in fraction 1-5 is probably thiophene (b.p. 84°C) and its alkyl derivatives, in fraction 8-9 there is probably benzothiophene (b.p.222°C) and in fraction 10-11 there can probably be alkyl derivatives of benzothiophene. The main source of nitrogen in fraction 6 is probably benzonitrile (b.p. 190°C) while it is indole in fraction 9-10. Content of sulfur and nitrogen is presented in Table III.

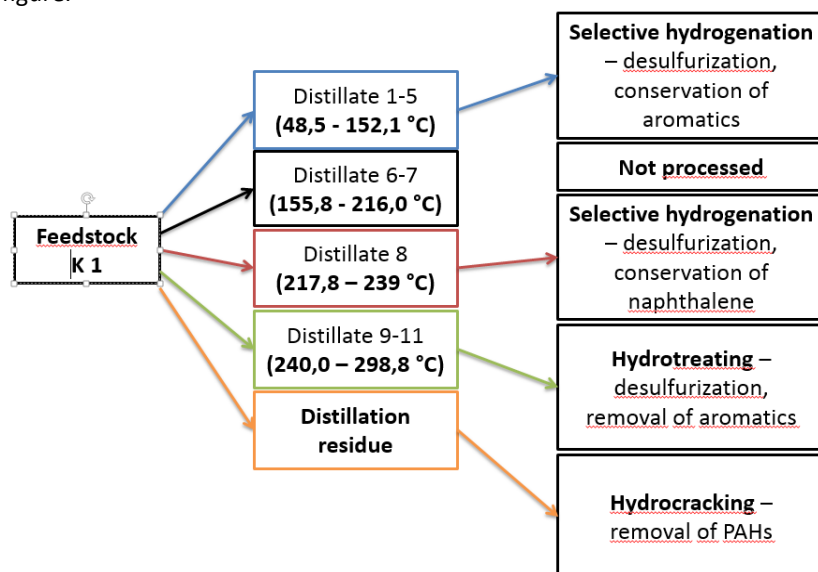
Table III: Content of sulfur and nitrogen in particular pyrolysis oil fractions.

fraction	S [w.%]	N [w.%]
1-5	0.46	0.22
6-7	0.29	0.6
9-11	1.39	0.6
dist. rest	1.204	0.4

High content of sulphur and nitrogen is characteristic for all distillation fraction which can be separated from the oil fraction from spent tires pyrolysis. These fractions, though very promising in terms of further utilization, have to be desulphurized prior to subsequent processing. Conventional hydroprocessing on sulphidic form on metal catalyst might be a suitable method but needs further research study.

### Conclusions

Pyrolysis oil, obtainable from waste tires seems to be very promising raw material for the use in both petrochemical industry and refineries. It can be an important source of diversity of aromatics and it can be comprehensively used. The oil fraction with boiling point ranging between 48 and 218°C, can be an interesting source of valuable petrochemical commodities like benzene, toluene, xylenes and naphthalene. The heavier fraction, of boiling range between 220 and 300°C can be used as a component of diesel fuel and the heavier residue can be the feedstock for hydrocracking. Single fractions obtained from pyrolysis oil from waste tires must be pre-treated prior to final processing. The proposed methods of treatment are summarized in following figure.



### Acknowledgment:

*This publication was created using the infrastructure supported in a frame of the project "Unipetrol centre for research and education" ev. No. CZ.1.05/2.1.00/03.0071, which is funded through the Operational Programme for Research and Innovation Development of the Structural Funds (specifically the European Regional Development Fund) and the state budget of the Czech Republic*

### Literature

- Overhoff, D., Tires. In Ullmann's Encyclopedia of Industrial Chemistry, Wiley-VCH Verlag GmbH & Co. KGaA: 2000.
- Gray, T., Tire Derived Fuel: Environmental Characteristic and Performance. The Southeast Regional Scrap Tire Management Conference, Nashville, Tennessee 1997
- González, J. F.; Encinar, J. M.; Canito, J. L.; Rodríguez, J. J., Pyrolysis of automobile tyre waste. Influence of operating variables and kinetics study. Journal of Analytical and Applied Pyrolysis 2001, 58-59, 667-683.

4. Cunliffe, A. M.; Williams, P. T., Composition of oils derived from the batch pyrolysis of tyres. *Journal of Analytical and Applied Pyrolysis* 1998, 44, 131-152
5. Juchelková, D.; Poláčková, Z.; Iva Macháčková; Sassmanová, V.; Frantík, J., Srovnání podílů vybraných aromatických uhlovodíků v dehtové frakci po pyrolýze pneumatik. *Waste Forum* 2012, 4, 198 - 203.
6. Rodriguez, I. d. M.; Laresgoiti, M. F.; Cabrero, M. A.; Torres, A.; Chomón, M. J.; Caballero, B., Pyrolysis of scrap tyres. *Fuel Processing Technology* 2001, 72, 9-22.
7. VŠB, FITE a. s., Studie zařízení na pyrolytický rozklad odpadů I [online]. Dostupné z: <<http://www.opzp.cz/ke-stazeni/252/10821/detail/studie-zarizeni-na-pyrolyticky-rozklad-odpadu-i/>> 2010, staženo 2.11.2014.
8. Benallal, B.; Roy, C.; Pakdel, H.; Chabot, S.; Poirier, M. A., Characterization of pyrolytic light naphtha from vacuum pyrolysis of used tyres Comparison with petroleum naphtha. *Fuel* 1995, 74 (11), 1589-1594.
9. Mirmiran, S.; Pakdel, H.; Roy, C., Characterization of used tire vacuum pyrolysis oil. Nitrogenous compounds from the naphtha fraction. *Journal of Analytical and Applied Pyrolysis* 1992, 22, 205–215.

## A COMPARATIVE STUDY OF LIQUID- AND GAS-PHASE CYCLOPENTENE HYDRATION CATALYZED BY THE MCM-22 ZEOLITE

**Krupka J.**<sup>1</sup>, Otmar J.<sup>1</sup>, Pawlesa J.<sup>2</sup>

<sup>1</sup>*Department of Organic Technology, Faculty of Chemical Technology, University of Chemistry and Technology, Prague, Czech Republic*

*Jiri.Krupka@vscht.cz*

<sup>2</sup>*J. Heyrovský Institute of Physical Chemistry, Academy of Sciences of the Czech Republic, Prague, Czech Republic (Present address: Engineering Design Centre, Poland)*

### Abstract

The study deals with technological aspects of the direct hydration of cyclopentene to cyclopentanol. The catalytic properties of the MCM 22 zeolite were studied in the case of cyclopentene hydration both in liquid and gas phases. MCM-22, unlike other solid acid catalysts, is highly selective for the formation of cyclopentanol in the liquid-phase hydration in the slurry arrangement. It suppresses completely the undesirable etherification of cyclopentanol and allows obtaining cyclopentanol with almost 99% selectivity. But the liquid-phase hydration was found to lead to rapid deactivation of the zeolite. The deactivation is caused mainly by a formation of carbon deposits in the pores of the zeolite. When hydrating in the gas phase on the fixed bed of granular catalyst, it could be easy to periodically reactivate the catalyst in situ. However, it has been found that the exceptional selectivity of MCM-22 to the cyclopentanol formation is characteristic only for the liquid-phase hydration; the reaction in the gas phase is unselective. Furthermore, the equilibrium conversion of cyclopentene to cyclopentanol in the gas-phase hydration has been found to be industrially unusable - below 1 % (e.g. under atm. pressure, at 120 °C and with a molar ratio of cyclopentene to water 1:5, it is as low as 0.3 %).

### Introduction

The present study deals with technological aspects of the direct hydration of cyclopentene (CPEN) to cyclopentanol (CPOL) and represents a part of a broader research aimed at alternative possibilities of the production of cyclopentanone and other cycloC5 derivatives from accessible petrochemical materials<sup>1,2</sup>. The hydration of cyclopentene is a potential intermediate in their production<sup>3,4,5</sup>.

Basically, the cyclopentene hydration or, generally, olefin hydration are simple chemical reactions but their implementation in industrial scale brings considerable complications. There are several variants of how to solve the olefin hydrations:

- so-called indirect two-stage process using a mineral acid
- direct process with phosphoric acid deposited on a solid carrier
- or a liquid-phase process catalyzed by an cation exchanger or zeolites.

Each of the variants has its drawbacks and complications to be eliminated or solved. For example, a common negative feature of the so-called direct processes catalyzed by cation exchangers or phosphoric acid deposited on a solid carrier is the releasing of the free acid into the reaction mixture which requires its neutralization. During the indirect process using sulfuric acid, cyclopentene first reacts with the acid to yield alkylsulfates which are, in the next step, hydrolyzed by water to cyclopentanol. In this way, 60 % of the theoretical yield of cyclopentanol is achieved. Significant drawbacks of this technological solution are:

- corrosion of the device caused by the presence of the acid
- necessity of an energy consuming concentration of the diluted acid prior to reusing
- undesirable dehydration of cyclopentanol during its isolation by a rectification of the reaction mixture after hydrolysis.

An unfavorable shift of the reaction equilibrium is another important negative feature of all direct processes of hydration of cyclopentene. The hydration equilibrium is strongly shifted toward reactants, much more than in case of, e.g., hydration of cyclohexene. For the hydration in the liquid phase at 120 °C and water:cyclopentene 5:1 molar ratio, the equilibrium conversion of cyclopentene is as low as 4 % (cit.)<sup>6</sup>. Another complicating factor of the hydration of cyclopentene is that the reaction system consists of two phases, organic and aqueous, wherein each of them contains a part of the product. Moreover, cyclopentanol forms an azeotrope with water (b.p. 96.6 °C, 43 vol.% cyclopentanol) which makes the industrial solution to the problem of the product separation complicated and costly.

Hydration of cyclopentene catalyzed by cation exchangers, alumina, amorphous aluminosilicates and common types of commercial zeolites (ZSM-5, Beta, Mordenit, Ferierit) is totally non-selective<sup>6,7</sup>. Large amounts of undesirable by-products are formed, especially dicyclopentylether and cyclopentylcyclopentene (Figure 1). At

achieving the reaction equilibrium, the selectivity for desirable cyclopentanol is lower than 80 % (120 °C, molar ratio H<sub>2</sub>O/CPEN = 5).

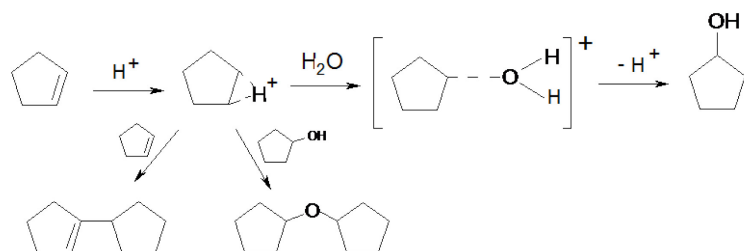


Figure 1. Reaction mechanism and formation of main by-products

Direct hydration of cyclopentene is selective only with zeolite of the type MCM-22 which suppresses totally the etherification of cyclopentanol, and can be used to produce cyclopentanol with a selectivity ( $S_{\text{CPOL}}$ ) close to 99 % (cit.<sup>6-8</sup>). MCM-22 is a zeolite with a medium porosity and a three-dimensional channel structure. Similarly to ZSM-5, it contains two 10-MR pore openings which, unlike ZSM-5, do not intersect and are independent of each other. Moreover, within the channel structure of MCM-22, cavities larger than the pores themselves are present. The size of the pores of MCM-22 is only by ca. 1 Å smaller than for ZSM-5, and such a difference is sufficient to influence dramatically the selectivity of the hydration of cyclopentene. While in the pores of ZSM-5 a more spacious by-product, i.e., dicyclopentylether, can be formed, no such formation takes place in the pores of MCM-22. The MCM-22 zeolite is used industrially in several technologies of the benzene alkylation with propylene and ethylene<sup>9</sup>.

In the past, we have dealt in detail with the liquid-phase hydration of cyclopentene in the batch slurry arrangement<sup>7,8</sup>. We have also tested the extent of deactivation, namely in the form of the reuse of the catalyst in the next batch hydration cycle. No such information has been published for the MCM-22 catalyst in the literature so far. Our research revealed an essential weak point in the use of MCM-22 and other zeolite catalysts for this reaction: their rapid deactivation. Already at the first repeated use of MCM-22 in the next hydration batch cycle, the reaction rate of hydration drops to half. The reason is a formation of carbon deposits in the pores of the zeolite. Also cyclopentadiene present as an impurity in the raw material is partially responsible for the rapid deactivation, but the activity of the zeolite substantially decreases also when cyclopentene freed from dienes is used. Oligomeric deposits in the pores of the catalyst are probably formed also by an acid-catalyzed reaction of the olefinic cyclopentene. Furthermore, also a partial undesirable dealumination of the zeolite contributes to the drop of its activity. It was found that the catalytic activity of the MCM-22 zeolite can be restored to original value neither by its reactivation by air oxygen in the calcination oven at 550 °C, nor by wet oxidation using hydrogen peroxide (Table I).

Table I

Repeated use of the MCM-22 catalyst for the batch hydration of cyclopentene in a liquid phase<sup>8</sup>

Catalytic cycle	Catalyst use degree	Reaction time [h]	$X_{\text{CPEN}}$ [mol. %]	$S_{\text{CPOL}}$ [mol. %]
1.	Fresh	72 <sup>d</sup>	4.24 (equilibrium)	98.22
1.	Fresh	8 <sup>e</sup>	2.35	97.21
2.	1x used	8 <sup>e</sup>	1.93 <sup>a</sup>	95.42
3.	2x used	8 <sup>e</sup>	1.52 <sup>a</sup>	92.08
4.	3x used	8 <sup>e</sup>	1.45 <sup>a</sup>	92.88
5.	Reactivated <sup>b</sup>	8 <sup>e</sup>	1.41	93.33
6.	Used	8 <sup>e</sup>	1.04 <sup>a</sup>	91.74
7.	Reactivated <sup>c</sup>	8 <sup>e</sup>	0.46 <sup>a</sup>	85.82

120°C, weight ratio CPEN/H<sub>2</sub>O/catalyst = 34/45/1,8; 10 ppm of cyclopentadiene in starting cyclopentene

<sup>a</sup> Corrections on catalyst weight loss

<sup>b</sup> Catalyst reactivated by air oxygen at temperature programme 1 K.min<sup>-1</sup>/823 K/9 h

<sup>c</sup> Catalyst reactivated by liquid hydrogen peroxide at 353 K

<sup>d</sup> long-term experiment to determine the equilibrium conversion of cyclopentene

<sup>e</sup> short 8h-experiments to monitor changes in the catalyst activity

Hence, an alternative variant of the realization of the direct cyclopentene hydration was tested, namely the process running in the gaseous phase of the reactor with a fixed bed of the granulated MCM-22 catalyst. Under

such conditions, the catalyst could periodically be reactivated *in situ*. The results of this experimental research are the subject of this paper.

### Experimental

Na<sup>+</sup> form of zeolite MCM-22 was prepared using a method published by Corma et al.<sup>10</sup>. Catalyst was transferred into NH<sub>4</sub><sup>+</sup> form using the conventional ion-exchange method: A calcined catalyst sample was treated with 0.5M NH<sub>4</sub>NO<sub>3</sub> solution (100 ml of solution to 1 g of catalyst sample) for 4 hours at 293 K four times under vigorous stirring. The ion exchanged catalyst sample was filtered, washed with distillate water, and dried. Catalyst was activated (transferred into H<sup>+</sup> form) by calcination at temperature of 823 K (1K/min, and maintained at 823 K for 6 hours). Thus, a sample with Si/Al ratio of 15 and with an average grain size of 1 μm was obtained. For the reaction in the gas phase, the catalyst powder was further tabletted (using 3% graphite), crushed and granulated to final size of 1 mm.

The research of the hydration in the gas phase was performed in a laboratory through-flow reactor with a fixed bed of the catalyst grains, at 120, 140 and 160 °C. A heated, tube integral reactor with controlled jacket temperature was used. The inner diameter of the reactor was 1.5 cm and the length of the catalyst bed was 12 cm. The catalyst bed contained 5.6 g of the MCM-22 zeolite in a form of granules with the size of 0.8-1.2 mm. Cyclopentene and water were injected on the top of the reactor in mole ratios of 1/1, 1/5, 1/15 and 1/30 (using independent pumps). A condenser was placed on the reactor outlet. After attaining a steady state, the reaction mixture behind the condenser was collected into a solvent, namely isopropylalcohol, with which it was simultaneously homogenized. The content of organic substances in the reaction mixture was determined by the GC analysis. The assessment was performed by the method of inner normalization. By-products were identified using GC/MS. The content of cyclopentadiene in cyclopentene used for the experiments was below 10 ppm.

### Results

One of the aims was to find out how the reaction conditions (temperature, cyclopentene/water mole ratio, catalyst load) affect the selectivity of the reaction and the degree of conversion of cyclopentene. The next task was to follow the deactivation of the catalyst and to verify if it can be reactivated *in situ*. Hydration experiments in the gaseous phase were performed under atmospheric pressure. During the hydration reaction, the molar number decreases. Therefore, a higher pressure should be favorable for the equilibrium but there was no pressure apparatus at our disposal. Nevertheless, even the results obtained under atmospheric pressure can yield useful information about the extent of the catalyst deactivation and the effect of reaction conditions on the course of the hydration.

Since it was found out that the catalyst deactivates only very slowly, the effect of the reaction conditions (catalyst load, cyclopentene/water mole ratio, reaction temperature) was tested in a single continuous experiment without the necessity of the catalyst reactivation. To verify the possibility to reactivate the catalyst, the catalyst deactivation was accelerated by adding first 0.1 % and then 1 % cyclopentadiene to cyclopentene being injected into the reactor. The catalyst reactivation was performed *in situ*: first by the nitrogen/air mixture and then by air only at 480 °C for the time period of 10 hrs.

#### **Effect of catalyst load**

At 120 °C and the cyclopentene/water molar ratio of 1/5, hydration experiments were performed with the catalyst loads of 0.54, 0.89 and 1.79 g<sub>cat</sub>·hr/g<sub>CPEN</sub>, and it was followed if, under the chosen conditions, the equilibrium conversion of cyclopentene was achieved. Concentrations of cyclopentanol in the reaction mixture in the reactor outlet were virtually the same for all the three loads. It follows that, in the range of the catalyst load under study, the obtained values of the outlet cyclopentanol concentration can be considered as equilibrinous. Regrettably, the equilibrium conversion of cyclopentene is very low: below 1%. This was confirmed also by experiments performed in the same apparatus and the same reaction conditions with another catalyst (ZSM-5).

#### **Effect of the cyclopentene/water molar ratio**

To assess the effect of the cyclopentene/water molar ratio on the course of the hydration of cyclopentene in gaseous phase on the MCM-22 zeolite, experiments were performed with the cyclopentene/water molar ratios of 1/1, 1/5, 1/15 and 1/30. Reaction temperature was 120 °C. Results are presented in Table II. A higher excess of water in the feed has a favorable effect on the selectivity to cyclopentanol. With the change of the cyclopentene/water mole ratio from 1/5 to 1/30, the concentration of the most significant by-products, i.e., 1-cyclopentylcyclopentene and dicyclopentylether, decreased markedly. On the contrary, the equilibrium

concentration of cyclopentanol increased from 0.36 to 0.53 %. When the hydration of cyclopentene in the gaseous phase is to be done on the industrial scale, a high excess of water in the inlet to reactor cannot be applied because its evaporation would consume a large amount of energy. This problem could be solved by recycling cyclopentene and water in the gaseous phase. However, this is complicated by the formation of the water-cyclopentanol azeotrope with a minimum of the boiling point (96.6 °C at atmospheric pressure). Cyclopentanol (b.p. 140 °C) should be removed from the column base. If, instead of this, all cyclopentanol together with recycled cyclopentene leaves from the column head to the reactor, its separation would be hindered and, moreover, the equilibrium of the hydration reaction would be unfavorably affected.

Table II.

The effect of the CPEN/water ratio on the composition of the hydration product in the gaseous phase

Molar ratio CPEN : H <sub>2</sub> O	1/1	1/5	1/15	1/30
Catalyst loading [g <sub>cat.</sub> · hr / g <sub>CPEN</sub> ]	1.79	0.89	0.71	0.39
Q <sub>m(CPEN)</sub> [g/h] <sup>a</sup>	10	5	4	2.2
Q <sub>m(water)</sub> [g/h] <sup>a</sup>	2.6	6.6	16	18
Compound	Composition [wt. %] <sup>b</sup>			
Cyclopentene	99.30	99.17	99.41	99.36
cyclopentanol	0.19	0.36	0.48	0.53
1-cyclopentylcyclopentene	0.07	0.07	0.01	0.01
dicyclopentylether	0.30	0.30	0.04	0.04
others	0.15	0.11	0.05	0.07
X <sub>CPEN</sub> [mol.%]	0.40	0.52	0.44	0.49
S <sub>CPOL</sub> [mol.%]	38.50	55.25	86.56	85.63

S<sub>CPOL</sub> - Selectivity to CPOL defined on molar basis, T=120°C, 5.6 g of MCM-22, equilibrium conversion of CPEN reached;

<sup>a</sup> feed rate into the reactor, <sup>b</sup> related to the organic part

### Effect of temperature

The hydration of cyclopentene is an exothermic reaction. Therefore, the value of the equilibrium constant decreases with increasing temperature. The effect of temperature on the conversion of cyclopentene and the selectivity to cyclopentanol was studied at 120, 140 and 160 °C. In all cases, the water/cyclopentene molar ratio was 1/5. It is evident from Table III that increasing temperature has a very unfavorable effect on the selectivity to cyclopentanol. Upon increasing temperature from 120 to 160 °C, the equilibrium concentration of cyclopentanol decreased from 0.36 to 0.08 %.

Table III

Effect of temperature on the product composition

Reaction temperature [°C]	120	140	160
Compound	Composition [wt. %] <sup>a</sup>		
cyclopentene	99.17	98.94	98.18
cyclopentanol	0.36	0.18	0.08
1-cyclopentylcyclopentene	0.07	0.14	0.3
dicyclopentylether	0.3	0.52	1.02
others	0.11	0.22	0.43
X <sub>CPEN</sub> [mol.%]	0.52	0.58	0.89
S <sub>CPOL</sub> [mol.%]	55.25	24.77	7.35

S<sub>CPOL</sub> - Selectivity to CPOL defined on molar basis, molar ratio CPEN/H<sub>2</sub>O – 1/5, 5.6 g of MCM-22, equilibrium conversion of CPEN reached; <sup>a</sup> related to the organic part

### Deactivation of the catalyst

The extent of the deactivation of the MCM-22 catalyst was studied at the reaction temperature of 120 °C and the cyclopentene/water molar ratio of 1/5. The value of the cyclopentanol concentration decreased with

increasing time of the catalyst exposition only very slowly. After 60 hrs of continuing the experiment, during which approx. 300 g of cyclopentene was processed, the concentration of cyclopentanol at the reactor outlet dropped from 0.36 to 0.31 %. To check the possibility of the catalyst reactivation, the deactivation of the catalyst was enhanced by injecting cyclopentene with cyclopentadiene added which is responsible for a rapid deactivation of the zeolite catalysts. Shortly before dosing cyclopentene containing cyclopentadiene, the concentration of cyclopentanol in the reaction mixture was 0.31 %. After 6 hrs of dosing cyclopentene with 0.1 % cyclopentadiene, the outlet concentration of cyclopentanol decreased to 0.26 %. In order to attain an even higher decrease of the cyclopentanol concentration, the content of cyclopentadiene in injected cyclopentene was increased to 1 %. After further 6 hrs, the reactivation of the catalyst was started. The catalyst reactivation *in situ* can be performed by various methods. Low-temperature processes using hydrogen peroxide or ozone as the oxidation agents represent one of the possibilities. In our case, the catalyst reactivation was done by an oxidation of the carbon deposits by air at 480 °C. The heating in order to achieve the required temperature lasted 4 hrs. During this process the flow rate of air was 20 mL/min and that of nitrogen 10 mL/min. Upon attaining 480 °C, the catalyst was reactivated for the period of 10 hrs with 30 mL/min air flow rate. The experiment with reactivated catalyst was performed under identical conditions as the preceding experiments. Reactivation of the catalyst restored fully its activity. The concentration of cyclopentanol in the reaction mixture increased to 0.38 % (Table IV).

Table IV.

Course of the catalyst deactivation and restoring its activity by air oxygen

Status of catalyst	fresh	) <sup>a</sup>	1%	After reactivation
Content of CPD in starting CPEN	< 10 ppm	< 10 ppm	1%	< 10 ppm
TOS [h]	6	64	76 <sup>b</sup>	80 <sup>c</sup>
Compound	Composition [wt. %] <sup>a</sup>			
cyclopentadiene	< 10 ppm	< 10 ppm	1.3	< 10 ppm
cyclopentene	99.11	99.56	97.91	99.14
cyclopentanol	0.36	0.31	0.26	0.38
1-cyclopentylcyclopentene	0.08	0.007	0	0.06
dicyklopentylether	0.33	0.036	0	0.26
others	0.12	0.08	0.54	0.17
$X_{CPEN}$ [mol.%]	<b>0.54</b>	0.31	-	<b>0.55</b>
$S_{CPOL}$ [mol.%]	<b>53.0</b>	<b>76.07</b>	-	<b>54.47</b>

$T=120^{\circ}\text{C}$ , 5.6 g of MCM-22, molar ratio CPEN/ $\text{H}_2\text{O}$  – 1/5; catalyst loading 0.89  $\text{g}_{\text{cat}} \cdot \text{hr} / \text{g}_{\text{CPEN}}$

Reactivation *in situ* by air at 480°C (heating of 4hr to 480°C, flow rate 10 ml  $\text{N}_2$  /min + 20 mL air /min, then 30 mL air/min for 10 hrs); <sup>a</sup> 300g of CPEN processed, <sup>b</sup> after 12 hrs feeding CPEN with CPD, <sup>c</sup> 4hr on stream after the reactivation by air,

<sup>d</sup> related to the organic part

It is interesting that, with increasing period of the catalyst exposition, the concentration of the main by-products in the reaction mixture, that is, 1-cyclopentylcyclopentene and dicyclopentylether, gradually decreased. When cyclopentene with cyclopentadiene added was dosed into the reactor, during 12 hrs these compounds disappeared completely from the reaction mixture. The reactivation of the catalyst resulted in increasing the formation of 1-cyclopentylcyclopentene and dicyclopentylether to the original values. Gradual drop and repeated rise of the concentration of the discussed substances is evident from Table IV. The reason why the spacious molecules of by-products of the cyclopentene hydration disappeared is probably the presence of carbon deposits which can diminish the catalyst pores and thus prevent the formation of these compounds. Such a phenomenon is described in a paper<sup>11</sup> by M. W. Kim *et al.* dealing with a selective alkylation of 2-isopropyl-naphthalene by isopropylalcohol on the MCM-22 zeolite. Also zeolites of the type Beta, mordenite and Y were studied. Of all catalysts under study, the increase of the selectivity to  $\beta,\beta$ -diisopropyl-naphthalene with increasing time of catalyst exposition was observed only for the MCM-22 zeolite. Another possible explanation of this phenomenon is that the carbon deposits can block the acidic Brønsted centers of the catalyst located predominantly on its outer surface. These acidic centers are “shape non-selective” and can be the cause of the formation of spacious molecules of the by-products. In a paper<sup>12</sup> by Z. Shanga *et al.*, the number of acidic Brønsted centers on the outer surface of the MCM-22 zeolite is

intentionally reduced in order to increase the selectivity of the catalyst to isobutane during the isomerization of *n*-but-1-ene. For this purpose, a method of chemical deposition of organic substances onto the catalyst surface was used. The best results were gained for the deposition of tetraethoxysilane.

### Conclusion

During the cyclopentene hydration in the liquid phase, zeolites are gradually deactivated. The catalytic activity of MCM-22 cannot be restored to the original state by the reactivation of the catalyst, be it by air oxygen in a calcination oven at 550 °C or by the wet oxidation using hydrogen peroxide. An alternative variant of a direct cyclopentene hydration was therefore checked, namely the process running in the gas phase in a reactor with a fixed bed of the MCM-22 granulated catalyst. Under such conditions, the catalyst could periodically be reactivated *in situ*. It was found out that also during the reaction in the gas phase the catalyst activity decreases with the time of the catalyst exposition. Nevertheless, the activity can completely be restored by the catalyst regeneration *in situ* using air oxygen at 480 °C. However, it was proved experimentally that the exceptional selectivity of the MCM-22 catalyst to the cyclopentanol formation is characteristic only for the hydration in the liquid phase; the reaction in the gas phase is non-selective. Moreover, it was found experimentally that the equilibrium conversion of cyclopentene to cyclopentanol during hydration in the gas phase under atmospheric pressure, at 120 °C and with the cyclopentene/water molar ratio of 1/5, is as low as 0.3 %. An increase of the reaction pressure which would shift the equilibrium composition toward the product would be impossible in this case due to the condensation of the reaction components in the catalyst bed. As we found out, the condensation of the components in the catalyst bed leads to a perceptibly more rapid deactivation of the catalyst. In order to eliminate the condensation, the effect of the increased pressure can be compensated for by an increase of the reaction temperature but, in case of the direct cyclopentene hydration, it leads to a dramatic drop of the reaction selectivity and to a repeated shift of the equilibrium to the reactants. It can be concluded that the gas-phase arrangement of the direct hydration of cyclopentene to cyclopentanol is unsuitable.

### Acknowledgment

*This study was financially supported by the project of the Ministry of Industry and Trade of the Czech Republic FT-TA3/079 "The Research of Progressive Chemical Products Based on Dicyclopentadiene"*

### Literature

1. Krupka J., Pašek J., Patera J., Fíla V.: Process for continuous production of cyclopentene of polymerization purity, Patent CZ 298 994, 26 Mar 2008.
2. Krupka J., Štěpánek J., Herink T.: *Chem. Listy.*, 102, 1107 (2008).
3. Miki H., Ota G., Fujisawa H. (Nippon Zeon Co.): JP 2001 335527, 2001.
4. Kikuchi T., Miki H., Fujisawa H. (Nippon Zeon Co): JP4055403, 2003.
5. Zeon Corporation: Press Release, May 23, 2001. [http://www.zeon.co.jp/pres\\_e/010523.html](http://www.zeon.co.jp/pres_e/010523.html).
6. Nuntasri D., Wu P., Tatsumi T.: *J. Catal.*, 213, 272 (2003).
7. Krupka J., Provazníková M.: Liquid-phase cyclopentene hydration over commercial heterogeneous acid catalysts, XXXVIII Symposium on Catalysis, 06 - 07 November 2006, Prague.
8. Hlavačková A., Krupka J., Kubů M., Otmar J., Lederer J.: *Procedia Engineering*, 42, 1917 (2012).
9. Perego C., Ingallina P.: *Catal. Today* 73, 3 (2002).
10. Corma A., Corell C., Perez-Pariente J.: *Zeolites* 15, 2 (1995).
11. Myung-Wan Kim, Jong-Ho Kim, Yoshihiro Sugi and Gon Seo Korean: *J. Chem. Eng.*, 17, 480 (2000).
12. Shang Y., Yang P., Jia M., Zhang W., Wu T.: *Catal. Commun.* 9, 907 (2008).

## HYDROCARBON CRACKING IN THE PRESENCE OF ALCOHOL: THEORETICAL STUDY

**Karaba A.**<sup>1,2\*</sup>, Zámstný P.<sup>2\*</sup>, Lederer J.<sup>1</sup>

<sup>1</sup>Research Institute of Inorganic Chemistry, Ústí nad Labem, Czech Republic

<sup>2</sup>Department of Organic Technology, Faculty of Chemical Technology, University of Chemistry and Technology Prague, Prague, Czech Republic

\*e-mail: adam.karaba@vscht.cz; petr.zamostny@vscht.cz

### Introduction

Steam-cracking is very important industrial process for large-scale olefins production. The most of ethylene, substantial part of propylene, butenes and butadiene production is obtained by cracking hydrocarbons. Aromatic compounds, such as benzene, toluene or naphthalene are also important products of steam-cracking. Ethane, liquefied petroleum gas (LPG) or gasoline are commonly processed type of feedstock but the importance of atmospheric gas oils and other refinery streams grows. Processing of heavy hydrocarbons feedstock has certain disadvantages, firstly a significant fraction of products is formed by pyrolysis oil which is not desired in such quantity for its limited consumption. The commonly known fact that coke-forming process running on the reactor coil wall is much faster during heavy feedstock cracking which makes reactor operation period significantly shorter is another significant disadvantage<sup>1</sup>.

Ethane gives the best results of cracking, providing high yield of ethylene, negligible yield of heavy pyrolysis products and the coke-formation is very slow, which allows longer operational period. However, it is common knowledge, that steam cracking of ethane is very energy-intensive. Optimal cracking conditions (high temperature, minimal pressure-drop and specific spent time) are on the edge of industrial coils construction limits and still the conversion of ethane approaches at most 65 %. Non-converted ethane is usually separated and recycled to the cracker. Cracking of LPG meets similar troubles even not of such range. Explanation of this fact is in the cracking reaction mechanism<sup>1-3</sup>.

The hydrogen abstraction reactions are the rate-controlling step, which determines the total conversion reached by the feedstock in non-equilibrium conditions. The rate of this reaction is determined by the concentration of active radicals which are formed by initiation reaction and then renewed by the propagation chain. Ethane is difficult to crack due to higher energy of its C-C bond (in comparison to heavy feedstock) which causes low rate of initiation reaction. Corresponding concentration of active radicals in the reaction mixture is therefore low and thus H-abstraction reaction rate is also low. So in the case of light feedstock, slow initiation reaction is slowing down entire reaction chain. One of possible way to accelerate entire cracking under constant reaction conditions is to support total radical's activity in reaction mixture by presence of a better radical source than original feedstock. This principle is well known. For example, LPG is often blended by gasoline fraction to accelerate the cracking of LPG because the gasoline provides significantly higher level of radical's activity<sup>4,5</sup>. But we decided to explore another way. In the scale of ethane cracking, there is no possibility for bending of hydroperoxides or similar initiator usually utilized for industrial processes. Direct dosing of oxygen or air would transform the cracking process into "oxidative pyrolysis" which requires significant modifications of entire production unit. Our preliminary research<sup>6</sup> indicates that alcohols are a good type of candidate for this purpose. Moreover, possible ways of utilization of alcohols is in the center of interest in the last decade.

However, there are only few mechanistic models of alcohols pyrolysis in the literature in contrast to wide palette of hydrocarbons cracking models. To the best our knowledge, there is no study which presents a mechanistic model describing the cracking behavior of mixtures, comprising hydrocarbons and alcohols. Therefore as an initial step, we decided to compile available mechanistic models of cracking of pure components. This study is aimed at developing the combined model to describe the behavior of ethane/methanol mixture.

### Modeling methodology

Kinetic model utilized for this study is a compilation of published models of ethane and methanol cracking.

### Ethane cracking model

A comprehensive mechanistic model of ethane cracking published by Sun and Saeys<sup>3</sup> was designed to describe the behavior of ethane under industrial cracking conditions. The model involves all molecular species H<sub>2</sub> - C<sub>4</sub> and all possible radicals up to C<sub>3</sub>. C<sub>4</sub> radicals include but-3-en-1-yl, 1-butyl and 2-butyl radicals, 20 species in

total and 150 chemical reactions forming 75 pairs of reversible reactions that can be grouped to following classes:

- Initiation and corresponding termination reactions
- Hydrogen abstraction caused by an attack of radical to a molecule and the reversed one
- $\beta$ -scissions of single C-C and C-H bonds in radicals and reverse radical additions
- Reversible isomerization of  $C_3$  and  $C_4$  saturated radicals

Kinetic parameters of reactions considered to be in forward directions (exothermic direction) were originally estimated by theoretical tools, such as CBS-QB3, W1U, etc. (for more details see the original paper). Kinetic parameters of those reactions in reverse direction were determined using previously determined forward ones and equilibrium constants of reversible reactions. Therefore kinetic parameters are thermodynamically consistent in this model.

Simulations were compared to experimental results specifically for following reactions conditions:

- Three different reactors
- Reactor inlet temperature 925-750 K
- Reactor outlet temperature 1110-1135 K
- Reactor inlet pressure 200-350 kPa
- Reactor outlet pressure 160-240 kPa
- Ethane reached conversion 51-61 %

Maximum deviation in predicted conversion of ethane was 1.5 % (relative error 3 %). Maximal deviations in predicted mass fraction of ethylene 1.8 wt. % (rel. 4.3 %), methane 1 wt. % (rel. 30 %).

#### **Methanol cracking model**

A detailed model of methanol thermal decomposition, published by Norton and Dryer<sup>7</sup> considers 23 reaction species and 66 elementary reactions including bond scission, radical recombination, hydrogen abstractions, radical additions and more specific reactions always in a pair with its antagonist form. Kinetic parameters of these reactions were also estimated using theoretical tools considering extended Arrhenius dependency of rate parameters and its pressure dependence. Developed model was tested for agreement with experimental data obtained on static, flow and shock tube reactor under conditions:

- Three different reactors
- Reaction temperature 973-2000 K
- Reactor modes: isothermal and adiabatic
- Reaction pressure 35-100 kPa
- Residence time 140  $\mu$ s-120 s
- Methanol reached conversion 60-99 %

Deviations in predicted reaction mixture composition are comparable with the ethane model.

#### **Combined model**

Reproduced model maintains the reactions rates being of the first order with respect to all reactants for each given chemical reaction. Eventually, in the case of third body interfering, model respects original models definitions. Rate coefficients are also considered in original form using the Arrhenius, respectively extended Arrhenius, expression. High-pressure limits of the rate coefficients were considered and the dependency of reaction coefficients on total pressure was neglected for its low significance in the range of reaction conditions for which this study is interested in. Connection of both models is provided via small active radicals, due to the interaction of both feedstock molecules (ethane and methanol) with these small radicals (H, O, OH, HO<sub>2</sub>, CH<sub>3</sub>, CH<sub>2</sub>O, ethyl, vinyl, allyl). Moreover, these radicals are connected via mutual interactions, such as hydrogen abstraction.

#### **Reactor model**

The aim of this theoretical pre-study is to evaluate the impact of alcohol (methanol) presence to conversion reached by hydrocarbon (ethane) which is difficult to be cracked individually and to delimit reactions conditions range for future experimental verification. For easy future experimental verification, we have chosen to utilize the apparatus of pyrolysis gas chromatograph; therefore it is needed to define reactor in this apparatus and its model. We have already established appropriate model of this equipment that was verified in

recently published papers<sup>8,9</sup>. For model equation see *ibid*. Simplifying assumptions that can be applied in this reactor are summarized below:

- Steady state in time
- Plug-flow of reaction mixture
- Isobaric mode
- Temperature profile typical for heating regulator settings (independent on all other conditions)

## Results

The main subject of this study is to evaluate the influence of methanol initial concentration to the conversion reached by ethane during cracking (co-pyrolysis) and specify appropriate area of reaction conditions for future experimental investigation, therefore a figure 1 is offered.

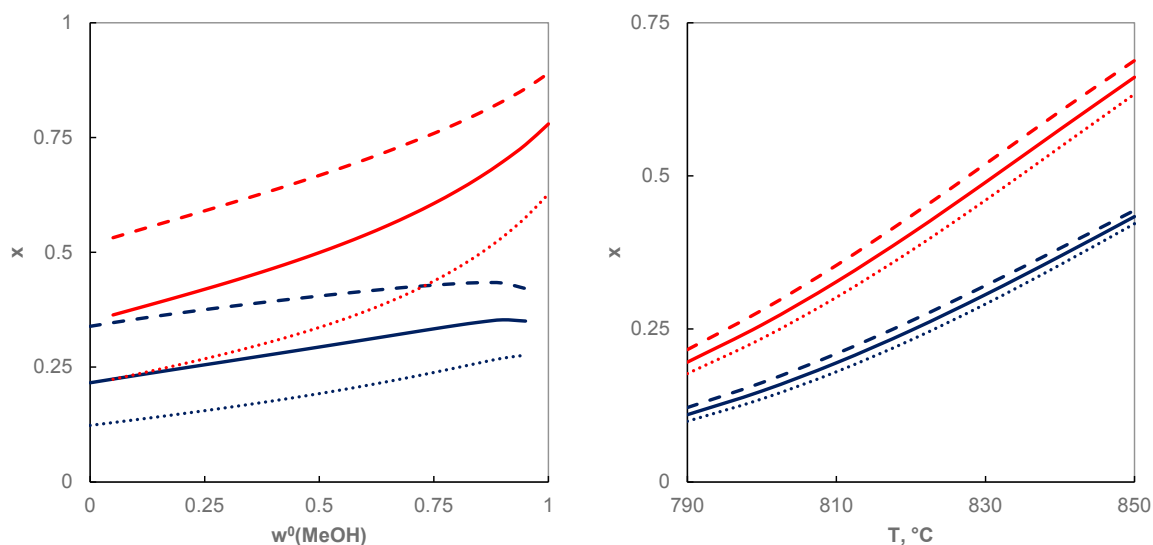


Figure 1. Predicted ethane conversion (blue) and methanol conversion (red). Left: Dependence of conversion on the initial mass-fraction of methanol in the feedstock for temperatures: 820 °C (solid), 840 °C (dashed) and 800 °C (dotted). Right: Dependence of conversion on the temperature for mixtures: 20 wt. % (solid), 30 wt. % (dashed), 10 wt. % (dotted) of methanol. Other conditions stays constant: reaction pressure 4 Bar, inlet volume flow 100 Nml·min<sup>-1</sup>. Modelled for the laboratory pyrolysis reactor PYR-4A (Shimadzu) 1.75x75 mm

Under selected reactions conditions pure ethane conversion is quite low (~ 20 %) on selected equipment as it was already experimentally verified in contrast to pure methanol conversion which is significantly higher (~ 80 %). Those conditions are selected purposefully because it is needed to investigate the mixture behavior under the conditions, where the kinetics of both species is “alive” (the ethane cracking is just running but the methanol cracking cannot finish along the reactor). Under these conditions, easily initiated methanol provides radicals for self- and co- pyrolysis with ethane which is more difficult to be initiated. As initial concentration of methanol in feedstock increases, conversion of ethane increases as well, as it could be expected because methanol produces active radicals more easily than ethane. These radicals interfere with ethane as well as methanol and shifts total conversion of ethane higher. Methanol conversion is lower in the mixture with ethane in comparison to pure methanol cracking because active radicals are partially drained by ethane and cannot be consumed by methanol. As the concentration of methanol in feedstock rises more, this effect seems to be equalized because methanol conversion rises too (rising probability of interaction) and the increase of ethane conversion is reduced as its concentration in feedstock is lower. And finally, when the concentration of ethane in methanol is low, radicals draining is not so significant and methanol cracking rate is less affected.

The next figure shows further investigation of the mixture behavior under varying reaction conditions. As it can be expected, with growing inlet flow of the feedstock, the residence time falls down and therefore conversion of ethane and methanol decreases. For shorter residence time (higher inlet flow), the conversion of ethane seems to be more affected by the presence of methanol than for longer residence time. Increasing reaction pressure causes small increasing of conversion because the concentration of reactions species grows which also illustrates the fact, the conversion is directed by the kinetics and not by the thermodynamics because the

on the thermodynamic limit, the conversion must generally fall down with increasing pressure in the case of cracking reaction.

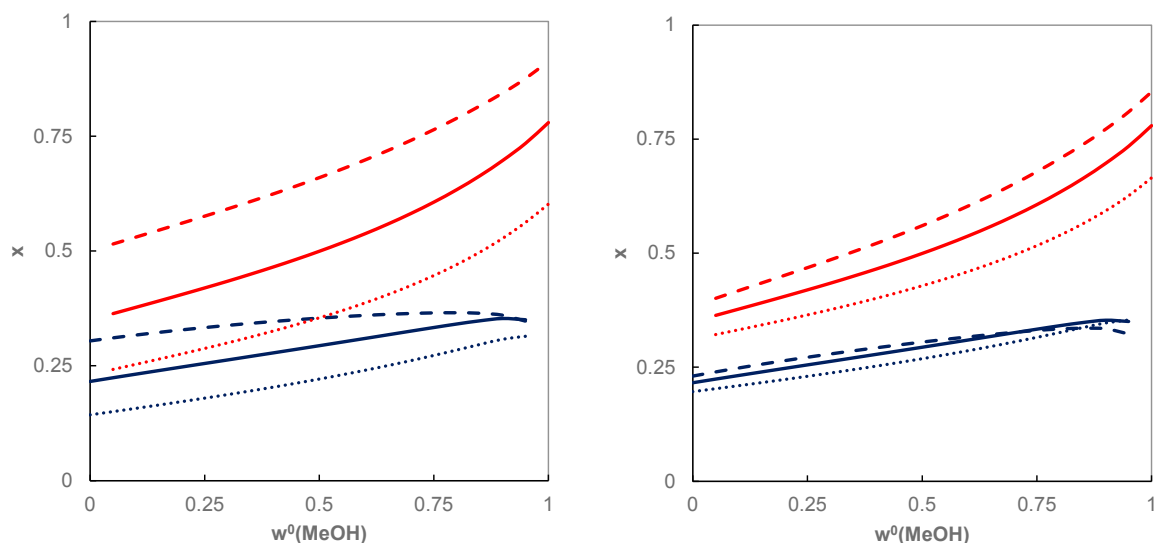


Figure 2. Predicted ethane conversion (blue) and methanol conversion (red) on the initial mass-fraction of methanol in the mixture. Left: for settings of inlet feedstock flow  $100 \text{ Nml}\cdot\text{min}^{-1}$  (solid),  $50 \text{ Nml}\cdot\text{min}^{-1}$  (dashed) and  $200 \text{ Nml}\cdot\text{min}^{-1}$  (dotted). Right: settings of reaction pressure 4 Bar (solid), 5 Bar (dashed) and 3 Bar (dotted). Reaction temperature constantly  $820 \text{ }^\circ\text{C}$ . Modelled for the laboratory pyrolysis reactor PYR-4A (Shimadzu)  $1.75 \times 75 \text{ mm}$

The next figure shows concentration profiles of selected radicals along the reactor length coordinate during pure ethane cracking in comparison to a mixture (80 wt. % ethane, 20 wt. % methanol) cracking. As it can be expected, level of active radicals is higher in the case of mixture cracking because methanol is more active than ethane. Not only radicals provided by methanol (such as  $\text{CH}_2\text{OH}$ ,  $\text{HCO}$ , etc.) are increased, but hydrocarbon radicals as well (such as ethyl, allyl or methyl radical). This is caused by the fact active radicals can abstract hydrogen atom to transfer the radical center to each other, therefore the presence of radical source (methanol) increases the total radical activity in the reaction mixture. This changes in the radical levels influence the rate of hydrogen abstraction reactions which affects total conversion of both reactants.

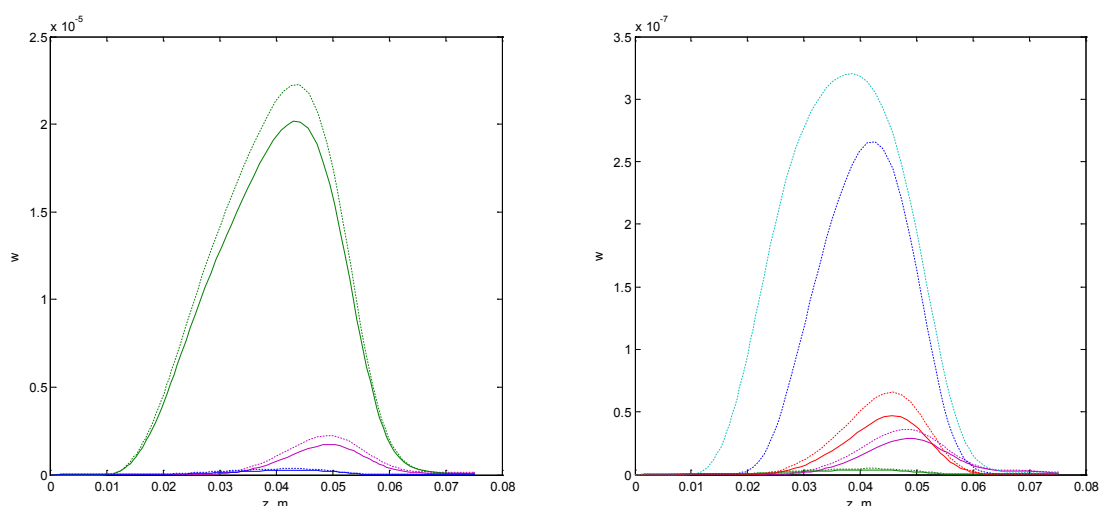


Figure 3. Predicted profiles radicals mass-fractions along the reactor with pure ethane cracking (solid line) and the cracking ethane containing 20 wt. % of methanol (dotted line) mixture under referential conditions ( $820 \text{ }^\circ\text{C}$ , 4 Bar,  $100 \text{ Nml}/\text{min}$ ), Left: ethyl (green), allyl (magenta), methyl (blue), right:  $\text{CH}_2\text{OH}$  (aqua),  $\text{HCO}$  (blue), vinyl (red), butenyl (magenta), hydrogen (green)

## Conclusions

A mechanistic model of methanol-ethane mixture has been created by a compilation of individual compounds cracking models. Using previously verified reactor model, a final model has been developed for this theoretical pre-study.

The presence of methanol in the ethane affects the total conversion reached by the ethane significantly. Conversion of ethane is increased with increasing initial concentration of methanol in the mixture under constant cracking conditions. And in opposite, the conversion of methanol is lowered by increasing initial ethane concentration in the mixture. This interfering effect seems to be depended on reaction conditions only faintly. The effect is more significant for lower temperature and shorted residence time.

Analysis of concentration profiles indicates that presence of methanol causes increase of radicals concentration along entire reactor under selected conditions.

Limits of reaction conditions area has been established in this study specifically for PYR-4A (Shimadzu) laboratory pyrolysis reactor for future experimental investigation. Kinetic study should be initiated in the temperature range 760-820 °C, under constant reaction pressure 4 bar and possibly with variable inlet gas flow 50-100 Nml/min. Appropriate range of methanol concentration for considered study could remain on 0-20 wt. % of methanol.

## Acknowledgement

*The publication was created using the infrastructure supported by the UniCRE project (reg. no. CZ.1.05/2.1.00/03.0071), funded by the EU Structural Funds and the state budget of the Czech Republic.*

## Literature

1. Albright L.F., Crynes B.L., Corcoran W.H., in book: *Pyrolysis: Theory and Industrial Practice*. Academic Press 1983.
2. Matheu D.M., Grenda J.M.: *J. Phys. Chem. A*, *109*, 5332 (2005).
3. Sun W., Saeys M.: *Comput. Chem. Eng.*, *57*, 2458 (2011).
4. Herink T., Belohlav Z., Zamostny P., Dorskocil J.: *Pet. Chem.*, *46*, 237 (2006).
5. Herink T., Fulin P., Lederer J., Belohlav Z.: *Oil Gas J.*, *99*, 50 (2001).
6. Karaba A., Zamostny P., Belohlav Z., *Effect of initiator presence on the conversion of ethane during thermal cracking*, in *21st International Congress of Chemical and Process Engineering CHISA 2014*, Czech Society of Chemical Engineering, Prague, CZ, 2014.
7. Norton T., Dryer F.: *Int. J. Chem. Kinet.*, *22*, 219 (1990).
8. Karaba A., Zamostny P., Lederer J., Belohlav Z.: *Ind. Eng. Chem. Res.*, *52*, 15407 (2013).
9. Zamostny P., Karaba A., Olahova N., et. al.: *J. Anal. Appl. Pyrol.*, *109*, 159 (2014).

### PILOT-SCALE POSTCOMBUSTION CO<sub>2</sub> CAPTURE USING ACTIVATED CARBON

**Smutná J.**<sup>1</sup>, Štefanica J.<sup>1</sup>, Hájek P.<sup>1</sup>, Ciahotný K.<sup>2</sup>, Machač P.<sup>2</sup>

<sup>1</sup>ÚJV Řež, a. s., Hlavní 130, Řež, 25068, Husinec

<sup>2</sup>UCT Prague, Technická 5, 16628, Prague

jana.smutna@ujv.cz

#### Introduction

Carbon dioxide capture, transport and storage (CCS) is one of the tools that can help to continually lower CO<sub>2</sub> emissions from large anthropogenic point sources. The whole CCS chain should be tailored to the conditions and needs of a certain country and designed with regard to local specifics. In the Czech Republic, there is an ongoing national research project no. TA02020205 supported by the Technology Agency of the Czech Republic. One of the main goals of the project is the development of an experimental device for a long-term study of the adsorption process and materials for CO<sub>2</sub> separation from flue gas in operational conditions of a power plant. Experiments with model gas mixture and real flue gas have already been conducted, using the commercially available activated carbon AP4-50 (Chemviron Carbon). Experiments with model gas mixture were focused on testing different conditions of adsorption and setting the optimal conditions for subsequent experiments with real flue gas.

#### Experimental settings and results: Model gas mixture

The model gas mixture was prepared by mixing pure CO<sub>2</sub> (calibration gas, class III.) with laboratory air, mixing volume ratio air:CO<sub>2</sub> varied approximately from 9:1 to 6:1 depending on required gas flow. Concentration of CO<sub>2</sub> in the gas mixture varied from 10% to 14% v/v. The model gas mixture was free of SO<sub>2</sub> and NO<sub>x</sub>. Humidity of the gas mixture was determined by water content in the air. The course of adsorption and desorption is significantly affected by temperature and the following parameters which were changed during the experiments: height of adsorption bed, gas flow in adsorption and desorption part of the rotational adsorber and time of rotation. Settings of operational parameters are in Table I.

Table I

Operational parameters, model gas mixture

Exp.	Bed height [cm]	Adsorbent weight per 1 column [kg]	Adsorption bed volume [m <sup>3</sup> ]	Temp. ADS [°C]	Temp. DES [°C]	Air flow ADS [m <sup>3</sup> /s]	Air flow DES [m <sup>3</sup> /s]	CO <sub>2</sub> flow [l/min]	Time of rotation [s]
PEZ14/08	10,5	2	0.0033	50	120-150	10	60	21	120
PEZ15/08	10,5	2	0.0033	50	200	10	60	21	240
PEZ19/08	10,5	2	0.0033	50	200	10	60	21	120
PEZ22/08	22.92	3.75	0.0072	50	200	10	60	21	360
PEZ25/08	22.92	3.75	0.0072	50	200	10	60	21	180
PEZ26/08	22.92	3.75	0.0072	50	200	10	60	21	300
PEZ27/08	22.92	3.75	0.0072	50	200	10	60	21	360
PEZ28/08	22.92	3.75	0.0072	50	200	10	60	21	480
PEZ29/08	22.92	3.75	0.0072	50	200	5	60	12	240
PEZ03/09	22.92	3.75	0.0072	50	200	5	60	12	360
PEZ05/09	22.92	3.75	0.0072	50	200	5	60	12	120
PEZ08/09	22.92	3.75	0.0072	50	200	5	10	12	240
PEZ12/09	22.92	3.75	0.0072	50	200	10	10	21	120
PEZ16/09	22.92	3.75	0.0072	50	200	10	10	21	240
PEZ17/09	22.92	3.75	0.0072	50	200	10	30	21	120

Activated carbon was regenerated before each experiment at 150°C for 2 hours. At the beginning of each measurement, the adsorber was tempered in the air regime for 2 hours to ensure stable operational

conditions. Amount of adsorbed CO<sub>2</sub> and CO<sub>2</sub> capture effectiveness was evaluated on the basis of obtained data. The results are in Table II.

Table II

Results – adsorption capacity and CO<sub>2</sub> capture effectiveness, model gas mixture

Exp.	Adsorbed CO <sub>2</sub> MAX [g]	Adsorbed CO <sub>2</sub> MIN [g]	Adsorption capacity MAX [% w/w]	Adsorption capacity MIN [% w/w]	Capture effectiveness MAX [%]	Capture effectiveness MIN [%]	Average CO <sub>2</sub> conc. [% v/v]
PEZ14/08	33.457	26.313	0.558	0.439	57.39	-10.71	11.9
PEZ15/08	60.387	45.239	1.006	0.754	66.07	4.94	10.4
PEZ19/08	29.471	24.188	0.491	0.207	58.49	0.00	10.8
PEZ22/08	136.857	99.693	1.215	0.885	75.23	25.00	10.6
PEZ25/08	9.243	4.217	0.082	0.037	67.68	35.48	10.4
PEZ26/08	111.755	82.108	0.993	0.729	68.14	33.66	11
PEZ27/08	131.778	104.529	1.170	0.928	69.37	29.21	10.7
PEZ28/08	189.061	150.332	1.679	1.335	76.58	34.07	10.6
PEZ29/08	43.571	33.255	0.387	0.295	66.07	30.38	10.6
PEZ03/09	81.721	60.901	0.726	0.541	98.08	35.90	10.4
PEZ05/09	34.522	21.880	0.307	0.194	97.20	59.68	9.6
PEZ08/09	43.571	33.255	0.387	0.295	66.0	30.38	10.6
PEZ12/09	63.970	46.638	0.568	0.414	84.13	57.89	11.4
PEZ16/09	110.396	97.989	0.980	0.870	75.41	44.95	11.7
PEZ17/09	42.912	32.987	0.381	0.293	69.39	29.59	10.3

The best capture effectiveness was found in case of PEZ12/09, considering the gas flow of 10 m<sup>3</sup>/h in the adsorption part. The course of effectiveness of CO<sub>2</sub> capture is in Figure 1, adsorbed amount of CO<sub>2</sub> in each step (120 s of rotation) is in Figure 2.

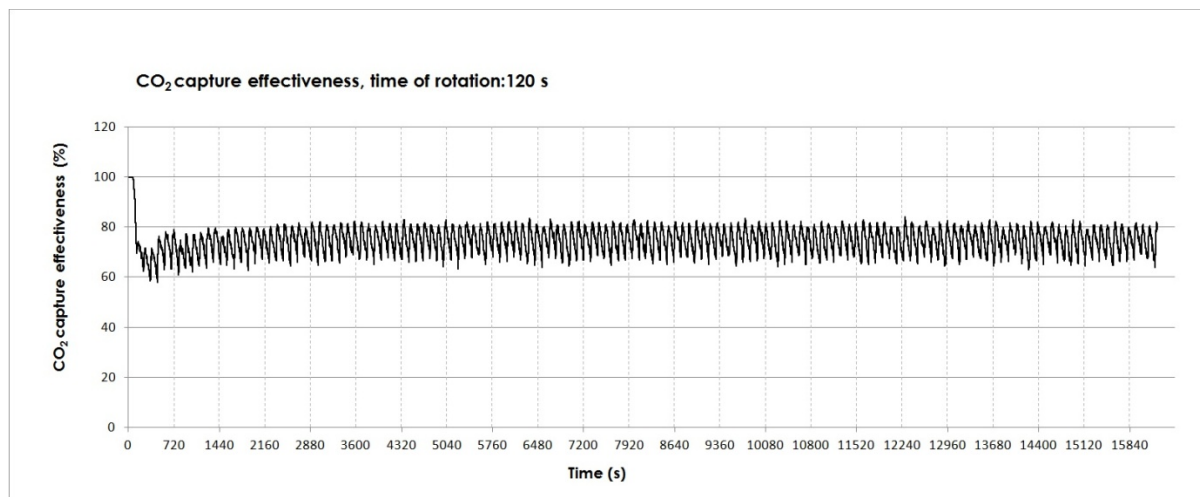


Figure 1. CO<sub>2</sub> capture effectiveness, experiment no. PEZ12/09

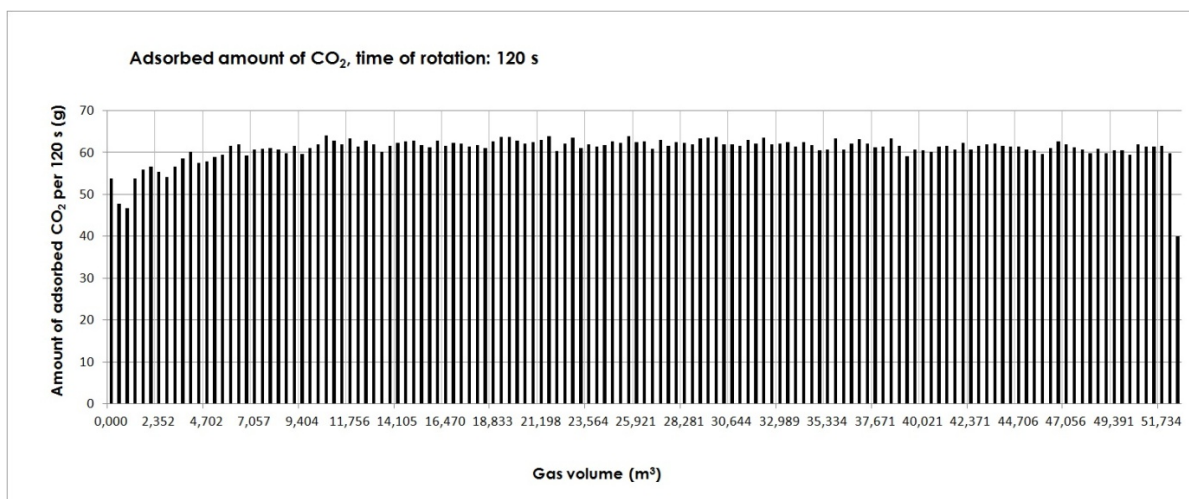


Figure 2. Adsorbed amount of CO<sub>2</sub>, experiment no. PEZ12/09

### Experimental settings and results: Real flue gas

The following experiments with real flue gas were set according to the optimal operational conditions given by the results from model gas mixture experiments. Operational parameters were: bed height: 22.92 cm; adsorbent weight per 1 column: 3.75 kg; adsorption bed volume: 0.0072 m<sup>3</sup>; adsorption temp.: 50°C; desorption temp.: 200°C; flue gas flow: 10 m<sup>3</sup>/s; air flow-desorption: 30 m<sup>3</sup>/s; time of rotation: 120 s. The results are in Table III.

Table III

Results – adsorption capacity and CO<sub>2</sub> capture effectiveness, real flue gas

Exp.	Adsorbed CO <sub>2</sub> MAX [g]	Adsorbed CO <sub>2</sub> MIN [g]	Adsorption capacity MAX [% w/w]	Adsorption capacity MIN [% w/w]	Capture effectiveness MAX [%]	Capture effectiveness MIN [%]	Average CO <sub>2</sub> conc. [% v/v]
PEZ23/10	57.321	13.266	0.509	0.118	100	45.24	8.05
PEZ29/10	44.801	8.873	0.398	0.018	100	65.52	5.45
PEZ30/10	34.283	2.850	0.304	0.025	100	79.17	4.97
PEZ31/10	52.119	3.201	0.463	0.004	100	46.25	6.98

During the experiments with real flue gas the concentration of CO<sub>2</sub> and other compounds in inlet flue gas varied in time. It was caused by conditions at a pilot desulphurization unit where flue gas from power plant were pre-treated before entering the adsorber. In case of experiment no. PEZ23/10, the conditions of inlet gas were the most similar to this from power plant after desulphurization. The course of effectiveness of CO<sub>2</sub> capture is in Figure 3, adsorbed amount of CO<sub>2</sub> in each step (120 s of rotation) is in Figure 4.

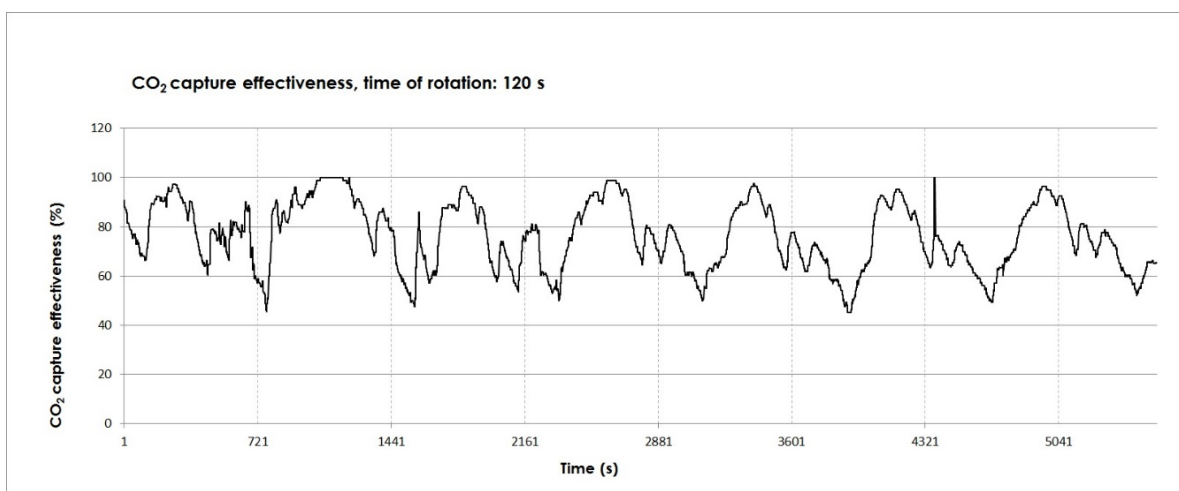


Figure 3. CO<sub>2</sub> capture effectiveness, experiment no. PEZ23/10

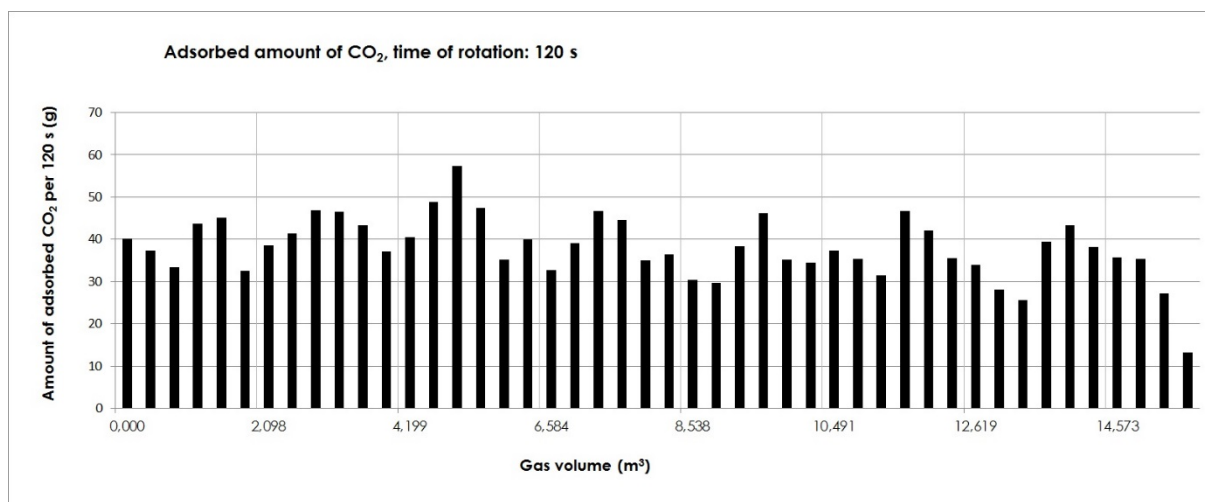


Figure 4. Adsorbed amount of CO<sub>2</sub>, experiment no. PEZ23/10

### Conclusion

Adsorption of CO<sub>2</sub> from model gas mixture and real flue gas after desulphurization using activated carbon was tested. Rotational adsorber with a system of relevant measurements (temperature, pressure, gas flow, gas concentration) was designed for this purpose. CO<sub>2</sub> capture effectiveness and adsorbed amount of CO<sub>2</sub> during the experiments was evaluated. In case of model gas mixture, the best operational parameters were set in case of experiment no. PEZ12/09. These parameters were used for the experiments with real flue gas. From the Figure 3 (experiment no. PEZ23/10), it is obvious that the minimum of the CO<sub>2</sub> capture effectiveness was lower compared to the experiment no. PEZ12/09.

These experiments will be further extended by analyses of adsorption of other compounds in flue gas and the main results will be published in the final report of the project TA02020205.

### Acknowledgment

*This work was supported by Technology Agency of the Czech Republic, project no. TA02020205.*

## 40<sup>TH</sup> ANNIVERSARY FROM COMMISSIONING OF THE NEW REFINERY KRALUPY N. VLT. – HOW IMPORTANT WAS FOR PROCESSING OF CRUDE OIL IN CR

**Kittel H.**<sup>1</sup>, Krch J.<sup>1</sup>, Tlustý J.<sup>2</sup>

<sup>1</sup>ČESKÁ RAFINÉRSKÁ, a.s., O. Wichterleho 809, 278 52 Kralupy n. Vlt., CR

<sup>2</sup>UNIPETROL RPA, s.r.o., Záluží 1, 436 70 Litvínov, CR

### Introduction

The New Refinery Kralupy (NRK) has been commissioned stepwise within the years 1974 – 1975. In this time, it was the biggest investment project in the chemical industry of the Czech Republic (CR). The project has been noted for certain break-through solutions, which anticipated features of the next chemical investments in CR. In 2001, NRK has been expanded by a new modern FCC complex and has become to produce modern clean motor fuels, including also biocomponents.

On the occasion of 40<sup>th</sup> anniversary of NRK commissioning, the paper introduces the most interesting solutions of the original NRK project and the consequent important development milestones of the refinery, until now.

### The project and commissioning of the new refinery Kralupy n.Vlt.

The history of NRK is in details described in the book "The Century of Petrol"<sup>1</sup>. Thirty years development of NRK summarizes presentation prepared for APROCHEM 2005 conference<sup>2</sup>. Material facts dealing with development of NRK after privatization in 1995 comprises paper in the journal "Paliva"<sup>3</sup>.

Decision to construct a new, fully modern crude oil refinery, constituted a response to the next past challenges:

- Ambition to complete in CR the transition phase from coal to crude oil as a key raw material source for production of fuels and petrochemical products.
- Since 1962, availability in CR of crude oil from pipeline Družba, without any hindrance.
- Existence at this time in the CR only technologically obsolete and small refineries, as concerns capacity.
- The rapid development of motorization and the related increase in motor fuels consumption.
- To feed growing production of poly-olefins, polystyrene, PVC, synthetic rubber and other petrochemical products.
- A relatively high share of fuel oils on energy portfolio in CR. Infrastructure for natural gas supplies has only begun to develop in this time.

The decision to build a new refinery just in Kralupy n.Vlt. was enforced by possible synergies with the activities, infrastructure and human resources here already operated state enterprise "Kaučuk". For the construction, there was also available the necessary grass – route plot.

At the time of construction, NRK represented the biggest and really break - through chemical project in the post-war country. Challenges mentioned above were transformed into a bright concept of a new refinery and this concept was implemented at the right time, on the right place and with the significant features as follows:

- Based on the visits of the newest oil refineries and consultation with renowned multinational engineering company Foster Wheeler, the modern concept and the best available technologies have been implemented.
- Deeply integrated facility (as mono-block) with only one Crude oil distillation unit (CDU) capacity of 3 million t/a was big at that time.
- To supply crude oil, Družba pipeline located since 1965 near Kralupy n.Vlt and delivering crude oil to Litvínov, has been used. NRK was therefore designed to process the West Siberian oil.
- Four modern oil floating roof storage tanks, capacity of each 30 thousand m<sup>3</sup>, have represented the largest facility of this type in CR at all.
- The hydroskimming technology scheme has been implemented, i.e. hydrotreating of the entire gasoline pool and all middle distillates. Therefore, NRK has produced Mogas with 1 mgkg<sup>-1</sup> S 20 years ahead a EU Clean Fuels policy. Due to relatively high consumption and mild quality of fuel oils in CR at this time, it was not necessary to consider neither a Vacuum distillation unit nor conversion of petroleum residues, as part of NRK. However, in the long view it was considered to add a lubes factory and in the late 80s also a new Hydrocracker.
- The central NRK unit featured a Semi-regenerative catalytic reforming (SRR), with a capacity of 300 kt/a, producing high-octane reformat as a component of Mogas and hydrogen for all hydrotreating units. The SRR's peculiarities represented a preheater, consisting of three chambers equipped in the radiant section with vertical U-tubes. Further, single-way heat exchangers equipped with a bellow compensator of the

tube bundle thermal expansion and, in particular, the first application of a bimetallic Pt - Re catalyst (CK 433, Ketjen) in Europe, which in comparison to the previously used Pt catalysts was characterized by a high stability, excellent selectivity, and good activity. Important part of the SRR was also solution how to start-up the unit – a battery of four horizontal pressure vessels (20 MPa each), to store electrolytic hydrogen.

- Facilities to dose modern technological and product additives were installed.
- Despite the existing embargo on import from US, NRK managed to buy a new IBM 1800 computer, which then processed all important technological data, controlled technological processes, inclusive of control loops (pre APC phase) and the modern "in-line" blender of motor fuels. A relatively high number of automatic analyzers have been employed to monitor and control the processes. With the computer, it was possible to solve variety of chemical - engineering problems. A linear programming package was also available.
- Four operators controlled NRK from a Central control room.
- Integral and important part of NRK constituted the automated Road and rail – tank loading facilities, the liquid products tank-farm, including also LPG, and modern chemical laboratory.

For technological scheme of NRK in 1975, see fig. 1, not-interrupted black line boxes only. At that time, NRK design was very modern also in terms of environmental protection:

- All production facilities were placed on a relatively small construction area of 200 times 200 m. This was achieved putting individual facilities into multi – store steel structure platforms.
- To be hydrocarbon-proof, technology units' background areas and tank-farm backyards were concreted and treated using special impermeable and resistant to hydrocarbons coatings and sealants.
- All technology units were deeply thermally integrated, i.e. exchanged mutually the heat and were feeded by hot streams without intermediate cooling or storing.
- All hydrogen sulfide in gases from crude oil distillation and hydrotreating units was absorbed in DEA scrubbers and then converted in a Claus unit to liquid sulfur.
- Radiation - convection heaters were equipped with analyzers of oxygen in the flue gas, to minimize excess of air. Moreover, some of them were equipped with a steam generator. The thermal efficiency of these devices was > 85%.
- The central technological fuel represented desulfurized refinery gas (mixture of hydrogen, methane, and ethane), and light fuel oil.
- With the aim to disperse emissions over the larger area, flue gases from all technology heaters were led via two horizontal flue gas ductings, provided with inner lining, to a central 160-meter high chimney.
- To cool the reaction products, primarily modern air coolers were used on the place of water coolers. Performance of air coolers could be partially regulated turning blades.
- For water cooling was, instead using one – through river water, built up a closed circuit, which part was a concrete hyperbolic cooling tower. This concept facilitated to monitor any leak of coolers as well as to control the quality of cooling water.
- It was built sewer system splitting the different types of water.
- All water contaminated with hydrocarbons was drained into a new Wastewater treatment plant, equipped with a biological stage. Sludge from the wastewater was centrifuged, dried and used as fuel.
- In case of accidental leak of hydrocarbons into groundwater, there was a system of wells with continuous water draining, creating a hydraulic trap.

Chemoprojekt Brno prepared NRK project documentation, in cooperation with Královopolská machinery Brno (KS), Jiskoot and Premaberg companies. Majority of construction and electrical works were carried out by Czech companies. The larger part of the apparatus, equipment, and instruments was made in the Czech engineering companies - KS Brno, Škoda Pilsen, and ZPA Prague. Some special compressors, pumps, automatic analyzers, and computers were imported.

To manage construction works and commissioning of units, critical path method (CPM) was used.

NRK units were put into operation stepwise. CDU was started - up in Nov. 1974, but after a few weeks was shut-down due to leaking bearing surfaces of heat exchangers. Some of them had to be replaced finally. In the summer 1975, SRR was put into operation. However, Pt - Re catalyst has coked rapidly and had to be regenerated soon. Second start - up of SRR was already without problems. Other issues associated with NRK start - up were:

- Corrosion of steel air coolers on CDU (were later replaced by brass ones), kerosene and gas oil hydrotreaters.
- Such rapid increase of pressure drop in the hydrotreating reactors that was necessary after several months of operation to shut – down the unit and to replace the top layer of the catalyst. A procedure has been

developed to replace the top layer of the catalyst in nitrogen atmosphere and upper catalyst layer design was significantly improved.

- Vibrations and frequent trips of SRR turbo-compressor.
- Vibrations caused by reciprocating compressors with horizontally moving pistons, circulating hydrogen at hydrotreating units.

Because CR at that time was a big exporter of refinery equipment, specialists of Chemoprojekt and VÚCHZ Brno verified design parameters on all technology units put into operation, to improve design methods of chemical equipment for the next similar projects. In parallel, this procedure has also provided number of valuable information for the next operation of the units. Therefore, it was very beneficial for all parties.

#### Development of the new refinery Kralupy n.Vlt within time period 1975 - 2014

Within 40 years period of operation, NRK had to face very fundamental changes of business environment, which have principally influenced its development, especially after 1989 year. These were:

- Significant changes in the economic (taxes and depreciation) and environmental (REACH, BAT, and BREF) legislation and in the rules how to operate chemical enterprises.
- Liberalization of petroleum market, which opened fully the CR to foreign competitors.
- Fluctuating refinery margin, increasing generally economic risks of refinery business and specifically, complicating justification and approval of new investments by shareholders. However, the refiners not investing in the conversion technologies lost quickly competitiveness.
- Since 2008, based on the emerging economic crisis, legitimated requirements of refinery shareholders on significant reduction of variable and fixed costs.
- Changes in ownership of refineries - the major oil companies stepwise left this business, focusing on up – stream activities.
- Tightening of quality standards of refinery products in the key technology parameters, such as the ban on the use of Pb additives into Mogas, reduction of sulfur and aromatics content in motor fuels etc.
- Significantly changing market of petroleum products, at first increasing motor fuels consumption generally, then, after 2005, declining Mogas demand and stagnant consumption of Diesel, shift to consumption of high octane Mogas, significant drop in deliveries of fuel oils because of natural gas, growing demand for LPG, etc.
- Launching and growth of bio-components blending into motor fuels (bioethanol and FAME) and the quick entrance of alternative motor fuels (especially CNG, LPG, and recently electricity), which compete with petroleum hydrocarbons more and more.
- Growth in prices of electricity, catalysts, additives, chemicals and other utilities, which are indispensable for the operation of refineries.

Additionally to the construction and commissioning of NRK, important milestones for the NRK operation were

- The cessation of activities of the Czech chemical concern Chemopetrol in 1990 (inter alia owner of refineries).
- The privatization of the Czech refining industry in Apr. 1995
- The transformation Czech refining Co (CRC) to processing refinery in Aug. 2003,
- Currently changes in ownership structure of CRC.

Crucial mandatory requirements to NRK over the discussed period summarizes exhibit 1.

**Table I: Central mandatory requirements on NRK activities**

Mandate	Valid from	Mandate	Valid from
Max. 3500 mgkg <sup>-1</sup> S in Diesel	1983	Max. 1% hm. S in fuel oils	2001
Max. 1500 mgkg <sup>-1</sup> S in Diesel	1987	Max. 50 mgkg <sup>-1</sup> S in Mogas and Diesel	2005
Max. 500 mgkg <sup>-1</sup> S in Mogas and Diesel	1995	Max. 35% vol. of aromatics in Mogas	2005
Quality audit of motor fuels performed by an independent authority	1996	Max. 10 mgkg <sup>-1</sup> S in Mogas and Diesel	2009
Mandate to produce motor fuels in line with valid Czech Norms only	1998	FAME into Diesel	min. 2.5% vol. min. 4.5% vol. min. 6.0% vol. 2007-09 2009-01 2010-06
CAPPO ecologic initiative (Mogas max. 300 mgkg <sup>-1</sup> S, max. 3 % vol. benzene; Diesel max. 400 mgkg <sup>-1</sup> S and max. 11 %	1998	Bioethanol into Mogas, min. 2.0% vol.	min.3.5% vol. min 4.1% vol. 2008-01 2009-01 2010-06

wt. of poly-aromatics)			
Mandatory recuperation of hydrocarbons' vapors	1999	REACH	2008
Max. 150 mgkg <sup>-1</sup> S in Mogas	2000	Max. 8% wt. poly-aromatics in Diesel	2011
Phase – out of Pb additives from Mogas	2001	CO <sub>2</sub> emissions reduction from motor fuels min. 2 %	2014
Max. 1% vol. of benzene in Mogas	2001		

**Table II: New, revamped and modernized units**

Unit	Commissioned
New MTBE unit (Hüls) [Complex project 2]	1981
Air preheating for NRK heaters [8]	1987
Replacing of the control computer IBM 1800 for HONEYWELL 2000 [7]	1989
New Font reactor R0 on SRR [7]	1988
New n - pentane / i - pentane splitter [7]	1990
Connection to Ingolstadt – Kralupy pipeline (IKL) [3]	1996
New Recuperation unit [1]	1997
New Isomerization unit (UOP, PENEX) [2]	1997
New Re-distillation of reformat [2]	1997
Additivation of Mogas RON 91 with additive protecting valve seats [2]	2000
New Vacuum distillation unit, as integral part of the FCC complex [3]	2001
New Semi-residual fluid catalytic cracking – FCC (UOP) [3]	2001
Revamp of MTBE [1, 7]	2001
New SULFREEN unit [9]	2001
New second stage De-salter [7]	2001
New Central control room and new control system FOXBORO [7, 11]	2001
Refurbishment and revamp of Gas oil hydrotreater [4]	2001
Refurbishment of Naphtha hydrotreater [4]	2001
New 3-cut-splitter of FCC gasoline [4]	2004
New facility to unload, store, and blend bio-ethanol to Mogas and FAME to Diesel [5]	2006
New Selective FCC heard-cut desulfurization unit (Axens, PRIME G+) – PETROL award 2008 [4]	2007
The first phase of FCC complex revamp – increase of propylene production. PETROL award 2009 [6]	2009
Slurry oil filtration [7]	2011

Majority of the investments were part of certain complex projects, which were often related not only to NRK as such, but the whole CRC. The important projects and investments can be commented as follows:

- 1) "Minimization of hydrocarbon emissions (1995 – 2000)":** It included the installation of secondary seals of floating roof tanks, a new Recovery unit of hydrocarbon vapors from the road- and rail-tank loading and fixed roof storage tanks.
- 2) "Reduction of Pb content in Mogas and phase - out of leaded Mogas (1995 – 2000)":** It was managed through the "National program of phase - out of leaded Mogas in the CR". The central part of the Pb phase - out represented MTBE unit, built in 1981, primarily to convert i-butene from the pyrolysis C<sub>4</sub> fraction to Mogas. It was the second MTBE unit in Europe. Moreover, MTBE unit was revamped in 2001. To balance the loss of octanes related to Pb additives, components from the new Isomerization unit (PENEX), the new FCC complex, and the new Re-distillation of reformat were also used. For a certain transitional period was Mogas 91 "Special" treated with additives protecting valve seats. Mothballing of assets for Mogas additivation with Pb additives represented a demanding, environmentally sensitive and therefore costly activity.
- 3) "Deep crude oil conversion (1996 – 2001)":** Implementation of this complex project was driven by strategic requirements of the new shareholders, after privatization in Apr. 1995 and was focused on the whole CRC, not only NRK. The major investment in Kralupy n.Vlt. represented construction of a new semi-residual FCC complex, see fig. 1, feeded with a mixture of atmospheric residue and vacuum gas oil. The new FCC complex consists of several technology units and includes, inter alia, a new Vacuum distillation unit and production of propylene. So, the original hydroskimming scheme of NRK was transformed into a



mgkg<sup>-1</sup> S in the product, but also to continue to process light cycle oil (LCO) from FCC complex as a Diesel component.

- 5) **“Addition of biocomponents in motor fuels (2004 – 2007)”**: In NRK were built new unloading and storage capacities for bioethanol and FAME, and modified Blenders of Mogas and Diesel. Capacity anticipated future concentration of bio-components in motor fuels of 10% vol., what looks as the right vision now.
- 6) **“FCC Petrochemization (2007 – 2009)”**: It aimed exploiting full design capacity of FCC complex and significant increase of propylene production. The 1<sup>st</sup> phase of the project, i.e. removal of bottlenecks in the gas separation section, was already implemented. For the 2<sup>nd</sup> phase of the project was envisaged to increase the production of propylene dosing ZSM5 additive, to construct a new parallel Propylene column, a new Metathesis unit, and new Alkylation unit. These options are under scrutiny now.
- 7) **“Development and modernization of existing technological units (implemented continuously)”**: It included:
  - Installation of a new front reactor at the SRR in 1988, to solve the uneven heat loading of individual sections of the reforming heater, and consequent revamp of this unit. From the technology point of view, it was the worldwide unique solution, verified exploiting a proper SRR’s kinetic model.
  - Regular modernization of the control system and the Central control room, as per exhibit 2.
  - Optimization of refinery operations - since 1996 was systematically developed an optimization model based on the Aspen Tech., Inc., PIMS software
  - Improved management of hydrocarbon streams – the project implemented within years 2007 – 2008, in the tight collaboration with UOP.
  - Phase – out Mogas RON 91, leaded and unleaded as well.
  - Reduction of benzene content in Mogas, exploiting components from Re-distillation of reformat and Isomerization.
  - ETBE production on original MTBE unit commissioned in 1981.
  - Optimization of components for Diesel production – integration of FCC hydrocarbons.
  - New Slurry oil filtration, as part of the FCC complex, to reduce mechanical impurities in fuel oil.
  - Substantial changes in management of NRK tank farm.
- 8) **“Energy savings”**: Achieved based on continuous evaluation of NRK energy performance, in collaboration and applying methodologies of Solomon, Inc., Shell Global Solutions, Inc. (SGSI), KBC and Linhoff’s PINCH. Consumption of energies was included into PIMS model. As concerns concrete facilities, these were mainly:
  - Preheating of air for refinery heaters.
  - More effective control of electric motor of SRR turbo-compressor (a 2.4 MW device).
  - Stepwise efficiency increase of FCC steam boiler.
- 9) **“Reduction of Green-house gases”**: As important NRK activities have to be mentioned in particular a new Sulfreen unit, processing off-gas from the Claus unit, which has increased the efficiency of H<sub>2</sub>S conversion to 98.5% and modernization of burners in refinery heaters to a low-NO<sub>x</sub> type.
- 10) **“Improved management of catalysts, additives, and chemicals”**: These consumptions and scope grew – up significantly in line with the implementation of FCC complex and "Clean Fuels" project. For example, reactors in GO HDS unit are containing four times higher catalyst volume now, in comparison to the situation before 2001. Nowadays, additives constitute an important part of modern refinery products and are exploited as an important tool for marketing differentiation of individual distributors.
- 11) **Increase of safety and reliability of facilities**: First of all, it included the construction of a new Central control room in 2001 resistant to any eventual fire or explosion, automation of start-up and shut-down of the central NRK facilities, new cameras, monitoring equipment, installation of automatic gas leakage detectors, modern tools of communication, risk assessment applying so called "Risk Assessment Matrix (RAM)" etc.

## Conclusions

The New Refinery Kralupy n.Vlt. (NRK) project, put into operation stepwise within the years 1974 - 1975, has significantly changed the capacity and scope of technologies of crude oil processing in the Czech Republic. It has substantially influenced and surpassed the standards of investments in the Czech chemical industry. During the next forty years of operation, NRK has undergone significant organizational and ownership changes and essential technological development as well. NRK owners managed always to respond properly to all business challenges and petroleum products market demands and so to maintain the role of refinery as an important

supplier of motor fuels in the Central Europe. Several major development projects, great even on a national scale, have been invented, prepared and implemented. Based on these projects, NRK has managed processing of diverse crude oils to design, introduced clean motor fuels, implemented biocomponents, significantly increased the output of Mogas, mastered the production of polymer grade propylene, and substantially reduced production of fuel oil. This was because the long-term interests of the owners to operate the refinery, strategic thinking of managers, and systematic effort and activities of the operators of NRK. To successful operation of the refinery has also contributed a number of engineering, service, and consulting organizations. **Forty years history of NRK can be characterized as extremely successful and inspiring for the future activities of the chemical industry in the Czech Republic and for the new generation of chemists as well.**

#### Literature

1. Holub L. a kol.: The Century of Petrol“. Asco – Publishing, s r. o., Prague, Apr. 2005. ISBN 80-85377-97-7.
2. Souček I., Kittel H., Ballek P.: Nová rafinérie Kralupy – od hydroskimmingu k hlubokému zpracování ropy. Sborník konference APROCHEM 2005, str. 17. Mílovy, 24. – 26.10.2005.
3. Kittel H., Souček I.: 15 let rozvoje zpracování ropy v České rafinérské, a.s.. Paliva (1), č. 2, s.1, (2010).

#### List of abbreviations

3CS	3-Cut-splitter	Ke HDS	Kero Hydrodesulphurization
APC	Advanced Process Control	LCO	Light Cycle Oil
AR	Atmospheric Residue	LPG	Liquefied Petroleum Gases
BAT	Best Available Technologies	MeOH	Methanol
BREF	BAT Reference Documents	NHT	Naphtha Hydrotreater
CAPPO	Czech Association of Petroleum Industry and Trade	NRK	New Refinery Kralupy
CDU	Crude-oil Distillation Unit	PIMS	Process Industry Modeling System
CNG	Compressed Natural gas	PINCH	The method to save energies, developer by Bodo Linnhoff
CPM	Critical Path Method	PVC	Polyvinylchloride
CR	Czech Republic	REACH	Registration, Evaluation, Authorization and Restriction of Chemicals
CRC	Czech Refining Co.	REB	Russian Export Blend
C3=	Propene	SGSI	Shell Global Solutions International
FAME	Fatty Acids Methyl Ester	SRR	Semi-regenerative Reformer
FCC	Fluid Catalytic Cracking	TAL	Transalpine pipeline
GO	Gas Oil	VDU	Vacuum Distillation unit
GO HDS	Gas Oil Hydrodesulphurization	VR	Vacuum Residue
IKL	Ingolstadt – Kralupy pipeline		

## EFFICIENCY OF SUPERCRITICAL WATER GASIFICATION: PROCESS CONDITIONS

Purkarová E.<sup>1</sup>, Šváb M.<sup>2</sup>, Ciahotný K.<sup>1</sup>

<sup>1</sup>University of Chemistry and Technology Prague, Department of gas, coke and air protection, Czech Republic

<sup>2</sup>Dekonta, a.s., Prague, Czech Republic  
purkaroe@vscht.cz

Worldwide we are confronted with the problem of waste streams and thus with the development of new technologies, such as SCWG (super critical water gasification) to deal with them. The main principle of this process is thermochemical conversion, where the organic substances are converted into gaseous products in water under high pressures and temperatures. This conversion represents a potential application for the technology on degradation of liquid organic wastes to produce energetically usable gases (methane, hydrogen, CO, higher hydrocarbons) along with the treatment of waste water<sup>1</sup>.

Supercritical water (SCW) under supercritical conditions, that means at temperature above critical temperature (374 °C) and at pressure above critical pressure (22,1MPa). Under these conditions dramatic changes in water properties can be observed, which is no longer a mixture of ions, but clusters of water molecules. For example the dielectric constant with increasing temperature decreases significantly to as low as 5, as shown in Fig. 1. Under normal conditions the dielectric constant of water is 80. Thus SCW behaves as a non-polar solvent. Therefore SCW dissolves organic substances and the solubility of inorganic substances decreases. Additionally important characteristics are low density, viscosity and surface tension that positively affect dissolution of organic compounds, macromolecular structures and the course of gasification reactions<sup>2</sup>.

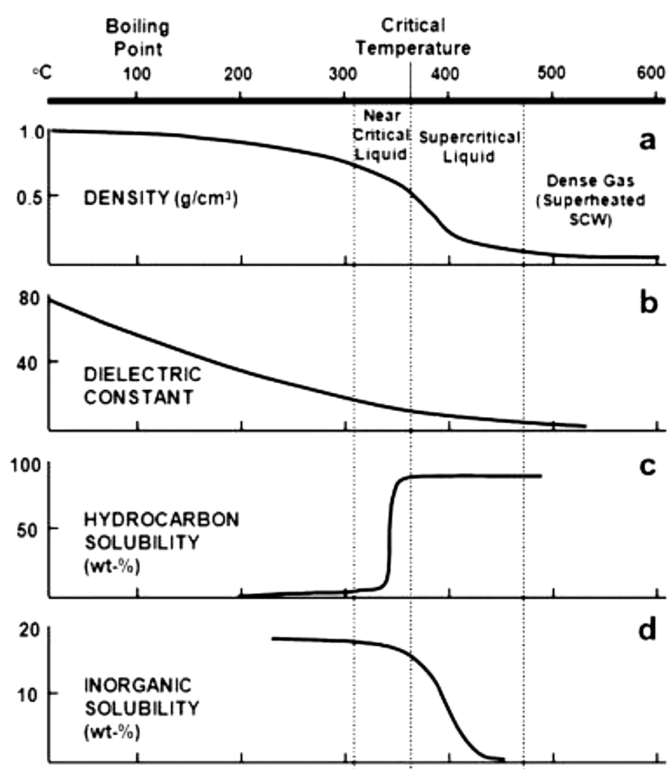


Figure 1. Changes in the properties of water in the transition to the supercritical conditions.

It is fundamental to SCWG process to bring the input of organic materials into the supercritical reactor in an aqueous suspension. Water acts during the conversion as solvent, reagent and gasifying medium at the same time. Processing liquid organic materials, preferably waste, is a major advantage of hydrothermal gasification over conventional methods which often require a dry substrate<sup>1</sup>.

SCWG proceeds either at lower temperatures (around 500 °C) or at higher (above 600 °C) differently, according to literature. At the lower temperatures occurs a higher production of tars. Thus is crucial to use catalyst to prevent formation of tars, chars and other undesirable products. Due to carbon monoxide and

carbon dioxide hydrogenation is the yielded gas rich on methane. Higher temperature prevents the formation of tar and the yielded gas is rich on hydrogen due to water-gas shift reaction<sup>3</sup>.

In this work this process was examined in a laboratory unit using a horizontal continuous flow reactor. The scheme of the laboratory unit is shown in Fig.2. The reactor worked under the following conditions: pressure settings at 25MPa, temperatures in the reactor was in the range off 500 - 650 °C, residence time in SCW 57-226 s, concentration of substrate 5-10 % wt. On this apparatus were performed a series of experiments with two different model compounds: glucose and glycerol. The experiments were carried out under various working conditions. The influence of temperature range, residence time of the substrate in the reactor and catalyst (K<sub>2</sub>CO<sub>3</sub> concentration range 0,5-4%wt.) were tested. The results of this work will be discussed and compared with literature.

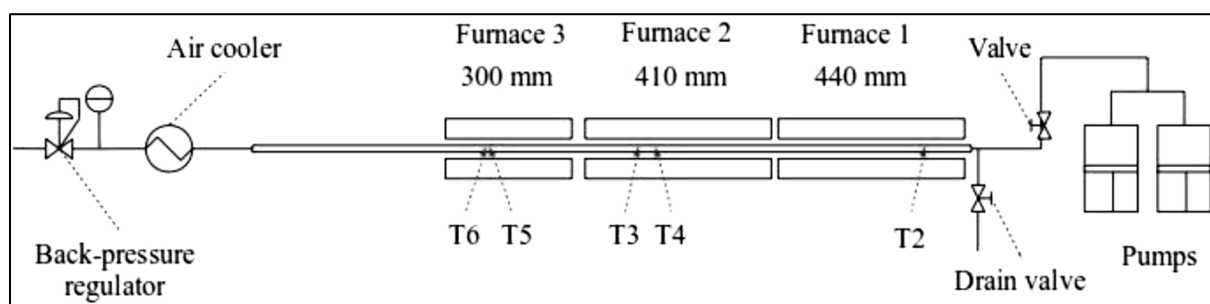


Figure 2. Schema of laboratory apparatus.

All published experiments were also performed on a continuous flow reactor. A comparison of output values from this work and literature on SCWG experiment with glucose was carried out. Experimental conditions are depicted in Tab. I. Compared were CE (carbon efficiency) values, which is ration between the amount of carbon in the input organic substrate and the amount of carbon in output gas. Further composition of emerging gas, especially content of hydrogen, methane and carbon dioxide were compared. From the results is can be seen that CE has higher values in the published experiments, even though their experimental conditions were similar to the ones applied in this work and residence time was only half the time . Furthermore even at higher temperature was not possible to achieve high hydrogen yield in the product. It was observed that neither at low temperature was not achieved high methane yield in the product. These results contradict literature statements as be seen in the published experiments.

The influence of the catalyst has been tested also on glucose, since this model compound showed the highest production of tars, even at higher temperatures. Without adding a catalyst liquid product was dark brown and opaque. As catalyst amount was increased colouring disappeared, so the tars formation was prevented and gasification efficiency increased. However higher catalyst concentration is not appropriate, since efficiency of the process at concentrations above 2 % wt. of K<sub>2</sub>CO<sub>3</sub> is no longer significantly increased. Inorganic catalyst can also, due to poor solubility in supercritical water, cause plugging of the reactor.

Table I

Comparison of experimental results with studies from the gasification of glucose.

Output values	Glucose			
	Laboratory exp. [25MPa, 600-680°C, 5%wt. glucose, residence time in SCW 57 s]	Laboratory exp. [25MPa, 480-550 °C, 5%wt. glucose, residence time in SCW 57 s]	Published exp <sup>4</sup> . [25MPa, 600 °C, 3,6%wt. glucose, residence time in SCW 30 s]	Published exp <sup>4</sup> . [25MPa, 750 °C, 1,8%wt. glucose, residence time in SCW 2,6-26,3 s]
CE [%wt.]	56.9	40.2	80	81
H <sub>2</sub> [%wt.]	19.3	17.2	68	52.5
CH <sub>4</sub> [%wt.]	12.7	13.6	2.1	-
CO <sub>2</sub> [%wt.]	24.7	25.3	24.8	-

In Tab II. is compared output values from our research and literature of SCWG experiment with glycerol, which differ even more than in comparison with glucose. Published experiments were also performed on continuous flow reactor. As you can see published experiment reaches almost same value of carbon efficiency as ours, but

in considerably less residence time. Also production of hydrogen is more than 10%wt. higher against obtained values from our laboratory apparatus, despite lower temperatures in reactor.

Table II

Comparison of experimental results with studies from the gasification of glycerol.

Output values	Glycerol		
	Laboratory exp. [25MPa, 580 °C, 10%wt. glycerol, residence time in SCW 226 s]	Laboratory exp. [25MPa, 580 °C, 10%wt. glycerol, 1%wt. K <sub>2</sub> CO <sub>3</sub> , residence time in SCW 226 s]	Published exp <sup>5</sup> . [25MPa, 567 °C, 10%wt. glycerol, residence time in SCW 4,2-7,3 s]
CE [%wt.]	86.4	89.2	80
H <sub>2</sub> [%wt.]	43.2	45.9	58
CH <sub>4</sub> [%wt.]	12.1	12.9	6
CO <sub>2</sub> [%wt.]	34.8	35.1	18

In conclusion SCWG is a technology with high potentials for the treatment of liquid organic waste materials. Its main advantage are energy recoverable gaseous products. The Main parameters – temperature, residence time, catalysts that influence the process, were examine and compared with literature. Increasing temperature, and catalyst addition have positive effects on conversion of organic substrate and prevents char, tar and other undesirable products formation. Residence time is one of the most important parameters of the technology and it is essential to be long enough so that the desired conversion reaction proceeds. However the results obtained in this work from the laboratory continuous flow reactor, especially residence time are not in agreement with the results found in literature. Composition of the gas produced by the technology also does not entirely agree with the publications, which produced much more hydrogen in notably shorter residence time. More information on the technology, can be seen on the results obtained from the pilot-scale plant build in the Framework of the same project, which is not discussed in this paper. In addition it must be stated that hydrothermal gasification is a very complex process due to the challenging process conditions (high temperature, pressure), thus is necessary its further and detailed examination.

#### Acknowledgment

*This work was supported by the Technology Agency of Czech Republic No.TA03011105.*

#### Literature

1. Kruse A. in book: *Biomass Gasification and Pyrolysis*, chap. 7, p. 229, Prabir Basu (2010).
2. Zychová M., Růžičková M., Macák J., Janda V.,: *Chem. Listy* 107, 126-129 (2013).
3. Kruse A.: *J. Supercrit. Flu.* 47, 392 (2009).
4. Susanti R.F., Diannigrum L.W., Yum T., Kim Y., Lee B.G., Kim J.: *Int. J. Hydr. En.* 37, 11679 (2012).
5. Guo S., Guo L., Cao C., Yin J., Lu Y., Zhang X.: *Int. J. Hydr. En.* 37, 5561 (2012).

## EXPERIMENTAL AND INDUSTRIAL DEACTIVATION OF HDS CATALYSTS IN THE PRODUCTION OF DIESEL FUEL

Zbuzek M.<sup>1,2</sup>, Vráblík A.<sup>2</sup>, Černý R.<sup>2</sup>, Prokešová A.<sup>3</sup>, Veselý M.<sup>3</sup>, Tukač V.<sup>3</sup>

<sup>1</sup>Unipetrol RPA, Section of Technology Development and Efficiency, Litvínov, Czech Republic

<sup>2</sup>Research Institute of Inorganic Chemistry, Department of Efficient Refining Technologies, Litvínov

<sup>3</sup>University of Chemistry and Technology, Department of Organic Technology, Prague

Contact: [michal.zbuzek@unipetrol.cz](mailto:michal.zbuzek@unipetrol.cz),

### Introduction

The hydrodesulphurization (HDS) of motor fuel is important refining process. Often it is supported by laboratory-scale testing facilities with a big benefit. Laboratory trickle bed reactors are frequently used for the prediction of catalyst performance, especially for the verification of catalyst HDS activity under specific conditions. HDS catalysts are important industrial catalysts. Their activity significantly affects the quality of the diesel fuel and any inappropriate choice would have a negative impact on the economy of diesel production<sup>1-3</sup>. The successful industrial catalytic system is dependent on the data obtained in the laboratory scale. They help to predict the behavior of the processing unit. The significant progress has been achieved in the development of new HDS catalysts in the recent years<sup>4</sup>. The research and development of the new catalysts increases the importance of testing for catalyst producers to verify catalytic activity and other properties.

Frequently, only the initial catalytic activity is tested. The result of the initial catalyst activity informs how the catalyst will perform during the first weeks of an operation<sup>5-6</sup>. However, the initial activity does not express how the catalyst could be operated under the specified conditions in a given industrial reactor. The catalysts, mostly based on Ni, Co, Mo and W sulphides, are susceptible to several deactivation mechanisms during their life cycle. The deactivation is going to be more critical due to the ongoing trend in increasing HDS severity and maximizing the catalyst performance. The deactivation of the catalyst is attributed to the three main causes: (i) the coke deposition (including both – the pore plugging and the catalytic site blocking), (ii) the metals deposition and (iii) the segregation of the active phase<sup>4</sup>.

In the industrial reactors the catalyst deactivation is compensated by temperature increase to the maximum permissible end-of-run (EOR) to maintain the catalyst performance<sup>7-8</sup>. Deactivation rate is different for each catalyst and depends on several factors – such as textural characteristics of used catalyst and their composition, process parameters, feedstock source and its quality. Hydrorefining reactors are usually operated under a constant performance to achieve the desired product specifications. The determination of the long term activity of HDS catalysts is not often applied to incorporate time constraints and economic factors. The HDS catalysts are so stable, that the change of their activity in a laboratory scale reactor is not observed during the length of a test for about 1-2 month<sup>9</sup>. Hence our research is focused on the creating of a new experimental accelerated methodology which can be used for the prediction of the long term activity during the test length of about 14 days.

### Experimental

The HDS catalyst activity determination was carried out in a trickle bed reactor. The diagram of the pilot plant unit, which is heart of the experimental accelerated method, is described in Figure 1.

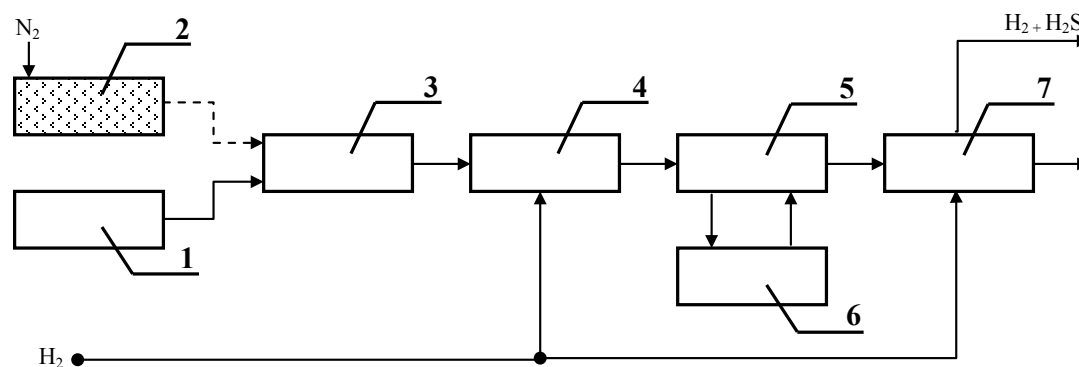


Figure 1. The detailed diagram of a pilot plant unit

**where:** (1) – The feedstock container, (2) – The container for deactivating agent, (3) – The pump, (4) – The mixer, (5) – The reactor, (6) – The heat exchanger, (7) – The stripper and separator

The reactor (length 0.9 m, diameter 0.03 m) was placed in a mixed salt bath. The bath ensured the isothermal operation of the experiments. A thermo-well with the outer diameter of 0.009 m was mounted in the centre of reactor. The temperature inside the reactor was monitored by three thermocouples. Their positions were adjustable and they were placed at the top, middle and bottom of the catalyst bed. The reaction mixture was cooled down at the reactor outlet. The products were withdrawn after were stripped with hydrogen to remove dissolved hydrogen disulfide. The raw material (AGO) and also the deactivating agent (LCO) are described in detail (analytical results can be seen from Tab. I.)

Table I. The detailed characterization of injected raw materials (AGO, LCO)

Feedstock	AGO	LCO	Feedstock	AGO	LCO
Density 15°C, kg.m <sup>-3</sup>	857.1	977.8	Distillation curve – D86	-	-
Refractive index 20°C	1.4763	1.5637	IBP, °C*	215	142
Color – ASTM D1500	0.9	2.6	5 % v/v	257	205
Sulphur, ppmw	12 900	5 000	95 % v/v	373	340
Nitrogen, ppmw	201	800	FBP, °C**	380	349
GCxGC, wt. %	-	-	IR spectroscopy, wt. %	-	-
parafins	29.8	4.7	aromatic carbon	16.9	85.4
isoparafins	37.1	8.1	paraffinic carbon	62.5	7.1
naphthenes	23.5	1.7	naphthenic carbon	20.6	7.5
monoaromatics	5.8	18.1	Cloud point, °C	-1	+13
di+polyaromatics	3.9	67.4	Cetane index	55.8	20.8

The testing reactor was loaded with 100 mL of HDS catalyst. The catalysts were tested in the original form. Before loading into the testing reactor the catalyst was diluted 1:1 volumetric with an inert (silicon carbide - SiC, MESH 80) to ensure the proper hydrodynamic conditions over the catalytic bed. SiC (MESH 12) was placed below and on the top of the catalyst bed too. SiC in the lower part of the testing reactor fixed the catalyst bed in the isothermal zone of the reactor. SiC in the upper part of the reactor ensured the preheating and proper mixing of the feedstock and hydrogen before the entering on the catalyst bed.

The catalyst activation was realized inside the testing reactor. A standard catalyst activation procedure using AGO with dimethyl disulfide (DMDS) was used. The activation procedure consists from several steps. (1) – the reactor was heated up to 120°C (rate 20°C/h) under nitrogen flow rate. After reaching 120°C the gas flow from nitrogen to hydrogen was switched and at the same time the injection of sulphidation feedstock (AGO + 3% DMDS) was started. (2) – the reactor was heated up to 220°C (rate 10°C/h). At 220°C was first stabilization period, 10 hours. After stabilization period, the reactor was heated up to 280°C (rate 10°C/h). At 280°C was second stabilization period, 10 hours. (3) – the last step was increasing of temperature up to 360°C still with feeding AGO + 3% DMDS. At 360°C was finished activation procedure, and all reaction parameters were switched to the first reaction condition, the feedstock as well.

The catalysts were also placed in a special basket into the industrial reactor and kept there over operating period for the real deactivation (i.e. 16 months). The industrial reactor was operated under conditions: AGO, 2.85 MPa, WHSV 1.0 h<sup>-1</sup>, 200 Nm<sup>3</sup>/m<sup>3</sup> and temperature in the ratio 360 – 380°C (see from Fig. 5). After catalysts removing from the industrial reactor, their residual activity was determined in pilot plant unit.

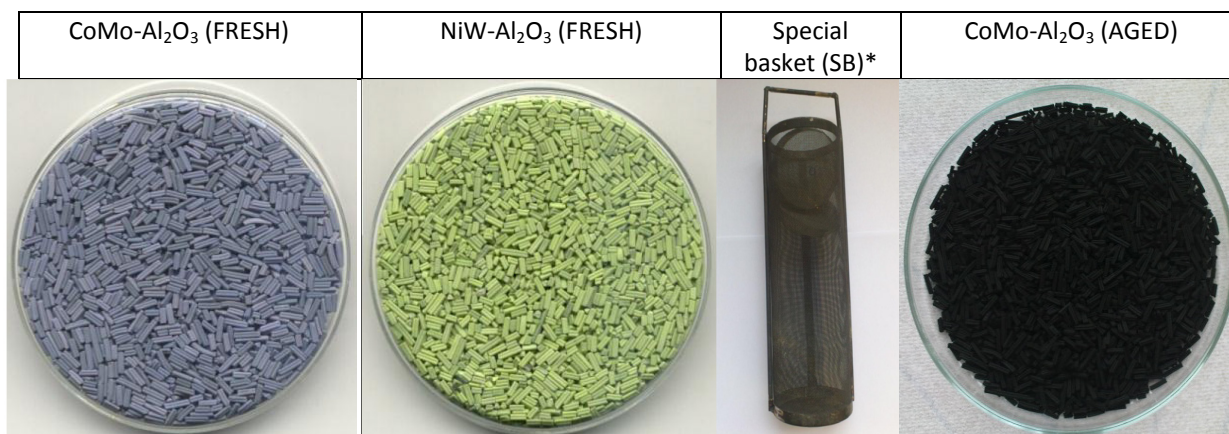


Figure 2. The tested catalysts and special basket

\*SB from stainless steel, resistant to aggressive hydrogen disulfide, cylinder shape,  $\phi$  120 mm, length 350 mm

## Results and discussion

The verification of experimental accelerated deactivation method for the testing of long-term activity of HDS catalysts was divided into three parts. The first part focused on the initial activity of fresh catalysts and residual activity on the industrially deactivated catalysts. The second part was focused on the deactivation step (experimental accelerated deactivation method). Finally, the differences in activity were calculated and compared. The developed method of experimental accelerated deactivation was completed by the detailed structure characterization of the aged catalysts.

### INITIAL AND RESIDUAL ACTIVITY OF INDUSTRIALLY DEACTIVATED CATALYSTS

The initial and residual activity determinations of two commercial HDS catalysts based on CoMo-Al<sub>2</sub>O<sub>3</sub> and NiW-Al<sub>2</sub>O<sub>3</sub> were performed under the typical conditions for the deep HDS: atmospheric gas oil (AGO) as a raw material, pressure 4.5 MPa, weight hourly space velocity (WHSV) 1.0 h<sup>-1</sup>, ratio of hydrogen to feed 300 Nm<sup>3</sup>/m<sup>3</sup>. The HDS reaction was realized at temperature 350 – 410 °C and the activity of tested catalyst was derived from the results of sulphur value. The initial HDS activity was expressed as the temperature, where the reaction liquid product contained less than 10 ppmw of sulphur. This value was obtained at 364 °C for the catalyst based on CoMo-Al<sub>2</sub>O<sub>3</sub> and at 375 °C for the NiW-Al<sub>2</sub>O<sub>3</sub> catalyst. The sulphur content result on each tested temperature is described in Tab. II and Tab III

Table II. The HDS activity results determined by CoMo-Al<sub>2</sub>O<sub>3</sub> catalyst

Reaction temperature, °C	Fresh cat. Sulphur, ppmw	Aged cat. Sulphur, ppmw
350	47.7	-
360	18.9	-
365	8.9	66.5
380	-	23.3
390	-	7.9
<b>10 ppmw, °C</b>	<b>364</b>	<b>388</b>

Table III. The HDS activity results determined by NiW-Al<sub>2</sub>O<sub>3</sub> catalyst

Reaction temperature, °C	Fresh cat. Sulphur, ppmw	Aged cat. Sulphur, ppmw
350	153.0	-
360	42.1	-
375	9.9	61.4
395	-	17.7
410	-	9.9
<b>10 ppmw, °C</b>	<b>375</b>	<b>410</b>

The residual activity of 10 ppmw sulphur was obtained at 388 °C for the catalyst CoMo-Al<sub>2</sub>O<sub>3</sub> and at 410 °C for the NiW-Al<sub>2</sub>O<sub>3</sub> catalyst. The effect of initial and residual HDS activity on the temperature is described in Figure 3. From the well-known combination of catalysts industrial operated period, knowledge and comparison of initial and residual activities, the rate of activity decrease can be calculated. It was 1.44 °C per month for the catalyst based on CoMo and 2.18 °C per month for the catalyst NiW. From the figure can be seen that the catalyst based on NiW was deactivated much faster than the CoMo catalyst. This fact is important for the verification of the developed experimental accelerated deactivation methodology.

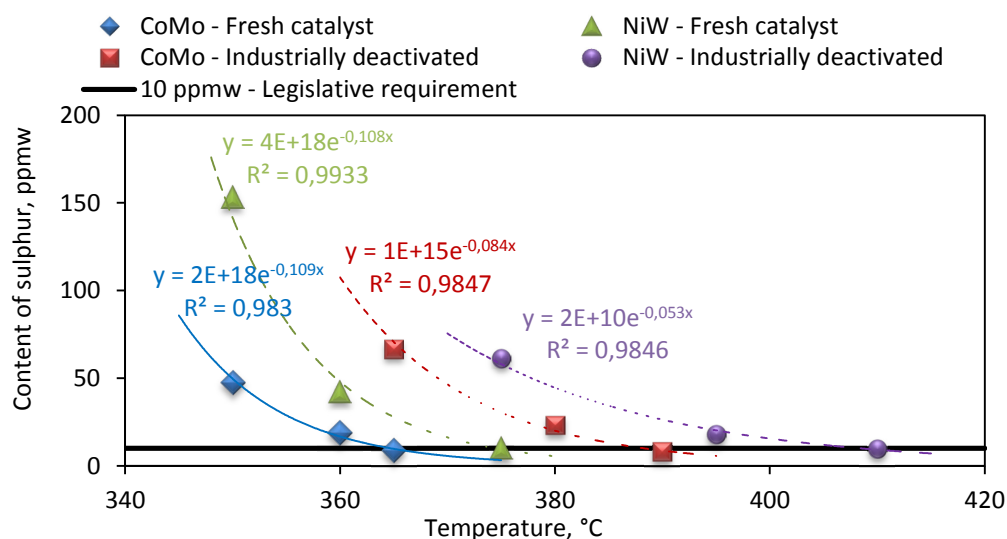


Figure 3. The initial and residual HDS activity determined on the CoMo and NiW catalysts

### Deactivation step

The accelerated experimental deactivation method included (i) testing of the initial activity (ii) deactivation step and (iii) determination of the decreasing rate of activity. The deactivation step with different time length was implemented by the injection of highly aromatic raw material "LCO" with a coking tendency under the conditions (temperature 360°C, atmospheric pressure, hydrogen flow 10-15 Nm<sup>3</sup>/m<sup>3</sup>, WHSV 3.0 h<sup>-1</sup>).

Before and after the deactivation step the typical HDS conditions were set (the feed –AGO, pressure 4.5 MPa, hydrogen flow 300 Nm<sup>3</sup>/m<sup>3</sup>, and WHSV 1.0 h<sup>-1</sup>). Subsequently, the reaction temperature for sulphur level 10 ppmw was determined. All measured data, denoting the initial and residual activity of the industrially deactivated CoMo catalyst and the initial and residual activity of the CoMo catalyst deactivated by experimental deactivation methods with time length (1 hr., 1+1 hr., 2 hrs., 4 hrs.) can be seen from the Fig. 4. The activity of the catalysts from the experimental deactivation was higher compared with the activity of the catalysts from the industrial reactor.

The length of experimental method has big effects on the rate of HDS activity (see Fig. 4). The deactivation procedure with a length 1 hour has a negligible impact on the long-term HDS catalyst activity, while the deactivation procedure with a length more than two hours has significant impact on the HDS activity change.

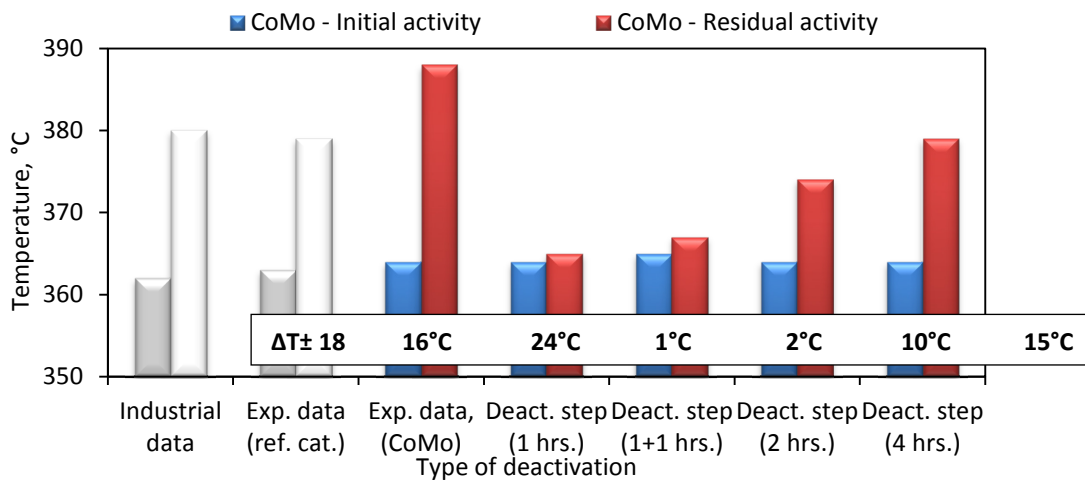


Figure 4. HDS activity set for CoMo catalyst vs. time length of deactivation step

### Comparison of experimental and industrial deactivation

The long-term HDS activity, which catalysts exhibit after approximately 7 and 11 months in an industrial reactor, can be predicted by the experimental accelerated method with the length of two, respectively four hours. The experimental accelerated deactivation method can be optimized also for the simulation of the longer operating period. From the Fig. 5 can be seen, that carbon content determined on the aged CoMo and NiW catalysts correspond with the result of HDS activity as well.

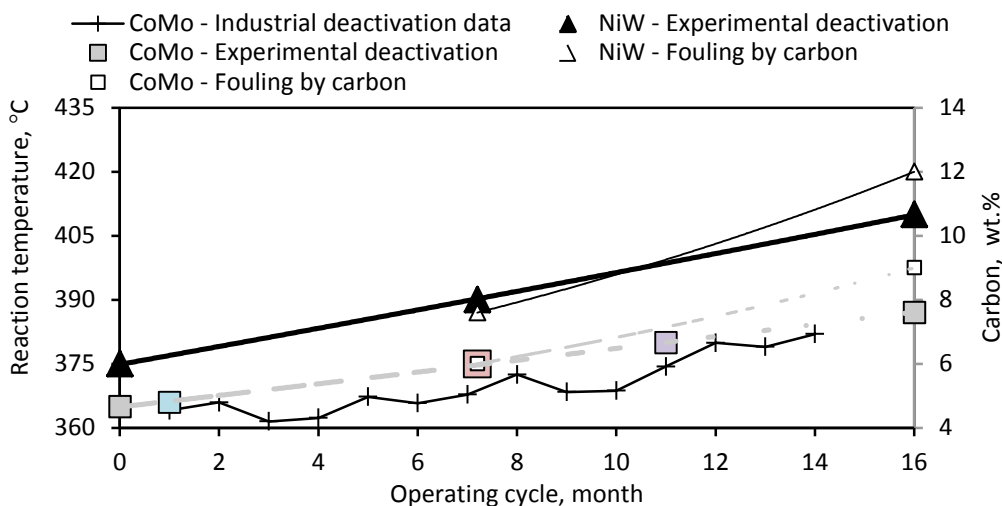


Figure 5. HDS long-term activity predicted based on the results from the accelerated deactivation methods

### Basic physico-chemical properties of fresh and aged catalysts

The catalyst structure was characterized by several analytical methods. The evaluations of physico-chemical properties of the fresh catalysts and also the catalysts after experimental respectively industrial deactivation are shown in Tab. IV.

The fresh catalyst was characterized in oxides form, i.e. before sulfidation step. The fresh CoMo catalyst is characterized with the highest pore volume, i.e. 359.9 mm<sup>3</sup>/g. The content of carbon and sulphur was characterized by optical emission spectrometry (ICP-OES) and the carbon was higher in the catalyst deactivated in the industrial reactor. The carbon content in the catalyst based on CoMo was 9.0 mass %, while the carbon content in the catalyst deactivated by experimental accelerated methodology was 6.0 mass %. The content of sulphur bounded in the active form was same for both catalysts.

The pore volume and distribution of pore size was determined by Hg porosimetry. The gradual decrease of the total pore volume during deactivation was observed. This decrease is due to causes by clogging the pores by carbonaceous deposits. The preferential clogging was seen in the pore sizes from 8.4 to 11.6 nm (Tab. IV). The results of physicochemical properties were in accordance with the results of HDS activity determination.

Table IV. Basic physico-chemical properties of HDS catalysts

Quality parameter	CoMo-Al <sub>2</sub> O <sub>3</sub>			Quality parameter	Fresh catalyst
	Fresh catalyst	Industrial deact.	Accelerated deact.		
Content of sulphur, wt. %	-	10.2	10.3	Content of cobalt, wt. %	-
Content of carbon, wt. %	-	9.0	6.0	Content of Mo*, wt. %	-
Pore volume, mm <sup>3</sup> /g	359.9	282.8	310.0	**CBD, kg.m <sup>-3</sup>	792
Pore size 11.6 – 9.8 nm, mm <sup>3</sup> /g	178.6	84.4	148.3	Length, mm	3.26
Pore size 9.8 - 8.4 nm, mm <sup>3</sup> /g	56.2	36.6	48.2	Diameter, mm	1.30
Pore size 8.4 – 6.0 nm, mm <sup>3</sup> /g	56.8	55.9	51.6	Strength D4179, N	5.2
Average pore size, nm	9.4	10.5	10.4	***LOI at 600°C, wt. %	1.3

\*Mo – molybdenum, \*\*CBD – compact bulk density, \*\*\*LOI – loss of ignition

### Carbon deposits on deactivated catalysts

The characterization of the carbon deposits was realized by thermogravimetry (TGA-IR), Raman spectroscopy and by SEM-EDS microscope technique.

The Raman spectroscopy allowed characterization of carbon hybridization – sp<sup>2</sup> bonds (*graphite like*) and sp<sup>3</sup> bonds (*diamond like*). The Raman spectra of disordered graphite showed two quite sharp modes, the peak around 1580 – 1600 cm<sup>-1</sup> and the peak around 1350 cm<sup>-1</sup>. The carbon structures were almost the same for experimental and industrial deactivation for both catalysts. The different intensities of response were found because the catalysts deactivated by experimental accelerated method were not clogged by carbon deposits so much as the industrially deactivated catalysts. The results from Raman spectroscopy correspond with the residual HDS activity of tested catalysts.

TGA-IR was used for the characterization of the carbon deposits type. From the Fig. 6, can be seen two peaks with different intensities. These peaks characterize the two basic types of carbon, i.e. *soft-coke*, which is during operation gradually transferred to the *hard-coke*. For the catalyst deactivated in the operating plant dominates hard-coke, while the catalyst deactivated by the specially developed accelerated method dominates soft-coke.

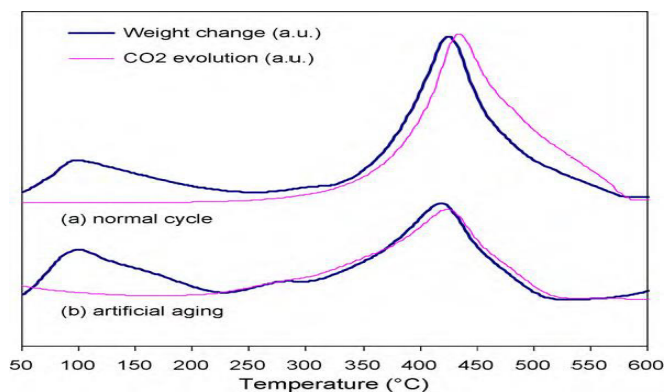


Figure 6. TGA-IR analysis of carbon deposits on the HDS catalysts based on CoMo-Al<sub>2</sub>O<sub>3</sub> deactivated in the industrial reactor (a), respectively by experimental accelerated method with the deactivating agent (b)

Visualization of carbon deposits was realized by SEM-EDS. The samples were coated with platinum in an argon atmosphere at 50 Pa, 18 mA, for about 180 seconds. The scanning of a sample was carried out with energy of 5 keV and current of 300 mA.

From the Fig. 7 can be seen, that the catalyst deactivated by experimental accelerated procedure was clogged in some places, whereas the industrially deactivated catalyst was clogged much higher, but it was also in line with other results.

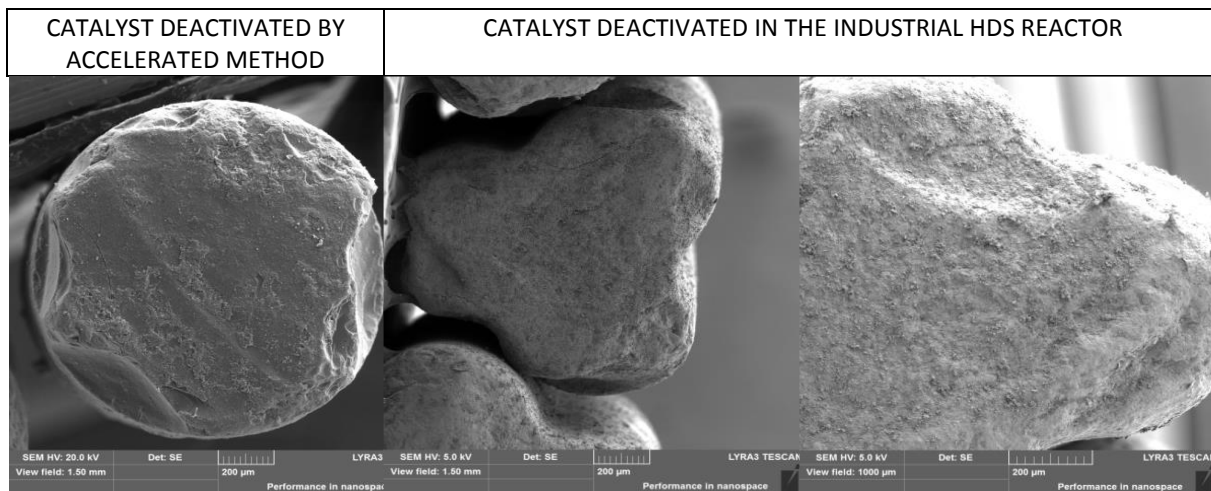


Figure 7. The carbon deposits by SEM-EDS microscope on aged HDS catalysts

### Conclusion

The described accelerated method of experimental deactivation can be used for the estimation of the HDS catalysts deactivation rate. The long-term HDS activity, which catalysts exhibit after approximately 11 months in an industrial reactor, can be predicted by the experimental accelerated method with the length four hours.

The experimental accelerated deactivation method can be easily optimized for the simulation even longer operating period. With an optimizing of the deactivation step length can be achieved the similar deactivation level like in an industrial reactor.

The results of physico-chemical characterization of the aged catalysts confirmed that the deactivation in the industrial reactor occurred especially due to the fouling of catalyst surface by carbon or dust. Simultaneously with this, the average pore size and the total pore volume were decreased. Evaluation of both deactivation procedures were realized by TGA-IR, Raman spectra and SEM-EDS. The results indicated that both deactivation occurs from the same cause (*deactivation by carbon deposits*) and the same way (*sp<sup>2</sup> and sp<sup>3</sup> bonds of disordered carbons*). Important fact is that all mentioned facts and dependencies were valid for both types of deactivation – industrial and experimental.

### Acknowledgment

*This publication is a result of the project no. FR-T13/084, supported by the Ministry of Industry and Trade of Czech Republic, which is being carried out in the UniCRE centre whose infrastructure was supported by the European Regional Development Fund and the state budget of the Czech Republic.*

### Literature

1. H. Topsøe, B. Hinnermann, J.K. Nørskov, J.V. Lauritsen, F. Besenbacher, P.L. Hansen, G., Hytowitz, R.G. Egeberg, K.G. Knudsen, *Catal. Today* 12 (2005) 107-108.
2. T. Fujikawa, *Top. Catal* 52 (2009) 872.
3. K.G. Knudsen, B.H. Cooper, H. Topsøe, *Appl. Catal. A. Gen* 189 (1999) 205-215.
4. A. Stanislaus, A. Marafi, M.S. Rana, *Catal. Today* 153 (2010) 1-68.
5. G.F. Froment, G.A. Depauw, V. Vanrysselberghe, *Ind. Eng. Chem. Res.* 33 (1994) 2975.
6. V. Tukač, A. Prokešová, J. Hanika, M. Zbuzek, D. Kubička, *Reliability of HDS Catalyst Tests in Trickle-bed Reactor, EuropaCat-XI, Lyon (France), 2013*, pp. 1-6.
7. S.K. Sahoo, S.S. Ray, L.D. Singh, *Appl. Catal. A: Gen.* 278 (2004) 83-91.
8. J.A. Moulijn, A.E. Diepen, F. Kaptein, *Appl. Catal. A: Gen.* 212 (2001) 3-16.
9. Zbuzek M., Kubička D., Kundertová N., *Vývoj metodiky pro zrychlené testování dlouhodobé aktivity odsiřovacích katalyzátorů, APROCHEM 2012, Kouty nad Desnou (2012)*.

## STABILIZATION OF ASPHALTENES IN FUEL OILS

**Vráblík A.**, Černý R.

*Research Institute of Inorganic Chemistry (VÚAnCh), Department of Efficient Refining Technologies (UniCRE-EFFRET), Chempark Litvínov, 436 70 Litvínov, Czech Republic  
Ales.Vrablik@vuanch.cz*

### Abstract

The stability or incompatibility of the fuel oils depends on the presence, amount, and character of asphaltenes tendency to precipitation. The significant technical problems during transport as well as storage or final processing can be connected with this fact.

The stability of fuel oils is classified by the determination of the total sediment content. The method for assessment of the accelerated total sediment (TSA) is a very good tool for determination of the fuel oil stability or compatibility. In the TSA chemical ageing procedure the asphaltenes in fuel oil are gradually flocculated using n-hexadecane (cetane).

Our work is focused on the comparison of the laboratory prepared fuel oils containing different amount of resin-based material. The effect of resin-based material on final stability is showed and described. The TSA method was optimized and verified for fuel oils containing higher content of the resin-based materials. The positive impact of the resin-based materials on the TSA parameter was detected.

### Introduction

The surplus of heavy fractions is formed during crude oil processing. These fractions are usually used for the production of bitumens or fuel oils and the useless residues are utilized by this way. However, viscosity of heavy residues must be reduced before their subsequent utilization. One of the possibilities for viscosity reduction is thermal cracking process – visbreaking.

Under the natural circumstances all the components of petroleum, bitumen and heavy oils are in an ideal balance. The balance can be deteriorated by physical or chemical processes during the processing of crude oil in the refinery. The changes in this equilibrium system can be followed-up by asphaltenes precipitation, phase separation or sediment formation.<sup>1</sup> Many changes are also caused in the external structures of the asphaltenes during the visbreaking process. It can lead to the formation of sludge, sediments and unstable structures.<sup>2</sup>

The asphaltenes precipitation may cause incompatibility of the whole mixture. This incompatibility induces many technical problems during transport, storage and final processing.<sup>3</sup> The asphaltene precipitation is very complex process often described as an intricate colloidal dispersion.<sup>4,5</sup> Molecules of asphaltenes are in this structure in micelles form and are affected of many factors.<sup>6</sup> These factors include the peptisability of the asphaltene core, the peptising power of the resins, the relative amounts of asphaltenes and resins and the aromaticity of the oil phase.<sup>6</sup>

One of the possibilities of fuel oil production is the use of streams from thermal cracking (visbreaking). The fuel oil is produced from heavy vacuum residues. The heavy residues are usually blended with low-boiling crude oil fractions to the achievement the required properties and meet the relevant standards. While respecting the requirements the minimal content of diluents should be used because of the stability of the resulting mixture.<sup>7</sup> The stability of asphaltenes can also be disrupted by using different residues for fuel oil production.<sup>6</sup>

The fuel oils are often characterized using the specific parameters connected with their stability.<sup>8</sup> For the fuel oil characterization and classification it is very important to know for example their viscosity, pour point, content of particles insoluble in toluene or total sediment content. All these parameters can identify technical problems during their processing. Last but not least the total time of production, transportation and processing affects the stability of petroleum products.<sup>1</sup>

Asphaltenes in the crude oil are characterized as a fraction insoluble in n-heptane but soluble in toluene. The content of asphaltenes can vary depending on the type and origin of the crude oil. The same situation is in the case of fuel oils.<sup>9</sup>

The quality of the fuel oil which is used as a marine fuel must be in accordance with ISO 8217, Petroleum products – Fuels (class F) – Specifications of marine fuels.<sup>10</sup> In this standard all the required parameters as well as relevant test methods are prescribed. The method for content of total sediment accelerated (TSA) is a very good tool for determination of the fuel oil stability and compatibility. In the TSA method the asphaltenes are gradually flocculated by the addition of n-hexadecane.<sup>11,12</sup>

This study is focused on the possibility of fuel oil stabilization by the addition of resin-based material. Samples of fuel oil with different content of resins were prepared in the laboratory scale. The samples were evaluated

for stability using the sediment determination by hot filtration after chemical ageing. The positive impact of higher resin content on the TSA parameter was detected and described.

### Experimental

The fuel oils were prepared using a heavy residue and a relevant diluent. All the components were preheated and carefully homogenized. Two different fuel oils with different content of the resin-based material were used for the final blending in this study. The final content of the resin-based material in this blend was calculated. The stability was assessed using the hot filtration according to ISO 10307.

### Methods and materials

**Total Sediment (TS)** was assessed using the hot filtration according to ISO 10307-1. A sample was filtered through the preheated apparatus at 100 °C and after solvent washing and drying the total sediment on the filter was weighted. This determination was performed in duplicate and the total sediment by hot filtration is reported as the average of the two determinations. The mass percentage of the total sediment for each test specimen was calculated using Equation (1).

$$S = \frac{(m_5 - m_4) - (m_3 - m_2)}{10 \cdot m_1} \quad (1)$$

where S is the total sediment, expressed as a percentage by mass;  $m_1$  is the mass of the test portion, expressed in grams;  $m_2$  is the mass of the lower filter before filtration, expressed in milligrams;  $m_3$  is the mass of the lower filter after filtration, expressed in milligrams;  $m_4$  is the mass of the upper filter before filtration, expressed in milligrams and  $m_5$  is the mass of the upper filter after filtration, expressed in milligrams.

The difference between the satisfactory test results, expressed as the average of duplicate determinations, obtained by the same operator with the same apparatus under the constant operating conditions on the identical test material would, in the long run, in the normal and correct operation of the test method, exceed the values below in only one case in twenty. The repeatability,  $r$ , for residual fuels was calculated according to Equation (2)

$$r = 0,089 \cdot \sqrt{x} \quad (2)$$

where  $x$  is the average of the test results, expressed as a percentage by mass.

**Total Sediment Accelerated (TSA)** was carried out in accordance with ISO 10307-2. TSA is determined after the accelerated ageing where a sample of residual fuel oil is diluted with a specified amount of n-hexadecane (cetane) under carefully controlled conditions. The sample is then heated to 100 °C for 1 hour, followed by hot filtration in accordance with ISO 10307-1.

**Wash solvent**, consisting of 85 % (V/V) heptane (P. A., lach:ner) and 15 % (V/V) toluene (P. A. lach:ner).

**n-Hexadecane** in the purity  $\geq 99$  %, Merck

**Fuel Oil** was blended in the laboratory scale from industrial streams. The fuel oil contained vacuum residue and a lighter component for dilution. Two types of fuel oils were used in this work. The fuel oil with the resin-based material in the content of 35 wt. % and the second one which had less than 1 wt. % content of the resin-based material. The resulting quality of the prepared fuel oils was varied depending on the content as well as on the properties of the diluting components.

### Results and discussion

The manipulation with the filter papers, especially with the lower one, was the most problematic point of the stability verification during this study. The higher content of the resin-based materials in the fuel oil caused the clogging of the lower filter paper (Fig 1). The resin-based materials are clearly visible in the following figure as a darker spots on the right side.

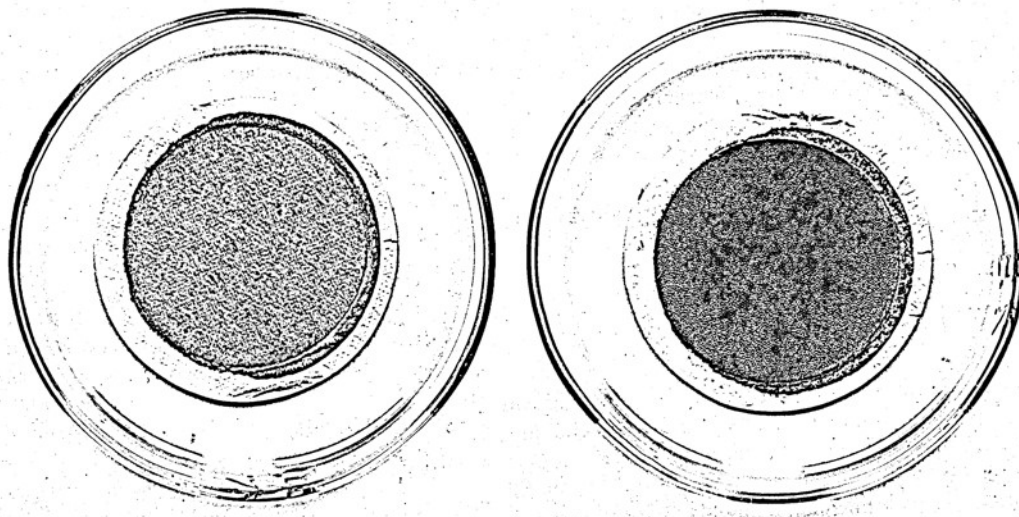


Figure 1. Comparison of the upper (left) and the bottom (right) side of the lower filter paper

The resin-based materials, which have passed through the filter paper but not through the frit, caused not correct increase of the lower filter weight in the overall balance. This fact caused the unreal results of the total sediment assessment as it can be seen in Figure 2.

This problem could be solved using the third filter paper as an auxiliary mechanism. The third paper is prepared for the measurement by the same way as the others (according to ISO 10307) but it is not incorporated into the final balance. The results with the third filter are illustrated in the Figure 2 as well.

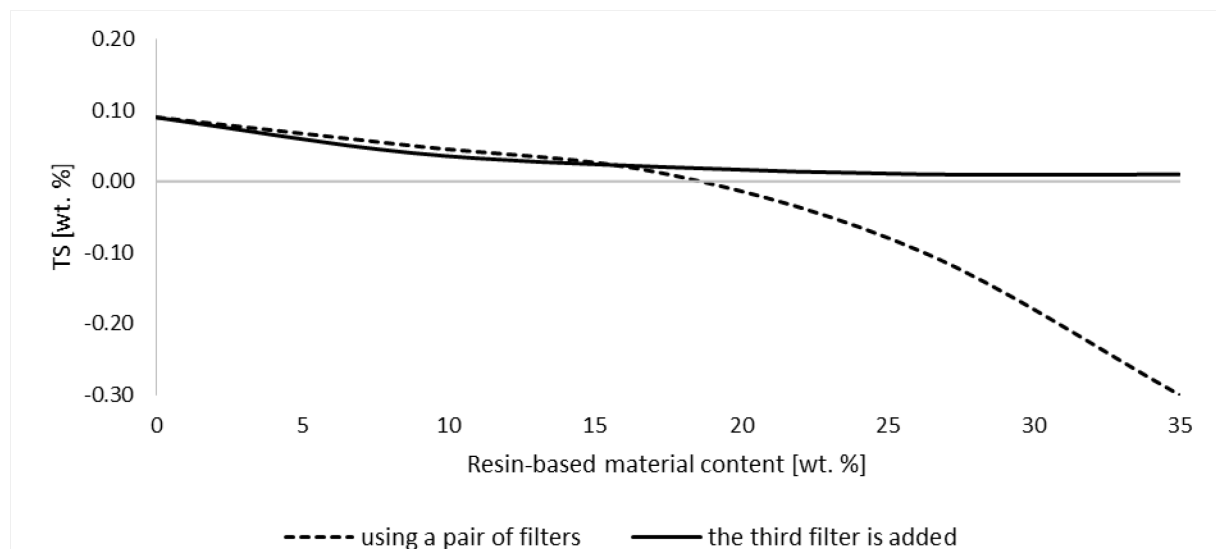


Figure 2. Comparison of TS obtained using of two or three filters

According to the Figure 2, the TS was closer to the reality using the third filter. The result with the pair of filters were in the negative values in the case of the higher content of the resin-based material - above 17 wt. %. In the following Figure 3 the bottom sides of the lower and the third filter paper are illustrated. The higher presence of the resin-based materials on the bottom side of the third filter paper is evident. The difference between weight of the lower and the third (lowest) filter was ranged from 3 to 28 mg depending on the resin-based material content. It must be pointed that there was also difficult handling during the taking off the filter from the frit. The third filters were often damaged.

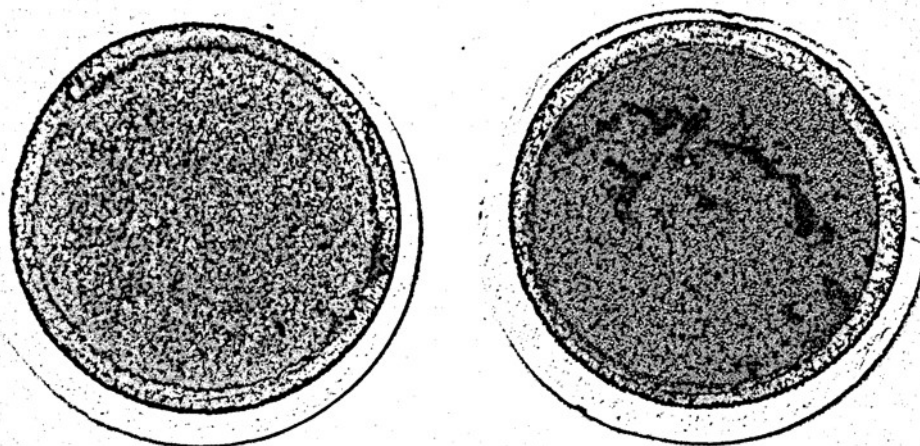


Figure 3. Comparison of the bottom sides of the lower (left) and the third (right) filter paper

The effect of the addition of resin-based materials into the fuel oil was investigated using the third filter paper. This procedure was in accordance with the method ISO 10307. In this method it is mentioned that the same results are achieved by the use of a fine wire mesh support screen in combination with a third, disposable filter. This third filter can be placed below the two test filters on the support screen and the same pre-drying regime followed as for the test filters, but without weighing the third filter before placement, discarding it when filtration is complete (NOTE 2 – part 9, Filter preparation).<sup>11</sup>

We found out that the results are different with the third filter when the resin-based materials content was more than 17.5 wt. %. This fact is not in accordance with the note mentioned in the relevant standard.

All the prepared fuel oils as well as the measured TSA values are mentioned in the Table I. The maximum TSA value according to ISO 8217 is 0.10 wt. %.

Table I

Stability (TSA) of the prepared fuel oils

Resin-based material content [wt. %]	< 1	9	18	26	35
Fuel Oil A – TSA [wt. %]	0.10	0.06	0.04	0.03	0.01
Fuel Oil B – TSA [wt. %]	0.18	0.16	0.12	0.10	0.05
Fuel Oil C – TSA [wt. %]	0.15	0.12	0.11	0.09	0.06
Fuel Oil D – TSA [wt. %]	< 0.01	< 0.01	< 0.01	< 0.01	< 0.01

The TSA value is really related to the content of resin-based materials. These materials may affect the stability of present asphaltenes because of their acid-base interaction with the micellar core in the structure of asphaltenes. The resin-based materials wrap the micellar core which increases the overall stability of the whole colloidal system. The stabilized molecules of asphaltenes are more resistant to precipitation. It should be noted that the precipitation of asphaltenes is basis for the TSA parameter assessment.

The typical trends for TSA changes in connection with the increasing content of the resin-based materials were constructed (Figure 4). The limit value according to ISO 8217 for TSA is mentioned in the figure as well.

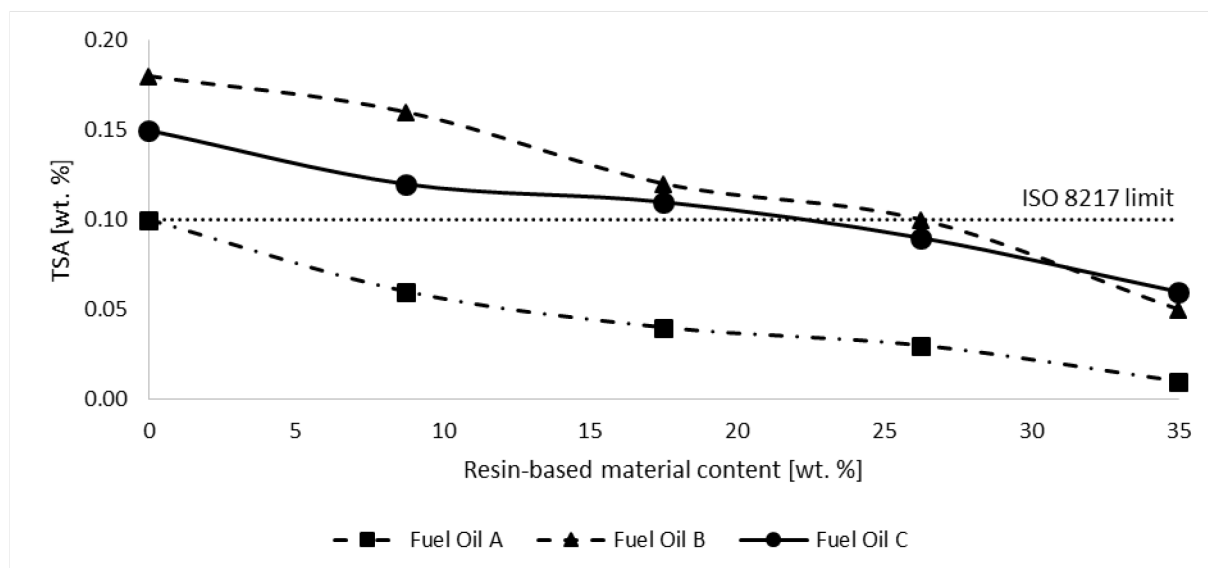


Figure 4. TSA vs. content of resin-based material

The increasing content of resin-based material had an observable effect on the TSA value. The increasing content resulted TSA reduction. It was found there is a possibility to improve the fuel oil which is out of the specific requirements (fuel oil B and C) for TSA value. This improvement was carried out by addition of the resin-based materials. The TSA for fuel oils B and C met the relevant minimal value in the case of 26 wt. % content of the resin-based material. The fuel oil A was improved by the same way as well. The fuel oil D (Table I) was without any significant changes because of the very low initial TSA value.

### Conclusions

The several fuel oils with different content of resin-based material and different stability (TSA) were prepared in the laboratory scale.

The test method for TS/TSP/TSA assessment was optimized and tested on the fuel oils containing higher amount of the resin-based materials. This method is reliable with application of the third filter paper as an auxiliary tool. The prepared fuel oils were assessed and compared using the optimized method of the hot filtration after their chemical aging (TSA).

The effect of the resin-based material content on the final stability of the prepared fuel oils was showed and described in this work. We found out that there is a possibility how to improve the stability of fuel oils using the higher content of resin-based materials. It was demonstrated that the individual prepared fuel oils (A; B; C and D) were significantly different in the comparison of the TSA values.

All the prepared fuel oils were successfully treated with the help of resin-based materials to meet the minimal TSA value according to ISO 8217. It should be noted that it really depends on the stability or quality of the initial fuel oils and thus the effect of the resin-based material addition was varied, but still was effective. The specific fuel oil should be tested in the real condition.

### Acknowledgment

*This publication is a result of research project solved in a frame of UniCRE centre which infrastructure was supported by the European Regional Development Fund and the state budget of the Czech Republic. The publication was supported by institutional funds (Ministry of Industry and Trade of the Czech Republic).*

### Literature

1. Chang S.H., Robinson P.R.: Practical Advances in Petroleum Processing. New York: Springer, 2006.
2. Vermeire M.B.: Everything You Need to Know About Marine Fuels. Ghent: Chevron Global Marine Products, 2007.
3. Alvarez P., Menendez J.L., Berruoco C., Rostani K., Milan M.: Fuel Processing Technology, 96: 16–21 (2012).
4. Perez-Hernandez R., Mendoza-Anaya D., Mondragon-Galicia G., Espinosa M. E., Rodriguez-Lugo V., Lozada M., Arenas-Alatorre J.: Fuel, 82: 977-982 (2003).

5. Kamenchuk Y. A., Pisareva S. I., Andreeva L. N., Unger F. G.: Chemistry and Technology of Fuels and Oils, 42: 39-42 (2006).
6. Spencer E.T.: Fuel, 77: 821-828 (1998).
7. Stratiev D., Dinkov R., Petkov K., Kirilov K.: Oil & Gas Journal, 106: 46-49 (2008).
8. Singh I., Kapoor M., Ramaswany V.: Fuel, 70: 195-199 (1991).
9. Holmes J.W., Bullin J. A.: Bryan Research and Engineering, Inc - Technical Papers, 1-6 (2006).
10. ISO 8217:2012 Petroleum products – Fuels (class F) – Specifications of marine fuels.
11. ISO 10307-1:2009 Petroleum products – Total sediment in residual fuel oils, Part 1: Determination by hot filtration.
12. ISO 10307-1:2009 Petroleum products – Total sediment in residual fuel oils, Part 2: Determination using standard procedures for ageing.

# ULTRA PURIFICATION OF ENERGETIC GAS FROM BIOMASS GASIFICATION

**Machač P.**, Duong V. M.

*University of Chemistry and Technology Prague, Prague, Czech Republic*

## 1. Introduction

Solid fuels gasification provides opportunities for the bio-energy conversion, extraction and contribution to electricity. The primary advantage is using high purified energetic gas in the combined cycle steam-gas turbine, or another combined application is for the fuel cell. Combustible components of the produced gas mixture such as CO, CH<sub>4</sub>, H<sub>2</sub> accompanied by H<sub>2</sub>S, COS and tar are dependent quantities, varied on the energy self-gasification process, setting conditions and the type of selected solid fuel. However, these impurities must be removed at the required concentration level for the specific use. The ultra-purification of generated gas using selected solid oxide based sorbents was experimentally investigated in a series of experiments.

Wood constitutes one the most abundant agricultural bio-fuels for production of electric energy due to its heating, calorific value and availability. Specific compositions, defining the contents of hydrocarbons, mainly hydrogen and sulfur compounds, of energetic gas for the fuel cell must be conformed in terms of long-term stable operation. Especially, the common operating value for high temperature fuel cell is at 1000°C in which gas concentration required at the inlet of the fuel cell is below 1ppmv.

The research aimed to investigate the hot cleaning method of model gas simulating the composition of the raw gas from the gasification of solid fuels. Purification was performed toward sulfur compounds H<sub>2</sub>S and COS to select or develop and produce suitable sorbent of mentioned sulfur compounds. The application ensures an optimum condition on the moist syngas at high temperatures (over 300°C), which properly meets up with the operational requirements of SOFC - Solid Oxide Fuel Cells. A laboratory reactor for testing selected sorbents was designed and tested to achieve this prior prerequisite.

## 2. Methodology

### 2.1 Fuel cell characteristics

The difference between the fuel cell and electric battery lies in the fact that the chemicals are not part of the anode and cathode, but they are continuously fed from outside. Both electrodes act only as a catalyst, are not reset during operation, and their composition is not changed. The fuel cell thus requires a very clean fuel, which may contain only acceptable levels of sulfur compounds<sup>1</sup>.

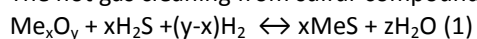
Table I. Electricity generators performance and their efficiency of conversion

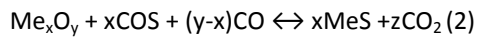
Type of device	Typical performance	Conversion efficiency
Micro turbines	10 ÷ 60 kW	20 ÷ 25%
Gas engines	100 ÷ 1000 kW	25 ÷ 35%
Gas turbines	3 000 ÷ 5 0000 kW	25 ÷ 35%
IGCC - Integrated Gasification Combined Cycles	30 000 ÷ 120 000 kW	35 ÷ 45%
MCFC - Molten Carbonate Fuel Cells	500 ÷ 8 000 kW	45 ÷ 50%
SOFC - Solid Oxide Fuel Cells	750 ÷ 10 000 kW	50 ÷ 55%
SOFC + Turbine - Solid Oxide Fuel Cells Turbines hybrids	2 000 ÷ 80 000 kW	55 ÷ 65%

Different ways of electricity producing from the heat can be categorized according to their performance and efficiency. Table 1 indicates that the SOFC working at high temperature reaches the maximum of efficiency<sup>2</sup>.

### 2.2 Adsorbents consideration

In practical, the sorbents considered for hot removal of sulfur compounds (mainly H<sub>2</sub>S and COS) are oxides of a certain metals like ZnO or binary metal oxides. Specific surface and mechanical properties are required to improve the usability of the sorbents. Especially for the ultra-desulphurization, sorbents need high reactivity, suitable texture (specific surface, porosity, and pore size distribution), mechanical and thermal ruggedness. Sorption products also have to be stable in a variety of hot gas cleaning temperature (between 400 and 900°C). The hot gas cleaning from sulfur compounds is based on reversible reactions:





Reactions 1 and 2 produce solid sulfides and water or carbon dioxide. It is technically possible to regenerate the spent sorbent by hydrolysis, partial oxidation or by reaction with sulfur dioxide, but not in gasification. The feasibility of the sorbent regeneration depends on the initial sulfur content of the gas. Oxidation of  $\text{H}_2\text{S}$  to  $\text{S}$  or  $\text{SO}_2$  at the expense of the metal oxides or even the thermal decomposition  $\text{H}_2\text{S}$  to the  $\text{S}$  and  $\text{H}_2$  catalyzed by metal oxides. In the following paragraphs, the suitability of particular metals or their compounds as a sorbents for the hydrogen sulfide removal will be discussed 4.

#### Alkaline Earth Metals

The only promising compound from this group is the  $\text{CaO}$ . The oxides of  $\text{Sr}$  and  $\text{Ba}$  would not be active at temperatures below  $1000^\circ\text{C}$  as they form thermal stable carbonates.  $\text{MgO}$  is not suitable for high temperature cleaning for its generally low affinity to hydrogen sulfide.

#### Zinc Oxides

The zinc oxide is used in industry already because of its high affinity to the  $\text{H}_2\text{S}$  even at high temperatures. There are nevertheless two problems in the zinc oxide usage. Firstly, the originating zinc sulfide is more voluminous than the original oxide and therefore clogs the sorbent pores and limits its sorption capacity. Secondly, at temperatures over  $700^\circ\text{C}$  and in the reduction atmosphere the zinc oxide susceptible to reduction to elementary zinc which in turn has the vapor pressure of the order of  $1\text{Pa}$  and therefore may appreciably vaporize into cleaned gas. The reduction and vaporization of the zinc may be limited by the use of  $\text{ZnO}\cdot\text{TiO}_2$  sorbent.

#### Manganese Oxides

The manganese may form several oxides in the reducing environment, final one being the manganese oxide  $\text{MnO}$  which shows good desulphurization efficiency in the temperature range  $500\text{--}800^\circ\text{C}$ .

#### Copper Oxides

The copper oxide reacts with sulfur compounds in the oxidizing as well as in the reducing environment, but below the temperature range of hot gas cleaning. The spent copper sorbent should be regenerated by air-steam mixture to prevent the formation of the copper sulfate.

### 2.3 Experimental design

Laboratory equipment for measuring the sorption efficiency of sulfur compounds from an energetic gas from biomass gasification is shown in Figure 1.

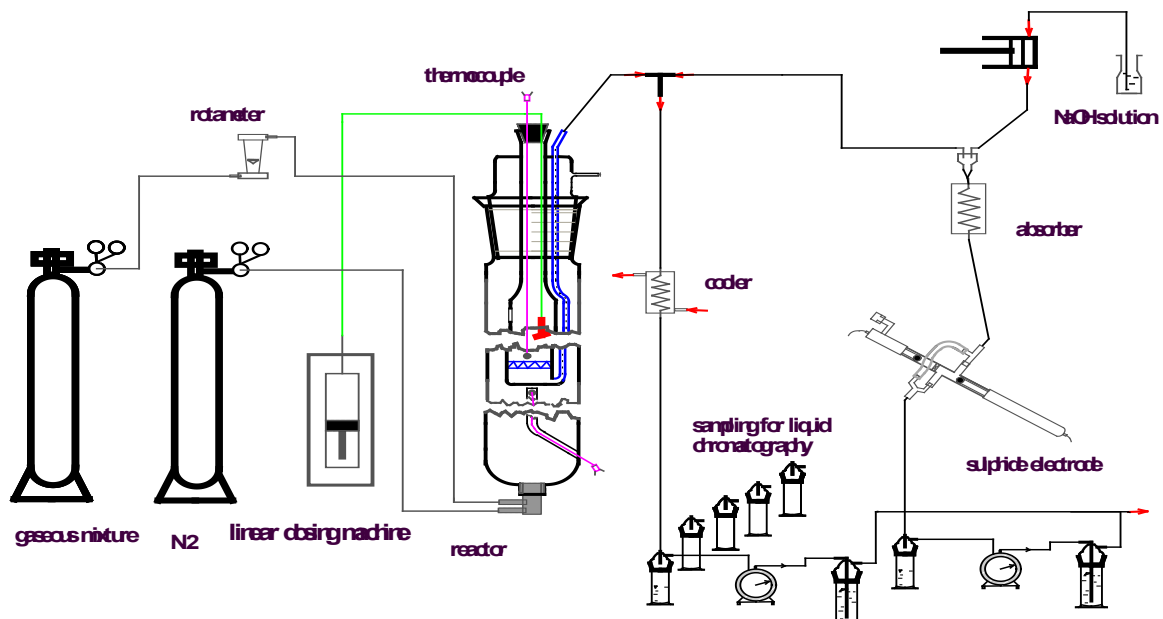
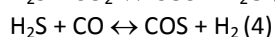
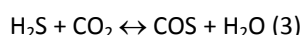


Figure 1. Scheme of the apparatus for  $\text{H}_2\text{S}$  and  $\text{COS}$  chemisorption

## 2.4 Influence of moisture content

Two main factors disadvantageous to the process, the elevated temperature and moisture content of the gas. Elevated temperature is required or seen as advantageous because it saves the sensible heat content of the gas for application. Various authors set the lower limit of temperature differently (400-550°C) but in general, the higher temperature is better process control. The moisture content of the gas is around 13vol. % at usual temperatures in procedure processing the biomass (800-900°C). Water vapor as a product of sorption reactions is substantially shifting the equilibrium to the higher concentrations of contaminants downstream of cleanup equipment.

Water content in gas is parameter influencing the whole sulfur removal process. Residual concentration of H<sub>2</sub>S as well as sorbent capacity is considerably affected by actual concentration of water in gas. Presence of water vapor in gas influences also the distribution of sulfur forms in gas.



Reactions 3 and 4 indicate that the water content in the gas may have great influence on COS creation from H<sub>2</sub>S. Previous experiments show the applicable concentrations of H<sub>2</sub>S and COS for purification of hydrogen in fuel cell are 0.02 ppm and 0.01 ppm<sup>3</sup> respectively.

Preparation of the gaseous fuel for the fuel cells plays a key role in the ultra-desulphurization. However, the degree of desulphurization strongly depends on the concentration ratios for the H<sub>2</sub>/ H<sub>2</sub>O and CO/CO<sub>2</sub>. Water and CO<sub>2</sub> shift the equilibrium towards the reactants i.e. decreases the degree of desulphurization. Carbon dioxide also decreases the decomposition of the carbonates (which is preliminary stage of the desulphurization mechanism when using the carbonates as sorbents) in the same manner.

## 3. Result and discussion

Several solid sorbents in terms of efficiency of sorption of sulfur compounds H<sub>2</sub>S and COS present in the model gas containing water vapor at elevated temperatures above 500°C were tested. Figure 2 shows that there are two stages of sorption efficiency - at the initial phase the sorption is almost total, then follows the phase with the outlet H<sub>2</sub>S concentration about half of the inlet concentration. Two effects immediately occurred when the moisture changed : (a) the outlet H<sub>2</sub>S concentration substantially fell down, i.e. there was some more capacity for the H<sub>2</sub>S sorption blocked by the water; (b) the COS began to develop from the H<sub>2</sub>S.

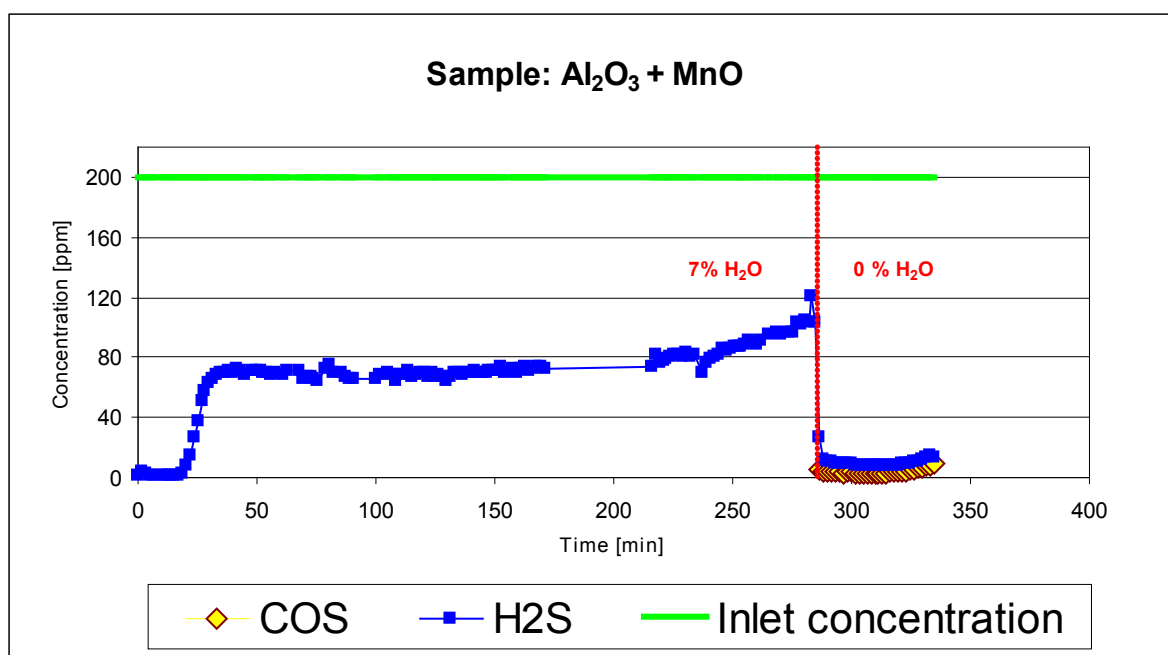


Figure 2. Breakthrough curves of H<sub>2</sub>S on sorbent ICT-Z2 (MnO 23.5%, MgO 23.5%, graphite 3%, Al<sub>2</sub>O<sub>3</sub> 50%)

An important property of the solid sorbents is their mechanical strength in conditions of frequent heating and cooling. Sample DI/500 has granular shape it is dolomite fine gravel, grain size about 4mm; composition: 58,75 %CaCO<sub>3</sub>, 36,96 %MgCO<sub>3</sub>, and 4,29% the residue is SiO<sub>2</sub> + Al<sub>2</sub>O<sub>3</sub>. The stability of the sorbent particles prevents the disintegration connected with an increase in pressure drop of model gas passes through sorbent. Hence, the calcination of dolomite was treated at 500° C for 30min before the H<sub>2</sub>S sorption measurement.

Components H<sub>2</sub>S and COS were detected in the reaction mixture by chromatography. Results in Figure 3 indicate a breakthrough curve of H<sub>2</sub>S during the an adsorption process with 3 grams of solid sorbents in the reactor and the flow rate of model mixture was 1.4 L [20°C; 101kPa] / min corresponding to the inlet concentration 188ppm. Other volume fractions of CO, H<sub>2</sub>, CO<sub>2</sub>, N<sub>2</sub> were 19.97, 17.51, 17.66 and 44.86% respectively.

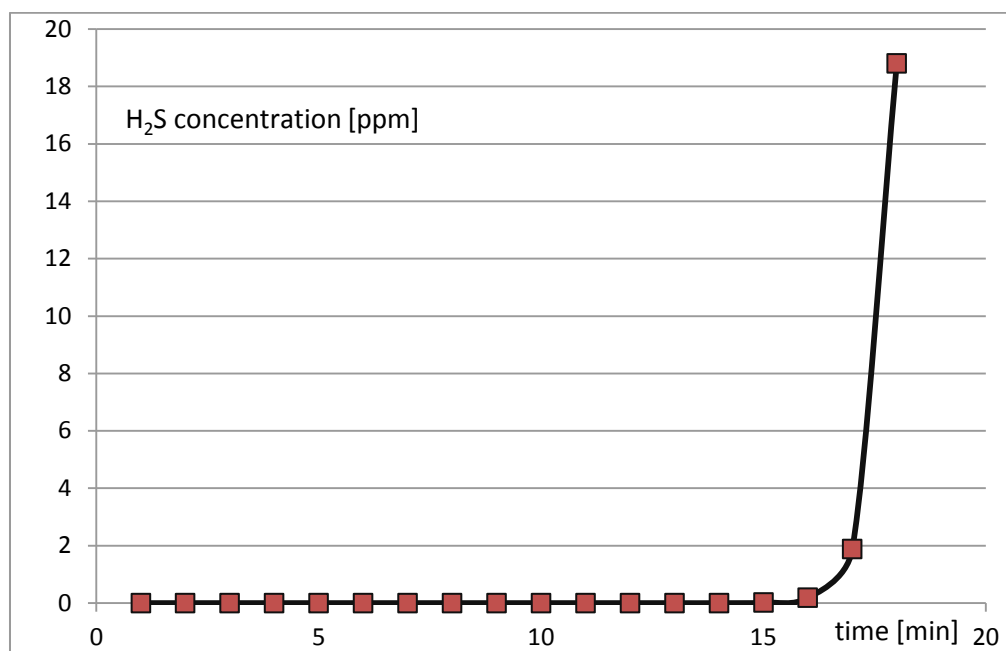


Figure 3. Detailed breakthrough curve of H<sub>2</sub>S (inlet volume fraction 188 ppm) during the adsorption process

Obtained results indicate that it is possible to operate a combined system of biomass gasification, a unit of ultra-purification and a high temperature fuel cell in compliance with operational conditions. In addition, the system could perform higher energy efficiency compared to the conventional production of electricity from fossil fuels.

**Keywords:** fuel cell, H<sub>2</sub>S, COS, moisture, adsorption, purification

#### Acknowledgment

*This work was supported by Project Green Fuel Cell No. SES6-CT-2004-503122. Authors also gratefully appreciate the Wageningen University and Research Center for providing the assistance and facilities.*

#### Literature

1. Powell M., Meinhardt K., Sprenkle V., Chick L., McVay G.: Demonstration of a highly efficient solid oxide fuel cell power system using adiabatic steam reforming and anode gas recirculation, *Journal of Power Sources*, Volume 205, pages 377-384, [http://www.science ... 7753120019911](http://www.science...7753120019911), (2012).
2. Doležal I., PoweWiki: elektroenergetika [online]. [cit. 2010-08-29]. Palivové články-princip, konstrukce, vlastnosti a využití. WWW:<<https://www.Powerwiki.cz/attach/APE/palivo.doc>>, (2010).
3. Hadrava J., Vokatý R.: Čištění vodíku pro použití v palivových článcích. *PALIVA* 6, 2, s. 66-72, (2014).
4. Machač P.: Green fuel cell project - ICT experimental part - laboratory equipment - gas cleaning (2005).

## ANALYSIS OF OPTIMAL HYDROGEN-RICH REFINERY OFFGAS UTILIZATION

**Mierka O.,** Variny M.

*Faculty of Chemical and Food Technology, Slovak university of Technology in Bratislava, Radlinského 9, 812 37 Bratislava, Slovak republic*  
*GRUCON s.r.o., Nezábudková 24, 821 01 Bratislava, Slovak republic*  
*miroslav.variny@stuba.sk*

### Introduction

In a refinery, hydrogen supply, quality and management of its production costs and utilization efficiency contributes significantly to the overall crude refining costs. Commonly the heavy gasoline platforming and steam methane (natural gas) reforming (SMR) contribute mostly to the refinery hydrogen pool, the latter usually being its marginal source<sup>1</sup>. Even in case the given steam reforming process can accept only light hydrocarbons as feed (e.g. the pre-reformer is absent), various hydrogen-rich refinery offgases (ROGs) can be utilized in this process, thus partially replacing the natural gas feed<sup>2-4</sup>. ROGs can alternatively be processed in a separate PSA (or membrane) unit, or fed to the refinery fuel gas network<sup>5</sup>.

The analysis of optimal ROGs utilization always has to consider local media (natural gas, water steam, electric energy) prices as well as any technologic, capacity, reliability, hydrogen purity etc. constraints<sup>6,7</sup>. Questions that need to be correctly answered include following:

- Which of the available alternatives enables to produce most hydrogen? (In case the hydrogen production capacity is or is to become the refinery's bottleneck in the near future.)
- What is the impact of each of the alternatives on the refinery's overall natural gas (NG) consumption both from qualitative and quantitative point of view? (Natural gas usually is both the marginal hydrogen production feed as well as the marginal refinery's fuel gas pool contributor)
- What is the impact each of the alternatives on the refinery's overall steam balance? (The SMR usually is a net steam exporter.)
- How does the resulting refinery's steam balance shift further impact the refinery's fuel and electricity costs? (E.g. what is the marginal steam source for the refinery and what type of fuel does it use? Is it just a steam source or a cogeneration unit? Or, in case there is excess steam in the refinery, how does the refinery's steam balance shift influence its marginal utilization? – F.e. on purpose electricity production in condensing steam turbines, or excess steam venting into the atmosphere.)
- Is there an impact of each of the alternatives on the overall refinery's electric energy consumption and if yes, what is its magnitude?
- What is the true marginal cost of each of the media whose balances are impacted?

We thus see that, due to the possible study complexity, a correct balance border construction is essential as each of the above mentioned aspects exclusion from the balancing process may seriously deform the resulting economic balance<sup>8,9</sup>. The second, equally crucial step is to determine the correct calculation basis for all analyzed alternatives meaning that in all considered calculation cases:

- The total amount of hydrogen supplied to its consumers is the same;
- The refinery's fuel gas network is balanced in terms of the total fuel lower heating value, e.g. if any of the considered alternatives increases or decreases the fuel gas production and/or consumption, the balance has to be restored by the respective marginal fuel consumption change;
- The refinery's steam network is balanced in terms of total steam enthalpy (the applied balancing principle is the same as in the fuel gas case);
- The refinery's electric energy balance needs to reflect each change imposed on it both from its production (side effect of steam balance shift on cogenerated mechanical or electric energy) and consumption point of view (changes in electric energy consumption due to more/less intense operation of any significant compressor, blower, pump etc. included in the balance borders)

This contribution aims at providing an analysis procedure of optimal ROGs utilization by means of a case study, considering the above aspects, each to the extent they deserve. In order to objectivize the calculation procedure, the SMR design and operating data were used separately and the obtained results were compared.

### System understudy

The analyzed system is depicted in the Figure 1. The correct balance borders have been constructed in compliance with the aspects listed in the Introduction. The system specification is as follows:

- The ROGs from two individual production units, containing 5 to 10 % wt. hydrogen and over 60 % wt. of C2 and higher hydrocarbons can either be fed to the SMR unit or to an independent PSA units or (exceptionally) directly to the fuel gas network;
- The SMR unit is the marginal hydrogen producer;
- NG is both the marginal feed to the SMR unit and to the fuel gas network;
- The SMR unit is a significant steam exporter, mostly on the high pressure (3.5 MPa) level; the marginal source of steam is the combined steam and power plant (CSPP) that produces very high pressure steam (9 MPa) that is expanded in steam turbines to different pressure levels and exported to the refinery whereby electric energy is cogenerated;
- The refinery consumes all electric energy produced in the CSPP and imports the rest from the outer grid

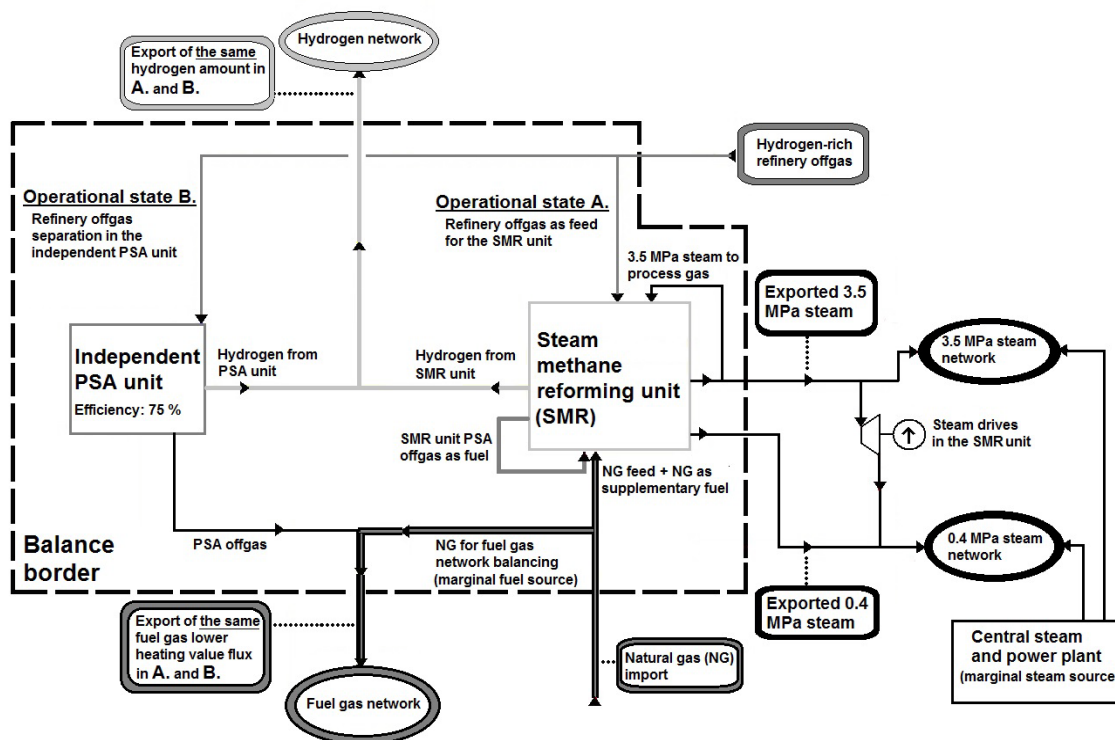


Figure 1. Schematic depiction of the system under study

Let us define two possible operational states, based on Figure 1:

- ROGs are fed to the SMR unit, serving as co-feed with NG
- SMR unit operates solely with NG feed; ROGs are processed in an independent PSA unit operating with 75% hydrogen recovery efficiency; PSA offgas is routed to refinery's fuel gas network

These two operational state possibilities are analyzed from the point of design as well as operational data point of view.

### Design data analysis

In following Tables I and II we provide key parameters and input data needed to perform calculation procedure based almost solely on SMR unit design data. As is obvious, the two SMR unit design states #1 and #2 exhibit the same reactor outlet temperature and almost the same steam to process ratio that are the two most important adjustable operational parameters. Except for feed composition both design states operate under almost the same conditions and can therefore serve as platform for comparison.

In order to recalculate the SMR design state #1 operational parameters to lower hydrogen production, one cannot use specific values but has to use the marginal ones. As the design documentation does not include other operational states from which the needed marginal values could be calculated, we had to extract them from operational data (natural gas consumption and steam export) that were plotted against net produced hydrogen. The data sets were fitted with linear dependences; the slopes of the linear fits representing the marginal values. Obtained marginal values are listed in the lower part of Table I. Are the ROGs fed to the independent PSA unit, they can be split into (virtually pure 99.9% vol.) hydrogen stream and PSA offgas. The material balance of the PSA unit is provided in Table II.

Table I. SMR unit design parameters and marginal values of NG consumption and steam export

Operational parameter	SMR design state #1: pure NG feed	SMR design state #2: NG + ROG mixture feed
Reactor outlet temperature, °C	850	850
Steam to process gas ratio, t/t	3.299	3.304
Net hydrogen produced, t/h	3.475	3.475
NG consumption (feed + extra fuel for SMR furnace), t/h	13.065	7.561
ROGs feed t/h	0	4.696
3.5 MPa / 0.4 MPa steam export, t/h	42.206 / 3.015	36.564 / 3.556
Marginal SMR unit values obtained by operational data linear regression; with pure NG feed to the SMR unit; per 1 ton of net hydrogen produced		
Natural gas consumption	4.42 tons	
Steam (3.5 + 0.4 MPa) export	18.5 tons (56.5 GJ)	

Table II. ROGs mixture composition and material balance of its processing in the independent PSA unit. Considered natural gas lower heating value is 48.86 GJ/t and its composition in % vol. as follows: Methane 96.66; Ethane 1.57; Propane 0.47; C4 and higher 0.2; Carbon dioxide 0.24; Nitrogen 0.84

Constituent, kg/h	ROG mixture feed	Hydrogen from PSA unit	PSA offgas
Hydrogen	371.0	285.7	85.3
Methane / Ethane	1127.9 / 1036.7	-	1127.9 / 1036.7
Propane / Butanes	1086.1 / 701.8	-	1086.1 / 701.8
C5 and higher / Inerts	370.0 / 2.5	-	370.0 / 2.5
Total	4696.0	285.7	4410.3
NG equivalent in lower heating value, kg/h	5098.3	699.0	4399.3

Table III. Comparison of **A.** and **B.** states. Employed prices: NG 430 €/t; 3.5 MPa steam 32 €/t; 0.4 MPa steam 22 €/t. Steam prices already incorporate the cogenerated electric energy value in the CSPP

Operational parameter / state	<b>A.</b>	<b>B.</b>
Net hydrogen production, t/h	3.475	3.189 + 0.286 = 3.475
Natural gas fed to SMR unit (feed + extra fuel), t/h	7.561	11.802
Produced PSA unit offgas NG equivalent, t/h	-	4.399
NG total consumption, t/h	7.561	11.802 - 4.399 = 7.403
Δ NG total consumption <b>B.</b> minus <b>A.</b> , t/h		7.403 - 7.561 = -0.158
3.5 MPa steam export from the SMR unit, t/h	36.564	36.92
Δ 3.5 MPa steam export <b>B.</b> minus <b>A.</b> , t/h		36.92 - 36.564 = +0.356
0.4 MPa steam export from the SMR unit, t/h	3.556	3.015
Δ 0.4 MPa steam export <b>B.</b> minus <b>A.</b> , t/h		3.015 - 3.556 = -0.541
Variable hydrogen production cost <b>B.</b> minus <b>A.</b> , €/h		+ 64

Since in both cases the same amount of hydrogen is to be generated (3.745 t/h), from Tables I,II it is obvious, that the SMR unit needs to produce just  $3.475 - 0.286 = 3.189$  t/h in **B.**. The SMR unit operation parameters at 3.189 t/h net hydrogen production are derived from Table 1, using the design state #1 definition and the SMR marginal operational parameters. F.e. the total natural gas consumption in the SMR unit at 3.189 t/h hydrogen production can thus be calculated as follows: NG consumption =  $13.065 \text{ t/h} - 4.42 \text{ t/t} \cdot (3.475 - 3.189) \text{ t/h} = 11.802 \text{ t/h}$ . In the same manner, the net 3.5 MPa steam export (supposing the 0.4 MPa steam export does not change) at 3.189 t/h hydrogen production is as follows:  $42.206 \text{ t/h} - 18.5 \text{ t/t} \cdot (3.475 - 3.189) \text{ t/h} = 36.92 \text{ t/h}$ . The following Table 3 provides the comparison between the 3.475 t/h hydrogen production by the operational state **A.** and **B.**. Obviously, both hydrogen AND PSA offgas are produced in **B.**, whereas only hydrogen is produced in **A.**. Thus the PSA offgas value in form of NG heating equivalent has to be incorporated into calculations as an extra NG stream lowering the NG consumption in **B.**

As appears from Table 3, **state B.**, compared to **A.**, is accompanied by lower natural gas consumption and slightly lower total steam export while keeping the net produced hydrogen flow the same. Expressed in financial terms and using the model prices of energy media, hydrogen production by **B.**, compared to **A.**, is cheaper by 64 €/h, e.g. it is cheaper to produce hydrogen from pure natural gas and process the ROGs in the

independent PSA unit. Obviously this difference would further increase if the PSA efficiency were higher. Recently, after adsorbent change, the given PSA efficiency has been reported to increase to 85 %, that in the considered case would enable to recover additional 37 kg/h of hydrogen resulting in additional 10 €/h benefit. The fact itself that feeding ROGs to SMR unit, instead of their separation in the independent PSA unit is economically unfavorable is perhaps a bit surprising but it can be effectively explained considering the stoichiometry and equilibrium data for the light hydrocarbons steam reforming:

- Per 1kg of produced hydrogen, consumption of C2 and higher hydrocarbons is higher than that of methane (natural gas), due to lowering hydrogen content with increasing number of carbon atoms;
- Per 1kg of produced hydrogen, steam reforming of C2 and higher hydrocarbons consumes more water steam than in the case of methane (natural gas) reforming;
- Hydrogen present in the ROGs shifts the reaction equilibrium back towards the reactants

### Operational data analysis

The long term operational parameters of the SMR unit understudy differ from design: lower reactor outlet temperature (790 to 820 °C) and a somewhat higher steam to process gas ratio (appr. 3.6) is applied. In order to confirm the results obtained from comparing design states by real SMR unit operational states analysis, we processed the operational states in the same manner as described above, with minor adjustments. The data provided were in form of daily averages, comprising all relevant calculation inputs including the amount and composition of ROGs processed in the SMR unit. The calculation procedure is shown in Table IV.

Table IV. Calculations example based on operational data.\*: 11.9 €/h have been subtracted, representing the by appr. 0.54 t/h lower design 0.4 MPa steam export (see Table 3) in **B.**, compared to **A.**

Operational parameter / date	22.8.2010	29.10.2010
Net hydrogen produced, t/h	2.779	2.749
NG consumption (feed + extra fuel for SMR furnace), t/h	11.288	9.565
ROGs feed; hydrogen content, t/h	0	1.473 ; 0.174
3.5 MPa steam export, t/h	36.61	35.49
Hydrogen obtainable in the independent PSA unit; PSA offgas NG equivalent, t/h	0.131; 1.305	
Adjusted 22.8.2010 operational state (= <b>B.</b> ), matching the 29.10.2010 state (= <b>A.</b> )		
Hydrogen to be produced in the SMR, t/h	2.749 – 0.131 = 2.618	
Adjusted NG consumption, t/h	11.288 – 4.42.(2.779-2.618) = 10.576	
NG consumption incl. the PSA offgas credit, t/h	10.576 – 1.305 = 9.271	
Adjusted 3.5 MPa steam export, t/h	36.61 – 18.5.(2.779-2.618) = 33.63	
Comparison of <b>B.</b> vs. <b>A.</b>		
Δ NG total consumption <b>B.</b> minus <b>A.</b> , t/h	9.271 – 9.565 = -0.294	
Δ 3.5 MPa steam export <b>B.</b> minus <b>A.</b> , t/h	33.63 – 35.49 = -1.86	
Variable hydrogen production cost <b>B.</b> minus <b>A.</b> , €/h*	55.0	

Generally the operational data analysis comprises:

- A longer time period comprising days  $D_{1...n}$  has been chosen when the ROGs have been processed in the SMR unit (thus representing operational states  $A_{1...n}$ );
- An adjacent time period comprising days  $D_{1...m}$  has been defined when the SMR unit has been operated solely on NG feed
- For a chosen i-th day from  $D_{1...n}$  period (representing the  $A_i$  state) and a chosen j-th day from  $D_{1...m}$  the j-th day SMR unit operational parameters have been adjusted to match hydrogen production from i-th day, lowered by the hydrogen that could be produced in the independent PSA unit on the i-th day. This adjusted  $D_j$  operation defines the operational state  $B_j$ .
- Comparison of  $B_j$  vs.  $A_i$  state yields differences  $\Delta NG_{ij}$  and  $\Delta steam_{ij}$  and thus the financial effect  $F_{ij}$  representing the variable hydrogen production costs difference

Average values  $\overline{\Delta NG}$ ;  $\overline{\Delta Steam}$  were obtained by averaging all differences  $\Delta NG_{ij}$  and  $\Delta steam_{ij}$  over i and j (1a,b),

whereby in the end the average financial effect  $\overline{F_{ij}}$  was obtained:

$$\overline{\Delta NG} = \frac{\sum_{i=1}^n \sum_{j=1}^m \Delta NG_{ij}}{n.m}; \quad \overline{\Delta Steam} = \frac{\sum_{i=1}^n \sum_{j=1}^m \Delta Steam_{ij}}{n.m} \quad (1a,b)$$

The following Figure 2. shows the financial effects  $F_{ij}$  for  $i = 29.10.2010$ . Its aim is to show that even within a period when the SMR unit operates purely on NG, the variable hydrogen production costs vary within  $\pm 60$  €/h (or appr.  $\pm 20$  €/t produced hydrogen) that indicates the influence of other operational parameters and certainly would merit further attention. It also includes autocorrelation of operational data within the  $D_{1...n}$  period, that show a similar pattern, but their values are lower by some 50 to 60 €/h on average.

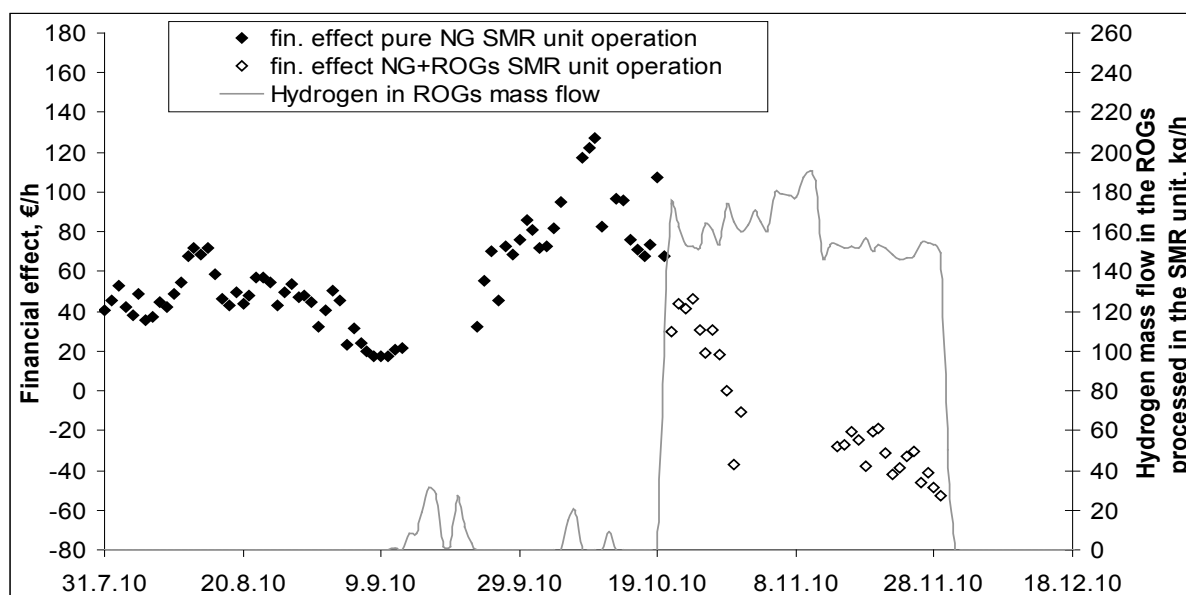


Figure 2. Financial effects  $F_{ij}$  for  $i = 28.10.2010$ . Solid dots:  $D_{1...m}$  period; open dots:  $D_{1...n}$  period

Table V. Results of operational data analysis for three individual time periods characterized by SMR unit operation solely on NG compared to ROGs coprocessing in the 20.10.2010 – 30.11.2010 period

Parameter	31.7.2010 – 18.10.2010	1.12.2010 – 26.3.2011	23.4.2011 – 22.6.2011	20.10.2010 – 30.11.2010
Average SMR unit hydrogen production, kg/h	2686	2686	3029	2711
Average reactor outlet temperature, °C	799	798	807	799
Average steam to process gas ratio, t/t	3.61	3.65	3.59	3.57
$\overline{\Delta NG}$ , t/h	-0.280	-0.140	-0.224	-
$\overline{\Delta Steam}$ , t/h	-1.51	-0.4	-1.42	-
$\overline{\Delta FE}$ , €/h	+61	+37	+40	-

Table V. shows comparison of three individual time periods when the SMR unit has been operated solely on NG with the 20.10.2010 to 30.11.2010 when the ROGs have been coprocessed in the SMR unit. These three periods are characterized by varying process parameters, however in all three cases it is obvious, that pure NG operation of the SMR unit yields lower hydrogen production costs compared to ROGs coprocessing.

It can be concluded that both in case of design data analysis and operational data evaluation, the obtained impact of ROGs coprocessing on the SMR unit operation is similar: pure NG operation means lower total natural gas consumption and lower steam export. In financial terms the hydrogen production by pure NG operation and ROGs processing in the independent PSA unit is by 40 to 60 €/h less costly than that of ROGs coprocessing in the SMR unit.

Due to limited space exhaustive electric energy balance is not provided. Its preliminary analysis yields the conclusion, that the electric energy costs related to the problem under study do not play an important role in the variable hydrogen production costs. The calculated electric energy difference between state **B.** and **A.** obtained from the design state analysis is in the order of tens of kW. As the electric energy consumption in the main process equipment within the balance borders is not measured separately, no quantitative conclusions can be drawn related to operational electric energy consumption difference between **B.** and **A.**

## Conclusions

This contribution aims at elucidating the key importance of correct balance borders settings and correct calculation base construction. In order to demonstrate this necessity a case study bearing on analysis of

optimal hydrogen rich refinery offgases utilization is presented here. The ROGs can either be fed to the SMR unit, respresented by operational state **A.** or be processed in a separate PSA unit in operational state **B.** In both cases hydrogen is produced, however in the second one a valuable by-product is obtained in form of PSA offgas. The correct economic calculation includes hydrogen and fuel gas network balancing as well as correct calculation of steam export change from the SMR unit. In the calculation process, marginal values of natural gas consumption and steam export are made use of. Both the analysis of design SMR unit operational state and operational data analysis confirm that the ROGs utilization in a separate PSA unit is economically favorable over their feeding to the SMR unit. The typical benefit resulting from preferential **B.** operation ranges between 40 and 60 €/h for the considered media prices, resulting from lower overall NG consumption and lower steam export. Such result can qualitatively be explained by combining the reaction stoichiometry, as ethane and higher hydrocarbons present in the ROGs produce less hydrogen and consume more steam per hydrocarbon unit, compared to methane or natural gas. Moreover due to the chemical equilibrium principle the hydrogen present in the ROGs acts against additional hydrogen formation in steam reforming process.

Only the results of electric energy balance are presented in this paper due to limited space; they indicate that it does play only minor role in variable hydrogen production costs and would thus affect the above financial effect only in terms of several €/h.

It must be remembered that **A.**, e.g. feeding the ROGs to the SMR unit at the same time means decrease of maximal hydrogen production capacity in the refinery: the design SMR unit cases enable 3.475 t/h hydrogen production both from pure NG and from ROGs and NG mixture. In case **B.** the ROGs are processed in the separate PSA unit, increasing the hydrogen production capacity by up to nearly 300 kg/h.

Concludingly there is one other aspect that deserves attention: the C2 and higher hydrocarbons in the ROGs have been assigned value only as NG fuel substitute. However these might represent an interesting and valuable feed f.e. for ethylene production in the adjacent Steam Cracker unit if separated from the ROGs. In this case their value would be higher than their fuel value and would significantly contribute to preferential use of **B.** operation over **A.** Recently a project aimed at valuable C2 and higher hydrocarbons recovery has been launched in the refinery, counting with the offgases form the separate PSA unit as one of their important sources. It is thus expected that the operation **A.** will be preferred only in extraordinary cases for very short periods, on the contrary to its preferential use in the past.

## Literature

1. Rostrup-Nielsen J. R., Rostrup-Nielsen, T.: Large-scale hydrogen production, p. 5. Available online at: [http://www.topsoe.com/sites/default/files/topsoe\\_large\\_scale\\_hydrogen\\_produc.pdf](http://www.topsoe.com/sites/default/files/topsoe_large_scale_hydrogen_produc.pdf). Accessed on 27.3.2015.
2. LINDE Engineering: Hydrogen, p. 10. Available online at: [http://www.linde-engineering.com/internet.global.lindeengineering.global/en/images/H2\\_1\\_1\\_e\\_12\\_150dpi19\\_4258.pdf](http://www.linde-engineering.com/internet.global.lindeengineering.global/en/images/H2_1_1_e_12_150dpi19_4258.pdf). Accessed on 29.3.2015.
3. Farnand S., Ratan S., Li J.: *Hydrocarb. Process.* 9, p.73 (2014).
4. Farnand S., Li J., Peng X. D., Ratan S.: *Hydrocarb. Process.* 2, p.53 (2015).
5. Rabiej, Z.: *Petrol. Coal* 4, p.360 (2012).
6. Saleh M., Jahantighy Z. F., Gooyavar A. S., Samipourgiry M., Majidian N.: *Int. J. Mod. Opt.* 2, 85 (2012).
7. De Prada C., Gutierrez G., Sarabia D., Gómez E., Méndez C. A., Sola J. M., González R.: Implementing optimal hydrogen networks management. In Preprints of the 8th IFAC Symposium on Advanced Control of Chemical Processes, Singapore 2012, p.115.
8. Jia N.: Refinery Hydrogen Network Optimisation with Improved Hydroprocessor Modelling. Doctoral thesis submitted to The University of Manchester, p. 86 (2010).
9. Collodi G., Bressan L., Ruggeri F., Uncuoglu D.: Hydrogen production for upgrading projects in refineries, p. 4. Available online at: <http://www.fwc.com/getmedia/fb57aa36-ebec-49b8-b753-986f12cc7a1d/Hydrogen-Production-for-Upgrading-in-Refineries.pdf.aspx?ext=.pdf>. Accessed on 2.4.2015.

## EXPLORING DIFFERENT POTENTIAL CZECH ELECTRICAL MIXES WITH ELEXTERN

**Wertz F.**<sup>1,2</sup>, Karásková Nenádálová L.<sup>1</sup>, Kočí V.<sup>2</sup>

<sup>1</sup>Centrum Výzkumu Řež, Husinec-Řež 130, 25068 Czech Republic

<sup>2</sup>UCT Prague, Technická 3, 16000 Prague 6, Czech Republic  
frederic.wertz@cvrez.cz

### Abstract

Electricity is a fantastic innovation to boost mankind productivity and creativity, however, there is no miraculous way to produce it and every technology has a price to pay. To reduce CO<sub>2</sub> emissions and fossil fuel dependency, Europe is engaged to switch from mainly coal-based to low-carbon technologies for electricity generation. Though determination of the different economic, social and environmental impacts belongs to scientists and specialists, valuing them on a unique scale is of societal matter. Thus, physical impacts must be distinguished from social assumptions that are scenario-dependent, to be chosen by the user. This is the aim of ELEXTERN, freely available at [www.elextern.eu](http://www.elextern.eu).

Besides showing user-customized cost structures of different electricity technologies (including externalities), ELEXTERN helps building, exploring, and comparing different virtual electrical mixes. To do so, additional information are required, such as minimum, average and maximum demand for power. Indeed, electricity is not intrinsically storable (storage requires expensive technologies), and power supply must be able to adapt to the actual demand anytime. Demand-side management can also be considered, which reduces the constraints. ELEXTERN is then a decision support tool for designing the future mix. It can also be used as a communication tool, since people can transparently adjust their own parameters and explore different pathways.

### Background

The Czech electricity mix (Figure 1) consists of various sources and technologies. About half of electricity (including auto-production) is made out of coal in conventional thermal power plants. Another 36% share is produced by Nuclear power plants, while gas-fired and hydro power plants are used for peak-demand and compensate some intermittent production (mainly Solar Photovoltaic).

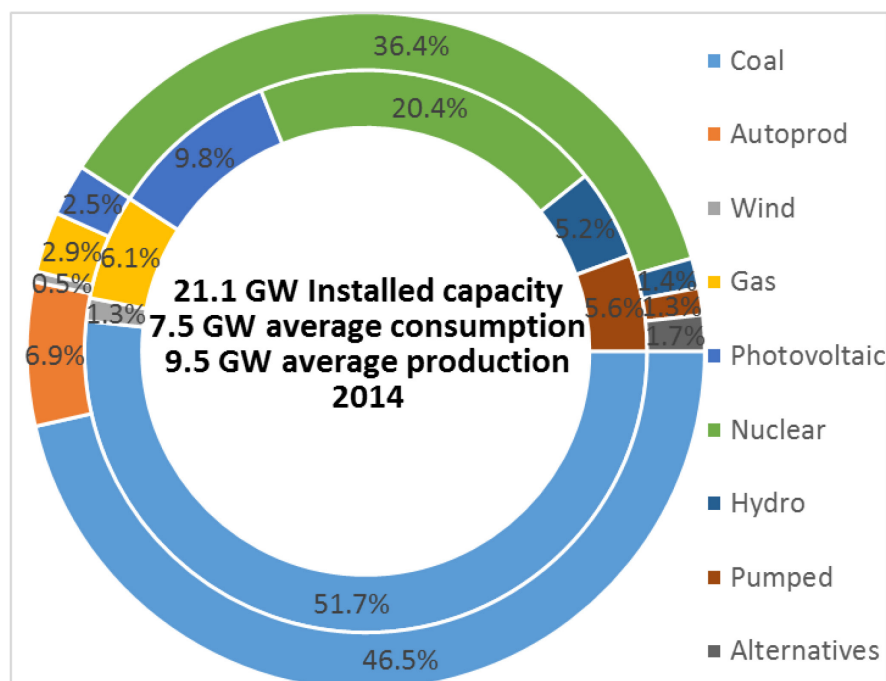


**Figure 1. Czech capacities (inner diagram) and average production (outer diagram) per source (ČEPS 2014<sup>1</sup>)**

Czech electricity infrastructure is besides interconnected with neighbouring countries and within the European context, electricity market has been liberalized (96/92/EC directive<sup>2</sup>). Thus, since July, 1st, 2007, all European

customers are given the choice of electricity providers. Consequently, electricity is simply another commercial product that must be generated for profit by private companies who desire a maximum return on investment. The adequate tool to value different electricity technologies is then the LCOE criterion – Levelised Cost Of Electricity – that represents the average cost of producing electricity for a given technology. It combines investment costs (CAPEX), fixed operation costs (OPEX) and variable fuel costs.

However, electricity production also causes undesirable consequences which must be weighed against its societal benefits. These externalities have impacts on the economic, social and environmental level and affect the whole society, both present and future. Natural resources do not belong more to us than to our children and resource depletion deprives future generations. Additionally, some technologies or resources may come from abroad, endangering the energy supply security. Further, usage of some technologies leads to environmental degradation, climate change, or impacts human health. All these externalities are not taken into account by private actors when planning their next investments. However, administrative authorities can compute the real cost of electricity for the society over the entire life cycle of the plant, determine the ideal energy mix for a given territory, and then build incentives so that private actors meet these goals.

The different impacts from electricity technologies are well documented in the literature<sup>3,4</sup>. However, these impacts are from different nature and must be compared on a unique scale to take decision, which is difficult. Besides, though the determination of the physical impacts belongs to scientists, the social value of these impacts is not necessarily unique and definite. The determination of this social scale belongs to the society. Thus, ELEXTERN ([www.elextern.eu](http://www.elextern.eu)) clearly distinguishes physical impacts from social assumptions, and the user can adjust them to design his own optimal mix.

#### ELEXTERN Methodology

Following the methodology developed by Wertz *et al.*<sup>5</sup>, first LCOE is computed according to

$$LCOE = \frac{CAPEX}{8,76 \cdot LF} \cdot \left[ \frac{(1+R)^{CT} - 1}{CT [1 - (1+R)^{-LT}]} + OPEX\% \right] + Fuel$$

where the discount rate R plays a prominent role. The operation rate OPEX% is used here to factor investment costs CAPEX: Operation costs OPEX = OPEX% \* CAPEX / (8.76 \* LF). Life time LF and Construction Time CT are also important factor for high value of R. Using data from IEA-OECD<sup>6</sup>, Bloomberg<sup>7</sup> and Pilař<sup>8</sup>, we can reconstitute the cost structure of main used technologies in the Czech Republic (Table 1).

**Table I. Cost structure of the different technologies for a discount rate of 1%**

Technology	Unit	Coal FBC	FBC+ CCS	Gas CCGT	Nuclear Gen II	Small Hydro	Large Hydro	Pumped Hydro	Onshore Wind	Solar PV
Load Factor	%	40.4	40.4	21.2	85	45	14	8	15	12
Construction time CT	years	4	4	4	7	2	3	3	1	1
CAPEX	€/kW	2370	4262	955	3983	7886	1564	1564	755	1359
Grid Connection	€/kW	100	100	50	200	100	100	100	230	380
Lifetime LT	years	40	40	30	60	80	80	80	25	25
OPEX%	%	1.65	1.46	1.76	1.87	0.32	1.56	1.56	2.00	0.71
Fuel	€/MWh	14.0	19.4	41.3	4.8			29.3		
Actual CAPEX	€/MWh	21.6	38.1	21.1	12.9	37.1	24.9	43.7	34.0	75.1
Actual OPEX	€/MWh	11.0	17.6	9.0	10.0	6.4	19.9	34.8	11.5	9.2
<b>LCOE</b>	<b>€/MWh</b>	<b>46.6</b>	<b>75.1</b>	<b>71.4</b>	<b>27.6</b>	<b>43.5</b>	<b>44.8</b>	<b>107.8</b>	<b>45.5</b>	<b>84.3</b>

Electricity social value depends on the difficulty to match production and consumption every time. Some technologies are said dispatchable when electricity can be generated on demand. Dispatchability is a key

advantage as it allows a plant to adjust to the electrical demand. Thus electricity is traded at a higher price when it is highly demanded. Dispatchable sources are given here an additional “flexibility Yield”. That is subtracted to the LCOE of dispatchable electricity, and computed via the ELIX index (spot price electricity index of German, French, Swiss and Austrian markets, Figure 2) for the years 2012-2013 (European Energy Exchange EEX<sup>9</sup>). The flexibility Yield corresponding to an X% load factor is computed as the mean of the X% most expensive MWh minus the average MWh price. This Yield is also used for describing electricity storage. These electricity generation devices use, as fuel, cheap MWh during periods of low demand. Depending whether the technology has a yearly or daily cycle, annual or daily lowest prices are computed, as well as annual or daily flexibility Yields. The daily cycle yields less than the annual cycle since the difference between low and high prices is lower

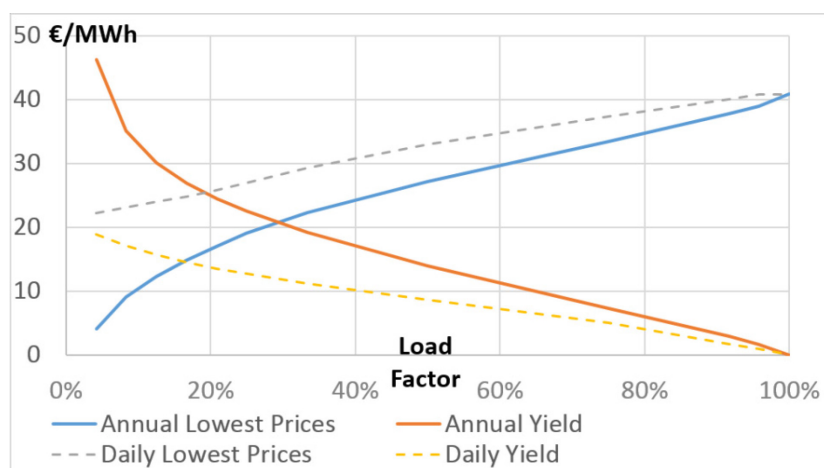


**Figure 2. Expected Daily/Annual electricity yield (for dispatchable sources) and price (for storage)**

Additional impacts are considered in the following sectors:

- Economic: depletion of natural resources, imports of fuels or technologies
- Social: impact on health due to air pollution, unplanned expulsions following disaster
- Environmental: loss of free services offered by nature when land is destroyed for electricity production
- Long-term: greenhouse gas emissions causing global climate change, storage of nuclear waste

Table II summarizes all considered input parameters used in ELEXTERN.

**Table II. Input parameter summary**

Socio-Economic parameters	Physical parameters
Discount rate R	Load Factor LF
Electricity price curve	Electricity demand curve
Capital expenditures CAPEX	Life Time LT
Operation expenditures OPEX	Construction Time CT
Decommission expenditures DECOMEX	Dispatch ability
Fuel Costs	Efficiency
Marginal Cost curve/Learning rate L	Reference Capacity
Value of Energy independency	Fuel and Technological Import share
Value of Statistical Life VSL	Mortality (air pollution)
Health costs and Sick leaves	Morbidity (air pollution)
Value of Biodiversity	Land Use
Costs of Climate Change	GHG emission
Costs of Nuclear wastes treatment	Nuclear wastes production
Value of other impact	Other Impact

### Czech electricity technologies assessment with ELEXTERN

ELEXTERN allows the user to choose assumptions concerning the social value of different impacts. Most of these values have a linear impact on the global costs. However, the discount rate plays a huge and non-linear role in the technologies assessment. Figure 3 and Figure 4 use the following values:

- Economic impact: 15% of CAPEX is expected to be bought abroad for basic technologies, 30% for CCS and Nuclear, 50% for Wind and Solar, 100% of fuels is reported as a loss (depleted or imported)

- Social impact: 45.6 €/sick days, 377 €/respiratory disease, 100 k€/cancer, 600 k€/death (VSL)
- Environmental impact: 0.5 €/m<sup>2</sup> for extended land use (including mining, nuclear incident...), 100 k€ for unplanned expulsion (nuclear incident)
- Long term impact: 4.5, resp. 2.86 €/MWh for nuclear waste treatment with a 1%, resp. 5% discount rate. 74.3, resp. 16 €/tCO<sub>2</sub> for climate change adaptation costs.

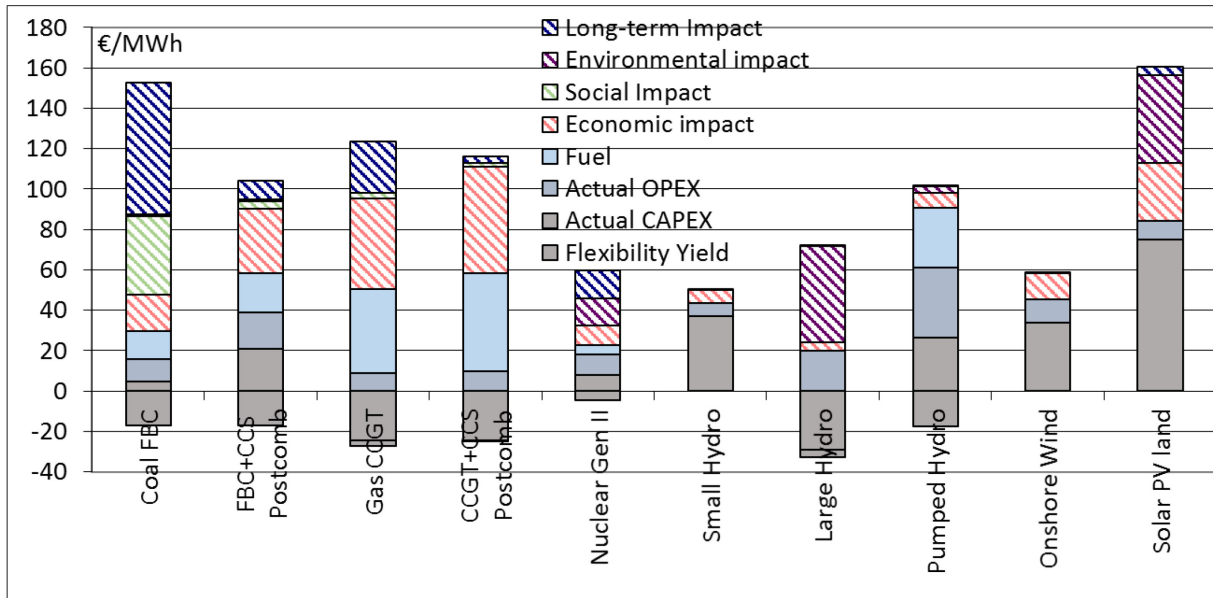


Figure 3. Czech electricity technologies assessment with a 1% Discount rate

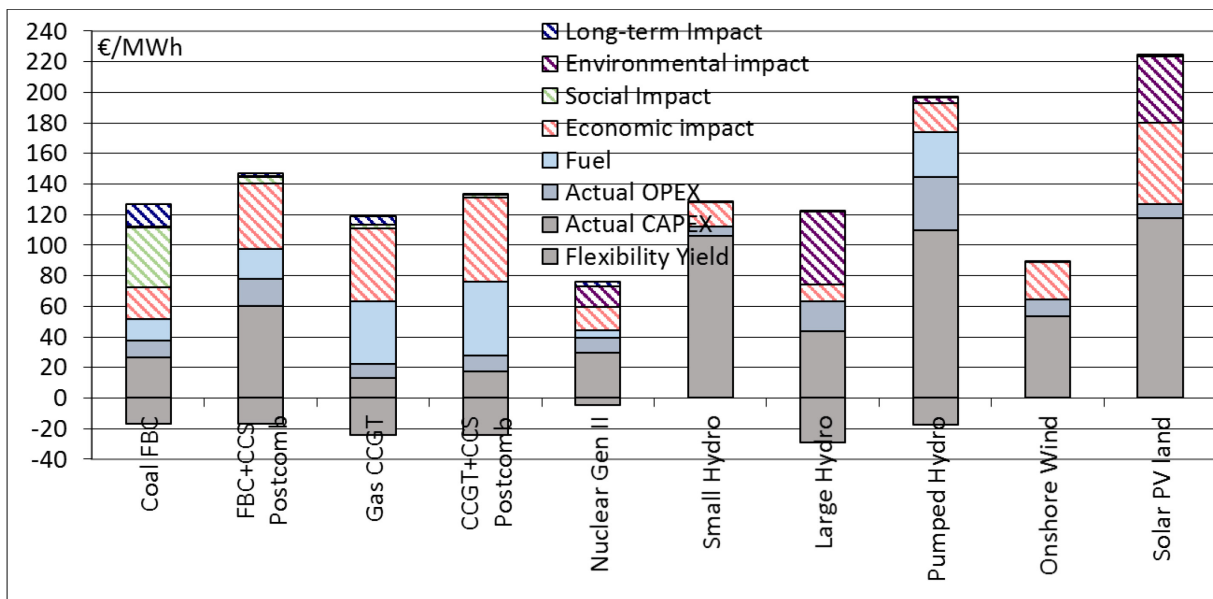


Figure 4. Czech electricity technologies assessment with a 5% Discount rate

#### Exploring different potential mixes with ELEXTERN

All mixes must respect some demand characteristics. Though bilateral trades with neighbours may help balancing the grid, capacities must be capable to answer themselves to the demand, since other countries will face similar constraints (sun, wind, peak demand). Figure 5 and Figure 6 use Czech 2014 demand characteristic: 5 GW minimum demand (except 5% extreme low demand), 7.5 GW average demand, and 10.3 GW maximum demand (except 5% extreme high demand). Different explored electrical mixes (with LF Load Factor of backup) are:

- Current 2014 Czech mix (40,4% Load factor for Coal, 21,2% for Gas)
- 100% Coal: 10.3 GW Coal (73% LF), with and without CO<sub>2</sub> Capture and Storage (CCS)

- Nuclear as base load, Gas for flexible adjustment: 6 GW Nuclear Generation III, 5.2 GW Gas (46% LF)
- 4 GW Nuclear Generation II, 3.2 GW Generation III, 3 GW Hydro and storage, 1.3 GW Gas (59% LF)
- 4 GW Nuclear Generation II, 6.3 GW Wind, 3 GW Hydro and storage, 3.9 GW Gas (66% LF)
- Intermittent generation + backup: 5 GW Wind or Solar PV, 10 GW Coal (65% or 67% LF)
- 100% Wind + storage: 63 GW Wind, 58 GW storage (to be found)
- 100% Solar PV + storage: 85 GW Solar PV, 80 GW storage (to be found)

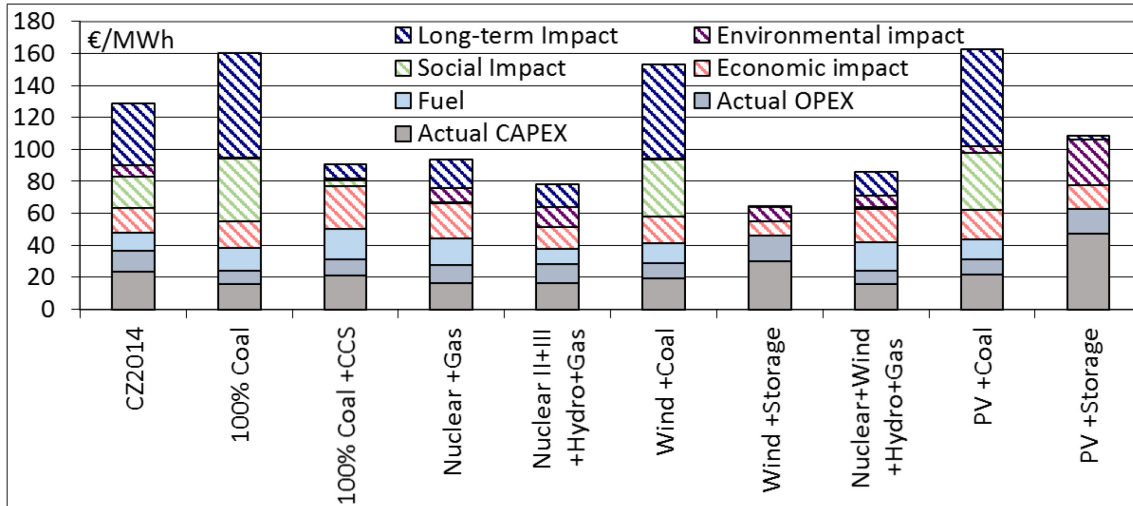


Figure 5. Virtual electrical mixes assessment with a 1% Discount rate

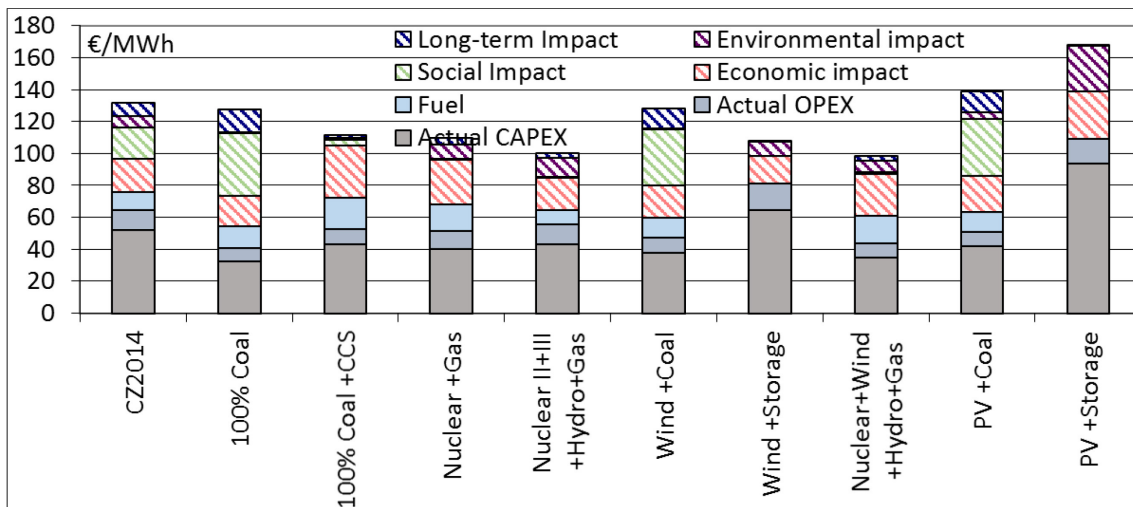


Figure 6. Virtual electrical mixes assessment with a 5% Discount rate

### Discussion

Results show that technologies with low LCOE (such as conventional coal power plants) are not necessarily serving society best interests. For each technology, the global cost (including externalities) depends itself on the value given to the different impacts, as well as on the applied load factor, and the considered discount rate. Even considering externalities, good performing technologies are not necessarily the best technologies to provide reliable electricity for a given country. Indeed Wagner<sup>10</sup> warns about tough constraints for an EU-wide use of renewable electricity. Thus, the optimal mix is difficult to reach and comprises various and complementary electricity sources, since storage is limited or expensive. Another solution to allow the further reduction of conventional electricity generation is to develop load management. Thus electricity use would better follow electricity intermittent generation.

The role of the discount rate predominates the investment phase of a project and continues to play a significant role in the valuation of long term impacts. Since we are considering the structural role played by electricity in our modern societies, electricity planning should rather obey public infrastructure schemes, with long-term return on investment. Thus a low discount rate such as 1% (close to countries' growth rate) should be used to virtually build the mix. Then energy policymakers can build different incentives so that private actors build similar mix with their own economical rules.

### **Conclusion**

Main features of ELEXTERN are the computation of LCOE, flexibility yield, social, environmental and economic impacts, as well as long term liabilities of any electricity technology. ELEXTERN can then reproduce results from previous studies, in term of direct costs (LCOE) and externalities. Besides, its flexible way to adjust assumptions allows easy sensitivity analyses. However, it consists on rough orders of magnitude and does not consider technical grid-constraints such as transmission lines and power gradients. Such dynamic problems must be specifically addressed by dynamic models coupled with geographical information systems.

### **Acknowledgment**

*This study has been funded by the SUSEN Project CZ.1.05/2.1.00/03.0108, realised in the framework of the European Regional Development Fund (ERDF).*

### **Literature**

1. ČEPS (2015) <http://www.ceps.cz/ENG/Data/Vsechna-data/Pages/Vyroba.aspx>.
2. European Commission, Directive 96/92/EC, Official Journal L 027 , 30/01/1997 P. 0020 – 0029 (1997)
3. Söderholm P., Sundqvist T.: Ecological Economics 46, 333 (2003).
4. Markandya A., Wikinson P.: Lancet 370, 979 (2007).
5. Wertz F., Nenadálová L., Kovařík P.: Proceedings of the Czech Nuclear Society, Young Generation meeting 2013, ISBN 978-80-02-02513-9, 57 (2014).
6. IEA/OECD, Projected Costs of Generating Electricity (2010)
7. Bloomberg new energy finance, Sustainable Energy in America 2013 Factbook (2013).
8. Pilař L.: Personal Communication (2015).
9. EEX, Power Spot Market (2014) <http://www.eex.com/en/market-data/power/spot-market/>
10. Wagner F.: Eur. Phys. J. Plus 129 (2014).

## LIGNITE GASIFICATION – MATHEMATICAL MODELING OF SYNGAS EQUILIBRIUM COMPOSITION

**Bártová Š.**<sup>1</sup>, Klajmon M.<sup>2</sup>, Kůs P.<sup>1</sup>, Stehlík K.<sup>1</sup>, Vonková K.<sup>1</sup>

<sup>1</sup>Research Centre Řež, Hlavní 130, Husinec-Řež, CZ-250 68, Czech Republic

<sup>2</sup>Department of Physical Chemistry, University of Chemistry and Technology Prague, Technická 5, Prague 6, CZ-166 28, Czech Republic

sarka.bartova@cvrez.cz

### Introduction

High-temperature reactor (HTR) is a generation IV nuclear reactor with high efficiency of electric energy production. The output temperature of HTR coolant can be higher than 1000 °C, which is suitable for its further use in other high-temperature applications (so called cogeneration). One of possible cogenerations is a coupling of the HTR with a gasification unit, at which water steam used as a gasification media is produced using HTR heat<sup>1,2</sup>.

In our work, we modeled lignite-gasification process, which utilizes heat from the HTR. For this purpose, we developed a mathematical model of a gasification unit in MATLAB<sup>3</sup> environment. The model is based on calculation of chemical equilibrium, which plays a crucial role in composition of syngas (synthesis gas) generated during a gasification process. Moreover, chemical equilibrium, as a thermodynamic phenomenon, indicates the upper limit of the gasification process efficiency. We studied the equilibrium syngas composition and its dependency on various operation conditions such as temperature, pressure, and composition of the feed mixture. For the calculation of chemical equilibrium, non-stoichiometric approach<sup>4</sup> was applied.

### Theory

From the thermodynamics point of view, calculation of chemical equilibrium in the lignite-gasification process is a non-trivial problem, mainly because of the complexity of the reacting system. At least 15 chemical reactions take place during the lignite-gasification process<sup>5,6,7</sup>, e.g., Boudouard and water-gas shift reactions, combustion of solid carbon, etc. Moreover, the number of compounds in the reacting system is greater than the number of chemical elements from which these compounds consist of. To solve chemical equilibrium in such complicated systems, methods requiring no stoichiometric analysis are recommended<sup>4</sup>.

Non-stoichiometric approach is a thermodynamic method for calculation of chemical equilibrium in complex systems consisting of many components and/or chemical reactions. It is based on minimization of Gibbs free energy of the whole reacting system while satisfying the mass-balance equations. Thus, stoichiometry of particular chemical reactions is not considered. It is sufficient to define the reacting system: a group of reactants and a group of products. Our reacting system was defined considering solid carbon C(s) and gaseous components CH<sub>4</sub>, H<sub>2</sub>O, CO<sub>2</sub>, CO, O<sub>2</sub> and H<sub>2</sub>. It can be described by the following scheme:



Here, the left side represents the hypothetical feed mixture of reactants and the right side represents products of the gasification process. The main interest of our work is focused on the determination of equilibrium concentrations of CO and H<sub>2</sub> because of their role as the major syngas components.

The reacting system (1) can be expressed by the matrix of constitution coefficients as follows:

$$A = \begin{pmatrix} 1 & 0 & 0 & 1 & 1 & 1 & 0 \\ 0 & 2 & 0 & 4 & 0 & 0 & 2 \\ 0 & 1 & 2 & 0 & 1 & 2 & 0 \end{pmatrix} \quad (2)$$

Columns of the matrix *A* represent the considered chemical compounds in the same order as in the scheme (1) and the rows are the numbers of C, H and O atoms involved in these compounds. The matrix of constitution coefficients is the only quantity describing the reacting system with respect to the elemental composition and is thus very important for expressing the mass-balance equations.

The reduced Gibbs free energy of the whole reacting system (1) is given by<sup>4</sup> the following equation:

$$Q_{\text{syst}} = \frac{G_{\text{syst}}}{RT} = \sum_{i=1}^N n_i q_i(T, p) + \sum_{i=1}^{N(\text{gas})} n_i \ln n_i - n \ln n, \quad (3)$$

Here,  $N$  is the total number of species in the reacting system,  $N(\text{gas})$  is the number of gaseous species and  $n$  is the molar amount of the gaseous phase. The reduced molar Gibbs free energy  $q_i$  of component  $i$  at temperature and pressure of the system is expressed in the form of following equation:

$$q_i(T, p) = \frac{G_{mi}^*(T, p^{st})}{RT} + \ln \frac{p}{p^{st}} \quad (4)$$

The mass-balance equations are as follows:

$$b_j = \sum_{i=1}^N a_{ji} n_i \quad j = 1, 2, \dots, M \quad (5)$$

Here,  $b_j$  is the constant molar amount of the  $j$ -th chemical element and  $a_{ji}$  is a respective element from the matrix of constitutional coefficients  $A$ .  $M$  is the number of chemical elements in the reacting system ( $M = 3$  in our reacting system).

The principle of non-stoichiometric approach is to find a minimum of the function (3) in a set of points  $(n_1, n_2, \dots, n_N)$  satisfying the additional conditions (5). For this kind of a mathematical-optimization problem with equality constraints (mass-balance equations), the method of Lagrange multipliers ( $\lambda$ ) was applied<sup>4,8</sup>. The resulting function  $L$  to be minimized is then following:

$$L(n_1, n_2, \dots, n_N, \lambda_1, \lambda_2, \dots, \lambda_M) = Q_{\text{syst}}(n_1, n_2, \dots, n_N) + \sum_{j=1}^M \lambda_j (b_j - \sum_{i=1}^N a_{ji} n_i) \quad (6)$$

Minimization of function  $L$  gives values of  $\lambda_1, \lambda_2, \dots, \lambda_M$ ,  $n$  and  $n_c$  (the equilibrium amount of solid carbon). For the detailed description of this problem solution (6), see the original literature<sup>4</sup>.

For evaluation of the reduced Gibbs free energy of each component in the ideal gas state,  $G_{mi}^*(T, p^{st})$ , an appropriate thermochemical data must be chosen. We used a collection of Bureš et al.<sup>9</sup> which provides temperature-dependent isobaric heat capacities in a form of semi-theoretical expressions, such as:

$$C_{pm}^\circ = A + B_1 \left(\frac{C_1}{T}\right)^2 \frac{e^{-C_1/T}}{(1-e^{-C_1/T})^2} + B_2 \left(\frac{C_2}{T}\right)^2 \frac{e^{-C_2/T}}{(1-e^{-C_2/T})^2} \quad (7)$$

Here,  $A$ ,  $B_1$ ,  $B_2$ ,  $C_1$ , and  $C_2$  are characteristic parameters for the given chemical compound. The main advantages of these expressions are their applicability in a wide temperature range (200–3000 K) and their safe extrapolations outside this temperature range. The pure-component Gibbs free energies are then evaluated using basic thermodynamic relations.

## Results and Discussion

Calculation of chemical equilibrium in the reacting system was carried out several times with various temperatures, pressures and compositions of the feed mixture in order to evaluate their effects on the syngas properties. The feed mixture always consisted only of solid carbon, water vapor and oxygen.

Figure 1 shows temperature dependence of the equilibrium molar fractions of CO and H<sub>2</sub> at pressure 1 bar and 10 bar. In general, it can be said that higher operation pressure required higher temperature for maintaining the same equilibrium molar fractions. The atmospheric pressure (1 bar) seemed to be the most appropriate for the gasification process.

Another phenomenon discovered in our computational study was that there is a certain temperature up to which the equilibrium amount of H<sub>2</sub> is higher than that of CO (cf. Figure 1). It is mostly connected with the fact that the reactions producing H<sub>2</sub> are predominant at lower temperatures<sup>7</sup>.

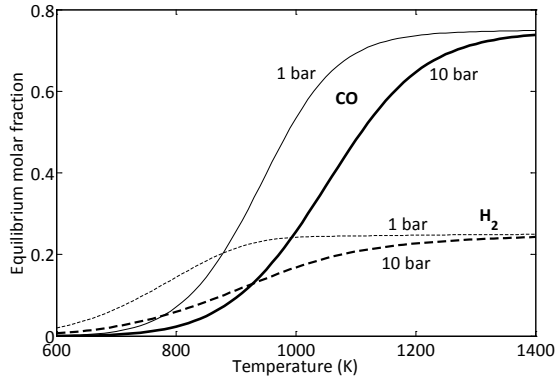


Figure 1. The equilibrium molar fractions of CO and H<sub>2</sub> as a function of temperature. The thin lines are results obtained at  $p = 1$  bar, while the thick lines at  $p = 10$  bar.

Conversion of solid carbon as a function of temperature at pressure 1 bar is illustrated in Figure 2. The initial molar amounts of C(s), O<sub>2</sub>, and H<sub>2</sub>O were always 5, 1, and 1 mol, respectively. Under these conditions, there is a significant change of the slope of the equilibrium curve starting at about 800 K and ending at 1100 K. Nevertheless, the equilibrium conversion approaches its limit of approximately 60% at the temperature of about 1200 K. In order to achieve the total C(s) conversion (100%), the ratio of the initial molar amounts of C(s) to (O<sub>2</sub> + H<sub>2</sub>O) has to be decreased.

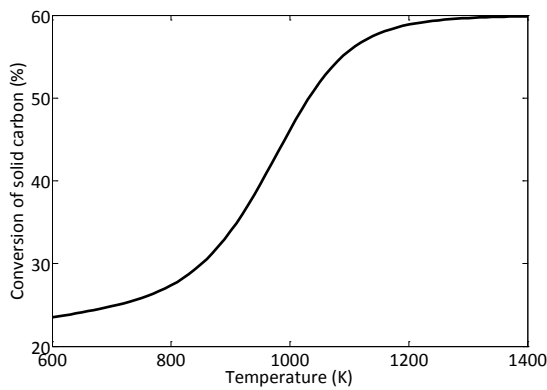


Figure 2. The equilibrium solid carbon conversion as a function of temperature obtained at  $p = 1$  bar. The initial amount of C(s) was always 5 mol.

Composition of the feed mixture also plays important role in the syngas equilibrium composition. We studied the influence of the ratio of the initial molar amounts of water vapor to oxygen ( $\alpha$ ). The calculations showed that the molar fractions of CO and H<sub>2</sub> are closer to each other as  $\alpha$  and operation temperature increase, as it is displayed in Figure 3. Thus, the CO and H<sub>2</sub> equilibrium amounts can be also modeled by the choice of  $\alpha$ .

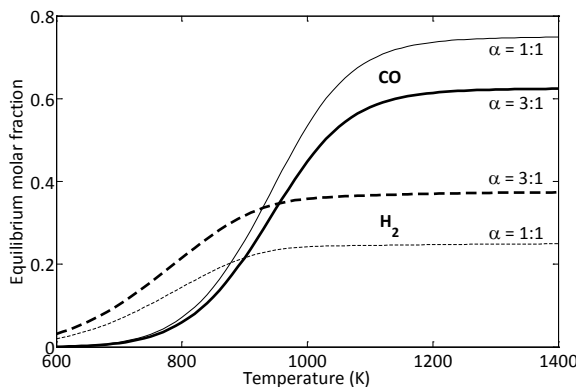


Figure 3. The equilibrium molar fractions of CO and H<sub>2</sub> as a function of temperature at  $p = 1$  bar. The Greek letter  $\alpha$  represents the ratio of initial molar amounts of water vapor to oxygen in the feed mixture.

Because the figures presented here illustrate only the equilibrium content of C(s), H<sub>2</sub> and CO, we provide also equilibrium composition of the whole reacting system as molar fractions and molar amounts of all components calculated at  $T = 1000$  K and  $p = 1$  bar (cf. Table I).

It is obvious that desired products of gasification, H<sub>2</sub> and CO, are in a significant excess. The third most abundant component in equilibrium mixture is CO<sub>2</sub>. We found that its equilibrium molar fraction usually approaches its limit of approximately 50 % at 700 K, but then steeply declines as temperature increases.

Oxygen, as one of the gasifying media, is practically not present in equilibrium mixture under any operation conditions. It indicates that not only gasification but also oxidation processes take place in the reacting system in quite a large extent.

Table I

Syngas composition at  $T = 1000$  K,  $p = 1$  bar,  $\alpha = 1$  mol/1 mol, and the solid carbon initial amount of 5 mol.

Component	$x$ [-]	$n$ [mol]
CH <sub>4</sub>	0.0056	0.0183
H <sub>2</sub> O	0.0516	0.1690
CO <sub>2</sub>	0.1643	0.5381
CO	0.5359	1.7549
O <sub>2</sub>	0.0000	0.0000
H <sub>2</sub>	0.2426	0.7943
C(s)	–	2.6887

### Conclusions

Our mathematical model calculating chemical equilibrium in the lignite gasification process can be successfully used for the modeling and optimization of the syngas equilibrium composition with respect to various operation conditions (temperature, pressure and composition of the feed mixture). As discussed in the previous sections, the operation conditions are of a significant influence on the final syngas composition and properties. Our further steps in extension of the model is to consider nitrogen (as a component of the air) and solid sulfur (as a lignite component) in the reacting system.

### Acknowledgment

*The work has been created with financial support of SUSEN Project CZ.1.05/2.1.00/03.0108 realized in the framework of the European Regional Development Fund (ERDF) and with the contribution of the institutional support that has been given to the research organization Centrum výzkumu Řež s.r.o. (Research Center Řež) for a long-term conceptual development.*

### Literature

1. Botha F., Dobson R., Harms T.: *J. Energy South. Afr.* 24, 37 (2013).
2. Berka J., Viden I.: *Paliva* 6, 7 (2014).
3. MATLAB Release R2013b, The MathWorks, Inc., Natick, Massachusetts, United States.
4. Holub R., Voňka P.: *The Chemical Equilibrium of Gaseous Systems*. Academia, Prague 1975.
5. Melgar A., Pérez J.F., Laget H., Horillo A.: *Energy Convers. Manage.* 48, 59 (2007).
6. Cempa-Balewicz M., Laczny M.J., Smolinski A., Iwaszenko S.: *J. Sust. Min.* 12, 21 (2013).
7. Li X., Grace J.R., Watkinson A.P., Lim C.J., Ergüdenler A.: *Fuel* 80, 195 (2001).
8. Gill P.E., Murray W., Wright M.H.: *Practical Optimization*. Academic Press, London 1981.
9. Bureš M., Holub R., Leitner J., Voňka P.: *Termochemické veličiny organických sloučenin (Thermochemical properties of organic compounds)*. VŠCHT, Praha 1992. (in Czech).

## DESIGN CALCULATIONS FOR ETHANOL – WATER MIXTURE SEPARATION USING IONIC LIQUID 1-BUTYL-3-METHYLIMIDAZOLIUM CHLORIDE

**E. Gracsová**, P. Steltenpohl

STU in Bratislava, FCHPT, Institute of Chemical and Environmental Engineering, Radlinského 9, 812 37 Bratislava, Slovakia  
elena.graczova@stuba.sk

### Abstract

Design of a separation equipment for the separation of azeotropic mixture ethanol – water in the presence of an ionic liquid (IL) is presented. In this study, 1-butyl-3-methylimidazolium chloride ([BMim]Cl) was chosen as the extractive solvent for the ethanol – water mixture separation at atmospheric pressure. Design calculations were accomplished for a distillation unit in which extractive distillation of an aqueous ethanol mixture containing 20 mole % of ethanol was carried out. Basic column design parameters, such as the number of theoretical stages, position of the solvent and feed input stages, reflux ratio, and ionic liquid consumption, were investigated. Calculations were based on the pre-set content of the desired product, ethanol, in distillate. Computations were done using a proprietary simulation program developed in the Matlab® program that solves a set of mass balances at individual theoretical stages of the distillation column combined with the vapor–liquid equilibrium (VLE) data. Non-ideal behavior of the liquid phase was assumed in the VLE calculations and the NRTL equation was used to calculate the components activity coefficients. Original NRTL parameters were taken from literature.

Due to the large number of variables, column design parameters were optimized in several computation cycles. Results of the calculations show that in order to achieve the required distillate purity (99.5 mole % of ethanol), a column with fifteen theoretical stages is required. The other optimum parameters were: reflux ratio of 1.4 and feed input stage no. 11. The results are presented in the form of temperature as well as vapor and liquid phase concentration profiles within the distillation column. Comparison of the results was carried out considering extractive distillation of the ethanol – water mixture in the presence of 1-butyl-3-methylimidazolium methylsulfate ([BMim][MSO<sub>4</sub>]), and 1-ethyl-3-methylimidazolium ethylsulfate ([EMim][ESO<sub>4</sub>]). Qualitative comparison of the economic efficiency of the aqueous ethanol mixture separation is also presented.

### Introduction

Ethanol as a polar compound is fully miscible with water, which is a polar solvent. Industrially produced ethanol is used as a fuel and gasoline additive<sup>1</sup>; as a solvent in the manufacture of varnishes, inks, paints, and cleaning products; in the cosmetic industry<sup>2</sup>; in food industry; as an extraction solvent and carrier in medicine and pharmaceutical industry<sup>3</sup>; etc. At atmospheric pressure, these components form an azeotropic mixture that contains 95,57 mole % of ethanol. Such a mixture cannot be separated using the traditional distillation process and, therefore, this procedure is not viable for anhydrous ethanol production. Separation, however, can be achieved employing extraction distillation that requires the use of an extractive solvent capable of altering the relative volatility of the original mixture components. As extractive solvents, various organic solvents were proposed. Nowadays, a new class of solvents, ionic liquids (ILs), is proposed as an alternative to traditional extraction solvents<sup>4, 5</sup>. ILs are ionic salts that are liquid at common temperatures. Due to their beneficial properties, such as high extraction selectivity and capacity, non-volatility, thermal stability, electrical conductivity, non-flammability, etc., ILs found wide applications in chemical industry<sup>6</sup>. The only substantial disadvantage of ILs is their elevated price.

### Phase equilibrium of multicomponent systems

To describe the vapor–liquid equilibrium (VLE) of a multi-component system, ideal behavior of vapor and real behavior of liquid phases was assumed. The condition of the equilibrium between a vapor and a liquid for a more component system at constant temperature and pressure,  $T$  and  $P$ , was written as:

$$Py_i = P_i^{\circ} x_i \gamma_i \quad i = A, B, C \quad [T, P] \quad (1)$$

where  $P_i^{\circ}$  is the saturated vapor pressure of the  $i$ -th component;  $y_i$  and  $x_i$  are the mole fractions of component  $i$  in the vapor and liquid phase, respectively. Activity coefficients,  $\gamma_i$ , were calculated using the original NRTL equation derived by Renon and Prausnitz<sup>7</sup>:

$$\ln \gamma_i = \frac{\sum_j \tau_{ji} G_{ji} x_j}{\sum_l G_{li} x_l} + \sum_j \frac{x_j G_{ij}}{\sum_l G_{lj} x_l} \left( \tau_{ij} - \frac{\sum_k \tau_{kj} G_{kj} x_k}{\sum_l G_{lj} x_l} \right) \quad i, j, k, l = A, B, C \quad (2)$$

Binary parameters  $\tau_{ij}$  and terms  $G_{ij}$  are defined by as follows:

$$\tau_{ij} = \frac{g_{ij} - g_{jj}}{RT} \quad G_{ij} = \exp(-\alpha_{ij} \tau_{ij}) \quad i, j = A, B, C \quad i \neq j \quad (3)$$

where  $\tau_{ij} \neq \tau_{ji}$ ,  $\tau_{ii} = \tau_{jj} = 0$ ,  $R$  is the universal gas constant,  $(g_{ij} - g_{jj})$  represent the extent of interactions between molecules  $i$  and  $j$ ; and  $\alpha_{ij}$  is the non-randomness parameter of the NRTL equation.

### Equipment design calculations

Design calculations were carried out for an extractive distillation column used for the separation of an aqueous ethanol mixture (20 mole % of ethanol). As extractive solvent, 1-butyl-3-methylimidazolium chloride ([BMim]Cl) ionic liquid was chosen. Simulations were carried out with the aim to optimize basic column operation parameters such as: relative solvent consumption, number of theoretical (equilibrium) column stages, position of the feed input stage, and reflux ratio. Optimization criterion was the prescribed distillate content of ethanol (99.5 mole %). Calculations were carried out in a proprietary program constructed in Matlab® capable of solving a set of material balances written for the column and its equilibrium stages considering the vapor-liquid equilibrium of a multicomponent system. Calculation of the components' activity coefficients in the liquid phase were assessed employing the NRTL equation. Binary NRTL parameters for the system ethanol – water – [BMim]Cl were taken from literature<sup>8</sup>. Comparison of the results was done for extractive distillation of the ethanol – water mixture in the presence of 1-butyl-3-methylimidazolium methylsulfate ([BMim][MSO<sub>4</sub>]) and 1-ethyl-3-methylimidazolium ethylsulfate ([EMim][ESO<sub>4</sub>]). Parameters of the NRTL equation for these two ternary systems were found in literature<sup>9,10</sup>.

### Results and discussion

Optimization of the column operation parameters was carried out at atmospheric pressure ( $P = 101325$  Pa). Due to the large number of optimized parameters, the calculations were done in three steps.

In the first step, relative solvent consumption, i.e. solvent to feed mole ratio, was optimized for the chosen value of the reflux ratio,  $RR$ , total number of the column equilibrium stages,  $N$ , and the feed input stage,  $f_2$ . Altogether eight combinations of the column parameters were used in this calculation step for the three selected ILs: [BMim]Cl, [BMim][MSO<sub>4</sub>], and [EMim][ESO<sub>4</sub>].

Results of these calculations showed that the lowest specific consumption of solvent necessary to reach the prescribed distillate purity,  $\dot{n}_s/\dot{n}_F = 1.5/10$ , was obtained with [BMim][MSO<sub>4</sub>]. In case of [BMim]Cl, the consumption was higher,  $\dot{n}_s/\dot{n}_F = 3/10$ . [EMim][ESO<sub>4</sub>] was the least appropriate (selective) from the chosen ILs since the prescribed distillate purity criterion could not be reached even at much higher relative solvent consumption and/or reflux ratio values<sup>11</sup> compared to those employed in simulations of the ethanol – water mixture separation in the presence of [BMim]Cl or [BMim][MSO<sub>4</sub>] ILs. Therefore, taking into account the elevated price of ionic liquids, further analysis was carried out for [BMim]Cl or [BMim][MSO<sub>4</sub>] ILs, only.

In the second step, the reflux ratio, number of the column theoretical stages, and the position of the feed input stage were optimized assuming the respective solvent to feed mole ratio ( $\dot{n}_s/\dot{n}_F = 3/10$  for [BMim]Cl and  $\dot{n}_s/\dot{n}_F = 1.5/10$  for [BMim][MSO<sub>4</sub>]) obtained in the first step of this procedure. Moreover, the solvent input stage,  $f_1 = 2$ , was fixed for the calculations. Due to the low IL volatility, there is no risk of IL loss due to its presence in the distillate. The reflux ratio was changed from  $RR = 1$  to  $RR = 2$  with the step of 0.2, the number of theoretical stages varied from  $N_{\min} = 10$  to  $N_{\max} = 20$ , and the position of the feed input stage of  $f_2 = N - 4$ ,  $N - 3$ , or  $N - 2$  was considered.

For both ILs, [BMim]Cl (Figure 1) and [BMim][MSO<sub>4</sub>] (Figure 2), calculation results are graphically represented as a variation of the ethanol mole fraction in distillate with the number of theoretical stages  $x_{D, \text{Ethanol}} = f(N)$ , or with the reflux ratio  $x_{D, \text{Ethanol}} = f(RR)$ , assuming different positions of the feed input stage, i.e.  $f_2 = N - 4$ ,  $f_2 = N - 3$ , and  $f_2 = N - 2$ . Based on these data, the optimum column parameters (number of theoretical stages and reflux ratio) were selected as the lowest values of the column design parameters at which the prescribed value of optimization criterion,  $x_{D, \text{Ethanol}} = 0.995$ , was obtained.

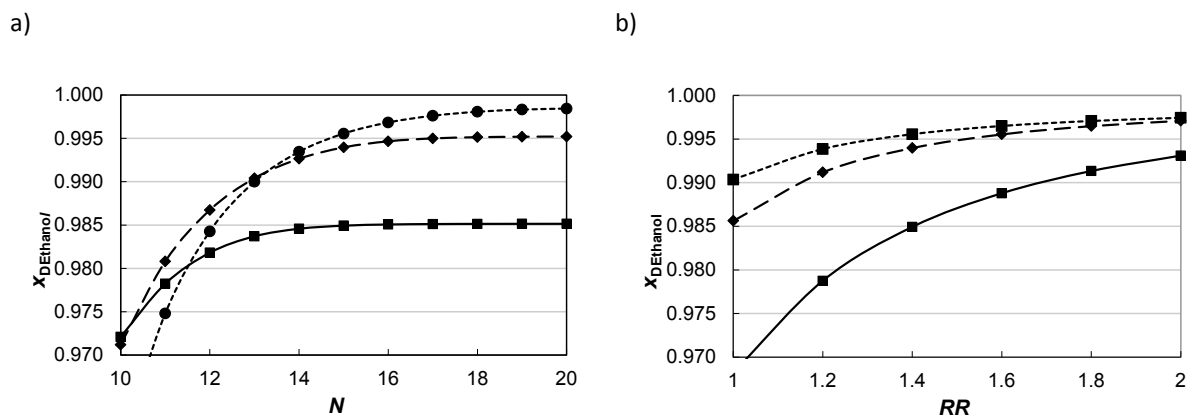


Figure 1. Results of simulations for [BMim]Cl as extractive solvent at  $\dot{n}_s/\dot{n}_F = 3/10$ . Variation of the ethanol mole fraction in distillate,  $x_{D, \text{Ethanol}}$ , with the number of theoretical stages,  $N$ , at  $RR = 1.4$  (a). Variation of the ethanol mole fraction in distillate,  $x_{D, \text{Ethanol}}$ , with the value of the reflux ratio,  $RR$ , at  $N = 15$  (b). Positions of the feed input stage:  $f_2 = N - 4$  (solid line),  $f_2 = N - 3$  (dashed line), and  $f_2 = N - 2$  (dotted line).

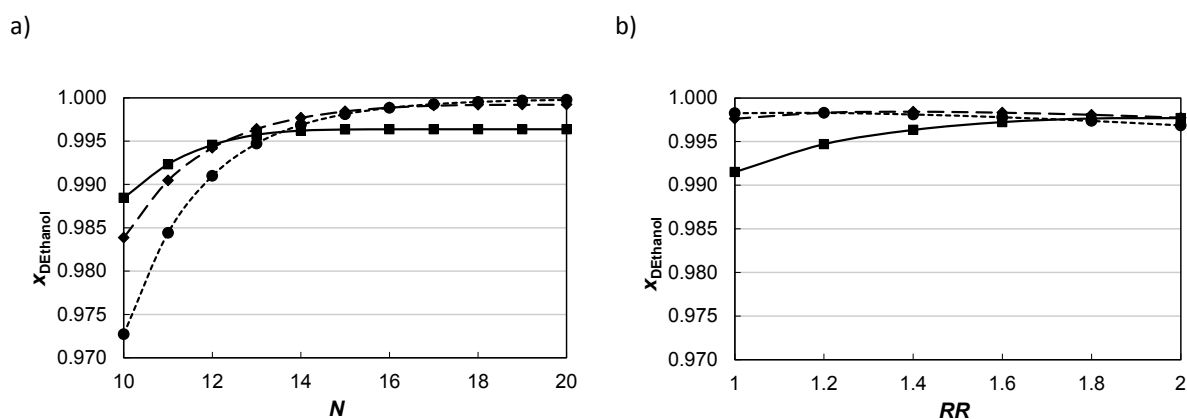


Figure 2. Results of simulations for [BMim][SO<sub>4</sub>] as extractive solvent at  $\dot{n}_s/\dot{n}_F = 1.5/10$ . Variation of the ethanol mole fraction in distillate,  $x_{D, \text{Ethanol}}$ , with the number of theoretical stages,  $N$ , at  $RR = 1.4$  (a). Variation of the ethanol mole fraction in distillate,  $x_{D, \text{Ethanol}}$ , with the value of the reflux ratio,  $RR$ , at  $N = 15$  (b). Positions of the feed input stage:  $f_2 = N - 4$  (solid line),  $f_2 = N - 3$  (dashed line), and  $f_2 = N - 2$  (dotted line).

From Figure 1 it is clear that to obtain the required content of ethanol in distillate, distillation column with 15 theoretical stages, feed to solvent mole ratio of 3/10, reflux ratio equal to or higher than 1.4, solvent input stage  $f_1 = 2$ , and feed input stage  $f_2 = N - 4 = 11$  are required for the separation in the presence of the extractive solvent assumed, [BMim]Cl.

A comparison of simulation results, yield of ethanol and water in distillate, for the obtained column design parameters and different feed input stage positions,  $f_2$ , is summarized in Table I.

From Table I it follows that the required separation efficiency was obtained only for the feed input stage position  $f_2 = N - 4$ .

For [BMim][MSO<sub>4</sub>] IL (Figure 2), the optimization criterion was met for  $\dot{n}_s/\dot{n}_F = 1.5/10$ ,  $N \geq 13$ , and  $RR > 1.2$  if the feed input stage position was  $f_2 = N - 2$ . In case of  $f_2 = N - 4$  or  $N - 3$ , the ethanol mole fraction in distillate was higher than 0,995 in a column with 15 theoretical stages at all assumed reflux ratios ( $RR = 1-2$ ).

Table I

Yield of ethanol and water in distillate for [BMim]Cl at  $\dot{n}_S/\dot{n}_F = 3/10$ ,  $N = 15$ , and  $RR = 1.4$

Feed input stage	Yield of ethanol in distillate, [%]	Yield of water in distillate, [%]
$f_2 = 10$	99.46 <sup>a</sup>	0.13
$f_2 = 11$	99.56	0.11
$f_2 = 12$	99.40 <sup>a</sup>	0.15
$f_2 = 13$	98.49 <sup>a</sup>	0.38

a) Preset distillate purity was not reached.

In the third step, simulation of the column for ethanol – water mixture separation in the presence of the chosen IL, [BMim]Cl, was carried out using the optimum column parameters obtained in the previous steps. Besides the values of the solvent to feed mole ratio  $\dot{n}_S/\dot{n}_F = 3/10$ , total number of equilibrium stages  $N = 15$ , position of the solvent input stage  $f_1 = 2$ , feed input stage  $f_2 = 11$ , and reflux ratio  $RR = 1.4$ , in simulations also the solvent and feed input stream quality  $q_1 = 1.5$  and  $q_2 = 1$ , respectively, were assumed. Results of the calculations for these conditions are illustrated by the concentration profiles in the liquid and vapor phases as well as the temperature profiles within the column for extractive distillation (Figure 3).

#### Economic analysis and qualitative comparison of the separation costs

As given above, in the first calculation step the ionic liquid consumption was investigated while changing the number of theoretical stages, reflux ratio, and the position of feed input stage. Taking into account the computed ethanol content in distillate, the minimum solvent to feed mole ratio necessary for the ethanol – water mixture separation in the presence of [BMim]Cl of  $\dot{n}_S/\dot{n}_F = 3/10$  was estimated. Even lower specific solvent consumption,  $\dot{n}_S/\dot{n}_F = 1.5/10$ , was found to be sufficient for this separation when [BMim][MSO<sub>4</sub>] IL was used as the extractive solvent. Computed yields of ethanol for the solvent to feed mole ratio  $\dot{n}_S/\dot{n}_F = 1.5/10$  are compared in Table II.

Table II

Yield of ethanol in distillate for different solvent to feed mole ratios and the two ILs considered; results computed for  $N = 15$ ,  $\dot{n}_S/\dot{n}_F = 1.5/10$ ,  $RR = 1.4$ , and  $f_2 = 12$

Ionic Liquid	Yield of ethanol in distillate, [%]	Yield of water in distillate, [%]
[BMim]Cl	99.11 <sup>a</sup>	0.22
[BMim][MSO <sub>4</sub> ]	99.95	0.01

a) Preset distillate purity was not reached.

It can be seen that the separation efficiency of [BMim]Cl is lower compared to that of [BMim][MSO<sub>4</sub>]. Bearing in mind elevated prices of ILs, ethanol – water mixture separation in the presence of [BMim]Cl is less economic compared to that employing [BMim][MSO<sub>4</sub>] as the extractive solvent. In case of the second IL, not only the operational (solvent purchase costs, heating and cooling media consumption, regeneration costs) but also the investment (size and number of stages of column for extractive distillation and regeneration) costs are reduced.

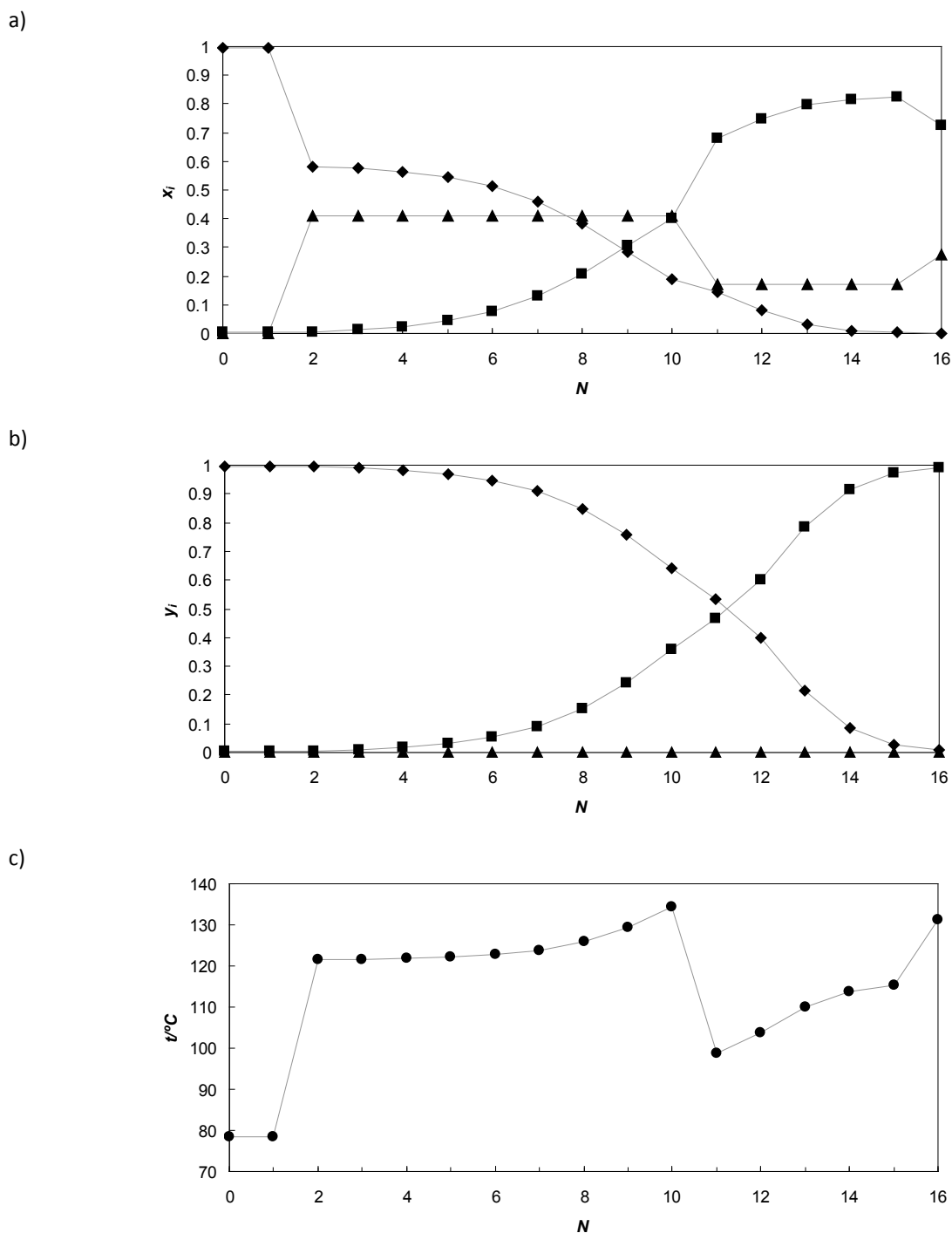


Figure 3. Calculated concentration profiles in the liquid (a) and vapor (b) phases and temperature profile (c) at individual stages of the distillation column for the extractive distillation of the ethanol – water – [BMim]Cl mixture at 101.3 kPa. Column design parameter values:  $\dot{n}_s/\dot{n}_f = 3/10$ ,  $N = 15$ ,  $RR = 1.4$ ,  $q_1 = 1.5$ ,  $q_2 = 1$ ,  $f_1 = 2$ , and  $f_2 = 11$ . Components: ethanol (diamonds), water (squares), and [BMim]Cl (triangles).

### Conclusions

In this study, optimization of the column parameters for extractive distillation of aqueous ethanol mixture separation in the presence of [BMim]Cl IL was carried out. For the required purity of distillate (ethanol mole fraction of 99.5 mole %), several column parameters such as the solvent consumption, number of column stages, reflux ratio, and position of the feed and solvent input stages. Optimization was carried in two consecutive steps that were repeated in a sequence.

Efficiency of [BMim]Cl in the ethanol – water mixture separation was compared with another ionic liquid that is structurally similar. For comparison, ionic liquid with the same cation, [BMim][MSO<sub>4</sub>], was considered. It was found that these extractive solvents possess identical separation efficiency at the corresponding values of the feed to solvent mole ratio (3/10 for [BMim]Cl and 1.5/10 for [BMim][MSO<sub>4</sub>]) assuming a column with fifteen theoretical stages, reflux ratio of 1.4, and the position of the feed input stage  $f_2 = 11$ .

Compared to [BMim]Cl, [BMim][MSO<sub>4</sub>] showed even higher efficiency in the ethanol – water mixture separation. For this extractive solvent, the required purity of distillate could be achieved at lower solvent to feed consumption. Thus, the use of [BMim][MSO<sub>4</sub>] is economically more advantageous compared to [BMim]Cl.

### **Acknowledgment**

*The authors acknowledge the Research and Development Assistance Agency (APVV-0858-12) for financial support.*

### **Literature**

1. Mills G.A., Ecklund E.E.: *Ann. Rev. Energy* **12**, 47 (1987).
2. Mayers R.L., Mayers R.L.: *The 100 Most Important Chemical Compounds: A Reference Guide*, p. 122, Greenwood Press, Westport, CT, USA 2007.
3. Parke S.A., Birch G.G.: *Food Chem.* **67**, 241 (1999).
4. Perreiro A. B., Araújo J. M. M., Esperança J. M. M. S., Marrucho I. M., Rebelo L. P. N.: *J. Chem. Thermodyn.* **46**, 2 (2012).
5. Ge Y., Zhang L., Yuan X., Geng W., Ji J.: *J. Chem. Thermodyn.* **40**, 1248 (2008).
6. Johnson K.E.: *The Electrochemical Society's Interface* **16**, 38 (2007).
7. Renon H., Prausnitz J. M.: *AIChE J.* **14**, 135 (1968).
8. Calvar N., Gonzáles B., Gómez E., Dominguez Á.: *J. Chem. Eng. Data* **51**, 2178 (2006).
9. Calvar N., Gonzáles B., Gómez E., Dominguez Á.: *J. Chem. Eng. Data* **54**, 1004 (2009).
10. Calvar N., Gonzáles B., Gómez E., Dominguez Á.: *J. Chem. Eng. Data* **55**, 2786 (2010).
11. Gracová E., Steltenpohl P.: *Chem. Eng. Trans.* **45**, in press (2015).

## ENVIRONMENTAL GAINS AND IMPACTS OF A CCS TECHNOLOGY – CASE STUDY OF POST-COMBUSTION CO<sub>2</sub> SEPARATION BY AMMONIA ABSORPTION

**Štefanica J.**<sup>1,2</sup>, Smutná J.<sup>1,3</sup>, Kočí, V.<sup>3</sup>, Machač P.<sup>3</sup>, Pilař L.<sup>1,2</sup>

<sup>1</sup>ÚJV Řež, a. s., Hlavní 130, Řež, 250 68, Husinec

<sup>2</sup>Czech Technical University in Prague, Faculty of Mechanical Engineering, Technická 4, 166 07, Praha 6 – Dejvice

<sup>3</sup>University of Chemistry and Technology, Prague, Technická 5, 166 28, Praha 6 - Dejvice

Jiri.stefanica@ujv.cz

### Abstract

Considering the impacts of human activities on the environment, emissions of greenhouse gases are one of the major concerns. The CCS technologies are seen as an option that can help to decrease the emissions of CO<sub>2</sub> and reduce potential effects that a heightened CO<sub>2</sub> concentration might have. The technical solution of capture, transport and storage of the CO<sub>2</sub> originating in large emission point sources (power plants, industry) is depending on local conditions and can vary significantly. The ammonia scrubbing was chosen for CO<sub>2</sub> separation from flue gas of lignite coal power plant (typical conditions for the Czech Republic) in the national project MPO FR-TI1/379. Environmental gains and impacts of the power plant and the optimized variant of the capture technology based on ammonia scrubbing were assessed on the basis of material and energy flow balance. The potential environmental impacts of the power plant with and without CO<sub>2</sub> capture were compared using LCA methodology.

### Introduction

Coal is one of the most important global energy sources. Despite being non-renewable coal is relatively evenly distributed around the world, it is providing electricity and heat with high reliability and the available known reserves are sufficient into far future. However, the energy production based on coal combustion is accompanied by significant environmental impacts – depletion of non-renewable resources and emissions of solid, liquid and gaseous compounds with potential negative impact on the environment and human health. The legislation is setting emission limits on sulfur dioxide, nitrogen oxides and particulates, which have environmental effects that can be observed in short term horizon as acid rain, photochemical smog and increased incidence of respiratory diseases. Reliable technological solutions are available to reduce the above mentioned emissions – flue gas desulphurisation, denitrification and dedusting. The situation is much more complex in case of CO<sub>2</sub> emissions as the long term effects must be considered. It also proves to be very difficult to exactly quantify the effect of anthropogenic CO<sub>2</sub> on global warming.

Coal will most likely remain an important element of the global energy production even in long term future. It is necessary to find ways how to utilize coal more efficiently and with fewer emissions, including CO<sub>2</sub>, in the future. As an illustration the Global CCS Institute specified long term CO<sub>2</sub> reduction measures: transfer to renewable energy sources, transfer to low carbon technologies and implementation of CCS (Carbon dioxide capture and sequestration) technologies on existing and newly planned facilities.<sup>1</sup>

The comparison of renewable energy sources and conventional thermal power plants with implemented CCS technology is often discussed. The study of Viebahn et al.<sup>2</sup> is using life cycle analysis (LCA) and cost analysis to compare the environmental impacts of pulverized combustion of hard coal, pulverized combustion of lignite, natural gas combustion in combined cycle and integrated gasification and combustion of hard coal – all option without and with CCS technology. These conventional energy sources are compared with renewables – wind and solar thermal systems. The authors point out that even with the best case of CCS technology the traditional sources still emit more CO<sub>2</sub> per 1 kWh of produced electricity than the renewables. However, thermal power plants are very significant source of energy (totaling e.g. about 52 % respectively 60 % of the energy mix in Czech Republic and Germany) and CCS technologies could help to mitigate its CO<sub>2</sub> emissions.

Many other studies were conducting LCA of parts of the whole CCS chain and also its parts comparing different types of energy applications with and without CCS.<sup>3-7</sup> The LCA is always applied on simulated power plants so the results can only function as an estimation. Moreover, modern power plant blocks with high power output and net efficiency around 45 % are used. This paper is using LCA to assess the environmental impacts of an existing lignite fired PCC power plant block (net efficiency 32 %), see parameters in Table I. The reference power plant environmental impacts are compared with the scenario of ammonia scrubbing CCS technology implementation.

## THE SCENARIOS FOR LCA

The aim of this paper is to compare the environmental impacts of an existing power plant with the scenario of ammonia scrubbing CCS technology implementation. The used background data were taken from the national project MPO FR-TI1/379, for more information see the project report<sup>8</sup>. The above mentioned project's aim was to suggest and design commercially available CCS technologies in the case their implementation on Czech existing power plants is needed in near future. The parameters of a power plant block in Table I are taken from a real facility and represent the existing conditions in the Czech Republic. The ammonia scrubbing was suggested as one of the options.

**Table I. The parameters of the power plant block without and with CO<sub>2</sub> capture**

Parameter	Power plant without CCS	Power plant with CCS
Nominal power output [MW]	250	250
Net power output [MW]	226	164
Yearly operation [h]	6 300	6300
Electricity produced [MWh/y]	1 423 800	1 033 200
CO <sub>2</sub> produced [t/MWh]	0.933628	0.128049
CO <sub>2</sub> captured [t/MWh]	0	1.158537

The LCA of environmental impacts is using the data related to the power plant and CO<sub>2</sub> capture operation. Impacts of CO<sub>2</sub> transportation and storage are not taken into account. Also the impacts of adsorber construction and additional auxiliaries and infrastructure are disregarded due to its minimal importance compared to construction of the whole power plant.

The analysis was carried out using SIMAPro software and CML 2001 methodology. All inputs' consumption and outputs'/wastes' production were related to the production of 1 kWh of electrical energy. Three scenarios were included in the analysis and compared:

Scenario 1: The reference power plant without CO<sub>2</sub> capture

Scenario 2: Power plant with CO<sub>2</sub> capture

Scenario 3: Power plant with CO<sub>2</sub> capture and with utilizing the ammonia salts as fertilizer (previous variant treated ammonia salts as solid waste)

Table II is showing the selected environmental impacts expressed in equivalent units representative for each category.

**Table II. Environmental impacts**

Category	Scenario 1: Power plant without CO <sub>2</sub> capture	Scenario 2 Power plant with CO <sub>2</sub> capture	Scenario 3 Power plant with CO <sub>2</sub> capture + fertilizer production
Mineral resources depletion [kg Sb eq.]	$6.67 \cdot 10^{-9}$	$1.31 \cdot 10^{-8}$	$1.23 \cdot 10^{-8}$
Fossil fuels depletion [MJ]	1.22	4.29	4.24
Climate change [kg CO <sub>2</sub> eq.]	2.18	$5.25 \cdot 10^{-1}$	$5.12 \cdot 10^{-1}$
Ozone layer damage [kg R-11 eq.]	$8.38 \cdot 10^{-12}$	$2.48 \cdot 10^{-11}$	$2.45 \cdot 10^{-11}$
Photochemical oxidation [kg C <sub>2</sub> H <sub>2</sub> eq.]	0.00011	0.00012	0.00012
Acidification [kg SO <sub>2</sub> eq.]	0.0024	0.0022	0.0022
Eutropication [kg PO <sub>4</sub> <sup>3-</sup> eq.]	0.00032	0.00022	0.00021

## Conclusions

The impact of CO<sub>2</sub> capture on climate change is expectedly positive and very significant. However, increased mineral resources and fossil fuel depletion can be observed for the power plant with CO<sub>2</sub> capture as well as increased ozone layer damage. The categories of photochemical oxidation and acidification seem unchanged,

slight decrease of eutropication occurred with including the CO<sub>2</sub> capture. The option with CO<sub>2</sub> capture and ammine salt utilization as fertilizers (Scenario 3) showed similar but slightly better results. Some other studies suggest that by including also the process of CO<sub>2</sub> transportation and storage the acidification and eutropication would increase compared to the reference power plant.<sup>2,3,7</sup>

#### Literature

1. Global CCS Institute: The Global Status of CCS 2012.
2. Viebahn R. et al.: Comparison of carbon capture and storage with renewable energy technologies regarding structural, economic and ecological aspects in Germany. *Greenhouse Gas Control* 2007, 1, p.121 – 133
3. Strube R. et al.: The environmental impact of post-combustion CO<sub>2</sub> capture with MEA, with aqueous ammonia, and with an aqueous ammonia-ethanol mixture for a coal-fired power plant. *Energy* 2011, 36, 3763 - 3770
4. Odeh N. A., Cockerill T. T.: Life cycle GHG assessment of fossil fuel power plants with carbon capture and storage. *Energy Policy* 2008, 36, 367 – 380
5. Koornneef J. et al.: Life cycle assessment of a pulverized coal power plant with post-combustion capture, transport and storage of CO<sub>2</sub>. *International Journal of Greenhouse Gas Control* 2008, 2, 448 – 467
6. Pehnt M., Henkel J.: Life cycle assessment of carbon dioxide capture, transport and storage from lignite power plants. *International Journal of Greenhouse Gas Control* 2009, 3, 49 – 66
7. Corsten M. et al.: Environmental impact assessment of CCS chains – Lessons learned and limitations from LCA literature. *International Journal of Greenhouse Gas Control* 2013, 13, 59 – 71
8. Dlouhý T. a kol.: Technicko-ekonomická analýza. Technicko-ekonomické porovnání dvou navržených konceptů zachytu CO<sub>2</sub>. Výzkumná zpráva ÚJV 14245 projektu TIP č. FR-TI1/379 (2009-2013). Řež-Husinec: ÚJV Řež a. s., 2013

## INFLUENCE OF REACTION CONDITION ONTO HYDROTREATING OF RAPESEED OIL

**Kočetková D.**, Váchová V., Blažek J., Šimáček P., Staš M.

*Department of Petroleum Technology and Alternative Fuels, University of Chemistry and Technology, Prague Technická 5, 166 28, Praha 6, Czech Republic, e-mail: Darja.Kocetkova@vscht.cz*

### Introduction

Due to our lifestyle and the fact that the human population is increasing, energy consumption has never been higher in the world than today. One of the major energy consumers is the transport sector counting about a fifth of the total consumption, and it is likely that will be only greater in the future<sup>1</sup>. Significant research is being conducted in an energy area in order to find alternative fuels to replace gasoline and diesel fuels.

According to the EU Directive on the promotion of the use of energy from renewable sources, a mandatory target of a 10 % share of energy from renewable sources in overall energy consumption has to be achieved by all Member States by 2020 and to be introduced in a cost-effective way<sup>2</sup>. Biofuel production also should be sustainable. Directives of the European Parliament and Council 2009/28/EC on the promotion of the use of energy from renewable sources<sup>2</sup> and 2009/30/EC on the quality of petrol, diesel and gas-oil<sup>3</sup> further reinforces the sustainability criteria for biofuels in relation to greenhouse gas emission savings and are trying to solve the problem of indirect land use changes due to growing biomass for biofuel production and reduces the contribution of biofuels made from food biomass to 5 %. These directives make the biofuel development to move from the first generation biofuels toward the second one. New researches are now focusing on developing other sources of biomass for the second generation such as agricultural, food and wood industries wastes.

Producing of FAME biodiesel by transesterification of triglycerides contained in vegetable oils (rapeseed, palm) with alcohol has showed a potential of fulfilling the sustainability criteria but there are still many disadvantages of these products (high viscosity, pour point, acid number, low heat value and stability because of its oxygen content and double bonds in molecule)<sup>4</sup>.

There is an alternative route for biodiesel production. Hydroconversion of the same oils provides hydrocarbons appropriate to use as a part of conventional diesel and even have higher cetane value as conventional ones<sup>4</sup>. Double bond hydrogenation, hydrodeoxygenation (HDO), hydrodecarbonylation (HDCN) and hydrodecarboxylation (HDCX) are the main reactions that occur during vegetable oil hydrotreating (Figure 1)<sup>5-8</sup>.

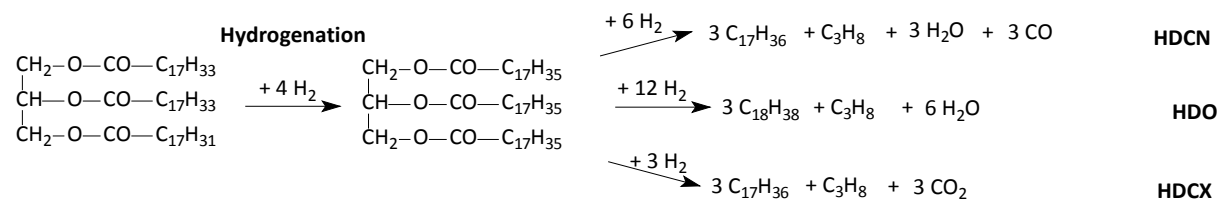


Figure 1. Main reactions occurring during hydrotreating of triglycerides

The catalysts used in hydrotreating processing are noble metals and transition metals, both on active support (alumina, carbon or mesoporous zeolite). Comparing with the transition metal catalysts, noble metal catalysts always have higher cost and shorter lifetime. Ni, Co and Mo are among the transition metals, which are usually used in form of monometallic or bimetallic catalysts. The reaction pathway is mainly dependent on the active metal<sup>5</sup>. Moreover, the product distribution, the yield and selectivity of hydrocarbons as well as the conversion of feedstock are usually affected not only by the catalysts but also by the operating conditions. Hydrotreating of vegetable oils and petroleum conventional fraction blends have also been investigated<sup>5,6</sup>.

In this work, the hydrotreating of rapeseed oil with regard to the use of the products as components of diesel fuel was researched. The effects of process parameters (temperature and pressure) of the hydrotreating on the oil conversion, the distribution of C<sub>17</sub> and C<sub>18</sub> components derived from HDO, HDCN, HDCX and subsequent isomerization, cyclization and dehydrocyclization were analysed.

### Experimental

Since middle petroleum distillates and products of their hydrotreatment contain a large variety of n-alkanes, isoalkanes, alkylated cycloalkanes and alkylaromatics, it is practically impossible to determine quantity and structure of the various hydrocarbons except the dominant C<sub>17</sub> and C<sub>18</sub> n-alkanes in products from hydrotreating of petroleum fraction and rapeseed oil blend. Therefore, hydrotreating of a mixture 83 wt% of

isooctane and 17 wt% of rapeseed oil was carried out. To ensure that model mixture hydrotreating would take place similarly as actual petroleum feedstock and hydrotreating catalyst remained in active sulphidic form, dimethyl disulphide (DMDS) was added to the model mixture in an amount same as sulphur concentration in conventional petroleum feedstock, i.e. 0.28 wt%.

Relative acyl representation in rapeseed oil used in this work is shown in Table I. It can be seen that C<sub>18</sub> acyl represents more than 91 wt% of acyl groups presented in the rapeseed oil. Rapeseed oil contained 4 mg·kg<sup>-1</sup> of sulphur and 8 mg·kg<sup>-1</sup> of nitrogen.

Table I  
Relative acyl representation in the rapeseed oil

Acyls <sup>a</sup>	C14:0	C16:0	C16:1	C18:0	C18:1	C18:2	C18:3	C20+
Amount [wt%]	0.1	5.5	0.4	2.0	60.0	20.3	8.8	3.0

<sup>a</sup> The first number next to C indicates carbon atoms number and the second one is double bonds number in an acyl. C20+ indicates acyls having 20 or more carbon atoms in molecule.

Hydrotreating of feedstock was performed at a flow apparatus equipped with a tubular trickle-bed reactor. The reactor was filled with a commercial Co-Mo/Al<sub>2</sub>O<sub>3</sub>+SiO<sub>2</sub> catalyst which is used for hydrotreating of middle distillates. Hydrotreating was performed at 320, 340, 360 and 380 °C, at LHSV of 1 hr<sup>-1</sup>, constant flow rate of feedstock at 100 g·hr<sup>-1</sup>, pressure of 4 and 8 MPa, and the ratio of hydrogen to feedstock of 230 m<sup>3</sup>·m<sup>-3</sup>. Products were collected for 5 hours.

Hydrogen sulphide was stripped off from liquid reaction products by hydrogen with a flow of 3.6 dm<sup>3</sup>·hr<sup>-1</sup> during the experiment and then by the same flow rate for 2 hours because of the possibility of its oxidation to elemental sulphur during next distillation of the liquid products, which would distort their sulphur content. Other gaseous and low-boiling compounds were removed during the procedure as well. Removal of isooctane from product was carried out using distillation apparatus FISCHER with a SPALTROHR HMS 500 column.

Completeness of rapeseed oil conversion into hydrocarbons was checked by simulated distillation on a gas chromatograph TRACE GC. Cetane index (CI) was calculated according to EN ISO 4264 using distillation data obtained from procedure specified in ASTM D2887. Density was determined according to EN ISO 12185 using oscillating densitometer DMA 48, kinematic viscosity was determined using STABINGER (SVM 3000) viscometer according to ASTM D7042.

Parameters of the simulated distillation and the parameters of high performance liquid chromatography (HPLC) that was used for an assessment of group composition of liquid products are listed in the previous work<sup>9</sup>. The sulphur content was determined according to ASTM D5453 on the Mitsubishi TOX-100 analyser. The content of n-alkanes was determined by gas chromatography with flame ionization detection (GC-FID) on HP 5890 chromatograph. Identification of n-alkanes was made by comparing peak retention times with retention times of n-alkanes presented in the standard mixture of C<sub>7</sub>-C<sub>30</sub> n-alkanes, which was analysed under the same conditions as the samples. The content of each n-alkane and group of isoalkanes was calculated as percentage of their area to a total area of the sample (without solvent and its decay products).

Additional information on the composition of liquid product was obtained using gas chromatography with mass spectrometric detection (GC-MS) on Thermo Focus GC-DSQ. This method was used primarily for the identification of other hydrocarbon (other than n-alkanes) presented in liquid products. Conditions for GC-FID and GC-MS analyses are shown in Tables II and III. Analysis of gaseous hydrotreating products was made using an HP 6890 gas chromatograph equipped with two analytical channels. Detailed analytical conditions are presented in Table IV.

Table II  
Conditions for GC-FID analysis

Parameters	Description
Analytical column	Agilent ULTRA 1 (12.5 m x 0.32 mm x 0.52 µm)
Injection	Split 1:100, injector temperature 320 °C, injection volume 0.2 µl
Carrier gas	Nitrogen 6.0, constant pressure of 20 kPa
Column temperature	isothermal 60 °C for 3 min, then a linear gradient of 8 °C·min <sup>-1</sup> to a temperature 280 °C, isothermally at this temperature for 5 min
FID detector	detector temperature 320 °C hydrogen flow rate 30 cm <sup>3</sup> ·min <sup>-1</sup> , airflow 300 cm <sup>3</sup> ·min <sup>-1</sup> , make-up gas flow (nitrogen) 20 cm <sup>3</sup> ·min <sup>-1</sup>

Table III

## Conditions for GC-MS analysis

Parameters	Description
Analytical column	Restek Rxi-1ms (20 m x 0,15 mm x 0,15 $\mu$ m)
Injection	Split 1:100, injector temperature 275 °C, injection volume 0.2 $\mu$ l
Carrier gas	helium (5.5), constant flow 1 cm <sup>3</sup> ·min <sup>-1</sup>
Column temperature	isothermal 35 °C for 2 min, then a linear gradient of 3 °C·min <sup>-1</sup> to a temperature 90 °C, then 15 °C·min <sup>-1</sup> to 310 °C, isothermally at this temperature for 5 min
MS detector	temperature of ion source 200°C, electron impact ionization (EI+); electron energy 70 eV, mass range m/z 30-450, scanning rate 3 scan·s <sup>-1</sup>

Table IV

## Conditions for gaseous products analysis

Parameters	Description
Analytical column	channel 1: Restek Alumina BOND/MAPD (30 m x 0.32 mm x 5 $\mu$ m) channel 2: pre-column, HayeSep Q (0.9 m x 3.2 mm, 80/100 mesh) column 1, HP PLOT Q (30 m x 0.53 mm x 40 $\mu$ m) column 2, HP Plot Molsieves 5 A (30 m x 0.53 mm x 50 $\mu$ m)
Oven temperature	isothermal 70 °C for 6 min, then a linear gradient of 10 °C·min <sup>-1</sup> to a temperature 90 °C, then 20 °C·min <sup>-1</sup> to 220 °C, isothermally at this temperature for 5 min
Detector	channel 1: flame ionization detector (detection of C <sub>1</sub> -C <sub>7</sub> hydrocarbons) channel 2: thermal conductivity detector (detection of permanent gases)

### Results and discussions

Eight products were prepared by hydrotreating of rapeseed oil dissolved in isooctane in two sets of experiments which differed in pressure. Reaction conditions of performed experiments and designation of the products obtained are given in Table V.

Table V

## Reaction conditions of hydrotreating and designation of the products obtained

Product	Temperature (°C)	Pressure (MPa)	Product	Temperature (°C)	Pressure (MPa)
ISR-4-320	320	4	ISR-8-320	320	8
ISR-4-340	340	4	ISR-8-340	340	8
ISR-4-360	360	4	ISR-8-360	360	8
ISR-4-380	380	4	ISR-8-380	380	8

The results of the simulated distillation of all liquid products did not show a presence of organic compounds in boiling range of 600-650 °C, which confirmed that conversion of rapeseed oil was complete. A part of a chromatogram of the ISR-4-320 product is shown in Figure 2 as an example. C<sub>17</sub> and C<sub>18</sub> n-alkanes were dominant in all products of the rapeseed oil conversion as expected. The content of other n-alkanes was considerably smaller, because C<sub>18</sub> acyl formed more than 91 wt% of acyl groups in the rapeseed oil (table I).

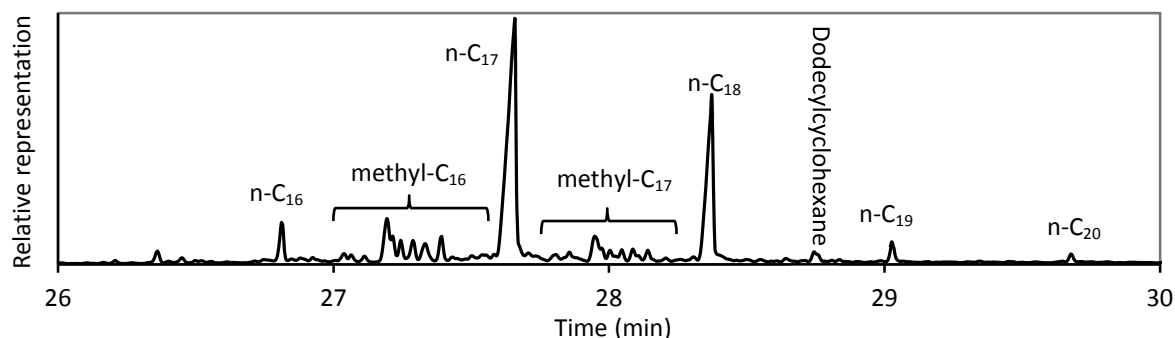


Figure 2. Identification of hydrocarbons in a part of ISR-4-320 chromatogram

Methylhexadecanes and methylheptadecanes were dominant isoalkanes determined in the products using GC-MS. Dodecylcyclohexane was identified as the only significant representative of cycloalkanes in all products excluding ISR-4-380. Methylphenanthrene or methylanthracene was identified only in ISR-4-380 product.

It can be seen in table VI, that content of C<sub>17</sub> and C<sub>18</sub> n-alkanes in reaction products decreases with increasing reaction temperature due to the subsequent reaction of n-alkanes formed by conversion of rapeseed oil. The products obtained at a pressure of 8 MPa contained larger amounts of C<sub>18</sub> and C<sub>17</sub> n-alkanes than the products obtained at the same temperature but 4 MPa. The amount of isoalkanes increased with increasing reaction temperature. Data in table VI reveal that ratio of C<sub>17</sub> to C<sub>18</sub> alkanes in products was growing with increasing temperature, which means that hydrodecarboxylation and hydrodecarbonylation were applied more in conversion of rapeseed oil compared to its hydrodeoxygenation at higher reaction temperatures.

Table VI

The content of individual groups of hydrocarbons in liquid products (wt%)

Product	ISR-4-320	ISR-4-340	ISR-4-360	ISR-4-380	ISR-8-320	ISR-8-340	ISR-8-360	ISR-8-380
C <sub>14</sub>	1.2	0.4	7.7	13.9	0.0	3.0	9.0	10.4
C <sub>15</sub>	2.4	2.1	3.4	4.9	4.2	2.7	3.3	3.9
C <sub>16</sub>	5.0	3.6	6.7	10.5	2.6	2.8	3.5	4.9
iso-C <sub>17</sub>	14.1	9.4	17.0	21.0	5.6	8.0	10.2	13.0
n-C <sub>17</sub>	31.6	34.4	26.5	19.9	41.2	42.3	37.0	29.8
iso-C <sub>18</sub>	11.4	8.7	13.3	12.9	5.2	6.0	6.8	8.5
n-C <sub>18</sub>	28.0	36.2	18.5	9.2	36.6	30.3	23.8	16.9
C <sub>19+</sub>	6.2	5.2	6.8	7.8	4.6	5.0	6.4	12.7
Sum	100	100	100	100	100	100	100	100
C <sub>17</sub> /C <sub>18</sub>	1.16	0.98	1.37	1.85	1.12	1.39	1.54	1.69

Properties of the liquid products obtained by hydrotreating of rapeseed oil are given in Table VII. The sulphur content of all products was less than 10 mg·kg<sup>-1</sup>. Viscosity of the products decreased with increasing reaction temperature. The products obtained at lower pressure had a bit lower viscosity than the ones obtained at higher pressure. All products meet the viscosity of EN 590 diesel standard, which must be in the range from 2.0 to 4.5 mm<sup>2</sup>·s<sup>-1</sup>.

Table VII

Yield and properties of hydrotreating liquid products

Sample	Yield (g)	Sulphur content (mg·kg <sup>-1</sup> )	Density at 25 °C (kg·m <sup>-3</sup> )	Pour Point (°C)	Viscosity at 40 °C (mm <sup>2</sup> ·s <sup>-1</sup> )	Cetane index	Monoarom. content (wt%)	Polyarom. content (wt%)
ISR-4-320	55.5	9	780	15.5	3.47	99.3	1.2	0.3
ISR-4-340	57.9	3	784	13.0	3.34	94.9	2.0	0.3
ISR-4-360	54.7	3	786	7.5	3.25	92.3	2.6	0.7
ISR-4-380	56.7	4	790	-1.5	2.98	82.1	5.5	3.3
ISR-8-320	55.2	5	782	20.0	3.93	98.7	0.9	0.3
ISR-8-340	58.7	8	782	17.0	3.73	98.7	0.9	0.3
ISR-8-360	57.9	3	783	14.5	3.67	97.3	1.2	0.3
ISR-8-380	57.8	6	784	7.5	3.37	92.2	3.0	0.6

Products had relatively high pour point which decreased with increasing reaction temperature. It was caused by partial isomerization of n-alkanes in higher reaction temperature. Products which were obtained at a lower pressure of hydrotreating had lower pour point than the ones obtained at the same temperature but at a higher pressure. Density had to be measured at 25 °C because of the high pour point of the products. The density of the products did not change too much with increasing reaction temperature or pressure. The cetane index of the products was very high and slightly decreased with increasing reaction temperature. Aromatics content of products increased with increasing temperatures, this trend was more marked when using lower pressure.

Analysis of gaseous products (Table VIII) showed increasing amount of butanes (mostly isobutane) and methane with increasing temperature. This was caused mainly by isooctane cracking. The products from conversion of rapeseed oil cracked a bit at higher reaction temperatures as well (increase in C<sub>14</sub> hydrocarbon

content, Table VI). Methane could also arise from reaction between carbon oxides and hydrogen (methanation)<sup>10</sup>.

Table VIII  
Composition of gaseous products from hydrotreating (vol%)

Compound	ISR-4-320	ISR-4-340	ISR-4-360	ISR-4-380	ISR-8-320	ISR-8-340	ISR-8-360	ISR-8-380
Hydrogen	87.80	87.43	85.52	74.02	88.47	87.44	86.87	79.34
Methane	1.67	1.66	1.62	2.30	1.90	2.72	2.80	3.50
Ethane	0.11	0.07	0.10	0.27	0.09	0.14	0.15	0.22
Propane	1.50	1.44	1.53	1.64	1.52	1.69	1.45	1.57
Butanes	1.21	1.89	3.31	15.01	0.12	0.64	2.17	9.11
CO	1.12	0.82	0.94	0.76	0.65	0.73	0.52	0.46
CO <sub>2</sub>	1.83	1.21	1.35	0.93	1.44	1.46	0.93	0.71
Other	5.01	5.58	5.62	5.06	5.81	5.18	5.11	5.09

### Conclusions

Rapeseed oil was completely converted into hydrocarbons under the reaction conditions. C<sub>17</sub> and C<sub>18</sub> alkanes were predominant in all products from hydrotreatment of rapeseed oil. Amount of isoalkanes and aromatic compounds in hydrotreating products increased with increasing reaction temperature and decreasing pressure. At increasing temperature, hydrodecarboxylation and hydrodecarbonylation were applied more in conversion of rapeseed oil compared to hydrodeoxygenation. Liquid products had relatively high pour point which decreased as a result of isomerization at higher reaction temperature. The cetane index of the products was very high (>90) and slightly decreased with increasing reaction temperature.

### Acknowledgment

*This work was supported by MSMT CR from specific university research (MSMT No 20/2014).*

### Literature

1. United Nations Department of Economics and Social Affairs, 2012, [http://esa.un.org/unpd/wpp/unpp/panel\\_population.htm](http://esa.un.org/unpd/wpp/unpp/panel_population.htm).
2. The European Parliament and the Council of the European Union: Directive 2009/28/EC of 23 April 2009 on the promotion of the use of energy from renewable sources and amending and subsequently repealing Directives 2001/77/EC and 2003/30/EC: Official Journal of the European Union L140, 16 (2009).
3. The European Parliament and the Council of the European Union: Directive 2009/30/EC of 23 April 2009 amending Directive 98/70/EC as regards the specification of petrol, diesel and gas-oil and introducing a mechanism to monitor and reduce greenhouse gas emissions and amending Council Directive 1999/32/EC as regards the specification of fuel used by inland waterway vessels and repealing Directive 93/12/EEC: A Official Journal of the European Union L140, 88 (2009).
4. Knothe G.: *Progr. Energ. Combust.* 36, 364 (2010).
5. Furimsky E.: *Catal. Today*: 217, 13 (2013).
6. Yang Y., Wang Q., Zhang X., Wang L., Li G.: *Fuel Process. Technol.* 116, 165 (2013).
7. Kiatkittipong W., Phimsen S., Kiatkittipong K., Wongsakulphasatch S., Laosiripojana N., Assabumrungrat S.: *Fuel Process. Technol.* 116, 16 (2013).
8. Choudhary T. V., Phillips C. B.: *Appl. Catal. A-Gen.* 397, 1 (2011).
9. Tomášek J., Blažek J., Bajer T.: *Paliva* 4, 1 (2012).
10. Selishcheva S. A., Babushkin D. E., Yakovlev V. A.: *Chem. Sust. Dev.* 19, 181 (2011).

## SBA-15 AND BENTONITE BASED CATALYSTS USED FOR THE VISCOSITY REDUCTION OF A REB VACUUM RESIDUE USING A LOW-TEMPERATURE HYDROVISBREAKING PROCESS.

Hidalgo J. M.<sup>1</sup>, Vráblík A.<sup>1</sup>, Jíša P.<sup>1</sup>, Černý R.<sup>1</sup>, Hamerníková J.<sup>1</sup>, Yepez A.<sup>2</sup>, Romero A. A.<sup>2</sup>

<sup>1</sup>Research Institute of Inorganic Chemistry (VUAnCh), Department of Efficient Refining Technologies (UniCRE-EFFRET), Chempark Litvínov, 43670 Litvínov, Czech Republic

<sup>2</sup>Universidad de Córdoba, Departamento de Química Orgánica, Campus de Rabanales, Edificio C-3, Carretera Nacional IV - A, Km. 396, 14014 - Córdoba (Spain)

### Introduction

Vacuum residue (VR) is the heaviest fraction of petroleum processed in the refinery industry; the increasing demand for petroleum have afforded a major impetus for the current research. The processing of heavy oils entails complications such as high viscosity, problems relating to transport and limited processing capacities for heavier fractions in the existing refineries. For these reasons, the properties of the heavy raw materials need to be improved to minimize any risk to the environment and to their processing in refineries [1-7]. The visbreaking process is a well-known conventional thermal treatment. It is based on a mild thermal decomposition resulting in a decrease in the viscosity of residues from petroleum, heavy oil, or bitumen. The reaction temperature is usually in the range of 350–450 °C. Usually, the heavier compounds are cracked at a low specific residence time to avoid coking reactions. The hydrovisbreaking process involves a visbreaking treatment in a hydrogen atmosphere; this can be a catalytic or non-catalytic reaction [6]. The use of cost-efficient catalysts is necessary for the catalytic process. The use of bentonites or other low-cost natural minerals as catalysts is another interesting alternative [8, 9].

This study was carried out with the aim of obtaining an active catalysts for the reduction of the viscosity of a vacuum residue using a low temperature process. Two bentonite based materials and two SBA-15 catalysts were used.

### Experimental

#### Hydrovisbreaking experiments

An autoclave Parr Instrument Company 4575/76 with a reactor controller “4848B” was used for the visbreaking experiments. The course of an experiment and the reaction conditions were as follows: The sample and an additive or catalyst were introduced into the reactor (autoclave) and heated from room temperature up to 300 °C with the rate of 8.3 °C/min. Then, the system was kept 30 min at 300 °C. Finally the system was cooled by air flow (-4.5 °C/min) to the room temperature and stabilized for 20 hours until the next day. Then a gas sample was taken and analyzed. The liquid product was analyzed (dynamic viscosity, elemental analysis, density, solubility in hexane and toluene and simulated distillation). One gram of catalyst and 99 g of feedstock were added for each test.

#### Analyses

The dynamic viscosity was evaluated using the standard EN 13302 with the “Brookfield Thermosel System”. The solubility in hexane and toluene of the product was determined according to the standard ČSN 65 6073.

The high temperature simulated distillation (SimDis) was performed by gas chromatography according to the procedure drawn up by “AC analytical controls”. It is used to determine the boiling point distribution of petroleum oils, their products and higher boiling residues. The minimum boiling range petroleum fractions, for which the method can be used, is 55 °C. The results obtained by this method are equivalent to the results of conventional distillation method ASTM D 2892, which is performed on a column with 15 theoretical trays at a reflux ratio of 5:1. The sample is sprayed on the gas chromatographic column, which separates the hydrocarbons according to their boiling point.

The density of the liquid products was carried out using a semi-hydrometer KYOTO DA-645.

Elemental analysis by the ICP method was measured on elemental analyzer Flash2000 (Thermo Scientific). The standard ASTM D 5291 was used.

The gaseous products were analysed by the method “Refinery Gas Analysis” RGA (Agilent Technologies) with the GC 7890A Agilent. It was configured to analyze refinery gas up to C6 hydrocarbons including H<sub>2</sub>S and carbonyl sulphides (COS).

## Raw material and catalysts

Vacuum Residue (VR) from Russian Export Blend crude oil (REB) was used as a raw material for the visbreaking experiments. Its properties were evaluated - elemental analysis, density, viscosity and solubility in hexane and toluene (Table I).

Table I.

### la. Feedstock properties.

Name	Dynamic Viscosity	Density	Elemental Analysis				Asphaltenes	
	mPa*s	kg/m <sup>3</sup>	%wt.				%wt.	
			C	H	S	N	<sup>2</sup> n-hexane	<sup>3</sup> Toluene
438-62-13-A	*	1007.6	85.9	10.4	3.1	0.7	6.9	0.031

<sup>2</sup>Amount of non-soluble compounds in n-hexane. (Asphaltene + others).

<sup>3</sup>Non-soluble compounds in n-hexane or toluene (others).

### lb. Dynamic Viscosity.

Dynamic Viscosity (mPa*s)	(60 °C)	(80 °C)	(100 °C)	(120 °C)	(135 °C)	(150 °C)
*438-62-13-A	24550	3290	822	267	125	74,5

### lc. Simulated Distillation.

Fraction	343-525 °C	525 °C +
%wt.	13	87

Four catalysts were tested:

**a)** Two catalysts which were used in previous published works [10, 11] were synthesized according to the next procedure: A solution (300 mL) of hydrochloric acid at pH = 1.5 was prepared and then added to a vessel containing 8.07 g of pluronics P123 as a structure-directing agent. The mixture was stirred until a transparent solution was obtained. Then, 0.93 g of Zr (IV) oxynitrate hydrate (or 0.82 g of aluminum isopropyl) was added to the mixture followed by the dropwise addition of 18 mL of TEOS (tetraethyl orthosilicate). The final mixture was stirred for 24 h, filtered, and eventually calcined at 600 °C for 8 h (4 h under nitrogen + 4 h under air). The catalysts were synthesized using Si/metal (Zr or Al) ratio of 30. Catalyst Al-SBA-15 presented a  $S_{BET}$  of  $756 \text{ m}^2 \text{ g}^{-1}$ ,  $D_{BJH}$  of 8.9 Å and  $V_{BJH}$  of  $0.72 \text{ mL g}^{-1}$ . Zr-SBA-15 presented a  $S_{BET}$  of  $660 \text{ m}^2 \text{ g}^{-1}$ ,  $D_{BJH}$  of 6.9 Å and  $V_{BJH}$  of  $0.58 \text{ mL g}^{-1}$  [10, 11].

**b)** The Activated Bentonite was a commercial bentonite "Sabencil Bentonite" (EINECS No. ES 215-108-5, with added sodium carbonate; max. 7 %wt.) from the company KERAMOST a. s. which is located in Most (Czech Republic).

**c)** The catalyst called "Fe-Citrate-Oxalate" was an extract from the commercial Activated Bentonite. The bentonite (100 g) was emulsified in a solution 0.88 M of Oxalic Acid (Lach:ner Oxalic Acid dihydrate) in distilled water (0.44 moles of acid calculated regardless the H<sub>2</sub>O of hydration "dihydrated" in 0.5 L of water) and stirred during 48 h. Then, the bentonite was filtrated and the aqueous solution dried obtaining a solid which was used as catalyst for testing the upgrading of vacuum residue. The final solid was mixed with Ferric ammonium citrate brown pure "Lach:ner" (20.5 - 23 %wt. of Fe content) in a weight ratio of solid/Ferric ammonium citrate brown = 70/10 (w/w). This final solid contained organic salts with 0.8 %wt. of Al, 11 %wt. of Fe, 1 %wt. of Mg, 1.2 %wt. of Na, 0.2 %wt. of Ca, 0.1 %wt. of K and much lower amounts (ppm) of Ti, Li, P and Mn.

## Results and Discussion

The results from the simulated distillation are shown in the table II. The reaction was carried out at 300 °C during 30 min. All tests supposed an increment of the amount of the fraction 343-525 °C. Concretely, from 13 %wt. (test without catalyst or with catalyst Zr-SBA-15) to 23 %wt. (test with the activated bentonite). The test using the commercial activated bentonite and VR-(Fe-Citrate-Oxalate) implied the biggest production of lighter fractions compared to the composition of the feedstock. The amount of the liquid fraction <177 °C was really low near to zero. And, fraction 177-343 °C was 1-4 %wt.

Table II.

Common four-fraction for feedstock from the liquid sample.

Common four-fraction / Test Name	%wt. <177 °C	%wt. 177-343 °C	%wt. 343-525 °C	%wt. >525 °C
<i>Feedstock</i>	0	0	13	87
VR-(test without catalyst)	0	<1	16-17	82-84
VR-(Zr-SBA-15)	<1	<1	11-13	87-89
VR-(Al-SBA-15)	0	1-2	15-16	84-82
VR-(Activated Bentonite)	<1	4	22-23	72-74
VR-(Fe-Citrate-Oxalate)	0	3-4	22	73-74

The viscosity was varying depending on the test carried out. The table III represents more clearly the differences between each product. Tests VR-(without catalyst) and VR-(Zr-SBA-15) generated the most viscous products. And, tests VR-(Activated Bentonite) and VR-(Fe-Citrate-Oxalate) the less viscous products. Test VR-(Al-SBA-15) produced a liquid mixture with a dynamic viscosity of 7717 mPa\*s (60 °C). The high content in Fe in the activated bentonite and in the organic salt Fe-Citrate-Oxalate could be the main reason of the highest activity. Nevertheless, catalyst Al-SBA-15 presented a high activity despite not having Fe (or other active metals such as Mo or Co) in its composition. This result suggest that an addition of Fe could improve the hydrovisbreaking activity.

Table III.

Dynamic Viscosity of the products and raw material.

<b>Dynamic Viscosity (mPa*s)</b>	<b>(60 °C)</b>	<b>(80 °C)</b>	<b>(100 °C)</b>	<b>(120 °C)</b>	<b>(135 °C)</b>	<b>(150 °C)</b>
<i>Feedstock</i>	24550	3290	822	267	125	74.5
VR-(without catalyst)	17700	2550	671	242	115	69.5
VR-(Zr-SBA-15)	16533	2420	671	225	117	66.5
VR-(Al-SBA-15)	7717	1340	381	148	79.5	47.8
VR-(Activated Bentonite)	3220	701	224	90.2	52.4	32.9
VR-(Fe-Citrate-Oxalate)	3590	725	234	94.5	53.8	32.9

The results represented in the table III showed really similar elemental analyses and densities. The amount of insoluble compounds in hexane and/or toluene increased after these tests. It could be due to the emulsion of particles from catalyst which are not soluble in these solvents. Interestingly, the highest amount of insoluble compounds in toluene was found in the SBA-15 materials which were the most porous and which presented the lowest density. The test using Activated Bentonite presented the biggest amount of insoluble compounds in n-hexane and the test using the catalyst Fe-Citrate-Oxalate the lowest content in hydrogen in the product. The elemental analysis and densities were similar for all products. The lowest amount of hydrogen was found in the product from the test using the organic salt. Nevertheless, this product had a low viscosity indicating possibly a lighter product with a bigger amount of olefins. This hypothesis cannot be confirmed due to the low difference (1-1.6 %wt.) in the amount of hydrogen between the different products. The amount of nitrogen or sulfur was the same for the product and feedstock. The density presented low differences between the feedstock and the products.

The Gas Refinery Analysis (only for gaseous products) indicated a low consumption or production of hydrogen (figure 1) during the reactions (from 2 %wt. (production from hydrocracking during the test without catalyst) to 4 %wt. (consumption during the test VR-(Activated Bentonite)).

Table III.

Selected properties of the liquid reaction products.

Name	Density <i>Kg/m<sup>3</sup></i>	Elemental Analysis (%wt.)				Insoluble (%wt.)	
		<i>C</i>	<i>H</i>	<i>S</i>	<i>N</i>	<sup>1</sup> <i>n-hexane</i>	<sup>2</sup> <i>Toluene</i>
<b>Feedstock</b>	1007.6	85.9	10.4	3.1	0.6	6.9	0.031
<b>VR-(without catalyst)</b>	1001	85.9	10.4	3.0	0.7	7.5	0.04
<b>VR-(Zr-SBA-15)</b>	998.4	85.5	10.7	3.1	0.7	7.5	0.44
<b>VR-(Al-SBA-15)</b>	1002.9	85.5	10.7	3.1	0.7	9.2	0.9
<b>VR-(Activated Bentonite)</b>	999	85.2	11.0	3.1	0.7	13.1	0.2
<b>VR-(Fe-Citrate-Oxalate)</b>	999.8	87.0	9.4	3.0	0.6	8.9	0.17

<sup>1</sup>Amount of non-soluble compounds in n-hexane. (Asphaltene + others).<sup>2</sup>Non-soluble compounds in n-hexane or toluene (others).

The analyses of gaseous products using GC presented a composition which contained not only hydrogen but also methane, ethane, and other gaseous compounds (Table IV). They suggested a main production to gas methane in the gaseous phase. Some carbon dioxide was found in the gases. The amount of hydrogen sulfide generated in the gases and the same amount of sulfur found in the liquid product indicated that only a small amount of sulfur was extracted from the feedstock.

Table IV.

Composition of the gaseous product collected after reaction at room temperature.

Table IVa. Gas-product composition for tests using the catalysts SBA-15 and blank-test.

<b>Test</b>	<b>VR-(without catalyst)</b>	<b>VR-(Zr-SBA-15)</b>	<b>VR-(Al-SBA-15)</b>
<b>Compound</b>	Mole%	Mole%	Mole%
<b>Hydrogen</b>	98.97	95.77	96.71
<b>Carbon Dioxide</b>	0.03	0.03	0.05
<b>Hydrogen Sulfide</b>	0.11	0.27	0.3
<b>Methane</b>	0.44	2.11	1.49
<b>Ethane</b>	0.16	0.76	0.56
<b>Others</b>	0.29	1.06	0.89

Table IVb. Gas-product composition for tests using the catalysts Fe-Citrate-Oxalate and Activated Bentonite.

<b>Test</b>	<b>VR-(Activated Bentonite)</b>	<b>VR-(Fe-Citrate-Oxalate)</b>
<b>Compound</b>	Mole%	Mole%
<b>Hydrogen</b>	92.05	93.48
<b>Carbon Dioxide</b>	0.09	0.16
<b>Hydrogen Sulfide</b>	0.66	0.66
<b>Methane</b>	3.48	3.03
<b>Ethane</b>	1.37	1.13
<b>Others</b>	2.35	1.54

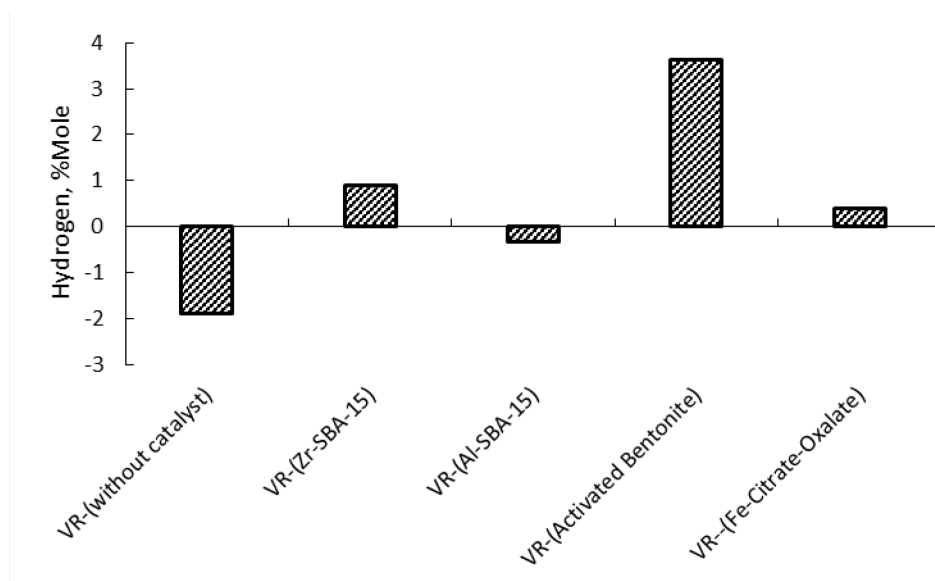


Figure 1. Relative consumption of hydrogen during reaction. Negative values mean a production of hydrogen and positive values consumption.

The methodology used to calculate the consumption of hydrogen was the same than the used by J. M. Hidalgo-Herrador [12] et al. The consumption of hydrogen (Fig. 1) during the reaction was monitored by a calibrated device of the experimental system (autoclave). The reactor was filled with an adequate amount of feedstock in order to achieve the same dead volume in each experiment. The total amount of added hydrogen was measured through a calibrated mass-flow controller. The pressure was measured using a digital pressure gauge. The equation for calculating the actual amount of hydrogen in the reactor was obtained as follows:  $A = 0.106B$ , where A is the number of moles of  $H_2$  and B is the pressure (MPa). This equation was used to calculate the amount of hydrogen in the gaseous phase (at 25°C) after the reaction. Knowing the gas composition and pressure, it was possible to calculate the amount of hydrogen in the gases and this amount was compared with the initial amount of free  $H_2$  present in the gas-product. According to information from the literature [13], this method could be generating an error of 0.1–6 % of total hydrogen consumption because the dissolved hydrogen in the liquid phase was not calculated. The total actual hydrogen consumption is  $H_{\text{cons}} = \Delta H_{\text{gas}} + H_{\text{diss}}$  [13]. For these reasons, the results should be taken as approximate.

### Conclusions

Five tests were carried out. The hydrovisbreaking of vacuum residue was investigated using four catalysts at low temperature. The biggest increment in the lighter fractions was found in the range of 343–525 °C. The main products, in the gaseous samples collected after reaction, were methane and ethane. Elemental Analyses and densities showed similar results for all the products. The main improvement found was the low dynamic viscosity of the products; 3220 and 3590 mPa\*s from tests VR-(Activated Bentonite) and VR-(Fe-Citrate-Oxalate) respectively. The tests were carried out at 300 °C.

### Acknowledgements

*This publication is a result of research project solved in a frame of UniCRE centre which infrastructure was supported by the European Regional Development Fund and the state budget of the Czech Republic. The publication was supported by institutional funds (Ministry of Industry and Trade of the Czech Republic).*

### Literature

1. Menoufy M. F., Ahmed H. S., Betiha M. A., Sayed M. A.: *Fuel* 119, 106–110 (2014).
2. Viet T. T., Lee J. H., Ma F. Z., Kim G. R., Ahn I. S., Lee C. H.: *Fuel* 103, 553–561 (2013).
3. Joshi J. B., Pandit A. B., Kataria K. L., Kulkarni R. P., Sawarkar A. N., Tandon D., Ram Y., Kumar M. M.: *Ind. Eng. Chem. Res.* 47, 8960–8988 (2008).
4. Liu Y. D., Gao L. A., Wen L. Y., Zong B. N.: *Recent Patents on Chemical Engineering*, 2, 22–36 (2009).
5. Lee S. H., Heo H. S., Jeong K. E., Yim J. H., Jeon J. K., Jung K. Y., Ko Y. S., Kim S. S., Park Y. K.: *Journal of Nanoscience and Nanotechnology* 11, 759–762 (2011).
6. Rana M. S., Sámano V., Ancheyta J., Diaz J. A. I.: *Fuel* 86, 1216–1231 (2007).

7. Hossain M., Kitaguchi T., Sato Y., Tago T., Masuda T.: 20th Annual Saudi-Japan Catalysts Symposium on "Catalysts in Petroleum Refining & Petrochemicals", "Heavy oil upgrading in supercritical water using iron based catalyst.", Dhahran, Saudi Arabia: King Fahd University of Petroleum & Minerals. December 5–6 (2010).
8. Emam E. A.: ARPN Journal of Science and Technology 3, 356–375 (2013).
9. Shah A. A.: The University of Birmingham, Ph.D. Thesis, "Experimental optimization of the CAPRI process", Birmingham, UK (2011).
10. Hidalgo J. M., Pineda A., Arancon R. A. D., Černý R., Climent M. S., Romero A. A., Luque R.: Journal of Flow Chemistry 4, 1 (2015).
11. Yopez A., Hidalgo J. M., Pineda A., Černý R., Jíša P., Garcia A., Romero A. A., Rafael Luque: **Green Chem.** 17, 565-572 (2015).
12. Hidalgo-Herrador J. M., Vráblík A., Jíša P., Černý R., Hamerniková J.: Chemical Papers, accepted manuscript. DOI: 10.1515/chempap-2015-0119 (2015).
13. Castañeda L. C., Muñoz J. A. D., Ancheyta J.: *Fuel* 90, 3593–3601 (2011).

## LOW-TEMPERATURE PROPERTIES OF DIESEL FUEL CONTAINING DIFFERENT FAME

**Vráblik A.**<sup>1</sup>, Zbuzek M.<sup>2</sup>, Hamerníková J.<sup>1</sup>, Němec J.<sup>3</sup>, Černý R.<sup>1</sup>

<sup>1</sup>Research Institute of Inorganic Chemistry (VÚAnCh), Department of Efficient Refining Technologies (UniCRE-EFFRET), Chempark Litvínov, 436 70 Litvínov, Czech Republic

<sup>2</sup>UNIPETROL RPA, Chempark Litvínov, 436 70 Litvínov, Czech Republic

<sup>3</sup>Kratolia Trade, Žukovova 59/34, 400 03 Ústí nad Labem, Czech Republic  
Ales.Vrablik@vuanch.cz

### Abstract

The low-temperature properties belongs to the most important parameters of diesel fuel, especially during the winter period. The unbranched paraffins (n-paraffins) form micro-crystals at the low temperatures deep below zero and they may cause significant problems in the fuel system of a car.

These complications can be magnified using a diesel fuel containing higher content of bio-components (FAME). The long chains of FAME show very similar behaviour like the n-paraffins and in this way they influence the final low-temperature properties of diesel – FAME blends. The resulting values of the standardized parameters are worse in comparison with the petroleum derived diesel. The diesel–FAME blends with higher content of FAME must be improved using the relevant additives (depressants). The content and type of FAME can influence the low-temperature properties as well as the oxidation stability.

This study is focused on the comparison of the low-temperature properties and the oxidation stability of diesel–FAME blends using two different types of FAME - RME and UCOME. The content of FAME was in the levels of 0; 7; 20; 30 and 100 % V/V. The blending procedure was carried out in the laboratory scale.

### Introduction

The motor fuels which are placed on the EU market must contain minimum share of biofuels according to the Directive No. 2009/28/EC. The bio components (FAME, bioethanol) must be presented in at least 6.0 % V/V in diesel and 4.1 % V/V in gasoline.<sup>1</sup> The mandatory target on reduction of emission greenhouse gases (GHG) produced by combustion of motor fuels follows the directive No. 1998/70/EC. The emissions should be reduced at least 4 % (from January 1, 2017) and subsequently at least 6 % (from January 1, 2020). The combustion of the motor fuel from fossil sources has a standard level of emission, i.e. 83.8 g/MJ. Other important fact is that only the biofuels with high sustainability criteria can be count into the obligations. The biofuels with sustainability criteria min. 35 % (to the end 2016), min. 50 % (from January 1, 2017) and min. 60 % (from January 1, 2018) can be count. Simultaneously, from 2020 the biofuels from food sources will be limited to 7 % of the final energy consumption in transport and at least 0.5 % should represent advanced biofuels. All these facts will play an important role in the production of motor fuels in coming years.<sup>2</sup>

The emission savings cannot be solved by the existing composition of raw materials and products especially it is necessary to increase the biofuels from non-food sources in the final mixture of motor fuels. The biofuels with a high sustainability are preferred also by legislation. The biofuels made from algae, bacteria can be counted 4 times. The biofuels produced from waste and residues (used cooking oil, animal fats) can be counted twice and the biofuels produced from straw, manure, lignocellulosic fibers, bark, branches, sawdust, shavings, etc. can be counted once. The biofuels from algae and bacteria are still not available in EU and their prices are high. The biofuels from waste and residues are therefore the raw material with the highest sustainability criteria, which are available on the EU market in an interesting quantity. The main aim of this article is to evaluate the effects of various biofuels on the low-temperature properties (cloud point, pour point, cold filtration plugging point as well as the oxidation stability) of the final diesel-FAME blends.<sup>1,2</sup>

The low-temperature properties of a diesel fuel are very important, especially during the winter period.<sup>3</sup> The cold filtration plugging point (CFPP) is the standardized parameter for diesel fuel according to the relevant standards (EN 590 and EN 14214 for FAME).<sup>4,5</sup> The low-temperature properties are depended on the presence of unbranched paraffins (n-paraffins) with higher melting point.<sup>6</sup> These molecules form micro-crystals at the low temperatures and it may cause problems in the fuel system.<sup>3</sup>

The long chains of methyl esters produced from vegetable oils or animal fats show similar behaviour as the n-paraffins. The low-temperature properties of a blend of diesel and biodiesel are influenced by several factors, especially by the FAME origin (rapeseed oil, palm oil, soybean oil, used cooking oil, etc.) as well as its production process and purity.<sup>7</sup>

The content of biodiesel in diesel fuel and the applied additives are very important for the resulting low-temperature properties (CFPP, CP, PP) and oxidation stability as well. Some additives may have a negative

effect because of overdose or contra-productivity, especially when they are applied separately for diesel and FAME before their blending.<sup>3, 8</sup> The addition of FAME to diesel fuel can affect the low-temperature properties and their resulting values may be higher.<sup>9, 10</sup>

This work is focused on the comparison of different FAMES (RME and UCOME) influence. Diesel fuel contained additives for regulating its low-temperature properties (depressant) based on WAFI (Wax Anti Fluid Improvement). WAFI is the most modern type of a flow additive. It is the combination of MDFI (Middle Distillate Flow Improvement) and WASA (Wax Anti-Sedimentation Additive). Through this type of additive the size of micro-crystals (n-paraffins) as well as the rate of its sedimentation in the tanks are modified.

The blends of diesel fuel containing specific level (0; 7; 20; 30 and 100 V/V %) of RME or UCOME were prepared in the laboratory scale. The low-temperature properties and the oxidation stability were measured. The different type of FAME as well as their various contents were compared.

### Experimental

Our work is focused on the comparison of different FAMES in diesel fuel containing additives based on WAFI regulating its low-temperature properties. The blends containing 0 % (V/V); 7 % (V/V); 20 % (V/V); 30 % (V/V) and 100 % (V/V) content of FAME were prepared in the laboratory scale. The petroleum diesel fuel was promoted with 120 ppm of depressant as well as the pure (100 % V/V) FAMES. The antioxidant in the level of 500 ppm was used for FAMES treatment. The ratio of the individual components for blending was calculated and weighed with the help of their density.

In the next step the low-temperature properties of the individual blends were evaluated. The comparison of the effect of different FAMES on the oxidation stability is described in this work as well.

#### *Analytical methods and materials*

**Cloud Point (CP)** was determined according to EN 23015 using the fully automated cloud point tester (NORMALAB NTE 450, France). The precision of the method is  $\pm 3$  °C.

**Pour Point (PP)** was assessed in accordance with ISO 3016 by the fully automated pour point tester (NORMALAB NTE 450, France). The precision of the method is  $\pm 3$  °C.

**Cold Filtration Plugging Point (CFPP)** was measured according to EN 116 with using the fully automated cold filter plugging point tester (NORMALAB NTL 450, France). The precision of the method is  $\pm 1$  °C.

**Oxidation stability** was carried out in accordance with ASTM D 7545. The PetroOXY method (Petrotest Instrument, Germany) was used for the assessment of induction period. The measured values were transferred in the line with Rancimat correlation (EN 15751) and the resulting values are given in hours.

**Diesel fuel**, respective winter type (F class) of diesel, was used as a model feedstock in this work. Diesel contained 120 ppm of the commercial additive regulating its low-temperature properties.

**Rapeseed-oil Methyl Ester (RME)** containing 500 ppm of an antioxidant was used in this paper.

**Used Cooking Oil Methyl Ester (UCOME)** containing 500 ppm of an antioxidant was used in this work.

**Additives** were used for diesel as well as for FAME treatment. The commercial additive affecting the low-temperature properties (depressant) was based on WAFI (Wax Anti Fluid Improvement). The antioxidant based on BHT (Butylated HydroxyToluene) was used for FAME treatment.

The low-temperature properties and oxidation stability of the raw materials are mentioned in the following table (Table I). It can be seen, that the pure UCOME have significantly worse low temperature properties in comparison with the pure RME. These results indicate, that the dosage of WAFI additive must be much higher for UCOME than RME to achieve the comparable low-temperature properties in the final diesel fuel.

Table I

Basic specification of raw materials

Component	CP [°C]	PP [°C]	CFPP [°C]	Ox. stability [h]
Diesel	- 5	- 26	- 20	34.2
RME	- 5	- 11	- 16	9.8
UCOME	+ 1	- 1	- 6	12.8

## Results and discussion

The prepared blends are differentiated according to the used FAMES (RME or UCOME) and the content of FAME (7; 20; 30 and 100 % V/V).

The CP parameter was not affected by any additive and it showed the same results for all the prepared blends (Table II). Better PP values were found for the blends containing RME and the PP had increased with higher content of both types of FAME – RME and UCOME. All the measured values of the low-temperatures properties are mentioned in the Table II.

Table II

CP; PP and CFPP values of the prepared blends containing 120 ppm of depressant

	Diesel	7 % (V/V)		20 % (V/V)		30 % (V/V)		100 % (V/V)	
		RME	UCOME	RME	UCOME	RME	UCOME	RME	UCOME
CP [°C]	- 5	- 5	- 5	- 5	- 5	- 5	- 4	- 5	+ 1
PP [°C]	- 26	- 28	- 22	- 26	- 16	- 24	- 15	- 12	- 1
CFPP [°C]	-20	-21	-22	-21	-20	-20	-17	-19	-6

The significant difference between the effects of depressant on different FAME is obvious from Table I and Table II. The low-temperature properties of RME were improved in comparison with UCOME which was not influenced by the addition of 120 ppm of depressant. This fact is also reflected in the results of the individual blends with various content of FAME.

The CFPP parameter was comparable for all the prepared blends containing RME. The interesting fact is that the PP value for RME blends was relatively stable to 20 % (V/V) of RME content. Subsequently the PP value was worsened by 30 % (V/V) and the higher content of RME. CFPP as well as PP values for UCOME blends were deteriorated with increasing content of UCOME. The specific trends connected with CFPP and PP values can be seen in the following figure 1.

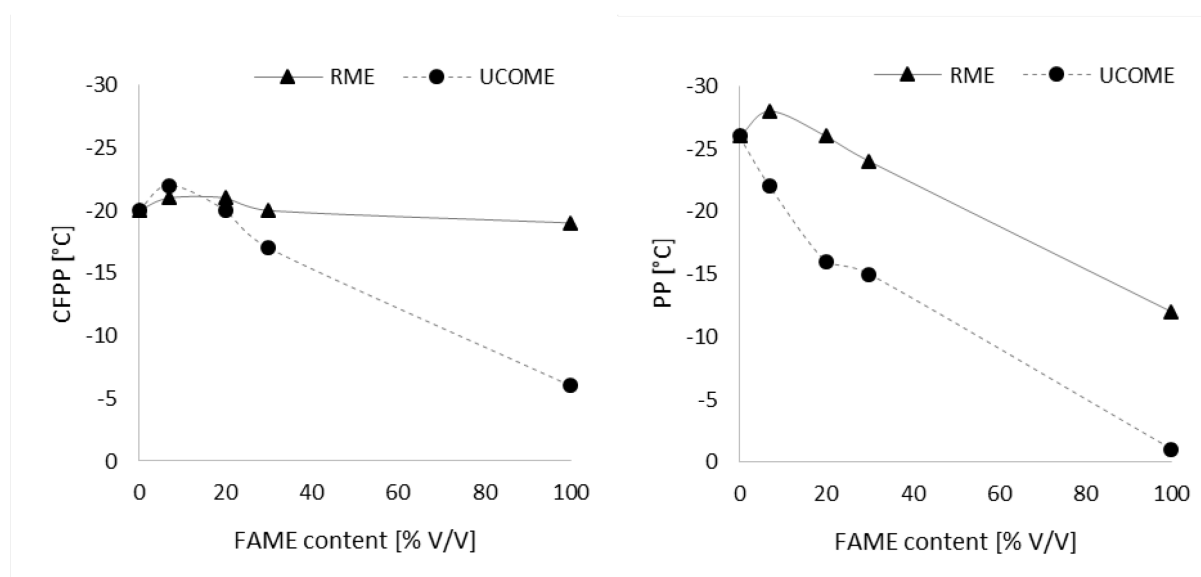


Figure 1. CFPP and PP values of the prepared blends containing 120 ppm of depressant

All the prepared blends (0; 7; 20 and 30 % V/V) met the relevant standard for CFPP parameter (Table II, Figure 1). The only exception is the CFPP value for blend with 30 % (V/V) UCOME. The maximum CFPP value (- 20 °C) is prescribed in the standard EN 590 for diesel – winter class F.

The 7 % (V/V) blends were quite comparable each other. The RME blends were better with increasing content of FAME starting from 20 % (V/V) in comparison with UCOME blends. The CFPP value for all the blends had the increasing trend with higher content of the FAME which was caused by increasing content of n-paraffins.

The Figure 2 represents the difference between CFPP and CP values that were detected in the prepared blends. The difference was calculated using the Equation (1).

$$\text{Difference} = \text{ABS}(\text{CFPP}) - \text{ABS}(\text{CP}) \quad (1)$$

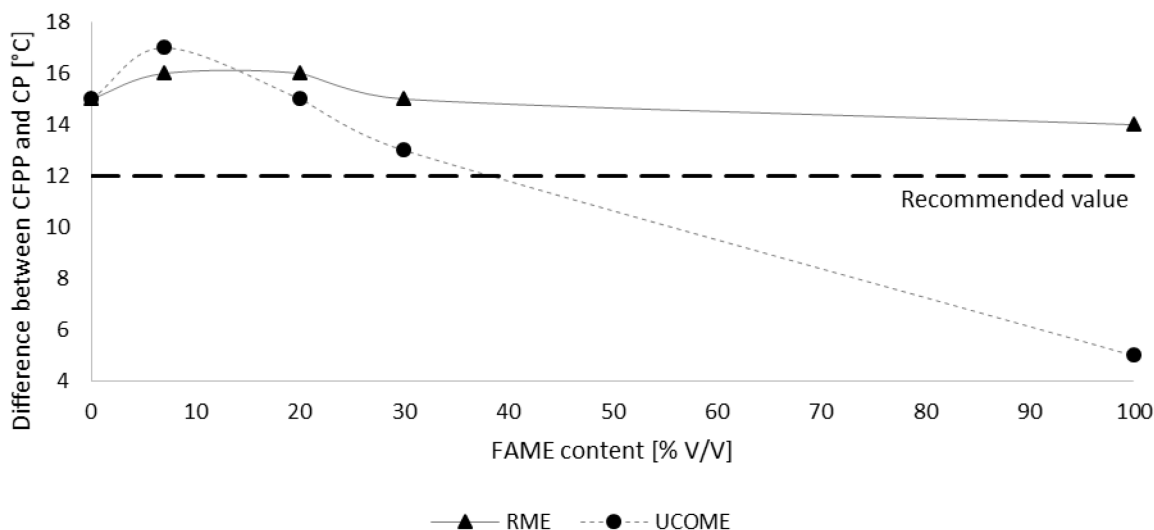


Figure 2. Difference between CFPP and CP values of the blends containing 120 ppm of depressant

The significant differences between CP and CFPP values were found. The recommended difference between CFPP and CP should not be higher than 12 °C.<sup>3</sup> However, all the prepared blends showed higher difference (Figure 2). In this case the n-paraffins can be precipitated at low temperatures significantly faster in the industrial conditions than during the laboratory determination of CFPP.<sup>3</sup>

The second interesting fact is that in the higher contents of FAME (100 % of RME and 20; 30 and 100 % of UCOME) the PP values are higher than the CFPP (Figure 3). It is not in compliance with the general trends. This discrepancy is probably caused by the ultrasonic method for determination of fluidity. The blends containing the higher content of FAME showed the creation of a solid layer on the surface of the testing sample. The solid layer is unfortunately in the same level as the ultrasonic sensors. There is not any stirring during the determination and it can affect the evaluation of PP parameter using the ultrasonic sensors and the resulting values can be inaccurate.

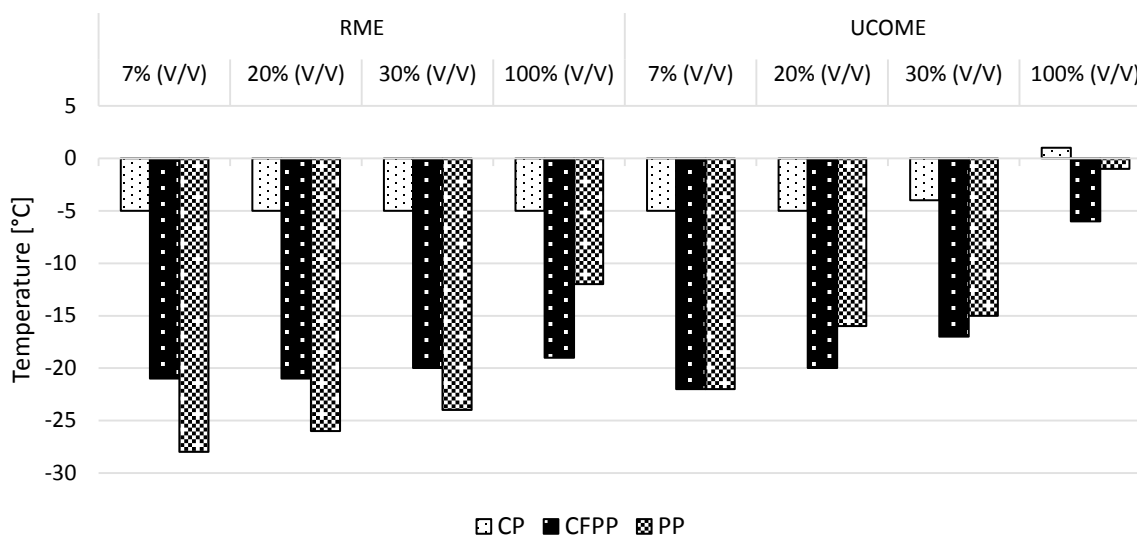


Figure 3. Comparison of the low-temperature properties

The oxidation stability was not found as a risky parameter for the FAME–diesel blends in this study. All the prepared blends met the standardized minimal value - 8 hours for FAME (EN 14214) or 20 hours for diesel fuel (EN 590). The oxidation stability of the individual components and the prepared blends are in the Table III.

Table III

Oxidation stability of the individual components and blends

Ox. stability [h]	Diesel	7 % (V/V)		20 % (V/V)		30 % (V/V)		100 % (V/V)	
		RME	UCOME	RME	UCOME	RME	UCOME	RME	UCOME
	34.2	39.6	39.7	25.7	21.0	20.5	25.2	9.8	12.8

The graphical interpretation of the oxidation stability is in the Figure 4. The minimum value for the oxidation stability according to EN 590 and EN 14214 is in the figure as well. The blends containing 7 % (V/V) of FAME showed better oxidation stability compared to the original petroleum diesel fuel. It might be caused by overdosing of the FAME component (RME or UCOME) by an antioxidant additive. The excess of the antioxidant in the FAME might affect the second component (diesel fuel) stability as well as the resulting blend.

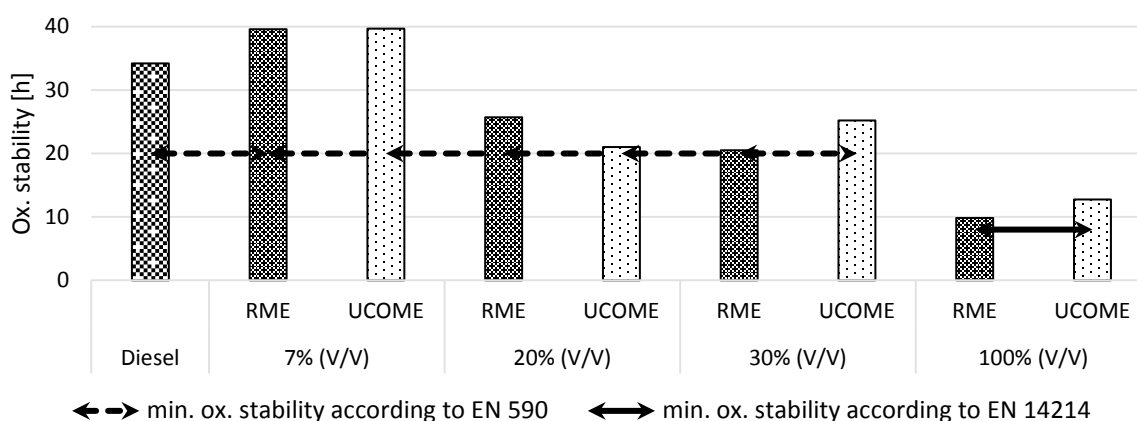


Figure 4. Oxidation stability of the individual components and blends

### Conclusions

The comparison of the low-temperature properties for the diesel-FAME blends containing 0; 7; 20; 30 and 100 % V/V of RME or UCOME in petroleum diesel fuel (winter type – class F) was done. The blends were also compared with pure RME and UCOME. The individual FAME was promoted by 500 ppm of antioxidant (based on BHT), and diesel fuel contained 120 ppm of depressant (based on WAFI). This content of depressant was also applied for pure FAME (100 % V/V) to do the comparison with the other blends. All the additives were added into the individual components before their blending. The low-temperature properties (CP; PP; CFPP) and oxidation stability were investigated.

The cloud point (CP) parameter was not affected by FAME content and it corresponds to the literature. The blends with RME showed better results in pour point (PP) compared to the blends containing UCOME. The PP increased with increasing content of RME or UCOME in the blends. The cold filtration plugging point (CFPP) parameter was problematic for UCOME blends with the content above 20 % V/V. The results indicated the need for higher dosage of depressant for UCOME than for RME blends to meet the required CFPP value.

The diesel-FAME blends had a higher difference between CP and CFPP values than it is recommended (12 °C). This difference can indicate problems with conformity of the laboratory and operational (industrial) CFPP results. The values of oxidation stability were very comparable for both types of FAME in the same level of content. All the prepared blends met the relevant standards (EN 590 for diesel fuel and EN 14214 for FAME) in the case of the oxidation stability.

The better results in some parameters (especially in the case of 7 % V/V blends) can be explained by the overdosing of the individual blending components. The excess of an additive (depressant in diesel fuel or antioxidant in FAME) could affect the properties of the resulting blend.

### Acknowledgment

*This publication is a result of research project solved in a frame of UniCRE centre which infrastructure was supported by the European Regional Development Fund and the state budget of the Czech Republic. The publication was supported by institutional funds (Ministry of Industry and Trade of the Czech Republic).*

## Literature

1. Directive 2009/28/EC of the European Parliament and of the Council on the promotion of the use of energy from renewable sources and amending and subsequently repealing Directives 2001/77/EC and 2003/30/EC.
2. Directive 1998/70/EC of the European Parliament and of the Council on the quality of petrol and diesel fuels and amending Council Directive 1993/12/EEC.
3. Matějovský V.: Automobilová paliva, Grada Publishing, Praha 2005.
4. EN 590:2014 Automotive fuels – Diesel – Requirements and test methods.
5. EN 14214+A1:2014 Liquid petroleum products – Fatty acid methyl esters (FAME) for use in diesel engines and heating applications – Requirements and test methods.
6. Schober S., Mittelbach M.: European Journal of Lipid Science and Technology, 105, 382 – 384 (2004).
7. Dittmar T., Ondruschka B., Haupt J., Lauterbach M.: Chemie Ingenieur Technik (2004).
8. Maliňáková M.: Thesis, VŠCHT Praha (1994).
9. Chiu Ch-W., Schumacher L. G., Suppes G. J.: Biomass and Bioenergy, 27, 485 – 491 (2004).
10. Knothe G.: American Society of Agricultural Engineers, 44 (2), 193 – 200 (2001).

## ADDITIVES FOR IMPROVEMENT OF THERMAL STABILITY OF BITUMINOUS BINDERS

Jíša P., Černý R.

*Research Institute of Inorganic Chemistry (VÚAnCh), Department of Efficient Refining Technologies (UniCRE-EFFRET), Chempark Litvínov, 436 70 Litvínov, Czech Republic  
petr.jisa@vuanch.cz*

### Abstract

The thermal stability is one of the key factors that influence durability of bitumen. The big emphasis is put on the monitoring of thermal stability of bitumen and the requirements for bitumen stability are getting stricter. The thermal stability of bitumen is evaluated by the methods for determination of short-term and long-term stability. The short-term stability is related to the bitumen processing including mixing with aggregate, laying, and compaction of an asphalt mixture. The long-term stability is related to the service life of an asphalt pavement on a road. Both the short-term and long-term stability are evaluated according to changes of different parameters during the ageing tests. The ageing tests can also be different especially when the long-term stability is determined.

The stability of bitumen depends on its colloidal structure and on the presence of reactive functionalities, i.e. free radicals and polar functional groups. The suitable additives can be used for the improvement of bitumen stability including radical scavengers, peptizing agents or additives with barrier effect.

The goal of our work was (i) testing of suitable additives for improvement of bitumen thermal stability, (ii) comparison of results from long-term ageing methods PAV and 3x RTFOT. Experiments were carried out with semi-blown bitumen produced from primary vacuum residues.

### Introduction

The thermal stability is one of the key factors that influences the durability of bitumen and road infrastructure. The big emphasis is put on the monitoring of thermal stability, furthermore the standardized requirements for bitumen stability are getting stricter.

The thermal stability of bitumen is evaluated by the short-term and the long-term ageing methods. The short-term stability is related to the bitumen processing including mixing with aggregate, laying and compaction of the asphalt layer. The long-term stability is related to the service life of asphalt pavement on the road, approximately for 5-10 years.

The short-term ageing is simulated by the method RTFOT according to EN 12 607. The long-term ageing can be simulated by various methods. The most preferred method is the pressure ageing vessel (PAV) according to EN 14 769. On the other hand, this method is substituted by the method 3x RTFOT – the variation of standard RTFOT according to EN 12 607 with extended duration time (225 minutes). Both PAV and 3x RTFOT give similar results when the binders are evaluated according to the standard methodology including test of softening point (EN 1427) and penetration (EN 1426). However, the conditions of the two tests are different and different impacts of the selected methods on the rheological properties of bituminous binders were observed<sup>1</sup>.

The thermal stability of bitumen can be improved by antioxidants and other additives that can stabilize the bitumen colloidal system<sup>2-6</sup>. The stabilizing effects of additives are influenced by their content in bitumen as well as by the properties of the original bituminous binder.

The goal of the presented work was the evaluation of stabilizing effects for the selected additives. Both the short-term and long-term stability were evaluated and the stabilization effects of additives were compared according to the changes of two quantities – softening point and DSR complex modulus at defined conditions. The results were also used for comparison of the difference between the long-term ageing method PAV and 3x RTFOT.

### Experimental

The samples were prepared by mixing of the base bitumen binder of grade 50/70 with the selected additives. The additives were aminoethoxylate, zinc octoate, aluminium stearane and magnesium stearane. Each of the selected additives was added to the base binder in content 1% by mass to compare their impact on the bitumen stability.

The ageing effect was evaluated using two criterions – the increase of softening point and change of complex modulus from the oscillatory rheology test at specified conditions. The increase of softening point is a standard criterion that is used for the evaluation of bitumen resistance to ageing according to EN 12 591. It is defined by the following formula where SP is the softening point according to EN 1427:

$$\Delta SP = SP_{after\ ageing} - SP_{original} \quad (1)$$

The ageing resistance can potentially be evaluated according to the changes of rheological properties although these criterions have not been standardized yet. For this purpose the rheology tests on dynamic shear rheometer Physica MCR 301 were carried out with the prepared samples. The tests were based on the application of oscillating shear stress on the loaded samples at temperature 60 °C, frequency 0.1 Hz and constant strain amplitude 1%. The changes of complex modulus were set as the criterion complex modulus ageing index  $G_i^*$  according to the following formula where  $G^*$  represents the complex modulus at the test conditions:

$$G_i^* = \frac{G_{after\ ageing}^*}{G_{original}^*} \quad (2)$$

### Results and discussion

According to the softening point increase the addition of aluminum stearane improves the resistance to short-term ageing while the other additives do not show remarkable effects – the changes in softening point increase are in the area of the test repeatability (Fig. 1). According to the complex modulus ageing index ( $G_i^*$ ) the stabilization effect was observed for all the additives except from zinc octoate. For aminoethoxylate and stearanes there was improvement from 3.5 for the base binder to 3.0 for the samples with these additives. The best result was found out for magnesium stearane (Fig. 1).

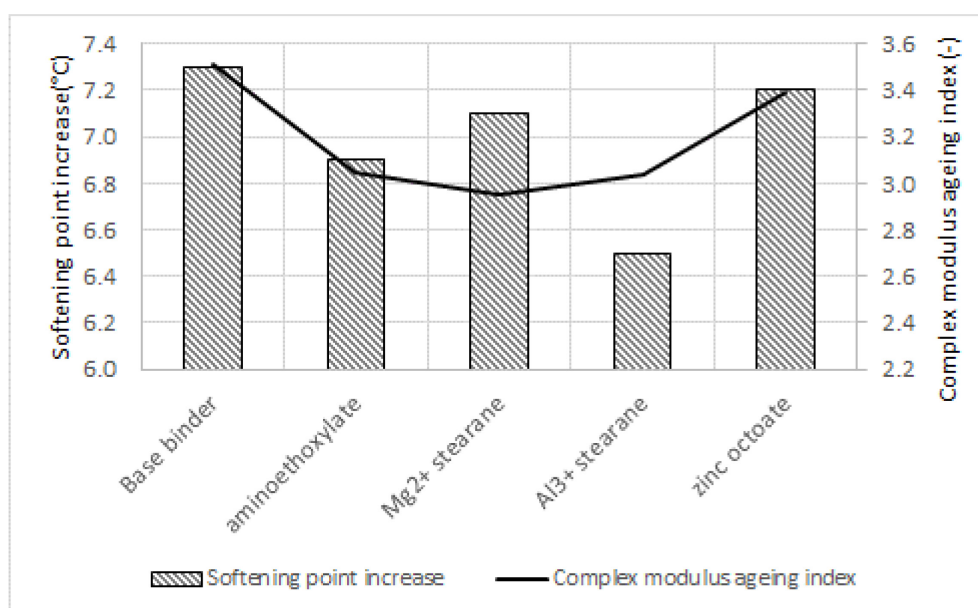


Figure 1: Changes of softening point and complex modulus after short-time ageing (RTFOT)

The increase of the resistance to long-term ageing according to softening point increase was observed for all the additives but without any significant differences between each other (Fig. 2). The resistance to long-term ageing according to  $G_i^*$  was confirmed for all the additives. While the ageing index for the base binder was near to 22, for the binders containing additives it never exceeded the value 15. The highest effect was found for magnesium stearane, in this case  $G_i^*$  was 13.(Fig. 2).

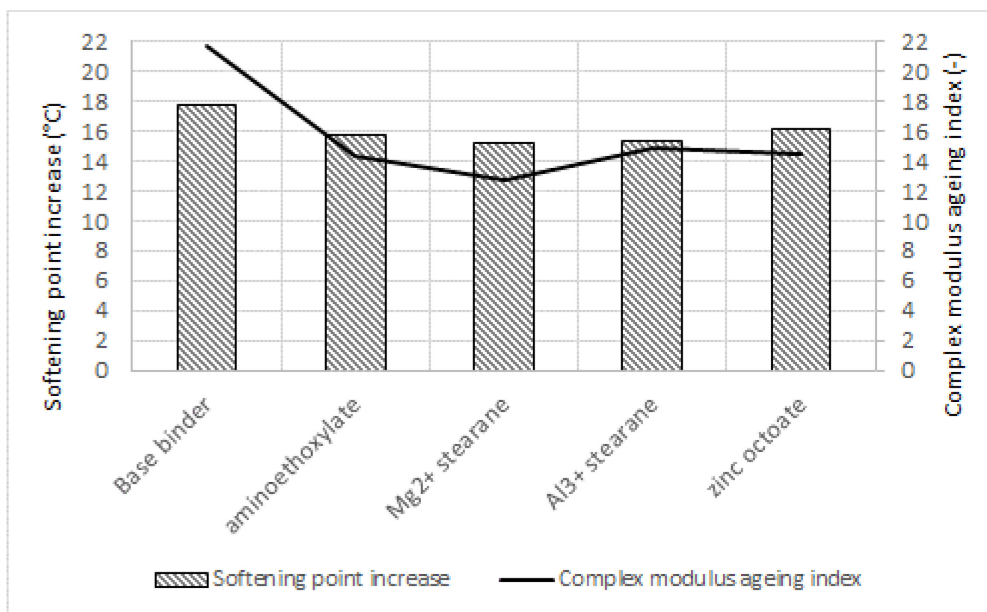


Figure 2: Changes of softening point and complex modulus after PAV

The evaluation of softening point increment provides similar results for both 3x RTFOT and PAV despite their different testing conditions for all the binders (Fig. 3). While the increase of softening point after carrying out the long-term ageing methods is approximately 17 °C for the binders with additives it is about 15 °C without significant differences between the two tests.

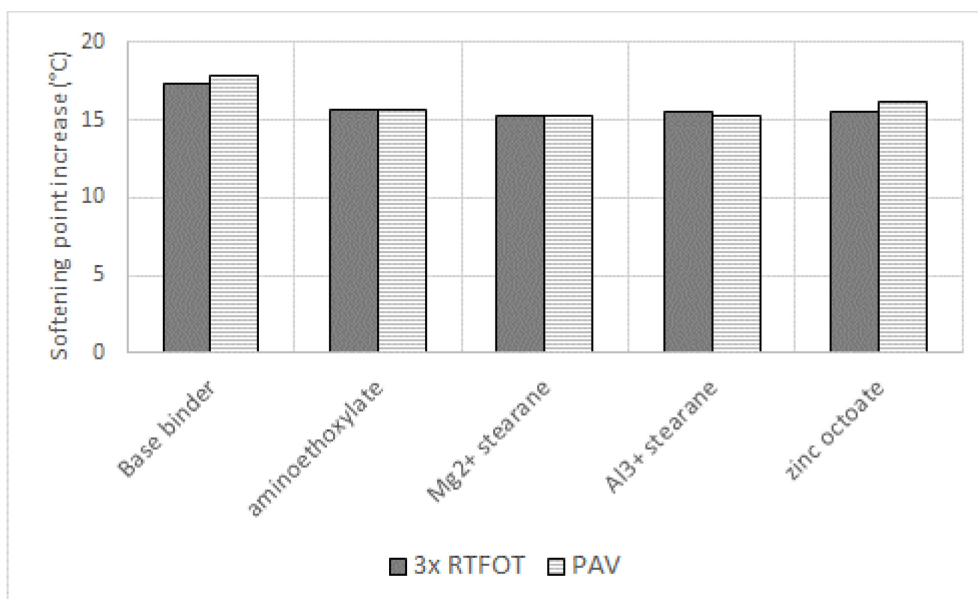


Figure 3: Softening point increase after 3x RTFOT and PAV

On the contrary to the softening point increase the results of the index  $G_i^*$  were significantly better for all the additivated samples and there were differences between the results after 3x RTFOT and PAV. The index  $G_i^*$  from PAV test gives higher  $G_i^*$  values for all of the analysed samples except from the sample containing aluminium stearane where no significant difference was observed.. These results indicate there are bigger changes in the rheological properties when the ageing is simulated by PAV compared to the changes during simulation by 3x RTFOT (Fig. 4).

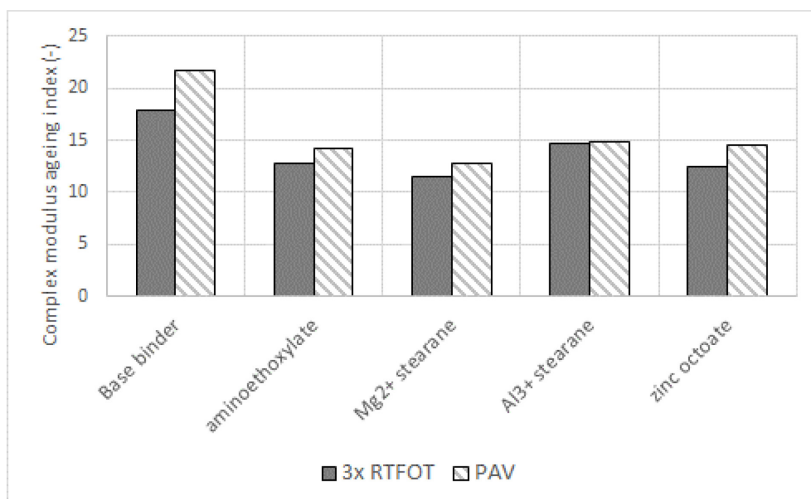


Figure 4: Complex modulus ageing index after 3x RTFOT and PAV

### Conclusions

The standard laboratory methods for short-term and long-term ageing were used to simulate the bitumen ageing. Four various additives for bitumen stabilization were tested and their effects were evaluated by the increase of softening point and complex modulus ageing index. The additives were aminoethoxylate, zinc octoate, aluminium stearane and magnesium stearane.

According to the softening point increase, the impact of the tested additives on resistance to short-term ageing was significant only for aluminum stearane. The stabilization effects were observed using the complex modulus ageing index for all the additives except from zinc octoate.

The resistance to long-term ageing was improved for all the samples containing additives. Increase of softening point was similar for all the samples with additives while complex modulus ageing index was different for each other and the best result was found for the sample with magnesium stearane.

The effectivity of additives was different depending on the criterion of evaluation. On the other hand it is clear that the weakest effects were found out for zinc octoate. The biggest improvement was observed for stearanes.

For the long-term ageing two methods, 3x RTFOT and PAV, were used. The increase of softening point for given sample was similar after 3x RTFOT and PAV. However, the ageing index  $G_i^*$  for the given sample was higher after PAV compared with the index after 3x RTFOT. Despite PAV and 3x RTFOT are often signed as commutable tests they have evidently different effects on the bitumen rheology and the conditions of PAV cause bigger changes in rheological properties compared with 3x RTFOT.

The complex modulus ageing index appears to be more sensitive compared with the softening point increase. It could be explored as an alternative criterion for the evaluation of bitumen stability.

### Acknowledgment

*This publication is a result of research project solved in a frame of UniCRE centre which infrastructure was supported by the European Regional Development Fund and the state budget of the Czech Republic. The publication was supported by institutional funds (Ministry of Industry and Trade of the Czech Republic).*

### Literature

- Hospodka, Markus. Alterungsmechanismen von Bitumen und Simulation der Alterung im Labor. Wien : Universität für Bodenkultur Wien, 2013.
- Petersen, J. C. A review of the fundamentals of asphalt oxidation. Transportation Research Circular E-C140, 2009.
- Apegyei, A. K. Laboratory evaluation of antioxidants for asphalt binders. Construction and Building Materials, 25(1), 47-53, 2011.
- Apegyei, A. K.; Buttlar, W.G.; Dempsey, B.J. Antioxidant Treatment Of Asphalt Binders. U.S. Patent Application 12/751,117, 2010.
- Zhang, H., Shi, C., Han, J., & Yu, J. Effect of organic layered silicates on flame retardancy and aging properties of bitumen. Construction and Building Materials, 40, 1151-1155, 2013
- Ouyang, C., Wang, S., Zhang, Y., & Zhang, Y. Improving the aging resistance of asphalt by addition of Zinc dialkyldithiophosphate. Fuel, 85(7), 1060-1066, 2006.

## HYDROTREATING OF LIGHT CYCLE OIL

**Tomášek J.**, Blažek J., Zbuzková B., Matějovský L., Kočetková D.

*Department of Petroleum Technology and Alternative Fuels, University of Chemistry and Technology, Prague  
Technická 5, 166 28, Praha 6, the Czech Republic  
e-mail: Josef.Tomasek@vscht.cz;*

### Introduction

Increasing consumption and demands on the quality of diesel fuel forces refineries to implement deeper refining of raw materials used in its manufacture. These facts also forces refineries to process larger amounts less appropriate fractions such as light cycle oil (LCO) from fluid catalytic cracking (FCC). Refineries must accept the quality requirements of diesel fuel during its production. In the European Union, it must meet strict legislative criteria<sup>1</sup>, such as very low sulphur content max. 10 mg/kg and the content of polycyclic aromatic hydrocarbons max. 8 wt%.

Hydrotreating of LCO is usually performed in a mixture with other middle distillates which are available in a refinery. Co-Mo/Al<sub>2</sub>O<sub>3</sub> or Ni-Mo/Al<sub>2</sub>O<sub>3</sub> catalysts are most frequently used in the middle distillate hydrotreating. Product superior in quality is usually obtained at higher reaction temperatures, higher pressure or lower space velocity of the feedstock<sup>2,3</sup>.

Al<sub>2</sub>O<sub>3</sub> is the most common support for hydrodesulphurization (HDS) catalysts because of its high stability, a relatively large surface area and porosity. It is easy to handle and relatively cheap<sup>4</sup>. Catalysts supported on carbon materials showed significant activity for HDS reaction in laboratory level. Availability methods for the preparation of oxides such as ZrO<sub>2</sub>, TiO<sub>2</sub>, MgO, which have a large surface, generate more interest in these materials as a component of bifunctional HDS catalysts. Mixtures such as TiO<sub>2</sub>-Al<sub>2</sub>O<sub>3</sub> and ZrO<sub>2</sub>-TiO<sub>2</sub> are frequently used because of their high activity<sup>5,6</sup>.

Slightly acidic non-polar carriers such as TiO<sub>2</sub> appear to be a good catalyst component. Deep desulphurization of highly aromatic LCO was achieved on the TiO<sub>2</sub> catalyst at temperatures from 340 to 360 °C. The HDS activity of the catalyst based on TiO<sub>2</sub> was better than Al<sub>2</sub>O<sub>3</sub> and cracking was lower<sup>7</sup>.

The sulphur and nitrogen content in LCO depends mainly on the amount of these elements in the feedstock for FCC. A significant part of the sulphur contained in the LCO is bound in alkyl dibenzothiophenes which are difficult to desulphurize. In LCO nitrogen is bound especially in alkyl carbazoles, which further hinders its hydrotreating. Another problem of processing the LCO on component for diesel fuels is its high content of aromatics, which affects its high density and low cetane number<sup>8</sup>.

Better quality LCO can be obtained by reducing the conversion of raw materials in the FCC unit. At a lower conversion, heavy cycle oil with higher content of hydrogen is obtained. The heavy cycle oil can be recycled which will contribute to greater LCO yield. A higher yield of LCO at the expense of gaseous hydrocarbons and gasoline is obtained in this way.

It is also possible to reduce initial boiling point of LCO at the expense of naphtha. This gives not only more LCO, but it also reduces the density, sulphur, nitrogen and polyaromatics content, which leads to easier hydrotreating of this fraction. Conversely, under high severity reaction conditions at the FCC unit, production of LCO decreases and an amount of unsaturated C<sub>3</sub> and C<sub>4</sub> hydrocarbons increases. Their subsequent oligomerization is then possible to produce high-quality, non-aromatic component of diesel fuel with a good cetane number<sup>9</sup>.

### Experimental part

Hydrotreating of LCO was performed on a commercial Co-Mo/Al<sub>2</sub>O<sub>3</sub>+SiO<sub>2</sub> catalyst in a laboratory tubular trickle-bed reactor. The catalyst bed was uniformly filled with 1:1 vol. of 87 g of catalyst (particle size from 0.25 to 0.42 mm) and inert material (SiC, particle size from 0.25 to 0.3 mm). The catalyst bed had a height of 280 mm and diameter of 30 mm. LCO was hydrotreated at a pressure of 4 MPa, temperature of 380 °C and 390 °C and at a constant hydrogen flow. The various feedstock space velocities of 0.6, 0.8 and 1.0 h<sup>-1</sup> (WHSV) changed the ratio of hydrogen to feedstock from 440 m<sup>3</sup>/m<sup>3</sup> to 260 m<sup>3</sup>/m<sup>3</sup>.

Stabilization of liquid products from LCO hydrotreating was carried out by distilling off products boiling below 150 °C (AET). Rectification was performed on a Fischer HMS 500 apparatus at a pressure of 10 kPa with a reflux ratio 1:1.

Cetane index was calculated according to EN ISO 4264. When calculating the cetane index, data from simulated distillation was used. These data were converted to a distillation curve according to ISO 3405. The conversion was performed according to ASTM D2887. Simulated distillation was performed according to ASTM D2887 on

a gas chromatograph TRACE GC. A calibration curve which was obtained by the simulated distillation of a standard mixture of n-alkanes with known boiling points was used for conversion of the retention times to the boiling points. The parameters of the simulated distillation are listed in the previous work<sup>10</sup>.

Cold filter plugging point (CFPP) was measured according to EN 116. Density was determined at Paar DMA 48 densitometer according to EN ISO 12185. Kinematic viscosity was determined at the Stabinger (SVM 3000) viscometer according to ASTM D7042. Determination of sulphur and nitrogen content was performed at Mitsubishi TOX-100 analyser according to ASTM D5453, ASTM D5762 and ASTM D4629 respectively. The content of polycyclic aromatic hydrocarbons was determined by high performance liquid chromatography (HPLC) according to EN 12916.

## Results and discussion

Yields of liquid product from LCO hydrotreatment varied between 97 and 98 wt. %. Yield of stabilized liquid products was about 99 wt. %. This means that the cracking of feedstock was negligible. Table I shows list of the properties of the LCO and stabilized products from hydrotreating. It is clear from this dates that the LCO had a high content of sulphur, nitrogen and polyaromatics. High polyaromatics content of the LCO caused its high density and very low cetane index.

Table I

Properties of LCO, stabilized products from its hydrotreating and EN 590 diesel fuel requirements

Product <sup>a</sup>	Sulphur content [mg·kg <sup>-1</sup> ]	Nitrogen content [mg·kg <sup>-1</sup> ]	Polyaromatic content [wt%]	Density at 15 °C [kg·m <sup>-3</sup> ]	Viscosity at 40 °C [mm <sup>2</sup> ·s <sup>-1</sup> ]	Cetane index	CFPP [°C]
LCO	7300	635	74	963	2.60	17	-23
V380-0.6	4	16	26.7	934	2.44	21	-26
V380-0.8	6	48	29.9	939	2.50	21	-28
V380-1.0	16	69	31.7	941	2.54	21	-29
V390-0.6	3	17	31.8	939	2.41	21	-28
V390-0.8	5	46	33.3	942	2.47	20	-29
V390-1.0	9	71	34.6	944	2.52	20	-29
EN 590	max. 10	n	max. 8.0	820-845	2.0-4.5	46	0 <sup>b</sup>

<sup>a</sup> The first number represents the reaction temperature (°C), the second space velocity (h<sup>-1</sup>) at which products were prepared, n - not required, <sup>b</sup> summer type diesel, for winter type -20 °C

Desulphurization of LCO increased with increasing temperature of hydrotreating. Only the product prepared at a temperature of 380 °C and a WHSV of 1 h<sup>-1</sup> failed to comply sulphur content required by EN 590. An increase in reaction temperature did not affect the denitrogenation. At the higher reaction temperature, product with higher content of polycyclic aromatic hydrocarbons and slightly higher density was prepared. Because of high polyaromatic content and very high density of LCO, each of the products failed with these parameters the EN 590 standard. Reducing the space velocity and increase the ratio of hydrogen to the feedstock had a positive influence on the content of sulphur, nitrogen, polyaromatics and density of hydrotreatment products.

The viscosity of LCO meet the requirement of the EN 590 standard, after refining it not changed so much. Cetane index was almost the same for all products. It improved slightly by hydrotreating, but not enough to meet the requirements of EN 590. Cold filter plugging point of LCO was very low, it slightly improved after refining.

Figure 1 illustratively show the distribution curves of LCO and the product obtained by hydrotreatment at 380 °C and a space velocity of 0.6 h<sup>-1</sup>. The figure shows a higher content of substances with a boiling point up to 245 °C in the V380-0.6 product compared with raw LCO. Distribution curves of all other products had only minimal differences from one of V380-0.6 product.

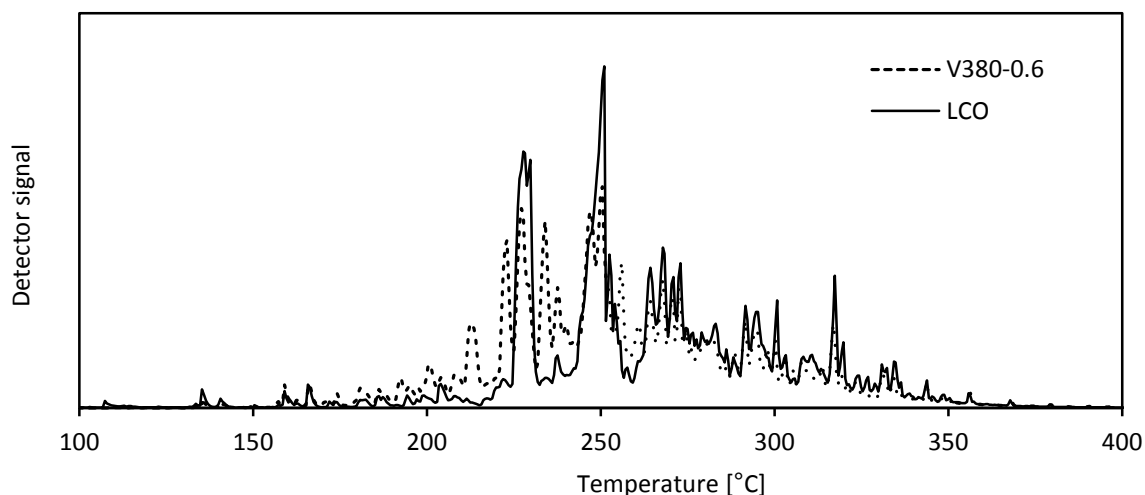


Figure 1. Comparison of the distribution curves of LCO and selected product of its hydrotreating

### Conclusion

High polyaromatic content of light cycle oil (LCO) is the cause of its high density and low cetane index. These properties are due to hydrogenation of diaromatics and triaromatics to monoaromatics improved slightly, but no product met the requirements of EN 590. Although the LCO contained large amounts of nitrogen and polycyclic aromatic hydrocarbons, a significant hydrodesulphurization and hydrodenitrogenation occurred in all the products. Sulphur content was high only in product prepared at reaction temperature of 380 °C, WHSV of 1 h<sup>-1</sup> and hydrogen to feedstock ratio of 260 m<sup>3</sup>/m<sup>3</sup>. Decreasing feed rate and an increasing ratio of hydrogen to the feedstock improve properties of hydrotreating products. Hydrodesulphurization was higher at the temperature of 390 °C than at the 380 °C. Polyaromatic content in the product was conversely lower at 380 °C which is probably associated with the balance and the exothermic hydrogenation of diaromatics and triaromatics to monoaromatics. Desulphurization of LCO is not a major problem for modern hydrotreating catalysts, in spite of this hydrotreated LCO cannot be used in a larger amount as a component of diesel fuel for its high density, high polyaromatic content and low cetane index.

### Acknowledgment

*The work was funded by the MŠMT ČR from institutional support for long-term conceptual development of research organization ID 60461373.*

### Literature

1. EN 590 Automotive fuels - Diesel - Requirements and test methods.
2. Raseev S.: Thermal and catalytic processes in petroleum refining, p. 624. Marcel Dekker, Inc., New York, Basel, 2003.
3. Stanislaus A., Marafi A., Rana M. S.: *Catal. Today* **153**, 1 (2010).
4. Topsoe H., Clausen B. S., Massoth F. E., in: Anderson J. R., Boudart M. (Eds.): *Catalysis Science and Technology*, vol. 11, Springer, New York, 1996.
5. R. Prins, V.H.J. Debeer, G.A. Somarjai.: *Catal. Rev. Sci. Eng.* **31**, 41 (1989).
6. H. Breyse, J.L. Portefaix, M. Vrinat.: *Catal. Today* **10**, 489 (1991).
7. Azizi N., Ali S. A., Alhooshani K., Kim T., Lee Y. J., Park J.-I., Miyawaki J., Yoon S.-H., Mochida I.: *Fuel Process. Technol.* **109**, 172 (2013).
8. Thakkar V. P., Abdo S. F., Gembicki V. A., Mc Gehee J. F: *Proceedings of AIChE Chicago Symposium*, October 9 - 10, 2006, Chicago, Illinois, USA.
9. Niccum P. K.: *Hydrocarb. Process.* **91**, 61 (2012).
10. Tomášek J., Blažek J., Bajer T.: *Paliva* **4**, 1 (2012).

## INCREASING SOLUBILITY AND DISSOLUTION RATE OF CANDESARTAN CILEXETIL

**Gruberová L.**, Kratochvíl B., Seilerová L.

Department of Solid State Chemistry, University of Chemistry and Technology Prague, Technická 5, 166 28, Prague, Czech Republic  
gruberol@vscht.cz

### Abstract

For a quality formulation, various formulation parameters play a crucial role. Solubility and rate of dissolution drug are the most important determinant of drug absorption from the gastrointestinal tract. The present investigation is an attempt to improve the solubility and dissolution rate using solid dispersion of a poorly soluble drug candesartan cilexetil prepared by hot-melt extrusion.

The first aim of the study was to investigate the solubility of candesartan cilexetil in a phosphate buffer with different ionic strength, pH value, type and amount of surfactant. The increased concentration of phosphate salt and pH value resulted in increase of CC solubility. Similarly, the increased concentration of surfactant Tween 20 resulted in increase solubility of CC. The increased concentration of surfactant Tween 80 resulted in slightly increase of CC solubility. Tween 20 is more suitable surfactant for dissolution medium.

The second aim of the study was characterized solid dispersion of candesartan cilexetil prepared using hot-melt extrusion. Polyvinylpyrrolidone and meglumine as carrier material was used for formulation of solid dispersions. The prepared solid dispersions were made into tablets by the direct compression method or filled into gelatine capsules. The dissolution profile of these dosage forms was studied in 0,05 M phosphate buffer pH 6,5 containing 0,35 % Tween 20. It was found that the dissolution rate of capsules containing solid dispersion EX\_4 were higher than the dissolution rate of physical mixture with the crystalline candesartan cilexetil.

### Introduction

In pharmaceutical candesartan cilexetil (CC) is an angiotensin II receptor antagonist and it is mainly indicated for the treatment of hypertension. Prodrug candesartan cilexetil is completely bioactivated by ester hydrolysis to candesartan, the active form, during a gastrointestinal absorption. The drug is having low solubility in fluids of the gastrointestinal tract, whereas, the use of the prodrug form increases the bioavailability after oral administration, therefore CC is described as BCS Class II drug<sup>1,2</sup>. Candesartan cilexetil is available as nonmodified release tablets in doses of 4, 8, 16 or 32 mg (an original product from Astra Zeneca and generics from Sandoz, Krka, Zentiva etc.)<sup>3</sup>.

Factors that are important to the kinetics of drug dissolution are the physicochemical properties of the compound itself and conditions in the gastrointestinal tract. Amphiphilic bile components have been shown to increase the solubility for numerous poorly soluble compounds<sup>4</sup>. Surfactants are regularly added into artificial dissolution medium to enhance the solubility. Tween 20 is a surfactant which is frequently used as a part of the dissolution media. The addition of Tween 20 enables to achieve sink condition during a dissolution test for poorly water soluble drugs. Tween 80 is a surfactant which is commonly used in solid oral dosage form (for examples SMEDDS)<sup>3,4</sup>. Poor solubility of active substance requires careful choice of dissolution medium in order to ensure that measurement of dissolution behavior is without the limitations imposed<sup>3</sup>.

Hot-melt extrusion (HME) is a process for the manufacturing of solid dispersion. The crystalline drug and amorphous polymer are melting under elevated temperatures and the material is exposed to shear inside the extruder; subsequently the melt is pressed out and further processed. The formulation of solid dispersion is one of the commonly used methods to improve the solubility of drug molecules<sup>5</sup>.

A required property of the polymer to be used in hot-melt extrusion is appropriate thermoplastic behavior and thermal stability. However, the number of corresponding polymers approved for pharmaceutical use is limited. Nevertheless, a range of suitable polymers with different structures and properties can be used in HME<sup>5</sup>. For this study were selected polymers polyvinylpyrrolidone (PVP) and meglumine. Till today any studies pursued solid dispersions of candesartan cilexetil produced by HME technology have been published.

### Materials and methods

#### Materials

Candesartan cilexetil (*I*) was obtained as a gift sample.

Tween 20, Tween 80 and excipients polyvinylpyrrolidone, meglumine, corn starch,  $\alpha$ -cellulose, D-lactose monohydrate, mannitol, magnesium stearate were purchased from Sigma-Aldrich. Excipient carboxymethyl

cellulose sodium salt was purchased from Acros organics. Potassium dihydrogen phosphate and sodium hydroxide were purchased from Lachner and hydrochloric acid (35 %) from Penta. All chemicals used in the study were analytical grade.

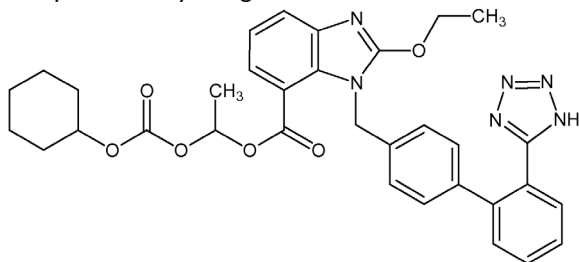


Figure 1. Structure of candesartan cilexetil (*I*)

### Sample preparation

Phosphate buffer (0,01; 0,05 and 0,10 mol/l) pH 6,2; 6,5 and 6,8 were prepared by dissolving potassium dihydrogen phosphate in distilled water and adjusting it to the desired pH with 0,1 M sodium hydroxide or 0,1 M hydrochloric acid solution. Solutions contained 0,35 % or 0,70 % (w/w) of Tween 20 or Tween 80. The pH value of the media was checked using a pH-meter (Hanna instruments, Edge HI 2020). Candesartan cilexetil was added in excess into prepared phosphate buffer and the resulting suspensions were shaken for 24 h at 37 °C under a thermostated orbital platform shaker (Heidolph, Unimax 1010 with Incubator 1000) to obtain the solubility equilibrium.

Solid dispersions were prepared by hot-melt extrusion. Candesartan cilexetil was blended with selected excipients and then the mixture was exposed to HME process. The mixture was heated in an extruder, the melted material was homogenized by a single screw and extruded through a round shape die 4 mm. The material left the extruder in the form of continuous strands which were ground in a ball mill and then sifted through a sieve number 0,80 to obtain uniform size particles. The pulverized extrudate was tableted or filled into gelatine capsules. Tablets (diameter of tablet was 10,0 mm) were made in a manual hydraulic press (Specac, 5–20 ton). Each tablets and capsules contained 4 or 8 mg of active substance. Candesartan cilexetil and selected excipients were blended in the same proportions as in the solid solution to the created physical mixture. The mixture was filled into gelatin capsules. The investigated pharmaceutical preparations (tablets or capsule forms) of solid dispersions or physical mixtures of candesartan cilexetil are described in Table I.

### Analyses of samples

The saturated solutions of candesartan cilexetil were filtrated through a 35 micron porous filter. The concentration of CC was analyzed by a UV-Vis spectrophotometer (Schimadzu UV Mini 1240) and HPLC apparatus (Waters Alliance HPLC System) equipped with C18 column (Symmetry C18; 3,5  $\mu\text{m}$ ; 4,6x75 mm) and UV-Vis detector at 256 nm. A mixture of 0,10% HCOOH:MeOH (1:9, V/V) was used as a mobile phase.

The powder X-ray diffraction patterns of solid dispersions were obtained using a powder X-ray diffractometer (PANalytical X'Pert Pro). The conditions of measurement were as follows: Cu target, graphite monochromator, range 0–40 °2-theta.

The measured mechanical characteristics of CC solid dispersion tablets were friability (Stuart rotator SB3) and in vitro dissolution. Dissolution test was likewise carried out on gelatine capsules of CC solid dispersion. Dissolution tests were performed with USP II (paddle apparatus) in 500 ml dissolution medium of 0.05 M  $\text{KH}_2\text{PO}_4$  with 0,35 % Tween 20 at 37 °C. Paddle speed was 50 rpm. The dissolution media was filtered through a 35 micron porous filter, pumped through a 10 mm flow cell using a peristaltic pump (Ismatic, Reglo Digital MS-2/6) and analyzed at  $\lambda = 256 \text{ nm}$  at time intervals of 5 minute using a UV-Vis spectrophotometer (Schimadzu UV Mini 1240). Data analysis was carried out using UV Probe software. All dissolution tests were determined in triplicate. The dissolution of physical mixtures was done similarly.

Table I

Prepared formulations of candesartan cilexetil

Samples	Excipients	Content of CC	Temperature of HME process
EX_1	Corn starch CMC Na PVP	1.1 %	40–130 °C
EX_2	Corn starch CMC Na PVP	1.1 %	60–150 °C
EX_3	Corn starch Meglumine	1.5 %	40–130 °C
EX_4	Corn starch Mannitole PVP	1.1 %	60–150 °C
EX_5	Magnesium stearate PVP	2.1 %	40–130 °C
EX_6	$\alpha$ -cellulose PVP	1.8 %	60–150 °C
EX_7	Lactose monohydrate PVP	3.7 %	–
FS_4	Corn starch Mannitole PVP	1.1 %	–
FS_6	$\alpha$ -cellulose PVP	1.8 %	–
CL_1	Lactose monohydrate	3.3 %	–

### Results and discussion

Solubility of CC in the phosphate buffer with an addition of 0,35 % Tween 20 is shown in Table II. The pH-dependent solubility profile of CC, as well as ionic strength dependent solubility profile of CC, was observed in the phosphate buffer containing 0,35 % and also 0,70 % Tween 20. The results suggest that solubilization of CC was more effective in the phosphate buffer with higher pH and higher concentration of phosphate salt. Tween 80 increased the solubility of CC in all solvents but a larger effect at higher concentration of this surfactant was not observed. In addition, HPLC analysis exposed unsuitability of Tween 80 because the peak at retention time of 4,5 min overlapped the peak of CC. The increase of the solubility of candesartan cilexetil did not achieve value present in the study<sup>3</sup>.

Table II

Solubility of candesartan cilexetil in the phosphate buffer containing 0,35 % Tween 20

Phosphate buffer with an addition of 0,35 % Tween 20		
Ionic strength	pH	Concentration
0,01 M	6.2	0.054 ± 0.001
	6.5	0.071 ± 0.001
	6.8	0.097 ± 0.003
0,05 M	6.2	0.065 ± 0.001
	6.5	0.093 ± 0.001
	6.8	0.135 ± 0.002
0,10 M	6.2	0.069 ± 0.001
	6.5	0.119 ± 0.001
	6.8	0.132 ± 0.002

The mixture marked EX\_7 was not convenient to HME considering agglomeration of particles after wetting a mixture of active substance and excipients.

The diffraction patterns confirmed that as a result of hot-melt extrusion method was formulated microcrystalline or amorphous solid dispersions. The patterns of solid dispersions showed decrease in the peak intensity or absence of peaks which indicated the amorphous nature of candesartan cilexetil in solid dispersion. The PXRD analysis was not carried out on EX\_3 because of extruded material was plastic and inappropriate to grinding.

The diffraction patterns of formulation EX\_1 and EX\_2 are identical. Composition of solid dispersion was not influenced by higher temperature of HME process. The experimental results suggest that tablet masses EX\_1 and EX\_2 prepared using carboxymethyl cellulose sodium salt (CMC Na) were highly friable (Table III). The CMC Na interfered with the CC in solid dispersion, it results in an increase in concentration value measured by UV-Vis spectrophotometer. Long disintegration time of tablet was caused by a gel layer that has formed on the surface of the tablet and has prevented a further wetting of the tablet. This effect was observed only for tablets containing CMC Na.

The hydrophobic nature of magnesium stearate leads to reduction of the dissolution rate of CC contained in EX\_5.

Table II  
Characterization of prepared formulations of candesartan cilexetil

Samples	Friability of tablets	Disintegration of tablets	% dissolved CC from capsule form at 120 minute
EX_1	100 % of tablet 2.0 ton	Limited disintegration	–
EX_2	10 % of tablet 2.0 ton	Limited disintegration	–
EX_4	1 % of tablet 1.5 t	Disintegration after 15 minute	95.28±3.55
EX_5	1 % of tablet 1.0 ton	Without disintegration	Without dissolution
EX_6	1 % of tablet 1.5 ton	Disintegration until 15 minute	750.2±3.29
FS_4	–	–	–
FS_6	1 % of tablet 0.5 ton	Disintegration after 15 minute	62.99±1.28
CL_1	100 % of tablet 2.0 ton	–	57.46±1.32

The dissolution results of CC capsules containing EX\_4, FS\_4 or CL\_1 are given in Fig. 2. At the end of the 120 minute dissolution experiment, the extent of dissolution was 97 % for EX\_4, 62 % for FS\_4 and 56 % for CL\_1. It is evident that solid dispersion EX\_4 considerably enhanced dissolution rate of CC. Physical mixture FS\_4 was not tableted, this mixture is sticky and inappropriate to tableting.

The in vitro dissolution behavior of two EX\_6 products (one uncoated tablet and one capsule formulation) are depict in Fig. 3. Little difference in the dissolution behavior of EX\_6 a FS\_6 was observed. The amount of dissolved drug at 120 minute was similar to both formulations. Intensity of tablet pressure had influence on dissolution profile of CC, with increase the pressure decrease the dissolution rate.

Dissolution profiles of candesartan cilexetil in solid dispersion prepared by hot-melt extrusion cannot be compared with some other data.

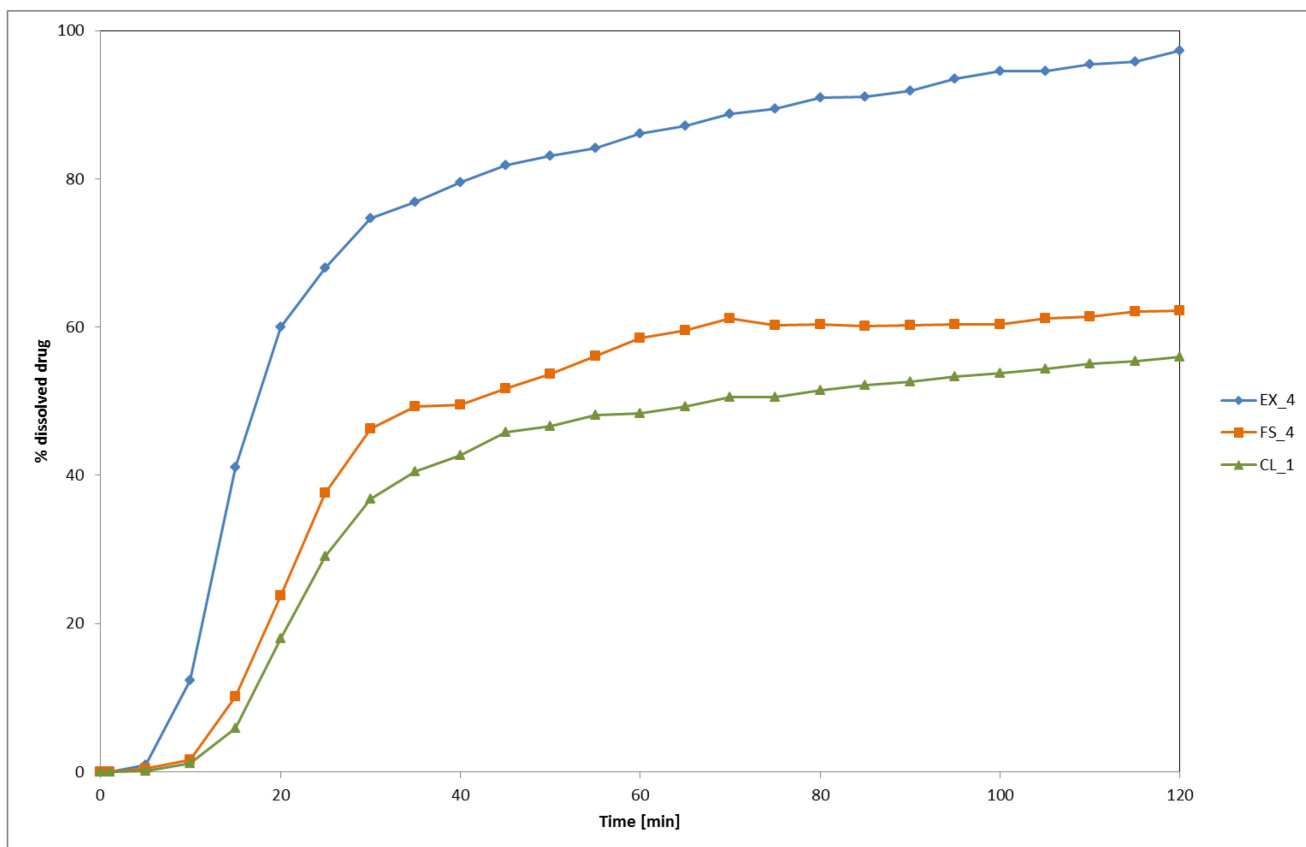


Figure 2. Dissolution profile of CC capsules containing EX\_4, FS\_4 and CL\_1

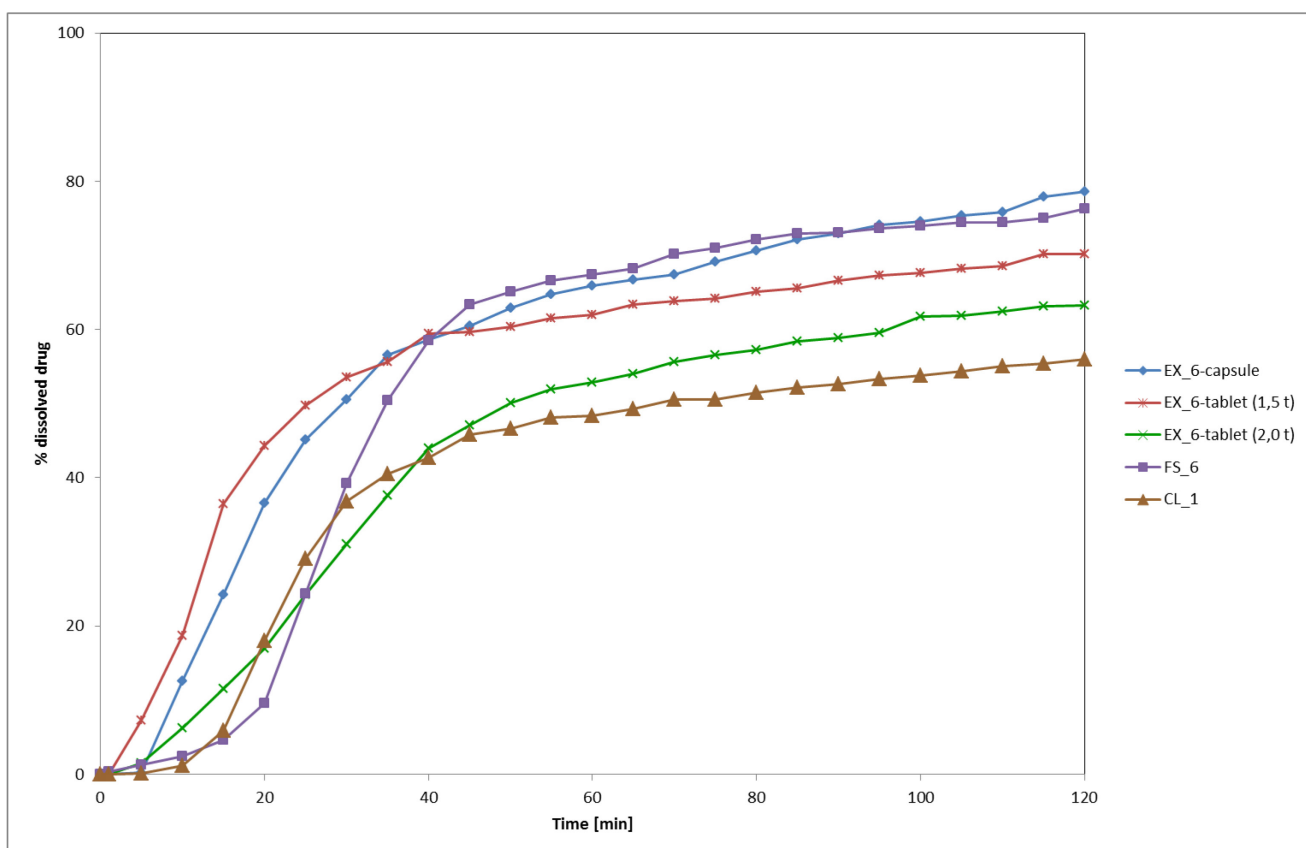


Figure 3. Dissolution profile of CC capsules containing EX\_6, FS\_6, CL\_1 and tablets containing EX\_6

## Conclusion

Solubility is the most important property for developing formulations. Candesartan cilexetil is poorly water soluble but once dissolved, CC rapidly pass biological membrane. As a consequence, slowly dissolve in the aqueous environment of the gastrointestinal tract after oral administration result in a poor bioavailability. While increasing the dissolution rate of CC the oral bioavailability will also improve. The solubility enhancement of poorly soluble drugs can be achieved by using surfactants. In this present work, the solubility of candesartan cilexetil in phosphate buffer was increased using Tween 20. Subsequent increase of the solubility of candesartan cilexetil was occurred in phosphate buffer with a higher pH, ionic strength and concentration of Tween 20. Hot-melt extrusion is the novel technology with aim to produce solid dispersion. Solid dispersion is an attractive approach to improve solubility of hydrophobic drugs. Nevertheless, to date have been published any studies dealing with solid dispersions produced by HME technology. Therefore in this study, solid dispersions were prepared by hot-melt extrusion method. Only specific formulation of candesartan cilexetil in solid dispersions showed an enhanced dissolution rate of the drug compared to the physical mixture. It was found that the dissolution rate of CC from capsules containing solid dispersion EX\_4 were higher than the dissolution rate of the crystalline candesartan cilexetil. The increase in the dissolution rate of the drug may be caused by a reduction of particle aggregation of the drug, an increased wettability and also possibility by a reduction in drug crystalline. Additional benefits of hot-melt extrusion are creation of a reliable drug release profile and higher strength of tablets. The study demonstrated that the dissolution rate of candesartan cilexetil can be enhanced by formulating solid dispersions of CC with PVP and chosen excipients.

## Acknowledgment

*Financial support from specific university research (MSMT No 20/2015).*

## Literature

1. Vishal S. K., Atul M. K., Sandip M. H., Shitalkumar P., Sachin P., Kiran B.: *IJPSR* 5(4), 1550 (2014).
2. Ramya K. S.: *The Pharma Innovation J.* 3(4), 72 (2014).
3. Hoppe K., Malgorzata S.: *AAPS Pharm. Sci. Tech.* 15(5), 1116 (2014).
4. Chen L. R., Wesley J. A., Bhattachar S., Ruiz B., Bahash K., Babu S. R.: *Pharm. Res.* 20(5), 797 (2003).
5. Kolter K., Karl M., Gryczke A. at book: *Hot-Melt Extrusion with BASF Pharma Polymers, Extrusion Compendium*, Ludwigshafen 2012.

# EFFECT OF $\beta$ -CYCLODEXTRIN ON PHYSICAL PROPERTIES OF ORALLY DISINTEGRATING TABLETS CONTAINING CETIRIZINE DIHYDROCHLORIDE

Škopková T.<sup>1</sup>, Krejzová E.<sup>1,2</sup>, Bělohav Z.<sup>1</sup>

<sup>1</sup>Department of Organic Technology, University of Chemistry and Technology Prague, Technická 5, 166 28 Prague, Czech Republic

<sup>2</sup>Zentiva k.s., A Sanofi Company, U Kabelovny 130, 102 37 Prague, Czech Republic  
skopkovt@vscht.cz

## Introduction

Cyclodextrins (CDs) are cyclic oligosaccharides composed of D-(+) glucopyranose units linked by  $\alpha$ -(1,4) glucosidic bonds. Hydrophilic outer surface and a hydrophobic inner cavity are characteristic for their molecular structure. CDs are well known as agents forming inclusion complexes with many active pharmaceutical ingredients (API) thereby achieving the taste masking, increase of drug solubility and stability, improve taste and odor and enhance bioavailability of the guest molecules<sup>1-5</sup>.  $\beta$ -CD (Figure 1a) is the most used CD in industry.

Active pharmaceutical ingredients Cetirizine dihydrochloride (CTZ, Figure 1b) is a second generation antihistaminic used in seasonal allergies and has a very unpleasant bitter taste<sup>6,7</sup>. In tablet formulation containing Cetirizine, CDs could be used in complexed and in physical mixtures for taste masking which is effective from molar ratio 1:2 (CTZ:  $\beta$ -CD)<sup>3,7</sup>.

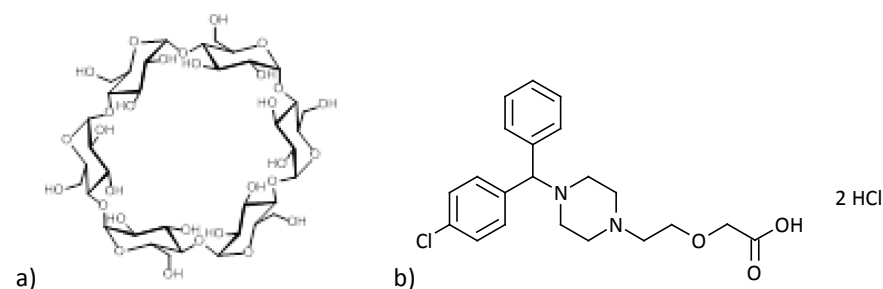


Figure 1. Chemical structure of  $\beta$ -cyclodextrin (a) and Cetirizine dihydrochloride (b)

## Materials and methods

Cetirizine dihydrochloride,  $\beta$ -cyclodextrin, Pearlitol flash mannitol, crospovidone, acid citric anhydrous, sucralose, cherry flavour and sodium laurylsulphate were used for the manufacture tablet.

## Orally disintegrating tablets preparation

Seven ODT formulations, differing in volume of  $\beta$ -CD and mannitol, were prepared by direct compression. All materials were passed through a mesh sieve with an aperture of 630  $\mu$ m. CTZ and the other ingredients (except sodium laurylsulphate) were blended in a Turbula T10B mixer (WAB, Switzerland) for 6 minutes at 30 rpm. Then sodium laurylsulphate was added, and the resulting mixture was homogenized for 2 minutes. Tablets were compressed on a StylOne compression machine (Kilian, Germany) with varying and constant pressures using 8.5 mm punches

## Hardness

The hardness of tablets was determined using Tablet Hardness Tester 8M (Dr. Schleuniger Pharmatron, Switzerland).

## Friability

Friability of the tablets was determined using Sotax FT2 Friability Tester (Sotax, Switzerland). Twenty of randomly selected tablets from each formulation were weighed and placed into the friabilator drum, and subjected to 100 revolutions in 4 min. The tablets were removed, dedusted and reweighed. Friability was calculated as the percentage weight loss.

Table I

## Formulations of orally disintegrating tablets

Formulation	F1	F2	F3	F4	F5	F6	F7
Substance	Quantity [mg/tbl.]						
$\beta$ -cyclodextrin	0.00	19.06	38.12	57.18	76.24	95.3	114.36
Pearlitol Flash mannitol	114.36	95.30	76.24	57.18	38.12	19.06	0.00

**In vitro drug disintegration**

*In vitro* disintegration time was measured by USP disintegration test apparatus Sotax DT2 (Sotax, Switzerland) and modified disintegration test. The USP disintegration test was used to determine disintegration times in 900 ml of distilled water at  $37.0 \pm 0.5^\circ\text{C}$  with 32 strokes per minute. In modified disintegration test three tablets were placed into the dish containing distilled water ( $37^\circ\text{C}$ , 7 ml). The end of the disintegrating time was when the last tablet disintegrated.

**In vitro dissolution**

Dissolution studies were carried out to determine differences in the release rate of the CTZ from tablets containing different amount of  $\beta$ -CD by using a dissolution machine (Sotax AT7 Smart, Sotax, Switzerland) with USP dissolution apparatus 2. The dissolution medium consisted of 500 ml of USP hydrochloride buffer pH 1.2 at  $37.0 \pm 0.5^\circ\text{C}$  and 75 rpm for the first 15 min and 150 rpm for the following 15 min. The absorbance maximum of samples was measured at 231 nm using the regression equation of a standard curve developed in the same medium.

**Surface characterization**

Surface characterization of  $\beta$ -CD and CTZ was performed by scanning electron microscopy (SEM MIRA\\LMU, Tescan, Czech Republic) measured at accelerated voltage of 7 kV. Samples were platinum coated before SEM observation.

**Tablet porosity**

The porosity of the tablets was calculated from the true and apparent density. The true density was measured by using Multi-Volume Pycnometer 1305 (MicroMeritics, USA). The apparent density was obtained by measuring the basic parameters of the tablet such as the weight, diameter and thickness of the tablet. Diameter was measured by caliper and thickness was measured by micrometer.

**In vivo testing**

*In vivo* testing was performed on 6 healthy human volunteers (3 men and 3 women with an average age of 25) from whom informed consent was first obtained. One tablet was put and held in the mouth and the time required for complete disintegration of the tablet was recorded. After the disintegration, the volunteers spat the disintegrated tablet out and rinsed the mouth cavity with water. A 20-min interval was given before testing next tablet. Volunteers evaluated tablet taste during waiting. To evaluate the intensity of taste (bitterness, sweetness, sourness and saltiness) was set-point scale of 0 - 5, where 0 meant no taste and 5 the most intense taste. Evaluation balance particles on the tongue was in the range of 0 (no residue on the tongue) to 3 (highest residue) and overall evaluation of tablets was scored from 1 (best) to 5 (worst).

**Results and discussion****Compression force**

The effect of  $\beta$ -CD amount on the compression force can be seen in Figure 2. Results showed that a rising amount of  $\beta$ -CD in tablet composition (ie. from F1 to F7) led to exponential decrease while the hardness  $22 \pm 2\text{ N}$  is constant. It can thus be concluded that  $\beta$ -CD is a suitable excipient for a formulation of ODTs due to its high compressibility which leads to increased abrasion resistance of tablets. However, it is generally known that the disintegration time is extended with increasing hardness. Therefore, in the case of ODT, where rapid disintegration is required in the mouth, it is important to reduce tablet hardness to the lowest value.

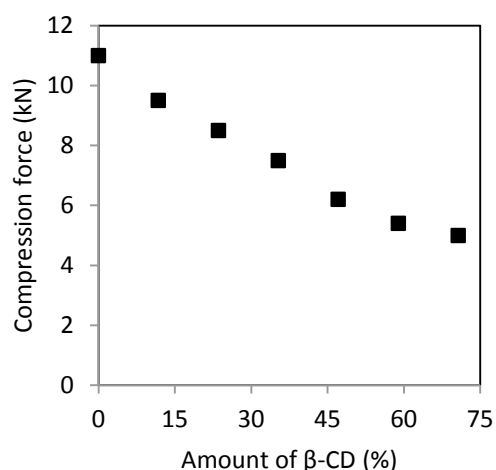


Figure 2. Effect of  $\beta$ -cyclodextrin amount on compression force

### Friability

Friability of ODTs can be seen in Table II. Measured friability values ( $< 1\%$ ) indicated good mechanical tablets hardness despite the fact that the tablets were prepared under relatively low compression forces (5 - 11 kN). The prepared tablets should not be packed in a special blister, which protects the product against mechanical damage.

Table II

Friability of seven ODTs formulations

Formulation	F1	F2	F3	F4	F5	F6	F7
Friability [%]	0.3	0.2	0.2	0.3	0.2	0.1	0.2

### In vitro drug disintegration

Disintegration times (Table III) fluctuated in a narrow range of values from 26 s to 27 s in the volume of 900 ml with the exception of the formulation without  $\beta$ -CD for which the time was distinctly shorter. Results showed that the presence of  $\beta$ -CD in the tablet extended the time of tablet disintegration. The disintegration time was realized in a smaller volume (7 ml, 37°C) to approximate the conditions in mouth. The results showed that the disintegration time was prolonged in case of smaller volume of 7 ml compared to standard disintegration test in 900 ml. The disintegration of the tablet is likely influenced by a different solubility of  $\beta$ -CD and mannitol. While the solubility of  $\beta$ -CD in water at 25 °C is 18.5 mg·ml<sup>-1</sup>, mannitol solubility under the same conditions is 216 mg·ml<sup>-1</sup>(ref. 8).

Table III

Disintegration time of seven ODTs formulations

Formulation	F1	F2	F3	F4	F5	F6	F7
<i>In vitro</i> disintegration, 7 ml [s]	25.0	34.0	44.3	46.7	72.3	77.0	79.7
<i>In vitro</i> disintegration, 900 ml [s]	16.0	26.0	26.0	27.0	26.0	27.0	27.0

### Dissolution studies

The dissolution profiles of CTZ in pH 1.2 are demonstrated in Figure 3. From the Figure 3 it is evident that the active substance was rapidly released from the tablets. On the other hand, it can be observed slowing release of the CTZ with rising content of  $\beta$ -CD. How it is shown more than 90 % of active ingredient was released during the first two minutes of the test for tablets without  $\beta$ -CD (F1) or with very low content of  $\beta$ -CD (F2). In contrast, for tablets with the high content of  $\beta$ -CD (F6, F7) more than 90 % of the active substance was released during 10 minutes. This test proved that with increasing amounts of  $\beta$ -CD the release rate of the CTZ from the tablet extended. Classic dissolution testing, which is the only pharmacopoeia method for determining the release of API from ODT, is inappropriate for this dosage form and should be modified. It is important to obtain the information about the amount of API that may be released from the tablet during the disintegration of the

tablet in the mouth (which is usually shorter than 180 s). This modification can be performed manually by sampling with short intervals between samples.

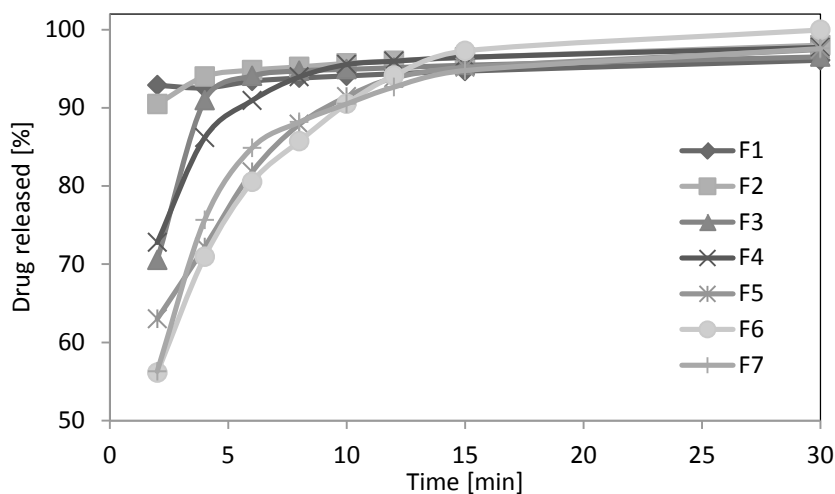


Figure 3. Dissolution profiles of CTZ from ODTs by conventional dissolution study. Each point represent the mean (n=3).

### Surface characterization

Particles with acicular shape are typical for Cetirizine and irregular block particles are typical for  $\beta$ -CD. It is generally known that the surface of manufactured tablets is primarily influenced by compression pressure. Large number of microcracks and pore size 4-20  $\mu\text{m}$  were also observed on the surface of tablets as it is shown in Figure 4. These frequent surface irregularities can be responsible for enhancement of the absorption of fluid that can penetrate into the interior of the tablet and result in a faster disintegration, which is desirable mainly in ODTs. In spite of this fact  $\beta$ -CD created large clusters of  $\beta$ -CD of size up to 2 mm which probably caused increasing tablet hardness, disintegration and thus the rate of release of CTZ. These clusters hold the tablet together and prevent penetration of fluid into the tablet core.

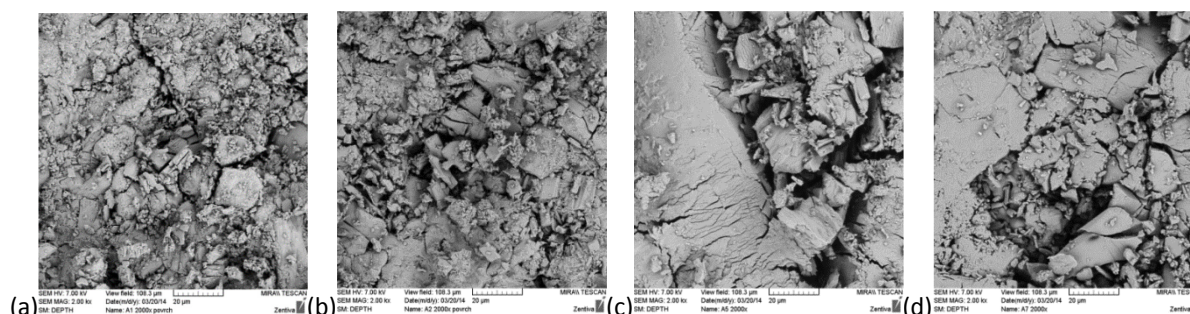


Figure 4. Scanning electron photomicrographs. Formulation F1 (a); F2 (b); F4(c); F (d). Images were magnified 2000x.

### Tablet porosity

Helium porosity was chosen because of the small size of the helium atom, which is able to fill very small pores, and its adsorption is negligible at ordinary temperatures. It was found (Figure 5) that the porosity and pore size of tablets decreased with increasing compression force.

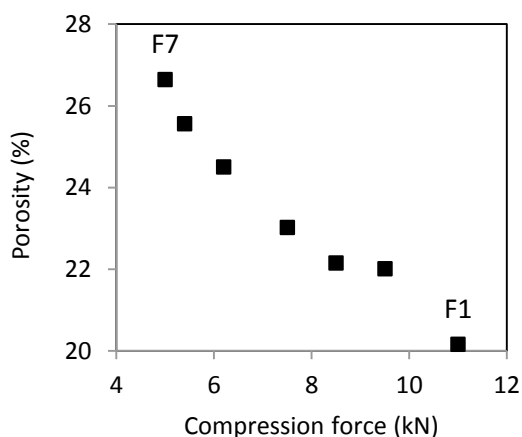


Figure 5. Dependence of porosity and compression force of ODTs

### In vivo testing

Prepared tablets had minimum saltiness, acidity and residue particles on the tongue how it can be seen in Table III. On the other hand, the tablets differed significantly in bitterness and sweetness. Volunteers evaluated formulations F5, F6 and F7 as the most delicious because minimal bitterness was observed in these tablets. Due to this fact it can be said that these formulations had sufficiently masked bitter taste of CTZ. The questionnaire also showed that even a small amount of  $\beta$ -CD (11 % relative to the total tablet weight) is sufficient to reduce the intensity of the bitterness of cetirizine more than one level. The amount of  $\beta$ -CD, when volunteer perceived weak or no bitterness intensity and also failed to recognize the higher content of  $\beta$ -CD tablets, was chosen as the optimal amount of  $\beta$ -CD in terms of taste masking efficiency. The optimum amount of  $\beta$ -CD was fixed in the tablet at 47 weight % (corresponding formulation F5).

*In vivo* disintegration times were widely different due to the influence of different amount of saliva in human mouth. Formulation F1 had the fastest disintegration time of the tablets which containing no  $\beta$ -CD, on the other hand formulation F4 showed the slowest disintegration time. Formulations F5 and F6 were chosen as the most delicious by 6 volunteers. In the end, volunteers preferred the overall palatability of the tablets at the expense of slower disintegration time of the tablet in the mouth.

Table III

Results of *in vivo* testing

Form.	Disintegration time [s]	Bitterness	Sweetness	Sourness	Saltiness	Residue on tongue	Total palatability
F1	27.0 ± 8.8	4.0 ± 0.6	1.5 ± 1.0	1.3 ± 1.6	1.3 ± 1.5	1.0 ± 1.0	4.3 ± 0.5
F2	35.4 ± 6.8	2.8 ± 0.9	2.6 ± 1.0	1.2 ± 1.2	0.8 ± 1.1	1.0 ± 0.7	2.6 ± 0.5
F3	39.3 ± 6.4	2.0 ± 1.0	2.5 ± 1.5	1.2 ± 1.5	1.0 ± 1.4	1.0 ± 1.2	2.8 ± 0.9
F4	43.7 ± 16.1	1.5 ± 1.0	3.2 ± 0.7	0.3 ± 0.5	0.8 ± 1.2	1.5 ± 1.3	2.5 ± 0.8
F5	35.0 ± 8.8	0.6 ± 0.8	3.4 ± 0.5	1.4 ± 0.8	0.6 ± 0.8	1.0 ± 1.0	1.8 ± 0.7
F6	40.5 ± 12.7	0.5 ± 0.5	3.2 ± 0.7	0.8 ± 1.1	0.8 ± 0.7	1.0 ± 0.8	1.5 ± 0.8
F7	38.2 ± 14.3	0.3 ± 0.5	3.7 ± 0.7	0.8 ± 0.4	0.0 ± 0.0	0.8 ± 0.7	1.5 ± 0.8

\* total palatability, residue on tongue and total palatability are expressed point evaluation

\*\* mean average value ± standard deviation

### Conclusions

In this study was demonstrated the effect of  $\beta$ -CD on the physical properties of the ODTs. For the purpose of this study, were prepared various formulations of ODTs by direct compression and which were evaluated in terms of friability, hardness, disintegration time, etc. The results of tests showed that with increasing amounts of  $\beta$ -CD tablet hardness and disintegration time are increased and compression force is decreased. Dissolution tests confirmed very rapid release of active substance from the tablets. The results of SEM and helium porosity confirmed that the surface of the prepared tablet included a large number of pores and cracks (size 4 - 20  $\mu$ m) which should allowed faster penetration of liquids into the interior of the tablet and thus causing a rapid disintegration. In spite of this fact  $\beta$ -CD created large clusters of  $\beta$ -CD of size up to 2 mm which probably caused increasing tablet hardness, disintegration and thus the rate of release of CTZ. These clusters hold the tablet

together and prevent penetration of fluid into the tablet core. This study recommends  $\beta$ -CD as excipient in amount unnecessarily to achieve the effective taste masking in ODTs as 47 weight %.

#### **Acknowledgment**

*Financial support from specific university research (MSMT No 20/2015).*

#### **Literature**

1. Lee C.-W., Kim S.-J., Youn Y.-S., Widjojokusumo E., Lee Y.-H., Kim J., Lee Y.-W, Tjandrawinata R. R.: *J. Supercrit. Fluids* **55**, 348 (2010)
2. Muankaew C., Jansook P., Stefánsson E., Loftsson T.: *Int. J. Pharm.* **474**, 80 (2014).
3. Szejtli J., Szenté L.: *Eur. J. Pharm. Biopharm.* **61**, 115 (2005).
4. di Cagno M., Terndrup Nielsen T., Lambertsen Larsen K. , Kuntsche J., Bauer-Brandl A.: *Int. J. Pharm.* **468**, 258 (2014).
5. Kurkov S. V., Loftsson T.: *Int. J. Pharm.* **453**, 167 (2013).
6. Skidgel A. R., Erdös G. E., in book: *Goodman and Gilman's The Pharmacological Basis of Therapeutics*, The McGraw-Hill companies, New York 2005.
7. Stojanov M., Wimmer R., Larsen K. I.: *J. Pharm. Sci.* **100**, 3177 (2011).
8. Rowe R. C., Sheskey P. J., Quinn M. E., in book: *Handbook of Pharmaceutical Excipients*, Pharmaceutical Press, 2009.

## **INORGANIC TECHNOLOGY**

### **PREPARATION AND COLOR PROPERTIES OF PIGMENTS BASED ON $YMnO_{3\pm\delta}$**

**Burkovičová A.**, Dohnalová Ž., Šulcová P.

*University of Pardubice, Faculty of Chemical Technology, Department of Inorganic Technology, Studentská 95, 532 10, Pardubice, Czech Republic  
aneta.burkovicova@student.upce.cz*

#### **Introduction**

Compounds with the general formula  $ABO_3$  can exhibit a wide range of structure types including perovskite. In addition to this structural variability, many  $ABO_3$  samples exhibit special physical properties such as superconductivity or magnetoresistivity<sup>1</sup>. The hexagonal  $YMnO_3$  is one of the most intensively studied manganates. This structure type attracts attention as a promising material with application electrochemical potentials<sup>2</sup>. These new compounds can be an alternative to currently used pigments due to their lower impact on the environment and their stability<sup>3</sup>. The structure of  $YMnO_3$  is constituted by non-connected layers of  $MnO_5$ , where each Mn ion is surrounded by three oxygen in plane and two apical oxygen ions forming a trigonal bipyramids, which are two dimensionally connected to each other through corners and separated by a layer of  $Y^{3+}$  ions<sup>4,5</sup>. Manganites with the general formula  $RMnO_3$ , where R denotes rare-earth cation, can be found within two crystal symmetries: a perovskite orthorhombic structure, when the R cation has a large ionic radius, on the other hand, when the rare-earth has a small ionic radius ( $R=Ho-Lu$ , including Y and Sc), manganites crystallize in a hexagonal structure<sup>6</sup>.

Over the past few years there have been several attempts to minimize negative impacts on the environment and to reduce the cost of ceramic pigments. For example, M. Ocaña et. al.<sup>7</sup> examined Mn - doped  $YInO_3$  blue pigments without cobalt, which have been synthesized at a much lower temperature (1100 °C) than is required for conventional solid state reaction (1400 °C). The method is based on pyrolysis of aerosols generated from aqueous nitrate solutions Y, In, and Mn.

The research was focused on the preparation of  $YMn_x(MCu)_{1-x}O_{3\pm\delta}$  pigments with  $x = 1; 0.9; 0.5; 0.1$  and  $M = Sn; Ti$  or  $Zr$ . All samples were synthesized by mechanical activation in solution and subsequently applied into an organic matrix and ceramic glaze G 073 91. Pigment  $YMn_{0.9}(SnCu)_{0.1}O_{3\pm\delta}$  was also prepared using mineralisers to improve purity of crystalline phase. The main aim of the research was find the best composition and calcination temperature suitable for the preparation of black pigment with blue tint. X-ray diffraction analysis and particle size distribution measurement were also used for these studies.

#### **Experimental**

The pigments  $YMn_x(MCu)_{1-x}O_{3\pm\delta}$ , where  $x = 1; 0.9; 0.5; 0.1$ ; and  $M = Sn; Ti$  or  $Zr$ , were prepared by mechanical activation in solution. The reagents  $Y_2O_3$  (99,99% purity, Alfa Aesar, Germany),  $MnCO_3$  (99% purity, Lachema Pliva a. s., Czech Republic),  $CuO$  (99% purity, Lachema Pliva a. s., Czech Republic) were weighted and mixed with oxides of doping ions:  $SnO_2$  (99% purity, Sigma Aldrich, s.r.o., Czech Republic) and  $TiO_2$  (99% purity, AV-01, Precheza a. s., Czech Republic) or  $ZrO_2$  (99% purity, Sigma Aldrich, s.r.o., Czech Republic). Molar proportions of starting materials were ground manually in a porcelain mortar and subsequently milled in the planetary mill (Pulverisette 5; FRITSCH, Germany) for 5 h. As a liquid medium the mixture of deionised water and ethanol in volume ratio 1:1 was used. All homogenous reaction mixtures were fired successively in the first step at 700 °C with a soaking time of 6 h and in the second step at 1000-1200 °C with a soaking time also 6 h. Prepared pigments were applied into an organic matrix (dispersive acrylic paint Parketol, Balakom, a.s., Czech Republic) in mass and diluted tone. Pigments were also applied into ceramic glaze G 073 91 (Glazura, s.r.o, Roudnice nad Labem, Czech Republic). The mixture of pigment in amounts of 10 % w/w a glaze on ceramic biscuit was glazed at 1000 °C for 15 min.

The applications of pigments into organic matrix and ceramic glaze were evaluated by measuring of spectral reflectance in the visible region of light (400 - 700 nm) using a ColorQuest XE (HunterLab, USA). As the measurement conditions were used an illuminant D65, measuring geometry  $d/8^\circ$  and  $10^\circ$  complementary observer. The colour properties were described in the CIE  $L^*a^*b^*$  system. The value  $a^*$  (the red-green axis) and  $b^*$  (the yellow-blue axis) indicate the colour hue. The value  $L^*$  represents the lightness or darkness of the colour.  $L^*$  is ranging from 0 (black) to 100 (white). The value  $C$  (chroma) represents saturation of the colour and is calculated according to the formula:

$$C = (a^{*2} + b^{*2})^{1/2}. \quad (1)$$

From previous values it is also possible to calculate the colour of pigment as a hue angle:

$$H^\circ = \text{arc tg } (b^*/a^*) \quad (2)$$

The hue angle  $H^\circ$  expresses colour using an angular position in the cylindrical colour space ( $H^\circ = 350\text{-}35^\circ = \text{red}$ ,  $H^\circ = 35\text{-}70^\circ = \text{orange}$ ,  $H^\circ = 70\text{-}105^\circ = \text{yellow}$ ,  $H^\circ = 105\text{-}195^\circ = \text{green}$ ,  $H^\circ = 195\text{-}285^\circ = \text{blue}$  and  $H^\circ = 285\text{-}350^\circ = \text{violet}$ ).

Mastersizer 2000 MU (Malvern Instruments, Ltd. GB) was used for measurements of particle size distribution. The device uses the laser diffraction on particles dispersed in liquid medium and it allows evaluation of measured signal either based on Mie's theory or Fraunhofer diffraction. As the source of light was used He-Ne laser (wavelength 633 nm) and blue light (466 nm). The samples were ultrasonically homogenized for 120 s and measured in a solution with  $\text{Na}_4\text{P}_2\text{O}_7$  ( $c = 0.15 \text{ mol}\cdot\text{dm}^{-3}$ ).

The crystal structures and phase purity of the powdered materials were studied by XRD analysis. The diffractograms of the samples were obtained by using a Bruker diffractometer D8 Advance (Bruker, GB) with a goniometer of 17 cm in the range  $2\theta$  of  $10\text{-}80^\circ$ .  $\text{Cu K}\alpha_1$  ( $\lambda = 0.15418 \text{ nm}$ ) radiation was used for angular range of  $2\theta < 35^\circ$  and  $\text{Cu K}\alpha_2$  ( $\lambda = 0.15405 \text{ nm}$ ) for the range of  $2\theta > 35^\circ$ . A scintillation detector was used.

## Results and discussion

### $\text{YMnO}_{3\pm\delta}$

At first, the pure  $\text{YMnO}_{3\pm\delta}$  was prepared and used as a standard. Samples were fired in the temperature range  $900\text{-}1300^\circ\text{C}$  (step  $100^\circ\text{C}$ ) and applied into the organic matrix. At the lower firing temperatures ( $900$  and  $1000^\circ\text{C}$ ), starting materials still did not completely react and the resulting powders have a brown color – axis  $a^*$  is in the positive region ( $a^* = 2.39$  to  $1.80$ ). After raising the temperature to  $1100^\circ\text{C}$  brightness decreased and color shade has changed to black with blue hue ( $b^* = -3.80$ ). After further increase of the firing temperature at  $1200$  and  $1300^\circ\text{C}$  powders became lighter and the value of the blue axis  $-b^*$  decreased. At the highest temperature the product has been already sintered. Pigment with best color properties was obtained at  $1100^\circ\text{C}$  ( $L^* = 26.19$ ,  $a^* = -0.28$ ,  $b^* = -3.80$ ). Therefore, the firing temperature range for doped samples was regulated only from  $1000$  to  $1200^\circ\text{C}$  (Table I).

Table I

The effect of calcination temperature on particle size and colour properties of the  $\text{YMnO}_{3\pm\delta}$  and  $\text{YMn}_{0.9}(\text{CuSn})_{0.1}\text{O}_{3\pm\delta}$  pigments applied into organic matrix.

T [ $^\circ\text{C}$ ]	$\text{YMnO}_{3\pm\delta}$						$\text{YMn}_{0.9}(\text{CuSn})_{0.1}\text{O}_{3\pm\delta}$					
	$L^*$	$a^*$	$b^*$	C	$H^\circ$	$d_{50}$ [ $\mu\text{m}$ ]	$L^*$	$a^*$	$b^*$	C	$H^\circ$	$d_{50}$ [ $\mu\text{m}$ ]
1000	29.85	1.80	-0.15	1.81	355.24	3.09	28.26	0.14	-2.66	2.66	273.01	2.94
1100	26.19	-0.28	-3.80	3.81	265.79	3.03	28.06	-0.08	-2.78	2.78	268.35	2.70
1200	26.58	-0.19	-3.01	3.02	266.39	3.57	20.02	-0.11	-3.01	3.01	267.91	3.28

### $\text{YMn}_x(\text{SnCu})_{1-x}\text{O}_{3\pm\delta}$

Pigments doped with ions  $\text{Sn}^{4+}$  and  $\text{Cu}^{2+}$  have the best color properties in the composition  $\text{YMn}_{0.9}(\text{CuSn})_{0.1}\text{O}_{3\pm\delta}$ . Effect of firing temperature on the color coordinates after application to the organic binder is shown in Table I. With increasing temperature product becomes darker (axis  $L^*$  decreases) and  $a^*$  passes from red to green region. Blue coordinate  $-b^*$  and chroma C also increases with higher temperature. The results show, that the most suitable firing temperature of these pigments is  $1200^\circ\text{C}$  - the darkest sample with the strongest blue tint. The final color of these samples varies from dark brown to black with blue shade. When the content of doping elements increases to  $x = 0.5$ , brighter shade of the product is obtained, but  $b^*$  axis values are still in negative region and their color is black with blue tint. By increasing  $x$  to  $0.1$  the color spectrum shifts more to the green area and the color of pigments is dark greenish blue.

### $\text{YMn}_x(\text{TiCu})_{1-x}\text{O}_{3\pm\delta}$

Perovskite pigment  $\text{YMnO}_{3\pm\delta}$  was also doped by  $\text{Ti}^{4+}$  and  $\text{Cu}^{2+}$  ions and powder products have been applied to the organic binder and evaluated in the same manner as the previous samples. Table II shows the effect of

firing temperature on the color properties of the pigment  $\text{YMn}_{0.5}(\text{CuTi})_{0.5}\text{O}_{3\pm\delta}$ , which composition was evaluated as most interesting, due to the highest content of blue shade. With rising temperature brightness of the samples decreases and it becomes darker. The lowest value ( $-a^*$ ) and highest value ( $-b^*$ ) was measured for a pigment fired at 1100 °C. This temperature was evaluated as the most suitable for the preparation of product with composition  $x = 0.5$ . The hue of these pigments is black with a blue tint. The samples with  $x = 0.9$  have higher values of  $L^*$  axis (25.15 to 28.68) and a lower content of red ( $+a^* = 0.02$  to 0.46) and blue ( $-b^* = 3.14$  to 1.87) color. The applications in organic binder are also black. Low values of coordinates  $a^*$  and  $b^*$  were achieved for pigments with  $x = 0.1$ , which are slightly lighter than previous samples ( $L^* = 25.83$  to 33.30).

Table II

The effect of calcination temperature on particle size and colour properties of the  $\text{YMn}_{0.5}(\text{CuTi})_{0.5}\text{O}_{3\pm\delta}$  and  $\text{YMn}_{0.9}(\text{CuZr})_{0.1}\text{O}_{3\pm\delta}$  pigments applied into organic matrix.

T [°C]	$\text{YMn}_{0.5}(\text{CuTi})_{0.5}\text{O}_{3\pm\delta}$						$\text{YMn}_{0.9}(\text{CuZr})_{0.1}\text{O}_{3\pm\delta}$					
	$L^*$	$a^*$	$b^*$	C	$H^\circ$	$d_{50}$ [µm]	$L^*$	$a^*$	$b^*$	C	$H^\circ$	$d_{50}$ [µm]
1000	27.80	-0.06	-2.01	2.01	268.29	3.26	28.04	0.27	-2.54	2.55	276.07	2.93
1100	23.72	0.80	-3.31	3.41	283.59	3.86	27.30	-0.19	-2.84	2.85	266.17	3.62
1200	20.06	0.70	-2.60	2.69	285.07	6.07	26.95	0.15	-2.24	2.25	273.83	4.90

#### $\text{YMn}_x(\text{ZrCu})_{1-x}\text{O}_{3\pm\delta}$

After application into an organic binder the color properties of the pigment doped with  $\text{Zr}^{4+}$  and  $\text{Cu}^{2+}$  were also evaluated. Values of coordinates  $L^*$ ,  $a^*$ ,  $b^*$ , C and  $H^\circ$  of the products with best composition ( $x = 0.9$ ) are shown in Table II. With increasing firing temperature samples became darker, which is confirmed by decreasing values of brightness  $L^*$ . The highest content of the blue shade was achieved at 1100 °C ( $b^* = -2.84$ ). Values of  $a^*$  axis are in a narrow range from -0.19 to 0.27, and they have minimal effect on the resulting color perception. Darkest sample was prepared for the composition with  $x = 0.5$  (1200 °C), where  $L^* = 20.72$ . However this product contained a smaller amount of blue hue than previous samples ( $b^* = -1.64$ ). Pigments  $\text{YMn}_{0.1}(\text{CuZr})_{0.9}\text{O}_{3\pm\delta}$  prepared at temperatures 1000 and 1100 °C have dark green hue, which is confirmed by negative values of  $a^*$  axis (-4.45 and -2.49). These pigments are also significantly lighter ( $L^* = 30.46$  to 38.74).

#### Particle size distribution

Particle size distribution (PSD) is one of the most important properties of powder materials, because it affects both the characteristics of the products and the possibility of using these materials. For this reason, PSD analysis was also used to characterize prepared pigments. The measurements were made for unmilled samples which were grinded in an agate mortar and results were expressed using values  $d_{10}$ ,  $d_{50}$  and  $d_{90}$ . The value  $d_{50}$  of samples with most interesting color properties are shown in Table I and II. With increasing temperature and higher content of doping elements particle size mostly increases. Value  $d_{50}$  for pure  $\text{YMnO}_3$  ranges from 2.1 to 3.5 µm. Similar range (2.7 to 3.3 µm) was also achieved for samples doped with  $\text{Sn}^{4+}$  and  $\text{Cu}^{2+}$  ions. Doping by  $\text{Ti}^{4+}$  and  $\text{Zr}^{4+}$  ions caused a slight increase of  $d_{50}$  to level 3.2 to 6.1 µm for titanium and 2.9 to 4.9 µm for zirconium. These values allow the use of these perovskite pigments without subsequent mechanical treatment.

#### XRD analysis

Prepared samples were also examined by X-ray diffraction analysis. It was verified that the single-phase hexagonal  $\text{YMnO}_3$  (PDF No. 04-011-9577)<sup>8</sup> with perovskite structure was obtained at 1100 °C. Higher calcination temperature (1200 °C) caused an increase of the peak intensity of perovskite phase. Doped samples ( $x = 0.9$ ) were also investigated by the X-ray diffraction analysis (Figure I). Single phase pigments were obtained at 1200 °C. The highest intensity of crystalline phase was achieved for the sample doped by tin ions (480 a.u.). This value is still relatively low, due to the need of high quality and stability of the prepared products.

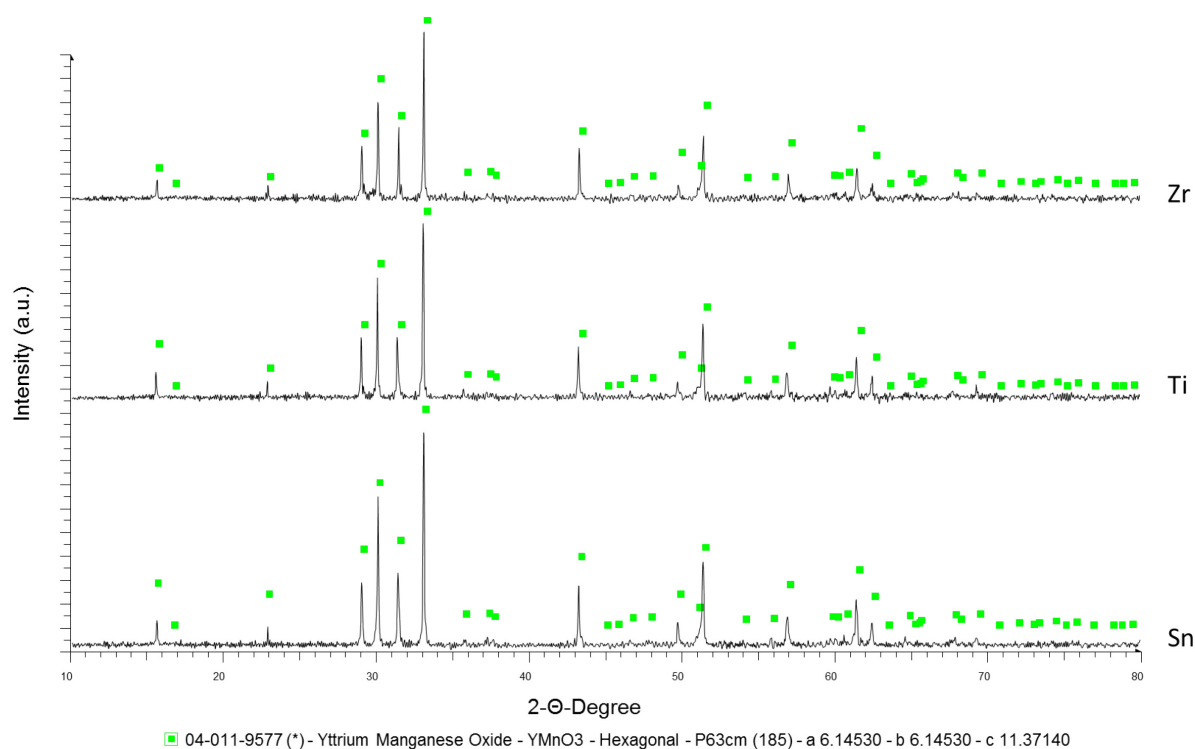


Figure 1. Diffractograms of pigment  $YMn_{0.9}(MCu)_{0.1}O_{3\pm\delta}$  (1200 °C) where M = Zr; Ti; Sn.

### Conclusion

The main aim of this research was to prepare inorganic pigments based on  $YMnO_{3\pm\delta}$ , which were doped by ions of tin, titanium and zirconium with general formula  $YMn_x(MCu)_{1-x}O_{3\pm\delta}$ , where  $x = 1; 0.9, 0.5, 0.1$  and M = Sn; Ti or Zr and verify their colour properties and possibility to use these powders as the new inorganic ceramic pigments. All samples were prepared by mechanical activation in solution and subsequently applied into an organic matrix and ceramic glaze G 073 91. At first the pure  $YMnO_{3\pm\delta}$  was prepared and it served as a standard. Pigment doped by  $Sn^{4+}$  and  $Cu^{2+}$  ions provides black samples with blue shade. Composition  $YMn_{0.9}(CuSn)_{0.1}O_{3\pm\delta}$  and firing temperature 1200 °C were evaluated as a most suitable synthesis conditions for preparing of these kind of pigment. Samples doped by  $Ti^{4+}$  and  $Cu^{2+}$  ions provide also black pigments, but the most interesting color was obtained by  $YMn_{0.5}(TiCu)_{0.5}O_{3\pm\delta}$  (1100 °C). Similar results were obtained by doping of this system by ions of  $Zr^{4+}$  and  $Cu^{2+}$ . Pigments were also black with blue shade except samples  $YMn_{0.1}(ZrCu)_{0.9}O_{3\pm\delta}$ , which provides dark green product. Application in the ceramic glaze G 073 91 has proven to be inappropriate, because of low stability of pigments in aggressive environment of molten glaze. The XRD analysis showed that single-phase perovskite hexagonal  $YMnO_{3\pm\delta}$  is formed at the temperature 1100 °C. Single-phase products were also proved for doped samples with  $x = 0.9$  (1200 °C).

### Acknowledgment

This work has been supported by University of Pardubice under the project SGSFChT\_2015005.

### Literature

1. S. Malo, A. Maignan: *Mater. Res. Bull.* 47 (2012) 974–979.
2. L. J. Downie, R. J. Goff, W. Kockelmann, S. D. Forder, J. E. Parker, F. D. Morrison, P. Lightfoot: *J. Solid State Chem.* 190 (2012) 52–60.
3. M. El Amrani, V. Ta Phuoc, M.R. Ammar, M. Zaghrioui, F. Gervais: *Solid State Sci.* 14 (2012) 1315-1320.
4. L. Yang, Q. Duanmu, L. Hao, Z. Zhang, X. Wang, Y. Wei, H. Zhu: *J. Alloy. Comp.* 570 (2013) 41–45.
5. M. Zaghrioui, J.M. Grenéche, C. Autret-Lambert, M.Gervais: *J. Magn. Magn. Mater.* 323 (2011) 509–514.
6. A. Alqat, Z. Gebrel, V. Kusigerski, V. Spasojevic, M. Mihalik, M. Mihalik, J. Blanusa: *Ceram. Int.* 39 (2013) 3183–3188.
7. M. Ocaña, J.P.Espinós, J.B. Carda: *Dyes Pigments* 91 (2011) 501-507.
8. Joint Committee on Powder Diffraction Standards, International Centre of Diffraction Data, Swarthmore, PA.

## HYDROGELS BASED ON GLUCOMANNAN AND THEIR UTILIZATION IN AGRICULTURE

**Hermann P.**, Svoboda L., Bělina P.

*University of Pardubice, Faculty of Chemical Technology, Department of Inorganic Technology, Doubravice 41, 532 10 Pardubice, Czech Republic  
petr.hermann@student.upce.cz*

### Introduction

During the last decades, an important part in agricultural development was to increase the productivity per unit area of land used for crop production to feed the growing population. This was achieved through excessive use of natural resources such as water and plant resources and overdose of fertilizers and pesticides. As the results of that were soil disturbance, the exhaustion of natural water resources and soil contamination by pesticides<sup>1</sup>. Nowadays, the agricultural development is focused on sustainable use of land, water and plant resources without threatening the environment. To contribute to achievement of this aim can soil conditioners on the basis of natural superabsorbents – hydrogels<sup>2</sup>.

Hydrogels are formed by polymeric networks, which can absorb large amount of water or biological fluid<sup>3</sup>. They are divided into two groups – physical and chemical, according to the process of gelation<sup>4</sup>. Physical or reversible hydrogels are held together by molecular entanglements, and/or secondary forces including ionic, hydrogen bonding or hydrophobic interactions. Chemical or permanent hydrogels are formed by covalently cross-linking<sup>5</sup>. Hydrogels are used in many sectors such as tissue engineering, agriculture, pharmaceutical, and biomedical fields (e.g. wound dressing, drug delivery, dental materials and implants)<sup>6</sup>.

Agricultural synthetic polymeric hydrogels are divided into three groups: starch–polyacrylonitrile graft polymers (starch copolymers), vinyl alcohol–acrylic acid co–polymers (polyvinylalcohols) and acrylamide sodium acrylate co–polymers (cross–linked polyacrylamides). These hydrogels can hold 400–1500 g of water per gram of dry hydrogel<sup>7</sup>.

Glucomannan is a nature polysaccharide, which forms linear random copolymer of (1→4) linked β-D-mannose and β-D-glucose. It contains mannose and glucose units at molar ratio 1,6:1 and acetyl groups along the glucomannan backbone are located at C–6 position<sup>8</sup>. Acetyl groups have an effect on solubility of polymer in aqueous solution<sup>9</sup>. Glucomannan is industrially extracted from the plant *Amorphophallus konjac*, which is grown primarily in the southeastern part of Asia<sup>10</sup>. Utilization of glucomannan is widespread in different technological areas. As a gelling agent is used in food, pharmaceutical, chemical, biotechnology and cosmetic industries<sup>11</sup>. The molecular structure of glucomannan is represented in Figure 1.

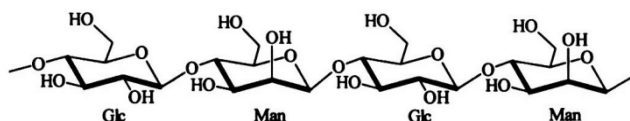


Figure 1. Structure of glucomannan<sup>12</sup>

### Experimental

#### Materials

For the experiments glucomannan (VUOS, Pardubice, Czech Republic), calcium hydroxide (Lachema, Brno, Czech Republic), sodium hydroxide (Penta, Chrudim, Czech Republic), urea and ammonium sulphate (Lach-Ner, Neratovice, Czech Republic) were used. Trisodium timethaphosphate, pentasodium tripolyphosphate, sodium dihydrogenphosphate monohydrate and disodium hydrogenphosphate dihydrate were obtained from Sigma-Aldrich (Steinheim, Germany). Aspartic acid, citric acid, malic acid and oxalic acid (Lach-Ner, Neratovice, Czech Republic) were used. Glutaric acid was purchased from Sigma-Aldrich (Steinheim, Germany) and succinic acid was delivered from Spolana (Neratovice, Czech Republic).

#### Preparation of hydrogel

Reaction of glucomannan with  $\text{Ca}(\text{OH})_2$

20 g of glucomannan was suspended with 160 ml of 50% aqueous solution of ethanol or pure distilled water and with 20 ml saturated solution of  $\text{Ca}(\text{OH})_2$ . The suspension was heated at the temperature about 100°C under continuous stirring for at least one hour. After cooling, the suspension was several times decanted with 50 ml of 50% ethanol, after each addition the suspension was stirred. After it the suspension was filtered on a Büchner funnel and the obtained hydrogel was dried at 105 °C to constant weight<sup>13</sup>.

#### Reaction of glucomannan with ethanol

10 g of glucomannan was dissolved in 500 ml of distilled water and 250 ml of ethanol. The suspension was boiled under stirring for one hour, then mixture was decanted three times with 250 ml of ethanol, the settled hydrogel was filtered through sintered glass and dried at room temperature to constant weight.

#### Reaction of glucomannan with STMP

Glucomannan was cross-linked using different fosforylating agent, which forms a three-dimensional network . In this case, as the fosforylating agent trisodium trimethaphosphate (STMP) was used. 0.5 g of STMP was dissolved in 100 ml of 0.001 M NaOH at room temperature, then glucomannan (1 g) was added into the solution under continuous stirring. The dispersion was mixed for 6 hours, after it the hydrogel was dried at 45 °C, washed several times with distilled water and dried again at 45 °C to constant weight<sup>14</sup>.

#### Reaction of glucomannan with STPP

Glucomannan was cross-linked with pentasodium tripolyphosphate (STPP). 0.947 g of STPP was dissolved in 30 ml of 0.01 M NaOH at room temperature, then glucomannan (0.648 g) was gradually added into the solution under continuous stirring. The reaction mixture was stirred for 6 hours at 60 °C. The obtained hydrogel was incubated in a dryer at 60 °C for 24 hours. Then the hydrogel was washed with distilled water and dried at 60 °C to constant weight<sup>15</sup>.

#### Reaction of glucomannan with Na<sub>2</sub>HPO<sub>4</sub> a NaH<sub>2</sub>PO<sub>4</sub>

13,80 g of NaH<sub>2</sub>PO<sub>4</sub>·H<sub>2</sub>O and 5,59 g Na<sub>2</sub>HPO<sub>4</sub>·2H<sub>2</sub>O were dissolved in 20 ml of de-ionized water at 35 °C and pH was adjusted to 6 by adding a few drops of 1 M aqueous NaOH solution. 10 g of glukomannan were added to the salt solution and the mixture was stirred for 20 min at ambient temperature. The resulting suspension was filtered using a Büchner funnel and the filter cake was crushed in mortar and dried for 24 hours at 55 °C. Then the temperature was increased to 65 °C for 90 min. For phosphorylation, the dried mixture was “baked” at 80 °C for 3 h, cooled down to room temperature and stirred in 50 ml of 50% aqueous methanol for 30 min. After filtering, the raw product was dehydrated by washing with 20 ml of absolute ethanol. The resulting paste was washed with a ten-fold amount of water and the glucomannan phosphate was precipitated with acetone. The product was vacuum-filtrated, repeatedly washed with denatured ethanol in order to remove water and acetone and finally dried at 45 °C to constant weight<sup>16</sup>.

#### Reaction of glucomannan and phosphorylated glucomannan with polycarboxylic acid

Cross-linking of glucomannan or phosphorylated glucomannan was proceeded using different polycarboxylic acid, such as aspartic, citric, glutaric, malic, oxalic and succinic. 0.071 mmol carboxylic acid in 10 ml de-ionized water was placed into the ultrasonic equipment and dissolved. After it glucomannan (1 g) was added and cross-linked at 80 °C for 3 hours. The resulting hydrogel was washed several times with distilled water and dried at 80 °C to constant weight<sup>17</sup>.

#### Characterization of hydrogel

Swelling ratio (SR) was determined by measuring the absorption capacity of the hydrogel using de-ionized water.

Swelling ratio (g H<sub>2</sub>O/g dry hydrogel) and swelling capacity (water content in swollen hydrogel, %) were calculated according to these equations:

Swelling ratio:

$$SR = \frac{w_2 - w_1}{w_1} \text{ [g/g]} \quad (1)$$

Swelling capacity:

$$SC = \frac{w_2 - w_1}{w_2} \cdot 100 \text{ [%]} \quad (2)$$

where  $w_1$  and  $w_2$  are the weights of dried and swollen hydrogel.

#### Results and discussion

##### Preparation of hydrogel

Glucomannan hydrogels were prepared by different methods using calcium hydroxide as the deacetylation reagent, ethanol as the precipitation agent, various polycarboxylic acids as the cross-linking agents, STMP, STPP, disodium hydrogenphosphate dihydrate and sodium dihydrogenphosphate monohydrate as the phosphorylated agents. Hydrogel sample A was represented by reaction of glucomannan with Ca(OH)<sub>2</sub> and ethanol without heating, sample B was prepared by reaction of glucomannan with Ca(OH)<sub>2</sub> and ethanol at increased temperature and sample C was obtained by reaction of glucomannan with Ca(OH)<sub>2</sub>. For preparation

of sample D only ethanol was used. Sample E is glukomannan cross-linked with STMP, sample F with STPP and sample G is glukomannan fosforylated with  $\text{Na}_2\text{HPO}_4$  and  $\text{NaH}_2\text{PO}_4$  mixture.

### Swelling studies

Swelling ratios of prepared hydrogels in distilled water are shown in Figure 2. It was observed that the highest values of SR were attained at samples A, B, and G (almost 60 g/g). For sample D was achieved 45 g/g, for sample C structure of hydrogel was not so perfect due to absence of ethanol as the precipitant. The low values of swelling ratios for samples E and F may be due to the fact that fosforylation led to cross-linking and rigid net structure of hydrogel was formed. Based on the results of the hydrogel swelling ratio samples B, D and G were selected for next investigation. The minimal time for maximum swelling of the hydrogel was determined as 2 hours.

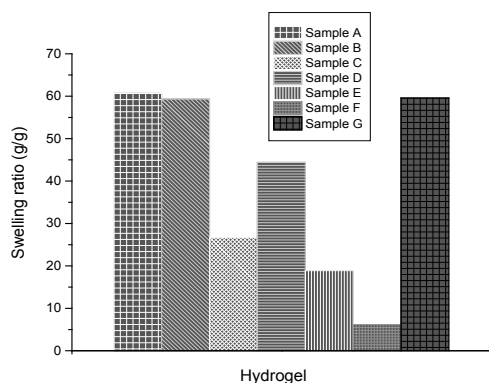


Figure 2. Dependence of swelling ratio on type of hydrogel

### Influence of temperature on the hydrogel swelling ratio and solubility of hydrogel

The influences of temperature on water capacity and solubility of hydrogels were investigated, the results are presented in Figure 3. It was observed that the hydrogel swelling ratio decreases with growing temperature and solubility of hydrogel increases with growing temperature. Hydrogel B was formed after deacetylation of glukomannan backbone in alkaline conditions, which resulted in increased number of free hydroxyl groups in glukomannan and higher hydrophilic interactions with molecules of water. Interaction un-deacetylated glukomannan with water was probably lower in hydrogel D. Hydrogel G was formed in slightly acidic conditions allowing binding of the phosphate groups as monoesters, which result in net structure formed with hydrogen bonds. For practical use of hydrogel is important value of its solubility, which reached values less than 0.05 g/100 g  $\text{H}_2\text{O}$  at 25 °C.

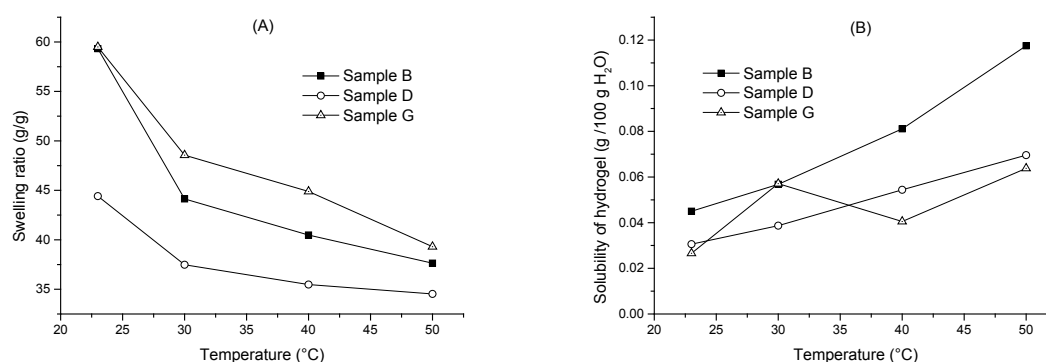


Figure 3. Effect of temperature on the swelling ratio (A) and solubility of hydrogel (B)

### Influence of swelling – drying cycles on hydrogel swelling ratio and solubility

The effect of repeating of swelling – drying cycles on water capacity (A) and solubility of hydrogels (B) was investigated, the results are shown in Figure 4. It can be seen that hydrogel swelling ratio decreases with

growing number of swelling – drying cycles of hydrogels, this fact corresponds with increasing solubility of hydrogel with raising number of swelling – drying cycles. The values of solubility of hydrogel after third cycle reached almost 0.12 g/100 g H<sub>2</sub>O. Nevertheless, the values of SR were relatively high (35 g/g) for samples B and G even after third swelling – drying cycle.

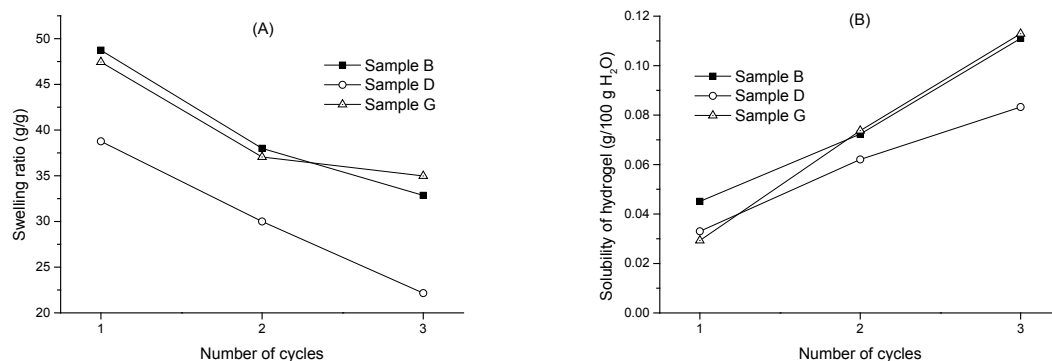


Figure 4. Effect of number of swelling–drying cycles on the swelling ratio (A) and solubility of hydrogel (B)

#### Rate of dehydration

Figure 5 shows the time dependence of swollen hydrogels dehydration at ambient temperature. It can be seen that all tested samples were dried-up during 22 – 30 hours.

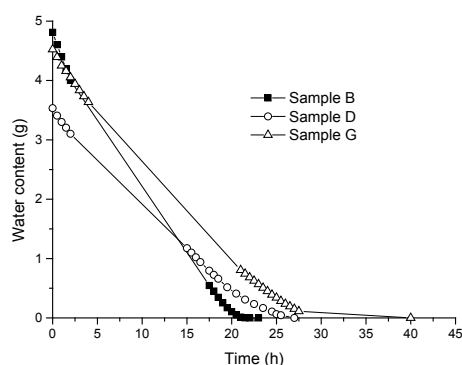


Figure 5. Time course of swollen hydrogels dehydration

#### Swelling behavior of hydrogels in saturated solutions of fertilizers

One of the important properties of the hydrogels is their swelling behavior in solutions of fertilizers. In our case, ammonium sulphate and urea were selected as representatives of fertilizing materials. Effect of type of fertilizer on swelling capacity of hydrogels in saturated solutions of fertilizers is presented in Figure 6. The highest value of swelling capacity in ammonium sulphate solution was obtained with sample G (70 %). Differences in swelling capacity of individual hydrogels in urea solution are not significant (SC ~ 50%).

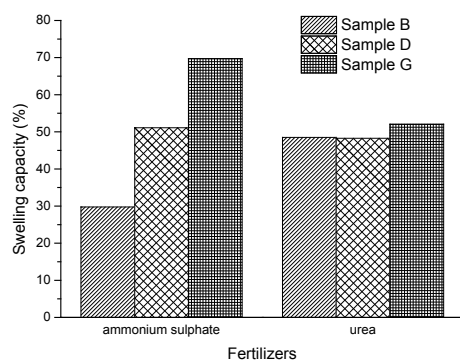


Figure 6. Dependence of swelling capacity of hydrogel on type of fertilizer

The influence of type of polycarboxylic acids on the swelling behavior of hydrogels

The influence of different cross-linking agents on gel formation and swelling behavior was investigated (Figure 7). It was also observed the effect of carbon chain length (spacer distance between the carboxylic groups) on the swelling ratio. The following cross-linkers were studied: aspartic acid, citric acid, glutaric acid, malic acid, oxalic acid, and succinic acid. The same amount of cross-linker (0.071 mmol) per gram mono-glucomannan phosphate was used. From Figure 7 it can be seen that significant value of SR (66 g/g) was achieved using succinic acid (C4) whereas the lowest SR value (55 g/g) was obtained with oxalic acid (C2).

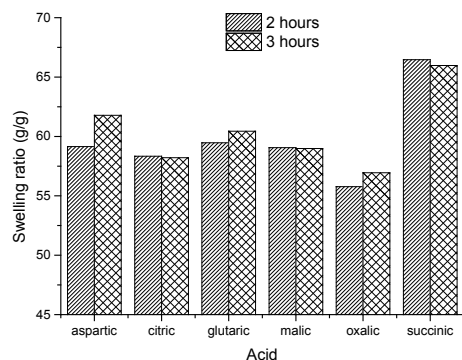


Figure 7. Dependence of type of polycarboxylic acid on the swelling ratio

#### Release study

Another important characteristic of studied hydrogels is rate of nutrient release. Conductometry and ion chromatography as useful methods for study releasing process were utilized. The release of compounds from hydrogels includes several steps: penetration of release medium into the polymeric network, dissolution of the dispersed fertilizers and release of the compounds from the hydrogel under swelling conditions. The results of release behavior of urea and ammonium sulphate from hydrogels into the distilled water are shown in Figure 8. It can be seen that release of urea from structure of both tested hydrogels took 4 minutes, in the case of ammonium sulphate 2 minutes.

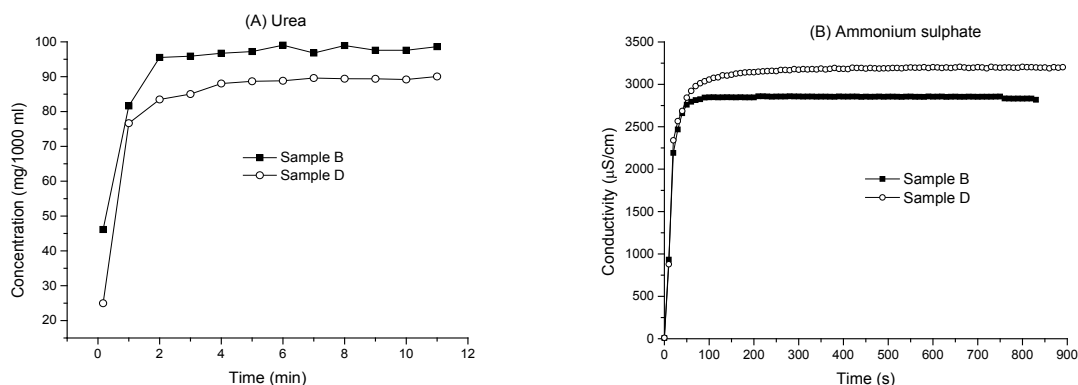


Figure 8. Release of urea (A) and ammonium sulphate (B) from hydrogels into distilled water

#### Conclusion

In this work was provided an overview of the preparation of glucomannan hydrogels using different agents as  $\text{Ca}(\text{OH})_2$ , ethanol, STMP, STPP,  $\text{Na}_2\text{HPO}_4$  and  $\text{NaH}_2\text{PO}_4$  and various polycarboxylic acids. According the results of swelling behavior of prepared hydrogels three methods were recommended for their synthesis: reactions glucomannan with  $\text{Ca}(\text{OH})_2$  and ethanol (sample B), with ethanol alone (sample D) and with  $\text{Na}_2\text{HPO}_4$  and  $\text{NaH}_2\text{PO}_4$  (sample G). The values of SR 60 g  $\text{H}_2\text{O}$  per g dried hydrogel were achieved for these hydrogels. Cross-linking glucomannan with polyphosphates led to lower swelling ratios. The investigations of influence of polycarboxylic acid on the SR have shown that only succinic acid provided a significant positive effect. Drying of

swollen hydrogels took approximately 1 day at 25°C. The results indicated that solubility of hydrogels increased with growing temperature, the values of 0.03 – 0.05 g per 100 g of water in a temperature range of 23 - 30°C are acceptable from practical point of view. Results of the release study demonstrated that prepared hydrogels show quick – release properties.

#### **Acknowledgment**

*This work has been supported by IGA University of Pardubice within the frame of project SGAFChT 2015005.*

#### **Literature**

1. Bhat N.R., Suleiman M.K., Abdal M.: *World J. Agric. Sci.* 5, 2 (2009).
2. Ekebafé L. O., Ogbefun D. E., Okieimen F. E.: *Biokemistri* 23, 2 (2011).
3. Kirschner Ch. M., Anseth K. S.: *Acta Mater.* 61, 931–944 (2013).
4. Hennink W. E., van Nostrum C. F.: *Adv. Drug Delivery Rev.* 54, 13–36 (2002).
5. Hoffman A. S.: *Adv. Drug Delivery Rev.* 43, 3–12 (2002).
6. Gulrez S. K. H., Al-Assaf S., O Phillips G., v knize: *Progress in Molecular and Environmental Bioengineering – From Analysis and Modeling to Technology Applications*, kap. 5, s. 124–126, 2011.
7. Yazdani F., Allahdadi I., Abas Akbari G.: *Pak. J. Biol. Sci.* 10, 23 (2007).
8. Davé V., McCarthy S. P.: *J. Environ. Polym. Degr.* 5, 4 (1997).
9. Williams M. A. K., Foster T. J., Martin D. R., Norton I. T.: *Biomacromolecules* 1, 3 (2000).
10. Chua M., Baldwin T. C., Hocking T. J., Chan K.: *J. Ethnopharmacol.* 128, 268–278 (2010).
11. Zhang Y.-q., Xie B.-j., Gan X.: *Carbohydr. Polym.* 60, 27–31 (2007).
12. Dhawan S., Kaur J.: *Crit. Rev. Biotechnol.* 27, 4 (2007).
13. Takata T.: Process for producing glucomannan gel particles. US Patent Appl. Publ. US 20030060518 A1, 27 March 2003.
14. Liu M., Fan J., Wang K., He Z.: *Drug Deliv.* 14, 397–402 (2007).
15. Chen L. G., Liu Z. L., Chen Y. J., Zhuo R. X.: *Chinese Chem. Lett.* 16, 12, (2005).
16. Passauer L., Liebner F., Fischer K.: *Macromol. Symp.* 244, 180–193 (2006).
17. Passauer L., Liebner F., Fischer K.: *Starch/Stärke* 61, 621–627 (2009).

## APPLICATION POSIBILITIES OF ZINC OXIDE NANOPARTICLES

Švrček J.<sup>1</sup>, Bierská L.<sup>1</sup>, Souček M.<sup>1</sup>, Krýsa J.<sup>2</sup>

<sup>1</sup>Bochemie a.s., Lidická 326, 735 95, Nový Bohumín

<sup>2</sup>Institute of chemical technology Prague, Technická 5, 166 28, Prague  
jiri.svrcek@bochemie.cz

Zinc oxide is a white inorganic powder, which is presented in a lot of industrial processes and products of our daily life. The global usage of ZnO is over 1 million tons per year and the main applications include rubber, glass and ceramics, paints, agriculture, cosmetics and pharmaceuticals. Nanoscale ZnO (nano ZnO) is much younger but more advantageous and fast-growing type of this material. Nano ZnO has attracted great interest due to its better, in some cases unique, properties than common type ZnO (o-ZnO).

We have done vast research in the area of nano ZnO preparation and have studied its properties (vulcanizing, anti-microbial, photo-catalytic etc.). In this contribution we would like to present some of these results.

In Table I is mentioned typical characterization of our nano ZnO (nZ-BOCH). Figures 1(a) and 1(b) show morphology of nZ-BOCH and Figure 1(c) its comparison with o-ZnO (Johann Wiehart, Austria). From these figures is clearly visible difference in primary particles size of nZ-BOCH and o-ZnO. Specific surface area of ordinary ZnO was  $6 \text{ m}^2 \text{ g}^{-1}$ , thus one fold lower than nZ-BOCH.

Table I  
General technical specification of nZ-BOCH

Characterization parameter	Value	Unit	Evaluation technique
Crystalline phase	100 % ZnO - zincite		XRD
Primary particles size/crystallites	$7 \pm 1$	nm	XRD
Secondary particles size ( $D_{50}$ Number)	85 - 156	nm	DLS
Specific surface area	60 - 100	$\text{m}^2 \text{ g}^{-1}$	BET
Purity of ZnO	$\geq 99.8$	wt. %	XRF
Content of $\text{Cl}^-$	$< 0.1$	wt. %	XRF, argentometry
Content of Mn, Fe, Cu, Co	$< 1$	ppm	XRF
Content of Pb	$< 50$	ppm	AAS, XRF
Content of Cd	$< 10$	ppm	AAS, XRF
Sample colour	cream/yellowish		visual evaluation
Particles shape	near-spherical		HRTEM

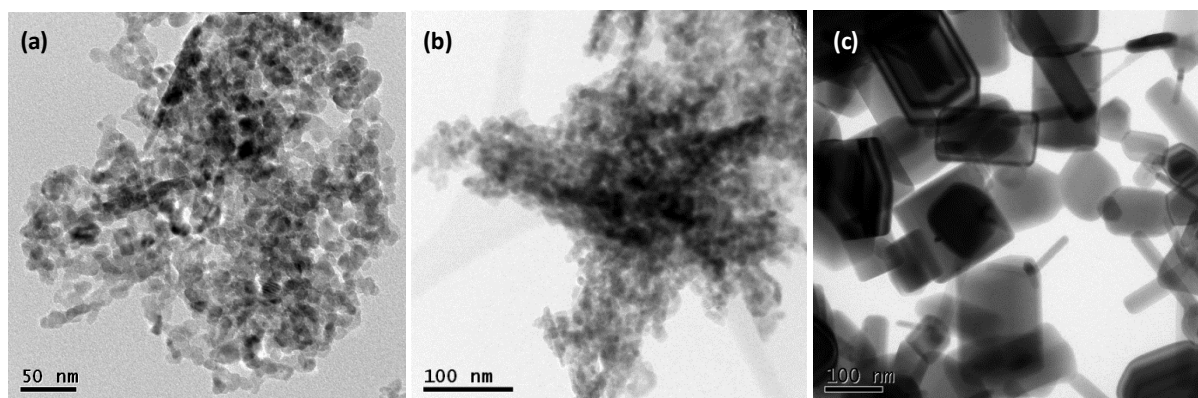


Figure 1. Transmission electron micrographs of nZ-BOCH (a, b) and o-ZnO (c)

ZnO is generally known as the best activator for sulphur vulcanisation of rubber. In recent years, due to the environmental and economic issues in relation to the amount of zinc in rubber products, there is the tendency to minimize content of zinc. If we want to reduce the required amount of ZnO, we have to increase the activity of zinc. Some recommended solutions include the application of so-called "active" or "nano" zinc oxide<sup>1,2</sup>.

We have done a lot of tests (in model and real rubber mixtures) which were focused on utilization of nano ZnO in rubber industry. Below is mentioned one example from these tests.

We investigated vulcanizing properties (Table II) of three nZ-BOCH samples in real rubber mixture used for tire manufacturing. Samples had different specific surface area but the size of primary particles (XRD determination) was in all cases between 7 to 8 nm. The ordinary zinc oxide Golden Seal R Q3 (Olawka Huta, Poland), with specific surface area  $5 - 6 \text{ m}^2 \text{ g}^{-1}$ , was chosen as a standard (o-ZnO). A standard amount of ZnO in this mixture was 3 phr.

First of all were determined vulcanization parameters on rheometer (the time of curve recording was 60 min and the temperature was  $150 \text{ }^\circ\text{C}$ ), after than the rubber mixtures were vulcanized in a laboratory vulcanizing press (at  $150 \pm 2 \text{ }^\circ\text{C}$ ). After vulcanization, we left mixtures for 24 hours, and then these mixtures were used for preparation of specimens in order to investigate the mechanical properties (Table III). All tests were done at room temperature ( $23 \pm 2 \text{ }^\circ\text{C}$ ).

Table II  
Vulcanizing properties of real mixtures with o-ZnO and nZ-BOCH

Type of ZnO	Dosage [phr]	S [ $\text{m}^2 \text{ g}^{-1}$ ]	M <sub>MIN</sub> [dN m]	M <sub>MAX</sub> [dN m]	t <sub>02</sub> [min]	t <sub>c(90)</sub> [min]	R <sub>V</sub> [ $\text{min}^{-1}$ ]	Cross-link density $\cdot 10^{-4}$ [ $\text{mol cm}^{-3}$ ]
o-ZnO	3.00	6	9.2	42.5	4.43	9.84	18.48	1.9534
nZ-BOCH 2	3.00	102	10.1	43.6	5.23	11.60	15.70	2.1202
	1.50		10.5	42.9	5.01	10.86	17.09	2.1811
	0.75		10.1	43.0	4.51	10.23	17.48	2.1945
nZ-BOCH 3	3.00	73	11.6	39.0	3.20	6.52	30.12	1.8724
	1.50		10.6	43.2	4.50	10.20	17.54	2.1801
	0.75		10.1	37.0	3.98	7.49	28.49	1.5900
nZ-BOCH 5	3.00	72	9.8	42.2	5.01	11.29	16.13	2.1517
	1.50		10.4	43.2	4.76	10.44	17.06	2.2022
	0.75		10.7	38.3	3.58	7.33	26.67	1.6019

Table III  
Mechanical properties of vulcanizates with o-ZnO and nZ-BOCH

Type of ZnO	Dosage [phr]	S [ $\text{m}^2 \text{ g}^{-1}$ ]	Strength [MPa]	Elongation at break [%]	Modulus 300 [MPa]	Hardness [IRHD]	Density [ $\text{g cm}^{-3}$ ]
o-ZnO	3.00	6	29.66	469	18.30	70.4	1.101
nZ-BOCH 2	3.00	102	29.94	422	18.70	71.2	1.100
	1.50		30.04	426	20.58	71.6	1.096
	0.75		29.56	432	20.06	71.4	1.107
nZ-BOCH 3	3.00	73	25.24	401	18.62	71.2	1.110
	1.50		26.04	437	17.26	69.8	1.091
	0.75		28.90	473	16.96	68.4	1.095
nZ-BOCH 5	3.00	72	29.20	435	19.40	69.0	1.102
	1.50		28.68	433	19.12	70.4	1.095
	0.75		26.52	446	16.78	68.6	1.097

On the basis of the measured results (Tables II and III) it is possible to conclude that all tested nano ZnO samples generally meet the requirements in relation to preparation of suitable rubber mixtures. It can be said that these samples achieved at lower dosage, 1.5 and 0.75 phr (respectively 50 and 25 %), the values which are comparable to the standard values (3 phr) of o-ZnO. These samples are not suitable when the dosage of nano ZnO is 3 phr (100 %). The best properties were observed for the sample nZ-BOCH 2, so nano ZnO with the largest specific surface area. Sufficient dosage of nZ-BOCH 2 is thus four times lower than required amount of o-ZnO. This discovery but also other better properties of nano ZnO (i.e. higher purity, positive influence on lifetime of rubber goods, better dispersibility in rubber mixture), compare to o-ZnO, invite nZ-BOCH for utilization in rubber industry.

Another very interesting functional property of ZnO is its antimicrobial activity. The mechanism of action and factors which influence this effect are still not well understood and actually exist several opinions - activity due to: electrostatic interaction, presence of reactive oxygen species generated by ZnO photocatalyst, release of  $\text{Zn}^{2+}$  or other unknown chemical species from ZnO or the abrasive surface texture of  $\text{ZnO}^{3-5}$ .

We have done comparative antimicrobial tests of our nZ-BOCH samples with competitive nano ZnO materials and o-ZnO. ZnO samples were tested in powder state and also in tailor-made lacquers, plastics or filters (evaluation primarily by Public Health Institute Ostrava).

In powder form (Table IV) all nano ZnO samples show a lower antimicrobial activity, in comparison with o-ZnO, which is possible to award to high agglomeration of primary particles. Absolutely opposite results were obtained when we have tested an activity of well dispersed ZnO nanoparticles in appropriate matrix (e.g. lacquers). In this case nZ-BOCH showed the best antibacterial activity. Examples of selected results are mentioned in Tables V, VI and VII.

Table IV

Antibacterial activity of nano (commercial materials or nZ-BOCH samples) and ordinary ZnO powders (exposition 24 hours)

Sample	Specific surface area, BET [m <sup>2</sup> g <sup>-1</sup> ]	Primary particle size, XRD [nm]	Minimum inhibitory concentration [wt. %]	
			<i>Escherichia Coli</i>	<i>Staphylococcus aureus</i>
o-ZnO	6	66 ± 9	0.156	0.156
nano ZnO	17	29 ± 8	0.313	0.313
nano ZnO	35	22 ± 5	0.313	0.313
nano ZnO	64	12 ± 1	0.313	0.313
nZ-BOCH	72	6 ± 1	0.313	0.625
nZ-BOCH	108	6 ± 2	0.313	0.313

Table V

Antibacterial activity (*Escherichia Coli*) of lacquers (on water-based) with nZ-BOCH and o-ZnO (ISO 27447:2009)

Lacquer with	Concentration of ZnO [wt. %]	0 h, CFU/50 µl	Exposition 4 hours, CFU/50 µl	
			Darkness	UV radiation
pure glass (blank)	0	7 300	4 300	3 000
nZ-BOCH	0.3		17	5
nZ-BOCH	1.0		0	0
o-ZnO	0.3		1 400	668
o-ZnO	1.0		976	364

Table VI

Antibacterial activity (*Staphylococcus Aureus*) of PVC with nano and ordinary ZnO (ISO 22196:2007)

Sample (48 h exposition)	ZnO [wt. %]	N [CFU cm <sup>-2</sup> ]	Activity = U <sub>t</sub> - A <sub>t</sub>
PVC, nano ZnO	0.5	< 1	> 4.9
	1.0	< 1	> 4.9
PVC, o-ZnO	0.5	1.8·10 <sup>3</sup>	1.6
	1.0	< 1	> 4.9
PVC	0	8.1·10 <sup>4</sup>	U <sub>t</sub> = 4.9
Concentration of the used bacterial suspension		6.7·10 <sup>6</sup> CFU ml <sup>-1</sup>	

Table VII

Antibacterial activity (*Klebsiella pneumonia*, density 10<sup>3</sup> ml<sup>-1</sup>) of PUR filters with nZ-BOCH (ASTM E 2149)

Exposition [min]	Daylight		Darkness	
	PUR	PUR, nZ-BOCH	PUR	PUR, nZ-BOCH
0	232	248	112	>300
60	185	228	122	220
120	160	150	193	186
180	130	92	163	125
240	>300	96	92	41
1440	>300	0	>300	0

In lacquers antibacterial effect appeared after 4 hours of exposure and after 24 hours the log reduction was 4 to 5 (Table V). The effect is a long-standing which we have confirmed by repeating tests after 10 months.

By addition of nano ZnO to polymeric matrix (e.g. PVC, Table VI) was prepared nanocomposite which meet the requirements of so-called "medical plastics". As well as by addition of nano ZnO to fibres (e.g. PUR or PVB, Table VII) it was possible to prepare antibacterial textiles or filters.

Next significant advantage of well dispergated nano ZnO is, compared to ordinary ZnO, its high transparency in a relevant matrix, which is for example a very interesting property for preparation of functional transparent lacquers (Figure 2).

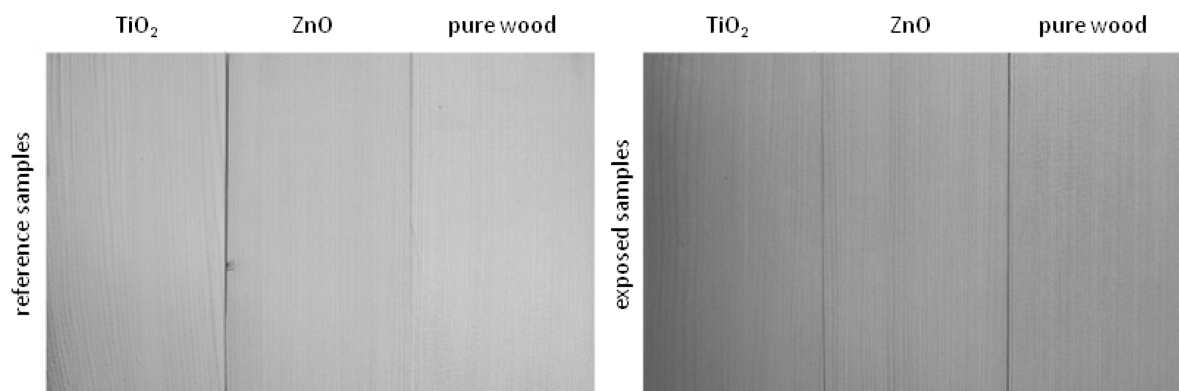


Figure 2. Photos of wood (spruce) with or without protection coating before (on the left side) and after 4 months of UV-C exposure (on the right side)

ZnO is known as a universal wide-spectral inorganic UV filter. So it offers utilization of nano ZnO as a transparent UV protective additive in lacquers, e.g. for protection of wood. We tested two types of commercial inorganic nano UV filters (ZnO a  $\text{TiO}_2$ ) for this purpose, but unfortunately the UV protection activity was in both cases in-sufficient (Figure 2). A possible reason of this negative finding could be a high photocatalytic effect of tested nanomaterials.

ZnO shows comparable photocatalytic properties as  $\text{TiO}_2$ , which is actually the most used photocatalyst. Nevertheless photocatalytic activity of our samples (nZ-BOCH) is significantly lower compared to the other tested nanomaterials (Figure 3). This property seems to be promising for application of nZ-BOCH in UV protection lacquers or for photo-stabilization of polymers (plastics, rubber) and also for utilization in cosmetics, more precisely sunscreens (note: the Scientific Committee on Consumer Safety (SCCS) concludes that ZnO nanomaterials of appropriate characteristics pose no or limited risk for use on the skin as UV filter in sunscreen formulations)<sup>6</sup>.

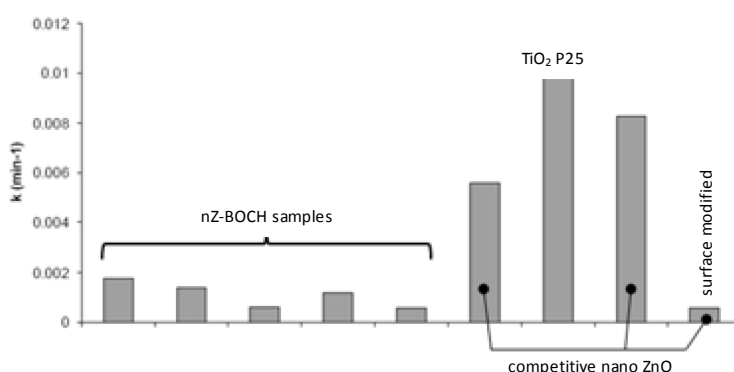


Figure 3. A comparison of photocatalytic activity of nZ-BOCH samples with competitive nano ZnO and  $\text{TiO}_2$  materials (photocatalytic activity was determined in suspension of model dye Acid Orange 7, intensity of UV radiation was  $2 \text{ mW cm}^{-2}$ )

We also have studied potential toxic properties of nano and ordinary ZnO (tests were done in cooperation with University of Ostrava and Tomas Bata University in Zlín).

First of all it is necessary to say that zinc is an essential trace element for humans, animals and plants. Zinc is the 24th most abundant element and ranks among the lowest harmful heavy metals. On the other side, zinc is classified "Very toxic to aquatic life with long lasting effects".

In our tests we focused on penetration through skin, cytotoxicity, DNA damage and phytotoxicity of nano and/or ordinary ZnO.

The aim of the first test was to quantitatively evaluate the skin (a pig) penetration of two types ZnO nanoparticles (primary particles size 12 and 38 nm). Experiments were performed in Franz-type of diffusion cells using a model pig skin. No or little penetration was observed for these nanomaterials through the *stratum corneum*. Our conclusion is in agreement with the opinion of SCCS on nano ZnO<sup>6</sup>.

In Table VIII are mentioned results from cytotoxicity test of five different ZnO nanomaterials (nZ-BOCH samples and commercial products) and one type of ordinary ZnO. From these results is not obvious difference between toxic effect of nano and ordinary ZnO. The same conclusion came out from the test of DNA damage.

In phytotoxicity tests nano ZnO showed higher effect than ordinary ZnO, but effects of both types of this material were significant (this is in accordance with above mentioned classification of zinc oxide).

Table VIII

Viability test/cytotoxicity - cells damage (human pulmonary tissue cells), standard 1 % H<sub>2</sub>O<sub>2</sub> - viability 77.4 %

Exposition 24 hours Sample/Concentration	Specific surface area, BET [m <sup>2</sup> g <sup>-1</sup> ]	Primary particle size, XRD [nm]	Viability (% check)		
			78.1 µg ml <sup>-1</sup>	19.5 µg ml <sup>-1</sup>	9.8 µg ml <sup>-1</sup>
o-ZnO	6	66 ± 9	0	57.7	77.5
nZ-BOCH 14	72	6 ± 1	59.9	76.5	82.8
nZ-BOCH 26	108	6 ± 2	0	34.5	60.5
nZ-BOCH 250	47	8 ± 1	57.4	57.9	91.2
nano ZnO (commercial)	64	12 ± 1	0	98.9	110.0
nano ZnO (commercial)	35	22 ± 5	64.7	95.7	100.5

The main goal of this contribution is to present some application possibilities of nano ZnO. From the mentioned results seems to be that our nano ZnO (nZ-BOCH) is a very interesting material which shows better parameters and functional properties (especially vulcanizing and antimicrobial activity) than o-ZnO but also tested competitive nano ZnO products.

BOCHEMIE has dealt with zinc chemistry over a long period of time and plans to be a producer of nano ZnO. The very significant advantage of our product (nZ-BOCH) will be its easy availability and thus its sale for a reasonable or even better a very interesting price, compared to actually available competitive nano ZnO products.

#### Acknowledgment

*This work was carried out with financial support from the state budget through the Ministry of Industry and Trade of the Czech Republic (MIT FR-T14/364).*

#### References

1. Heideman G.: *Ph.D. Thesis, University of Twente*, chap. 3, p. 45, Enschede 2004.
2. Li L., Liu L.: *Mater. Sci. Forum* 650, 367 (2010).
3. Sawai J., Igarashi H., Hashimoto A., Kokugan T., Shimizu M.: *J. Chem. Eng. Jpn.* 28, 288 (1995).
4. Singh P., Nanda A.: *J. Chem. Pharm. Res.* 5, 457 (2013).
5. Shi L. E., Li Z. H., Zheng W., Zhao Y. F., Jin Y. F., Tang Z. X.: 31, 173 (2014).
6. Scientific Committee on Consumer Safety: *SCCS/1518/13* (2014).

## STRUCTURE AND PROPERTIES OF LEAD-YTTRIUM PHOSPHATE GLASSES

**Račický A.**, Mošner P., Koudelka L.

*Faculty of Chemical Technology, University of Pardubice, 532 10, Pardubice, Czech Republic  
antonin.racicky@student.upce.cz*

### Introduction

Doping of phosphate glasses by trivalent oxides is generally known to improve their chemical resistance against atmospheric moisture, mechanical properties and thermal stability<sup>1</sup>. A number of studies have been devoted to aluminophosphate glasses and borophosphate glasses<sup>2-7</sup> over recent years. Phosphate and borophosphate glasses containing  $Y_2O_3$  have been studied in recent years as host matrix for rare-earth ions for a variety of optoelectronic and laser applications. Doping glasses with yttrium oxide is also known to improve their mechanical properties, chemical durability and thermal behaviour. A primary disadvantage of pure  $Y_2O_3$  is its high melting point which makes preparation of  $Y_2O_3$  glasses a little difficult. Angel and Hann studied glasses in the system  $Na_2O-Y_2O_3-SiO_2$  with maximal  $Y_2O_3$  content of 15 mol% (upper limit of melting temperature was 1550°C)<sup>8</sup>. Addition of  $Y_2O_3$  to lithium-aluminium-silicate glasses leads to lower melting temperature, lower viscosity and higher crystallization temperature<sup>9</sup>. Martin et al. studied glass system  $(Y_2O_3)_{0,31-z}(Al_2O_3)_z(P_2O_5)_{0,69}$  and concluded that with increasing  $Y_2O_3$  content the density of glasses increases whereas the Vickers hardness decreases<sup>10</sup>. The obtained results were compared to those obtained for pseudo-binary  $Al_2O_3-P_2O_5$  glasses. Bacon studied yttrium-silicate glasses in the system  $MgO-Y_2O_3-SiO_2$ . He managed to synthesize glass containing 36.5 mol % MgO and 12 mol %  $Y_2O_3$ <sup>11</sup>. The aim of this work is to investigate how the  $Y_2O_3$  oxide influences the structure, physicochemical properties and thermal behaviour of lead phosphate glasses.

### Experimental

$PbO-Y_2O_3-P_2O_5$  glasses were prepared by melting from an analytical grade  $PbO$ ,  $Y_2O_3$  and  $H_3PO_4$  using a total batch weight of 10g. The homogenized starting mixtures were slowly heated up to 1050-1400°C in a platinum crucible covered with a lid. The melting temperature increased with increasing  $Y_2O_3$  content. After 20 min reaction and mixing, the obtained melt was cooled by pouring into a preheated ( $T < T_g$ ) graphite mould. The weight loss measurements indicated that the volatilization losses were not significant, hence the batch compositions can be considered as reflecting actual compositions. The vitreous state was checked by XRD. A structureless spectrum was obtained for all glass compositions.

The glass density,  $\rho$ , was determined on bulk samples by the Archimedes' method using toluene as the immersion liquid. The molar volume,  $V_M$ , was calculated as  $V_M = M/\rho$ , where  $M$  is the average molar weight of the glass composition  $aPbO-bY_2O_3-cP_2O_5$  calculated for  $a+b+c = 1$ . The chemical durability of the glasses was evaluated from the measurements of the dissolution rate,  $DR$ , at 25°C. The measurement of  $DR$  was realized on glass cubes with dimensions of  $\approx 5 \times 5 \times 5$  mm. These cubes were leached in 100 cm<sup>3</sup> of distilled water for 48 hours. The dissolution rate,  $DR$ , was calculated from the expression  $DR = \Delta m/S \cdot t$ , where  $\Delta m$  is the weight loss [g],  $S$  is the sample area [cm<sup>2</sup>] before the dissolution test and  $t$  is the dissolution time [min]. The linear refractive indices were measured with the prism coupling method, using a Metricon Model 2010/M.

The thermal behaviour of the glasses was studied with the Netzsch DTA 404 PC operating in the DSC mode at a heating rate of 10 °C·min<sup>-1</sup> at a temperature interval of 30-900°C. The measurements were carried out with 100 mg powder samples (the average particle size was 10  $\mu$ m) in platinum crucible under an atmosphere of  $N_2$ . The values of the glass transition temperature,  $T_g$ , ("midpoint") and the values of the crystallization temperature,  $T_c$ , (the onset of the first crystallization peak) were determined from the DSC curves. Crystalline samples were prepared using isothermal heating of powdered glasses at 500-650°C (end of the last crystallization peak) for 2 hours and identified by XRD analysis using  $Cu K\alpha$  radiation on a Bruker D8 Advance diffractometer.

The glass transition temperature was also determined from dilatometric curves obtained from bulk samples with dimensions of 10×5×5 mm using a dilatometer DIL 402 PC (Netzsch) and a heating rate of 5°C·min<sup>-1</sup>. The glass transition temperature,  $T_g$ , was determined from a change in the slope of the elongation versus temperature, the dilatometric softening temperature,  $T_d$ , from the maximum of the expansion trace corresponding to the onset of viscous deformation and the coefficient of the thermal expansion,  $\alpha$ , as a mean value in a temperature range of 150- 250°C.

The Raman spectra were measured on bulk samples at room temperature using a Horiba-Jobin Yvon LaBRam HR spectrometer in a range of 1760 – 60 cm<sup>-1</sup>. The spectra were recorded in back-scattering geometry under excitation with Nd:YAG laser radiation (532 nm) on the sample. The exposition time was 3 s, the accumulation 10x and the grid had 600 streaks/mm.

## Results and discussion

Four homogeneous, transparent and colourless glasses of the system (40-x)PbO-xY<sub>2</sub>O<sub>3</sub>-60P<sub>2</sub>O<sub>5</sub> (x=0-15 mol% Y<sub>2</sub>O<sub>3</sub>) were prepared and studied. Their composition is summarized in Table I, just as the values of their density,  $\rho$ , molar volume,  $V_M$ , dissolution rate,  $DR$ , index of refraction,  $n$ , and Abbe number,  $v_d$ .

Table I  
Physicochemical properties (40-x)PbO-xY<sub>2</sub>O<sub>3</sub>-60P<sub>2</sub>O<sub>5</sub> glasses

Sample	PbO	Y <sub>2</sub> O <sub>3</sub>	P <sub>2</sub> O <sub>5</sub>	$\rho \pm 0.02$	$V_M$	n(532nm)	$v_d$	$DR \cdot 10^6 \pm 0.05$
		[mol%]		[g·cm <sup>-3</sup> ]	[cm <sup>3</sup> ·mol <sup>-1</sup> ]			[g·cm <sup>-2</sup> ·min <sup>-1</sup> ]
Y 00	40	0	60	4.03	43.2	1.68	35.3	0.455
Y 05	35	5	60	3.92	44.5	1.68	35.9	0.056
Y 10	30	10	60	3.81	45.9	1.67	36.8	0.134
Y 15	25	15	60	3.70	47.3	1.64	42.4	0.157

As can be seen in Table I, glass density decreases linearly with increasing Y<sub>2</sub>O<sub>3</sub> content from 4.03 g/cm<sup>3</sup> (x=0) down to 3.7 g/cm<sup>3</sup> (x=15), whereas molar volume increases within the range 43.2-47.3 cm<sup>3</sup>/mol, as the total number in the molar formula increases when only 2 atoms in PbO are replaced by 5 atoms in Y<sub>2</sub>O<sub>3</sub>. The reason for the decrease of the density with Y<sub>2</sub>O<sub>3</sub> additions is mostly due to the lower atomic weight of yttrium in comparison with lead. The dissolution rate of the glasses reveals a minimum for the glass with x = 5 mol% Y<sub>2</sub>O<sub>3</sub>. The lowest chemical durability was observed for the starting lead phosphate glass with composition 40PbO-60P<sub>2</sub>O<sub>5</sub>. We have also measured the index of refraction of the studied glasses at the three wavelengths. From Table I it is evident that glasses of the series xZnO-10In<sub>2</sub>O<sub>3</sub>-(90-x)P<sub>2</sub>O<sub>5</sub> showed only negligible decrease with increasing Y<sub>2</sub>O<sub>3</sub> content ranging from 1.68 to 1.64 ( $\lambda=532$  nm), whereas Abbe number slightly increases within the range 35.3-42.4.

DSC curves obtained for the studied glass series are shown in Fig 1. DSC curve of the starting glass 40PbO-60P<sub>2</sub>O<sub>5</sub> is characterized by a weak enthalpic effect at ~280-330°C corresponding to the glass transition phenomenon and by a broad exothermic peak with the onset at 436°C ascribed to the crystallization of the glass. DSC curves of the other studied glasses suggest that all of glasses crystallize on heating within the range ~420-650°C. The values of the crystallization temperature,  $T_c$  (onset of the crystallization peak) just as the values of the glass transition temperature ("midpoint") determined from DSC curves are summarized in Table II. As can be seen in this table the glass transition temperature,  $T_g$ , and crystallization temperature,  $T_c$ , increases with increasing Y<sub>2</sub>O<sub>3</sub> content within the range 299-491 °C ( $T_g$ ) and 436-606 °C ( $T_c$ ) respectively. The observed increase in  $T_g$  values show the increasing bonding strength in the glass structure with increasing Y<sub>2</sub>O<sub>3</sub> content. For the evaluation of thermal stability of glasses,  $\Delta T=T_c-T_g$ , criterion was applied. Higher values of  $\Delta T$  usually correspond to a higher thermal stability and glass-forming tendency. The values of the  $T_c-T_g$  obtained for studied glasses are given in Table II. As can be seen in this table, the highest thermal stability and therefore the lowest tendency towards crystallization was found for the glass containing 5 mol% Y<sub>2</sub>O<sub>3</sub> ( $\Delta T= 206^\circ\text{C}$ ), whereas the lowest thermal stability showed the glass containing 15 mol% Y<sub>2</sub>O<sub>3</sub> ( $\Delta T= 137^\circ\text{C}$ ).

Diffraction patterns of crystalline phases (see Fig.2), formed in the glasses after 2 hours of annealing of powdered samples at 500-650°C (end of the last crystallization peak), showed that the observed crystallization peak on DSC curve of the parent glass composition 40PbO-60P<sub>2</sub>O<sub>5</sub> corresponds only to the formation of lead metaphosphate Pb(PO<sub>3</sub>)<sub>2</sub> crystalline phase. With increasing addition of Y<sub>2</sub>O<sub>3</sub> the diffraction lines of Pb(PO<sub>3</sub>)<sub>2</sub> are gradually replaced by the diffraction lines of Y(PO<sub>3</sub>)<sub>3</sub>, Pb<sub>3</sub>P<sub>4</sub>O<sub>13</sub> and Pb<sub>2</sub>P<sub>2</sub>O<sub>7</sub> crystalline compounds.

The determination of the glass transition temperature from DSC curves is tedious, as the change in the thermal capacity  $c_p$  in the glass transition region of these samples is relatively small (see Figure 1). The glass transition region can be seen more clearly from the TD measurements. Results from TD analysis are summarized in Table II. It can be seen that incorporation of Y<sup>3+</sup> ions into the phosphate network results in an increase the glass transition temperature,  $T_g$ , (discussed before) and dilatation softening temperature,  $T_d$ , whereas values of thermal expansion coefficient,  $\alpha$ , reveal a maximum 13.2 ppm°C<sup>-1</sup> at the glass with 5 mol% Y<sub>2</sub>O<sub>3</sub>. Glass transition temperature obtained from TD curves was by 3-5°C lower than the values obtained from DSC curves.

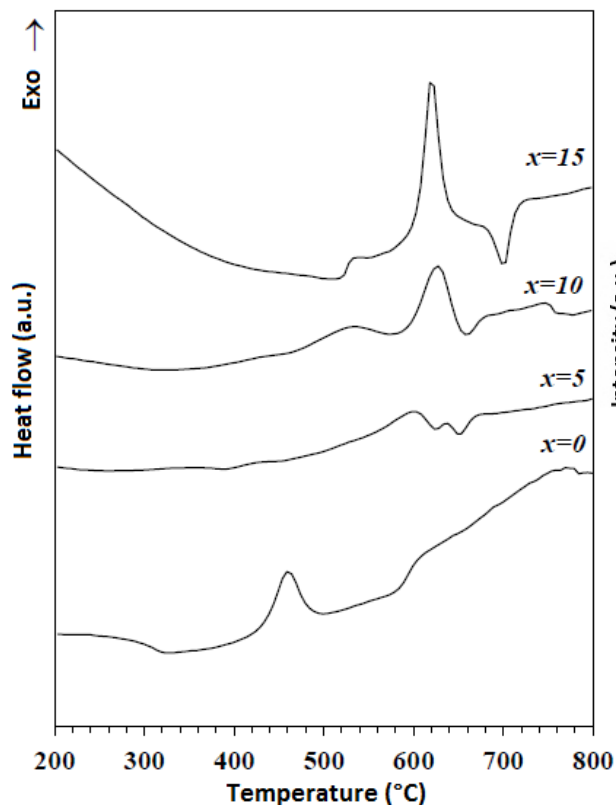


Figure 1. DSC curves of the glass series  $(40-x)\text{PbO}-x\text{Y}_2\text{O}_3-60\text{P}_2\text{O}_5$

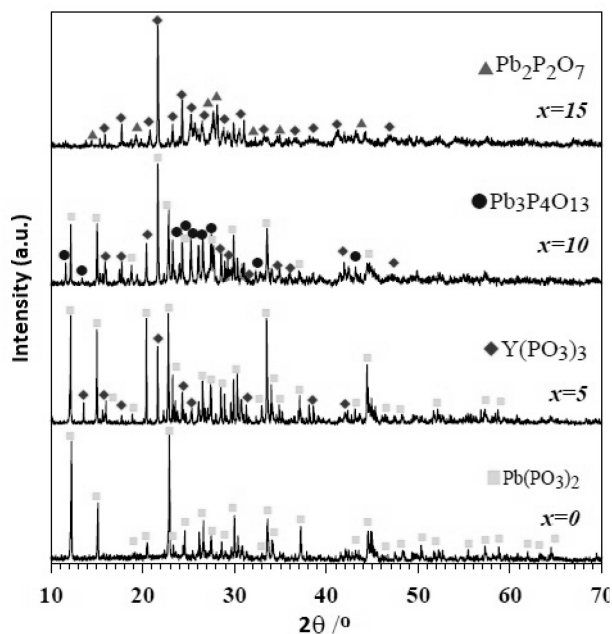


Figure 2. XRD patterns of the crystallized samples of the series  $(40-x)\text{PbO}-x\text{Y}_2\text{O}_3-60\text{P}_2\text{O}_5$

Table II  
Thermoanalytical parameters of  $(40-x)\text{PbO}-x\text{Y}_2\text{O}_3-60\text{P}_2\text{O}_5$  glasses

Sample	PbO	Y <sub>2</sub> O <sub>3</sub>	P <sub>2</sub> O <sub>5</sub>	DSC				DIL	
				T <sub>g</sub> ± 2	T <sub>c</sub> ± 2	T <sub>c</sub> - T <sub>g</sub>	α ± 0.5	T <sub>g</sub> ± 2	T <sub>d</sub> ± 2
	[mol%]			[°C]	[°C]	[°C]	[ppm °C <sup>-1</sup> ]	[°C]	[°C]
Y 00	40	0	60	299	436	137	10.4	295	321
Y 05	35	5	60	367	573	206	13.2	364	391
Y 10	30	10	60	404	601	197	11.9	399	441
Y 15	25	15	60	491	606	115	9.7	488	512

Raman spectra of the glass series  $(40-x)\text{PbO}-x\text{Y}_2\text{O}_3-60\text{P}_2\text{O}_5$  are shown in Fig. 3. The spectrum of the parent  $40\text{PbO}-60\text{P}_2\text{O}_5$  glass shows two vibrational bands in the high-frequency region with a maximum at  $1146\text{ cm}^{-1}$  and  $1269\text{ cm}^{-1}$  ascribed to the symmetric and asymmetric stretching vibration of non-bridging phosphate atoms in  $\text{Q}^2$  units (or  $\text{P}=\text{O}$  group in polymeric phosphate chains) and medium band with shoulder in the middle-frequency region at  $669\text{ cm}^{-1}$  ascribed to the vibrations of oxygen atoms in  $\text{P}-\text{O}-\text{P}$  bridges between metaphosphate ( $\text{Q}^2$ ) and diphosphate ( $\text{Q}^1$ ) units. The band of  $291\text{ cm}^{-1}$  on the Raman spectrum can be associated to bending vibrations of phosphate units. With increasing  $\text{Y}_2\text{O}_3$  content the dominant band at  $1146\text{ cm}^{-1}$  becomes weaker and shifts to shorter wavelengths up to  $1186\text{ cm}^{-1}$  at the glass with  $x=15\text{ mol}\%$   $\text{Y}_2\text{O}_3$ , which is probably due to partial transformation of  $\text{Q}^2$  into  $\text{Q}^3$  and  $\text{Q}^1$  phosphate species.

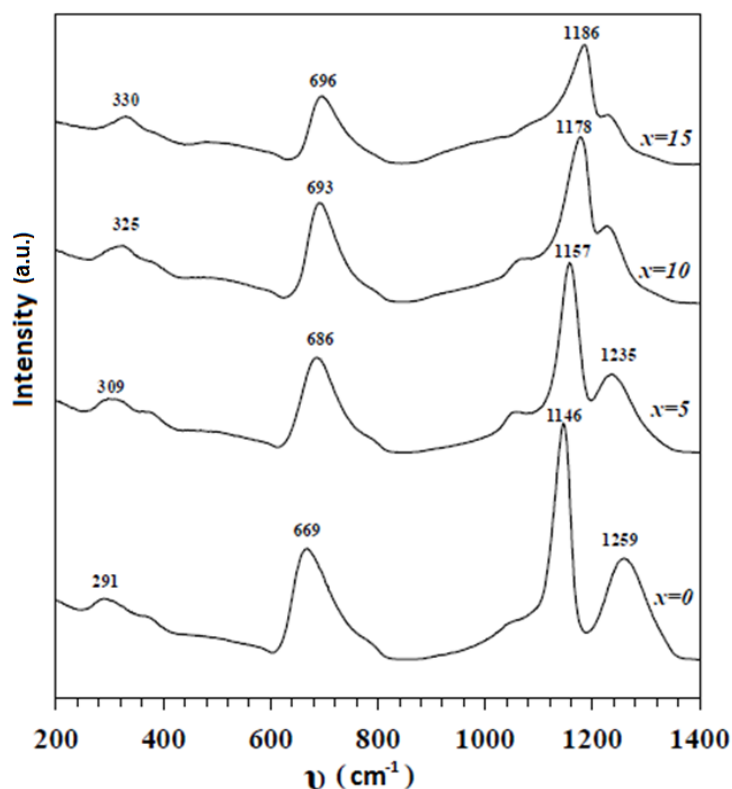


Figure 3. Raman spectra of the glass series  $(40-x)\text{PbO}-x\text{Y}_2\text{O}_3-60\text{P}_2\text{O}_5$

### Conclusion

Yttrium oxide is able to form glasses with the composition  $(40-x)\text{PbO}-x\text{Y}_2\text{O}_3-60\text{P}_2\text{O}_5$  in only a narrow concentration range of 0-15 mol%  $\text{Y}_2\text{O}_3$ , nevertheless the replacement of  $\text{PbO}$  by  $\text{Y}_2\text{O}_3$  leads to often significant changes in the physicochemical and thermal behaviour of these glasses. TD and DSC measurements showed that the incorporation of  $\text{Y}^{3+}$  ions into the structural network of the lead phosphate glasses results in an increase of the glass transition temperature and the crystallization temperature. The observed differences in the glass transition temperature indicate an increase in bonding strength with increasing  $\text{Y}_2\text{O}_3$  content. Raman spectra indicated that the structural network of the glasses is formed mainly from metaphosphate structural units  $\text{Q}^2$ . The addition of  $\text{Y}^{3+}$  ions into the structural network causes partial disproportionation of the phosphate groups according to  $2\text{Q}^2 \rightarrow \text{Q}^1 + \text{Q}^3$ .

### Acknowledgment

The authors are grateful for the financial support from the Grant Agency of the Czech Republic (Grant No. 13-00355S).

### Literature

1. Brow, R. K.: *J. Non-Cryst. Solids* 263-264, 1 (2000).
2. Brow, R. K., Tallant, D.: *J. Non-Cryst. Solids* 222, 396 (1997).
3. Koudelka, L., Mošner, P.: *Mater. Lett.* 421, 194 (1997).
4. Brow, R. K.: *J. Non-Cryst. Solids* 194, 267 (1996).
5. Brow, R. K.: *J. Am. Ceram. Soc.* 76, 913 (1993).
6. Smith, C. E., Brow, R. K., Montagne, L., Revel, B.: *J. Non-Cryst. Solids* 386, 105 (2014).
7. Tsuchida, J., Schneider, J., Rinke, M.T., Eckert, H.: *J. Phys. Chem.* 115, 21927 (2011).
8. Angel, P.W., Hann, R.E. J.: *Am. Ceram. Soc.* 75, 3278 (1992).
9. Zheng, W., Cheng, J., Tang, L.: *Thermochim. Acta* 456, 69 (2007).
10. Martin, R.A., Salmon P.S., Carroll D.L.: *J. Phys.: Condens. Matter.* 20, 115204 (2008).
11. Bacon, J.F.: NASA Contract. Rep., 1856 (1971).

## MECHANOCHEMICAL PREPARATION OF ALUMINA-CERIA

**JirátoVá K.**<sup>1</sup>, Spojakina A.<sup>2</sup>, Tyuliev G.<sup>2</sup>, Balabánová J.<sup>1</sup>, Kaluža L.<sup>1</sup>, Palcheva R.<sup>2</sup>

<sup>1</sup>*Institute of Chemical Process Fundamentals of the CAS, v.v.i, Prague, Czech Republic*

<sup>2</sup>*Institute of Catalysis, BAS, Sofia, Bulgaria*

*jiratova@icpf.cas.cz*

Ceria containing catalysts play an essential role in heterogeneous catalytic processes. However, ceria shows poor thermal stability and low specific surface area and therefore, many studies have been done to improve its properties by combination with other oxides. Alumina-ceria is substantial component of the three ways catalysts, due to the ceria ability to function as the buffer of oxygen and to enhance the oxygen storage capacity of the catalysts. Ceria in these catalysts also functions as structural promoting component, increasing alumina stability towards thermal sintering. Promising method of oxides preparation, very interesting and simple but not sufficiently studied yet is a mechanochemical synthesis. Here we report on the synthesis of nano-sized alumina, ceria and ceria-alumina of various compositions by a wet solid phase mechanochemical reaction of hydrous aluminum, and/or cerium nitrate with ammonium bicarbonate after addition of a small amount of water. The aim of this contribution is to study processes being in progress during synthesis of the mixed oxides, interaction between components and their mutual effect on the properties of resulting products. The phase evolution during mechanical milling and the subsequent heat treatment of precursors were studied by X-ray diffraction, DTA/TG, H<sub>2</sub>-TPR, NH<sub>3</sub>-TPD, CO<sub>2</sub>-TPD, N<sub>2</sub> adsorption at -195°C, IR, and XPS spectroscopy. Alumina and mixtures of alumina with different quantities of CeO<sub>2</sub> (1- 18 wt. %) were synthesized by mechanochemical method from aluminum nitrate, cerium nitrate and ammonia bicarbonate.

### Experimental

#### *Al, Al-Ce and Ce oxides preparation*

Aluminum oxide and aluminum/cerium mixed oxides were prepared by mechanochemical process from aluminum nitrate or from both aluminum and cerium (III) nitrate Ce(NO<sub>3</sub>)<sub>3</sub>·6H<sub>2</sub>O used in various proportions. The aluminum nitrate was first fused (m.p. 72.8°C) and after addition of NH<sub>4</sub>HCO<sub>3</sub> at 80 °C the mixture was grinded in an agate mill for 1 h. The reaction product was dried 20 h at 60°C and calcined 4 h at 500°C. Mixed aluminum-cerium and cerium oxide precursors were prepared similarly: Ce(NO<sub>3</sub>)<sub>3</sub>·6H<sub>2</sub>O was slowly added to the fused aluminum nitrate and then, NH<sub>4</sub>HCO<sub>3</sub> was added at 60°C; the mixture was grinded and further treated as described above. The products were labeled by the number of intended CeO<sub>2</sub> amount (wt. %) in the resulting oxides, e.g. Al<sub>2</sub>O<sub>3</sub>-18CeO<sub>2</sub>.

*Content of cerium* in the calcined precipitates was determined by chemical analysis using ICP-AES after dissolution of the samples in water solution of HCl.

*Surface area* was determined by nitrogen physisorption at -195°C using Micromeritics ASAP 2010 after drying the samples at 105°C and evacuating at 350°C (approximately 2–5 h).

*Thermogravimetry* (TG) and differential thermal analysis (DTA) of the selected dried samples were performed using a Setaram Setsys Evolution instrument. The heating rate 10°C min<sup>-1</sup>, air-flow rate of 75 ml min<sup>-1</sup> and 20-mg samples were used for the measurements. In the separate instrument equipped with a quadrupole mass spectrometer OmniStar (Pfeiffer Vakuu) the analysis of gaseous product evolving during calcination of the dried precipitates was performed under identical conditions as TG measurements were done. Gaseous products were continuously monitored for the mass numbers *m/z* (16-NH<sub>3</sub><sup>+</sup>, 18-H<sub>2</sub>O<sup>+</sup>, 30-NO, 44-CO<sub>2</sub>).

*X-Ray measurements* were performed using a Philips X'pert PW3020 instrument, equipped with a Cu K $\alpha$  Bruker AXS 2D Powder X-Ray analyzer with filtered CuK $\alpha$ <sub>1</sub> radiation ( $\lambda=0.154056$  nm), a graphite monochromator, and rate of 0.01° per 0.5 s.

*Infrared spectra* of the samples mixed with KBr at approximately 0.5 wt% concentration were recorded on a Nicolet Impact 400 FTIR spectrophotometer (Thermo Electron Corporation, USA). The spectra were taken in the region of 4000-400 cm<sup>-1</sup> at 0.4 cm<sup>-1</sup> resolution using 100 scans. Alumina absorption in the 400-1200 cm<sup>-1</sup> range was compensated by subtraction of a normalized spectrum of the equivalent amount of support from the spectra of the catalysts.

*Temperature-programmed reduction* (H<sub>2</sub>-TPR) of the calcined samples (0.025 g) were accomplished with an H<sub>2</sub>/N<sub>2</sub> mixture (10 molar% of H<sub>2</sub>) and a flow rate of 50 ml min<sup>-1</sup> with a linear temperature increase of 20 °C min<sup>-1</sup> up to 1000 °C. During the TPR measurement, the change in composition of H<sub>2</sub>/N<sub>2</sub> mixture was recorded by catharometer. Reduction of the grained CuO (0.16-0.315 mm) was performed to calculate the absolute values of the hydrogen consumed during the reduction.

*Temperature-programmed desorption of NH<sub>3</sub> and CO<sub>2</sub>* (NH<sub>3</sub>-TPD, CO<sub>2</sub>-TPD) was accomplished with a 0.050 g sample at 20-1000°C with a helium carrier gas and NH<sub>3</sub> or CO<sub>2</sub> as an adsorbing gas. Ten doses (912  $\mu$ l each) of

NH<sub>3</sub> (or CO<sub>2</sub>) were applied to the catalyst sample at 30°C before flushing of the sample with helium for 1 h and heating with ramp rate 20°C min<sup>-1</sup>. The mass contributions (*m/z*) 16-NH<sub>3</sub><sup>+</sup> or 44-CO<sub>2</sub> was collected using an Omnistar mass spectrometer (Pfeiffer Vakuu).

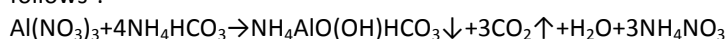
XPS measurements were performed with an ESCALAB-Mk II (VG Scientific) electron spectrometer with a base pressure of ~5.10<sup>-8</sup> Pa. The samples were excited with AlK $\alpha$  radiation (*hν*=1486.6 eV). The total energy resolution of the instrument was 1.2 eV as measured by the FWHM of the Ag 3d<sub>5/2</sub> photoelectron line. The following photoelectron lines were recorded: C 1s, O 1s, Al 2p, Ce 3d<sub>3/2</sub>, and Ce 3d<sub>5/2</sub>. All binding energies were related to the C 1s photoelectron line centered at 285.0 eV. The surface atom concentrations were evaluated using the photoelectron peak areas divided by the corresponding sensitivity factors taken from<sup>1</sup>.

## Results and discussion

In addition to pure alumina and ceria, eight alumina-ceria mixed oxides samples with various CeO<sub>2</sub> and Al<sub>2</sub>O<sub>3</sub> concentrations were prepared mechanochemically. Concentration of cerium oxide in the alumina samples varied from 0.05 to 18 wt. %. Small deviation of the real CeO<sub>2</sub> concentrations from the intended was found which could be accounted to inaccuracies caused by losses during samples preparation.

The precipitates produced by mechanochemical reaction of the corresponding nitrates with NH<sub>4</sub>HCO<sub>3</sub> differed in dependence on their composition. In case of Al and Al-Ce nitrates, the use of ammonium bicarbonate as a precipitating agent resulted in a voluminous white precipitates, while yellowish precipitate was obtained in case of Ce(III) nitrate. SEM images of the Al ions precipitate, of the mixed Al-Ce precipitate having 18 wt. % CeO<sub>2</sub> and Ce ions precipitate prepared mechanochemically showed that dried alumina precipitate consists of nearly spherical particles, while pure Ce precipitate formed substantially larger platelets. The shape of the particles and sizes of the mixed Al<sub>2</sub>O<sub>3</sub>-18CeO<sub>2</sub> sample resembled that of pure alumina precipitate. The finding is in accord with the data published by Djuricic and Pickering<sup>2</sup> who found that amorphous precipitates such as aluminum hydroxide consisted of spherical particles whereas crystalline precipitates often contained faceted particles. Agglomeration of primary particles of amorphous precipitate in a suspension usually proceeds to form densely packed agglomerates. The agglomerates often have a narrow size distribution and tend to be spherical when the precipitates were amorphous. Agglomerate diameters up to 1 micron are frequently obtained. Akinc and Sordelet<sup>3</sup> and Chen and Chen<sup>4</sup> prepared non-spherical well-crystalline Ce(OH)CO<sub>3</sub> microplates as the precursor particles. The shape of the Ce(OH)CO<sub>3</sub> microplate was sustained<sup>5</sup> after thermal decomposition/oxidation to CeO<sub>2</sub>.

Crystal structure and phase identification of the mechanochemically prepared precursors, dried at 60°C, are analyzed from the X-ray diffraction patterns. Fig. 1 shows diffraction lines of three samples: a) alumina with low amount of cerium (sample Al<sub>2</sub>O<sub>3</sub>-0.05CeO<sub>2</sub>), b) Al<sub>2</sub>O<sub>3</sub>-18CeO<sub>2</sub> and c) pure CeO<sub>2</sub>. Diffraction lines of the alumina precursor show peaks indicating rather low crystallinity of the sample. The main component is aluminum ammonium carbonate hydroxide NH<sub>4</sub>Al(OH)<sub>2</sub>CO<sub>3</sub> (PDF 71-1314), accompanied with a rest of unwashed ammonium nitrate (PDF 01-0809). The main chemical reaction of Al nitrate precipitation can be written as follows<sup>6</sup>:

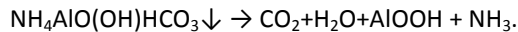


XRD analysis of the Al<sub>2</sub>O<sub>3</sub>-18CeO<sub>2</sub> precursor indicated that presence of ceria in the amount of 18 wt% led to formation of less crystalline precipitate than pure alumina precursor. In the precipitate, aluminum ammonium carbonate hydroxide NH<sub>4</sub>Al(OH)<sub>2</sub>CO<sub>3</sub> in the highest extent was found together with aluminum hydroxide gibbsite Al(OH)<sub>3</sub> (PDF 07-0324). Cerium in the precipitate appeared as cerium nitrate hydrate Ce(NO<sub>3</sub>)<sub>3</sub>·5H<sub>2</sub>O (PDF 22-0544).

XRD analysis of the dried Ce precipitate prepared by milling of Ce nitrate with ammonium bicarbonate revealed somewhat complicated picture. Following compounds containing cerium were identified: cerium carbonate hydroxide Ce(OH)CO<sub>3</sub> (PDF 41-0013), cerinite Ce<sub>2</sub>(CO<sub>3</sub>)<sub>3</sub>·6H<sub>2</sub>O (PDF 30-0295) and a small amount of cerium hydroxide Ce(OH)<sub>3</sub> (PDF 74-0665). Unfortunately, the peak found at 2 $\theta$ =8.170° having the highest intensity and the peak at 2 $\theta$ =18.4° was not possible to classify even using the XRD database from the 2011 year. All cerium compounds recognized in the dried precipitate occur in the (III) oxidation state and therefore, oxidation of Ce<sup>3+</sup> to Ce<sup>4+</sup> during precursor preparation did not take place like in case of precipitation of Ce nitrate with ammonium hydroxide at high pH values<sup>2</sup>. XRD analysis revealed no compounds containing nitrogen in this dried precipitate.

IR spectra of the dried precipitates confirmed presence of all ions in the compounds mentioned above. The large band centered at 3500 cm<sup>-1</sup> is assigned to the O-H stretching modes of interlayer water molecules and of H-bound OH groups, and the peak at 1630 cm<sup>-1</sup> is due to the bending mode of water molecules<sup>7</sup>. Intensities of the peaks are higher in the spectra of the samples containing alumina. Four weak bands at 850, 1100, 1354, and 1450 cm<sup>-1</sup> are characteristic of carbonate ions<sup>8</sup>. Three of them are visible in the spectra, only the band at

1354  $\text{cm}^{-1}$  is overlapped by the peak with maximum at 1380  $\text{cm}^{-1}$  ascribed to  $\text{NO}_3^-$  ion. Presence of  $\text{NH}_4^+$  ions in the solid samples is documented<sup>9</sup> by the peak centered at 3150  $\text{cm}^{-1}$  and at 1430–1390  $\text{cm}^{-1}$ . The highest concentrations of  $\text{NH}_4^+$  ions are observed in the samples in which aluminum ammonium carbonate hydroxide was identified. Ce precipitate showed the least concentration of ammonium ions, very likely, incorporated in the compound non-identified by XRD. After calcination of the as-prepared samples at 500 °C, poor peaks indicating low crystallinity of the high-concentrated alumina samples were observed (Fig. 2). Formation of the gamma- and/or eta-alumina could be assumed<sup>11</sup> in the calcined alumina precursor



As the cubic gamma-alumina (PDF 50-0741) and eta-alumina are hardly distinguishable, it cannot be surely concluded which of these two alumina phases are present in the examined catalysts. X-ray diffraction peaks at 28.54, 33.17, 47.462 and 56.278, characteristic of  $\text{CeO}_2$  in cubic fluorite structure (JCPDS data file 34-0394, 43-1002) and clearly seen in the XRD spectrum of the pure  $\text{CeO}_2$  sample (Fig. 2) are in good agreement with the data (28.58, 33.38, 47.58 and 56.48°) published previously<sup>11,12</sup>.

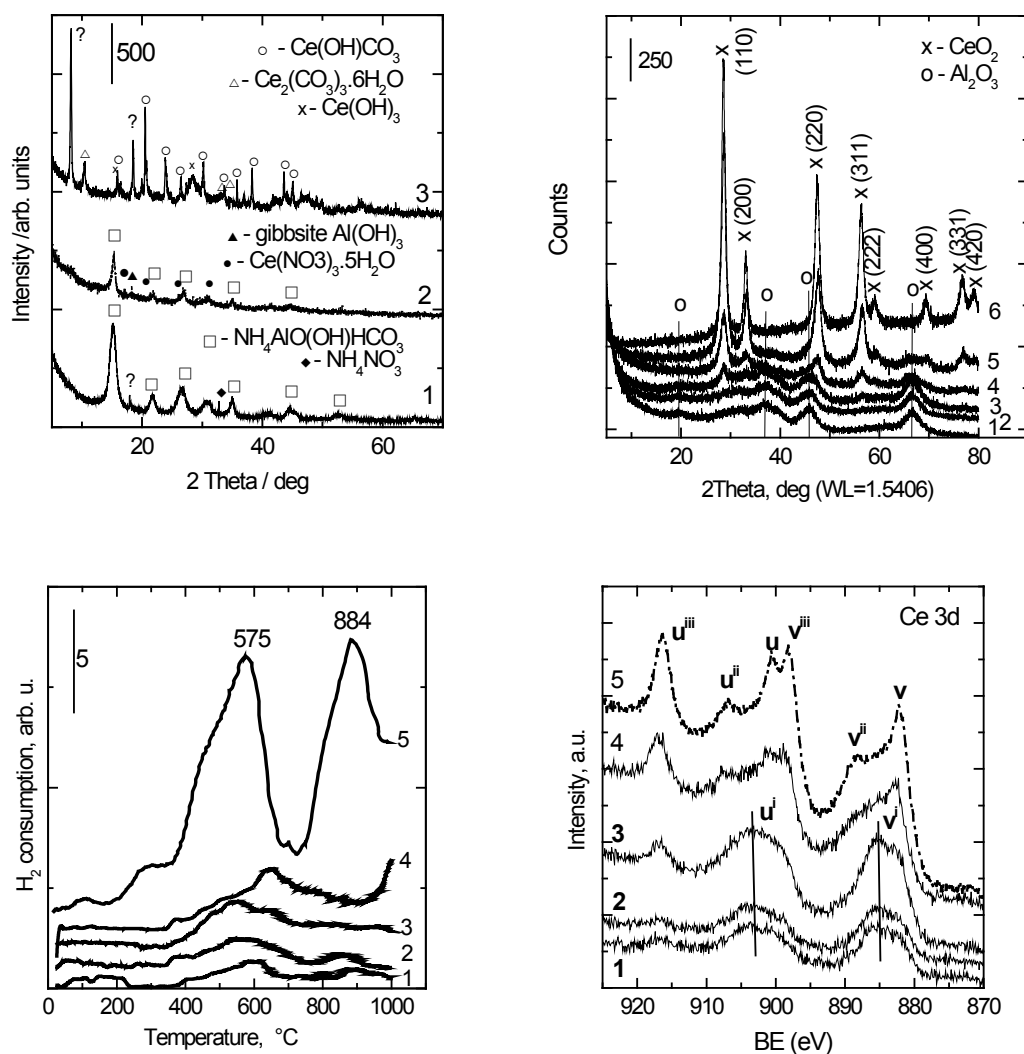


Figure 1. XRD patterns of the precursors: 1:  $\text{Al}_2\text{O}_3$ -0.5 $\text{CeO}_2$ , 2:  $\text{Al}_2\text{O}_3$ -18 $\text{CeO}_2$ , 3:  $\text{CeO}_2$

Figure 2. XRD patterns of the calcined precursors. 1:  $\text{Al}_2\text{O}_3$ , 2:  $\text{Al}_2\text{O}_3$ -0.5 $\text{CeO}_2$ , 3:  $\text{Al}_2\text{O}_3$ -1.5 $\text{CeO}_2$ , 4:  $\text{Al}_2\text{O}_3$ -4 $\text{CeO}_2$ , 5:  $\text{Al}_2\text{O}_3$ -10 $\text{CeO}_2$ , 6:  $\text{CeO}_2$

Figure 3. TPR profiles of the calcined precursors. 1:  $\text{Al}_2\text{O}_3$ -0.5 $\text{CeO}_2$ , 2:  $\text{Al}_2\text{O}_3$ -1.5 $\text{CeO}_2$ , 3:  $\text{Al}_2\text{O}_3$ -4 $\text{CeO}_2$ , 4:  $\text{Al}_2\text{O}_3$ -10 $\text{CeO}_2$ , 5:  $\text{CeO}_2$

Figure 4. XPS spectra of Ce 3d core electron levels for the calcined precursors. 1:  $\text{Al}_2\text{O}_3$ -0.05 $\text{CeO}_2$ , 2:  $\text{Al}_2\text{O}_3$ -1.5 $\text{CeO}_2$ , 3:  $\text{Al}_2\text{O}_3$ -4 $\text{CeO}_2$ , 4:  $\text{Al}_2\text{O}_3$ -10 $\text{CeO}_2$ . Dashed line corresponds to bulk  $\text{CeO}_2$ .

In the mixed  $\text{Al}_2\text{O}_3\text{-CeO}_2$  samples, the presence of nanocrystalline phase, cubic  $\text{CeO}_2$  (cerianite), is confirmed by (111) reflection at  $2\theta=33.3^\circ$ . Other intense  $\text{CeO}_2$  reflections (200 and 311) cannot be found because they are either not present or overlapped by  $\gamma$ -alumina (220) and (422) reflections. d-Spacing of  $\text{Al}_2\text{O}_3$  planes (Table 2) gradually decreases with increasing amount of ceria added to the alumina and is the lowest for the sample containing 10 wt. %  $\text{CeO}_2$ . The value found for pure ceria is higher than that for the mixed Al-Ce oxides but lower than for pure alumina. In contrast to Sasikala et al.<sup>13</sup>, formation of  $\text{CeAlO}_3$  was not observed by XRD. The finding is very likely connected with high dispersion of  $\text{Al}_2\text{O}_3$  in which cerium is included.  $\text{CeAlO}_3$  could exist as a dispersed phase where  $\text{Ce}^{4+}$  is stabilized in cation vacancies on the alumina surface or is inserted and forms solid solution. Presence of  $\text{CeO}_2$  in alumina stabilizes its structure. Very likely, cerianite starts nucleating at the defects of oxygen (oxygen vacancies) forming bridges with  $\text{O}_2$  between  $\text{Al}_2\text{O}_3$  and  $\text{CeO}_2$  saving alumina structure, as  $\text{Ce}^{4+}$  (ionic radius  $\text{Ce}^{4+}=0.092$  nm) can substitute  $\text{Al}^{3+}$  (ionic radius  $\text{Al}^{3+}=0.051$  nm) in  $\text{Al}_2\text{O}_3$  structure.  $\text{CeO}_2$  continues to grow with its increasing content in alumina forming bulk cubic  $\text{CeO}_2$  nanocrystals<sup>14</sup>.

Thermogravimetric mass-loss measurements accompanied with mass spectrometry of effluent of the three selected precursors,  $\text{Al}_2\text{O}_3\text{-0.05CeO}_2$ ,  $\text{Al}_2\text{O}_3\text{-18CeO}_2$ , and  $\text{CeO}_2$  were done to find temperature ranges in which transformation of the precursor proceeds. Transformation of the dried Ce precipitate proceeded in the narrow temperature range  $194\text{-}275^\circ\text{C}$ . In these temperatures, substantial part (26.3 %) of the total weight loss (35.6 %) was realized. Maximum rate of the weight loss caused by exothermic reaction, probably decomposition of ammonium nitrate, was found at  $T_{\text{max}}=206^\circ\text{C}$ . In the gas effluent formed at  $170^\circ\text{C}$ , the mass spectrometer detected masses  $m/z$  16 ( $\text{NH}_3$ ), 18 ( $\text{H}_2\text{O}$ ), 30 ( $\text{NO}$ ), and 44 ( $\text{CO}_2$ ). The findings indicate that apart from sample dehydration, decomposition of carbonates e.g. cerium carbonate hydroxide  $\text{Ce}(\text{OH})\text{CO}_3$  and/or cerinite  $\text{Ce}_2(\text{CO}_3)_3\cdot 6\text{H}_2\text{O}$  proceeds. Appearance of ammonia in the effluent reveals presence of small amount of ammonium salts in the precursor, e.g.  $\text{NH}_4\text{NO}_3$ . In contrast to relatively simple process of thermal transformation of the Ce precursor, the alumina sample containing negligible amount of  $\text{CeO}_2$  ( $\text{Al}_2\text{O}_3\text{-0.05CeO}_2$ ) showed behavior that is more complex. Dehydration of the sample was in progress at  $71^\circ\text{C}$  what is proved by 9 % of weight loss and presence of the gas with  $m/z=18$  in this DTG peak. Two maxima of  $\text{H}_2\text{O}$  appearance were observed in the effluent at  $222$  and  $285^\circ\text{C}$  connected with the loss of water produced by dehydroxylation of the hydroxides. Another 33.5 % of mass loss was observed in this temperature range. As ammonia was detected in the effluent in the first peak ( $T_{\text{max}}=222^\circ\text{C}$ ), decomposition of aluminum ammonium carbonate hydroxide  $\text{NH}_4\text{Al}(\text{OH})_2\text{CO}_3$ , found in the dried precipitate by XRD, has to proceed. In the second peak of the effluent,  $\text{CO}_2$  ( $m/z=44$ ) was identified, and therefore, carbonates are decomposed. Mass spectroscopy also identified some amount of  $\text{NO}$  (temperature range  $250\text{-}550^\circ\text{C}$ ) arising due to decomposition of nitrate ion.

TG/DTA analysis of the sample containing 18 wt%  $\text{CeO}_2$  resembles the analysis of the pure alumina sample with some marks of  $\text{CeO}_2$  analysis. Up to  $152^\circ\text{C}$ , weight loss 22.6 % was found, and another 22.2 % was observed up to  $227^\circ\text{C}$ . The rest of 9.6 % of weight loss was observed up to  $868^\circ\text{C}$ . Two main endothermic peaks with  $T_{\text{max}}$  139 and  $206^\circ\text{C}$  correspond to dehydroxylation and decomposition of aluminum ammonium carbonate hydroxide  $\text{NH}_4\text{Al}(\text{OH})_2\text{CO}_3$ . Nitrates in cerium nitrate hydrate  $\text{Ce}(\text{NO}_3)_3\cdot 5\text{H}_2\text{O}$  could be decomposed in higher temperature range with  $T_{\text{max}}=282^\circ\text{C}$ .

Porous structure measurement of the calcined precipitates confirmed high surface area (Table I) of the pure aluminum oxide ( $285\text{ m}^2\text{g}^{-1}$ ). Increasing amount of ceria in the mixed alumina-ceria resulted in a gradual, non-linear decrease in the surface area, pure ceria surface area being the lowest ( $70\text{ m}^2\text{g}^{-1}$ ). The observed decrease in the surface area with increasing concentration of ceria does not correspond with the weight parts of both components (alumina and ceria) in the mixed oxides, as the decrease in the mixed oxides surface area is more substantial. The phenomenon can be likely caused either by formation of a new compound based on alumina-ceria or by changes in primary particles size. Volume of micropores gradually decreased with increasing ceria concentration in the Al-Ce mixtures from  $52\text{ mm}^3\text{g}^{-1}$  (calcined aluminum oxide) to  $13.8\text{ mm}^3\text{g}^{-1}$  (ceria). The findings are very likely connected with the size of primary particles. The micropores are formed in the space among the smaller primary particles and these were found in the samples with high concentration of aluminum hydroxide. A larger space among the larger platelets of dried Ce precipitates exists and therefore, larger diameter of pores can be observed. Volume of mesopores, similarly as the average diameter of pores, did not change substantially with the varying composition of the supports.

Table I

Amount of CeO<sub>2</sub>, crystalline phase in the precursors, lattice parameter *d* of the cubic oxides and characteristic values of porous structure of the calcined Al-Ce mixed oxides

Sample	CeO <sub>2</sub> [wt.%]	Crystalline phase [%]	<i>d</i> [nm]	S <sub>BET</sub> [m <sup>2</sup> g <sup>-1</sup> ]	V <sub>meso</sub> [cm <sup>3</sup> g <sup>-1</sup> ]	V <sub>micro</sub> [mm <sup>3</sup> g <sup>-1</sup> ]	D [nm]
Al <sub>2</sub> O <sub>3</sub>	0.01	Amorphous	1.9835	285	0.56	52.2	6.7
Al <sub>2</sub> O <sub>3</sub> -0.05CeO <sub>2</sub>	0.05	23.4	1.9770	259	0.56	47.2	7.6
Al <sub>2</sub> O <sub>3</sub> -1.5CeO <sub>2</sub>	1.74	23.5	1.9641	285	0.53	50.1	6.3
Al <sub>2</sub> O <sub>3</sub> -4CeO <sub>2</sub>	4.09	36.5	1.9100	237	0.52	45.5	7.8
Al <sub>2</sub> O <sub>3</sub> -10CeO <sub>2</sub>	10.5	63.3	1.9048	169	0.44	30.0	8.8
CeO <sub>2</sub>	100	74.3	1.9142	70	0.15	13.8	5.8

$$D=4V_{\text{meso}}/S_{\text{BET}}$$

IR spectra of the prepared oxides, excluding spectrum of CeO<sub>2</sub>, revealed very similar picture. Broad absorption in the region 450–800 cm<sup>-1</sup>, characteristic of the gamma-Al<sub>2</sub>O<sub>3</sub> phase<sup>15</sup>, was detected in the spectrum of the synthesized alumina. The band with maximum at 1120 cm<sup>-1</sup> is connected with the deformation vibrations of OH<sup>-</sup> groups on the Al<sub>2</sub>O<sub>3</sub> surface. Absorption in the region 450–800 cm<sup>-1</sup> was significantly increased in the sample containing 0.5 and 1.5 wt. % CeO<sub>2</sub> and this band could be connected with formation of Al-O aluminate bond. In the spectrum of the sample having substantially higher concentration of CeO<sub>2</sub> (Al<sub>2</sub>O<sub>3</sub>-10CeO<sub>2</sub>), the band at 670 cm<sup>-1</sup>, observed in the spectrum of the pure CeO<sub>2</sub>, was also seen. In the literature, the band at 700 cm<sup>-1</sup> was observed in IR spectrum of pure ceria, and it was ascribed to the envelope of the phonon band of the metal oxide (CeO<sub>2</sub>) network<sup>16</sup>. The shift in the band position can be caused by different procedure of the sample preparation. Decrease in the intensity of the 1120 cm<sup>-1</sup> band with increasing concentration of CeO<sub>2</sub> in the mixed oxides permits to suggest that this phase, lowering the number of surface Al-OH groups, is present on the sample surface. The bands around 1170–1000 and 960–850 cm<sup>-1</sup> could be associated with the formation of „carbonate-like“ species on the ceria surface<sup>17</sup>.

Temperature programmed reduction patterns of the synthesized oxides are presented in Fig. 3. Two main reduction regions are observed in the TPR profile of CeO<sub>2</sub>. The two principal regions appear at 300–600 °C with T<sub>max</sub> 520–550 °C and at 750–1000 °C with T<sub>max</sub> around 850 °C. The two reduction regions are characteristic of ceria reduction and they are attributed to the reduction of Ce<sup>4+</sup> to Ce<sup>3+</sup> (maximum at about 525 °C) and bulk ceria reduction (maximum at 875 °C), respectively<sup>18,19</sup>. In the literature, following reduction maxima can be found in the TPR profiles for ceria: two main reduction peaks at 577 and 886 °C together with a shoulder at 269 °C. The shoulder at 269 °C can be attributed to the reduction of surface cerium oxide<sup>18</sup> and thus, it corresponds to the reduction of Ce<sup>4+</sup> to Ce<sup>3+</sup>. The peak at 577 °C is ascribed to reduction of CeO<sub>2</sub>, for this peak was identified as the main peak in the TPR profiles of CeO<sub>2</sub>-Al<sub>2</sub>O<sub>3</sub> supports with different CeO<sub>2</sub> loading after calcination at 500 °C<sup>12</sup>. The peak observed at 438 °C was attributed to the reduction of surface cerium oxide<sup>20</sup>. The peak at 560 °C was ascribed to the reduction of bulk CeO<sub>2</sub>; this peak was identified as the main peak in the TPR profiles of CeO<sub>2</sub>-Al<sub>2</sub>O<sub>3</sub> supports with different CeO<sub>2</sub> loading and calcined at 500 °C<sup>21</sup>.

High mobility of surface oxygen species in ceria is known, and for that reason, oxygen can be removed under reduction atmosphere forming<sup>22</sup> non-stoichiometric ceria CeO<sub>2-x</sub>. At low temperature, the surface oxygen ions can be removed more easily than bulk oxygen, which requires transportation to the surface before reduction. The TPR results show that the major part of oxygen ions in the Al-Ce mixed oxides is more mobile than those in the pure CeO<sub>2</sub> are, as the reduction process proceeds more easily, i.e. at lower temperatures. The shift of the reduction peaks to lower temperature indicates interaction between the oxides in their mixture. Only the sample with 18 wt. % CeO<sub>2</sub> is reduced with more difficulty than the other samples (Fig. 3). The phenomenon could be connected<sup>23</sup> with partial reduction of Ce<sup>4+</sup> to Ce<sup>3+</sup> during precursor decomposition in the stage of its calcination Ce-(H<sub>2</sub>O) → Ce<sup>3+</sup>-OH + H<sup>+</sup>.

The obtained reduction curves were integrated in two temperature ranges, the first one being 25–500 °C (interesting for catalytic reactions), the second one 25–1000 °C. The highest amount of hydrogen consumed in the temperature range 25–500 °C was found with pure ceria (0.48 mmol g<sup>-1</sup>), while the lowest one (0.08 mmol g<sup>-1</sup>) showed the sample with the lowest concentration of ceria. In accord with expectation, the mixed Al-Ce oxides samples showed reducibility within these two limits.

NH<sub>3</sub>-TPD of the calcined precipitates proceeded in the temperature range of 25–350 °C only. It indicates that the oxides do not comprise very strong acidic sites. The principal part of the sites can be ascribed to the sites of very low acidity with a distinct desorption peak at about 60 °C. Low acidity was also observed in case of pure alumina, which comprises, apart from very weak sites, slightly stronger sites appearing as a shoulder at about

148 °C. The shoulder decreases with increasing amount of CeO<sub>2</sub>. Acidity of the pure alumina was lower (0.28 mmol g<sup>-1</sup>) than that observed with Sasol alumina (around 0.35 mmol g<sup>-1</sup>) prepared by other method. Increasing concentration of ceria in alumina led to decreased amount of the sites with low acidity. Basicity of all prepared samples determined by CO<sub>2</sub>-TPD was in all cases higher than their acidity. The amount of basic sites in alumina-ceria samples increased with increasing amount of ceria in the samples. Pure ceria showed, however, lower basicity than that of the mixed Al<sub>2</sub>O<sub>3</sub>-10CeO<sub>2</sub> sample. This finding is in accord with its higher acidity.

XPS spectra of Ce 3d core electron levels for Al<sub>2</sub>O<sub>3</sub>-CeO<sub>2</sub> mixed oxides with varying CeO<sub>2</sub> loadings after calcination at 500°C are shown in Fig. 4. The XPS spectrum of bulk CeO<sub>2</sub> is complex, consisting of six components, corresponding to three pairs of spin-orbit doublets: *v* represents the Ce 3d<sub>5/2</sub> contribution, and *u* represents the Ce 3d<sub>3/2</sub> contribution<sup>24</sup>. It is seen that XPS spectra of the Al<sub>2</sub>O<sub>3</sub>-CeO<sub>2</sub> mixed oxides are different from that of the pure CeO<sub>2</sub>, and depend on the CeO<sub>2</sub> loading. The broadening of the XPS lines for oxide samples suggests the presence of several surface cerium oxide species; a new weak band (*v*<sup>j</sup>) at about 885.4 eV appears in the samples with 0.5-4 wt% CeO<sub>2</sub>. The increasing intensity of the *v*<sup>j</sup> band and disappearance of *v*<sup>ii</sup> with increasing CeO<sub>2</sub> loading (up to 4 wt. %) points out that cerium at low content (0.5-4 wt. %) is in a reduced state (III). In addition, it should be noted that some photoreduction of Ce<sup>4+</sup> might take place during exposure of the samples to a high X-ray flux under ultra-high vacuum employed during data acquisition. It is seen in Fig. 4 that the intensity of *u*<sup>iii</sup> increases with increasing CeO<sub>2</sub> loading, what means an increase in the relative amount of Ce(IV). We can thus conclude that the Ce<sup>4+</sup>/Ce<sup>3+</sup> redox couple exists on the surface of the Al<sub>2</sub>O<sub>3</sub>-18CeO<sub>2</sub> mixed oxide. It should suggest formation of CeO<sub>2</sub> crystallites, whose presence were proved by XRD in this sample. The XPS atomic ratios of Ce/(Ce+Al) for the calcined mixed oxides are listed in Table II. The data demonstrate that

Table II  
Surface concentrations of Al, O and Ce (at%) in the Al<sub>2</sub>O<sub>3</sub>-CeO<sub>2</sub> mixed oxides

Sample	Al 2p	O 1s	Ce 3d	Ce/(Ce+Al) <sup>a</sup>	Ce/(Ce+Al) <sup>b</sup>
Al <sub>2</sub> O <sub>3</sub>	36.23	53.72	0	0	0.000
Al <sub>2</sub> O <sub>3</sub> -0.05CeO <sub>2</sub>	35.72	52.06	0.19	0.005	0.0001
Al <sub>2</sub> O <sub>3</sub> -1.5CeO <sub>2</sub>	36.15	53.02	0.25	0.007	0.005
Al <sub>2</sub> O <sub>3</sub> -4CeO <sub>2</sub>	35.58	52.93	0.40	0.011	0.012
Al <sub>2</sub> O <sub>3</sub> -10CeO <sub>2</sub>	36.35	54.08	0.64	0.017	0.034
CeO <sub>2</sub>	0	48.64	18.85	1	1.000

<sup>a</sup> Atomic ratio calculated from XPS, <sup>b</sup> Atomic ratio based on chemical analysis

the Ce/(Ce+Al) ratios in surface layers increase with increasing CeO<sub>2</sub> loading. Surface concentration of cerium is higher than concentration in bulk for the samples having low cerium concentration (< 4 wt. %). With increasing CeO<sub>2</sub> loading bulk concentration is higher than the surface what confirms formation of separated CeO<sub>2</sub> crystallites in the calcined precipitates.

## Conclusions

Pure alumina, pure ceria and mixtures of both oxides having 0.05 up to 18 wt. % CeO<sub>2</sub> were prepared mechanochemically from aluminum and/or cerium nitrates with ammonia bicarbonate. Aluminum ammonium carbonate hydroxide NH<sub>4</sub>Al(OH)<sub>2</sub>CO<sub>3</sub> was found to be main product in the dried Al precipitate, while cerium carbonate hydroxide Ce(OH)CO<sub>3</sub> was prevailing in the dried Ce precipitate. After calcination at 500 °C, amorphous structure of alumina and cubic fluorite crystallites of ceria with preferred orientation along (1 1 1) direction were detected by XRD. XPS spectrum confirmed the existence of Ce<sup>4+</sup> oxidation states in the calcined mixed oxides when concentration of CeO<sub>2</sub> is higher than 6 wt. %. Surface acidity of the mixed oxides prepared mechanochemically is lower than that observed at oxides prepared by other methods because of presence of adsorbed ammonia on the surface. IR spectroscopy results are in accord with the findings. Addition of CeO<sub>2</sub> to alumina slightly decreases surface area and mesopore volume of the resulting mixed oxides. Surface concentration of Ce in the mixed Al-Ce oxides increases faster with increasing bulk Ce concentration than could be expected from the data of chemical analysis. The reason is likely the insertion of Ce ions into the Al<sub>2</sub>O<sub>3</sub> lattice. Mechanochemical procedure of the Al-Ce mixed oxide preparation is relatively simple and facile which does not produce large quantities of wastewaters influencing unfavorably the life environment. Moreover, due to the use of initial reactants (nitrates and ammonium salt) the products do not contain sodium, which is very often not advantageous in catalytic supports. The products are suitable as supports of heterogeneous catalysts for hydrodesulfurization reactions or directly as catalysts for total oxidation reactions.

## Acknowledgment

This work was carried out in the framework of bilateral Czech-Bulgarian scientific cooperation and was supported by Czech Science Foundation (grant GA 14-13750S).

## Literature

1. Scofield J.H.: J Electron Spectrosc. Relat. Phenom. 8, 129 (1976).
2. Djuricic B., Pickering S.: J. Euro. Ceram. Society 19, 1925 (1999).
3. Akinc M., Sordelet D.: Adv. Ceram. Mat. 2, 232 (1987).
4. Chen P.L., Chen L.W.: J. Am. Ceram. Soc. 76, 1577 (1993).
5. Guo Z., Du F., Li G., Cui Z.: Inorg. Chem. 45, 4167 (2006).
6. Zhisen Wu, Youde Shen, Yan Dong, Jianqing Jiang: J. Alloys Comp. 467, 600 (2009).
7. Zhu Y., Li H., Kolytyn Y., Gedanken A.: J. Mater. Chem. 12, 729 (2002).
8. Labajos F.M., Sastre M.D., Trujillano R., Rives V.: J. Mater. Chem. 9, 1033 (1999).
9. Nakanishi Koji, Solomon P.H.: *Infrared Absorption Spectroscopy*, 2nd edn., Holden-Day Inc., San Francisco, 1977.
10. Wefers K., Misra Ch.: Technical Report No. 19 Revised. Alcoa Laboratories (1987).
11. Fathi M., Bjorgum B., Viig T., Rockstad O.N.: Catal. Today 63, 489 (2000).
12. Santos A.C.S.F., Damyanova S., Texeira G.N.R., Mattos L.V., Noronha F.B., Passos F.B., Bueno J.M.C.: Appl. Catal. A 290, 123 (2005).
13. Sasikala R., Sudarsan V., Kulshreshtha S.K: J. Solid State Chem. 169, 113 (2002).
14. Jun Fang, Xinzhen Bi, Dejun Si, Zhiquan Jiang, Weixin Huang: Appl. Surf. Sci. 253, 8952 (2007).
15. Uvarov A.V., Antipina T.V., Tihomirova S.P.: Zhur. Fiz. Khim. (Rus) 41, 3059 (1967).
16. Zawadzki M.: J. Alloys Comp. 454, 347 (2008).
17. Suresh R., Ponnuswamy V., Mariappan R.: Appl. Surf. Sci. 273, 457 (2013)
18. Ranga Rao G., Mishra B.G.: Bull. Catal. Soc. India 2,122 (2003)
19. Martin D., Duprez D.: J. Phys. Chem. 100, 9429 (1996).
20. Bernal S., Calvino J.J., Cauqui M.A., Gatica J.M., Larese C., Perez-Omil J.A., Pintado J.M.: Catal. Today 50, 175 (1999).
21. Trovarelli A., Dolcetti G., Leitenburg C., Kaspar J., Finetti P., Santoni A.: J. Chem. Soc. Faraday Trans. 88, 1311 (1992).
22. Hardacre C., Ormerod R.M., Lambert R.M.: J. Phys. Chem. 98, 10901 (1994).
23. Araujo A.S., Aquino J.M.F.B., Souza M.J.B, Silva A.O.S.: J. Solid. State Chem. 171, 371 (2003).
24. Burroughs P., Hamnett A., Orchard A.F., Thornton G.: J. Chem. Soc. Dalton Trans. 17, 1686 (1976).

## PYROCHLORES OF LANTHANIDES DOPED BY ZIRCONIA

**Hablovičová B.**, Šulcová P.

University of Pardubice, Faculty of Chemical Technology, Department of Inorganic Technology, Studentská 573, 532 10, Pardubice  
blanka.hablovicova@student.upce.cz

### Introduction

Many of ceramic pigments used in ceramic industry contain transition and heavy metals. Interest of environmental pigments without toxic elements (such as e.g. Pb, Hg, Cd, Sb, As or Cr) is growing for this reason. These are mainly materials where transition elements are exchanged by lanthanides<sup>1</sup>. Lanthanide zirconates with pyrochlore structure have very interesting properties and therefore they paid great attention<sup>2-4</sup>. Pyrochlores are characterized by composition  $A_2B_2O_7$  with space group  $Fd\bar{3}m$ <sup>5</sup>. Many of these compounds have been prepared by combination of the various  $A^{3+}$  and  $B^{4+}$  ions<sup>6</sup>. Lanthanide ions were used as  $A^{3+}$  ions and  $Ce^{4+}$  with  $Zr^{4+}$  were used as  $B^{4+}$  ions. Lanthanide oxides are polymorphic. They are characterized by three forms at temperatures lower than 2000 °C: A form (hexagonal), B form (monoclinic) and C form (cubic). At temperatures above 2000 °C forms H and X are found<sup>7</sup>. Lanthanide oxides are stable with composition  $Ln_2O_3$  except  $CeO_2$ ,  $Pr_6O_{11}$  and  $Tb_4O_7$ . Melting points are ranging about 2400 °C and their refractive indexes have interval from 1.90 to 1.99<sup>8,9</sup>.  $ZrO_2$  has three solid polymorphic phases at atmospheric pressure. Monoclinic is stable at temperatures below 1170 °C, tetragonal is stable between 1170 - 2370 °C and cubic is stable above 2370 °C<sup>10</sup>. Refractive index varies by modification, for tetragonal and cubic is 2.19 and for monoclinic has value 2.24<sup>11</sup>. This article is focused on environmental friendly pigments based on lanthanide zirconates with pyrochlore structure  $Ln_2CeZrO_7$  ( $Ln = Nd, Sm, Gd, Dy, Er, Yb$  and  $Y$ ) prepared by solid-state reaction. Particle size distribution, color properties, band gaps and phase composition were determined.

### Experimental

Compounds with general formula  $Ln_2CeZrO_7$  ( $Ln = Nd, Sm, Gd, Dy, Er, Yb, Y$ ) were prepared by solid-state reaction. As starting materials were used  $CeO_2$  (99.5 %, ML chemica, CZ),  $Nd_2O_3$ ,  $Sm_2O_3$ ,  $Gd_2O_3$ ,  $Dy_2O_3$ ,  $Er_2O_3$ ,  $Yb_2O_3$ ,  $Y_2O_3$  (all 99.9 %, Alfa Aesar) and  $ZrO_2$  (98.5 %, Roudnice nad Labem, CZ). Calcination was carried out at temperatures 1400, 1450 and 1500 °C for 3 hours (heating rate was 10 °C·min<sup>-1</sup>). Obtained pigments were applied into organic matrix (dispersive acrylic paint Parketol, Balakom, CZ) in mass tone and pigments, which were calcined at 1500 °C, were applied into ceramic glaze G 070 91 (Glazura, Roudnice nad Labem, CZ) in 10 wt.% (calcination at 1000 °C for 15 min, heating rate 10 °C·min<sup>-1</sup>).

Particle size distribution of powder materials was measured by Mastersizer 2000/MU (Malvern Instruments, UK). Signal was evaluated by Fraunhofer bend. Spectrophotometer ColorQuest XE (HunterLab, USA) was used for color measurements (geometry d/8°). Device used color system CIE  $L^*a^*b^*$  for measure,  $L^*$  represents lightness and coordinates  $a^*$  and  $b^*$  describe color hues. Coordinate  $a^*$  indicates color hue from green ( $-a^*$ ) to red ( $+a^*$ ) and color hue from blue ( $-b^*$ ) to yellow ( $+b^*$ ) is characterized by coordinate  $b^*$ . Chroma  $C$ , which shows saturation of sample, was calculated from equation 1. Degree of color tone  $H^\circ$  (Figure 1) has interval from 0° to 360° (350-0-35° = red, 35-70° = orange, 70-105° = yellow, 105-195° = green, 195-285° = blue, 285-350° = violet) and it is denoted by equation 2<sup>12</sup>. Band gaps (Figure 2), which correspond with colors, were calculated by Kubelka-Munk theory from spectrophotometric data (transferring data to  $K/S$ ). It is equation 3, where  $K$  is effective absorption and  $S$  is scattering coefficient<sup>13,14</sup>. Phase composition of the most interesting compounds was measured by diffractometer D8 Advance (Bruker AXS, UK) with vertical goniometer and in range 10-80°.

$$C = (a^{*2} + b^{*2})^{1/2} \quad (1)$$

$$H^\circ = \arctg\left(\frac{b^*}{a^*}\right) \quad (2)$$

$$F(R_\infty) \equiv \frac{(1 - R_\infty)^2}{2 \cdot R_\infty} \equiv \frac{K}{S} \quad (3)$$

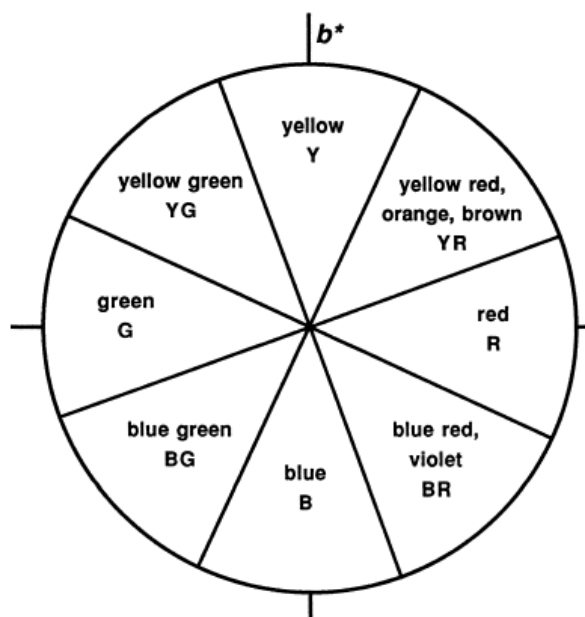


Figure 1. CIEL\*a\*b\* color plane<sup>12</sup>.

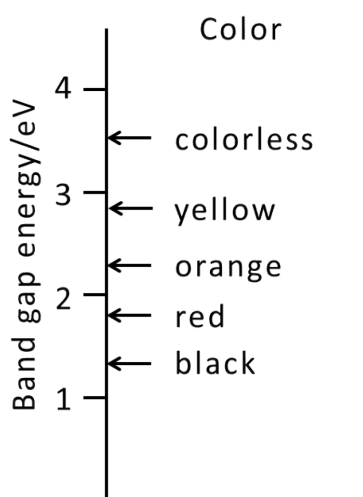


Figure 2. Color corresponding to band gap<sup>14</sup>.

### Results and discussion

Prepared compounds were applied into organic matrix in mass tone at first. Table I contains color coordinates  $a^*$  and  $b^*$  which correspond with degree of color tone in Table II. Color coordinates  $b^*$  are positive for all prepared compounds. Pigment doped by neodymium has green shades at all calcination temperatures which prove color coordinate  $a^*$  in range from -7.95 to -8.74 (decreasing with temperature) and degree of color tone with values from 125.34° to 131.36°. These pigments have the lowest values of lightness from all samples (75.73 - 78.75). Color of pigments doped by erbium exhibits pink shades due to high values of coordinate  $a^*$  (11.96 - 12.61) which is connected with degree of color tone (28.93 - 31.47). Other pigments are characterized

by very low or negative values of coordinate  $a^*$  which mean yellow or yellow-green colors and degrees of color tone are ranging from  $82.88^\circ$  to  $97.60^\circ$ . Pigments are very light except  $\text{Nd}_2\text{CeZrO}_7$  ( $L^* = 85.85 - 92.61$ ), but all of them obtained low values of chroma, only from 9.08 to 23.23.

Table I

Color coordinates  $a^*$  and  $b^*$  of compounds  $\text{Ln}_2\text{CeZrO}_7$  applied into organic matrix in mass tone and into ceramic glaze G 070 91 in 10 wt.% (calcination temperature  $1500^\circ\text{C}$ ).

Ln	1400 °C		1450 °C		1500 °C		G 070 91	
	$a^*$	$b^*$	$a^*$	$b^*$	$a^*$	$b^*$	$a^*$	$b^*$
Nd	-7.95	9.03	-8.29	11.69	-8.74	10.63	-1.65	19.88
Sm	-0.84	14.95	-0.99	20.60	-1.35	17.45	0.24	32.09
Gd	2.35	19.47	0.26	18.60	2.88	23.05	-0.55	30.27
Dy	-1.25	15.18	-2.52	16.94	-1.74	19.14	-1.03	29.69
Er	12.41	7.42	11.96	7.32	12.61	6.97	8.13	26.20
Yb	-0.67	9.06	-1.35	11.98	-1.33	11.12	-1.39	28.48
Y	-0.17	12.37	-0.96	13.60	-1.26	9.44	-1.02	27.66

Table II

Color properties of pigments  $\text{Ln}_2\text{CeZrO}_7$  applied into organic matrix in mass tone and into ceramic glaze G 070 91 in 10 wt.% (calcination temperature  $1500^\circ\text{C}$ ).

Ln	1400 °C			1450 °C			1500 °C			G 070 91		
	$L^*$	C	$H^\circ$	$L^*$	C	$H^\circ$	$L^*$	C	$H^\circ$	$L^*$	C	$H^\circ$
Nd	78.75	12.03	131.36	75.73	14.33	125.34	78.49	13.76	129.43	74.40	19.95	94.74
Sm	90.75	14.97	93.22	89.43	20.62	92.75	90.67	17.50	94.42	83.27	32.09	89.57
Gd	87.29	19.61	83.12	89.60	18.60	89.20	86.17	23.23	82.88	84.05	30.27	91.04
Dy	91.54	15.23	94.71	91.39	17.13	98.46	91.23	19.22	95.19	84.31	29.71	91.99
Er	85.85	14.46	30.88	86.93	14.02	31.47	86.22	14.41	28.93	81.03	27.43	72.76
Yb	91.75	9.08	94.23	91.34	12.06	96.43	92.61	11.20	96.82	85.00	28.51	92.79
Y	90.90	12.37	90.79	91.34	13.63	94.04	91.39	9.52	97.60	85.17	27.68	92.11

Pigments calcined at temperature  $1500^\circ\text{C}$  were applied into ceramic glaze G 070 91 in 10 wt.%. Color properties are shown in Table I and Table II. Values of coordinate  $b^*$  are higher than in application into organic matrix (interval 19.88 - 32.09). Pigment doped by erbium obtained orange shade which proves coordinate  $a^*$  (8.13). Other compounds have yellow-green colors, because coordinates  $a^*$  reached very low values, negative mostly. Degrees of color tone respond color shades. Lightness decreased and chroma increased rapidly because of this application.

Particle size distribution was also evaluated. Values of mean particle size are shown in Table III. Optimal particle size of inorganic pigments for applications into organic matrix (plastics) is about  $2\ \mu\text{m}$  and for applications into ceramic glazes is ranging from 5 to  $15\ \mu\text{m}$ . Mean particle size increases with calcination temperature mainly and is located in range  $3.59 - 8.50\ \mu\text{m}$ , so pigments are suitable for applications into ceramic glazes, but for applications into organic matrix particle size should be modified (e.g. milling).

Band gaps of compounds  $\text{Ln}_2\text{CeZrO}_7$  were calculated as next (Table IV). Values of band gaps correspond with colors of semiconductors in which pigments belong (Figure 2). Calcination temperature does not have big impact to band gaps. Values for pigment doped by erbium are ranging from 1.85 to 1.87 eV which agree with red color even if true color is pink. Band gaps of pigment with neodymium acquired value 2.03 eV which concurs green shade (between red and orange). Other compounds have band gaps about 3 eV which confirm yellow shades (even yellow with green addition).

Table III

Mean particle size of compounds  $\text{Ln}_2\text{CeZrO}_7$ .

Ln	1400 °C	1450 °C	1500 °C
	$d_{50}/\mu\text{m}$	$d_{50}/\mu\text{m}$	$d_{50}/\mu\text{m}$
Nd	3.59	5.01	7.48
Sm	5.68	6.24	6.42
Gd	4.20	5.39	5.28
Dy	3.93	5.01	5.31
Er	6.69	7.31	8.36
Yb	5.88	6.34	6.05
Y	6.06	7.06	8.50

Table IV

Band gaps of pigments  $\text{Ln}_2\text{CeZrO}_7$ .

Ln	1400 °C	1450 °C	1500 °C
	$E_g/\text{eV}$	$E_g/\text{eV}$	$E_g/\text{eV}$
Nd	2.03	2.03	2.03
Sm	3.00	3.00	3.01
Gd	2.99	3.00	2.99
Dy	3.01	3.01	3.01
Er	1.85	1.87	1.87
Yb	3.01	3.01	3.01
Y	3.01	3.01	3.02

Table V

Phase compositions of compounds  $\text{Ln}_2\text{CeZrO}_7$  calcined at temperature 1500 °C.

Ln	Phase composition	Crystal structure	JPDF number <sup>15</sup>
Nd	$\text{CeNdO}_3$	cubic	04-017-4168
	$\text{Ce}_{1.6}\text{O}_3$	cubic	04-002-5591
	$\text{Ce}_{0.65}\text{Zr}_{0.35}\text{O}_2$	tetragonal	04-012-8035
	$\text{ZrO}_2$	monoclinic	00-037-1484
Sm	$\text{Ce}_{0.6}\text{Sm}_{0.4}\text{O}_{1.8}$	cubic	04-013-8942
	$\text{ZrO}_2$	monoclinic	00-037-1484
Gd	$\text{Ce}_{0.4}\text{Gd}_{1.6}\text{O}_{3.2}$	cubic	04-016-3967
	$\text{Gd}_{0.3}\text{Zr}_{0.7}\text{O}_{1.85}$	cubic	04-006-5311
	$\text{ZrO}_2$	monoclinic	00-037-1484
Dy	$\text{Ce}_2\text{Zr}_2\text{O}_7$	cubic	04-015-7156
	$\text{CeDyO}_{3.5}$	cubic	04-017-4475
	$\text{ZrO}_2$	monoclinic	00-037-1484
Er	$\text{Er}_2\text{O}_3$	cubic	04-008-8242
	$\text{Ce}_{0.9}\text{Zr}_{0.1}\text{O}_2$	cubic	04-013-4359
	$\text{Ce}_2\text{Zr}_2\text{O}_{7.5}$	cubic	04-015-7157
	$\text{ZrO}_2$	monoclinic	04-004-4339
Yb	$\text{Ce}_{0.75}\text{Zr}_{0.25}\text{O}_2$	tetragonal	01-077-8790
	$\text{Yb}_2\text{O}_3$	cubic	04-001-2438
	$\text{ZrO}_2$	monoclinic	00-037-1484
Y	$\text{Y}_{1.5}\text{Ce}_{0.38}\text{O}_3$	cubic	04-002-0294
	$\text{Y}_2\text{O}_3$	cubic	00-041-1105
	$\text{Y}_{0.8}\text{Ce}_{0.2}\text{O}_{1.6}$	cubic	04-006-9426
	$\text{ZrO}_2$	monoclinic	00-037-1484

Phase composition of pigments  $\text{Ln}_2\text{CeZrO}_7$  calcined at 1500 °C was studied as well (Table V). Two-, three- and four-phase compounds were prepared. All samples contain non reacted  $\text{ZrO}_2$ . Pyrochlore structure was obtained only for the sample doped by dysprosium and  $\text{Ce}_2\text{Zr}_2\text{O}_7$  was formed. Perovskite structure  $\text{CeNdO}_3$  was

synthesized for compound with neodymium which has four-phase composition. Samples doped by erbium, ytterbium and contain starting lanthanide oxides as  $\text{Er}_2\text{O}_3$ ,  $\text{Yb}_2\text{O}_3$  and  $\text{Y}_2\text{O}_3$ .

### Conclusion

The inorganic pigments based on lanthanide oxides and zirconium oxide with general formula  $\text{Ln}_2\text{CeZrO}_7$  ( $\text{Ln} = \text{Nd, Sm, Gd, Dy, Er, Yb, Y}$ ) were prepared by solid-state reaction with calcination temperatures 1400, 1450 and 1500 °C. Compounds applied into organic matrix in mass tone have green (Nd), pink (Er), yellow (Gd) and yellow-green (Sm, Dy, Yb, Y) color shades. Best color properties were obtained for compounds calcined at the highest temperature, therefore these pigments were applied into ceramic glaze G 07091 in 10 wt.% which final color tones were green (Nd), orange (Er), yellow (Sm) and yellow-green (Gd, Dy, Yb, Y). Prepared compounds are suitable for applications in ceramic glazes due to mean particle sizes which have been proven by color properties in glaze G 070 91. Band gaps respond with color shades of all pigments. XRD analysis confirmed presence of two to four phases in prepared samples. Pigments with required composition were not prepared. For the preparation of single phase sample would be necessary to increase the firing temperature. Single-phase pigment is not necessary, but it should have interesting color and thermal stability. Synthesized compounds have the potential to become inorganic environmental friendly ceramic pigments.

### Acknowledgment

Research of inorganic pigments is supported by IGA University of Pardubice (SGSFChT\_2015005).

### Literature

1. De la Luz V., Prades M., Beltrán H., Cordoncillo E.: J. Eur. Ceram. Soc. 33, 3359 (2013).
2. Wang Ch., Wang Y., Cheng Y., Huang W., Zou B., Cao X.: Powder Technology 225, 130 (2012).
3. Fabrichnaya O., Kriegel H. J., Seidel J., Savinykh G., Ogorodova L. P., Kiseleva I. A., Seifert H. J.: Thermochem. Acta 526, 50 (2011).
4. Popa K., Konings R. J. M., Wastin F., Colineau E., Magnani N., Raison P. E.: J. Phys. Chem. Solids 69, 70 (2008).
5. Yamamura H., Nishino H., Kakinuma K.: J. Ceram. Soc. JPN. 112(10), 553 (2004).
6. Yamamura H., Nishino H., Kakinuma K., Nomura K.: J. Ceram. Soc. JPN. 111(12), 902 (2003).
7. Adachi G., Imanaka N.: Chem. Rev. 98, 1479 (1998).
8. Kilbourn B. T., in book: *A Lanthanide Lanthology, Part II, M – Z*, s. 18-20, Molycorp, Mountain Pass, CA, U.S.A. 1994.
9. Medenbach O., Dettmar D., Shannon R.D., Fischer R.X., Yen W.M.: J. Opt. A.: Pure Appl. Opt. 3, 174 (2001).
10. Swab J. J.: Army Research Laboratory, ARL-TR-2591 (2001).
11. Torres-Huerta A.M., Domínguez-Crespo M.A., Onofre-Bustamante E., Flores-Vela A.: J. Mater. Sci. 47, 2300 (2012).
12. Völz H. G., in book: *Industrial Color Testing*, kap. 2, s. 26-35. Wiley-VCH, Weinheim 2002.
13. Radhika S. P., Sreeram K. J., Nair B. U.: J. Adv. Ceram. 1(4), 301 (2012).
14. Nassau K, in book: *Color for science, art and technology*, kap. 4, s. 145. Elsevier Science, Amsterdam 1998.
15. The International Centre for Diffraction Data, Newtown Square 2012.

## THE INFLUENCE OF AMOUNT OF CHROMOPHORE ON THE COLOR PROPERTIES OF MALAYAITE PIGMENT

Luxová J., Šinkovská M., Šulcová P.

*University of Pardubice, Faculty of Chemical-Technology, Department of Inorganic Technology, Doubravice 41, Pardubice 532 10, Czech Republic  
email: jana.luxova@upce.cz*

### Introduction

Protection of the environment plays a primary role nowadays. Elimination of some chemical elements, which is in accordance with current legislation classified as toxic or dangerous, the production of many materials based on these elements has been restricted. From the viewpoint of the inorganic ceramic pigments, this restriction affects many pigments containing these elements; this reduces the possibility of their use for high temperature applications. The cobalt was also included among undesirable and problematic elements together with Pb, Cr<sup>6+</sup> and it can be denoted as the only traditional chromophore providing pigments with blue shade. The second negative aspect of the ceramic pigments containing cobalt is their high price. Therefore, the research of the inorganic pigments with cobalt is nowadays performed so that the content of cobalt would be lower on the necessary minimum or so that new non-traditional pigments are discovered.

The malayaite is calcium tin silicate compound derived from natural occurring mineral the Malayaite, which has the chemical formula CaSnOSiO<sub>4</sub> or more precisely CaSnSiO<sub>5</sub>. As the name of this mineral says, there are large deposits of malayaite compounds to be found in Malaysia as well as in Brazil, Madagascar, Russia, or Germany. Malayaite belongs to a large family of sphenic pigments. According to the nomenclature CPMA (Colour Pigments Manufacturers Association) they belong into a large group of pigments with the highest thermal stability<sup>1</sup>. Malayaite is characterized by monoclinic crystal structure consisting of infinite chains of octahedra SnO<sub>6</sub> connected with tops of tetrahedra SiO<sub>4</sub>, respectively polyhedral CaO<sub>7</sub>. This structure is then stable for bond of metal ion and takes part in the final pigment colouring<sup>2</sup>.

Malayaite pigments of the chemical formula CaSn<sub>(1-x)</sub>Co<sub>x</sub>SiO<sub>5-6</sub> were prepared in this work. Cobalt has been chosen as chromophore providing the colour, even though this element is in the current legislation referred to as problematic.

The purpose of this work was to prepare non-traditional cobalt pigment with blue colouring with a minimum content of cobalt. Moreover, in the case of incorporation of the pigment into the vitreous surface of leadless glaze, there is only minimum change of the contamination of the environment. For the synthesis of these compounds the classical ceramic method was used. This method is based on the solid state reaction. Older ceramic methods of the solid state reaction phase were carried out only with one calcination temperature. However, the late works<sup>3,4</sup> emphasize the appropriateness of the use of multiple calcination procedures for obtaining of products with higher quality. Therefore, the objective of this work was to compare samples, which were prepared not only by one-step calcination but also by two-step calcination procedure.

### Experimental part

Compounds corresponding to the chemical composition of CaSn<sub>(1-x)</sub>Co<sub>x</sub>SiO<sub>5-6</sub>, where x=0; 0.005; 0.01; 0.015; 0.025; 0.03; 0.04; 0.055; 0.065; 0.075; 0.085 and 0.1 were prepared by using the ceramic method. The following powder raw materials were used for the preparation: precipitated CaCO<sub>3</sub> (98.5%, the Merck Group KGaA, Germany), SnO<sub>2</sub> (99.9%, Alfa Aesar GmGH&KG, Germany), nature micro-milled SiO<sub>2</sub> (99.6%, Sklopísek Střeleč, a.s., Czech Republic) and mixed Co<sub>3</sub>O<sub>4</sub> (content 73.8% of Co, The Shepherd Color Company, USA). Stoichiometric amounts of the starting materials for the given sample of the pigment were homogenised in the agate mortar, then inserted into corundum crucibles and calcinated in the electric furnace with the heating rate 10°C.min<sup>-1</sup>. The calcination procedure was kept at temperatures 1250 – 1400°C in steps 50°C for the time of 4 hours<sup>5</sup>. This working methodology was used for the samples, which were prepared by the so called the one-step calcination procedure.

The same quantity of the doped element was compared with pigments prepared by the two-step calcination procedure, which was carried out due to the improvement of pigment application and structural properties, but also due to the assumption that the creation of malayaite compounds takes place in two stages. In the first stage CaSnO<sub>3</sub> is created (approx. 1100°C), into which SiO<sub>2</sub><sup>6</sup> is then incorporated. In this case, the calcination procedure was carried out at two temperatures, during which the first calcination was always held at 1100°C for 4 hours. The following second calcination was at the appropriate temperature 1200 – 1400°C/4 hours. After the firing, all the calcinates were grinded in the agate mortar.

The aim of this work was to assess the influence of the cobalt amount on the colour properties of the malayaite pigment. These have been studied both in the case of powder pigments as well as after the application of two binding systems, namely into the transparent leadless glaze P 07410 in the weight ratio 10% (Glazura Roudnice, a.s., Czech Republic); and into the organic acrylate matrix (Parketol, Akzo Nobel Coatings CZ, a.s., Opava, Czech Republic) in the mass tone. The colour properties were measured in the visible region of the light (400-700 nm) using the spectrophotometer ColourQuest XE (HunterLab, USA). The colour was evaluated in the system CIE  $L^*a^*b^*$  (1976), where the value  $L^*$  represents lightness of darkness of the pigment. The value  $a^*$  (red-green axis) and  $b^*$  (yellow-blue axis) indicate colour hue. Other colour characteristics have been calculated for better defining of the colour: the chroma  $C$ , the hue angle  $H^\circ$  and for observing of colour changes the total colour difference  $\Delta E^*_{CIE}$ . The standard sample (without the presence of chromophore, i.e.  $x=0$ ) and the sample with the appropriate amount of cobalt content (the content as stated above  $x=0.005-0.1$ ) have been compared. The chroma was calculated using the formula:  $C=(a^{*2}+b^{*2})^{1/2}$ . The hue angle  $H^\circ$  is expressed in degrees and moves in the range within  $0^\circ-360^\circ$ . The value of the hue angle can be found out from the formula:  $H^\circ=\arctg(b^*/a^*)$ . The interval  $H^\circ$  for this studied system of malayaite pigments with cobalt is following: 195-285 blue hue, 285-350 violet hue. The total colour difference can be found out from formula:  $\Delta E^*_{CIE}=[(\Delta L^*)^2+(\Delta a^*)^2+(\Delta b^*)^2]^{1/2}$ , where  $\Delta L^*$  - brightness difference between the standard and given sample,  $\Delta a^*$ ,  $\Delta b^*$  - difference of the colour coordinates  $a^*$  and  $b^*$  between the standard and the given sample<sup>7</sup>.

The phase composition of the tested powder samples was studied by the X-ray diffraction analysis using the device D8 Advance (Bruker, GB), working with radiation  $CuK_\alpha$  and the scintillation detector (the range  $2\theta$  from 10 to 80). The particle size of prepared compounds was observed too. It was measured by the device Mastersizer 2000/MU (Malvern Instr., GB), which enables evaluation based on Fraunhofer bending or based on the Miehe theory. In this case the evaluation has been examined based on Fraunhofer bending.

## Results and discussion

The main objective of this work was to assess the influence of the amount of cobalt, which was used as a chromophore for colouring of the malayaite lattice. On Fig. 1 is graphically shown the quantitative dependence of the dopant on the result colour properties of samples applied into the transparent leadless glaze P 07410. The Fig. 1a is devoted monitoring of this dependence of the compounds, which were prepared by using the one-step calcination at  $1250^\circ\text{C}$ . A shift to bluer hues together with the increasing content of the cobalt was recorded (decrease of the coordinate  $b^*$  towards more negative values). The decrease of the coordinate  $a^*$  was recorded for the composition corresponding to  $x$  from 0 to 0.015, but after that coordinate  $a^*$  together with increasing of the cobalt content gradually increased. The values of colour coordinates  $a^*$  and  $b^*$  for the samples containing Co in the amount of  $x=0.055-0.1$  changed only slightly. The slow move toward bluer hues was recorded in the case of the Fig. 1b), which corresponds to the samples prepared by two-step calcining process at  $1200^\circ\text{C}$ . From this figure it is also evident, that in the case of the two-step calcination process at  $1200^\circ\text{C}$ , very similar results as at the samples, which were calcinated by the one-step firing method at  $1250^\circ\text{C}$ , were achieved. The colour appearance of the ceramic tiles moved from white ( $x=0$ ), through greyish ( $x=0.005-0.01$ ), blue-grey ( $x=0.015-0.04$ ) over to blue-violet ( $x=0.055-0.1$ ). Lower hiding power was negative aspect common for both compared ways of calcination caused by inappropriate particle size and by insufficient distribution of pigment in the glaze. This defect was seen particularly in tiles with applied pigments with higher cobalt content and which were prepared at higher temperatures.

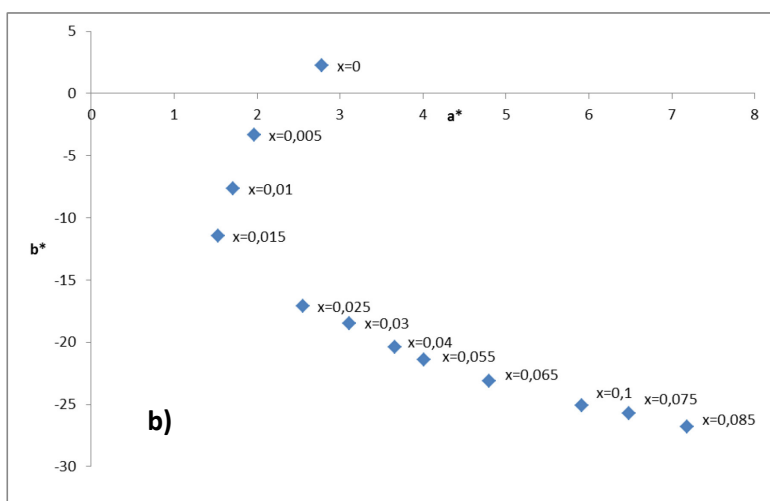
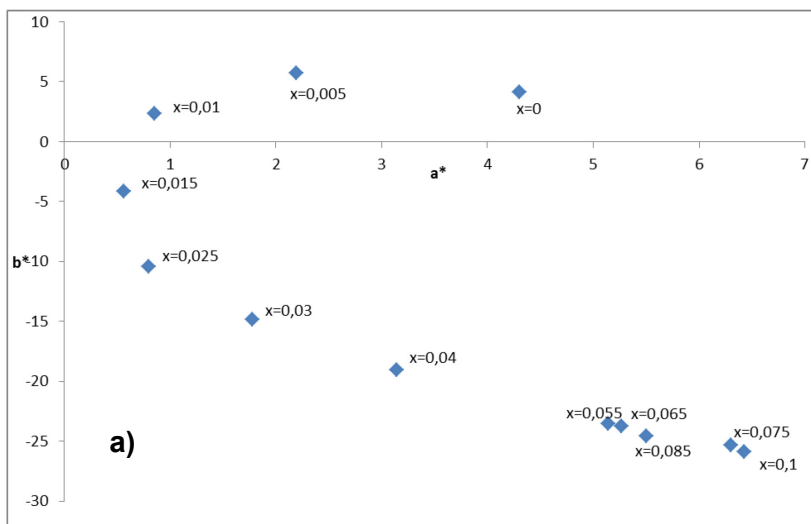


Fig. 1: The influence of the cobalt amount on the colour properties of the  $\text{CaSn}_{(1-x)}\text{Co}_x\text{SiO}_{5-8}$  pigment prepared by: a) the one-step way at  $1250^\circ\text{C}$ ; b) two-step way at  $1200^\circ\text{C}$ ; application – glaze P 07410

The recommended particle size for uniform surface covering of the ceramic tile by glaze with pigments is from 5 to  $15\ \mu\text{m}$ . In the case of samples prepared by one-step way at the temperature  $1250^\circ\text{C}$  the mean particle size lay from 3.4 to  $10.3\ \mu\text{m}$ . The malayaite pigments prepared at  $1300^\circ\text{C}$  satisfy the above mentioned condition only into amount  $x=0.4$ . The pigment particles for composition  $x=0.055$  and more had the mean particle size in interval 18.1- $25.1\ \mu\text{m}$ , where the biggest value  $d_{50}$  was measured for  $x=0.075$ . Particles calcinated at  $1350^\circ\text{C}$  and  $1400^\circ\text{C}$  were very similar in characteristics – the increase of  $d_{50}$  up to cobalt content  $x=0.03$ , where the highest value was found out ( $1350^\circ\text{C} - 24.7\ \mu\text{m}$  a  $1400^\circ\text{C} - 24.9\ \mu\text{m}$ ) followed by gradual decrease of this value. The analysis of samples prepared by two-step process proved that mean particle size of compounds prepared at the calcination temperatures  $1200^\circ\text{C}$  and  $1250^\circ\text{C}$  achieved again up to  $15\ \mu\text{m}$ . The pigment particles prepared at the temperature of  $1300^\circ\text{C}$  had the higher values of  $d_{50}$ . The highest values were determined for  $x=0.065$  ( $26\ \mu\text{m}$ ), after which they started to decrease. The particles synthesized at  $1350^\circ\text{C} - 1400^\circ\text{C}$  had the values of mean particle size which gradually increased together with the content of cobalt up to  $x=0.085$ , resp.  $x=0.075$ . The biggest values of  $d_{50}$  for these compositions were  $25.7\ \mu\text{m}$ , resp.  $24.7\ \mu\text{m}$ . Even during these calcination temperatures the recommended size was exceeded - at  $1350^\circ\text{C}$  ( $x=0.025$ ) and at  $1400^\circ\text{C}$  ( $x=0.015$ ). However, it was found out when comparing both presented way (one-step and two-step calcination) that the two-step way shows the more balanced and more considerate growth of particle sizes, even though two calcination procedures were used for the preparation.

An acrylate matrix was chosen as the second binding system, into which the monitored samples were applied in the mass tone. Although from point of view of particle size the studied pigments are not suitable for application into this binding system (recommended about 2  $\mu\text{m}$ ), the evaluation of colour properties in this binding system was realized. Mainly due to two reasons: the appropriateness of the acrylate matrix (whether it came about to interact with malayaite pigment); but also from the reason of future evaluation of determination of the total colour difference with regard to the quality of grinding. The calcination temperature 1350°C was chosen for visualizing of the dependence of the influence of cobalt amount on the colour properties of pigments applied into the organic binding system. Again, one-step way (Fig. 2a) and two-step way (Fig. 2b) have been compared. From this figure it is obvious that in this binding system the coordinate  $b^*$  is pointed down (it gains more negative values against the glaze), but a slight shift to the III. quadrant was also recorded, i.e. even the negative value of the coordinate  $a^*$  asserts (a contribution of the green hue).

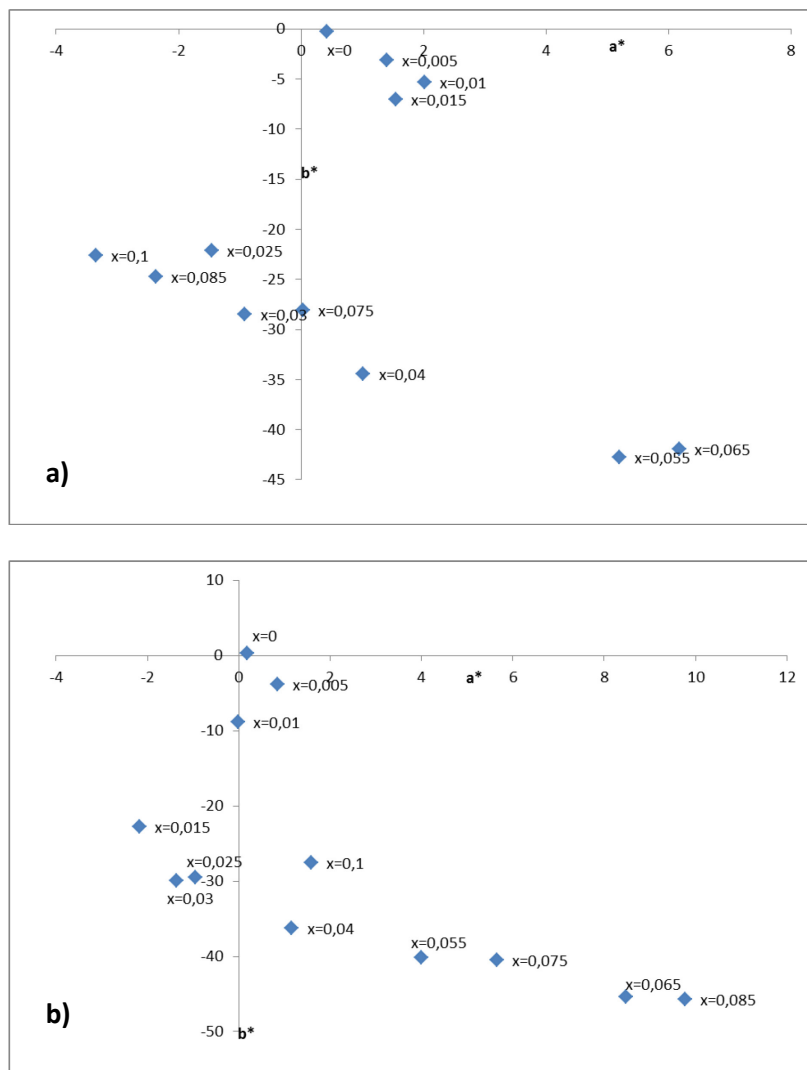


Fig. 2: The influence of the cobalt amount on the colour properties of the  $\text{CaSn}_{(1-x)}\text{Co}_x\text{SiO}_{5-6}$  pigment calcinated at 1350°C and prepared by: a) the one-step way; b) two-step way; application – organic matrix

The sample corresponding to the chemical formula  $\text{CaSn}_{0.945}\text{Co}_{0.055}\text{SiO}_{5-6}$  (Fig. 3) was chosen for better evaluation of the quality of the compared methods and for the evaluation of the best calcination temperature, because the first large colour change in this sample was monitored. It corresponds to the requirement of the minimum Co content with good colour hue. The colour coordinates  $a^*$  and  $b^*$  of the pigment of this composition are compared in the Fig. 3a, which was prepared by one-step and two-step way and applied in the transparent glaze P 07410. An apparent shift to the bluer colours for samples calcinated at two temperatures is recorded. In the case of the calcinations at one temperature, the sample at 1350°C showed the highest value of the coordinate  $b^*$  (-25.18). However, the value of the coordinate  $b^*$  was got over at two-step calcination

already at the temperature of 1300°C (-25.89). Moreover, the samples prepared at temperatures 1350°C and 1400°C had the colour coordinate  $b^*$  even higher, i.e.  $b^* = -26.70$  and  $-27.14$ . Fig. 3b demonstrated the colouring coordinates of the powder pigment and after the application in the organic binding system too. Again the one-step and two-step ways of preparation have been compared. It is visible, that the trend connected with colouring coordinates of the powders is retained even in the case when the pigment was applied into the acrylate binder. Thus it is obvious that the mutual reaction between the organic matrix and the studied pigment does not occur and the pigment is inert in the binder. Significant changes in colouring coordinates were recorded for both studied methods at temperatures of 1300°C and 1350°C when the samples showed the bluest hues. They are placed in the IV. quadrant of the colouring cross. The shift to the III. quadrant of the colouring cross was in both cases during the increase of the calcinations temperature up to 1400°C. The pigment gained more of the green tone (shift from positive values of the coordinate  $a^*$  into the negative), moreover the blue values of coordinate  $b^*$  decreased. Even in this case, it can be noted that better values have been obtained for two-step calcinations procedure.

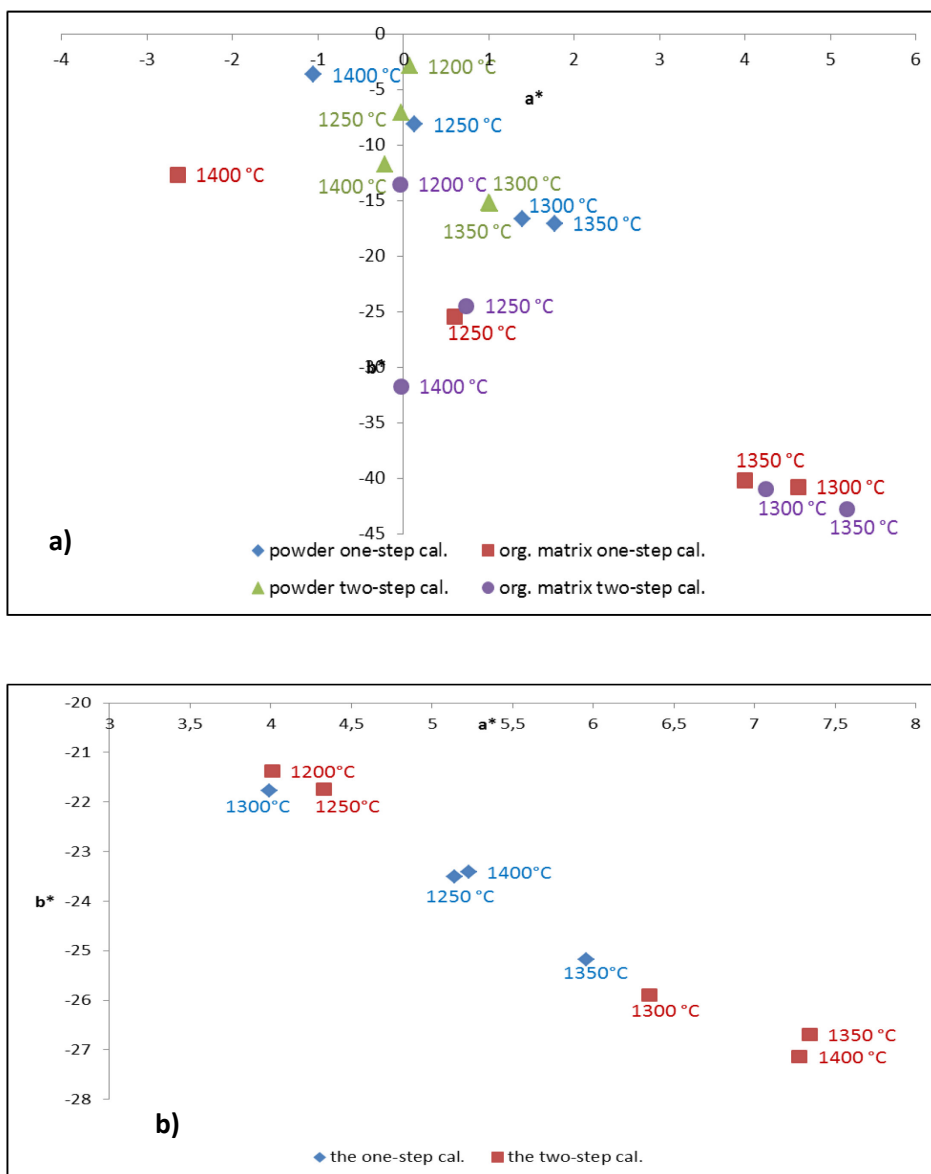


Fig. 3: The influence of calcination temperature on colour properties of  $\text{CaSn}_{0.945}\text{Co}_{0.055}\text{SiO}_{5-6}$  pigment, compared the one-step and two-step firing after application: a) into transparent glaze P 07410; b) without application (powders) and into the organic binder matrix (mass tone)

Table I: The impact of calcination temperature on colour characteristics and the mean particle size  $d_{50}$  of  $\text{CaSn}_{0.945}\text{Co}_{0.055}\text{SiO}_{5-6}$  malayaite pigment after application into glaze P 07410 (10 wt.%) -  $L^*$ - the brightness, C- the chroma,  $H^\circ$  - the hue angle,  $\Delta E^*_{\text{CIE}}$  – The total colour difference

Calcination temperature [°C]	The one-step calcination					The two-step calcination				
	The colour characteristics				$d_{50}$ [µm]	The colour characteristics				$d_{50}$ [µm]
	$L^*$	C	$H^\circ$	$\Delta E^*_{\text{CIE}}$		$L^*$	C	$H^\circ$	$\Delta E^*_{\text{CIE}}$	
1200	-	-	-	-	-	67.55	18.72	279.44	36.01	5.85
1250	56.63	24.07	282.33	42.64	9.32	59.82	22.17	281.26	38.52	10.30
1300	58.46	22.14	280.38	41.64	18.10	53.93	26.66	283.78	46.93	28.26
1350	53.81	25.88	283.32	48.14	22.49	50.06	27.69	285.37	50.19	21.21
1400	54.16	24.00	282.59	45.60	11.77	51.03	28.10	285.02	50.17	23.99

The Table I shows the values of the colour characteristics, which have been established for both mentioned methods of prepared malayaite pigments with the chemical formula  $\text{CaSn}_{0.945}\text{Co}_{0.055}\text{SiO}_{5-6}$  (applied into the transparent leadless glaze P 074710). In the case of evaluation of the one-step method, it can be concluded that the brightness coordinate  $L^*$  was decreasing together with the increasing temperature, the chroma C almost did not change (it was moving around the value 24) and the hue angle  $H^\circ$  was near the area of violet (285 – 350). Namely the values  $H^\circ$  oscillated around of 283 and they indicated low stabilization of the colour hue. The values of the total colour difference  $\Delta E^*_{\text{CIE}}$  are very large, the highest value was obtained for the temperature 1350°C. The mean particle size increased together with the temperature up to 1350°C (22.49 µm), then they decreased. Better results were determined for the two-step calcination method of preparation. The shift towards darker colours together with increasing temperature was recorded (the values of the brightness coordinate  $L^*$  gradually went down); the chroma (C) was progressive growing with the increasing temperature and the values of hue angle were moving from blue – violet area towards violet. In this case it can be claimed that the hue angle was stabilized. The total colour difference increased together with the increasing temperature of calcination up to the values 50.2 and after that it didn't change. The values of the mean particle size indicated the largest growth at the temperature of 1300°C, when the highest value  $d_{50}=28.26$  µm was measured.

Table II: The impact of firing temperature on the colour characteristics of  $\text{CaSn}_{0.945}\text{Co}_{0.055}\text{SiO}_{5-6}$  malayaite pigment after application into the organic matrix (mass tone) -  $L^*$ - brightness, C - the chroma,  $H^\circ$  - the hue angle,  $\Delta E^*_{\text{CIE}}$  – the total colour difference

Calcination temperature [°C]	The colour characteristics							
	The one-step calcination				The two-step calcination			
	$L^*$	C	$H^\circ$	$\Delta E^*_{\text{CIE}}$	$L^*$	C	$H^\circ$	$\Delta E^*_{\text{CIE}}$
1200	-	-	-	-	69.23	13.59	180.17	28.88
1250	62.65	25.49	271.35	41.28	59.87	24.49	271.73	41.25
1300	56.01	41.07	276.46	55.95	58.50	41.24	275.90	54.76
1350	59.84	40.41	275.08	52.46	56.87	43.09	276.92	56.08
1400	52.85	12.94	191.77	41.78	61.16	31.71	180.05	43.91

In the table II there are shown the colour characteristics for the same pigment composition after application into the organic matrix, and it is obvious that the brightness component decreases with the increasing temperature of the calcination at both monitored methods. A slight shift to the darker hues is very evident in the case of the two-step calcination method. The sample calcinated at 1400°C is the exception, when the pigment was lightened again (growth of the coordinate  $L^*$ ). The highest value of the chroma C at calcination at one-step calcination was found out at the sample with the firing temperature of 1300°C. On the contrary for the two-step calcination method it was increasing together with the growing temperature up to the maximum value 43.09 at 1350°C, then decrease occurred. These results are in agreement with the results of the total colour difference  $\Delta E^*_{\text{CIE}}$ . The greatest value of the chroma corresponds to the highest value of the total colour difference. The values of the hue angle  $H^\circ$  correspond with above stated graphical dependence of colour properties on the firing temperature (see Fig. 3b). The colour shade of samples prepared by the one-step calcination moves more towards the blue-violet area (growth of the coordinate  $b^*$ ), however at 1400 °C it is in the area of blue-green. The shift from the blue-green shade to the bluer is very well evident in case of the two-

step calcination method and subsequently again towards the blue-green. In both cases it is caused by the effect of the negative coordinate  $a^*$  (contribution of the green undertone).

Table III: The phase composition of studied pigments in dependence of chromophore amount and the way of preparation

Amount of dopant	Identified phase composition (structure)	
	The one-step calcination at 1350°C	The two-step calcination at 1100°C/1350°C
x=0.005	CaSn(SiO <sub>4</sub> )O (monoclinic); SnO <sub>2</sub> (tetragonal); CaSnO <sub>3</sub> (orthorhombic)	CaSn(SiO <sub>4</sub> )O (monoclinic); SnO <sub>2</sub> (tetragonal); CaSnO <sub>3</sub> (orthorhombic)
x=0.015	CaSn(SiO <sub>4</sub> )O (monoclinic); SnO <sub>2</sub> (tetragonal)	CaSn(SiO <sub>4</sub> )O (monoclinic); SnO <sub>2</sub> (tetragonal)
x=0.03	CaSn(SiO <sub>4</sub> )O (monoclinic); SnO <sub>2</sub> (tetragonal)	CaSn(SiO <sub>4</sub> )O (monoclinic); SnO <sub>2</sub> (tetragonal)
x=0.055	CaSn(SiO <sub>4</sub> )O (monoclinic); SnO <sub>2</sub> (tetragonal)	CaSn(SiO <sub>4</sub> )O (monoclinic); SnO <sub>2</sub> (tetragonal)
x=0.065	CaSn(SiO <sub>4</sub> )O (monoclinic); SnO <sub>2</sub> (tetragonal)	CaSn(SiO <sub>4</sub> )O (monoclinic); SnO <sub>2</sub> (tetragonal)
x=0.085	CaSn(SiO <sub>4</sub> )O (monoclinic); SnO <sub>2</sub> (tetragonal); Ca <sub>2</sub> Co(Si <sub>2</sub> O <sub>7</sub> ) (tetragonal)	CaSn(SiO <sub>4</sub> )O (monoclinic); SnO <sub>2</sub> (tetragonal)
x=0.1	CaSn(SiO <sub>4</sub> )O (monoclinic); SnO <sub>2</sub> (tetragonal); Ca <sub>2</sub> Co(Si <sub>2</sub> O <sub>7</sub> ) (tetragonal)	CaSn(SiO <sub>4</sub> )O (monoclinic); SnO <sub>2</sub> (tetragonal)

The results of the X-ray diffraction analysis (see Table III.) proved that one phase compound was not prepared. XRD patterns for the temperature 1350°C indicated the presence of two or three-phase compounds depending on the dopand content and on the method of preparation. The three compounds in the case of the one-step calcination for sample with the cobalt content  $x = 0.005$  were identified: CaSn(SiO<sub>4</sub>)O (malayaite), CaSnO<sub>3</sub> (perovskite) a SnO<sub>2</sub> (cassiterite). The XRD patterns for the other formula  $x = 0.015-0.065$  prove the presence of two-component compound, namely malayaite as major phase and cassiterite as minor. Malayaite with the highest cobalt content  $x = 0.085$  and  $x = 0.1$  had besides mentioned malayaite and cassiterite also Ca<sub>2</sub>Co(Si<sub>2</sub>O<sub>7</sub>) (Co-akermanite) suggesting that one-step calcination method of preparation is not sufficient for incorporation of cobalt into the malayaite structure. Presumably, higher cobalt amount supports the creation of calcium cobalt silicate, which then it can subsequently to influence the resulting colour properties. Only two compounds were identified in all cases for the two-step calcination method of preparation – as the main part - CaSn(SiO<sub>4</sub>)O (malayaite) and SnO<sub>2</sub> (cassiterite). It is evident that the two-step calcination method of preparation affords the better quality of product. Therefore this method of preparation can be recommended for the preparation of the malayaite compounds. The work of authors dealing with malayaite cobalt pigments<sup>8</sup> points also to the presence of cassiterite structure, it can be stated that the required malayaite compound in both comparative methods of preparation was prepared. Moreover, from the pigmentary point of view it is not necessary to prepare one-phase pigment but the synthesis conditions are the most important, which must be suitable for industrial use.

### Conclusion

In this work blue pigments corresponding to the chemical composition CaSn<sub>(1-x)</sub>Co<sub>x</sub>SiO<sub>5-6</sub> with the different cobalt content were prepared. The compounds were synthesized by calcinations at temperatures 1250 – 1400°C/4 hrs. In order to improve both the quality of the pigment, phase composition of the pigment as well as better colour properties, the second comparable method has been used. This second method was consisted in the two-stage calcination procedure. The first calcination was carried out at the temperature 1100°C/4hrs and the following one at the temperature 1200 – 1400°C/4hrs. The impact of cobalt amount on the resulting colour properties of blue pigments was mainly assessed in this work. The first major and fundamental changes occurred in the pigment containing cobalt  $x = 0.055$ , which it is a very small amount of the unwanted element. The most suitable temperature that can be recommended for the calcination is 1350°C. From the results of evaluation of the colour properties, size of particles and X-ray phase analysis it can be summarised, that the pigments prepared by the two-stage calcination method were the more quality, with the better particle sizes

more suitable into the ceramic glaze and with the better colour properties. But in terms of evaluation of the particle size it is necessary to recommend the operation of grinding with the aim positively to influence the particle size, which relates to the optical properties.

*This work has been supported by IGA University Pardubice within the project SGSFChT\_2015005.*

**Literature:**

1. Classification and chemical descriptions of the complex inorganic color pigments. 4th ed. Alexandria, Virginia: Color Pigments Manufacturers Association, Inc.2010; pp. 24.
2. Higgins J.B., Ross F.K.: *Crystal Structure Communications* 6, 179 (1977).
3. Mouyane M., Womes M., Jumas J.C., Olivier-Fourcarde J., Lippens P.E.: *J. Solid State Chem.* 184, 2877 (2011).
4. Pavlov S.R., Marzá V.B., Carda J.B.: *J. Mater. Chem.* 12, 2825 (2002).
5. Luxová J., Šulcová P., Trojan M., Trojan J.: *J. Therm. Anal. Calorim.* 116, 571 (2014).
6. Šolc Z., Trojan M., Kuchler M.: *Thermochim. Acta.* 88, 421 (1985).
7. Šulcová P.: *Vlastnosti anorganických pigmentů a metody jejich hodnocení*, Pardubice (2008).
8. Piña C., Arriola H., Nava N.: *Hyperfine Interact.* 161, 93 (2005).

## SYNTHESIS OF Mn/Mg FERRITES USING UNUSAL PREPARATION METHODS – COMPARATIVE STUDY

**Bělina P.**, Strouhal J., Pluhařová L., Šulcová P., Svoboda L.

*Department of Inorganic Technology, Faculty of Chemical Technology, University of Pardubice, Studentska 95, 532 10, Pardubice, Czech Republic*  
*petr.belina@upce.cz*

### Introduction

Spinel of the type  $M^{2+}M_2^{3+}O_4$  attract the research interest because of their practical applications. In the case of  $M^{3+} = Fe^{3+}$ , the resulting spinel ferrites having a general composition of  $MFe_2O_4$  ( $M = Cu, Mn, Mg, Zn, Ni, Co$  etc.) are widely used in the field of inorganic pigments, information storage, magnetic separation, catalyst, magnetic resonance imaging, gas sensors. Optical, magnetic and electric properties of ferrites combined with their chemical, thermal and mechanical stability are important for listed applications<sup>1,2</sup>.

The conventional preparation of ferrites compounds is the solid state synthesis under high temperature and co-precipitation method in alkaline environment with subsequent calcination<sup>3,4</sup>. The insufficiency of solid state method is that it required a quite high calcination temperature (approx. 800 – 1200°C), the co-precipitation method is very sensitive to changing conditions. In addition, not only the particle size distribution of powder material obtained is wide (nonuniform), the specific surface area is quite low. This may be restrictive for some application of these materials.

In this study, preparation of  $MnFe_2O_4$ ,  $MgFe_2O_4$  and  $Mg_{0.5}Mn_{0.5}Fe_2O_4$  and characterization of some physico-chemical properties was undertaken. The powder materials were prepared by classical methods – solid state reaction and precipitation in alkaline environment. Next, these materials were synthesized by unusual methods from a technological point of view – precipitation of mixed oxalates, preparation of mixed oxalates in solid state and preparation using suspension mixing of starting materials<sup>5-9</sup>. The properties of the prepared materials which were determined as a part of this work have been selected with regard to their potential application as inorganic pigments. Color properties, particle size distribution of milled and nonmilled powders, thermal stability, specific surface area and oil consumption were observed depending on the method of preparation.

### Materials and methodology

For solid state synthesis (in tables marked as ceramic method),  $MnCO_3$  (Shepherd Color Comp., USA),  $MgCO_3$  (Penta, CZ) and  $Fe_2O_3$  (Precheza, CZ) were weighted in proper molar ratio and subsequently mixed in mortar grinder for 30 minutes. Mixture was transferred to a corundum firing crucible and calcined at 750°C/6 hours in an electric furnace (heating rate 10°C/min was used in every calcination steps).

For two step synthesis by suspension mixing of reactants (in tables marked as suspension mixing of RM),  $MnSO_4 \cdot H_2O$  (Lach-Ner, CZ),  $MgSO_4 \cdot 7H_2O$  (Lach-Ner, CZ),  $FeSO_4 \cdot 7H_2O$  (Lach-Ner, CZ) and  $Na_2CO_3$  (Penta, CZ) were weighted in proper molar ratio and mixed in ceramic mortar into homogenous mixture. After addition of urea  $CO(NH_2)_2$  (Penta, CZ) and fumaric acid  $C_4H_4O_4$  (Merck, DE), which serve as the foaming agent, the water suspension was prepared. Flowable suspension was transferred on hot plate made from stainless steel at temperature 400°C for 15 minutes. The intermediate powder product was finally calcined at 700°C/3 hours in an electric furnace in ceramic crucibles.

For co-precipitation method in alkaline region of pH (in tables marked as precipitation pH 10),  $MnCl_2 \cdot 4H_2O$  (Lach-Ner, CZ),  $MgCl_2 \cdot 6H_2O$  (Lach-Ner, CZ) and  $FeCl_3 \cdot 6H_2O$  (Lach-Ner, CZ) were weighted in proper molar and dissolved in water (0.05M solution of metal salts). The ammonia solution (12.5 %) was added into mixture of metal salts solutions until reached pH 10 and at this pH the solution was stirred for 15 minutes. After filtration careful washing and drying (95°C) the intermediate product was calcined at 600°C/3 hours in an electric furnace in ceramic crucibles.

For oxalate co-precipitation method (in tables marked as precipitation oxalic acid),  $MnSO_4 \cdot H_2O$ ,  $MgSO_4 \cdot 7H_2O$ ,  $FeSO_4 \cdot 7H_2O$  were weighted in proper ratio and dissolved in water. The solution of oxalic acid  $C_2H_2O_4$  (Merck, DE) in equivalent amount was added into solution of metal sulfates and then stirred for 15 minutes. The filtered precursor was washed by deionized water and dried (95°C). Final product was obtained using thermal decomposition of precursors in an electric furnace in ceramic crucible at 400°C/3 hours.

For preparation of oxalate precursors by solid state reaction (in tables marked as oxalate preparation in solid state),  $MnSO_4 \cdot H_2O$ ,  $MgSO_4 \cdot 7H_2O$ ,  $FeSO_4 \cdot 7H_2O$  were weighted in proper ratio and mixed in mortar grinder for 15 minutes.  $Na_2C_2O_4$  (Merck, DE) and surfactant polyethylene glycol (PEG 400, 50 vol.%, Merck, DE) were put in the mortar grinder and ground for 35 minutes. The reactant mixture gradually became damp, and then a paste formed. The reaction mixture was kept at room temperature for 2 hours. The mixture was washed with

deionized water and finally dried at 95°C. Final product was obtained using thermal decomposition of precursors in an electric furnace in ceramic crucible at 400°C/3 hours.

### Characterization techniques

Crystallochemical characterization of the final ferrite powders was performed by X-ray diffraction analysis (monochromatic CuK $\alpha$  radiation, a scintillation detector, equipment Diffractometer D8 Advance, Bruker, GB). Data were collected by step scanning over 2 $\theta$  range from 10° to 80° with a step size of 0.02°.

The color properties of the powdered samples pressed into a glass cuvette were analyzed by measurement of the spectral reflectance in the visible region of light (400–700 nm) using a spectrophotometer (ColorQuest XE, HunterLab, USA). The measurement conditions were the following: an illuminant D<sub>65</sub>, 10° standard observer and measuring geometry d/8°. The color properties are described in terms of CIE L\*a\*b\* system. In this system, the values of a\* (the green (-) → red (+) axis) and b\* (the blue (-) → yellow (+) axis) indicate the color hue, the value of L\* represents the lightness or darkness of color as related to a neutral grey scale which is described by numbers from 0 (black) to 100 (white).

The particle size distribution of the samples was measured using a laser scattering system based on Mie theory (Mastersizer 2000/MU, Malvern Instruments, UK) after dispersion of the sample in 0.1% solution of sodium hexametaphosphate (Fosfa, CZ). The samples were measured after calcination and the same samples after the wet milling process. The samples were milled using planetary mill with agate milling container and zircon balls with diameter 1-1.2 mm (weight ratio sample:balls was 20:1) and environment of ethanol and water (1:1). Color properties, critical pigment volume concentration, thermal stability and specific surface were measured for milled samples.

Thermal stability was tested using a heating microscope with automatic image analysis (EM201-12, Hesse Instruments, DE). For measurement, a pellet of cylindrical form with dimensions of 3 × 3 mm was prepared. The test was performed with temperature intervals between 20 and 1300 °C at a heating rate of 10 °C.min<sup>-1</sup>.

The Critical Pigment Volume Concentration – CPVC was determined using method of linseed oil consumption according to CSN EN ISO 787-10.

The specific surface area S<sub>BET</sub> was measured using Nova 1200 (Quantachrome, USA) using the nitrogen sorption technique. The adsorption isotherms were fitted using the Brunauer-Emmett-Teller (BET) method for specific surface area determination, adsorption data were obtained in the relative pressure range between 0.05 and 0.25. Before each sorption measurement the sample was degassed (250°C, 4 hours).

### Results and discussion

The preparation method has a major impact on particle size distribution of prepared powders. The tables I, III and V show the highest value d<sub>90</sub> and the lowest value d<sub>10</sub> in all cases for preparation using co-precipitation method with ammonia solution (hydroxides as intermediates). The particle size distribution in this case is the widest, the samples contain small particles and probably solid particle aggregates. In absolute values, then the highest value d<sub>50</sub> provides precipitation method using oxalic acid. Other preparation methods in terms of particle size distribution are similar. After the milling the particle size distribution is comparable for all preparation method and it is possible to use the samples for comparative study.

The samples prepared by both precipitation methods and by method using suspension mixing of raw materials are darker than samples prepared by other methods. For Mg<sub>0.5</sub>Mn<sub>0.5</sub>Fe<sub>2</sub>O<sub>4</sub> (Tab. I) the ceramic method provides powder with higher proportion of red hue. The same situation occurs for the sample MgFe<sub>2</sub>O<sub>4</sub> (Tab. V). The samples Mg<sub>0.5</sub>Mn<sub>0.5</sub>Fe<sub>2</sub>O<sub>4</sub> and MnFe<sub>2</sub>O<sub>4</sub> are brown, MgFe<sub>2</sub>O<sub>4</sub> is red.

The specific surface area (S<sub>BET</sub>) is strongly influenced by the selected method of preparation. The highest value of the specific surface area showed all three prepared compounds if using method of preparation oxalate by solid state reaction with subsequent calcination at 400°C. This soft chemical method combined with low calcination temperature provides higher values S<sub>BET</sub> than 75 m<sup>2</sup>.g<sup>-1</sup> (MgFe<sub>2</sub>O<sub>4</sub>, Tab. VI). In other cases the specific surface area values ranging from 10 to 30 m<sup>2</sup>.g<sup>-1</sup>.

The thermal stability of prepared powders measured on heating microscope means the first dimensional change of prepared tablets. Most often it is the beginning of the sintering process. Measurement in this case showed that the precipitation methods provide powders with lower thermal stability than in the case of solid state reactions. The thermal stability of samples prepared by classical ceramic method is 100°C higher than for samples prepared by precipitation methods (pH 10). An unexpected result is that also the samples prepared using oxalate preparation in solid state have the similar thermal stability as method using suspension mixing of raw materials and ceramic method.

The CPVC number represents the dispersion ability and as pigment volume concentration increases above CPVC, void space and porosity increase while tensile properties decrease. Prepared samples provide middle

number of CPVC for every method of preparation. Samples prepared by precipitation method (pH 10) are characterized by higher value of CPVC.

Table I

Particle size distribution and color properties of  $Mg_{0.5}Mn_{0.5}Fe_2O_4$  according to the preparation method

$Mg_{0.5}Mn_{0.5}Fe_2O_4$	PSD [ $\mu m$ ]			PSD after milling [ $\mu m$ ]			Color coordinates		
	$d_{10}$	$d_{50}$	$d_{90}$	$d_{10}$	$d_{50}$	$d_{90}$	L*	a*	b*
Precipitation (pH 10)	0.32	2.22	27.78	0.18	0.37	1.81	39.07	1.92	3.84
Precipitation (oxalic acid)	5.51	9.03	14.04	0.35	0.84	8.24	37.76	2.69	5.85
Oxalate prep. in solid state	0.43	1.93	31.90	0.34	0.72	3.92	42.55	3.42	8.17
Suspension mixing of RM	0.46	1.59	11.71	0.24	0.52	1.24	39.79	2.26	3.17
Ceramic method	0.40	1.69	14.74	0.26	0.59	12.18	41.21	8.17	5.80

Table II

Specific surface area, thermal stability and critical pigment volume concentration of  $Mg_{0.5}Mn_{0.5}Fe_2O_4$  according to the preparation method

$Mg_{0.5}Mn_{0.5}Fe_2O_4$	$S_{BET}$ [ $m^2 \cdot g^{-1}$ ]	$T_{stab.}$ [ $^{\circ}C$ ]	CPVC [%]
Precipitation (pH 10)	$25.80 \pm 1.60$	760	51.5
Precipitation (oxalic acid)	$52.73 \pm 3.31$	755	42.6
Oxalate prep. in solid state	$58.87 \pm 1.04$	845	43.0
Suspension mixing of RM	$17.63 \pm 0.59$	840	44.9
Ceramic method	$16.08 \pm 0.84$	900	41.0

Table III

Particle size distribution and color properties of  $MnFe_2O_4$  according to the preparation method

$MnFe_2O_4$	PSD [ $\mu m$ ]			PSD after milling [ $\mu m$ ]			Color coordinates		
	$d_{10}$	$d_{50}$	$d_{90}$	$d_{10}$	$d_{50}$	$d_{90}$	L*	a*	b*
Precipitation (pH 10)	0.28	4.94	36.20	0.22	0.49	1.75	28.82	1.72	3.06
Precipitation (oxalic acid)	6.29	11.91	22.37	0.29	0.73	1.88	36.34	2.17	4.03
Oxalate prep. in solid state	0.66	3.38	22.49	0.41	0.95	2.44	41.22	3.26	6.08
Suspension mixing of RM	0.68	1.95	13.38	0.24	0.49	1.06	36.86	1.60	1.75
Ceramic method	0.33	0.87	17.96	0.21	0.42	0.98	38.81	2.73	3.31

Table IV

Specific surface area, thermal stability and critical pigment volume concentration of  $MnFe_2O_4$  according to the preparation method

$MnFe_2O_4$	$S_{BET}$ [ $m^2 \cdot g^{-1}$ ]	$T_{stab.}$ [ $^{\circ}C$ ]	CPVC [%]
Precipitation (pH 10)	$15.80 \pm 1.10$	780	53.05
Precipitation (oxalic acid)	$19.81 \pm 0.44$	780	46.65
Oxalate prep. in solid state	$49.29 \pm 2.12$	870	42.44
Suspension mixing of RM	$9.82 \pm 1.63$	825	49.61
Ceramic method	$11.12 \pm 1.60$	880	44.88

Table V

Particle size distribution and color properties of  $\text{MgFe}_2\text{O}_4$  according to the preparation method

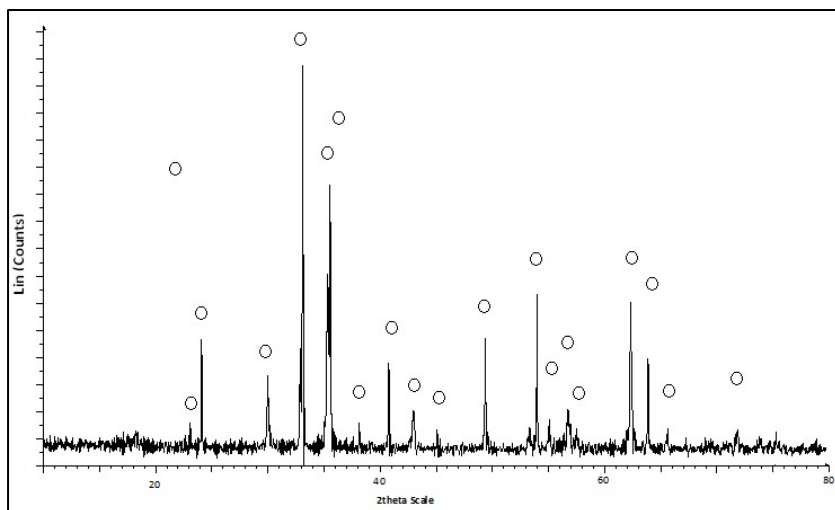
$\text{MgFe}_2\text{O}_4$	PSD [ $\mu\text{m}$ ]			PSD after milling [ $\mu\text{m}$ ]			Color coordinates		
	$d_{10}$	$d_{50}$	$d_{90}$	$d_{10}$	$d_{50}$	$d_{90}$	$L^*$	$a^*$	$b^*$
Precipitation (pH 10)	0.34	9.23	49.00	0.28	0.97	14.47	47.48	15.18	15.78
Precipitation (oxalic acid)	6.99	13.54	24.74	0.24	0.49	2.15	44.69	17.61	13.05
Oxalate prep. in solid state	0.63	4.00	19.41	0.40	1.29	17.00	48.30	15.77	17.41
Suspension mixing of RM	0.48	1.68	8.62	0.35	0.89	14.05	45.50	15.07	14.48
Ceramic method	0.38	1.56	29.87	0.26	0.62	13.50	47.86	18.87	15.42

Table VI

Specific surface area, thermal stability and critical pigment volume concentration of  $\text{MgFe}_2\text{O}_4$  according to the preparation method

$\text{MgFe}_2\text{O}_4$	$S_{\text{BET}}$ [ $\text{m}^2 \cdot \text{g}^{-1}$ ]	$T_{\text{stab.}}$ [ $^{\circ}\text{C}$ ]	CPVC [%]
Precipitation (pH 10)	$26.40 \pm 0.20$	780	53.69
Precipitation (oxalic acid)	$32.54 \pm 0.22$	755	50.60
Oxalate prep. in solid state	$75.98 \pm 0.58$	785	38.37
Suspension mixing of RM	$20.48 \pm 3.08$	800	34.39
Ceramic method	$29.94 \pm 1.17$	870	36.54

To confirm the resulting spinel structures, all samples were subjected to X-ray diffraction analysis. The relevant spinel formation was confirmed for all the methods of preparation. As an example, in Figure 1, the diffraction pattern of the sample  $\text{Mg}_{0.5}\text{Mn}_{0.5}\text{Fe}_2\text{O}_4$  is given in Fig. 1. The lines corresponding to the spinel cubic grid were only identified (marked).

Figure 1. Diffractogram of  $\text{Mg}_{0.5}\text{Mn}_{0.5}\text{Fe}_2\text{O}_4$  – oxalate preparation in solid state,

### Conclusions

In this study, there were compared several laboratory methods of preparation for compounds of spinel – ferrites. XRD showed that all the methods result in preparation of compounds having the desired composition. The co-precipitation method using ammonia at pH 10 provides final powders with width particle size distribution, with low thermal stability and with a darker tone. The powder samples with highest absolute value of particle size were obtained by co-precipitation method using oxalic acid. The thermal stability is comparable

with previous method but lower if compared by others. Classical method provides a ceramic powder having excellent thermal stability, average value of particle size and specific surface area. Samples prepared by this method are different in color. High energy consumption is the main disadvantage of this method. Characteristics of the powders obtained by the two step method associated with the suspension by mixing the raw materials are very similar to ceramic method. The method using preparation of mixed oxalates with subsequent calcination provides the highest value of specific surface area, high thermal stability, average value of particle size, good color properties and CPVC.

#### **Acknowledgment**

*This work was supported by IGA University of Pardubice (SGFChT04).*

#### **Literature**

1. Jaswal L., Singh B.: J. Integr. Sci. Technol. 2, 69 (2014).
2. Diodati S., Nodari L., Natile M.M., Caneschi A., Fernandez C.J., Hoffmann C., Kaskel S., Lieb A., Di Noto V., Mascotto S., Saini R., Gross S., Eur. J. Inorg. Chem. 2014, 875 (2014).
3. Topfer J., Dieckman R.: J. Eur. Ceram. Soc. 24, 603 (2004).
4. Yang G., Han B., Sun Z., Yan L., Wang X.: Dyes Pigments 55, 9 (2002).
5. Ozel E., Turan S.: J. Eur. Ceram. Soc. 23, 2097 (2003).
6. Zhou K., Wu W., Li Y., Wu X., Liao S.: J. Therm. Anal. Calorim. 114, 205 (2013).
7. Tanaka Y., Takeguchi T., Kikuchi R., Eguchi K.: Appl. Catal. A-Gen. 279, 59 (2005).
8. Hessien M.H., Zaki Z.I., Mohsen A.: Adv. Mater. Phys. Chem. 3, 1 (2013).
9. Belina P., Sulcova P.: J. Therm. Anal. Calorim. 88, 107 (2007).

## STUDY OF PROPERTIES OF MODIFIED COMMERCIAL HYDROGEL

**Sustek S.**, Svoboda L.

*University of Pardubice, Department of Inorganic Technology, Doubravice 41, 532 10, Pardubice  
stanislav.sustek@student.upce.cz*

### Introduction

During the last decade, efforts are conducted to substitute superabsorbents based on petrochemicals by natural materials or prepare composite superabsorbents. These eco-friendly hydrogels should be lead to improve soil water retention and nutrient utilization by plants<sup>1</sup>. The presented work was focused on evaluation of properties of modified commercial hydrogel. The modification of commercial hydrogel was done by encapsulation in a mixture of gelatine collagen and clay. The study of effect of encapsulated hydrogels on water-holding capacity of soil was carried out, when different amounts of encapsulated hydrogels were mixed with dry soil. Also swelling capacity of modified hydrogels was tested at different pH. The encapsulating mixture could be suitable to decrease content of acrylic components and non-biodegradable residues in soil after using polyacrylate hydrogel as a soil conditioner in agricultural or horticultural applications. In addition, collagen gelatine is a source of nutrients after its mineralization in the soil and a presence of bentonite should contribute to improving the structure and properties of the soil due to its high cation exchange capacity.

### Experimental

In presented study, water-holding capacity of modified hydrogel was studied. Also swelling capacity of modified hydrogels was tested in solution of potassium nitrate. At selected samples, swelling capacity in different pH was studied.

### Materials

Collagen and gelatine were purchased from Tanex Vladislav and were used without further purification. Nanoclay, hydrophilic bentonite (nBentonite) was purchased from Aldrich, bentonite B75 was supplied from Keramost and bentonite BS was received from Sedlecky Kaolin. Hydrogel Floria was made by Degussa AG and delivered by Agro CS. Also all of these materials were used without further purification. Other agents were in analytical grade purity and all solutions were prepared using distilled water.

### Preparation of encapsulated hydrogel

Encapsulation of commercial hydrogel was done by the following procedure. Weighed amounts of collagen were mixed with small amount of distilled water. Subsequently, the solution was transferred into beaker with magnetic stirrer. Temperature was set on 60°C. Meanwhile bentonite was agitated in distilled water by means of ultrasonic device and consequently by magnetic stirrer. Then clay was added to collagen solution and allowed to stir for 30 minutes. After this time, hydrogel was added and solution was stirred an hour. At the end, product was filtrated and gel particles were dried in an oven at 50°C for 8 hours, then at 80°C for 6 hours. Encapsulated hydrogel was stored in absence of moisture. Overall 30 samples were prepared.

### Swelling capacity in distilled water

For determination of swelling capacity were used tea bags made of 100 mesh nylon screen. The quantity of dried sample was placed into tea bag, immersed in distilled water and its weight was recorded at room temperature. Swelling capacity was calculated according the formula:

$$SC (g/g) = (W_s - W_D) / W_D \quad (1)$$

where  $W_s$  is weight of swollen gel,  $W_D$  is weight of dried hydrogel<sup>1</sup>.

### Swelling capacity in solution of potassium nitrate

Loading of a hydrogel with chemical compounds is possible to carry out by two methods. In the first method, loaded material is added to the encapsulating mixture and built in situ whereby compound is trapped within hydrogel and collagen gelatin cover. In second approach, the dry hydrogel is allowed to swell in the saline solution and after equilibrium swelling, the hydrogel is dried. In the present study, the second method was

followed by swelling the dry hydrogel in a solution of  $\text{KNO}_3$  of known concentration. Modified gel was placed into the tea-bag which was then immersed in 5% solution of  $\text{KNO}_3$ . The swollen gels were dried and stored<sup>2</sup>.

### Swelling capacity in various pH solutions

The pH of absorbed solutions was adjusted using aqueous NaOH and HCl solutions. The method used was the same as the absorbency in distilled water was measured. At selected samples, swelling capacity in different pH was studied<sup>3</sup>.

### Water-holding capacity of soil<sup>4</sup>

Effect of the encapsulated hydrogel on water-holding capacity of the soil was studied. 2 g of modified hydrogel were mixed with 200 g of dried soil (below 2 mesh) and placed in a 4.5 cm diameter plastic tube. The bottom of the tube was sealed with nylon fabric and weighted ( $W_1$ ). The soil sample was drenched by distilled water from the top of the tube until water seeped out from the bottom. When no water seeped at the bottom, the tube was weighed again ( $W_2$ ). A control experiment without the hydrogel was also carried out. The water-holding capacity (WH %) of the soil was calculated from equation 2.

$$\text{WH (\%)} = (W_2 - W_1) \times 100 / 200 \quad (2)$$

## Results and discussion

### Determination of swelling capacity

Samples were immersed in distilled water and their weight after 24 hours was recorded. The best swelling capacity had a value about 41 grams of water per one gram of dried hydrogel (Fig 2.).

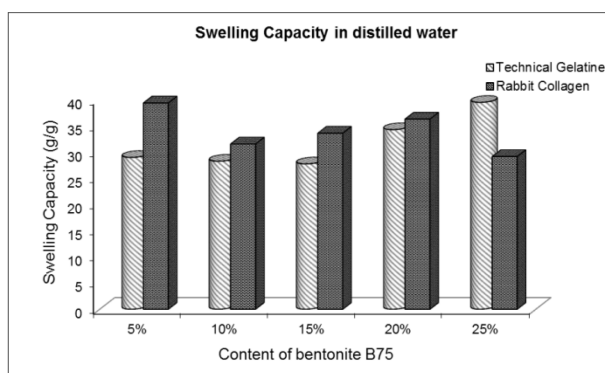


Fig.1. Swelling capacity, samples with bentonite B75

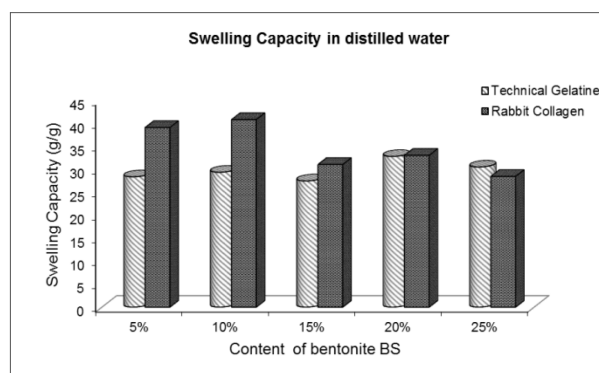


Fig.2. Swelling capacity, samples with bentonite BS

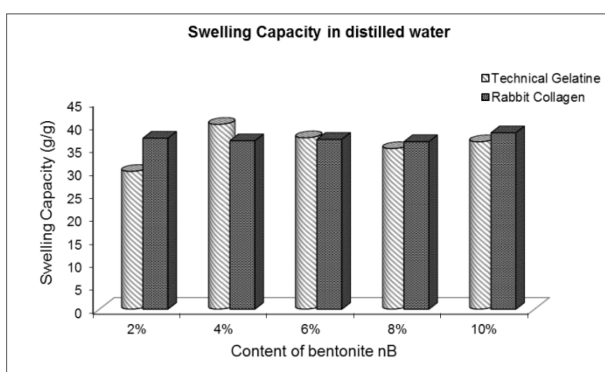


Fig.3. Swelling capacity, samples with bentonite B75

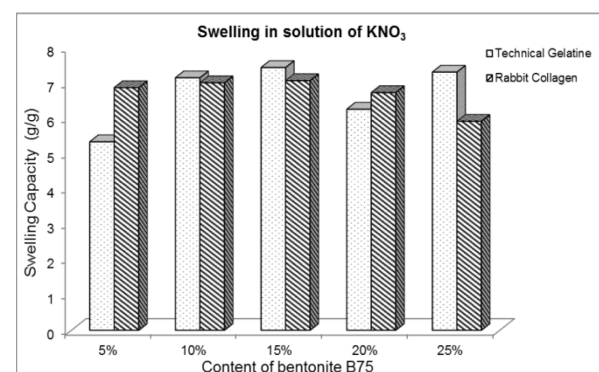


Fig.4. Swelling in saline solution (bentonite B75)

### Water absorbency in saline solution of potassium nitrate

Swelling studies indicated that the hydrogels are sensitive to the ion presence in solution and it is very important to know swelling behaviour of hydrogels in a salt solution, especially for agricultural and horticultural applications<sup>3</sup>. Due to this fact the samples were also tested for swelling in a 5% solution of potassium nitrate. The swelling capacities for modified hydrogels are shown in Figs 4-6, where first and second chart represents commercial hydrogel modified by gelatine, collagen and bentonite B75 and BS. Third chart shows results for modified hydrogel with bentonite nB. The best swelling ratio was 7.7 grams of potassium nitrate solution per one g of the encapsulated hydrogel.

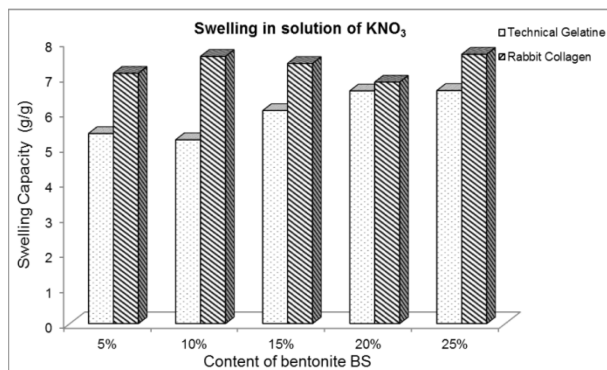


Fig.5. Swelling in saline solution (bentonite BS)

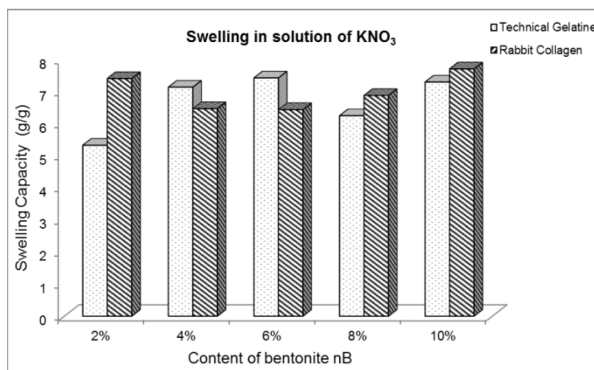


Fig.6. Swelling in saline solution (bentonite nB)

### Absorbency in solutions of various pH

The pH of absorbed solutions was adjusted using aqueous NaOH and HCl. The water absorbency decreases drastically as pH decreases from 4 to 2 and increases from 10 to 12 (Figs 7 and 8). This is because most of the  $\text{-COO}^-$  groups are protonized into  $\text{-COOH}$  groups when the  $\text{pH} \leq 4$  and then the repulsion between polymeric chains decreases, which leads to the decrease of water absorbency. When the pH is too high, most of the  $\text{-COOH}$  groups change into  $\text{-COO}^-$  groups, the screening effect of the counter ion (Na) on the poly-anionic chain of polymer is more evident, which also leads to a decrease of the water absorbency<sup>3</sup>.

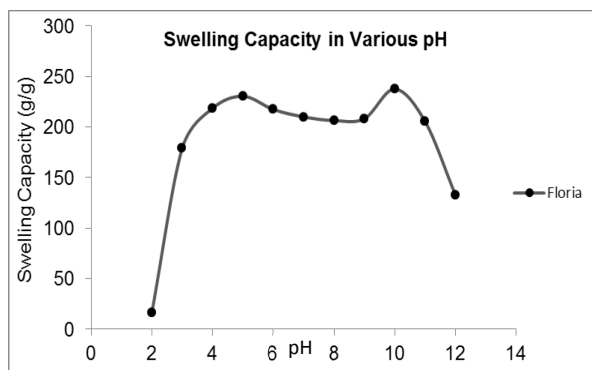


Fig.7. Swelling in different pH (commercial hydrogel)

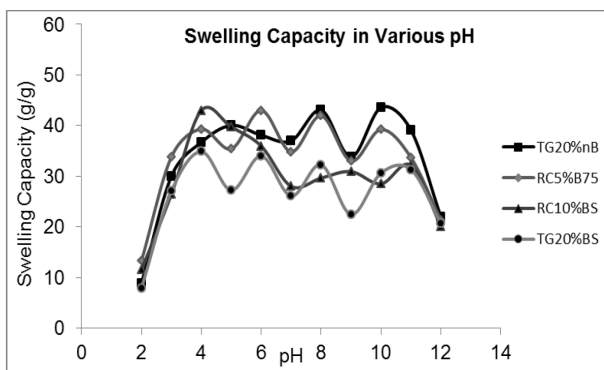


Fig.8. Swelling in different pH (modified hydrogel). TG – technical gelatine, RC – rabbit collagen

### Effect of the modified hydrogel on water-holding capacity of soil.

The water is one of the essential conditions for plant growth. Liquid water ensures the feeding of plants with nutritional elements, which increases the growth quality of plants<sup>5</sup>. Soils in arid areas are characterized by low water-holding capacity and excessive drainage of rain and irrigation water below the root zone, leading to weak water efficiency by crops. Due to it, we tested hydrogel effect on water-holding capacity of soil. As shown in Fig. 9 and 10 the best water-holding capacity of soil (1 day) is 49.0% for the encapsulated hydrogel, and that of soil without hydrogel is 43.9%. It is noted that soil/hydrogel mixture retains more water than the control soil. However, in comparison to the water retained by the free hydrogels in distilled water, the soil/hydrogel mixtures retain much less water. First, in the soil/hydrogel mixtures, each granule is surrounded by soil particles and subjected to a confining pressure by these particles<sup>6</sup>. Second, the presence of ions in soil solution makes the osmotic pressure difference between the polymeric network and the external solution decrease, resulting in a decrease in the water absorbency of

the hydrogel. Therefore, the swelling degree of the modified hydrogel in the soil is limited in comparison to that in distilled water<sup>7,8</sup>. However, as we can see in figures, in comparison to the control sample (soil without hydrogel, labelled as None), the modified hydrogel improved the water-holding capacity of soil.

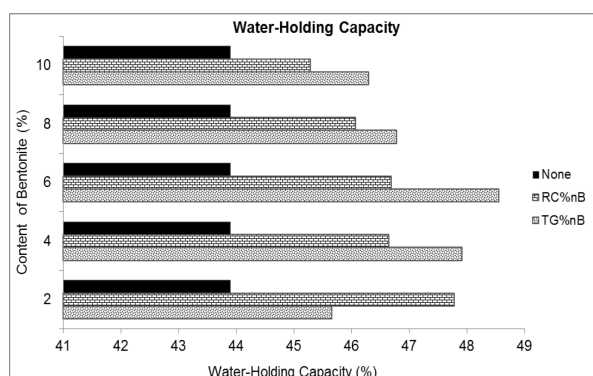


Fig.9. Water-holding capacity in soil

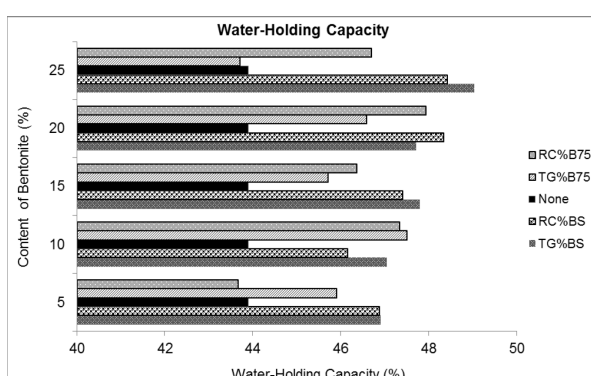


Fig.10. Water-holding capacity in soil

### Conclusions

This work was concentrated on study of properties of modified commercial hydrogel. Various modifications of composite hydrogels were prepared and tested. The best swelling capacity had value 7.7 grams of 5%  $\text{KNO}_3$  solution per 1 g of the encapsulated hydrogel. The best water-holding capacity of soil is 49.0% for the encapsulated hydrogel, and that of soil without hydrogel is 43.9%. It is noted that soil/hydrogel mixture retains more water than the control soil. Test of releasing of potassium nitrate out of the hydrogel will be carried out and reviewed in other work.

### Acknowledgements

*This work has been supported by IGA University of Pardubice in the project SGSFChT 2015005*

### References

- Kabiri K., Omidian H., Zohuriaan-Mehr M.J., Superabsorbent Hydrogel Composite and Nanocomposites: A Review. *Polymer Composites*, 2011, vol. 32, p. 277-289
- Bajpai A.K., Giri A., Swelling dynamics of a macromolecular hydrophilic network and evaluation of its potential for controlled release of agrochemicals, *Reactive & Functional Polymers*, 2002, vol. 53, p. 125-141
- Zhang J. P., Li A., Wang A. Q., Study on superabsorbent composite. V. Synthesis, swelling behaviors and application of poly (acrylic acid-co-acrylamide)/sodium humate/attapulgit superabsorbent composite, *Polym. Adv. Technol.*, 2005, vol. 16, p. 813-820
- Ni B., Liu M., Lu S., Xie L., Wang Y., Environmentally Friendly Slow-Release Nitrogen Fertilizer, *Journal of Agricultural and Food Chemistry*, 2011, vol. 59, p. 10169-10175
- Bakass, M.; Mokhlisse, A.; Lallemand, M. Absorption and desorption of liquid water by a superabsorbent polymer: Effect of polymer in the drying of the soil and the quality of certain plants. *J.Appl. Polym. Sci.*, 2002, vol. 83, p. 234-243.
- Bhardwaj, A. K.; Shainberg, I.; Goldstein, D.; Warrington, D. N.; Levy, G. J. Water retention and hydraulic conductivity of crosslinked polyacrylamides in sandy soils. *Soil Sci. Soc. Am. J.*, 2007, vol. 71, p. 406-412.
- Ni, B.; Liu, M. Z.; Leu, S.; Xie, L.; Zhang, X.; Wang, Y. Novel slow-release multielement compound fertilizer with hydroscopicity and moisture preservation. *Ind. Eng. Chem. Res.*, 2010, vol. 49, p. 4546-4552.
- Zhang, J. P.; Chen, H.; Wang, A. Q. Study on superabsorbent composite. III. Swelling behaviors of polyacrylamide/attapulgit composite based on acidified attapulgit and organo-attapulgit. *Eur. Polym. J.*, 2005, vol. 41, p.2434-2442.

## THE EFFECT OF LANTHANIDES ON COLOUR PROPERTIES OF THE MIXED OXIDE PIGMENTS BASED ON Bi-Ce-Nb

**Těšitelová K.**, Šulcová P., Gorodylova N. O.

*Department of Inorganic Technology, Faculty of Chemical Technology, University of Pardubice, Studentská 95, 532 10, Pardubice, Czech Republic*  
*katerina.tesitelova@student.upce.cz*

### Introduction

Natural inorganic pigments, derived mainly from mineral source, have been known since prehistoric times. The oldest natural yellow inorganic pigments are yellow ochre containing ferric oxide hydroxide. In ancient Egypt, but later also in Assyria and China pure yellow was prepared by grinding of natural mineral auripigment ( $\text{As}_2\text{S}_3$ ) and used for painting walls and in paintings and illuminated manuscripts. One of the oldest manufactured yellow pigment was Naples yellow ( $\text{Pb}_2\text{Sb}_2\text{O}_7$ ), which was already identified on glass and ceramics of ancient Egypt and Mesopotamia. Depending on the composition, respectively, on the mass ratio of antimony/lead and thermal conditions of preparation, it can provide a sulphur-yellow up to orange-yellow tint. The cheaper yellow pigments, which were used for industrial and commercial purposes, such as Mars yellow ( $\text{FeOOH}$ ), chrome yellow ( $\text{PbCrO}_4$ ) and cadmium yellow ( $\text{CdS}$ ), completely replaced the Naples yellow in the 18<sup>th</sup> century<sup>1,2</sup>.

In the area of powder materials it is a currently most discussed topic the environmental impact of the synthesized inorganic compounds. In this respect, it is recalled that a series of previously used pigments contains toxic metals such as lead, cadmium and hexavalent chromium that can adversely affect the environment and human health. The environmental regulatory restrictions make necessary to modify current pigments containing these "problematic" elements and substitute or reduce them. For this reason, it is considered important for the development of new safe inorganic pigments.

Ceramic pigments are chemically and thermally stable compounds which are characterized by absolute light stability, inertness to media and weathering. These properties are ideal for high-temperature applications. They are an integral part of many decorative and protective coatings for colouring many materials, including glaze, ceramic bodies and porcelain enamels. The essence of these fine powders is a highly stable host lattice of the mineral which is in its pure form colourless and therefore into its structure incorporation of chromophore dopant which provides the colour. Nowadays research in the fields of ceramic pigments is oriented toward the enlargement of the chromatic set of colours together with an increased thermal and chemical stability<sup>3</sup>.

Compounds based on  $\text{Bi}_2\text{O}_3$  have found increasing popularity because they provide interesting colour hue from yellow to orange. The intense colours of these powder materials are the results from the incorporation of  $\text{Ln}^{3+}$  ions ( $\text{Ln}$  = rare earth elements) into the stable host lattice of  $\text{Bi}_2\text{O}_3$ . The  $\text{Bi}_2\text{O}_3$  itself is a light yellow powder. Compounds based on  $\text{Bi}_2\text{O}_3$  produce not only interesting colours, but also contribute to a growth of the thermal stability. The high-temperature stable modification of  $\text{Bi}_2\text{O}_3$  is a  $\delta$ -phase, which is recognized as one of the best solid-state oxygen ion conductors<sup>4,5</sup>. This phase is stable between 730 °C and 835 °C temperature range, but may be stabilized below room temperature by partial cationic substitution for  $\text{Bi}^{3+}$  ions<sup>6,7</sup>.

This study is focused on the preparation of pigments basing on  $\text{Bi}_2\text{O}_3$  doped with selected lanthanides. The aim was to develop conditions for the synthesis of  $\text{Bi}_{1.5}\text{Ln}_{0.5}\text{Ce}_{1.5}\text{Nb}_{0.5}\text{O}_7$  pigments and to determine the influence of lanthanides and temperature of calcination on the colouring properties of this type of inorganic pigments. Research of these synthesized compounds gives interesting hues in the organic matrix and ceramic glaze. Prepared powder materials also represent the inorganic pigments alternative from the environmental point of view.

### Experimental

Compositions based on  $\text{Bi}_{1.5}\text{Ln}_{0.5}\text{Ce}_{1.5}\text{Nb}_{0.5}\text{O}_7$  (where  $\text{Ln}$  = Y, Sm, Gd, Er, Eu, Dy, Ho, Yb, Lu and Tm) were prepared by the conventional ceramic route using corresponding oxides:  $\text{Bi}_2\text{O}_3$  (99 % purity, Lachema Pliva a.s., Brno, CZ),  $\text{Nb}_2\text{O}_5$  (99.5 % purity, Bochemie, a.s. Bohumín, CZ),  $\text{CeO}_2$  (99 % purity) and  $\text{Ln}_2\text{O}_3$  of 99.9 % purity, which were obtained from Rare Earth Products Ltd., India. Precursors for the traditional solid state reaction were initially manually homogenised in a porcelain mortar with a pestle. The homogenous mixture was calcinated in corundum crucibles in an electric furnace with the heating rate 10 °C/min. In the temperature interval from 800 °C to 1,000 °C with the step 50 °C, the calcination was maintained in isothermal conditions for 3 h. After each heating cycle, the samples were gradually cooled down to room temperature and ground in a porcelain mortar.

All prepared pigments were applied to organic matrix (Parketol, Balakom a.s., Opava, CZ) in mass tone and middle-temperature borate-silicate (transparent leadless) glaze G 070 91 (Glazura, s.r.o., Roudnice nad Labem, CZ). Coating films on a shiny white non-absorbing paper containing the pigments in an organic matrix were prepared so called dragging test using a Bird applicator slit width of 100  $\mu\text{m}$ . The mixture of pigment (10 % w/w) and glaze was applied to a dry white ceramic fragments of dimensions 25 x 25 mm. Ceramic body coated with a glaze suspension was first dried at room temperature and then calcinated in an electric furnace at 1,000  $^{\circ}\text{C}$  at a heating rate of 10  $^{\circ}\text{C}/\text{min}$ , keeping this temperature for 15 min. Colourimetric study of final coating films and coloured glazes were carried out by a ColorQuest XE (HunterLab, USA) spectrophotometer in the 400-700 nm wavelength range. The study of chromatic properties requires the use of an appropriate system to measure the colour objectivity. The CIE  $L^*a^*b^*$  system (1976) colour scales were used for the assessment of the colour properties of the pigment powder. In this system, the value  $L^*$  represents the lightness or darkness of a colour in relation to scale extending from white ( $L^* = 100$ ) to black ( $L^* = 0$ ). The value  $a^*$  is the green (-)/red (+) axis,  $b^*$  is the blue (-)/yellow (+) axis, which describe the colour hue. Thorough description of colour is done by recalculation of chrome extent  $C$  (chroma) according mathematical formula  $C = (a^{*2} + b^{*2})^{1/2}$ . The colour of pigment is also expressed by the hue angle  $H^{\circ}$  ( $H^{\circ} = \arctg(b^*/a^*)$ ) defined by an angular position in the cylindrical colour space (for the orange  $H^{\circ} = 35^{\circ}$ - $70^{\circ}$  and for the yellow  $H^{\circ} = 70^{\circ}$ - $105^{\circ}$ ). The next measurement conditions were D65 illuminant,  $10^{\circ}$  complementary observer and geometry of measurements  $d/8^{\circ}$ .

The distribution of particle size distribution of the calcinated powder materials was obtained by laser scattering using a Mastersizer 2000/MU (Malvern Instruments, Ltd., UK). It is a compact, highly integrated laser measuring device for analysis of particle size in the range from 0.02 to 2,000  $\mu\text{m}$ . The system evaluates the particle size using red light (He-Ne laser, wavelength 633 nm) and blue light (solid-state light source, wavelength 466 nm). The signal was evaluated on the base of Fraunhofer bending. The measurement of particle size distribution has three steps and instrument calculates average automatically like values  $d_{10}$ ,  $d_{50}$ ,  $d_{90}$  or as a frequency or cumulative function.

## Results and discussion

Colour properties are the most important characteristic of the inorganic pigments. The aim of the present work was to investigate the influence of several lanthanides on the colouring effect of  $\text{Bi}_{1.5}\text{Ln}_{0.5}\text{Ce}_{1.5}\text{Nb}_{0.5}\text{O}_7$ . Pigments applied to the organic binder system in mass tone provide yellow-orange colour hues.

Based on the  $a^*$  and  $b^*$  values measured for the pigments calcinated at 800  $^{\circ}\text{C}$  and applied into organic matrix, it can be seen in the Table I that all lanthanides have the positive values of the colour coordinate  $a^*$  (red hue) and  $b^*$  (yellow hue). All prepared samples show positive values of the colour coordinate  $a^*$ , which lies in the interval from 0.80-12.88. The lowest contribution of red and yellow shade has a sample containing the element Sm, which is also characterized by a maximum value  $L^*$  (86.60) and value  $H^{\circ}$  (88.87). As a consequence provides lightest yellow hue from the series of the prepared samples. Pigments containing Ln = Y, Gd, Er, Eu, Dy and Ho have lower values of hue  $H^{\circ}$  and in combination with relatively high values of chroma  $C$  provide most interesting deep yellow-orange colour (Table II). The increase of calcination temperature up to 900  $^{\circ}\text{C}$  produces in some cases lower values  $L^*$  and chroma  $C$ , and it means that the colour becomes darker. Considering that the value  $H^{\circ}$  of these powder materials ranges from  $\sim 73$  to  $79$  so the samples are characterized by yellow-orange colour. The biggest shift recorded pigment with the formula  $\text{Bi}_{1.5}\text{Sm}_{0.5}\text{Ce}_{1.5}\text{Nb}_{0.5}\text{O}_7$ , in which value colour coordinates  $a^*$  increased from 0.80 to 9.59 (Table I). Contribution of yellow shade at this calcination temperature decreases which corresponds to values of coordinates  $b^*$  (in the range 40.34-46.21). The interesting colour samples can again identify those which contain rare earth elements Gd, Er, Dy and Ho since they have the lowest values  $L^*$  and with high values  $C$ . The compounds  $\text{Bi}_{1.5}\text{Eu}_{0.5}\text{Ce}_{1.5}\text{Nb}_{0.5}\text{O}_7$  and  $\text{Bi}_{1.5}\text{Dy}_{0.5}\text{Ce}_{1.5}\text{Nb}_{0.5}\text{O}_7$  have the smallest values  $H^{\circ}$  and  $L^*$ , and therefore provide darkest yellow-orange tinges. A further increase of calcination temperature to 1,000  $^{\circ}\text{C}$  did not induce too great changes colour properties of prepared pigments. The highest temperature of calcination a slightly increased by almost all values of colour coordinates  $a^*$  and  $b^*$  (Table I). All powder materials at this calcination temperature are characterized by a deep yellow-orange shade. From the values of the hue  $H^{\circ}$ , it is obvious that the most significant hue change is evident for the sample with formula  $\text{Bi}_{1.5}\text{Gd}_{0.5}\text{Ce}_{1.5}\text{Nb}_{0.5}\text{O}_7$  (Table II). The value  $C$  for all samples containing the lanthanides is at this calcination temperature in the range of values from 43.34 (Er) to 48.43 (Y). At the same time brightness decreased for all pigments. Simultaneously pigments containing lanthanides are darker than identical samples prepared at lower calcination temperature. Generally, increasing calcination temperature caused the colour darkening, deeper colour tint and the colour hue shifts to the orange area. The colour range for all pigments moves from pale yellow, over yellow-orange to darker orange. The best results were obtained for the pigment  $\text{Bi}_{1.5}\text{Gd}_{0.5}\text{Ce}_{1.5}\text{Nb}_{0.5}\text{O}_7$  which indicates the lowest

lightness value ( $L^* = 73.81$ ), high values of colour coordinate  $a^*$ ,  $b^*$  and chroma  $C$  for calcination temperature 1,000 °C. The prepared powder material provides a yellow-orange shade that matches the value hue  $H^\circ = 73.40$ .

Table I

The effect of calcination temperature on colour properties of the  $\text{Bi}_{1.5}\text{Ln}_{0.5}\text{Ce}_{1.5}\text{Nb}_{0.5}\text{O}_7$  pigments applied into organic matrix

Ln	Temperature [°C]								
	800			900			1,000		
	$L^*$	$a^*$	$b^*$	$L^*$	$a^*$	$b^*$	$L^*$	$a^*$	$b^*$
Y	81.85	8.86	46.26	80.02	9.56	42.33	77.18	12.75	46.72
Sm	86.60	0.80	40.43	78.80	9.59	40.34	78.07	10.66	46.21
Gd	78.82	9.17	41.39	79.73	10.65	46.02	73.81	12.98	43.53
Er	79.69	11.81	45.19	78.53	12.20	44.68	75.29	12.36	41.54
Eu	81.16	7.83	41.80	76.64	12.40	41.84	76.98	12.29	42.71
Dy	78.77	12.88	46.43	77.85	12.34	44.23	78.96	10.05	47.02
Ho	79.97	10.00	47.38	77.89	11.99	46.21	75.93	10.69	43.04
Yb	83.12	6.19	47.22	80.56	9.47	45.12	78.90	10.35	44.08
Lu	83.66	5.65	47.47	81.22	8.26	42.90	80.17	9.41	45.93
Tm	82.18	7.86	48.55	79.95	9.83	44.71	77.62	11.44	45.53

Table III shows the colour properties ( $L^*$ ,  $a^*$ ,  $b^*$ ) of the pigments applied to ceramic glaze. Powder materials containing rare earths give a light yellow colour with little greenish tint at all calcination temperature. The colour coordinates  $a^*$  provide negative values. The exception is the pigment  $\text{Bi}_{1.5}\text{Er}_{0.5}\text{Ce}_{1.5}\text{Nb}_{0.5}\text{O}_7$  which has this coordinate positive. The lightness of all prepared pigments corresponds with high values of brightness  $L^*$ . Generally, the pigments in ceramic glaze have worse colour properties than the same pigments in an organic binder system in mass tone.

Optical properties of the compounds and also their application preferences are determined by their particle size distribution (PSD). The test was performed with reference to the unmilled pigments. The growing trend of the mean size of the pigment particles  $d_{50}$  (Table II) is observed with increasing calcination temperature. The lowest value of particle size was obtained for the sample with Gd (2.28  $\mu\text{m}$ ) calcinated at 800 °C. On the other hand, the highest value has pigment with the presence of Eu ( $d_{50} = 7.37 \mu\text{m}$ ) calcinated at 1,000 °C. The condition, good applicability of prepared pigments to the ceramic glaze is met in the case of powder material calcinated at 1,000 °C, when the mean particle size is in the interval from 5.09  $\mu\text{m}$  to 7.37  $\mu\text{m}$ .

Table II

The effect of calcination temperature on purity of color, degree of colour tone and mean particle size of the  $\text{Bi}_{1.5}\text{Ln}_{0.5}\text{Ce}_{1.5}\text{Nb}_{0.5}\text{O}_7$  pigments

Ln	Temperature [°C]								
	800			900			1,000		
	$C$	$H^\circ$	$d_{50} [\mu\text{m}]$	$C$	$H^\circ$	$d_{50} [\mu\text{m}]$	$C$	$H^\circ$	$d_{50} [\mu\text{m}]$
Y	47.10	79.16	3.41	43.40	77.27	5.07	48.43	74.74	5.84
Sm	40.44	88.87	3.21	41.46	76.63	3.56	47.42	77.01	5.58
Gd	42.39	77.51	2.28	47.24	76.97	3.69	45.42	73.40	5.24
Er	46.71	75.35	4.45	46.32	74.73	4.83	43.34	73.43	5.97
Eu	42.53	79.39	2.39	43.64	73.49	3.77	44.44	73.95	7.37
Dy	48.18	74.50	2.76	45.92	74.41	3.68	48.08	77.94	5.50
Ho	48.42	78.08	3.06	47.74	75.45	4.06	44.35	76.05	5.15
Yb	47.62	82.53	3.98	46.10	78.15	4.37	45.28	76.79	5.18
Lu	47.81	83.21	4.05	43.69	79.10	4.43	46.88	78.42	5.09
Tm	49.18	80.80	3.76	45.78	77.60	4.69	46.95	75.90	5.43

Table III

The effect of calcination temperature on colour properties of the  $\text{Bi}_{1.5}\text{Ln}_{0.5}\text{Ce}_{1.5}\text{Nb}_{0.5}\text{O}_7$  pigments applied to ceramic glaze

Ln	Temperature [°C]								
	800			900			1,000		
	$L^*$	$a^*$	$b^*$	$L^*$	$a^*$	$b^*$	$L^*$	$a^*$	$b^*$
Y	85.28	-0.13	30.88	85.80	-1.13	35.57	85.25	-1.06	35.39
Sm	85.89	-0.72	33.49	85.60	-0.76	34.65	85.36	-0.39	35.99
Gd	85.85	-0.89	33.82	85.88	-0.66	31.76	85.11	-0.80	33.47
Er	85.80	0.10	33.67	85.72	0.13	33.33	84.99	0.39	33.89
Eu	85.87	-0.70	34.54	86.06	-0.87	32.91	85.78	-0.86	34.11
Dy	85.77	-0.92	33.03	86.35	-1.41	33.70	85.16	-0.63	34.96
Ho	85.88	-0.96	33.74	85.69	-1.06	34.81	84.94	-0.71	34.71
Yb	86.52	-1.07	33.32	86.69	-1.41	33.94	85.95	-1.24	34.65
Lu	86.61	-1.46	33.25	86.22	-1.50	34.65	85.93	-1.47	35.25
Tm	86.40	-1.50	33.19	86.04	-1.18	34.51	84.96	-1.12	32.72

### Conclusion

The influence of selected rare earths (Ln = Y, Sm, Gd, Er, Eu, Dy, Ho, Yb, Lu and Tm), temperature of calcination on the colour properties and mean particle size distribution of Bi-Ln-Ce-Nb-O pigments was investigated.

All prepared pigments give the yellow-orange colour in the organic matrix in mass tone. It is evident that for most samples with increasing calcination temperature decrease value of lightness  $L^*$  occurs. The values of hues  $H^e$  are close to the orange area. Pigment with formula  $\text{Bi}_{1.5}\text{Gd}_{0.5}\text{Ce}_{1.5}\text{Nb}_{0.5}\text{O}_7$  and calcination temperature 1,000 °C was evaluated as the best. Overall range of mean particle size of discussed pigments is from 2.28 to 7.37  $\mu\text{m}$ . For the highest temperature of calcination (1,000 °C) pigments are suitable for ceramic glaze. This type of pigments is environmentally friendly and could contribute to the basic assortment of yellow and orange inorganic pigments.

### Acknowledgment

The authors would like to thank for the financial support IGA University of Pardubice (SGSFChT\_2015005).

### Literature

1. Buxbaum G., Pfaff G.: *Industrial Inorganic Pigments*, 3<sup>rd</sup> ed., Wiley-VCH, Verlag GmbH & Co. KGaA, Weinheim, 2005.
2. Rosi F., Manuali V., Miliani C., Brunetti B.G., Sgamellotti A., Grygar T., Hradil D.: *J. Raman Spectrosc.* **40**, 107-111 (2009).
3. Faulkner E.B., Schwartz R.J.: *High Performance Pigments*, 2<sup>nd</sup> ed., Wiley-VCH, Verlag GmbH & Co. KGaA, Weinheim, 2009.
4. Šulcová P.: *J. Therm. Anal. Calorim.*, **109**, 639-642 (2012).
5. Ling Ch. D., Withers R. L., Schmid S., Thompson J. G.: *J. Solid State Chem.*, **137**, 42-61 (1998).
6. Adachi G., Imanaka N.: *Chem. Rev.*, **98**, 1479-1514 (1998).
7. Bosacka M., Szkoda I.: *Cent. Eur. J. Chem.*, **7**, 512-518 (2009).

## THE EFFECT OF ADMIXTURES Ti a Zr ON THE COLOUR PROPERTIES OF CASSITERITE PIGMENTS DOPED BY Cr

**Karolová L.**, Trojan J., Trojan M., Luxová J.

*Department of Inorganic Technology, Faculty of Chemical Technology, University of Pardubice, Studentská 95, 532 10, Pardubice, Czech Republic  
lucie.karlova@student.upce.cz*

### Introduction

Ceramic pigments are inorganic chemical compound, which provide colour and they are insoluble in a medium with which they do not interact physically or chemically. They are characterized by high thermal and chemical stability. Structures of ceramic pigments contain chromophore ions, which impart colour to the originally colourless system<sup>1</sup>. Cassiterite pigments are based on tin dioxide respectively they are mixed oxides, where tin dioxide is the main component. Thanks to their high thermal stability they are used in ceramic industry (for colouring ceramic glazes and enamels) and for their high refractive index also in paint applications or textile dyeing. The advantage of cassiterite pigments is their easy preparation and great availability of raw materials<sup>2</sup>. These pigments are based on tin dioxide which crystallizes in tetragonal structure to form bipyramidal crystals and which plays dominant role in final compound<sup>3</sup>. Tin dioxide is used as a host lattice for important ceramic pigments, e.g. Chrome Tin Orchid Cassiterite, Tin Vanadium Yellow Cassiterite and Tin Antimony Grey Cassiterite<sup>4,5</sup>.

Chromium Tin Orchid Cassiterite of the general formula  $Sn_{1-x}Cr_xO_2$  (according to the CPMA classification with numerical designation 11-23-5) is one of the most important chromium pigment used in ceramic industry. Chrome Tin Orchid Cassiterite is usually synthesized by the conventional ceramic method, involving homogenization of tin dioxide and chromium (III) oxide mixture and its high-temperature calcination<sup>6</sup>. Nowadays this pigment is the only alternative to cadmium-containing pigments for deep violet shades in the pottery chemistry<sup>7</sup>. However, its colouring mechanism is a subject of debate. Its colouration can only be achieved in a narrow range of the chromium oxide and evidences show that the colouration is only present if chromium is above its solubility in cassiterite. Solubility limit of chromium in the inner part of tin dioxide grain is substantially smaller than 1.6 wt% as  $Cr_2O_3$ . The violet colour of the pigment is probably caused with chromium (IV) ions, which are dissolved in cassiterite lattice to form a solid solution. But in the microstructure of pigment are present chromium (III) oxide clusters and small amount of chromium (IV) oxide nanoparticles as well<sup>8,9</sup>.

The aim of this work was to prepare pigment with suitable chromophore agents. Titanium dioxide  $TiO_2$  and zirconium dioxide  $ZrO_2$  were chosen as admixture. The influence of admixtures on colour properties of  $SnO_2/Cr$  pigments in terms of their violet colour intensification to reach higher contribution of desired blue shades in final pigment colouration, especially when applied into ceramic glaze, was observed. In this research the effect of the calcination temperature (1,350, 1,400, 1,450, 1,500°C) on colour properties and particle size distribution was also studied. Synthesized pigments  $Sn_{1-2x}Cr_xM_xO_2$  (where M = Ti or Zr) were always compared with concurrently prepared pigment  $Sn_{1-x}Cr_xO_2$  depending on the calcination temperature and the composition of pigment.

### Experimental

Pigments of general formula  $Sn_{1-2x}Cr_xM_xO_2$  (where M = Ti or Zr) were synthesized by conventional ceramic method. The method makes use of homogenization of starting raw materials presented in form of powder oxides  $SnO_2$  (>99% purity, Shepherd Color Company, USA),  $Cr_2O_3$  (98.5% purity, Lachema a.s., Czech Republic), eventually  $TiO_2$  (>99% purity, Precheza a.s., Czech Republic),  $ZrO_2$  (>99% purity, Honeywell, Germany). The reagents were weighed in suitable molar proportions and then ground manually in porcelain mortar to gain a homogenous reaction mixture. These mixtures were calcinated in corundum crucibles in resistance electric furnace at temperatures from 1,350 to 1,500°C with a step 50°C and with increase of the temperature 10°C  $min^{-1}$  and for the duration 3 hours. All synthesized samples were left to cool to room temperature after each heating stage and subsequently ground in an agate mortar. After spontaneous cooling, prepared pigments were applied into the organic matrix (dispersive acrylic paint Parketol, Balakom, a.s. Opava, Czech Republic) in mass tone and into medium temperature ceramic glaze G 070 91 (Glazura, s.r.o. Roudnice nad Labem, Czech Republic), with amount of a pigment sample 10 wt%. For testing in organic matrix, suspension containing 1 g of the sample and 1.5  $cm^3$  of binder were homogenized. This suspension was converted by a pestle to dense paste able to flowing. Coloured coating films were prepared by application of the paste on white nonabsorbing glossy paper. The coating layer of film was created by dragging the Bird's applicator. Prepared coating films were kept to dry spontaneously in the open air. Then they were ready for an evaluation of colour properties of pigments

into organic matrix in mass tone. In the case of application into the ceramic glaze, an aqueous suspension containing 10 wt% of pigment and 90 wt% of transparent ceramic glaze with an appropriate amount of distilled water was prepared by hand-grinding. The suspension was applied by using brush on unglazed ceramic tile and after drying in open air was glazed at 1,000°C for 15 min.

The colour properties of all final applications were objectively evaluated by measuring of spectral reflectance in the visible region of light (400-700 nm) by using a spectrophotometer ColorQuest XE (HunterLab, Inc. Reston, USA). Standard illuminant D65 was used as internationally recommended white daylight, measurement conditions are as follows: 10° supplementary standard observer, measuring geometry d/8°. For description of colour properties, CIE  $L^*a^*b^*$  colour system (1976) was used. The value  $L^*$  represents the lightness or darkness of the colour as related to the natural grey scale. There is described by numbers from 0 (black) to 100 (white). The values  $a^*$  and  $b^*$  indicate colour tones from  $+a^*$  (red) to  $-a^*$  (green) and from  $+b^*$  (yellow) to  $-b^*$  (blue). Chroma  $C$  represents saturation for the colour and determines colour purity from 0 (grey) to 100 (pure colour). It means that chroma is the degree of difference between a colour and the grey. The colour hue of pigments is also possible to express as a hue angle  $H^\circ$ . It is expressed in degrees;  $H^\circ = 350 - 35^\circ$  for red colour,  $H^\circ = 35 - 70^\circ$  for orange colour,  $H^\circ = 70 - 105^\circ$  for yellow colour,  $H^\circ = 105 - 195^\circ$  for green colour,  $H^\circ = 195 - 285^\circ$  for blue colour and  $H^\circ = 285 - 350^\circ$  for violet colour. Chroma  $C$  and hue angle  $H^\circ$  of samples were calculated according to the Eqs. (1) and (2)<sup>10</sup>.

$$C = [(a^*)^2 + (b^*)^2]^{\frac{1}{2}} \quad (1)$$

$$H^\circ = \arctg \frac{b^*}{a^*} \quad (2)$$

The overall colour difference  $\Delta E_{CIE}^*$  in the CIE  $L^*a^*b^*$  system indicates the degree of colour difference between two samples. This difference is defined by the Eq. (3).

$$\Delta E_{CIE}^* = [(\Delta L^*)^2 + (\Delta a^*)^2 + (\Delta b^*)^2]^{\frac{1}{2}} \quad (3)$$

Parameters between colour of two samples  $\Delta L^*$ ,  $\Delta a^*$ ,  $\Delta b^*$  show difference in lightness and colour tones.

The distribution of particle sizes of the synthesized pigments was measured by using apparatus Mastersizer 2000/MU (Malvern Instruments, Ltd. Worcestershire, UK). The measured signal is assessed by means of Mie scattering theory and Fraunhofer diffraction. The particle size distribution was analysed by two lasers – red light (He-Ne laser,  $\lambda = 633$  nm) and blue light (laser diode,  $\lambda = 466$  nm). The blue light was used for wide-angle forward and back scattering in combination with the red light for forward, side and back scattering. Before the measurement, the samples were gently ground in agate mortar. For the measurement, 0.5 g of sample was dispersed in solution with  $\text{Na}_4\text{P}_2\text{O}_7$  ( $c = 0.15$  g  $\text{L}^{-1}$ ) by using an ultrasonic bath for 2 min. During dispergation, 4.8 ml of  $\text{Na}_4\text{P}_2\text{O}_7$  ( $c = 3$  g  $\text{L}^{-1}$ ) was got into the solution immediately after dispergation up to maximum concentration  $12.5 \pm 0.5\%$  and measuring was launched. The signal was evaluated on the basis of Fraunhofer diffraction. Each measurement was performed three times, results are automatically calculated as average and present as  $d_{10}$ ,  $d_{50}$ ,  $d_{90}$  values.

## Results and discussion

### Colour characteristics

The effect of admixtures and calcination temperature on the colour properties of synthesized pigment after their applications into an organic matrix and ceramic glaze was studied. This part will be focused on application of pigments in ceramic glaze, as for research ceramic pigments, this application is a priority. The obtained results show, that the colour coordinates are changing in the dependence of the pigment composition and the calcination temperature.

In case of  $\text{Sn}_{0.98}\text{Cr}_{0.01}\text{Ti}_{0.01}\text{O}_2$  pigments, the rising calcination temperature caused a considerably decreases value  $L^*$  (lightness) and samples seemed darker. For prepared pigments, the rising temperature caused the increase of the saturation  $C$ . The highest value  $C$  ( $C = 22.74$ ) was observed at temperature of 1,500°C and this pigment provided the purest colour. It is obvious that the increasing value of  $C$  results from the increase of both colour coordinates ( $+a^*$ ,  $-b^*$ ). The values of coordinate  $a^*$  were in interval from 17.38 to 20.58 and coordinate  $b^*$  reached values from -7.44 to -9.67. The values of  $H^\circ$  moved in the narrow range, from 334.83° to 336.83° and this range corresponds to violet colour shade.

The comparison of synthesized pigments  $\text{Sn}_{0.99}\text{Cr}_{0.01}\text{O}_2$  and  $\text{Sn}_{0.98}\text{Cr}_{0.01}\text{Ti}_{0.01}\text{O}_2$  in terms of acquired colour properties showed that pigments with titanium ions provided higher values of lightness  $L^*$ . Furthermore, titanium doped pigments provided the increase of saturation. All of prepared titanium-doped pigments had higher values of both colour coordinates ( $+a^*$ ,  $-b^*$ ). This fact is confirmed by mostly decreasing values of angle

$H^\circ$ . It means that  $Sn_{0.98}Cr_{0.01}Ti_{0.01}O_2$  pigments in comparison with  $Sn_{0.99}Cr_{0.01}O_2$  were a shift closer toward blue-violet shades. All measured results are presented in *Table I*.

Table I

The effect of admixture and calcination temperature on colour properties and particle size distribution of pigments  $Sn_{0.98}Cr_{0.01}Ti_{0.01}O_2$  and their comparison with similarly prepared pigments  $Sn_{0.99}Cr_{0.01}O_2$ .

T [°C]	Pigment	L*	a*	b*	C	H°	$\Delta E_{CIE}^*$	$d_{50}$ [µm]
1,350	$Sn_{0.99}Cr_{0.01}O_2$	54.51	15.64	-6.12	16.79	338.63	3.33	6.90
	$Sn_{0.98}Cr_{0.01}Ti_{0.01}O_2$	57.03	17.38	-7.44	18.91	336.83		5.70
1,400	$Sn_{0.99}Cr_{0.01}O_2$	53.34	16.37	-7.37	17.95	335.76	3.25	8.41
	$Sn_{0.98}Cr_{0.01}Ti_{0.01}O_2$	54.88	18.80	-8.88	20.79	334.72		8.60
1,450	$Sn_{0.99}Cr_{0.01}O_2$	52.11	17.93	-8.29	19.75	335.19	2.49	10.33
	$Sn_{0.98}Cr_{0.01}Ti_{0.01}O_2$	53.10	19.85	-9.53	22.02	334.35		10.07
1,500	$Sn_{0.99}Cr_{0.01}O_2$	49.89	19.26	-8.54	21.07	336.09	2.05	14.43
	$Sn_{0.98}Cr_{0.01}Ti_{0.01}O_2$	50.98	20.58	-9.67	22.74	334.83		12.51

In case of the  $Sn_{0.98}Cr_{0.01}Zr_{0.01}O_2$  pigments, increasing synthesis temperature causes a decrease of value  $L^*$ . For these types of pigments, rising temperature caused the slight increase of the saturation  $C$ . However the red colour has a bigger share in the increasing of  $C$  and values  $a^*$  were increasing with temperature. On the other hand the blue shade shows insignificant increase. The values of coordinate  $a^*$  ranged between 18.89 to 20.00 and coordinate  $b^*$  reached values from -6.43 to -6.64. This trend is apparent also from marginally increasing values of angle  $H^\circ$  within a very narrow range (from 341.20° to 341.63°) and these pigments provided red-violet hue.

The comparison of synthesized pigments  $Sn_{0.99}Cr_{0.01}O_2$  and  $Sn_{0.98}Cr_{0.01}Zr_{0.01}O_2$  in terms of acquired colour properties demonstrated that pigments with zirconium ions provided lower values of lightness  $L^*$ . Zirconium-doped pigments as well as titanium-doped pigments provided higher values of saturation  $C$  than  $Sn_{0.99}Cr_{0.01}O_2$  pigments. The largest contribution to an increase of saturation  $C$  had a distinct increase of value  $a^*$  compared with standard pigments  $Sn_{0.99}Cr_{0.01}O_2$ . It can be stated that  $Sn_{0.98}Cr_{0.01}Zr_{0.01}O_2$  that with slightly higher values of  $H^\circ$  provided (in comparison  $Sn_{0.99}Cr_{0.01}O_2$ ) rather toward red-violet hue.

Table II

The effect of admixture and calcination temperature on colour properties and particle size distribution of pigments  $Sn_{0.98}Cr_{0.01}Zr_{0.01}O_2$  and their comparison with similarly prepared pigments  $Sn_{0.99}Cr_{0.01}O_2$ .

T [°C]	Pigment	L*	a*	b*	C	H°	$\Delta E_{CIE}^*$	$d_{50}$ [µm]
1,350	$Sn_{0.99}Cr_{0.01}O_2$	54.51	15.64	-6.12	16.79	338.63	3.46	6.90
	$Sn_{0.98}Cr_{0.01}Zr_{0.01}O_2$	55.66	18.89	-6.43	19.95	341.20		6.05
1,400	$Sn_{0.99}Cr_{0.01}O_2$	53.34	16.37	-7.37	17.95	335.76	3.38	8.41
	$Sn_{0.98}Cr_{0.01}Zr_{0.01}O_2$	52.01	19.42	-6.80	20.58	340.70		7.37
1,450	$Sn_{0.99}Cr_{0.01}O_2$	52.11	17.93	-8.29	19.75	335.19	3.50	10.33
	$Sn_{0.98}Cr_{0.01}Zr_{0.01}O_2$	49.53	19.59	-6.60	20.67	341.38		9.65
1,500	$Sn_{0.99}Cr_{0.01}O_2$	49.89	19.26	-8.54	21.07	336.09	2.05	14.43
	$Sn_{0.98}Cr_{0.01}Zr_{0.01}O_2$	50.10	20.00	-6.64	21.07	341.63		12.80

#### Particle size distribution

The calcination temperature and the admixture do not affect only colour properties, but also particle size distribution. The mean particle size of inorganic pigments should lie in the range of 0.01 – 15 µm. The obtained values of mean particle size ( $d_{50}$ ) of the powder compounds are presented in *Table I* and *Table II*. The results show, that growing synthesis temperature causes the increase of values  $d_{50}$  for both types of admixtures. Titanium-doped and zirconium-doped pigments are characterized by lower values of  $d_{50}$  in comparison with the standard pigments with any other admixture. Their interval ranges from approx. 5 to 13 µm. A suitable

granulometric composition for application of pigments into ceramic glaze is about 5 – 15  $\mu\text{m}$ . These values were attained for all prepared pigments. For their potential use in painting coats it would be necessary to treat the size mechanically, especially for pigments synthesized at higher temperature (1,450 and 1,500°C).

### Conclusions

The main aim of research was to synthesize  $\text{Sn}_{0.98}\text{Cr}_{0.01}\text{Ti}_{0.01}\text{O}_2$  and  $\text{Sn}_{0.98}\text{Cr}_{0.01}\text{Zr}_{0.01}\text{O}_2$  compounds and to find out whether the presence of admixtures can affect the colour properties and particle size distribution. The use of these  $\text{TiO}_2$  or  $\text{ZrO}_2$  as dopants components in pigments had a major importance of their proven positive effects on the course of solid state reactions. Changes in their modification during synthesis support its course (use of Hedvall effect), which had a positive influence on the particle size of synthesized pigments. Mean particle size moved in range 5.70 to 12.80 in dependence on firing temperature. The effect of calcination temperature on colour properties was studied as well. From the obtained results, it can be concluded that higher heating temperature stimulates the formation of darker pigments with higher saturation C. The biggest abundance of the desired blue shade as well as an overall shift closer toward blue-violet colour in ceramic glazes were observed in  $\text{Sn}_{0.98}\text{Cr}_{0.01}\text{Ti}_{0.01}\text{O}_2$  pigment, which was calcinated at 1500°C. The resulting  $\text{SnO}_2/\text{Cr}$  compounds doped with titanium or zirconium ions allow an extension of the scale of the attainable violet colours that are in shortage in the field of high-temperature ceramic pigments.

### Acknowledgment

This work was supported by IGA University of Pardubice (SGSFChT\_2015005).

### Literature

1. Buxbaum G., Pfaff G.: *Industrial Inorganic Pigments*. 3<sup>rd</sup> ed., Wiley-VCH, Verlag GmbH & Co. KGaA, Weinheim, 2005.
2. Eppler D.R., Eppler R.A.: *Ceram Eng Sci Proc*, 18, p. 139 (1997).
3. Batzill M., Diebold U.: *Prog. Surf. Sci.*, 79, p. 47-49 (2005).
4. Joo I.D., Hwang D.H., Lee H.S., Park J.S., Lee B.H.: *J. Korean Chem. Soc.*, 46, p. 639-642 (2009).
5. Tena M.A., Sorlí S., Llusar M., Badenes J.A., Forés D., Monrós G.: *Anorg. Allg. Chem.*, 631, p. 2188-2191 (2005).
6. CPMA Classification and Chemical Description of the Complex Inorganic Color Pigments, 4th ed. Alexandria, Virginia: Color Pigments Manufacturers Association, Inc., p. 21-22 (2010).
7. Papp J.F.: *Am. Ceram. Soc. Bull.*, 74, p. 118 (1995).
8. Ren F., Ishida S., Takeuchi N.: *Ceram. Bull.*, 71, p. 759 (1992).
9. López-Navarrete E., González-Eliphe O. R., Ocaña M.: *Acta Mater.*, 51, p. 2371-2381 (2003).
10. Völz H.G.: *Industrial Color Testing: Fundamentals and Techniques*, 2<sup>nd</sup> ed., Wiley-VCH Verlag GmbH & Co. KGaA, Weinheim, 2002.

## **MATERIAL ENGINEERING**

### **CHEMICAL ASPECTS OF ANTIBALLISTIC CERMETS PREPARATION**

**Brozek V.**<sup>1</sup>, Kubatik F.T.<sup>1</sup>, Chraska T.<sup>1</sup>, Musalek R.<sup>1</sup>, Janata M.<sup>1</sup>, Mastny L.<sup>2</sup>

<sup>1</sup>*Institute of Plasma Physics ASCR v.v.i, Za Slovankou 3, 18200 Prague, Czech Republic*

<sup>2</sup>*University of Chemistry and Technology, Technicka 5, 16628 Prague, Czech Republic*  
brozek@ipp.cas.cz

#### **Abstract**

Antiballistic ceramics, either for individual personal protection or for protection of combat equipment, is always composed of materials with the highest attainable hardness and toughness simultaneously. An important property determining the choice of suitable compounds is low density. These criteria are fulfilled only by certain borides, carbides, nitrides and oxides of elements with their atomic number smaller than 22. In practice, these materials are based especially on aluminium oxide, boron carbide, silicon nitride and carbide and borides of titanium, characterized in particular by high Young's modulus of 200 GPa and micro-hardness values above 20 GPa. That is convenient for deformation of projectiles, but results in small fracture toughness and inappropriate energy dissipation of the impacting projectile. Wearable personal antiballistic protection solves this issue by mechanically anchoring the antiballistic material in matrices of high strength polymers, e.g. Kevlar. Antiballistic protection of combat equipment is adhesively bonded with metal armour. Reactive plasma coating technology enables the preparation of both the ceramic materials, and their attachment to a metal matrix. It also promotes perfect adhesive bonding with a metal or another ceramic substrate. The advantage of reactive plasma deposition lies in its ability to coat complex geometric shapes of otherwise difficult to machine semi-finished products and also in the possibility of preparing functionally graded materials. Chemical approach to problems of the reactive plasma deposition at temperatures above 4000 K is related to the fact that the deposition occurs in an interval of a few milliseconds. In such circumstances, the rules of chemical kinetics do not apply and the extremely rapid cooling of the deposited product can result in new stable structures that are poorly understood as they are created from the original precursors.

The paper aims to demonstrate the possibilities of metal-ceramic material deposition on different types of metal or ceramic substrates using plasma spraying. A number of self-supporting components and the preparation of metal-braced composites are described and the results of plasma depositions of two particular extremely hard ceramic materials, boride and nitride of titanium are presented. The plasma deposition of these materials is performed in technological conditions which prevent undesirable high-temperature oxidation. The paper describes deposition conditions that may lead to materials suited to create anti-ballistic protection and complicated shapes or improve parameters of surface layers of present anti-ballistic ceramics.

**Key words:** anti-ballistic ceramics; armour ceramics; corundum-baddeleyite ceramics; plasma spraying; titanium boride; titanium nitride;

#### **Introduction**

There are a number of requirements placed on modern antiballistic armour, in particular with regard to the level of ballistic protection, basis weight, price, production technologies and potential reparability. At present, for passive protection of an individual, layered structures are used where an outer level of the armour is made of resistant ceramics whose main aim is to blunt or disturb a falling projectile and spread acting energy to a large area<sup>1</sup>. Residual energy of a projectile is later absorbed by an underlying metal layer, especially by its plastic deformation. Obviously it is vital to ensure good binding, be it chemical or adhesive, between the two layers. Outer antiballistic or armour ceramics passes through continuous material changes, especially affected by new findings from the field of quarry mechanics. In essence, the choice is oriented at materials from compounds appropriate for personal protection means of an individual (the so-called light armour) and materials for protection of light combat technique – see e.g. the armament of our armoured vehicles with Pandur antiballistic corundum or carbide ceramics<sup>2</sup>. The paper does not aim at the discussion of advantages or disadvantages of individual antiballistic ceramics variants; unequivocal conclusion based on practical combat experience relates to a fact that the front part of the armour must be made of a material with the highest achievable hardness in a given system to ensure the diversion of a trajectory or major geometric deformation of a metal projectile or shrapnel<sup>3</sup>. The significance and functions of individual layers of composite armours

have been studied and presented in a number of publications, e.g.<sup>4</sup>. They are a subject of numerous patents<sup>5</sup> and supposedly even top-secret information.

Among main chemical compounds from which antiballistic ceramic parts are made belong aluminium oxide, silicon carbide and silicon nitride, boron carbide and borides of titanium. They are substances which are generally characterised by high hardness ( $> 20$  GPa), high melting points ( $2000\text{ }^{\circ}\text{C} - 3000\text{ }^{\circ}\text{C}$ ) and low density  $< 4\text{ g/cm}^3$ , for even low weight belongs among main selection criteria.

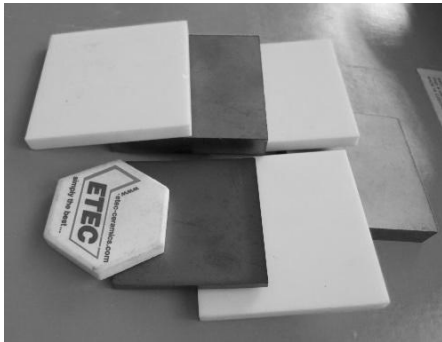


Figure 1. Commercial products of antiballistic ceramics

High hardness of these materials which causes their difficult workability is a reason why they are produced in simple geometrical shapes, most often as flat plates of square or hexagonal shape (Figure 1), from which large parts are comprised in a mosaic-like style<sup>6</sup>.

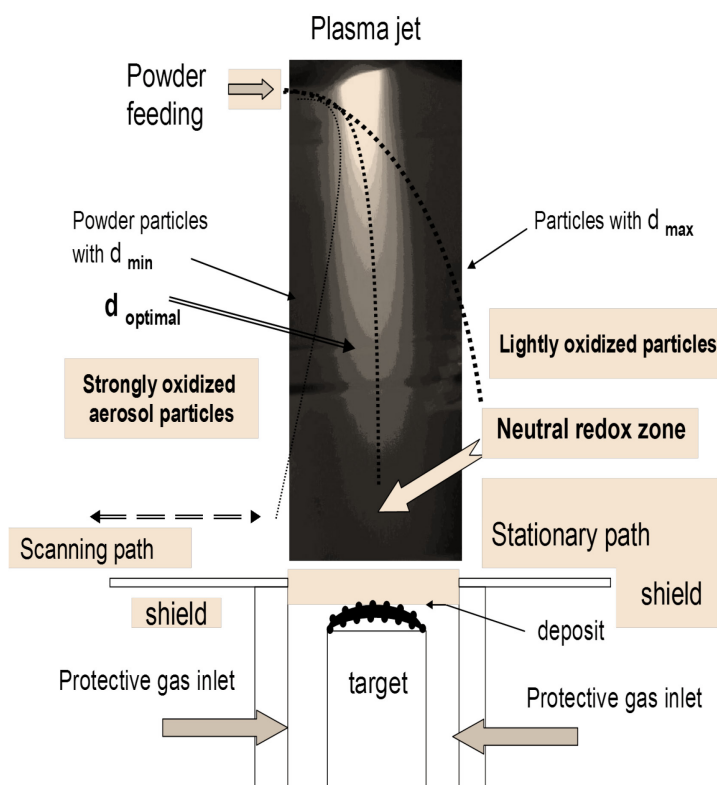


Figure 2. Scheme of plasma deposition experiment arrangement;

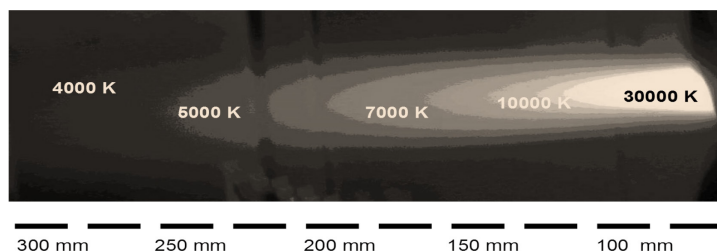


Figure 2a. Plasma isotherms produced by WSP®H-500 generator.

As opposed to classical approach to sintering ceramics, plasma deposition technology has several potential advantages. It is easier to process compounds with extremely high melting points and hardness into different complicated shapes or deposit a layer straight to a substrate without further coupling. It is further possible to deposit various materials or their mixtures and create functionally graded layers. As potentially very convenient

is regarded a possibility to carry out repairs of damaged layers. Plasma deposition enables the preparation of planar and shaped armours from compounds with the highest melting points ( $\text{TiB}_2$  2980°C,  $\text{ZrC}$  3520°C), with low density ( $\text{SiC}$  3.21 g/cm<sup>3</sup>,  $\text{B}_4\text{C}$  2.49 g/cm<sup>3</sup>), with incorporated metal inter-layers, with incorporated grids of metal fibres and fibres from metal glass and materials with nano-composite structure<sup>7</sup>.

The use of unique stabilised WSP<sup>®</sup> plasmatron, developed in the Institute of Plasma Physics ASCR, potentially enables efficient deposition of layers on large areas in technologically interesting depths.

The paper focuses on the preparation of sandwich antiballistic ceramics based on ultra-hard titanium compounds from Ti, TiN,  $\text{TiB}_2$ ,  $\text{B}_4\text{C}$  precursors by both their direct deposition and reactive deposition to commercial antiballistic corundum substrates  $\text{SiC}$  and  $\text{ZrO}_2$ . In the first phase the behaviour of input substances during the plasma deposition was verified. In other phases individual variants of the preparation of sandwich antiballistic elements was tested. In conclusion, compatibility and bond strength with combat technique steel bases was verified.

### Experimental part

Initial substances: Powder titanium of grain 20-63 μm, powder boron carbide of grain 50–63 μm. Commercial  $\text{TiB}_2$  Ventron Alfa Aesar production, powder corundum from Carborundum Electrite Inc., Benátky n/Jiz. The WSP<sup>®</sup>H-500 plasma generator with operating parameters 320-550 A, 280-320 V, power up to 180 kW, stabilising medium flow 0.2 l/min (note: General parameters of plasma deposition on our WSP<sup>®</sup> device are described in more detail in e.g. <sup>8</sup>). Powder input to plasma flow by means of two independent pneumatic feeders TecFlo, carrier gas a) nitrogen b) argon with 7% hydrogen. The amount of powder discharged into the plasma flow was regulated in the scope 5 – 20 kg/h by the change of pressure and flow of carrier gas between 0.30 – 0.50 MPa. Argon was used as carrier gas; in case of reactive deposition nitrogen was used. The reactive deposition of borides of titanium was performed in two ways, a) independently, from two separate feeder nozzles Ti and  $\text{B}_4\text{C}$  powder was brought into the plasma using argon with 0.5 MPa overpressure and b) Ti +  $\text{B}_4\text{C}$  mixture was homogenized in the ratio  $\text{Ti}:\text{B}_4\text{C}$  1:1.15 and brought simultaneously from two feeders. In reactive TiN deposition Ti powder was brought into plasma by nitrogen in excess provided by 0.30 MPa overpressure, feeding distance 45 mm to 115 mm. Ultra-hard coatings were applied to ceramic substrates from corundum,  $\text{SiC}$  and  $\text{ZrO}_2$ , simulating qualities of commercial antiballistic older generation elements. Experiment instrument arrangement is schematically described in Figure 2 and Figure 2a.

### Results and discussion

Plasma deposition of powder precursors into metal, ceramic or graphite substrates provided products whose characteristics is mentioned in Table 1.

Table I

Mechanical qualities of antiballistic coatings on substrates from  $\text{Al}_2\text{O}_3$ ,  $\text{SiC}$ ,  $\text{ZrO}_2$  or steel EN-S235JR – 1.0038

Starting powder	Phase composition of coating	HV [GPa]	Density [g.cm <sup>-3</sup> ]	E-module [GPa]
$\text{TiB}_2$	$\text{TiB}_2$ , TiB	20.7	4.52	315
Ti + $\text{B}_4\text{C}$ separate feeding	TiB, $\text{Ti}_3\text{O}$	15.7	4.54	230
Ti + $\text{B}_4\text{C}$ mixture	TiB, $\text{TiB}_2$ , $\text{Ti}_3\text{O}$	22.1	5.08	294
Ti + $\text{N}_2$	TiN, $\text{Ti}_{0.83}\text{N}_{0.17}$	22.2	5.28	374
$\alpha\text{-Al}_2\text{O}_3$	$\gamma\text{-Al}_2\text{O}_3 > \delta\text{-Al}_2\text{O}_3 > \alpha\text{-Al}_2\text{O}_3$	14.2	3.98	274
Eucor *	$\text{ZrO}_2$ , $\text{Al}_2\text{O}_3$ + 30-90 % amorphous phase	15.3	3.50	315
$\text{SiC}$ substrate ( $\text{SiSiC}$ )	$\text{SiC}$ 6H, $\text{SiC}$ 4H, YAG	42.0	3.08	536

\*Eucor – corundum-baddeleyite ceramics with amorphous phase, product of Eutite Ltd. Mar. Lazne

Product parameters after conjoint deposition of titanium and boron carbide applied to the plasma from two independent feeders in the ratio 1: 1.15 (i.e. with excess 15 % B) are also in Table 1. Reactive deposition of titanium with a stoichiometric excess of nitrogen provided a product which has all features of cermet material. The acquired products of plasma deposition were subjected to analysis on FISCHER Picodentor Scope HM500 device which, using an indentation method, analyses values of Vickers surface micro-hardness and flexibility modules. Results are summarised in Table 1 and documented in Figure 3. Values of indenter penetration maximal depth and minimal depth measured after relieving indentation load are described in Figure 3 for the

firmest material on the basis of sintered SiC (curve 4) and for substrate from ZrO<sub>2</sub> baddeleyite ceramics which was used as a limit material with the lowest parameters that is applied in the area of antiballistic ceramics (curve 1). Values of the examined coatings from corundum and Eucor (curve 2), TiN (curve 3) including TiB and TiB<sub>2</sub> lie in the interval between the above mentioned limit examples.

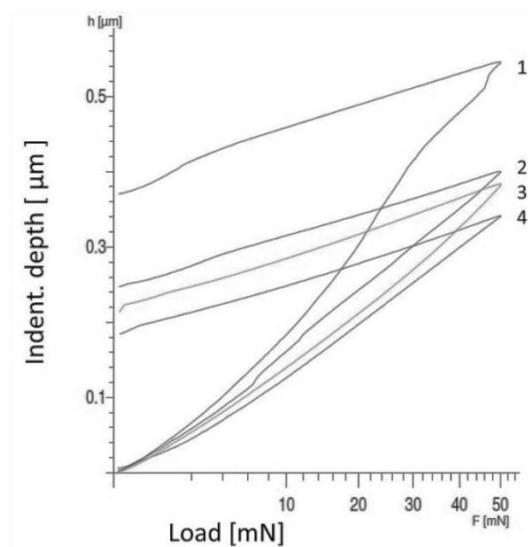


Figure 3. Indentation measurement of hardness and flexibility modules with maximum load 50 mN  
The following examples demonstrate possibilities of plasma deposition technology in creating multilayers from materials with the highest mechanical parameters both independently and in substrates of commercial antiballistic segments.

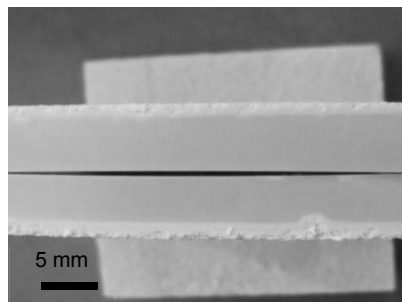


Figure 4. Aluminium oxide coating on ZrO<sub>2</sub> substrate

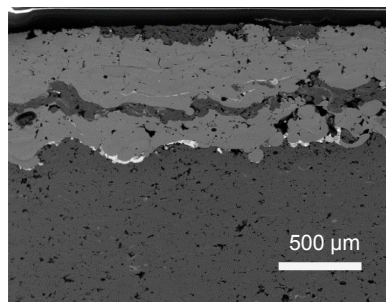


Figure 5. Microstructure of TiB<sub>2</sub> on corundum substrate (SEM)

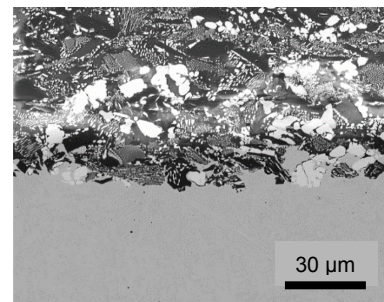


Figure 6. Microstructure of the Eucor coating on steel S235JR

In reactive deposition of titanium and boron carbide applied to plasma from two independent feeders in the ratio 1: 1.15, with 15% B<sub>4</sub>C excess, using the XRD method, presence of cubic boride TiB and deficit Ti<sub>3</sub>O with hexagonal structure (P-31c) was discovered in 2 mm thick coatings. What is remarkable is the absence of titanium carbide in flow, which may correspond with the so-called auto-shrouding effect already observed before, e.g. in wolfram carbide deposition<sup>9</sup>. In plasma flow, or in its turbulent composition with entrained air tracks, the oxidation of boron carbide occurs and produced carbon monoxide creates a protective atmosphere around the surface of flying powder particles. Normally, in air, boron carbide oxidation creates boron oxide. In boron carbide deposition<sup>10</sup> the boron oxide was created, however, it was not found in product diffractograms, probably due to the development of its glassy amorphous phase. After leaching the products with hot water boron ions were identified in the solution using atom absorption spectrometry. Further experiment was therefore performed with beforehand concocted powder mixture in the ratio Ti: B<sub>4</sub>C 3:1 with the aim to gain a final reaction:



Even in this case Ti<sub>3</sub>O hexagonal phase of two cubic phases was discovered in the product, with two close grid parameters corresponding to compounds TiB and TiN.

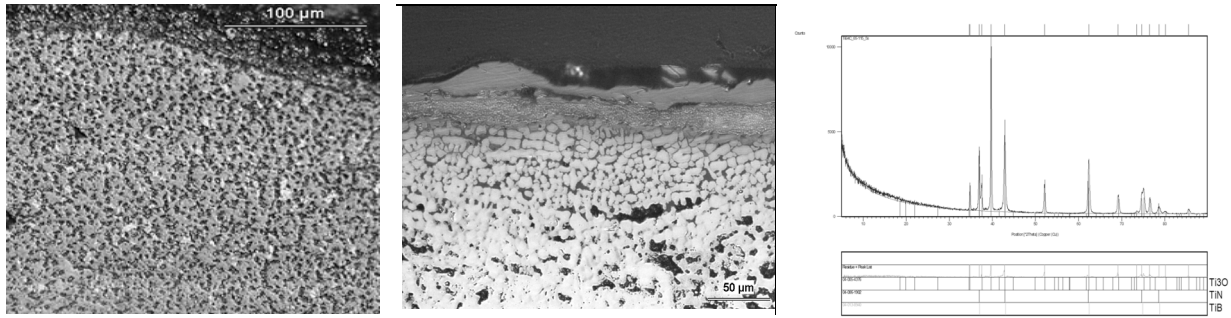


Figure 7. Surface microstructure and cross-section through the product of Ti + B<sub>4</sub>C plasma-chemical reaction

If culled coarse-grained boron carbide and Ti + B<sub>4</sub>C mixture was applied to a less warm part of a plasma cone, only titanium fusion and B<sub>4</sub>C grain fixation into this metal matrix occurred. Besides titanium and B<sub>4</sub>C, a phase analysis of the product confirmed the presence of TiO<sub>2</sub>, which implies that the selected deposition temperature was already low after the fusion and reaction with B<sub>4</sub>C. Only the oxidation of undersized titanium particles occurred and a shrouding effect of boron carbide did not take place. This was also proved by a high share of non-deformed B<sub>4</sub>C grains in titanium matrix. In boron carbide fusion (m.p. 2450 °C) the creation of splats typical for plasma deposition would have to occur.

Further reactive deposition experiments were performed with powder titanium applied to plasma flow by nitrogen. Coating samples were surrounded by protective nitrogen atmosphere. TiN with lattice parameter  $a = 0.4216$  nm was identified in the products, which according to verified literary data indicates achieving nearly ideal stoichiometry. Also a hexagonal phase Ti<sub>0.83</sub>N<sub>0.17</sub> (P63/mmc) appeared in the product, which develops in high-temperature titanium nitration only<sup>11</sup>. In marginal parts of a plasma cone (spatial angle 0.03 – 0.05 sr) even TiO<sub>2</sub> oxidation occurred. Its presence at the level of sensitivity of the XRD method was apparent when the covering of the substrate surface was necessary due to a large target dimensionality. In small targets situated in a flow axis of plasma fused particles oxidation did not occur. After verifying deposition system capability to process both boride and nitride of titanium, we aimed at the preparation of combined multi-layered segments for antiballistic protection and we verified its ballistic resistance (Fig. 8-10).

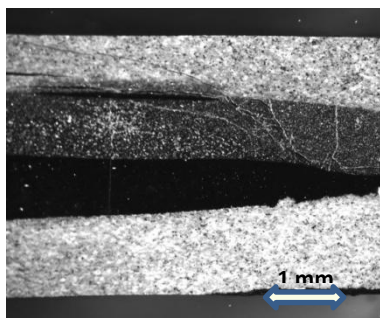


Figure 8. Microstructure of multilayers Eucor-TiN-Ti-TiB<sub>2</sub> (Canon EOS 500D)

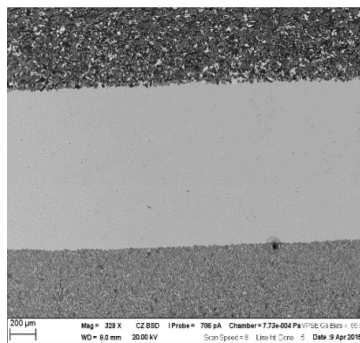


Figure 9. Microstructure of multilayers Eucor-steel-TiN

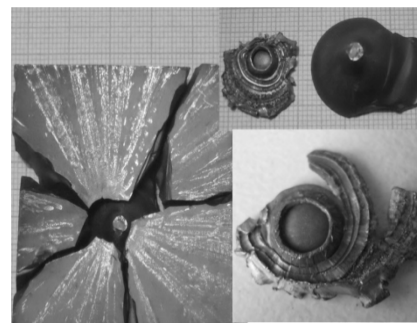


Figure 10. Projectile degradation on TiB<sub>2</sub>/SiC antiballistic ceramics

The temperature of substrate surface in plasma deposition can be programmatically regulated and reduced without external cooling under 300 °C, which means, for example, that while reinforcing with metal wires or other fibres or mesh no secondary heat influence will occur, which usually reduces convenient parameters of reinforced texture materials. Figure 11 and 12 show details of corundum spraying on metal grid which is used as a combined reinforcing feature which combines ceramic armours using alkyl-glycol-carbonates or epoxydes<sup>3</sup>. The figure shows an initial phase of metal grid coating. By continued spraying, using original corundum or boron titanium, another mesh and total compaction occurs.

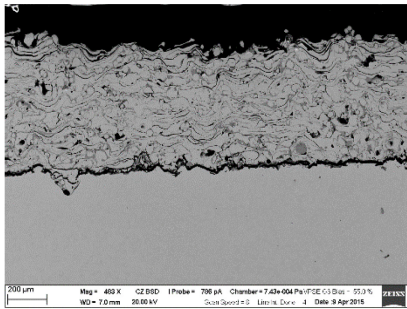


Figure 11. Corundum surface microstructure on steel

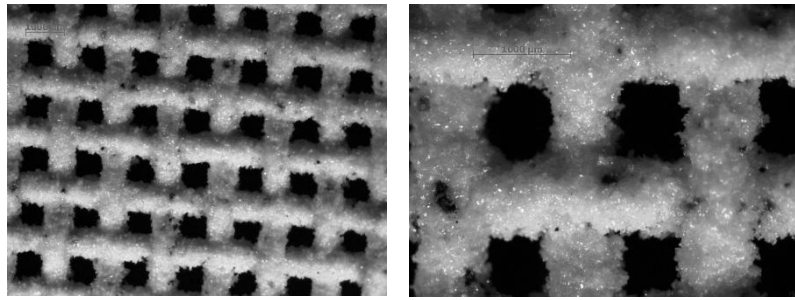


Figure 12. Initial phase of corundum deposition on steel reinforcing grid 50 mesh

Adhesion between individual ceramic layers and adhesion to metal military technique armouring was also measured for multilayer products. Using a pull-off technique with the Loctite 3425 A&B Hysol adhesive, in all cases of ceramic deposition on EN-S235JR, steel bond strength values between 12-20 MPa were discovered. Ceramic layers shared a higher value than that of the adhesive, i.e. 27-29 MPa.

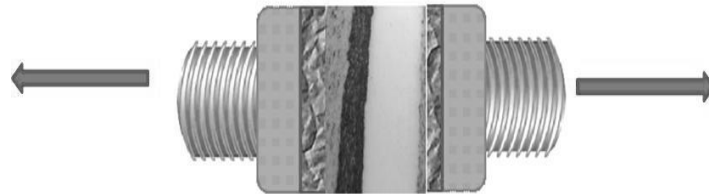


Figure 13. Scheme of pull-off test of multi-layered ceramic coatings

## Conclusion

It was confirmed that it is possible to deposit advanced ceramics in a thermic way using plasma spraying on ceramic substrates. Ultra-hard surfaces of borides and nitrides of titanium with a minimal amount of sub-stoichiometric oxide phases of titanium on pads from corundum, silicon carbide and zirconia ceramics can also be prepared using plasma deposition. Ballistic resistance of the samples prepared in this series following the EU norms was not analysed yet, however, two mechanical parameters which have a decisive impact on the required quality of such materials were measured. Indentation methods were used to measure hardness and flexibility modules. Products of a titanium plasma-chemical reaction with boride and nitrogen compounds reach micro-hardness 15.7 – 22.2 GPa, E-module value 230 - 374 GPa. When compared with known commercial products on  $Al_2O_3$  CoorsTek Comp. basis, it is clear that boride micro-hardness in plasma deposited coating will be higher and, in contrast, module flexibility will drop about 25 %. The reason is rather high porosity of a plasma deposited coating, which may reach as high as 10 %. This corresponds with generally acknowledged exponential dependence of hardness on porosity of material  $H = H_0 \cdot (\exp -bP/100-P)$  with empirically stated constant  $b = 0.42$ . ( $P = \% \text{ porosity}$ ,  $H_0 = \text{theoretical or maximum elicited hardness value}$ ).

If porosity is reduced during deposition by technological changes, for example by additional sintering or impregnation<sup>12</sup>, much more favourable final values can be expected. From a small number of up to now verified samples it is impossible to arrive at statistical conclusions concerning the impact of variable oxygen content bound in the  $Ti_3O$  phase which develops during the deposition of titanium with boron carbide and TiN. This hexagonal phase, detected by XRD, is homogeneously scattered in the whole sample volume and it is impossible to isolate it or prepare it in order to measure its individual parameters and characteristics. Nothing is known about the behaviour of this phase in literature, however, physical parameters can be assumed not to significantly differ from other titanium oxides. These values at any rate exceed parameters of corundum materials processed using ceramic technology and they suggest that a front surface boride layer even with a mild content of oxide phases applied by plasma spraying can significantly increase antiballistic resistance of ceramic parts prepared in a classical sintering technology.

It should also be noted that the lamellar microstructure of plasma-deposited layers are fundamentally different from the mechanism of fracture microstructure conventional sintered ceramics for ballistic purposes. It is therefore to be expected that their properties are significantly different.

The aim of our further research of the preparation technology development of combined or laminated metal-ceramic layers will focus on the use of unique qualities of plasma spraying, such as its increased ability of energy dissipation, non-linearity of deformation course, differences in disturbance micro-mechanisms or possibilities of gradient layer formation and so on.

#### **Acknowledgment**

*This work was supported by a grant from Ministry of Industry and Trade Czech Republic, MPO No. FR-T12/702*

#### **Literature**

1. Medvedovski E.: American Ceramic Society Bulletin, 81, 3, pp. 27-32 (2002).
2. Zdobinsky M.: *Pandurs for Afghanistan*. ATM, 10, 4-5 (2010).
3. Gama A. A., Bogetti T. A., Fink B. K.: Composite structures 52, pp. 381-395 (2001).
4. Hallam D., Heaton A., James B.: J. Eur. Ceram. Soc. 35, 2243-2252 (2015).
5. Saforeen G.M.J.: US Patent Office 2964501
6. Hazell P. J., Roberson C. J., Moutinho, M.: Materials and Design, 29, 8, pp. 1497-1503 (2008).
7. Chraska T., Neufuss K., Dubsky J.: J. Thermal Spray Technology. 17, pp. 872-877 (2008).
8. Neufuss K., Chraska P., Kolman B., Sampath S., Travnicek Z.: J. Thermal Spray Technology 6, 434-438 (1997).
9. Brozek V., Matejicek J., Neufuss K.: Powder Metallurgy Progress 7, 4, 213-220 (2007).
10. Nanobashvili S., Matejicek J., Zacek F.: Journal of Nuclear Materials, 307-311, 1334-1338 (2002).
11. Bars J.P., David D., Debuigne J.: Metall Trans A, 14, 1537-1542 (1983).
12. Kocik J., Ctibor P., Brozek V.: Chem. Listy 104, 6, 518 (2010).

## SYNTHESIS AND APPLICATIONS OF INTERMETALLICS

**Novák P.**<sup>1</sup>, Salvetr P.<sup>1</sup>, Kříž J.<sup>1</sup>, Marek I.<sup>1</sup>, Kubatík T.F.<sup>2</sup>

<sup>1</sup>University of Chemistry and Technology, Prague, Department of Metals and Corrosion Engineering, Technická 5, 166 28 Prague 6, Czech Republic

<sup>2</sup>Institute of Plasma Physics AS CR, v.v.i., Za Slovankou 1782/3, 182 00 Prague 8, Czech Republic  
panovak@vscht.cz

### Abstract

Intermetallic compounds, intermetallics, are characterized by interesting properties, such as e.g. excellent high-temperature oxidation resistance, shape memory or ability to store hydrogen reversibly. Their positive, but also negative, properties are a combination of the behaviour of metals and ceramics. Their wider application in industry is limited due to low room-temperature ductility and problematic production, associated with high melting points of many intermetallics, high reactivity of metals at high temperatures and problematic processing.

In this paper, the overview of the methods for synthesis of intermetallic compounds is presented, ranging from conventional casting processes to modern powder metallurgy technologies. Selected interesting applications from industry and medicine, where their unique properties are used.

### Introduction

Metallic materials are used in structural applications for their typical properties, such as good strength and ductility at common temperatures, formability, ductility, electric and thermal conductivity etc. In addition to these typical applications, metallic materials are also designed to be applied under the conditions near their limits, such as at high temperatures, in strongly aggressive corrosion environment or under the conditions of extreme abrasive or adhesive wear. For these conditions, intermetallics can be possible candidates, combining the properties of metals and ceramics. Intermetallics are usually characterized by high melting points, good corrosion resistance in electrolytes as well as at high temperatures or by special material-specific properties (shape memory, magnetic properties etc.). However, the larger utilization of intermetallics is strongly limited by low room-temperature ductility and also by problematic production and processing.

### Synthesis of intermetallics

Such as for other metallic materials, melting metallurgy is a dominant production method of intermetallics. Melting and casting is applicable technology for many intermetallics, but connected with serious problems. These complications are high melting points (e.g. titanium aluminide melts at 2130 °C [1]), poor casting properties and also high reactivity of the melts at high temperatures (mainly in the case of the processing of titanium-based intermetallics [2]). All of those obstacles can be overcome by the modification of the processing route, such as the use of ultrasound during casting [3], hot isostatic pressing of the castings to heal the voids and cracks in castings [4] or the application of alternative less reactive materials for crucibles and molds (e.g. ZrO<sub>2</sub>, Y<sub>2</sub>O<sub>3</sub>) [2]. However, these solutions increase the production cost and are not applicable generally. Forming processes are almost non-applicable for most of the intermetallics due to low plasticity even at elevated temperatures, except for e.g. NiTi shape memory phase.

These facts imply that powder metallurgy can be very promising alternative route for the production and processing of intermetallics. Among powder metallurgy techniques, two kinds of non-conventional processes play an important role worldwide. First one is mechanical alloying, which allows for the production of nanocrystalline intermetallics. Mechanical alloying is a solid-state powder processing method, involving repeated welding, fracturing and re-welding of powder particles [5] during high-energy ball milling (Figure 1). This method produces ultrafine structures which are far from equilibrium state.

Mechanical alloying enables to achieve following materials attributes:

- production of fine dispersion of strengthening phase particles,
- extension of solubility limits,
- refinement of the grains down to nanometre scale,
- synthesis of metastable crystalline phases,
- formation of amorphous powders,
- alloying even by insoluble elements,
- low-temperature initiation of solid state reactions.

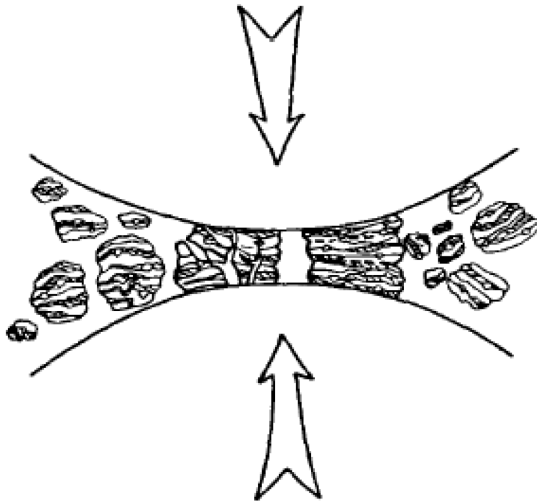


Figure 1: Schematic description of the mechanical alloying process [5]

Mechanical alloying produces ultrafine-grained powder that has to be consolidated to produce a bulk intermetallic phase. The number of applicable consolidation techniques is very limited in the case of intermetallics due to low plasticity and poor sinterability of the intermetallics' powders. In practice, hot isostatic pressing or Spark Plasma Sintering are applicable. Spark Plasma Sintering, i.e. the consolidation by uniaxial pressing combined with the passage of pulsed electric current, seems to be the most promising technique due to low process duration and lower process temperature required. It prevents coarsening of the grains of intermetallics [6].

Second possible method is a group of Self-propagating High-temperature Synthesis (SHS) processes. In these processes of reaction synthesis, energy is supplied to the compressed mixture of pure metallic powders or other precursors by heating or by electric discharge. Due to the exothermic nature of the reactions leading to the formation of intermetallics, the energy is necessary only for the initiation of the reactions (Figure 2). After that, heat produced by the reactions sustains and propagates the reaction towards the body of the reactants [7]. In the case of heating of the sample, the process is usually called reactive sintering [7].

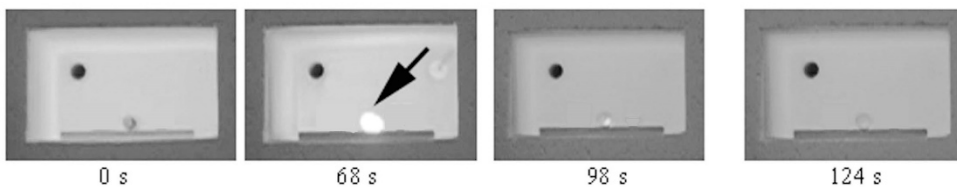


Figure 2: SHS progress in TiAl<sub>15</sub>Si<sub>15</sub> powder mixture [8]

Reactive sintering is the simplest method for the manufacture of bulk intermetallics. However, in some systems (e.g. Fe-Al or Ti-Al), this process results in highly porous products [7]. The solution of this problem is the pressure-assisted reactive sintering. In some cases, reactive sintering or SHS in general can be applied for the synthesis of the materials with controlled porosity, such as NiTi scaffolds [9].

### Applications of intermetallics

One of the most typical applications of intermetallics is the high-temperature use. In our department, continuous research of high-temperature materials based on iron aluminide (FeAl) and titanium aluminide (TiAl) has been carried out since 2006. During this research, the in-situ composite TiAl-Ti<sub>5</sub>Si<sub>3</sub> (Figure 3) and its production route by reactive sintering were developed. During testing of this material it has been found that in addition to excellent high-temperature oxidation resistance (Figure 4) this material exhibits also excellent abrasive wear resistance. Our preliminary results of mechanical testing and tribological tests show that this material can be potentially applied as a tool material.

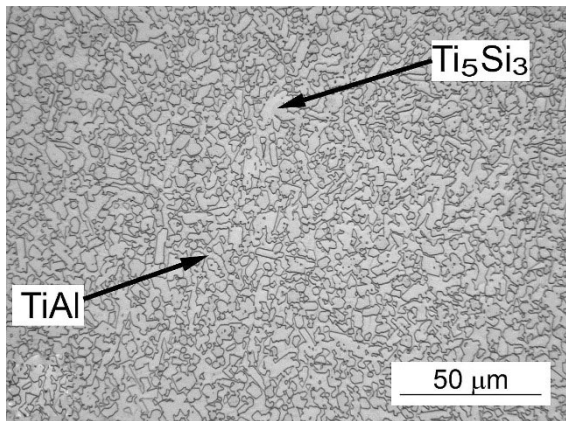


Figure 3: Microstructure of TiAl<sub>15</sub>Si<sub>15</sub> alloy prepared by reactive sintering at 900 °C for 15 min

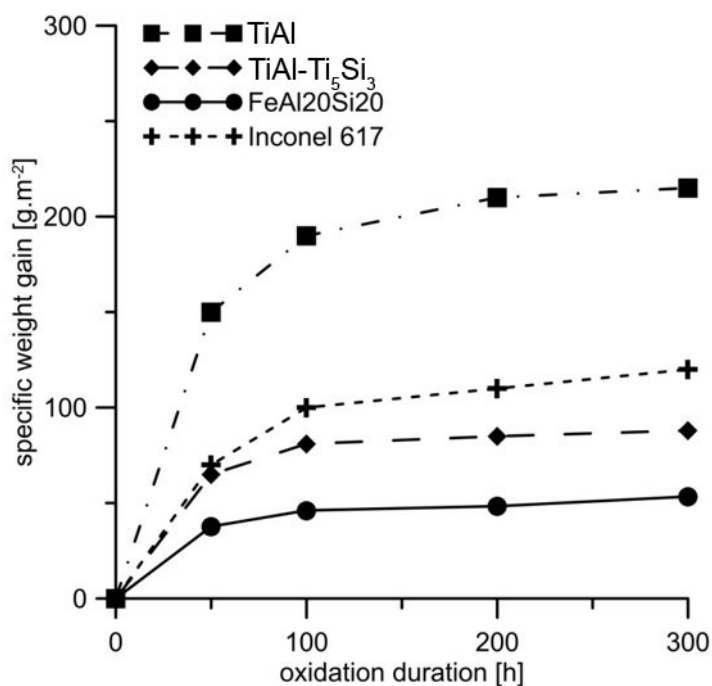


Figure 4: Weight gain during oxidation vs. oxidation duration at 900 °C in air

Reactive sintering also allows the preparation of intermetallic matrix composite materials with ceramic reinforcement that can be potentially applicable as the substitute for cemented carbide. In our previous work [10], the route for the synthesis of nickel aluminide NiAl reinforced by Al<sub>2</sub>O<sub>3</sub> particles (Figure 5a) or short fibres (Figure 5b).

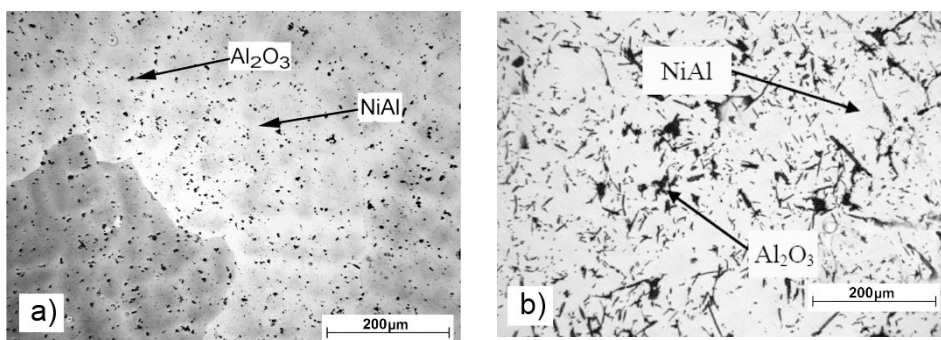


Figure 5: Microstructure of TiAl<sub>15</sub>Si<sub>15</sub> alloy prepared by reactive sintering at 900 °C for 15 min

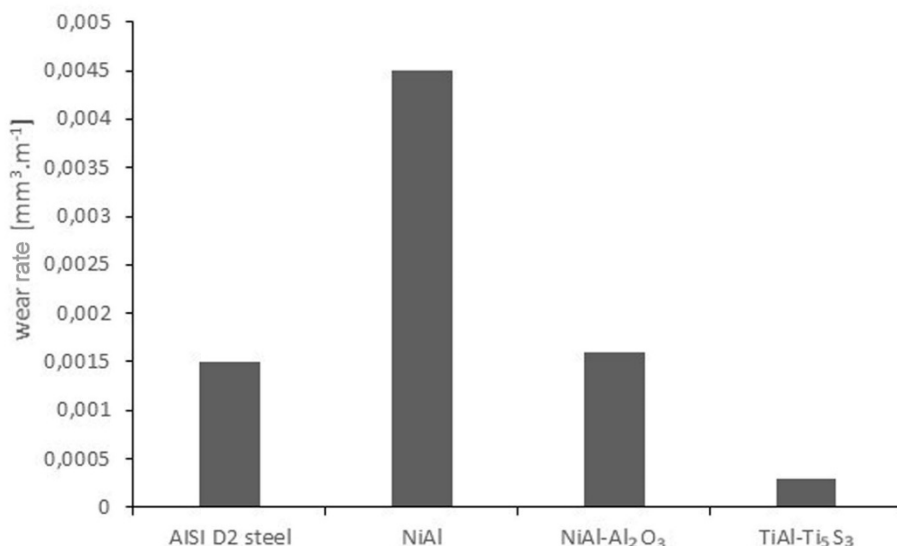


Figure 6: Abrasive wear rate of selected materials based on intermetallics (load 5.8 N, sliding distance 2500 m, grinding paper P1200)

Abrasive wear rate of selected materials based on intermetallics are presented in Figure 6 in comparison with highly wear resistant tool steel AISI D2. Results show that single-phase intermetallics do not exhibit high wear resistance. On the other hand, the intermetallic-based composite materials achieve comparable (NiAl-Al<sub>2</sub>O<sub>3</sub>) or even much better wear resistance (TiAl-Ti<sub>5</sub>Si<sub>3</sub>) than highly wear resistant tool steel. The big advantage is that these materials achieve the wear rate in the same range as tool steels without the need of heat treatment.

The next non-conventional application of intermetallics is in the medicine. The branch of surgical and dental implants is usually a domain of conventional materials as stainless steels, titanium- or cobalt-based alloys. The exception is a NiTi shape memory alloy applicable e.g. for stents or braces. When this material is prepared by SHS, high porosity is usually achieved. This phenomenon is practically applied in the production of porous scaffolds made of NiTi phase [9]. It is considered or already applied in special medical applications, e.g. bone replacement. However, NiTi phase is not very biocompatible due to high amount of allergenic nickel. In our department we developed novel material containing titanium and silicon [11]. In this material, high porosity can be achieved during reactive sintering (Figure 7) under specific conditions without any additive. The pores form by Kirkendall effect and lattice distortion connected with the formation of silicides in the alloy. This material, covered by suitable bioactive surface layer, can be applied as a bone replacement, having porosity, mechanical properties and bioactivity comparable with human bone.

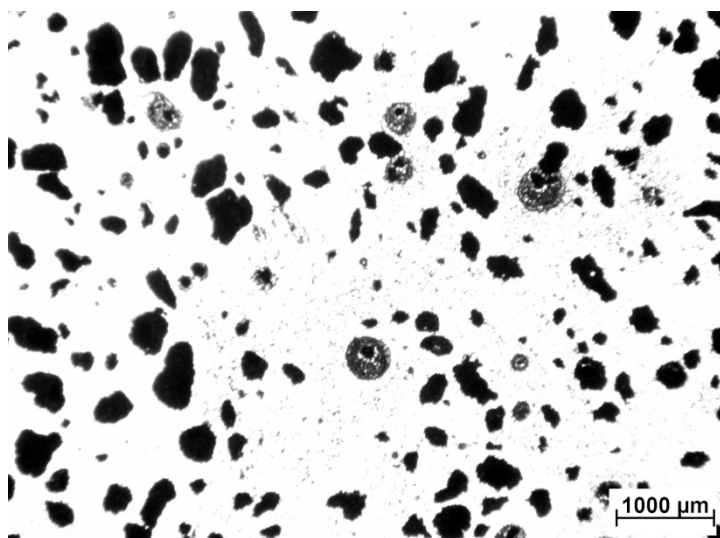


Figure 7: Structure of new titanium and silicon containing intermetallics-based biomaterial

## Conclusions

This paper presents non-conventional methods for the synthesis of intermetallic compounds. These processes are based on modern powder metallurgical methods. Combination of mechanical alloying and suitable compaction technique (Spark Plasma Sintering) and reactive sintering of compressed powders seem to be the future of the production of intermetallics and intermetallics-based composite materials.

Among the applications of intermetallics, the utilization as tool materials and new biomaterials for surgical applications can exceed the current application range in the near future.

## Acknowledgement

This research was financially supported by Czech Science Foundation, project No. 14-03044S.

## Literature

1. Massalski T.B., Binary Alloy Phase Diagrams, Materials Park, ASM, 1990.
2. Sadrnezhad S.K., Raz S.B: Metallurgical and Materials Transactions B, 36, 395-403 (2005)
3. Šíma V., Kratochvíl P., Kozelský P., Schindler I., Hána P.: International Journal of Materials Research, 100, 382-385 (2009).
4. Lapin J., Hecht U., Effect of processing parameters on microstructure and mechanical properties of cast TiAl based alloys, In: Metal 2008 conference proceedings, CD (2008).
5. Froes F.H., Suryanarayan C., Russell K., Li C.-G: Materials Science and Engineering A192/193, 612-623 (1995).
6. Novák P., Kubatík T., Vystrčil J., Hendrych R., Kříž J., Mlynář J., Vojtěch D.: Intermetallics, 52, 131-137 (2014).
7. Novák P., Michalcová A., Šerák J., Vojtěch D., Fabián T., Randáková S., Průša F., Knotek V., Novák M.: Journal of Alloys and Compounds, 470, 123-126 (2009).
8. Novák P., Popela T., Kubásek J., Šerák J., Vojtěch D., Michalcová A.: Powder Metallurgy, 54, 50-55 (2011).
9. Kaya M., Orhan N., Tosun G.: Current Opinion in Solid State and Materials Science, 14, 21-25 (2010).
10. Novák P., Šotka D., Novák M., Michalcová A., Šerák J., Vojtěch D.: Powder Metallurgy, 54, 308-313 (2011).
11. Novak P., Titanium alloy for the manufacture of porous medical implants, UV 26361 (2014).

## MECHANICAL AND CHEMICAL PROPERTIES OF PLASMA-SPRAYED BRONZE CuAl10 COATING ON MAGNESIUM AND MAGNESIUM ALLOY AZ 91

**Kubatík F.T.**, Vilémová M., Mušálek R., Janata M.

*Department of Materials Engineering, Institute of Plasma Physics AS CR, v.v.i. Za Slovankou 1782/3, 182 00 Prague 8, Czech Republic, Tel.: (+420) 266 053077, kubati@ipp.cas.cz*

### Abstract

The most common magnesium alloy AZ91 is widely used as a structural material, but its use is limited at higher temperatures and high humidity. Plasma spraying is a technology that allows to prepare protective metallic and nonmetallic coatings on a wide variety of substrates including magnesium and its alloys. In this study, CuAl10 was plasma sprayed on magnesium and magnesium alloy AZ91 with the aim to study corrosion resistance of the magnesium substrates. The work focuses on optimization of the plasma spraying process, on chemical composition of the coatings, on interface between the coating and substrate, as well as on adhesive strength of the coatings. The coatings were deposited after two passes of the spraying torch resulting in thickness of 150  $\mu\text{m}$  on magnesium substrate and 110  $\mu\text{m}$  on AZ91 substrate. Chemical microanalysis showed that deposition of CuAl10 alloy on magnesium results in formation of an intermetallic layer at the interface. The layer provides a metallurgical bond between the magnesium substrate and the coating. Adhesive strength of CuAl10 coatings reaches an average value of 14 MPa.

### Introduction

Magnesium and its alloys have excellent ratio of density and strength, are suitable for lightweight construction in the automotive, aerospace, but also for bio-medical applications due to their high specific strength and stiffness. However, due to the poor corrosion resistance, their massive use is very limited<sup>1</sup>. There are methods to reduce the reactivity of magnesium; among the easiest methods belongs alloying of magnesium with aluminum and manganese. Magnesium and its alloys can also prevent the formation of surface protective layers deposited e.g. by plasma spraying technology, which allows to prepare protective metallic and nonmetallic coatings<sup>2,3</sup>. There are several works dealing with research of plasma sprayed coatings for magnesium and magnesium alloys<sup>4</sup>. These works are primarily concerned with the preparation of layers, which greatly enhance the hardness ( $\text{Al}_2\text{O}_3$ ,  $\text{TiO}_2$ )<sup>5</sup>, improve abrasion resistance (e.g.  $\text{TiC}$ ,  $\text{TiB}_2$ ,  $\text{WC}$ )<sup>6</sup> or further improve its corrosion resistance by plasma-sprayed deposit of AlSi12 alloy<sup>4</sup>. In this work, corrosion rate values of AZ91 alloy in a solution of 5% NaCl was reduced from 4.31 ( $\text{mg}/\text{cm}^2\text{day}$ ) to 3.89, and further improvement was achieved by laser remelting reaching values of 1.78. In this work, it has been also reported that during the corrosion of plasma spray coatings prevails crevice corrosion attack<sup>4</sup>. The adhesive strength of metallic coatings on magnesium alloy AZ91 was studied<sup>5</sup>. Plasma spraying aluminum onto AZ91 reached strength 6-15 MPa. For NiAl5 alloys, AZ91 alloy achieves adhesion strength 17-25 MPa<sup>3</sup>. Aluminium bronze CuAl10 is very resistant to corrosion in both acids and alkaline environments, but also resistant to heat up to temperatures of 800 °C. From literature, it is known that connection of noble and non-noble metals can cause formation of the corrosion cell and corrosion rate of non-noble metal is increased. In cases that it is a porous material, corrosion products may block the open pores and thus decrease rate of oxidation. This work is focused on study of the chemical changes during plasma spraying of CuAl10 alloy by hybrid plasma torch onto magnesium and magnesium alloy AZ91 substrates, and adhesion strength of deposited layers.

### Experimental

In this work, CuAl10 powder with grain size of -63 +40  $\mu\text{m}$  was sprayed by hybrid plasma torch WSP-H 500 with an output of 160 kW. Powder is injected by compressed air at rate of 260 g / min. Spray distance was determined experimentally by spraying on laboratory glass slides with graded distance of 50 mm from 300 to 550 mm. After optimization of the spray distance, coatings were deposited on commercially pure magnesium and magnesium alloy AZ91 substrates (dimensions 70 \* 20 mm, thickness 5 mm). Substrates were degreased in acetone and grit-blasted with corundum. CuAl10 alloy was sprayed onto the substrate preheated to 180 °C with 1, 2 or 5 spraying passes. Spray powder and metallographic cross-sections of the deposits were observed with an scanning electron microscope (SEM) equipped with point elemental chemical microanalysis (EDS). Adhesion test was performed according to ASTM C 633 standard. The substrates for this test were machined from commercially pure magnesium and magnesium alloy AZ91 with the diameter of 25 mm and a height of 50 mm. Again, substrates were preheated to 180 °C before deposition of the CuAl10 coating. Thickness of the coating deposited with 5 spraying passes was at least 350  $\mu\text{m}$  in order to a

substrate. Low-carbon steel counterparts, adhesive epoxy and universal tensile tester Instron 1362 (Instron, UK) were used for evaluation of the coating adhesion/cohesion strength. Strength value represents mean value of adhesion tests results from 6 valid measurements.

### Results and discussion

Fig. 1 shows the feedstock powder. The powder consists of regular spherical particles, irregularly shaped particles, and elongated particles having a length of up to 140  $\mu\text{m}$ .

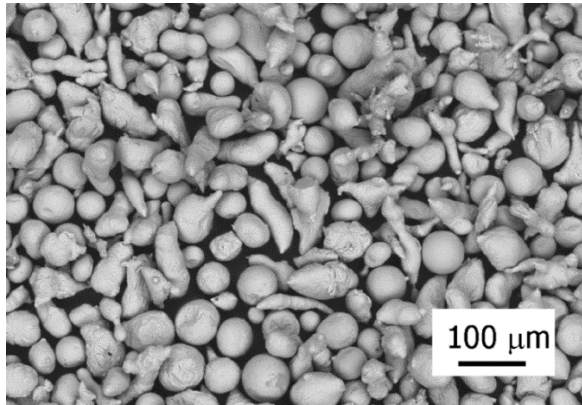


Figure 1. Feedstock powder, Aluminium brass, Fraction -63 +40  $\mu\text{m}$  (SEM)

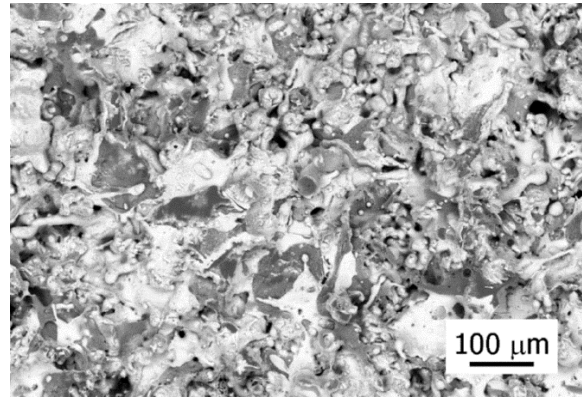


Figure 2. Free-surface of plasma-sprayed CuAl10 aluminium brass on Mg alloy (SEM-BSE).

The first experiments were carried out to find the optimal feeding distance of the powder into jet, which was visually evaluated in laboratory slides. Next, the best experimentally determined spraying distance of 350 mm spraying on laboratory slides with graded distance of 50 mm. After optimizing the spraying and feeding distance followed plasma spraying onto the commercially pure magnesium and AZ91 magnesium alloy substrates. Samples were prepared with layers prepared during one, two or five spraying passes. The surface microstructure shown in Fig. 2 is formed by splats, some are oxidized and some are variously fragmented. Among splats are present small un-molten particles of spherical shape, and size below  $50 \mu\text{m}$ . Cross-sections of deposited layers are presented in Fig. 3 to 6. In all cases, deposits show structure of a standard plasma spray coating which is formed by splats, pores and un-melted particles. The layers have markedly uniform thickness as can be seen in the cases with one spraying pass. Figures 3 to 5 show a layer prepared onto pure magnesium with one, two, and five spraying passes, with an average thickness of  $56 \pm 17 \mu\text{m}$ ,  $146 \pm 32 \mu\text{m}$  respectively. Figures 6 to 8 is shows layers prepared on the magnesium alloy AZ91 with one, two and five spraying passes, with thickness of  $87 \pm 18 \mu\text{m}$ ,  $110 \pm 14 \mu\text{m}$  respectively. It is also clear that in the case of plasma spray coatings on pure magnesium with two spraying passes, formation of the new interface takes place. This new interface consists of a sub-layer with an average thickness of  $60 \mu\text{m}$ . This sub-layer is uniform and present in under almost entire width of the sprayed layer. In the case of plasma spraying on pure magnesium with one spraying pass only, penetration of molten particles deeper into the substrate was observed, see Figure 3.

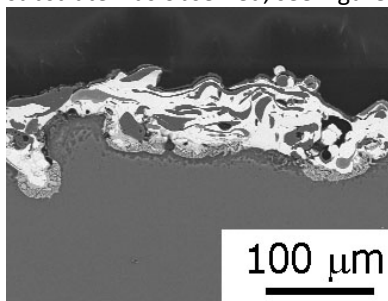


Figure 3. Microstructure on the cross-section of CuAl10 sprayed on magnesium, after one pass (SEM).

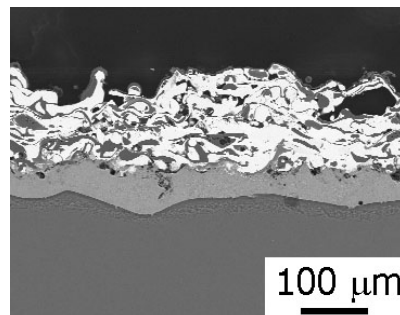


Figure 4. Microstructure on the cross-section of CuAl10 sprayed on magnesium, after two passes (SEM).

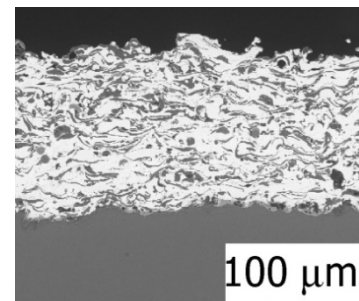


Figure 5. Microstructure on the cross-section of CuAl10 sprayed on magnesium, after five passes (SEM).

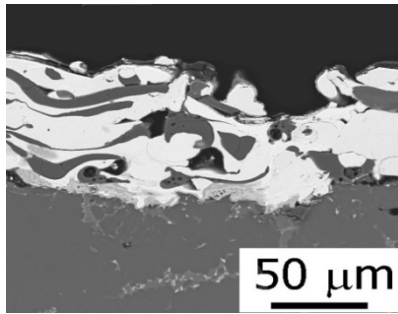


Figure 6. Microstructure on the cross-section of CuAl10 sprayed on magnesium alloy AZ91, after one pass (SEM).

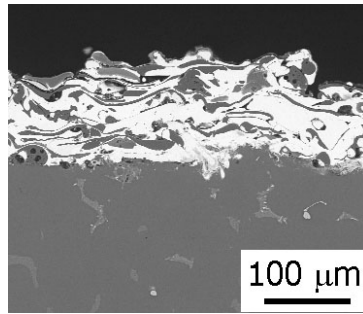


Figure 7. Microstructure on the cross-section of CuAl10 sprayed on magnesium alloy AZ91, after two passes (SEM).

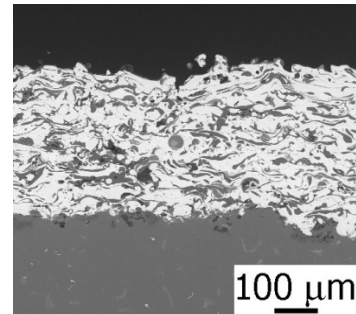


Figure 8. Microstructure on the cross-section of CuAl10 sprayed on magnesium alloy AZ91, after five passes (SEM).

In Fig. 4 is visible newly formed interface consisting of the supersaturated solid solution of copper in magnesium. From Fig. 5 with 3 additional spraying passes, it seems that when the additional heat was the supersaturated solution was trying to reach a steady state. Precipitation of binary or ternary phases of an Al-Cu-Mg in small quantities was observed.

#### EDX Analysis

For chemical elemental analysis were selected samples with two spraying passes (Fig. 9 and 10). For both types of substrates, the plasma sprayed layer consists in majority of splats with chemical composition close to the original feedstock. However, oxidized splats with chemical composition ranging from almost pure  $Al_2O_3$  to copper oxides and pores were also observed. This may be explained by local segregation of alloy components during plasma spraying in open air atmosphere.

Table 1, shows the results of chemical elemental microanalysis for points indicated in Figure 9. The newly formed interface consisted of magnesium with small amount of copper (up to 1 at. %). From the Cu-Mg phase diagram, it is known that magnesium-copper forms a solid solution containing about 0.013 wt. % Cu. It can be expected that a new interface is formed by almost pure magnesium and very small content of  $Mg_2Cu$  intermetallic phase. Further, from the analysis results, it can be seen that there is a diffusion of magnesium from the substrate into the interface layer and the coating. The results of chemical microanalysis indicate that there is no diffusion of Cu into the substrate.

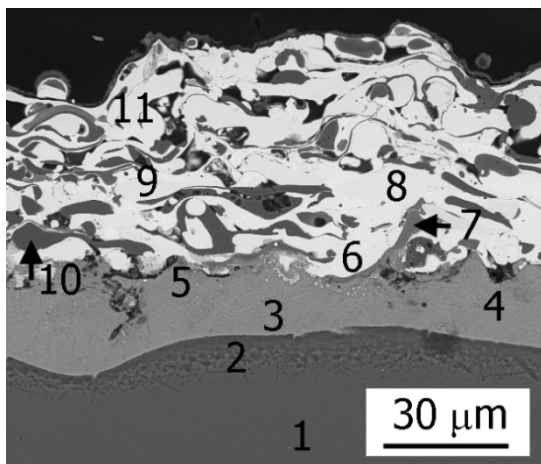


Figure 9. Position of areas on CuAl10 coating on pure magnesium substrate selected for elemental analysis whose results are in Tab. 1.

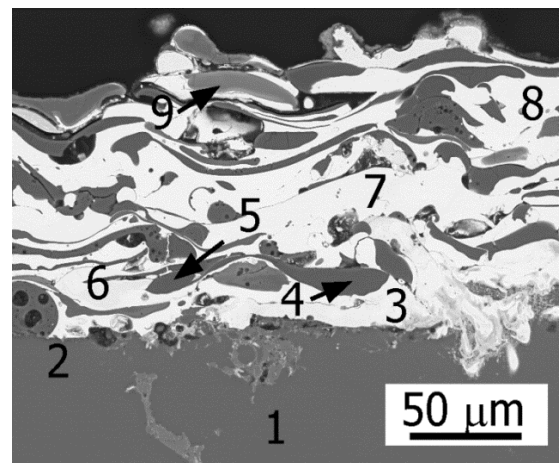


Figure 10. Position of areas on CuAl10 coating on magnesium alloy AZ91 substrate selected for elemental analysis whose results are in Tab. 1.

The results of chemical elemental analysis of CuAl10 layer on AZ91 alloy (Fig. 10, Tab. 1) are similar to those of a coating on pure magnesium. The formation of interface layer was in this case not observed. However, from cross-section details, it could be seen that in this case localized diffusion of copper into AZ91 substrate was observed up to distance the of several micrometers. Diffusion of magnesium into the CuAl10 coating is more extensive than for the pure magnesium, as is evident from the analyzes in tab. 1. Even in the outer layer of coating, magnesium content was up to about 30 at. %.

Table I. Elemental analysis (at.%) in selected areas from figure 9 and 10

	on Mg			on AZ91				
	O	Mg	Al	Cu	O	Mg	Al	Cu
1	4.88	95.12	-	-	4.40	90.17	5.43	
2	4.37	95.63	-	-	5.42	88.07	4.85	1.65
3	11.48	88.31	-	0.22	4.86	45.88	8.65	40.61
4	10.43	88.73	-	0.84	46.92	11.34	39.20	2.54
5	6.52	77.26	16.21	-	47.54	10.92	39.35	2.19
6	8.22	9.35	13.67	68.76	5.34	40.54	4.91	49.21
7	55.52	0.90	43.05	0.53	5.73	36.73	8.79	48.75
8	7.23	6.45	12.64	73.68	6.68	31.87	10.12	51.33
9	12.56	2.80	13.92	70.72	47.50	10.81	33.86	7.82
10	54.37	0.90	44.21	0.52				
11	40.15	13.06	8.37	38.39				

The adhesion strength was measured on samples with coatings deposited with 5 spraying passes. The strength is significantly higher for the coatings on the magnesium alloy AZ91, i.e.  $18.94 \pm 1.29$  MPa for CuAl10 on AZ91 and  $3.52 \pm 0.77$  MPa for CuAl10 on pure magnesium. Figure 11 and 12 show a characteristic appearance of the respective fracture surfaces with revealed substrate surface (dark areas) and coating residuals (light areas). In both cases, dominantly adhesion failure was observed. Pure magnesium substrate surface (Fig. 11) showed signs of oxidation which probably worsened bonding of first layer of splats to the substrate.

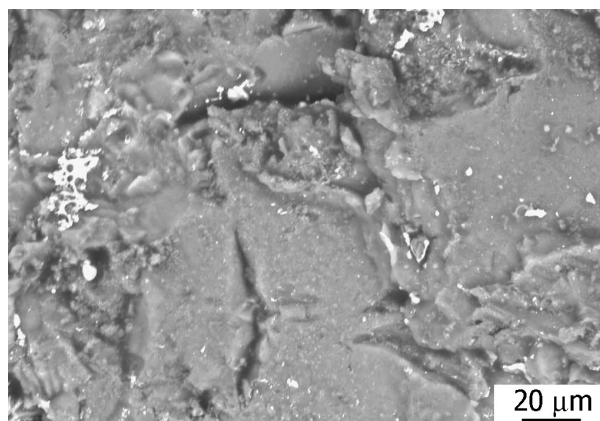


Figure 11. Fracture surface of CuAl10 on pure magnesium (SEM).

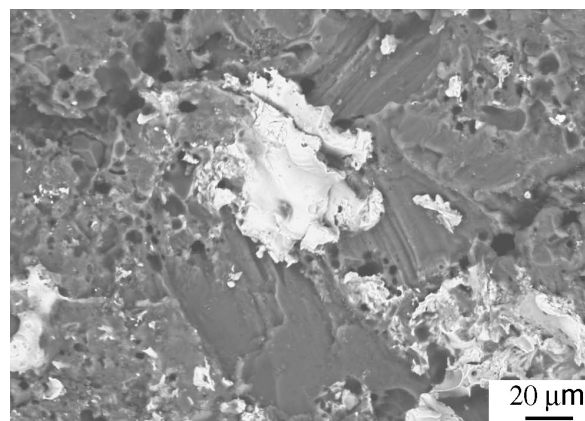


Figure 12. Fracture surface of CuAl10 on magnesium alloy AZ91 (SEM).

### Conclusion

The layers were prepared by plasma spraying of aluminum bronze CuAl10 onto pure magnesium and magnesium alloy AZ91. Layers having a thickness of 470 μm and 351 μm on Mg and AZ91 were prepared, which appear sufficient for a corrosion barrier. Chemical analysis showed that during the plasma spraying magnesium diffuses into the coating in the content of more than 30 at. %, and the copper diffuses into the substrate in the case of coatings on AZ91 alloy. Adhesion tests showed that the coating of CuAl10 on magnesium alloy reaches values of adhesion strength up to 19 MPa which is significantly higher than for pure magnesium. Values breakaway spraying CuAl10 on pure magnesium is 3.5 MPa, and are the biggest cause of the oxidation of the surface of magnesium for preheating before plasma spraying.

### **Acknowledgement**

*This work was supported by the Grant Agency of the Czech Republic through the project with a number 14-31538P "Evaluation of bonding interface during and after plasma spraying of metallic materials on magnesium and magnesium alloy."*

### **Literature**

1. Padekar, B. S. Raja, V.S. Singh Raman, R.K. Lyon, P.: *Mat. Corr. Sci. E.*, 583, 2013.
2. Zou, B. Tao, S. Huang, W. Khan, Z. S. Fan, X. Gu, L. Wang, Y. Xu, J. Cai, X. Ma, H. Cao X.: *Apl.S. S.*, 264, 1, 2014.
3. Parco M., Zhao L., Zwick J., Bobzin K., Lugscheider E.: *Surf. Coat. T.*, 201, 4, 2006.
4. Qian, M. Li, D. Liu, S.B. Gong, S.L.: *Corr. Sci.*, 52, 10, 2010.
5. Xu J., Zou B., Fan X., Zhao S., Hui Y., Wang Y., Zhou X., Cai X., Tao S., Ma H., Cao X.: *Jour. All. C.*, 596, 25, 2014.
6. Villalobos-Gutiérrez C.J., Gedler-Chacón G.E., La Barbera-Sosa J.G., Piñeiro A., Staia M.H., Lesage J., Chicot D., Mesmacque G., Puchi-Cabrera E.S.: *Surf. Coat.T.*, 202, 15, 2008.

## RESEARCH OF THE CHEMICAL PRE-TREATMENTS APPLIED ON THE SURFACE OF THE LOW CARBON UNALLOYED STEEL SHEET USING SEM AND EDS ANALYSIS

**Svobodová J.**, Weiss V., Cais J.

*Faculty of Production Technology and Management, University of J. E. Purkyně in Ústí nad Labem, Pasteurova 3334/7, 400 96, Ústí nad Labem  
svobodova@fvtm.ujep.cz*

### Introduction

The surface of the material must be free from all impurities. It is necessary for the final coating quality and its good adhesion. This is achieved with surface pre-treatment technologies. The surface pre-treatment technology has the influence on the basic material surface geometry, thus on its roughness and anchor profile. The most important aim of surface treatment is the removing of contaminants, corrosion products etc. from the material surface and getting such a surface of material which will provide sufficient adhesion of the coating to the steel surface<sup>1,2</sup>. The pre-treatment of the surface before the application of the final coating have usually two stages and can be divided on the two groups of operations – mechanical pre-treatment and chemical pre-treatment of the material surface. The subject of this paper is the research of chemical pre-treatments applied on the surface of the low carbon unalloyed steel sheet using SEM and EDS analysis.

Chemical pre-treatments of the surface are used for the removing of impurities and corrosion products from the surface of the material. Thanks to chemical pre-treatment we achieve such a surface of the basic material, which will have good corrosion resistance and good conditions for the final coatings adhesion. When choosing the chemical pre-treatment it is necessary to consider if the degree of the surface treatment provides required level of surface cleanliness and also the surface roughness and anchor profile before the final coating application<sup>3,4</sup>. The article is focused on the evaluation of chemical pre-treatment applied on the steel sheet. On this low carbon unalloyed steel sheet were excluded the coatings of chemical pre-treatments – alkaline degreasing, iron phosphate and as the next the pre-treatment based on nanotechnology. This nanotechnology pre-treatment product is the chemical from the new group of zirconium nanopassivations, which are developed like a substitute of the classical phosphating technologies. We prepared several types and combinations of coatings on which was observed the character of excluded layers on the electron microscope in different magnifications. For the purpose of this article we chose only two types of pre-treatments which are the most important for the application in real conditions in companies using chemical pre-treatments before powder coating.

Nanotechnologies start its rise and development from the second part of 20<sup>th</sup> century. To this area of nanotechnologies belong also nanolayers which protect the material surface against corrosion. These nanolayers are developed like alternative technologies to the methods of chemical pre-treatment using currently. The goal of these nanotechnologies is the increasing of the corrosion resistance, increasing the resistance of the material surface against the mechanical wear and also increasing better aesthetic appearance of the material surface. If we'll speak about corrosion so nanolayers have the importance just in the surface pre-treatments where they can replace the classical phosphating processes in the future and this from the reasons written bellow<sup>4,5</sup>. These nanolayers based on zirconium, titanium and other elements create for example good conditions for the adhesion between the coating surface and the basic material which is coated by these nanolayers. It is the possibility of surface pre-treatment before the application of the powder coating and these nanolayers should gradually replace the classical phosphate for some reasons: technological, economical and also ecological. From the technological point of view are the nanolayers:

- applied at lower temperatures,
- have longer lifetime,
- are less time consuming,
- do not produce waste sludge,
- have universal use for the pre-treatment of steel or aluminium,
- corrosion resistance should be comparable with the phosphate,
- remove unwanted elements from the environment (Zn, Ni, Mn, Cr),
- better liquidation.

From the view of costs we don't have the cost for the heating of the baths where are the materials coated and the liquidation of the waste sludge. The products based on nanotechnologies are multimetallic it means that the one product is possible to use for more types of materials. Thanks to these nanolayers are expanding and improving the possibilities of the corrosion protection and material surface treatment technologies<sup>6</sup>.

### Experimental samples preparation

Basic material – low carbon unalloyed steel sheet, was chemically pre-treated under certain technological conditions in two combinations (for the purpose of these article, it is a part of the wide research in this area we realised).

- Alkaline degreasing (**Alk**) + nanopassivation Alfipas ENVIROX SG (**Zr**) – variant 1.
- Alkaline degreasing (Alk) + iron phosphate (**Feph**) + nanopassivation Alfipas ENVIROX SG (Zr) – variant 2.

The product Alfipas is nanopassivation based on zirconium, composition: zirconium complex with the six atoms of fluorine, fluorides, polymeric compound – polyacrylic acid or phenolic resin, creating of the layer by sol-gel process.

The process of the basic material pre-treatment is shown on the figure 1 and 2.

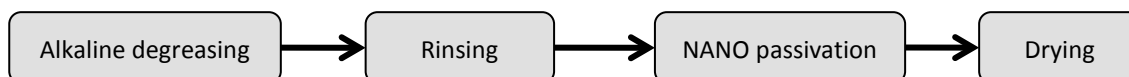


Figure 1. Scheme of the technological process of chemical pre-treatment – variant without phosphate



Figure 2. Scheme of the technological process of chemical pre-treatment – variant with phosphate

### SEM and EDS analysis of excluded coatings of chemical pre-treatment

Using electron microscopy were examined the excluded layers of chemical pre-treatment on the surface of the basic material. Using SEM and EDS analysis was examined the character of excluded layer of the pre-treatment and measured the chemical composition or the excluded layers. Subsequently both variants were compared.

### SEM analysis

The scanning electron microscope TESCAN VEGA 3 were used for evaluation of excluded coatings of chemical pre-treatment and their connection with the basic material. Both variants are shown on the following figures.

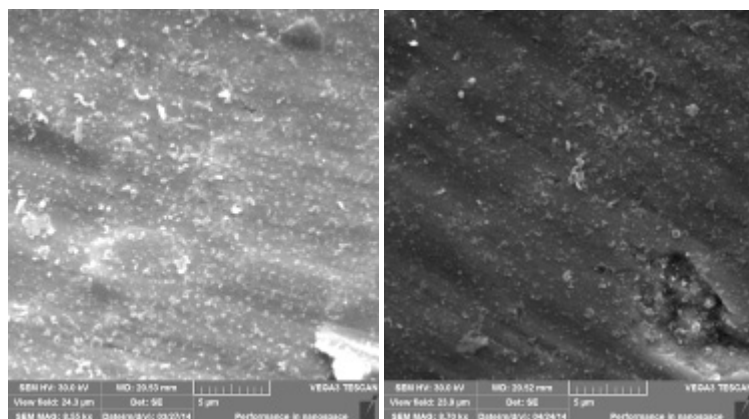


Figure 3. Surface of the experimental sample variant 1

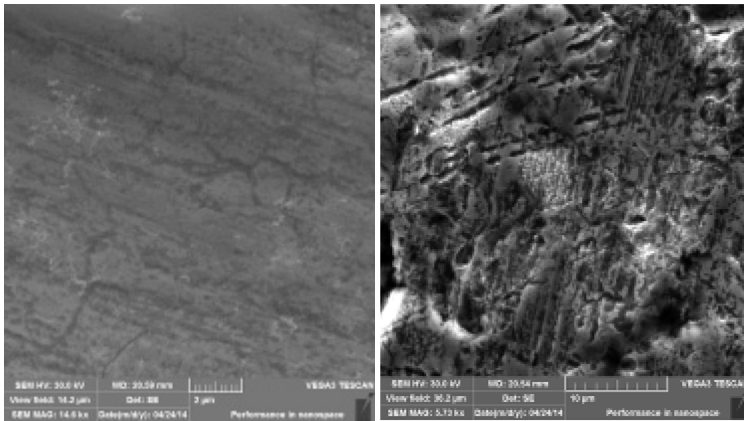


Figure 4. Surface of the experimental sample variant 2

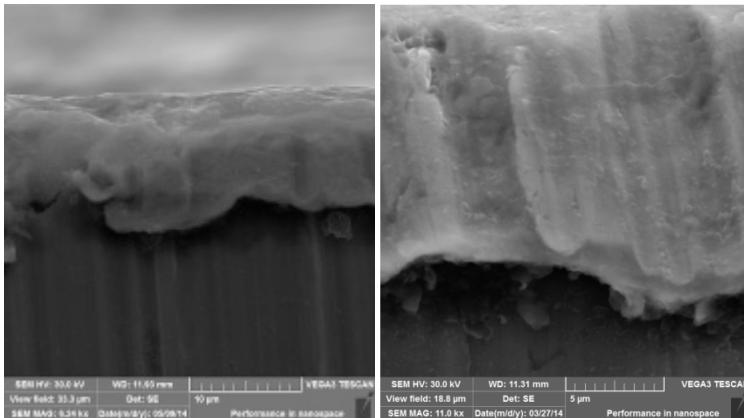


Figure 5. Layer of the experimental sample variant 1

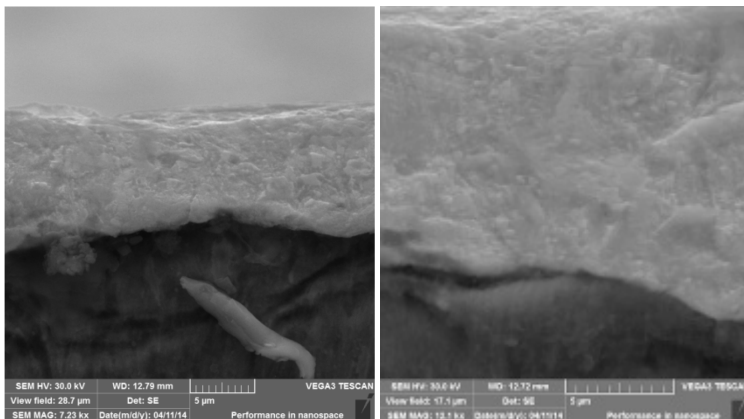


Figure 6. Layer of the experimental sample variant 1

The documentation from the electron microscope is shown on the figures 3 – 6. The figures were created with the analysis of the each sample surface (variant 1 and 2) and as the next comparison of the excluded layers of individual samples. For the analysis of the excluded layer was necessary the experimental samples diagonally grind. Thanks to it was excluded layer easily observed and was possible to perform EDS analysis of the transition between the basic material and excluded chemical pre-treatment.

Samples of the variant 1 have a chemical pre-treatment alkaline degreasing + nanopassivation Alfipas. This type of pre-treatment is excluded on the surface material in the form of particles covering the whole surface of the material. The surface was highly reactive after application of the chemical pre-treatment and after drying. It reacted into several minutes in air in a laboratory environment and on the surface of the material began to form surface corrosion.

Samples variant 2 with chemical pre-treatment alkaline degreasing + Fe phosphate + nanopassivation Alfipas have completely different character of the layer. The excluded coating is not in particulate form on the surface of the material, but the compact layer which is broken with cracks.

## EDS analysis

The EDS method was chosen for evaluation of individual excluded coatings of chemical pre-treatment which is used for the measurement of concentration of individual elements. Using this method was possible to analyse chemical composition of excluded chemical products by prepared samples both on the surface so after the preparation of the oblique cut. The point (B1, B2) and surface (P1, P2) EDS analysis was performed on the experimental samples. The analyzer BRUKER was used for analysis which is the part of electron microscope.

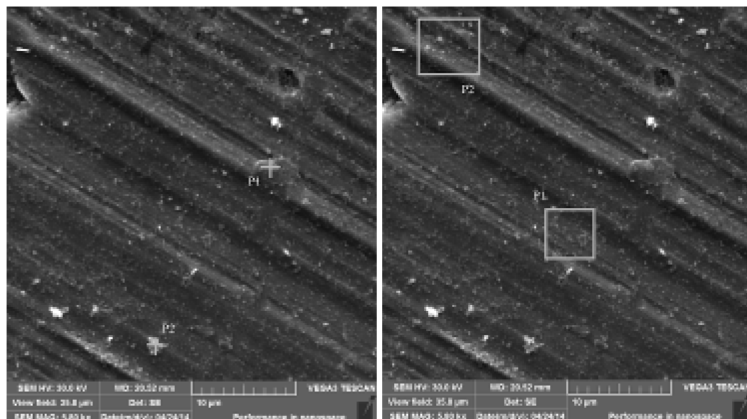


Figure 7. Surface of the sample variant 1

Table I

EDS analysis of the sample variant 1 (surface)

Analysed elements	B1	B2	P1	P2
O [hm. %]	5.47	3.07	2.85	3.34
Zr [hm. %]	0.79	0.54	0.92	0.86
Si [hm. %]	0.21	0.13	0.08	0.10
F [hm. %]	3.39	3.43	4.12	3.69

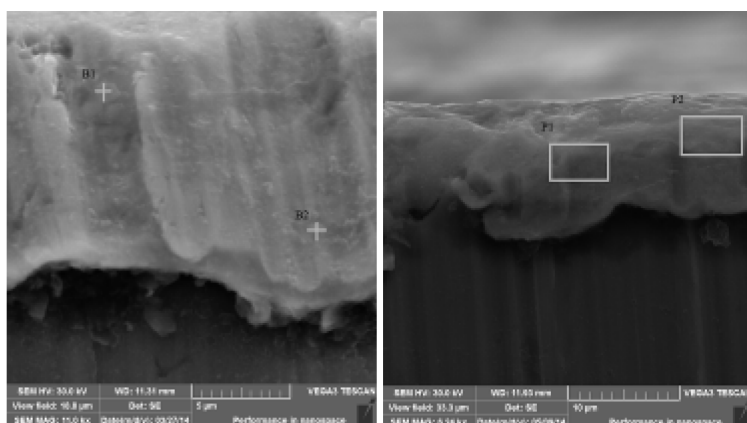


Figure 8. Layer of the sample variant 1

Table II

EDS analysis of the sample variant 1 (layer)

Analysed elements	B1	B2	P1	P2
O [hm. %]	10.02	6.47	6.17	8.07
Zr [hm. %]	2.21	2.08	2.82	3.29
Si [hm. %]	6.60	0.18	-	-
F [hm. %]	3.57	4.68	4.13	5.09

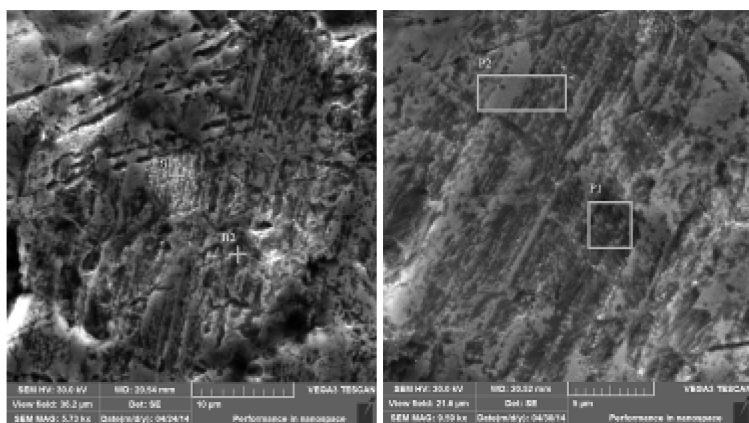


Figure 7. Surface of the sample variant 2

Table III

EDS analysis of the sample variant 2 (surface)

Analysed elements	B1	B2	P1	P2
O [hm. %]	2.43	7.12	4.14	10.49
Zr [hm. %]	0.71	0.41	0.51	0.83
Si [hm. %]	0.04	0.14	0.03	0.07
F [hm. %]	3.56	3.55	3.32	3.28

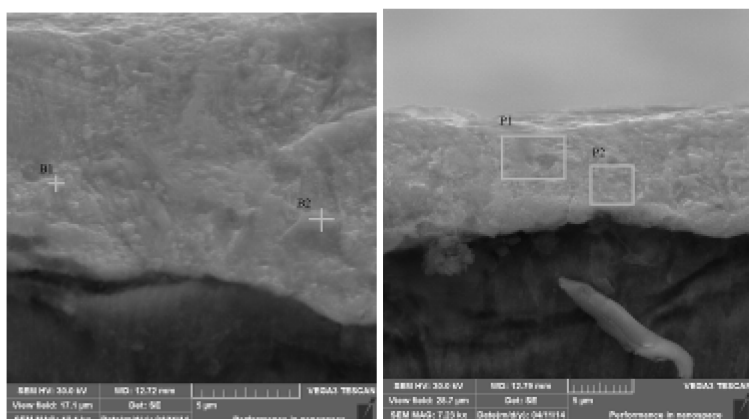


Figure 8. Layer of the sample variant 2

Table IV

EDS analysis of the sample variant 2 (layer)

Analysed elements	B1	B2	P1	P2
O [hm. %]	4.13	4.92	7.33	9.21
Zr [hm. %]	0.62	0.65	0.65	0.52
Si [hm. %]	0.22	0.35	0.25	0.44
F [hm. %]	4.51	4.82	4.98	-
P [hm. %]	-	-	-	0.45

All samples were subjected to more testing measurements in different locations than indicated in the figures and tables. The results were similar for each sample, for this article were selected two points for point analysis, two surfaces for surface measurement, when the measurement results of concentration of elements are listed in the tables.

## Conclusion

The aim of this paper was evaluation of the excluded coatings variant 1 – alkaline degreasing + Zr nanopassivation; variant 2 – alkaline degreasing + Fe phosphate + Zr nanopassivation using SEM and EDS analysis.

In this evaluation were observed the differences between individual variants of chemical pre-treatment. Chemical pre-treatment Alk + Zr was excluded in the form of small particles when these particles uniformly cover the surface of the material and forms clusters. The pre-treatment Alk + Feph + Zr created on the surface of the material have completely different structure from the variant 1. To this pre-treatment resulted effect of sol-gel technology. Sol-gel technology forming layers on the surface of the material after oven drying (samples dried at 130°C) causes cracking of conversion protective layer 7. These cracks are visible on the surface of the samples in Fig. 6, 11, 12. Cracks can cause a reduction of the protective effect conversion layer against corrosion. During SEM analysis were also observed individual layers on the prepared oblique cut. For this analysis were prepared grinded samples. Thanks to it is the layer better visible and it was possible to observe its character and measure the elements concentration at the transition between excluded chemical layer and basic material during subsequent EDS analysis. On the prepared oblique cut of the samples were observed compact excluded layer. For pre-treatment Alk + Feph + Zr were again observed the cracks on the layer surface. After performed SEM picture analysis were the samples submitted to EDS analysis. With EDS analysis we documented the occurrence of particular elements that each chemical pre-treatment contain, therefore by nanopassivation Zr, F, Si and O and P for phosphate. Distribution of chemical elements of excluded layers is very uneven and depends of course of the analysed place. From the measurement of the concentration of elements on excluded layers of chemical pre-treatment can say that the content of elements forming a protective layer of chemical pre-treatment is very low and it corresponds to the corrosion resistance thus pre-treated samples, especially in the case of chemical pre-treatment Alk + Zr where is the content of zirconium less than 1 wt. %. These samples begin in a laboratory environment after oven drying very quickly react with the surrounding environment and cover with a layer of corrosion products. The results listed in the article are linked with the wide research in this area which is engaged with the research of the influence of the surface pre-treatment based on nanotechnology on the corrosion resistance of the lacquered low carbon unalloyed steel material. The corrosion tests were performed of the listed pre-treatments after their application on the steel sheet and applying of the final powder coating, when the variant 2 had better results than variant 1 after the corrosion load with salt spray during different time regimes 8 9.

In conclusion we can say that the use of zirconium nanopassivation Alfipas in the form in which it was tested, it is not practical for use in enterprises without the use of phosphates appropriate. Despite the advantages that come with this nanotechnology carries, phosphating technology is still preferable especially in higher corrosion resistance and thus increases the life of the pre-treated materials. Nanotechnological product Alfipas is then particularly suited as a sealant for phosphate which pores are sealed and phosphate may result in increasing the corrosion resistance of phosphated materials.

## Literature

1. Philip A., Schweitzer P.E.: Paint and Coatings: Applications and Corrosion Resistance, Corrosion Technology – Vol. 23, Taylor&Francis, p. 672, ISBN 1574447025 (2005).
2. Voevodin A. A., Shtansky D. V., Levashov E., A., Moore J. J.: Nanostructured Thin Films and Nanodispersion Strengthened Coatings, Springer, Nato Science Series II: - Vol. 155, ISBN 1-4020-2221-2 (2004).
3. Cavaleiro A., Hosson J. T.: Nanostructured Coatings, Nanostructure Science and Technology, Springer, p. 648, ISBN 0-387-25642-3 (2006).
4. Groysman A.: Corrosion for Everybody, Springer, ISBN: 9048134765 (2009).
5. Hošek J.: Úvod do nanotechnologie, ČVUT v Praze, ISBN 978-80-01-04555-8 (2010).
6. Narayanan S.: Surface Pretreatment by Phosphate Conversion Coatings – A Review, Rev.Adv.Mater.Sci. 9, p. 130 – 177 (2005).
7. Chou T. P., Chandrasekaran C., Limmer S., Nguyen C., Cao G. Z. Organic-inorganic sol-gel rating for corrosion protection fo stainless steel, Journal of Materials Science, Letters 21, p. 251-255, ISSN 0261-8028 (2002).
8. Svobodová J., Kuśmierczak S.: Analysis of the state of the lacquered layer of the metal sheet after corrosion load, Engineering for Rural Development, 12<sup>th</sup> International Scientific Conference, ISSN 1691-5976 (2013).
9. Kuśmierczak S., Svobodová J.: Microscopic Evaluation of Protective Coating by Coated Sheets after Corrosion Load, Manufacturing Technology, Journal for Science, Research and Production, Vol. 12, No. 13, p. 151-157, ISSN 1213-2489 (2012).

## RESEARCH AND EVALUATION OF CRYSTAL SEGREGATION DURING CASTING OF THE ALLOY Al-Zn-Cu-Mg

**Weiss V.**, Svobodová J., Cais J.

*Fakulty of Production Technology and Management, University of J. E. Purkyně in Ústí nad Labem, Pasteurova 3334/7, 400 96, Ústí nad Labem  
svobodova@fvtm.ujep.cz*

In the course of homogenizing annealing of aluminium alloys being cast continually or semi-continually it appears that chemical inhomogeneity takes off within separate dendritic cells (crystal segregation). It is about a diffusion process that takes place at the temperature which approaches the liquid temperature of the material. In that process the transition of soluble intermetallic compounds and eutectic to solid solution occurs and it suppresses crystal segregation significantly<sup>1</sup>. The temperature, homogenization time, the size of dendritic cells and diffusion length influences homogenizing process. The article explores the optimization of homogenizing process in terms of its time and homogenizing annealing temperature which influence mechanical properties of AlZn5.5Mg2.5Cu1.5 alloy.

Homogenization is defined as a method of heat treatment that happens at high temperature approaches liquid (approximately 0.7 - 0.8 of melting temperature) with the purpose of eliminating chemical inhomogeneity by the means of diffusion processes. In the process of crystallization a long interval between a liquid and a solid state causes the difference in chemical composition in the middle and on the borders of the dendrite. The presence of balanced and not balanced eutectics which appears in the structure of AlZnMgCu alloy casts deteriorates mechanical properties of the alloy. It is possible to minimize or even to eliminate completely chemical inhomogeneity in crystal segregation by the means of homogenizing annealing. The article describes heat treatment process optimization in the terms of the structure and chosen mechanical properties of AlZn5.5Mg2.5Cu1.5 alloy<sup>2,3</sup>.

### Experiment

Raw material that was given by a producer was used for making a cast of a tested material. Casts of tested alloys were prepared taking into consideration chemical composition defined by CSN 42 4222 standard. The material was melted in a furnace at the temperature of 730 °C, the furnace temperature was read by a digital thermometer with ± 2°C accuracy. In the process of melting the melt was treated with a refining salt and melt surface skimming was done. A prepared material was cast into a preheated (at the temperature of 220 °C) mould in a gravitational way. The casts were in a form of a conical cylinder in size of 40 /50 x 100 mm. The chemical composition of a prepared tested alloy (mass percentage) is shown in Tab.1.

Table 1.

The chemical composition of AlZn5.5Mg2.5Cu1.5 alloys

AlZn5.5Mg2.5Cu1.5 metallic form [mass %]	Zn	Mg	Cu	Si	Fe	Al
	5.21	1.89	1.47	0.05	0.06	91.30

Being composed in such a way the alloy was divided into two sets of specimens which were subjected to homogenizing annealing. Annealing was carried out in a LAC furnace, the temperature was read by a digital thermometer with ± 2°C accuracy. The first set of specimen was subjected to different temperature conditions with temperature ranges of 410-530 °C with 20°C intervals (410; 430; 450; 470; 490; 510; 530°C), annealing lasted 8 hours.

The second set of specimen was made at a constant temperature of homogenizing annealing (T=470°C), but with a different time period of a heat treatment process. The time of homogenizing annealing was from 2 hours to 24 hours (2; 4; 6; 8; 10; 12; 16; 20; 24 o'clock). For microstructure and micro-hardness analysis, according to Vickers, with a load of 20 g. with a 5-second duration metallographic grinds were made out of the specimen before and after homogenizing annealing.

AlZn5.5Mg2.5Cu1.5 alloy structure was accentuated by the method of color etching, when a color contrast appears as a response of a specimen to an etching agent (KMnO<sub>4</sub>)<sup>4</sup>. By the means of that method the inhomogeneity of chemical composition of dendritic cells was revealed.

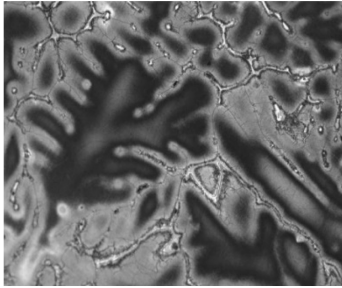


Figure 1. AlZn5.5Cu2.5Mg1.5 alloy microstructure before homogenizing annealing, mag. 200x

After homogenizing annealing the microstructure of the specimens (of their metallographic grinds) was analyzed with a confocal laser microscope LEXT with magnification 100x.

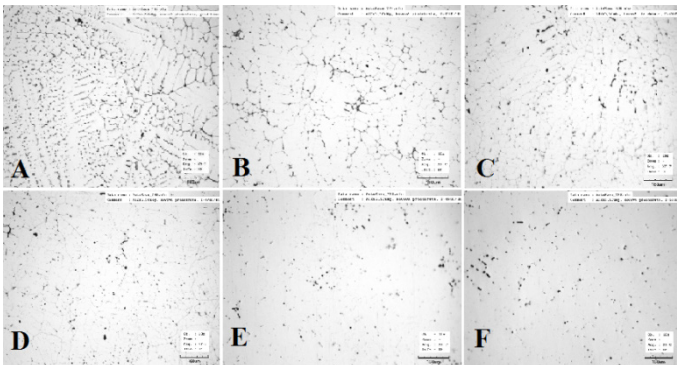


Figure 2. Microstructure after homogenizing annealing (A – before homogenizing, B – 430°C, C – 450°C, D – 470°C, E – 490°C, F – 510°C)

The AlZn5.5Cu2.5Mg1.5 alloy microstructures at constant annealing lasting 8 hours are shown above, magnification 100x.

The analysis of microstructure of an experimental alloy being heat treated constantly with a changeable temperature shows that the temperature of 430 – 450°C is insufficient for crystal segregation suppression. It is obvious according to images (Fig. 2 B, Fig. 2 C) of AlZn5.5Mg2.5Cu1.5 structure that not all present soluble eutectics and intermetallic compounds have melted. At the temperature of 510°C it is possible to observe the structure and it is evident that at such a high temperature melting eutectics, which are arranged along dendritic cells, and spheroid melting eutectics appear. After AlZn5.5Mg2.5Cu1.5 alloy structure observation it is possible to state that homogenizing annealing at the temperature of 430 – 530°C is the optimal condition for homogenization at the temperature range of 470 – 490°C.

After microstructure evaluation all these AlZn5.5Mg2.5Cu1.5 alloy specimens, particularly their micro-hardness, that were subjected to constant 8-hour annealing were analyzed according to Vickers with a load of 20 g. with a 5-second duration, that determines the optimal temperature of 470°C for homogenizing annealing (Fig. 4). The same temperature was chosen to treat another set of specimens which were subjected to annealing lasting from 2 up to 24 hours.

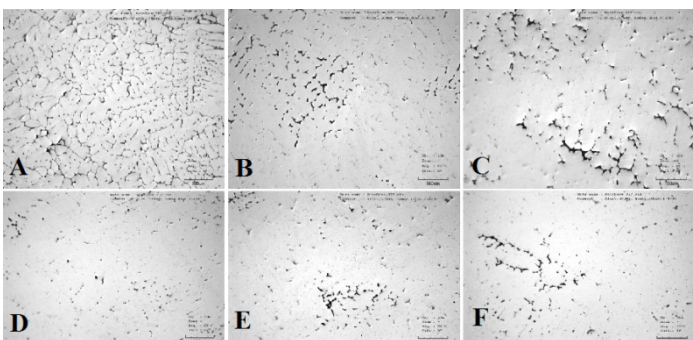


Figure 3. Microstructure after homogenizing annealing (A – before homogenizing, B – 2 hours, C – 6 hours, D – 8 hours, E – 12 hours, F – 20 hours)

The AlZn5.5Cu2.5Mg1.5 alloy microstructures at constant annealing temperature of 470°C are shown above, magnification 100x.

It is known that homogenizing time depends on the structure of a tested alloy. As it is seen from the Fig. 3 A, showing the structure of AlZn5.5Mg2.5Cu1.5 alloy before homogenizing, the structure of a prepared alloy which is poured into a preheated mold is finely reticular and the melting of intermetallic compounds and the diffusion of presented elements inside dendritic cells will not be time-consuming.

From the Fig. 3 B and Fig. 3 C it is possible to state that annealing time at the temperature of 470°C is not sufficient. Considering the structure it is possible to specify an optimal homogenizing time ranging from 8 to 10 hours when the melting of melting eutectics and the diffusion of elements into a solid solution  $\alpha$  is completed. With a longer homogenizing time the elimination of precipitate occurs and pores appear as a result of melting and eutectics solidification of a tested alloy, it is obvious from the Fig. 3 F. The hardness of all the specimens of a tested alloy was defined according to Vickers, it characterizes material hardness properties and is influenced by the chemical composition and structure of the material. Micro-hardness of metallographic grinds in the center of dendritic cells with a load of 20 g with a 5 - second duration was defined<sup>5,6</sup>. The dependence of tested alloy hardness on the temperature and homogenizing time is presented graphically on the Fig. 4. and Fig. 5.

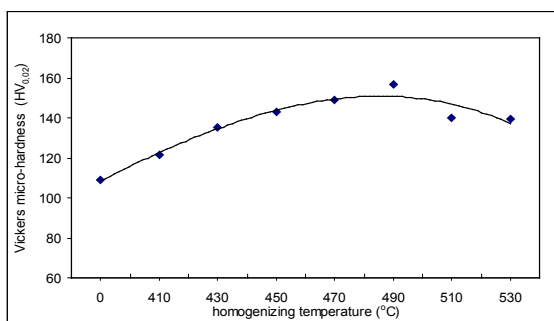


Figure 4. The dependence of AlZn5.5Mg2.5Cu1.5 alloy hardness on homogenizing temperature along 8 hours according to Vickers

From the Fig. 4 it is possible to state that with the increase of homogenizing annealing temperature ( $T = 410 - 490^\circ\text{C}$ ) the micro-hardness of a tested AlZn5.5Mg2.5Cu1.5 alloy, according to Vickers, in the centre of dendritic cells is growing. The specimens of a tested alloy which were homogenized with the temperature of 470 up to 490°C during 8 hours demonstrate the maximum micro-hardness value according to Vickers. With further temperature increase the hardness is getting lower, it occurs because of a melting eutectic which appears on the borders of the grains and because of a spheroid melting eutectic which appears inside the grains.

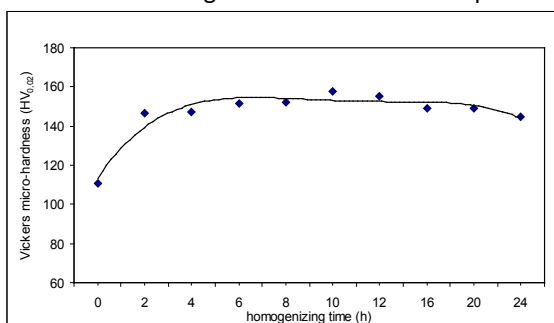


Figure 5. The dependence of AlZn5.5Mg2.5Cu1.5 alloy hardness, according to Vickers, on homogenizing time with a constant temperature  $T = 470^\circ\text{C}$

As it is shown graphically, in the terms of AlZn5.5Mg2.5Cu1.5 alloy micro-hardness, according to Vickers, and its dependence on homogenizing time with a constant temperature of 470°C, it is possible to state the following: after 2 hours of homogenizing annealing the micro-hardness of the material is growing expressively; with a longer homogenizing (8-12 hours) of a tested material the hardness of a tested material, according to Vickers, is growing gently; homogenizing annealing with the temperature of 470°C and which lasts more than 20 hours causes a gentle decrease of a tested material hardness that occurs because of eliminated precipitate coarsening inside dendritic cells in a solid solution  $\alpha$ . In general, it is possible to state that 2 hours of

homogenizing annealing of that experimental alloy with the temperature of  $T = 470^{\circ}\text{C}$  is enough to gain maximal micro-hardness value, according to Vickers, which is analyzed in the central part of dendritic cells.

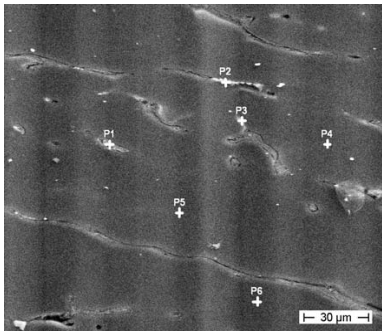


Figure 6. Pattern EDX analysis of AlZn5.5Mg2.5Cu1.5 alloy before annealing, the places of analysis are marked as P1-P6

Table 2.

Pattern EDX analysis values of AlZn5.5Mg2.5Cu1.5 alloy's marked places Fig. 6 P1-P6

wt. %	Mg	Al	Cu	Zn
P1	1.77	76.14	7.43	14.67
P2	1.42	64.00	22.60	11.98
P3	2.17	76.66	4.68	16.49
P4	2.16	85.03	1.20	11.60
P5	2.17	85.07	1.28	11.48
P6	2.10	81.06	2.56	14.27

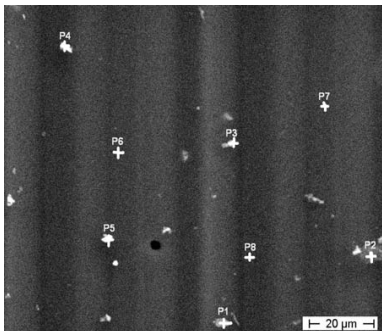


Figure 7. Pattern EDX analysis of AlZn5.5Mg2.5Cu1.5 alloy after annealing with the temperature of  $T = 470^{\circ}\text{C}$  during 8 hours, the places of analysis are marked as P1-P8

Table 3.

Pattern EDX analysis values of AlZn5.5Mg2.5Cu1.5 alloy's marked places Fig. 7 P1-P8

wt. %	Mg	Al	Cu	Zn
P1	2.05	77.51	3.92	16.52
P2	1.83	75.85	6.90	15.41
P3	2.03	77.28	3.93	16.75
P4	1.91	76.80	5.50	15.79
P5	2.12	77.17	4.18	16.53
P6	1.91	77.40	4.17	16.52
P7	2.01	77.19	4.06	16.75
P8	2.20	77.27	3.84	16.70

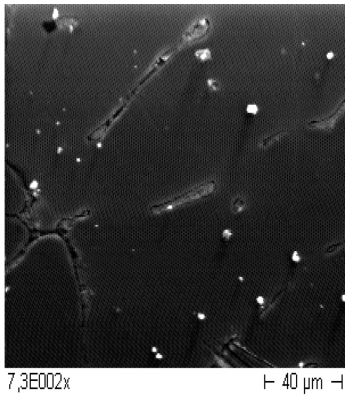


Figure 8. Analyzed area EDX analysis AlZn5.5Mg2.5Cu1.5, homogenized T = 470°C/8 h, scanning electron microscope

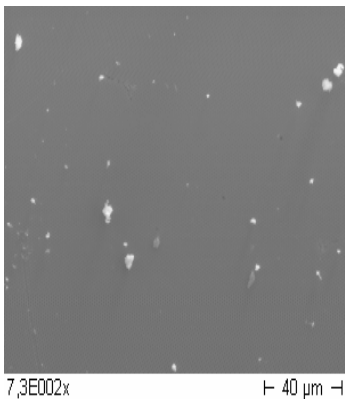


Figure 9. Analyzed area EDX analysis AlZn5.5Mg2.5Cu1.5, homogenized T = 470°C/8 h, scanning electron microscope

Considering pattern EDX analysis values of an experimental AlZn5.5Mg2.5Cu1.5 alloy before homogenizing annealing it is possible to state the following:

- the structure of an experimental AlZn5.5Mg2.5Cu1.5 alloy before homogenizing is composed of  $\alpha$  – solid solution and a soluble and insoluble eutectic of a type  $\alpha + \text{Mg}_3\text{Zn}_3\text{Al}_2$  (quasibinary) or an insoluble eutectic of a type  $\alpha + \text{CuMgAl}_2$ . It is also possible to reveal the presence of soluble tertiary eutectics  $\alpha + \text{Mg}_5\text{Al}_8 + \text{Mg}_3\text{Zn}_3\text{Al}_2$  and  $\alpha + \text{Mg}_3\text{Zn}_3\text{Al}_2 + \text{MgZn}_2$ . The presence of copper causes the growth of eutectic of a type  $\alpha + \text{CuMgAl}_2 + \text{Mg}_3\text{Zn}_3\text{Al}_2 + \text{MgZn}_2$ , the most part of it will dissolve into  $\text{MgZn}_2$  or  $\text{Mg}_3\text{Zn}_3\text{Al}_2$ .
- from the Fig.6 it is possible to define the presence of eutectic of a type  $\alpha + \text{CuAl}_2$ , which can also appear after a short period of ageing.

Due to pattern EDX analysis of specimens after homogenizing annealing with the temperature of T = 470°C during 8 hours it is possible to conclude the following:

- the solubility of copper and zinc under homogenizing is extremely high, and during homogenizing very sound and fast diffusion of that elements into a solid solution  $\alpha$  occurs;
  - from the Fig. 7 it is evident that the most number of presented soluble eutectics had dissolved at the temperature of 470°C after 8 hours. It is about a soluble low-meltable eutectic  $\alpha + \text{Mg}_5\text{Al}_8 + \text{Mg}_3\text{Zn}_3\text{Al}_2$ , which dissolves at the temperature over 450 °C. It is possible to state that even eutectic  $\alpha + \text{Mg}_3\text{Zn}_3\text{Al}_2 + \text{MgZn}_2$ , which can dissolve at the temperature of 475°C, has dissolved under those homogenizing conditions.
  - from the structure and EDX analysis values of an experimental alloy under the homogenizing temperature of 470 °C and time of 8 hours Fig. 7 it is evident that existing eutectics  $\alpha + \text{CuMgAl}_2$  are not dissolved (P2,P4).
- ined caption and be positioned in flush-left alignment with the text margin within the column. If they do not fit into one column they may be placed across both columns in which case place them at the top or at the bottom of a page.

## Conclusion

After the experiments with AlZn5.5Mg2.5Cu1.5 alloy it is possible to conclude the following:

1. From the microstructure of AlZn5.5Mg2.5Cu1.5 alloy that was homogenized during a constant time of 8 hours with a changeable temperature it is possible to state that considering the microstructure of

AlZn5.5Mg2.5Cu1.5 alloy, homogenizing annealing with the temperature of 430 up to 530 °C is an optimal homogenizing condition with the temperature range of 470 up to 490°C. At the higher temperature over 510°C as it is seen from the microstructure melting eutectics set along the borders of dendritic cells and spheroid melting eutectics appear.

2. After microstructure evaluation of experimental alloy sets being made with the constant temperature of  $T=470^{\circ}\text{C}$  it is possible to conclude that annealing time of 2-6 hours is not sufficient. Considering the microstructure after treatment with  $470^{\circ}\text{C}$  the optimal homogenizing time is 8 up to 10 hours, when the dissolution of soluble eutectics and the diffusion of elements into a solid solution  $\alpha$  are completed.
3. Considering the micro-hardness of a solid solution  $\alpha$ , according to Vickers, with a load of 20g. with a 5-second duration (the micro-hardness of all the specimens was analyzed in the middle part of dendritic cells) it is possible to determine the optimal annealing condition - it is constant annealing time of 8 hours with the temperature range of 470 up to  $490^{\circ}\text{C}$ .
4. From an experimental alloy made with the constant temperature of  $470^{\circ}\text{C}$  (Fig. 5) it is possible to observe a considerable hardness growth of a solid solution  $\alpha$ , according to Vickers, after 2 hours of homogenizing annealing. Homogenizing annealing which lasts 20 hours causes a gentle micro-hardness decrease of a tested material, it takes place because of eliminated precipitate coarsening inside dendritic cells in a solid solution  $\alpha$ .
5. The results of EDX analysis of an experimental AlZn5.5Mg2.5Cu1.5 alloy before and after homogenizing with the temperature of  $470^{\circ}\text{C}$  lasting 8 hours show that the structure of AlZn5.5Mg2.5Cu1.5 alloy before homogenizing is made with a solid solution  $\alpha$  and a soluble and insoluble eutectic of a type  $\alpha + \text{Mg}_3\text{Zn}_3\text{Al}_2$  (quasibinary) or an insoluble eutectic of a type  $\alpha + \text{CuMgAl}_2$ . It is possible to presuppose the presence of soluble tertiary eutectics  $\alpha + \text{Mg}_5\text{Al}_8 + \text{Mg}_3\text{Zn}_3\text{Al}_2$  and  $\alpha + \text{Mg}_3\text{Zn}_3\text{Al}_2 + \text{MgZn}_2$ . Copper influences the growth of eutectic of a type  $\alpha + \text{CuMgAl}_2 + \text{Mg}_3\text{Zn}_3\text{Al}_2 + \text{MgZn}_2$ , the most part of it will dissolve into  $\text{MgZn}_2$  or  $\text{Mg}_3\text{Zn}_3\text{Al}_2$ . From the the Fig. 6 (P2) it is possible to disclose the presence of eutectic of a type  $\alpha + \text{CuAl}_2$ , which can also appear after a short period of ageing. From the Fig. 7 of a homogenized alloy it is evident that the most number of presented soluble eutectics had dissolved at the temperature of  $470^{\circ}\text{C}$  after 8 hours. It is about the eutectic of a type  $\alpha + \text{Mg}_5\text{Al}_8 + \text{Mg}_3\text{Zn}_3\text{Al}_2$  and the eutectic of a type  $\alpha + \text{Mg}_3\text{Zn}_3\text{Al}_2 + \text{MgZn}_2$ . The eutectics of a type  $\alpha + \text{CuMgAl}_2$  under the temperature of  $470^{\circ}\text{C}$  during 8 hours are not dissolved (P2, P4).

#### Literature

1. Grígerová, T., Lukač, I., Kořený, R.: Foundry of non-ferrous metals, Praha (1988).
2. Michna, Š., Lukáč, I., Louda, P., Očenášek a kol.: Aluminium materials and technologies from A to Z, Adin s.r.o., ISBN 978-80-89244-18-8 (2005).
3. Lukač, I., Michna, Š.: Colour contrast, structure and defects in aluminium and aluminium alloys, Cambridge International Science Publishing, ISBN 18-983-26-70-3 (2001).
4. Michna, Š., Nová, I.: The technology and treatment of metallic material, Adin, s.r.o. Prešov, ISBN 978-80-89244-38-6 (2008).
5. Pisarek, B. (2012). Effect of Annealing Time for Quenching CuAl7Fe5Ni5W2Si2 Bronze on the Microstructure and Mechanical Properties. Archives of Foundry Engineering. Volume 12 (Issue 2/2012), pp. 187-204, ISSN 1897-3310.
6. Pezda, J. (2012). Heat Treatment of AlZn10Si7MgCu Alloy and its Effect on Change of Mechanical Properties. Archives of Foundry Engineering. Volume 12 (Issue 2/2012), pp. 135-138, ISSN 1897-3310.

## THE INFLUENCE OF GERMANIUM ON THE PROPERTIES OF COMMERCIAL MAGNESIUM ALLOYS

Šerák J., Kovalčík T., Vojtěch D., Novák P.

*Institute of Chemical Technology, Prague, Department of Metals and Corrosion Engineering,  
Technická 5, 166 28 Prague 6, Czech Republic  
serakj@vscht.cz*

### Abstract

The effort to develop new magnesium alloys working at elevated temperatures is very intensive at the present time. Ge forms more stable intermediary phases with magnesium compared to silicon. That is why the effect of additions of Ge on mechanical properties at different temperatures of selected commercial magnesium alloys (AZ31, EZ33, WE43, AJ62 and MRI153) was studied. It was found that Ge additions have significant effect on the properties of some magnesium alloys.

### Key words

magnesium alloys;germanium;mechanical properties

### Introduction

Magnesium alloys represent modern structural materials with very good ratio between their mechanical properties (especially yield strength) and density. The requirement for a combination of high mechanical properties of the alloy and its low density results from the particular requirements of the automotive and aerospace industries. Reducing vehicle weight has a positive effect in lowering fuel consumption and exhausts emissions and also allows increase the weight of goods transported<sup>1-5</sup>. Most of magnesium alloys is applicable only for normal temperature. Mechanical properties of magnesium alloys begin to fall significantly even at temperature above 150° C. This phenomenon is affected with gradual change in the microstructure of alloy that occurs due to the presence of aluminum as alloying element. Common commercial magnesium alloys are alloyed with aluminum in particular and therefore they are unusable at high temperatures. Therefore, the quest for new affordable magnesium alloy stable at higher temperatures. Magnesium and aluminum form instable intermediate phase Mg<sub>17</sub>Al<sub>12</sub>. This phase is in the microstructure of magnesium alloys present in the form of the Mg + Mg<sub>17</sub>Al<sub>12</sub> eutectic, surrounding the dendrites of magnesium solid solution. Low difference in the electronegativity between the aluminum and magnesium and existence of the Mg<sub>17</sub>Al<sub>12</sub> phase in relatively wide area of chemical composition imply the low stability of the Mg<sub>17</sub>Al<sub>12</sub> phase. Low melting point of this intermediary phase (455°C) and low value of the hardness also documents the low stability of this phase, which causes the decrease in yield strength and tensile strength of magnesium alloys alloyed with aluminum at the temperatures higher than 150°C<sup>7-8</sup>. For this reason, aluminum is not used as alloying element for magnesium alloys working at elevated temperatures. Number of commercial magnesium alloys is alloyed with silicon or other elements to achieve increased thermal stability<sup>9-12</sup>. Currently, as additions stabilizing properties of magnesium alloys at elevated temperatures, rare earth metals are used<sup>3-5</sup>. However, they are expensive. One possible way is to study the influence of unconventional alloying elements on the properties of magnesium alloys at elevated temperatures.

Germanium is element which could have positive effect on the properties of magnesium alloys.

Germanium is an element discovered in 1886 by Clemens Vinkler, named after his native country - Germany<sup>1,2</sup>. Germanium is an element relatively little widespread in the earth's crust (5-7 mg/kg). This is a very hard and brittle material. Chemically, its properties are very similar to silicon or tin. Selected properties of germanium, silicon and tin are shown in tab. I.

Germanium does not yet have important uses in metallurgy. The use of germanium in various branches is summarized in tab. II.

Binary alloys Mg-Al-Ge and Ge show higher mechanical properties than the corresponding Mg-Si and Al-Si alloys<sup>1,2</sup>. Magnesium forms with silicon an intermediate phase Mg<sub>2</sub>Si. A similar phase Mg<sub>2</sub>Ge is formed with

Table I  
Selected properties of Ge, Si and Sn<sup>1</sup>

	Ge	Si	Sn
Density, 20°C [kgm <sup>-3</sup> ]	5 323	2 330	7 310
Vickers hardness	300	410	40
Melting point [°C]	938.3	1 415	231.9
Structure, 20°C	cubic	cubic	tetragonal
Atomic radius [pm]	125	111	145
Oxidation states	- IV, II, IV	- IV, II, IV	- IV, II, IV

magnesium and germanium. Phase diagrams<sup>7</sup> show a high stability of intermediate phases. The stability of these intermediate phases is substantially higher than in the case of phase  $Mg_{17}Al_{12}$ . The highest melting temperature (1117.4°C) has  $Mg_2Ge$  phase. Thermal stability of  $Mg_2Ge$  phase is the basis of increased thermal stability of magnesium alloys after alloying with germanium<sup>13-18</sup>.

Table II  
Technical use of germanium<sup>1-2</sup>

Branch	Use
Optics	- $GeO_2$ - high index of refractory, low optical dispersion → optical glass (fiber optics), wide-angle camera lenses, microscopy - production of chalcogenide glasses ( $GeTe$ )
Electronics	- manufacturing of semiconductor parts - Ge, SiGe (diodes, transistors) - construction of sensitive IR detectors (high transparency to infrared radiation - night vision devices) - manufacturing of solar panels - $MgGeF_6$ - use as phosphors high pressure mercury lamps - use of alloys $GeSbTi$ in new types of capacitive batteries - DVD rewritable media (active layer from $GeSbTe$ alloy)
Industrial production	- catalyst in the production of polyethylene terephthalate (PET)
Medicine	- use of organic compounds Ge (eg, bis-carboxyethyl germanium sesquioxide) in chemotherapy - alloying element in some dental alloys
Metallurgy	- jewelry solder $AuGe_{12}$ - Ge lowers the transformation temperature in Ti-Nb shape memory alloys

AZ31, EZ33 and WE43 alloys are frequently used magnesium alloy. AZ31 alloy is commercial alloy for work at normal temperature, the WE43 and EZ33 alloys are alloyed with rare earth metals and usable at elevated temperatures. AJ62 and MRI153 alloys contain significant levels of Sr, and Ca respectively. These elements also have very favorable effect on the resistance of magnesium alloys at elevated temperatures. The influence of Ge additions to AZ31, EZ33, WE43, AJ62 and MRI153 alloys were studied in this work. Microstructure, hardness and compressive mechanical properties at room (20°C) and elevated temperatures (150, 200°C) were studied.

### Experimental

The influence of germanium on the microstructure and mechanical properties (hardness, compressive yield strength and compressive strength) of several commercial magnesium alloys was studied in this work. Commercial alloys were alloyed with germanium in levels of 2 and 5 wt.%. Overview of 15 investigated alloys is shown in tab. III.

Samples were prepared from commercial alloys and germanium (5N5 purity) by melting in an electric induction furnace under protective atmosphere of Ar. Melt was

Table III  
Overview studied alloys

AJ62	AZ31	EZ33	MRI153	WE43
AJ62Ge2	AZ31Ge2	EZ33Ge2	MRI153Ge2	WE43Ge2
AJ62Ge5	AZ31Ge5	EZ33Ge5	MRI153Ge5	WE43Ge5

cast into a brass mold with a diameter of 20 mm and after cooling the samples were removed from the mold and used for experiments. The chemical composition of the samples was determined by x-ray fluorescence spectrometry. Chemical composition of studied alloys is shown in tab IV.

Metallographic samples were made by conventional metallographic procedure. The microstructure of the samples was studied by light microscope Olympus PME 3 and by scanning electron microscope TESCAN VEGA 3 LMU with EDS analyzer. Brinell hardness measurements were carried out using a Heckert WPM machine. Hardness of each sample was determined three times. Mechanical testing of alloys in uniaxial pressure was performed using a universal tensile machine LabTest 5.25OSP1. Uniaxial pressure test was performed at the temperatures of 20, 150 and 200° C.

Table IV

Chemical composition of studied alloys [wt.%]

	Al	Mn	Zn	Sr	Ge	Ca	Zr	La	Ce	Nd	Y	Gd	Mg
AJ62	6.3	0.3	0.1	2.9	-	-	-	-	-	-	-	-	bal.
AJ62 Ge2	6.2	0.3	0.1	2.7	1.6	-	-	-	-	-	-	-	bal.
AJ62 Ge5	5.1	0.3	-	2.1	4.7	-	-	-	-	-	-	-	bal.
AZ31	2.8	-	1.2	-	-	-	-	-	-	-	-	-	bal.
AZ31 Ge2	2.7	-	1.3	-	2.2	-	-	-	-	-	-	-	bal.
AZ31 Ge5	2.2	-	1.3	-	4.4	-	-	-	-	-	-	-	bal.
EZ33	-	-	2.2	-	-	-	0.3	0.7	1.4	0.6	-	-	bal.
EZ33 Ge2	-	-	2.0	-	1.6	-	0.3	0.6	1.3	0.4	-	-	bal.
EZ33 Ge5	-	-	1.8	-	4.8	-	0.3	0.5	1.1	0.3	-	-	bal.
MRI153	7.7	0.2	-	0.1	-	0.7	-	-	-	-	-	-	bal.
MRI153 Ge2	7.4	0.2	-	0.1	1.7	0.7	-	-	-	-	-	-	bal.
MRI153 Ge5	7.1	0.2	-	0.1	4.7	0.6	-	-	-	-	-	-	bal.
WE43	-	-	0.1	-	-	-	0.2	-	-	2.2	2.8	0.8	bal.
WE43 Ge2	-	-	-	-	1.7	-	0.2	-	-	2.0	2.4	0.6	bal.
WE43 Ge5	-	-	-	-	4.8	-	0.2	-	-	1.8	2.1	0.5	bal.

## Results and discussion

### Microstructure of alloys

Microstructure of all studied alloys is very similar. It consists of the dendrites of the magnesium solid solution with dissolved elements. The remaining part of the alloying elements that are not dissolved in magnesium solid solution forms intermediate phases, which occur in the space between the dendrites. The examples of the microstructures of EZ33 alloy without the addition of germanium and after addition of germanium in amount of 2 and 5 wt.% are in the fig.1. Germanium added to alloy forms with magnesium  $Mg_2Ge$  phases. These phases are shown in the fig.1b,c.  $Mg_2Ge$  particles have polyhedral morphology and black color.

Germanium also forms intermediate phases with some alloying elements added to magnesium to reach higher stability at elevated temperatures. Particles of  $MgYGeNd$  intermediary phase were observed in the microstructure of WE43 alloy with addition Ge in amount of 5%. These phase contain about 40 wt.% of Y and about 40 wt.% of Ge. Formation of this phase leads to decrease in rare earth metals content in magnesium solid solution and decrease in the mechanical properties of alloy.

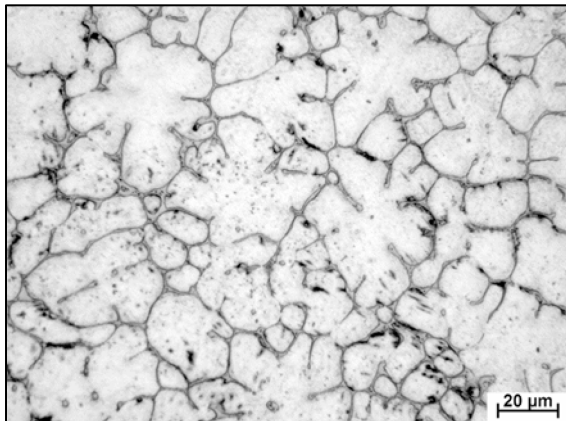


Figure 1a. Microstructure of EZ33 alloy, LEM, as-cast

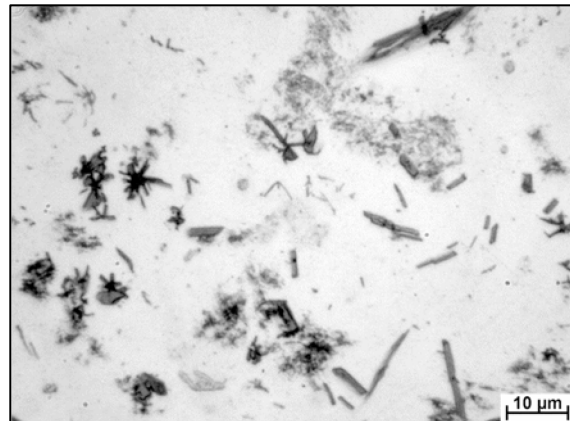


Figure 1b. Microstructure of EZ33Ge2 alloy, LEM, as-cast

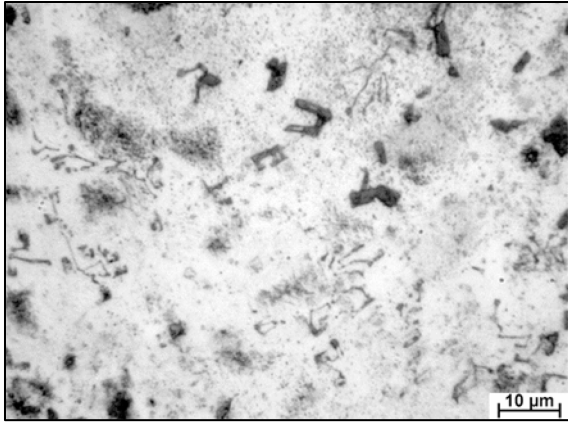


Figure 1c. Microstructure of EZ33Ge5 alloy, LEM, as-cast

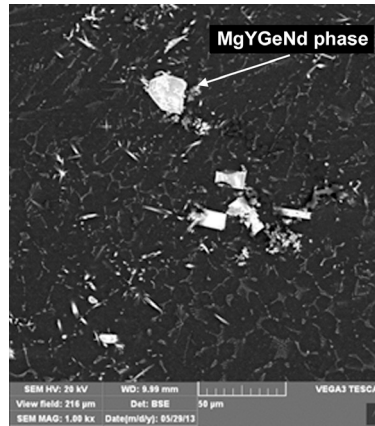


Figure 1d. Microstructure of WE43Ge5 alloy, SEM, as-cast

## Mechanical properties

### Hardness

The addition of Ge has different effect on mechanical properties of commercial magnesium alloys. Hardness of alloys containing Al increases with increasing Ge content. Hardness of alloys without Al content (EZ33, WE43) slightly decreases after addition 2% Ge. The addition of 5% Ge to alloy on the contrary increases the hardness of alloy, see fig.2. Explanation for this is the formation of intermediate phases between Ge and rare earth metals, thereby reducing the content of rare earth metals in the magnesium solid solution, leading to a decrease in hardness of the alloy. Higher Ge addition leads to the formation  $Mg_2Ge$  phase, resulting in an increase in hardness of alloy.

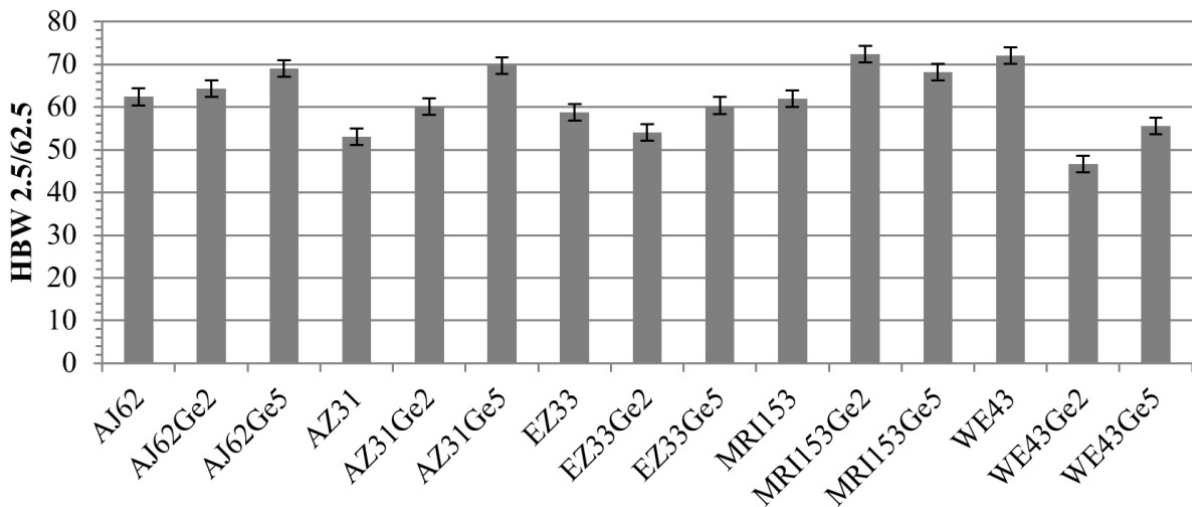


Figure 2. Brinell hardness of studied alloys

### Compressive test

The uniaxial pressure test was performed at room temperature (20 °C) and at elevated temperatures (150 and 200 °C). Due to the sample preparation by gravity casting method the effect of casting defects on the results of compressive test cannot be excluded. Compressive yield strength (fig.3a) and compression strength (fig.3b) were calculated. The effect of Ge addition on the compressive yield strength of commercial magnesium alloys is very different. In the case of AJ62 and MRI153 alloys the effect of Ge is insignificant and the values of compressive yield strength of alloys do not change much even at different temperatures. Compressive yield strength increases with increasing Ge content in the case of AZ31 alloy. Additions of Ge to commercial WE43 alloy lead to a significant reduction in compressive yield strength.

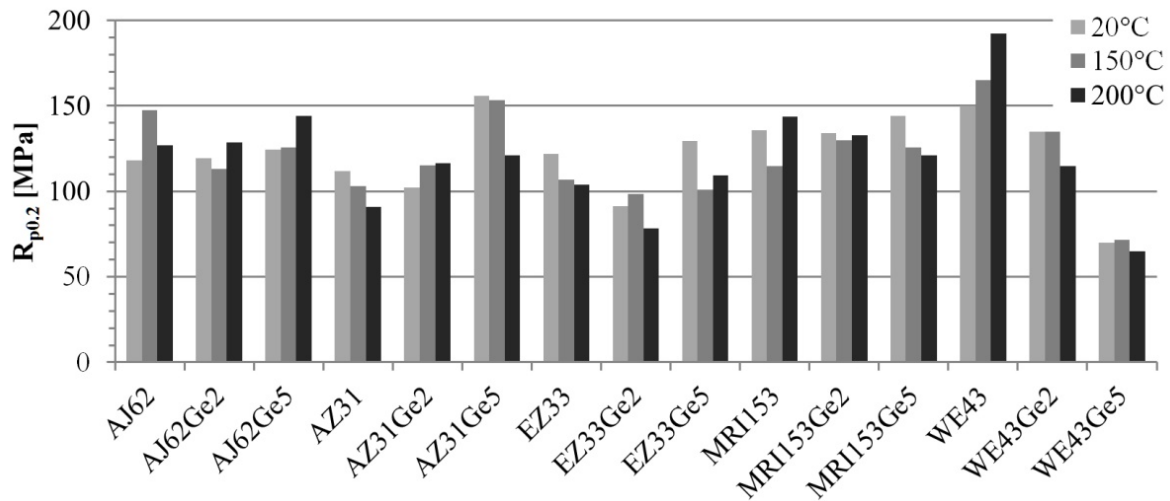


Figure 3a. Yield strength of studied alloys at various temperatures

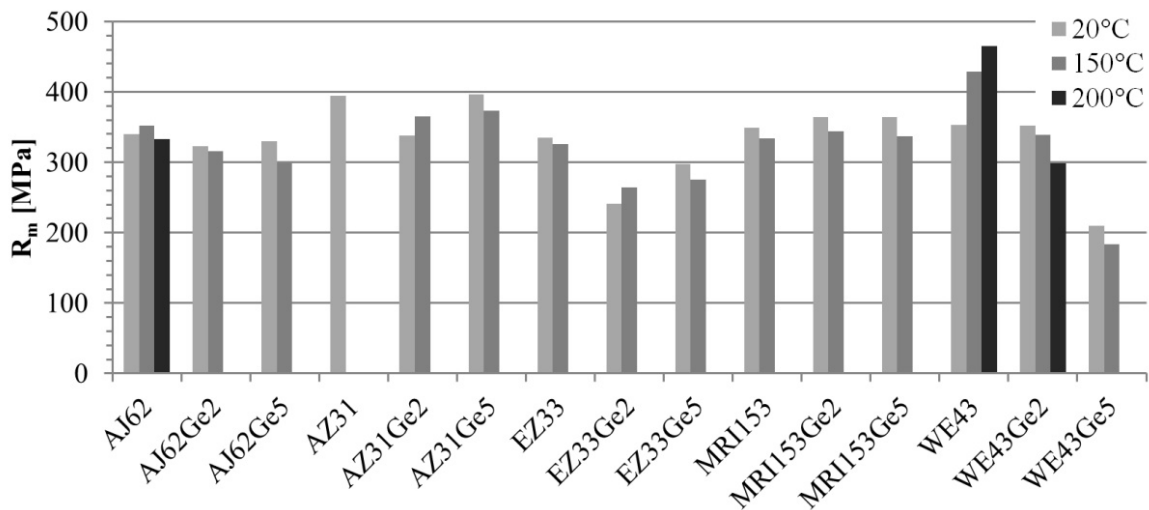


Figure 3b. Compressive strength of studied alloys at various temperatures

The effect of Ge addition to compressive strength of studied commercial magnesium alloys is similar to effect of the compressive yield strength. The most distinctive effect has Ge on compressive strength of WE43 alloy. High plasticity of several alloys at elevated temperatures did not allow compute the value of their compressive strength.

### Conclusions

The microstructure of all investigated alloys is very similar. It consists of the dendrites of magnesium solid solution with dissolved alloying elements. The particles of intermediate phases are segregated on the grain boundaries. The addition of Ge to alloy leads to further formation of intermediary phases ( $Mg_2Ge$ ) segregated on the grain boundaries. It was found that Ge forms intermediate phases with other alloying elements (Y, Zr, Nd). The level of these elements dissolved in magnesium solid solution is much lower and mechanical properties of alloy significantly decrease.

Very different influence of Ge additions on the mechanical properties of selected commercial magnesium alloys was found. The effect of Ge additions on the mechanical properties of AJ62 and MRI153 is not significant. Ge additions to AZ31 alloy increase the mechanical properties of alloy. Mechanical properties of WE43 and EZ33 alloys decrease after Ge additions to these alloys.

### Acknowledgment

The presented results were obtained within the frame of the research project GA CR No. P108/12/G043.

## Literature

1. Scoyer J., Guislain H., Wolf H. U., Germanium and Germanium Compounds in Ullmann's Encyclopedia of Industrial Chemistry, Wiley-VCH Verlag GmbH & Co. KGaA: Weinheim, (2012), pp. 629–641.
2. Buttermann W. C., Jorgenson J.D., Germanium, 2005. Mineral Commodity Profiles: Germanium. <http://pubs.usgs.gov/of/2004/1218/2004-1218.pdf> (cited 25. 4. 2014).
3. Šerák J., Kovalčík T., Vojtěch D., Novák P., 13-th Conference Contribution of Metallography to Solving of production Troubles, Lázně Libverda, 17.-19. June (2014), pp. 72–78.
4. Cherubinia F., Raugei M., Ulgiati S., LCA of magnesium production: Technological overview and worldwide estimation of environmental burdens. *Resources, Conservation and Recycling*, 52, (2008), pp. 1093–1100.
5. Gupta M., Nai M. L. S, Magnesium, Magnesium Alloys, & Magnesium Composites [online]; John Wiley & Sons Inc., 2010, [onlinelibrary.wiley.com](http://onlinelibrary.wiley.com) (cited 25. 4. 2014).
6. Cramer S. D., Covino B. S., Corrosion of Magnesium and Magnesium Base Alloys. *ASM Handbook, Volume 13B: Corrosion: Materials*; ASM International, (2005), pp. 205–227.
7. Avedesian M. M., Baker H., Magnesium and Magnesium Alloys [online]; ASM International, 1999. [http://books.google.cz/books?id=0wFMfJg57YMC&printsec=frontcover&hl=cs&source=gbs\\_ge\\_summary\\_r&cad=0#v=onepage&q&f=false](http://books.google.cz/books?id=0wFMfJg57YMC&printsec=frontcover&hl=cs&source=gbs_ge_summary_r&cad=0#v=onepage&q&f=false) (cited 25. 4. 2014).
8. Yang Z., et al., Review on research and development of magnesium alloys. *Acta metallurgica sinica (English letters)*, 21 (5), (2008), pp. 313–328.
9. Nie J.F., Precipitation and Hardening in Magnesium Alloys. *Metall. Mater. Trans. A*, 43, (2012), pp. 3891–3939.
10. Zhu S. M., et al., The relationship between microstructure and creep resistance in die-cast magnesium–rare earth alloys, *Scripta Materialia*, 63 (5), (2010), pp. 698–703.
11. Luo A., Pekguleryuz M. O., Review: Cast magnesium alloys for elevated temperature applications. *Journal of Material Science*, 29, (1994), pp. 5259–5271.
12. Pekguleryuz M. O., Kaya A. A., Creep resistant magnesium alloys for powertrain applications. *Advanced engineering materials*, 5 (12), (2003), pp. 866–878.
13. Liao Z., et al., The effect of Ge addition on Al–3.5Cu–0.4Mg alloy. *Scripta materialia*, 66, (2012), pp. 447–450.
14. Liu H. B., Qi G. H., Ma Y. T., et al., Microstructure evolution and mechanical properties of Mg-Ge binary magnesium alloys. *Materials research innovations*, 14 (2), (2010), pp. 154–159.
15. Liu H. B., Zhang X. G., Qi G. H., et al., Microstructure and mechanical properties of as cast AZ31 with addition of germanium. *Materials research innovations*, 14 (4), (2010), pp. 342–347.
16. Serak J., Voderova M., Vojtech D., Novak P. Microstructure and Properties of magnesium alloys working at elevated temperatures. *Manufacturing Technology*, June 2014, Vol.14, No.2 (2014), pp. 238-244.

## INFLUENCE OF HEAT TREATMENT ON MICROSTRUCTURE AND MECHANICAL PROPERTIES OF AlSi9CuMgNiMn ALLOY

**Cais J.**, Weiss V., Svobodová J.

*J. E. Purkyně University in Ústí nad Labem, Faculty of Production Technology and Management, Department of Technology and Material engineering, Pasteurova 3334/7, 400 0,1 Ústí nad Labem  
cais@fvvm.ujep.cz*

### Abstract:

The article examines the influence of heat treatment process on the mechanical properties of the castings made from AlSi9CuMgNiMn alloy. Examination were subjected to a mold for pressing of tires which are made by low-pressure casting technology. The part of research was carried out analysis of the microstructure by optical and electron microscopy. Investigation of mechanical properties was performed by a static tensile testing and measuring Brinell hardness.

Keywords: hardening, tensile strength, ductility, intermetallic phase, SEM, EDS analysis

### Introduction

Aluminum alloys of Al-Si-Cu are currently commonly used in the automotive industry especially in the production of cylinder heads, transmission housings and pistons of internal combustion engines. The heat treatment of these alloys causes a substantial increase of the mechanical properties, for this reason, the process for casting this type of alloys is often applied. Alloys based on Al-Si-Cu is heat-treated by the hardening process. This process consists of heating the dissolution, the subsequent cooling, supercritical speeds and subsequent aging (natural or artificial). The copper content in these alloys in addition to guaranteeing the possibility of heat treatment (precipitation of intermetallic phases Al<sub>2</sub>Cu) also improve their properties at elevated temperatures (up to 250 ° C). These alloys excel in good casting properties, not prone to cracking under heat and does not significantly shrinkage. The mechanical properties of Al-Si-Cu alloys can be further affected by the addition of other alloying elements, which with changes in the microstructure of the material cause changes in the mechanical properties. Addition of Mg is another element contributing to the improvement of mechanical properties through heat treatment by creating intermetallic phase Mg<sub>2</sub>Si. Nickel is alloyed in order to increase the strength properties at elevated temperatures and reduced thermal expansion coefficient. The main reason for the addition of manganese suppress the formation of iron in a plate shape and create favorable intermetallic phase  $\alpha$ -AlFeMnSi

### Experimental work

Input sample was cut from the segment mold for pressing of tires. This casting was made by low pressure casting technology, where the initial charge had a weight of 530 kg, the weight of the cast segment itself according to the size of the tire produced in the range 12 to 25 kg. Cleaning melt is then done through the addition of refining salt and degassing of molten is implemented by FDU technology with using argon. The chemical composition of the casting is captured in Tab. I

Tab. I Chemical composition of the casting

Chem. element	Si	Fe	Cu	Mn	Mg	Ni	Ti	Sr	Al
Content [wt. %]	8.462	0.542	1.144	0.314	1.130	0.605	0.067	0.032	base

Microstructure analyzed alloy were evaluated by optical and scanning electron microscopy (SEM). The chemical composition of the individual structural components have been analyzed by electron dispersive spectroscopy (EDS).

The microstructure of the alloy is formed by dendrites  $\alpha$  solid solution, eutectic, and the amount of different intermetallic phases. Fig. 1 and 2 shows the microstructure examined polycomponent alloy. Fig. 3 shows extensive bone formations emerging in the investigated alloy microstructure. Picture of these intermetallic phases taken by the SEM is indicated as Fig.4, in this image is marked area from which it was subsequently created EDS surface analysis. The spectrum of the chemical elements detected in this area is reported in Fig. 5. Quantification of the results of the EDS analysis is in Tab. II. Based on the results of EDS analysis it can be concluded that it is an intermetallic phase of  $\alpha$ -AlFeMnSi.

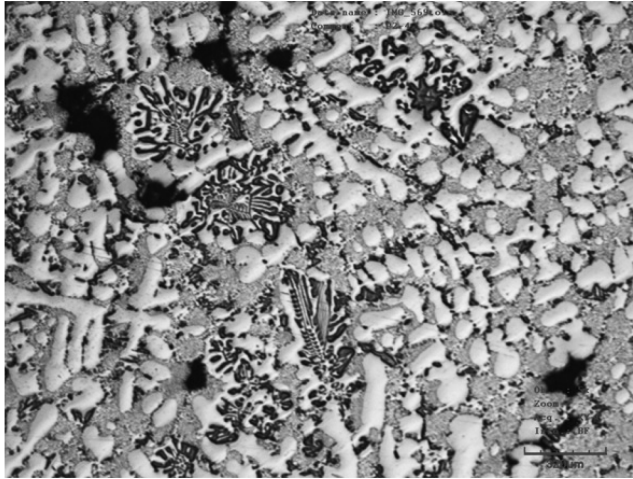


Fig. 1 Alloy microstructure

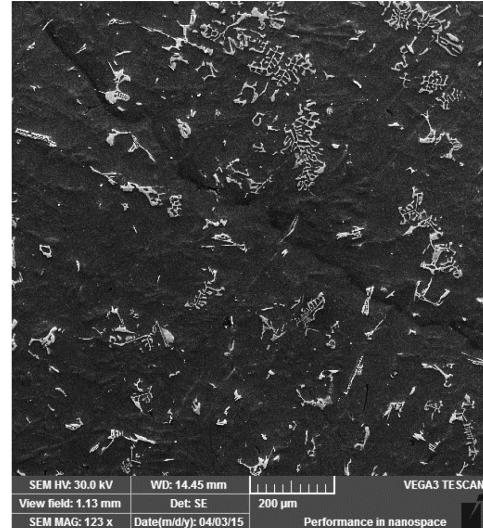


Fig. 2 Alloy microstructure(SEM)



Fig. 3 Intermetallic phase  $\alpha$ -AlFeMnSi

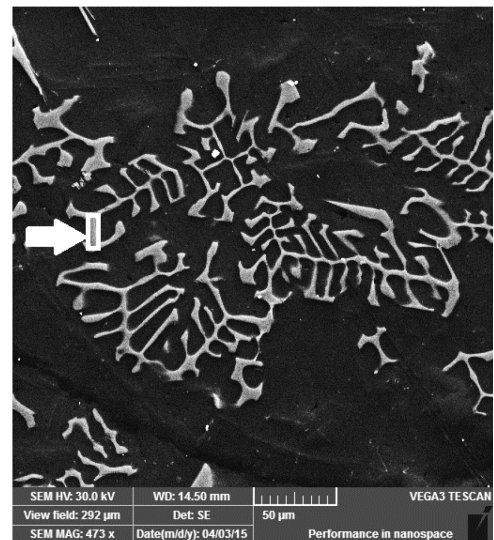


Fig. 4 Intermetallic phase  $\alpha$ -AlFeMnSi(SEM)

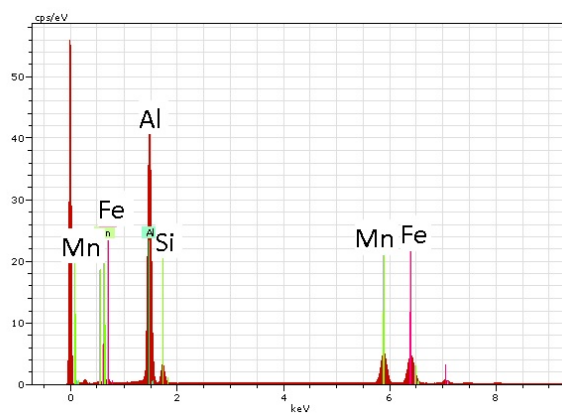


Fig. 5 Analysis of intermetallic phase  $\alpha$ -AlFeMnSi

Tab. II Analysis of intermetallic phase  $\alpha$ -AlFeMnSi

Ch. element	Content [wt. %]	Content [at. %]
Al K	59.38	71.53
Si K	8.13	9.41
Mn K	16.38	9.69
Fe K	16.11	9.38
SUMA	100.00	100.00

Another recognized type of intermetallic phases is depicted in Fig. 6 (surface area of EDS analysis is indicated by an arrow in the picture). Identified spectrum of chemical elements in the selected area is shown in Fig. 7. EDS

analysis results from selected areas are shown in Tab. III. Based on the quantification of the results sheet EDS analysis is possible to say that the structure is recognized polycomponent intermetallic phases of Al-Ni-Si-Cu-Fe-Mn.

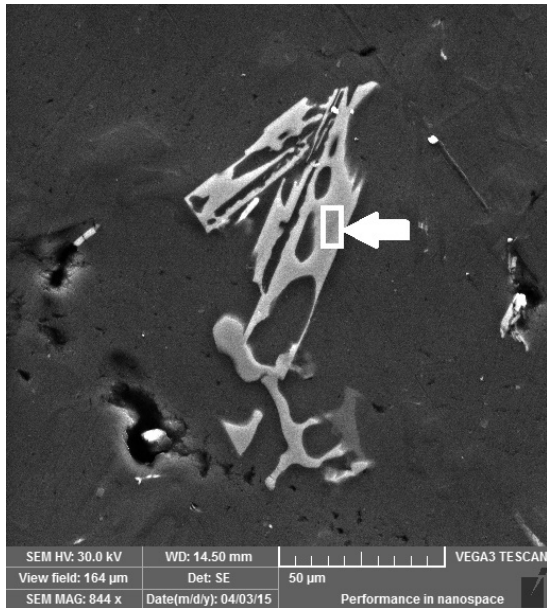


Fig. 6 Intermetallic phase type Al-Ni-Si-Cu-Fe-Mn

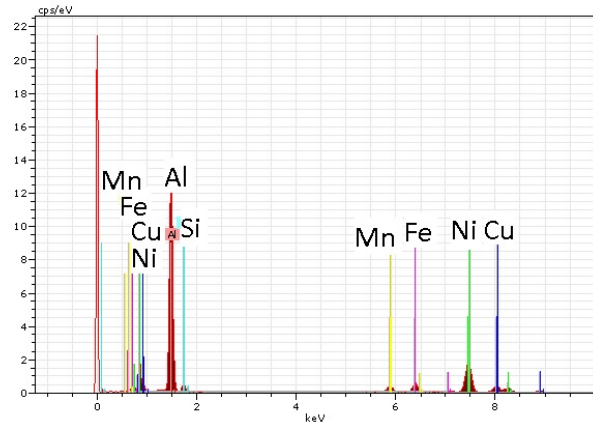


Fig. 7 Analysis of intermetallic phase type Al-Ni-Si-Cu-Fe-Mn

Tab. III Analysis of intermetallic phase type Al-Ni-Si-Cu-Fe-Mn

Ch. element	Content [wt. %]	Content [at. %]
Al K	61.65	75.93
Ni K	21.61	12.24
Cu K	6.02	3.15
Si K	3.86	4.57
Fe K	4.04	2.41
Mn K	2.81	1.70
SUMA	100.00	100.00

The heat treatment of the investigated alloys consisted of dissolver heating at 520 °C for 8 hours and subsequent cooling in water at 60 °C. Followed process of artificial aging at 170 °C for 12 hours.

For measuring the hardness of the investigated alloys was used Brinell hardness test. Measured parameters have been set in accordance with the standard ČSN EN ISO 6506-1. Samples were subjected to measurement in a state without heat treatment and after heat treatment. The measurement results are shown in Table IV.

Another type of test applied to samples made from a cast to determine the mechanical properties is the static tensile test. Test parameters including the shape and dimensions of the test samples were adjusted according standards EN 10002-1 (420310). The results of the static tensile test specimens made of casting are in Tab. V.

Tab. IV The Brinell hardness test results

Numberofmeasurement	Withoutheattreatment[HB <sub>10</sub> ]	Afterheattreatment[HB <sub>10</sub> ]
1	73	144
2	78	139
3	72	136
4	76	153
5	79	141
6	76	138
7	75	140
8	83	152
9	76	162
10	75	143
<b>Average value [HB<sub>10</sub>]</b>	<b>76.3</b>	<b>144.8</b>

Tab. V Static tensile test results

Sample identification	R <sub>m</sub> [MPa]	∅ R <sub>m</sub> [MPa]	A [%]	∅ A [%]	Sample status
Sample 1	126	<b>143.5</b>	4.9	<b>4.8</b>	Without heattreatment
Sample 2	132		5.2		
Sample 3	129		5.0		
Sample 4	158		6.3		
Sample 5	149		6.0		
Sample 6	167		7.0		
Sample 7	227	<b>258.3</b>	5.4	<b>5.8</b>	After Heat treatment
Sample 8	228		5.4		
Sample 9	264		5.8		
Sample 10	266		5.9		
Sample 11	279		5.8		
Sample 11	286	6.2			

### Conclusions

During the experiment was analyzed casting alloy AlSi9CuMgNiMn produced by low-pressure casting technology. Experiment was focused on the exploration of microstructure and the impact of heat treatment on the mechanical properties of the investigated alloy.

The microstructure of the investigated alloy AlSi9CuMgNiMn was recognized by the presence of intermetallic phase  $\alpha$ -AlFeMnSi. This intermetallic phase in the microstructure was excreted in the form of extensive bone formations. As the it was recognized in the microstructure polycomponent intermetallic phases of type Al-Ni-Si-Cu-Fe-Mn.

The heat treatment was comprised of dissolution by heating, cooling in water and the subsequent artificial aging caused an increase in hardness of the investigated alloy by 90% (144.8 versus 76.3 HB<sub>10</sub> HB<sub>10</sub> in a thermally untreated state). The tensile strength was increased with heath treatment of 80% (258.3 MPa compared with 143.5 MPa in in a thermally untreated state) and ductility increased of 21% (5.8% vs. 4.8% in a thermally untreated state).

### Acknowledgement

*The article was supported by an internal student grant competition SGS 2015 UJEP.*

### Literature

1. Michna, Š., Lukáč, I., Louda, P., Očenášek a kol.: Aluminium materials and technologies from A to Z, Adin s.r.o., ISBN 978-80-89244-18-8 (2005).
2. Lukač, I., Michna, Š.: Colour contrast, structure and defects in aluminium and aluminium alloys, Cambridge International Science Publishing, ISBN 18-983-26-70-3 (2001).

3. CAIS, J., WEISS, V., SVOBODOVÁ, J.: Relation between Porosity and Mechanical Properties of Al-Si Alloys Produced by Low-Pressure Casting, Archives of Foundry Engineering, Vol. 14, Issue 2, 2014, ISSN 1897-3310
4. CAIS, J., V., SVOBODOVÁ, J, WEISS, V...: Influence of Modification and Heat Treatment on the Mechanical Properties of the AlSi7Mg0,3 Alloy, International Scientific Conference „Cluster -Casting- Future“ Świełcza 2014, s. 67-70, ISBN 978-83-63666-90-3

## **POLYMERS, COMPOSITES**

### **OPTIONS FOR REDUCTION OF CONTENT OF ZnO IN RUBBER COMPOUNDS**

**Božek M.**<sup>1</sup>, Švrček J.<sup>2</sup>, Olšovský M.<sup>3</sup>

<sup>1</sup>*Faculty of industry technologies, I. Krasu 491/30, 020 01 Puchov, Slovak Republic*

*e-mail: marian.bozek@gmail.com*

<sup>2</sup>*BOCHEMIE, a. s., Lidická 326, 735 95 Bohumín*

*e-mail: jiri.svrcek@bochemie.cz*

<sup>3</sup>*MSM Martin, s. r. o. Duklianska 60, 971 72 Nováky*

#### **Introduction**

The paper presents the investigation about the nano zinc oxides used in the rubber compounds. In recent years, due to the environmental and economic issues in relation to the amount of zinc in rubber products, is the tendency to minimize content of zinc. If we want to reduce the required amount of ZnO, we must increase the activity of zinc. Therefore, the availability of Zn<sup>2+</sup> ions should be maximized on the surface of the crystals. Some recommended options include the application of "active zinc oxide" or the use of so-called. "Nano zinc oxide" and use it in the system of chemical reaction between the accelerator, stearic acid and ZnO to addition to the rubber mixture. Several studies suggest the possibility of reducing ZnO without deterioration of the properties of vulcanizates [1-3].

The properties of vulcanized NR (including the mechanical properties and the properties of rubber compound after aging) were studied in work [4]. The results showed that highly dispersed nano-ZnO in the NR compound has a higher resistance to temperature, the degree of cross-linking and resistance to aging are better than the standard ZnO with 99.5% of ZnO in the compound under the same vulcanization conditions. 80% amount of nano-ZnO was mixed in the compound and the mechanical properties and resistance to atmospheric aging of NR were superior to admixture compared to the classic type of ZnO in the traditional formula. The reasons may be better dispersion of nano-ZnO and nano-ZnO is thus better receive the contact with the multiple bonds NR and the sulfur surface in rubber matrix to increase the efficiency of rubber vulcanization, physical and mechanical properties of vulcanizates prepared based on NR were increased too [4].

The regulation of the European Union (EU) leads to a reduction in the amount of materials used in tires with the growing interest in environmental. The researchers in [2] deal with the question of reduction of ZnO in the mixture. The ZnO nano-particle sizes of 30-40 nm and a surface of 25 - 50 m<sup>2</sup>.g<sup>-1</sup> was used instead of the conventional ZnO in a compound of NR/BR. The task was to reduce the content of zinc oxide in the compound. Used was only 20% by weight. of nano-ZnO in the conventional to standard ZnO. The results showed that the curing characteristics and the mechanical properties of vulcanizates were the same. The increase of specific surface of nano-ZnO results increased the number of cross-links. For curing characteristics and mechanical properties the effect of nano-ZnO was more pronounced in compounds filled with silica (SiO<sub>2</sub>). The NR/BR compound (with silica containing from 0.3 to 3 phr nano-ZnO) had better mechanical properties (modules 100, 300, tensile strength) compared to compounds containing 5 phr of classical ZnO. The optimal amount of nano-ZnO and stearic acid were 1 and 0.1 phr [2].

Study [5] is divided into two parts. The first part deals with the reduction and optimization of ZnO. The researchers selected two different rubbers to monitor the effectiveness - SBR and EPDM. The results show that the physical and mechanical properties can be preserved if the content of ZnO is 1 or 2 phr. The curing characteristics indicate that the nano-ZnO may reduce the content of ZnO in the compound. In the second part the researchers mixed the model mixtures and the observed the impact of ZnO during the various stages of vulcanization. They described two models (squalene and 2,3-dimethyl-2-butene), and as a vulcanization accelerator was used the benzothiazole sulfenamide. The results showed the impact of nano-ZnO during the various stages of vulcanization. The reducing of particle size of nano-ZnO had a positive impact on curing characteristics, especially in the beginning of vulcanization (at the onset of the vulcanization curve) [5].

#### **Results and discussion**

First we have prepared mixtures of nano - ZnO forms at a dosage of 100, 50, 25 and 12.5 % by weight of standard + 1 standard composition to compare the results and tested activating effect of nano - ZnO samples in the model compounds based on NR. The preparation of the model rubber compounds were made in a laboratory kneading machine BRABENDER Plastograph at 110 °C, the speed of rotation of the pinion was 50 turns/min and elaborated of 1 minute and embeded rubber vulcanization for 5 minutes.

In addition to the vulcanization activity were assessed by as indicative parameter influence on the strength properties of the cross-link density. Second the samples, which were evaluated how best were the curing parameters in the model mixtures we undergone comprehensive evaluation of a rubber compound that is normally used in the manufacture of tires. Real rubber mixtures were prepared for laboratory kneading machine plastograph BRABENDER for two-stage mixing. The first step consisted of rubber, fillers and other additives (except for the vulcanization system). We have been working at a temperature of 130 °C and the rotational speed of pinion 50 rev/min. First we elaborated rubber for 1 min left, then gradually were added carbon black and other ingredients and mixed for 5 min. First stage of the rubber mixture were left to stand for 24 hours and were mixed up vulcanization system - again in a kneading machine BRABENDER plastograph at 110 °C at a speed of rotation of the pinion 50 rev/min. We elaborated rubber for 1 min, and then we had 5 minutes left to incorporate vulcanization system. We compared vulcanization characteristics physical and mechanical properties, and cross-link density of these mixtures [6 - 10].

We compared 4 different samples of nanoforms ZnO to research the curing activity of nano-ZnO. Table I shows the characterization of these samples.

Table I  
Characteristics of samples of ZnO nanoforms

Sample	Specific surface BET [m <sup>2</sup> /g]	XRD phase	amorphous phase [%]	particle size [nm]	ZnO content [weight %]
1	114.2	100 %	18	6.0 ± 0.7	99.75
2	83.6	100 %	18	6.6 ± 0.9	99.95
3	104.6	100 %	18	6.8 ± 1.6	99.91
4	84.9	100 %	18	6.7 ± 2.3	99.95

We were given the task to try these 4 samples nanoforms ZnO in the model and the real composition based on NR in this series of measurements. Next, we tested the impact of the extension of the mixing time of 1 and 2 minutes in model compounds. We determined the vulcanizing activity, cross-link density and physical and mechanical properties of the compounds. We chose a commercial product labeled zinc oxide Zinc Oxide GoldenSeal RQ3 (manufacturer: Olawa Huta, Poland) as a standard sample. The sample was delivered directly to a rubber manufacturing plant, the specific surface area is 5-6 m<sup>2</sup>/g. Formulation and all procedures with stirring and determining were the same as the recipe of model and real compounds.

Table II  
Vulcanization characteristics of model compounds

Sample, dosage [%]	ML [dN.m]	MH [dN.m]	TS [min]	TC(90) [min]	RV [min <sup>-1</sup> ]	The shape of vulcanization curve
Standard	6.7	21.1	6.00	12.56	15.2439	slight reversion
1 - 12,5 %	6.9	18.2	6.01	10.36	22.9885	reversion
1 - 25 %	7.2	20.0	6.35	12.75	15.6250	reversion
1 - 50 %	7.3	21.2	5.58	13.28	12.9870	slight reversion
2 - 12,5 %	6.7	18.0	4.28	8.61	23.0946	reversion
2 - 25 %	6.9	19.7	4.85	10.73	17.0068	reversion
2 - 50 %	6.9	20.8	4.67	11.73	14.1643	slight reversion
3 - 12,5 %	6.8	18.5	4.96	9.12	24.0384	reversion
3 - 25 %	7.0	20.0	5.10	11.08	16.7224	reversion
3 - 50 %	7.2	21.1	4.50	11.93	13.4590	slight reversion
3 - 100 %	7.9	21.7	2.92	10.30	13.5501	slight reversion
4 - 12,5 %	7.0	18.5	4.75	8.99	23.5849	reversion
4 - 25 %	7.4	20.2	5.70	12.47	14.7710	reversion
4 - 50 %	7.4	21.5	5.53	13.30	12.8700	fixed curve

The values of minimum torque (ML) where we used nano-ZnO were the same (6-8 dN.m) in all mixtures and very approximate standard. This means that the reinforcing force is similar to classic ZnO. The values of the maximum torque (MH) are also comparable to a standard (18-22 dN.m). The nano-ZnO significantly not affects the viscosity from the aspect of the torque. The torque properties of rubber compounds should not be significantly different from the standard sample. All compounds showed a reverse in terms of the shape of the vulcanization curves except of the sample 4 at 50 % dosage of the composition. The vulcanization cross-link was not thick enough and over time the ties were regrouped. The optimum vulcanisation time was shortened in all samples, in particular for a sample 3 and a dose of 100 %. Coefficients of cure rate were increasing with decreasing amounts of nano-ZnO in compound. Samples with dosing of 12.5% in the mixture had the highest cure rate coefficients. This means that the dosage of 12.5 % of nano-ZnO in rubber compound was not suitable for vulcanization.

Then we tried to extend the period of mixing samples. Curing characteristics of these samples are reported in table III.

Table III  
Comparison of the effect of mixing time on curing characteristics of model mixtures

Sample, dosage [%]	ML [dN.m]	MH [dN.m]	TS [min]	TC(90) [min]	RV [min <sup>-1</sup> ]	The shape of vulcanization curve
Standard	6.7	21.1	6.00	12.56	15.2439	slight reversion
Standard + 1 min	5.9	22.6	4.25	9.70	18.3486	slight reversion
Standard + 2 min	6.01	22.1	3.08	8.16	19.6850	slight reversion
2 - 25 %	6.9	19.7	4.85	10.73	17.0068	reversion
2 - 25 % + 1 min	7.2	20.6	4.33	10.52	16.1551	reversion
2 - 25 % + 2 min	6.8	20.2	2.54	9.54	16.6667	reversion
2 - 50 %	6.9	20.8	4.67	11.73	14.1643	slight reversion
2 - 50 % + 1 min	7.8	22.3	3.98	11.78	12.8205	slight reversion
2 - 50 % + 2 min	7.2	21.7	4.00	11.47	13.3869	slight reversion
3 - 25 %	7.0	20.0	5.10	11.08	16.7224	reversion
3 - 25 % + 1 min	7.5	21.2	3.88	9.90	16.6113	reversion
3 - 25 % + 2 min	6.9	20.6	3.18	9.20	16.6113	reversion
3 - 50 %	7.2	21.1	4.50	11.93	13.4590	slight reversion
3 - 50 % + 1 min	7.2	21.6	3.65	10.99	13.6240	slight reversion
3 - 50 % + 2 min	6.9	21.7	3.25	10.58	13.6426	slight reversion

The measured values showed that the extension of the mixing time was not affect for the curing characteristics of these samples. The measured torques were almost identical. The time of beginning of vulcanization was slightly reduced, in particular in sample 2 – 25 % with extended mixing time of 2 min. The optimum vulcanization time of the standard sample decreased about 4,5 min with extension of stirring at 2 minutes. From this aspect the cure rate of this sample was increased. The shape of the vulcanization curves were observed equal reversed for all samples, with some slight reversal. This means that after reaching the maximum torque the sulfur bonds were ruptured.

We were subjected all samples to the determination of the cross-link density. The measured values are shown in table IV.

Table IV  
Cross-link density of model compounds

Sample Mixing time	Cross-link density [mol.cm <sup>-3</sup> ] . 10 <sup>-4</sup>			Sample Mixing time	Cross-link density [mol.cm <sup>-3</sup> ] . 10 <sup>-4</sup>		
	5 min	+ 1 min	+ 2 min		5 min	+ 1 min	+ 2 min
Standard	1.1327	1.1385	1.5525				
1 – 50 %	1.2735			3 - 50 %	1.3941	1.4738	1.4412
1 - 25 %	1.0241			3 – 25 %	1.0908	1.1115	1.2527
1 – 12.5 %	0.9884			3 – 12.5 %	0.9920		
2 - 50 %	1.3617	1.3211	1.2729	4 - 50 %	1.3223		
2 - 25 %	1.1339	1.0643	1.1449	4 - 25 %	1.1127		
2 – 12.5 %	0.8911			4 – 12.5 %	0.8113		

The results showed that the prolongation of mixing time of the samples had a different influence. The standard sample and the 3 – 25 % sample increased the number of generated cross-links. Conversely the extended mixing time had no significant effect on the cross-link density values of sample 2. The best results presented sample 3 with the highest number of cross-links formed after sulfur vulcanization.

We selected samples 1, 2 and 3 from the model compounds, which were suitable for the mixing of real compounds. Mixing procedure and the determination of the parameters of the vulcanization activity and cross-link density was identical with previous determinations. Next, we determined the physical and mechanical properties of real mixtures (tensile strength, elongation, Young's modulus 300, density). Vulcanization characteristics of real mixtures third series are recorded in table V.

Table V  
Vulcanization characteristics of real compounds

Sample, dosage [%]	ML [dN.m]	MH [dN.m]	TS [min]	TC(90) [min]	RV [min <sup>-1</sup> ]	The shape of vulcanization curve
Standard	9.2	42.5	4.43	9.84	18.4843	reversion
1 – 12.5 %	10.2	32.0	3.40	5.32	43.6681	reversion
1 - 25 %	10.0	39.1	5.38	9.89	19.4553	reversion
1 – 50 %	9.1	39.8	5.93	11.39	16.0514	reversion
1 – 100 %	10.6	44.0	6.11	13.12	12.5945	slight reversion
2 – 12.5 %	11.0	34.5	3.11	5.09	43.6681	reversion
2 – 25 %	10.7	38.5	5.19	9.38	20.8333	reversion
2 – 50 %	10.9	43.3	5.35	11.26	15.2905	reversion
2 – 100 %	11.3	45.0	5.89	12.68	13.3156	slight reversion
3 – 12.5 %	10.5	33.0	3.49	5.59	40.3226	reversion
3 – 25 %	10.2	37.8	5.30	9.48	21.0084	reversion
3 – 50 %	11.4	43.3	5.75	11.72	14.9925	reversion
3 – 100 %	11.0	44.6	6.10	12.80	13.3511	slight reversion

Determination of curing characteristics of real mixtures showed that the standard values were closest to the sample with 50 and 25 % dosage of mixed nano-ZnO. The samples with 100 % dosage were extended the period of the start of vulcanization; on the other hand the cure rate coefficients for these samples were significantly reduced. Conversely, the samples with a dose of 12.5 % of nano-ZnO in compounds were unsuitable, because the beginning of vulcanization was too early, optimal time of vulcanization was very short too.

Table VI  
Physico-mechanical of real compounds

Sample, dosage [%]	Tensile strength [MPa]	Elongation [%]	Young's modulus 300 [MPa]	Density [g.cm <sup>-3</sup> ]	Cross-link density .10 <sup>-4</sup> [mol.cm <sup>-3</sup> ]
Standard	29.66	469	18.30	1.101	1.9534
1 – 100 %	29.39	438	19.69	1.094	1.4042
1 – 50 %	29.12	426	20.02	1.088	2.1614
1 – 25 %	28.47	504	15.31	1.059	1.4883
1 – 12.5 %	24.23	502	13.34	1.081	2.0821
2 – 100 %	28.57	415	19.79	1.095	2.1427
2 – 50 %	26.91	404	19.35	1.086	1.9469
2 – 25 %	25.70	503	14.18	1.083	2.0509
2 – 12.5 %	23.29	494	12.45	1.079	1.8588
3 – 100 %	28.98	432	19.36	1.090	1.8202
3 – 50 %	28.66	443	18.53	1.085	2.0144
3 – 25 %	26.66	508	13.97	1.088	1.6567
3 – 12.5 %	22.03	482	11.94	1.085	1.4005

The results showed that the values of tensile strength of all the samples are very close to the standard. The best values reached sample 1 at 50 % dosage, but the other samples (1-25, 2-50 and 3-50 and 25 and 25) lagged only slightly. The values of elongation were approximately the same (with only minor variations) in all samples compared to the standard compound. The Young's modulus 300 values of all the samples with 100 and 50 % dose were approximately the same compared standard compound. The density and the cross-link density values were differed only minimally in all samples and it was negligible.

### Conclusion

The measured results of the model and real rubber compounds showed that the best parameters achieved sample 1, but the other samples lagged only slightly. These compounds reached the best values in model compounds. After testing in real rubber compounds of the three selected samples at a dosage of 100, 50 and 25 % by weight to the standard we can conclude that the dosage of 100 % of nano-ZnO was unreasonable compared to the standard compound. The same amount of nanoforms had a negative impact not only on vulcanization characteristics, but also on physical and mechanical properties too. The amount of 50 and 25 % of nano-ZnO was preferred from the aspect of curing parameters and the physical and mechanical properties. The values of density and cross-link density were comparable to the standard compound. All three samples (1, 2, and 3) generally fulfill the requirements, respectively these samples could be used in large scale.

### Acknowledgment

*This work was carried out with financial support from the state budget through the Ministry of Industry and Trade of Czech Republic (MPO FR-T14 / 364).*

### Literature

1. Thomas S. P. et al.: Journal of Applied Polymer Science 124, 3099 - 3107 (2012).
2. Il-Jin K. et al.: Journal of Applied Polymer Science 117, 1535 - 1543 (2010).
3. Mottaghi M. et al.: Journal of Elastomers & Plastics 44, 443 - 451 (2012).
4. Ling L. - Lan L.: Energy and Environment Materials (Book Series: Materials Science Forum), 650, 367-373, 2010.
5. Vatansever N. - Polat, S.: Materials and Design, 31, 1533–1539 (2010).
6. STN 62 1425: Kaučuky - príprava a vulkanizácia kaučukových zmesí, 1984.
7. STN 62 1415: Kaučuky a gumárenské zmesi. Stanovenie viskozity a navulkanizovania na viskozimetri Mooney, 1989.
8. ISO 37: Rubber, vulcanized or thermoplastic - Determination of tensile stress-strain properties, 2011.
9. ISO 48: Rubber, vulcanized or thermoplastic - Determination of hardness (hardness between 10 IRHD and 100 IRHD), 1999.
10. ISO 2781: Rubber, vulcanized or thermoplastic - Determination of density, 2008.

## THE EFFECT OF PURE BIOFUELS ON PHYSICAL AND MECHANICAL PROPERTIES OF FLUORORUBBER BLENDS

**Dubovský M.**<sup>1</sup>, Haninčík S.<sup>1</sup>, Olšovský M.<sup>2</sup>

<sup>1</sup>*Faculty of Industrial Technologies, I. Krasku 491/30, 020 01 Púchov, Slovakia*

<sup>2</sup>*MSM Martin, s. r. o. Duklianska 60, 972 71 Nováky, Slovakia*  
*dubovskymichal7@gmail.com*

Apprehensions relating to rapid exhaust of fossil fuels, environmental problems and strict laws referring to fossil fuels led to the interest improvement in biofuels as an alternative fuel in order to satisfy the increasing energy demand in the transport sector. Since conventional automotive fuel systems are adapted to petroleum fuels, their exchange for biofuels causes the properties deterioration of rubber blends which are used in aircraft industry nowadays [1]. This paper presents the overall review regarding to the influence of different types of pure fuels (fatty acid methyl ester FAME, bioethanol, ethanol E85 and aviation fuel JET A1) on physical, mechanical and morphological properties of the elastomers at different exposure conditions including temperature (laboratory temperature and 100 °C). The elevated temperature simulates actual operating conditions which occurs in internal combustion engines. At week intervals, the samples were pulled out of the solvents and thoroughly dried by filter paper and subsequently, the change of weight, hardness, mechanical properties and surface morphology were observed by optical microscopy. The measured results indicate that with increasing temperature, there is decrease in physical and mechanical properties of the examined rubber seals. The worst results were reached in the case of samples which were immersed into bioethanol and aviation fuel JET A1 at elevated temperature.

### Introduction

FKM elastomers are relatively often produced with fluorine content (it is between 64-70 wt. %). Even small differences in the fluorine content in FKM have a great influence on the rubber resistance to biofuels. From FKM introduction before more than half century, FKM is known as a high-performance rubber with an ability to withstand a wide range of aggressive solvents and fuels. Although the composition and application of this polymer is used for biofuel engines and this type of FKM is more resistance than NBR and curing system of this rubber is still "Achilles heel" in relation to the operating conditions. Nowadays, FKM blends are cured by ionic reactions (bisphenol) or free radical mechanism (peroxides). These two curing systems are usually activated by bivalent inorganic metal oxides or metal hydroxides, such as MgO and Ca(OH)<sub>2</sub> [2]. When FKM blends are exposed to biofuels, these oxides and hydroxides reacted with an allylic hydroperoxides what can lead to biofuels oxidative degradation. The final products of this reaction can have harmful effect on physical and mechanical properties of FKM. The above mentioned influence was studied by Thomas et al. [3], where samples were immersed in rapeseed biodiesel as well as their blends with 80 and 95 vol. % of diesel fuel (B5, B20, B100). When the samples were crosslinked by bisphenol and peroxides, the volume change was 45-65 vol. %. On the other hand, when the metal oxides were used as curing agents, the volume change was 4-6 vol. % after 3024 hours of exposure in biofuel. In the case of peroxide curing agent consisting of Ca(OH)<sub>2</sub>, there was the volume change 1.5 phr, the volume change was 5,19 % while in connection with dosage 3 phr it was 33 %. The decrease in hardness, tensile strength and elongation of FKM blends in biodiesel was increased with increasing content of metal oxides in the curing system. In other study [4], there was the evaluation of the crosslink mechanism effect on the performance of FKM blend, where samples were immersed in ethanol, butanol as well as their mixtures with diesel fuel. The composition of diesel fuel was: 50 % of isooctane and 50 % of toluene. FKM contained 66 wt. % of fluorine. The samples swelling volume (crosslink by peroxides) was higher in comparison with samples, which were cured by bisphenol after exposure in pure ethanol as well as its mixtures with diesel fuel. Similar tendency was observed for FKM samples, where hardness was decreased by action of bioalcohol fuels. Tensile strength and elongation for samples (FKM blends cured by peroxides) was decreased more in comparison with blends which were cured by bisphenol after exposure in biofuels.

### Results and Discussion

Rubber materials contain a high ratio of curing agents, excipients, various oils, stabilizers and fillers. It can lead to swelling and degradation of elastomer structure, i.e. curing additives diffuse to fuel and create chemical reaction between fuel and rubber [5]. In this paper, there is the evaluation of the long-term and short-term impact of biofuels on the behaviour of different elastomers. In the contact with medium, the degradation change in comparison with standard was observed. The discussion is divided into several sections and it deals with the structural and physical changes in rubber blends which are exposed different biofuels. The tested

samples were produced of fluororubber blend which is commonly used in internal combustion engines. The exact composition and material properties are “Know How” of producer. In this paper, there is the evaluation of the physical and mechanical properties changes of the samples (in the shape of double-sided blades according to the relevant ISO standard). These tested samples were exposed to four different fuels at various exposure conditions and change in weight (ISO 1817), change in hardness (ISO 48), tensile properties (ISO 37), crosslink density were evaluated according to the method [6] while the change of surface morphology was investigated by optical microscopy. Fuel identification and test conditions of the experiments are shown in table I. For each measurement, there three parallel samples were used. Considering the test, arithmetic average for a better results evaluation was performed.

Table I  
Test conditions

Test samples	Test conditions	
	Fuel type [%]	Temperature [°C]
0	Standard – without the effect of fuels and temperature	
1	100 % of FAME	23 ± 2
2	100 % of Ethanol E85	23 ± 2
3	100 % of Bioethanol	23 ± 2
4	100 % of Aviation fuel JET A1	23 ± 2
5	100 % of FAME	100 ± 2
6	100 % of aviation fuel JET A1	100 ± 2

#### Properties of rubber blends exposed to pure biofuels at laboratory temperature

FKM samples were immersed to pure biofuels at laboratory temperature. In the table II, there are the measurements results of weight and hardness changes of samples which were exposed to different fuels during 1500 hours. In fuel engines, hydroperoxides that are present in biofuels are decomposed into free radical products, especially in the presence of water, oxygen and metal ions. These substances are often present in commercial biodiesels. Free radicals bind hydrogen atom from an alkyl esters chains and these radicals form allylic radicals. Subsequently, allylic radicals form peroxide radicals by reaction with the molecular oxygen, and these peroxide radicals form allylic hydroperoxides by elimination of further hydrogen atom. After penetration of these hydroperoxides into the structure of rubber blends, carboxylic acid salts, metal halides and Lewis acids can be formed. These factors could cause the degradation of sealing materials in aviation transport. The weight change is in the range of 0-5 wt. % and it can be attributed to the high content of fluorine (64-70 wt. %) in rubber blends as well as to low extraction of some insoluble ingredients, such as stabilizers and plasticizers. The lowest degree of swelling and the lowest permeability (to 0.05 vol. %) was observed for samples which were exposed to aviation fuel JET A1. The highest degree of swelling was recognized for samples which were exposed to ethanol E85 (85 % of ethanol and 15 % of kerosene NATURAL 95) and these results are in good correspondence with foreign papers [8-9] which presented that the suitable fuel has to contain 10 % ratio of ethanol maximum in mixtures because solubility parameter is close to values of many rubbers. The immersion temperature was decisive factor for fuel diffusion through the polymer matrix during the sorption and desorption processes.

Table II  
Relative change of samples weight and hardness by the influence of different fuels at laboratory temperature

Influence of fuel in time [hours]	Relative change of weight [%]				Relative change of hardness [%]			
	1	2	3	4	1	2	3	4
168	0.42	1.50	0.55	0.04	-1.81	-1.39	2.72	5.30
336	0.11	1.86	0.97	-0.09	-2.27	-5.82	2.28	4.03
504	0.17	2.10	1.06	-0.09	0	-5.30	-0.46	3.16
672	0.20	2.55	1.06	-0.04	-1.81	-1.39	2.72	3.60
840	0.21	2.76	1.06	0	-1.81	-2.83	2.72	4.03
1008	0.20	3.17	1.20	0	-0.90	-2.83	2.72	3.60
1176	0.23	3.17	1.20	0	-1.13	-3.31	1.83	3.60
1500	0.25	4.54	1.39	0.04	-1.13	-4.30	0.46	4.20

For the estimation whether solvent will dissolve the given polymer, mathematical relation can be used and it was proposed by Flory and Huggins [9]. The solvent and soluble substances (in this case fuel and rubber) which have similar solubility parameters have a higher affinity for the solvent absorption in comparison with those which have different values. The total solubility parameters for mixtures of kerosene and ethanol are shown in figure 1 as a simplified way to show this effect. As it can be seen, the total solubility of mixture of kerosene and ethanol increases linearly with increasing ethanol content. At the concentration of ethanol from 0 to 15 vol. %, the fuel solubility parameter is close to the many rubber values and therefore it is the potential for a higher solubility in the fuel as well as polymer swelling and the fuel absorption into polymer. At the concentration of 15-49 vol. %, there is the maximum swelling of rubber blends in fuels. Bioethanol as hygroscopic fuel causes much more serious problems in comparison with the biodiesel from the aspect of the metals corrosion. Bioethanol in comparison with kerosene is electrically conductive. Moreover, bioethanol can be oxidized to acetic acid and it can be caused by pH decrease. This can lead to the deterioration of its functional and performance properties [9].

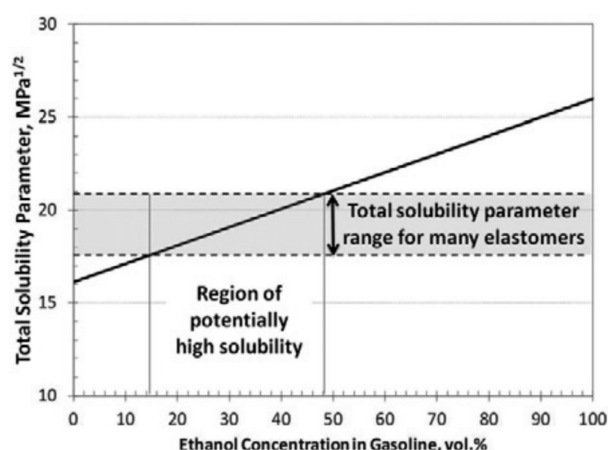


Figure 1. The solubility parameter for fuel mixtures of kerosene/ethanol [8]

After 1500 hours, the samples were pulled out, thoroughly dried by filter paper and investigated from the aspect of mechanical properties. The mechanical properties values of the samples after aging or after the influence of pure fuels were compared with samples which were not exposed to solvent and temperature. The modulus 300 value for the reference sample was 10.98 MPa. The elongation values were decreased after the fuel influence, therefore, there was not possible to calculate this variable for other samples. In relation to the crosslink density, there was not any significant values fluctuation and it can be attributed to FKM rubber. The changes of mechanical properties were in the range from 0 to -20 vol. %. The negative percentage changes showed a decrease of mechanical properties in comparison with reference sample. The worst results were observed for the samples which were exposed to the influence of bioethanol and aviation fuel JET A1. The swelling in FAME biofuel was relatively low in comparison with the above-mentioned fuels. The reduction of mechanical properties could be caused by several physical and chemical phenomena: permeability (solvent penetration based on controlled chemical activity by gradient), swelling (interaction between the solvent and polymer matrix) and extraction of soluble substances (the decrease of antioxidants, fillers, heat stabilizers, plasticizers due to the penetration of the solvent).

Table III

The change of samples mechanical properties in various fuels at laboratory temperature

Type samples	Tensile strength [MPa]	Elongation [%]	Hardness [IRHD]	Hardness [ShA]	Density [g.cm <sup>-3</sup> ]	Crosslink density [mol.cm <sup>-3</sup> ].10 <sup>-4</sup>
0	10.88	304.50	78.33	68.5	1.82	5.24
1	10.36	262.37	73.66	67.2	1.81	5.12
2	10.13	252.60	69.33	66.4	1.80	4.98
3	9.54	250.91	72	67.7	1.82	5.05
4	9.24	254.40	73.66	67.4	1.82	4.72

At the end of experiment, the samples were thoroughly dried, washed in acetone and prepared for investigation process relating to surface morphology change and it was performed by optical microscopy, i.e. "stereomicroscope". This is a trinocular stereo microscope which is used for observing materials surface changes. It was examined whether the fuel has the negative influence on the samples surfaces which are commonly used as rubber seals. The each sample was compared with standard (without the influence of fuel and temperature). Moreover the examination was connected with any deterioration of the samples surface structure under the influence of selected solvents after the specified time of immersion. As it is shown in figure 2, the used fuels have the significant influence of samples surface morphology. In relation to rubber seals, FAME biofuel represents "internal plasticizer". There is the increase of the macromolecules mobility in polymer matrix and thus there was the rupture of the material surface structure.

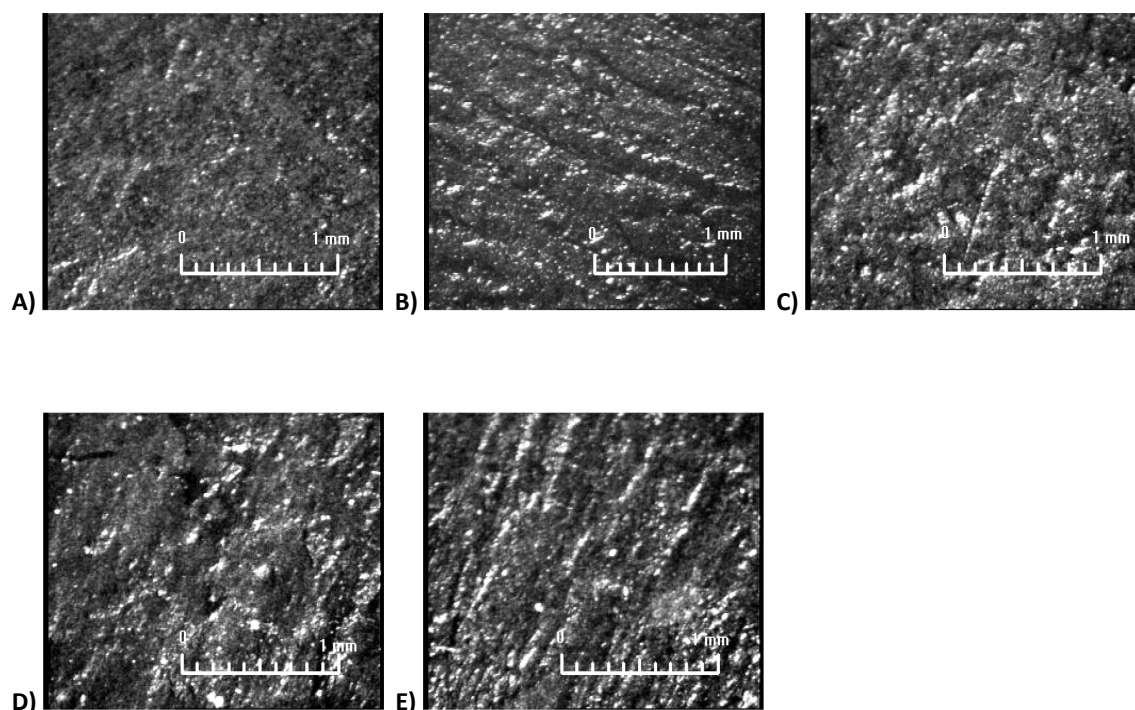


Figure 2. The change of samples surface morphology under the effect of various fuels at laboratory temperature during 1500 h.; A) Standard (without the influence of fuel and temperature); B) 100 % of FAME; C) 100 % of Ethanol E85; D) 100 % of Bioethanol; E) 100 % of aviation fuel JET A1

#### Properties of rubber blends exposed to pure biofuels at 100 °C

In other experiment, the samples were placed into testing vessel and poured by suitable solvent at 100 °C under the various time periods up to 400 hours. This temperature simulates actual operating conditions which are used in aviation engines.

Table IV

Relative change of samples weight and hardness by the influence of different fuels at 100 °C

Influence of fuel vs. time [hours]	Weight change (%)		Hardness change (%)	
	5	6	5	6
52	4.75	11.41	-10.39	-2.36
103	7.26	15.74	-8.78	-12.43
128	8.07	17.88	-9.30	-11.27
188	9.35	18.73	-10.39	-14.80
218	10.31	19.73	-8.25	-14.80
266	11.49	19.73	-5.68	-13.01
322	12.82	20.32	-7.21	-13.01
364	13.89	20.72	-7.20	-12.43
400	14.69	20.97	-8.25	-12.43

The samples were cut from cured sheets in the shape of double-sided blades and these samples were evaluated comprehensively from the aspect of physical and mechanical properties. At the end of experiments, the samples were pulled from the testing vessel and material surface structure change was observed on the basis of the solvents influence and elevated temperature. The samples were investigated from the aspect the change of weight, hardness after 168 hours during the overall time which was 400 hours. After the performance of the experiments, mechanical properties were investigated by ZWICK/ROELL Z2.5 with moving jaw 500 mm/min and then hardness and crosslink density were also evaluated. In the table IV, the obtained results of the measured weight and hardness change are shown and moreover the liquid absorbed by rubber and stabilization degree of swelling can be also seen in this table (the degree of swelling was at 2518-266 hours). This phenomenon can be observed for fuels, such as methylester of rapeseed oil (FAME) and aviation fuel (JET A1). It is caused by evaporation and washing out of some soluble ingredients (antidegradants, plasticizers) of rubber seals. On the basis of observation, the last reaction between rubber seals and used solvents led to the increase of the weight again and this change in weight could be caused either rubber swelling in liquid or chemical reaction of rubber with liquid. Absorption at 100 °C was significantly higher than at laboratory temperature and these results indicate that a high temperature significantly accelerates liquid diffusion into polymer matrix. It can be attributed to the decreasing viscosity of fuel at elevated temperature. Liquid penetration into material structure is easier and esters which have increased polarity have also some the influence on physical properties of cured rubber. The table V shows the results which are characteristic for mechanical properties of samples which were exposed to FAME biofuels and JET A1 aviation fuel at 100 °C. The reduction in tensile properties of the other samples is probably caused by plasticizing influence of FAME which acts as "internal plasticizer". The reduction of mechanical properties was in the range from 0 to -30 % and it is significantly higher than at laboratory temperature. During the curing process, the three-dimensional spatial grid is created and there is the occurrence of coupling bonds. To determine the swelling of our samples, 1 % solution of Dusantox (IPPD) in xylene was used for rubber stabilization while the chains of this rubber are significantly stressed during the swelling process and it can lead to the degradation [6]. The value of the crosslink density decreased and it was caused by damaged of coupling bonds in cured structure after the influence of solvent penetration into polymer matrix. The most notable change in tensile properties was observed for both biofuels, i.e. FAME biofuel and JET A1 aviation fuel which were exposed to higher temperature and it caused deterioration of rubber samples. Our experiments showed that the effect of biofuels as well as nowadays used fuels in aviation sector significantly deteriorate physical and mechanical properties of rubber seals.

Table V

The change of mechanical properties for samples exposed to various fuels at 100 °C

Samples type	Tensile strength [MPa]	Elongation [%]	Hardness [IRHD]	Hardness [ShA]	Density [g.cm <sup>-3</sup> ]	Crosslink density [mol.cm <sup>-3</sup> ].10 <sup>-4</sup>
0	10.88	304.50	78.3	68.5	1.82	5.24
1	9.02	230.45	67.7	61.8	1.65	4.12
2	9.45	270.52	64	57.4	1.67	4.37

In the picture 3, there is the photograph of seals samples which were exposed to the influence of two fuels at elevated temperature. As it can be seen, from the aspect the influence of increased temperature, there was the occurrence of extraction of non-rubbers additives (the highest extraction was observed for carbon black) into solvent as well as the solvent colour was changed and it could cause the properties changes of the given fuel as well as the destruction of the fuels themselves and risk of service safety.

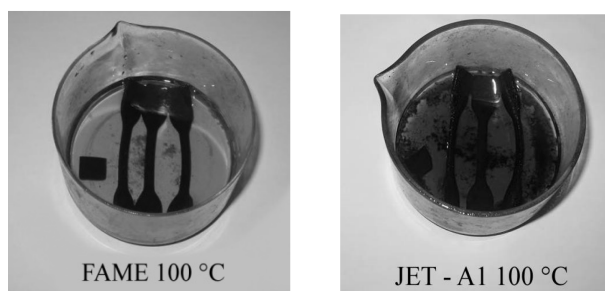


Figure 3. The photograph representing the destruction of seals exposed to various fuels at 100 °C

After 400 hours, the samples were pulled from tested vessel, thoroughly dried by filter paper, washed out by acetone to remove of excess oil from samples surface. From these prepared samples, the surface structure changes were observed under optical microscopy (figure 4). FAME biofuel caused the formation of cracks and holes and it can be attributed to high temperature which had substantially destructive effect during the operation process.

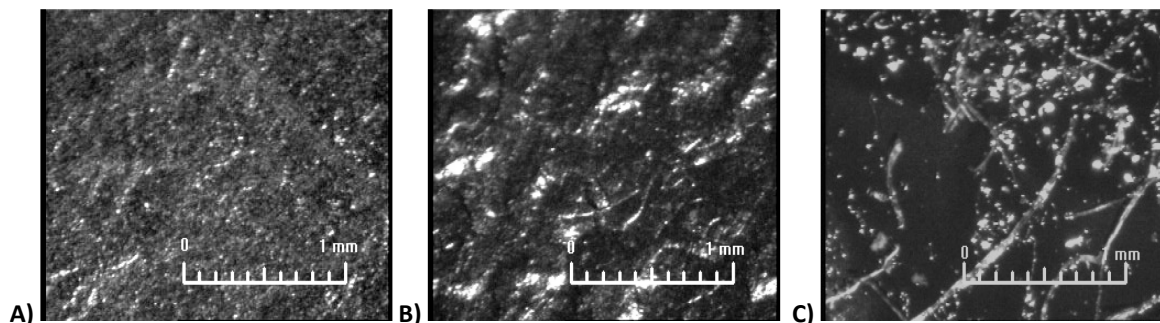


Figure 4. The change of samples surface morphology based on exposure to various fuels at 100 °C during 400 hours.; A) Standard (without the influence of fuel and temperature); B) 100 % of FAME; C) 100 % of Aviation fuel JET A1

### Conclusion

This paper discusses the influence of fatty acid methyl esters (biodiesel of rapeseed oil), ethanol E85, bioethanol and JET A1 aviation fuel on properties deterioration of FKM blends. The results presented in our paper are limited only by laboratory temperature and 100 °C. These temperatures simulate the actual operating conditions of aviation engines in simplified form. Relating to observation, there was the abnormal sorption kinetics of biodiesel in rubber, the gradual increase of sample weight under the influence of various fuels at 100 °C, the tensile test data and findings based on optical microscopy which shows the presence of “cracks”. The given summary above shows that biofuels strongly influence the interface between “polymer – carbon black” and it is caused by embrittlement and cavitations in high-swelling solvents.

### Literature

1. Singh P.N., Singh A.: *Prog. Energ. Combust.* 37, 74 (2011).
2. Baena L., Jaramillo F., Calderón J. A.: *Fuel* 95, 312 (2012).
3. Thomas W. E.: *SAE International Journal of Fuels and Lubricants* 2, 462 (2009).
4. Kass M., Theiss T., Janke C., Pawel S., Chapin J. T., Yang E., Boyce K.: *Sealing Technology* 2012, 7 (2012).
5. Akhlaghi S., Gedde W., Hedenquist M. S., Conde Brana M. T., Bellander M.: *Renew. Sust. Energ. Rev.* 43, 1238 (2015).
6. Olšovský M., Krmelová V., Máziková V., Šulcová J., Božek M., Dubovský M.: *Laboratory seminars of polymeric materials*, cap. 17, p. 38-42. University of Alexander Dubček, Trenčín 2013.
7. Akhlaghi S., Hedenquist M., Conde Brana M. T., Bellander M., Gedde W.: *Polym. Degrad. Stabil.* 111, 211 (2015).
8. Kass M. D., Pawel S., Theiss T.: OAK ridge national laboratory-technical memorandum ORNL/TM-2012/88 2012 (research report).
9. FINK J. K.: *Petroleum Engineer's guide to oil field chemicals and fluids*, p. 678 – 680, Elsevier, Amsterdam 2012.
10. Haseeb A. S. M. A., Masjuki H. H., Siang C. T., Fazal M. A.: *Renew. Energ.* 35(10), 2356 (2010).
11. Linhares N. F., Corrêa L. H., Khalil N. C., Leite M. A. C. M., Furtado G. R. C.: *Energy* 49, 102 (2013).

# INFLUENCE OF NITROGEN OXIDE ATMOSPHERE ESPECIALLY N<sub>2</sub>O<sub>4</sub> ON AGING PROCESSES OF POROUS LIGNOCELLULOSE MATERIALS

**Filipi M.**, Milichovský M., Mikala O.

*Department of Wood, Pulp and Paper, University of Pardubice, 532 10, Czech Republic,  
michaela.filipi@upce.cz (M. Filipi).*

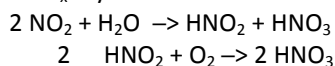
**Keywords:** N<sub>2</sub>O<sub>4</sub>, aging, porous materials

## Abstract

Exhibits deposited in museums or depositories, are exposed to surrounding environment, effecting material lifetime. Many factors are concerned, effecting the material degradation. Among the factors which cannot be influenced, there is material composition. Into second group, so called, external factors, belongs: temperature, relative humidity, solar radiation and atmospheric impurities. Due to continuously rising of nitrogen oxide content in atmosphere, it is inevitable to deal with questions, what are the impacts of this atmosphere on the cellulose materials, new and historical, deposited in archives and book depositories.

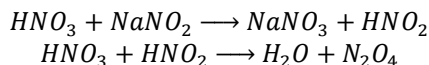
## Introduction

More than 90% of the total nitrogen oxides in the outside environment is being emitted in form of NO<sup>1</sup>. NO<sub>2</sub> forms relatively quickly by reaction of NO with ground ozone or radicals of <sup>\*</sup>HO<sub>2</sub> or <sup>\*</sup>RO<sub>2</sub><sup>1</sup>. NO and NO<sub>2</sub> are named as NO<sub>x</sub>. By a series of chemical reactions, NO<sub>x</sub> converts into HNO<sub>3</sub>/NO<sub>3</sub><sup>-1</sup>.



## Experiment

Preparation of N<sub>2</sub>O<sub>4</sub> atmosphere was used these chemical reactions



N<sub>2</sub>O<sub>4</sub> atmosphere was prepared by blending of 125 ml of concentrated nitric acid (63%), 10 ml of concentrated sulphuric acid (96%), and, 7 g of sodium nitrite, in wash bottle, immersed in ice bath. After that, the wash bottle was tempered 30 minutes at 20 °C. Gas was, by the means of vacuum pump drawn into apparatus.

## Preparation of samples

For the experiments two time intervals were chosen hours (1, 3, 5). For one exposure time, always two desiccators were used, one was exposed to day-light (marked A), the second was in dark (marked B). After the end of the exposure time, the atmosphere of nitrogen oxides was evacuated and the desiccators were washed by clean air by vacuum pump for period of 10 minutes. Then they were placed into air conditioned room and post-tested. The samples were weighed and the weight difference before and after the exposure was recorded.

## Materials

Hands of paperboard weighing 400±15 g.m<sup>-2</sup> prepared from following composition

- 1) Sa-L – bleached sulfate pulp hardwood Ružomberok, 25 SR
- 2) Sa-J – bleached sulfate softwood Štětí, 25 SR
- 3) Si – MgBi sulphite spruce bleached pulp (Biocel Paskov, 25 SR )
- 4) R.P. – hand-made paper (Velké Losiny, 60 % linters , 40 % z cultivated flax, 28 - 29 SR

## Methods

- Optical characteristic were measured by Elrepho from Lorentzen & Wettre.
- Compressive strength tested by TIRAtest 270025 (ISO 9895:2008).
- Stiffness were by TIRAtest 26005.
- Degree of polymerization cadoxen solutions with Ubbelohde viscometer.

## Parameters

A content of free glucuronic acid - is connected with a gradual chains scission of cellulose, which takes place during oxidation<sup>2</sup>.

$$c_{GA} = \frac{(A-B_{GA})}{k_{GA}} \quad (1)$$

$$x_{GA} = \frac{c_{GA}}{c_{vz}} \quad (2)$$

Present of destabilizing substances - they cause faster aging and loss of mechanical properties

$$DS_{PAGA} = (3,9555 \cdot x_{COOH} - 0,91752x_{GA}) / (100 - x_{GA}) \quad (3)$$

The degree of polydispersity - predicate about evenness of material oxidation. The closer the value to the zero is, the more homogeneous the material is. And vice versa. The higher it is, the more diverse the size of segments are<sup>2</sup>.

$$P_{DP} = \frac{(DP_H - DP)}{(DP_H - DP_{HL})} \quad (4)$$

The quality of substitution of COOH in PAGA (destabilizing substances) - indicates real percentage substitution of COOH groups in PAGA<sup>2</sup>.

$$DS_m = 1 \cdot x_{GA} + (1 - x_{GA}) \cdot DS_{PAGA} \quad (5)$$

$$x_{DS} = \frac{DS_{PAGA} \cdot 100}{DS_m} \quad (6)$$

## Results and Discussion

The weight change of the samples after exposure to nitrogen atmosphere, was effected at short-time exposure. At the samples exposed for one hour, the highest increase of weight by 5 % was recorded. The samples exposed to day-light, showed during the exposure higher rise of weight, than the samples placed in darkness.

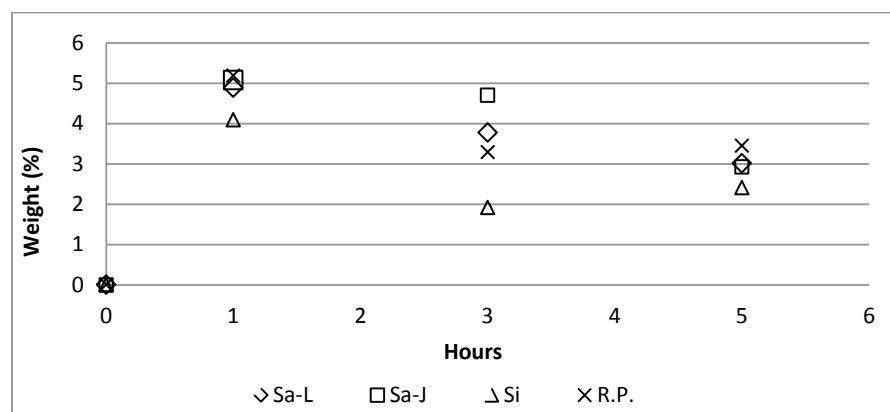


Figure 1. Change of weight versus hours exposed to day-light

## Evaluation of Optical Properties of the Samples

Degradation of the material did not show any yellowing or decrease in whiteness. On the contrary, the whiteness went up with Sa-L samples, only after an hour-exposure, by more than 4 % and the yellowness dropped from 9.19 % to less than 6 %. Similar increase in whiteness and decrease in yellowness achieved also samples Sa-J and Si. With samples of hand-made paper, the increase in whiteness was only up to 1 % and decrease in yellowness was also minimal. Increase in whiteness and decrease in yellowness for samples exposed to day-light was higher than for samples stored in darkness. The highest increase in the whiteness occurred only after one-hour exposure to nitrogen oxides, and, by extending of exposure time the rise of whiteness was only minimal. The most stable were optical properties of hand-made paper cellulose. Improvement of the optical properties was given by the content of nitric acid in the capillary system of the material. The samples were bleached by the nitric acid in the initial phase.

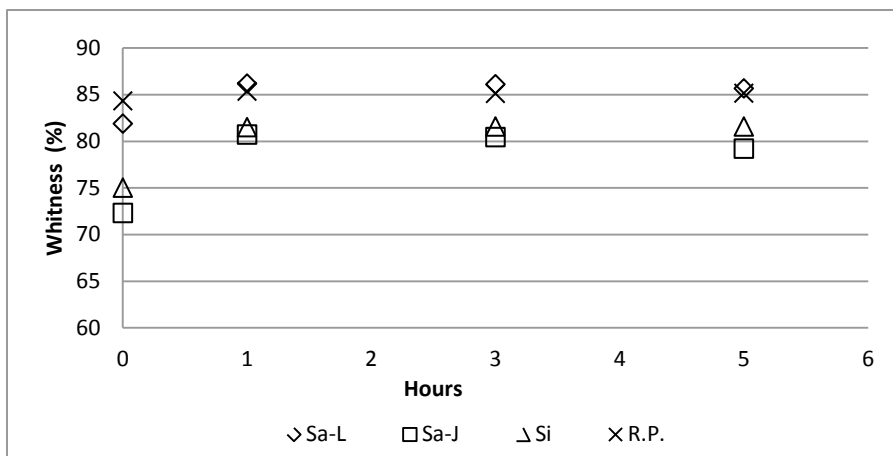


Figure 2. Whitensness versus hours exposed to day-light

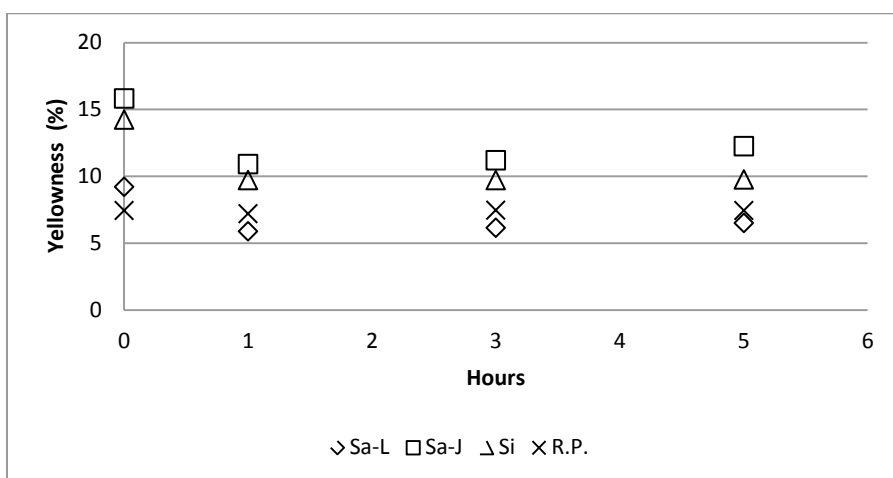


Figure 3. Yellowness versus hours exposed to day-light

### Tensile properties

Out of the computed values of compressive strength and index of compressive strength, the decrease was noticeable only after an hour exposure in nitrogen oxide atmosphere. Gradual drop in the index of compressive strength, which could be seen more with the samples Sa-L, Sa-J and R.P., than with Si samples, where was the decrease minimal, chiefly with the samples stored in darkness.

The samples showed an evident drop with the exposure time in the atmosphere. Only with the samples made of sulphite pulp, there was an obvious initial increase of unit stiffness after one day exposure, but after further days, the unit stiffness went down again. Elasticity index after a several-day exposures dropped significantly only with Sa-L samples, and that was with the samples exposed to a day-light and darkness too. Elasticity index drop occurred with the other samples only after several days. Rising of fragility with the exposure time was evident from the values of a relative drop of strength.

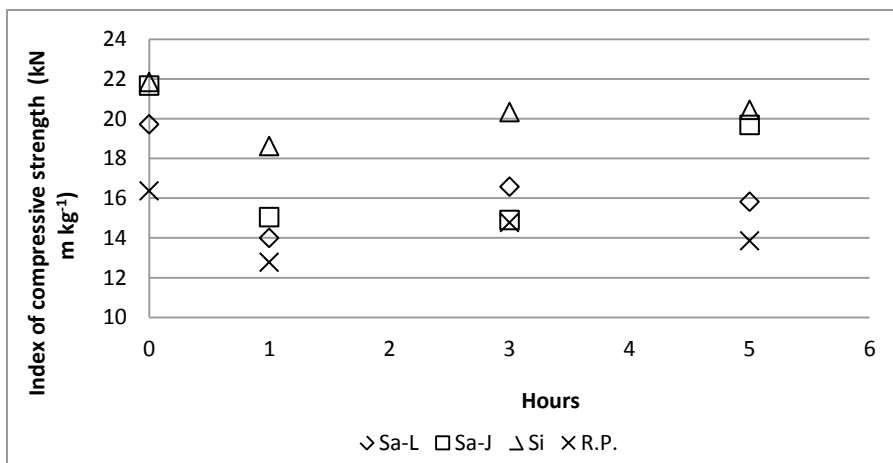


Figure 4. Index of compressive strength versus hours exposed to day-light

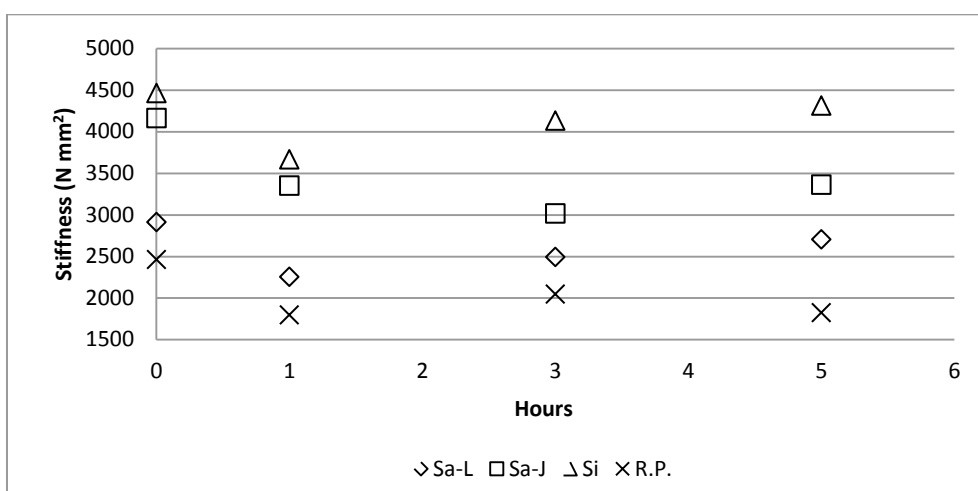


Figure 5. Stiffness<sub>T<sub>0</sub></sub> versus hours exposed to day-light

### Degree of polymerization

Drop in degree of polymerization with all the samples. Polymerization degree of the sulphite pulp, measured before exposure to nitrogen oxide atmosphere, was the highest ever (813.02), which led to better mechanical properties of this material after exposure, in comparison with other sample types. After a long-term exposure (29 days), the degree of polymerization of all the samples dropped to a value of 100 to 160.

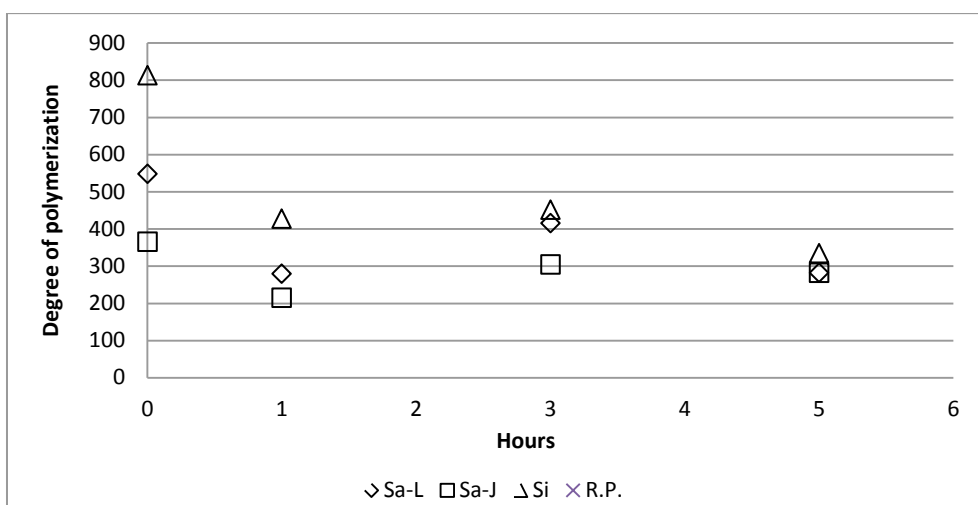


Figure 6. Degree of polymerization versus hours exposed to day-light

## Conclusion

### Oxidation of oxycelluloses

An important role in oxidizing gas plays the content of dioxide nitrogen (NO). Its high, as well as low, content, results in slowing down the reaction speed. By a method of ultraviolet spectrum of oxidizing cellulose, the authors Jermolenko, Kapuckij and Pavljučenko proved, that in the initial state of the reaction, unstable esters of nitrous acid form - those decay easily by the effect of humidity. See the scheme of cellulose oxidation by the nitrogen oxides<sup>3</sup>.

The nitride formed at the beginning of the reaction, decay to radical, which can stabilize itself by oxidation to carbonyl, then to carboxyl group by acting of N<sub>2</sub>O<sub>4</sub>.

Materials containing PAGA are of very versatile lifetime. During storage of those materials, decaying of PAGA takes place, which is manifested by colour change (yellowing to browning) and by loss of material properties. Further degrading products come up, which initialise a total destruction of the cellulose matter down to furan, its dimers and tetramers in case of hemicellulose. In the case of cellulose, it is a degrading product HMF (5-hydroxymethyl-2-furaldehyd)<sup>4</sup>.

### Degradation of celluloses

The first-phase products of the oxidation are various forms of polyanhydroglucuronic acid, collectively called oxycellulose. Schematic depiction of the chemical reactions, in the process of oxidation<sup>2</sup>.

Due to the presence of the nitrogen oxides, mainly N<sub>2</sub>O<sub>4</sub> and water, selective oxidation of cellulose to poly-β,D-1,4-anhydroglucuron acid (PAGA), takes place. Already at the beginning of the oxidation process, an enormous degradation of cellulose chain happens.

During the aging of paper, also cellulose degrades due to acidic hydrolysis. This cellulose is responsible for the stress and mechanical properties of lignocelluloses materials. Oxidation of the present lignin, caused in some cases yellowing of the samples. The reason for yellowing and poor whiteness stability of the pulps is attributed to the creation of the end groups of the hexenuronic acid (HexA) in hemicelluloses<sup>4,5</sup>.

## Acknowledgements

*The authors thank the ESF and state budget of Czech Republic for financial support. This research was supported by grants VEPACZ.1.07/2.3.00/20.0236.*

## Literature

1. Johansson A., Kolseth P., Lindqvist O.: Restaurator, 21, 117 (2000).
2. Milichovský M., Milichovská Sv.: J. Appl. Pol. Sc., 107, 2045 (2007).
3. Milichovský M., Sopuch T., Richter J.: J. Appl. Pol. Sc., 106, 3641 (2007).
4. Vuorinen T.; Fagerström P.; Buchert J.; Tenkanen M.; Teleman A.: J. Pulp and Paper Sc. 25, 155 (1999).
5. Łojewski T., Zięba K., Knapik A., Bagniak J., Lubańska A., Łojewska J.: Applied Physics A, 3, 809 (2010).

## ALTERNATIVE SOURCE OF NATURAL RUBBER - TKS AND GUAYULE

**Brejcha J., Herzigová L.**

*MITAS a.s., Švehlova 1900/3, 106 00, Praha 10  
jiri.brejcha@mitas-tyres.com*

Natural rubber is one of the most strategic materials for European industry and society. Every day all inhabitants use at least one product which contains natural rubber. Most of natural rubber, as well as generally rubber, is used for tyre production. Tyres are key object for transportation, agriculture, industry. Any movement is unimaginable without service of tyre. But tyres are not only one. Others are shoes, medical tools and materials, gloves and plenty of different rubber parts in all different services. For more than 100 years, natural rubber we obtain as results of coagulation of latex tapped from rubber trees – *Hevea Braziliensis*. This plant was originally planted in Amazon's area of Brazil. Later on was moved to South East Asia and West Africa region, where is currently majority of rubber plantations. But year consumption is increase every year, for 2015 – 2017 is estimated 3,0 - 3,3 % increase. Long distance, high transport cost, risk of non-deliveries is everyday task for purchasing managers of all rubber production plants. Also high volatility of price with year and period is not acceptable for a lot of not only EU based companies. Together with discovering of allergy reactions of 16% of people works as medical staff in Europe and 17% of post – surging complications we see big request to find alternative source for natural rubber. Other request is sustainable source which will be planted in area of use – Europe. Reason for this is use of staff from European countries as positive impact to solving global European problem.

The idea to find safe source of rubber is not new. More than 2000 of species content latex or 1,3 – polyisoprene. Two of them look very promising.

*Taraxacum koksaghyz* (TKS) well known as Kazakh or Russian dandelion. Homeland of his plant is located in Kazakhstan close to mountain area of Tan Šan near to boarder with Uzbekistan and China. This plant grows in moderate climate with long and hard winter similar to Nord and Central European climate. It would be positive point to plat dandelion in areas close to big part of European rubber industry and also in the area of not expensive land. Other very interesting task would be possibility of use of machinery in earth moving and harvesting operations which decrease dependency on labour costs. Last but not least jump over 7 years gap between start of planting and first latex production as we know from *Hevea* trees looks promising for this way of covering rubber demands.

Second plant related to alternative rubber source is Guayule (*Parthenium argentatum*). Original ecology of this desert shrub is northern part of Mexico or south of USA. Discovering of Guayule is dated to 1852. But real begging of first Guayule period is in begging of previous century. Within 1930's big boom of this plant was coming. Next big interests of alternative rubber source is related to 2nd World war. But very early after the end of war were all projects stopped again. Same as Dandelion case in Soviet Union. In time of oil crises in 1970's renaissance of Guayule is updated. 1990's and increase of allergy and strategic task came to priority and Guayule is one of research tasks again.

Number of different research groups established different projects. Two of them look very promising. EUNARS (ETRMA – European Tyre and Rubber Manufacture Association) is one of stakeholders concern about Guayule. Second, DRIVE4 EU, members of consortium – Wageningen UR, KeyGene, Rusthoeve, Apollo Tyres, QEW Engineered Rubber (all Neatherland), Institute of Botany and MITAS (Czech republic), InExCB (Kazakhstan), ILVO (Belgium), Tereos Syral (France), Netzsch and GEA Westfalia (Germany), Joanneum Research (Austria) is focused on Kazakhs or Russian dandelion *Taraxacum koksaghyz* (TKS). All of this subjects are leading players in different fields of complete chain, from breeding, throw agronomy, rubber production to final users – tyre and GRG manufactures. Goal of projects is establishing of supply chain of natural rubber without 100% dependency on tropic areas and production of European products (e. g. agricultural tyres) from sustainable European raw materials. From rubber point of view as a side effect, but also very important we can find TKS as source of inulin, important saccharide for food industry as well as potential source for bio based (furan) polymers and chemicals.

### Literature

1. Kappen F.: Natural rubber alternatives, 2<sup>nd</sup> World Elastomer Summit (March 2015).
2. Simmons R.: Natural rubber market: outlook and challenges, 2<sup>nd</sup> World Elastomer Summit (March 2015).

## SIMULATION OF MECHANICAL PROPERTIES OF HETEROPHASE POLYPROPYLENE COPOLYMER

**Grůza J.**, Kratochvíla K.

*POLYMER INSTITUTE BRNO, spol. s r.o., Tkalcovská 36/2, Brno, Czech Republic*

*Jan.Gruza@polymer.cz*

### Introduction

Industrial production of impact polypropylene copolymers is relatively complex manufacturing process, which is rather demanding from the process control point of view<sup>1,2</sup>. Already small change in polymerization conditions, as for example the change in polymerization temperature, in hydrogen and external donor concentration, in ethylene content in copolymer or its ratio in propylene/ethylene in rubber phase, can cause unexpected changes in structure, composition and properties of the resulting copolymer<sup>3-5</sup>. Particularly complicated is the case, when the changes are combined, e.g. in the case of simultaneous change of several polymerization conditions at the same time. The newly developed copolymerization model enables simulation of such various polymerization parameters and prediction of the resulting mechanical properties of heterophase copolymers.

In the first part of the study, the influence of homopolymerization conditions (polymerization temperature, hydrogen and external donor concentration) was investigated on properties of polypropylene homomatrix, which is created in the first part of the copolymerization run. Subsequently, in the second part of the study, the influence of copolymerization parameters (the molecular weight of homomatrix, the content, molecular weight and composition of rubber phase) was investigated on the whole heterophase (homomatrix + rubber) copolymer mechanical properties.

### Experimental

Polymerization conditions and corresponding polymer properties create the data set, which is essential for the parametrization of the copolymerization model.

Polymerization experiments comprising the necessary range of polymerization conditions and corresponding polymer properties of heterophase copolymer materials were performed using the high-yield Ziegler-Natta catalyst system L-01/DIBDMS/TEA in 2-L (homomatrix synthesis) and in 50-L (heterophase copolymer synthesis) reactors and in industrial gas-phase PP plant of Unipetrol RPA (heterophase copolymer production) in gas-phase at the polymerization pressure of 2.2 MPa at the following conditions:

1. The influence of particular homopolymerization conditions was simulated in the following ranges:
  - Al/Si molar ratio: 2 - 10 mol/mol,
  - Polymerization temperature T: 60 - 90°C,
  - Hydrogen concentration H<sub>2</sub>/C<sub>3</sub>: 3.5 - 60 mmol/mol.

For the purpose of simulation we have used the polypropylene homomatrix materials, which cover the specified ranges, as laboratory samples synthesized in bench 2-L reactor (55 samples).

2. The influence of particular copolymerization conditions was simulated in the following ranges:
  - MFR1: 0.5 - 100 g/10 min (homomatrix),
  - MFR2: 0.3 - 30 g/10 min (heterophase copolymer),
  - RC: 12 - 24 wt. %,
  - RCC2: 40 - 60 wt. %.

For the purpose of simulation we have used the heterophase copolymer materials, which cover mentioned ranges, partly as laboratory samples prepared in bench 50-L reactor (50 samples) and partly as commercial Innovene™ PP process samples from the industrial gas-phase PP plant of Unipetrol RPA, Litvinov (49 samples).

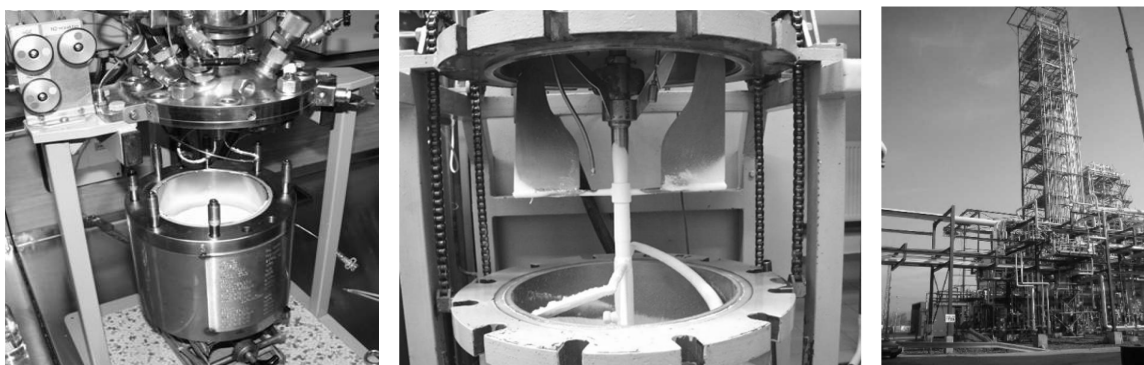


Figure 1: The polymer materials necessary for copolymerization model parametrization were synthesized under specified polymerization conditions in 2-L reactor (left side), in 50-L reactor (middle), and in industrial gas-phase PP plant of Unipetrol RPA (right side).

## Results and discussion

### Copolymerization model - homomatrix properties simulation

Mechanical properties of heterophase copolymers must particularly comply with the requirements related to the balanced combination of stiffness and toughness.

Concerning the stiffness of heterophase copolymer, it is mainly represented by the properties of its homomatrix, particularly by its stereospecificity controlled mainly by the Al/Si ratio. The lower the Al/Si ratio, the higher the stereospecificity and stiffness are as it is apparent from the Figure 2 (Al/Si - H<sub>2</sub>/C<sub>3</sub> - X.S. dependency). However, the decrease in this ratio is also manifested by some additional effects - decrease in polymerization activity as it is apparent from the Figure 2 (Al/Si - T - Activity dependency) and decrease in melt flow rate of homomatrix homopolymer.

Concerning the melt flow rate of resulting heterophase copolymer, it is influenced (increased) synergistically with the increase in polymerization temperature and the increase in hydrogen concentration, as it is apparent from the Figure 2 (H<sub>2</sub>/C<sub>3</sub> - T - MFR 21N dependency). The same way acts the increase in Al/Si ratio.

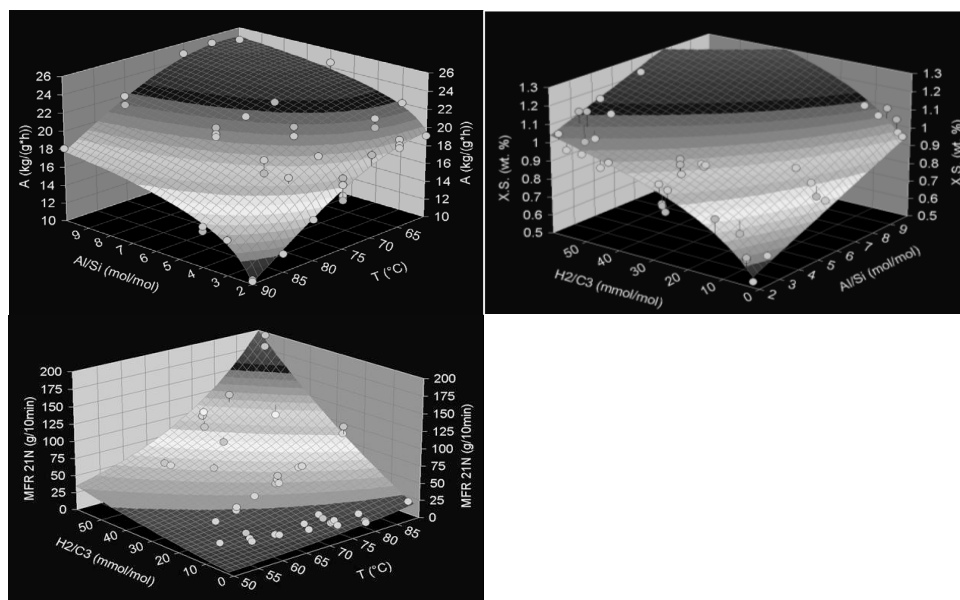


Figure 2: Fundamental correlations of polymerization activity and homomatrix polymer properties with propylene homopolymerization conditions for the high-yield Ziegler-Natta catalyst system L-01/DIBDMS/TEA.

Based on these expectations, all the three above mentioned parameters (co-catalyst / external donor molar ratio Al/Si, polymerization temperature T, and hydrogen / propylene molar ratio H<sub>2</sub>/C<sub>3</sub>) had to be taken into consideration in the newly developed copolymerization model.

The model was created based on the multidimensional regression analysis using the SigmaPlot 2000 software. This multidimensional regression analysis of the influence of the three above mentioned parameters (Al/Si ratio, polymerization temperature T, and H<sub>2</sub>/C<sub>3</sub> ratio) on polymerization activity (A), amorphous portion of

homomatrix homopolymer (X.S.) and melt flow rate of polypropylene homomatrix (MFR 21N) has resulted in the model, represented by three equations: Equation 1 defines the polymerization activity (A), Equation 2 defines the amorphous portion of homomatrix polypropylene (X.S.) and Equation 3 defines the melt flow rate of homomatrix polypropylene (MFR 21N).

$$A = a + \frac{b}{(Al/Si)} + c * (T)^3 + d * (H2/C3) + e * (H2/C3)^2, \quad (1)$$

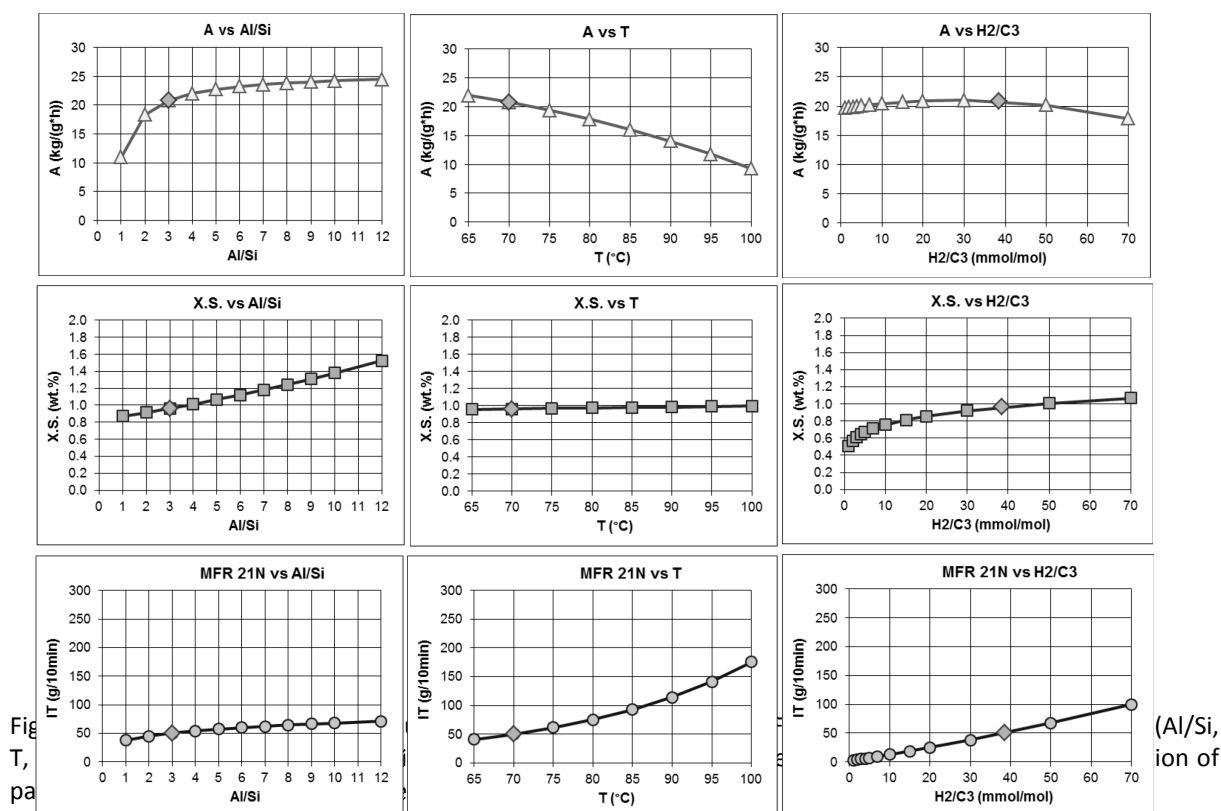
where a, b, c, d, e are best-fitted correlation coefficients

$$X.S. = 2.718^{(a+b*(Al/Si)+c*(T)+d*\ln(H2/C3))}, \quad (2)$$

where a, b, c, d are best-fitted correlation coefficients

$$MFR\ 21N = 2.718^{(a + b*\ln(Al/Si) + c*(T) + d*(T)^2 + e*(T)^3 + f*\ln(H2/C3) + g*(\ln(H2/C3))^2)}, \quad (3)$$

where a, b, c, d, e, f, g are best-fitted correlation coefficients



Model input			Model output		
Al/Si ratio	T °C	H2/C3 mmol/mol	A kg/(g*hr)	X.S. wt.%	MFR 21N g/10min
3	70	38.5	20.8	0.96	50.0

Table I: The input variables values and corresponding output parameters of the homopolymerization part of the copolymerization model. The data are depicted in trend graphs in figure 3 as diamond points.

Based on the input 3 variables the resulting model enables to calculate the resulting polymerization activity A, the portion of amorphous polypropylene X.S. and the melt flow rate MFR 21N of the resulting polymer. The dependencies of particular parameters (A, X.S., MFR 21N) on the particular variables (Al/Si, T, H2/C3) are depicted in 9 correlation graphs in Figure 3. These correlations can be summarized as follows:

- The decrease of external donor concentration indicated by **Al/Si increase** (at constant Al concentration) brings about a significant increase in polymerization activity (A), an increase in amorphous PP content (X.S.) and an increase in homomatrix polypropylene melt flow rate (MFR 21N).
- The **increase in polymerization temperature T** causes a significant decrease in polymerization activity (A), practically no change in the content of amorphous polypropylene (X.S.), and a significant increase in homomatrix polypropylene melt flow rate (MFR 21N).

- The **increase in hydrogen / propylene molar ratio H<sub>2</sub>/C<sub>3</sub>** brings about the polymerization activity (A) maximum at the range 20-30 mmol/mol, the content of amorphous polypropylene (X.S.) slightly increases due to the extraction of short polymer chains and the homomatrix polypropylene melt flow rate (MFR 21N) significantly increases.

Based on the documented knowledge, the newly developed homopolymerization part of copolymerization model can be utilized in the following ways:

- Prediction of polymerization activity and polymer properties under specified polymerization conditions.
- Construction of polymerization activity and polymer properties correlations within specified ranges of polymerization conditions (one or two variables – 2D or 3D correlations).
- Searching for optimum polymerization conditions related with polymer properties of requested polypropylene homomatrix.

*Copolymerization model - simulation of mechanical properties of heterophase copolymer*

Toughness of heterophase copolymer is mainly influenced by the rubber phase, particularly by ethylene-propylene rubber (RC) domains content in heterophase copolymer, and ethylene content in the rubber phase (RCC2). Generally, the higher the rubber content, the higher the toughness. But the increase in this parameter is manifested also by some additional effects - e.g. by decrease of the heterophase copolymer stiffness. The melt flow rate of homomatrix homopolymer (MFR1) and resulting heterophase copolymer (MFR2) have a minor effect concerning the mechanical properties of heterophase copolymer.

This part of the model was again created based on the multidimensional regression analysis using the SigmaPlot 2000 software. This multidimensional regression analysis of the impact of four above mentioned parameters (MFR1, MFR2, RC, RCC2) on the heterophase copolymer stiffness and toughness has led to the model, represented by Equation 4, specifying the heterophase copolymer stiffness (FM), and by Equation 5, specifying the heterophase copolymer toughness (Charpy).

$$FM = a + b * \ln(MFR1) + c * \ln(MFR2) + d * (RCC2) + e * (RCC2)^2 + f * (RC) + g * (RC)^2, \quad (4)$$

where a, b, c, d, e, f, g are best-fitted correlation coefficients

$$Charpy = a + b * \ln(MFR1) + c * \ln(MFR2) + d * (RCC2) + e * (RCC2)^2 + f * (RC) + g * (RC)^2, \quad (5)$$

where a, b, c, d, e, f, g are best-fitted correlation coefficients

Based on the input of these 4 variables the resulting copolymerization model enables to calculate the stiffness and the toughness of resulting heterophase copolymer. The dependencies of the particular parameters (stiffness and toughness) on the particular variables (RC, RCC2) are depicted in three-dimensional graphs in Figure 4. These correlations can be summarized as follows:

- The **increase in RC content** causes a significant decrease in stiffness (FM) and a significant increase in toughness (Charpy impact resistance) of the heterophase copolymer.
- The **increase in RCC2 concentration of ethylene in EPR rubber phase** brings about the maximum in stiffness (FM) in the range 52 - 54 wt. % and a slight decrease in toughness of the heterophase copolymer.

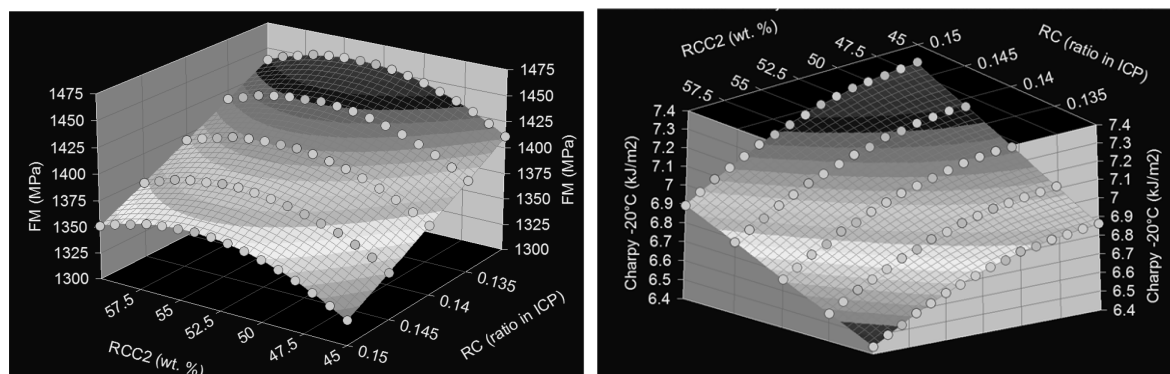


Figure 4: Dependencies of heterophase copolymer mechanical properties (stiffness - FM and toughness - Charpy) on copolymer composition (RC and RCC2).

Input of Copolymerization model				Output of Copolymerization model	
MFR1	MFR2	RC	RCC2	FM (23°C)	Charpy (-20°C)
g/10min	g/10min	wt. %	wt. %	MPa	kJ/m2
<b>0.8</b>	<b>0.4</b>	<b>15.0</b>	<b>50</b>	<b>1358</b>	<b>7.3</b>

Table II: Input variables values and corresponding output parameters of the copolymerization model.

The developed copolymerization model can be used in following ways:

- For the on-line prediction of mechanical properties during the simulation of particular copolymer grade production - based on the current process variables input (MFR1, MFR2, RC content, RCC2).
- For finding polymerization conditions leading to the synthesis of new copolymer grades with a requested combination of stiffness/toughness properties.

### Conclusion

The copolymerization model enables in its homopolymerization part the simulation of production rate and structure and properties of the related homomatrix material, such as the portion of amorphous chains in polypropylene (X.S.) and melt flow rate of resulting polypropylene (MFR 21N). If we further take into account the composition of the heterophase copolymer (represented by content of ethylene-propylene rubber and its composition) and the molecular weights of homomatrix polypropylene and the whole heterophase copolymer (represented by their particular MFR's), we can finally simulate the mechanical properties (stiffness and toughness) of the resulting heterophase copolymer.

The newly developed copolymerization model can be utilized in 2 principal ways, as a tool for an *on-line prediction of mechanical properties during the particular copolymer grade production*, and as a tool for the *determination of polymerization conditions leading to the synthesis of completely new copolymer grades with a convenient combination of stiffness/toughness properties*.

### Abbreviations

A - polymerization activity, kg/(g\*h)

Al/Si - co-catalyst/external donor ratio, mol/mol

C2 - ethylene

C3 - propylene

DIBDMS - diisobutyldimethoxysilane, external donor

FM - flexural modulus at 23°C, stiffness, MPa, ISO 178

H2 - hydrogen

H2/C3 - hydrogen / propylene ratio in polymerization, mmol/mol

Charpy - notched Charpy impact at -20°C, toughness, kJ/m<sup>2</sup>, ISO 179

MFR - melt flow rate of polypropylene homopolymer, g/10 min, ISO 1133

MFR1 - melt flow rate of homomatrix homopolymer in heterophase copolymer, g/10 min, ISO 1133

MFR2 - melt flow rate of heterophase copolymer, g/10 min, ISO 1133

RC - ethylene-propylene rubber phase content in heterophase copolymer, wt. %

RCC2 - ethylene content in ethylene-propylene rubber phase in heterophase copolymer, wt. %

T - polymerization temperature, °C

TEA - triethylaluminum, co-catalyst

X.S. - amorphous portion in polypropylene (xylene solubles at 23°C), wt. %, ISO 16152

### Acknowledgments

This work was financially supported by Ministry of Industry and Trade as project FR-TI1/140.

### Literature

1. Kiparissides K.: J. Process Control 16, 205 (2006).
2. Qin S. J., Badgwell T. A.: Control Engineering Practice 11, 733 (2003).
3. Zhang Y.-Q., Fan Z.-Q., Feng L.-X.: J. Appl. Polym. Sci. 84, 445 (2002).
4. Fu Z., Dong Q., Li N., Fan Z., Xu J.: J. Appl. Polym. Sci. 101, 2136 (2006).
5. Fan Z., Deng J., Zuo Y.-M., Fu Z.-S.: J. Appl. Polym. Sci. 102, 2481 (2006).

## RHEOLOGICAL BEHAVIOUR OF PROPYLENE COPOLYMERS AND TERPOLYMERS

**Balgová V.**, Sadílek J.

*Polymer Institute Brno, Tkalcovská 36/2, Brno 656 49, Czech Republic  
balgova@polymer.cz*

### Introduction

Rheology is very useful technique enabling to study polymer composition and its structure<sup>1,2</sup>. Within the scope of this project the impacts of polymerization conditions and effect of presence of various co-monomers in polypropylene matrix on the structure a copolymer composition were studied. For this purpose propylene copolymers with ethylene, 1-butene, 1-hexene and propylene-ethylene-butene and propylene-ethylene-hexene terpolymers were prepared. Besides, comparison between one-step and two-step polymerization procedure was evaluated. Rheological measurement in oscillatory mode gave us information about polydispersity index and samples were compared from the view of average molecular weight, presence of high molecular weight fraction, molecular weight distribution, structural strength of the melt and melt elasticity<sup>3,4</sup>. Consequently, the correlation among the copolymer and terpolymer structure and mechanical properties and fracture behaviour were explored<sup>5</sup>.

### Experimental

Ethylene (butene) - propylene do-polymerization

Two types of the experiments were performed. Monomodal (one step) polymerization with constant gas phase composition during the whole experiments was governed at temperature 75 °C and pressure 2.2 MPa. Catalyst Z-7S was used in combination with diisopropyl(dimethoxy)silane (DIPDSM) as an external donor and co-catalyst triethyl aluminum (TEA). External donor and co-catalyst were dosed at 40 °C. Polymerization was initiated by catalyst injection at 45 °C then within two minutes polymerization temperature was reached. Two-step (bimodal) synthesis procedure was constituted of two different steps. As the first the copolymerization step proceeded. Ethylene (butene) - propylene copolymerization occurred in the hydrogen absence and the polymerisation was led to the exact polymer yield. This fraction can be denoted as ultra-high molecular weight fraction (UHMW-RCP). Degassing of the reactor followed and new propylene monomer and hydrogen were dosed for the second step, thus the following polymerization was conducted as propylene homopolymerization. In a consequence of hydrogen presence polypropylene homopolymer was composed of the middle-low molecular weight macromolecules. Content of UHMW-RCP component ranged from 20 to 50 wt. %. Polymerization conditions in both steps were chosen in order to obtain statistical copolymer with the melt flow rate in the range from 0.1 to 0.4 g/10min and total ethylene content in the range of 2 – 5 wt. %.

Ethylene-butene (hexene)-propylene ter-polymerization

The polymerization experiments were performed in two-step mode in 2L reactor at temperature 75 °C and pressure 2.2 MPa with continuous dosage of propylene, ethylene and hydrogen. Catalyst Z-7S was used in combination with diisopropyl(dimethoxy)silane (DIPDSM) as an external donor and co-catalyst triethyl aluminum (TEA). External donor and co-catalyst were dosed at 40 °C. Calculated amount of 1-butene or hexene was dosed at the beginning of the experiment. The polymerization was initiated by the catalyst injection at 45 °C then within two minutes polymerization temperature was reached. During the synthesis constant ratio of C<sub>2</sub>/C<sub>3</sub> was assured by continuous dosage of the individual component. When determined amount of the terpolymer was obtained, degassing of the reactor was performed and again pressurized with propylene monomer. Terpolymerization step was followed by propylene homopolymerization with hydrogen presence contrary to the first step where hydrogen was absent. The polymerization was terminated when required weight ratio of two components was achieved.

Extrusion

Prior to the granulation polymer powder was stabilized with 0.2 wt. % of Irganox B225 and homogenized in mixer. Polymer samples were processed via extrusion at 220 °C, 100 rpm, BRABENDER L/D=30. D=19 mm.

<sup>13</sup>C-NMR analysis

NMR analyses were performed on NMR spectrometer Bruker DRX 500. 210 mg copolymer sample is weighed into the NMR cuvette of 10 mm diameter. The solution of 0.4 cm<sup>3</sup> benzene-D<sub>6</sub> and 1.7 cm<sup>3</sup> 1,2,4-trichlorobenzene is added. The sample is dissolved under nitrogen atmosphere at 130 °C for ca. 8 h.

Measurement parameters were following: Temperature 120-125 °C, pulse angle 77 °, pulse interval 15 s. Number of accumulations was set so as to reach signal/noise ratio  $S/N > 500$ . Spectrum was calibrated on the Sdd peak. Maximum LB is 1 Hz. Spectra were measured with a minimized cuvette rotation. Waltz type decoupling was used.

#### Rheological measurement

Rheological behaviour was studied with rotational rheometer Bohlin Gemini II with plate-plate geometry for characterization of viscoelastic properties. Sample used for measurement was in the form of pressed sheet about 2 mm thick. Measurement was performed at 200 °C with 0.5 % deformation in the oscillation range 0.0499 – 100 rad/s.

#### Mechanical properties

Tensile and flexural properties were measured with the use of INSTRON 4466. Notched Charpy impact strength test were performed on ZWICK HIT25T instrument.

### Results and discussion

Mechanical properties and rheological behaviour of ethylene-propylene copolymers

Series of the samples with different ethylene content was prepared via bimodal synthesis procedure and the results were compared with one-step statistical copolymer. Rheological analysis was performed with the view to obtain information about the polymer structure such as i) average molecular weight, ii) molecular weight distribution, iii) presence of ultra-high molecular weight fraction.

Our two-step material exhibited dominant elastic behaviour in the wide frequency range. On the base of the result depicted on Figure 1A can be said that two-step synthesis procedure led to the material with wider molecular weight distribution and higher average molecular weight as the crossing point of the elastic and viscous modulus  $G' = G''$  is significantly shifted to the lower frequency and lower  $G'$  - values. The presence of ultra-high molecular weight fraction is clear from the elastic modulus curve that lead up to very low frequencies. Bimodal material exhibited dominant elastic behaviour in the wider frequency range contrary to monomodal samples. On the Figure 1B the impact of the ethylene content on viscoelasticity is shown. According to expectation melt elasticity increased with increasing ethylene content. Polydispersity index was not affected but average molecular weight decreased with lower ethylene content. Higher molecular weight of the UHMW-RCP (ultra-high molecular weight) fraction was connected with the ethylene concentration during the synthesis in the hydrogen absence.

Another series consisted of statistical copolymers with different content of UHMW fraction. This fraction was synthesized without presence of hydrogen. Aliquot part of ultra-high molecular weight fraction (UHMW-RCP) was 20, 30, 40 and 50 wt. %, thus ethylene content in this fraction varied 19, 13, 9, 7 wt. %, respectively with the aim to obtain similar total ethylene concentration in the range of 3.0 – 3.5 wt. %. Second polymer fraction was polypropylene homopolymer synthesised in the presence of hydrogen, thus molecular weight of this fraction was significantly lower than of the UHMW-RCP fraction. Mechanical properties are summarized in Table 1 and revealed significantly higher Charpy impact strength of two-step copolymers in comparison with one-step material with the same ethylene content. It is also clear that bimodal material have significantly improved toughness already at lower ethylene content about 2.6-3.2 wt. %. Comparing samples with similar ethylene content values of notched Charpy impact test of bimodal copolymers with UHMW-RCP content 30 and 40 wt. % were seven times higher than for one-step material. For the samples with content of ultra-high molecular fraction 20 and 50 wt. % the distinction in toughness was lower, however values were still high. These results suggested an optimal composition of the statistical copolymer with the meaning of content of ultra-high molecular weight fraction, ethylene concentration in this fraction and average molecular weight, see Figure 2A. In order to obtain material with high toughness besides maintenance of sufficient strength i) presence of high molecular weight component was necessary ii) total ethylene content was in the range 3.5 – 4.0 wt. % and iii) ratio between low-middle molecular weight homopolymer fraction and ultra-high molecular weight statistical copolymer fraction was about 60 : 40 wt.%. Statistical copolymers with high Charpy impact strength featured by high melt elasticity depicted as low phase angle see Figure 2B.

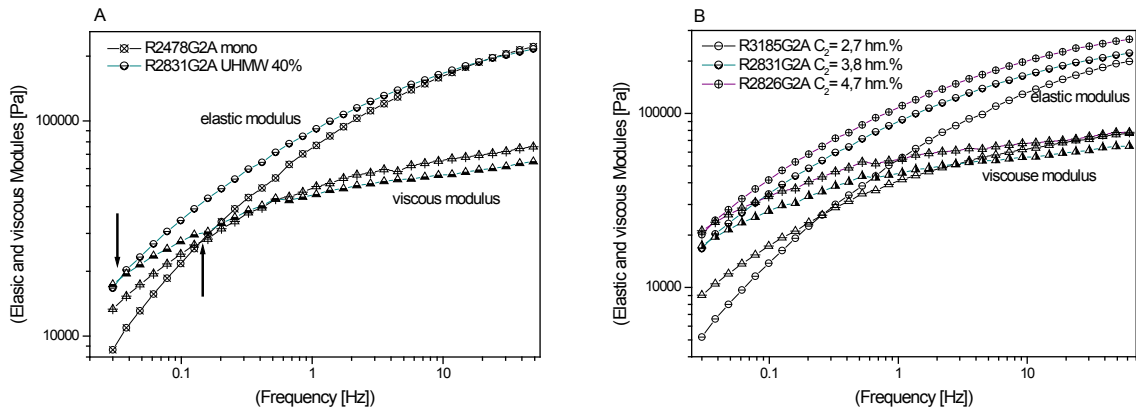


Figure 1: A) comparison of one-step and two-step material with 40 wt. % of UHMW; B) The effect of ethylene content on elastic and viscous modules.

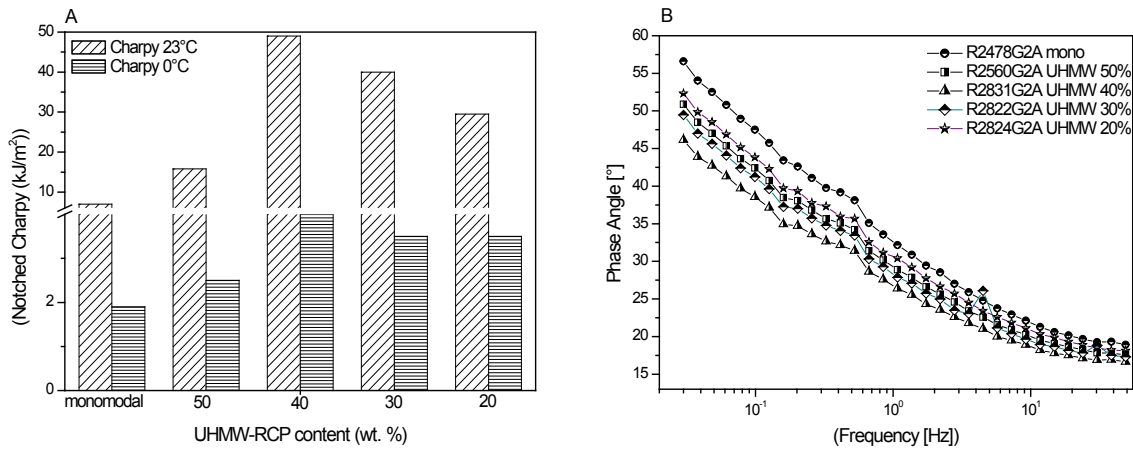


Figure 2: A) The effect of ethylene content on elastic and viscous modules; B) the effect of UHMW-RCP content on phase angle

Table I: One-step and two-step statistical ethylene-propylene copolymers

Material	MFR g/10min	XS %	UHMW content wt. %	C <sub>2</sub> wt. %	Yield strength [MPa]	Flexural modulus [MPa]	Notched Charpy 23 °C [kJ/m <sup>2</sup> ]	Notched Charpy 0 °C [kJ/m <sup>2</sup> ]
R2478G2A*	0.15	8.63	-	3.5	23.3	768	7.0	1.6
R3185G2A	0.32	8.20	40	2.7	24.5	880	11.0	2.4
R3184G2A	0.31	9.35	40	3.8	23.9	805	26.2	2.7
R2826G2A	0.11	10.46	40	4.7	19.8	730	70.5	7.7
R2560G2A	0.11	10.83	50	3.2	25.0	800	13.9	2.7
R2831G2A	0.11	7.38	40	3.8	22.5	846	49.0	5.1
R2822G2A	0.13	8.60	30	3.5	23.9	754	40.1	3.5
R2824G2A	0.16	6.80	20	2.6	26.7	1046	29.5	3.5

note: \* one-step polymerization

### Mechanical properties and rheological behaviour of ethylene-butene-propylene terpolymers

In the Table 2 mechanical properties of the ethylene-butene-propylene terpolymers are summarized. For the comparison butene-propylene copolymer was added. Presence of butene in polypropylene matrix led to increase of strength however toughness remained unaffected and comparable to the polypropylene homopolymer. Structural analysis revealed that incorporation of butene did not have impact on the high level of isotacticity of the polypropylene matrix which is connected with high strength of the copolymer. If butene together ethylene was present the toughness of the terpolymers improved. The values of Charpy impact strength at 23 °C were two or three times higher than that of butene-propylene copolymer. However, only slight decrease of Yield strength and modulus (around 20 %) was noted. Rheological analyses revealed distinction at low frequencies among the terpolymers with various ethylene and butene contents. Increasing comonomers content (sample R3578G2A  $C_{2+4} = 4.1$  wt.%) led to a decrease of the molecular weight as the elastic modulus was shifted to the higher frequencies and besides that lower polydispersity index  $PI = 4.4$  was determined. On the other hand material with the lower comonomer content (R3584G2A  $C_{2+4} = 3.4$  wt. %) had high polydispersity index  $PI = 5.6$  and according to the elastic modulus reaching lower frequencies presence of the fraction with higher molecular weight was clear. Butene-propylene copolymer behaved differently. Presence of the high molecular fraction was accompanied by low polydispersity index and narrower MWD determined by shift of  $G'$  curve to higher frequencies and steepness of the elastic modulus curve ( $G'$ ), respectively. High  $G'_{plateau}$  of butene-propylene copolymer indicated high melt strength in comparison with terpolymers.

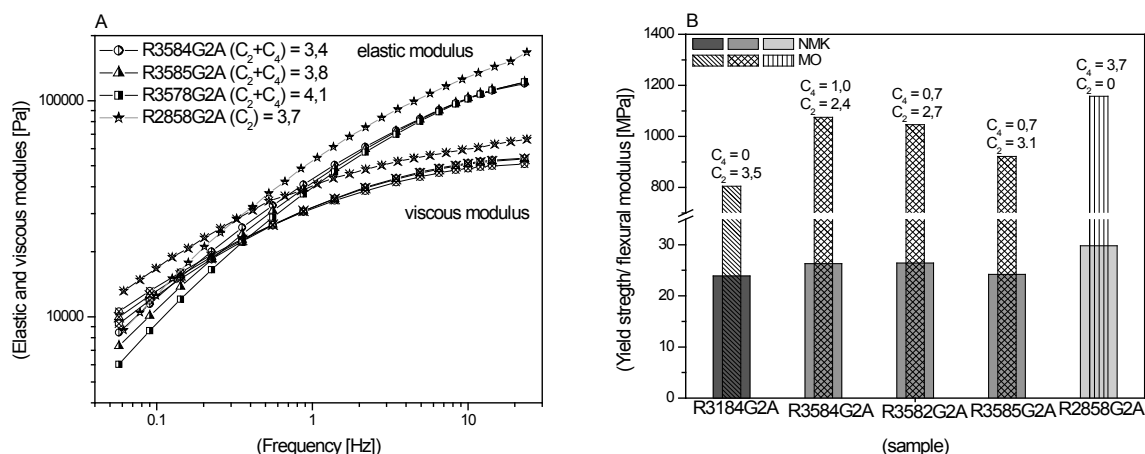


Figure 3: The effect of co-monomers content on A) rheological properties; B) mechanical properties

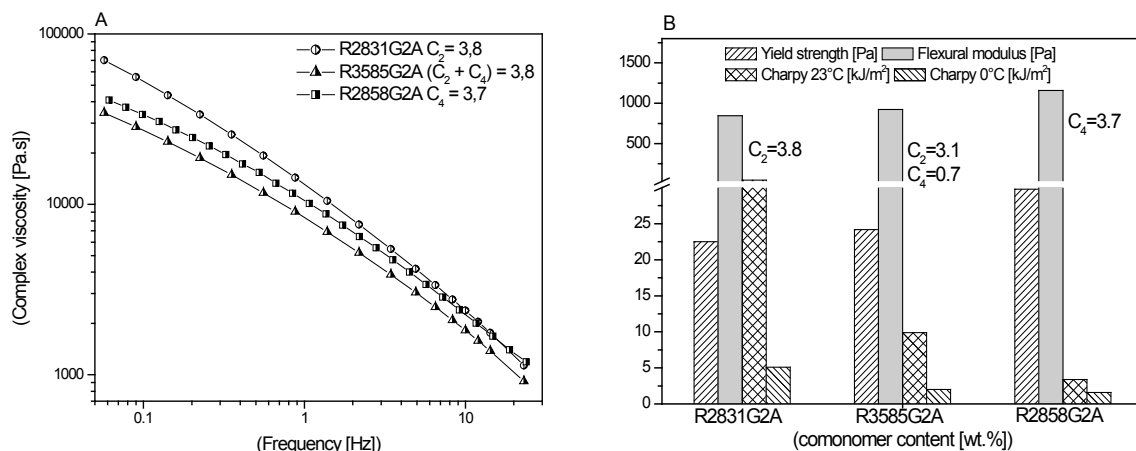


Figure 4: Comparison of ethylene-propylene and butene-propylene copolymers with ethylene-butene-propylene terpolymer A) complex viscosity B) mechanical properties

Table II: Statistical ethylene-butene-propylene terpolymers

Material	MFR g/10min	XS %	C <sub>2</sub> wt.%	C <sub>4</sub> wt.%	Yield strength [MPa]	Flexural modulus [MPa]	Notched Charpy 23 °C [kJ/m <sup>2</sup> ]	Notched Charpy 0 °C [kJ/m <sup>2</sup> ]
R2858G2A	0.37	2.11	-	3.7	29.8	1157	3.4	1.6
R3578G2A	0.36	9.05	3.5	0.6	23.5	925	11.2	2.0
R3585G2A	0.37	8.50	3.1	0.7	24.2	922	9.9	2.0
R3580G2A	0.37	8.74	2.9	0.6	24.7	922	10.7	2.0
R3582G2A	0.29	6.64	2.7	0.7	26.4	1046	8.3	1.8
R3584G2A	0.31	6.15	2.4	1.0	26.3	1075	7.7	1.6

Mechanical properties and rheological behaviour of ethylene-hexene-propylene terpolymers

Rheological properties as well as mechanical properties of the ethylene-hexene-propylene terpolymers exhibited distinction in comparison with the butene-propylene copolymer and corresponding terpolymer. Closer look at the cross point ( $G' = G''$ ) showed shift to the higher frequencies revealing decrease of the average molecular weight if butene or hexene was present together with ethylene during the copolymerization stage, see Figure 5A, 5B. According to the elastic modulus curve high molecular weight fraction was found in ethylene-propylene and also hexene-propylene copolymers however,  $G'$  curves of butene-propylene copolymer together with both terpolymers were significantly shifted to the higher frequencies. As steepness of  $G'$  curve gives information about molecular weight distribution the broadest molecular weight distribution was determined in the case of ethylene-propylene copolymer. Interestingly, both terpolymers showed wider distribution contrary to propylene copolymers containing butene and hexene only, see Figure 6A. On the Figure 6B, above discussed material were compared from the point of mechanical properties. Copolymers with butene and hexene exhibited significantly higher Yield strength and flexural modulus, however surprisingly higher toughness of the hexene-propylene copolymer was determined despite of the lower hexene content. These results indicate that high Charpy impact strength can be connected with the wide molecular weight distribution accompanied the presence of ultra-high molecular weight fraction. Both conditions were fulfilled for the ethylene-propylene copolymers. Hexene-propylene copolymer contained ultra-high molecular weight fraction that led to improved toughness. Introduction of butene or hexene instead of ethylene into the polypropylene matrix led to higher isotacticity of the polymer thus higher strength and modules were determined.

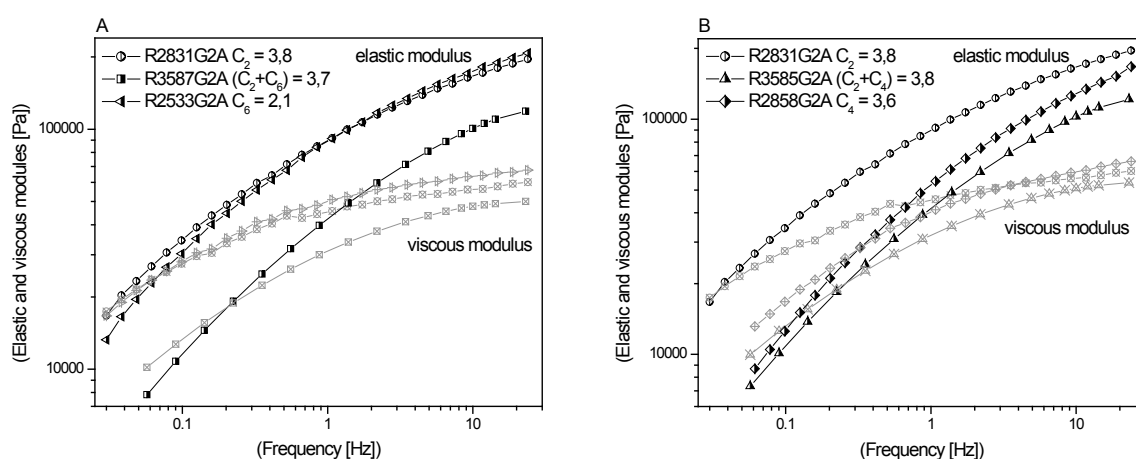


Figure 5: Elastic and viscous modules of C<sub>2</sub>-C<sub>3</sub> copolymers compared with A) C<sub>4</sub>-C<sub>3</sub> copolymer and C<sub>2</sub>-C<sub>4</sub>-C<sub>3</sub> terpolymer B) C<sub>6</sub>-C<sub>3</sub> copolymer and C<sub>2</sub>-C<sub>6</sub>-C<sub>3</sub> terpolymer

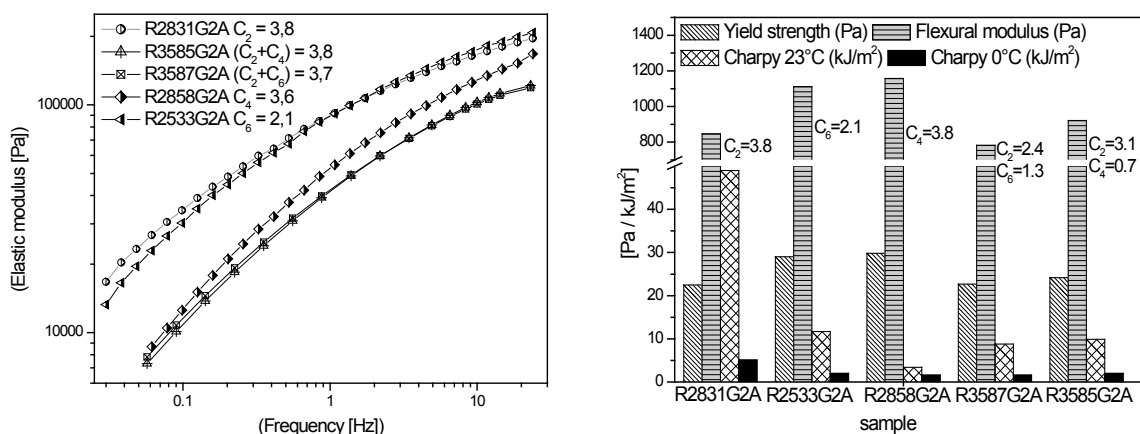


Figure 6: A) Elastic modulus of C<sub>2</sub>-C<sub>3</sub>, C<sub>4</sub>-C<sub>3</sub>, C<sub>6</sub>-C<sub>3</sub> copolymers and C<sub>2</sub>-C<sub>4</sub>-C<sub>3</sub>, C<sub>2</sub>-C<sub>6</sub>-C<sub>3</sub> terpolymers; B) mechanical properties of copolymers and terpolymers

Table 3: Statistical ethylene-hexene-propylene terpolymers

Material	MFR g/10min	XS %	C <sub>2</sub> wt. %	C <sub>6</sub> wt. %	Yield strength [MPa]	Flexural modulus [MPa]	Notched Charpy 23 °C [kJ/m <sup>2</sup> ]	Notched Charpy 0 °C [kJ/m <sup>2</sup> ]
R2533G2A	0.11	2.05	-	2.1	-	1112	11.7	-
R3450G2A	0.27	13.86	4.0	0.6	18.6	713	50.9	5.1
R3451G2A	0.25	15.33	3.7	1.0	18.5	646	40.1	5.7
R3586G2A	0.35	7.69	2.6	0.9	24.4	871	8.1	1.1
R3591G2A	0.35	10.47	1.9	1.7	21.9	855	7.9	1.8
R3587G2A	0.29	9.03	2.8	1.3	22.7	782	8.8	1.6

## Conclusions

Obtained results showed interesting distinctions among ethylene-propylene, butene-propylene, hexene-propylene copolymers and ethylene-butene-propylene, ethylene-hexene-propylene terpolymers. Increasing content of ethylene in the copolymer caused higher elasticity and increase of the average molecular weight. These materials also exhibited wide molecular weight distribution determined by low steepness of G' curve. However introduction of butene instead of ethylene led to the copolymer with lower average molecular weight and UHMW fraction was absent. High melt strength accompanied by high isotacticity of butene-propylene copolymer was responsible for significant improvement of the Yield strength and elastic modulus in comparison with ethylene-propylene copolymer. The copolymer with hexene exhibited significantly higher Yield strength and flexural modulus, however surprisingly also higher toughness of hexene-propylene copolymers was determined despite of lower hexene content. These results indicate that high Charpy impact strength can be connected with wide molecular weight distribution accompanied by the presence of ultra-high molecular weight fraction. Both conditions were fulfilled only for ethylene-propylene copolymers. Also hexene-propylene copolymer contained ultra-high molecular weight fraction that led to improved toughness to some measure. In the case of ethylene-butene(hexen)-propylene terpolymers elastic and viscous modules were shifted to higher frequencies and no UHMW fraction was detected. However, all terpolymers showed gradual increase of G' modulus with increasing frequency indicating wide molecular weight distribution. Presence of butene in the terpolymer increased strength however toughness was not affected. Increasing content of ethylene was responsible for improvement of the toughness. Contrary to that, hexene in the terpolymer had not such impact on the strength but rather participated on the increase of toughness.

## Literature

1. Subhasis P., Kale P.P.: J.Appl.Polym.Sci. 84, 665-671 (2002)
2. Ana-Lúcia. N. Da Saliva, Marisa C.G. Rocha, Fernanda M.B. Coutinho, Rosário E.S. Bretas, Marcelo, Farah: Polymer Testing 21, 647-652 (2002)
3. Costello B.: Annual Transaction of the Nordic rheology society 13, 61-64 (2005)
4. TA Instruments - Understanding Rheology of Thermoplastic Polymers AANO13
5. Shang-Guan YongGang, Chen Feng, Zheng Qiang: Science China 55, 698-712 (2012)

## BIODEGRADABLE POLYPROPYLENE BLEND WITH CONTROLLED DEGRADATION

**Balgová V.**, Vrátničková Z., Babka M.

*Polymer Institute Brno, Tkalcovská 36/2, Brno 656 49, Czech Republic  
balgova@polymer.cz*

### Introduction

The aim of our research was modification of the polypropylene matrix with an additive causing fast/controlled photo-oxo-degradation<sup>1</sup> followed by biodegradation in composting environment. Several additives consisting of various components playing specific role in the degradation process were prepared<sup>2,3</sup>. Individual components were chosen based on thorough study of the effect of individual component on the degradation process in relation to the creation of a new different functional groups, rate of functional groups evolution and disintegration assistance<sup>4,5,6</sup>. Final additive, with polypropylene as a matrix, was composed of polyethylene glycol combined with copper oxide and manganese stearate. In order to support disintegration of the synthetic material calcium carbonate was added. The additive operated on the photo-oxo degradation principle. Presence of the functional groups increased UV light absorption capacity of the composite and the presence of copper enabled easy creation of the new carbonyl and others groups and further facilitated cleavage reactions, which led to the formation of new reactive radicals. Due to an increase of the concentration of polar functional groups in the process of time hydrophilic character of the composite become dominant. Hydrophilic character is one of the necessary conditions to be fulfilled besides sufficiently low molecular weight of the remaining material in order to allow microbial attack. The degradation process of the polypropylene blend with additive was studied on foils which were exposed to i) accelerated aging on QUV-A test ii) natural environment and iii) exposition to UV-light followed by the composting test. The progress of the disintegration and degradation was followed by FTIR, DSC and GPC analyses.

### Experimental

#### Extrusion modification

Concentrate of individual component such as copper oxide, manganese stearate, Socal 312 (CaCO<sub>3</sub>), Irganox B25, polyethylene glycol in polypropylene matrix was prepared via extrusion at 220 °C, 100rpm, BRABENDER L/D=30. Final blend was composed of 20 wt. % of Concentrate and standard polypropylene GB 002.

#### Thermal analysis

Thermal analysis was performed with DSC-7 differential scanning calorimeter (Perkin Elmer). 4mg of sample was used for analysis. The DSC temperature program consist of three steps when sample is heated from 50 to 200 °C at 10 °C/min rate, then kept 10 min. at 200 °C and cooling occurring at the same rate come after.

#### Infrared spectroscopy

FTIR spectrometer Nicolet nexus in the transmission mode with 4 cm<sup>-1</sup> resolution was employed. For the analysis foil with thickness 0.2-0.3mm was used.

#### Gel permeation chromatography

GPC analysis was performed on instrument Polymer Laboratories (Agilent), model PL-GPC 220 with PL-220DRI (refractive index detector) and VISCOTEK model 220R (viscosity detector) equipped with columns 3x PL gel 10 μm MIXED-B, 300 x 7.5 mm, with guard column PL gel 10μm MIXED-B, 50 x 7.5 mm. As a mobile phase 1,2,4-trichlorobenzene for chromatography (Scharlau) containing 0.025 wt. % Santonox R, to prevent oxidative degradation of polymers, was used. For the analysis 200 μL of sample with concentration 1.0 mg/cm<sup>3</sup> was injected.

#### Degradation tests

QUV-A test was carried out according EN SI 4892-2. The chamber was programmed to operate at cycles. At temperature of 50 °C the sample was subjected UV light exposure for 20hours followed by condensation stage, when temperature was decreased to 40 °C and moisture was introduced. Condensation step last for 4 hours. Such procedure should simulate natural environment where sunlight, temperature and humidity have impact on polymeric material and its degradation. Composting the test was carried out in ordinary composting container for 6 month.

## Results and discussion

Prior to the preparation of pro-degradation additive the effect of individual components on degradation process was studied. Various polymers containing functional groups, such as hydroxyl, esters, carbonyl etc., were mixed with polypropylene matrix. Besides, polypropylene was modified by in-situ polymerization when higher olefins and dienes were applied and incorporated into polypropylene matrix. Introduction of Cu ions in the form Cu-Zeolite into polypropylene (PP-Cu) by in-situ procedure and oxidation of polypropylene by nitric acid was also performed (PP-Ox). In-situ preparation of PP-Cu showed more homogenous distribution of Cu ions in polymer powder and degradation through the whole testing foil occurred more uniformly contrary to foil prepared from the blend based on mixing of polypropylene with CuO in extruder. All types of functional groups had positive effect on the degradation however glycols were determined as the most suitable, when shortening of initiation period was more pronounced and also in the same time higher concentration of new functional group was detected. Various transition metals such as Zn, Fe, Mo, Mn, Cu in the form of oxides, were tested in order to increase degradation rate. The presence of transition metal caused significantly easier creation of new functional groups, mainly carbonyl and hydroxyl groups, during the initiation period. However, ester dominates above carbonyl groups when transition metal is absent. The decrease of molecular weight was more extensive with the used of Cu or Fe oxides. Thus for further research CuO was applied as a component of the complex additive. In order to support disintegration of the synthetic material calcium carbonate was added together with manganese stearate as a metal with different redox potential.

Two series B-P and B-E of additives were prepared. This additives B-P and B-E contained polypropylene glycol (pluriol P 2000) and polyethylene glycol (pluriol E 6000) as source of functional groups, respectively. Polypropylene denoted as GB 002 (Unipetrol RPA) was used as a matrix. Final blend consisted of 80 wt. % of PP matrix and 20 wt. % of additive composed of individual components as described in the **Table 1**.

Table 1: Composition of polypropylene/additive blends

Blends	B-P1	B-P2	B-P3	B-E1	B-E2	B-E3
GB 002 - matrix	x	x	x	x	x	x
Additive						
Irganox B225	x	x	x	x	x	x
PP-Cu	x	x	-	x	x	-
PP-Ox	x	x	-	x	x	-
Pluriol P 2000	x	x	x	-		-
Pluriol E 6000	-	-	-	x	x	x
Mn-stearate	-	x	x	-	x	x
Socal 312	-	x	x	-	x	x
Mn-stearate	-	x	x	-	x	x
CuO	-	-	x	-	-	x

Note: PP-Cu - in-situ modified polypropylene; PP-Ox - oxidized polypropylene

The additive operated on the photo-oxo degradation principle. Functional groups increased initial UV light absorption capacity of the composite. The presence of copper enabled easy creation of new carbonyl groups and further facilitated cleavage reactions which led to the formation of new reactive radicals. Due to an increase of the concentration of polar functional groups in process of time hydrophilic character of the composite became dominant. Hydrophilic character is one of the necessary conditions to be fulfilled besides sufficiently low molecular weight of the remaining material in order to allow microbial attack. Degradation process of the polypropylene blends, modified with the additive, was studied on foils which were exposed to i) accelerated aging on QUV-A test, ii) natural environment and iii) exposition to UV-light followed by the composting test. Decrease of molecular weight after degradation tests, determined by GPC analyses, is summarized in the **Table 2**. On the **Figure 1A** are depicted DSC spectra and **Figure 1B** GPC analyses portraying comparison among raw material B-E1 prior to degradation (B-E3 0), samples after 259 hours exposition on QUV-A (B-E3 259h) and sample after exposition on QUV-A flowed by 6 month composting test (B-E3 K200). Unmodified polypropylene after composting test is added.

Table II: GPC analysis before and after composting test, comparison with standard PP after composting test

Material	Mn g/mol	Mw g/mol	Mz g/mol	Mw/Mn	Intrinsic viscosity [dl/g]
B-P1	76 220	422 400	1 149 000	5.6	1.94
B-E1	62 285	398 200	1 095 000	6.4	1.89
PP ref K200	17 740	75 005	237 150	4.2	0.56
B-P1 K200	9 843	95 445	443 600	9.7	0.59
B-P2 K200	8 972	62 825	335 500	7.0	0.35
B-P3 K200	8 598	27 233	79 955	3.2	0.21
B-E1 K200	10 900	55 695	217 350	5.1	0.39
B-E2 K200	8 406	43 710	204 300	5.2	0.28
B-E3 K200	9 146	31 040	88 040	3.4	0.27

All composites exhibited significant decrease of molecular weight. However, it was clear that efficiency of copper oxide (B-P2-P3 and B-E2-E3 blends) was higher than Cu ions incorporated via in-situ procedure directly into polypropylene (B-P1 and B-E1 blends). Presence of carbon dioxide unambiguously supported erosion of the testing species (B-P2-P3 and B-E2-E3 blends). Additives containing CuO (B-P3 and B-E3) showed the wastes degradation through the whole mass of the testing specimen. High molecular weight fraction disappeared as molecular weight Mz dropped to ~ 8 % of the initial Mz value, see **Table 2**.

On the Figure 1A and 1B are depicted results of DSC and GPC analyses that compare polypropylene blend with additive and pure polypropylene after composting test. GPC curve of PP/additive blend (B-E3 K200) after composting test was significantly shifted to lower molecular weights. DCS results showed shift of the whole curve to lower values and drop of the melting temperature about 20 °C was determined. These results are consistent with GPC analyses. Generally, the best results were obtained in the case of B-E3 and B-P3 composites. Prior to the composting test foils were exposed to the UV-light and humidity in QUV-A test for 259 hours, in order to simulate “life cycle” of the plastic product. On the **Figure 2** and **Figure 3** are depicted photographs of foils before and after composting test for pure PP sample and B-E3 sample containing additive with polyethylene glycol as a source of initial functional groups. After composting test six month long pure PP foil remain almost untouched, however it was almost impossible to recover some residuals of B-E3 sample. Only about 20 wt. % of this sample was detectable by eye and usable for analyses. According to FTIR analyses very high concentration of functional groups were present and hydrophilic character became dominant.

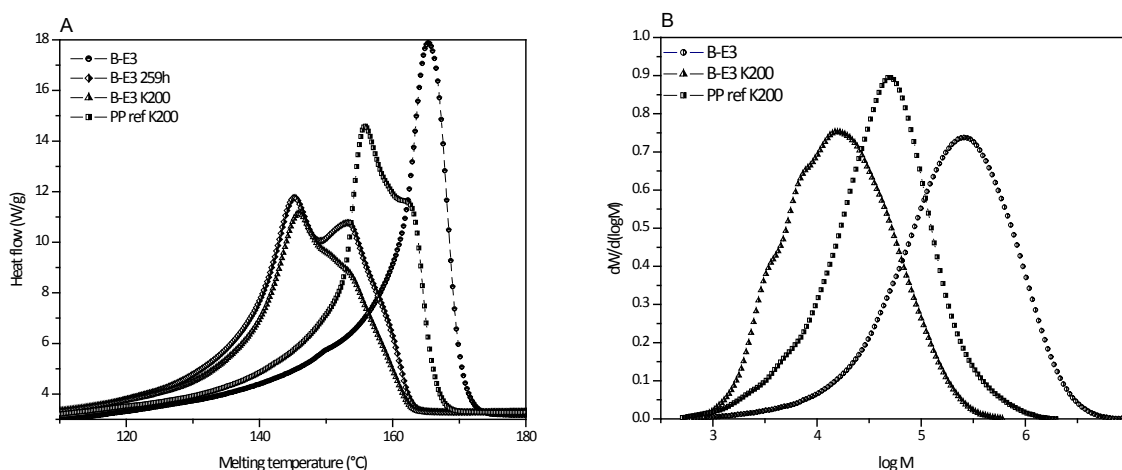


Figure 1: A) DSC spectra B) GPC analyses of PP/polyethylene glycol blend: B-E3 0 – sample before exposition, B-E3 259h – sample after 259h on QUV-A test, B-E3 K200 – sample after 6 month composting test, PP ref K200 – pure PP sample after composting test.

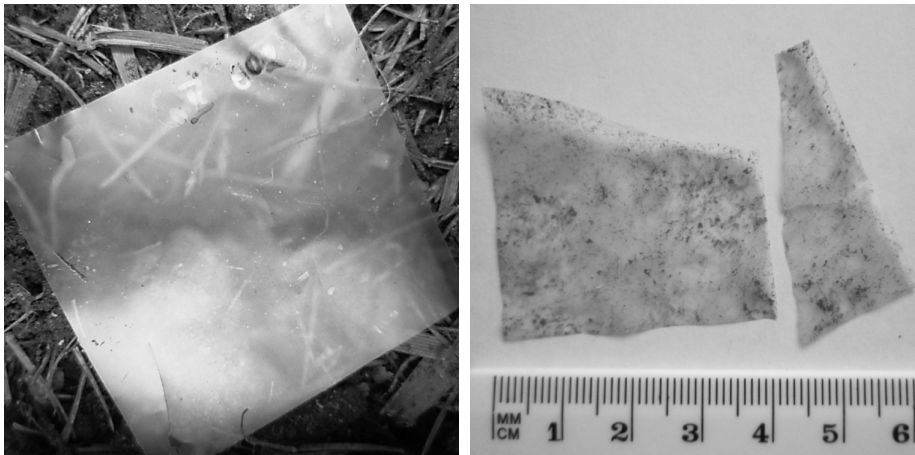


Figure 2: Foil of pure PP before and after composting test

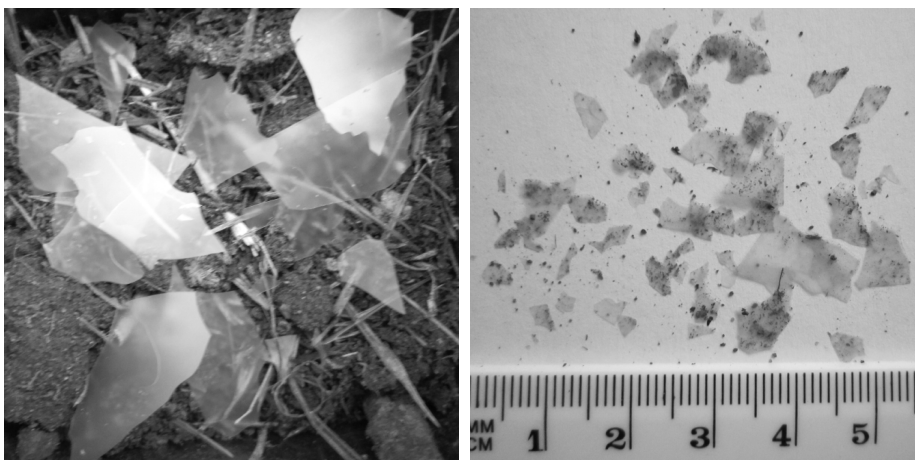


Figure 3: Foil of B-E3 composite before and after composting test

### Conclusions

Within the scope of our project additive enabling governed degradation followed by biodegradation in composting environment was developed. Additive composed of five components added in 20 wt. % in maximum did not affect mechanical properties and processability of the polypropylene composite. Degradation of the foil was activated by exposition to environment, especially to UV-light. However during storage in the room mechanical properties of the foil remain unaltered for one year. Degradation rate can be effectively governed by additive dosage and via alternation of concentration of individual component.

### Literature

1. [www.biodeg.org](http://www.biodeg.org) - Oxo-biodegradable Plastic Association
2. Gross R.A. and Klara B.: Green Chemistry 297, 803 (2002)
3. Chiellini E., Corti A., Antone S.D., Baci R.: Polym.Degrad.Stab., 91, 2739 (2006)
4. Koutný M., Sancelme M., Dabin C., Pichon N., Delort A-M., Lemaire J.: Polym.Degrad. Stab., 91, 1495 (2006)
5. M. Arnold, S. Bornemann, T. Schimmel, T. Heinze: Macromol.Symp. 181, 5, (2002)
6. Paavola S., Uotila R., Löfgren B., Seppälä J.V.: Reactive and Functional Polymers 61, 53 (2004)

## WASHING OF SODA PULP FROM RAPESEED STRAW

**Potůček F.**, Hájková K.

*University of Pardubice, Faculty of Chemical Technology, Institute of Chemistry and Technology of Macromolecular Materials, 532 10 Pardubice, Czech Republic  
Phone: 420-466038016; fax: 420-466038039; e-mail: frantisek.potucek@upce.cz*

The aim of this work was to investigate the displacement washing process of soda pulp cooked from rapeseed straw. Displacement washing process was described by displacement washing curves recorded for alkali lignin like a tracer. The shape of the washing curves obtained experimentally indicated that the displacement of black liquor was non-ideal, *i. e.*, it was between the ideal limits of plug flow and perfectly mixed flow. Mathematical treatment of the washing curves, which were obtained as a response to the step input signal, gave a dimensionless criterion known as the Péclet number characterizing the displacement of lignin from the pulp pad.

The preliminary results obtained showed that the differences in intrinsic properties between soda rapeseed and kraft wood fibres have an impact on the displacement washing of soda pulp. Similarly as for kraft softwood and hardwood fibres, the wash yield determined for soda rapeseed pulp was found to be lower than that for non-porous incompressible particles. Comparing our results for soda pulp with those reported for softwood and hardwood pulps earlier, the displacement front becomes irregular owing to the heterogeneity of soda pulp fibre bed having much greater hydraulic resistance.

**Key words:** displacement washing, soda rapeseed pulp, wash yield

### Introduction

Over the past years, the world demand for paper increased steadily while the existing wood resources seem to be inadequate to fulfil this requirement. Non-wood fibres including agricultural residues and annual plants could be effective source to produce pulp and paper with acceptable properties, especially in countries with insufficient forest resources<sup>1</sup>. Compared to wood, non-wood raw materials are similar in cellulose, lower in lignin and higher in pentosans (hemicelluloses) and silica content.

Non-wood raw materials such as wheat straw, rice straw, and sugarcane bagasse are used successfully in pulp and paper industries. Besides agricultural residues, some annual plants, *e. g.*, hemp, and flax, have been traditionally used for the production of common, writing, and printing papers, as well as for specialty papers like bible, filter, cigarette, currency, insulating, and condenser papers. Chemical composition and morphological properties along with pulping procedures of non-woody plants were reported in the review article<sup>2</sup>, including also strength properties of non-woody pulp fibres.

Rapeseed, the third most important oilseed crop after soybean and palm, has been cultivated to produce seeds for oil and biodiesel production. The world wide planted area for rapeseed increases continuously. After harvesting, the amount of rapeseed straw remaining in the field is of 2.8 to 4.5 t/ha (ref.<sup>3</sup>). Recently, several authors<sup>4-7</sup> reported soda pulping of rapeseed straw and their results obtained in the laboratory scale showed that rapeseed straw can be considered as one of the basic resources of non-woody materials to pulp and paper production.

Both chemical cooking of wood and non-wood materials and chemical bleaching of pulp introduce chemicals into pulp in order to release organic compounds from it. These cooking and bleaching chemicals and organic compounds should be removed from the pulp prior to further processing. High efficient washing systems are desired because dissolved solids remaining with the pulp after pulp-liquor separation increase the cost of bleaching, pulping, chemical make-up, effluent treatment, and fuels. Hence, the objective of washing is to separate cellulose fibres from black liquor while using a minimal amount of wash water. Pulp washing can be carried out by dilution/drainage or by displacement of the liquor, and most of the industrial washers combine both principles. However, a substantial amount of filtrate is trapped inside the fibre walls and between the fibre bundles, and is therefore not relevant to the drainage process. Appropriate displacement washing is of primary importance in obtaining good washing efficiencies with all types of washing equipment.

Although pulp washing together with cooking rank among the key unit operations in pulp manufacture, no research work concerning washing of rapeseed pulp was found in the literature. Therefore, the objective of this study was to conduct displacement washing of soda pulp cooked from rapeseed straw.

## Experimental

Rapeseed straw (*Brassica napus* L. convar. *napus*, in our case winter hybrid genotype Rohan) collected from the field in Bohemian-Moravian Highlands was used for the pulping process. Raw materials consisted mainly of stalks, but approximately one third of total mass were valves of siliques.

Prior to cooking experiments, the rapeseed straw was cut into 2–3 cm length chips. Batch soda pulping of rapeseed straw was carried out in a laboratory rotary digester comprising six autoclaves of 750 cm<sup>3</sup> capacity, immersed in an oil bath. The cooking conditions, when rejects amount was acceptable, were selected as follows: liquor-to-raw material ratio of 5:1, alkali charge of 19 mass % expressed as Na<sub>2</sub>O per oven-dried raw material, and cooking temperature of 160 °C.

The degree of delignification of pulp cooked by the batch soda process expressed by the kappa number was 33.9. Using the Kajaani FS-100 instrument, the distribution of the fibre length was also measured for soda pulp cooked from rapeseed straw.

Displacement washing experiments simulated under the laboratory conditions were performed in a cylindrical glass cell with inside diameter of 35 mm under constant pulp bed height of 30 mm. The fibre pulp bed occupied the volume between the permeable septum and a piston, covered with 45 mesh screens to prevent fibre losses from the bed.

Pulp beds were formed from a dilute suspension of unbeaten unbleached soda pulp in black liquor. Properties of black liquor were as follows: solids content of 11.3 mass % (of which ash presented 56 % and organic substances 44 %), density of 1061 kg m<sup>-3</sup> at 22 °C, pH value of 9.2, and alkali lignin concentration of 27 g dm<sup>-3</sup>. After compressing to desire thickness of 30 mm, the consistency, *i. e.*, mass concentration of moisture-free pulp fibres in the bed varied within the limits from 68 to 88 kg m<sup>-3</sup>. The pulp beds were not mechanically conditioned and were used as formed.

To investigate the displacement washing process, the stimulus-response method was chosen. Distilled water at the temperature of 22 °C employed as wash liquid was distributed uniformly through the piston to the top of bed at the start of the washing experiment, approximating a step change in alkali lignin concentration. At the same time the displaced liquor was collected at atmospheric pressure from the bottom of the bed through the septum. The washing effluent was sampled at different time intervals until the effluent was colourless. Samples of the washing effluent leaving the pulp bed were analysed for alkali lignin using an ultraviolet spectrophotometer operating at a wavelength of 280 nm. Displacement washing experiments with pulp fibres including washing equipment were described in detail in the preceding paper<sup>8</sup>.

After completing the washing run, the volumetric flow rate of wash liquid was measured gravimetrically at the pressure drop of 7 kPa to determine a permeability and average porosity of the pulp bed. Analogous measurements at various consistencies of the bed were focused on the determination of the effective specific volume and surface of pulp fibres according to Ingmanson<sup>9</sup>.

## Results and Discussion

### Soda rapeseed pulp characteristics

The fibre characteristics of soda pulps cooked from rapeseed straw are compared with those for kraft pulp from a blend of hardwoods, namely beech 55 %, oak 16 %, Turkey oak 8 %, acacia 4 %, hornbeam 5 %, poplar 6 %, and other 6 % (ref.<sup>10</sup>) and from a blend of softwoods containing ¾ spruce and ¼ pine (ref.<sup>11</sup>) in Table I. Pulp fibres manufactured from rapeseed straw are short, with an average length less than 1 mm. The presence of silique valves in straw resulted in greater polydispesity in fibre length in comparison with the soda pulp cooked from stalks only.

Table I. Fibre characteristics for pulp cooked from rapeseed straw, blend of hardwoods<sup>10</sup>, and blend of softwoods<sup>11</sup>

Pulp	Kappa number	Weighted average length, mm	Arithmetic average length, mm	Effective volume cm <sup>3</sup> g <sup>-1</sup>	specific Effective surface m <sup>2</sup> g <sup>-1</sup>	specific
Rapeseed straw	33.9	0.82	0.36	3.04	1.07	
Hardwoods	29.9	0.90	0.75	2.92	0.988	
Softwoods	32.0	3.34	1.46	2.82	0.793	

## Wash yield

For a better and more detailed description of the washing operation, a microscopic model has to be used. The dispersed plug flow model<sup>12</sup> can be chosen to characterize the displacement of the black liquor from the pulp fibre bed. The response to the step input signal can be recorded as a time dependence of the solute (*e. g.*, alkali lignin) concentration in the output stream of effluent. Breakthrough curves obtained experimentally were normalized by plotting them on coordinates of the ratio of the instantaneous outlet to the initial mother liquor concentration in the bed *versus* the wash liquor ratio defined as the ratio of the mass of the wash liquor passed through the bed and the mass of the mother liquor present in the packed bed. Typical examples of washing curves measured for alkali lignin are illustrated in Fig. 1, which shows also the logical limits of plug flow without diffusion and of infinite diffusion as with a fully stirred vessel.

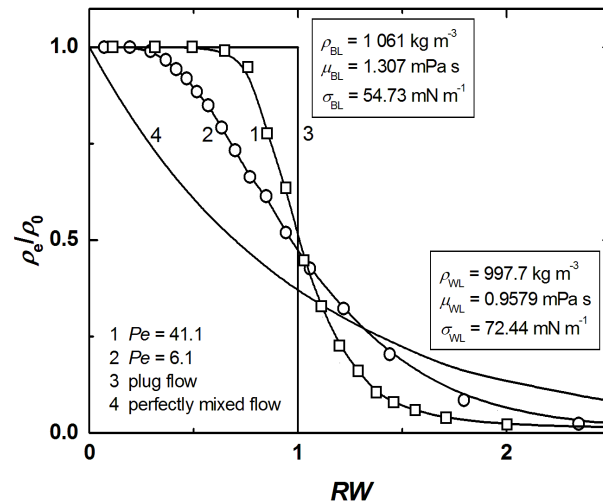


Figure 1. Typical breakthrough washing curves for soda pulp:  $Pe = 41.1$  (line 1),  $Pe = 6.1$  (line 2), plug flow (line 3), perfectly mixed flow (line 4).

Intrinsic properties of effluent stream leaving the bed are changed during displacement process. In Fig. 1, the density,  $\rho$ , viscosity,  $\mu$ , and surface tension,  $\sigma$ , measured at a temperature of 22 °C for the black liquor (BL) and wash liquid (WL) are mentioned. At the beginning of a displacement, the first portions discharged from the bed are fully as concentrated as was the mother liquor. As soon as the first portion of wash liquid passes through the bed, the concentration of lignin drops very rapidly. The major part of mother liquor in interparticle voids is removed and replaced by wash liquid. In the last period, only remains of black liquor are removed from inside narrow pores and fibre walls. In contrast to the first two periods, in which the displacement operation is a dominant one, the leaching referring to the desorption and diffusion of solute from within the fibres prevails. The shape of washing curve including its tail is strongly influenced by a highly complex network of pores and by leaching of solute from within fibre walls into the wash liquid. It is necessary to note that the shorter time contact between the wash liquid and fibres the longer the tail on the washing curve can be achieved. Under our laboratory conditions, the average interstitial velocity of the wash liquid in the bed was quite low in the range from 0.039 to 0.18 mm s<sup>-1</sup>. Then, the wash liquid was in contact with the fibres for a relatively long time. Owing to a tortuosity of pores, the wash liquid is forced to take a longer path than the bed thickness is.

The area below breakthrough curve expressed as the dependence of the dimensionless concentration of a solute upon the wash liquor ratio,  $RW$ , is directly proportional to the amount of a solute removed from the pulp bed. Then, the quality of the displacement washing process can be characterized by the traditional wash yield,  $WY_{RW=1}$ , evaluated at the wash liquor ratio equal to unity as follows

$$WY_{RW=1} = \frac{\int_{RW=0}^{RW=1} \frac{\rho_e}{\rho_0} d(RW)}{\int_{RW=0}^{RW \rightarrow \infty} \frac{\rho_e}{\rho_0} d(RW)} \quad (1)$$

where  $\rho_e$  is the exit lignin concentration from bed, and  $\rho_0$  is the initial lignin concentration in bed.

A measure of lignin dispersion in the bed is indicated by the dimensionless Péclet number defined as

$$Pe = \frac{hu}{D\varepsilon} \quad (2)$$

where  $h$  is the bed height,  $u$  is the superficial wash liquid velocity,  $D$  is the longitudinal dispersion coefficient, and  $\varepsilon$  is the average effective bed porosity. This dimensionless criterion based on the height of the bed also signifies a ratio of the convective to the diffusive transport mechanisms. Details of the evaluation of the Péclet number can be found elsewhere<sup>8</sup>.

Wash yield data are illustrated as a function of the Péclet number in Fig. 2. The experimental points measured for pulp fibres are located below the curve which was derived for the packed bed of non-porous particles by Brenner<sup>13</sup>. In contrast to the packed bed of non-porous particles, when the washing process is reduced to the displacement mechanism and interfacial mixing between the displaced and displacing fluid, the leaching can play a significant role in the case of compressible porous fibres in the swollen state.

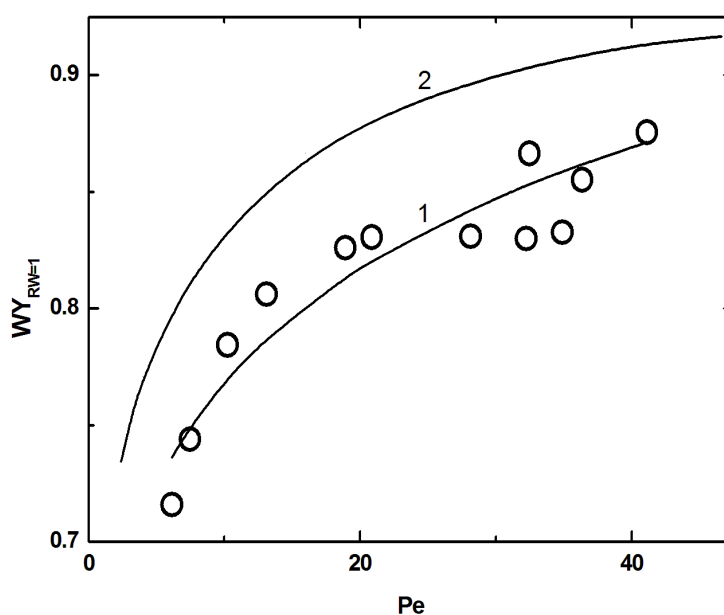


Figure 2. Displacement wash yield as a function of the Péclet number for soda pulp from rapeseed straw (○). 1 Equation (3) (line 1), non-porous particles according to Brenner<sup>13</sup> (line 2)

For the data illustrated in Fig. 2, the influence of the Péclet number on the wash yield can be correlated by the following equation

$$WY_{RW=1} = 0.63Pe^{0.087} \quad (3)$$

valid in the range of the Péclet number of 6 to 41. The equation (3) fitted the data with a mean relative quadratic deviation,  $\delta$  (defined in Symbols) of 1.9 %. Since the values of regression coefficients, which were evaluated by the least square method, represent an estimate of the real values, the 95% confidence intervals were also calculated. They are for the coefficient  $0.63 \pm 0.012$ , and for the power of the Péclet number  $0.087 \pm 0.0063$ . The equation (3) confirmed again that the wash yield depends upon the Péclet number in a small degree.

The wash yield measured for soda rapeseed pulp is compared with that of softwood<sup>11</sup> and hardwood<sup>10</sup> in Fig. 3. However, in case of soda rapeseed pulp, values of the Péclet number varying in the relative wide range revealed that the bed formation may be a critical step influencing wash liquid dispersion. It is worth mentioning that soda pulp bed manifested greater hydraulic resistance in comparison with kraft pulp from hardwood and softwood. Even through both rapeseed pulp and hardwood pulp rank among short-fibred pulps, the permeability measured for hardwood pulp<sup>10</sup> was in the range from  $0.9 \times 10^{-12}$  to  $2.8 \times 10^{-12}$  m<sup>2</sup> at pulp bed consistencies within the limits of 108 to 116 kg m<sup>-3</sup>, while, for soda rapeseed pulp, the permeability of

$0.5 \times 10^{-12}$  to  $1.9 \times 10^{-12}$  m<sup>2</sup> at significantly lower pulp bed consistencies within the limits of 67 to 87 kg m<sup>-3</sup> was evaluated for streamline flow regime.

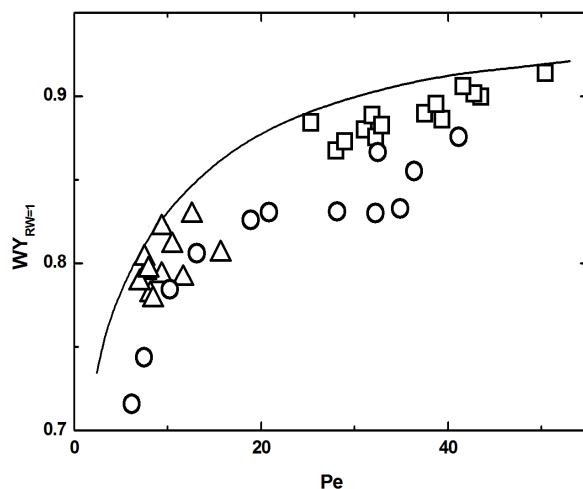


Figure 3. Comparison of the traditional wash yield for soda rapeseed pulp (○) with kraft pulp from hardwood<sup>10</sup> (□) and softwood<sup>11</sup> (△). Non-porous particles according to Brenner<sup>13</sup> (solid line)

### Conclusion

The morphological properties analysis indicated that despite the thicker cell wall, the morphological properties of rapeseed straw fibres were comparable to those of non-woods and hardwoods fibres. Of course, the pith of non-wood plants is composed mainly of parenchyma cells and vessel elements and causes serious problems such as increasing chemical consumption in pulping and bleaching, washing problems, and drainage problems in papermaking.

The hydraulic resistance of the soda pulp fibres cooked from rapeseed straw to the delignification degree expressed by the kappa number of 34 was much greater than that for kraft softwood or hardwood pulp fibres. The beds of soda pulp fibres presented much greater longitudinal dispersion in comparison with non-porous particles. The displacement wash yield for soda pulp fibres showed an increasing trend with increasing the Péclet number in agreement with the results obtained for softwood and hardwood fibres in the previous papers<sup>10,11</sup>.

### Acknowledgements

*This work was supported by the Internal Grant Agency of University of Pardubice under the research project SGFChT04/2014.*

### Symbols

$D$	axial dispersion coefficient, m <sup>2</sup> s <sup>-1</sup>
$h$	height of bed, m
$n$	number of measurements
$Pe$	Péclet number based on bed height defined by Eq. (2)
$RW$	wash liquor ratio (dimensionless)
$u$	superficial wash liquid velocity, m s <sup>-1</sup>
$WY_{RW=1}$	wash yield at $RW = 1$ defined by Eq. (1)

### Greek letters

$\delta$  mean relative quadratic deviation of wash yield defined as

$$\delta = \left[ \frac{1}{n} \sum_{i=1}^{i=n} \left( \frac{WY_{exp} - WY_{calc}}{WY_{exp}} \right)_i^2 \right]^{1/2} \times 100, \%$$

$\varepsilon$	average effective bed porosity
$\mu$	dynamic viscosity, Pas
$\rho_e$	exit lignin concentration from bed, $\text{kg m}^{-3}$
$\rho_p$	consistency (mass concentration) of pulp bed, $\text{kg m}^{-3}$
$\rho_0$	initial lignin concentration in bed, $\text{kg m}^{-3}$
$\sigma$	surface tension, $\text{N m}^{-1}$

### Literature

1. Mohieldin S. D.: *J. For. Prod. Ind.* 3(2), 84 (2014).
2. Gurung B., Potůček F.: *Pap.Celul.* 68(5), 147 (2013).
3. Petříková V.: *Plants for energy purposes* (in Czech), p. 34, Česká energetická agentura, Praha 1999.
4. Enayati A. A., Hamzeh Y., Mirshokraie S. A., Molaii M.: *BioResources* 4(1), 245 (2009).
5. Mousavi S. M. M., Hosseini S. Z., Resalati H., Mahdavi S., Garmaroody, E. R.: *J. Cleaner Prod.* 52, 420 (2013).
6. Potůček F., Milichovský M.: *Cellul. Chem. Technol.* 45(1–2), 23 (2011).
7. Potůček F., Gurung B., Hájková K.: *Cellul. Chem. Technol.* 48(7–8), 683 (2014).
8. Potůček F.: *Collect. Czech. Chem. Commun.* 62, 626 (1997).
9. Ingmanson W. L.: *Chem. Eng. Prog.* 49(11), 577 (1953).
10. Potůček F., Miklík J.: *Chem. Pap.* 64(2), 147 (2010).
11. Potůček F., Pulcer, M.: *Chem. Pap.* 58(6), 377 (2004).
12. Levenspiel O.: *Chemical Reaction Engineering*, Wiley, New York 1962.
13. Brenner H.: *Chem. Eng. Sci.* 17, 229 (1962).

## INFLUENCE OF CHEMI-MECHANICAL PULP ADDITION TO SECONDARY FIBRES UPON BENDING STIFFNESS

**Potůček F.**, Gurung B., Říhová M.

*University of Pardubice, Faculty of Chemical Technology, Institute of Chemistry and Technology of Macromolecular Materials, 532 10 Pardubice, Czech Republic*  
*frantisek.potucek@upce.cz*

### Abstract

The aim of this study was to investigate bending stiffness characteristics for handsheets made of a blend of secondary fibres and chemi-mechanical pulp from rapeseed straw. To manufacture chemi-mechanical pulp, three cold processes, namely neutral sulphite, alkaline sulphite, and caustic soda, were applied under laboratory conditions. The chemi-mechanical pulping comprises four main operations, viz. chipping, grinding, leaching, and beating. The chemi-mechanical pulp was characterized by its average degree of polymerization which was measured in the range of 75 to 110 with respect to relatively great amount of low molecular substances presented in pulps prepared by cold pulping process. The results obtained showed that the addition of chemi-mechanical pulp to secondary fibres led to a decrease in the bending stiffness, bending modulus of elasticity in the region of reversible deformation, as well as in the maximum curvature in the region of reversible deformation, and in critical curvature in the region of plastic deformation. However, the bending modulus of elasticity and maximum curvature was found to be comparable with those measured for moulded fibre products in our previous studies.

Keywords: rapeseed straw, cold pulping process, secondary fibres, chemi-mechanical pulp, bending stiffness

### Introduction

Nowadays, wood is the dominant resource for pulp and paper production which is increased continuously. However, since wood is not available in sufficient quantities in many countries, alternative new non-wood raw materials such as annual plants and agricultural waste are searched for exploitation as the potential substitution of wood<sup>1</sup>.

Rapeseed is widely cultivated throughout the world and considered as the third most oilseed crop after soybean and palm. Its seeds are basically used for production of edible oil and further utilized in biodiesel production<sup>2</sup>. The influence of European Union's legislation to reach the consumption of biofuel to 10 % of the total at minimum by 2020 has led the production of rapeseed to be doubled in last 10 years<sup>3</sup>. After the harvest of grains, the straw is left in the field as residue and let to be composted or burnt otherwise. Depending upon the irrigation facilities, the total amount of biomass produced varies from 5 to 10 t/ha and approximately 20 % of the rapeseed biomass in the field possesses stem portion<sup>4</sup>. In the Czech Republic, the planted area achieved over 400 thousand hectares. After rapeseed seed collection, the total amount of straw produced per unit area varies from 2.8 to 4.5 t/ha (ref.<sup>5</sup>). However, these agricultural wastes can be utilized as fibrous raw material for pulp and paper production. Fibers from rapeseed straw used as secondary fibers bring better mechanical properties than recycled papers<sup>3</sup>. Moreover, Yousefi<sup>6</sup> has found promising results in utilizing the rapeseed straw pulp in medium density fiberboard.

The objective of the present study was to manufacture chemi-mechanical pulp from rapeseed straw by the cold pulping process at a room temperature under laboratory conditions. For blends of secondary fibres with chemi-mechanical pulp, the bending stiffness, bending modulus of elasticity, maximum curvature in the region of elastic deformation, and critical curvature in the region of plastic deformation were measured using the three-point loading method. The results obtained in this work were compared with those determined for moulded fibre specimens made from secondary fibres only.

### Material and methods

Rapeseed straw (*Brassica napus* L. convar. *napus*, line genotype Labrador) collected from the field in Polabian lowlands near the city of Pardubice was used as a raw material to chemi-mechanical pulping experiments. The stalks and valves of silique were cut manually into small chips having a length of about 20 mm. After drying at 60 °C for 5 hours, the chips of stalks and of silique valves were ground for 20 – 25 s using a laboratory vibrating mill containing a roller and collar in the milling space. Fine mass of accepts retained on +50 mesh size was used for leaching. The samples of fine material to be leached were blends of the stalks and silique valves in a mass ratio of 2:1. Three various cold pulping processes, viz. neutral sulphite, alkaline sulphite and caustic soda, were applied at an active alkali charge of 16 mass % of Na<sub>2</sub>O on oven dry straw. For the liquor-to-straw ratio of 15:1,

the leaching was performed for 18 hours at a temperature of 21 – 23 °C. For comparison, the leaching of a blend of stalks and silique valves into tap water was carried out as well.

After four-stage batch washing, the wet pulp was beaten to 43 – 46 °SR using a laboratory conical beater. The beating degree was measured by the Schopper-Riegler method according to ISO 5267-1 Standard. The suspension of beaten chemi-mechanical pulp was mixed with the secondary fibres obtained by slushing of egg trays in water in a mass ratio of 1:3, and 1:1. Egg trays from Huhtamaki Czech Republic, a. s., were manufactured from a blend of waste papers, namely newspapers, magazine paper, waste corrugated board and non-sorted waste papers. The secondary fibres and chemi-mechanical pulp, as well as their blends were used to prepare pulp hand sheets having basis weight of 520 g m<sup>-2</sup> on a Rapid-Köthen sheet forming machine. To determine the stiffness properties, the stripes, 15 mm in width and 90 mm in length, were cut from the pulp handsheets. Using a TIRA test 26005 device, the bending stiffness was determined by the three-point loading method when the distance between supports was kept at 50 mm (Figure 1). Strength characteristics were measured under a constant room temperature of 23±1 °C and relative humidity of 50±2 %. All the strength measurements were performed at least on 20 replicates per each tested sample. A typical dependence between specimen deflection, *y*, and acting force, *F*, for chemi-mechanical pulp made from rapeseed straw using cold caustic soda process is illustrated in Figure 2.

To characterize chemi-mechanical pulps, the average degree of polymerization was determined by a viscosity test using FeTNa solution, *i. e.*, iron (III) sodium tartrate complex as a solvent for chemi-mechanical pulp according to ISO 5351/2-1981.

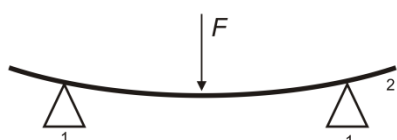


Figure 1. The 3-point loading method.  
1 supports, 2 specimen of pulp sheet

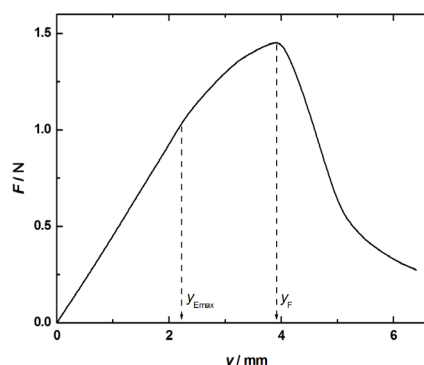


Figure 2. Typical dependence between specimen deflection, *y*, and acting force, *F*, measured for chemi-mechanical pulp hand sheet

## Results and discussion

To characterise chemi-mechanical pulps, the average degree of polymerization of 77, 100, 108, and 112 was determined for mechanical pulp (MP), neutral sulphite, alkaline sulphite, and caustic soda pulps, respectively. The low values of degree of polymerization can be attributed to the presence of low molecular substances, mainly hemicelluloses, in chemi-mechanical pulps (CMP). Moreover, the rapeseed contains short fibres having the average length below 1 mm (ref.<sup>7</sup>).

The influence of adding chemi-mechanical pulp to secondary fibres (SF) upon bending parameters is shown in the following Figures 3 – 6.

The bending stiffness, *S*, as a property of paper and board, which expresses its rigidity or resistance to bending, is defined as

$$S = \frac{Fl^3}{48y} \quad (1)$$

where *F/y* corresponds to the slope in the region of elastic deformation, at low acting forces, when the dependence of the acting force on the deflection is straight, and *l* is the distance between supports<sup>8</sup>.

Bending stiffness as a function of mass fraction of chemi-mechanical pulp in the blend of fibres is illustrated in Figure 3. The results show that the bending stiffness decreases with the addition of chemi-mechanical pulp into secondary fibres. In comparison with secondary fibres, the bending stiffness measured for a blend of secondary fibres and CMP in a mass ratio of 1:1 was lower by nearly 30 %. For a blend with 25 % of CMP, the bending

stiffness of handsheets containing MP and CMP after cold caustic soda process is greater than that of pulp containing CMP after cold neutral sulphite and alkaline sulphite processes.

However, it is known that the bending stiffness increases strongly with increasing the thickness of test specimen,  $h$ , theoretically with the third power of pulp sheet thickness, *e. g.*, Potůček *et al.*<sup>8</sup> found that  $S \approx h^{2.81}$  and  $S \approx h^{3.11}$  for moulded fibre products, depending on manufacturing conditions. Hence, the bending stiffness results depend not only on composition of stock used for handsheets, but also on their thickness. While for secondary fibres the thickness of hand sheet was only 0.88 mm, the addition of 25 % and of 50 % of CMP to the secondary fibres stock brought an increase in handsheet thickness of 0.96 to 1.16 mm, and of 1.00 to 1.43 mm, respectively. It should be noted that, for both charge of CMP, the thickness of hand sheet increased in the following order, *viz.* of caustic soda pulp < alkaline sulphite pulp < neutral sulphite pulp < mechanical pulp made after water leaching process. Furthermore, it is worth mentioning that pulp handsheets made from blends of secondary fibres and chemi-mechanical pulp had a much higher bulk in comparison with hand sheets made from secondary fibres only.

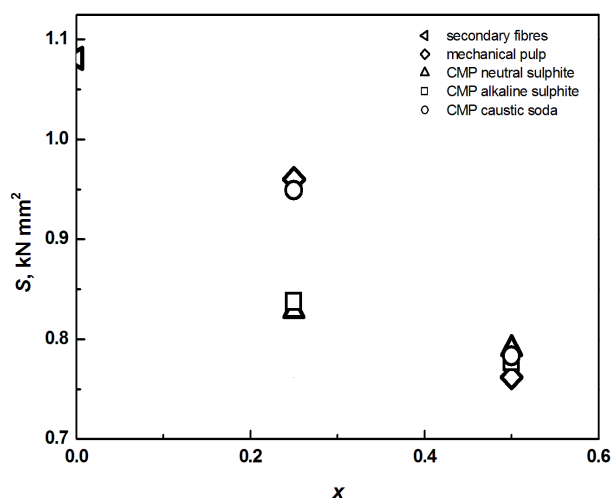


Figure 3. Influence of mass fraction of CMP,  $x$ , on the bending stiffness,  $S$

The bending modulus of elasticity in the region of reversible deformation,  $E$ , is defined as

$$E = \frac{Fl^3}{4yb h^3} \quad (2)$$

where  $b$  is the specimen width,  $h$  is the specimen thickness, and the meaning of other symbols is the same as in equation (1). Thus, Equation (2) may be written as  $E = 12 S / (b h^3)$ . Our previous results<sup>9</sup> show that the bending modulus of elasticity is not appreciably different for groundwood specimens with various thicknesses.

The influence of the presence of CMP in a blend with secondary fibres on the bending modulus of elasticity is shown in Figure 4. It is evident that the bending modulus of elasticity decreases with increasing the mass fraction of CMP and MP. The greatest values of the bending modulus were measured for a blend of secondary fibres with caustic soda chemi-mechanical pulp. On the contrary, the lowest values of the bending modulus were achieved for neutral sulphite chemi-mechanical pulp in a blend with secondary fibres at both levels of CMP addition.

The maximum curvature in the region of reversible deformation,  $C_E$ , defined by the following relationship

$$C_E = \frac{12 y_{E_{\max}}}{l^2} \quad (3)$$

is plotted against the mass fraction of CMP in Figure 5.

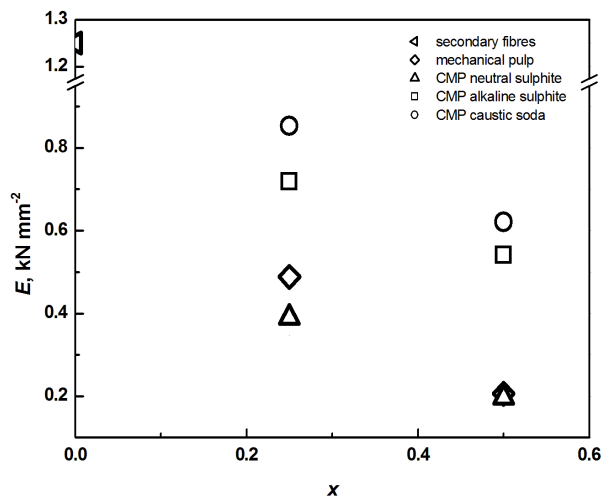


Figure 4. Influence of mass fraction of CMP,  $x$ , on the bending modulus of elasticity,  $E$ , in the region of reversible deformation

Comparing with the secondary fibres, the lower values of the maximum curvature in the region of elastic deformation were measured for pulp handsheets prepared from a blend of secondary fibres with addition of CMP or MP. The pulp handsheets prepared from a blend of secondary fibres with addition of CMP or MP were less elastic in comparison with sheets from secondary fibres only. However, the influence of CMP addition is ambiguous. Increasing increment of CMP led to an increase in the maximum curvature for MP and CMP made by cold caustic soda process. On the contrary, the maximum curvature was not influenced by the different amount of neutral sulphite CMP added to secondary fibres, while for alkaline sulphite pulp addition the maximum curvature decreased with increasing amount of CMP in a blend with secondary fibres.

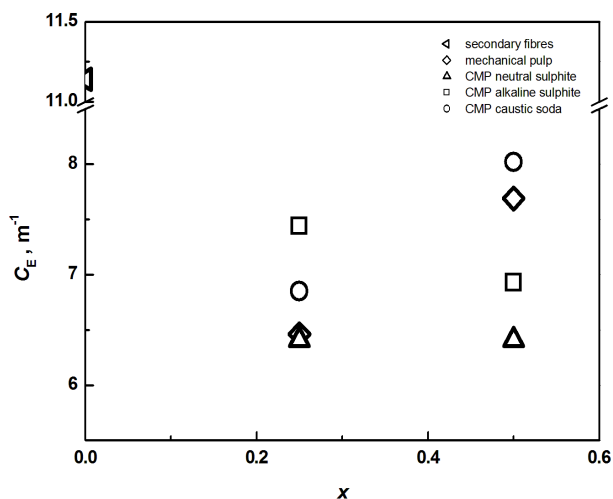


Figure 5. Maximum curvature,  $C_E$ , in the region of reversible deformation as a function of mass fraction of CMP

The influence of CMP addition on the critical curvature for tensile crack is illustrated in Figure 6. The critical curvature,  $C_F$ , is given by the following equation

$$C_F = \frac{12 y_F}{l^2} \quad (4)$$

Tensile crack occurs in the region of irreversible or plastic deformation and is evident in the convex side of specimen below the neutral plane.

For MP, alkaline sulphite and caustic soda CMP, the quantity of the critical curvature was found to increase with their increment in secondary fibres. However, the greatest values of the critical curvature were measured for neutral sulphite CMP addition in the secondary fibres even if the critical curvature slightly decreases with increasing amount of CMP. In spite of this fact, the addition of MP and CMP had a positive impact on the critical curvature of pulp handsheets which were less fragile in comparison with those made from secondary fibres only.

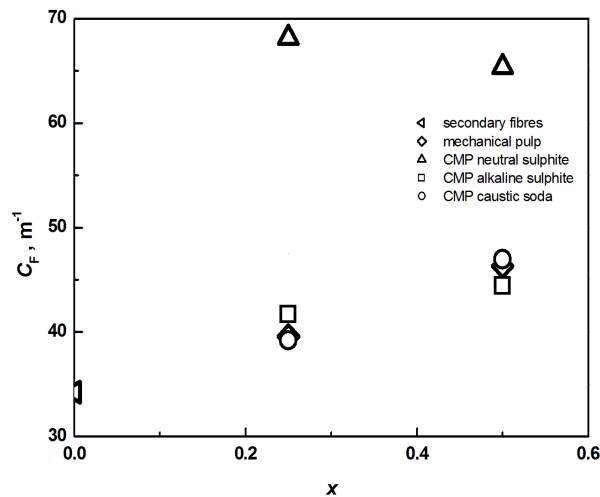


Figure 6. Curvature for tensile crack,  $C_F$ , as a function of mass fraction of CMP

Finally, the results obtained in this study were compared with those measured for specimens made from moulded fibre products with basis weight of 360 to 620  $g\ m^{-2}$  in the previous paper<sup>8</sup>. It showed that the bending modulus of elasticity for pulp sheets from a blend of secondary fibres and MP or CMP (Figure 4) is comparable with that of 0.18 to 0.56  $kN\ mm^{-2}$  determined for moulded fibre specimens having the thickness of around 1 mm, while the maximum curvature in the region of reversible deformation (Figure 5) is comparable with that ranging from 5.2 to 8.2  $m^{-1}$  for moulded fibre specimens with the thickness close to 2 mm.

### Conclusion

The preliminary results obtained in the scope of our study proved that, the addition of chemi-mechanical pulp prepared by the three cold processes to secondary fibres led to a decrease in bending stiffness properties. Nevertheless, the results showed that the bending modulus of elasticity, as well as the maximum curvature in the region of elastic deformation are comparable to those measured for moulded fibre specimens in the previous paper<sup>8</sup>. With respect to current knowledge on chemi-mechanical pulping of rapeseed straw, further studies should be developed to confirm the suitability of rapeseed as a future non-wood fibre source.

### Acknowledgements

*This work was supported by the Internal Grant Agency of University of Pardubice under the research project SGFChT04/2014.*

### Symbols

$b$	specimen width, mm
$C_E$	maximum curvature in the region of elastic deformation, $m^{-1}$
$C_F$	critical curvature in the region of plastic deformation, $m^{-1}$
$E$	bending modulus in the region of elastic deformation, $N\ mm^{-2}$
$F$	force, N
$h$	thickness of specimen, mm
$l$	distance between two support points, mm
$S$	bending stiffness, $N\ mm^2$
$y$	deflection, mm
$y_{E_{max}}$	maximum deflection in the region of reversible deformation, mm

$y_F$  deflection attained in the region of non-reversible deformation where tensile crack occurs, mm

#### Abbreviations

CMP chemi-mechanical pulp  
MP mechanical pulp  
SF secondary fibres

#### Literature

1. Gurung B., Potůček F.: *Pap. Celul.* 68(5), 147 (2013).
2. Potůček F., Milichovský M.: *Cellul. Chem. Technol.* 45(1–2), 23 (2011).
3. González I., Alacalá M., Arbat G., Vilaseca F., Mutjè P.: *BioResources* 8(2), 1697 (2013).
4. Samariha A., Kasmani J. E., Kiaei M., Shurmasti D. K.: *World Appl. Sci. J.* 13(5), 1000 (2011).
5. Petříková V.: *Plants for energy purposes* (in Czech), p. 34, Česká energetická agentura, Praha, 1999.
6. Yousefi H.: *Waste management*, 29(10), 2644, (2009).
7. Potůček F., Gurung B., Hájková K.: *Cellul. Chem. Technol.* 48(7–8), 683 (2014).
8. Potůček F., Češek B., Domin P., Milichovský M.: *Cellul. Chem. Technol.* 41(4–6), 277 (2007).
9. Potůček F., Češek B., Milichovský M.: *Cellul. Chem. Technol.* 42(7–8), 413 (2008).

## CONDUCTIVE POLYMERS IN PROTECTIVE COATINGS

**Kalendová A.**, Hájková T.

*Faculty of Chemical Technology, University of Pardubice, 532 532, Pardubice, Czech Republic  
Andrea.kalendova@upce.cz*

### Abstract

The use of conductive polymers in protective organic coatings was studied. The conductive polymers were represented by polyaniline phosphate (PANI) and polypyrrole (PPY), which are potential metal corrosion inhibitors. The polymers were used in the form of active layers on inorganic pigments – CaTiO<sub>3</sub> and TiO<sub>2</sub> mixed oxides – and the effect of surface treatment with PANI and PPY on the properties of the pigment particles, in particular on the corrosion resistance of protective organic coatings pigmented with them, was investigated. The coatings were formulated by using modified alkyd resin as the binder. The anticorrosion efficiency of the surface treated pigments was evaluated based on the results of corrosion tests of the pigmented coatings exposed to a sodium chloride solution (mist). The results indicate a good anticorrosion efficiency of coatings with low pigment volume concentrations. Polypyrrole was found to be superior to polyaniline phosphate from the anticorrosion efficiency aspect.

### Key words

Conductive polymer, corrosion, coating, pigment.

### Introduction

The use of conductive polymers is a promising option in the protection of metals by using anticorrosion coatings. They appear to be suitable substitutes for heavy metal-containing corrosion inhibitors. Among the organic materials are, for instance, polyaniline, polypyrrole, polyphenylene and polythiophene. Such materials have been extensively studied and new and new areas are identified for their application. The feasibility of pigment surface treatment with polyaniline and polypyrrole was also examined in this work.

The use properties of conductive polymers in a number of applications can be extended by preparing composite particles of pigments and fillers coated with layers of such substances. Polyaniline as a conductive polymer has been known for many years.<sup>1</sup> It is classed among electrochemically and electrically active corrosion inhibitors, most frequently used in the powder form as a pigment. Both polyaniline and polypyrrole are prepared by chemical polymerization oxidation.<sup>2</sup>

The use of composites (composite materials used as composite pigments) consisting of inorganic particles coated with layers of a conductive polymer in paints intended for corrosion protection of metals appears to be promising.<sup>3,4</sup> The polymer's conductive property, however, must be maintained. For polyaniline phosphate and polypyrrole this means that the environment must be slightly acidic. Polyaniline exists basically in five species differing in their chemical structure, stability, electrochemical properties, colour, and oxidation/protonation state. By contrast, polypyrrole exists in one species only.<sup>5,6</sup>

Two titanium (Ti) based mixed pigments were selected to examine the anticorrosion efficiency of the organic materials: perovskite CaTiO<sub>3</sub> and commercially available neutral rutile type TiO<sub>2</sub> pigment. Perovskites derive from a natural material, viz. crystalline calcium titanate with very diverse impurities, e.g. rare earth elements such as Ta, Zr and Nb.<sup>7</sup>

### Experimental

*Synthesis of the mixed metal oxide based pigments and their surface coating with layers of a conductive polymer*

The conductive layer was prepared by polymerization on the pigment surface in laboratory conditions. Aniline or pyrrole was dispersed in phosphoric acid and the pigment was added. A potassium peroxodisulfate solution was prepared and after perfect dissolution, the two solutions were combined to initiate the polymerization reaction. The system was stirred for 1 hour, after which the product was allowed to stand in the beaker overnight. The next day the solution was filtered on a Büchner funnel in air. The product on the funnel, i.e. the pigment coated with a layer of the conductive polymer, was rinsed first with dilute phosphoric acid in order to remove low-molecular-weight products and then with acetone to facilitate drying. The rinsed product was

dried in air for 24 hours and then in a drier at 105 °C to constant weight. The basic properties of the pigments, i.e. density, oil number, critical pigment volume concentration (CPVC), pH, and conductivity of aqueous extracts of the pigments, determined by standard procedures, are listed in Table I.

Table I

Physico-chemical properties of the bare pigments and pigments coated with the conductive polymer

Properties	Density [g/cm <sup>3</sup> ]	Oil consumption [g ol./100g pig.]	KOKP	pH [21.days]	Spec. elec. conductivity [μS/cm]
CaTiO <sub>3</sub>	3.613	26.55	49.22	11.52	5620
TiO <sub>2</sub>	3.8539	18.37	56.78	6.58	190
CaTiO <sub>3</sub> /PANI	2.9881	24.33	56.13	5.02	3050
TiO <sub>2</sub> /PANI	2.9400	21.68	59.33	6.84	1640
CaTiO <sub>3</sub> /PPY	3.3052	33.48	45.66	3.89	5280
TiO <sub>2</sub> /PPY	3.1944	27.67	51.27	3.45	4720

#### Formulation and preparation of the model paints

The model paints were based on an alkyd resin modified with soy oil. The paints with no surface treatment were formulated to possess pigment volume concentrations (PVC) 1%, 3%, 5%, 10%, 15%, 20%, 30%, 40%, and 50% and the critical pigment volume concentration (CPVC). The pigments coated with a thin layer of polyaniline were formulated to PVC = 1%, 3%, 5%, 10%, 30%, and CPVC. The constant PVC to CPVC ratio in the paints was modified with a silicate type filler whose trade name is Plastorit. Plastorit Micro is a mix of mica, quartz and chlorite.

#### Preparation of steel panels coated with the paint

The paints were applied to stainless steel panels (deep-drawing cold-rolled Class 11 steel). A vertical cut 10 cm long was made on the steel panels coated with the crosslinked paint films for comparison with the behaviour of an undisturbed paint film.

#### Accelerated cyclic corrosion test in neutral salt mist

This test was performed in accordance with ČSN ISO 92 27 in order to simulate seaside weather conditions or roads with winter salt treatment. The test samples were exposed to a 5% NaCl mist at 35 ± 1°C for 1000 hours. The corrosion effects were examined after the tests.

The parameters evaluated included the degree of blistering in the paint area and in the paint film cut (ASTM D 714 87), metal corrosion in the cut (ASTM D 1654-92), and degree of corrosion of the painted steel surface (ASTM D 610-85).

#### Determination of the degree of metal surface corrosion

The corrosion effects were evaluated by the method described in ASTM D 610-85. After evaluation, the panels were submerged in a 10% NaOH solution for 24 hours in order to remove the paint, rinsed with distilled water, wiped with chloroform, and newly evaluated by the same procedure.

#### Overall evaluation of the accelerated corrosion tests

The above methods of evaluation of the corrosion effects on the metal surface and on the film itself were combined in order to obtain a combined overall protective efficiency indicator.

The following formula was used (1):

$$\text{Overall anticorrosion efficiency} = \frac{A+B+C+D}{4} \quad (1)$$

where A is the degree of blistering in the paint film surface

B is the degree of blistering in the paint film cut

C is the degree of metal surface corrosion

D is the degree of corrosion in the cut on the metal substrate

## Results and discussion

Results of the accelerated corrosion test of the painted panels with a vertical cut

A single paint layer whose dry film thickness was 65±10 μm was prepared on the steel panel (the paint film thickness plays a role in the corrosion tests [8]). The panels with the paint films in which a vertical cut had been made were exposed to the salt mist for 1000 hours, after which the corrosion effects were evaluated.

Osmotic blisters in the cut were observed for the TiO<sub>2</sub> paint films with PVC = 20%, 30%, and 40%. Blisters on the surface were observed for all the TiO<sub>2</sub> paint films except for PVC = 3% and 15%.

Corrosion on the metal surface attained largely 50% or more. The best results were obtained with paints containing PPY or PANI at PVC= 5%,10% and 15%.

The paint with the surface-untreated TiO<sub>2</sub> at PVC = 20%, 30%, and 40 % exhibited a mere 20% overall anticorrosion efficiency whereas the remaining paints reached about 60%.

Evaluation of corrosion of painted panels after 1000 hours' exposure to salt mist

Table II

Results of the accelerated corrosion test in a salt chamber: steel panels with films of paint containing CaTiO<sub>3</sub> pigment, DFT = 65 ± 10 μm

Pigment	Blister in the cut	Blister in paint film	Corrosion in the cut [mm]	Surface corrosion [%]	Overall anticorrosion efficiency
1% CaTiO <sub>3</sub>	0	0	5	33	58
3% CaTiO <sub>3</sub>	0	0	5	10	68
5% CaTiO <sub>3</sub>	0	0	5	10	68
10% CaTiO <sub>3</sub>	0	0	5	>50	53
15% CaTiO <sub>3</sub>	0	0	5	50	55
20% CaTiO <sub>3</sub>	0	0	5	50	55
30% CaTiO <sub>3</sub>	0	0	5	>50	55
40% CaTiO <sub>3</sub>	0	0	5	50	53
49% CaTiO <sub>3</sub>	0	0	5	>50	53
55% CaTiO <sub>3</sub>	0	0	5	>50	56

Table III

Results of the accelerated corrosion test in a salt chamber: steel panels with films of paint containing TiO<sub>2</sub> pigment, DFT = 65 ± 10 μm

Pigment	Blister in the cut	Blister in paint film	Corrosion in the cut [mm]	Substrate corrosion [%]	Overall anticorrosion efficiency
1% TiO <sub>2</sub>	0	8M	5	33	48
3% TiO <sub>2</sub>	0	0	5	33	58
5% TiO <sub>2</sub>	0	2F	5	16	54
10% TiO <sub>2</sub>	0	2F	5	16	54
15% TiO <sub>2</sub>	0	0	5	16	63
20% TiO <sub>2</sub>	2MD	2MD	5	33	20
30% TiO <sub>2</sub>	6D	2M	5	>50	18
40% TiO <sub>2</sub>	2MD	2M	4	>50	24
50% TiO <sub>2</sub>	0	2M	5	>50	39
56% TiO <sub>2</sub>	0	6MD	5	>50	36
60% TiO <sub>2</sub>	0	2MD	5	>50	34

Table IV

Results of the accelerated corrosion test in a salt chamber: steel panels with films of paint containing CaTiO<sub>3</sub>/PANI pigment, DFT = 65 ± 10 μm

Pigment	Blister in the cut	Blister in paint film	Corrosion in the cut [mm]	Substrate corrosion [%]	Overall anticorrosion efficiency
1% CaTiO <sub>3</sub> /PANI	0	0	5	16	63
3% CaTiO <sub>3</sub> /PANI	0	0	5	10	68
5% CaTiO <sub>3</sub> /PANI	0	0	5	10	68
10% CaTiO <sub>3</sub> /PANI	0	0	5	16	63
30% CaTiO <sub>3</sub> /PANI	0	0	5	33	58
56% CaTiO <sub>3</sub> /PANI	0	0	5	>50	53

Table V

Results of the accelerated corrosion test in a salt chamber: steel panels with films of paint containing TiO<sub>2</sub>/PANI pigment, DFT = 65 ± 10 μm

Pigment	Blister in the cut	Blister in paint film	Corrosion in the cut [mm]	Substrate corrosion [%]	Overall anticorrosion efficiency
1% TiO <sub>2</sub> /PANI	0	0	5	16	63
3% TiO <sub>2</sub> /PANI	0	0	5	10	68
5% TiO <sub>2</sub> /PANI	0	0	5	10	68
10% TiO <sub>2</sub> /PANI	0	0	5	33	58
30% TiO <sub>2</sub> /PANI	0	0	5	>50	53
59% TiO <sub>2</sub> /PANI	0	0	5	>50	53

Table VI

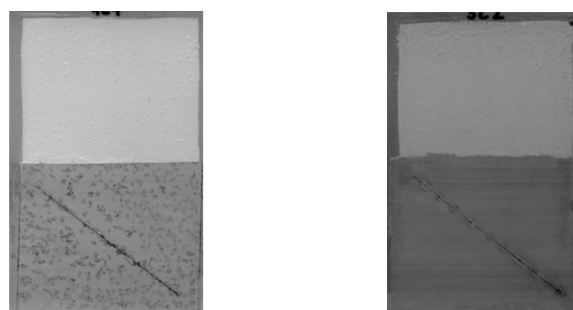
Results of the accelerated corrosion test in a salt chamber: steel panels with films of paint containing CaTiO<sub>3</sub>/PPY pigment, DFT = 65 ± 10 μm

Pigment	Blister in the cut	Blister in paint film	Corrosion in the cut [mm]	Substrate corrosion [%]	Overall anticorrosion efficiency
1% CaTiO <sub>3</sub> /PPY	0	0	5	16	63
3% CaTiO <sub>3</sub> /PPY	0	0	5	10	68
5% CaTiO <sub>3</sub> /PPY	0	0	5	3	70
10% CaTiO <sub>3</sub> /PPY	0	0	5	10	68
30% CaTiO <sub>3</sub> /PPY	0	0	5	16	63
46% CaTiO <sub>3</sub> /PPY	0	0	5	>50	53

Table VII

Results of the accelerated corrosion test in a salt chamber: steel panels with films of paint containing TiO<sub>2</sub>/PPY pigment, DFT = 65 ± 10 μm

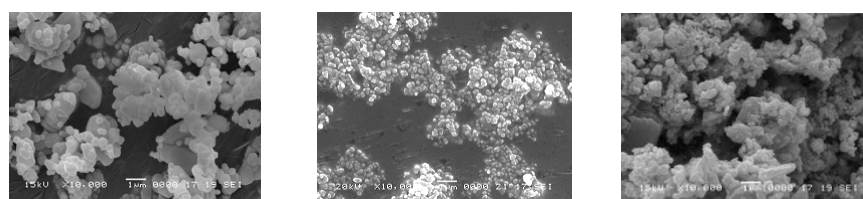
Pigment	Blister in the cut	Blister in paint film	Corrosion in the cut [mm]	Substrate corrosion [%]	Overall anticorrosion efficiency
1% TiO <sub>2</sub> /PPY	0	0	5	16	63
3% TiO <sub>2</sub> /PPY	0	0	5	10	68
5% TiO <sub>2</sub> /PPY	0	0	5	10	68
10% TiO <sub>2</sub> /PPY	0	0	5	10	68
30% TiO <sub>2</sub> /PPY	0	0	5	33	58
51% TiO <sub>2</sub> /PPY	0	0	5	>50	53



a) TiO<sub>2</sub> (OKP = 30%)

b) CaTiO<sub>3</sub> (5%)

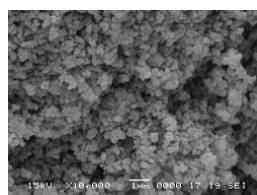
Figure 1. Photographs of panels coated with selected paints and exposed to an atmosphere with NaCl mist after 1000 hours. In each photograph, the top part shows the condition of the paint film, while the bottom part shows the condition of the substrate metal after removing the coating.



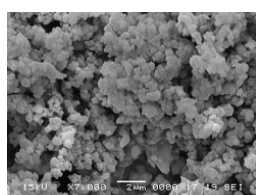
a) particles CaTiO<sub>3</sub>

b) particles TiO<sub>2</sub>

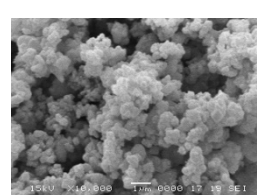
c) particles CaTiO<sub>3</sub>/PANI



d) particles TiO<sub>2</sub>/PPY



e) particles CaTiO<sub>3</sub>/PPY



f) particles TiO<sub>2</sub>/PPY

Figure 2. SEM photographs, magnification 10 000x

## Conclusion

The properties of pigments whose surface had been treated with polyaniline (PANI) and polypyrrole (PPY) were studied. Two pigments possessing different structures, viz. perovskite  $\text{CaTiO}_3$  and the white  $\text{TiO}_2$ , were used. An alkyd resin served as the coating material binder, the filler was the commercially available Plastorit Micro. Different pigment concentrations were used, and the results obtained with the coated pigments were compared with those for the untreated pigments. Perovskite  $\text{CaTiO}_3$  was classed as an anticorrosion pigment,  $\text{TiO}_2$  (rutile), as a barrier pigment. A total of 45 concentration series of the pigments were prepared. All paints were subjected to 1000 hours' exposure to a salt mist in a test chamber (accelerated corrosion test). Mechanical test were also performed on the painted steel panels, and improved flexibility was observed with all the model films. The anticorrosion efficiency of the paints was found to depend on the pigment volume concentration. The best results with respect to anticorrosion efficiency were obtained with paints containing the pigments at low concentrations, i.e. PVC = 1% to 5%.  $\text{CaTiO}_3$  as the pigment proved to be superior to  $\text{TiO}_2$ , both in the surface-treated and untreated forms.

## Literature

1. Tüken T., Yazıcı B., Erbil M.: Prog. Org. Coat., 50, 115–122 (2004).
2. Armelin E., Pla R., Liesa F., Ramis X., Iribarren J.I., Alemán C.: Corros. Sci., 50, 721–728 (2008).
3. Sathiyarayanan S., Syed Azim S., Venkatachari G.: Electrochim. Acta, 52, 2068–2074 (2007).
4. Brodinová J., Stejskal J., Kalendová A.: J. Phys. Chem. Solids, 68, 1091–1095 (2007).
5. Prokeš J., Nešpůrek S., Stejskal J.: Vesmír 80, 35 – 38 (2001).
6. Prokeš J., Stejskal J., Omastková M.: Chemické listy 95, 484 – 492 (2001).
7. Ramadass N.:  $\text{ABO}_3$  – type oxides, Their structure and properties: A Bird's Eye View, Material Science and Engineering, , 231-239 (1978).
8. Stejskal J., Kratochvíl P., Jenkins A.D.: Collect. Czech. Chem. Commun. 60, 1747-1755 (1995).

## THE SATURATED VAPORS OF SELECTED COMPONENTS OF ESSENTIAL OILS AND ITS INFLUENCE ON THE PROPERTIES OF THE LIGNOCELLULOSE MATERIALS

**Mikala O.**, Gojný J., Milichovský M., Hájek M.

*University of Pardubice, Faculty of Chemical Technology, Institute of Chemistry and Technology of Macromolecular Materials, Department of Wood, Pulp and Paper, Studentská 95, 532 10, Pardubice  
ondrej.mikala@gmail.com*

### Abstract

The aging process of cellulose and lignocellulose materials is done by several ways. Some examples could be the hydrolytic cleavage of glycoside bonds, oxidation, photo-oxidation, photolysis and biological attack. The biological attack on cellulose and lignocellulose materials can be caused by bacteria or fungi (moulds). This work is focused on the possibility of using vapours of the selected essential oils or their components to protecting archival materials against biological attacks. Essential oils with the highest bactericidal activity were used. Before use in a real environment, it was necessary to prove whether vapours of these active compounds do not degrade cellulose and lignocellulose materials in the library depositories. For testing of properties after the exposition in saturated vapours of the active compounds were selected sheets based on the following materials: coniferous sulphate pulp, deciduous sulphate pulp, sulphite pulp, groundwood and pulp for the production of handmade paper.

### Introduction

To apply the correct protective mediums and procedures in an effort to rescue historical materials based on cellulose and lignocellulose materials is important to know the following degradation processes. Damage of paper materials occurs by hydrolysis of glycosidic bonds, oxidation, photo-oxidation and photolysis and also may be caused by biological attack of microorganisms. During degradation process are monitored correlations between paper properties (optical or mechanical) and structural or microscopic characteristics of materials in the paper (degree change of polymerization of cellulose, increasing the proportion of low molecular weight fractions)<sup>1, 2, 3, 4, 5</sup>.

Among the microorganisms that most frequently attack the paper-based materials include *Aspergillus fumigatus*, *Aspergillus niger* and *Penicillium* genus. In nature, plants prevent from infestation by microorganisms by production of essences (essential oils). Essential oils (EO) are complex mixtures of substances, consisting most often terpenes and derivatives thereof, hydrocarbons, alcohols, aldehydes, ketones and carboxylic acids. The use of EO for protection against microorganisms appears to be an alternative to synthetic fungicidal agents<sup>6, 7</sup>. Antimicrobial effects of EO are associated with hydrophilic and lipophilic properties of EO or rather its components, as they are described in a work by Kalemba<sup>8</sup>. Competitive absorption processes for condensation of water and EO in the pores of cellulose and lignocellulose materials are described in article by Češek et al<sup>6</sup>. Bactericidal effects of different EO have been demonstrated in several studies<sup>9</sup>. Bactericidal activity of components EO of eucalyptus was tested by Elaissi et al<sup>10</sup>. Main constituents of EO were determined eucalyptol,  $\alpha$ -pinene, p-cymene and limonene. Mechanism of *Escherichia coli* deactivation using limonene and terpenes from the EO is described by Chueca et al<sup>11</sup>. Bacteriostatic and bactericidal activity of EO of two kinds of sage (*Salvia officinalis*, *Salvia triloba*), growing in southern Brazil, is devoted to the study of Delamare et al<sup>12</sup>. Main components of the EO are eucalyptol, camphor, borneol and  $\beta$ -pinene.

This study is aimed at investigation the effect of saturated vapour mixtures of five components of essential oils and two pure EO on cellulose and lignocellulose materials. This part of the research was focused on monitoring of mechanical properties (represented by bending stiffness and compressive strength) and changes in optical properties. Verification of saturated vapours of substances from EO on mechanical or optical properties on the paper pad can be further used in the library depositories. This application could reduce the risk of microbial infestation of archival documents.

### Materials and Methodics

Lignocellulose material:

In order to best simulate the real printed matter stored in archives, 5 lignocellulose materials which are commonly used in the paper and printing industry, have been chosen for testing. These are:

- 1) SaL – deciduous sulphate pulp from Ružomberok, the beating degree 25 °SR
- 2) SaJ – coniferous sulphate pulp from Štětí, the beating degree 25 °SR
- 3) Si – sulfite pulp from Biocel Paskov, the beating degree 25 °SR

- 4) RP – the raw material for the production of handmade paper of the Velké Losiny, consists of 60% cotton linters and 40% of pulp of flax, the beating degree from 28 – 29 °SR  
 5) DS – groundwood with the addition of 10% of sulphite pulp, as described above.

#### Components of essential oils:

Five components of EO and two EO with the highest microbicide effect have been chosen for testing. Microbicide effectiveness was tested on microorganisms *Aspergillus brasiliensis*, *Penicillium aurantiogriseum ex-niger*, and *Cladosporium cladosporioides*. The components of essential oils and two EO are shown in table 1.

**Tab. 1 Used components of essential oils and essential oils**

Mixture No.	Components
1	$\alpha$ -pinene, camphene, $\beta$ -pinene, myrcene
2	limonene, eucalyptol, ocimene
3	linalool, linalyl acetate, camphor
4	$\alpha$ -phellandrene, 1,4-cineole, $\alpha$ -terpinene, cymene
5	$\gamma$ -terpinene, terpinolene, $\alpha$ -terpineol
6	<i>Lavandula angustifolia</i>
7	<i>Citrus aurantifolia</i>

#### Description of the apparatus:

The apparatus was composed of seven desiccators. A relative humidity of 75% using saturated solution of NaCl was maintained inside. Inside each desiccator was placed Petri dish with 2.5 ml of mixture no. 1-7 and after 40 days of exposure has been completed with a further 2.5 ml of fresh mixture thereof. Samples of cellulose and lignocellulose materials were exposed to saturated vapours of substances no. 1-7 for 40 and 80 days.

#### Determination of mechanical properties:

Sheets with basis weight about  $400 \text{ g m}^{-2}$  have been prepared from 5 fibrous materials on Rapid-Köthen – Sheet former. The sheets were cut to yield test samples measuring  $15 \times 100 \text{ mm}$  and a thickness was also measured. After 40 days of expiry half of the samples have been removed while the other half of the samples continued experiment for the next 40 days.

The bending stiffness of the exposed and comparative samples was measured by the 3-point method (Fig. 1) (always at least 10 times) using TIRAtest 26005 equipment. The distance between the supports was set at 50 mm. The bottom part of the sample is exposed to traction and the upper part to pressure forces. From the deflection curve (Figure 2) there has been determined the slope of the linear portion of the curve  $F/\delta \text{ (N mm}^{-1}\text{)}$  and maximum deflection at the end of the reversible deformation  $\delta_{\text{max}} \text{ (mm)}$ .

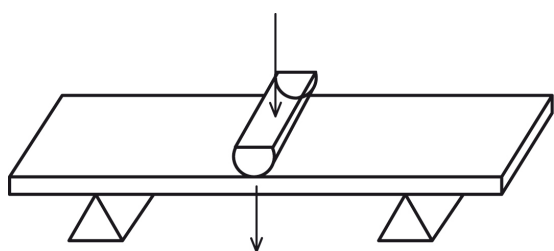


**Fig. 1 The 3-point bending stiffness method**

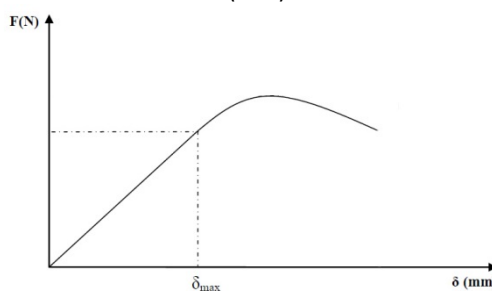


**Fig. 2 Deflection curve**

Parameters obtained from the deflection curve are used to calculate the bending stiffness  $T \text{ (N mm}^2\text{)}$  according to equation 1,

$$T = \frac{F}{\delta} \cdot \frac{l^3}{48} \quad (1)$$

where  $F/\delta \text{ (N mm}^{-1}\text{)}$  is the linear portion of the curve and the  $l$  is distance between the supports. A standard bending stiffness  $T_0 \text{ (N mm}^2\text{)}$  eliminates the influence of different material thickness and shall be calculated according to equation 2,

$$T_0 = T \cdot \frac{t_0^3}{t^3} \quad (2)$$

where  $t_0$  is the standard sample thickness of 1 mm and  $t$  is the thickness of the measured sample.

Compressive strength – SCT (ISO 9895:2008)

A test piece, 15 mm wide, is clamped between two clamps, mutually spaced 0.7 mm (fig. 3), which are forced towards each other until a compressive failure occurs. The maximum force is measured and the compressive strength (kN m) is calculated from Equation 3.

$$\sigma_C^b = \frac{\bar{F}_C}{b} \quad (3)$$

Where  $\bar{F}_C$  (N) is the mean maximum compressive force and  $b$  (mm) is the initial width of the test piece. If required, calculate the compressive index (kN m kg<sup>-1</sup>) from Equation 4.

$$\sigma_C^g = \frac{1000 \times \sigma_C^b}{g} \quad (4)$$

Where  $\sigma_C^b$  (kN m) is compressive strength and  $g$  (g m<sup>-2</sup>) is grammage.

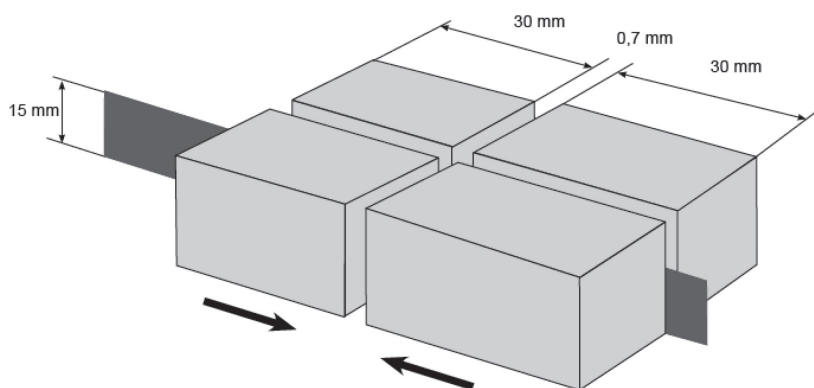


**Fig. 3 Compressive strength clamps**

Determination of optical properties:

Optical properties of samples before and after exposure to the vapours of saturated components of essential oils have been measured (always at least 5 times) by the spectrophotometer Elrepho Lorentzen & Wettre Company. The ISO brightness was measured at D65 illumination and L\* a\* b\* coordinates were determined from which, the colour difference  $\Delta E^*$  from the unexposed sample has been calculated (Equation 5).

$$\Delta E_{ab}^* = \sqrt{\Delta L^{*2} + \Delta a^{*2} + \Delta b^{*2}} \quad (5)$$

The scale of colour difference is given in table 2.

**Tab. 2 Scale of colour difference  $\Delta E^*$**

$\Delta E^*$	The Difference
0.0 to 0.2	imperceptible
0.2 to 0.5	very weak
0.5 to 1.5	weak
1.5 to 3.0	clearly perceivable
3.0 to 6.0	medium
6.0 to 12.0	significant
12.0 to 16.0	very significant
greater than 16.0	interfering

## Results and Discussion

In order to present the rigidity results the standard bending stiffness  $T_0$  was chosen, because it eliminates the influence of the sample thickness. Picture 4a is evident (see fig. 4a) that samples made of groundwood were more susceptible to saturated vapours. The stiffness of these samples decreased after 80 days exposure by an average of 41%, no one environment appeared to be significantly destructive. In case of RP materials (fig. 4b), stiffness increased just slightly by an average of 16%. Data in figs. 4c and 4d show no significant decrease in rigidity (maximum change was 10%). Due to the significant dispersion of measurements (confidence interval 95%), a maintenance of original properties of samples can be considered. Because of the lack of material samples of SaJ, measurements were taken only after 80 days of exposure. Figure 4e shows no significant change in stiffness.

Measurement of compressive strength confirmed deterioration of mechanical properties particularly in DS material (fig. 5a). The material for the production of hand-made paper (fig. 5b) had decreased compressive index on average by 8% after 80 days of exposure. Mechanical properties of materials Si and SaL (fig. 5c, 5d) decreased approximately by 12% or more precisely by 15%. A similar decline occurred even in SaJ material (fig. 5e).

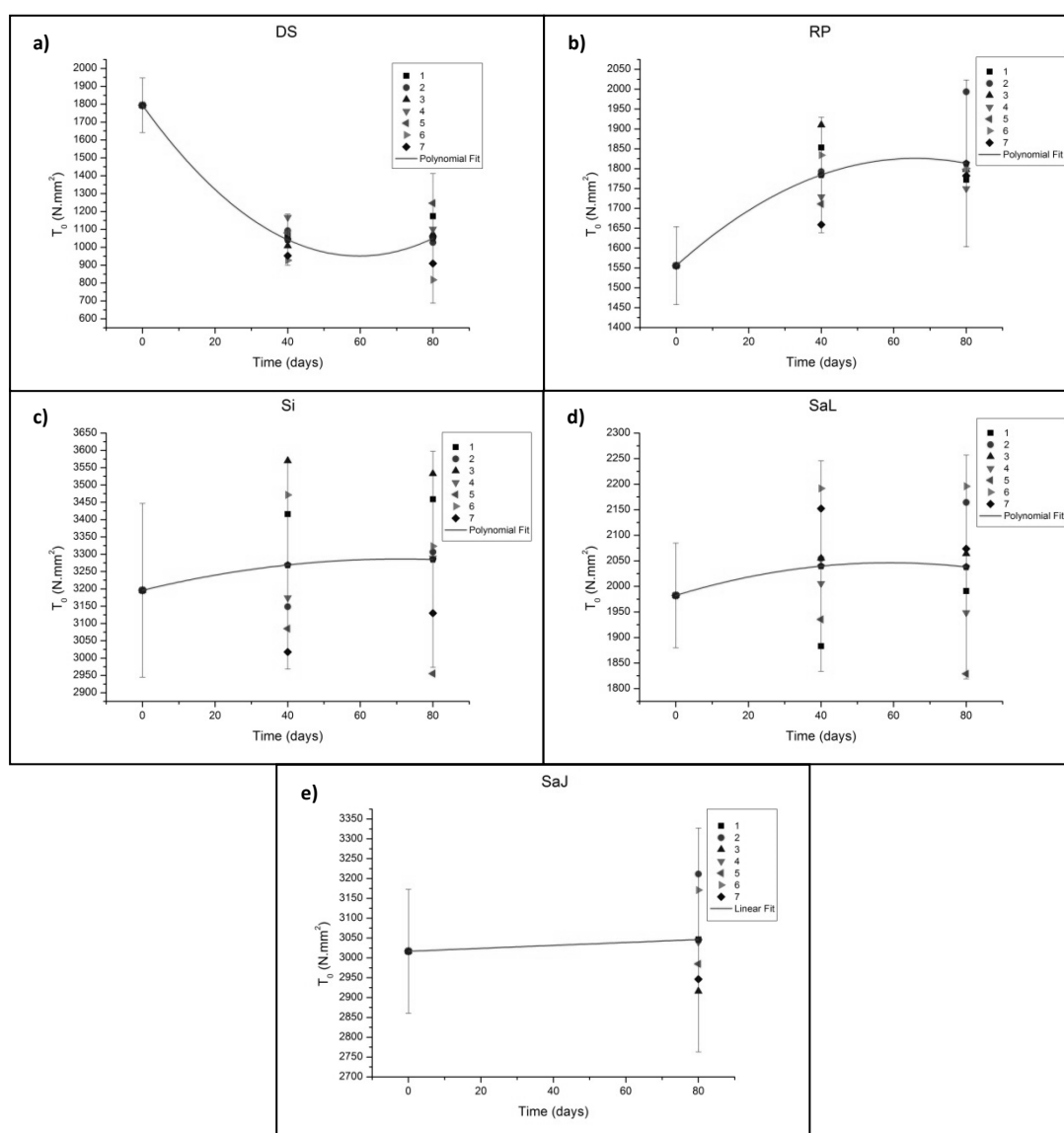


Fig. 4 Dependence of bending stiffness per thickness unit of samples (DS, RP, Si, SaL, SaJ) on exposure time in saturated vapours substances 1 – 7.

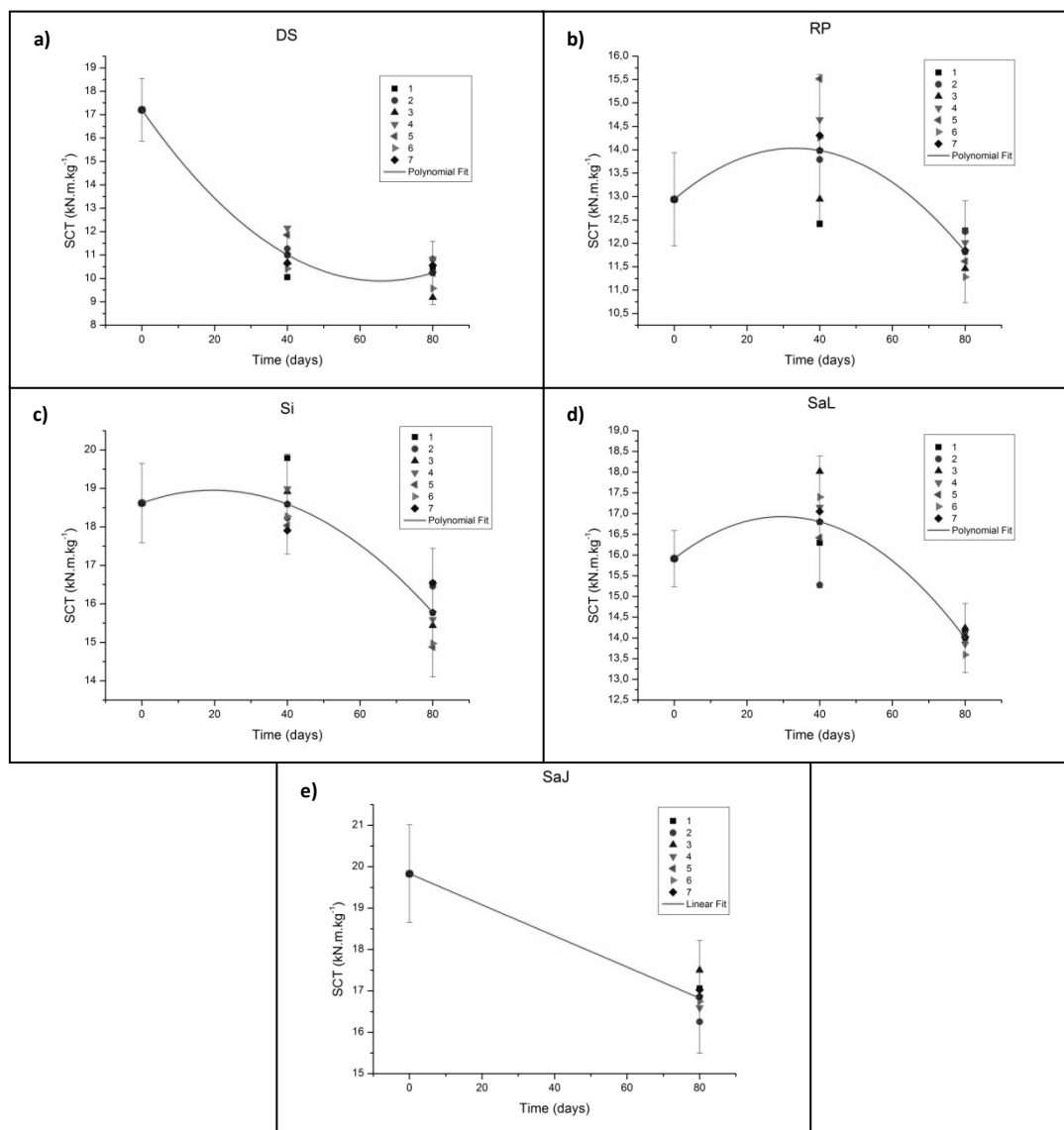


Fig. 5 Dependence of compressive index of samples (DS, RP, Si, SaL, SaJ) on exposure time in saturated vapours substances 1 – 7.

Tab. 3: Value of colour difference  $\Delta E^*$  after exposure 40 and 80 days

Mixture No.	40	80	40	80	40	80	40	80	40	80
	days									
	DS	DS	RP	RP	SaJ	SaJ	SaL	SaL	Si	Si
	$\Delta E$									
1	0.45	0.52	0.22	0.70	0.31	0.28	0.13	0.21	0.35	0.64
2	0.52	1.01	0.90	1.41	0.30	0.47	0.66	1.20	0.46	0.89
3	0.20	0.14	0.07	0.10	0.08	0.20	0.17	0.21	0.28	0.32
4	0.16	0.28	0.20	0.27	0.08	0.25	0.10	0.10	0.28	0.31
5	0.30	0.46	0.13	0.31	0.42	0.47	0.03	0.10	0.38	0.45
6	0.25	0.32	0.02	0.04	0.25	0.33	0.17	0.19	0.29	0.42
7	0.22	0.12	0.13	0.06	0.28	0.40	0.17	0.15	0.34	0.48

Optical properties presented by the colour difference  $\Delta E^*$  are listed in table 3. Effect of saturated vapours composed of substances 1-7 appeared on the paper in a color change only minimally. Highest hue deviation was measured when exposing mixture no. 2, which contained limonene, eucalyptol and ocimene. Color deviation in this case was the highest in the material for production of hand-made paper, but the value of 1.41 can be considered as slight change. Other substances changed the hue of cellulose and lignocellulose materials only negligibly.

## Conclusions

This part of the research focused on the effect of essential oils and their components on cellulose and lignocellulose materials is an important part of the project, which aims to protect archival documents. Despite the fact that tested ingredients EO and EO alone have proven bactericidal effects, it is important to find a suitable substance or combination of substances, which also does not affect the paper pad in mechanical, optical and chemical way. It has been proven that saturated vapours of 7 compounds, which we had tested, had a negative effect on the mechanical properties of wood-based material. Stiffness and compressive strength after exposure of saturated vapours decreased approximately by 40%. This significant decline can be attributed to plasticity of fibres and loosening connections among them. In case of other cellulose materials the change of mechanical properties was only about 15%. It is necessary to take into account that the samples were exposed to saturated vapours, which could not be applied in the library depositories or more precisely they would have to be diluted many times. Change in optical properties is reflected by slight color variation with a maximum value of 1.41 when applying mixtures of substances no. 2 (limonene, eucalyptol, ocimene) on the material for production of handmade paper. Other saturated vapours didn't affect significantly optical properties of paper pads.

For real application EO or their components in the archives with paper artefacts, which threaten to microbial attack, it is necessary to follow up convenient composition of protective vapours and suitable method of application into the space.

## Literature

1. Bansa, H. 2002. Accelerated Ageing of Paper: Some Ideas on its Practical Benefit. In *Restaurator*, 23(2), 2002, s. 106-117, ISSN 0034-5806
2. Calvini, P., Gorassini, A. 2006. On the Rate of Paper Degradation: Lessons From the Past. In *Restaurator*, 2006, s. 275-290, ISSN 0034-5806
3. Čabalová, I., Kačík, F., Sivák, J. 2011a. The changes of polymerization degree of softwood fibers by recycling and ageing process. In *Acta Facultatis Xylologiae*, Zvolen, 53(1), 2011, s. 61-64. ISSN 1336-3824
4. Čabalová, I., Kačík, F., Geffert, A., Kačíková, D. 2011b. The effects of recycling and its environmental impact, In: *Elżbieta Broniewicz (ed.): Environmental management in Practice*. INTECH, 2011, s.329- 350, ISBN 978-953-307-686-7
5. Milichovský, M., Češek, B., Filipi, M., Gojny, J. 2013. Cellulose Aging as Key Process of Paper Destruction. In *Przeglad Papierniczy*. 69. 2013. p. 291-298. ISSN 0033-2291.
6. Češek, B., Milichovský, M., Gojny, J. 2014a. Mutual Competitive Absorption of Water and Essential Oils Molecules by Porose Ligno-Cellulosic Materials. In: *Journal of Biomaterials and Nanobiotechnology*. Journal of Biomaterials and Nanobiotechnology, Vol.5 No.2(2014), ISSN 2158-7027
7. Češek, B., Milichovský, M., Gojny, J. 2014b. Essential Oils Influence upon Chemical Aging Process of Lignocellulosic Materials. In *PROGRESS'14 Papers*. Łódź : Stowarzyszenie Papierników Polskich, 2014, s. 1-13. ISBN 978-83-60419-08-6.
8. Kalembe, D., Kunicka, A. 2003. Antibacterial and Antifungal Properties of Essential Oils. *Current Medicinal Chemistry* [online]. 2003, č. 10, s. 813-829 [cit. 2015-04-05]. Available from: <http://www.ingentaconnect.com/content/ben/cmc/2003/00000010/00000010/art00002>
9. Miladinović, D., L., ILIĆ, B., S., Mihajilov-Krstev, T., M., NIKOLIĆ, N., D., MILADINOVIĆ L., C., Cvetković, O., G. 2012. Investigation of the chemical composition–antibacterial activity relationship of essential oils by chemometric methods. *Analytical and Bioanalytical Chemistry* [online]. 2012, vol. 403, issue 4, s. 1007-1018 [cit. 2015-04-05]. DOI: 10.1007/s00216-012-5866-1. Available from: <http://link.springer.com/10.1007/s00216-012-5866-1>
10. Elaissi, A., Hadj Salah, K., Mabrouk, S., Larbi, K., M., Chemli, R., Harzallah-Skhiri, F. 2011. Antibacterial activity and chemical composition of 20 Eucalyptus species' essential oils. In: *Food Chemistry* 129 (2011) 1427-1434. ISSN 0308-8146 .
11. Chueca, B., Pagán, R., García-Gonzalo, D. 2014. Oxygenated monoterpenes citral and carvacrol cause oxidative damage in *Escherichia coli* without the involvement of tricarboxylic acid cycle and Fenton reaction. In: *International Journal of Food Microbiology* 189 (2014) 126–131, ISSN 0168-1605.
12. Delamare, A., P., L., Moschen-Pistorello, I., T., Artico, L., Atti-Serafini, L., Echeverrigaray, S. 2007. Antibacterial activity of the essential oils of *Salvia officinalis* L. and *Salvia triloba* L. cultivated in South Brazil. In: *Food Chemistry* 100 (2007) 603–608, ISSN 0308-8146.

## INFLUENCE OF SELECTED DISINFECTANTS AND DEACIDIFICATION MEANS ON LIGNOCELLULOSIC MATERIALS

**Hájek M.**, Milichovský M., Filipi M., Mikala O.

*University of Pardubice, Faculty of Chemical Technology, Institute of Chemistry and Technology of Macromolecular materials, Department of Wood, Pulp and Paper, Studentská 95, 532 10 Pardubice, Czech Republic  
st20744@student.upce.cz*

### Abstract

The aim of this work was to study the effect of disinfectants and deacidification means for lignocellulosic materials. For the experiments were selected four the most commonly used pulp in paper industry. It was deciduous kraft pulp (SaL), coniferous kraft pulp (SaJ), sulphite pulp (Si) and pulp for the manufacture of handmade paper (RP). In cooperation with the National Archives in Prague, these pulp exposed to the influence three different disinfectants and three deacidification means and then were measured their mechanical, optical and chemical properties.

Key words: lignocellulosic materials; disinfection; deacidification

### Introduction

The basic restoration work to protect rare and papermaking artefacts stored in archives and libraries are disinfection and de-acidification through various means. These interventions can have an impact on the mechanical, optical and chemical properties. A measurement of these changes is the focus of this work.

From the surface and volume of the paper in case of microbial attack, disinfection eliminates microorganisms present. Disinfection can be do in several ways. Samples can immerse in disinfectant or antiseptic samples to paint it or we spray. Further still be allowed to remain in pairs disinfectants or sample put between filter papers, which impregnated with disinfectant means<sup>1</sup>.

To prevent the emergence of resistance of microorganisms to disinfectants, it is necessary to strictly follow the application process (reaction time, concentration)<sup>1</sup>.

According to the mechanism of action of disinfectants divided into two groups. Destroy either the physical mechanisms or ongoing destruction of microorganisms by direct chemical reaction with the product. The major chemical disinfectants include alcohols (methanol, ethanol, butanol, amyl alcohol, etc.), which leads to denaturation of proteins of microorganisms. Alcohols are effective in vapour form in the presence of water. The amount of water creates a suitable environment for moisture recovery sporulation microorganisms (optimally 80% relative humidity environment)<sup>1</sup>.

Gaseous ethylene (see Figure 1) penetrates the porous materials. Because of its explosiveness, a mixture of 10% ethylene oxide and 90% carbon dioxide, which supplied in the storage bottles under the commercial name ETOXEN. It also has a sterilizing effect, therefore, can kill all the living and the spore-forming microorganisms. The effect of ethylene is immediate and killing germs and fungi mycelia is necessary odstranit<sup>3</sup>.

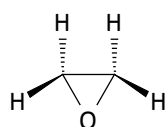
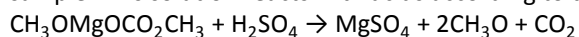


Figure 7. Structure of ethylene oxide (ACD/ChemSketch 12)

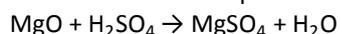
Disinfection often connected with deacidification samples. The deacidification used most of the magnesium compound. Magnesium ions slow down the oxidative degradation of cellulose and have a positive effect on mechanical and physical properties of the lignocellulosic materials. Therefore, it is currently the most widely used means deacidification compounds bicarbonates of magnesium and calcium (HERCO). However, these two bicarbonate to neutralize acidity current only and does not form an alkaline reserve for the future<sup>2</sup>.

For a lot of damage to paper, it is necessary to use anhydrous environment. The organic magnesium compound in the form of deposits provide bicarbonate or magnesium hydroxide. The most commonly used means is a methanol solution methoxymagnesiummethyl carbonate (MMMK) which is resistant to water contained in the sample. This solution reacts with acids according to the equation:



The volatile products are formed and neutral salts. Excess MMMK reacts with atmospheric carbon dioxide to magnesium carbonate. The solution leaving the necessary alkaline reserve caused magnesium carbonate and the pH value after treatment move within 8 – 9<sup>2</sup>.

Bookkeeper technology is suitable for mass deacidification. This is a dispersion of MgO in perflourheptane and deacidification takes place successively in the presence of moisture according to the equation:



Dispersion particle aggregation prevented by adding a suitable surfactant<sup>2</sup>.

### Experiment

We have chosen four most used lignocellulosic materials, which used in the paper industry. These are sulphite pulp from Biocel Paskov (Si; freeness 25 according to Schopper Riegler (SR)), coniferous kraft pulp from Štětí (SaJ; 25 SR freeness), deciduous kraft pulp from Ružomberok (SaL; freeness 25 SR) and pulp production of handmade paper from Velké Losiny (RP; 60% cotton linters and 40% linen, freeness 28-29 SR).

These selected samples exposed to three different disinfectants (butanol, ethylene oxide and  $\gamma$ -rays) and three deacidification (Bookkeeper, HERCO and MMMK).

Deacidification HERCO solution performed by immersion in this solution for 20 minutes. In this solution monitored by conductivity (2.5 mS cm<sup>-1</sup>) and pH (6.79). Deacidification MMMK solution at a concentration of 0,8 % carried out by immersion for 1 minute, then the sample was dried in an open fume hood. Last deacidification were carried out on both sides by spraying with a solution Bookkeeper (manufacturer Preservation Technologies, USA)<sup>3</sup>.

Disinfection in vapours of 96% butanol performed in an ambient temperature of 25 °C and at 80% relative humidity for an exposure time 48 hours (see Figure 2). On disinfection  $\gamma$ -radiation was used irradiance of 2,2 kGy. Material for the disinfection of ethylene oxide (EtOX) placed in a porous paper packages (boxes, bags, etc.). Straightened loosely into special containers with wire ends (easy access of gas) and placed into the chamber. Before the disinfection has introduced into the steam chamber until reaching 80% relative humidity. The reason was the need to revive spore-forming microorganisms, which subsequently liquidated. Introduced into the chamber ethylene oxide, created pressure 160 kPa at 30 °C and disinfection carried out approximately 16 hours. Thereafter, the gas was evacuated from the chamber, and catalytically burned container sanitized material was placed in a tunnel where conducted venting residual EtOX. Ethylene oxide is able to bind to the material surface, which gradually released. This relaxing the residual amounts may be dangerous to humans, it was necessary for the ventilation control measuring concentrations of ethylene oxide in air. Only after thorough removal, EtOX was handling requires<sup>3</sup>.

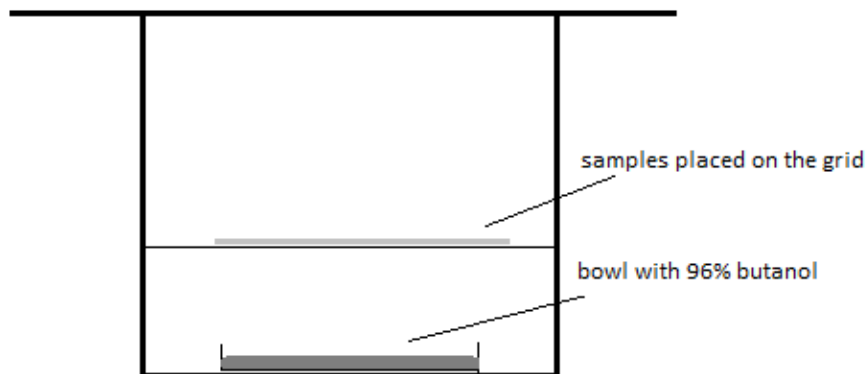


Figure 8. Placing the samples in vapours butanol<sup>3</sup>

For the treated samples were measured optical properties before and after exposure to disinfectant and deacidification means. Measurements were performed on an ELREPHO spectrophotometer from Lorentzen & Wettre. For each sample were measured coordinates L\*a\*b\*, the ISO brightness.

From the mechanical properties of the device was 26005 TIRAtest stiffness of samples was measured. This method used to determine the three-point bending; the sample placed on two supports and then the pressure on the bent middle portion of the sample. The distance between the lower supports (*l*) was set at 50 mm (see Figure 3).

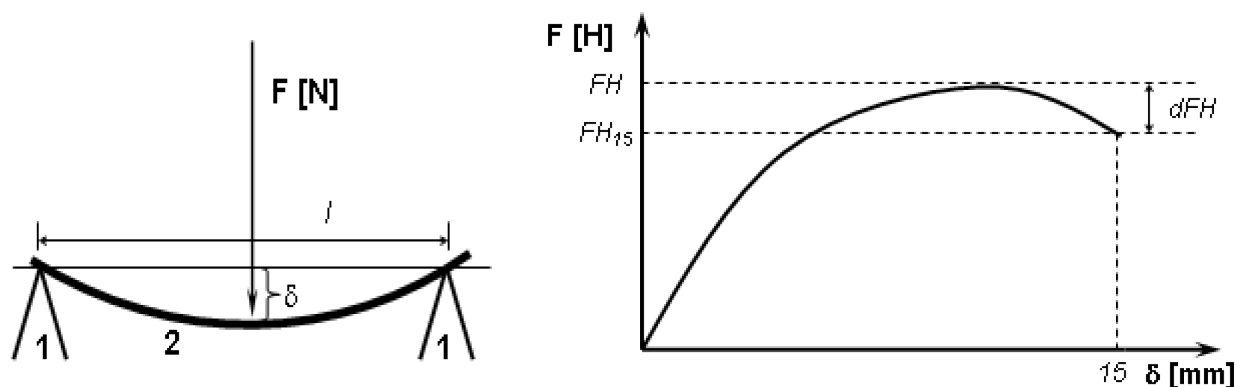


Figure 9. Diagram of three-point bending and deflection curves typical course of lignocellulosic materials

Note: 1 - support points, 2 - measured sample,  $F$  - acting force [N],  $\delta$  - bending [mm],  $FH$  - maximum force [N],  $FH_{15}$  - the force deflection at 15 mm,  $dFH$  - absolute decrease in strength,  $l$  - distance of supports

Deflection curve was recorded (Figure 3), which has deduced from the value of force at 15 mm deflection, slope of the linear part of the curve (area elastic deformation), the maximum force and the maximum deflection distance of the end of the recoverable strain.

In addition to the optical and mechanical properties were measured and chemical properties. Values were determined pH salty extract (a solution of 0,1 M KCl) and an aqueous extract (distilled water). The measured values of the original samples compared with samples that have exposed to treatment compositions.

### Results and discussion

This study aimed to investigate the influence of disinfectants and acidification means on lignocellulosic materials. The samples were exposed to three different disinfectants and three acidification means. After exposure for pulp samples measured, optical, mechanical properties, the pH of the extracts.

When measuring the optical properties of the treated pulps did not show a reduction in ISO brightness. The samples Si after disinfection of improved optical properties of up to 5 %. For other pulps were change of optical properties was negligible.

**Table II Values of ISO brightness (%) of the samples after treatment**

ISO brightness [%]				
deacidification	SaJ	Si	SaL	RP
original sample	72.27	74.97	81.84	84.26
Bookkeeper	74.78	80.85	85.52	84.74
HERCO	73.58	80.08	84.92	83.81
MMMK	73.09	78.68	84.56	84.39
disinfection	SaJ	Si	SaL	RP
original sample	72.27	74.97	81.84	84.26
butanol	74.86	80.27	84.4	84.44
EtOX	74.36	80.03	77.23	83.94
$\gamma$ -rays	74.85	80.03	84.96	83.9

The stiffness of the material characterizes several quantities, preferably characterizes behaviour of samples called unitary stiffness that the stiffness of the material in the field of reversible deformation related to a thickness of 1 mm (see equation 1). For samples after deacidification a significant decrease after treatment Bookkeeper and HERCO. The smallest decrease in this parameter was observed in the samples after treatment with ethylene oxide (see Table II).

$$T_0 = \frac{F \cdot l^3}{48 \cdot \delta} \cdot \frac{t_0^3}{t^3} \quad (1)$$

Where  $t_0$  is the standard specimen thickness (1 mm), at  $t$  the current thickness of the samples (mm).

**Table III Values of unitary stiffness ( $N \cdot mm^2$ ) of the samples after treatment**

unitary stiffness [ $N \cdot mm^2$ ]				
deacidification	SaJ	Si	SaL	RP
original sample	4161.84	4462.51	2911.3	2463.44
Bookkeeper	2995.72	2210.87	1881.08	2228.95
HERCO	3798.56	3110.77	1231.76	1601.98
MMMK	3607.69	4489.07	2381.97	2364.92
disinfection	SaJ	Si	SaL	RP
original sample	4161.84	4462.51	2911.3	2463.44
butanol	3513.89	3981.27	2422.9	2210.87
EtOX	4205.02	4226.98	2917.02	2151.88
$\gamma$ -rays	3712.68	3945.294	2385.21	2116.84

When measuring the SCT samples after deacidification showed improvements only affect HERCO caused a slight decline this property. After disinfection an increase of this parameter for all treated samples (Table III).

**Table IV Values of SCT ( $kN \cdot m^{-1}$ ) of the samples after treatment**

SCT [ $kN \cdot m^{-1}$ ]				
deacidification	SaJ	Si	SaL	RP
original sample	9.16	9.13	8.43	6.63
Bookkeeper	11.97	10.75	8.79	7.11
HERCO	9.56	8.88	5.49	6.28
MMMK	11.55	11.18	7.84	6.96
disinfection	SaJ	Si	SaL	RP
original sample	9.16	9.13	8.43	6.63
butanol	10.97	10.51	7.46	7.66
EtOX	11.32	10.93	8.34	7.87
$\gamma$ -rays	10.97	10.63	8.1	6.42

Values of pH extracts samples after disinfection did not change significantly. Samples that passed deacidification it is assumed extracts pH increased up to values of 9-10 (see Table IV).

**Table V Values pH of the extract of samples after treatment**

pH extract									
saline extract	RP	SaJ	SaL	Si	saline extract	RP	SaJ	SaL	Si
original sample	7.05	6.34	6.36	5.42	original sample	7.05	6.34	6.36	5.42
butanol	8.35	5.75	5.9	5.83	Bookkeeper	10.39	10.13	10.14	9.94
EtOX	8.33	5.82	6.04	5.9	HERCO	9.69	9.25	9.03	9.13
$\gamma$ -rays	8.41	5.72	5.82	5.9	MMMK	10	9.91	10	9.9
aqueous extract	RP	SaJ	SaL	Si	aqueous extract	RP	SaJ	SaL	Si
original sample	7.05	6.34	6.36	5.42	original sample	7.05	6.34	6.36	5.42
butanol	8.18	6.12	6.26	6.15	Bookkeeper	10,1	10.05	10	9.9
EtOX	8.23	6.32	6.21	6.1	HERCO	9.58	9.4	9.07	9.14
$\gamma$ -rays	7.15	6.19	5.9	5.85	MMMK	10	10.04	10	10

### Conclusion

They were measured by four kinds of lignocellulosic materials before and after treatment with disinfectants and deacidification means. Measurements were mechanical properties (SCT, stiffness), optical properties (ISO brightness) and the pH of aqueous and saline extracts. Deterioration of mechanical properties after exposure

resulted HERCO, Bookkeeper and butanol. Values of pH extracts demonstrated the effectiveness deacidification means. Changes in optical properties were noticeable.

#### **Acknowledgment**

*This work was support by the project for the Science paper artefacts reg. CZ.1.07/2.3.00/20.0236 Operational Programme Education for Competitiveness. This project is co-finance by the European Social Fund and the state budget of the Czech Republic.*

#### **Literature**

1. VŠCHT v Praze, výukové materiály, Laboratorní cvičení - Restaurátorství a čištění papíru, [cit. 2014-03-18], dostupné z: [http://www.vscht.cz/met/stranky/vyuka/labcv/labor/res\\_cistení\\_papíru/teorie.htm](http://www.vscht.cz/met/stranky/vyuka/labcv/labor/res_cistení_papíru/teorie.htm)
2. Ďurovič, Michal a kol. *Restaurování a konzervování archiválií a knih*, nakladatelství Paseka, Praha, první vydání, 2002, 517 s., ISBN 80-718-5383-6.
3. Materiály Národního archívu, Národní archív Praha (2014)

# INFLUENCE OF SBR/BR BLENDS FORMULATION ON THE COURSE OF VULCANIZATION AND PROPERTIES OF THE VULCANIZATES

**Kadeřábková A.**, Ducháček V.

University of Chemistry and Technology Prague, Technická 5, 166 28, Prague  
alena.kaderabkova@vscht.cz

## Introduction

Since the development of new synthetic polymers is very expensive, the current polymers are often combined in order to obtain new materials with a broader spectrum of properties. Rubbers are mixed for many years, both from the processing reasons, and because of requirements for the properties of the resulting rubber goods. It is very important to choose carefully blended rubbers and the additives. Dissimilar elastomers can result in blends with inferior properties. This property failure has been ascribed to three types of incompatibility - (thermodynamic, different viscosity and cure rate incompatibility)<sup>1</sup>.

This work deals with blends of styrene-butadiene rubber (SBR) with butadiene rubber (BR), which are widely used, for example for the manufacture of tire treads, in which an addition of butadiene rubber increases resistance to abrasion and therefore the useful life of the tire.

## Experimental

To eliminate possible side effects of ingredients, the mixtures containing only mentioned rubbers and simple vulcanization system were prepared. For experiments, Kralex 1500 SBR (Mooney viscosity 54 ML (1+4) 100 °C) and Synteca 44 BR (Mooney viscosity 47 ML (1+4) 100 °C) were used.

On a laboratory two-roll mill, three sets of blends were prepared using standard vulcanizing system for butadiene rubber, standard vulcanizing system for styrene-butadiene rubber and sulphurless vulcanizing system. Table I shows SBR/BR ratios in the blends, Table II shows compositions of curing systems. In these blends, the influence of formulation on the course of vulcanization, tensile strength, compression set and resilience has been monitored. The dynamic mechanical analysis (DMA) has been used to determine whether the formation of the network common to both rubbers, i.e. mutual co-vulcanization takes place.

Table I

SBR/BR ratios in rubber blends

	S100B0	S90B10	S80B20	S60B40	S50B50	S40B60	S20B80	S10B90	S0B100
SBR [%]	100	90	80	60	50	40	20	10	0
BR [%]	0	10	20	40	50	60	80	90	100

Table II

Formulation of the vulcanizing systems [weight parts per hundred weight parts of rubber - phr]

	SBR standard	BR standard	Sulphurless system
ZnO	3	3	3
Stearin	1	2	1
sulphur	1.75	1.5	-
TBBS*	1	0.9	-
TMTD**	-	-	3

\*N-*tert*-butylbenzothiazole-2-sulphenamide, \*\*tetramethylthiuram disulphide

## Results

Influence of blends formulation on the course of vulcanization

The higher is the BR content in blends cured with BR standard system and SBR standard system, the higher is optimum curing time ( $t_{90}$ ) as well as scorch time  $t_{0,2}$ .  $T_{90}$  and  $t_{0,2}$  of the blends cured with a sulphurless system does not depend on the ratio of rubbers. (Fig. 1, Fig. 2).

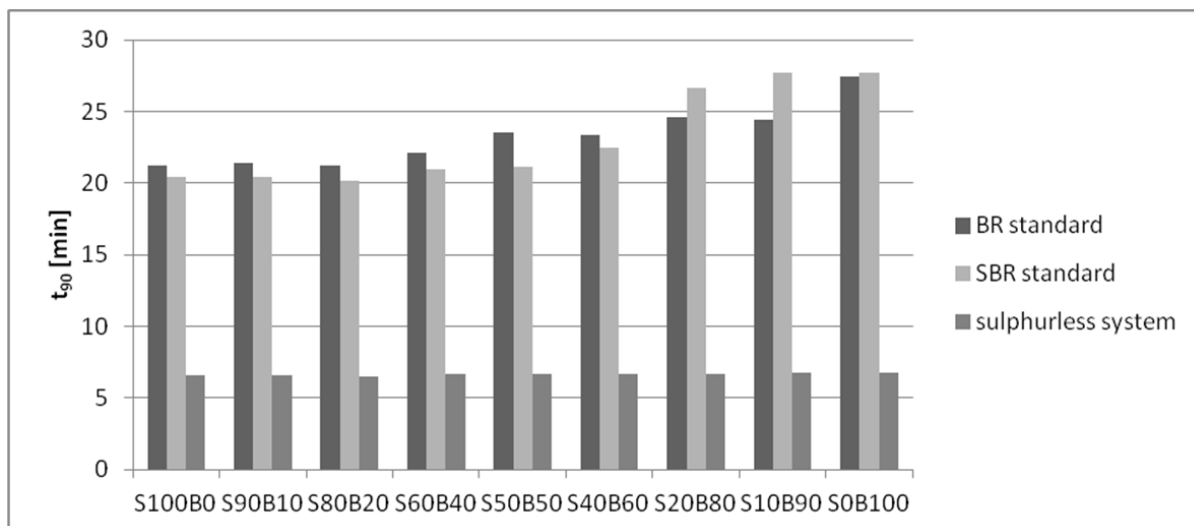


Figure 1. Dependence of optimum curing time ( $t_{90}$ ) on the composition of blends.

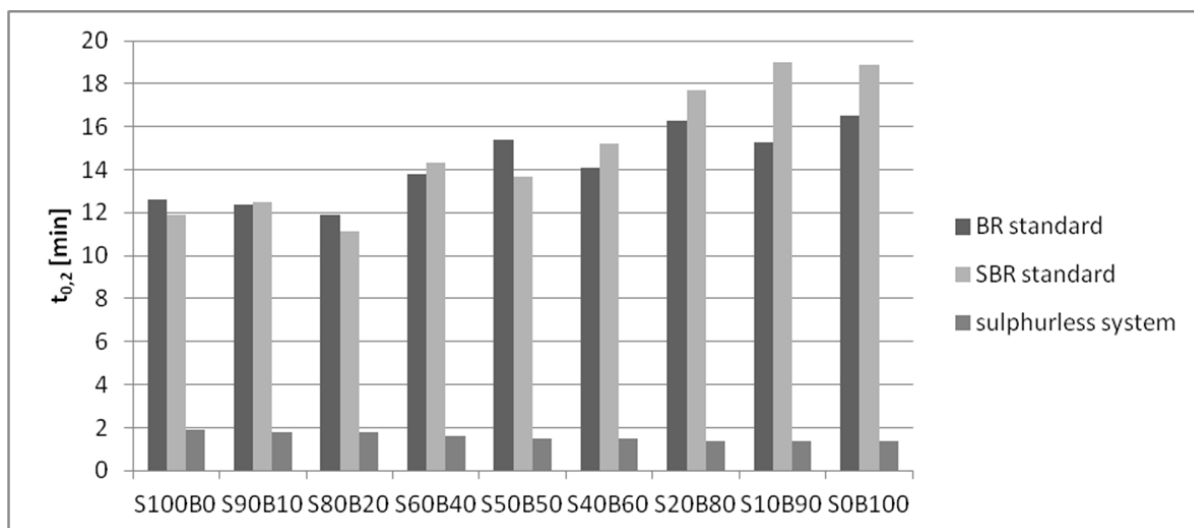


Figure 2. Dependence of scorch time ( $t_{0,2}$ ) on the composition of blends.

### Physical-mechanical properties

The tensile strength of blends cured with SBR standard system and BR standard system slightly deteriorates with decreasing content of SBR (Fig 3). For blends vulcanized with sulphurless system, an opposite trend has been observed. The resilience of vulcanizates increases with increasing content of BR. It does not depend on the curing system used (Fig 4). The blends cured with BR standard system shown highest compression set values (Fig. 5). On the other hand, the blends cured with the sulphurless system shown the lowest ones. The compression set values of the blends cured with BR standard system and sulphurless system does not depend on the rubbers ratio.

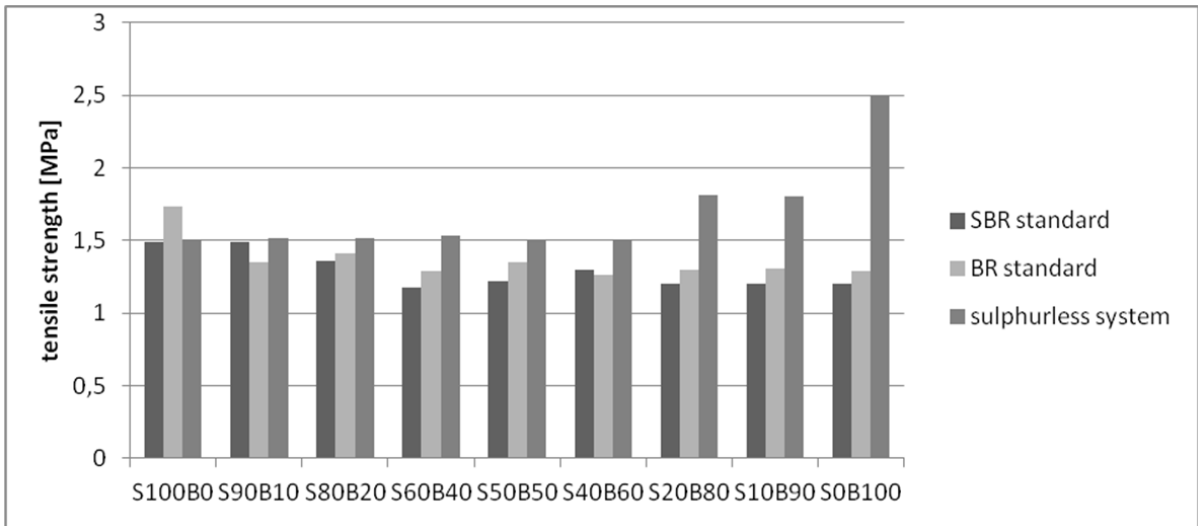


Figure 3. Dependence of tensile strength on the composition of the vulcanizates.

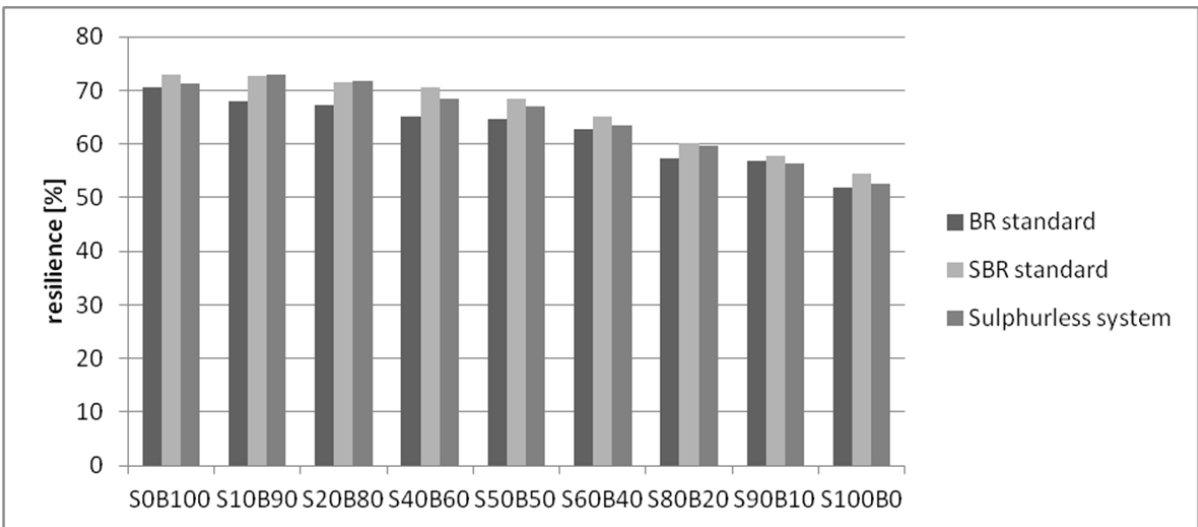


Figure 4. Dependence of resilience on the composition of the vulcanizates.

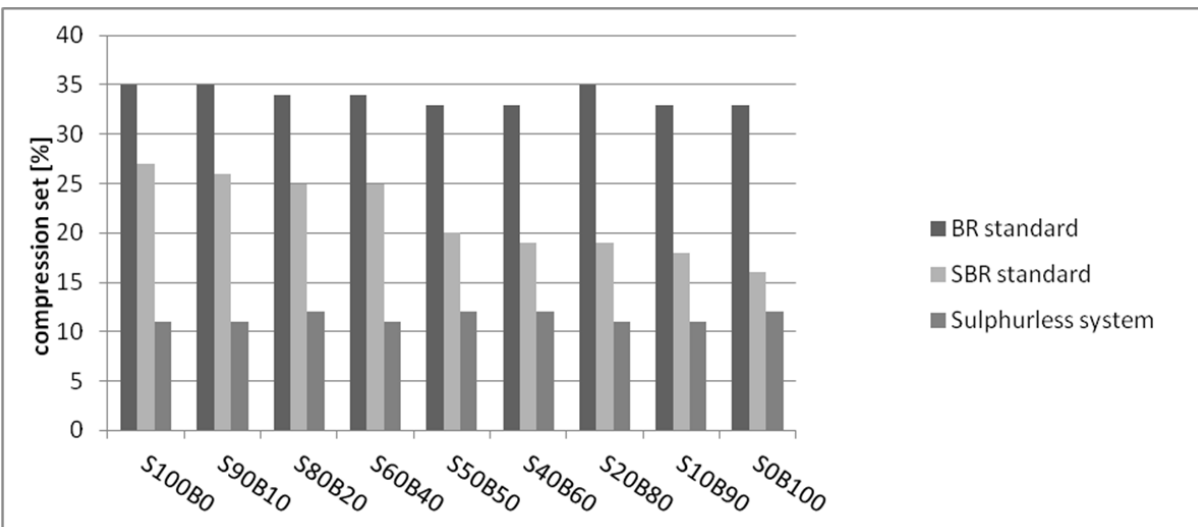


Figure 5. Dependence of compression set on the composition of the vulcanizates.

### DMA analysis

Results of DMA study have shown only one glass transition temperature ( $T_g$ ) for all vulcanizates. Decreasing SBR content, the glass transition temperature value moves to the lower one (Fig 6, Fig 7).

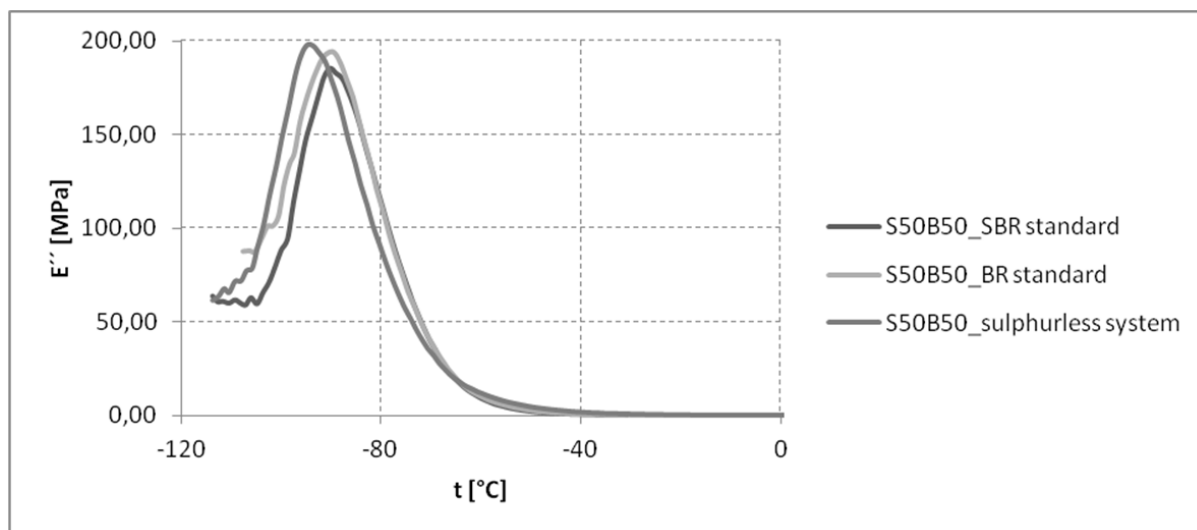


Figure 6: Temperature ( $t$ ) dependence of loss modulus ( $E''$ ) of S50B50 vulcanizates with different curing systems.

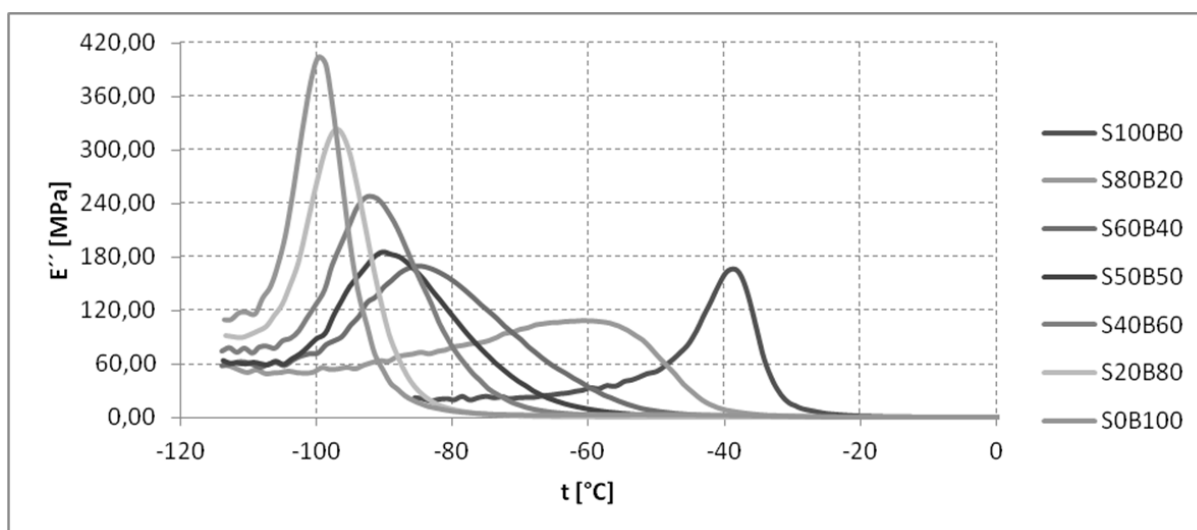


Figure 7: Temperature ( $t$ ) dependence of loss modulus ( $E''$ ) of vulcanizates with SBR standard vulcanizing system.

### Conclusions

- $T_{90}$  and  $t_{0,2}$  values of blends cured with sulphurless system are almost equal.
- Resilience values do not depend on curing system used.
- Compression set values of the blends cured with BR standard system and sulphurless system do not depend on the rubbers ratio .
- Results from DMA show that the formation of the network common to both rubbers may occur. To confirm these results, further studies are necessary.

### Acknowledgment

Financial support from specific university research (MSMT No 20/2015).

### Literature

1. Ghosh A. K., Debnath S. Ch., Naskar N., Basu D. K.: J. Appl. Polym. Sci. **81**, 800-808 (2001).

## **WASTE PROCESSING, AIR AND WATER PROTECTION, TECHNOLOGIES FOR THE DECONTAMINATION OF SOILS**

### **FEASIBILITY STUDY OF THE PARTICULATE MATTER FILTRATION FROM THE AIR STREAM IN GRANULATED FERTILIZER PRODUCTION**

**Jecha D.**, Brummer V., Lestinsky P., Skryja P.

*Institute of Process and Environmental Engineering, Brno University of Technology  
Technická 2896/2, 616 69 Brno, Czech Republic  
jecha@fme.vutbr.cz*

#### **Abstract**

In this contribution, results of the 34 days test of particulate matter (PM) removal from air stream emerging from granulated fertilizers production (NPK and mixed ammonium sulphate fertilizers) are presented. Management of the plant want to replace older wet scrubber preferably by filter bags which can provide waste less operation of the technology, because separated PM can be reintroduced to the production. Because of the assumption of the sticky and problematic deposits formation on the filter bags that could increase excessively the pressure loss, test on the pilot unit with 15 filter bags with pulse-jet bags cleaning was carried out. During the test, various technological conditions were tested. Temperatures, stream humidity, pressure loss of bags and inlet and outlet PM concentrations were monitored. It was find out, that dry cleaning of this air stream is problematic as expected, but feasible. Filter bags were absorbing considerable amount of water from dust stream (fertilizers are granulated by steam and water). This fact leads to hard removable deposits formation and increased pressure loss, but if the stream was preheated by small natural gas burner, the depositions creation was reduced. According to results of the long term test, recommendations for the technological conditions for full scale bag filter were provided for given type of technology and production.

#### **Introduction**

Particulate matter (PM) gets to the air by both natural and anthropogenic activities. Traffic is the major anthropogenic source of PM releasing road dust, particles from tires and brake pads, etc. Other anthropogenic sources of PM are emerging from industrial plants, agriculture activities, construction sites, mines and so on, and some of them can be prevented or at least reduced by secondary measures<sup>1</sup>.

The negative effects of both fractions of PM – PM 2.5 and PM 10.0 on the human health are already known and well described<sup>1-4</sup>. PM poses more health risk when comparing to common air pollutants like carbon monoxide and even ground level ozone<sup>1</sup> created by photochemical oxidation reactions between nitrogen oxides (NOx) and volatile organic compounds (VOC).

Industrial PM emission can be mostly well treated. There are a several possible ways for particulate matter (PM) mitigation emerging form stationary industrial sources. Sometimes only single step cleaning is needed, but many times it is necessary to clean air waste stream with subsequently placed devices, where first step significantly lowers the PM concentration (for example cyclones) and second step lowers the PM concentration even further to meet legislation limits for stationary source.

Filtering elements such as fabric or rigid bag filters (baghouses) are providing very high PM removal efficiencies<sup>4</sup>. Even 99.99 % in terms of efficiency can be achieved<sup>5</sup>. This is the reason, why they are used in industry for dust treatment so frequently<sup>4-7</sup>. The limitation in filter applications lies in the maximum allowable temperature given by used material of the filter bag or candle<sup>4,6</sup>. Temperature upper limit for natural fibres is about 90 °C and fabrics made from glass and synthetic fibres are usable up to 230-260 °C during continuous operation - PAN (125°C), PES (140 °C), PPS (180 °C), PI (240 °C), glass (260 °C)<sup>4</sup>. Fabric filters are made from the flexible material, so this makes them less susceptible to thermal shocks, rough handling and excessive temperature, which can lead to premature material damage<sup>6</sup>.

The industrial filter units are operated usually at the constant flow and as the differential pressure on filter material ( $\Delta P$ ) is increasing due to particles deposition on the filter bags forming cake, the downstream blower must be present for pressure compensation<sup>5,8</sup>.

When the filtration starts, dust particles are being captured on the filter material forming the cake, which properties depends on particle size distribution and particle shape which also play a role on the cake structure and detachment<sup>9</sup>. The developed cake is often fragile<sup>9</sup>. The cake properties as well as increase of  $\Delta P$  further

depend on many factors like filtration velocity, dust concentration<sup>10</sup>, permeability of the filtering elements<sup>6</sup>, types and surface treatment of filter media, operating conditions, gas and dust properties, and equipment design<sup>11</sup>.

Generally, it would be preferable to monitor the performance of an industrial filter bags dust collector over a long period instead of using artificial ageing techniques, to get truly representative results, as we tried to achieve in our industrial case study

### Materials and methods

Current state of technology for the production of granulated fertilizers

In manufacturing facility, mixed granulated fertilizers are produced by mixing, granulating, drying and subsequent cooling of individual fertilizer components. The design production capacity is 20 t / h. Granular fertilizer is prepared from loose raw material from the warehouse in the desired amounts and ratios transported by conveyor into a blender, where it will form a perfect mixture of components. To the mixture, portions of the granular product, which do not meet the particle size requirement for the product, are returned by transport pathways along with dusty shares of cyclones are added. This mixture is subsequently granulated in two heating steam granulators. The mixture is then transported by the conveyor into a rotary co-current dryer, wherein the granulated mixture is dried. Drying takes place co-currently, the drying medium is a flue gas produced by combustion of natural gas (NG) in a burner. Drying is regulated according to the desired temperature for each dried granulate. Flue gas from the dryer is carried through a battery of cyclones by suction created by the blower. New pipeline branch was created for pilot unit (source of dust gas) downstream a cyclones battery and a blower. The cyclone battery includes 8 identical cyclones. Dust stream from dryer proceeds through the cyclones and the blower to a wet scrubber. The wet scrubber is composed of a trickle column and a droplet separator. Mechanical state of the wet scrubber is not good and management is considering to exchange it either by a new wet scrubber or dry gas cleaning using textile filter bags. The results of paper are used to help the implementation of the full-scale filtration unit for dust stream from the rotary dryer based on of the long term pilot test.

#### Pilot unit

The pilot test lasted for 34 days, in which several technical measurements were performed. Pilot unit for PM removal is dimensioned for treatment of 1000 m<sup>3</sup>/h of waste gas (flue gas) at max. temperature of 250 °C and the suction up to 10 kPa.

The construction of designed experimental unit is specific in many aspects. The most important feature is the ability of easy transportation of experimental unit and its installation directly in the industry. For this reason, the entire unit is autonomous entity and excluding power connection and pressurized air supply is entirely self-sufficient. From a structural point of view, unit is divided into several parts. Visualization of basic pilot unit parts can be seen in Figure 1.

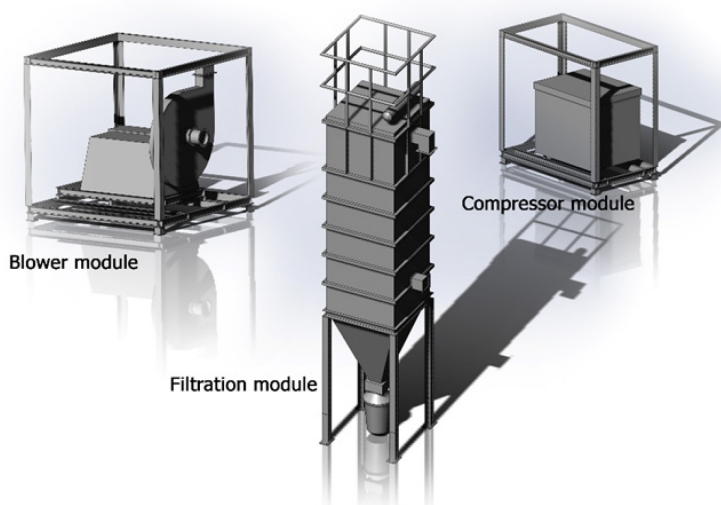


Figure 1: Visualization of the experimental pilot unit.

#### Filtration module and bag filters

The filtration module consists of filter construction, a discharge hopper and support structure. On the filter is possible to test PM filtration, optionally deNOX or removal of PCDD/F by filtration or catalytic filtration. The filter itself contains 15 filter sleeves (Gutsche AR055AR15S1.350) with a diameter of 152 mm and a length of 2500 mm. Total filtration area is approx. 18 m<sup>2</sup>, corresponding to the filtration rate of 0.92 m<sup>3</sup>/(m<sup>2</sup>.min) for real gas flow rate 1000 m<sup>3</sup>/h. Regeneration of filter bags is performed using pressure jet pulses by compressed air with pressure 5 or 6 bar (the desired pressure of air can be set).

Filter module is controlled by software "Control Web", which allows to monitor process parameters such as temperature and pressure at various points of the unit, to control pulse regeneration of filter bags and propulsion (the blower) and compressor module. Further the heating of the discharge hopper can be turned on/off, all measured data are saved in real time to external files and it is possible to track trends and individual parameters. Flow sheet of the filtration unit with measured and controlled variables is shown in Figure 2.

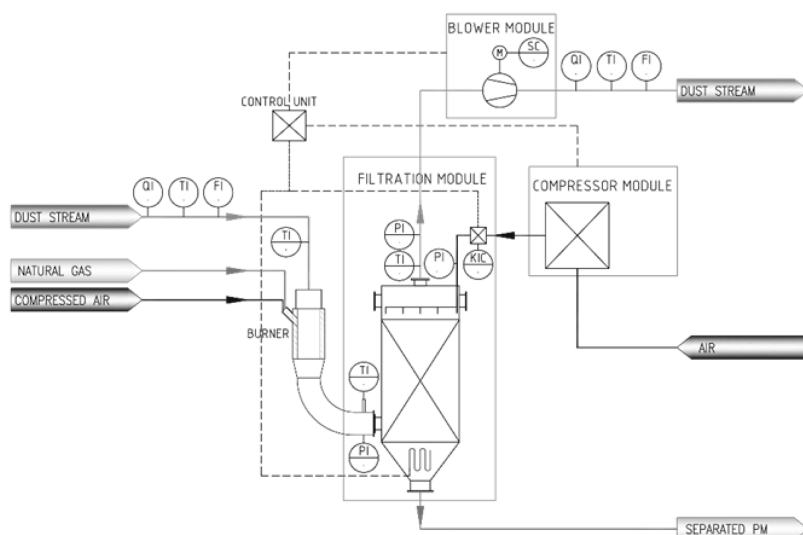


Figure 2: Flow sheet of the filtration unit

### Burner

For heating of the dust stream, which is collected downstream of the blower, the natural gas burner with approximate output of 18.5 kPa has been incorporated into the piping before the filtration unit. Heat applied to the dust stream replaced the heat loss of dust stream created before it enters the filtration unit and warmed it even more, thereby achieving greater difference between the current temperature of the stream and dew point of the stream.

### Measured parameters

Following parameters were monitored on filtration unit: inlet temperature (before the burner), inlet temperature (after the burner), outlet temperature, inlet pressure (after the burner), outlet pressure, blower rpm (downstream the filtration unit), activation of discharge hopper heating, period of filter regeneration (pressure jet pulses), see Figure 2. Other monitored parameters of the dust stream at inlet and outlet of the filtration unit, such as temperature, humidity and gas velocity were measured manually. Following waste gas parameters were further analysed several times during the long term test: outlet and inlet PM concentrations and gaseous substances (O<sub>2</sub>, CO, CO<sub>2</sub>, SO<sub>2</sub>, NO<sub>x</sub>, HCl and HF).

### Results and discussion

Based on the results of measurements and analyses, recommendations to improve the current state and recommendations for the implementation of the future full-scale filtration unit were suggested. The test was performed in real industrial plant. Production of fertilizers followed the normal monthly production plan. During the test, there were frequent outages of technology that could not be controlled or reduced. During the test, the following fertilizer types were processed: granular ammonium sulphate (GR-SA) - approximately 70 % of the production time; fertilizers containing nitrogen, phosphorus and potassium (NPK) - various types, some containing sulphur - about 30 % of production time.

Table 1 shows calculated water concentration in the inlet and the outlet gas, gas velocity and real flow, PM inlet and outlet concentration and calculated PM removal efficiency. Observed PM removal efficiency was on the expected high level about 94-99 %. Humidity of the inlet and outlet gas was measured, due to the fact that

fertilizers were granulated by water and steam and water capture by filter material with negative impact on deposits and  $\Delta P$  was anticipated. As can be seen on Table 1, inlet water concentration is sometimes quite high and filter material captured 10-40 g/kg of dry gas from the gas stream. The blower rpm were adjusted periodically to get real gas flow close to 1000 m<sup>3</sup>/h. Pulse pressure was 5 bar until day 30, after that was changed to 6 bar.

The following figures shows only selected parts of measurements. The unit was started-up without heating of the gas stream during the manufacture of GR-SA.

Table I: Measured and calculated parameters

day	hour	gas velocity	real flow	water - gas inlet	water - gas outlet	PM <sub>IN</sub>	PM <sub>OUT</sub>	PM rem. effec.
[d]	[h]	[m/s]	[m <sup>3</sup> /h]	[g/kg of dry gas]	[g/kg of dry gas]	[mg/m <sup>3</sup> ]	[mg/m <sup>3</sup> ]	[%]
1	0	8.7	984	41.43	33.42	94.2	0.1	98.89
4	72	–	–	36.85	–	–	–	–
5	96	–	–	27.25	–	–	–	–
6	120	–	–	77.99	–	–	–	–
7	144	–	–	110.27 ; 44.31	–	–	–	–
8	168	8.5	961	45.57	34.14	–	–	–
9	192	–	–	55.33	–	–	–	–
10	216	–	–	42.60 ; 61.34	–	–	–	–
11	240	–	–	51.35	–	–	–	–
12	264	–	–	60.45	–	–	–	–
15	336	10	1131	123.42	–	132.0	8.0	93.94
16	360	–	–	159.47	–	–	–	–
22	504	11.2	1267	66.58	–	–	–	–
29	672	14, 12	1583; 1357	79.57 ; 113.16	49.64; 74.95	94.2	4.2	95.54

3 days measurement for NPK manufacture, can be see in Figure 4. NPK fertilizer was extensively granulated by steam and water, which caused the filter saturation with water and increase of  $\Delta P$  to 2.2 kPa. The impact of gas stream heating on  $\Delta P$  was tested. There is a clear dependence of  $\Delta P$  on the gas temperature. The higher temperature helps to provide better filtering and lower  $\Delta P$ , conversely, if the temperature of the stream suddenly decreases, the increase of  $\Delta P$  is rapid and significant. Heating of gas above 100 °C decreased  $\Delta P$  back to 1.6 kPa. Finally, the last part of the test was performed with the GR-SA but without heating,  $\Delta P$  only slightly increases over time up to 2.1 kPa.

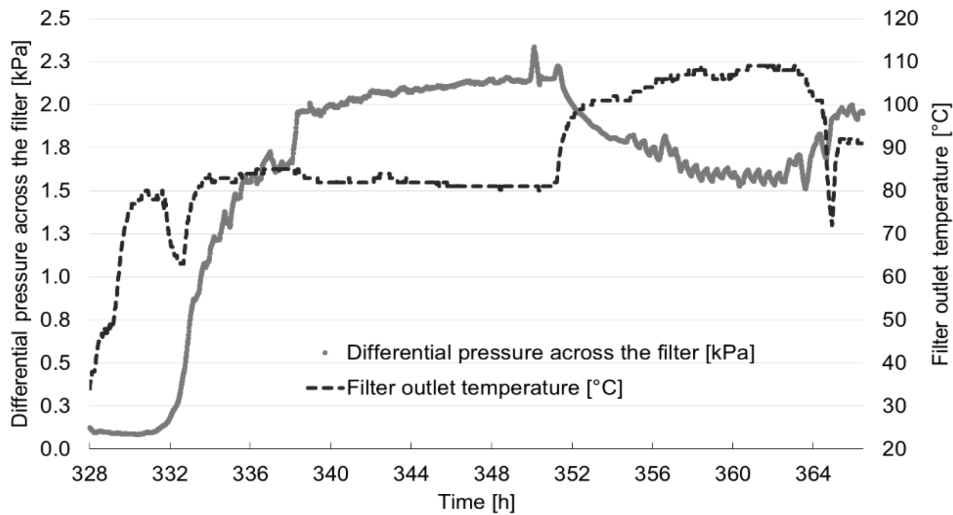


Figure 4: Pilot unit start-up – NPK

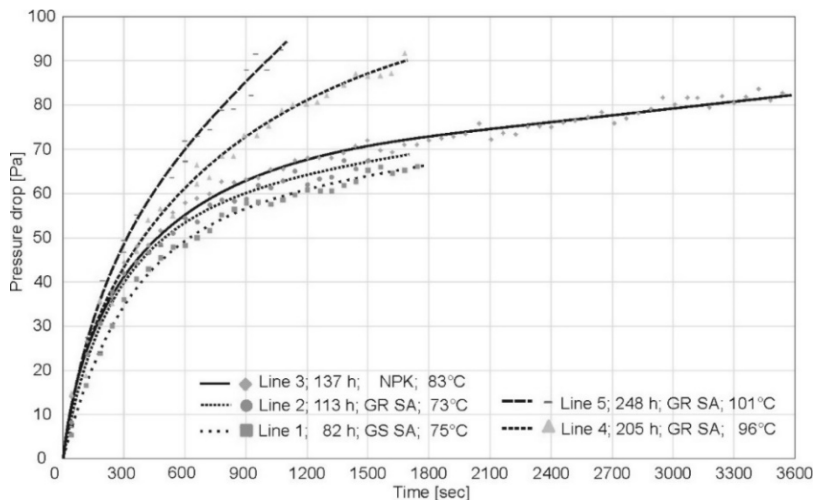


Figure 5: Characteristic trends of pulse jet cleaning - the time dependence of  $\Delta P$  for cleaning between two successive pulses

From the course of long-term test, characteristic lines of pulse jet cleaning were selected, i.e. the time dependence of  $\Delta P$  between two consecutive cleaning pulses. These lines characterizes as well the overall time course of the test, another result will be achieved, if for each condition and fertilizer, fresh filter bags were used. Lines in Figure 5 corresponds to relatively fresh new filter bags, lines in Figure 6 corresponds to more established filter bags. At the beginning of the test mostly granulated ammonium sulphate (GR-SA) has been made. When this product is made, only steam is used for the granulation (not steam-water combination as for NPK), therefore there is no more significant “clogging” of the filter, see Figure 5 lines 1 and 2 – lines looks very similar.

When switching to NPK granulate, slightly faster “clogging” of the filter was observed as can be seen in line 3. At the approximate time of 25 min. (1500 s) the time dependence of  $\Delta P$  becomes linear.

Subsequently, the production returned to GR-SA with the temperature rise in the filter due to gas heating (lines 4 and 5). For these lines, increase of pressure loss comes more quickly, which corresponds to the separation of larger pieces of dust particles during cleaning pulse and thus increased pressure loss can be generated in shorter time after the pulse. Particles are probably making more dense cake, leading in quick rise of  $\Delta P$ . Subsequent change of the product from the GR-SA to NPK granulate led to even more significant increase in the pressure loss between pulses (Figure 6, line 6), the further increases in the differential pressures were caused by heating of the filter above 100 °C and thus causing better cleaning of filtration surfaces (falling away of larger pieces of formed filter cake during pulse).

Line 6 could be also be negatively affected by excessive granulation by water-steam. After this point the filter was used without further preheat of inlet gas and thereby ordinary technology conditions were simulated at

first for Cererit (GSH NPK) production, lines 7 and 8, was again observed the gradual clogging of the filter and removal of larger pieces of the filter cake.

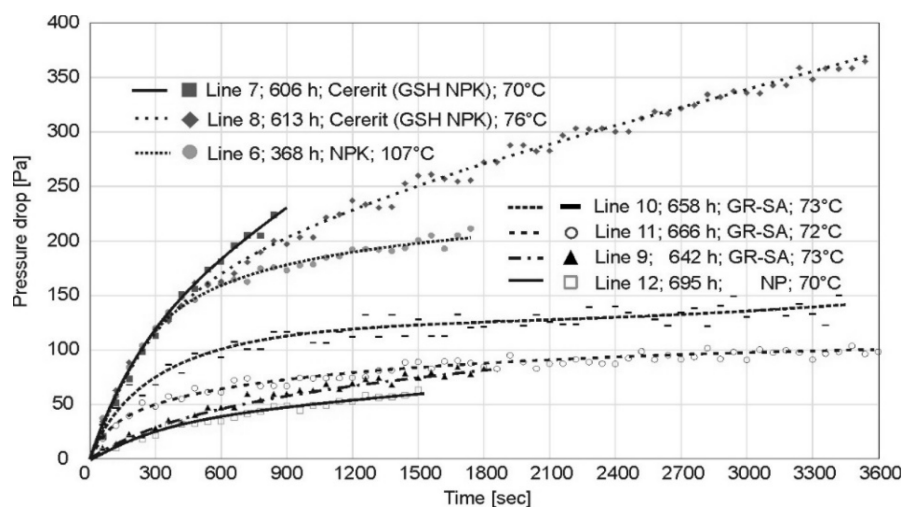


Figure 6: Characteristic trends of pulse jet cleaning - the time dependence of  $\Delta P$  for cleaning between two successive pulses – continued

In the subsequent production of GR-SA, the filter surface has been cleaned of newly deposited material only partially after each pulse. The cleaning pulse efficiency was not affected by the change of the pulse period or pulse pressure increase from 5 to 6 bar (lines 9-12). During prolonged operation (last hours of the test) filter material stayed partially clogged even after pulse, causing consequently reduction of the  $\Delta P$  between pulses up to 50 %. Major changes in the filter cleaning have been always a consequence of the production change or production outages.

### Conclusions

34 days test of PM removal from air stream emerging from granulated fertilizers production in industrial plant was performed. Filter bags captured water which gets into the gas stream after granulation - about 10 g and 40 g  $H_2O$  / kg of dry gas for GR-SA and NPK, respectively. Filtration of dust stream cannot be operated without increasing the temperature of gas above 100 °C. The best solution for full-scale unit seems to be the installation of a separate burner upstream of the filter and to keep filtration temperature above 80 °C and 110 °C for GR-SA (with no outages) and NPK respectively, during filtration and also outages. Average efficiency of PM capture by filter unit was 96 %. Outlet gas meets local emission limit for PM. Different cleaning pulses periods (7-60 min.) and pulse pressure (5-6 bars) had no impact on filter  $\Delta P$ . More flat lines of time dependence of  $\Delta P$  between two consecutive cleaning pulses were observed with more difficult deposits already located on the filtration material and lower temperatures.

### Acknowledgment

„The results of this project NETME CENTRE PLUS (LO1202) were co-funded by the Ministry of Education, Youth and Sports within the support programme „National Sustainability Programme I“. The authors also gratefully acknowledge financial support of the project CZ.1.07/2.3.00/30.0039 Excellent young researcher at BUT and the project Waste-to-Energy (WtE) Competence Centre no. TE02000236.

### Literature

1. Kim, K., Kabir, E. & Kabir, S., A review on the human health impact of airborne particulate matter. *Environ. Int.*, 74, pp. 136-143, 2015.
2. Borgie, M., Ledoux, F., Verdin, A., Cazier, F., Greige, H., Shirali, P., Courcot, D. & Dagher, Z., Genotoxic and epigenotoxic effects of fine particulate matter from rural and urban sites in Lebanon on human bronchial epithelial cells. *Environ. Res.*, 136, pp. 352-362, 2015.
3. Donaldson, K., Mills, N., Macnee, W., Robinson, S. & Newby, D., Role of inflammation in cardiopulmonary health effects of PM. *Toxicol. Appl. Pharmacol.*, 207(2), pp. 483-488, 2005.
4. Morcos, V., Performance analysis of industrial bag filters to control particulate emissions. *Energy*, 21(1), pp. 9-14, 1996.

5. Saleem, M. & Krammer, G., Optical in-situ measurement of filter cake height during bag filter plant operation. *Powder Technol.*, 173(2), pp. 93-106, 2007.
6. Lupion, M., Alonso-Fariñas, B., Rodriguez-Galan, M. & Navarrete, B., Modelling pressure drop evolution on high temperature filters. *Chem. Eng. Process.: Process Intensif.*, 66, pp. 12-19, 2013.
7. Saleem, M., Krammer, G., Khan, R. & Tahir, M., Influence of operating parameters on cake formation in pilot scale pulse-jet bag filter. *Powder Technol.*, 224, pp. 28-35, 2012.
8. Simon, X., Chazelet, S., Thomas, D., Bémer, D. & Régnier, R., Experimental study of pulse-jet cleaning of bag filters supported by rigid rings. *Powder Technol.*, 172(2), pp. 67-81, 2007.
9. Lupion, M., Rodriguez-Galan, M., Alonso-Fariñas, B. & Gutierrez Ortiz, F., Investigation into the parameters of influence on dust cake porosity in hot gas filtration. *Powder Technol.*, 264, pp. 592-598, 2014.
10. Saleem, M. & Krammer, G., Effect of filtration velocity and dust concentration on cake formation and filter operation in a pilot scale jet pulsed bag filter. *J. Hazard. Mater.*, 144(3), pp. 677-681, 2007.
11. Saleem, M., Krammer, G. & Tahir, M., The effect of operating conditions on resistance parameters of filter media and limestone dust cake for uniformly loaded needle felts in a pilot scale test facility at ambient conditions. *Powder Technol.*, 228, pp. 100-107, 2012.

## A PRACTICAL APPROACH FOR PREDICTING A RIGHT GEOMETRY OF CYCLONE SEPARATORS

### Kušnierik O.

ZVU Engineering a.s., Pražská třída 155, 500 04 Hradec Králové  
ondrej.kusnierik@zvuengineering.cz

Cyclones are exploited everywhere solids particles from a gas stream are to be separated. As examples of their useful application the following industries can be introduced: food processing plants, mine industries, coal industries, chemical industries, spray dryers, pneumatic transport, metallurgy and also technologies protecting environment.

### **Advantages and disadvantages of cyclone separation**

#### Pros

- Simple construction, a robust one but with no moving parts
- Low investment costs
- Low operation costs and maintenance
- Collected phase remains dry and processable
- Compactable in installations
- Various construction materials including liners with regards to operational conditions
- Possible separation of solids or liquid particulates
- Can be used at high temperatures

#### Cons

- Effective separation only for particles with diameter higher than 10 microns and not effective under the size of particles less than 2.5 microns in diameter.
- Higher pressure drop
- Possible subject to erosion in case of abrasive solids
- Possible fouling in case of sticky solids
- Can operate below expectations if not designed and/or operated properly <sup>1</sup>

The last point of cons determines the subject of the lecture aimed to help engineers and designers with mathematic simulation of cyclone separation and its consequent right proposal and design.

### **Principle of separation**

In principle a cyclone is a special settling chamber which the separation takes place due forces caused by centrifugal acceleration. Practically the dusty gas enters into the cyclone tangentially and makes an eddy. The movement becomes spiral and the solid particulates are thrown off from the stream of gas to the wall of equipment by the impact of tangential forces. The separated solids consequently fall down into a hopper. In the bottom the gas changes the direction upside down and streams to the gas out opening. Thus there are two vortices in the separator: the outer one from inlet of gas to the bottom of cyclone and separating majority of heavy particulates and the inner one leading from the bottom of cyclone to the outlet of gas and carrying finer particles out. When several cyclones are needed the cyclones can be arranged in a multicyclone (battery) consisting of a number of cyclones operating in parallel with one inlet and one outlet.

When modelling gas swirling down and up a cyclone two basic flows should be considered:

- a) Forced vortex flow having the same tangential velocity distribution as a rotating solid body – in this case the fluid elements of all radial positions have the same angular velocity
- b) Free vortex flow of frictionless fluid when the swirling fluid is without viscosity and the motion of a given element is not influenced by neighbour element; the result is the moment –of-momentum is conserved and the tangential velocity will increase.
- c) Simulated flow has a core of near solid rotating body surrounded by a region of fluid without rotation. This is the so-called Rankine vortex.

More practical is an access respecting the Bernoulli equation in spite of the fact it is valid for steady flow of a frictionless fluid with constant density. In a real flow the fluid is never frictionless. Frictional energy dissipation is the cause of decreasing value of the sum of Bernoulli's equation in the direction of the fluid flow, nevertheless, results based on the Bernoulli's equation lead to reasonable results with technically acceptable approximation.

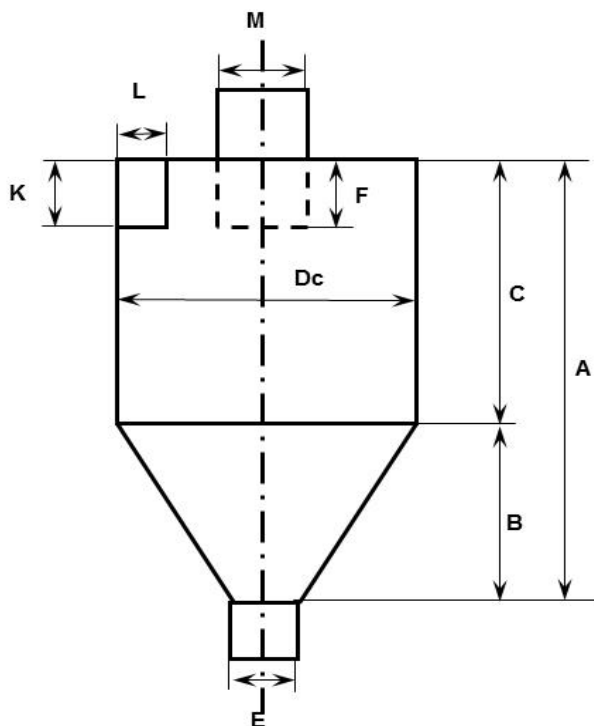


Figure 1. Basic dimensions of cyclone taken into ordinary simulations: A – cyclone height, B – conical height, C - cylindrical height, Dc – cyclone body diameter, E – dust outlet diameter, F – outlet duct length, K – inlet height, L – inlet width, M – gas outlet diameter

### Input parameters

Solving a cyclone proposal several parameters must be known. Firstly the properties of gas have to be considered: flow (velocity), density, viscosity, temperature, pressure. The solid is used to be characterized by density, shape of particles, their diameter and distribution, mass loading. The construction parameters of cyclone as an apparatus influence the cyclone performance, too. Basic dimensions of cyclone as it is a convention are illustrated in the Figure 1. Such parameters as shape and eccentricity of vortex finder and wall roughness are to be also considered.

So, there is a lot of degrees of freedom when solving the cyclone separator so the work is not easy and the unambiguous solution is not possible. Cyclones are generally designed to meet specified pressure drop limitations respecting the fan possibilities. The default design value of inlet velocity is usually about 15 m/s. Normal range<sup>2</sup> is considered between 8 and 30 m/s.

There is a habitual technical practice to design the cyclone by comparing of its both cylindrical and conical lengths to the body diameter. Thus, the configurations 1D2D or 1D3D or 2D2D are used as typical<sup>3</sup>. Their relative dimensions to the body diameter are in the Table 1. Another kind of cyclone configurations are mentioned in<sup>4,5</sup> as conventional (CNVN) and high efficiency (HE) and high throughput (HTOP) configurations, whose dimension relations are also in the Table I.

Table I

Relative dimensions of basic configuration of cyclones

Configuration	1D2D	1D3D	2D2D	CNVN	HE	HTOP
Dimension parameter						
B	2 D	3 D	2 D	2 D	2.5 D	2 D
C	1 D	1 D	2 D	1.75 D	1.4 D	1.7 D
D	1 D	1 D	1 D	1 D	1 D	1 D
E	½ D	¼ D	¼ D	0.4 D	0.4 D	0.4 D
F	9/8 D	9/8 D	5/8 D	0.6 D	0.5 D	0.85 D
K	½ D	1D	½ D	0.5 D	0.44 D	0.8 D
L	¼ D	1/8 D	¼ D	0.25 D	0.21 D	0.35 D
M	5/8 D	½ D	½ D	0.5 D	0.4 D	0.75 D

### Cyclone Operation Modelling

It is reasonable to evaluate the operation of a chosen cyclone by calculations. Several methods can be used. The classical cyclone design requires the determination of the number of turns, the cut-point, the fractional collection efficiency and the pressure drop.

First application of aerocyclones has been dated<sup>1</sup> to 1886. Since this date large amount of theories and equations have been created. The reviews of different models can be found in<sup>1, 3, 6, 7</sup>. Increasing spreading of computers is connected with beginning of the new era when computational fluid dynamics have been using for models development<sup>8, 9</sup>. In spite of large number of publications concerning computational fluid dynamics models in technical practice the preference is given to default historical models and their modifications e.g. Sheperd's and Lapple's model developed in 1939. Very interesting is also the development of experimental methods enabling the evaluation of performance of modelled cyclones. The either laser doppler anemometry or particle image velocimetry are used for this aim.

### Example from engineering practice

The production capacity of the plant producing inorganic salts has been increased. So, the producer required firstly the checking of possible operation of existing cyclone battery, secondly the alternative design of the new unit and thirdly proposal of the two step separation unit.

The solids have been carried by the stream of the hot air (109 °C) with capacity of 6,000 Nm<sup>3</sup>/h. Input pressure has been 1.056 bar(a). Two different salts have been to be separated. One salt with the capacity 2,292 kg/h and the density 1,520 kg/m<sup>3</sup> (Salt No. 1), the other's capacity has been 2,000 kg/h and the density 1,596 kg/m<sup>3</sup> (Salt No.2). The distribution of size particulates is introduced in the Table II. The existing unit has been created by the battery of six identical cyclones. The alternative design of one step separation has been proposed as six member battery. Two step design consisting from six members battery as first separation step and the battery of three cyclones has created second separation step.

Calculation method

As collection characteristic the cut diameter of 50 % efficiency was calculated in accordance with Lapple model:

$$X_{50} = \sqrt{\frac{9\mu L 10^6}{2N_s V_i \pi (\rho_s - \rho_g)}} \quad (1)$$

Table II

The distribution of size particles

Salt No. 1			Salt No 2		
Size	Group percentage	Cumulative percentage	Size	Group percentage	Cumulative percentage
$\mu\text{m}$	% wt.	% wt.	$\mu\text{m}$	% wt.	% wt.
25	0	0	25	5	5
75	3	3	100	39	44
125	6	9	200	24	68
175	22	31	325	9	77
250	49	80	550	7	84
350	15	95	750	6	90
500	5	100	850	5,5	95,5
650	0	100	950	4,5	100

The effective number of spiral turns  $N_s$  was determined by the polynomial extrapolation of figure 17-38 in<sup>10</sup>

$$N_s = -1.067 \cdot 10^{-9} v^6 + 2.50864 \cdot 10^{-7} v^5 - 2.31872 \cdot 10^{-5} v^4 + 1.076931058 \cdot 10^{-3} v^3 - 2.7783953751 \cdot 10^{-2} v^2 + 0.475672419177 v \quad (2)$$

Fractional efficiency for a particle size was calculated by

$$G_l(x_l) = \frac{x_l^2}{(x_l^2 + x_{50}^2)} \quad (3)$$

Pressure drop of cyclone was determined from equation

$$\Delta P = 8 * 10^7 Eu \frac{\rho_g V_g^2}{\pi^2 D_C^4} \quad (4)$$

where

$$Eu = \frac{\pi^2 D_C^4}{L K M} \quad (5)$$

For obtaining the geometry parameters of cyclones the numerical calculation methods have been used.

## Results and Discussion

The results of mathematical modelling for individual required design are in the Table III.

The operation of individual cyclones creating the battery was being judged in relation to the pressure drop and flow rate of solids in the gas stream out of the cyclone. The determined values of pressure drop of existing cyclone battery has been rather higher and with relation to the absorption unit placed downstream found values have been practically unacceptable. The problem of pressure drop can be solved by installing the cyclone with larger body diameter. The cyclone parameters designed for proposed battery working as single separation step are in the columns of the Table 3 headed as 1 step proposal. As it can be seen the values of pressure drop implies to accept this solution but the producer has refused to accept the amount of solids in the gas stream downstream the cyclone battery. From the point of the process characteristics the most acceptable solution is an installation of two batteries in series working as two steps separation. The amount of separated solids is excellent and the pressure drop is still in the acceptable range of values. Nevertheless, this solution leads to the higher investment costs and requires larger installation area. The next step should be global optimization of the project.

Table III

Results of mathematical modelling of cyclones

Tag	Parameter Name	unit	Existing		1 step proposal		2 steps proposal			
			Salt No. 1	Salt No. 2	Salt No. 1	Salt No. 2	Salt No. 1		Salt No. 2	
							1st step	2nd step	1st step	2nd step
F <sub>M</sub>	Flow rate (Gas)	kg/h	1292	1292	1292	1292	1292	2584	1292	2584
ρ	Density, gas	kg/m <sup>3</sup>	0,874	0,874	0,874	0,874	0,874	0,915	0,874	0,915
μ	viscosity	mPa.s	0,022	0,022	0,022	0,022	0,022	0,021	0,022	0,021
ρ <sub>p</sub>	Particle density	kg/m <sup>3</sup>	1520	1596	1520	1596	1520	1520	1595,5	1596
	Required diameter	mm	484	405	362	405	422	575	422	575
D <sub>C</sub>	Selected diameter	mm	309	309	350	350	450	575	450	575
A	Total height cyclone B+C	mm	1380	1380	1564	1564	1755	2156	1755	2156
B	Conical height of cyclone	mm	750	750	850	850	1125	1150	1125	1150
C	Cylindrical height	mm	630	630	714	714	630	1006	630	1006
E	Product outlet diameter cyclone	mm	150	150	170	170	180	230	180	230
F	Height of gas outlet pipe in cyclone	mm	300	300	340	340	225	345	225	345
K	Height cyclone inlet	mm	239	239	271	271	198	288	198	288
L	Width cyclone inlet	mm	84	84	95	95	94,5	144	94,5	144
M	Gas outlet diameter cyclone	mm	138	138	156	156	180	288	180	288
v <sub>N</sub>	Gas inlet velocity	m/s	20,44	20,45	15,95	15,95	21,94	18,99	21,94	18,99
v <sub>OUT</sub>	Gas outlet velocity	m/s	27,44	27,45	21,48	21,48	16,13	12,09	16,13	12,09
Eu	Euler value	-	316	316	316	316	668	316	668	316
N <sub>s</sub>	Effective number of turns	-	5,17	5,17	4,63	4,63	4,22	3,94	4,22	3,94
X <sub>G0</sub>	Cut diameter	mm	3,02	2,93	3,82	3,73	4,60	6,24	4,49	6,09
E <sub>T</sub>	Total collection efficiency	%	99,98	99,89	99,96	99,83	99,95	99,76	99,75	96,36
dP	Pressure drop cyclone	mbar	41,35	41,37	25,13	25,13	19,44	13,19	19,44	13,19
F <sub>S</sub>	Flow rate solids (feed)	kg/h	381,94	333,33	381,94	333,33	381,94	0,26	333,33	1,05
F <sub>S</sub>	Flow rate solids (in gas stream out)	kg/h	0,09	0,36	0,14	0,58	0,21	0,00	0,83	0,04
F <sub>S</sub>	Flow rate solids (solid stream out)	kg/h	381,86	332,98	381,80	332,76	381,74	0,26	332,50	1,02

## Symbols

- $V_g$  – gas flow rate in  $\text{Nm}^3/\text{s}$   
 $\rho_g$  – gas density in  $\text{kg}/\text{m}^3$   
 $\rho_s$  – solid particle density in  $\text{kg}/\text{m}^3$   
 $\mu$  – gas viscosity in  $\text{mPa}\cdot\text{s}$   
 $v$  – design inlet velocity of cyclone in  $\text{m}/\text{s}$   
 $N_s$  – number of effective turns in a cyclone  
 $x_i$  – particle size in  $\mu\text{m}$   
 $X_{50}$  – cut diameter in  $\mu\text{m}$   
 $F_i(x_i)$  – mass percentage of particle size  $x_i$   
 $G_i$  – fractional efficiency of particle size  $x_i$

## Literature

1. Khairy Elsayed: Analysis and Optimization of Cyclone Separators Geometry Using RANS and LES Methodologies, Thesis submitted in fulfilment of the requirements for the award of the degree of Doctor in de Ingenieurswetenschappen, Vrije Universiteit Brussel, FACULTY OF ENGINEERING, Department of Mechanical Engineering, October 2011
2. Perry's Chemical Engineering handbook, 5<sup>th</sup> edition, p. 20-85, McGraw Hill Book Company, 1973
3. Wang L., Parnell C.B., Shaw B.W., Lacey R. E.: A theoretical approach for predicting number of turns and cycle pressure drop, Transactions of the ASABE, Vol. 49(2): 491-503
4. Procestechnieken en – engineering afl. 24(1998), 49, 22130 Cyclonen en hun ontwerp
5. Cooper, C. D., Alley F.C.: Air Pollution Control, Waveland Press; 3rd edition edition (2002)
6. S. Altmeyer S., Mathieu V., Jullemier S., Contal P., Midoux N., Rode S., Leclerc J.P.: Comparison of different models of cyclone prediction performance for various operating conditions using a general software, Chemical Engineering and Processing, 43(2004), 511–522,
7. Fayed M. E., Otten L.: Handbook of Powder Science and Technology, 2<sup>nd</sup> edition, New York, Chapman & Hall, 1997
8. Boysan F., Ayer W. H., Swithenbank J.A.: Fundamental mathematical-modelling approach to cyclone design, Transaction of Institute Chemical Engineers, 60(1982)222–230,
9. Zhao B., Su Y.: Artificial neural network-based modeling of pressure drop coefficient for cyclone separators, Chemical engineering research and design, 88(2010)606–613,
10. Perry's Chemical Engineering handbook, 7<sup>th</sup> edition, p. 17-28, McGraw Hill Book Company, 1997

## SOIL DECONTAMINATION OF POPS BY THERMAL DESORPTION, APPLYING OF THERMAL DESORPTION FOR SOIL DECONTAMINATION PROCESS.

Grof A., Uotilla J.

Savaterra Oy, Rovaniemi, Finland

Keywords : soil treatment, POPs, thermal desorption

Thermal desorption is non-incineration method of soil treatment. This is the way to treat soils contaminated with organic wastes. By heating these soils to temperature 350-800 degrees C<sup>o</sup>, contaminants will vaporise and separate from the soil. The vaporised gases are collected and treated in cyclone, oxidiser and bag-house and finally washed by gas scrubber. Vaporised contaminants are destroyed in oxidiser in high temperature 850-1100 degrees C<sup>o</sup> (with a gas retention >2 sec). The design has been made according to the EU rules for waste incineration :

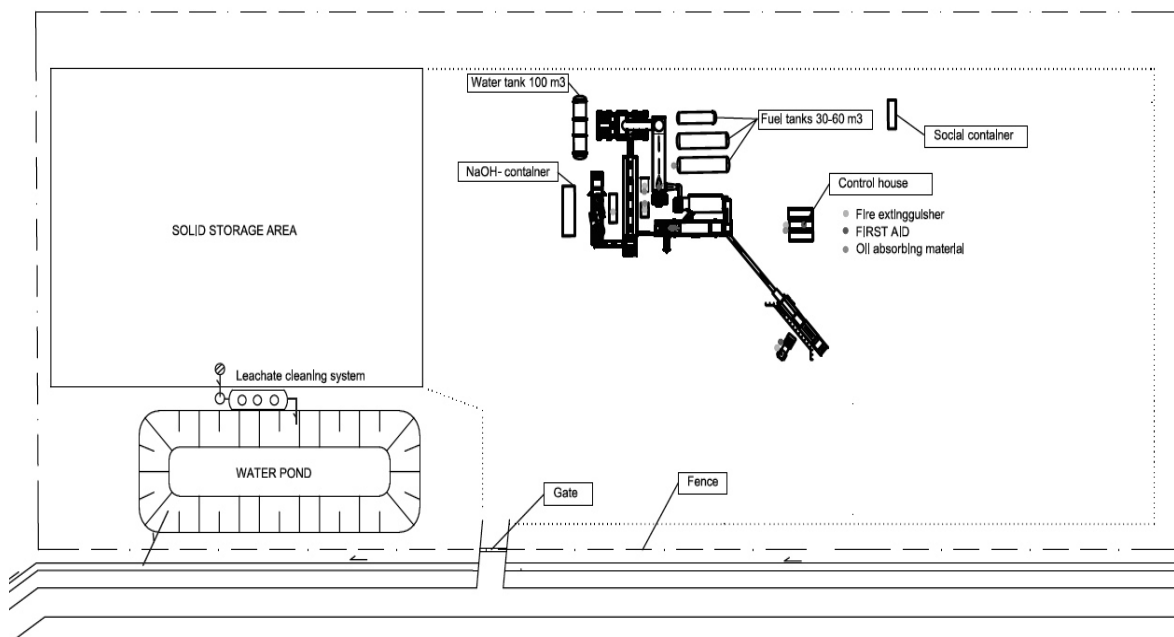
*REGULATION (EC) No 166/2006 OF THE EUROPEAN PARLIAMENT AND OF THE COUNCIL of 18 January 2006 concerning the establishment of a European Pollutant Release and Transfer Register and amending Council Directives 91/689/EEC and 96/61/EC*

Savaterra thermal desorption has six established permits in EU for mobile thermal treatment facility, three in Finland, by one in France, Sweden and Norwegian .

In all Savaterra's environmental permits authorities have given following regulations :

- 1) all treated samples must be analysed by outside independent accredited laboratory
- 2) emission (air) must be made similar way

Picture 1 : Site plan layout :



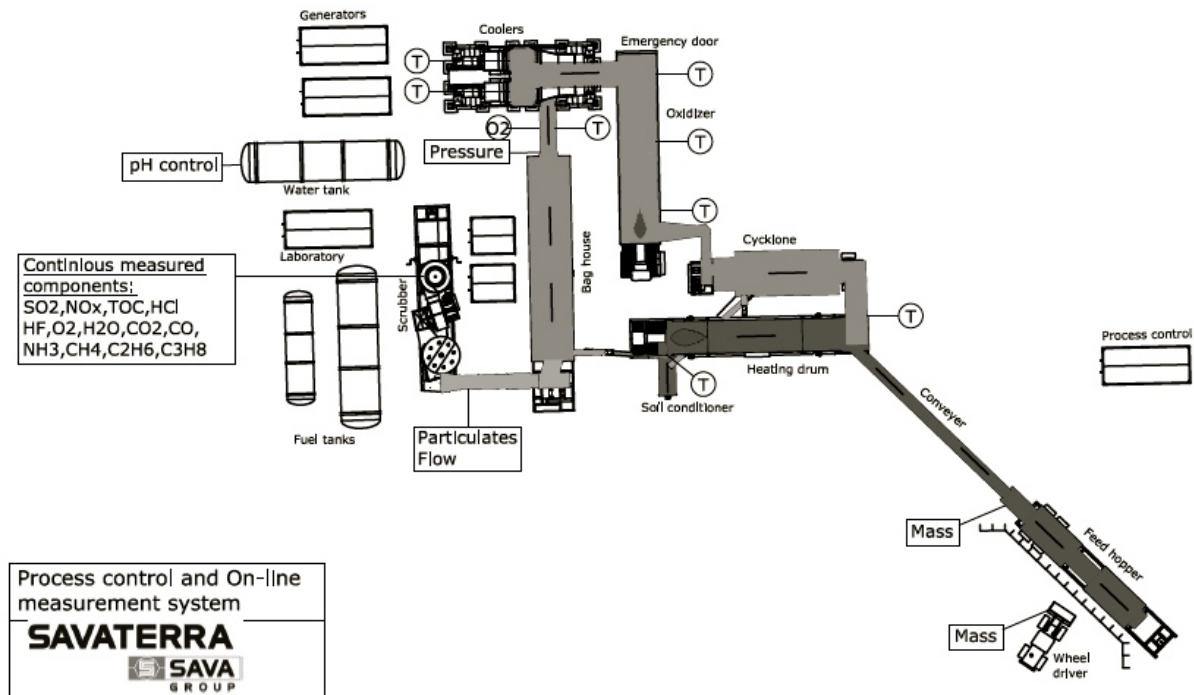
The soil under plant must have good carrying capacity and sustain the wheel loader traffic. The compacting of the soil should be made for 60 ton load. The area needed is about 40 x 50 m.

The water for dust binding and cooling the material will be pumped from water system of the gas washer or directly from water pipe.

The electricity needed in process will be provided by a generator or by normal electric network if available. The thermal desorption plant is made up of unconnected units, which build-up / build-down will take about couple weeks.

The air emissions are monitored by on-line measurements. For the on-line instruments and their measurement points. Periodical measurements carried out by an outside consultant (a certified lab) two times per year. This time also the on-line instruments are tested (calibration functions) by the outside lab. The on-line instruments are calibrated daily basis according to the manufacturers instructions. The plant can be operated from Monday to Saturday 24h per day.

Picture 2 : Measurement system :



The on-line instruments are calibrated daily basis according to the manufacturers instructions.

Picture 3,4 : Online emission measurement and Dust-particles measurement:

**Gasmet CEMS II**

The Gasmet CEMS II FTIR measuring system is designed for continuous emissions monitoring measurements (CEM). Typical application is H<sub>2</sub>O, CO<sub>2</sub>, CO, N<sub>2</sub>O, NO<sub>x</sub>, SO<sub>2</sub>, HCl, HF, NH<sub>3</sub>, CH<sub>4</sub>, C<sub>2</sub>H<sub>6</sub>, C<sub>3</sub>H<sub>8</sub>, C<sub>4</sub>H<sub>10</sub> monitoring from Waste Incinerator or Large Combustion Plants. Measured components and calibration ranges can be changed according to application.

The Gasmet CEMS II is an ideal tool to use for measuring trace concentrations of pollutants in wet, corrosive gas streams. All parts of the Gasmet CEMS II are heated up to 180 °C. It can be used for undiluted gases and the sample gases do not need drying beforehand.

The Gasmet CEMS II consists of Gasmet FTIR Gas Analyzer, Gasmet Industrial cabinet, Gasmet sampling system. As an option the system can be equipped with Gasmet TDL or ZrO<sub>2</sub> oxygen analyzer and/or with total hydrocarbon analyzer (THD). All parts of the system are 10" rack mounted and are installed on the pull-out shelves. The Gasmet CEMS II includes all power connections and temperature controllers for heated lines and heated sample probe. The operation of the system is fully automatic and controlled by the Calmet software. Additionally all functions of CEMS II can be controlled manually.

Comprehensive I/O functions make possible to connect CEMS II into all kind of automation or reporting systems. Measuring data and alarms can be transferred from Gasmet CEMS II to other systems with analog or digital format. Gasmet CEMS II is also equipped with analog / digital inputs for external data (other analyzers or process).

Gasmet CEMS II provides different alarm functions such as System alarm, Service request, Maintenance on progress (can be set also manually), Concentration alarm, and Result valid. Combination for each alarm can be set on Calmet. If any of the critical alarm is activated, instrument air starts to flow automatically into the system to prevent condensation.

Standard CEMS II is equipped with a two span gas valve to allow automated spanzero checks as required by the new legislation.

Gasmet CEMS II is air conditioned with a compressor-cooling unit on top of the cabinet. Cabinet includes ready made through-leading submers on each side and top of the cabinet for all cables and lines. Gasmet CEMS II is also supported by full remote control.

The Gasmet CEMS II FTIR has a very low cost of ownership; the equipment is extremely well designed, and requires very little maintenance. The system also has a number of built-in safety devices to protect the instrument from potential damage.

**DUSTHUNTER SP100**  
Scattered Light Particulate Monitor

Continuous Measurement of Dust with Low to Medium Concentrations

**Intended Purpose**  
The DUSTHUNTER SP100 monitor provides continuous measurement of particulates in industrial plants for process control and PS-11 compliance.

**Models**  
The DUSTHUNTER SP100 (probe version) is available with the following probe lengths:

- 17.13 in (435 mm)
- 28.94 (735 mm)
- 40.75 in (1,035 mm)
- 52.56 in (1,335 mm)

This makes the DUSTHUNTER SP100 ideal for a wide range of applications.

The DUSTHUNTER SP100 consists of the following components:

- DH-SP sender/receiver unit
- Flange with tube
- MCU control unit (with/without purge air supply)
- External purge air unit (option)
- Connection cable
- Purge air hose for MCU-P control unit with integrated purge air supply

General parameters	
Measuring principle:	FTIR (Fourier Transform Infrared)
Performance:	Simultaneous analysis of up to 50 gas components
Operating temperature:	20 ± 20 °C, non-condensing
Storage temperature:	-20 - +60 °C
Response time, T <sub>90%</sub> :	< 180 s, 20m heated line
Gas cell temperature:	180 °C
Sample gas:	Non-condensing, particle free
Flow rate:	~4 liters per minute
Sample gas pressure:	Ambient
Installation place:	Dust free and clean ambient air, without external vibrations

The operation will take place in two shifts of three men. Sunday is reserved for maintenance work. The plant personnel consist of two operator, one foreman and one wheel loader driver. The personnel fill the daybook of production. Quality and quantity of production, disturbances, maintenance work etc. are written into daybook.

Table 1 : Measurements of flue gas emissions at the thermal processing unit of contaminated soil on and measurements of flue gas emissions at the thermal processing unit of contaminated soil (heavy metals):

Parameter	Result	Reference	Parameter	Result	Reference
Volumetric flow of flue gas (dry fl.gas.)	8,2 m <sup>3</sup> /s	1	Mercury (reduced O <sub>2</sub> level 11 %)	μg/m <sup>3</sup>	2
Flue gas temperature (dry flue gas) after gas washing unit	9°C	5	Cadmium (reduced O <sub>2</sub> level 11 %)	,10μg/m <sup>3</sup>	0
Flue gas humidity (dry flue gas)	9%	1	Thallium (reduced O <sub>2</sub> level 11 %)	< 0.01μg/m <sup>3</sup>	<
O <sub>2</sub> (dry gas)	3,6%	1	Antimony (reduced O <sub>2</sub> level 11 %)	.001μg/m <sup>3</sup>	0
CO <sub>2</sub> (dry gas)	,0%	6	Arsenic (reduced O <sub>2</sub> level 11 %)	,01μg/m <sup>3</sup>	0
CO (dry gas)	.0006%	0	Cobalt (reduced O <sub>2</sub> level 11 %)	μg/m <sup>3</sup>	2
CO (reduced O <sub>2</sub> level 11 %)	1mg/m <sup>3</sup>	1	Chromium (reduced O <sub>2</sub> level 11 %)	,3μg/m <sup>3</sup>	0
SO <sub>2</sub> (reduced O <sub>2</sub> level 11 %)	mg/m <sup>3</sup>	5	Copper (reduced O <sub>2</sub> level 11 %)	,8μg/m <sup>3</sup>	0
NO <sub>x</sub> (reduced O <sub>2</sub> level 11 %)	11mg/m <sup>3</sup>	1	Lead (reduced O <sub>2</sub> level 11 %)	,1μg/m <sup>3</sup>	0
TOC (reduced O <sub>2</sub> level 11 %)	mg/m <sup>3</sup>	6	Manganese (reduced O <sub>2</sub> level 11 %)	,5μg/m <sup>3</sup>	0
Solids (reduced O <sub>2</sub> level 11 %)	mg/m <sup>3</sup>	7	Nickel (reduced O <sub>2</sub> level 11 %)	,4μg/m <sup>3</sup>	0
			Vanadium (reduced O <sub>2</sub> level 11 %)	,04μg/m <sup>3</sup>	0

The total concentration obtained in dioxin and furan (I-TEQ) measurements was 0.003 ng/m<sup>3</sup>N reduced to the oxygen level of 11%.

## II. Process description

The thermal desorption plant will be transported the nearness of remediation site. Contaminated soils are excavated and transported to plant.

Description of parts :

**1.Feed hopper** - The wheel loader unloads the contaminated soils to **feed hopper** where material larger than 150 mm in diameter are removed. Larger material will be crushed and recycled into the feed or delivered to landfill. The capacity is adjusted in feed hopper according the concentration and quality of contaminant. If contaminated soil is very wet or has a lot contamination, it may need to be mixed with less contaminated or workable soil for treatment in desorption unit. Metal material will be removed by **magnetic** after feed hopper. **A conveyor belt (2)** will load the material into desorption unit.

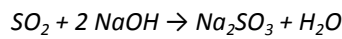
**3.Desorption unit** - The desorption unit is used to heat contaminated soil to a high enough temperature and for a long enough time to dry it and vaporize the contaminants from soil. The unit is a rotary desorber which has a rotating ,cylindrical metal drum. The rotation speed and the angle of the drum will adjust treatment rate (tons/hour) Temperature in the drum can be adjusted in the range of 350-800°C depending on the contaminant. Typical retention time of the material in the desorption drum is approx.. 20 minutes. The desorber has direct flame in the oven. This means that the material has direct contact to flame. The material can heat up to 1000°C. Oven will always have under-pressure.

**4. Cyclone** - As the soil is heated, the contaminants will vaporize and become a part of gas stream of air which is caused by blowers. Gas flow from desorber is guided by under-pressure to cyclone where most of the particulate matter will be removed.

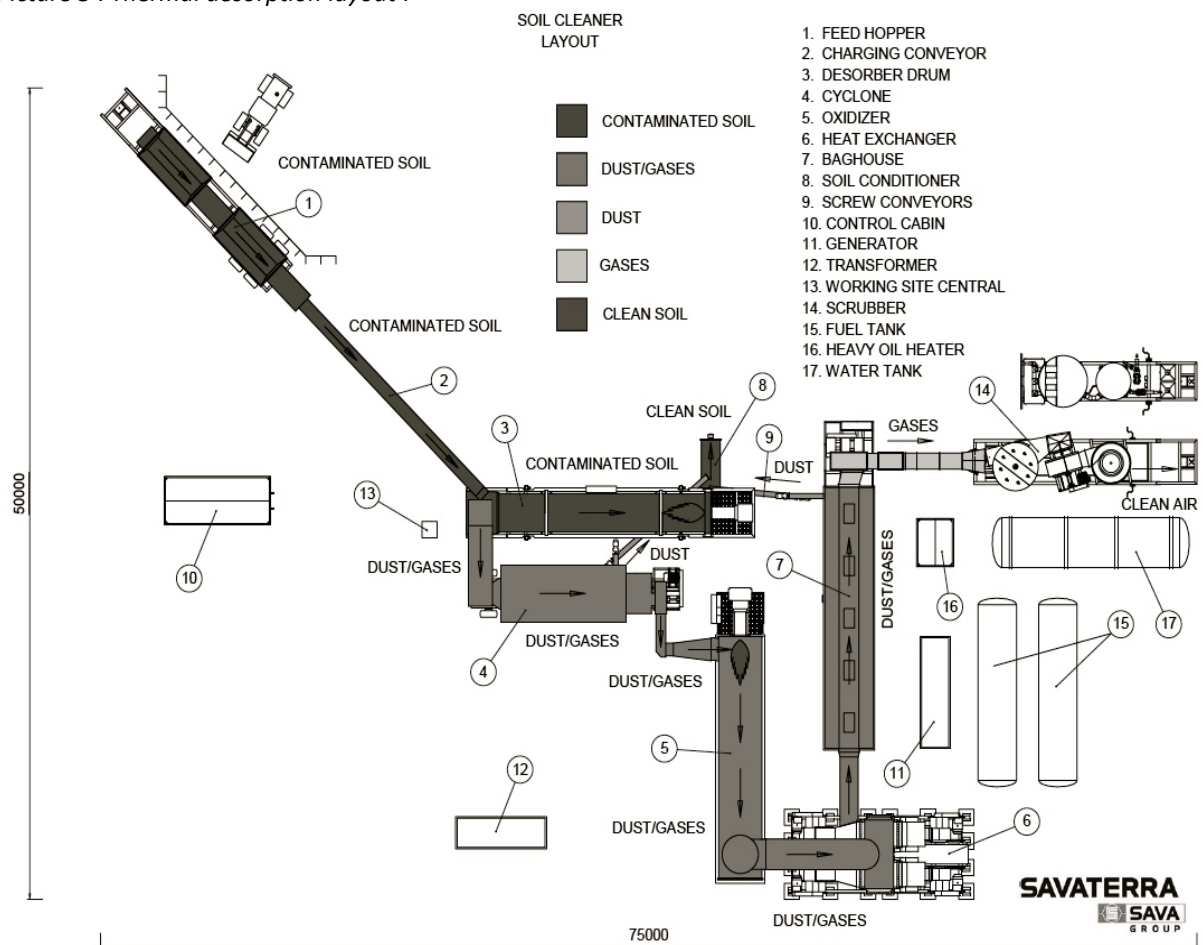
**5. Afterburner** - After cyclone, vaporized contaminants will be burned in an afterburner (oxidizer). Temperature 850-1100 degrees C destroys the contaminants into CO<sub>2</sub>.

**6. Heat exchanger** - The flue gas is cooled to 180°C before entering the bag house.

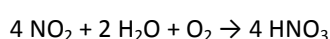
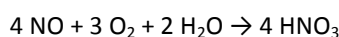
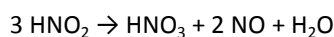
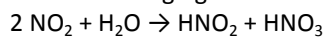
**7. Bag house** takes away most of particles. Activated carbon can be utilized in the bag house to remove Hg from the flue gases. **14. Gas scrubber** is connected to process if sulphur (SO<sub>x</sub>) concentration in soil or fuel is exceptional high level. SO<sub>x</sub> will react with water and sodium hydroxide as follows:



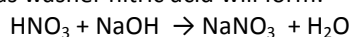
Picture 5 : Thermal desorption layout :



Scrubber also helps to remove last particles. Water of the scrubber will be treated in water treatment process and re-used in dust binding of soil. Gas washing unit will also take some nitric oxides :



In the gas washer nitric acid will form:



However, in prevention of most of the nitric oxide formation has been done by optimization of treatment temperatures and by adjustment of the burners.

Water in the process (steam) will also reduce nitric oxide emission. The gas scrubber will also neutralize possible HF and HCl emissions as follows:

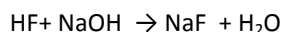
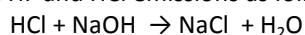


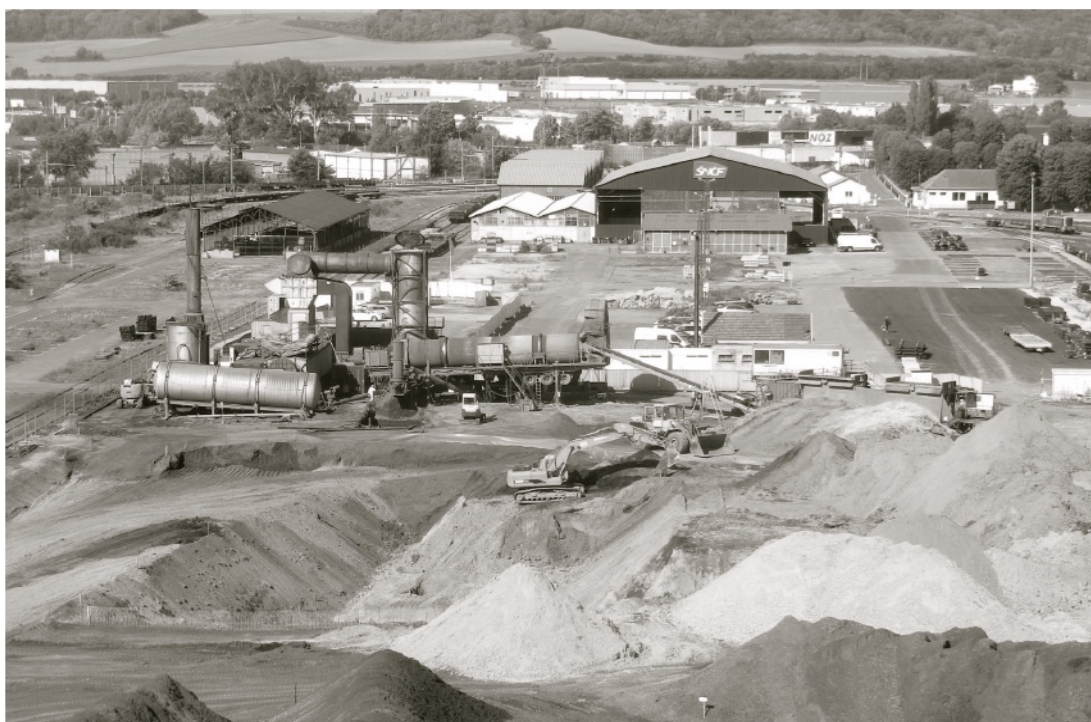
Table 2 : Contaminants, temperature of desorption, oxidation, input and output content of contaminant in soil :

Contaminant	Temperature of desorption/boiling point	Temperature of oxidation	Content of contaminant in soil in input - before	Content of contaminant in soil in output -after
SemiVOC	200-300°C	850°C	<80.000mg/kg	0,02-10mg/kg
PAH	>400°C	850°C	<20-30g/kg	<5mg/kg
PCB	>500°C	>1000°C	<10.000mg/kg	<0,5mg/kg
Pesticides and herbicides	200-300°C	850°C	<10.000mg/kg	Less than detection limit
VOC	200-300°C	850°C	<80.000mg/kg	0,02-10mg/kg
Total hydrocarbons TOC	200-400°C	850°C	<80.000mg/kg	<50mg/kg
Chlorophenols (CP)	>400°C	850°C	<10.000mg/kg	<5mg/kg
PCDD/Fs	>600°C	>1000°C	<1.000mg/kg*	<0,00005mg/kg
Cyanid's (CN)	>400°C	850°C	<40.000mg/kg	<10mg/kg
Metals of 12.groups table of elements (f.e. Mercury Hg)(volatile metals)	>400°C	850°C	<10.000mg/kg	0,005mg/kg
Heavy metals	>400°C	850°C	<10.000mg/kg	Insoluble Salt

Table 3 : Savaterra Oy references in soil treatment:

Year	Ref.	Description	Compound	Concentration	Amount (t)
2002	1	Receptory site operated by ST	VOC+C <sub>10</sub> -C <sub>40</sub>	0.7-3%	20000
2002	2	Receptory site operated by ST	VOC+C <sub>10</sub> -C <sub>40</sub>	3 %	5000
2002	3	Maarjehavn oilharbour	VAC+C <sub>10</sub> -C <sub>40</sub>	5 %	20000
2003-2004	4	Puistolanniemi oilharbour	VOC+C <sub>10</sub> -C <sub>40</sub>	0.3%+ 1%	100000
2003-2004	5	Puistolanniemi oilharbour	VOC+C <sub>10</sub> -C <sub>40</sub>	0.3%+ 1%	30000
2004-2005	6	Refinery waste site	VOC+C <sub>10</sub> -C <sub>40</sub> + PAH	7-20%	175000
2005	7	Impregnation site	VOC+C <sub>10</sub> -C <sub>40</sub> + PAH	0.8-3% + 0.2-0.5%	18000
2003-2008	8	Receptory site operated by ST	VOC+C <sub>10</sub> -C <sub>40</sub> + PAH+PCB	>2% + >0.5% +0.1-0.2%	100000
2003->	9	Receptory site operated by ST	C <sub>10</sub> -C <sub>40</sub> + PAH	>3% + >0.5%	150000
2003->	10	Receptory site operated by ST	C <sub>10</sub> -C <sub>40</sub> + PAH - PCDD/F –metals, pesticides, TNT	0.1-5%+0.1-0.5%	250000
2009	11	Oil drilling mud	C <sub>10</sub> -C <sub>40</sub> + PAH	22 %	3000
2010	12	Pulpmill site	C <sub>10</sub> -C <sub>40</sub> + PAH+turpentine+ black liquor	0.05-4%	55000
2012	14	Impregnation site	VOC+C <sub>10</sub> -C <sub>40</sub> + PAH	0.8-3% + 5%	60000
2012	15	Impregnation site	CP+PCDD/F	1.5-2000µg/kg	15000
2014	16	Impregnation site	CP+PCDD/F	1.5-150µg/kg	12000
2014	17	Mustard gas	military compounds	not public	200
				Total	1013200

Picture 6 : SAVATERRA'S EVO1 in Chambly France



Picture 7 : EVO 1 in Paris Chambly

Table 3 : Capacity of EVO 1

Technology	Daily capacity (t/day)	Short time capacity (t/hour)	Monthly production (tons)	Yearly capacity (tons)
Thermal treatment of contaminated soils by EVO 1	350	80	7 000 -16 000	84 000- 200 000

Table 4 : Extract from Patent office register

(19)  Europäisches Patentamt European Patent Office Office européen des brevets	
	(11) <b>EP 2 749 361 A1</b>
(12) <b>EUROPEAN PATENT APPLICATION</b>	
(43) Date of publication: <b>02.07.2014 Bulletin 2014/27</b>	(51) Int Cl.: <b>B09B 3/00 (2006.01) B09C 1/06 (2006.01)</b> <b>F23G 7/14 (2006.01)</b>
(21) Application number: <b>12199796.9</b>	
(22) Date of filing: <b>31.12.2012</b>	
(84) Designated Contracting States: <b>AL AT BE BG CH CY CZ DE DK EE ES FI FR GB GR HR HU IE IS IT LI LT LU LV MC MK MT NL NO PL PT RO RS SE SI SK SM TR</b> Designated Extension States: <b>BA ME</b>	(72) Inventor: <b>Aho, Olli</b> <b>96300 Rovaniemi (FI)</b> (74) Representative: <b>Kolster Oy Ab</b> <b>Iso Roobertinkatu 23</b> <b>PO Box 148</b> <b>00121 Helsinki (FI)</b>
(71) Applicant: <b>Savaterra Oy</b> <b>96300 Rovaniemi (FI)</b>	
(54) <b>Direct contact high temperature thermal desorbtion</b>	

## EVALUATION OF UV, UV/H<sub>2</sub>O<sub>2</sub> AND UV/Na<sub>2</sub>S<sub>2</sub>O<sub>8</sub> SYSTEMS FOR THE TREATMENT OF INDUSTRIAL WATERS – ORGANICS DEGRADATION AND DISINFECTION

**Bártová Š.**<sup>1</sup>, Šveda H.<sup>2</sup>, Kůs P.<sup>1</sup>, ŠmejdoVá V.<sup>1</sup>, Říhová Ambrožová J.<sup>2</sup>, Vonková K.<sup>1</sup>

<sup>1</sup>Research Centre Řež, Hlavní 130, 250 68, Husinec-Řež

<sup>2</sup>University of Chemistry and Technology Prague, Technická 3, 166 28, Praha sarka.bartova@cvrez.cz

### Introduction

Non-potable (river or lake) water is used for cooling in cooling water circuit system (cooling towers). This water itself contains high amount of organic compounds and microorganisms, however, further organic compounds and microorganisms can get into the cooling system from the surroundings. Furthermore, the cooling tower system is an ideal environment for the growth of microorganisms. To minimize the effects of microorganism pollution, cooling waters are biologically monitored and consequently treated<sup>1</sup>.

Currently, water treatment is based on physicochemical and mechanical methods with further biological treatment, which is not sufficient enough for the whole range of organic compounds<sup>2,3</sup>. One of possible alternatives is to use UV light, which damages microorganisms DNA and, thus, results in the loss of their reproducibility. Furthermore, irradiation of water by UV light leads to formation of very reactive OH radicals, which are capable of non-selective mineralization of all organic pollutants<sup>3,4</sup>. The UV light efficiency in disinfection process and organics degradation can be enhanced by the presence of oxidizing agents (e.g. H<sub>2</sub>O<sub>2</sub>) due to their ability to form loose radicals, and, thus, initiate radical reaction<sup>5</sup>. The main advantage of the suggested technology is that it is universal and non-selective and that it is environment friendly.

Real cooling water from cooling towers of fossil power plant was used for the evaluation of UV, H<sub>2</sub>O<sub>2</sub> and UV/H<sub>2</sub>O<sub>2</sub> systems in disinfection and organics degradation. In our work, we focused our attention on the efficiency of these systems in water disinfection, on the determination of microscopic image and biological analyses. Furthermore, the overall process efficiency was monitored by determination of TOC value (TOC – Total Organic Carbon).

### Experimental

For the experiments testing the efficiency of UV and UV/H<sub>2</sub>O<sub>2</sub> systems in TOC decrease, a laboratory apparatus was constructed. It consists of UV lamp Sterilight S1Q-PA/2 (radiation wavelength 254 and 185 nm), feed solution reservoir, H<sub>2</sub>O<sub>2</sub> reservoir and two pumps for dosing feed solution and H<sub>2</sub>O<sub>2</sub> (cf. scheme in Fig. 1). The experiments were performed in a continuous mode with various flow rates of feed solution and H<sub>2</sub>O<sub>2</sub>. As the feed solution, real samples of cooling water from Czech fossil power plant were used. The samples of water were analyzed before and after each experiment to determine TOC and microbiological indicators of water quality. In microbiological analyses we focused on the presence of culturable microorganisms (at 22 °C and 36 °C), coliforms and *E. coli*, enterococci, *Pseudomonas aeruginosa* (biofilms, sliming), *Clostridium perfringens* (anaerobic, endospores), *Staphylococcus aureus* (resistant to chemical treatment), algae and cyanobacteria.

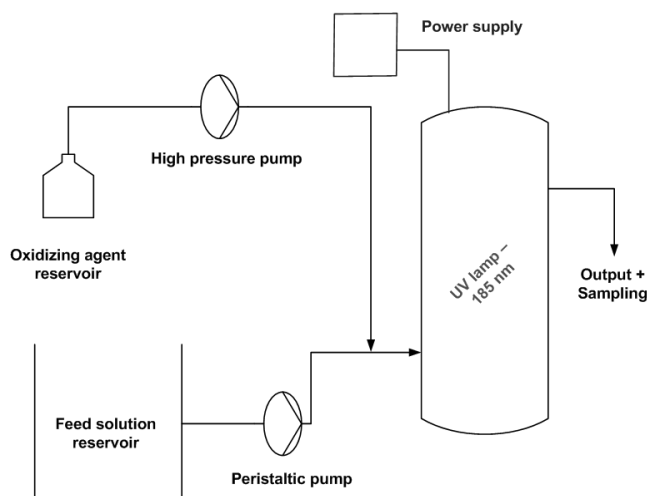


Figure 1. Scheme of laboratory apparatus used for the experiments with real cooling water from cooling water circuit system of fossil power plant.

## Results and discussion

The results obtained from microbiological analysis are summarized in Tables I and II. Quite a significant amount of culturable microorganisms was identified in the system treated solely by UV light. Applying 1.0 % H<sub>2</sub>O<sub>2</sub> resulted in much lower amount of identified microorganisms (Table I), however applying 0.1 % H<sub>2</sub>O<sub>2</sub> resulted in much more identified microorganisms. The best results were achieved with a combined UV/H<sub>2</sub>O<sub>2</sub> system with both H<sub>2</sub>O<sub>2</sub> concentrations.

Table I

Microbiological values obtained in the cooling water before and after the experiments performed with UV, H<sub>2</sub>O<sub>2</sub> and UV/H<sub>2</sub>O<sub>2</sub> systems. Q<sub>BA</sub>=30 ml/min, Q<sub>OX</sub>=2 ml/min (1.0 % H<sub>2</sub>O<sub>2</sub>).

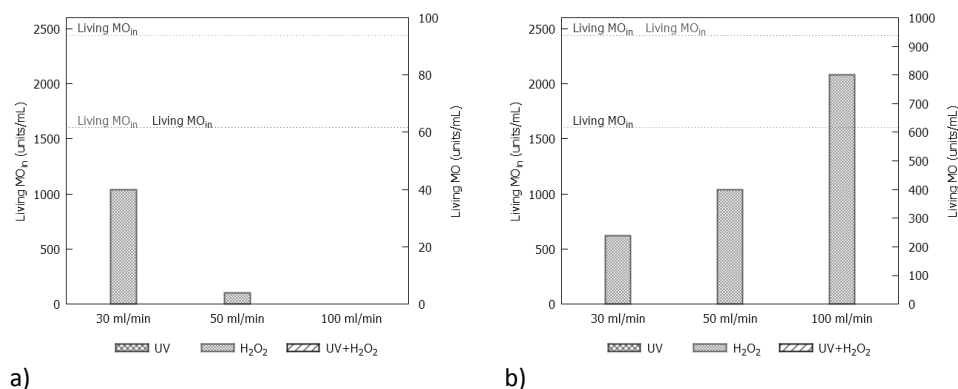
Indicator	Feed solution	past UV	Feed solution	past H <sub>2</sub> O <sub>2</sub> [1%]	Feed solution	past UV+H <sub>2</sub> O <sub>2</sub> [1%]
Coliforms [CFU/100ml]	200	10	530	0	530	0
<i>Escherichia coli</i> [CFU/100ml]	1380	1	420	0	420	0
Enterococci [CFU/100ml]	870	50	510	0	510	0
Staphylococci [CFU/100ml]	170	0	140	14	140	1
<i>Pseudomonas aeruginosa</i> [CFU/100ml]	200	0	20	0	20	0
<i>Clostridium perfringens</i> [CFU/100ml]	370	0	240	0	240	0
Culturable microorganisms at 22 °C [CFU/ml]	472	423	421	160	421	0
Culturable microorganisms at 36 °C [CFU/ml]	1080	487	2340	220	2340	0

Table II

Microbiological values obtained in the cooling water before and after the experiments performed with UV, H<sub>2</sub>O<sub>2</sub> and UV/H<sub>2</sub>O<sub>2</sub> systems. Q<sub>BA</sub>=30 ml/min, Q<sub>OX</sub>=2 ml/min (0.1 % H<sub>2</sub>O<sub>2</sub>).

Indicator	Feed solution	past UV	Feed solution	past H <sub>2</sub> O <sub>2</sub> [0.1%]	Feed solution	past UV+H <sub>2</sub> O <sub>2</sub> [0.1%]
Coliforms [CFU/100ml]	200	10	200	20	530	0
<i>Escherichia coli</i> [CFU/100ml]	1380	1	1380	17	420	0
Enterococci [CFU/100ml]	870	50	870	0	510	0
Staphylococci [CFU/100ml]	170	0	170	240	140	2
<i>Pseudomonas aeruginosa</i> [CFU/100ml]	200	0	200	0	20	0
<i>Clostridium perfringens</i> [CFU/100ml]	370	0	370	30	240	0
Culturable microorganisms at 22 °C [CFU/ml]	472	423	472	490	421	20
Culturable microorganisms at 36 °C [CFU/ml]	1080	487	1080	560	2340	3

Microscopic image did not reveal any living microorganisms after treatment by UV and UV/H<sub>2</sub>O<sub>2</sub> systems (cf. Fig. 2 a, b) under any experimental conditions. However, when only H<sub>2</sub>O<sub>2</sub> was used for the treatment, some living microorganisms were identified. In case of 1.0 % H<sub>2</sub>O<sub>2</sub>, the amount of identified living microorganisms was in orders of tens of units per mL (cf. Fig. 2a). Unexpectedly, the amount of identified living microorganisms decreased as the feed flow increased, but the deviations can be included in the measurement error in this case because of very little absolute numbers. In case of 0.1 % H<sub>2</sub>O<sub>2</sub>, the amount of identified living microorganisms was in orders of hundreds of units per mL and it increased as the feed solution increased (cf. Fig. 2b), as expected. The initial amount of living microorganisms with 1.0 % H<sub>2</sub>O<sub>2</sub> was little lower (ca. 1600 units/mL) than with 0.1 % H<sub>2</sub>O<sub>2</sub> (ca. 2480 units/mL). However, such a little difference in the feed water can not be a reason for such a significant difference in the treated water (ten times higher efficiency in case of 1.0 % H<sub>2</sub>O<sub>2</sub>) and it can be said that 0.1 % H<sub>2</sub>O<sub>2</sub> was not sufficient enough in microorganisms' damage.



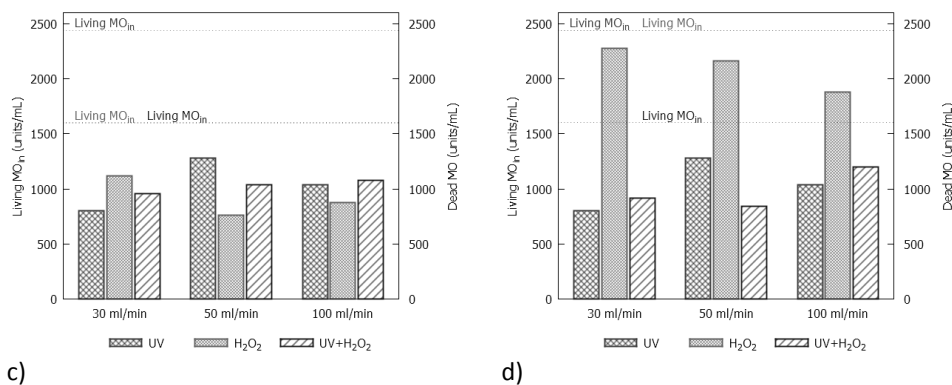


Figure 2. Microscopic image, i.e. the amount of a), b) living and c), d) dead microorganisms identified before and after the experiments with cooling water from fossil power plant.  $Q_{BA}=30/50/100$  ml/min, a), c)  $Q_{ox}=2$  ml/min (1.0 % H<sub>2</sub>O<sub>2</sub>) and b), d)  $Q_{ox}=2$  ml/min (0.1 % H<sub>2</sub>O<sub>2</sub>).

TOC concentrations determined in the samples before and after the experiments are depicted in Fig. 3. When only UV light was used, TOC concentration in the treated samples decreased as the feed flow increased. However, general UV light efficiency in organics degradation was low. There are two possible explanations for such a low UV light efficiency: (i) organics present in water are quite resistant towards UV light, and/or (ii) mainly microorganisms contribute to overall TOC value and even though they are damaged, they are still present in water and, thus, contribute to TOC value.

When only H<sub>2</sub>O<sub>2</sub> was used, the best results were achieved with higher H<sub>2</sub>O<sub>2</sub> concentration (1.0 % H<sub>2</sub>O<sub>2</sub>) at the lowest feed flow. Higher feed flows and lower H<sub>2</sub>O<sub>2</sub> concentration resulted in worse efficiency indicating that lower "H<sub>2</sub>O<sub>2</sub> flow/feed flow" ratio is not sufficient for most of the organics degradation.

When UV/H<sub>2</sub>O<sub>2</sub> system was used, a high improvement in organics degradation was observed at low and middle feed flow with both H<sub>2</sub>O<sub>2</sub> concentrations. In these cases, about 50 % of organic compounds were damaged independently of "H<sub>2</sub>O<sub>2</sub> flow/feed flow" ratio. However, increase of feed flow to 100 mL/min. resulted in lower organics degradation and obtained results were comparable with results of solely UV and H<sub>2</sub>O<sub>2</sub> systems.

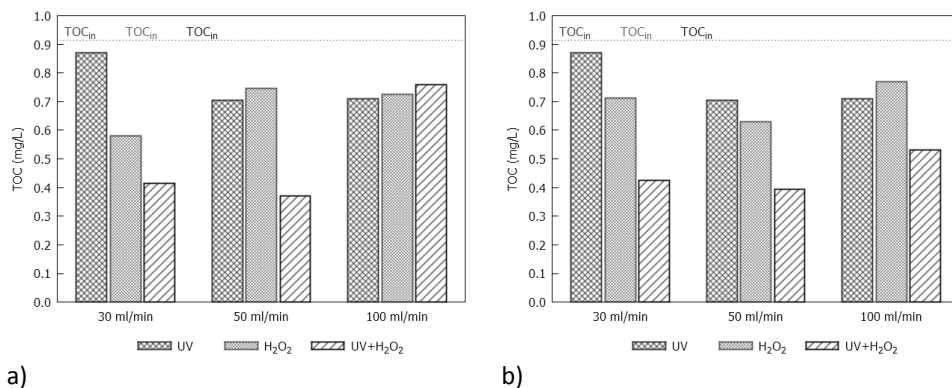


Figure 3. TOC concentration before and after the experiments with cooling water from fossil power plant.  $Q_{BA}=30/50/100$  ml/min, a)  $Q_{ox}=2$  ml/min,  $c_{ox}=1.0$  % H<sub>2</sub>O<sub>2</sub> and b)  $Q_{ox}=2$  ml/min,  $c_{ox}=0.1$  % H<sub>2</sub>O<sub>2</sub>.

## Conclusion

UV, H<sub>2</sub>O<sub>2</sub> and UV/H<sub>2</sub>O<sub>2</sub> systems were tested for the treatment of cooling water from cooling towers. The efficiency of these systems in disinfection and organics degradation was evaluated with various experimental setups. A combined UV/H<sub>2</sub>O<sub>2</sub> was evaluated as the most efficient giving satisfactory results.

## Acknowledgement

The work has been performed with the support of project Effective Infrastructure for R&D Commercialization CZ.1.05/3.1.00/14.0322 (ERDF) and with the contribution of the institutional support that has been given to the research organization Centrum výzkumu Řež s.r.o. (Research Center Řež) for a long-term conceptual development.

### Literature

5. Říhová Ambrožová J., Matulová T., Chemické listy 101(10), 820-836 (2007)
6. Munter R., Proc. Estonian Acad. Sci. Chem. 50, 59 (2001).
7. Baycan Parilti N., Ekoloji 77, 9 (2010).
8. Ruppert G., Bauer R., Heisler G., Chemosphere 28, 1447 (1994).
7. Beneš J., Sborník konference Pitná voda, 135 (2008).

## INFLUENCE OF PHOSPHORUS TO DENITRIFICATION WITH THIOBACILLUS DENITRIFICANS

**Blažková Z.**, Slehová E., Trousil V., Slezák M., Palarčík J., Čákl J.

University of Pardubice, Faculty of chemical technology, Institute of Environmental and chemical engineering, Studentská 573, 532 10, Pardubice  
Zuzana.Blazkova@upce.cz

*Thiobacillus (Th.) denitrificans* is gram-negative, chemolithoautotrophic and facultative anaerobic microorganism. These bacteria use oxidation of reduced inorganic sulfur compounds for respiratory reduction of oxygen or, under anaerobic conditions, of nitrate (or nitrite) to dinitrogen gas<sup>1,2</sup>. This is the way of obtaining energy for bacterial cells and it is used for effective fixation of carbon dioxide by the Calvin cycle under both aerobic and anaerobic conditions<sup>3</sup>.

*Th. denitrificans* is found in soil, mud, marine and freshwater sediments, domestic sewage, industrial waste-treatment lagoons and digestion tanks. From an environmental perspective it is very important microorganism. Denitrification capacity of *Th. denitrificans* could be used in the future as an alternative method for the removal of nitrates and nitrites from contaminated water<sup>4</sup>. Denitrification can be affected by many factors such as pH, temperature and the ration C/N and S/N<sup>5-8</sup>. This work is focused on influence of phosphorus to denitrification, because phosphorus belongs to compounds accelerating denitrification. The aim of the work was to determine the effectiveness of autotrophic denitrification with phosphorus, determine the speed of these processes and defining the amount of consumed phosphorus.

Two series of batch experiments were prepared to verify effect of phosphorus on the course and speed of denitrification by *Th. denitrificans*.

In the first series of batch experiments, we compared the course of denitrification in the presence of phosphorus with the course of denitrification with no phosphorus. The experiments were carried out in glass bottles of one liter (total 2 pieces). Bottles were labeled A and K, and they contained sulfur pearls (with size from 0,5 to 5 mm) with bacteria *Th. denitrificans*, limestone rubber for pH control and solution of sodium nitrate at concentration 100 mg/l NO<sub>3</sub><sup>-</sup>. Limestone rubber and sulfur pearls were purchased from the company Aqua Medic. In the bottle labeled A was added phosphorus at concentration 0,5 mg/l P. Experiments in this series were studied for 160 days.

In the second series of batch experiments, we compared the speed denitrification in the presence of different concentrations of phosphorus. The experiments were carried out in the same bottles as in previous case. Four bottles were prepared and they were labeled P1 - P4. Bottles contained sulfur pearls (with size from 0,5 to 5 mm) with bacteria *Th. denitrificans*, limestone rubber for pH control, solution of sodium nitrate at concentration 100 mg/l NO<sub>3</sub><sup>-</sup> and phosphorus at concentration range from 0,1 to 2,5 mg/l P. Experiments in this series were studied for 80 days.

In all experiments the values of nitrate, nitrite and phosphorus concentration, pH, redox, temperature and dissolved oxygen concentration were measured. All assays were performed according to appropriate standards<sup>9-15</sup>. It was also observed the presence of bacteria in all experiments by phase contrast microscopy. Specific contents of bottles in all series of batch experiments is shown in Table I.

Table I. Summary of experiments and conditions

Bottle	Sulfur with <i>Th. Denitrificans</i> [g]	CaCO <sub>3</sub> [g]	NO <sub>3</sub> <sup>-</sup> [mg/l]	P [mg/l]
A	50	50	100	0,5
K	50	50	100	-
P1	50	50	100	2,5
P2	50	50	100	1,0
P3	50	50	100	0,5
P4	50	50	100	0,1

The course of denitrification by bacteria *Th. denitrificans* in the bottle A and K is graphically illustrated in the Figure 1. There are used values depending nitrate and nitrite concentration versus time. These experiments demonstrated, that the bacteria need 5 days to adapt (lag phase). In this phase can be seen minimal loss of nitrates and the formation of corresponding amount of nitrites. It is also caused by presence of oxygen, because oxygen has preference as a terminal electron acceptor. After lag phase, there are significant changes

in the monitored parameters - reduction of nitrate concentration and the corresponding increase of nitrite concentration. Although in both cases the values of nitrite concentrations have increased trend, resulting nitrite ions are degraded immediately - there is a loss of total nitrogen determined by the sum of nitrate and nitrite nitrogen. In the first half period of the reduction of nitrite, more nitrite ions are formed than reduced. Opposite occurs in the second half of this time, nitrite ions no longer have to form. We can conclude, that the reduction of nitrate ions is faster than the reduction of nitrite ions.

Wide range of substances as phosphorus can affect these processes positively or negatively. If we focus on both processes as a whole, we can say, that even a slight addition of phosphorus (0,5 mg/l P to 100 mg/l  $\text{NO}_3^-$ ) has a positive effect to autotrophic denitrification by bacteria *Th. denitrificans* - we compared the course and speed of denitrification in bottles A and K in Figure 1 (when bottle labeled A contained phosphorus) and we observed approximately four-fold acceleration of reduction of nitrate ions to nitrite ions. Unfortunately, we could not unequivocally determine acceleration of nitrite reduction during denitrification at presence of phosphorus and during denitrification with no phosphorus, because the rate of formation of nitrite ions is different. In the bottle labeled A, there is faster reduction of nitrate ions than in the bottle K and it is consequence of faster formation of nitrite ions in the bottle A than in the bottle K. Therefore, it is not possible to objectively asses the rate of nitrite reduction in this case.

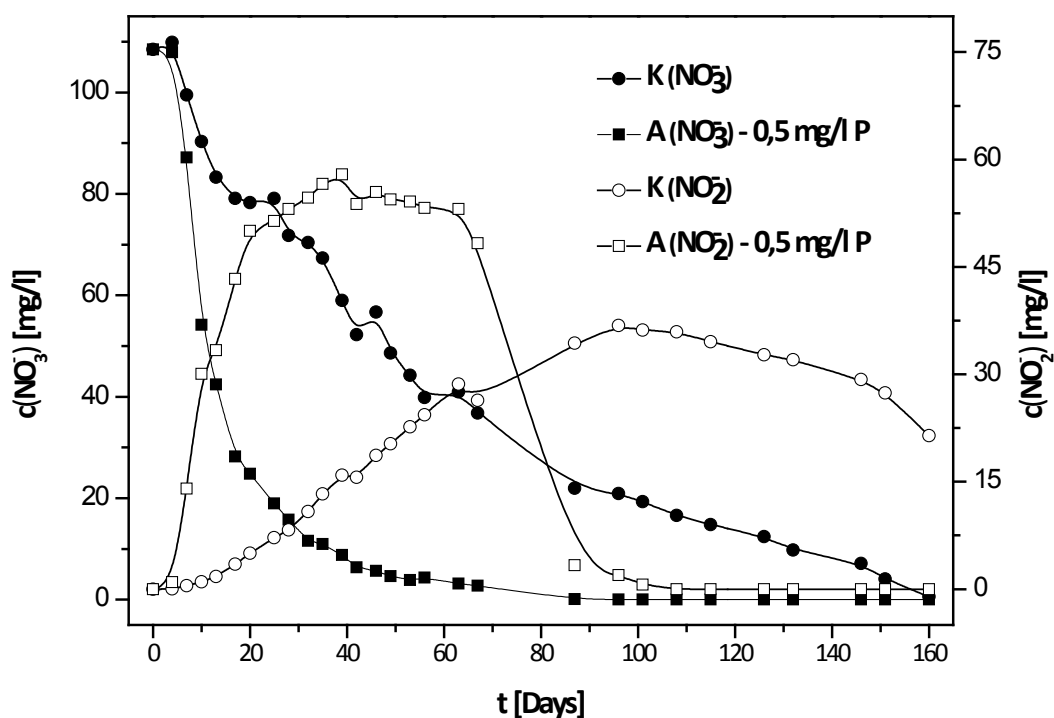


Figure 1. The course of denitrification by *Th. denitrificans* in the presence of phosphorus and the course of denitrification by *Th. denitrificans* with no phosphorus

Four batch reactors (labeled P1 - P4) were prepared for study of influence of different concentrations of phosphorus during the denitrification by bacteria *Th. denitrificans*. A phosphorus was added into bottles at concentration range from 0,1 to 2,5 mg/l P. Figure II shows the time correlations of the concentration of nitrate ions in all four bottles. In the first five days, we observed lag phase again. Further progress of the nitrate reduction takes place identically in these bottles. The selected range of phosphorus concentrations showed only a minimal influence each other on the course and speed denitrification.

Conversely, the selected range of concentrations of phosphorus showed different effect each other on the course and speed denitrification processes. There are time correlations of the concentrations of nitrite ions in all four bottles in the Figure III. After the lag phase, the fastest degradation of nitrite ions was observed at concentrations of phosphorus 0,5 mg/l P and 1,0 mg/l P for degradation of 100 mg/l  $\text{NO}_3^-$ .

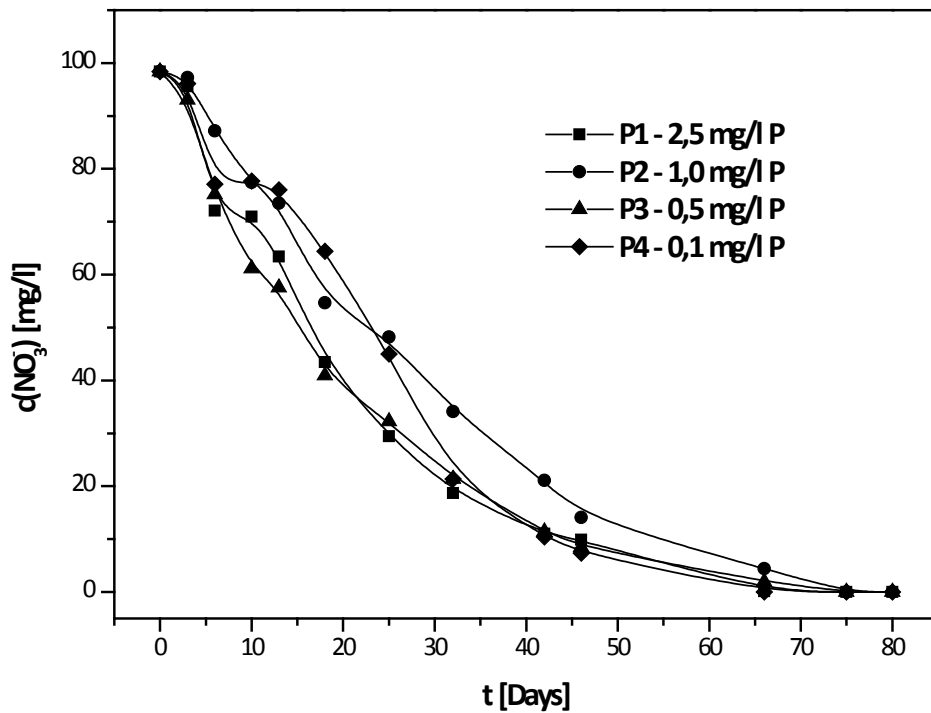


Figure 2. Degradation of nitrate during denitrification by *Th. denitrificans* in the presence of different concentrations of phosphorus

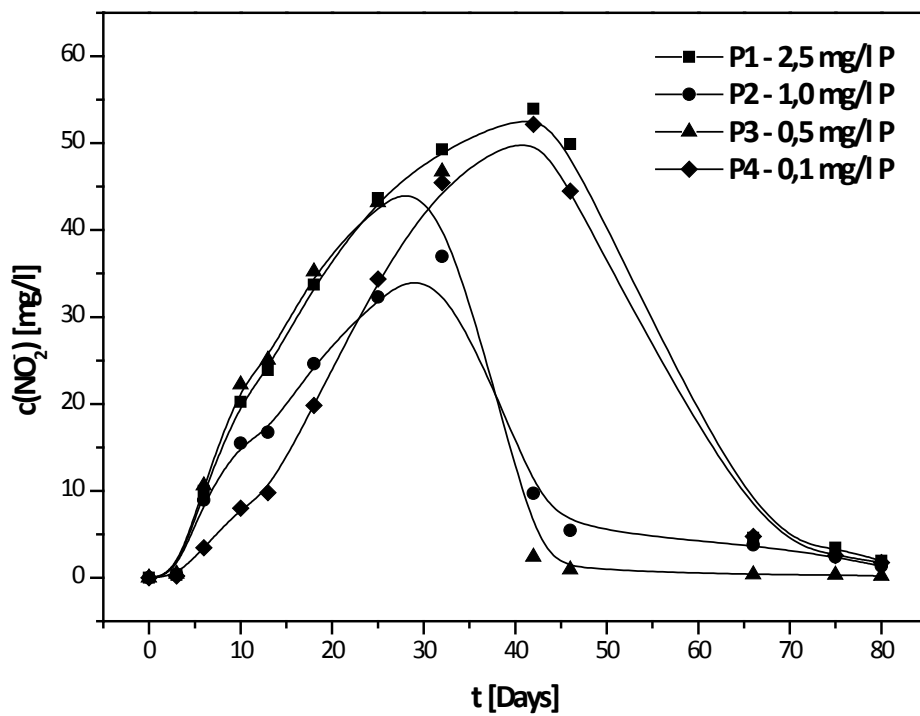


Figure 3. Formation and degradation of nitrite during denitrification by *Th. denitrificans* in the presence of different concentrations of phosphorus

The experiment confirmed, that the low addition of phosphorus (0,5 mg/l P to 100 mg/l NO<sub>3</sub><sup>-</sup>) leads to a significant acceleration of denitrification processes of bacteria *Th. denitrificans*. The concentration optimum of added phosphorus for remove 100 mg/l NO<sub>3</sub><sup>-</sup> should be in the range from 0,5 to 1,0 mg/l P to ensure the highest speed of denitrification. Correct settings of ratio of these nutrients are important for effective management of autotrophic denitrification bacteria *Th. denitrificans*.

#### Acknowledgement

*This work was supported by Ministry of Education, Youth and Sports (SGSFCHT\_2015006).*

#### Literature

1. Kelly D. P., Wood A. P.: *Int J Evol Microbiol* 50/2, 547 (2000).
2. Beller H. R., Letain T. E., Chakicherla A., Kane S. T., Legler T. C., Coleman M. A.: *J Bacteriol* 188/19, 7005 (2006).
3. Beller H. R., Chain P. S. G., Letain T. E., Chakicherla A., Larimer F. W., Richardson P. M., Coleman M. A., Wood A. P., Kelly D. P.: *J Bacteriol* 188/4, 1473 (2006).
4. Moon H. S., Ahn K.-H., Lee S., Nam K., Kim J. Y.: *Environmental Pollution* 129, 499 (2003).
5. Oh S.-E., Kim K.-S., Choi H.-C., Cho J., Kim I. S.: *Wat Sci Tech* 42/3-4, 59 (2000).
6. Liu L. H., Koenig A.: *Proc Biochem* 37, 885 (2002).
7. Marconi I., Carruci A., Lens P.: *Biotech Bioeng* 98/3, 551 (2007).
8. Shao M., Zhang T., Fang H. H.: *Appl Microbiol Biotechnol* 88/5, 1027(2010).
9. ČSN ISO 7890-3 (75 7453): *Jakost vod. Stanovení dusičnanů s kyselinou sulfosalicylovou*. Praha: Český normalizační institut (1994).
10. ČSN EN 26777 (75 7452). *Jakost vod. Stanovení dusitanů. Molekulární absorpční spektrofotometrická metoda (ISO 6777:1984)*. Praha: Český normalizační institut (1995).
11. ČSN EN ISO 6878 (75 7465). *Jakost vod. Stanovení fosforu. Spektrofotometrická metoda s molybdenanem amonným*. Praha: Český normalizační institut (2005).
12. ČSN ISO 10523 (75 7365). *Jakost vod – Stanovení pH*. Praha: Český normalizační institut (2010).
13. ČSN ISO 757342 (75 7342). *Kvalita vod – Stanovení teploty*. Praha: Český normalizační institut, 2013
14. ČSN ISO 757367 (75 7367). *Jakost vod – Stanovení oxidačně redukčního potenciálu (ORP)*. Praha: Český normalizační institut (2011).
15. ČSN EN ISO 5814 (75 7463). *Kvalita vod. Stanovení rozpuštěného kyslíku. Elektrochemická metoda membránovou sondou*. Praha: Český normalizační institut (2013).

## HOME WASTE TREATMENT PLANTS WITH ELECTROCHEMICAL CLEANING

Dušek L.<sup>1</sup>

*Institute of Environmental and Chemical Engineering, Faculty of Chemical Technology, University of Pardubice, Studentská 573, 532 10, Pardubice, Czech Republic  
libor.dusek@upce.cz*

### Abstract

The paper deals with the technical solution, arrangement and procedural conditions of an electrolyser suitable for indirect electro-oxidation of mostly organic pollutants present in waste water and treated water.

The device works on the basis of the electro-Fenton reaction, using internally synthesized hydrogen peroxide as a precursor for the preparation of hydroxyl radical and as an ecological oxidization agent in acid environments. The electrolyser may be operated independently or in combination with mechanical and biological cleaning processes, i.e. as a supplement of existing waste water treatment plants. Its technical arrangement and possible miniaturization make it suitable also for the final treatment of waste water from small home water treatment plants, given that the efficiency of the majority oxidiser – the hydroxyl radical – makes it possible to oxidise, with high efficiency, also biologically persistent organic pollutants.

### Introduction

Although modern technologies of home waste water treatment plants make it possible to meet the statutory requirements and, when combined with membrane modules, use microfiltration to remove insoluble compounds, bacteria, protozoa and turbidity, they are not sufficiently effective to remove a whole range of pharmaceuticals and personal care products (PPCP) <sup>1</sup>. Though it might be objected that the attested concentrations of PPCPs do not directly threaten human health, neither in surface water, underground water, or drinking water, these are evidently biologically active substances that are capable of affecting water organisms even in minute concentrations. For this reason, it is desirable to develop new effective technologies and increase the efficiency of existing cleaning technologies with a focus on biologically active micropollutants. What is also problematic is the use of classic water treatment technologies, such as chlorination, and the application of hypochlorites and hypochlorous acid, which often cause partial chlorination of micropollutants. When such organic micropollutants are present, this is accompanied by an increase of the AOX parameter.<sup>2</sup>

Apart from the application of high pressure membrane processes (mainly ultrafiltration and nanofiltration, which need not – unlike reverse osmosis – be complemented with the remineralization of released water), possible solutions to this situation include the use of AOP processes (advanced oxidation processes) with the key role of hydroxyl radicals for the highly effective non-selective oxidation. An available source of hydroxyl radicals can be hydrogen peroxide decomposed catalytically with, for instance, Fe<sup>2+</sup> ions in the sense of Fenton's reaction. The degree of efficiency of the oxidizers arises from its oxidizing potential of 2.8V.<sup>3</sup> It also needs to be pointed out that the agents necessary for the creation of OH<sup>•</sup> radicals are still expensive (H<sub>2</sub>O<sub>2</sub>, O<sub>3</sub>). It is more economical to use AOP processes for the treatment of waste water with CHSK < 5000 mg/l or combine them with aerobic biological cleaning. This means that the use of Fenton's oxidation is suitable when waste waters are pre-cleaned or post-cleaned not only in municipal and domestic waste-water treatment plants but also in the processing and treatment of industrial waste waters and process waters, provided that:

- H<sub>2</sub>O<sub>2</sub> is used in low concentrations and is continuously added into the reaction environment of the water that is being treated, or it is produced directly *in situ*, which calls for its economically acceptable preparation in the place of application.
- Fe<sup>2+</sup> ions are continually added or regenerated for catalysing Fenton's reaction, while their optimal proportion with respect to H<sub>2</sub>O<sub>2</sub> is assured.
- the reaction location reaches and maintains, for the duration of the reaction, pH within the range of 2-4, and, it is assured that it fluctuates only minimally from the optimum value because of its significant effect on the value of the speed constant of OH<sup>•</sup> creation, and thus the speed of oxidization of organic pollutants.

These prerequisites may be met using the electro-Fenton's process<sup>5-7</sup>. Hydrogen peroxide is prepared (unless it is added from an external source) regardless of the type of cathode by means of a two-electrode reduction of oxygen that is either clean or present in the air. The potential placed on the working cathode is selected so that reduction of oxygen occurs without the electrolyte being decomposed. That requires taking into account the

effect that the material and the surface of electrodes has on the overstress of oxygen, which means that the work has to be carried out under exact conditions and by using a potentiostat to regulate the electro-Fenton's process.

The catalyser, i.e.  $\text{Fe}^{2+}$  ions, are added into the reaction space either from an external source in the form of inorganic salt (e.g.  $\text{FeSO}_4$ ,  $\text{FeCl}_2$ ,  $\text{Fe}(\text{NO}_3)_2$ ,  $(\text{NH}_4)_2\text{Fe}(\text{SO}_4)_2 \cdot 6\text{H}_2\text{O}$  etc.) or they may be generated by means of a sacrificed iron or steel anode. The regeneration of the  $\text{Fe}^{2+}$  catalyser then occurs on the surface of the cathode, cf. Figure 1A-B. In either case, it is necessary to modify the pH value before starting the electro-Fenton reaction, usually by means of a strong mineral acid. After the oxidization, the acid must be neutralized with suitable alkali and, simultaneously, the treated water becomes salted. In the event of low conductivity of the treated water, this parameter needs to be increased – usually by adding auxiliary electrolyte, which again contributes towards increasing the salinity of the treated liquid.

### Experimental part

For the purpose of the final treatment of waste water by means of the electro-Fenton reaction, we tested an electrolyser consisting of a decontamination chamber and a neutralization chamber, which were separated with fritted glass. The decontamination chamber contained a platinum anode-cathode and a sacrificed iron anode. The space between the Pt anode and the cathode was filled with Pd/C catalyser in a 3D electrode bed, see Figure 1A<sup>8</sup>.

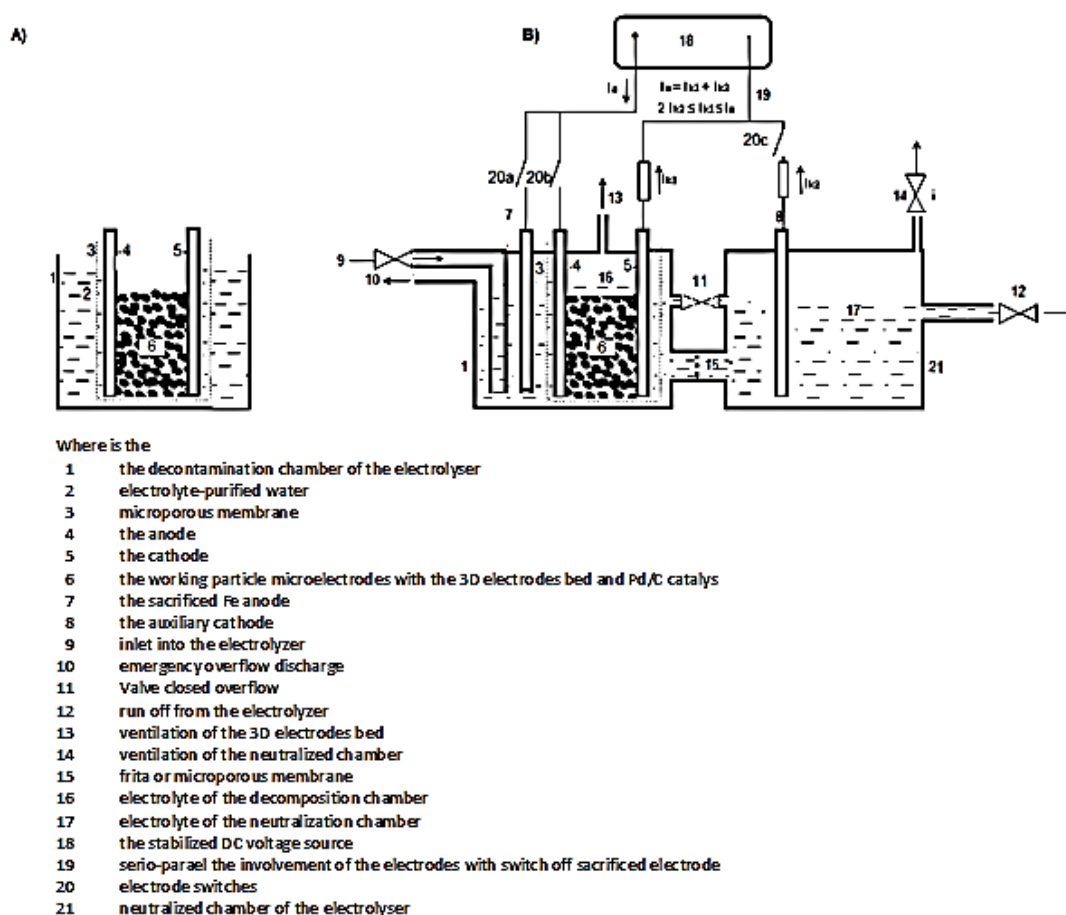


Figure 1. The electrolyser suitable for indirect electro-oxidation by the electro-Fenton reaction, using internally synthesized hydrogen peroxide and the sacrificed Fe anode. A - the decontamination chamber of the electrolyser with 3D electrodes bed and Pd/C catalyst. B - An overall view and schema of the bichamber electrolyzer

The device is suitable for carrying out the treatment of waste water by means of the electro-Fenton reaction. Inside the device, which is filled with waste water, water is decomposed, by means of putting on electrodes a potential higher than the value of the decomposing potential of the water electrolyte, into hydrogen and

oxygen, which further react in the presence of the catalyser held between electrodes in a 3D electrode bed. This leads to the generation of hydrogen peroxide, which is, in the presence of ferrous ion supplied by the sacrificed electrode or the external addition of ferrous salt, subject to Fenton's reaction giving  $\text{OH}^\bullet$  hydroxyl radical, which eventually oxidizes organic pollutants in waste water.

During the classic electro-Fenton reaction, hydrogen peroxide is prepared *in situ* on the surface of the cathode (or, where the same volume is supplied by 3D gas diffusion electrodes) by means of reduction of dissolved oxygen (see equation 1 below). In the newly invented device, however, the electro-Fenton reaction uses a higher potential on the electrodes than the value of the decomposing potential of the aqueous electrolyte. The passage of current results in the electro-chemical decomposition of water, giving rise to oxygen gas on the anode and hydrogen on the cathode, cf. equations (2) and (3).



The sum of the equations (2) and (3) gives us equation (4), which describes, together with equations (5), (6), (7) and (8), the main actions in the decontamination chamber of the electrolyser producing Fenton's agent.



During the electro-chemical decomposition of the electrolyte (the water that is being treated), the area around the anode becomes more acid as a result of the  $\text{H}^+$  generated, while  $\text{OH}^-$  ions produced by the cathode increase the pH of the surrounding area. This leads to the conclusion that equation (4) explains the experimentally observed decrease of pH in the decontamination chamber, while equation (3) describes the growth of the pH in the neutralization chamber of the electrolyte. Hydrogen peroxide is, once again, produced *in situ*, but this is done as a result of direct synthesis of hydrogen and oxygen, as indicated in equation (9), in the presence of the Pd/C catalyser.



In this manner, it is possible to produce, under normal temperature and pressure in acid environment, no more than 1 per cent strong aqueous solution of hydrogen peroxide that is continually consumed during the oxidization of the organic pollutants by means of the electro-Fenton's reaction (10) happening in acidic environment.



The electrolyser uses the internally synthesized hydrogen peroxide both as a precursor for the preparation of hydroxyl radical and as the actual ecological agent of oxidization in acidic environment. Apart from that, there is direct oxidization of pollutants on the anode. Therefore, in the presence of Pd and  $\text{Fe}^{2+}$  catalysers, there are at least three parallel oxidization reactions that are competing for a common substrate – the organic pollutant. The resulting speed constant of the oxidization of the organic pollutant that we observe is thus given as the sum of the partial speed constants, as described in equation (11).

$$k_{obs} = k_{\text{OH}^\bullet} + k_{\text{H}_2\text{O}_2} + k_{anoda} \quad (11)$$

#### Example of cleaning model waste water

The decontamination chamber of the H-cell of the electrolyser, equipped with fritted glass, was filled with 250 ml of model waste water containing urine diluted with distilled water in the ration of 1:100, with the dry matter of  $415 \text{ mg l}^{-1}$ ,  $\text{TOC} = 117 \text{ mg l}^{-1}$ ,  $\text{BOD}_5 = 182 \text{ mg l}^{-1}$ ,  $\text{COD} = 347 \text{ mg l}^{-1}$ . The overall current  $I_a$  was set to  $I_a = 100 \text{ mA}$  and the current flowing through the auxiliary cathode in the neutralization chamber was  $I_{k2} = 10 \text{ mA}$ .

After the settling of the conditions, the pH of the decontamination chamber was  $\text{pH} = 2 \pm 0,25$ , and that of the neutralization chamber was  $10 \pm 0,25$ . We used Pt electrodes with the surface area of  $1 \text{ cm}^2$  and the 3D electrode bed of the decontamination bed was filled with 0.5 g of Pd/C catalyser. After two hours of operation,  $\text{Fe}_2\text{SO}_4$  was added in the form of a solution, with its initial modal concentration of  $c_{\text{Fe}^{2+}} = 2,93 \cdot 10^{-4} \text{ mol l}^{-1}$ . After 24 hours of oxidization, we measured the final COD by means of cuvette tests LCK 514 (supplied by Hach-Lange). The final value was  $9 \text{ mg l}^{-1}$ , which means that the oxidization had 97.4% efficiency. The value of TOC dropped to  $5,4 \text{ mg l}^{-1}$  (reduction by 95,4 %) and the final value of  $\text{BSK}_5$  was  $13 \text{ mg l}^{-1}$  (reduction by 92,9 %).

### Conclusion

The electrolyser may be operated individually or in combination with mechanical and biological treatment processes, i.e. also as a supplement to existing waste water treatment plants, including home waste water treatment plants. It may be efficiently used for the pre-cleaning of waste waters containing toxic pollutants in the activated sludge of the waste water treatment plant, as well as for the final cleaning of waste waters containing micropollutants that are hard to degrade biologically – such as are typical for select pharmaceutical substances and personal care products (PPCPs). Thanks to its technical layout and the possibility of miniaturization, the device is ideal for the final treatment of waste water from small home waste water treatment plants with the advantage that the efficiency of the majority oxidiser, namely hydroxyl radical, enables a maximum efficiency of oxidization of biologically persistent organic pollutants.

### References

1. Oulton R. L., Kohn T., Cwiertny D. M. a kol.: J. Environmental Monitoring 12(11), 1956 (2010).
2. Dušek L., Vystrčilová B., Novotný L.: Chemické Listy, 106 (11), 1054 (2012).
3. Dušek L. Chemické Listy, 104 (9), 846 (2010).
4. Panizza M., Cerisola G. *Chem. Rev.*, 109, 6541(2009).
5. Oturan M. A., Brillas E.: *Portugaliae Electrochimica Acta* 25, 1 (2007).
6. Brillas E., Sires I., Oturan M. A.: *Chem. Rev.*, 109, 6570 (2009).
7. Xiong, Y.J., Fan, J., Zhu, X.H.: *Industrial Water Treatment*, 18, 5-8 (1998)
8. Liu Z., Ai Z., Zhang L.: *Journal of Hazardous Materials*, 243, 257– 264 (2012).

## REDUCTION OF NEGATIVE IMPACTS OF INFRASTRUCTURE CONSTRUCTIONS ON THE SURFACE WATER QUALITY

**Hnátková T.**<sup>1</sup>, Šereš M.<sup>1</sup>, Kriška M.<sup>2</sup>, Rozkošný M.<sup>3</sup>, Vymazal J.<sup>4</sup>

<sup>1</sup>*Dekonta, a.s., Dřetovice 109, 273 42, Stehelčevy*

<sup>2</sup>*Vysoké učení technické v Brně, Žižkova 17, 602 00, Brno*

<sup>3</sup>*Výzkumný ústav vodohospodářský TGM, v.v.i., Mojmírovo nám. 16, 612 00, Brno*

<sup>4</sup>*Czech University of Life Sciences Prague, Faculty of Environmental Sciences, Kamýcká 1176, 165 21, Prague  
hnatkova@dekonta.cz*

### Introduction

The high number of released pollutants that can affect many elements of the environment and the human health are caused by car traffic (Hvited-Jacobson & Yousef, 1991; Sansalone, 1999). The origin of particular pollutants in surface run-off from roads and parking areas is summarized in detail by Lee and Touray (1998) and Bäckström et al. (2004). A part of the harmful substances dissolved in water flows away with the rain water and another part of noxious substances is bound to suspended particles (Norrström & Jacks, 1998). Monitoring of the surface run-off at the control network of selected profiles at various motorways and expressways was carried out in a period 2005 – 2009 within two research projects of the Czech Ministry of Transport (Beránková et al., 2008; 2009). The current situation leads to pressure to provide an appropriate treatment of the surface run-off by accurate treatment facilities. Existing solutions, which are typified rainwater settling tanks (DUN) or open settling tanks are primarily implemented in order to capture the main portion of storm water pollution (run-off) to reduce water pollution in rivers or other recipient. These solutions don't represent an active stage of purification, but only mechanical pre-treatment.

Study of Aryal et al. (2006) summarizes the results of a longitudinal twenty-year-long monitoring of the cleaning effect of retention and infiltration facilities where the cleaning of surface run-off from roads in the filtration bed of defined filter material was carried out. Use of chemical substances for road and parking areas maintenance (e. g. salting) has an significant impact on hydraulic characteristic changes of filtration beds and also on mobility of metals. The detailed information is summarized by Novotny et al. (1998) and Bäckström et al. (2004). As a consequence of salting and presence of dust in run-off, changes in granularity, porosity and thus the hydraulic conductivity of the filtration beds are observed. Changes in hydraulic conductivity are progressively leading to the colmatage (clogging) processes (Dierkes et al., 2006). Use of the filtration beds of constructed wetlands in combination with a sedimentation components described by Bulc and Sajn Slak (2003) shows a positive influence on the run-off treatment efficiency.

The presented research was focused on the study of existing surface run-off treatment facilities (DUN, storm water tanks) efficiency, mathematical modelling of these facilities, designing of new constructions of treatment facilities with better hydraulic characteristics and mathematical modelling validation with added semi-operated validation. Part of the research was focused on constructed wetland filters as a final purification step after the pre-treatment of surface run-off by the storm water tanks.

### Methods

The research focused on the study of existing surface run-off treatment facilities (DUN, storm water tanks) efficiency was divided in to these parts: i) monitoring of existing facilities along selected parts of highway network; ii) monitoring of storm water tanks built in commercial zones; iii) mathematical modelling of existing facilities (different types of DUN and storm water tanks); iv) designing of construction changes in existing facilities based on modelling; v) mathematical modelling of newly developed facilities; vi) pilot testing of newly developed facilities and vii) study of the role of macrophyte on treatment processes.

Monitoring of operating DUN and storm water tanks was carried out in the period 2013 - 2015. Description of these facilities is provided in the project database published the web sites of company Dekonta. Water samples were collected by standardized methods into pre-set sample containers for different types of pollutants. Sampling was carried out 3 - 6 times a year in relation to the rainfall periods, that affects the supply of water into retention part and its delay.. The physicochemical indicators (water temperature, pH, electrical conductivity using a portable device Hach Lange HQ40D) of water quality were measured samples in-situ. Concentrations of the following water quality parameters: turbidity, suspended solids and volatile solids,

chlorides, nutrients (total nitrogen, total phosphorus), organic compounds (TC, TOC, DOC, COD), PAHs, petroleum substances (expressed as C10–C40), heavy metals (Al, Cd, Cr, Cu, Hg, Ni, Pb, Zn) were determined in accredited laboratory. Indicators were selected based literature review (Hvited-Jacobson & Yousef, 1991; Bayerisches Landesamt für Umwelt, 2008 etc.) and author's own findings from monitoring of surface run-off at highways and expressways (Beránková et al., 2008; Beránková et al., 2009).

The process of monitoring and mathematical modelling was divided into several stages. Since the beginning of the research we have focused on the use of Comsol Multiphysics software and implementation of numerical models for simulation of the mixture of two different liquids in the newly designed storm water settling tank. The mixture of two liquids was different combinations of water + gasoline and water + oil substances. For creation of the numerical model the simulation software Comsol Multiphysics in combination with additional CFD modules were used. These models were selected to allow of modelling of two liquids flow. In order to make the simulations faster we have replaced all rounded edges of the settling tank with flat walls (e. g. the circular inlet pipe is replaced by a square profile,; Similarly, the rounded part in the plan view was replaced by octagon. Modeled water inflow is 0,5 l/s that means 62,5 l/s in real facility. By generating of finite element mesh arises the geometry with following characteristics (see the Figure 1): number of vertex elements: 162; number of edge elements: 1226; number of boundary elements: 11951; number of elements: 106026.

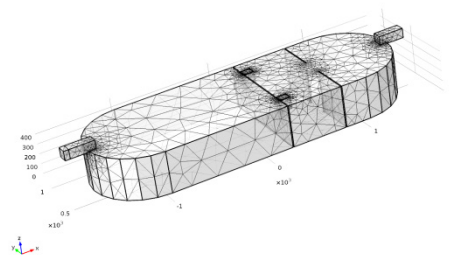


Figure 1. Finite element mesh generated for the model of DUN stormwater settling tank

To eliminate inaccuracy of the simulations for the purposes of results applicability into practice, the model calibration and subsequent verification based on real laboratory measurements is required. Size of the real DUN usually doesn't enable performance of accurate measurements and simulations of water flow and pollution transfer. We therefore initially focused on the development of a physical model in scale 1:5 (Figure 2a), that was used for observation of real processes in contamination transport. We expected similar results of cleaning efficiency of the model analogous to real DUN during emergency situations and during standard operation conditions, when the pollutants are in trace concentrations. The validation of mathematical modelling was performed at the pilot scale model of newly designed storm water tank type DUN by tracer tests. For these test NaCl was used as a tracer and electrical conductivity was measured. The methods of electrical conductivity measurement is often used to monitor the water quality of streams and effluent from industrial sites (Binkley et al., 2000) and wastewater treatment facilities (Prieto et al., 2001). These measurements have been also used to determine the salinity, ionic strength (Lind, 1970) and major solute concentrations (McNeil and Cox, 2000) of natural waters.

In the experiment physical model was initially filled with fresh water, which we have deliberately adjusted so as to have an increased electrical conductivity by adding salty water. In the first step, the salt was diluted in 50 l vessels. Then the circulation of original fresh water in model was proceeded to be mixed with the salt water. The recirculation of the water was performed until the stabilization of electrical conductivity within the entire volume of the physical model (to  $6981.0 \pm 3.17$  mV;  $n = 10$ ). In accordance to verify the numerical model, we subsequently filled up the physical model with fresh water ( $547.82 \pm 0.853$  mV,  $n = 22$ ) and observed changes of conductivity in selected profiles. For purposes of comparison with numerical model the measured values at mV were expressed at % (initial water 6981 mV = 100%, the pumped water 547,82mV = 0% volumetric).

After calibration and adjustment of the mathematical model we have performed verification of the model. Principle of the verification consists in process of changings in the filling of the settling tank with different mixtures of two liquids: instead of mixing of salty water with fresh water we conducted an experiment in which oil substances were added to the pumped fresh water (Figure 2b). In result, the ratio of water and oil was 0.9998:0.0002. Samples were taken in the outlet profile and in period 0-30-60-90-120-150 minutes.



Figure 2a,b. Semi-operated model of DUN storm water tank (left). Accumulation of oil substances at the water surface during validation testing (right).

The part of research given to the study of final purification of the storm water settling tanks by constructed wetlands is presented by analysis of heavy metals uptake by macrophyte vegetation. Four constructed wetlands (two with horizontal flow, two with vertical flow) were planted by next mentioned plants. For experiments, *Phalaris arundinacea* L. (Reed canary grass) and *Glyceria maxima* Hartman. Holmberg (Mannagrass) were selected. Both plants are common wetland species that tolerate higher level of pollution, and, therefore they are used for constructed treatment wetlands. Contrary to *Phragmites australis* (Cav.) Trin. Ex Steud.) (Common reed) which grows very slowly, both *Phalaris* and *Glyceria* grow very fast. The biomass was divided into leaves (including leaf sheaths), stems, roots and rhizomes and dried at 60 °C to a constant weight and weighed. The biomass was then homogenized using a cutting mill (Pulverisette 15, FRITSCH) and mineralized in nitric acid (Ultrapur, Merck Millipore) in a microwave (Berghof, Speedwave MWS-2) under high temperature and pressure. The concentrations of heavy metals (Cu, Ni and Zn) in leaves, stems, roots and rhizomes were determined in triplicate samples using the atomic absorption spectroscopy (Agilent AAS DUO 55B/240Z). For the evaluation of measurement precision and accuracy the certified reference material (CRM) METRANAL TM3 (*Fragaria vesca*, QCM03, Analytica Ltd., Czech Republic) was used. The triplicate determinations agreed to within 5%, and CRM recoveries were found within 90–105% range.

### Results and discussion

Concentrations of copper, nickel and zinc in various parts *Phalaris* and *Glyceria* are presented. The highest concentrations of all heavy metals were found in roots, followed by rhizomes. On the other hand, the lowest concentrations were found in stems with higher concentrations in leaves. The ranges of values (in mg/kg) for the wetlands were: Cu – *Phalaris* – 13-27 roots, 7-13 rhizomes, 2-10 leaves, 1-5 stems / *Glyceria* – 25-35 roots, 4-10 rhizomes, 1-4 leaves, 1-6 stems; Ni – *Phalaris* – 12-27 roots, 7-13 rhizomes, 2-10 leaves, 1-5 stems / *Glyceria* – 4-26 roots, 2-7 rhizomes, 2-9 leaves, 2-8 stems; Zn – *Phalaris* – 37-98 roots, 25-53 rhizomes, 18-41 leaves, 6-34 stems / *Glyceria* – 81-98 roots, 19-39 rhizomes, 18-31 leaves, 21-80 stems (all in mg/kg). This finding is in agreement with results reported from constructed as well as natural wetlands (Schierup and Larsen 1981; Pevery et al. 1995; Windham et al. 2003; Bonano and Lo Guidice, 2010).

The results also revealed that higher copper and nickel concentrations were found in *Phalaris* while zinc concentrations were comparable in both plants. During the harvest, only aboveground biomass could be removed, and, therefore, high concentrations in the aboveground biomass is desirable. Both plants used in the experiments could be harvested several times during the year. However, the concentration itself does not provide information about the accumulation of heavy metals in the biomass. In order to evaluate accumulation, it is necessary to take biomass into consideration.

Both plants are very productive with aboveground biomass in the range of 1000-2000 g dry matter /m<sup>2</sup> with 50-70% of the biomass being stems. Concentrations of all monitored heavy metals determined in the experiment varied within the range commonly found in wetland plants in natural and constructed wetlands for wastewater treatment. (Table I).

Table I. Concentration (mg/kg) in biomass of wetland plants growing in natural and constructed wetlands

wetland	metal	leaves	stems	roots	rhizomes	references
Natural	Cu	2.1-10.7	0.5-19.2	9.0-184	4.3-12.6	1,2,3,4,5,6,7,8,9,10
Constructed	Cu	6.1-15	5.1-25	5.3-64	6.5-33	1,3 11,12,13,14,15,16,17,18
Natural	Ni	0.5-5.8	0.2-10.3	7.7-25,5	1.6-3.8	2,4,5,6,7,8,9,15
Constructed	Ni	0.47-2.8	0.54-2.0	4.9-16.7	1.87	3,13,14,15,18,19
Natural	Zn	11-1300	10-137	1.3-588	17-66.8	1,2,4,5,6,7,8,9,10,
Constructed	Zn	29-59	18-70	46-165	12.2-22	1,3,11,12,13,15,17,18

1- Peverly et al. (1995), 2-Obolewski et al. (2011), 3-Lesage et al. (2007b), 4-Duman et al. (2007), 5-Szymanowska et al. (1999), 6-Samecka-Cymerman a Kempers (2001), 7-Du Laing et al. (2006), 8-Baldantoni et al. (2009), 9-Bonano and Lo Guidice (2010), 10-Windham et al. (2003), 11- Yeh et al. (2009), 12-Samecka-Cymerman et al. (2004), 13-Lesage et al. (2007a), 14-Khan et al. (2009), 15-Galletti et al. (2011), 16-Liu et al. (2010), 17-Bragato et al. (2006), 18-Vymazal et al. (2009), 19-Bragato et al. (2009)

Table II and III show the range of values found in water samples from selected DUN during monitoring in years 2013 to 2015. The ranges of values are shown for the inlet sections of the DUN (IN) and the outlet sections (OUT).

Table II

Range of values of selected pollutants analysed in samples from stormwater tanks monitoring

Locality		ENT [CFU 1ml <sup>-1</sup> ]	Cl [mg l <sup>-1</sup> ]	SS105 [mg l <sup>-1</sup> ]	SS550 [mg l <sup>-1</sup> ]	COD [mg l <sup>-1</sup> ]	TOC [mg l <sup>-1</sup> ]	TN [mg l <sup>-1</sup> ]	TP [mg l <sup>-1</sup> ]
DUN1 IN	Min	0	21	3	0	149	5.0	3.3	0.04
DUN1 IN	Max	18	3040	388	336	2230	17.6	12.5	0.60
DUN1 OUT	Min	1	11	7	3	67	5.8	2.1	0.05
DUN1 OUT	Max	12	1930	232	228	1880	15.8	12.0	0.32
DUN2 IN	Min	0	40	0	0	83	1.7	2.3	0.00
DUN2 IN	Max	13	760	104	90	201	11.7	8.7	0.35
DUN2 OUT	Min	0	20	0	0	90	2.9	2.8	0.00
DUN2 OUT	Max	18	1480	108	92	219	20.1	8.6	0.40
DUN3 IN	Min	1	3	3	0	16	4.7	0.6	0.07
DUN3 IN	Max	8	1960	54	35	1660	16.9	3.2	0.14
DUN3 OUT	Min	0	3	0	0	18	2.9	0.7	0.05
DUN3 OUT	Max	5	3420	20	13	189	18.1	2.6	0.12
DUN4 IN	Min	0	15	0	0	132	6.0	1.0	0.00
DUN4 IN	Max	3	535	53	45	253	13.3	16.1	0.27
DUN4 OUT	Min	0	16	3	2	126	5.2	1.0	0.03
DUN4 OUT	Max	1	765	60	48	232	13.6	10.0	0.27

ENT – Enterococci, Cl – chlorides, SS105 – suspended solids, SS550 – volatile suspended solids, TN – total nitrogen, TP – total phosphorus

Table III

Range of values of selected pollutants analysed in samples from stormwater tanks monitoring

Locality		C10C40 [mg l <sup>-1</sup> ]	PAH [ $\mu$ g l <sup>-1</sup> ]	Cd [ $\mu$ g l <sup>-1</sup> ]	Cu [ $\mu$ g l <sup>-1</sup> ]	Hg [ $\mu$ g l <sup>-1</sup> ]	Ni [ $\mu$ g l <sup>-1</sup> ]	Pb [ $\mu$ g l <sup>-1</sup> ]	Zn [ $\mu$ g l <sup>-1</sup> ]
DUN1 IN	Min	<0.1	<0.002	0.0	8.5	0.0	2.0	0.0	7
DUN1 IN	Max	1.4	6.4	0.3	58.7	0.4	34.3	5.4	210
DUN1 OUT	Min	<0.1	<0.002	0.0	11.0	0.0	2.5	0.0	33
DUN1 OUT	Max	1.6	5.8	0.1	50.5	0.2	32.3	7.0	179
DUN2 IN	Min	<0.1	<0.002	0.0	0.0	0.0	14.3	0.0	0
DUN2 IN	Max	0.6	1.5	0.1	24.3	0.3	41.8	3.5	93
DUN2 OUT	Min	<0.1	<0.002	0.0	0.0	0.0	14.5	0.0	12
DUN2 OUT	Max	1.2	5,5	0.2	64.3	0.3	45.2	2.3	201
DUN3 IN	Min	<0.1	<0.002	0.0	8.5	0.0	0.0	0.0	41
DUN3 IN	Max	0.7	1.4	0.2	35.5	0.2	20.1	3.4	239

DUN3 OUT	Min	<0.1	<0.002	0.0	5.7	0.0	0.0	0.0	37
DUN3 OUT	Max	0.3	0.7	0.4	22.7	0.3	0.0	1.5	366
DUN4 IN	Min	<0.1	<0.002	0.0	2.4	0.0	0.0	0.0	0
DUN4 IN	Max	0.2	0.3	0.1	17.0	5.6	0.0	2.1	73
DUN4 OUT	Min	<0.1	<0.002	0.0	3.0	0.0	0.0	0.0	6
DUN4 OUT	Max	0.3	0.4	0.0	14.8	1.0	3.6	2.4	51

Recording of conductivity values during the validation experiments was performed in twelve selected profiles of the physical model at 10 minute intervals until stabilization of values after 205 minutes. Subsequent comparison of the mathematical model with physical model, which was filled with salty water and subsequently filled with fresh water ( $Q = 0.5 \text{ l/s}$ ), indicates that model results corresponds to the conducted experiment (Figure 3). The model was then verified using a precisely defined dose of oil with precisely defined physical characteristics (viscosity, density).

Statistical evaluation of the real experiment shows, that the portion of oil in the inflow is 0,0002 while in the outflow it is  $0,000079 \pm 0,00007$  (median 0,000063). The mathematical simulation shows different results -  $0,000092 \pm 0,00007$  in the outflow (median 0,000080). That means 11,6% difference between mathematical simulations and real experiments.

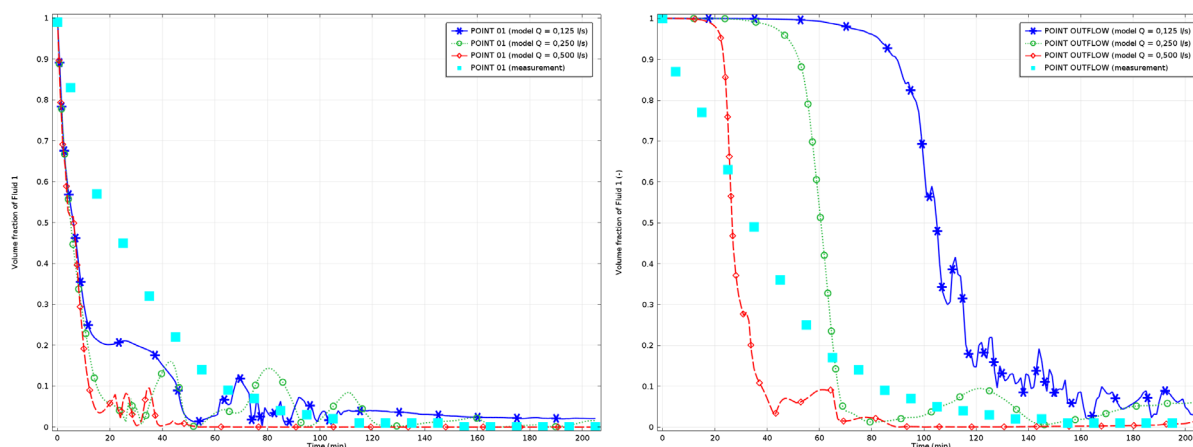


Figure 3. Correlation of measurements and mathematical modelling – course of liquid amount in the selected measurement profiles of the DUN physical model (first profile after inflow – left chart, outflow profile – right chart)

## Conclusions

The retention efficiency of existing DUN settling tank was calculated from the databasis of selected pollutants monitoring. It is necessary to take into account that, due to a residence time dependent on the precipitation events, the time samples collected from the inlet and outlet sections during each visit of subscribed objects can not exactly match. Efficiencies were therefore calculated for long-term average value. The results shown high differences between the four presented DUN facilities in the treatment efficiency for selected metals (e.g. Cd – DUN1 46%, DUN2 32%, DUN3 5%, DUN4 100%; Hg – DUN1 33%, DUN2 -9%, DUN3 9%, DUN4 80%; Ni - DUN1 6%, DUN2 2%, DUN3 100%, DUN4 >-100%; Zn - DUN1 -9%, DUN2 -63%, DUN3 -36%, DUN4 22%) PAH (DUN1 10%, DUN2 -174%, DUN3 59%, DUN4 -11%), but also for nutrients (TN – DUN1 18%, DUN2 -2%, DUN3 32%, DUN4 27%; TP – DUN1 23%, DUN2 -13%, DUN3 26%, DUN4 -4%), suspended solids (between -34% and 66%) and chlorides (between -49% and 22%). That can be caused by low concentrations in the samples from monitoring period in the case of metals, and by contact and exchange of pollutants between water and sediments accumulated in the monitored parts of DUN facilities.

The results of mathematical and physical modelling shows that this approach can be used for designing and subsequent operation, reconstruction and maintenance of real DUN. Knowledge obtained based on the project results can be applied for designing of operation scheme of settling tanks for emergency situations (e. g. high concentrations of oil products).. Mathematical modelling have 11% error compared to real experiments in this case study.

## Acknowledgment

*This work was supported by Technology Agency of the Czech Republic, project TA03030400 Wetland – “Development of technologies for road and other paved areas stormwater runoff cleaning”.*

## Literature

1. Aryal, RK., Muramaki, M., Furumai, H., Nakajima, F., and Jinadasa, HKPK. Prolonged deposition of heavy metals in infiltration facilities and its possible threat to groundwater contamination. *Wat. Sci. Tech.*, vol. 54, No. 6–7, p. 295–212 (2006).
2. Bäckström, M., Karlsson, S., Bäckman, L., Folkesson, L., and Lind, B. Mobilisation of heavy metals by deicing salts in a roadside environment. *Wat. Research* 38, p. 720–732 (2004).
3. Beránková, D., Brtníková, H., Kupec, J., Huzlík, J., and Prax, P. Pollution of the highways runoff. *Transactions on Transport Sciences*, vol. 2008, No. 2, p. 31–38. ISSN 1802-971X (2008).
4. Beránková, D., Brtníková, H., Kupec, J., Mlejnková, H., Huzlík, J. a Prax, P. Parametry jakosti a množství povrchového splachu z dálnic. *VTEI (Vodní hospodářství)* 6/2009, Vol. 51, No. 3, p. 8–11. ISSN 0322-8916 (2009).
5. Binkley J., Simpson J. A. and McMahon P. Characterisation of textile aerobic-activated sludge plant by conductivity and pH measurement. *J. Text. Inst.* 91, 523–529 (2000).
6. Bodenkundliche Untersuchungen im Rahmen des Entwicklungsvorhabens „Versickerung des Niederschlagwassers von befestigten Verkehrsflächen“. Augsburg : Bayerisches Landesamt für Umwelt. ISBN 978-3-940009-96-8 (2008).
7. Bonano, G. and Lo Guidice, R. Heavy metal bioaccumulation by the organs of *Phragmites australis* (common reed) and their potential use as contaminant indicators. *Ecol. Indicators* 10: 639-645 (2010).
8. Hvited-Jacobson, T. and Yousef, YA. Highway Runoff Quality, Environmental Impacts and Control. In *Highway Pollution* (eds Hamilton, RS. and Harrison, RM). Amsterdam: Elsevier, p. 165–208 (1991).
9. Lee, PK. and Touray, JC. Characteristics of a polluted artificial soil located along a motorway and effects of acidification on the leaching behavior of heavy metals (Pb, Zn, Cd). *Wat. Res.*, vol. 32, No. 11, p. 3425–3435 (1998).
10. Lind C. J. Specific conductance as a means of estimating ionic strength. *U.S. Geol. Surv. Prof. Pap.* 700-D, D272–D280 (1970).
11. McNeil V.H., Cox M.E. Relationship between conductivity and analysed composition in a large set of natural surface-water samples, Queensland, Australia, *Environ. Geol.*, 39 , pp. 1325–1333 (2000).
12. Norrström, AC. and Jacks, G. (1998) Concentration and fractionation of heavy metals in roadside soils receiving de-icing salts. *Sci. Tot. Env.*, 218, p. 161–174.
13. Novotny, V. et al. Cyanide and metal pollution by urban snowmelt: impact of deicing compounds. *Wat. Sci. Tech.*, vol. 38, No. 10, 1998, p. 223–230.
14. Peverly, J.H., Surface, J.M. a Wang T. Growth and trace metal absorption by *Phragmites australis* in wetlands constructed for landfill leachate treatment. *Ecol. Eng.* 5: 21-35 (1995).
15. Prieto F., Barrado E., Vega M. and Deban L. Measurement of electrical conductivity of wastewater for fast determination of metal ion concentration. *Russ. J. Appl. Chem.* 74, 1321–1324 (2001).
16. Sansalone, JJ. (1999) Adsorptive infiltration of metals in urban drainage – media characteristics. *Sci. Tot. Env.*, 235, p. 179–188.
17. Schierup, H.-H. a Larsen, V.J. Macrophyte cycling of zinc, copper, lead and cadmium in the littoral zone of a polluted and non-polluted lake. I. Availability, uptake, and translocation of heavy metals in *Phragmites australis* (Cav.) Trin. *Aquat. Bot.* 11: 197-210 (1981).
18. Windham, L., Weis, J.S. a Weis, P. Uptake and distribution of metals in two dominant salt marsh macrophytes, *Spartina alterniflora* (cordgrass) and *Phragmites australis* (common reed). *Estuar. Coast. Shelf Sci.* 56: 63-72 (2003).

## SACRIFICIAL ANODES CATALYZING ELECTRO-FENTON OXIDATION OF WASTEWATER

**Kočanová V.**, Dušek L., Novotný L.

*Institute of Environmental and Chemical Engineering, Faculty of Chemical Technology, University of Pardubice, Studentská 573, 532 10 Pardubice, Czech Republic  
st26815@student.upce.cz*

### Abstract

Technologies which are based on electro-Fenton processes could be considered as a modern and effective way in wastewater treatment. Commonly used catalysts of Fenton oxidation are ions of  $\text{Fe}^{2+}$ . New and modern catalyst found more use as selective agents for specific pollutants yet Catalyst in form of  $\text{Fe}^{2+}$  is meeting important attributes and could be suitable dosage by electrochemical dissolving of sacrificial steel anode. It was comparison between two material types of sacrificial anode – Steel 17 240 Cr-Ni (DIN X 5 CrNi 18 10, AISI 304) and Steel 11 373 (DIN USt 37-2). Both steels are common commercially available products with excellent stable quality and reasonable price, which are produced in the Czech Republic. It is necessary to take into account the specific properties of both materials under conditions of electro-Fenton process. The main influence of pH range 2-4 in which experiments were processed. Steel 17 240 Cr-Ni (DIN X 5 CrNi 18 10, AISI 304) has a lower corrosion losses under the same conditions. Non-alloy steel 11 373 (DIN USt 37-2) has enough corrosion rate to dose to electro-Fenton process necessary amount of catalytic  $\text{Fe}^{2+}$  ions dependence of surface and current density. The usage of alloy steel 17 240 Cr-Ni is materially five times more expensive. It is necessary to connect power supply to increase small corrosion rates. Ferrous and ferric sludge which are in water could be effectively precipitated by neutralization purified water and removed by sedimentation. Residual concentration of total iron  $0,37 \text{ mg}\cdot\text{l}^{-1}$  meets the conditions in Government Regulation No. 61/2003 Coll., about values of pollution by iron in the surface and wastewaters, where is a limit for iron  $0,55 \text{ mg}\cdot\text{l}^{-1}$ .

### Key words

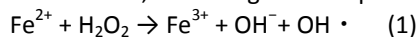
electro-Fenton, catalyst, iron, wastewater treatment, oxidation

### Introduction

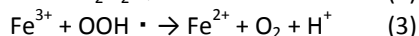
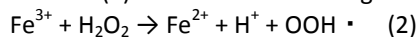
Wastewater treatment is end technology and is expensive process, however, is nowadays necessary and almost indispensable. Target is to remove persistent and dangerous substances from wastewater, which could damage human health or the environment. Typical examples are heavy metals and organic substances which can be converted into harmless products by using chemicals which are friendly for the environment. It is also necessary to prevent the dispensing of chemicals in large quantities, so as to prevent consequent contamination and environmental pollution by other agents. Processes using electro-Fenton oxidation can be effectively applied especially in the area of wastewater treatment using ion  $\text{Fe}^{2+}$  as a catalyst.

### Fenton's oxidation

In the Fenton reaction at first reacted  $\text{Fe}^{2+}$  with hydrogen peroxide in acidic medium to give the hydroxyl radical and the  $\text{Fe}^{3+}$ , according to the equation (1).



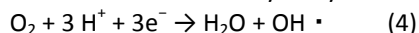
In the next step could be reaction of  $\text{Fe}^{3+}$  with hydrogen peroxide again. It will be formed hydroperoxyl radical, formula (2). And then  $\text{Fe}^{2+}$  are regenerated, equation (3).



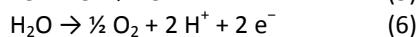
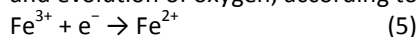
Efficiency of the Fenton's reaction depends on various factors, such as pH, temperature, concentration and form of catalyst ( $\text{Fe}^{2+}$ ) and concentration of  $\text{H}_2\text{O}_2$ . A main quantity for the right process of Fenton's reaction is pH value, which depends on the catalytic activity of the iron. Optimal pH range is 2-4. It is also important to choose the correct molar ratio of Fenton reagent  $[\text{Fe}^{2+}] / [\text{H}_2\text{O}_2]$  and make a practical control of reaction temperature. The optimal molar ratio of ferrous ion to hydrogen peroxide is 1:10 to 1:5<sup>1</sup>.

### Electro-Fenton oxidation

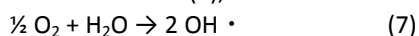
Method of electro-Fenton oxidation is based on classical Fenton reaction where hydrogen peroxide is produced by reduction of dissolved oxygen on the surface of cathode. And then formed peroxide reacted with added ferrous ions to form a hydroxyl radical. This process summarizes next equation (4).



The main step in electro-Fenton oxidation is regeneration of ferrous ions by reducing ferric ions on the cathode, equation (5) Oxidation of water runs in anodic area simultaneously acidification around the anode and evolution of oxygen, according to equation (6).



Overall reaction (7), which leads to the formation of hydroxyl radicals runs in the electrolytic cell.



For the production of hydroxyl radicals is necessary presence of oxygen, water and power supply<sup>2</sup>.

### Options of arrangement electro-Fenton process

Nowadays exist many modifications and options in electro-Fenton process. It can define four main configurations. Hydrogen peroxide is added externally at the first set up. Sacrificial iron anode is used as a source of ferrous ions. Second option is electrochemical preparation of ferrous ions and hydrogen peroxide. Anode is sacrificial again. The cathode space is bubbled with oxygen. Iron ions are externally added in another configuration. Hydrogen peroxide is generated at the oxygen sparging cathode. In the last option are ferrous ions regenerated by reduction of ferric ions in the cathode area<sup>3</sup>.

### Other catalyst of the electro-Fenton process

Processes based on the electro-Fenton reaction can be also sometimes catalysed by other metal ions  $\text{Fe}^{2+}$  as usually in classical electro-Fenton oxidation. It could be transition of metal ions for example  $\text{Ag}^+$ ,  $\text{Cu}^{2+}$ ,  $\text{Co}^{2+}$ ,  $\text{Mn}^{2+}$  or  $\text{Fe}^{3+}$ . This finding extends the opportunities of electro-Fenton processes. The catalytic activity of transition metal ions strongly depends on the pH value of the solution. They are useful in the acidic medium. The greatest efficiency is achieved about pH 1<sup>4</sup>. This fact must be taken into account when applying electro-Fenton reaction in practice. Transition metal ions may be used as selective catalysts for the oxidation of specific organic substances<sup>5</sup>.

### Application of electro-Fenton oxidation

Electro-Fenton process is considered as one of the most effective and most economic methods to the environment. Technologies based on the electro-Fenton oxidation are used especially in the wastewater treatment, containing organic substances. Most of these are aromatic compounds. It can remove the drugs, phenol compounds, dyes, pesticides and herbicide from the wastewater<sup>6</sup>. It is also possible to purify water and wastewater from metals such as e.g. Pb, Cd, Cr, As, Mn, Cu, Zn, Ni, Al, Fe, Co, Sn, Mg, Se, Mo, Ca and Pt with electro-Fenton process. Further, after the anions -  $\text{CN}^-$ ,  $\text{PO}_4^{3-}$ ,  $\text{SO}_4^{2-}$ ,  $\text{NO}_3^-$ ,  $\text{F}^-$  or  $\text{Cl}^-$ . From the non-metals it could be removed for example P from wastewater<sup>7</sup>.

### Types of materials used for sacrificial anode

It was used sacrificial anode as steel Cr-Ni and non-alloy steel. Types of stainless Cr-Ni steel, according to the marking ČSN 41 7240, see the table I, it is Steel 17 240 Cr-Ni. It is austenitic, weldable, unstabilized and stainless steel. It is resistant to intergranular corrosion of welded metal sheets up to a thickness of about 6 mm. The final product is sold in the form of rods, tubes or plates. It could be used for construction of chemical equipment and pressure vessels, which are designed to work in elevated temperatures. It is suitable for oxidation environments, for weak organic acids to medium concentrations and temperatures, while aeration. If it is used for strong inorganic acids (e.g.  $\text{H}_2\text{SO}_4$ ), and only at very low concentrations in the low temperature, it can be used in environments where high purity of the product, but the influence of corrosion is negligible (e.g. food or pharmaceutical industries). It could be used for components of cold devices except environment of brine<sup>8</sup>.

Tab. I Chemical composition of non-alloy steel according to norm ČSN 41 7240

Chemical composition (analysis of meltage) [%]	C	Mn	Si	Cr	Ni	P	S
	max.	max.	max.			max.	max.
	0,07	2	1	17,0 - 20,0	9,0 - 11,5	0,045	0,030
Permissible variations of chemical composition in final product [%]	+ 0,01	+ 0,15	+0,05	+ 0,5	+ 0,5	- 0,3	- 0,3

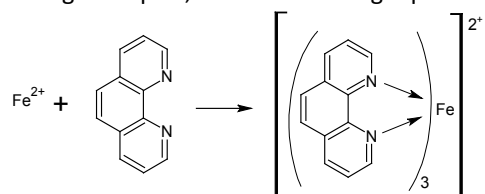
Non-alloy steel is named as Steel 11 373 according to the marking ČSN 41 1373. This plain structural steel is suitable for welding of steel structures. It could be part of the construction and equipment of smaller thicknesses which are a fusion welding statically and dynamically. They're less stressed welded pipes and couplers, weir structures, objects pouring water turbines, discharge, stop-log or board floodgates. These are bars rolled, rolled wire, hot-rolled, wide hot-rolled steel, hot-rolled strip, cold drawn bars, rods peeled, thin cold-rolled sheets, strip and cold rolled strips, strips slit cold rolled hollow sections of cold-formed thin-walled sections and wide curved profiles<sup>9</sup>. Chemical composition of non-alloy structural steel according to the norm ČSN 41 1373 is summarize in the next table II.

Tab. II Chemical composition of non-alloy steel

Chemical composition (analysis of meltage) [%]	C	P	S	N
	max.	max.	max.	max.
	0,17	0,045	0,045	0,07
Permissible variations of chemical composition in final product [%]	0,04	0,01	0,01	0,02

#### Monitoring the current amount of catalyst

Dissolved iron in oxidation state II was determined by absorption spectrophotometry after reaction with 1,10-phenanthroline. The principle of this method is the reaction of  $\text{Fe}^{2+}$  with 1,10-phenanthroline to form a red-orange complex, see the following equation, Formula I.



Formula I. Reaction  $\text{Fe}^{2+}$  with 1,10-phenanthroline

This complex is formed in the range of pH 2,5 – 9, but it is the most stable at pH 3 – 4. Dependence of intensity of coloration is proportional to the mass concentration of  $\text{Fe}^{2+}$  to  $5 \text{ mg} \cdot \text{l}^{-1}$ . Conditions of Bouguer-Lambert-Beer law apply. Measurement was done at a wavelength of 510 nm in a cuvette optical path 1 cm. Dependence of absorbance to concentration shows a calibration curve it the following Figure I.

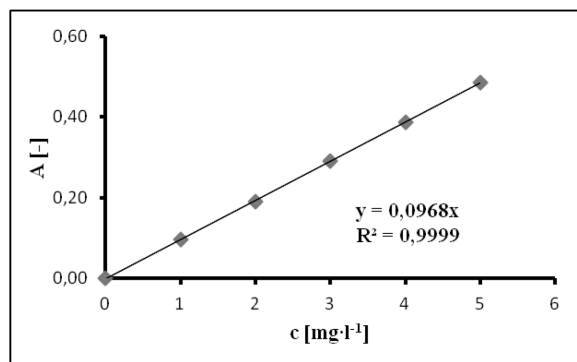


Figure I. Determination of  $\text{Fe}^{2+}$  - calibration curve

Total dissolved Fe was observed gravimetrically, which allows easy to uninstall active part of a sacrificial steel anode. This method is easy, very accurate, fast and also not depends on the human factor. Another benefit is to obtain the current value of total iron. Concentration of total and ferrous iron can be observed within 15 minutes.

### Electrochemical dissolution of Fe

Setup of electrochemical dissolving terms was always identical for both of those used materials of sacrificial anode. Cathode was made from Platinum. Supporting electrolyte was prepared at the beginning of each analysis. Selected value of pH was set by automatic titrator. Instrument always automatically dosed the required amount of  $H_2SO_4$  or  $NaOH$  until reaching the desired pH. Initial weight of the anode was found on the analytical balance. The current is kept constant for the whole duration of the experiment. Experiments were run at pH 2, 3 and 4. For each pH was measured at a current of 0,010 A, 0,025 A, 0,050 A, 0,100 A and 0,150 A. Collection of sample for determination of  $Fe^{2+}$  was carried out always at the same time during the experiment. Weight loss of sacrificial anode was found at the same time simultaneously. Evolution of all forms of iron concentration depending on time shown in the following Figure. II and III.

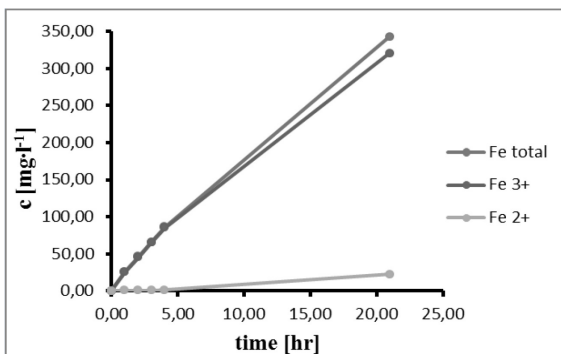


Figure II. Concentration of Fe (Steel 17 240 Cr-Ni), pH 2; 0,010 A

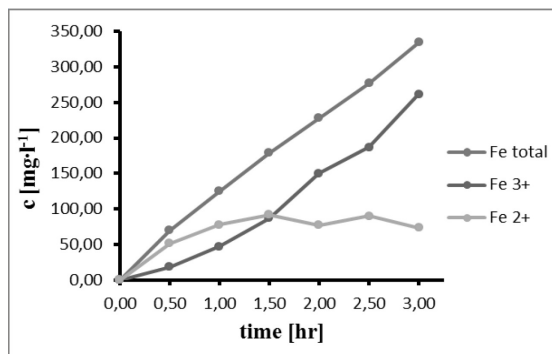


Figure III. Concentration of Fe (Ocel 11 373) při pH 2; 0,010 A

Because concentrations of  $Fe^{2+}$  were very low in comparison of total iron dependence concentration of  $Fe^{2+}$  on time summarize next Figure IV. and V.

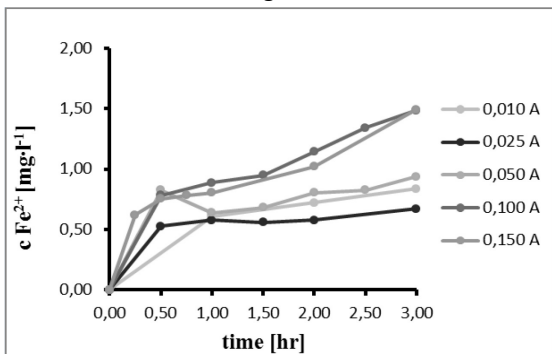


Figure IV. Concentration of  $Fe^{2+}$  (Steel ČSN 17 240 Cr-Ni), pH 2

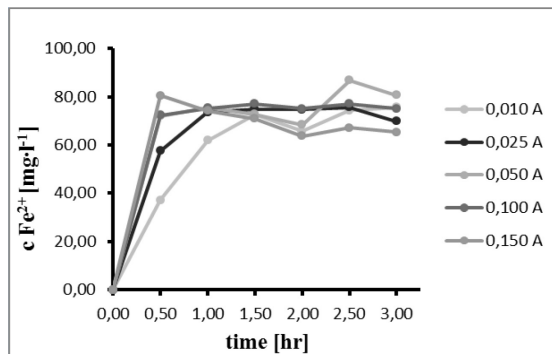


Figure V. Concentration of  $Fe^{2+}$  (Steel ČSN 11 373), pH 2

The following Figure VI. and VII. shows weight losses of iron anode during the duration of experiment.

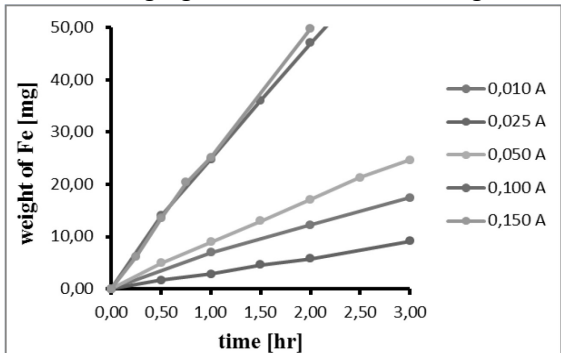


Figure VI. Weight losses (Steel ČSN 17 240 Cr-Ni), pH 2

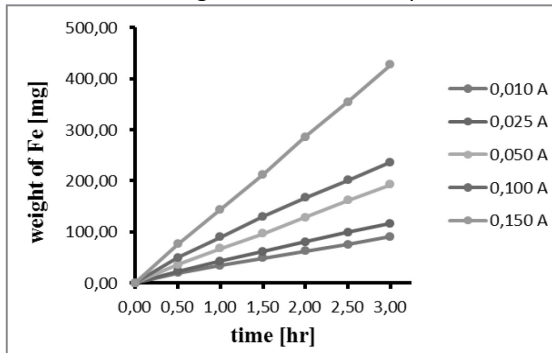


Figure VII. Weight losses (Steel ČSN 11 373), pH 2

### Corrosion tests without electric current

#### Alloy steel Cr-Ni

In these corrosion experiments was tested whether the Steel Cr-Ni which is used as an anode is dissolved only in an acidic medium without the current. At the beginning of the analysis all three anodes were weighed on an analytical balance. Three beakers of 250 ml were arranged. Electrolyte –  $0,05 \text{ mol} \cdot \text{l}^{-1} \text{ Na}_2\text{SO}_4$  was prepared to each of beaker. In each beaker was different pH. Tests were run 505 hours and 30 minutes with intensive stirring. After analysis anodes were dried and weighed again. The total iron was determined voltammetrically. The conducted corrosion test shows that the Steel Cr-Ni due to the high proportion of chromium without inserting current almost dissolve. On this basis, it can be concluded that the influence of atmospheric oxygen is insignificant. Although the concentration of Fe detected were very low it is evident that at a more acidic pH of the solution to release more of Fe. The corrosion rates and losses of Steel Cr-Ni are much lower than in the case using electrodes of unalloyed structural steel.

Tab. III Corrosion test without electric current - Steel 17 240 Cr-Ni

Beaker	pH	Time [hr]	Total loss [mg]	Corrosion loss [ $\text{g} \cdot \text{m}^{-2}$ ]	Corrosion rate [ $\text{g} \cdot \text{m}^{-2} \cdot \text{y}$ ]	Corrosion rate [ $\text{kg} \cdot \text{m}^{-2} \cdot \text{y}$ ]
1.	2	505,5	0,3	0,26	4,48	0,0045
2.	3	505,5	0,2	0,17	2,99	0,003
3.	4	505,5	0,1	0,09	1,49	0,0015

#### Non-alloy steel

Corrosion experiment was conducted also with electrodes made of non-alloy steel, which were used as the iron anode. The experiment was conducted under the same conditions as for Steel Cr-Ni. Test was run 61 hours with intensive stirring. Samples were collected during the experiment for determination of  $\text{Fe}^{\text{II}}$  which was detect spectrophotometrically after reaction with 1,10-phenanthroline. Total iron was observed gravimetrically. To achieve much higher corrosion rates of anodes made of non-alloy steel was enough corrosion tests sufficient corrosion tests carried out just 61 hours, compared to 505,5 hours duration of test with Steel Cr –Ni. Even this relatively short time of exposure was sufficient to achieve corrosion losses in case of chrome-nickel steel which could be achieved only with electric current in electrochemical dissolution. It is evident that the release of Fe from the electrodes is strongly depends on pH. The corrosion rate at pH 2 is more than three times higher than the pH 4. The change of color of electrolyte is evident too. Influence of oxygen and environmental conditions aren't negligible factors.

Tab. IV Corrosion test without electric current - Steel 11 373

Beaker	pH	Time [hr]	Total loss [mg]	Corrosion loss [ $\text{g} \cdot \text{m}^{-2}$ ]	Corrosion rate [ $\text{g} \cdot \text{m}^{-2} \cdot \text{y}$ ]	Corrosion rate [ $\text{kg} \cdot \text{m}^{-2} \cdot \text{y}$ ]
1.	2	61	492,7	425,02	61035,23	61,0352
2.	3	61	194,7	167,95	24119,26	24,1193
3.	4	61	148,2	127,84	18358,88	18,3589

#### Alkaline precipitation electrochemically dissolved $\text{Fe}^{2+}$ and $\text{Fe}^{3+}$ ions

Target of this experiment was precipitation  $\text{Fe}^{2+}$  and  $\text{Fe}^{3+}$  ions which form precursor of catalyst and catalyst Fenton's or electro-Fenton's oxidation. As a source of pollution was used electrolyte from analysis. Sacrificial electrode was steel anode (Steel Cr-Ni). Cathode was platinum. As electrolyte was used  $0,05 \text{ mol} \cdot \text{l}^{-1} \text{ Na}_2\text{SO}_4$  volume of 250 ml. The voltage was kept constant. The current density was regulated by increasing the electrical conductivity by the addition of  $\text{Na}_2\text{SO}_4$ . From the supporting electrolyte was collected twice 100 ml. The solutions were adjusted to pH 7 and 10,5 with automatic titrator TitraLab 856. Adjusted solutions were allowed to freely sedimented for 1 296 hours (54 days). In each beaker was evident distribution of solid and liquid phase after the experiment. Brown-orange iron sludge ferrous and ferric hydrated hydroxides were settled at the bottom of both beakers. The liquid layer was coloured green. Samples were collected to determine the total dissolved iron and dissolved ferrous iron. It was found from the measured values that after 54 days of continuous sedimentation of the iron concentration in solution are very low. Most of the iron is in the sludge at the bottom of beakers. Sludge can be removed by filtration. Concentrations of total iron 0,38 and 0,37  $\text{mg} \cdot \text{l}^{-1}$  met the conditions of the Government Regulation No. 61/2003 Coll., about values of pollution by iron in the

surface and wastewaters where is a limit for iron  $0,55 \text{ mg} \cdot \text{l}^{-1}$ . It was also found that the resulting concentration of iron does not depend on initial pH, because the resulting concentration of iron in both solutions was almost identical. In this way can be removed sufficiently dissolved  $\text{Fe}^{2+}$  and  $\text{Fe}^{3+}$  ions by neutralization of purified water. It was showed efficient efficacy of sedimentation at the same time when the sludge to settle for the second day after neutralization. After the Fenton or electro Fenton oxidation his provides the merging neutralization and precipitation process in purified water and the removal of ferrous-ferric sludge by the sedimentation.

### Conclusion

Fenton's oxidation is a perspective environmental technology for treatment and pretreatment for biologically difficult to clean wastewater and industrial process water regardless of the method of execution. Is necessary an effective catalyst in suitable concentration and molar ratio with hydrogen peroxide. Catalyst could be cheap, nontoxic, effective, regenerable and easily removable from purified water. Ion of  $\text{Fe}^{2+}$  meets all the demands. Electrochemical dissolution of sacrificial steel anode is very effective method of continuous dosing of  $\text{Fe}^{2+}$  which unnecessarily not salting treated water. Two types of material of sacrificial steel anode - Steel 17 240 Cr-Ni and Steel 11 373 were chosen. The price of these materials is favorable in both cases about 98 CZK respectively 22 CZK including VAT per 1 kg. Both steels are common commercially available products with excellent stable quality which are produced in the Czech Republic. Two types of sacrificial anodes are useful for electro-Fenton reaction, but it is necessary to take into account the specific properties of both materials under conditions of electro-Fenton process. This is the influence of the pH medium in the range of 2-4. Rapid corrosion of non-alloy structural steel 11 373 occurs under these conditions where the corrosion rate is achieved, depending on the pH, about  $18,36 \text{ kg} \cdot \text{m}^{-2} \cdot \text{year}$  (pH 4);  $24,12 \text{ kg} \cdot \text{m}^{-2} \cdot \text{year}$  (pH 3) to  $61,04 \text{ kg} \cdot \text{m}^{-2} \cdot \text{year}$  (pH 2). Steel 17240 Cr-Ni shows a corrosion losses about 1 420-1 640 lower under the same conditions which corresponds to the corrosion rate of  $1,5 \cdot 10^{-3} \text{ kg} \cdot \text{m}^{-2} \cdot \text{year}$  (pH 4), respectively,  $4,5 \cdot 10^{-3} \text{ kg} \cdot \text{m}^{-2} \cdot \text{year}$  (pH 2). Non-alloy steel 11 373 shows enough corrosion rate to supply the necessary amount of catalyst  $\text{Fe}^{2+}$  ions to the electro-Fenton process. This amount may be increased at low current densities and positive potentials, which also corresponds to high material yield of the process. Low level of regulation of process when disconnect the electric current is considerable corrosion rate under the conditions of pH electro-Fenton reaction. It can easily to lead increase concentrations  $\text{Fe}^{2+}$  and  $\text{Fe}^{3+}$  which will show at lower the efficiency of the process. The application of alloy steel 17 240 Cr-Ni material is five times more expensive. Connection to DC power supply is necessary to increase low corrosion rate. Energy costs are associated with. It is very well regulated source of  $\text{Fe}^{2+}$  ions which could be easily operated in electro-Fenton process with electronic controlled circuit and keep optimal molar ratio  $\text{Fe}^{2+} : \text{H}_2\text{O}_2 : \text{organic pollutant}$ . Only residual concentration of total iron meets the conditions in the Government Regulation No. 61/2003 Coll. where is a limit for iron  $0,55 \text{ mg} \cdot \text{l}^{-1}$ .

### Acknowledgement

*This work was supported by the Ministry of Education, Youth and Sports of the Czech Republic (project No. SG 350006).*

### References

1. Brillas E., Sirés I., Oturan M. A.: *Chem. Rev.* 109, 6570 (2009).
2. Kang Y. W., Hwang K. Y.: *Water Res.* 34, 2786 (2000).
3. Rosales E., Pazos M., Santoromán M. A.: *Chem. En.* 35, 609 (2012).
4. Sahoo M. K., Sinha B., Marbaniang M., Naik D. B., Sharan R. N.: *Chem. Eng. J.* 209, 147 (2012).
5. Balci B., Oturan M. A., Oturan N., Sirés I.: *J. Agric. Food Chem.* 57, 4888 (2009).
6. Nidheesh P. V., Gandhimathi R.: *Desalination* 299, 1, (2012).
7. Moreno C., Hector A., Cocke D. L., Gomes J. A. G., Morkovsky P., Parga J. R., Peterson E., Garcia C.: *Industrial* 48, 2275, (2009).
8. ČSN 41 7240: *Ocel 17 240 Cr-Ni* (1973).
9. ČSN 41 1373: *Ocel 11 373* (1994).

## METAMITRON DEGRADATION FROM MODEL WASTEWATER BY INDIRECT OXIDATION

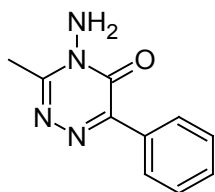
**Tomić A.**<sup>1</sup>, Dušek L.<sup>1</sup>, Palatý Z.<sup>1</sup>, Vojs M.<sup>2</sup>

<sup>1</sup>*Institute of Environmental and Chemical Engineering, Faculty of Chemical Technology, Pardubice, Studentská 573,*

<sup>2</sup>*Slovak University of Technology in Bratislava, Faculty of Electrical Engineering and Information Technology, Ilkovičova 3, 812 19 Bratislava, Slovak Republic*  
e-mail: aleksandar.tomic@upce.cz

### Introduction

Triazines and triazinones refer to persistent soil herbicides. If a large quantity is used (5 to 20 kg.ha<sup>-1</sup>), they act as a total herbicide. However, when a smaller quantity is used (1 to 4 kg.ha<sup>-1</sup>), it is possible to kill selectively a number of germinating weeds, e.g. in maize, asparagus, rape and beans<sup>1</sup>. Triazines and triazinones act on the surrounding weeds as the inhibitor of photosynthesis. The triazine group includes ametrifone, amibuzin, ethiozine, hexazinone, isomethiozine, metamiltron, metribuzin and trifludimoxazine. In the Czech Republic only metamiltron and metribuzin are used currently. Until 2007 also hexazinone was applied but due to the expiry of its valid registration<sup>2</sup> it is no longer used. Metamiltron is a synthetic compound belonging to the triazine group. From the point of view of efficiency, this herbicide is classified as a selective reagent. It is applied directly onto leaves where it is absorbed and subsequently impairs photosynthesis due to the inhibition of electron transport<sup>3</sup>. The target plants are fodder beets, red beet and the standard sugar beet. The herbicide can be used independently or in combination with another herbicide.



Metamiltron

(4-amino-4,5-dihydro-3-methyl-6-phenyl-1,2,4-triazine-5-one)

### Experiment

The chemical substances used for the experiments were sodium chloride NaCl p.a. Lach-Ner, s.r.o., sulphuric acid H<sub>2</sub>SO<sub>4</sub> 96%, manufactured by Penta s.r.o., sodium hydroxide NaOH p.a. Lach-Ner, s.r.o., demineralised water. Na<sub>2</sub>SO<sub>4</sub>, manufactured by Lach-Ner, s.r.o., H<sub>2</sub>O<sub>2</sub> - 30%, manufactured by Penta s.r.o., FeSO<sub>4</sub>·7H<sub>2</sub>O – manufactured by Lachema Brno., K<sub>2</sub>TiO(C<sub>2</sub>O<sub>4</sub>)<sub>2</sub>·2H<sub>2</sub>O - manufactured by AbcrGmbH, metamiltron – 97%, manufactured by Sigma – Aldrich, H<sub>3</sub>PO<sub>4</sub> 85%, manufactured by Penta s.r.o., H<sub>3</sub>BO<sub>3</sub> p.a. Lach-Ner, s.r.o., CH<sub>3</sub>COOH 98% Lach-Ner, s.r.o.

### Determination of metamiltron using UV-visible spectrophotometry

The current concentration of metamiltron within the concentration range of 1.5·10<sup>-5</sup> - 2·10<sup>-4</sup> mol.l<sup>-1</sup> in model waters used for degradation by chlorine-based oxidizing agents was monitored by UV-visible spectroscopy using the Libra S22 spectrophotometer in a 10mm silica glass cuvette at λ<sub>anal</sub> = 304 nm at the temperature of 20 °C. It has been verified that the presence of NaCl in the solution has no influence on measuring in the respective part of the spectrum. The current concentration of metamiltron was calculated based on a linear formula expressing the absorbance - concentration relationship A = 10,771 C<sub>metamiltron</sub> with the regression coefficient r<sup>2</sup> = 0.9999, see Fig. 1a, 1b.

### Determination of metamiltron using differential pulse (DP) voltametry

This method is based on the reduction of the metamiltron molecule on the hanging mercury drop electrode (HMDE) as the working electrode, the output of which is a cathodic reduction peak.

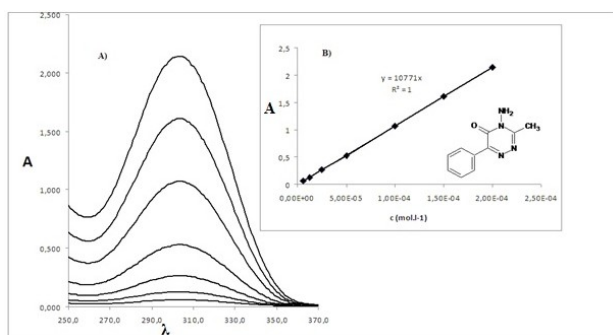


Figure 1a. Absorbance - wavelength relationship for metamitron (250 – 370 nm,  $t = 20\text{ }^{\circ}\text{C}$ )

Figure 1b. Calibration curve for metamitron

The differential pulse voltametry (DPV) measurement was employed for measuring the metamitron concentration with the concurrent electro-Fenton oxidation as spectrophotometry could not be used for this method due to the interfering absorbance of the substances present in the solution. However, the method was used for the reference determination of metamitron during the electrolysis of NaCl, but in this case, spectrophotometric measurements were an easier variant. The employed polarograph was equipped with a three-electrode microelectrode system. The reference electrode was an argentchloride electrode, the working electrode was a hanging mercury drop electrode (HMDE), the auxiliary electrode was a platinum wire electrode. The conditions of the measurement are provided in Table 1. For this measurement, the universal Britton-Robinson buffer was used. Oxygen was displaced from the measured solution by nitrogen.

Table I

Conditions applied during the DPV measurements of metamitron concentration with the concurrent electro-Fenton oxidation.

Parameters	Values
Initial potential [mV]	-200
Final potential [mV]	-800
Scan rate [mV/s]	20
Bubble time [s]	300
Number of scans	3
Pulse height [mV]	-50
Pulse width [ms]	80

The following voltamogram in Figure 2 shows the current responses on the HMDE with the increasing concentration of metamitron in the polarography vessel with the individual peaks corresponding with the concentrations of  $1 - 5 \cdot 10^{-6}\text{ mol.l}^{-1}$ . By way of experiment it was discovered that the position of the reduction peak is located within the potential range of -470 through -490 mV with the current reaching maximum values at the potential of approx. -480 mV.

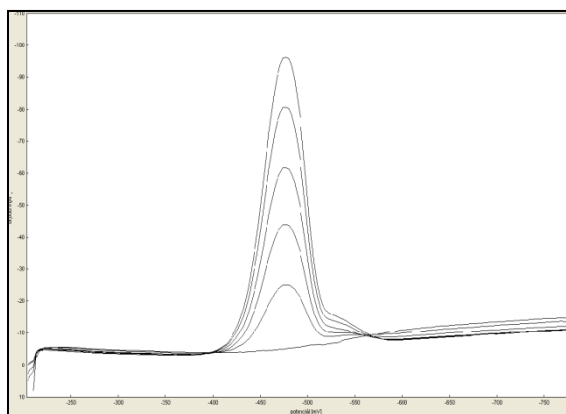
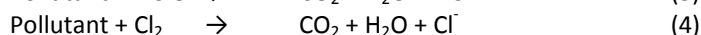
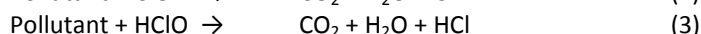
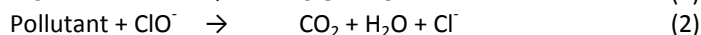
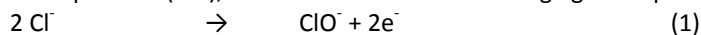


Figure 2. The DPV measurement of metamitron on the HMDE (Britton – Robinson buffer,  $\text{pH} = 3$ ), initial potential = -200 mV, final potential = -800 mV, scan rate =  $20\text{ mVs}^{-1}$ .

### Electrochemical oxidation with the formation of chlorine-based oxidizing agents

For the experimental measuring of metamitron electrooxidation, a single-chamber drum-shaped laboratory electrolyser was used. The initial concentration of metamitron was  $1.10^{-4} \text{ mol.l}^{-1}$ , which corresponds with  $20.22 \text{ mg.l}^{-1}$ . A supporting electrolyte based on NaCl or  $\text{Na}_2\text{SO}_4$ , both with the concentration of  $0.05 \text{ mol.l}^{-1}$ , was used for the improvement of conductivity and as a precursor of the electrochemically generated oxidizing agent. The temperature of the model wastewater during degradation was  $20^\circ\text{C}$ . The active surface of all electrodes was  $1 \text{ cm}^2$ . The connection used for the experiments was always with two electrodes.

During degradation metamitron was subjected to indirect electrochemical oxidation with the formation of chlorine-based oxidizing agents in situ using the electrolyse of a sodium chloride solution. As it is obvious from the equations (1-4), the formation of the oxidizing agent depends on the pH of the ambient environment.



Within the framework of individual measurements, the influence of reaction conditions was monitored, see Table II, in terms of the efficiency of the model wastewater decontamination. The reduction in concentration in time was calculated from the measured values, see Figure 3. Figure 4 provides for the influence of individual electrolysis parameters on the efficiency of the processes, which is expressed by a percentage reduction in metamitron concentration. The Figure compares the influence of pH and current densities on the efficiency of oxidation for individual concentrations of NaCl after 30 minutes of the experiment.

Table II  
Measuring conditions

Parameters	Values		
NaCl [ $\text{mol.l}^{-1}$ ]	0.025	0.05	0.075
pH	2	3	4
I [mA]	50	75	100

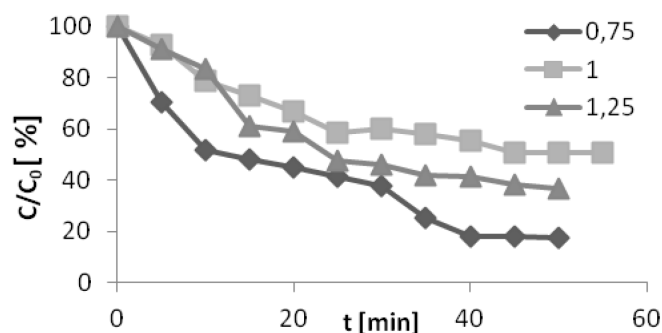


Figure 3. The metamitron concentration reduction - time relationship at pH = 3,  $t = 20^\circ\text{C}$ , platinum electrodes,  $S = 2 \times 1 \text{ cm}^2$ ,  $V = 250 \text{ ml}$ , spectrophotometric determination ( $\lambda = 304 \text{ nm}$ ),  $I = 50 \text{ mA}$ , key: concentration of NaCl ( $0.025 - 0.075 \text{ mol.l}^{-1}$ ).

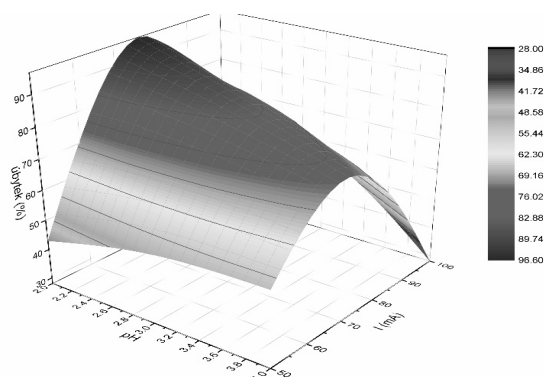
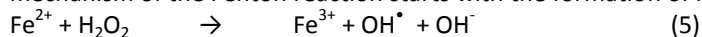


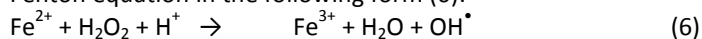
Figure 4. The influence of pH (2-4) and current densities (50-100 mA) on metamitron degradation at the concentration of NaCl  $0.025 \text{ mol.l}^{-1}$  (after time  $t = 30 \text{ min}$ ).

### Indirect electrochemical oxidation of metamitron using the electro-Fenton reaction

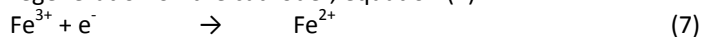
The method utilizing the formation of hydroxyl radicals as the products of the Fenton reaction was used. The reaction proceeds due to the catalysed electrosynthesis of hydrogen peroxide and an addition of  $\text{Fe}^{2+}$  ions. The mechanism of the Fenton reaction starts with the formation of hydroxyl radicals<sup>4</sup>, equation (5)



An important factor is pH, which must be in this case within the range of 2 to 4. Then it is better to write the Fenton equation in the following form (6):



An important role is played here by  $\text{Fe}^{2+}$ , which are added in a very small quantity. The reason is their regeneration on the cathode<sup>5</sup>, equation (7)



The influence of the reaction conditions on the efficiency of the model wastewater decontamination was examined, see Table III. The measured current reached the maximum values at the potential of approx. -480 mV. The reduction in concentration in time was calculated from the measured values, see Figure 5. Figure 6 provides for the influence of individual electrolysis parameters on the efficiency of the processes, which is expressed by a percentage reduction in metamitron concentration. The Figure compares the influence of pH and current densities on the efficiency of oxidation for individual concentrations of  $\text{FeSO}_4 \cdot 7\text{H}_2\text{O}$  after 30 minutes of the experiment.

Table III

The conditions of the measurements of indirect electrochemical oxidation of metamitron using the electro-Fenton reaction

Parameters	Values		
pH	2	3	4
$\text{FeSO}_4 \cdot 7\text{H}_2\text{O}$ [ml]	0.75	1	1.25
I [mA]	50	75	100

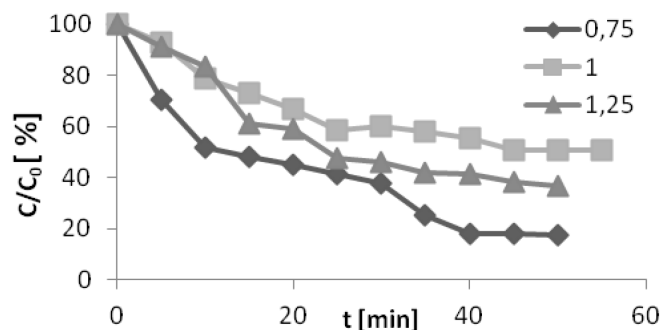


Figure 5. The metamitron concentration reduction - time relationship, at pH = 3,  $t = 20^\circ\text{C}$ ,  $I = 50\text{ mA}$ ,  $1\text{ g.l}^{-1}$  Pd/C catalyser, BDD cathode, Pt anode,  $S = 2 \times 1\text{ cm}^2$ , electrolyte  $\text{Na}_2\text{SO}_4$  ( $0.05\text{ mol.l}^{-1}$ ),  $V = 250\text{ ml}$ , key: concentration  $\text{Fe}^{2+}$  in the cell ( $0.75 - 1.25 \cdot 10^{-4}\text{ mol.l}^{-1}$ ).

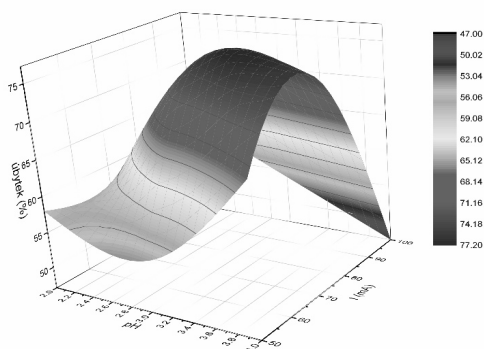


Figure 6. The influence of pH (2-4) and current densities (50-100 mA) on metamitron degradation at the concentration of  $\text{Fe}^{2+} = 1.25 \cdot 10^{-4} \text{ mol.l}^{-1}$  (after time  $t = 30 \text{ min}$ ).

### Discussion and conclusion

During the degradation of metamitron by the method of indirect electrochemical oxidation at the presence of chlorine compounds, the influence of current density (50-100 mA), the concentration of auxiliary electrolyte NaCl (0.025 – 0.075 mol.l<sup>-1</sup>) and pH (2-4) was monitored.

The NaCl concentration had a direct effect on the rate of degradation due to the fact that a larger quantity of oxidizing agents was allowed to be formed. Therefore, the degradation rate increased in the order of concentrations of NaCl  $0.025 < 0.05 < 0.075 \text{ mol.l}^{-1}$ . In addition, the increase in salinization resulted in a reduction in the process demands as reaching the same current densities required a lower voltage. The optimal current density in the respective connection of the electrochemical system and with respect to the size of electrodes and all the other aforementioned parameters was 75 mA. The degradation efficiency increased in the order of  $50 \text{ mA} < 100 \text{ mA} < 75 \text{ mA}$ . The suitability of the medium current density can be explained by the fact that its further increase resulted in a larger production of chlorine, which could not be dissolved in the reaction solution and leaked out of the cell.

In the case of Fenton oxidation, the influence of current density (50-100 mA), the quantity of added catalyst  $\text{Fe}^{2+}$  ( $0.75 - 1.25 \cdot 10^{-4} \text{ mol.l}^{-1}$ ) and pH (2-4) was monitored. Ferrous cations were added in the form of the solution of  $\text{FeSO}_4 \cdot 7\text{H}_2\text{O}$ . The influence of pH on the degradation of Metamitron was ascertained unambiguously using the electro-Fenton reaction at the optimal value of 3, which is in accordance with the quoted references. The optimal current density was determined at 75 or, where applicable, 100 mA. As far as the influence of the  $\text{Fe}^{2+}$  ions concentration on the course of the Metamitron degradation is concerned, it is difficult to state the optimal value as the efficiency was high throughout the entire concentration range, and due to the observed interferences as well. The disadvantage of this method in practice is the formation of sludge by the precipitation of  $\text{Fe}^{3+}$  in the form of hydroxides. The sludge may demonstrate hazardous properties depending on the content of contaminants in the treated waters.

In conclusion, it is possible to say that the promising potential of both methods for metamitron degradation from model wastewater using indirect electrochemical oxidation has been ascertained. With a suitable modification of parameters the methods can be implemented with a high efficiency thus offering a reasonable alternative to the conventional methods of water treatment.

### Acknowledgements

*This paper has been prepared with the support of the subsidy provided by the Ministry of Education, Youth and Sports of the Czech Republic under the number of SG 350006.*

### References

1. Martin, H., Worthing, C. R. (1974): Pesticide Manual. 4th edition British Crop Protection Council., 395 p.
2. Nera Agro. Safety Data Sheet: Velpar 5G. 5th edition 2000, 9 p.
3. Agromanál.cz: metamitron [online]. [quot. 23/02/2014]. Available at <http://www.agromanual.cz/cz/pripravky/ucinne-latky/ucinna-latka/metamitron.html>
4. Haber, F.; Weiss, J. Naturwissenschaften, 1932, 51, 948.
5. Aaron, J. J.; Oturan, M. A. Turk. J. Chem., 2001, 25, 509.

## REMOVAL OF SELECTED PHARMACEUTICALS BY HETEROGENEOUS PHOTOCATALYSIS

**Trousil V.**<sup>1</sup>, Blažková Z.<sup>1</sup>, Slehová E.<sup>1</sup>, Palarčík J.<sup>1</sup>, Machalický O.<sup>2</sup>, Cakl J.<sup>1</sup>

<sup>1</sup>Ústav environmentálního a chemického inženýrství, Fakulta chemicko-technologická, Univerzita Pardubice, Studentská 573, 532 10 Pardubice

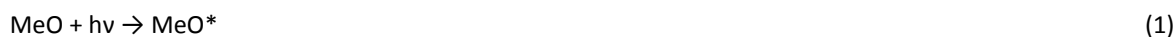
<sup>2</sup>Ústav organické chemie a technologie, Fakulta chemicko-technologická, Univerzita Pardubice, Studentská 573, 532 10 Pardubice  
Vojtech.trousil@upce.cz

### Theoretical

Pharmaceuticals belong to substances, which are designed to have a strong biological effect at low doses. They are often designed to not to be inactivated before own therapeutic effect (they are structurally stable substances). Some are also highly lipophilic. Although these properties are widely used in pharmacology, in the environment are pharmaceuticals dangerous xenobiotics. Furthermore, in the human metabolism from the original drugs are formed metabolites, which can be more persistent or bioactive than the original compound (e.g. carbamazepine or diclofenac metabolites). These substances then go along with sewage water into the sewage treatment plant. Big drawback of current wastewater treatment plants is that they are not able to successfully eliminate this kind of pollutant in such a low concentration (the amount ranges from units of ng/l to tens of µg/l) Removal of pharmaceuticals in wastewater treatment plants is for each drug different <sup>[1, 2]</sup>.

Subsequently, pharmaceuticals and their metabolites are released into the water recipient. Their amount is relatively low and thus usually do not cause acute toxic effect, but due to the above mentioned properties pharmaceuticals cause chronic effects on non-target (mostly water) organisms. One of the strongest effects have sex hormones, which cause bioaccumulation in the tissue, changes in fish population, or organ malformations. Other effects which pharmaceuticals cause include inhibition of the growth of water plants and algae, Crustaceans and Cnidarian <sup>[3, 4]</sup>.

Ibuprofen and paracetamol were removed from model water samples by method of heterogeneous photocatalysis. Its principle is the generation of chemical oxidants on the surface of oxide (sulfide) of transition metals. The system is composed of catalyst, oxidising agent and excitation light. The TiO<sub>2</sub> is the most frequent catalyst- for example more than CdS or CeO<sub>2</sub>. After the irradiation the catalyst become polarized and the electron is transferred on the oxygen (1-2). So the superoxide radical ·O<sub>2</sub><sup>-</sup>, then ·HO<sub>2</sub> radical (3-4) is generated. This radicals cause oxidative degradation of the pharmaceuticals. Heterogeneous photocatalysis itself has the advantage that it works under mild reaction conditions, and also it can better managed <sup>[5-7]</sup>.



### Equipment and chemicals

Chromatograph HPLC (Watrex), UV-LED lamp (Helling), circulation thermostat (Thermo Haake), Ibuprofen 98% C<sub>13</sub>H<sub>18</sub>O<sub>2</sub> (Sigma Aldrich), Titanium dioxide TiO<sub>2</sub> (Precheza a.s.), Paracetamol C<sub>8</sub>H<sub>9</sub>NO<sub>2</sub> (Penta), Acetonitrile C<sub>2</sub>H<sub>3</sub>N (Lach-Ner), Phosphoric acid H<sub>3</sub>PO<sub>4</sub> (Penta), Hydrogen peroxide 30% H<sub>2</sub>O<sub>2</sub> (Lach-Ner), Hydrochloric acid HCl (Penta), Sodium hydroxide NaOH (Penta), BOD cuvette tests LCK 555 (Hach-Lange), COD cuvette tests LCI 500 (Hach-Lange)

### Practical

Stock solutions were prepared by dissolving the appropriate amount of pharmaceutical in distilled water. Ibuprofen was also converted into its sodium salt with NaOH. The catalyst suspension of TiO<sub>2</sub> was prepared by dispersion of appropriate amount of oxide in distilled water by sonication. The amount of TiO<sub>2</sub> in the reaction vessel was 0.5 g/l. The drug content was 10 mg/l. Photocatalytic removal of pharmaceuticals was set in a double layer 1l batch reactor. Cooling was provided by a circulation thermostat (Thermo Haake) which drew cool water between the reactor walls.

Experiments were carried out at 25 °C. As a source of UV radiation was used UV-LED lamp Helling (4.2 V) with a maximum absorbance at 365 nm. The intensity of UV radiation was from 1700 to 8000 mW/cm<sup>2</sup>. The lamp was placed over the actual reaction vessel. Mixing was carried out using a magnetic stirrer at a speed of 450 rpm. During irradiation the samples were taken at regular 10 minute intervals and experiment lasted 1 hour.

Additionally experiments were carried out with pH adjustment to acidic and basic area (pH 3 and 10) and with 30% hydrogen peroxide H<sub>2</sub>O<sub>2</sub>. Its content in the reaction vessel was 2,5; 0,5; and 0,25 g/l. Prior the analysis, the samples were filtered through a membrane filter with a porosity of 0,2 µm. The samples were analysed by high performance liquid chromatography (HPLC) under these reaction conditions: reverse phase Nucleosil C18 column 250x4 mm, MF = 50% ACN and 50% H<sub>2</sub>O acidified with H<sub>3</sub>PO<sub>4</sub> (1 liter of MF contains 0,75 ml H<sub>3</sub>PO<sub>4</sub>), p = 11,2 MPa, flow rate 1 ml/min. As a detector was used diode array detector (DAD). Paracetamol measurement was at 245 nm and ibuprofen at 226 nm. In these separation conditions, the retention time was 2,3 minutes for paracetamol and 13,3 minutes for ibuprofen. As a general parameter of removal efficiency there was determined chemical and biochemical oxygen demand.

## Results and discussion

Before heterogeneous photocatalysis were separately investigated the effects of UV irradiation in the absence of catalyst. It was found that this effect on the removal of drugs from water is relatively small. During UV irradiation of pharmaceuticals without addition of a catalyst the conversion of paracetamol was 15 %. For ibuprofen the efficiency was less than 8 %. Further the effect of TiO<sub>2</sub> for removal of pharmaceuticals without the presence of UV radiation was examined. For both mentioned drugs was the removal efficiency only less than 5%. Several phenomena may occur in this case: elimination of the pharmaceutical can be happened by adsorption on the catalyst surface, photocatalysis induced by sunlight, or a combination of the two mentioned processes.

The graph in Figure 1 shows the removal efficiency of paracetamol by heterogeneous photocatalysis together with the oxidizing effect of H<sub>2</sub>O<sub>2</sub>. For paracetamol without added peroxide the conversion was achieved almost 80 %. Paracetamol degradation also in this case can be monitored visually during the experiment – by colour change of the solution from clear to light brown. This is attributable to formation of phenolic substances (degradation products of paracetamol). Subsequently, the removal efficiency was determined after a single addition of 30% H<sub>2</sub>O<sub>2</sub>. It was found that when the hydrogen peroxide content was 2,5 g/l there was a significant increase in removal efficiency of paracetamol. The removal efficiency was over 95 %. When the peroxide content was 0,5 g/l, the removal efficiency of paracetamol was 75 % and with the content of peroxide 0,25 g/l, the rate of elimination of the drug was 73 %.

Although the removal rate of paracetamol in this case is not significantly different from experiments without addition of hydrogen peroxide, the graph shows that the rate of reaction with peroxide was increased, however, later has been exhausted. This phenomenon is also evident in the HPLC chromatogram where in sample in 60 minutes there is not apparent peak of hydrogen peroxide. Similar results were achieved during degradation of ibuprofen as can be seen in a graph in Figure 2. The removal efficiency was 70 % with the content of H<sub>2</sub>O<sub>2</sub> 2,5 g/l, 58 % with H<sub>2</sub>O<sub>2</sub> content of 0,5 g/l and 59 % with H<sub>2</sub>O<sub>2</sub> content of 0,25 g/l. The literature states that hydrogen peroxide as the electron acceptor is more efficient than oxygen during electron transfer (5). The radical scavenging by hydrogen peroxide and thus reaching the limit concentration of peroxide did not occur, because in this case the removal efficiency was proportional to the amount of peroxide<sup>[8,9]</sup>.



The influence of pH on removal efficiency of pharmaceuticals was investigated. Graph in Figure 3 shows the removal efficiency of paracetamol at different pH. It was modified by 0.1 molar HCl or NaOH to pH 3, respectively 10. From the graph it is clear that a very significant increase in the effect of heterogeneous photocatalysis was achieved when pH was adjusted in the acidic range. After 40 minutes of experiment has been paracetamol already eliminated from water. On the other hand when pH was adjusted to an alkaline area the conversion of paracetamol occurred only from 30 %. The graph in Fig. 4 shows the conversion of ibuprofen at different pH values. During acidic conditions there was ibuprofen removal of 95 % after one hour of the experiment. Conversion of ibuprofen in the alkaline area was nearly 50 %. If the pH of the medium is below the isoelectric point of TiO<sub>2</sub>, its surface generates large amounts HO<sup>-</sup> ions. Subsequently, during the reaction of these ions with positive holes of semiconductors arises large amount of radicals participating the oxidative degradation compared to the untreated pH.

In most cases there was a satisfactory elimination of paracetamol or ibuprofen during irradiation, but from the HPLC chromatogram it is evident that in the system arise degradation products from the original organic substance. The literature states that the degradation products of pharmaceuticals may be more dangerous for the environment. There was exhibited higher toxicity to aquatic ecosystems or their biodegradability is lower. Therefore, the ratio between COD<sub>Ct</sub>/BOD<sub>5</sub> was determined. This ratio is used to determine the biodegradability of the substances. In the case of paracetamol, before the heterogeneous photocatalysis this ratio was 7,2. For

ibuprofen this ratio was 10,3. Only degradation of ibuprofen gave the satisfactory results. This value of  $COD_{Cr}/BOD_5$  after one hour of irradiation was 1.6 (heterogeneous photocatalysis at neutral pH) and 1,9 (degradation in acidic pH). For paracetamol was obtained the lowest value of 3,3 (again for heterogeneous photocatalysis at neutral and acidic pH). The graph in Fig. 5 then shows ratio of  $COD_{Cr}/BOD_5$  in time for paracetamol and ibuprofen. The graph shows that during the heterogeneous photocatalysis is reduced chemical and biochemical oxygen demand. The ratio of  $COD_{Cr}/BOD_5$  was 7 and 13 ( $t_0$ ), after 60 minutes it was 1,9 and 3,3. Low biodegradability is probably caused due to degradation products that are formed during irradiation. For example, paracetamol, whose peak was eluted in 2.5 minute, is transferred to an intermediate which peak is located in 1.6 minute. The signal of this substance after one hour of irradiation increased from an initial value of 83 mAU.s to 640 mAU.s. This formation is linear ( $R = 0.97$ ). Generally, the lowest number of intermediates was achieved by combination of heterogeneous photocatalysis with hydrogen peroxide at a concentration of 2.5 g/l and adjusting the pH into the acidic range. These experiments also showed the lowest ratio of  $COD_{Cr}/BOD_5$  for both mentioned pharmaceuticals<sup>[10,11]</sup>.

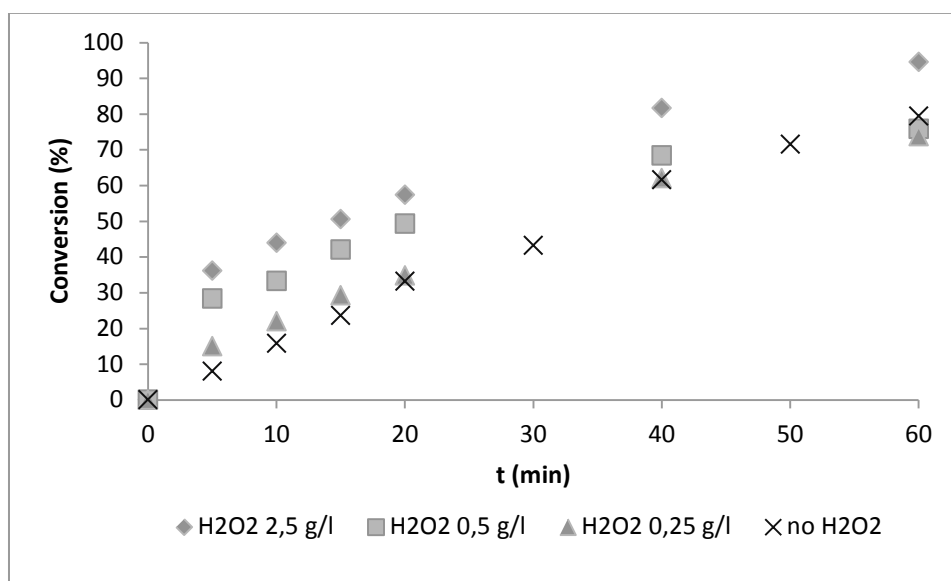


Fig. 1: Conversion of paracetamol by heterogeneous photocatalysis with addition of  $H_2O_2$

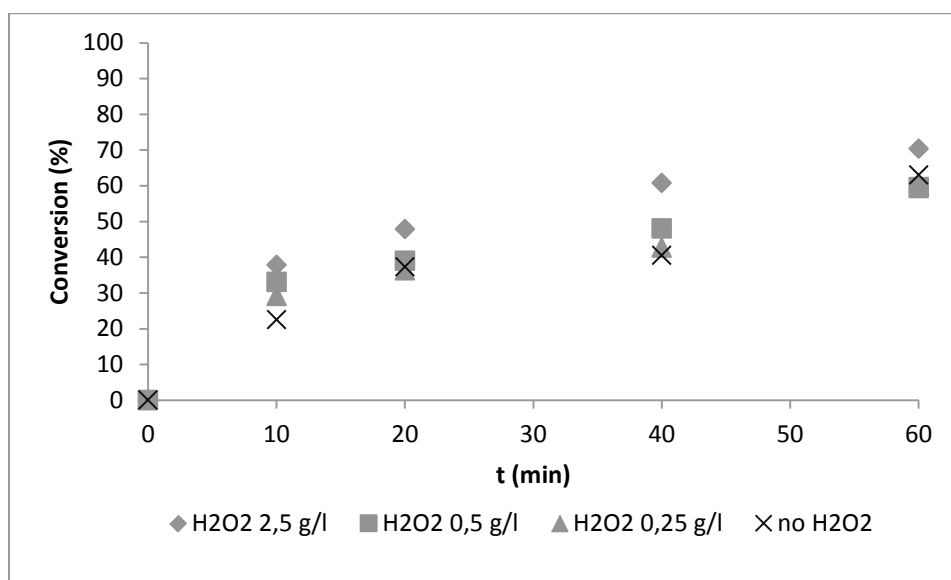


Fig. 2: Conversion of ibuprofen by heterogeneous photocatalysis with addition of  $H_2O_2$

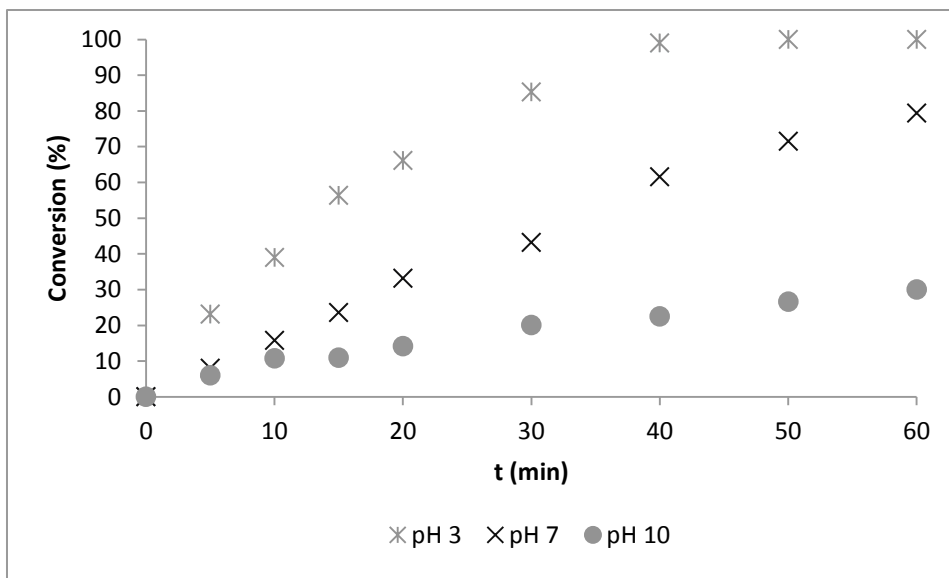


Fig. 3: Conversion of paracetamol by heterogeneous photocatalysis with various pH

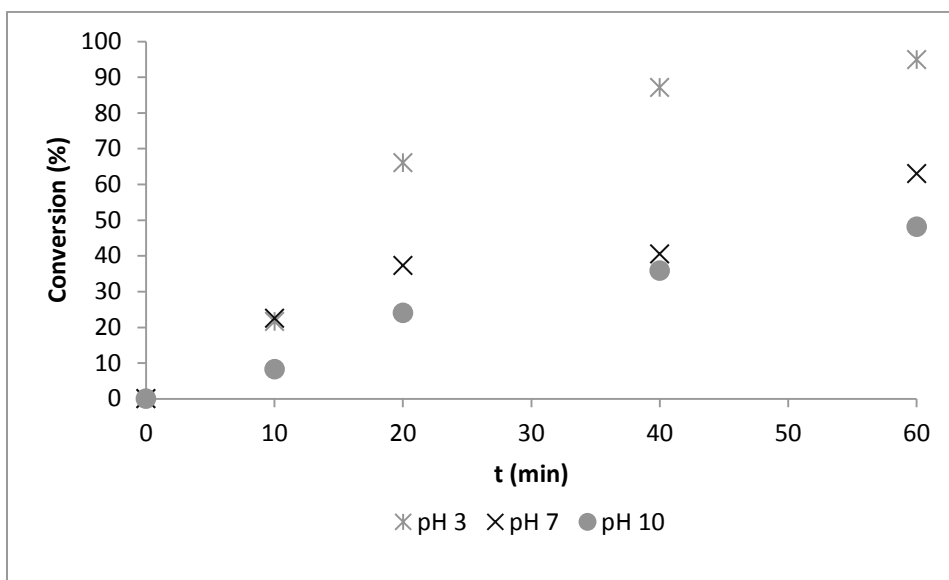


Fig. 4: Conversion of ibuprofen by heterogeneous photocatalysis with various pH

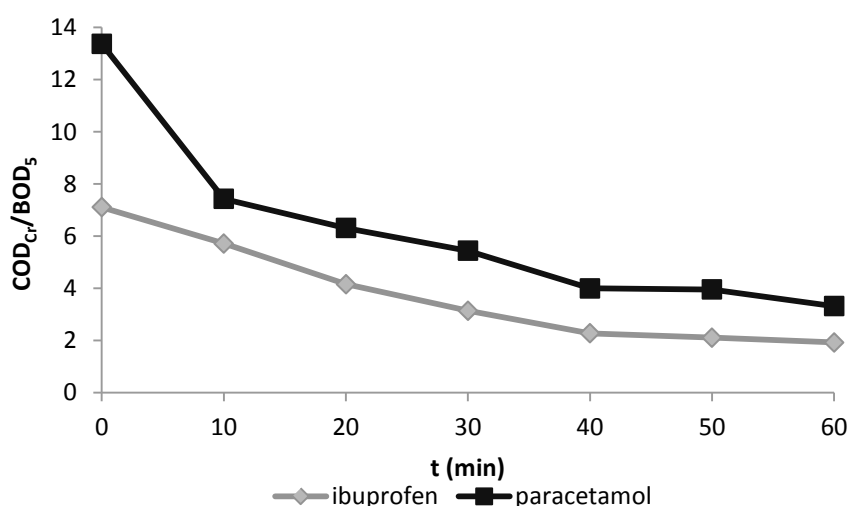


Fig. 3: Decrease of COD<sub>Cr</sub>/BOD<sub>5</sub> ratio heterogeneous photocatalysis

### Conclusion

Pharmaceuticals ibuprofen and paracetamol were removed from the model water samples by heterogeneous photocatalysis. In general, the more degradable was paracetamol than the ibuprofen. Reaction conditions were modified by adjusting pH or by single addition of hydrogen peroxide H<sub>2</sub>O<sub>2</sub>. The highest conversions were achieved by adjusting pH into the acidic range, wherein the paracetamol was removed 100% and ibuprofen was removed from 95%. Although it was reached so high removal efficiency of these substances, subsequent biological degradation (measured by the ratio COD<sub>Cr</sub>/BOD<sub>5</sub>) would be possible only for ibuprofen.

### Acknowledgement

Authors would like to thank Ministry of Education, Youth and Sports for financial support (SGSFCHT 2015006).

### Literature

- PETROVIC, M. a D. BARCELO. *Comprehensive analytical chemistry: Analysis, fate and removal of pharmaceuticals in the water cycle*. Amsterdam, Netherlands: Elsevier, 2007. ISBN 978-0-444-53052-3.
- BOTTONI, P. Pharmaceuticals as priority water contaminants. *Toxicological and Environmental Chemistry*. 2010, č. 92.
- JJEMBA, Patrick K. *Pharmacology: The occurrence and fate of pharmaceuticals and personal care products in the environment*. Hoboken, New Jersey: Wiley & Sons, Inc., 2008. ISBN 978-0-470-04630-2.
- AGA, Diana s. *Fate of pharmaceuticals in the environment and water treatment systems*. Boca Raton, 'Florida: CRC Press, 2008. ISBN 1-4200-5232-2.
- DE LA CRUZ, N. Degradation of 32 emergent contaminants by UV and neutral photo-fenton in domestic wastewater effluent previously treated by activated sludge. *Water Research*. 2012, č. 46.
- DUPREZ, Daniel. *Handbook of advanced methods and processes in Oxidation catalysis: From laboratory to industry*. London: Imperial College Press, 2014. ISBN 978-1-84816-750-6.
- BARCELÓ, D. a M. PETROVIC. Emerging contaminants from industrial and municipal waste: Removal technologies. Berlin: Springer-Verlag, 2008. ISBN 978-3-540-79209-3.
- AKPAN, U.G. Parameters affecting the photocatalytic degradation of dyes using TiO<sub>2</sub>-based photocatalysts: A review. *Journal of Hazardous Materials* [online]. 2009, č. 170 [cit. 2015-03-23]. Dostupné z: <http://chemical.eng.usm.my/bassim/PDF/photocatalytic%20degradation.pdf>
- PISCOPO, Antoine. Influence of pH and chloride anion on the photocatalytic degradation of organic compounds: Part I. Effect on the benzamide and para-hydroxybenzoic acid in TiO<sub>2</sub> aqueous solution. *Applied catalysis*. 2001, č. 35.
- FERNANDÉZ, J. Orange II photocatalysis on immobilised TiO<sub>2</sub>: Effect of the pH and H<sub>2</sub>O<sub>2</sub>. *Applied catalysis*. 2004, č. 48.
- MENDÉZ-ARRIAGA, Fabiola. Photocatalytic degradation of non-steroidal anti-inflammatory drugs with TiO<sub>2</sub> and simulated solar irradiation: Effect of the pH and H<sub>2</sub>O<sub>2</sub>. *Water research*. 2008, č. 42.

## DEVELOPMENT OF A PILOT PLANT FOR REDUCTION Hg EMISSION FROM LARGE POWER PLANT

**Pilař L.**<sup>1</sup>, Vlček Z.<sup>1</sup>, Zseliga Z.<sup>3</sup>, Veselý V.<sup>2</sup>

<sup>1</sup>ÚJV Řež, a.s. division ENERGOPROJEKT PRAHA, Na Žertvach 2247/29, 180 00 Praha 8, Czech republic

<sup>2</sup>Department of Chemical processes, Czech Academy of Sciences ČR, v. v. i., Rozvojová 135, 16500 Praha – Lysoláje, Czech republic

<sup>3</sup>VŠB – Technical university Ostrava, 17. Listopadu, 70800 Ostrava – Poruba, Czech republic  
Lukas.pilar@ujv.cz

### Abstract

The contribution introduces the project TAČR TA04020723 „Development of a pilot plant for monitoring of Hg emissions reduction from large and medium capacity energy sources“. The project responds to the new EU BAT legislative, where both emission limits for Hg concentration in flue gas and continual Hg concentration measurement requirements are stated. The objective of the contribution is an introduction of the project and the results gained in 2014. Analyses of certain lignite and coal samples were done to specify the Hg amount and balance of other compounds concentration was calculated with regard to the specifics of combustion process of a particular power source. At the end of 2014, a measurement was carried out at the large power plant. Hg concentrations were measured in the combustion products and were compared with balance calculation.

### Introduction

Effort for global protection of air environment is realized in the field of emissions. Reason for this is the fact, that emission of pollution exhausted in the air are transported by wind away, contaminate the surroundings regardless of regional borders. Therefore, EU also focuses its pursuit of environment protection on limit of emissions exhausted into the air. On the other hand, solid wastes are usually treated on the national level via regulations and acts.

Based on proved negative effects on livestock, actual topic addressed on international level is the lowering of mercury emissions exhausted into the air. Mercury concerned is mercury emitted during combustion of fossil fuels. Mercury in the living environment present serious health risk, and therefore its occurrence in the environment is watched carefully. Mercury is strongly neurotoxic and accumulates in food chains. Mercury gets into the human body mainly by inhaling its vapors, which have comparatively long half-life of permanence in atmosphere, where they appear in elementary form, ( $\text{Hg}^0$ ), as oxides ( $\text{Hg}^{2+}$ ) or bound to very fine-grain particles in aerosols. Its presence in human body results in damages to nervous system, kidneys, respiratory ways, damage of blood production and another diseases.

Therefore the newly prepared documentation in the EU called „Best Available Techniques (BAT) Reference Document for the Large Combustion Plants“, that sets emission limits for mercury concentration both for existing and new devices. Emission limits are sets in the following table:

Table I Emission limits

Combustion facility of rated heat intake ( $\text{MW}_t$ )	Hg emissions ( $\mu\text{g}/\text{Nm}^3$ )		rated period	monitoring
	new source	existing source		
coal: anthracite and black bituminous				
< 300	0.5 - 5	1 - 10	average taken from samples gathered during one year period	4times a year
> 300	0.2 - 2	0.2 - 6	year average	Continual measurement
coal: sub-bituminous and lignite				
< 300	1 - 10	2 - 20	average taken from samples gathered during one year period	4times a year
> 300	0.5 - 5	0.5 - 10	year average	Continual measurement

Presented confirmed base measurements will be implemented into legislation of EU member states after 2019. In The Czech Republic, actually no continual measurement of mercury concentration in flue gas is carried out and no technological solution or facility aiming for emission reduction of mercury in flue gas is in place.

### Projects objectives

Objectives of the projects are to identify actual distribution of emitted mercury and subsequently to design solution of the problem in order to reach expected emission limits. Actual condition will be verified on chosen representative energy sources combusting fossil fuels in the Czech Republic. Design of technical economical solution for reaching expected future emission limit of mercury will be tested on pilot unit, that will be using catalytic effects of the SCR method. Optimal conditions will be investigated, when necessary level of denitrification has been reached and mercury has been sufficiently oxidized at the same time. Results of this project solution will verify assumptions, on which the principle is based and new technical documentation of changes in existing facilities will be carried out or preliminary documentation of new facilities for mercury emissions elimination will be carried out. Necessary analytical methods for checking of the emission limits will be verified as a part of the project.

### Hg forms

During coal combustion at temperatures of 700-800°C decomposition of mercury compound is taking place while elementary mercury  $Hg^0$  is formed. This mercury leaves the combustion chamber in the form flue gas flow. After the flue gas is cooled while going through heat-exchange surfaces (on 200-250°C) of mercury reacts with present halogens, in particular with  $HgCl_2$ , eventually  $Hg_2Cl_2$ . Mercury is also trapped on the surface of escaping ash ( $Hg^p$ ), which is subsequently eliminated in ash separator. Remaining part is then emitted in the air. See fig n.1.

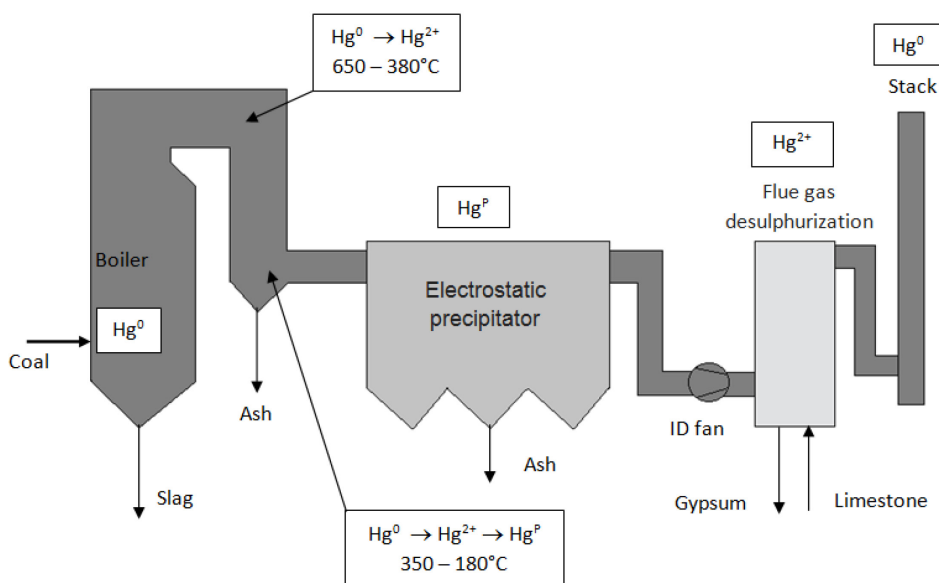


Figure 1. Scheme Hg distribution in the flue gas.

Mercury is then present in the flue gas in metallic form as atomic  $Hg^0$ , oxidized as  $Hg^{2+}$  ( $HgCl_2$ ,  $Hg_2Cl_2$  or  $HgO$ ) or further adsorbed;  $Hg^p$ . Oxidized form can be eliminated by wet or dry desulphurization of flue gas. On the other hand, elimination of elementary mercury is very difficult and escapes into the air. Resulting from continuous measurements, 15 % of total mercury entering as a part of the fuel is trapped on the ash and 5 to 10% of mercury goes. The rest is emitted with the flue gas into the air. This situation of emissions is fulfilling actual limits, but the expected change of limit concentration raises the necessity of redistribution of mercury and its compounds.

### Methods for mercury concentration reduction in the flue gas

Following methods can be used industrially for reduction of mercury concentration. As one of the most widely used methods of heavy metals adsorption but also of persistent agents (PCDD/F), adsorption using carbon sorbents is used. This technology is commonly used for purification of flue gas from incinerators. Sorbent is added together with an additive ( $Ca(OH)_2$ ,  $NaOH$ ,  $NaHCO_3$  etc.) into the stream of flue gas during semi-dry or

dry method of purification.. Contaminated carbon sorbent together with purification products is trapped by ash separator.

Another method of Hg concentration reduction is using the BBA method (Boiler bromide addition). The core of the method is the addition of halogenides into the combustion place. As a result of the additive, mercury is oxidized into soluble forms, so entrapment rate of mercury is increased in subsequent facilities formed by filters and wet purification of flue gas. The method is very debated with respect to creation of not only halogenides of mercury creation, but also of other persistent agents, in particular polybrominated dibenzodioxins and dibenzofurans.

Another method is to use catalyser primarily designed for elimination of emissions of NO using SCR method. (Selective Catalytic reduction) It is assumed, that increased oxidation of gaseous  $\text{Hg}^0$  will take place in comparison with actual condition without catalyser. Subsequently,  $\text{Hg}^{2+}$  can be trapped in existing desulphurization facilities. Implementation of catalytic reduction into flue gas mains and requested division of mercury is shown on Figure n.2.

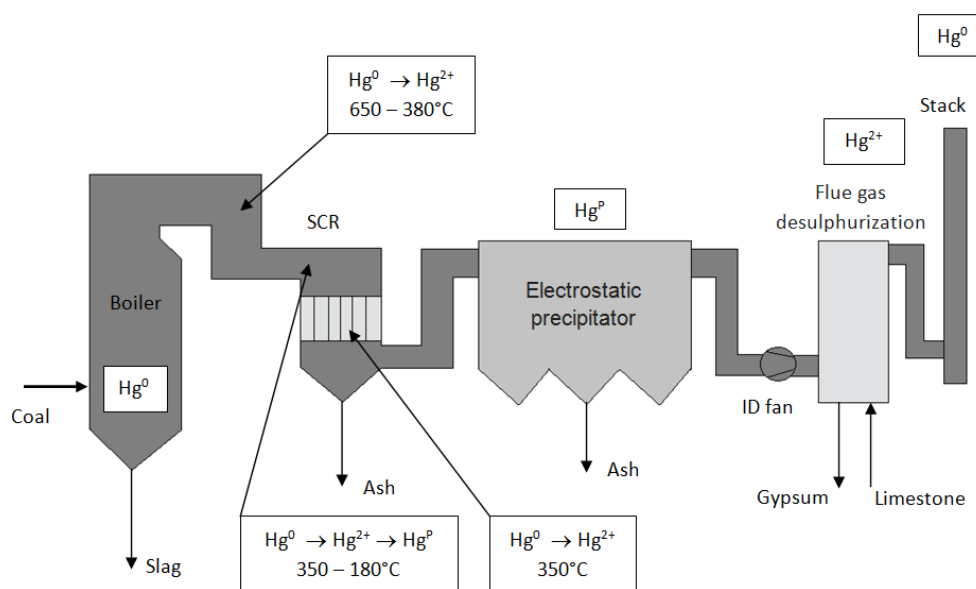


Figure 2. Scheme of Hg distribution in the flue gas using SCR for fulfillment of expected emission limits.

### Analysis of fuel composition

In 2013, around 40.6 mil tons<sup>1</sup> of lignite (in 2014 the prediction was 38.5 mil. tons of coal<sup>2</sup>) in the Czech Republic and the amount is almost completely used as energy fuel both in power plants or heat production facilities. Main areas of coal mining are situated in the area of Podkrušnohoří in Chebská plateau, Sokolovská plateau and North-Bohemian coal plateau.

Fuel selection for carrying out analyses in order to investigate mercury concentration was based on several criteria:

- coverage of wider spectrum of fossil fuels used in large and extra large combustion sources
- expected sufficient availability in the future, i.e. sufficient and reachable supplies
- real usability in the conditions of the Czech republic, especially with respect to transportation options.

### Lignite

Based on the criteria stated above, following types of lignite we selected after carrying out the analyses. 3 samples weighting 1 kg each were taken from each type of the lignite. Samples of the lignite were further analyzed in the Coal research department in Most.

- North-Bohemian coal plateau – Nástup Tušimice mine and Bílina mine  
Nástup Tušimice mine (DNT) – sample "Industrial mixture" - PS2  
Bílina mine (DB) - sample "Rough gravel" HP1, "Industrial mixture" PS1 a PS2
- Mostecká coal plateau  
Vršany mine - sample – sample "Industrial mixture" PS3
- Sokolovská coal plateau  
Jiří mine – sample DT - NS II

Analyses results are shown in the following Table II.

Table II Hg concentration in different types of lignite

Mine	Sample name	Fuel type	Wtr % mass.	Hg mg/kg dry.
Bílina mine	81887	HP1	27.43	0.157 ± 0.011
	81888	PS1	26.44	0.182 ± 0.013
	81889	PS2	24.42	0.200 ± 0.015
	81893	HP1	28.10	0.153 ± 0.011
	81894	HP1	27.30	0.176 ± 0.013
	81895	PS2	25.11	0.325 ± 0.024
	81896	PS2	25.49	0.259 ± 0.019
	81897	PS1	26.42	0.225 ± 0.016
	81898	PS1	27.62	0.158 ± 0.012
DNT	81899	PS2	28.95	0.233 ± 0.017
	81900	PS2	28.75	0.218 ± 0.016
	81901	PS2	29.66	0.256 ± 0.019
Jiří mine	81890	PS2	34.89	0.510 ± 0.040
	81891	PS2	34.05	0.358 ± 0.026
	81892	PS2	34.21	0.540 ± 0.040
Vršany	81902	PS3	26.19	0.192 ± 0.014
	81903	PS3	26.50	0.284 ± 0.021
	81904	PS3	25.98	0.256 ± 0.019

From the analyses above it follows, that Hg concentration is changing according mining area. According to power generation institute [ 1 ] in 2014 33.6 mil. tons of lignite was exploited (Bílina mine – 9.5 mil. tons/year, Nástup Tušimice mine – 12.0 mil. tons/year, Jiří mine – 6.1 mil. tons/year, Vršany mine – 6.00 mil. tons/year) and around 6.41 tons of mercury is released into air by its combustion. Mercury concentration is observed in the long term and its values are stated in the coal catalogue. Stability of mercury concentration in mined coal is obvious from these data. Some variations are caused by changing the mining bed. Result is obvious from the following figure, where analyzed mercury concentrations are compared with mercury concentration stated in available coal catalogues of given mining area.

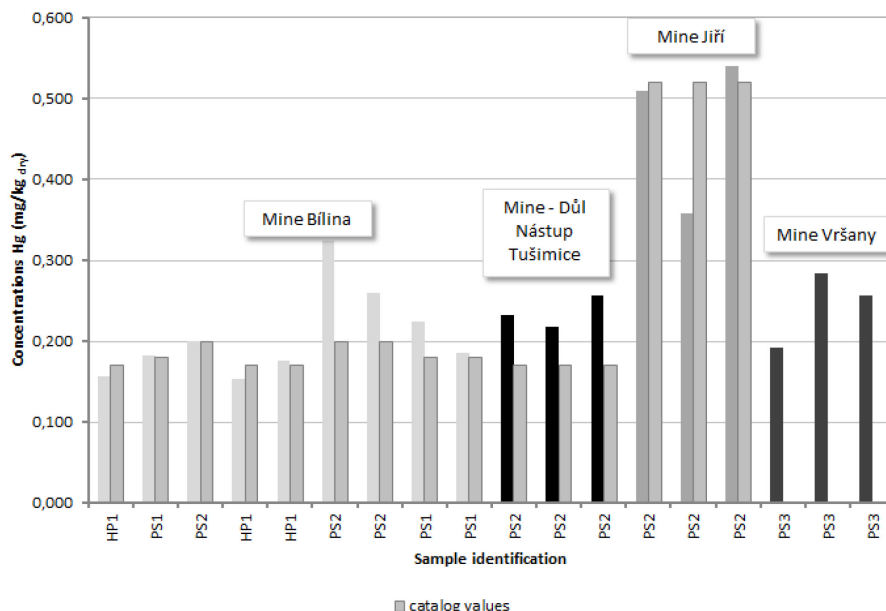


Figure 3. Comparison of cataloged Hg concentrations with analyzed concentrations in taken samples.

### Coal

Coal is mined in deep mines and in 2013 8.6 mil tons was exploited in the Czech republic. In Karviná mine 2.62 mil. tons was mine, in Darkov mine 2.65 mil. tons was mined and in ČSM mine 2.48 mil. tons was mined and in

Paskov 0.86 mil. ton was mined. Samples of coal were analyzed and Hg concentration was within range from 0,109 mg/kg<sub>dry matter</sub> to 0,152 mg/kg<sub>dry matter</sub>.

### Discussion of measures

For measurement design it is necessary to base them on balance calculations, which point to concentrations of observed samples with knowledge of usual combustion mode in chosen sources. Knowledge of these concentrations then give the notion of analytical methods and procedures of samples taking in single points of flue gas flows. They subsequently the baseline for mathematical models of processes involved in mercury distribution as a main observed element. Balance calculation is an essential part of relevant data set for facility design and for measurements for change in distribution of mercury along flue gas mains.

Balance compounds then must be set and these should be compliant with observed elements. This choice has to be harmonized with measurement equipment available, so we can carry out the balance calculation also based on the experimental data. Another essential part of balance calculation is a technology-balance scheme.

Let's assume a boiler combusting lignite as a source of energy. Dross is produced as part of ash products. Compliant with scheme on Figure 2., catalytic denitrification SCR unit is equipped in the flue gas mains, at temperatures 350 to 400°C. Flue gas then goes through recuperation exchanger (LUVVO), where part of the ash parts is trapped. Main part of the fine ash is separated in electric separator. Flue gas with main part of the fine ash eliminated are led into the process of wet desulphurization. Desulphurization is carried out using a calcite and energoplaster is formed. Technology-balance scheme is shown on the Figure 4 following. Single arrows denote the mass flow direction and each flow is denoted by a number.

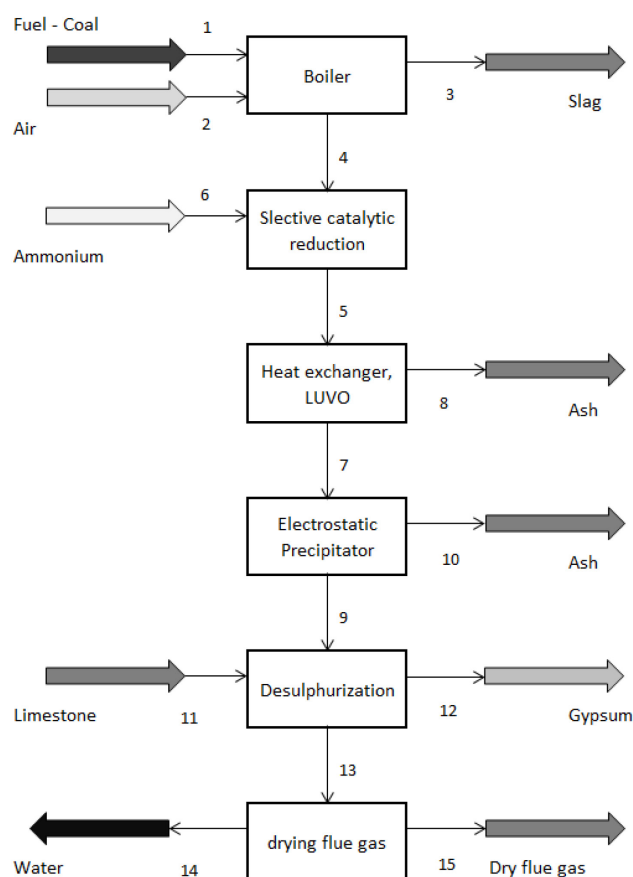


Figure 4. Technology-balance scheme of energetic unit with SCR denitrification and wet limestone purification. Calculation will be carried out with the assumption, that Hg concentration is equal to 0.5 mg/kg in dry fuel. Amount and composition of fuel entering the burning place is given by following table.

Table III Inlet - fuel

Flow no. 1	Fuel
Weight:	245.64 kg
element	X
carbon	0.2634
hydrogen:	0.0232
nitrogen:	0.0048
sulphur:	0.0199
oxygen:	0.0955
chlorine:	7.21E-05
fluorine:	1.19E-04
ash:	0.2829
mercury:	2.04E-07
water:	0.31

X column contains the mass ration of a given element. Along with fuel, air is taken to the combusting place. Amount and composition is shown in Table IV:

Table IV combustion air – inlet

Flow no. 2	combustion air
Weight:	1075.41 kg
element	X
nitrogen:	0.7479
oxygen:	0.2321
water:	0.02

Solution condition for compliance with emission limits for lignite for sources < 300 MW are emissions with limits of 2 $\mu$ g Hg/Nm<sup>3</sup>. Wet flue gas is formed as a result of the combustion. Analyses is given with respect to dry flue gas and therefore amount and composition of dry flue gas is given in Table V.

Table V Dry flue gas

Flow no. 15	Dry flue gas				
Weight:	1096.822	kg	801.8677	Nm <sup>3</sup>	
		X		kmol	
nitrogen:		0.7349	28.788		
oxygen:		0.0428	1.467	4.098	% vol.
ash:		1.00E-05			
mercury:		2.50E-09		3.42E+00	$\mu$ g/Nm <sup>3</sup>
CO <sub>2</sub> :		0.222	5.535		
CO:		1.29E-04	0.005054	176.463	mg/Nm <sup>3</sup>
SO <sub>2</sub> :		7.30E-05	0.001252	99.892	mg/Nm <sup>3</sup>
NO:		5.18E-05	0.001893	70.835	mg/Nm <sup>3</sup>

### Summary

Analyses of lignite has shown, that mercury concentration varies from 0.2 mg/kg up to do 0.5 mg/kg according to mining area and mine respectively. Mercury content in black coal is roughly half.

Based on mathematical model, necessary conditions for mercury redistribution were set with compliance with expected emission limits at the same time. Amount of mercury emitted into the air for combustion of brown air is at the level of 5.4% of total mercury entering the combusting place with the fuel. Remaining part is therefore necessary to be redistributed into outlet streams. It is mostly fine ash and plaster. Amount of dross and fine ash from heat exchanger (LUVA) is negligible in comparison with other streams. Based on calculations, assumed redistribution of mercury between streams is shown on the following chart:

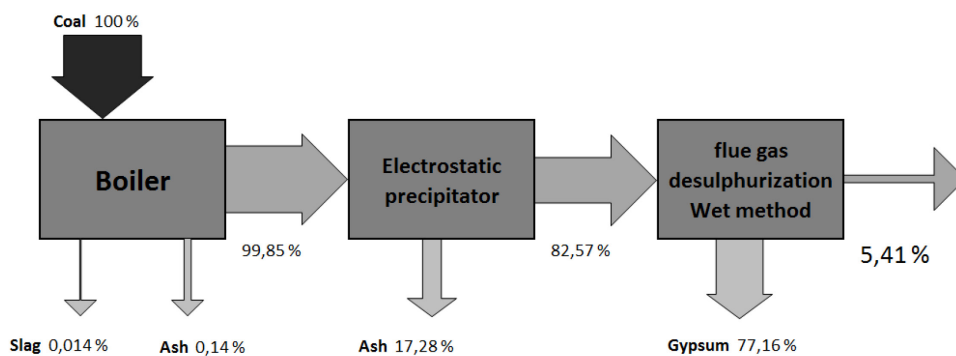


Figure 6. Assumed Hg distribution when using its oxidation on the catalyser for flue gas denitrification using ammonium.

Thermic and concentration conditions have to be found, when catalytic oxidation transforms the atomic mercury into easily separable compounds, especially in wet limestone purification.

#### Acknowledgment

*In this paper, results from solution of TAČR project no. TA04020723 were used.*

#### Literature

1. Energostat, power generation in the Czech Republic v ČR: information, data, comments, laws, <http://energostat.cz/>
2. M. Bedjanová, V. Jaroš, J. Ruml, INERGIN – institut energetických informací, Aktuální vývoj trhu s hnědým uhlím v ČR v kontextu energetických transakcí roku 2013, sektorová analýza, april 2013
3. L. Pelcl, Vupek-economy, s. r. o., Současný a budoucí trh tuhých paliv v ČR, 2011
4. Joint research center, Best Available Techniques (BAT) Reference Document for The Large Combustion Plants – Draft 1 (June 2013).

## NUMERICAL SIMULATION OF MIXED LAYER EVOLUTION CONSIDERING THE INFLUENCE OF BUOYANCY AND SHEAR PRODUCTION

**Duong V. M.**

*University of Chemistry and Technology Prague, Technicka 5, Praha 6 Dejvice, 16628, Czech Republic  
Duong.Van.Minh@vscht.cz*

### **Keywords**

Boundary layer growth, boundary layer modelling, mixed layer depth, mixing height, inversion layer height.

### **Introduction**

The height of the convective boundary layer (CBL) or mixed layer height is a key variable to characterize the dispersion potential of the lower troposphere. It determines the total volume of air available for the dispersion of passive pollutants, especially in numerical transport simulations of flow fields<sup>1</sup>. Mixing height plays an important role to determine the turbulence domain in which dispersion takes place or as a scaling parameter to describe the vertical profiles of CBL variables<sup>2</sup>. It involves in many predictive and diagnostic methods, particularly the measured and predicted concentrations of trace gases and aerosols. Data of mixing height is strongly required for both operational air quality monitoring and needed as a direct input to dispersion models.

Mixed layer height is not measured by standard meteorological practices and moreover it is often a rather unspecific parameter whose definition and estimation is not straightforward. As a result, the determination of mixing height is often ambiguous under realistic atmospheric conditions, even over relatively homogeneous terrain at specific sites and for limited time periods. Therefore, parameterizations are very widely developed to compute mixing height as well as other CBL variables from routinely available meteorological data<sup>3</sup>. However, there is a lack of appropriate consideration of moisture contents and shear term in the control of stability and the surface energy balance. These large changes in energy fluxes and temperature profile may cause the changes of mixed layer development.

The major purpose of this research is firstly better understanding of the sensitivity of the CBL evolution to the surface and entrainment variables, then secondly the evolution of mixed layer height in humid meteorology conditions using computational methods with consideration on moisture contents influence. Two mixed layer preprocessors are numerically analyzed to determine the daytime development of the convective boundary layer. Then, comparative analysis of mixed layer height simulations was conducted, in order to study the influence of shear term and moisture contents.

### **Mixed layer parameterization**

Most current mixed layer models are based on the considerations the CBL as a single bulk layer and hereby uses the Eulerian approach. In this approach, the CBL is considered as a box in which quantities are influenced by all the incoming and outgoing fluxes at all sides of the box. The box is closed, which implies that all sources and sinks have to be compensated and here is no energy lost. As an example one can consider heat: if there is more heat coming into the box than going out, the temperature in the box has to increase<sup>4</sup>.

The structure of CBL is therefore often represented by just two layers instead of four in common. The bulk layer incorporates the surface layer and the free atmosphere. The inversion layer is here simply a sharp discontinuity representing the difference between values in the bulk layer and the free atmosphere. This is called the zero-order jump approach of the CBL, in which quantities are nearly constant with height.

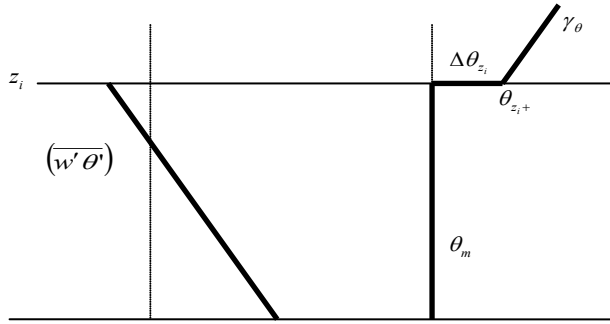


Figure 1. The zero-order jump approach of the mixed layer

The mixed layer model assumes a quasi steady state and horizontal homogeneity, no radiative or latent heating effects or any other sources of scalar quantities. Only the bottom and top of the box are considered as possible source or sink of quantities, thus only surface fluxes respectively entrainment fluxes play a role. However, where the surface fluxes in the mixed layer model are explicitly specified for the entire model simulation, the entrainment fluxes are not. These fluxes need to be resolved in the actual model simulation and they are only specified as an initial value at the start of the simulations.

Considering those assumptions, the mixed layer model can be studied numerically with the equations. More specifically, in the model the equation for the heating rate of temperature is:

$$\frac{\partial \theta_m}{\partial t} = \frac{(\overline{w'\theta'})_s - (\overline{w'\theta'})_e}{z_i} \quad (1)$$

where  $(\overline{w'\theta'})_s$  is the surface heat flux [ $\text{K.m.s}^{-1}$ ],  $(\overline{w'\theta'})_e$  is the entrainment heat flux (at the top of mixed layer) [ $\text{K.m.s}^{-1}$ ],  $\theta_m$  is the mixed layer potential temperature [K],  $z_i$  is the mixed layer height [m]. The tendency of the inversion jump  $\Delta\theta_{z_i}$  [K] is expressed as follow:

$$\frac{\partial \Delta\theta_{z_i}}{\partial t} = \frac{\partial \theta_{z_i+}}{\partial t} - \frac{\partial \theta_m}{\partial t} = \gamma_\theta \left( \frac{\partial z_i}{\partial t} - w_s \right) - \frac{\partial \theta_m}{\partial t} \quad (2)$$

where,  $\gamma_\theta$  is the temperature lapse rate [ $\text{K/m}$ ],  $z_i^+$  is the height [m] just above  $z_i$ ;  $w_s$  is the subsidence velocity which has a negative value [ $\text{m/s}$ ]. The entrainment heat flux,  $(\overline{w'\theta'})_e$ , is obtained by the Eq. 3:

$$(\overline{w'\theta'})_e = -\Delta\theta_{z_i} \left( \frac{\partial z_i}{\partial t} - w_s \right) \quad (3)$$

*The bulk mixed layer estimation (BMLM):*

An additional closure equation specified the entrainment flux as a certain fraction  $\beta_\theta$  of the surface flux<sup>5</sup> is:

$$(\overline{w'\theta'})_e = -\beta_\theta (\overline{w'\theta'})_s \quad (4)$$

This closure assumption requires the prescription of a constant value of  $\beta_\theta$ . We take the value of 0.4 is often used as an average value that represents a turbulent boundary layer mainly driven by free convection<sup>6</sup>.

*The boundary layer evolution simulation (BLES)*

This simple slab-type model is also based on the zero-order scheme<sup>7</sup>. The derivations are essentially based on a combination of 3 governing equations from the heat conservation budget mentioned above (Eq. 1, 2, 3) and the budget equation for the turbulent kinetic energy as follows<sup>8</sup>:

$$-(\overline{w'\theta'})_h = A(\overline{w'\theta'})_s + \frac{Bu_*^3}{(g/T)h} - \frac{Cu_*^2}{(g/T)h} \frac{dh}{dt} \quad (5)$$

where  $h$  is the mixed layer height (mentioned as  $z_i$  in the BMLM),  $g = 9.81 \text{ [m/s}^2\text{]}$  is the gravitational acceleration,  $(g/T)$  is the buoyancy parameter  $[\text{m/K}^{-1}\cdot\text{s}^{-2}]$ ,  $u_*$  is the friction velocity  $[\text{m/s}]$ . The usual value of  $A$  is  $0.2^9$  but recent experimental results from different climatic regions suggest a higher value of around  $0.4^{10}$ . The proposed value of  $B$  is 2.5, and the chosen value of  $C$  can be estimated approximately 8 recommended by Zilitinkevich<sup>11</sup> and Tennekes<sup>9</sup>.

### Numerical simulation

In this numerical experiment, the integration of time of equations begins at 07:00 UTC with total simulation time 36000 [s]. Table 1 summarizes the initial values for sensitivity analysis of several modified simulations in order to study the influence of moisture content in the development of the CBL.

Table I. Summary of input values for the control run of BMLM

RH [%]	Bowen ratio, $\beta$	$\theta_v$ [K]	$\overline{w'\theta'_v}$ [K.m.s <sup>-1</sup> ]	$q$ [g/kg]	$\overline{w'q'}$ [g/kg.m.s <sup>-1</sup> ]	max $z_i$ [m]	max $\Delta z_i$ [m]	$\Delta z_i$ [%]
45	0.954	296.60	0.272	08.91	0.12	1787	73	4.3
75	0.573	297.67	0.286	14.85	0.20	1835	121	7.1
95	0.452	298.38	0.296	18.81	0.25	1866	152	8.9

In combination of these equation sets, in which  $(\overline{w'\theta'_v})_s$  and  $w_s$  are explicitly specified as boundary conditions, we are left with four following unknowns:  $(\overline{w'\theta'_v})_s$ ,  $\Delta\theta_{z_i}$ ,  $\theta_m$ ,  $z_i$ . The used temperature lapse rate  $\gamma_\theta$  is 0.007 K/m, being somewhat higher than the value of  $\gamma_\theta = 0.005 \text{ K/m}$  recommended by Hanna and Chang (1992). During simulation with BLES, the constant value of  $A$  for the Eq. 5 is 0.4, which is equal to the value of  $\beta_\theta$  in Eq. 4. The friction velocity  $u_*$  is set to 0.05 m/s in order to neglect the shear effect presents by the second and third terms on the right-hand-side of Eq. 5.

The influence of moisture content in the daytime development of the CBL were numerically expressed with the replacements of  $\overline{w'\theta'_v}$  and  $\theta_v$  into the simulation steps, which leads to significant variations in the growth. In terms of the atmospheric water vapor mixing ratio ( $q$ , [ $\text{g of water vapor} \cdot \text{g of total air}^{-1}$ ]) consideration, we used the virtual potential temperature,  $\theta_v$ , can be written as the Eq. 6.

$$\theta_v = \theta \left[ \frac{1+1.61q}{1+q} \right] \cong \theta(1+0.61q) \quad (6)$$

The usual form for kinematics virtual potential temperature (buoyancy) flux,  $\overline{w'\theta'_v}$  is given as Eq.7<sup>12</sup>:

$$\overline{w'\theta'_v} \cong (\overline{w'\theta'}) [1+0.61\bar{q}] + 0.61\bar{\theta}(\overline{w'q'}) \quad (7)$$

The Bowen ratio,  $\beta$ , which is defined as the ratio of sensible to latent heat fluxes at the surface, is also an important calculation to account for the surface evaporation is expressed as:

$$\beta = \frac{Q_H}{Q_E} = \frac{c_p(\overline{w'\theta'})_s}{L_v(\overline{w'q'})_s} = \gamma \frac{(\overline{w'\theta'})_s}{(\overline{w'q'})_s} \quad (8)$$

where  $\gamma = 0.4 \text{ [(g}_{\text{water}}/\text{kg}_{\text{total air}})\cdot\text{K}^{-1}]$  is the psychrometric constant,  $Q_H$  and  $Q_E$  are the sensible and latent heat fluxes respectively  $[\text{W/m}^2]$ ,  $c_p = 1004.67 \text{ [J.kg}^{-1}\text{K}^{-1}]$  is the specific heat of dry air at constant pressure,  $L_v = 2.45 \times 10^6 \text{ [J.kg}^{-1}]$  is the latent heat of vaporization at 20°C. This approach indicates the surface energy budget and fluxes balance with the influence of evapotranspiration.

### Influence of moisture content

Development of mixing height simulated with the BMLM with two major options of with and without atmospheric water vapor mixing ratio  $[q, g_{\text{water vapour}} \cdot (g_{\text{total air}})^{-1}]$  allowed us to account for air density with effect of moisture content only (moist air is lighter). The hourly results were presented in order to make further comparison with hourly heights derived from actual measurements and those from reference models.

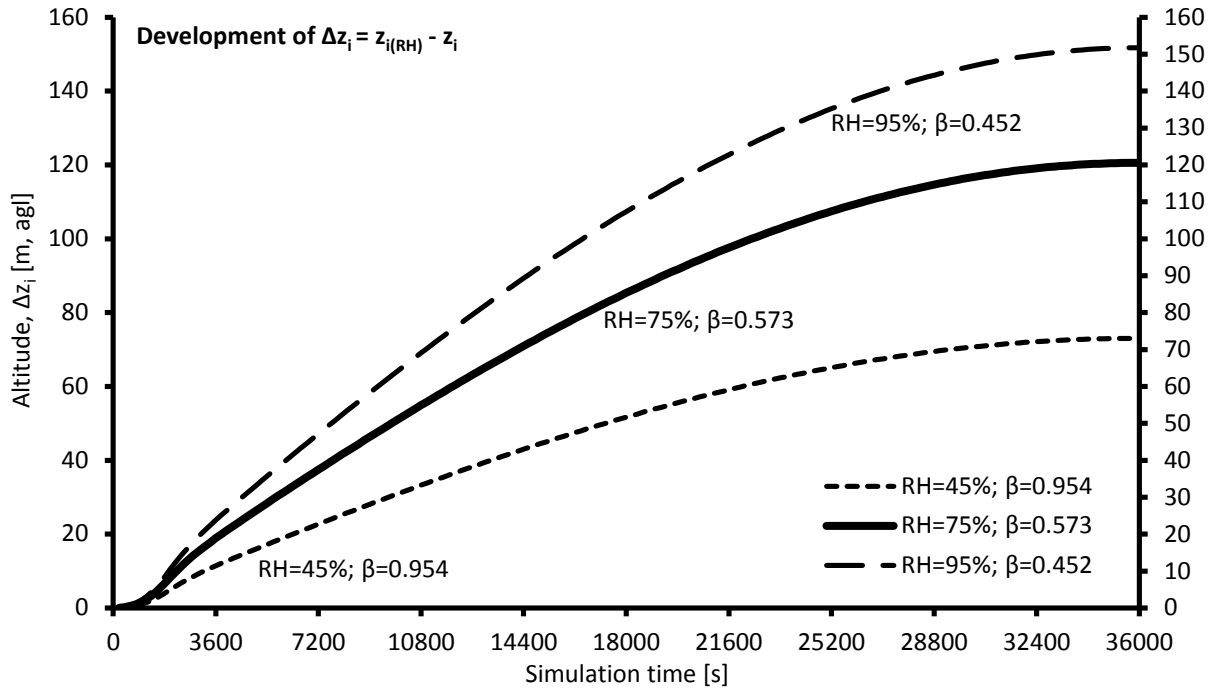


Figure 2. Average difference in daytime evolution of mixed layer height considering moisture content

Analysis from Fig. 2 shows that simulations with moisture content consideration give the average difference,  $\Delta z_i$ , between 120m ÷ 150m, in correlation with the average increasing of mixing heights between 7% ÷ 9%.

The Bowen ratio ranges from  $0.4 < \beta < 0.6$  over the moist surface where a large of energy goes into evapotranspiration in the humid condition. The values verified that surface evaporation plays an important role in convective mixing processes. However, attempts to use this approach need further research in details due to the fact that the  $\beta$  value usually varies with time, net radiation budget, and surface characteristic.

### Influence of shear contribution

In comparison between the BMLM and BLES runs, the derivations based on governing equations (Eq. 1, 2, 3) from the heat conservation budget are straightforward. The difference is caused by the use of additional closure equation specified the entrainment flux,  $(\overline{w'\theta'})_e$ , which is obtained by the Eq. 4 for the BMLM and the constant  $A = 0.4$  in the first term on the right hand side of Eq. 5 for the BLES<sup>12</sup>. An additional turbulence production is processed by the second and third terms which specify the role of mechanical turbulence.

The relative contribution to the growth of the mixed layer from mechanical and convective turbulence and spin-up term can be deduced from Eq. 9 in BLES<sup>7</sup>. On the left-hand-side, the first term accounts for the combined effect of mechanical and convective turbulence, and the second term is the Zilitinkevich correction term due to the spin-up effect which is important only when the mixed layer is shallow, typically less than a hundred meters<sup>7</sup>.

$$\left[ \frac{h^2}{(1+2A)h-2B\kappa L} + \frac{Cu_*^2 T}{\gamma_\theta g \{(1+A)h-B\kappa L\}} \right] \times \left( \frac{dh}{dt} - w_s \right) = \left( \frac{\overline{w'\theta'}_s}{\gamma_\theta} \right) \quad (9)$$

In the former case, initial geotropic wind is assumed to be constant with height and shear production occurs only at the surface with represent of friction velocity,  $u_*$  [m/s], which considers the relative amounts of surface mechanical production changes, and therefore enhance development pattern as shown in Fig. 3.

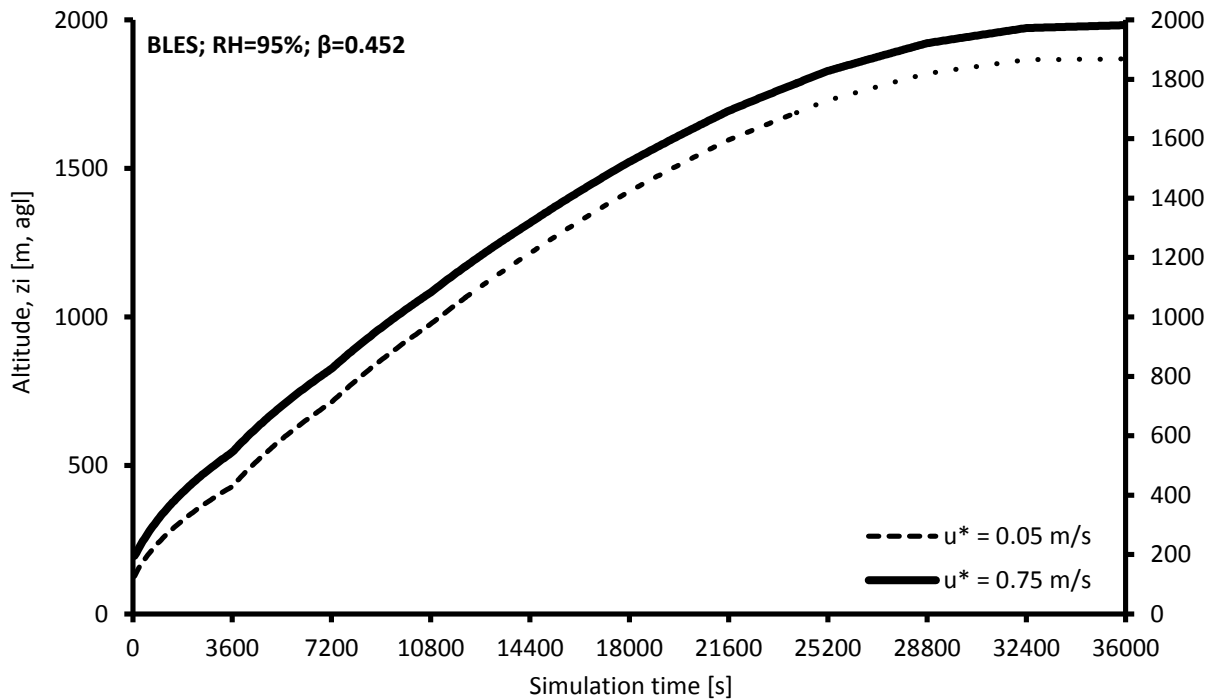


Figure 3. Daytime evolutions of mixed layer height considering mechanical production

Meanwhile, we considered the initial shear production occurs at the surface which physically can influence surface flux by using the constant value  $\beta_\theta = 0.25$  is suggested in the BMLM<sup>4</sup>. Shear production was also accounted at the entrainment zone with changes geotropic wind,  $u_g$  [m/s] and the suggested value of  $\beta_\theta = 0.4$ . The  $\beta_\theta$  ratio formulation contains parameterized terms is proposed and expressed as:

$$\beta_\theta = -\frac{(\overline{w'\theta'})_e}{(\overline{w'\theta'})_s} = C_F \left[ 1 + \eta^3 \left( \frac{u_*}{w_*} \right)^3 \right] \frac{1}{1 + C_T / Ri_t - C_M / Ri_{GS}} \quad (10)$$

where different constants have been proposed for  $A$ ,  $C_F$ ,  $C_T$ ,  $C_M$ ,  $\eta = 2$  when  $\eta^3 = A/C_F$ ,  $u_*$  and  $w_*$  are the velocity scales, the ratio  $u_*/w_* = 0.4$  is the relevant parameter in sheared convection,  $Ri_t$  and  $Ri_{GS}$  are the Richardson numbers<sup>4</sup>. During the additional shear contribution analysis, BMLM gives the  $\beta_\theta$  value change in time. Initial and surface input values for the control run of BMLM with shear contribution analysis as described in the Fig. 1. Additional information are the surface momentum flux  $(\overline{w'u'})_s = 0.5 \text{ m}^2/\text{s}^2$ ; the initial surface wind speed,  $u_s = 10 \text{ m/s}$ ; the geotropic wind speed,  $u_g = 10 \text{ m/s}$  and  $15 \text{ m/s}$  relatively.

#### Influence of the temperature jump at the inversion

Fig. 4 confirmed a pattern agreement with the theoretical evolution of convective mixed layer when maximum values reached  $1700 \text{ m} \div 1900 \text{ m}$ . Similar increasing trend of  $z_i$  simulated by 2 models were obtained between 08:00 and 17:00, however BLES gives higher values than the BMLM. Difference as a result of the initial growth rate during the first hour, from 07:00 to 08:00, when the morning radiation inversion occurs was  $140 \text{ m}$ .

The BMLM growth was delayed from 07:00 to 08:00 for heating of the air close to the ground with given initial temperature inversion jump  $\Delta\theta_{zi} = 0.45 \text{ K}$ , while the BLES approximates the value of  $\Delta\theta_{zi} = 0.21 \text{ K}$  by the analytical solution neglecting the influence of the initial conditions is suggested<sup>7</sup>:

$$\Delta\theta_{zi} = \frac{Ah - B\kappa L}{(1 + 2A)h - 2B\kappa L} \gamma h \quad (11)$$

where  $\kappa = 0.4$  is the von Karman constant,  $L$  is the Monin-Obukhov length,  $A$  and  $B$  are the parameterized constants mentioned above.

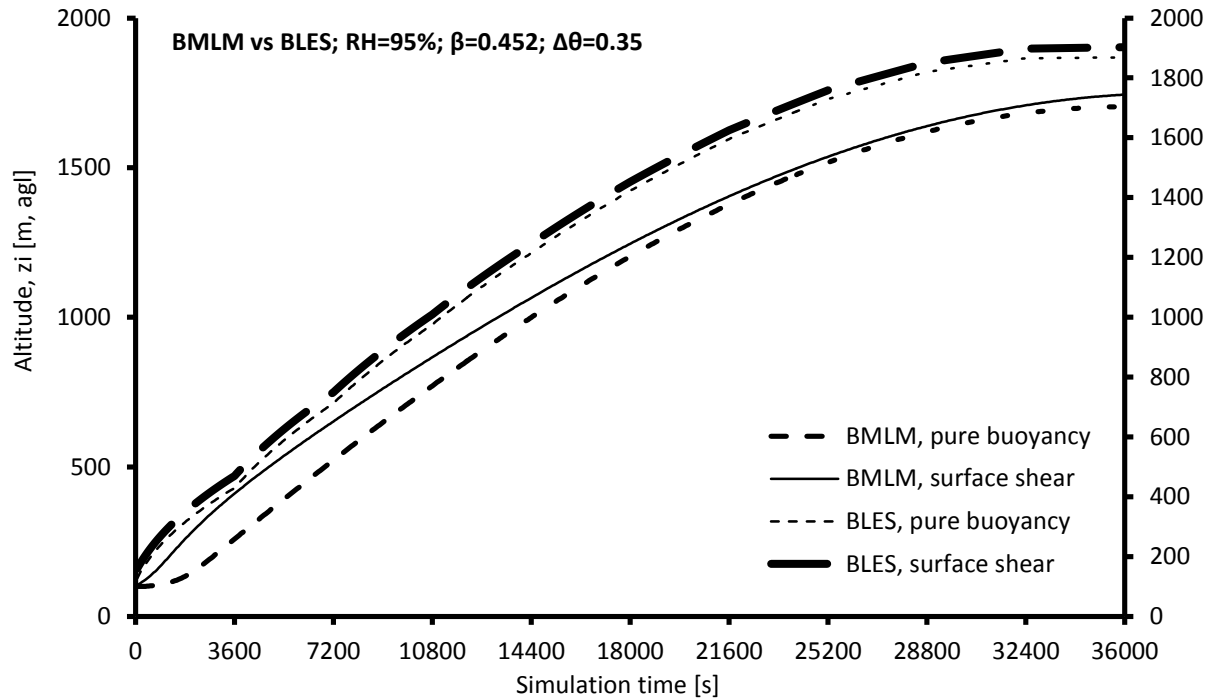


Figure 4. Daytime evolutions of  $z_i$  with different initial control options

Sensitivity analysis shows that the mixed layer height with shear production cases increases similarly in both models in comparison to the pure buoyancy cases. By comparing the simulations, the value given by BLES when the vertical wind profile only reproduces the shear at the surface, was higher than those simulated by the BMLM, even at which shear was also presented in the entrainment zone.

The occurrence of different growth during the first hour still strongly influences the mixed layer daytime development. Further sensitivity analysis and comparison with actual observations should be done for better understanding of the gap in determinations of initial  $\Delta\theta_{zi}$ , which effect to the mixed layer growth rate can be rewritten from Eq. 3:

$$\frac{\partial z_i}{\partial t} = \frac{-(\overline{w'\theta'})_e}{\Delta\theta_{zi}} + w_s \quad (12)$$

## Conclusion

Two mixed layer preprocessors were numerically analyzed to determine the daytime development of the convective boundary layer. Simulation results confirmed the theoretical evolution of convective mixing height, where daily maximum value of  $z_i$  reached approximately  $1700 \div 1900\text{m}$ . Influence of moisture content creates a significant change in daytime development, with an increasing of  $130\text{m} \div 150\text{m}$ . The range of analyzed Bowen ratio from  $0.4 < \beta < 0.6$  verified that surface evaporation plays an important role in convective mixing processes.

BLES generated higher values than the BMLM with the maximum difference,  $\Delta z_i$ , was about  $140\text{m}$ . Different developments started with the initial growth rate during the first hour due to the initial temperature jumps,  $\Delta\theta_{zi}$  when the morning inversion occurs. The difference was caused by the use of additional closure specified the entrainment flux,  $(\overline{w'\theta'})_e$ . Shear productions supported an increasing of  $z_i$  value comparing to the pure buoyancy cases. It is necessary to take the shear term into parameterization because that indicates the influence of turbulence kinetic energy in the entrainment zone. Besides that, the parameterized the fluxes ratio,  $\beta_\theta$ , should be proposed in order to improve the simulation results.

## Acknowledgment

*The report was supported by the University of Chemical Technology Prague . Authors also gratefully appreciate the Wageningen University and Research Center for providing the assistance and facilities.*

#### **Literature**

1. Vach M., Duong V. M.: Numerical modeling of flow fields and dispersion of passive pollutants in the vicinity of the Temelin Nuclear Power Plant; Journal of Environmental Modeling and Assessment; 16, 135-143 (2011).
2. Beyrich F., Gusten H., Sprung D., Weisensee U.: Comparative analysis of sodar and ozone profile measurements in a complex structured boundary layer and implications for mixing height estimation. Boundary Layer Meteorology 81, 1-9 ( 1996).
3. Beyrich F.: Mixing height estimation in the convective boundary layer using sodar data. Boundary Layer Meteorology 74, 1-18 (1995).
4. De Arellano J.V.-G.: Transport and transformation of chemical compounds in the atmosphere. Practical documents. Wageningen University and research center (2010).
5. Pino D., De Arellano J.V.-G., Duynkerke P. G.: The contribution of shear to the evolution of a convective boundary layer. Journal of the Atmospheric Sciences 60, 1913-1926 (2003).
6. De Arellano J.V.-G., Gioli B., Miglietta F., Jonker H.J.J., Baltink H.K., Hutjes R.W.A., and Holtslag A.A.M.: Entrainment process of carbon dioxide in the atmospheric boundary layer. Geophysical research 109, D18110 (2004).
7. Gryning S.E.: The height of the atmospheric boundary layer during unstable conditions. Riso-Report-1536 ., Riso National Laboratory, Denmark (2005).
8. Batchvarova E., Gryning S.E.: Applied model for the growth of the daytime mixed layer. Boundary Layer Meteorology 56, 261-274 (1991).
9. Tennekes H.: A model for the dynamics of the inversion above a convective boundary layer. Journal of the Atmospheric Sciences 30, 558-567 (1973).
10. Betts A.K.: FIFE atmospheric boundary layer budget methods. Journal of Geophysical Research 97, 18, 523-531 (1992).
11. Zilitinkevich S.S., Fedorovich E.E., Shabalova M.V.: Numerical model of a non steady atmospheric planetary boundary layer, based on similarity theory. Boundary Layer Meteorology 59, 387-411 (1992).
12. Stull R. B.: An Introduction to Boundary Layer Meteorology, Kluwer Academic Publishers., Norwell, Mass.
13. Gryning S.E., Nyren K.: Nomogram for the mixing height of the daytime mixed layer. Boundary Layer Meteorology 91, 307-322 (1999).

## LIFE CYCLE ASSESSMENT (LCA) METHOD IN NUCLEAR ENERGY FIELD: A CRITICAL OVERVIEW

Zakuciová K.<sup>1,2</sup>, Kočí V.<sup>1</sup>

<sup>1</sup>Research Centre Rez, 250 68, Husinec-Řež, Česká republika

<sup>2</sup>University of Chemistry and Technology, Technická 5, 166 28 Praha 6 – Dejvice, Česká republika  
Kristina.Zakuciova@cvrez.cz

### Introduction

Life Cycle Assessment (LCA) is considered as analytical tool which can perfectly described whole life cycle of the systems processes and evaluate GHG emissions. LCA is commonly used in different areas of energy sector. It is important method how to gain results and data which could show concrete potential environmental harm. LCA in nuclear field has been already used and described in nearly 300 papers and scientific journals. Documents about Life Cycle Inventories of different energy systems of different countries usually include assessment of oil, natural gas, coal, nuclear, hydro power, photovoltaic and wind power energy systems<sup>1,2</sup>. The main goal of LCA methodology for nuclear power production is to estimate the current GHG footprint of nuclear power based largely on the global average nuclear fuel cycle<sup>3</sup>. Nuclear energy production is based on two different cycles – either open fuel cycle or closed fuel cycle.

This paper is based on selected papers and documents which are critically assessing different LCA approaches in nuclear energy sector and trying to describe two parts essential for further LCA modelling:

Product system description and overall impact categories with indicators for nuclear power production

Basic elements for open and closed nuclear fuel cycle needed for LCA modelling

### LCA methodology overview for nuclear fuel cycle

Life cycle of the systems and products generally includes raw material acquisition and input materials production through product production, utilization and removal or recycling. Environmental impacts of product are evaluated on a basis of impact evaluation of material and energetic flows. Important contribution of LCA is in specification of environmental impact by so-called impact category. Impact category is the specific environmental problem as global warming, eutrophication, etc. Precise specification of environmental impacts by impact category helps to identify undesirable transferring of problem from place to place. It means transferring of problem from one category to another<sup>4</sup>.

LCA study is described by 4 phases:

1. Goal and scope definition
2. Inventory analysis
3. Impact assessment
4. Interpretation

The goal and scope of the LCA study include determination of functional unit, product system boundary, data quality requirements and data allocation. Inventory analysis requires modelling of products system and determination of environmental profile of product. Impact assessment means evaluation in impact categories. Interpretation includes identification of key findings, evaluation of LCA study, critical analysis, and suggestions for innovation of the product system<sup>4</sup>.

### Product System Description of open fuel and closed fuel cycle

LCA methodology requires knowledge of described product system. In a case of nuclear energy production it means description of nuclear fuel cycle which is showed below in a figure 1. The focus of the literature sources is on open fuel cycle (once through) because the reference LCA methods were made for currently operating NPP`s. Open fuel cycle requires uranium ore processing (mining, milling), conversion and enrichment of uranium and, at the end of the cycle, the final disposal of the spent fuel. All stages of open nuclear fuel cycle can be summarized into three main processes:

1. Upstream – Mining and Milling, Conversion, Enrichment, Fuel Fabrication;
2. Core (Operational phase) – Operation of NPP, Operation of Fuel Storage, Operation of Waste Repository, Construction and Decommissioning of facilities;
3. Downstream – Electricity distribution<sup>5,6</sup>.

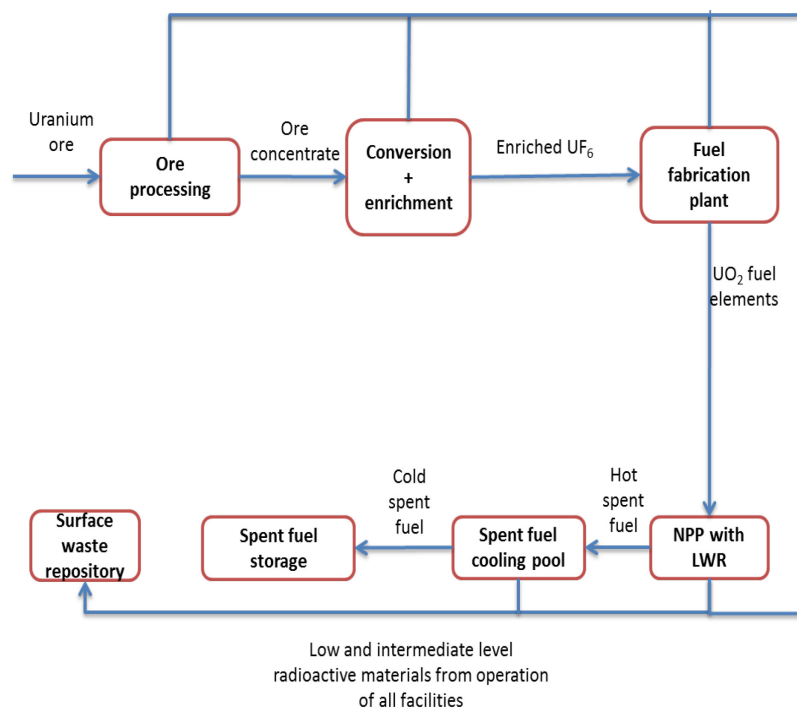


Fig. 1 Scheme of open fuel cycle

On the other hand, closed fuel cycle involves spent fuel reprocessing which means that the spent fuel from Light Water Reactors (LWR) instead of final disposal, is reprocessed to recover uranium and plutonium (about 95% of the spent fuel of LWRs), which are recycled for the fabrication of mixed oxide fuel (MOX) for use in the reactor. In the literature, the description of closed fuel cycle represents French twice-through nuclear fuel cycle<sup>7</sup>. According to Poisson<sup>7</sup> the processes of twice-through nuclear fuel cycle can be divided as:

1. Upstream processes- Mining and Milling, Conversion, Enrichment, Fuel Fabrication;
2. Core – Operational phase of reactor and services;
3. Downstream processes - Reprocessing of spent fuel, recycling of uranium and plutonium, and waste management<sup>8</sup>.

As it is mentioned above, the closed fuel cycle performance cannot be performed without open fuel cycle. Connecting part is the cold spent fuel from LWRs which is entering reprocessing plant where the separation of uranium, plutonium and minor actinides (MA) is performed. MOx (Mixed Oxide) fuel elements consisting of UO<sub>2</sub> and PuO<sub>2</sub> are the fuel elements which are entering Fast Reactor (FR). Cold spent fuel from FR is reprocessed in a second Reprocessing plant with different technology for spent MOx fuel then Reprocessing plant for fuel based on uranium oxides. From the second reprocessing plant, uranium and plutonium is coming back to the fuel fabrication plant for MOx fuel and minor actinides to the uranium, plutonium and minor actinides stock repository. Fission products and low and intermediate level radioactive materials from operation of the facilities is tend to be disposed in surface waste repository. This approach of disposal in surface waste repository can allow us to avoid concept of geological deep repository where required data are worldwide scarce and poor. The whole scheme of general closed fuel cycle performance with the main processes essential for LCA modelling is showed in the following figure.

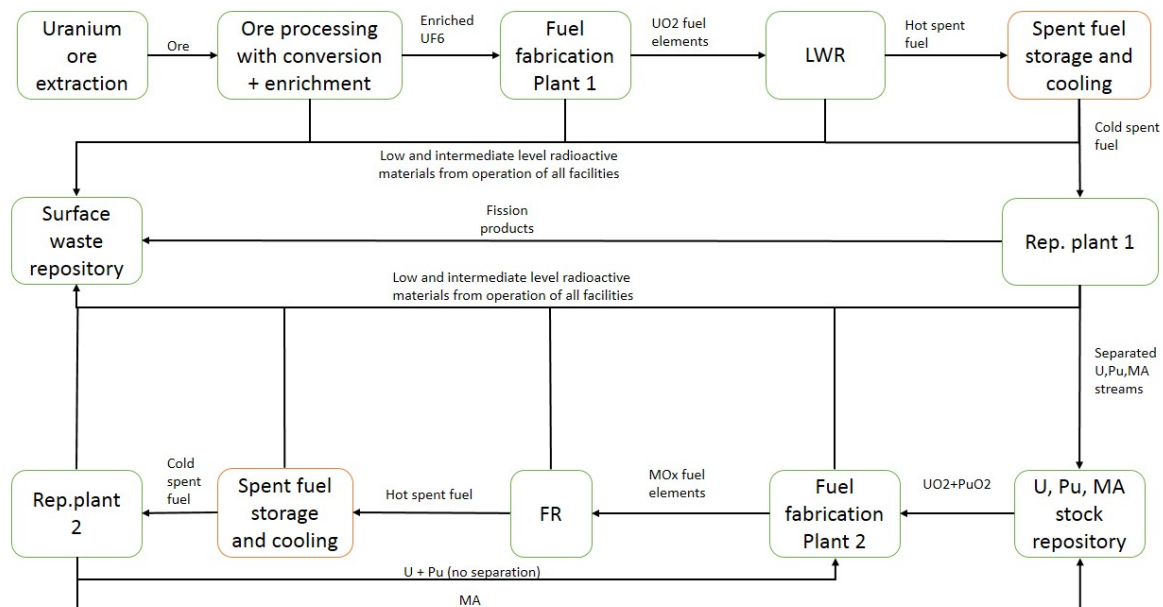


Fig. 2 System description of closed fuel cycle as a baseline for LCA modelling

LCA analysis requires a definition of the functional unit. Some literature sources Lenzen defines functional unit as the actual quantity in kWh of delivered electricity<sup>9</sup>. On the other hand, Norgate defines the functional unit as 1MWh of electricity produced by a 1GWe PWR nuclear reactor<sup>3</sup>. A functional unit should be connected also with a time range (distribution of electricity during the reference period)<sup>6</sup>. Definition of the systems boundaries is another starting point for LCA modelling. Defining system boundaries means the determination of processes which will be included in a product system. Usually, majority of literature sources consider the whole processes of the nuclear fuel cycle into the system boundaries<sup>4,5</sup>. Allocation is another important process in LCA. It describes a distribution of environmental impacts of one process among two or more products which are the outputs from this process<sup>4</sup>. Allocation for the nuclear fuel cycle is usually straightforward because most of the stages are mono-functional.

### Impact categories and indicators for nuclear energy production

An impact category is described as a specific problem in the environment which is caused by human activity. The choice of the impact categories is a very important step for LCA, showing how the study will be complex and objective. In general there are 10 basic impact categories for LCA in nuclear field:

Global warming, stratospheric ozone depletion, acidification, eutrophication, photochemical ozone creation, potential terrestrial toxicity, aquatic toxicity, human health, resource depletion and land use<sup>8</sup>.

For nuclear energy the following potential environmental impacts per functional unit shall be reported and divided into core, upstream and downstream modules:

- Emissions of GHG in CO<sub>2</sub> equivalents (kg(CO<sub>2</sub>eq)/MWh)
- Emissions of acidifying gases in SO<sub>2</sub> equivalents (kg(SO<sub>2</sub>eq)/MWh)
- Emissions of gases that contribute to the creation of ground level ozone expressed in C<sub>2</sub>H<sub>4</sub> equivalents (kg(C<sub>2</sub>H<sub>4</sub>eq)/MWh)
- Emission of substances to water contributing to oxygen depletion, expressed in PO<sub>4</sub><sup>3-</sup> equivalents (kg(PO<sub>4</sub><sup>3-</sup>eq)/MWh)<sup>10</sup>

There are also 3 basic categories monitored for radioactive impact:

- The solid radioactive waste production (kg/MWh or dm<sup>3</sup>/MWh)
- Gaseous emissions of radioactive isotopes in kBq, at a minimum C-14, Rn-222 and Kr-85 (kBq/MWh)
- Radioactive water emissions: radium, tritium, mixed nuclides and actinides (kBq/MWh)

Radioactive gaseous releases can be divided in four categories: radon (Rn-222, Rn-226), other noble gases (Ar, Kr, Xe), non-noble gases (H-3, C-14) and aerosols. Radioactive water emissions are distributed also into four categories: radium, tritium, mixed nuclides and actinides<sup>11</sup>. According to the figure 2, reprocessing plants are dealing with the fission products and minor actinides production. Fission products are generally considered as a waste and minor actinides should be reprocessed.

### Defining basic elements for LCA methodology for open and closed fuel cycle

LCA methodology required description of basic units and flows to be able to define the model. For comparative reasons functional units have to be the same. In a case of nuclear energy production it means production of 1MWh of electricity produced by a 1GWe nuclear reactor during the reference year. After defining the functional unit, it has to be quantified the amount of product needed to fulfill this function. The result of this quantification is the reference flow. System boundaries should be defined according to the defined function of the system. Functional unit defines the system boundaries in open fuel cycle from uranium mining and milling till the utilization of nuclear fuel in the reactor. The type of the reactor will be selected according to the available data for LCA software performance (usually Light Water Reactor – LWR or Boiled Water Reactor- BWR). At first, system boundaries of closed fuel cycle will be defined separately from open fuel cycle, even though these two are connected. It means, spent fuel from LWRs will be considered as the resource in other words elementary flow. Spent fuel in FR is utilized and again reprocessed for the FRs utilization. Allocation in the open fuel cycle is essential for the uranium ore processing. When the uranium ore consists of other metals than uranium, allocation of the mine's environmental impact is based on market prices of the metals<sup>12</sup>. On the other hand, in the closed fuel cycle it can be assumed that reprocessing of spent fuel will be defined as closed loop of recycling which is the one of the three cases of allocation utilization<sup>3</sup>.

Speaking about the phases of the specific processes which should be involved into modeling, the operation and construction of the facilities seem to lead into significant contribution to environmental burden. For radioactive waste management we are counting with surface waste repository. From the LCA modeling point of view, it is not essential to include deep geological repository for the final radioactive waste disposal. The main problem is lack of data and robustness of the system. Impact categories which need to be evaluated will be preliminary the same as is noted in different literature sources.

The interesting part is to point out technological differences between comparative nuclear systems which can result in different categories and amounts of the particular indicators which define impact categories.

Regarding open fuel cycle, several literature sources consider the enrichment technology and uranium ore grade as the main factors which can significantly change environmental footprint in nuclear energy production. Norgate<sup>4</sup> in his study shows the fact that as the grade of the uranium ore mined for falls, a greater amount of energy and other material inputs are required in the mining and milling stage and this will cause an increase of the GHG footprint of nuclear power<sup>4</sup>. Nian states that enrichment technology using gaseous diffusion technology captures more than 80% of the overall upstream energy inputs<sup>13</sup>. Storm and Smith's and also Hondo's studies show that emissions from operational and construction phase of the Life Cycle of the open fuel cycle corresponds to a share of 80-90 %<sup>3,14</sup>. Operations of nuclear reactors (usually LWRs) for open fuel cycle contribute to the production of low and intermediate active radioactive waste.

Closed fuel cycle should be evaluated from the storage of the spent fuel from LWRs where the fuel is cooling down and stored for further reprocessing. It is assumed there won't be any significant environmental burden from operational point of view. Construction phase of spent fuel cooling storage can contribute to GHG emissions. The reprocessing plant for U, Pu separation can result into different kind of GHG emissions but mainly in a construction phase. Regarding the reprocessing, plant will contribute to the radioactive waste production. MOx fuel fabrication facility uses dioxides of plutonium and uranium. Again construction is assumed as the greatest contribution to the GHG emissions. Because of the processing of radioactive material it is assumed of radioactive waste production. Fast reactors construction and operation will also result into GHG emissions as well as radioactive waste. These all will highly depend on the type of the reactors, type of moderator, cooling substances and purification systems.

### Results and discussion

The main goal of the LCA method is to compare two or more systems and technologies and show up the way how to improve parts of the systems to decrease or erase certain environmental burden. Definition of the functional unit of compared systems has to be the same. In our case it means that the functional unit for closed fuel cycle will be the same as for open fuel cycle, it means production of 1MWh of electricity produced by a 1GWe nuclear reactor during the reference year. The reference flow has to fulfill the functional unit. In our case it will be:

- For the open fuel cycle – amount of uranium (mass) required for production of 1MWh
- For the closed fuel cycle – amount of spent fuel (mass) required for production of 1 MWh

System boundaries of the open and closed fuel cycle will be clearly separated. This will simplify the modelling for both cycles and enable to clearly see the differences in environmental footprint of both systems. Then, it will be much simpler to connect these two systems and optimize the model. Proposed system boundary is not counting with surface waste repository. Surface waste repository is the part of waste

management which is different part of the systems boundaries. We are focused only on the production of the fuel and utilization for the energy production. Regarding, surface waste repository, allocation process could be assumed for the open fuel cycle in a process of uranium ore processing and for the closed fuel cycle in the phase of reprocessing. But it is highly possible that closed fuel cycle will define allocation in more processes or in totally different processes. This will be shown by actual modelling of the system. The most robust part of LCA method is to understand and compare both technologies. For both systems, operation and construction seem to be the most contributing phases to environmental footprint.

Operation of reactors in open fuel cycle results into production of radioactive waste, in particular:

- low and intermediate level radioactive waste in a form of concentrates, sorbents, spent ion exchange resins, active corrosion products, radioactive liquid effluents of tritium and C-14, fission products and actinides;
- high level radioactive waste in a form of spent fuel

The reason for the high share of environmental burden for uranium ore processing are following:

- High water consumption
- High land occupation or land use
- Solid waste from the milling process
- High SO<sub>2</sub> and NO<sub>x</sub> emissions from uranium extraction process
- Radioactive tailings from mining and milling<sup>12</sup>

Conversion and enrichment processes contribute to the high environmental footprint by:

- Very high energy consumption
- Potential environmental impact by tributyl phosphate, NO<sub>x</sub> effluents and heavy metals
- Release of depleted UF<sub>6</sub> and hydrofluoric acid

Spent fuel storage and cooling system as a starting point for LCA of closed fuel cycle won't represent environmental footprint because the quantity of water is large enough and evaporation gradual enough for a temporary disruption of the cooling not to pose any danger<sup>12</sup>.

Reprocessing plants environmental footprint will be dependent highly on a choice of the reprocessing process. Actinides and fission products from reprocessing are considered as the high level radioactive waste. Separated plutonium is a potential proliferation risk, and the minor actinides remain in the separated waste, which means that its radioactivity is longer-lived than if it comprised fission products only<sup>15</sup>.

Fast Reactors contribution into environmental footprint and mainly to radioactive waste production will highly depend on the choice of the technology of reactors systems and their cooling. For instance, Lead-cooled Fast Reactors as a representative of Generation IV reactors can result into Polonium effluents which are highly radiotoxic. Purification systems for lead are also required and therefore different kinds of anti-corrosive materials for construction of the reactor.

MOx fuel fabrication plant needs to be studied in a detail in a sense of all inputs, outputs and waste coming from operational phase. One of the biggest advantages for the fast reactor is that spent fuel is no longer considered as a high level active waste in a sense of LCA process because it is again used and reprocessed. That means decrease of environmental burden for closed fuel cycle. Further reprocessing and storage will have some impact but the energy and land use as well as fossil fuel utilization will decrease because of no separate mining and ore processing.

## Conclusion

LCA method for the open fuel cycle is well defined in many documents and literature reviews. That is the main reason that overall consideration of environmental aspects can be clearly discussed. The hardest part for LCA is to gain relevant and specific data, mainly for nuclear industry. Utilization of data from publicly available sources can be also used for LCA modeling of open fuel cycle.

Closed fuel cycle is the subject of the further detailed LCA analyses. It is clear that for LCA purposes whole processes from storage and cooling of spent fuel till second reprocessing of spent fuel coming from FRs need to be modelled. That will depend on the choice of the specific systems and technologies which will be essential for further fuel utilization in the specific fast reactor. LCA consideration of closed fuel cycle will highly depend on a choice of 3 basic systems:

- Reprocessing technology
- MOx fuel fabrication process
- Fast Reactor systems

The fast reactor systems seem to be promising technology. One of the main facts is, that closed fuel cycle can save low cost uranium source for 10 000 years which leads to no need of permanently committed land. Closed

fuel cycle also promises efficient spent fuel reprocessing and reducing of final radioactive waste. On the other hand, there are many technical issues which are subjects of the further research which will show the way for the environmental footprint and optimization of the systems.

### **Acknowledgement**

*This work has been supported by the SUSEN Project CZ.1.05/2.1.00/03.0108 realized in the framework of the European Regional Development Fund (ERDF). Authors would also like to express the greatest thanks to Giacomo Grasso (ENEA) for professional guidance and providing information on reactors technology and associated fuel cycle*

### **Literature**

1. Hondo, H.: Life cycle GHG emission analysis of power generation systems: Japanese case. *Energy* 30, 2042 (2005).
2. Dones R., Bauer C., Bolliger R., Burger B., Faist Emmenegger M., Frischknecht R., Heck T., Jungbluth N., Röder A., Tuchschnid M.: Life Cycle Inventories of Energy Systems: Results for Current Systems in Switzerland and other UCTE Countries. *Ecoinvent report No. 5*. Paul Scherrer Institut Villigen, Swiss Centre for Life Cycle Inventories, Dübendorf, 2007.
3. Norgate, T.: The impact of uranium ore grade on the greenhouse gas footprint of nuclear power. *J. Cleaner Prod.* 84, 360.
4. Kočí, V. : Environmentální dopady: Posuzování životního cyklu, p. 131, VŠCHT, Praha 2013.
5. Vattenfall AB.: Certified Environmental Product Declaration EPD® of Electricity from Ringhals Nuclear Power Plant. Group 171 – Electrical Energy, Germany, 2014.
6. EDF Energy Nuclear generation Ltd.: Environmental Product Declaration of electricity from Sizewell B nuclear power station No.4, Gloucester, 2014.
7. Poinssot, C.: Assessment of the environmental footprint of nuclear energy systems. Comparison between closed and open fuel cycles. *Energy* 69, 199 (2014).
8. EDP Sciences: Nuclear Fuel Cycle 2013. <<http://www.laradioactivite.com/en/site/pages/FuelCycle.htm>>
9. Lenzen, M.: Life cycle energy and greenhouse gas emissions of nuclear energy: A review. *Energy Convers.manage.* 49, 2178 (2008).
10. Weisser, D.: A guide to life-cycle greenhouse gas (GHG) emissions from electricity supply technology. *Energy*, 32, 9 (2007).
11. Sovacool, B. K.: Valuing the greenhouse gas emissions from nuclear power: A critical survey. *Energy Policy* 36, 2950 (2008).
12. EPD International AB: Improving Swiss energy generation. Sweden, 2014. <<http://www.environdec.com/en/Articles/EPD/XXXX/#.VTdZkpMt7Uk>>
13. Voorspools, K. R. : Energy content and indirect greenhouse gas emissions embedded in 'emission-free' power plants: results for the Low Countries. *Appl. Energy* 67, 307 (2000).
14. Storm van Leeuwen J W., Smith Ph., Nuclear power - the energy balance, Ceedata, Chaam (Netherlands), 2008.
15. World Nuclear Association: Processing of used Nuclear fuel, 2015. <<http://www.world-nuclear.org/info/Nuclear-Fuel-Cycle/Fuel-Recycling/Processing-of-Used-Nuclear-Fuel>>

## THE ROLE OF ADDITIVES IN HYDRODEHALOGENATION OF HALOGENATED ANILINES USING Al-Ni ALLOY

**Weidlich T.**<sup>1</sup>, Opršal J.<sup>1</sup>, Beneš L.<sup>2</sup>, Vlček M.<sup>2</sup>

<sup>1</sup>*Institute of Environmental and Chemical Engineering, Faculty of Chemical Engineering, University of Pardubice, Pardubice, Czech Republic*

<sup>2</sup>*Joint Laboratory of Solid State Chemistry, Faculty of Chemical Engineering, University of Pardubice, Pardubice, Czech Republic*

tomas.weidlich@upce.cz

Halogenoanilines, being important intermediates in the production of a very wide range of synthetic organic chemicals including phenylurea herbicides, such as Monuron (4-chloroaniline, 4-CAN, as the intermediate), Metobromuron (4-bromoaniline, 4-BAN), Diuron, Linuron or Neburon (3,4-dichloroaniline, 3,4-DCA) or fungicide Vinclozolin (3,5-dichloroaniline, 3,5-DCA), antibacterial agent Chlorohexidine, pharmaceuticals such as the antidepressant Aripiprazole (2,3-dichloroaniline, 2,3-DCA), non-steroidal anti-inflammatory drug Diclofenac (2,6-dichloroaniline, 2,6-DCA), kinase inhibitors and immunosuppressants (2-chloro-5-methoxyaniline), anticancer drug Gefitinib (3-chloro-4-fluoroaniline, 3-Cl-4-FAN), dyes and pigments (2,5-dichloroaniline, 2,5-DCA) are common water pollutants. Halogenated anilines are toxic compounds and their water solubility depends on the type, position and number of the halogen substituents on the aromatic ring<sup>1</sup>.

In addition, halogenated anilines are much less biodegradable than aniline<sup>2</sup>, which increases their environmental impact. Therefore, a rapid and simple wastewater treatment removing XAN's is urgently required at present.

Various methods have been reported for the chemical degradation of halogenoanilines and their derivatives<sup>3-10</sup>. Methods based on chemical or photochemical oxidation are widely tested for their effective treatment<sup>3-7</sup>.

However, the oxidation techniques are often accompanied by the formation of stable and very toxic halogenated by-products like of polychlorinated dibenzodioxines and dibenzofuranes (PCDD/Fs) and similar heterocyclic compounds<sup>6</sup>.

However, they are known very effective methods for quantitative hydrodehalogenation of some Ar-X compounds without risk of polychlorinated dibenzo-*p*-dioxines and dibenzofuranes (PCDD/Fs) formation (reduction conditions, temperature less than 100°C, Fig. 1) using catalytic hydrogenation over special types of hydrogenation catalysts for destruction of chlorinated anilines in aqueous solution<sup>8-10</sup>. The catalytic hydrogenation method, however, often requires expensive apparatus for high-pressure operations.

A few reduction methods at ambient pressure for hydrodehalogenation halogenated anilines caused by and their low valent compounds in the presence of noble metals<sup>11</sup> by transfer hydrodehalogenation using 2-propanol in the presence of Pd or Rh catalysts<sup>12</sup>.

Recently, we described studies focused on the action of commercially available aluminium alloys (Raney Al-Ni alloy and Devarda's Al-Cu-Zn alloy) for the rapid and quantitative hydrodehalogenation of halogenated anilines in alkaline aqueous solution even at room temperature<sup>13-15</sup>. Similarly, we tested Arnd alloy and duralumin as effective dehalogenation agents in many cases. As we often observed, the Devarda's alloy shows interesting selectivity in dehalogenation of halogenated anilines. Both Devarda's and Raney Al-Ni alloys are cheap and easy to handle. In addition, we proved that using substoichiometric quantities of both Al-Ni and Devarda's alloys together with aluminium as the reductant, at least debromination proceeds effectively.

The aim of this report is to describe the application of Raney Al-Ni alloy to dehalogenation of various industrially important halogenated anilines in alkaline aqueous solutions at room temperature with the emphasis put on elaboration of a method short enough and suitable for decentralised treatment of wastewaters contaminated with XAN's and/or for ex-situ decontamination of ground water.

The effects of the amount of base, the amount of the Raney Al-Ni alloy and the co-action of different reductants used for the dehalogenation have been investigated under various conditions using 0.01 M aqueous solution of 3-chloroaniline (3-CAN) and 4-chloroaniline (4-CAN) as the substrates (Tables I and II).

The reaction is selective, i.e. only dehalogenation takes place, aniline being the only product detected (verified using <sup>1</sup>H NMR and GC-MS spectroscopy). The dechlorination of 3-CAN in alkaline solutions other than aq. NaOH was investigated. Aniline was obtained selectively with complete conversion in KOH, K<sub>2</sub>CO<sub>3</sub> or in Na<sub>2</sub>CO<sub>3</sub> aqueous solutions.

Table I

Dechlorination of 3-CAN<sup>a</sup> under various conditions

Entry	Reducing agent (mmol of Al)	Quantity of base	Time	Conversion to aniline by <sup>1</sup> H NMR
1	540 mg Al-Ni (10)	2 g (50 mmol) NaOH	17 h	100 %
2	270 mg Al-Ni (5)	1 g (25 mmol) NaOH	17 h	100 %
3	270 mg Al-Ni (5)	1.4 g (25 mmol) KOH	17 h	100 %
4	270 mg Al-Ni (5)	2.1 g (20 mmol) Na <sub>2</sub> CO <sub>3</sub>	17 h	100 %
5	270 mg Al-Ni (5)	2.76 g (20 mmol) K <sub>2</sub> CO <sub>3</sub>	17 h	100 %
6	270 mg Al-Ni (5)	1 g (25 mmol) NaOH	4 h	100 %
7	270 mg Al-Ni (5)	0.8 g (20 mmol) NaOH	4 h	100 %
8	135 mg Al-Ni (2.5)	1 g (25 mmol) NaOH	4 h	93 %
9	270 mg Al-Ni (5)	0.6 g (15 mmol) NaOH	4 h	81 %
10	270 mg Al-Ni (5)	0.8 g (20 mmol) NaOH	2 h	89 %

<sup>a</sup> 100 ml 0.01 M (1 mmol) aqueous solution of 3-CAN, 500 rpm, 25 °C

In subsequent experiments, NaOH was used as the most common and cheap strong base. When using NaOH solution, the dehalogenation was found to be finished after 4 h when 5 equivalents of Al in the form of Al-Ni alloy and 20 equivalents of NaOH were used and the reaction was performed at room temperature (Table I, Entries 7-8).

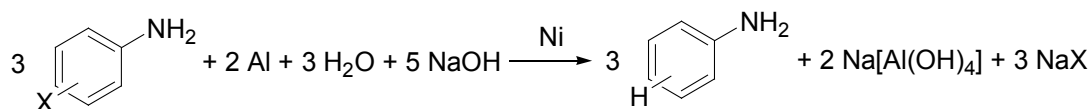


Figure 2. Scheme of the dehalogenation reaction of XAN's using Al-Ni alloy in alkaline aqueous solution

When the amount of Al-Ni alloy was reduced (e.g., to 2.5 eq.), 7 mol. % of 4-CAN remained unchanged (NMR ratio). Similarly, when the quantity of NaOH was decreased (to 3 equivalents), the dechlorination became sluggish and 19 % of 4-CAN remained unchanged (NMR ratio). Moreover, alloys and metals, such as Al, Cu-Sn, Cu-Zn and Al-Cu-Zn (Devarda's alloy) were tested for the dehalogenation of 4-CAN using prolonged reaction time for investigation of the role of Al and Ni in Al-Ni alloy (Table II).

Table II

Dechlorination of 3- and 4-CAN using various reductants after 17 h of vigorous stirring at room temperature<sup>a, 16</sup>

Entry	Reducing agent	Quantity of base	Conversion of 3-CAN to aniline	Conversion of 4- CAN to aniline
1	540 mg Al powder (20 mmol)	4 g (100 mmol) NaOH	4 %	0 %
2	1.8 g of Devarda's alloy (1.4 mmol Zn and 30 mmol Al)	6 g (150 mmol) NaOH	100 %	3 %
3	2.2g Cu-Zn (70/30) (10 mmol Zn)	2 g (50 mmol) NaOH	0 %	0 %
4	1.84g H <sub>2</sub> CuSn (10 mmol Sn)	2 g (50 mmol) NaOH	0 %	0 %
5	0.11 g Al-Ni (2 mmol Al)	2 g (50 mmol) KOH	49 %	42.2 %
6	0.11 g Al-Ni (2 mmol Al) + 0.33 g of Zn powder (5 mmol)	2 g (50 mmol) NaOH	81 %	59 %
7	0.11 g Al-Ni (2 mmol Al) + 135 mg Al powder (5 mmol)	2 g (50 mmol) NaOH	100 %	100 %
8	0.11 g Al-Ni (2 mmol Al) + 100 mmol of glucose	2 g (50 mmol) NaOH	100 %	48.9 %
9	270 mg Al-Ni (5 mmol Al)	1 g (25 mmol) NaOH	100 %	100 %
10 <sup>b</sup>	Ni (cat.) + H <sub>2</sub> (balloon)	no base was used	23 %	11 %

<sup>a</sup> NaOH dissolved in 100 mL water was added dropwise to 100 mL 0.01 M aqueous solution of 4-CAN within 1 hour<sup>b</sup> Raney Ni obtained by decantation after dehalogenation (entry 9)

In the presence of aluminium dust alone, dechlorination did not take place, and 4-CAN was recovered. However, when aluminium or zinc dust was employed in the presence of low quantity of Al-Ni alloy, different

results were obtained. Application of Zn dust in the presence of small amount of Al-Ni alloy leads to dehalogenation with 59% conversion (for comparison: the same amount of Al-Ni alloy without reducing agent leads to dehalogenation of 42.2 % 4-CAN or 49 % 3-CAN) (Table 2, entries 5-6). Under the same reaction conditions and with the use of Al dust, the conversion of dehalogenation reaction is 100 %. Replacing of non-noble metals as the hydrogen source by hydrazine, which is used for transfer hydrogenation, leads to 4-CAN conversion which is only by 6.7 % higher than that achieved with Al-Ni alloy without reducing agent (Table 2, entries 5, 7-8). In order to develop a reducing system with Ni catalysis, the dechlorination of 4-CAN was tested using gaseous H<sub>2</sub> as reducing agent in the presence of Raney nickel from Al-Ni alloy (Table 2, entries 9, 10). However, the dehalogenation was found to be very slow (11 % of aniline after 17 h). With Devarda's alloy, the reductive dechlorination of 4-CAN hardly occurred at all. In the presence of brass (Cu-Zn) or bronze (Cu-Sn), the dechlorination did not proceed. The results presented show that nickel is an efficient catalyst of the dehalogenation. The experiments also confirm that Al is not only a source of hydrogen but in the presence of nickel its acts itself as a reducing agent<sup>14-16</sup>. Among the tested reduction agents, we also tested glucose, which (as other aldoses) is well-known by its reduction properties. And it was just glucose, which gave very interesting results in the dehalogenation experiments performed with industrially used halogenated anilines even at RT, see Table 3. The experiments with the use of glucose as additive in the medium of 10 mM aqueous solution of 3-CAN in 1% or 0.5% NaOH solution showed that the charge of reducing Al-Ni alloy can be decreased down to one half as compared with the dehalogenations performed without its addition.

Table III

Reduction of halogenated anilines by action of glucose in aqueous solution of NaOH with catalysis of in-situ prepared Raney nickel; reaction time 17 hours at RT with intensive stirring<sup>16</sup>

Exp. No.:	XANs (mmol)	Quantity of NaOH (g)	Quantity of glucose <sup>a</sup> (g)	Quantity of Al-Ni (mmol of Ni)	Conversion to aniline (or another product)
1	2,5-dichloroaniline (0.5)	0.8	0.5	0.08 g (0.67)	90.7 %
2	2-chloroaniline (2)	0.5	1.0	0.06 g (0.5)	100 %
3	2-chlorophenylene-1,4-diamine (1)	0.5	1.0	0.06 g (0.5)	100 % phenylene diamine
4	2,5-dichloro-phenylene-1,4-diamine (1)	1.0	2.0	0.06 g (0.5)	100 % phenylene diamine
5	5-chloro-2-methoxyaniline (1)	1.0	1.0	0.06 g (0.5)	100 % 2-methoxyaniline
6	2-chloro-5-methylaniline (1)	1.0	1.0	0.06 g (0.5)	100 % 3-methylaniline
7	2-methyl-5-chloroaniline (1)	1.0	1.0	0.06 g (0.5)	100 % 2-methylaniline
8	2-chloro-5-methyl-phenylene-1,4-diamine (1)	1.0	1.0	0.06 g (0.5)	100 % <i>o</i> -methyl-phenylene diamine
9	3-chloro-2-methylaniline (1)	1.0	1.0	0.06 g (0.5)	100 % 2-methylaniline
10	4-bromoaniline (1)	0.5	1.0	0.06 (0.5)	100 % aniline
11	4-chloroaniline (1)	0.5	1.0	0.06 g (0.5)	47.7 % aniline

<sup>a</sup> 1 g NaOH was used per 1 mmol AOX

<sup>b</sup> NaOH was added in the form of 10% aqueous solution

As it is documented in Table III, even with the addition of a catalytic amount of the Raney alloy (0.5 mmol Ni) it is possible to dehalogenate quantitatively all the studied substituted *ortho*- and *meta*-chloroanilines by action of glucose in alkaline medium. From Table 2 it is obvious that 4-bromoaniline is debrominated distinctly more easily by action of glucose in alkaline medium (see experiment no. 10). In the attempt to dehalogenate *para*-chloroaniline, the reduction of chlorine is markedly slower (the conversion to aniline is only 47 %). In the course of dehalogenation of 2,5-dichloroaniline with Al-Ni alloy, it is only possible to find in the reaction mixture the starting 2,5-dichloroaniline and aniline; neither 2-chloroaniline nor 3-chloroaniline (as potential intermediates of dehalogenation) were found in the reaction mixture, which indicates a markedly higher reactivity of these monochloroanilines as compared with 2,5-dichloroaniline.

*Dehalogenation of halogenoanilines (XANs) in glucose/NaOH solution (general method):* The reactions were carried out in 250-cm<sup>3</sup> round-bottomed flasks equipped with magnetic stirrer; outlet of the flask was fitted to a

glass tube filled with granulated charcoal. The reaction flasks were attached on the Starfish attachment heated at the temperature of  $25 \pm 1$  °C. In  $200 \text{ cm}^3$  of 10 mM aqueous solution of XAN (2 mmol) was dissolved appropriate amount of solid base (see Tables), glucose or another additive and Al-Ni alloy (see Tables) was added. The reaction mixture was stirred at 500 rpm at the temperature of 25 °C for appropriate time, filtered through the filter paper (*solution 1*) and a  $20\text{-cm}^3$  aliquot of the filtrate was extracted with three portions of  $\text{CDCl}_3$  ( $1 \times 1 \text{ cm}^3$  and  $2 \times 0.5 \text{ cm}^3$ ). The relative integral intensities of signals in  $^1\text{H}$  NMR spectrum of this  $\text{CDCl}_3$  extract indicate conversion of XANs to aniline (identified using aniline as internal standard).

$^1\text{H}$  and  $^{13}\text{C}$  NMR spectroscopy of  $\text{CDCl}_3$  extract:  $\delta_{\text{H}}$  (360.13 MHz,  $\text{CDCl}_3$ ) 5.0 (bs, 2H,  $\text{NH}_2$ ), 6.68 (m, 2H, H-*o*), 6.76 (m, 1H, H-*p*), 7.15 (m, 2H, H-*m*).  $\delta_{\text{C}}$  (90.55 MHz,  $\text{CDCl}_3$ ) 115.1 (2 $\times$ CH), 118.5 (CH), 129.2 (2 $\times$ CH), 147.3 (C).

According to AOX analysis, *solution 1* contains 382  $\mu\text{g/l}$  of AOX (Adsorbable Organic Chlorine) and 1710 mg/L Al and 0.941 mg/L Ni (according to the ICP-OES measurement). *Solution 1* was adjusted at pH 7 using 20 wt % aqueous solution of HCl and insoluble part was filtered off. The filtrate contains less than 0.05 mg/L of Al and less than 0.05 mg/L of Ni.

### Conclusion

We have proved that an addition of glucose to alkaline aqueous solutions of *meta*- and *ortho*-chloroanilines and *para*-bromoaniline makes it possible to markedly decrease the charge of reducing Al-Ni alloy in dehalogenation at room temperature. A probable reason of the described influence of glucose is its effect on stabilization of nickel nano-particles which are formed during the dissolution of Al-Ni alloy in the alkaline medium during reductive dehalogenation. The formed Ni nano-particles catalyze the hydrodehalogenation of the above-mentioned monohalogenoanilines by the hydrogen being formed *in-situ* during dissolution of Al from Al-Ni alloy. However, we also proved that the dehalogenation of less reactive chlorinated anilines, such as 4-chloroaniline and 2,5-dichloroaniline, is virtually unaffected by added glucose.

### Literature

1. C. Tixier, M. Sancelme, S. Ait-Aissa, P. Widehem, F. Bonnemoy, A. Cuer, H. Veschambre: *Chemosphere* 46 519 (2002).
2. F.J. O'Neill, K.C.A. Bromley-Challenor, R.J. Greenwood, J.S. Knapp: *Water Res.* 34, 4397 (2000).
3. I. Casero, D. Sicilia, S. Rubio, D. Perez-Bendito: *Water Res.* 31, 1985 (1997).
4. K. Nick, H.F. Scholer: *Vom Wasser* 86, 57 (1996).
5. C. Richard, S. Bengana: *Chemosphere* 33, 635 (1996).
6. G. Mailhot, L. Hykrdová, J. Jirkovský, K. Lemr, G. Grabner, M. Bolte: *Appl. Cat. B: Environmental.* 50, 25 (2004).
7. J.M. Herrmann: *Catal. Today* 53, 115 (1999)
8. R. Kang, X. Ouyang, J. Han, X. Zhen: *J. Mol. Catal. A: Chemical* 175, 153 (2001)
9. A. David, M.A. Vannice: *J. Catal.* 237, 349 (2006)
10. C. Noubactep: *J. Hazard. Mat.* 164, 394 (2009).
11. Alonso, Francisco; Beletskaya, Irina P.; Yus, Miguel: *Chem. Rev.* 102(11), 4009 (2002).
12. Yuji Ukisu, Tatsuo Miyadera: *J. Mol. Catal. A: Chemical* 125, 135 (1997).
13. Weidlich T., Krejčová A., Maturová M.: *Waste Forum* 2, 117 (2009)
14. Weidlich T., Prokeš L.: *Cent. Eur. J. Chem.*, 9(4), 590-597 (2011).
15. Weidlich T., Krejčová A., Prokeš L.: *Monatsh. Chem.*, 141, 1015 (2010).
16. Weidlich T., Obršal J., Krejčová A., Jašůrek B.: *Monatsh. Chem.*, 146, 613 (2015).

## APPLICATION OF IONIC LIQUIDS FOR THE PRODUCTION OF BROMAMINE ACID

Šimek M.<sup>1</sup>, Vyňuchal J.<sup>2</sup>, Weidlich T.<sup>1</sup>

<sup>1</sup>Faculty of Chemical Technology, University of Pardubice, Studentská 573, 532 10, Pardubice

<sup>2</sup>Synthesia, a.s., Semtín 103, 530 02, Pardubice  
miroslav.simek@upce.cz

### Introduction

Bromamine acid (BAK) shown in Figure 1 is an important intermediate of many organic colorants based on anthraquinone structure and represents the basic component of various products of dye industry (Pigment Red 177, Acid Blue 25, Acid Blue 138). Annual worldwide production is more than thousands of tons. Nowadays the biggest producer of Bromamine acid is China.

Until 2003, BAK was produced also in Synthesia, a.s. Pardubice. However, facing the environmental problems connected with its production – mostly waste water treatment, caused the termination of the production as well as in many companies in Europe.

Wastewater analysing during BAK production are typical for containing water-soluble brominated organic compounds – Adsorbable organic halides (AOX), Bromine and significant amount of waste acid. Among others, aromatic sulphate acids can be found in the wastewater composition as well.

The production of 1-amino-2-sulfoanthraquinone acid is illustrated in Figure 1.

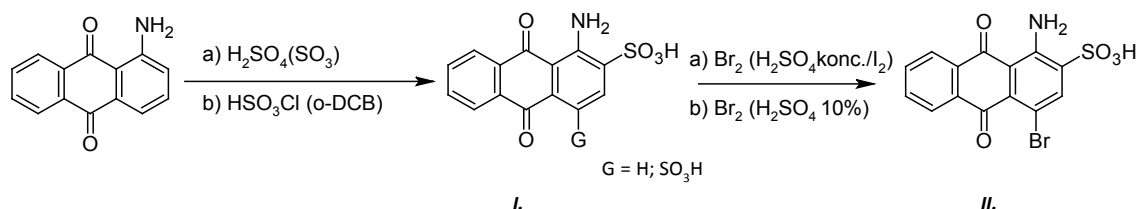


**Figure 1:** Production of 4-brom-2-sulfo-1-aminoanthraquinone acid by bromination of 1-amino-2-sulfoanthraquinone acid (I.).

Many ways of production of BAK have been studied so far. They differ mainly at sulfonating agent used, environment, where the sulphonation and bromination take place, reaction temperature during bromination and concentration of reaction component.

Production technology can be divided according to the environment:

- production of BAK in water solution (without organic solvent);
- production of BAK with use of organic solvent.

The fundamental of BAK production from 1-aminoanthraquinone is similar for both technological methods. In the first step sulphonation of 1-aminoanthraquinone is carried out, followed by the bromination of created intermediate I. In both cases of BAK production high amount of wastewater is detected.

This article describes the possibility of novel economical way of BAK production which is based on the minimizing of the AOX, absorbance and chemical oxygen demand (COD) in wastewaters.

Using of ionic liquids (quaternary ammonium or phosphonium salts)<sup>1</sup> and the coagulation agent provides an environmentally friendly production of BAK and other dyes. This method is described in the University of Pardubice Patent CZ20120359. This patent describes the removal of sulfo-substituted acid dyes from the aqueous solution by using of ionic liquids (ILs) and coagulation agent (aluminium and ferric salts)<sup>2</sup>.

Benzalconium chloride (Figure 2; III.) is a commercially available ionic liquid which was used in this research.

If suitable amounts of ionic liquid and coagulation agent are used, following parameters can be decreased: COD (chemical oxygen demand), BOD (biochemical oxygen demand), metal traces, adsorbable organic halides and the overall colour of wastewaters.

When ionic liquid is applied and ion-pairs are created, the solubility of undesired substances in wastewater decreases which simplifies the removal of pollutants. However, the pollutant solubility in organic solvents is very good (ion-pair benzalconium chloride/bromamic acid).

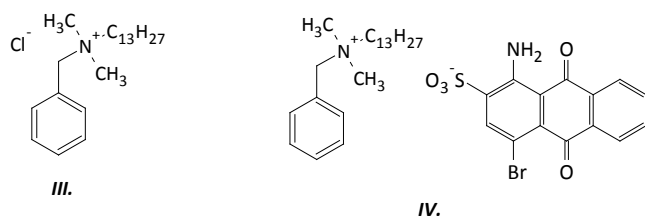


**Figure 2:** Benzalconium chloride (III.) and ion-pair BAC/BAK (IV).

The following wastewater treatment can be applied to the production of organic colorants with bromamine acid as a precursor. Pigment Red 177, produced by Synthesia, a.s, can be mention as an example. However, these days the wastewater are treated by other ways.

Pigment Red 177 is formed by Ullmann reaction when the C-C coupling takes place by reaction of 2 BAK molecules in the presence of powder-based copper. As a result of  $-SO_3Na$  groups present, the intermediates' looses are huge. This represents a challenge to face because of economical and ecological aspects. By applying an ionic liquid, the intermediate could be recycled from wastewaters and used further.

#### Preparation of bromamic acid in aqueous solution

The procedure for BAK preparation is known since 1948 and is described in patents US 2503254 A<sup>3</sup> and US 4213909<sup>4</sup>. In Synthesia, a.s. the bromamine acid was produced according to this procedure until 2003.

The first step is the sulphonation of 1-aminoanthraquinone by oleum (20%  $SO_3$  in  $H_2SO_4$ ) and is followed by bromination of 1-amino-2-sulfoanthraquinone by bromine. Then the bromamine acid is isolated in the form of BAK sulphate which is further neutralized and then rinsed by solution of sodium sulphate giving sodium salt of BAK. This is further treated by the use of active carbon and undergoes alkali "clearation" (= the filtrate is processed). All the steps are done in aqueous solution.

If 10 g of bromamine acid is desired, 8.31 g of aminoanthraquinone, 11.84 g of sodium sulphate, 0.015 g of iodine, 4.8 g of bromine and 48 g of oleum (20%) is necessary.

Several steps in the production are connected with high amount of wastewaters which content non-degradable compounds. The overall wastewater volume was 600 ml.

Wastewater is treated according to the patent of University of Pardubice CZ20120359. Benzalconium chloride and ferric sulphate were added to the wastewater sample. Decreasing tendency of AOX, absorbance and COD were detected. The results can be seen in Table 1 and Table 2.

**Table I:** Wastewater after desalting – isolation of a product.

	AOX [mg/l]	COD <sub>Cr</sub> [mg/l]	Absorbance
WW-US1	46.04	2 338	0.34 (100x)
WW-US1 coagulation	1.31	1 256	1.27

(WW-US1 = wastewater after coagulation of BAK; WW-US1 coagulation = wastewater after adding of ionic liquid and coagulant)

**Table II:** Wastewater after alkali clearation — product purification

	AOX [mg/l]	COD <sub>Cr</sub> [mg/l]	Absorbance
WW-US2	11.98	1 022	0.11 (100x)
WW-US2 coagulation	0.08	903	0.506

(WW-US2 = wastewater after product rafination; WW-US2 coagulation = wastewater after adding of ionic liquid and coagulant)

In the case of water technology, it is necessary to face problems with reactants entering the reaction – especially in the bromination part, where iodine is added. In addition, more steps are necessary for the whole reaction to proceed. As a result, huge amount of wastewater with many environmentally unfriendly compounds is created.

### BAK preparation with use of solvent

BAK production with use of solvent (1,2-dichlorobenzene) is described by the patent CN 102617412A<sup>5</sup>. Sulphonation of reagent – 1-aminoanthraquinone is the first step of this method, where the functional group – SO<sub>3</sub>H is substituted at the position 2 using of chlorosulphonic acid at 1,2-dichlorobenzene environment. Then stratification of the reaction mixture takes place by adding sulphuric acid. Another step is the bromination of the intermediate (1-amino-2-sulphoanthraquinone acid) by bromine at 0-2°C. Bromination is carried out in 10% sulphuric acid. Further, the desalting of BAK by sodium carbonate is done.

Formed bromamine acid is raffinated by hot water which leads to remove of soluble compounds from water, mainly 1-amino-2-sulphoanthraquinone acid.

If 10 g of product – bromamine acid is desired, 7.35 g of 1-aminoanthraquinone, 38.1 g 1,2-dichlorobenzene, 5.42 g chlorosulphonic acid and 3 g bromine.

Wastewater production is connected with desalting (WW-CN1) and following raffination (WW-CN2) process of BAK. According to this technology 300 ml of wastewater was produced in the lab conditions. Wastewater was isolated and tested by AOX, COD and Absorbance methods. Further, the treatment with ionic liquid was carried out (benzalconium chloride + coagulation agent ferric sulphate). As the presence of 1,2-dichlorobenzene represented a risk (it is partly soluble in acidic solutions), active carbon was applied for the its adsorption.

When applying ionic liquid agents to filter treatment, which was created after desalting of BAK, it was found out that all parameters tested (AOX, COD and Absorbance) decreased rapidly which can be seen in Table 3. Higher initial value of AOX and COD was caused by traces of non-desalted BAK and 1-amino-2-sulphoanthraquinone acid present in water.

**Table III:** Wastewater after desalting treatment – isolation of the product.

	AOX [mg/l]	COD <sub>Cr</sub> [mg/l]	Absorbance
WW-CN1	244.51	1 807.9	0.15 (100x)
WW-CN1 precipitation	3.1	1 334	0.19 (10x)
WW-CN1 precipitation and sorption	0.53	1 088	0.13

(WW-CN1 = wastewater after desalting of BAK; WW-CN1 coagulation = WW after addition of ILs and coagulant; WW-CN1 coagulation and sorption = WW after addition of ILs, coagulant and activated carbon)

The filtrates after raffination of BAK proved lower values of AOX and COD compared to values after desalting. The reason for this is the presence of partly dissolved product. After the coagulation with ionic liquid, the drop of halides content in wastewater is more than 99 % (Table 4).

**Table IV:** Wastewater after raffination – product purification.

	AOX [mg/l]	COD <sub>Cr</sub> [mg/l]	Absorbance
WW-CN2	47.64	1 134	0.098 (100x)
WW-CN2 precipitation	1.31	985	0.12 (10x)
WW-CN2 precipitation and sorption	0.12	835.8	0.03

(WW-CN2 = wastewater after product raffination; WW-CN2 coagulation = WW after addition of ILs and coagulant; WW-CN2 coagulation and sorption = WW after addition of ILs, coagulant and activated carbon)

The great advantage of this method is represented by the used solvent – 1,2-dichlorobenzene – which can be regenerated by distillation so the wastewater treatment for this compound is not necessary. Compared to the manufacture of BAK in water solution, less wastewater is generated. Moreover low acidity of wastewater is provided as the bromination takes place in presence of 10% sulfuric acid.

On the other hand, this technology faces some problems when using chlorosulphuric acid. The cooling of reaction mixture is energetically more complicated than heating step. As a consequence of high viscosity of reaction mixture after stratification, the complications with stirring are quite often.

Another tested method for environmentally friendly production of BAK was bromination of 1-amino-2-sulphoanthraquinone acid in a solid state according to bromination of Diketo-Pyrrolo-Pyrroles (DPP)<sup>6</sup>. It is suggested that the bromination takes place only on DPP chromophore, bromination on anthraquinone structure has not been proven yet.

### Applying of patent CZ20120359 during production of Pigment Red 177

Scheme of Pigment Red 177 production can be seen in the Figure 3. The production procedure is described in patents GB926514, CH477417 or CS 217252. It is based on specific Ullmann reaction taking place in aqueous solution. P.R.177 is created by reaction of 2 BAK molecules with powder-based copper in aqueous or slightly acidic solution. Then isolation of the intermediate is carried out (4,4'-diamino-1,1'-dianthraquinon-3,3'-disulphonic acid), followed by the desulphonation by diluted sulphuric acid.<sup>7</sup>

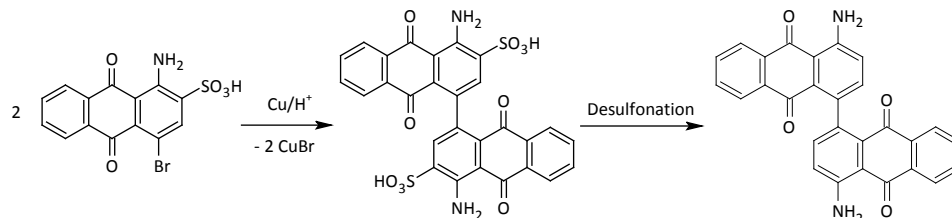


**Figure 3:** Synthesis of Pigment Red 177.

During the production of P.R.177 there are several problems with dissolving of intermediate and other compounds in wastewaters. According to patent of University of Pardubice CZ20120359 when wastewater treatment is described, the overall values of absorbance, AOX, COD and metal traces are decreased. Results can be seen in table 5.

The mass of benzalconium chloride to be applied for wastewater treatment is calculated according to the overall content of compounds with –SO<sub>3</sub>H group present in wastewaters. During the coagulation, tar products were produced causing complications with filtrations of solutions.

**Table V:** Wastewater from P.R. 177 production after purification treatment - 1

	AOX [mg/l]	Absorbance	Cu content [ppm]
WW-PR177 original	1.42	0.38 (100x)	405
WW-PR177 after coagulation	0.52	0.19	270

(WW-PR177original = WW after filtration of DADADSK; WW-PR177 after coagulation = WW after addition of ILS and coagulant)

A significant drop in the copper content in filtrates was observed when applying of benzalconium chloride in combination with coagulation agent. This can be the reason for presence of copper-complex with sulphonated anthraquinone. The decreased Cu content proposes the effective production and lower costs for wastewater treatment.

**Table VI:** Wastewater treatment from production of P.R.177-2.

	COD <sub>Cr</sub> [mg/l]	BOD [mg/l]	Ratio BOD/COD
WW-PR177 original	4 202.2	340.78	0.081
WW-PR177 after coagulation	858.5	235.45	0.27

(WW-PR177original = WW after filtration of DADADSK; WW-PR177 after coagulation = WW after addition of ILS and coagulant)

BOD (biochemical oxygen demand) is another important parameter which was observed to find out the degradability of compounds present in water.

BOD provides water characterization in terms of biological degradability of organic compounds present. The ratio between BOD and COD is detected. The higher the ratio, the more easier-bio-degradable compounds are present in water.

From values in Table 6 is evident that the ratio BOD : COD from the original filtrate is lower than 0.1. This proves low bio-degradability of wastewater. In contrast, when applying ionic liquids in combination with coagulation agent, the ratio changes to 0.27. In conclusion, coagulant can help with efficient removing of nonbio-degradable compounds.

The use of ionic compound is not only in wastewater industry, where the created ionic pair is characterized as a waste. It can be applied for isolation of compounds that are supposed to be used further as well. Figure 3

represents an appropriate example – isolation of intermediate P.R.177 in filtrates and wastewater by ionic liquid. After desulphonation part Pigment Red 177 is created.

Filtrates, resp. wastewater, can contain following intermediates: 4,4'-diamino-1,1'-dianthraquinon-3,3'-disulphonic acid (DADADSK), 1-amino-2-sulphoanthraquinon acid (ASK), 1-amino-4-hydroxyanthraquinon-2-sulphonic acid (AHASK) and unconverted BAK. All mentioned compounds can be isolated from the solution by applying of ionic liquids.

### Conclusion

In chemical industry water represents the „green“ solvent. However, considering the cost of purification treatment in the case of mass production of bromamine acid, the solvent technology is more suitable. For economical and ecological comparison, more detailed study should be done. Ionic liquids can be applied not only for waste water treatment (described by patent of University of Pardubice) but for the synthesis of ionic pairs as well. This promises a new perspective in production of new colorants.

If the ionic liquids are used during wastewater treatment, the overall absorbance, COD and metal traces content are increased, whereas the bio-degradability is improved. Proposed technological procedure provides production with less AOX present in wastewater. Low-waste and economically available technology for production of BAK, P.R.117 and other colorants can be obtained by appropriate optimization.

### Acknowledgement:

This work was done in cooperation of Synthesia, a.s. and University of Pardubice.

### Literature

1. Meindersma G., Maase M., De Haan A.; Ullmann's Encyclopedia of Industrial Chemistry: Ionic Liquids, s.13076, (2007)
2. Martinková J., Weidlich T.; Dye precipitation process from aqueous solutions; Patent, CZ20120359, (2013)
3. Gen Aniline & Film corp.; Process of preparing 1-amino-4-bromoanthraquinone-2-sulfonic acid. Patent, US2503254 A. (1950)
4. Berg G., Hohmann W., Proces for preparation of 1-amino-4-bromo-anthraquinone-2-sulfonic acid, Patent, US 4213909, (1978)
5. Preparation method of bromamine acid, Patent, CN 102617412A, (2014)
6. Luňák, Jr.S., Vyňuchal J., Vala M., Havel L., Hrdina R., The synthesis, absorption and fluorescence of polar diketo-pyrrolo-pyrroles, Dyes and Pigments 2009 (1-7).
7. Šimek M., The issue of recycling of metal used in the homocoupling reaction; Thesis, University of Pardubice (2014)

## OPTIMIZATION OF WALL TEMPERATURE IN VACUUM FILM EVAPORATOR

**Timár P.**, Stopka J., Bálaš V., Timár P.Jr., Hanus K.

*Department of Chemical and Biochemical Engineering, Institute of Chemical and Environmental Engineering, Faculty of Chemical and Food Technology, Radlinského 9, 812 37 Bratislava  
pavel.timar@stuba.sk*

### Abstract

This contribution deals with task to find optimal conditions for vacuum distillation of waste liquids, e. g. used oils. Important part of new proposed technology for material evaluation of waste oils is vacuum distillation from falling liquid film. Ultimate factors for rate of distillation process are optimal heat transfer conditions. When distillation pressure is fixed, it is necessary choose most suitable temperature of heating surface or heating agent. Optimal value of this temperature is possible to find out on the basis of known liquid boiling curve. Original experimental equipment was constructed and used for experimental setting of optimal temperature from boiling curve for various liquids, first for atmospheric pressure and consequently for vacuum.

Keywords: waste oils, boiling curve, boiling regime, optimum temperature

### Introduction

Understanding the different boiling regimes is very important for industrial evaporation processes. Over the past decades, many studies on the optimal heat flux versus have been presented. However, the importance of the boiling curve has not been fully understood yet, especially in the transition regime from nucleate to film boiling Chai & Shoji<sup>5</sup>. Boiling heat transfer is characterized by an S-shaped curve relating the heat flux to the temperature difference between the fluid and the heating surface Tong and Tang<sup>19</sup>, Fig. 1). This curve, first obtained by Nukiyama<sup>13</sup>, is the dependence of the heat flux on the wall superheat boiling curve and on the boiling transition Chai & Shoji<sup>5</sup>. Pool boiling is of interest in high heat flux applications because of its potential to remove large amounts of heat resulting from the latent heat of evaporation and a small pressure drop for the coolant circulating through the system Cooke & Kandlikar<sup>6</sup>. Many theoretical and empirical correlations for the estimation of the boiling heat transfer coefficient (HTC) and the critical heat flux under different conditions have been proposed Piro & Piro<sup>16</sup>. The classical boiling process studied was the nucleate pool boiling, boiling on a surface submerged in a pool of liquid. Many types of boiling surfaces: plates Berenson<sup>3</sup>; Tolubinskiy<sup>18</sup>; Lee et al.<sup>10</sup>; Piro et al.<sup>14</sup>; Piro<sup>15</sup>, strips Young & Hammel<sup>22</sup>, wires Tolubinskiy<sup>18</sup>; Addoms<sup>1</sup>, and single tubes Cryder & Finalbargo<sup>7</sup> made of various materials have been investigated over a wide range of boiling conditions. In the work by Nakoryakov et al.<sup>12</sup>, the authors deal with water drop behaviour on heated surface. The measurement principle is similar to that of the present work and the boiling curve found for water has the same trend as the one reported here. The curve displaying temperature dependence on the rate of droplets evaporation showed a minimum at 130°C, which is in good agreement with our results. Also in the work of Rops et al.<sup>17</sup>, the authors used the same measurement principle. This topic has been dealt with in a number of works but none of them measured boiling curves under vacuum conditions. Only a few recent studies dealing with the behaviour of fluids at the heating surface could be found Nakoryakov et al.<sup>12</sup>; Misale et al.<sup>11</sup>; Kim et al.<sup>8</sup>; Wang et al.<sup>20</sup>. Fig. 1 shows a typical boiling curve, where the horizontal axis represents the temperature difference ( $\Delta T = T_w - T_{sat}$ ) and the vertical axis represents the heat flux density ( $q''$ ). According to the ascending temperature difference, the boiling curve is divided into four basic regions:

- i) region I – natural convection
- ii) region II – nucleate boiling
- iii) region III – transition boiling
- iv) region IV – film boiling

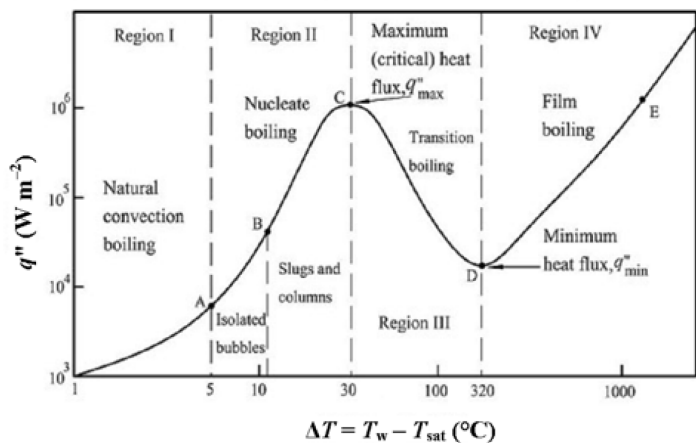


Fig. 1. Boiling curve with different boiling regimes.

For each boiling regime, a characteristic change of the heat transfer driving force, i.e. the temperature difference between the heating surface and the heated liquid ( $\Delta T = T_w - T_{sat}$ ), is defined. If this difference is less than  $5^{\circ}C$  (Fig. 1, region I), heat transfer occurs by natural convection where the movement of the fluid is caused by the temperature gradient. In this regime, it is possible to evaluate the heat transfer coefficient by semi-empirical correlations for natural convection. As the heat transfer driving force increases, natural convection boiling changes to nucleate boiling (Fig. 1, region II).

The transition boiling regime (Fig. 1, region III) is a combination of nucleate and film boiling. It is characterized by intense formation of vapour bubbles on the heating surface. Bubble formation intensifies with the increasing temperature of the heating surface. As a consequence, there is a significant decrease of the  $\alpha$  and  $q''$  values (Fig. 1). Vapour layer covering the heating surface works as insulation and reduces the heat transfer efficiency. Finally, the whole heating surface is covered with a boiling liquid vapour layer, and  $\alpha$  and  $q''$  reach their minimum values. This is called the Leidenfrost effect (Fig. 1, point D).

Film boiling begins at the Leidenfrost point. This boiling regime (Fig. 1, region IV) is characterized by a continuous vapour layer which separates the heating surface from the liquid. The whole heating surface is covered with a thin vapour layer which isolates the liquid from the heating surface decreasing thus the heat transfer efficiency significantly. Film boiling usually occurs during the hardening process in metallurgy. However, it is usually desirable to work in the nucleate boiling regime to achieve maximum efficiency. This work deals with the determination of optimum process conditions for vacuum distillation of waste transformer oils. For maximum efficiency and quality of waste oil regeneration it is necessary to find optimum temperature and pressure. Under atmospheric conditions, it is possible to determine optimum distillation conditions using the boiling curves.

## Experimental

The assembled equipment was first used under atmospheric conditions to examine the evaporation of polar and non-polar liquid drops. The time of drop evaporation was measured as it is indirectly proportional to the heat flux. The longer the drop evaporates, the lower is the heat flux density and vice versa.

The advantage of this approach is in its lower investment costs. The measuring equipment included also a thermocouple and a stopwatch. Curves depicting the dependence of the vaporization time decrease on the heating surface temperature were obtained by these measurements; they are symmetrical with the liquid boiling curves about the x-axis, depicting the heat flux density dependence on the temperature difference. In terms of the heat transfer intensity, the optimum temperature difference is given by the difference of the heating surface temperature and the boiling point of the liquid.

The main part of the experimental equipment (Fig. 2) is a cylindrically shaped copper block heated by a regulated electric heater. Temperature of the copper block was measured by a thermocouple (K type) placed 3 mm under the surface from which a drop of the studied liquid evaporates. The time from the drop landing on the surface to its complete evaporation was measured. It is clear that the most intensive heat transfer from the heating surface to the boiling liquid takes place when the drop evaporation time is minimal.

Liquids such as oils are multicomponent materials containing a wide range of components. It is not possible to distillate oils under atmospheric pressure due to their thermal degradation at high temperatures, which is the reason why the experiments have to be performed under vacuum conditions.

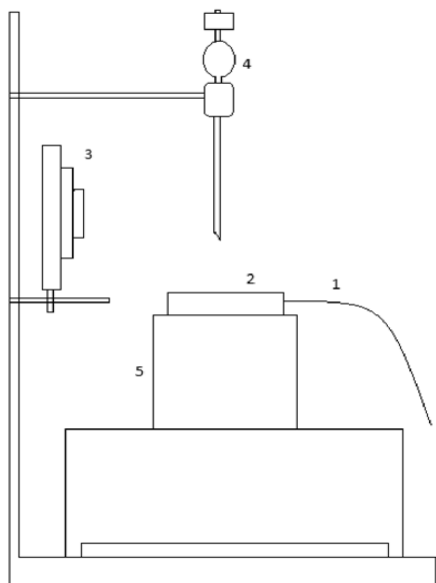


Fig. 2. Equipment designed for optimum distillation temperature measurement: 1 –thermocouple type K, 2 – copper block, 3 – camera, 4 – remotely controlled valve, 5 – electric heater.

### Results and Discussion

Results of the experiment with water are presented in Fig. 3. We obtained typical curve and optimum temperature was around 130°C and the optimal temperature difference for maximum heat flux was 30°C. This means that the water drop fallen on the surface of the copper block needed the shortest time to evaporate at the surface temperature of 130°C. The most intensive heat transfer occurs when the temperature of the heating surface is 30°C higher than the boiling point of water. Available literature presents the optimum temperature difference of around 25–30°C.

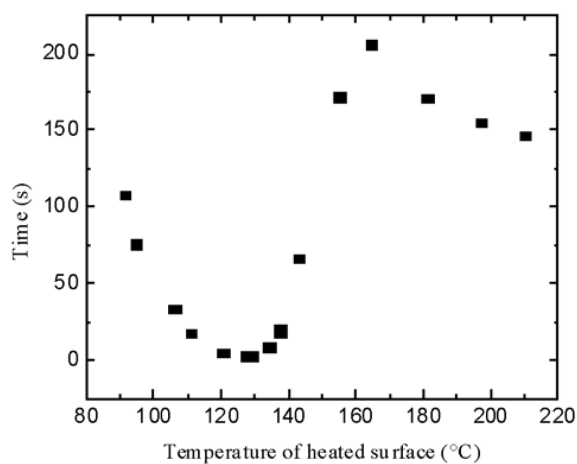


Fig. 3. Experimental curve of the optimum temperature difference for water.

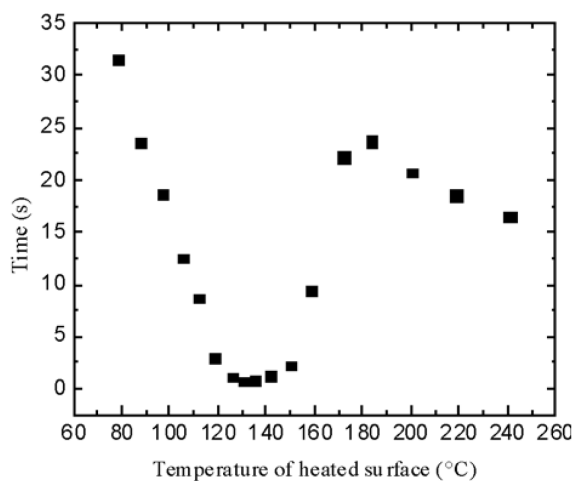


Fig. 4. Experimental curve of the optimum temperature difference for heptane.

The other examined liquids were mainly hydrocarbons with defined boiling points, which are resistant to thermal degradation in the given temperature range. These liquids together with measured optimal temperature difference are listed in Table 1.

From Table 1 it is clear, that optimal temperature difference between temperature of copper block and boiling point of liquid is within the range 24 and 39 °C. This optimal temperature difference is complex function of many physical and chemical properties of examined liquid. Our next effort will be target to find some empirical equation for forecast of it. Besides this, above mentioned method is very useful for testing of not pure substances but for many components solutions too.

Table I. Experimental results of the examined substances.

Sample	Molecular formula	Temperature °C		
		Boiling point	Optimum	Difference
Water	H <sub>2</sub> O	100.0	130.0	30.0
Ethanol	C <sub>2</sub> H <sub>6</sub>	78.3	102.3	24.0
Pentane	C <sub>5</sub> H <sub>12</sub>	36.0	74.0	38.0
Hexane	C <sub>6</sub> H <sub>14</sub>	69.0	98.4	29.4
Heptane	C <sub>7</sub> H <sub>16</sub>	99.0	130.0	31.0
Decane	C <sub>10</sub> H <sub>22</sub>	174.0	205.0	31.0
Dodecane	C <sub>12</sub> H <sub>26</sub>	216.4	250.4	34.0
Isooctane	C <sub>8</sub> H <sub>18</sub>	99.3	138.3	39.0

As mentioned before, presented experimental method is valid for multicomponent mixtures. Some substances degrading at high temperatures. Measurements of their optimum temperature difference had to be performed under vacuum conditions. The entire experimental equipment was adapted to vacuum conditions. All parts were placed under a sealed glass cover to enable experiment observation even at low pressures. Drop dosing had to be performed by a remotely controlled solenoid valve. The rest of the equipment was the same as that used under atmospheric conditions. Vacuum was generated by a vacuum pump. Results obtained for pure dodecane under vacuum and atmospheric conditions are displayed in Fig. 5. The boiling point of the dodecane is 214°C at the atmospheric pressure and 173°C at 32 kPa. The shortest drop evaporation time was observed at 250°C (36°C higher than boiling point) at the atmospheric pressure and at 202°C under vacuum conditions (28,9°C higher than boiling point).

As least was experimentally found optimal conditions for the vacuum distillation of waste oil refer to the temperature and pressure of the most intensive heat transfer to the boiling oil. Boiling curves of four different oil samples are displayed in Fig. 6. The highest heat transfer for sample 1 was reached at 261°C. Sample 2 reached its optimum at 301°C, sample 3 at 241°C and sample 4 at 264°C. All four measurements were performed at the pressure of 1.3 kPa.

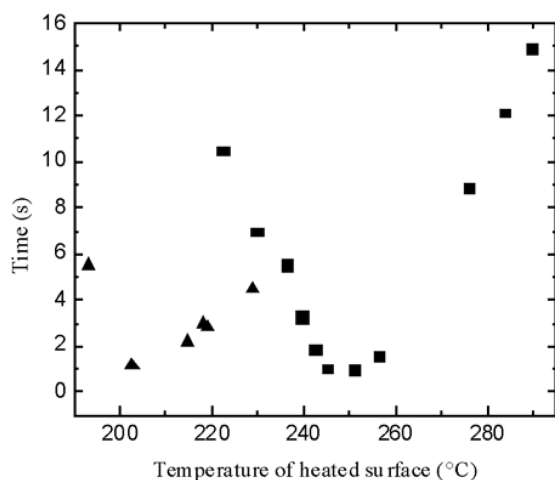


Fig. 5. Comparison of the evaporation time of dodecane under atmospheric (■) and vacuum (32 kPa) conditions (▲).

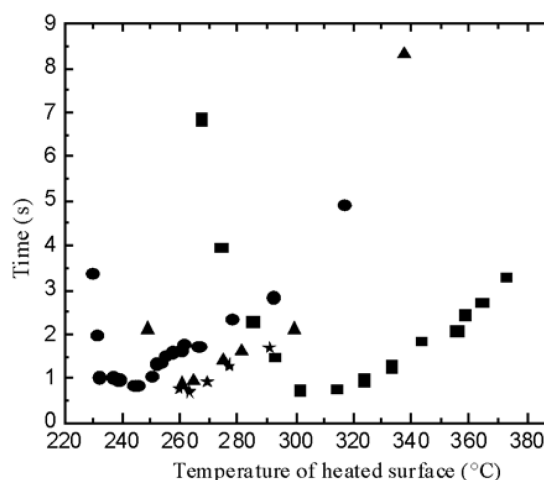


Fig. 6. Comparison of the evaporation time of waste oil samples 1 (●), 2 (■), 3 (★), and 4 (▲) at 1.3 kPa.

From the results of experiments depicted in Fig. 5 and 6 one can see, that optimal temperature difference strongly depends on pressure. Lower pressure shifts the optimum point to the left – see Fig. 5 for dodecane, when optimal temperature difference changed due to pressure from 36°C to 28,9°C. In the literature<sup>23</sup> we can find, that it is caused mainly by changing of evaporation heat and surface tension of liquid.

In case of various oil samples (Fig. 6) situation is more complex, because at the same pressure optimal heating point depends on kind of oil and width of fraction. But with above mentioned experimental technique is possible quite simple to measure it.

## Conclusion

Original experimental equipment was built in laboratory conditions to provide measurements of liquid drop evaporation time and temperature of the heating surface under atmospheric and vacuum conditions. Various substances pure and mixtures were measured using this device. Curves depicting the dependence of the drop vaporization time on the heating surface temperature were thus obtained. These curves are symmetrical with the liquid boiling curves depicting the heat flux density dependence on the temperature difference about the x-axis. These results showed the optimum temperature of the heating surface at which the distillation process provides the best performance. The distillation process is slow at low temperatures and heavier components do not appear in the distillate, which leads to the decrease of the distillate quality. At high distillation temperatures, the distilled liquid is separated from the heating surface by a continuous vapour film and the film boiling worsens the conditions of the heat transfer decreasing thus significantly the performance of the process.

Formation of thermal degradation products covering the surface of the distillation equipment is also possible. Yang and Shivpuri<sup>21</sup>, Bernardin and Mudawar<sup>4</sup>, and Auracher and Buchholz<sup>2</sup> measured the boiling curves similarly as it is given in the present paper. However, the behaviour of materials in vacuum has not been studied until now. None of the published papers mentions the optimum temperature of the heating medium under reduced pressure. Oils are high-boiling substances decomposed at high temperatures and they cannot be distilled under atmospheric conditions. Therefore, these experiments were performed to determine the optimum temperature of the heating medium under vacuum.

## Acknowledgement

*This article was created with the financial support from the Structural Funds of EU, project in progress: "Industrial research focused on material evaluation of liquid waste, mainly from the automotive industry", ITMS: 26220220074, is appreciated.*



## Literature

1. Addoms, J. N. (1948). Heat transfer at high rates to water boiling outside cylinders. D.Sc. Thesis, Massachusetts Institute of Technology, Cambridge, MA, USA.
2. Auracher, H., & Buchholz, M. (2005). Experiments on the fundamental mechanisms of boiling heat transfer. *Journal of the Brazilian Society of Mechanical Sciences and Engineering*, 27, 1–22.
3. Berenson, P. J. (1962). Experiments on pool-boiling heat transfer. *International Journal of Heat and Mass Transfer*, 5, 985–999.
4. Bernardin, J. D., & Mudawar, I. (1999). The Leidenfrost point: Experimental study and assessment of existing models. *Journal of Heat Transfer*, 121, 894–903.
5. Chai, L. H., & Shoji, M. (2001). Boiling curves – bifurcation and catastrophe. *International Journal of Heat and Mass Transfer*, 44, 4175–4179.
6. Cooke, D., & Kandlikar, S. G. (2011). Pool boiling heat transfer and bubble dynamics over plain and enhanced microchannels. *Journal of Heat Transfer*, 133(5), 052902.
7. Cryder, D. S., & Finalbargo, A. C. (1937). Heat transmission from metal surfaces to boiling liquids: Effect of temperature of liquid on liquid film coefficient. *Transactions of AIChE*, 50, 346–362.
8. Kim, S. H., Ahn, S. H., Kim, J. W., Kaviani, M., & Kim, H. M. (2013). Dynamics of water droplet on a heated nanotubes surface. *Applied Physics Letters*, 102(23), 233901.
9. Kobayashi, & K. Oshima (Eds.), *Proceedings of the 4th International Heat Pipe Symposium*, May 16–18, 1994. Tsukuba, Japan: Japan Association for Heat Pipes.

10. Lee, Y., Pioro, I., & Park, H. J. (1994). An experimental study on a plate type two-phase closed thermosyphon. In Y. Kobayashi, & K. Oshima (Eds.), *Proceedings of the 4th International Heat Pipe Symposium*, May 16–18, 1994. Tsukuba, Japan: Japan Association for Heat Pipes.
11. Misale, M., Guglielmini, G., & Priarone, A. (2011). Nucleate boiling and critical heat flux of HFE-7100 in horizontal narrow spaces. *Experimental Thermal and Fluid Science*, 35, 772–779.
12. Nakoryakov, V. E., Misyura, S. Ya., & Elistratov, S. L. (2012). The behavior of water droplets on the heated surface. *International Journal of Heat and Mass Transfer*, 55, 6609–6617.
13. Nukiyama, S. (1934). Maximum and minimum values of heat transmitted from metal to boiling water under atmospheric pressure. *Journal of Japanese Society of Mechanical Engineering*, 37, 367–374.
14. Pioro, I. L., Park, H. J., & Lee, Y. (1996). Heat transfer in a two-phase closed thermosyphon: Horizontal flat plate type. In *Proceedings of the 5th International Symposium on Thermal Engineering and Science for Cold Regions*, May 19–22, 1996 (pp. 489–494). Ottawa, Canada.
15. Pioro, I. (1997). Boiling heat transfer characteristics of thin liquid layers in a horizontally flat two-phase thermosyphon. In *Proceedings of the 10th International Heat Pipe Conference*, September 21–25, 1997 (Paper H1-5). Stuttgart, Germany.
16. Pioro, L. S., & Pioro, I. L. (1997). *Industrial two-phase thermosyphons (Chapters 2 and 3)*. New York, NY, USA: Begell House.
17. Rops, C. M., Lindken, R. H., Velthuis, J. F. M., & Westerweel, J. (2009). Enhanced heat transfer in confined pool boiling. *International Journal of Heat and Fluid Flow*, 30, 751–760.
18. Tolubinskiy, V. I. (1980). *Heat transfer under boiling (Chapters 4 and 5)*. Kiev, URSS: Naukova Dumka. (in Russian)
19. Tong, L. S., & Tang, Y. S. (1997). *Boiling heat transfer and two-phase flow (2nd ed.)*. Washington, DC, USA: Taylor & Francis.
20. Wang, X. F., Rahman, Md. A., Jacobi, A. M., & Hrnjak, P. S. (2013). Dynamic wetting behavior and water drops on microgrooved surfaces. *Heat Transfer Engineering*, 34, 1088–1098.
21. Yang, L., & Shivpuri, R. (2007). A water evaporation based model for lubricant dryoff on die surfaces heated beyond the Leidenfrost point. *Journal of Manufacturing Science and Engineering*, 129, 717–725.
22. Young, R. K., & Hammel, R. L. (1965). Higher coefficients for heat transfer with nucleate boiling. *Chemical Engineering Progress Symposium Series*, 61(59), 264–270.
23. Incropera F.P., DeWitt D.P., Bergman T.L., Lavine A.S.: *Fundamentals of Heat and Mass Transfer*. 6-th edition, John Wiley & Sons, Inc. 2007.

## HEAT TRANSFER COEFFICIENTS IN LIQUID FILM EVAPORATOR

**Stopka J.**, Timár P., Bálež V., Timár P. Jr.

*Department of Chemical and Biochemical Engineering, Institute of Chemical and Environmental Engineering, Faculty of Chemical and Food Technology, Radlinského 9, 812 37, Bratislava  
jan.stopka@stuba.sk*

### Abstract

Regeneration is the most efficient way of managing used oil. It saves money by preventing costly clean-ups and liabilities that are associated with mismanagement of used oil and it helps to protect the environment of course. A numerical study of the flow, heat and mass transfer characteristics of the vertical evaporating tube with the films flowing down on both the inside and outside tube walls has been carried out. Condensation occurs along the outside wall and evaporation at the free surface of the inside film. The calculation domain of two film flow regions and tube wall is solved simultaneously. The longitudinal variation of temperature, mass flow rate, and hence thickness of the films downward the tube may be obtained by applying conservation of energy requirement to the differential element.

### Introduction

Waste oils are dangerous for the environment so their regeneration is necessary. The aim of waste oils regeneration technologies is to maximal rate of recycling at minimal financial cost and of course low ecological impact. This means complex processing of mineral oils in order to achieve the recreation of all the oils properties, to the same quality as fresh oil has. Regeneration takes place in conventional vacuum columns, similar to those used in petrochemical industry, or in vacuum evaporators with falling or wiped film evaporation. One of developed methods is vacuum distillation of oils in thin falling oil film. In falling-film evaporator a thin film of liquid generally flows downward under gravity on the inner surfaces of vertical tube bundles. Heat is transferred in order to [1]: raise the temperature of the liquid and/or to evaporate some of the liquid.

The heating medium is mostly vapor that condenses on the outer surfaces of the tubes. Occasionally, the falling film is cooled by heat removal. Advantages of falling-film equipment are [1]: high heat transfer coefficients, short residence times, short liquid holdup, low pressure drops

Three dimensionless numbers suffice for the description of heat transfer. Those are:

- Nusselt number 
$$Nu = \frac{\alpha}{\lambda} \left( \frac{v^2}{g} \right)^{\frac{1}{3}} \quad (1)$$
- Reynolds number 
$$Re = \frac{d w \rho}{\mu} = \frac{\dot{m}}{\mu} \quad (2)$$
- Prandtl number 
$$Pr = \frac{v}{a} = \frac{\mu c_p}{\lambda} \quad (3)$$

The term  $(v^2/g)$  has the dimension of a length. It is used instead of the film thickness  $\delta$ , because  $\delta$  itself depends on  $Re$ . The wetting rate  $\dot{m}$  is the mass flow rate of liquid per unit of length of circumference.

In no boiling falling films, all the physical properties ( $\lambda$ ,  $\mu$ ,  $a$ ,  $v$ ,  $c_p$ ) are determined at the average of the inlet and the outlet temperatures, and in boiling films, at the boiling point  $t = t_{sat}(p)$

### Film thickness

A knowledge of the film thickness  $\delta$  is required for the determination of the liquid holdup. It can be obtained from the Nusselt theory [2] if the film is smooth and laminar:

$$\delta_{lam} = \left( \frac{3 v^2}{g} \right)^{\frac{1}{3}} Re^{\frac{1}{3}}, \quad Re < 400 \quad (4)$$

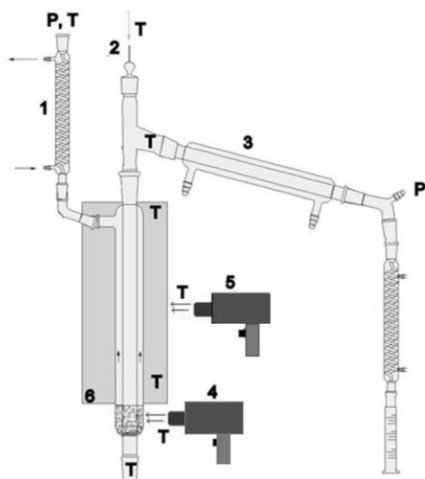
Kapitza [3] recommended that allowance for surface waves in laminar falling films be made by inserting a numerical value of 2.4 instead of 3 in equation (4). Brauer [4] determined the following relationship for turbulent falling films from optical measurements:

$$\delta_{turb} = 0,302 \left( \frac{3 v^2}{g} \right)^{\frac{1}{3}} Re^{\frac{8}{15}}, \quad Re > 400 \quad (5)$$

Equation (5) agrees well with the results obtained from semiempirical correlations derived from general laws on velocity distribution [5–7].

### Experimental equipment

In the following Figure 1 the simplified layout of the laboratory equipment is shown. It fundamentally works as vertical shell and tube heat exchanger.



1. Cooler of Dowtherm A
2. The top cap of apparatus
3. Cooler of oil
4. Heat gun for heating the Dowtherm A
5. Heat gun to compensate for heat loss from the system
6. Glass case

Figure 1 Experimental equipment description

On the Figure 1 letter P shows the places which were used for pressure measuring, letter T shows the places where thermocouples were placed to measure a temperature.

Oil fed into the equipment was pre-heated from its initial laboratory temperature, to the one close to its boiling point. Sensible heat used for this purpose was provided by heat guns located outside the body of distillation equipment. Pre-heated oil was fed into the apparatus with varying flow rates by peristaltic pump. Inside of the device the oils formed a falling film on the inner surface of the vertical tube. The equal distribution of oil along the circumference of the tube was provided by suitable distributor. Distributor should provide uniform distribution of oil on the entire circumference of inner tube. Saturated vapours of Dowtherm A were condensing on the outer surface of the tube and continuing to heat the oil on the inner surface. Once the vapours of distilled oil get into the contact with surface below their boiling point, they change their state of matter immediately.

The majority part of the equipment was made of glass. Glass has low heat conductivity. This influences the values of overall heat transfer coefficient, by decreasing them to lower values. However since it was necessary to measure behaviour of the system during the evaporation, this impact was negligible. High heat losses from the equipment were another issue during the experiment. The distillation device worked with temperatures around 300 °C. In order to minimize these losses into the environment during the measurement another outer glass tube was installed into the equipment. From the bottom of the device heat required for the boiling of Dowtherm A was provided by heat gun. Additional heat source was provided by another heat gun with heating regulation, which was blowing hot air at certain temperature between the apparatus and outer isolation. This was how the heat losses were reduced for the purpose of the experiment.

### Mathematical model

Mathematical model of the device was based on experimental equipment, Figure 1, currently used in laboratory conditions. In Figure 2 all the phenomena that take place in mathematical model of the device are shown. Mineral oil is distributed on the inner surface of the inner tube, while heating medium is supplied into the shell side (space between the tubes) of the distillation device. Evaporated Dowtherm A is used as the heating medium, which forms a condensate on the outer surface of the inner tube at atmospheric pressure. Our model works with the assumption that falling film of mineral oil is continuous. The thickness of the film slowly decreases due oil evaporation. On the shell side we considered vapour of Dowtherm A as saturated, so condensation only takes place during the heat transfer and a continuous film of liquid Dowtherm A is formed. Along the tube the thickness of the film increases.

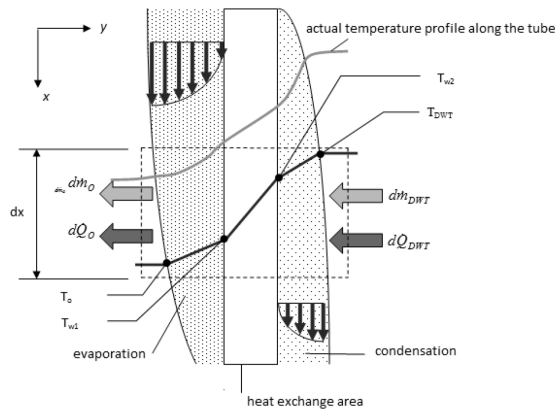


Figure 2 Temperature profile along the tube

Mathematical model was created with these assumptions

1. Each of section the tube is divided so that there is only laminar flow present. The temperature changes only along the tube and is constant in each section
2. Condensing vapour of heating medium is saturated thus only heat transfer caused by condensation takes place. Temperature of the vapour in the heating medium is constant in the entire volume of the shell side.
3. Stress on the phase boundary is negligible
4. Transfer of heat and momentum is provided only by convection, this means only the advective factor is negligible

#### Mass and energy balances:

We expect that in each of the differential segments of length  $dx$  the mass of condensing vapour is  $d\dot{m}_{DWT}$ . This causes an increase in the thickness of the film formed by the condensate. Heat given by condensing vapour in the section of the column is used either to increase the temperature of the oil, or also (after temperature reaches the boiling point) to evaporate part of the liquid oil.

For the flow analysis of the inner and outer films in a vertical tube evaporator, it is assumed that:

- (1) oil comes into the tube without turbulence
- (2) properties of the fluids are constant in an operating range,
- (3) interfacial shear forces at the film free surfaces are negligible because the surrounding steam viscosities are much smaller than the liquid films,
- (4) saturated state is maintained at the free surface of the outer condensation film,
- (5) boundary-layer approximation is adopted for the governing equations of the flow and heat transfer because the films are very thin and the flow has a distinct main flow direction.

$$d\dot{Q} = \Delta_{vyp} h \cdot d\dot{m}_{DWT} = c_p \Delta t \cdot d\dot{m}_{O,1} + \Delta_{vyp} h \cdot d\dot{m}_{DWO,2} \quad (6)$$

Previously mentioned assumptions simply says, that heat flow through phase boundary equals conductive heat flow through falling film of thickness  $\delta_{DWT}$ :

$$\dot{Q} = \Delta_{vyp} h \cdot d\dot{m}_{DWT} = \lambda_{DWT} \cdot dx \cdot W \cdot \frac{T_{DWT} - T_{w2}}{\delta_{DWT}} \quad (7)$$

Since all the calculations deal with the stationary state, heat flow continues through the wall of the tube into the boiling oil. These phenomena can be described by following equations:

$$\dot{Q} = \lambda_w \cdot dx \cdot W \cdot \frac{T_{w2} - T_{w1}}{\delta_w} \quad (8)$$

$$\dot{Q} = \lambda_o \cdot dx \cdot W \cdot \frac{T_{w1} - T_o}{\delta_o} \quad (9)$$

The iterative procedure of solving and updating was used.

## Results

The following Table 1 shows the measured mass flows of mineral oil which is supplied to the experimental laboratory equipment and the mass flows of distillate.

Table I The measured mass flows of feed and distillate

measurement	1	2	3	4	5	6	7
$\dot{m}_F \cdot 10^4 [kg s^{-1}]$	1.43	1.05	1.09	1.27	1.43	1.87	1.87
$\dot{m}_D \cdot 10^4 [kg s^{-1}]$	1.26	1.03	0.95	1.14	1.16	1.72	1.58
yield [%]	88.1	97.9	86.8	90.0	81.4	91.9	84.34

The temperatures in various points in the entire experimental device were measured using a system of thermocouples. Temperature on the site, where evaporation of oil takes place, was controlled by pressure level altered by an oil vacuum pump. A heat gun with regulation of temperature provided hot air into the space between the outer glass shell of the apparatus and the outer isolation. This helps to further reduce the heat loss from the shell side to minimum during measurement.

Variation of the local convection coefficient of the inner and outer film along the tube axis direction for various pressures of evaporation are shown on Fig. 3 and Fig.4. From Fig.3 it is evident the decrease of heat transfer coefficient of Dowtherm A from values of thousands of  $W \cdot m^{-2} \cdot K^{-1}$  to values of hundreds. This effect is probably due to the rapid increase of thickness of liquid film of condensate. On the other side the heat transfer coefficient of oil gently increased, which is result of evaporation of oil and consequential decrease of thickness of oil film.

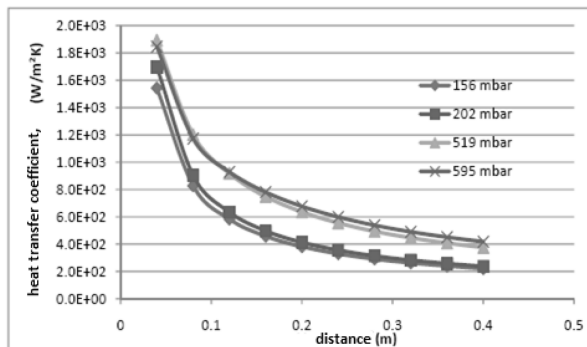


Figure 3 Heat transfer coefficients of Dowtherm A along the tube

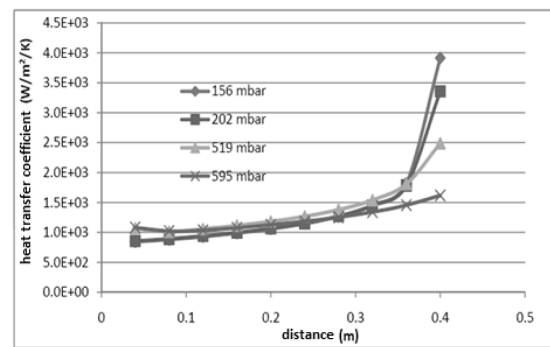


Figure 4 Heat transfer coefficients of oil along the tube

Among all of the measured temperatures the most important are the temperature of condensing Dowtherm A and the temperature of oil vapours leaving the inner tube or temperatures of wall in appropriate place of condensation or evaporation. These temperatures are shown in the Figure 5 for pressure of 20 kPa.

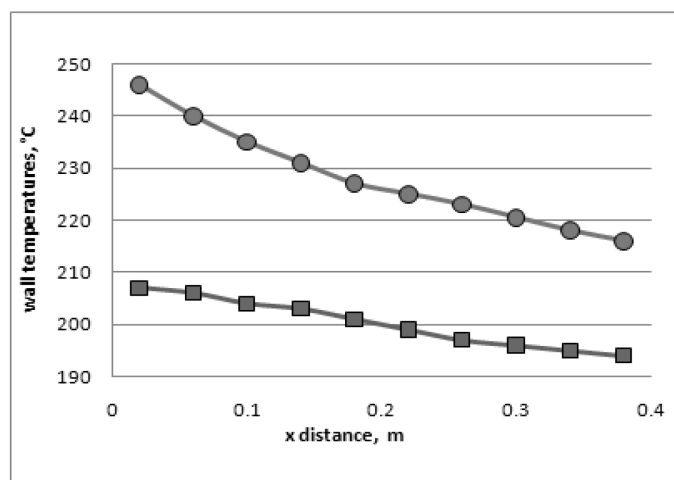


Figure 5. Variation of the mean wall temperatures of the inner and outer film along the tube axis direction for pressure 20 kPa

## Conclusions

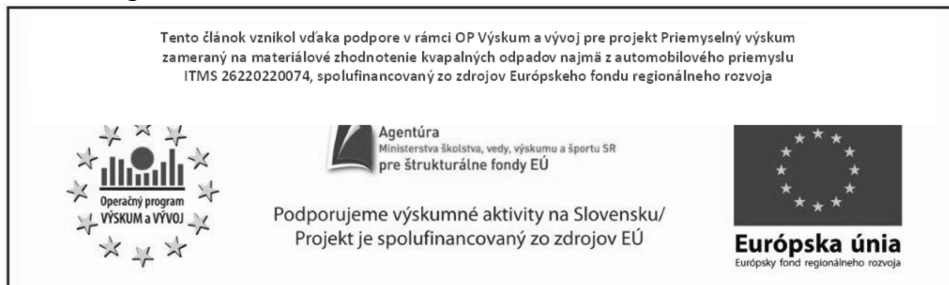
Mathematical model is based on the assumption that laminar falling films in the vertical direction are formed along the walls of the evaporator. Volumetric flow and temperature of waste oil fed into the device were measured before entering the evaporator. Temperature of oils vapor was measured by thermocouples placed inside the experimental device. Using the measured data we were able to calculate changes in laminar film thickness and also the thickness of film formed by condensing Dowtherm A. The calculations were used to evaluate the heat transfer coefficients. These coefficients have crucial role in falling film device design.

Our mathematical model was able to closely describe processes in the falling film evaporator. Even though some of models parameters had to be altered the calculated yield of distillation was close to the measured one.

## Literature

- [1] Frank P. Incropera, David P. DeWitt , Fundamentals of Heat and Mass Transfer. New York, JOHN WILEY & SONS, 1996
- [2] Nußelt W (1916) Die Oberflächenkondensation des Wasserdampfes. VDI-Zeitschrift 60:542–575
- [3] Kapitza PL (1948, 1949) Wellenströmung der dünnen Schichten einer viskosen Flüssigkeit. J ExpTheoretPhys (UdSSR) 18(1):3–18; 19(2):105–120
- [4] Brauer H (1956) Strömung und Wärmeübergang bei Rieselfilmen. VDI-Forsch., Heft 457
- [5] Kosky P (1971) Thin liquid films under simultaneous shear and gravity forces. Int J Heat Mass Transfer 14:1220–1224
- [6] Kutadladze S Fundamentals of heat transfer. Edward Arnold, London.
- [7] Portalsky S (1963) Studies of falling liquid film flow. ChemEngSci 18:787–804
- [8] Bays GS, McAdams WH (1937) Heat transfer coefficients in falling film heaters. Ind Eng Chem 29(11):1240–1246
- [9] Schnabel G (1980) Bestimmung des örtlichen Wärmeüberganges bei der Fallfilmverdampfung und Kondensation an gewellten Oberflächen zur Auslegung von Hochleistungsverdampfern. Diss. Univ. Karlsruhe
- [10] VDI- Gesellschaft Verfahrenstechnik und Chemieingenieurwesen (GVC) : VDI-Heat Atlas, Second edition Springer-Verlag, Heat Transfer to Falling Films at Vertical Surfaces, Heidelberg 2010, 1287-1294

## Acknowledgments



*Authors of this contribution want to thank for financial support from the Structural Funds of EU project in progress: "Industrial research focused on recycling the liquid waste, mainly from the automotive industry", ITMS: 26220220074.*

# THE DEGRADATION OF RESIDUES OF DRUGS IN WASTEWATER USING PHOTOCATALYSIS WITH TITANIUM DIOXIDE

Kořínková J.<sup>1</sup>, Bauerová D.<sup>1</sup>, Machalický O.<sup>2</sup>

<sup>1</sup>Univerzity of Pardubice, Faculty of Chemical Technology, Department of Environmental and Chemical Engineering, Studentská 95, 532 10, Pardubice

<sup>2</sup>University of Pardubice, Faculty of Chemical Technology, Institute of Organic Chemistry and Technology, Studentská 95, 532 10, Pardubice

[jaroslava.korinkova@upce.cz](mailto:jaroslava.korinkova@upce.cz)

## Introduction

Nowadays, techniques used to remove residues of pharmaceuticals from wastewater do not work with sufficient effectiveness. Disturbing information about the presence of some drugs in drinking water appear as more and more often in recent years, thus the issue is becoming a new environmental problem facing the world. More than a hundred species of medicinal products in groundwater, surface water and wastewater has been proved.

One of the possible solutions to the problem of cleaning such waste water is photocatalytic degradation<sup>1-4</sup>.

Titanium dioxide is often used as a catalyst. Among its advantages belong high photocatalytic activity, low cost, stability in water systems and low toxicity to the environment.

This work is focused on the use of heterogeneous photocatalysis for treatment of wastewater containing ibuprofen and paracetamol (Fig. 1) as model drugs. The aim was to achieve such concentrations of drug residues in water, which no longer pose risk to the environment and living organisms.

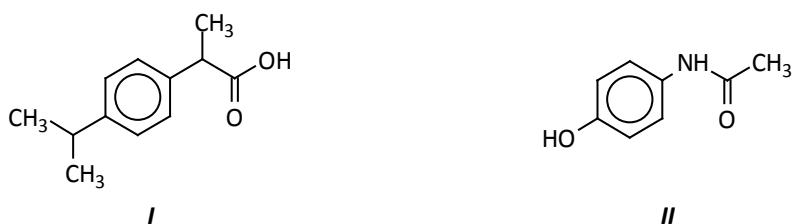


Figure 1. Chemical formulas of ibuprofen (I) and paracetamol (II)

## Results and discussion

Photochemical reactor used for degradation of selected drugs, emission spectrum and the distribution curve of radiation emitted by an arc high-pressure Hg lamp HPL-N-125 W are shown in Fig. 2.

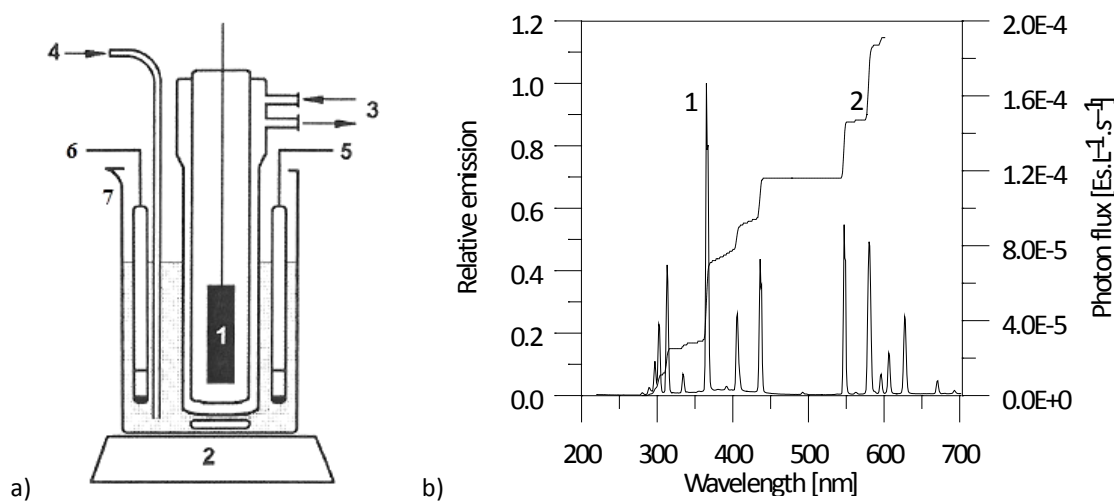


Figure 2. a) Immersion photoreactor: 1-radiation source, 2-magnetic stirrer, 3-cooling water, 4-oxygen inlet, 5-oxygen electrode, 6-pH electrode, 7-reactor vessel; b) The spectrum of the incident radiation (relative intensity, curve 1) and the photon flux (curve 2)

The decrease of concentration of ibuprofen (in form of sodium salt) by 50% after 70 min photolysis without the presence of  $\text{TiO}_2$  and constant  $\text{O}_2$  concentration (about 37 g/L) is shown in Fig. 3. The use of hydrogen peroxide resulted in a decrease of photolysis time to less than 50 min and also the decrease in the number of products of photolysis (as compared to using only  $\text{O}_2$ ).

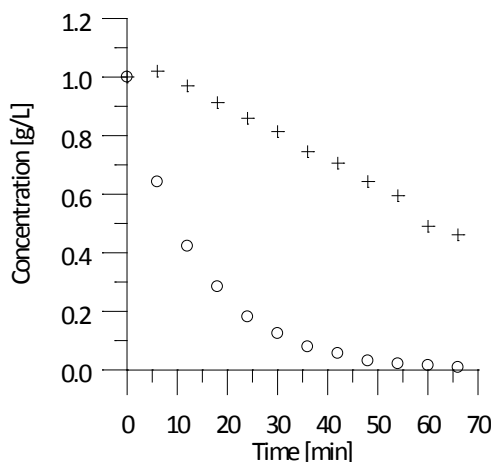


Figure 3. Concentration of ibuprofen depending on irradiation time without  $\text{TiO}_2$ ; using oxygen (+), using  $\text{H}_2\text{O}_2$  (O)

Heterogeneous photolysis of ibuprofen was also tested in suspensions containing 1-4 g/L of  $\text{TiO}_2$ , with oxygen as oxidizing agent. A very little influence of a catalyst concentration on the rate of photolysis is shown in Fig. 4a. The degree of conversion was over 70 min to about 60% at concentration 1 g/L of  $\text{TiO}_2$  and to about 80% at concentration 4 g/L of  $\text{TiO}_2$ . The exchange of oxygen as oxidizing agent for hydrogen peroxide significantly accelerated decomposition. Kinetic data of photolysis of ibuprofen using hydrogen peroxide and 1 g/L  $\text{TiO}_2$  are given in Fig. 4b. Complete decomposition of ibuprofen was achieved in the presence of peroxide after about 38 min but the reaction mixture contained residues of unreacted organic substances; but after 60 min no organic compounds were detected therein.

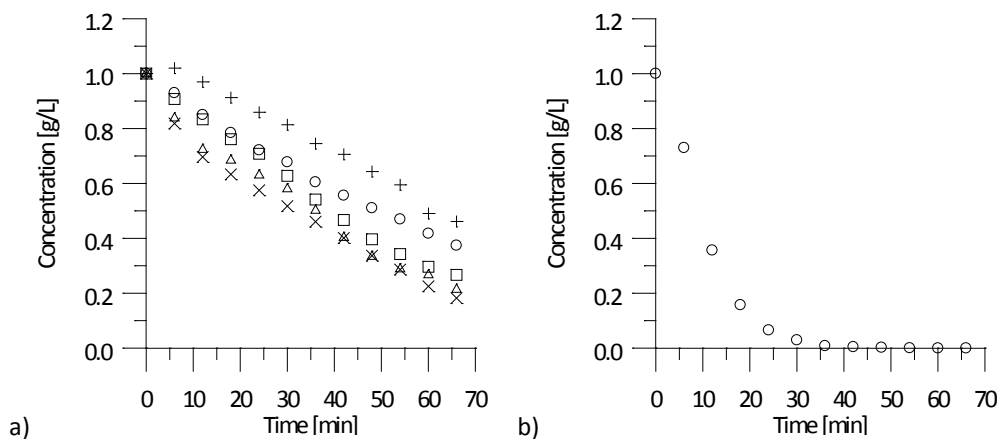


Figure 4. The dependence of ibuprofen concentration on irradiation time a) in the presence of  $\text{O}_2$  and different concentrations of  $\text{TiO}_2$ : 0 g/L (+), 1 g/L (O), 2 g/L (□), 3 g/L (△) and 4 g/L (x)  $\text{TiO}_2$ ; b) in the presence of  $\text{H}_2\text{O}_2$  with 1 g/L  $\text{TiO}_2$

The dependence of the concentration versus time for photolysis of paracetamol is depicted in Fig. 5. Practically no decrease of concentration during the irradiation without the presence of  $\text{TiO}_2$  and constant  $\text{O}_2$  concentration was observed even after about 110 min.

The exchange of oxygen for hydrogen peroxide has decreased the concentration of paracetamol by 50% after 110 minutes of irradiation.

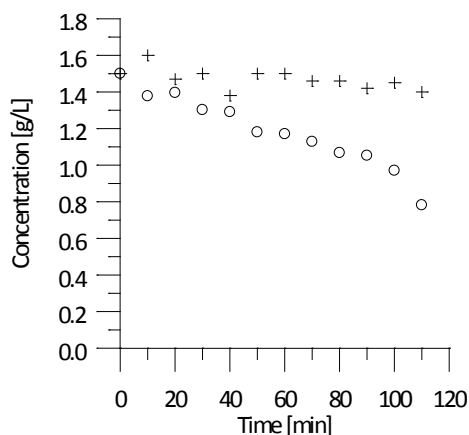


Figure 5. The dependence of the concentration of paracetamol on the irradiation time without  $\text{TiO}_2$  and using oxygen (+) or  $\text{H}_2\text{O}_2$  (O)

Heterogeneous photolysis of paracetamol was also tested in the suspensions containing  $\text{TiO}_2$  from 1 g/L to 4 g/L, and with oxygen as oxidizing agent. The dependence of a catalyst concentration on the course of photolysis is shown in Fig. 6a. Reaction rate was affected very little by increase of concentration of catalyst. The degree of conversion was about 20% at a concentration 1 g/L of  $\text{TiO}_2$  and about 30% at concentration 4 g/L of  $\text{TiO}_2$  after 110 min. By replacing oxygen with hydrogen peroxide, accelerated decomposition was achieved similarly as in the case of ibuprofen. Kinetic data on photolysis of paracetamol using hydrogen peroxide and 1 g/L of  $\text{TiO}_2$  are given in Fig. 6b.

The complete decomposition of paracetamol in the presence of  $\text{H}_2\text{O}_2$  and  $\text{TiO}_2$  was not achieved even after 110 min, but its concentration dropped most of all measurement experiments - by almost 90%.

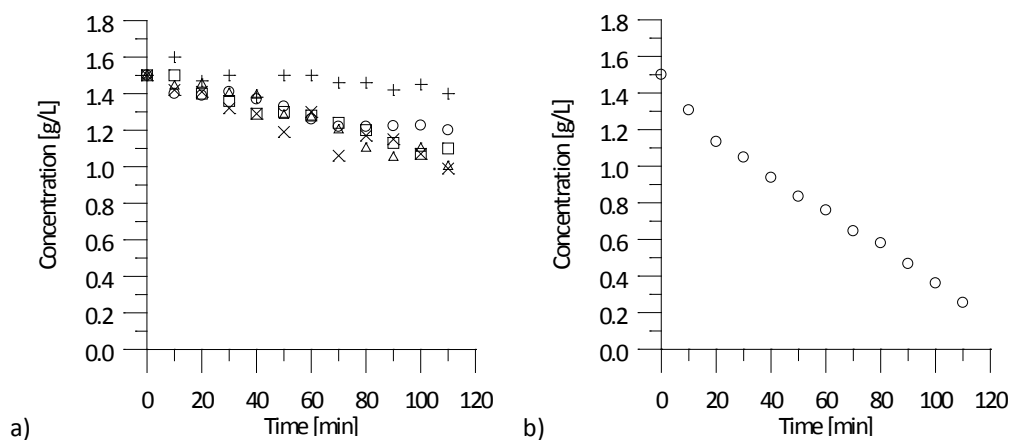


Figure 6. The dependence of paracetamol concentration on irradiation time a) in the presence of  $\text{O}_2$  and different concentrations of  $\text{TiO}_2$ : 0 g/L (+), 1 g/L (O), 2 g/L (□), 3 g/L (△) and 4 g/L (x)  $\text{TiO}_2$ ; b) in the presence of  $\text{H}_2\text{O}_2$  with 1 g/L  $\text{TiO}_2$  (O)

### Conclusion

Studying photolysis of ibuprofen, it was found that the substance decomposes under UV radiation even without using catalyst. Virtually constant rate of decomposition at  $4.0 \times 10^{-5}$  M/min was observed under the irradiation of  $4.9 \times 10^{-3}$  M ibuprofen at constant concentration of oxygen. Kinetics of homogeneous photolysis of ibuprofen using hydrogen peroxide (at starting concentration 1.2 g/L) showed an exponential character with an initial rate  $23 \times 10^{-5}$  M/min.

Photolysis intermediates were detected during oxidation using oxygen but complete mineralization of the sample was not achieved. On the other hand, no intermediates were detected and complete mineralization was achieved during photolysis of ibuprofen in the presence of hydrogen peroxide.

Addition of  $\text{TiO}_2$  catalyst in a concentration of 1 g/L and the use of  $\text{O}_2$  as oxidizing agent practically did not increased rate of photolysis ( $4.6 \times 10^{-5}$  M/min) compared with reaction without a catalyst. Increasing the

catalyst concentration to 4 g/L, the reaction rate increased only slightly to  $5.4 \times 10^{-5}$  M/min. A lot of reaction intermediates were observed under these conditions and no complete mineralization occurred; the nature of these products was different from ones raised by photolysis of ibuprofen with oxygen without a catalyst.

When using hydrogen peroxide at initial concentration 1.2 g/L and the concentration of  $\text{TiO}_2$  1 g/L the initial rate of photolysis  $26 \times 10^{-5}$  M/min was almost the same in comparison with homogeneous photolysis with  $\text{H}_2\text{O}_2$ . Under these conditions a complete mineralization of the sample of ibuprofen was achieved.

When studying the photolysis of paracetamol, it was found that the substance did practically not decompose without the use of a catalyst and at constant oxygen concentration (about 37 g/L). Using hydrogen peroxide (1.2 g/L) only slow decrease in the concentration of paracetamol ( $3.8 \times 10^{-5}$  M/min) was observed.

The use of  $\text{TiO}_2$  in concentration of 1-4 g/L and oxygen 37 g/L had practically no influence on the rate of photolysis of paracetamol ( $3-3.6 \times 10^{-5}$  M/min) compared with the reaction without a catalyst.

When using hydrogen peroxide in an initial concentration 1.2 g/L and the concentration 1 g/L of  $\text{TiO}_2$  the important initial rate of photolysis  $12 \times 10^{-5}$  M/min have been observed.

Based on the above findings, we can conclude that the method of photochemical degradation using titanium dioxide is a method effective especially in combination with hydrogen peroxide, and can thus be used for the removal of residues of drugs from wastewaters.

### **Acknowledgement**

*This work was supported by student grant SGSFChT\_2015006.*

### **Literature**

1. Jacobs L. E., Fimmen R. L., Chin Y., Mash H. E., Weavers L. K.: Fulvic acid mediated photolysis of ibuprofen in water, *Water Research* 45, 4449-4458 (2011).
2. Castell J. V., Gomez-L M. J., Miranda M. A., Torera I. M.: Photolytic degradation of Ibuprofen. Toxicity of the isolated photoproducts on fibroblasts and erythrocytes, *Photochemistry and Photobiology* 46, 6, 991-996 (1987).
3. Manu B., Mahamood S.: Enhanced degradation of paracetamol by uv-c supported photo-Fenton process over Fenton oxidation, *Water Science and Technology*, 64, 12, 2433-2438 (2011).
4. Velichkova F., Julcour-Lebigue C., Koumanova B., Delmas H.: Heterogeneous Fenton oxidation of paracetamol using iron oxide (nano)particles, *Journal of Environmental Chemical Engineering* 1, 1214-1222 (2013).

## ASSESSMENT OF SELECTED OPTIONS IN OPERATION OF WATER TREATMENT PLANT IN PILSEN BY MEANS LCA

**Klimtová M.**<sup>1</sup>, Kočí V.<sup>2</sup>

<sup>1</sup> VODÁRNA PLZEŇ a.s., Malostranská 2, 317 68, Pilsen, Czech Republic

<sup>2</sup> Department of Environmental Chemistry, Faculty of Environmental Technology, UCT Prague, Technická 5, 166 28 Prague, Czech Republic

*martina.klimtova@vodarna.cz*

*Vlad.koci@vscht.cz*

### Abstract

Water treatment plant in Pilsen (Czech Republic) uses as the source of raw water the surface water from a river. Water treatment technology is set with respect to variable quality of raw water. Some technological units are exacting for consumption of chemicals, others for electrical energy consumption. In this paper, we evaluated the waterworks facility of the WTP in Pilsen from an environmental point of view using the LCA (Life Cycle Assessment) method. In the previous studies, we evaluated waterworks facility in Pilsen using LCA as a whole. We used the obtained results and we concentrated on selected technological part of the waterworks operation. First, we compared environmental impacts of two specific coagulants - alum and ferric, by means of method LCA. Based on the results of the inventory and characterization analyses, we found out that the technology of water treatment which uses a ferric coagulant has a lower environmental impact.

Very interesting topic for WTP in Pilsen is consumption of electrical energy. A part of WTP in particular demanding in terms of the electrical energy is the distribution of produced water. Distribution of produced water into reservoirs is energy-intensive. The objective of this paper is also interpretation of the results of inventory analysis and Life Cycle Impact Assessment (LCIA) for the current state of water treatment plant with the use of all electricity from electricity grid. For comparison, we made different models that use electrical energy from alternative sources (e.g. solar, natural gas). We established the option with electricity from natural gas as the most suitable with respect to the environment.

### Introduction

We live in a period when the greater part of the civilized world starts to question its actions in relation to the environment. Environmental view appears in various fields of human activity, waterworks are no exception. Within the last few years, we encounter the development of new methods that can assess the impacts of human activities in relation to the environment. The methodology provides information about the environmental impacts of different production processes and it is a valuable tool for evaluating and comparing the impacts on the environment, for example LCA<sup>1</sup>, SEA<sup>2</sup>, EIA<sup>3</sup>. The Life Cycle Assessment (LCA) methodology enables calculating the environmental impacts on products, processes or services over its entire life cycle (from cradle to grave). The environmental impacts are classified in different impact categories (e.g. resource depletion, global warming, acidification, eutrophication, human toxicity, human health etc.). There was a number of interesting papers published concerning the application of LCA in the facility of drinking water production<sup>4,5</sup>.

The objective of this paper is to apply the method LCA to assess the water treatment plant in Pilsen (CZ), which uses surface water from the river Úhlava as a source of raw water. The main objective of our study was to compare the environmental impacts of the coagulants - aluminum sulphate and ferric sulphate and evaluate which option is better from an environmental perspective. Drinking water production process in the WTP in Pilsen is energy-intensive, this is true especially for some technology units (e.g. pumping of raw and treated water, distribution of treated water into reservoirs). For these reasons, we used models of alternative electricity sources for the operation of WTP in Pilsen and we assessed individual processes using LCA. We compared the process of drinking water production using electricity grid mix of the Czech Republic to the same technological process with the use of alternative sources of electricity production.

### Methodology and materials

Life cycle assessment is a tool to assess the potential environmental impacts and resources used throughout a product's life cycle, i.e. from raw material acquisition, via production and use phases, to waste management. The environmental impacts of all these stages are evaluated in the context of the method. All emissions of substances into the environment are counted at all stages of entire life cycle of the product. The obtained sums of emissions related to a specific amount of the product<sup>6,7</sup>. Life cycle assessment calculates all emissions, raw materials consumption, related environmental and health impacts, and resource depletion associated with any

goods or services throughout its life cycle. The LCA was performed according to the ISO framework. The method LCA complies with requirement of DIN EN ISO 14040<sup>11</sup> and 14044<sup>12</sup>. The LCA phase called the Life Cycle Impact Assessment (LCIA) quantifies all material and energy flows throughout the entire life cycle of product. The output data set is used to assign the results to particular categories of impact (for example resource depletion, global warming, acidification, eutrophication, human toxicity, human health etc.) and quantification of the extent of their exposure<sup>8</sup>. Mutual comparison of the different impact categories is allowed thanks to the development of characterization models and methodologies for LCA method, for example CML 2001<sup>9</sup>, EDIP, IMPACT 2002<sup>+</sup>, Recipe, USEtox<sup>10</sup>.

### **Product system description and system boundary**

The Water Treatment Plant in Pilsen uses the surface water from the river Úhlava as the source of water. The quality of the surface water is very variable. Technological line consists of two separate stages. Coagulant – aluminum sulphate is dosed into the raw water. After the homogenization, the water is discharged into settling tanks – it is the first separation stage. After the separation of the emerged flakes the water flows to the system of rapid filters – it is the second separation stage. The filtered water continues to the ozonization. The ozone is produced in the generator from dried air. In the next part of technological line the calcium hydroxide (lime water) and carbon dioxide are dosed into the treated water. In the storage tanks chlorine is added into the water. The function of chlorine is to secure the water hygienically<sup>13</sup>. After treatment, drinking water is pumped into the urban reservoirs. Later on, potable water is supplied to the population (approximately 180 000 inhabitants) by distribution network in Pilsen.

The functional unit is 1 m<sup>3</sup> of produced drinking water. We used the operation data from the year 2012 for calculations.

We considered the boundary of system assessment in following stages: raw water pumping - drinking water treatment - the production of chemicals, fuels and electricity consumption - the transportation of chemicals - sewage collection - wastewater treatment and disposal - potable water pumping into reservoirs. The distribution network of drinking water in Pilsen is complicated, it consists of 592 km of water distribution pipes, 12 water-pumping stations, 5 delivery points of drinking water, 6 water storage tanks and various pressure zones. The assessment of distribution of drinking water through water network is not included in this study.

### **Coagulation in the WTP**

The coagulant based on aluminum - aluminum sulphate is used in the WTP in Pilsen. This coagulant – aluminum sulphate complies with raw surface water experimentally and operationally. The technology of WTP is optimal for alum. For comparison, we considered coagulant based on iron - ferric sulphate. Ferric sulphate dosage was tested in the WTP in the past. For this option we calculated average dose of ferric sulphate, which is quantitatively related to the required dose of aluminum sulphate. Dosing of ferric sulphate brings along an increase in the consumption of lime and carbon dioxide by approximately 20%. This fact was also practically verified during the testing of ferric sulphate in the WTP in Pilsen. The coagulation with ferric sulfate proceeds at lower pH (4.5 - 5) than coagulation with aluminum sulphate<sup>14</sup>, this difference needs to be compensated by more intensive hardening of water before its distribution.

### **Results and discussion - coagulation**

In the inventory phase, we have compared the output values of raw materials used for both coagulants - aluminum sulphate (using) and ferric sulfate (alternative model). For clarity, we compared five economically important raw materials that are consumed to produce 1 m<sup>3</sup> of drinking water (crude oil, natural gas, hard coal, lignite, uranium). For all raw materials, the consumption was lower for the option with ferric coagulant. The Table I summarizes the results of selected impact categories. The table shows the output data using the characterization methodology CML 2013. Characterization CML methodology is based on midpoint impact category indicators. The values of all impact category indicators were higher in case of using aluminum sulphate for water treatment. It is obvious that the most striking differences are for the impact category abiotic depletion and global warming. These results clearly speak for the choice of ferric sulfate, which would reduce the environmental impact of the coagulation process.

Table I

Impact category results in the production of 1 m<sup>3</sup> drinking water in the WTP in Pilsen - using methodology CML 2013.

Indicators of impact category	Alternative coagulant	
	Al <sub>2</sub> (SO <sub>4</sub> ) <sub>3</sub>	Fe <sub>2</sub> (SO <sub>4</sub> ) <sub>3</sub>
Abiotic Depletion (ADP elements) [kg Sb-Equiv.]	1.15E-07	6.64E-08
Abiotic Depletion (ADP fossil) [MJ]	1.17E+01	6.53E+00
Acidification Potential (AP) [kg SO <sub>2</sub> -Equiv.]	4.70E-03	3.71E-03
Eutrophication Potential (EP) [kg Phosphate-Equiv.]	2.83E-04	2.37E-04
Freshwater Aquatic Ecotoxicity Pot. (FAETP inf.) [kg DCB-Equiv.]	1.76E-03	8.82E-04
Global Warming Potential (GWP 100 years) [kg CO <sub>2</sub> -Equiv.]	9.64E-01	7.18E-01
Human Toxicity Potential (HTP inf.) [kg DCB-Equiv.]	2.71E-02	2.01E-02
Marine Aquatic Ecotoxicity Pot. (MAETP inf.) [kg DCB-Equiv.]	2.78E+01	2.16E+01
Ozone Layer Depletion Potential (ODP, steady state) [kg R11-Equiv.]	4.57E-08	-2.26E-09
Photochem. Ozone Creation Potential (POCP) [kg Ethene-Equiv.]	3.49E-04	2.28E-04
Terrestrial Ecotoxicity Potential (TETP inf.) [kg DCB-Equiv.]	1.25E-03	1.12E-03

### Electricity in the WTP

The current operation of water treatment plant in Pilsen uses all its electricity from electricity grid. Considering that current energy mix of the Czech Republic, the majority part of the energy comes from the conventional resources. The extreme energetic intensity of some technological units (e.g. treated water pumping into the urban reservoirs, raw water pumping, ozonization) made us consider the alternative energy resources. First, we developed a model for the alternative solar energy related to the photovoltaic phenomenon. All necessary data and information concerning the production of photovoltaic cells has provided the company Lintech-solar<sup>15</sup>. This company based in Pilsen region is an independent producer of photovoltaic panels. For comparison, we have prepared two variants of photovoltaics representation of the total yearly consumption of electricity - 11% and 100% of photovoltaics. The value of the first proportion - 11% of the total yearly consumption of electricity is calculated from the real possibilities of water treatment plant. We considered every possible surface (roofs of buildings, roofs of underground storage tanks) for the theoretical location of the photovoltaic panels (4000 panels). The conversion of electrical energy produced related to the local climatic conditions corresponded to 11% of the electricity of the total annual consumption in the year 2012. The storage batteries and frequency converters are not considered in these variants of photovoltaics.

### Results and discussion - electricity

In the inventory phase, we compared the output values of these raw materials (crude oil, natural gas, hard coal, lignite, uranium) used in the operation of WTP for following options: the current state of the WTP, the option 11% substitution of the electricity grid by photovoltaic, the option with full replacement of electricity grid by photovoltaics and the option natural gas. The downward trend of values was legible for each of the listed raw material starting with the current state, through different alternatives with various contribution of photovoltaic, down to alternative of natural gas. The Table II summarizes the results of selected impact categories. The table shows the output data using the characterization methodology CML 2013. From the given results, there is a noticeable decrease in the majority of impact categories comparing the alternatives to the current state of operation. We can see the sharp decline for the impact category - global warming, acidification and photochem. ozone creation. Conversely, only slight difference is between the current state of operation of WTP and 11% share of photovoltaic, which represents real technical possibilities of photovoltaic. Use of electricity from natural gas (self generation) or from solar energy would significantly reduce the environmental impact of the entire process of WTP in Pilsen, because some technological parts (raw water pumping, treated water distribution, ozonization, coagulation) are very energy-intensive.

Table II

Impact assessment results associated with the production of 1 m<sup>3</sup> drinking water in the WTP in Pilsen- using methodology CML 2013.

Indicators of impact category	Alternative energy supply			
	Current WTP	11% of photov.	100% of photov.	Natural Gas
ADP elements [kg Sb-Equiv.]	1,15E-07	1,15E-07	1,09E-07	9,65E-08
ADP fossil [MJ]	1,17E+01	1,12E+01	6,74E+00	1,20E+01
AP [kg SO <sub>2</sub> -Equiv.]	4,70E-03	4,30E-03	1,06E-03	1,31E-03
EP [kg Phosphate-Equiv.]	2,83E-04	2,68E-04	1,40E-04	1,49E-04
FAETP inf. [kg DCB-Equiv.]	1,76E-03	2,08E-03	4,74E-03	1,17E-03
GWP 100 years [kg CO <sub>2</sub> -Equiv.]	9,64E-01	9,09E-01	4,59E-01	7,80E-01
HTP inf. [kg DCB-Equiv.]	2,71E-02	2,73E-02	2,85E-02	9,96E-03
MAETP inf. [kg DCB-Equiv.]	2,78E+01	2,80E+01	2,92E+01	-2,00E+00
ODP, steady state [kg R11-Equiv.]	4,57E-08	4,59E-08	4,71E-08	4,57E-08
POCP [kg Ethene-Equiv.]	3,49E-04	3,27E-04	1,45E-04	1,84E-04
TETP inf. [kg DCB-Equiv.]	1,25E-03	1,21E-03	8,74E-04	7,53E-04

### Conclusion

The water treatment plant in Pilsen is currently in a phase of extensive reconstruction. The LCA can provide a different view of the entire operation of the water treatment plant or its individual units. We found that the coagulant – aluminum sulphate, which is optimal for technological line of WTP in Pilsen in terms of quality of treated water leaves a deeper environmental footprint than ferric coagulant. Choosing ferric coagulant enables to improve environmental impacts of the operation WTP in Pilsen. Possible change of coagulant has not been discussed in the context of the reconstruction of WTP in Pilsen, since the operator of waterworks sets the quality of water produced as the priority.

Production of electric energy consumed by the water treatment process in Pilsen plays an important role. Given the LCA results, photovoltaics is not a reasonable energy supply alternative within the current technical possibilities of the WTP in Pilsen. The alternative where the electricity is generated from natural gas provided much better results in comparison to the current situation.

Currently, the environmental view of the technological operation of WTP does not have enough scope. The project documentation covers technical and economic aspect predominantly. Hopefully, the environmental criterion will be soon of the same significance as technical and economic criteria in the waterworks in Czech Republic.

### Acknowledgments

*The authors would like to thank the management of company VODÁRNA PLZEŇ a.s. for providing operation data and the possibility of data processing. This work benefited from the support of research projects MSM 6046137308 and with the support of the Technology Agency TA02030188.*

### Literature

1. Finnveden, G., Moberg, A.: Environmental systems analysis tools – an overview. *J. Cleaner Prod.* 13, 1165-1173 (2005).
2. Finnveden, G., Hauschild, M.Z., Ekvall, T., Guinée, J., Heijungs, R., Hellweg, S., Koehler, A., Pennington, D., Suh, S.: Recent developments in Life Cycle Assessment. *J. Environ. Manage.* 91, 1-21 (2009).
3. Ness, B., Urbel-Piirsalu, E., Anderberg, S., Olsson, L.: Categorising tools for sustainability assessment. *Ecol. Economics* 60, 498-508 (2007).
4. Igos, E., Dalle, A., Tiruta-Barna, L., Benetto, E., Baudin, I., Mery, Y.: Life Cycle Assessment of water treatment: what is the contribution of infrastructure and operation at unit process level? *J. Cleaner Prod.* 65, 424-431 (2014).
5. Mery, Y., Tiruta-Barna, L., Baudin, I., Benetto, E., Igos, E.: Formalization of a technical procedure for process ecodesign dedicated to drinking water treatment plants. *J. Cleaner Prod.* 68, 16-24 (2014).
6. Kočí, V.: Life Cycle Assessment – LCA., Chrudim: Ekomonitor (2009).

7. Kočí, V.: Metoda posuzování životního cyklu a chemický průmysl. *Chemické Listy* 104, 921-925 (2010).
8. Kočí V.: Posuzování environmentálních dopadů životního cyklu. Sb. konference Posuzování životního cyklu LCA, Praha. 12-15 (2008).
9. Heijungs, R., Guinée J.B., Huppes G., Lankreijer R.M., Udoede Haes H.A., Wegener-Sleeswijk A.: Environmental Life Cycle Assessment of products. Guide and Backgrounds., Leiden: CML, Leiden University (1992).
10. Rosenbaum, R.K., Bachmann, T.M., Gold, I.S., Huijbregts, M.A.J., Joliet, O., Juraske, R., Koehler, A., Larsen, H.F., MacLeod, M., Margni, M., McKone, T.E., Payet, J., Schuhmacher, M., van de Meent, D., Hauschild, M.Z.: USEtox-the UNEP-SETAC toxicity model: recommended characterization factors for human toxicity and freshwater ecotoxicity in life cycle assessment. *Int. J. LCA* 13, 532-546 (2008).
11. Environmental Management. Life Cycle Assessment. Principles and Framework. ISO 14040: International Organization for Standardization, Geneva, CH. (2006).
12. Environmental Management. Life Cycle Assessment. Requirements and Guidelines. ISO 14044: International Organization for Standardization, Geneva, CH. (2006).
13. Klimtová, M., Kočí, V.: Life Cycle Assessment of drinking water production within Water Treatment Plant in Pilsen by LCA. *Acta Environmentalica Universitatis Comenianae (Bratislava)*, 2012.20(1) (2012).
14. Strnadová, N., Janda, V.: *Technologie vody I.*, VŠCHT Praha, 94-140 (1995).
15. General information on photovoltaics, quotes from the web: <http://www.lintech-solar.cz/obecne-ofotovoltaice>, (2013-10-11)(2013).

## DETERMINATION OF SORPTION CAPACITY OF ORGANIC VAPORS ON ACTIVATED MESOCARBONS

**Špitová B.**<sup>1,2</sup>, Koutník I.<sup>1</sup>, Večeř M.<sup>1,2</sup>

<sup>1</sup>VSB-TU Ostrava, FMME, department of Chemistry, 17. listopadu 15, Ostrava, 708 33, Czech Republic  
barbora.spitova@vsb.cz

<sup>2</sup>VSB-TU Ostrava, FMG, ICT, 17. listopadu 15, Ostrava, 708 33, Czech Republic  
marek.vecer@vsb.cz

### Abstract

Specific surface of adsorbent is one of the key factors governing its application. Proposed paper deals with alternative experimental method based on weight registration during adsorption of pure organic vapors on tested samples.

Thermogravimeter TGA-HP50 has been used for sorption experiments, where activated mesocarbon microbeads were the sorbent and vapors of benzene, toluene, acetone and cyclohexane were used as organic adsorbate. Primary data has been actual weight of the tested sorbent and absolute pressure of organic vapor.

Solid sorbents have been prepared by chemical activation of pyridine insoluble matters (PI) using potassium hydroxide. Coal tar pitch as raw material was thermally treated together with Lewis acids ( $\text{FeCl}_3$ ,  $\text{AlCl}_3$ ) as catalytic agents. Temperature of activation was 850°C.

Experimental data were fitted by Langmuir model of adsorption isotherm. Specific surface was determined from evaluated parameters.

### Key words:

Coal tar pitch, Adsorption, Chemical activation, Thermogravimeter, Specific surface

### Introduction

Adsorption plays key role in many processes such as catalytic reactions, filtrations, oxidations and corrosions, chromatographic separations, and pharma processes of severe medical products and metabolites. Porous solids are fast growing group of inorganic and organic compounds<sup>1,2</sup>.

Consequence of increasing worldwide request for cheap, available but also high quality sorbents is permanent interest for new more effective methods of its preparation. Large group of sorbents, which are focused on are sorbents based on activated carbon.

Beside conventional methods based on natural organic materials, there are also severe methods using as a raw material coal tar pitch<sup>3</sup>. Value of specific surface of activated carbons prepared from coal tar pitch could be even more than 2 500  $\text{m}^2\text{g}^{-1}$ . Process typically consists of preparation of carbon mesophase by heating of coal tar pitch at temperature about 410°C for 5 hours and following chemical activation. Chemical activation is carried out in two steps. First, the solid sample is mixed with KOH in weight ratio 1:5. Second step is heating on 850-900 °C for 1 to 5 hours with nitrogen purge at the same time. The sample is washed by 2M HCl and distilled water up to neutral pH after heating.

Present paper describes the ability of activated carbons prepared from coal tar pitch to adsorb pure organic vapors. Four different organic liquids were used as an adsorptives. Primary data were treated by model of linearized Langmuir isotherm and evaluated parameters were used for estimation of specific surface of the used activated carbons.

### Experimental

All solid adsorbents have been prepared from coal tar pitch (type S090) with softening point about 86 °C. Coal tar pitch, was thermally treated for 30 minutes in microwave oven under 600W microwave power (sample A, B, and D). Lewis acids ( $\text{AlCl}_3$  sample C,  $\text{FeCl}_3$  sample E, F) were added in different amounts as catalytic agents. After heating was solid residue extracted by pyridine (10 ml pyridine per 1g of solid residue) for severe hours. Chemical activation of pyridine insoluble (PI) matters by KOH was carried out in tube furnace afterwards (sample B was not activated). Activation temperature was 850°C and heating period was 1 hour. Then, the 2M HCl was added to neutralize residue of KOH and solid samples were washed by distilled water until pH was stable at value 7. Six solid adsorbents were prepared by this specific procedure. Conditions are listed in table 1.

Table I  
Specification of solid adsorbents

Sample	Activation	Extraction	Additives	Concentration of additives
A	Yes	Solvent + Soxhlet extractor	-	-
B	No	Solvent + Soxhlet extractor	-	-
C	Yes	Solvent + Soxhlet extractor	AlCl <sub>3</sub>	10 %
D	Yes	Reflux condenser extraction	-	-
E	Yes	Solvent + Soxhlet extractor	FeCl <sub>3</sub>	10 %
F	Yes	Solvent + Soxhlet extractor	FeCl <sub>3</sub>	2.5 %

Four pure organic volatile liquids were chosen as adsorptive: cyclohexane, benzene, toluene and acetone. Tension of saturated vapors was key parameter for adjusting measuring procedures, for cyclohexane it was 97.63 torr, 95.17 torr for benzene, 28.44 torr for toluene and 229.88 torr for acetone (T = 298.15 K, 1 torr = 133.322 Pa).

Molecular cross section areas of used organic compounds, listed in Table 2, were used for assumption of surface area of adsorbents. Calculation was based on evaluated parameters of linearized Langmuir isotherm model. Assumption of monomolecular surface layer was used and capillary condensation was neglected.

Table II  
Molecular cross section areas from literature<sup>4</sup>

	Cyclohexane [nm <sup>2</sup> ]	Benzene [nm <sup>2</sup> ]	Toluene [nm <sup>2</sup> ]	Acetone [nm <sup>2</sup> ]	Reference
VdW	0.367	0.325	0.385	0.314	[5]
Cross section (calculated)	0.431	0.441	0.481	-	[6]

VdW –calculated from van der Waals' constants

### Adsorption experiment

Thermogravimeter TGA-HP50, (see Figure 1), is equipped by special container where organic adsorptives take place as pure liquids. Solid sample is placed inside the experimental cell and its weight is measured permanently. Sample is evacuated first (pressure 0.1 torr) then dried (120°C) and finally experimental temperature is adjusted (25°C). When experimental temperature is reached the first pressure step is adjusted. Absolute pressure was different with respect on used adsorptive. Maximal value of applied pressure can't exceed value of saturated vapor tension. Breaking conditions were following: if weight is stable for 5minutes ± 0.5 w%, or duration of pressure steps exceed 1 hour. When one of the conditions was accomplished the next pressure step was applied with the same breaking conditions.

Primary experimental data were experimental time, temperature, pressure, and weight of solid sample.

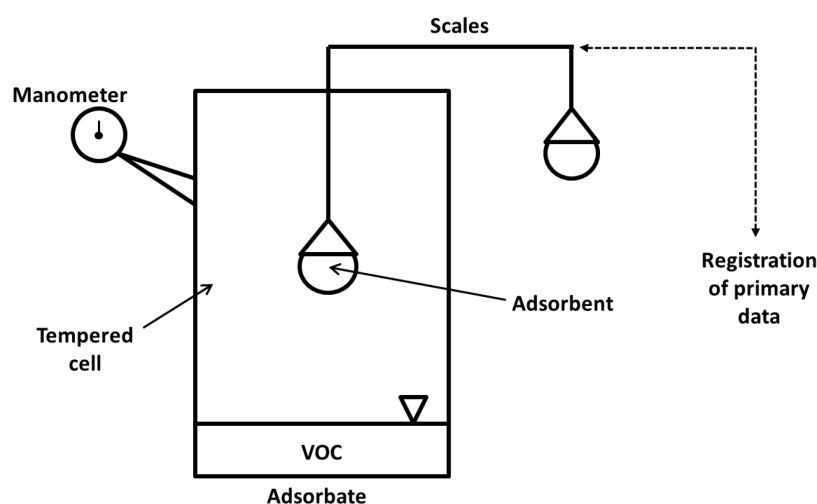


Figure 1. Principle of operation unit of thermogravimeter TGA-HP50 (TA Instruments, USA)

## Results and discussion

Determination of adsorption isotherm was carried out at temperature 25°C for pure vapors (cyclohexane, benzene, toluene and acetone) when the low pressures of saturated vapors were applied as a maximum absolute experimental pressures. Sorption capacity of each adsorbent with each adsorbate was determined. Maximum sorption capacity for cyclohexane vapors was determined for sample D. Maximum vapor uptake raises over 1g/g, see Figure 2 a). The same observation was made for benzene. Samples D and F displays similar behavior, and sorption capacity of benzene approaches value 1.1 g/g, see Figure 2 b). Determined sorption capacity of toluene is slightly lower than for cyclohexane and benzene. It corresponds to the higher molecular cross section areas reported in Table 2. Sorption capacity of acetone is lower than in others tested organic matters. Samples A, D, F approaches value 0.8 g/g, which is about 20% less than for the other tested cases. It is caused by polar character of the acetone molecule.

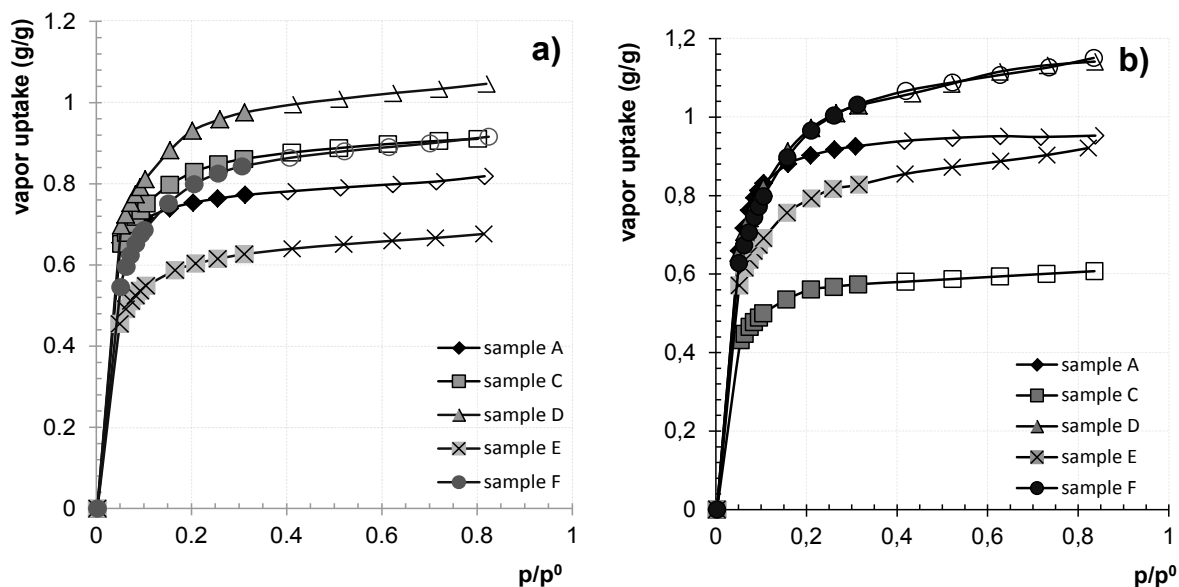
From Table 3, it is evident that all activated samples have significantly higher specific surface than sample B, which was not activated. On the other side, the addition of FeCl<sub>3</sub> on quantity of specific surface is negative regardless of concentration of additives (samples E and F). Effect of extraction procedure (Soxhlet – sample A contra reflux condenser extraction -sample D) is negligible.

The shapes of adsorption isotherms of all activated samples correspond to the types IV and IV+I, respectively, according to IUPAC classification<sup>2</sup>. This indicates the porous character of all activated adsorbents. Contrary the adsorption isotherm of nonactivated adsorbent corresponds to the type II, which indicates nonporous structure.

Activated sorbents show the specific surface area within the range of 1 231 to 3 272 m<sup>2</sup>.g<sup>-1</sup>. This property of activated sorbents corresponds to their significantly improved textural properties compared to the nonactivated one. While nonactivated mesocarbon (sample B) shows the specific surface area only within the range of 9.3 to 110 m<sup>2</sup>.g<sup>-1</sup>, activated ones possess the specific surface area of two orders of magnitudes higher. It can be concluded that the chemical activation of the carbon mesophase by KOH has a positive effect on the textural properties of produced sorbents. There is no effect of type of extraction procedure and the effect of addition of FeCl<sub>3</sub> and AlCl<sub>3</sub> on textural properties was found negative too.

Table III  
Surface areas of tested adsorbents (m<sup>2</sup>/g)

Sample	Organic volatile liquids			
	Cyclohexane	Benzene	Toluene	Acetone
A	2 327	3 045	2 629	2 634
B	9.3	68	36	110
C	2 551	1 869	2 097	788
D	2 859	3 272	2 344	2 070
E	1 855	2 675	1 313	1 578
F	2 453	3 246	1 555	2 244



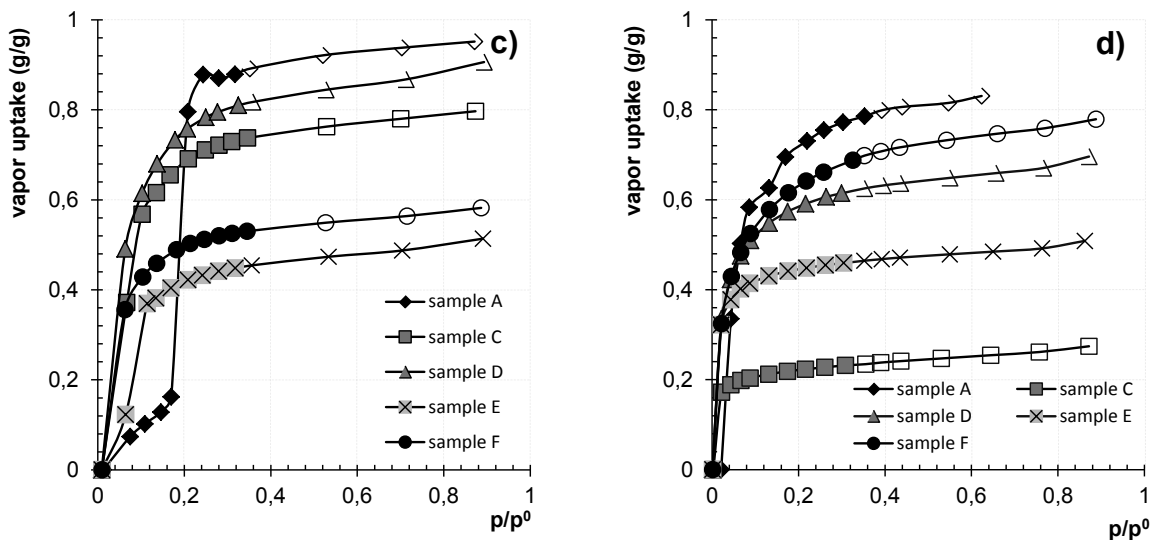


Figure 2. Adsorption isotherms of a) Cyclohexane, b) Benzene, c) Toluene, d) Acetone for activated sorbents at 25 °C

For calculation of specific surface area was used linearized model of Langmuir isotherm. For calculation of Langmuir parameters, were used points up to value of relative pressure 0.3. Counted data are shown as solid points at the Fig. 2. Open points are just for illustration of trends up to higher relative pressures. Calculated specific surface areas based on sorption experiments with organic volatile liquids are listed in table 3.

### Conclusion

Six solid sorbents were prepared from coal tar pitch by heating in microwave oven. Lewis acids were used as additives enhancing resulting surface area and pore volume. Effect of addition  $\text{FeCl}_3$  and  $\text{AlCl}_3$  is negligible (samples C, E and F). Chemical activation is of crucial importance (sample B is not activated).

Sorption capacity of prepared sorbents was tested on thermogravimeter TGA-HP50. Four pure organic liquids were used as adsorptives. It is evident, that all activated samples are suitable for capturing of selected adsorptives.

High pressure thermogravimeter TGA-HP50 seems to be suitable apparatus for sorption experiments of organic vapors.

### Acknowledgment

Generous support of this study by projects ICT- Sustainability program (LO1406) and Specific student project SP2015/76 is gratefully acknowledged.

### Literature

1. Rouquerol F., Rouquerol J., Sing K.: *Adsorption by powders and porous solids: principles, methodology, and applications*. Academic Press, San Diego 1999.
2. Bansal R.Ch., Meenakshi G.: *Activated carbon adsorption*. Taylor, Boca Raton 2005.
3. Fuhu L., Weidong Ch., Zengmin S., Yixian W., Yunfang L., Hui L.: Activation of mesocarbon microbeads with different textures and their application for supercapacitor. *Fuel Process Technol*; 91:17–24 (2010).
4. Věčeř M., Špitová B., Koutník I.: *J Therm Anal Calorim.*, in press.
5. Gray M.J., Mebane R.C., Womack H.N., Rybolt T.R.: Molecular Mechanics and Molecular Cross-Sectional Areas: A Comparison with Molecules Adsorbed on Solid Surfaces. *J Colloid Interf Sci.*; 170(1):98-101 (1995).
6. Livingston H.K.: The cross-sectional areas of molecules adsorbed on solid surfaces. *J Colloid Interf Sci.*; 4(5):47-458 (1949).

## BIOTIC METHODS FOR IDENTIFYING THE EFFECTS OF POLYPHENOLIC COMPOUNDS IN THE AQUATIC ENVIRONMENT

**Kobetičová K.**, Losonszky G., Pařízek O., Kočí V.

*Department of Environmental Chemistry, Faculty of Environmental Technology, University of Chemistry and Technology, Technická 5, 166 28 Prague, Czech Republic*  
*Klara.Kobeticova@vscht.cz*

### Introduction

Tannins belong among the polyphenolic compounds. Commonly used in industry for leather tanning, to produce iron gall ink or medicines, that is used against internal parasites and against bleeding. Natural tannins may also occur in food (tea, wine, fruits). Data of toxicities tannin are given for acute toxicity LD<sub>50</sub> in the rat by oral ingestion of amounts of 2,260 mg/kg. Information on ecotoxicity tannin is only available for the species of mosquito fish (*Gambusia affinis*), which was measured LC<sub>50</sub> at 96-hour exposure of 37 g/l. Other data currently not available, therefore this thesis deals with obtaining information on the effects of tannin for other selected representative model organisms from other groups.

For this study was selected tannin industrially manufactured (Merck)<sup>1</sup>. This was tested using a battery of ecotoxicity tests with Daphnia (*Daphnia magna*), enchytraeids (*Enchytraeus crypticus*), freshwater algae (*Desmodesmus subspicatus*) and mustard plant species (*Sinapis alba*) in aquatic arrangement. All tests were carried out under controlled conditions according to relevant methodologies<sup>2,3,4,5</sup>. The assay endpoints were: daphnia immobilization, enchytraeid mortality, mustard seed root length and algae growth rate and yield. For each test concentration range was chosen to obtain the 50% effective concentration for each measured endpoint. The effective concentrations were calculated by Statistical programme GraphPad Prism, version 5 (non-linear regression, the method of the least squares)<sup>6</sup>.

### Materials and methods

#### Test methodologies

#### Daphnia test<sup>2</sup>

Dissolved oxygen was measured in the test water to ensure intensive aeration of the dilution water before the test. Daphnia (up to 24 hours old) were caught in a beaker with dilution water. The test containers were prepared by dilutions of the test substances together with test in duplicates. 50 ml of the test solution was measured into a 100 ml beaker into which daphnia were deployed in the number of 10 individuals. Daphnia were deployed in beakers using a plastic pipette. Beakers wearing Daphnia were entered into the termostate at temperature 26 ± 1 °C. Immobilization was observed after 24 and 48 hours of exposure.

#### Enchytraeid test<sup>3</sup>

Reconstituted water was prepared. Subsequently, dilution series were prepared solutions of the test substances in concentrations of water-reconstituted 125; 250; 500; 1,000; 2,000 mg/l including control. 50 ml of the test solution was decanted into 100 ml beaker, into which was enchytraeid divided (into each beaker was put 10 enchytraeid). For each concentration were prepared by two parallels, including controls. Beakers containing enchytraeid been thoroughly covered to be adhered to during the test condition in the dark, and entered into the thermoluminostat at 20 ± 2 °C. Per 24 hours were recorded individuals make a living (dead enchytraeid which did not respond to mechanical stimuli were removed from the test vessels).

#### Algae test<sup>4</sup>

With a microscope, cell numbers were subtracted in 1 ml algal inoculum so that were randomly selected 20 squares in the chamber CYRUS II, where they were counted cell counts in individual squares. The amount of inoculum corresponding to 10 000 algae cells per ml was pipetted into test concentrations of tannin. The test and control flasks were plugged with wadding and were placed in termoluminostat at 25 ± 1 °C. The density of algal suspension cells in the counting chamber CYRUS II was determined by counting at the end of the test (after 96 hours of exposure).

#### Mustard test<sup>5</sup>

A dilution series of tested solutions of the tested substances was prepared. From each concentration and control were prepared after three repetitions. The tested concentrations of tannin were prepared by pipetting

the respective amount of the highest tested concentration and adding them to 50 ml volumetric flasks to the mark. To each Petri dish was introduced out of the bottom filter paper and pipetted 5 ml of test solution or pure dilution water (controls). On each filter paper, evenly spread throughout ten mustard seeds and each dish was covered with a glass lid and covered with aluminum foil to prevent light. The dishes were placed in a thermostat tempered at  $20 \pm 2^\circ\text{C}$  for 72 hours.

Subsequently, the calculated inhibition (or stimulation) for each endpoint and for each test concentration and control was expressed as:

$$I_{\mu i} = \frac{\mu_c - \mu_i}{\mu_c} \cdot 100$$

$\mu_i$  - inhibition in% for the tested concentration, if  $I < 0$  and if  $I > 0$  this is the stimulation

$\mu_i$  - is the measured endpoint for test concentration

$\mu_c$  - is the measured endpoint for the control sample

### Results and discussion

The results show (Table 1, 2, 3, 4) that the most sensitive organism were daphnia ( $EC_{50} = 40.77 \text{ mg/l}$ ) and algae ( $EC_{50} = 10\text{-}50 \text{ mg/l}$ ). Endpoints such as mustard root growth ( $IC_{50} = 100\text{-}500 \text{ mg/l}$ ) and survival of enchytraeids ( $LC_{50} = 280 \text{ mg/l}$ ) showed up to an order of magnitude smaller effects compared with the previous two tests.

Table 1. Results of test with dafnia

<i>Daphnia magna</i>						
Concentration [mg/l]	24 hours of exposition			48 hours		
	Number of immobilized daphnids		Immobilization [%]	Number of immobilized daphnids		Immobilization [%]
Control	0	0	0	0	0	0
15.625	1	0	5	2	0	10
31.25	1	1	10	3	2	25
62.5	3	4	35	8	9	85
125	7	6	65	9	10	95
250	6	8	70	10	10	100

Table 2. Results of test with enchytraeids

<i>Enchytraeus crypticus</i>						
Concentration [mg/l]	48 hours of exposure			96 hours of exposure		
	No. of dead worms		Inhibition [%]	No. of dead worms		Inhibition [%]
Control	0	0	0	0	0	0
125	1	0	5	2	3	25
250	5	5	50	10	10	100
500	7	8	75	10	10	100
1,000	10	9	95	10	10	100
2,000	10	10	100	10	10	100

Table 3. Results of test with algae

<i>Desmodemus subspicatus</i>					
Concentration [mg/l]	96 hours of exposure		96 hours of exposure		
	Growth rate	Inhibition [%]	Yield	Inhibition [%]	
Control	1.62	0	6415000	0	
0.5	1.59	2	5680000	11	
1	1.58	3	5440000	4	
5	1.46	10	3430000	37	
10	1.33	17	2065000	40	
50	0.58	64	90000	96	

Table 4. Results of test with mustard seeds after 72 hours of exposure

<i>Sinapis alba</i>							
Concentration [mg/l]	Mean lenght of root [mm]			Inhibition [%]			Mean inhibition of lenght [%]
Paralel	1	2	3	1	2	3	
Control	19.20	30.00	29.80	0.00	0.00	0.00	0.00
10	13.50	23.30	24.60	29.69	22.33	17.45	23.16
50	15.40	12.80	23.80	19.79	57.33	20.13	32.42
100	14.90	16.80	17.80	22.40	44.00	40.27	35.55
500	7.92	8.22	12.51	58.75	72.60	58.02	63.12
1.000	3.11	3.02	3.13	83.80	89.93	89.50	87.74

According to Safety Data Sheets<sup>1</sup>, tannin is harmful to aquatic organisms. Our results confirm and complement these conclusions of valuable information about ecotoxicity for other aquatic organisms (Table 1, 2, 3, 4). It is obvious that the aquatic organisms (algae, daphnia) were more sensitive than soil organisms that were used in aquatic assay arrangements (enchytraeids, mustard). Bioaccumulation is not expected for tannins but it is likely that adverse effects on different species in our study were caused by the chemical origin of tannin, since these substances are acids and can damage cells and lead to their various defects and death of organisms.

#### Literature

1. Merck Chemicals. 100773 Tannic acid (Tannin). <http://www.merckmillipore.com/czech> (24.4. 2014).
2. ČSN EN ISO 6341: Jakost vod – Zkouška inhibice pohyblivosti *Daphnia magna* Straus (Cladocera, Crustacea) – Zkouška akutní toxicity. Praha (2013).
3. Röembke J., Knacker T.: Aquatic toxicity test for enchytraeids. *Hydrobiol.* 180, 235 (1989).
4. ČSN EN ISO 8692: Jakost vod – Zkouška inhibice růstu sladkovodních zelených řas. Praha (2005).
5. Metodický pokyn odboru odpadů ke stanovení ekotoxicity odpadů. MŽP Praha, 2007 (28. 4. 2014).
6. GraphPad Prism 5 for Windows; GraphPad Software Inc. 1999-2007.

## QUARTZ CRYSTAL MICROBALANCE ODOR SENSOR OF VOLATILE AMINES BASED ON PHTHALOCYANINE FILM

Seidl J.<sup>1</sup>, Jirešová J.<sup>1</sup>, Hofmann J.<sup>1</sup>, Smolná K.<sup>2</sup>

<sup>1</sup>Department of Physics and Measurements, Faculty of Chemical Engineering, University of Chemistry and Technology Prague, Technická 5, Praha 6, 166 28, Czech Republic

<sup>2</sup>Department of Chemical Engineering, Faculty of Chemical Engineering, University of Chemistry and Technology Prague, Technická 5, Praha 6, 166 28, Czech Republic  
seidlj@vscht.cz

### Introduction

The freshness of fish is an important quality parameter in the food industry and in the fish-processing industry. Fish products are subject to rapid deterioration. Dimethylamine (DMA) and trimethylamine (TMA) vapors are the principal organic substances emitted from decaying fish and other seafood. It is known that after the death of fish, the adenosine triphosphate (ATP) in fish muscle breaks down and releases volatile amines such as NH<sub>3</sub>, DMA and TMA. The concentration of these amine vapors emitted from fish is closely related to its freshness<sup>1,2</sup>. The American Conference of Government Industrial Hygienists (ACGIH) has adopted threshold limit value–time weighted averages (TLV – TWA) in the range of 5 to 10 mg L<sup>-1</sup> for different alkylamines<sup>3</sup>.

There are many sensors for sensing amines that are usually based on the oxidation of amines. Other sensors are based on chromatography and mass spectrometry or on a change in resistance. In comparison with the conventional methods such as gas chromatography and enzyme-reactor-based systems a Quartz Crystal Microbalance (QCM) gas sensor for trimethylamine (TMA) detection offers a quick response, low detection limit and works at room temperature. Main disadvantage of QCM sensors is that they need of a thin crystal to increase the sensitivity that prevents their inclusion in multi sensor arrays.

The gas sensor proposed in this article is based on a QCM sensor<sup>4,5</sup>. The sensor works on the principle of a shift in the crystal oscillation frequency due to the absorption of gas molecules.

Changes in the fundamental oscillation frequency of a quartz crystal are described by the well-known Sauerbrey equation<sup>6</sup>:

$$\Delta f = - \left( \frac{2f_0^2}{A\sqrt{\rho_Q\mu_Q}} \right) \Delta m \quad (1)$$

where  $f_0$  is the natural frequency of quartz crystal,  $\mu_Q$  is the shear modulus,  $\rho_Q$  is the density of quartz,  $\Delta m$  is the change in mass and  $A$  is the piezoelectrically active crystal area.

A sensing layer is formed from a neodymium phthalocyanine (NdPc<sub>2</sub>). Metal phthalocyanines are suitable as the active layer of electrochemical sensors for the detection of amines and exhibit good reversibility and reproducibility<sup>7-9</sup>.

### Materials and Methods

A 40% wt. solution of dimethylamine in water (Sigma-Aldrich, Germany), a 25% wt. solution of trimethylamine in water (Sigma-Aldrich, Germany), a 25% wt. solution of ammonia in water (Lach-Ner, Czech republic) and chloroform (Lach-Ner, Czech republic) were used as received.

Neodymium bisphthalocyanine was synthesized by the method of Moskalev<sup>10</sup>. Neodymium acetate and o-Phthalonitrile mixed in the molar ratio of 1:10 were slowly heated in a test tube. The solid reaction product that formed after 1 h at 290 °C was pulverized and transferred to a vacuum chamber and heated at a temperature of 350 °C for 5 h to remove the remaining of phthalonitrile and side reaction products. The reaction product was successively washed with acetic anhydride and acetone and dried in air at 120 °C. In the next step, the product was dissolved in DMF with the addition of 1% vol. hydrazine hydrate. A Pt wire and a carbon rod were used as the anode and cathode electrodes, respectively. The spacing between the anode and cathode was about 2 cm. A DC bias voltage of 6 V was applied to the anode with respect to the cathode for 2 h. The initial current was 0.25 mA. The product of electrolysis produced at the anode was scraped off, washed with acetone and dried at 110 °C.

Optical measurements were carried out using a WPA S800 visible spectrophotometer (Biochrom, UK). The visible absorption spectrum of the prepared NdPc<sub>2</sub> in DMF solution is shown in Figure 1. The spectrum corresponds to that of the [PcNdPc] – ion<sup>11</sup>.

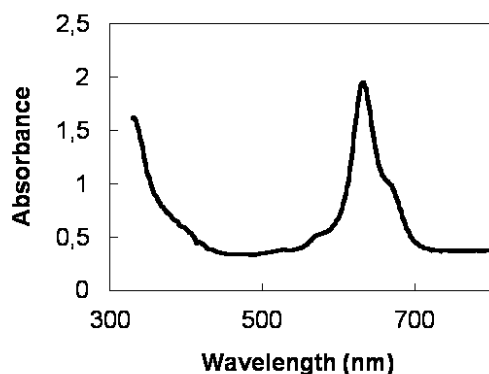


Figure 1. Visible absorption spectrum of NdPc<sub>2</sub> in DMF solution.

The FTIR spectrum was recorded on a Nicolet 740 spectrometer. The spectrum of the product in a KBr pellet is shown in Figure 2. The spectrum is in agreement with that published for NdPc<sub>2</sub><sup>12</sup>. To confirm the NdPc<sub>2</sub> structure, X-ray diffraction (XRD) measurement was made using Co K $\alpha$  radiation in a DRON-UM-1 XRD diffractometer (Burevestnik, Russia). It can be deduced from the XRD pattern (Figure 3) that the prepared NdPc<sub>2</sub> has the  $\alpha$ -phase structure.

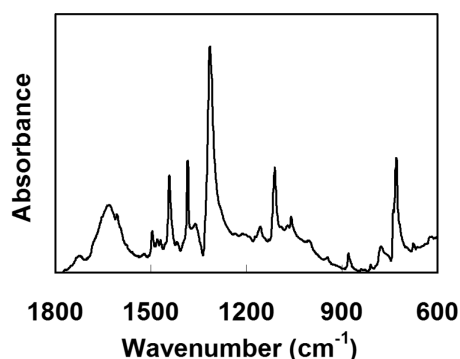


Figure 2. FTIR spectrum of oxidized NdPc<sub>2</sub> in a KBr pellet.

The sensor layer was prepared by the spin-coating technique. The basic principle of spin coating lies in the rapid drying of a solution as it rotates and spreads on a revolving plate. A film was prepared in a similar way by first adding the solution drop wise onto a stationary substrate and then accelerating the substrate to an appropriate speed.

NdPc<sub>2</sub> was dissolved in chloroform (3 g L<sup>-1</sup>) and spin-coated onto the quartz. A HC49-4U series, 10.059 MHz, AT-cut quartz crystal (Yuechung International Corp., Taiwan) and a WS-400E-LNPP-LITE single-wafer spin processor (Laurell Technologies Corporation, USA) were used. The dimensions of the rectangular quartz plate were (2 × 8) mm<sup>2</sup>.

The layer was activated for 24 h at room temperature. The film was investigated by atomic force microscopy (AFM) (Figure 4). The film thickness was about 1.5  $\mu$ m.

Such a morphology has proved to be very useful for gas sensing by promoting the absorption of gas molecules into the film.

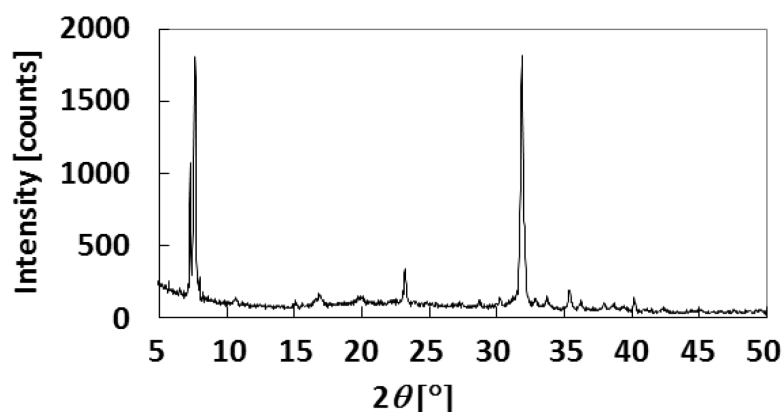


Figure 3. Visible absorption spectrum of NdPc<sub>2</sub> in DMF solution.

### Experimental setup

The QCM sensor was placed in a measuring cell (dead volume approx. 40 mL) and connected with an impedance analyzer (Agilent 4294A precision impedance analyzer, Agilent Technologies Japan, Ltd.) using a 4-TP professional adapter. Synthetic air, amine and ammonia vapors were alternately blown onto the sensor with a gas flow rate of 40 mL min<sup>-1</sup>. The frequency of the testing signal was maintained in a range close to the fundamental oscillation frequency of the QCM sensor (from 10 to 12 MHz). Its amplitude had a constant level of 500 mV and no bias DC voltage was applied. The resonant frequency was evaluated from the measured impedance spectrum. Resonant frequency was found for phase  $\neq 0$ .

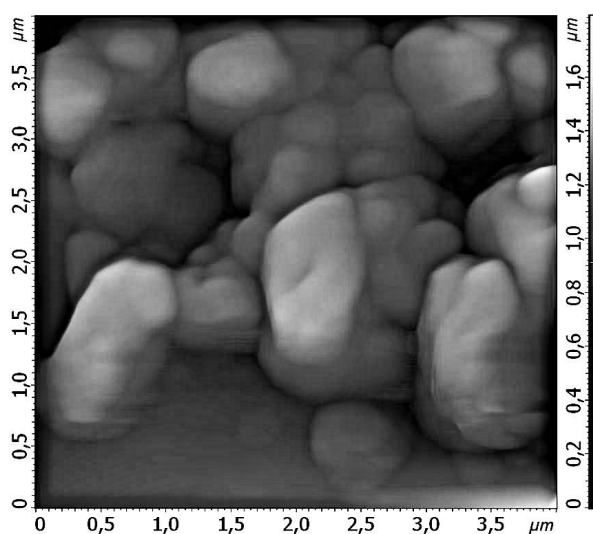


Figure 4. AFM image of the NdPc<sub>2</sub> film used for sensing.

### Results and discussion

The neodymium phthalocyanine (NdPc<sub>2</sub>) active layer of the QCM sensor was exposed to different concentrations of amine, ammonia and water vapors. The resulting frequency changes  $\Delta f$  of the sensor system are shown in Figure 5. Because aqueous amine solutions were used, the dependence of the frequency change on the concentration of water vapor was measured to distinguish the effect of the solvents.

The measured data were fitted by linear regression and the regression correlation coefficients are summarized in Table I. The QCM resonant frequency decreases owing to the absorption of the vapors.

The frequency change  $\Delta f$  increases linearly with increasing vapor concentration and is greatest for TMA. This trend is consistent with the results<sup>5</sup>. Our measurements were performed for lower concentrations (from 0.35 mg L<sup>-1</sup>) than those in reference<sup>5</sup>. We achieved sensitivities of 98 Hz/mg L<sup>-1</sup> for TMA and 49 Hz/mg L<sup>-1</sup> for DMA (Table I) in the concentration range investigated.

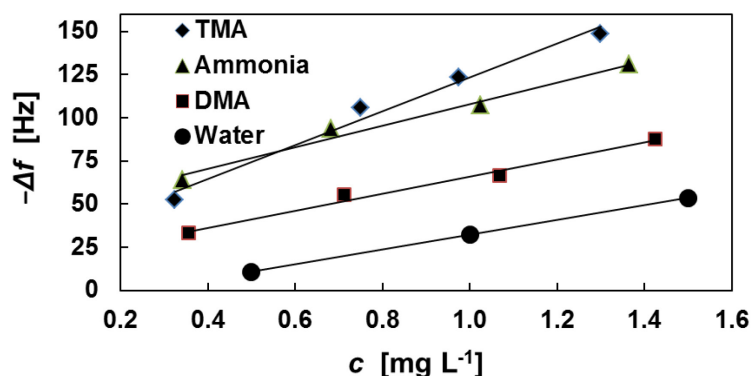


Figure 5. Frequency shift of the QCM sensor with a NdPc<sub>2</sub> layer exposed to amine, ammonia and water vapors of different concentrations.

Table I. Coefficients of linear dependence of frequency change  $\Delta f$  on vapor concentration of active layer for TMA, DMA and ammonia.

Compound	Sensitivity (Hz/mg L <sup>-1</sup> )	Correlation coefficient
Trimethylamine	98	0.981
Dimethylamine	49	0.986
Ammonia	62	0.982

It is obvious, that the resonant frequency of QCM sensor returned to initial value after repeated exposure to TMA vapor.

### Conclusions

A QCM sensor novelty based on a neodymium phthalocyanine (NdPc<sub>2</sub>) was investigated in this study. The QCM system was able to detect the odor of volatile amines (TMA, DMA), which are released during the degradation processes of marine fish and shellfish. The detection limit of the biosensors is about 0.35 mg L<sup>-1</sup>. The developed QCM sensor is inexpensive, easy to make, can obtain immediate results and works at room temperature.

### Literature

- 1 N. U. Karim, T. Kennedy, M. Linton, S. Watson, N. Gault and M. F. Patterson: Food Control 22 (2011) 476.
- 2 C. A. Campos, Ó. Rodríguez, V. Losada, S. P. Aubourg and J. Barros Velázquez: Int. J. Food Microbiol. 103 (2005) 121.
- 3 B. Sahasrabudhey, A. Jain and K. K. Verma: Analyst 124 (1999) 1017.
- 4 M. M. Ayad and N. L. Torad: Sens. Actuators B 147 (2010) 481.
- 5 M. R. Gomes, M. S. Veríssimo and J. P. Oliveira: Sens. Actuators B 57 (1999) 261.
- 6 G. Sauerbrey: Z. Phys. 155 (1959) 206.
- 7 R. Saja, J. Souto and M. L. Rodríguez-Méndez: Mater. Sci. Eng. C 8–9 (1999) 565.
- 8 T. Ceyhan, A. Altindal, M. K. Erbil and O. Bekaroglu: Polyhedron 25 (2006) 737.
- 9 A. Wilson and R. A. Collins: Sens. Actuators B 12 (1987) 389.
- 10 P. N. Moskalev, G. N. Shapkin and A. N. Darovskikh: Zh. Neorg. Khim. 24 (1979) 340.
- 11 C. Clarisse and M. T. Riou: Inorg. Chim. Acta 130 (1987) 139.
- 12 P. N. Moskalev, A. I. Sibilev and V. V. Klyubin: Zh. Neorg. Khim. 42 (1997) 1812.

## **BIOTECHNOLOGY**

### **PRESSURE HYDROLYSIS OF PROTEIN IN WASTE OF CHICKEN CARTILAGE AND FEATHERS IN THE PRESENCE OF CARBON DIOXIDE**

**Hanika J.**<sup>1</sup>, Šolcová O.<sup>1</sup>, Kaštánek P.<sup>2</sup>

<sup>1</sup>*Institute of Chemical Process Fundamentals AS CR, v. v. i., 165 02 Prague 6*

<sup>2</sup>*Ecofuel, s. r. o., Prague, Czech Republic*

*hanika@icpf.cas.cz*

#### **Abstract**

Proteins hydrolysis of chicken cartilage and feathers were carried out at increased temperature (till 120 °C) and in the presence of carbon dioxide (partial pressure 10 20 bar), which dissociates in water solution forming an acidic environment supporting the reaction. Carbon dioxide was easily detachable from the reaction mixture at the end of process. Bench scale tests were performed using a mixed autoclave (volume 2.5 lt, mixing time 5 hr). The resulting aqueous solution of amino acids contained in the same representation as peptides forming collagen and keratin of raw material. The reaction conversion was proportional to carbon dioxide partial pressure.

#### **Introduction**

One of the most important tasks of the Centre Biorefinery BIORAF is finding ways for obtaining valuable substances by chemical transformation of biomass, animal and vegetable origin. This task is undoubtedly important because it represents a unique biomass, a renewable raw material base. In the case of animal biomass, significant attention has been paid to the waste from agricultural, respectively. food plants - waste chicken cartilage and feathers that after acid hydrolysis to give a mixture of amino acids nutritional value. Collagen represents the main protein of the various connective tissues in animals, e.g. cartilage<sup>1</sup>. Producers of collagen-based food supplements containing hydrolyzed collagen sometimes claim the skin improvement and health support. For example, Schauss et al.<sup>2</sup> described also improved osteoarthritis-related symptoms in application of a low molecular weight dietary supplement consisting of hydrolyzed chicken sternal cartilage extract. The hard keratin forming e.g. feathers of birds represents fibrous structural protein<sup>3</sup>. Keratin has large amount of the sulfur-containing amino acid cysteine. Formation of disulfide bridges via intra- and inter-molecular hydrogen bonds brings rigidity and thermal stabile cross-linking of the keratin structure. Hydrolyzed keratin has become a common cosmetic ingredient. Studies have shown topical application of hydrolyzed keratin gives significant increases in skin elasticity and hydration<sup>4</sup>. Due to its moisturising properties, hydrolyzed keratin has also been incorporated into shampoo and conditioner. Difficult in poultry waste chicken feathers, whose liquidation is currently being dealt anaerobic fermentation biogas and mixed with other wastes from processing slaughter lines. Other methods of disposal of waste feathers - incineration, composting is problematic because the badly burning waste and composting very slowly decays. Hydrolytic cleavage of peptide bonds in the protein structure of feathers results in a mixture of amino acids. The resulting aqueous solution can be easily mixed with compost or as a component in dressings plants, thereby achieving a recycling biogenic elements in agricultural process.

#### **Pressure hydrolysis of chicken wastes**

Hydrolytic cleavage of peptide bonds in the protein structure, chicken cartilages and feathers, produces an amino acid mixture of high nutritional value. The resulting aqueous solution can be easily refined and modified thicken into valuable nutrients. For hydrolysis of collagen and keratin is however preferable to use as catalyst a mineral acid or alkali compound, since the product would be required for neutralization and thus final product is contaminated by salts.

The proposed technology eliminates the disadvantages mentioned, by applying pressure hydrolysis at elevated temperature in the presence of carbon dioxide which provides the necessary acidic environment for the successful progress of the reaction and after hydrolysis carbon dioxide is easily separable from the reaction mixture. The resulting aqueous solution contains valuable amino acids in the identical ratio as the starting collagen and keratin, respectively.

The pilot experiments were made using chicken cartilage and feathers, (Rabbit, a. s., Trhový Štěpánov). Starting materials were frozen, wrapped in icy water. The pressure mixed reactor (autoclave) with a regulated heating

was used for materials hydrolysis. Intensive mixing of reaction volume is necessary because the responsive system comprises three phases - carbon dioxide gas, a liquid aqueous medium, and a raw material in the solid phase. During the hydrolysis process, there is a gradual disappearance of solid phase and forming an aqueous solution of amino acids, optionally with a small proportion of unreacted peptides.

It is evident that a kinetic course of reaction conversion of animal waste into amino acids solutions is the faster the higher temperature and carbon dioxide pressure are used. By application of biomass to water mass ratio 1: 6 very promising results were achieved at reaction time of 5 hours, temperature interval 115-120 ° C and pressure 15-20 bar. Under these conditions, high peptides conversion to the desired amino acids was achieved (over 95%). But, choosing a higher temperature is undesirable due to possible thermal decomposition of raw materials or products, also carbon dioxide concentration in liquid reaction mixture is then reduced due to the higher water partial pressure. These facts demonstrate the following experimental data.

### Hydrolysis of chicken cartilage

For hydrolysis of 300 ml frozen cartilage was used. Chopped wet waste chicken cartilage of two different origin (minced and sliced forms) were fed along with 1000 ml of water into the autoclave volume of 2.5 lt. Experiments 1 and 2 were carried out at temperature 105 °C and pressure 1.5 MPa.

Elemental composition of dried product is given in Table I. and show a good reproducibility of elemental analysis. The process results did not depend on disintegration of cartilage prior to hydrolysis. A similar conclusion can be drawn when comparing amino acid content in the product from experiments 1 and 2, as shown in Figure 1. It is also confirm good reproducibility of cartilage hydrolysis.

Table I

Elemental analysis of dry product (wt. %)

Element	#1-Minced chicken cartilage	#2-Sliced chicken cartilage
Carbon	40.1	40.3
Hydrogen	5.61	5.58
Nitrogen	12.0	12.1
Sulfur	2.60	2.32
Oxygen (imputation)	39.7	39.7

A detailed picture of the resulting product gave HPLC-MS analysis of the hydrolysate, see Fig. 1. (UCT Prague, FFBT). From the results follows that the hydrolysate contains also undetermined components (unreacted collagen, glykosoaminoglykany, etc.) because total quantity of amino acids is significantly less comparing to processed batch cartilages. The most significantly represented in the hydrolysate represents asparagine, the content of the order exceeds the proportion of other amino acids.

Likewise, the chromatographic analysis of the hydrolysate is well reproducible. The hydrolysis product can be recommended to perform application tests both to stimulate growth of plants, algae, as well as nutritional tests for livestock and possibly after further evaluation as an ingredient for food supplements, etc.

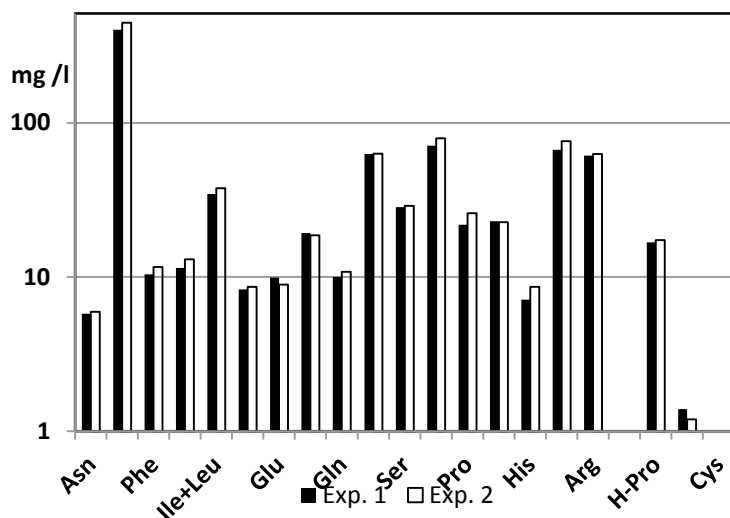


Figure 1. Comparison of amino acids content in liquid hydrolysate; experiments 1 and 2

### Hydrolysis of chicken feathers

For hydrolysis of waste chicken feather was chosen the same procedure as in the case of cartilage. In experiments 300 ml of wet waste chicken feathers (dry matter 25%) was used and poured over 1000 ml of water. The weight of dry solids feathers was 12.5 g. This mixture was submitted to a stainless steel autoclave 2.5 liter. The autoclave was filled with cold carbon dioxide and its pressure in experiments 1 and 2 was maintained at 11 and 21 bar, respectively. After heating the mixture (2 hr) to reaction temperature (105-112 °C) under stirring frequency of 1 Hz the feathers were hydrolyzated for 5 hours and autoclave was cooled down over night to ambient temperature (12 hr). The reaction products were brown colored without any solid rests. The very important parameter which significantly influences the kinetics of the hydrolysis process is the carbon dioxide pressure. Its higher concentration control lower pH value of reaction mixture which support the hydrolysis process. Thus, there was observed a direct proportionality between reaction conversion and carbon monoxide partial pressure applied during hydrolysis process, see Fig. 2.

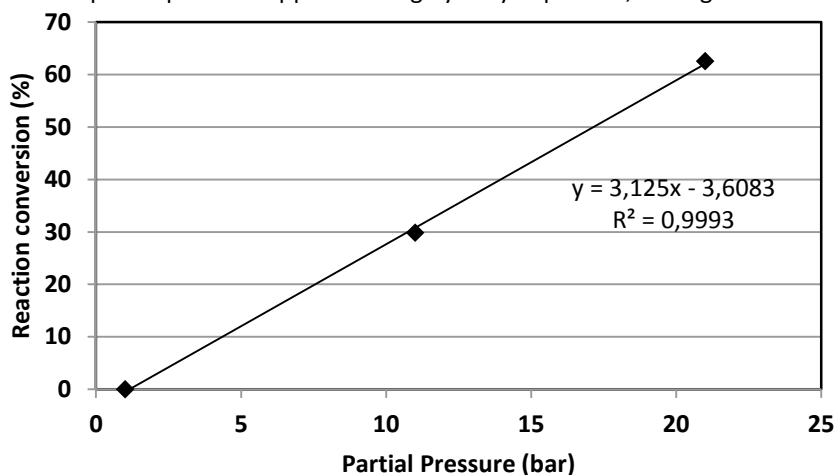


Figure 2: Effect of carbon dioxide pressure on reaction conversion of feather hydrolysis

A detailed product composition was investigated by HPLC/MS analysis (UCT – FFBT Prague). Figure 3 demonstrates a representation of amino acids in hydrolysate. The content of unreacted protein was determined by subsequent product hydrolysis in presence of hydrochloric acid. The reaction conversion was 29.8 % and 62.5 % in experiments 1 and 2, respectively. It is evident the hydrolyzate does not contain all the essential amino acids in the proportions that the human body requires.

From this analysis it was possible to further specify a representation of the individual elements and amino acids in a protein - carbon, hydrogen, nitrogen, sulfur and oxygen (determined by imputation up to 100%), which was compared with the elemental analysis of the dried residue of the hydrolyzate (3.6 and 4.8 g / 100 g hydrolyzate; Experiments 1 and 2, resp.). There was found very good agreement elemental representation in the hydrolyzate and its residue, as shown in Table II.

The liquid product was also analyzed by the classical elemental analysis for sulfur content in hydrolyzate of 0.118 g / lt and nitrogen 2.02 g / lt; the ratio corresponds very well to the content of these elements in the feathers (nitrogen, 13.69% and sulfur 0.80 % respectively). The data for nitrogen is also in relative good agreement with the mean content of nitrogen in the amino acid mixtures in both experiments, see Table II. Content of the other elements, except sulfur, in hydrolyzate corresponds very well to mean elemental composition of amino acids mixture determined by HPLC/MS method.

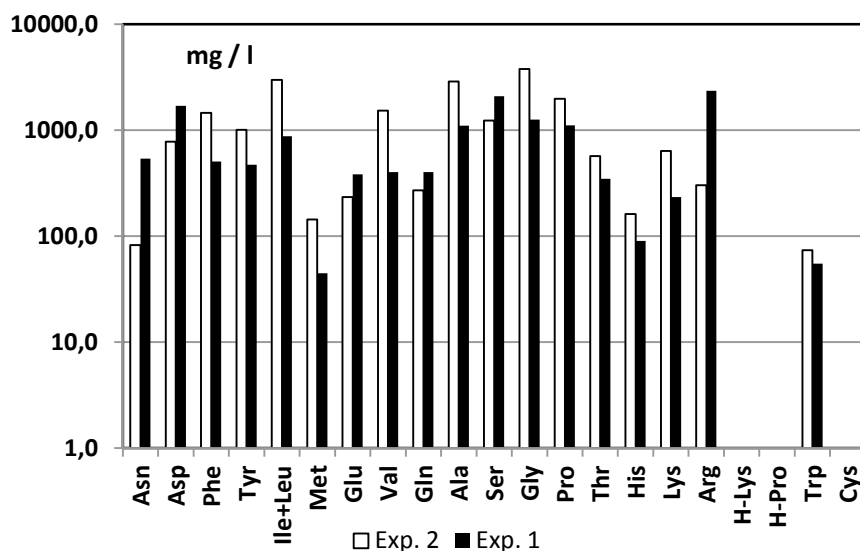


Figure 3: Comparison of the amino acids concentration in hydrolyzate; Experiments 1 and 2

Table II

Comparison of the elemental composition of dry feathers hydrolysis product and mean elemental composition of amino acids in hydrolyzate (Experiments 1 and 2)

Element	Dry residue (% wt.)	Amino acids (% wt.)
Carbon	46.7	44.0
Hydrogen	7.64	7.56
Nitrogen	12.0	14.0
Sulfur	1.18	2.73
Oxygen (imputation)	32.5	31.7

### Conclusion

The hydrolysis product is perspective one for various applications, first, for dampening the composted agricultural waste, next could be useful as nutritional additives to livestock feed and finally as a nutrient supporting growing algae for biotechnology applications. For any culture, or nutritional usage of hydrolyzate as ingredient in feed mixtures have to be necessary to perform additional relevant field tests.

### Acknowledgement

The study is dealt within the framework of the project "Centre of Competence for Biorefinery Research, BIORAF" (TE01020080) with the financial support of the Technology Agency of the CZECH REPUBLIC.

### Literature

1. <http://en.wikipedia.org/wiki/Collagen>
2. Schauss, A., Stenehjem, J., Park, J., Endres, J., and Clewell, A.: *Journal of Agricultural and Food Chemistry* **60** (16), 4096–4101, (2012); doi:10.1021/jf205295u.
3. <http://en.wikipedia.org/wiki/Keratin>
4. Barba C., Méndez S., Roddick-Lanzilotta A., Kelly R., Parra J. L., Coderch L.: *Skin Res. Technol.* **14** (2), 243–248 (2008); doi:10.1111/j.1600-0846.2007.00280.

## UTILIZATION OF LIGNOCELLULOSIC SUBSTRATES BY CLOSTRIDIUM BACTERIA

**Kolek J.**, Patáková P.

*University of Chemistry and Technology, Technická 5, 166 28, Praha  
kolekj@vscht.cz*

Cellulose is very common substance in the nature occurring mainly in cell walls of the plants. It is compact polymer consisting from glucose subunits which could be used as potential carbon and energy source for many biotechnological applications. Unfortunately, cellulose is very hard to decompose to monosaccharides and this is the main problem of its use as a fermentative substrate. In nature, cellulose decomposition is provided by strictly specialized microorganisms and fungi which could be potentially used for direct cellulose conversion to some valuable product. Another possibility is the use of cellulose enzymatic hydrolysis process for obtaining fermentable carbohydrates or gasification of dry biomass into synthetic gas, so called syngas. All of these processes are unfortunately very expensive and the products yields are very low, yet. Clostridia are gram-positive anaerobic bacteria which belong to typical cellulose decomposers of the anaerobic habitats (like soil, water sediments, digestion tract of animals etc.) in nature. Many of them are able to use cellulose contains in lignocellulosic complex and ferment it to the ethanol or other valuable products. Other species can utilize syngas to produce ethanol or butanol. In global, cellulolytic and syngas-utilizing clostridia are much unexplored group of microorganisms which could be important for many biotechnological processes in the future. Here we describe approaches for the isolation of new cellulolytic clostridia from natural reservoirs.

### Introduction

Cellulose is one of the most common compounds of the Earth. It is important component of cell walls of plants. In nature, cellulose typically does not occur as free substance but as one of the components of rigid lignocellulosic complex. This very stable matrix consists of three main components: cellulose, hemicelluloses and lignin. These components penetrate each other, create higher supramolecular structures (fibrils, plates) and are bounded together by covalent and non-covalent bonds (Fig. 1). Cellulose is polysaccharide consisting of glucose subunits which are bounded together by  $\beta$ -1,4 glycosidic bonds and creating very long unbranched chains. Hemicelluloses belong to very heterogeneous group of polysaccharides which typically contain many subunits of different saccharide molecules and also other components like e.g. uronic acids. Lignin is random copolymer of fenypropanoid units with typical side chains and is a major component of woody substrates and its main precursors are 4-coumaryl alcohol, coniferyl alcohol and sinapyl alcohol. Proportion of these three main elements varies widely depending on the lignocellulosic substrate<sup>1</sup> (Tab. 1). There are also next, minor components of lignocellulosic substrates like proteins, simple carbohydrates or minerals (inorganic salts, silica oxide etc.).

Table I

Examples of lignocellulosic substrates and their dry matter composition<sup>1</sup>.

Lignocellulosic material	Cellulose [%]	Hemicelluloses [%]	Lignin [%]
Hardwood (average values)	43-47	25-35	16-24
Softwood (average values)	40-44	25-29	25-31
Wheat straw	30-50	20-30	15
Barley straw	33-40	20-35	8-17
Switchgrass	45	31	12
Corn stalks	35	25	35
Grasses	25-40	35-50	10-30
Green algae	20-40	20-50	NA
Paper	85-99	0	0-15
Cattle manure	2-8	2-4	3-6

NA: not applicable

Due to its composition cellulose is potentially useful as a source of carbon and energy for bacterial fermentation. Unfortunately, lignocellulosic complex is generally very rigid and only a few microorganisms are able of its direct decomposition to the fermentable monosaccharides (predominantly glucose). Known, possible indirect approaches for the lignocellulosic substrate utilization are mainly their enzymatic hydrolysis to fermentable sugars or their gasification into the synthetic gas, also called syngas. The second option is to use

cellulolytic microorganisms for direct utilization of cellulose to valuable product (so-called consolidated bio-processing)<sup>2</sup>. Unfortunately, all of these three main ways of lignocellulosic utilization have many drawbacks like too high price of process and very low product yields.

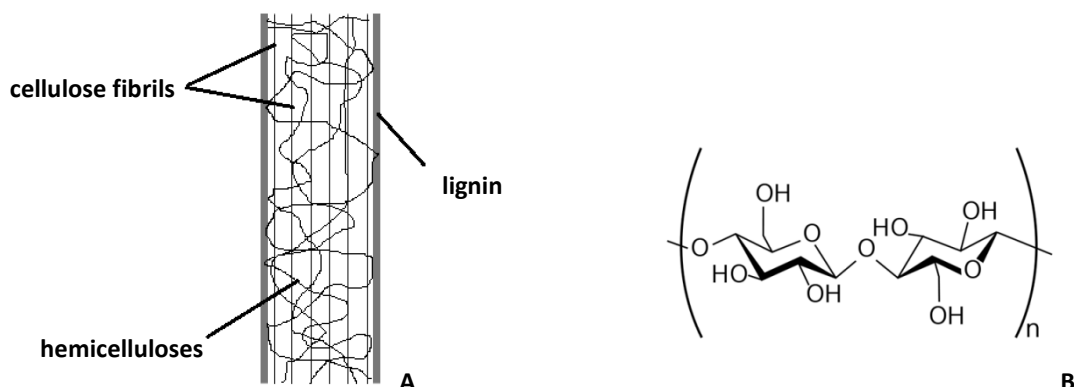


Figure 1. (A) typical arrangement of lignocellulosic complex in plant cell walls: cellulose fibrils interconnected by hemicelluloses and externally surrounded by lignin layer; (B) structure of cellulose: molecule of cellobiose (the basal subunit of cellulose).

In aerobic zone, there are the most important cellulose decomposers fungi and aerobic species of bacteria. On the other hand, there are mainly bacterial decomposers in anaerobic zone. Some species of bacteria belong to the genus *Clostridium* which are the most common cellulose decomposers in the nature. Clostridia are strictly anaerobic, gram-positive bacteria which typically occur in soil, anaerobic water sediments, digestion tract of animals and all other anaerobic habitats. Until today, several species of cellulolytic clostridia have been described. There are psychrophilic, mesophilic and thermophilic species whose are able to produce some organic acids or ethanol. Main previously described cellulolytic clostridia species are summarized in table II.

Table II  
Summary of the most important cellulolytic clostridium species and main products of their fermentation.

Species	Temperature relationship	Source	Main product of fermentation	Reference
<i>C. cellulolyticum</i>	Mesophilic	Composted grass	Acetate, ethanol	3
<i>C. cellulovorans</i>	Mesophilic	Anaerobic digester	Acetate, butyrate	4
<i>C. cellobioparum</i>	Mesophilic	Rumen fluid	Acetate, ethanol	5
<i>C. phytofermentans</i>	Mesophilic	Soil	Acetate, ethanol	6
<i>C. thermocellum</i>	Thermophilic	Anaerobic digester	Acetate, ethanol, lactate	7
<i>C. papyrosolvans</i>	Mesophilic	Compost	Acetate, ethanol, lactate	8
<i>C. josui</i>	Thermophilic	Sediment	Acetate, ethanol, butyrate	9
<i>C. termitidis</i>	Mesophilic	Termite gut	Acetate, ethanol	10
<i>C. cellulosi</i>	Thermophilic	Composted manure	Acetate, ethanol	11
<i>C. lentocellum</i>	Mesophilic	Fresh water sediment	Acetate, ethanol, lactate	12
<i>C. herbivorans</i>	Mesophilic	Pig intestine	Butyrate, formate, ethanol	13

The main goal of our work was the optimization of technique for isolation of new cellulolytic strains, esp. mesophilic clostridium bacteria from natural reservoirs. We have used two main approaches: simple isolation from samples collected in the nature and isolation from cellulose traps.

### **Cellulolytic clostridia isolation and characterization**

#### *Samples for simple isolation*

Samples for simple isolation were collected from several anaerobic places like deep soil layers, organic compost, fresh-water sediments, decaying grass and manure dumps. Samples were collected in 15ml falcon tubes in standard aerobic atmosphere.

#### *Cellulose-trap method*

Cellulose-traps were performed from stainless steel tea strainer or burlap sacks whose were filled by a piece of mashed filter paper. Traps were placed to the same places as described above. All traps were stored in place around 14 days and after this period samples (piece of partly decomposed filter paper) from every trap were collected as described above.

#### *Enrichment culture and growth of cellulolytic bacteria detection*

A modified P2 medium<sup>14</sup> was used for first round of enrichment culture. Our modification was prepared by mixing the following solutions (all dissolved in double-distilled water): 790 ml solution A (contain 2 g yeast extract; 5 g carboxymethyl-cellulose), 100 ml solution B (0.5 g  $\text{KH}_2\text{PO}_4$ ; 0.5  $\text{K}_2\text{HPO}_4$ ; 2.2 g ammonium acetate), 10 ml solution C (0.2 g  $\text{MgSO}_4 \cdot 7\text{H}_2\text{O}$ ; 0.01 g  $\text{MnSO}_4 \cdot \text{H}_2\text{O}$ ; 0.01 g NaCl; 0.01 g  $\text{FeSO}_4 \cdot 7\text{H}_2\text{O}$ ) and 1 ml solution D (1 mg *p*-amino benzoic acid; 1 mg thiamine-HCl; 0.01 mg biotin). Solutions A and B were autoclaved, for sterilization of solutions C and D filter sterilization were performed.

Small piece of each sample was transferred to the tube with 5 ml of modified P2 medium and every tube was challenged by heat (100 °C for 5 minutes) for suppression of all vital bacteria and thermostable bacterial endospores advantage. Tubes were cultivated in anaerobic chamber (Concept 400, Ruskinn, UK) or in anaerostat (Merck, Germany) in a stable anaerobic atmosphere suitable for clostridium growth (95 %  $\text{N}_2$ , 5 %  $\text{H}_2$ ) and temperature 37 °C or 30 °C. After two weeks, all cultures were subcultured in modified P2-P medium (without carboxy methyl cellulose in solution A) and small strips of sterile filter paper were added to each tube. Detection of cellulolytic activity was carried out by monitoring the decomposition of the paper.

#### *Morphology analysis*

Cultures where cellulolytic activity obtained were observed by light microscopy for endospores formation confirmation and basic morphology acquisition. Phase-contrast was used for better endospore recognition and bacterial cells characterization.

#### *Single strain isolation*

Cultures from tubes, where decomposition of the paper was observed, were serially diluted in sterile anaerobic water and spread onto RCM (Merck, Germany), P2 with 5 g/l carboxymethyl-cellulose and P2 with 5 g/l cellobiose. All media were solidified by adding of agar (Agar Bacteriological, Oxoid, UK) in final concentration 2 %. Plates were cultivated under the same conditions as above. After one to two weeks, single colonies were picked and transferred to the P2-P medium in glass tube with filter paper strips to confirm their potential cellulolytic activity. Cellulolytic strains were processed by cryopreservation in 20 % glycerol for long-term storage.

### **Results**

After two weeks of cultivation, significant filter paper decomposition was visible in glass tubes with culture containing cellulolytic strains (Fig. 2). Although the cultures were heat inactivated for a long time at the beginning of cultivation and cellulose was used as source of carbon and energy, significant background growth of non-cellulolytic bacteria was obtained in every stage of cultivation. Furthermore, non-cellulolytic and fast-

growing bacteria were outgrown the slow-growing cellulolytic bacteria on agar plates. Significant growths of several types of colony were obtained on all agar media.

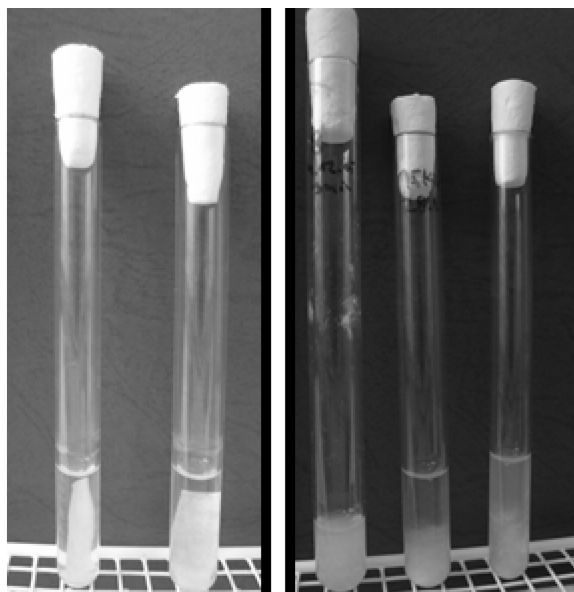


Figure 2. Screening of cellulolytic activity by filter paper decomposition test; culture without cellulolytic activity (left) and containing cellulolytic strains (right) after two weeks cultivation in 37 °C.

Characterization of cellulolytic activity by filter paper decomposition was proven as very fast approach for this issue. Other standard methods from literature like plating to agar media with insoluble cellulose particles and halo-zones observation were found as dubious methods (data not shown). Filter paper was generally decomposed (as shown in Fig. 2) and cellulose fibers were settled on the bottom of tube during one to two weeks at 37 °C and during three weeks at 30 °C.

Unfortunately, we obtained a very poor growth of single strain culture from one colony and only in a few cases we were able to isolate pure culture of cellulolytic bacteria. This probably might be caused by specific nutrient requirements of cellulolytic strains or their coherence with other soil non-cellulolytic bacteria metabolism (which also could produce some important growth factors to media). Spore formation (typical attribute of genus *Clostridium*) was verified at all new isolates by light microscopy, as shown in Fig. 3.

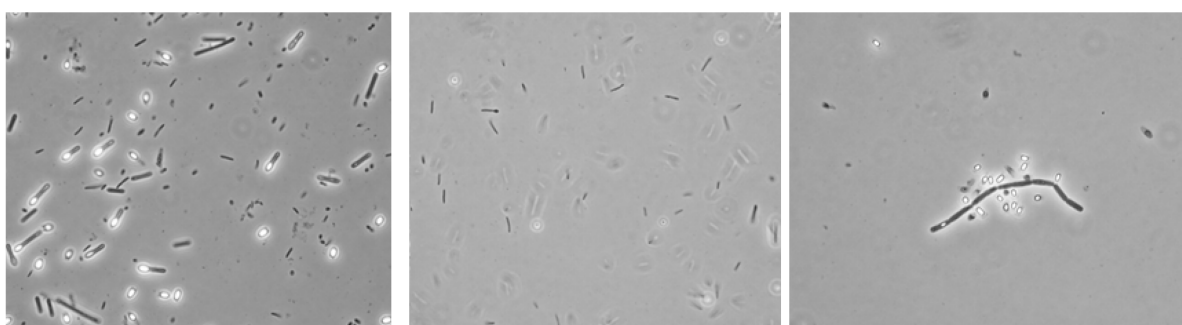


Figure 3. Examples of isolated cellulolytic strains (pure culture) observed by light microscopy with phase contrast (1000x magnification); typical endospore formation in some cases.

### Conclusion

Here we described system applicable for fast and specific isolation of cellulolytic mesophilic clostridium bacteria. Cellulolytic bacteria are relatively poor-described group of anaerobic bacteria which have a potential in biotechnology. It is relatively easy to isolate bacterial consortium with cellulolytic properties but the growth of pure culture of cellulolytic bacteria from these consortia were very low. This obstacle might be resolved for example by addition of mixed, sterile, soil-bacteria lysate or sterile, filter-sterilized soil infusion.

## Acknowledgement

*Financial Support from Specific University Research (MSMT No. 20/2015) and TAČR BIORAF (TE01020080).*

## Literature

1. Sun Y., Cheng J. Y.: *Bioresour. Technol.* **83**, 1 (2002).
2. Paulová L., Patáková P., Branská B., Rychtera M., Melzoch K. *Biotechnol. Adv.*, in press.
3. Petitdemange E., Caillet F., Giallo J., Gaudin C.: *Int. J. Syst. Bacteriol.* **34**, 155 (1984).
4. Sleat R., Mah R. A., Robinson R.: *Appl. Environ. Microbiol.* **48**, 88 (1984).
5. Hungate R. E.: *J. Bacteriol.* **48**, 499 (1944).
6. Warnick T. A., Methe B. A., Leschine S. B.: *Int. J. Syst. Evol. Microbiol.* **52**, 1155 (2002).
7. Ng T. K., Weimer T. K., Zeikus J. G.: *Arch. Microbiol.* **114**, 1 (1977).
8. Madden R. H., Bryder M. J., Poole N. J.: *Int. J. Syst. Bacteriol.* **32**, 87 (1982).
9. Sukhumavasi J., Ohmiya K., Shimizu S., Ueno K.: *Int. J. Syst. Bacteriol.* **38**, 179 (1988).
10. Hethener P., Brauman A., Garcia J. L.: *Syst. Appl. Microbiol.* **15**, 52 (1992).
11. He Y. L., Ding Y. F., Long Y. Q.: *Int. J. Syst. Bacteriol.* **41**, 306 (1991).
12. Murray W. D., Hofmann L., Campbell N. L., Madden R. H.: *Syst. Appl. Microbiol.* **8**, 181 (1986).
13. Varel V. H., Tanner R. S., Woese C. R.: *Int. J. Syst. Bacteriol.* **45**, 490 (1995).
14. Baer S. H., Blaschek H. P., Smith T. L. *Appl. Environ. Microbiol.* **53**, 2854 (1987)

# USING THE TYROSINASE FROM *AGARICUS BISPORUS* AND THE CYANIDE HYDRATASE FROM *ASPERGILLUS NIGER* K10 IN THE DEGRADATION OF PHENOL AND *o*-, *m*- AND *p*-CRESOL AND THE FREE CYANIDE FROM COKE PLANT WASTEWATER

**Chmátal M.**<sup>1</sup>, Veselá A. B.<sup>1,2</sup>, Rinágelová A.<sup>1</sup>, Kaplan O.<sup>1,3</sup>, Martínková L.<sup>1</sup>

<sup>1</sup>*Institute of Microbiology of the AS CR, v. v. i., Vídeňská 1083, 142 20, Praha 4*

<sup>2</sup>*Charles University in Prague, Faculty of Science, Hlavova 8, 128 40, Praha 2*

<sup>3</sup>*Institute of Macromolecular Chemistry, v. v. i., Heyrovského nám. 2, 162 06, Praha 6  
chmatal@biomed.cas.cz*

## Introduction

Coke plant wastewater contains a broad spectrum of organic compounds, primarily phenolics and tars, which have been partly utilized as raw materials in the chemical industry, but a significant portion of them remains in the wastewaters as pollutants. The most abundant of them are phenol (cca 56 %), cresols (cca 30 %) and xylenols (4 %), but also a variable amount of free and bound cyanides are present. Phenol, being a commodity chemical, has been previously produced in coke plants but this manufacture has been stopped, resulting in a high phenol content in their wastewaters (cca 1500 – 2000 mg/L; Dr. S. Czudek, Třinec Iron and Steel Works; *personal communication*) which represents a burden for the coke plant technology and their wastewater treatment plants.

Compared to chemo - physical methods of wastewater dephenolization, the use of oxidative enzymes of plant and microbial origin is a much cheaper alternative, which has the additional benefit of utilizing the wide substrate specificities of these enzymes for various pollutants. For this application, the use of oxidoreductases such as peroxidase, laccase or tyrosinase is promising<sup>1</sup>. However, in contrast to peroxidase, which requires hydrogen peroxide for its activity, laccase and tyrosinase make use of the readily available molecular oxygen as the electron acceptor. Laccases and tyrosinases degrade phenol into compounds which are poorly soluble in water and can then be easily separated by filtration or sedimentation<sup>2,3</sup>. Tyrosinase (polyphenol oxidase, EC 1.14.18.1) catalyzes the hydroxylation of monophenols to *o*-hydroquinones (catechols) and their subsequent dehydrogenation to quinones, which are then non-enzymatically polymerized, forming insoluble brown pigments<sup>4</sup>. Tyrosinase is easily available as a crude extract from the fruiting bodies of the common mushroom (*Agaricus bisporus*).

In this work we have exploited the catalytic properties of tyrosinase in combination with cyanide hydratase (CHT) for the degradation of phenols and cresols from coke plant wastewater. The free cyanide present in this wastewater strongly inhibits the tyrosinase<sup>5</sup>. To alleviate this inhibition we used a recombinant CHT (formamide hydrolyase EC 4.2.1.66) from *Aspergillus niger* K10 (CCF 3411)<sup>6</sup>. Using a two-step enzymatic reaction for the degradation of multiple components of the pollutant mixture, where the first enzyme degrades cyanide and thus creates the conditions for the degradation of another 2-3 pollutants (in our case phenols and cresols) in the wastewater, is an original way of using enzymes in e.g. coke plant or wastewater treatment technologies.

## Materials and methods

### Materials

The coke plant wastewater was kindly donated by the Třinec Iron and Steel Works (Dr. S. Czudek). The sample was withdrawn after the ammonia removal step and designated phenolic water (PW). Its properties were as follows: pH 7.4, phenol 16.5 mM (1552 mg/L), cresols 5.0 mM (540 mg/L), free cyanide (CN<sup>-</sup>) 0.32 mM (8.3 mg/L) as determined by the analytical methods described further in Materials and methods.

The following enzymes were used in the degradation experiments: a) a commercial tyrosinase (TYR) from *Agaricus bisporus* (EC 1.14.18.1) (Sigma, USA; specific activity 5771 units/mg of lyophilized powder), b) crude tyrosinase (TYR/AC) extracted from the fruiting bodies of *A. bisporus* with acetone (specific activity 112 U/g), c) CHT (specific activity 930 U/mg of protein).

A unit of activity of TYR = amount of enzyme which catalyzes a change in  $\Delta A_{280}$  of 0.001/min at pH 6.5 and 25 °C in a 3-ml reaction mixture containing L-tyrosine. A unit of activity of TYR/AC (U) = enzyme amount which catalyzes the transformation of 1  $\mu$ mol phenol/min at pH 7.4 and 25 °C. A unit of activity of CHT (U) = enzyme amount which catalyzes the transformation of 1  $\mu$ mol CN<sup>-</sup>/min at pH 8.0 and 30 °C.

#### Preparation of crude tyrosinase

350 g of commercially available fruiting bodies of the common mushroom (*A. bisporus*) was homogenized for 30 s in 800 ml of distilled acetone at 4 °C. The acetone was then removed by filtration through a Büchner funnel. Residual acetone was removed from the filter cake with filter paper and the resulting biomass was stored at – 20 °C. 150 g of the preparation was thus obtained (5.6 g of protein) with a specific activity of 3 U/mg of protein.

#### Preparation of cyanide hydratase

CHT was produced by recombinant *Escherichia coli* BL21-Gold expressing the *chy* gene from *Aspergillus niger* K10 (CCF 3411) as described previously<sup>6</sup>. Briefly, the strain was cultivated in LB medium and enzyme production was induced by IPTG; the cells were disrupted by sonication and the nitrilase purified by ion exchange and gel permeation chromatography. The purified enzyme exhibited its maximum activity at pH 8.0 and 45 °C and was stable at up to 30 °C<sup>6</sup>; it was stored at – 80 °C.

#### Enzymatic degradation of phenol and cresol by commercial tyrosinase

CHT (20 U/ml) was added to phosphate buffer (pH 8.0) with KCN (0.1 mM or 1.0 mM) and phenol (5 mM) or to PW diluted 1:1. After 10 min of incubation at 35 °C with shaking (750 rpm) samples were withdrawn for the determination of cyanide. Tyrosinase (250 units/ml) was then added and the reaction was carried out for 2-72h at 35 °C with shaking (750 rpm). Optionally, CHT (20 U/ml) and TYR (1000 units/ml) were added simultaneously or at different times, or different amounts of TYR (250, 500, 1000 or 2000 units/ml) were added after cyanide had been eliminated with CHT (20 U/ml). The reactions were carried out under the aforementioned conditions.

#### Enzymatic degradation of phenol and cresol by crude tyrosinase

20 g (2240 U) of tyrosinase TYR/AC was added to 50 ml of PW from which cyanide was eliminated using CHT (see above). The reaction was carried out for 20 h at 25 °C with shaking (350 rpm).

#### Analytical methods

The concentration of free cyanide was determined by the spectrophotometric method based on the reaction of cyanide with picric acid<sup>7</sup>. The concentrations of phenol and cresol were determined by HPLC with a Chromolith Speed ROD column, RP-18e, 50x4.6 mm, (Merck); mobile phase: 20% acetonitrile, 0.1% H<sub>3</sub>PO<sub>4</sub>, flow rate 2.0 ml/min; retention times: phenol 1.31 min, cresols 2.26 min (isomers not separated); detection by UV at 210 nm; 34 °C.

## Results

#### Alleviation of tyrosinase inhibition by cyanide hydratase

The effect of 0.1 mM and 1.0 mM KCN on the degradation of phenol by commercial tyrosinase was first monitored in model mixtures (buffer pH 8.0 with 5 mM phenol). The reaction mixtures contained: a) phenol + TYR (control), b) phenol + KCN + TYR, c) phenol + KCN + CHT + TYR. Whereas 0.1 mM KCN decreased the degradation of phenol by ca. 30 % after 72 h (Fig. 1), 1 mM KCN inhibited the phenol degradation completely (Fig. 2). However, the addition of CHT alleviated this inhibition effect and the degradation of phenol thus proceeded with a similar efficiency as in the reaction mixtures without cyanide (68% vs. 71%). Hence, the elimination of cyanide by CHT enabled an efficient degradation of the phenolic compounds by tyrosinase.

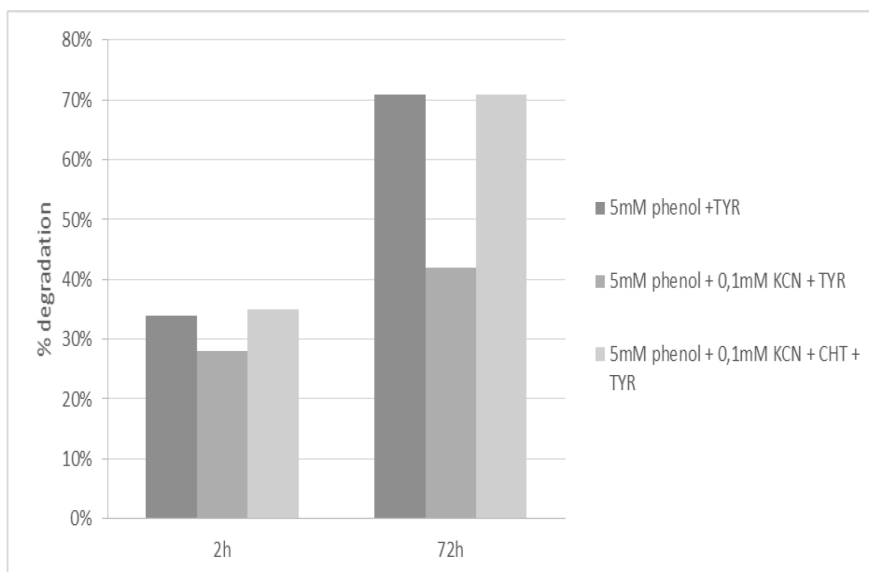


**Fig. 1**  
Inhibition of tyrosinase by 0.1 mM KCN and its alleviation by cyanide hydratase

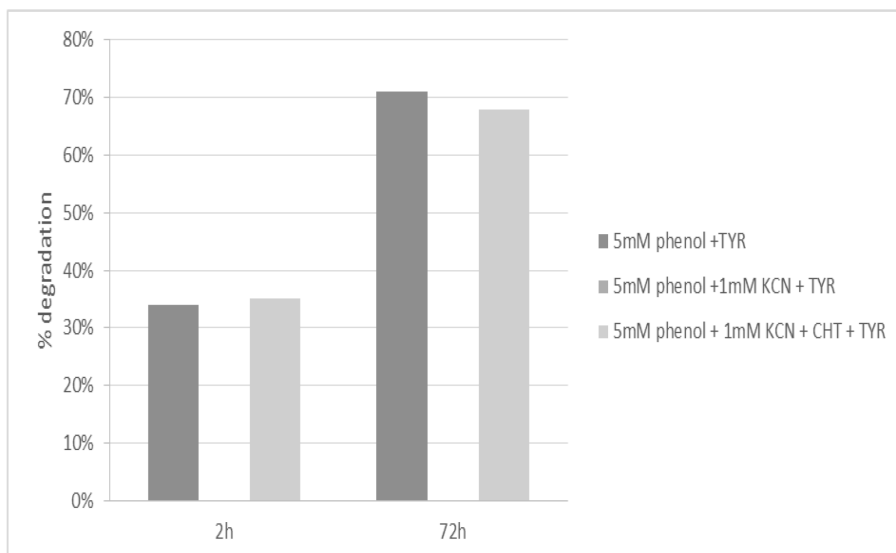


**Fig. 2**  
Inhibition of tyrosinase by 1 mM KCN and its alleviation by cyanide hydratase

Addition of the same tyrosinase to the PW sample did not result in a significant phenol degradation, which remained at ca. 11% after 20 h and was not substantially improved even after diluting this sample (1:1). This was probably caused by the presence of cyanide (0.32 and 0.16 mM in PW and diluted PW, respectively). The alleviation of tyrosinase inhibition by pre-treatment of the sample by CHT was also efficient in this case and enabled the degradation of phenol to increase to 33% after 20 h (Fig. 3). To achieve higher degradation within a short time, the tyrosinase amounts were increased in the next experiment (see below).

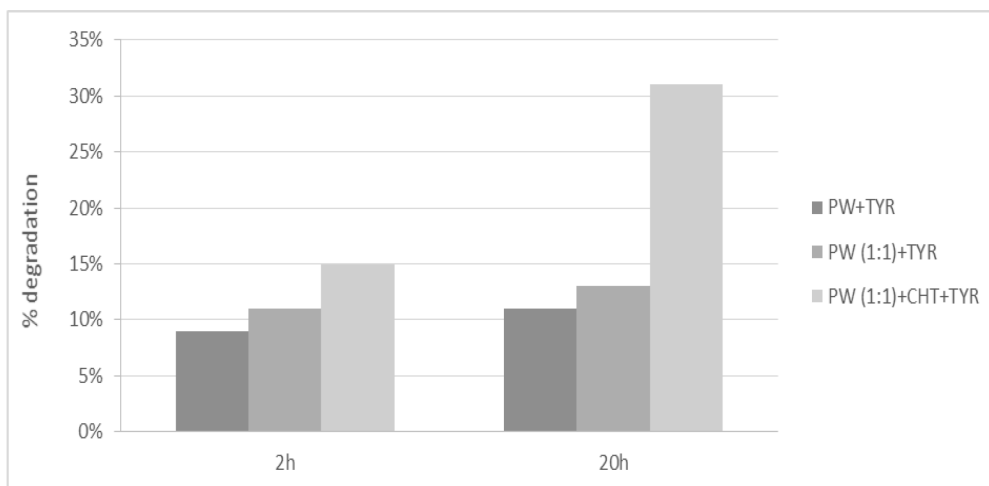


Fig. 3  
Inhibition of tyrosinase by cyanide in wastewater and its alleviation by cyanide hydratase

#### Effect of tyrosinase dosage on phenol and cresol degradation

In this experiment, the effect of the amount of tyrosinase on the degradation of phenol and cresol in PW was monitored (Fig. 4). The degradation increased with the amount of tyrosinase: with 250 U/ml the percentage of degradation of phenol and cresol was 8% and 17%, respectively, while increasing the enzyme amount to 2000 U/ml led to the degradation of 88% phenol and 62% of cresol within 4 h.

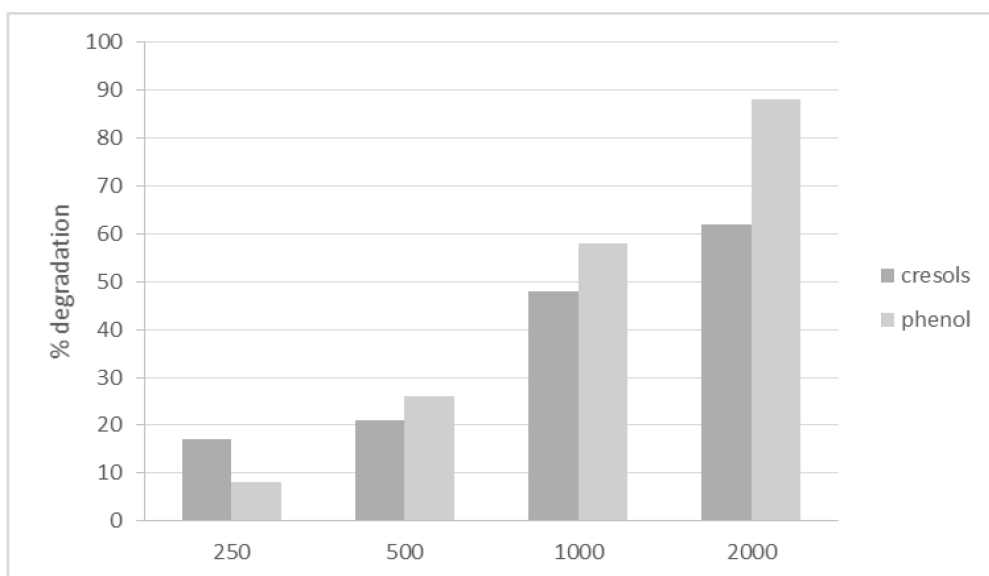


Fig. 4  
Effect of tyrosinase dosage on phenol degradation in wastewater

Note: reaction time 4 h

#### Effect of time of CHT application on phenol degradation by tyrosinase

In this part of the study the enzymes (CHT, TYR) were added simultaneously or at different times (Fig. 4). In the former method the efficiency of cyanide degradation remained low (cca 15%), suggesting an instantaneous inhibition of tyrosinase by the cyanide present. In contrast, the successive addition of CHT and tyrosinase led to degradation of cca 58 % phenol and 47 % cresol after 4-h reaction (Fig. 5).

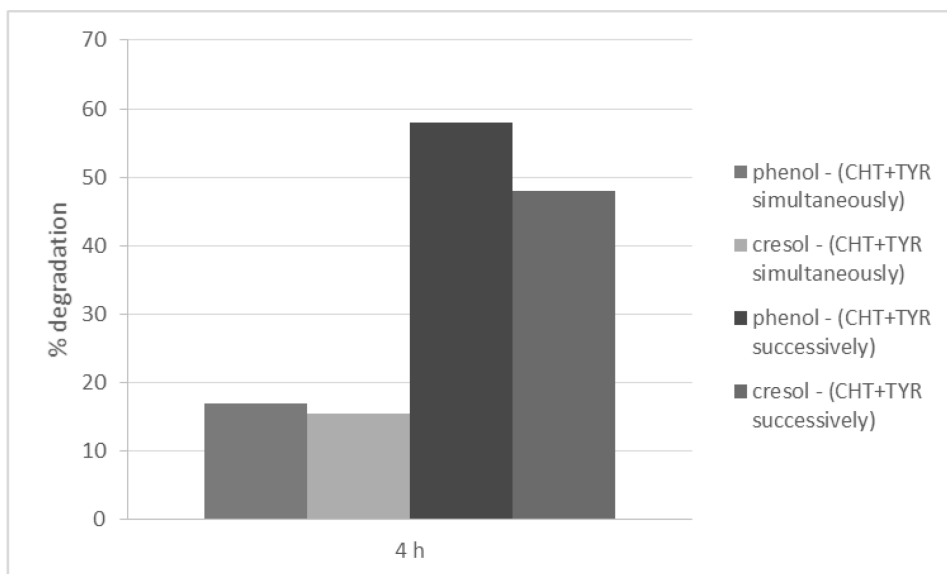


Fig. 5  
Effect of the simultaneous or successive addition of CHT and TYR on phenol degradation in wastewater

#### Degradation of phenol and cresol from wastewater by tyrosinase preparation TYR/AC

In the next experiment, the commercial tyrosinase was replaced with the enzymatic preparation obtained from the fruiting bodies. The preparation was tested for its potential to remove phenol and cresol from PW. Within 20 h, a complete degradation of phenol and 66% degradation of cresol was achieved (Fig. 6). The consumption of the phenolic compounds was almost linear with time for 8 h, at which point the degradation of phenol and cresol was 79% and 51%, respectively.

This form of the crude enzymatic preparation thus seems to be suitable for phenol degradation, and it may be also used for tyrosinase purification and immobilization.

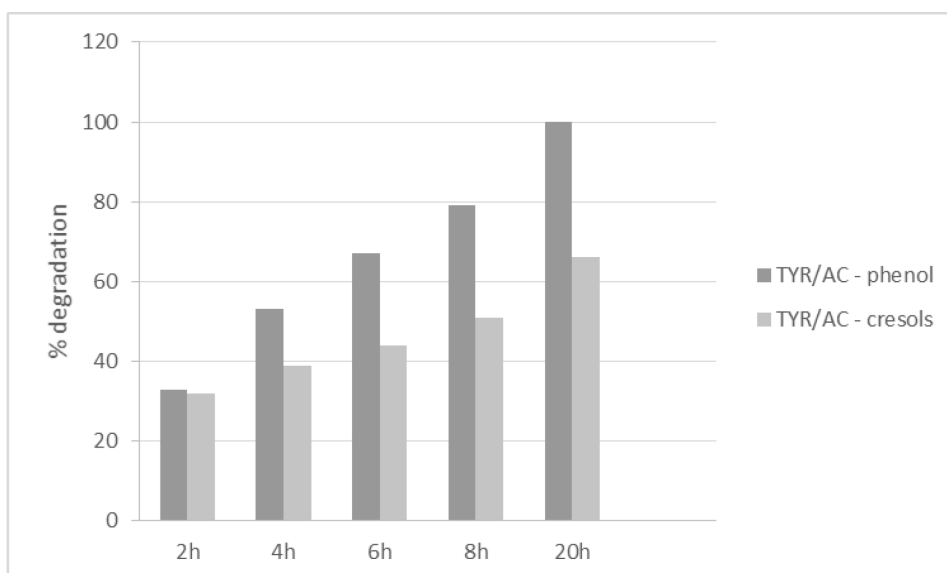


Fig. 6  
Degradation of phenol and cresols in wastewater by tyrosinase TYR/AC

#### Discussion

Natural and synthetic tyrosinase inhibitors are the focus of significant attention<sup>4</sup>. KCN, being one of the strongest inhibitors ( $K_i = 0.14\text{mM}$ ) of the tyrosinase activity, has been used in control experiments<sup>1</sup>. Here, a recombinant CHT from *Aspergillus niger* was used to eliminate  $\text{CN}^-$  ions from wastewater. This enzyme was previously demonstrated to exhibit a high specific activity for  $\text{CN}^-$  ions (930 U/mg) and to be resistant to the potential inhibitors present in coke plant wastewater such as sulfides and thiocyanates<sup>8</sup>. As a result, it degrades

cyanide in wastewaters at a high rate, while the reaction product - formamide – has no inhibitory effect on tyrosinase. Thus the enzymatic pre-treatment of the wastewater with CHT was necessary for an efficient elimination of phenol and cresol by tyrosinase. This solution was thus experimentally verified and seems to be an original approach to wastewater bioremediation.

The use of the tyrosinase from *A. bisporus* for the dephenolization of industrial wastewaters has been intensively studied in recent years. The suitability of various tyrosinase preparations such as crude extract or enzyme immobilized on silica gel<sup>11</sup>, alginate with PVP<sup>12</sup> or in CLEAs<sup>13</sup> was examined. However, these studies only rarely dealt with higher concentrations of phenol (940-1100mg/l)<sup>10,12</sup>, which are close to the concentrations in the wastewater we used (1552 mg/L). Here we succeeded in degrading this high phenol concentration with 100% efficiency, using the crude extract. Moreover, to the best of knowledge, no previous study made use of a combination of enzymes degrading phenolic pollutants on the one hand and cyanide-degrading enzymes on the other. Here, the step-by-step application of CHT and tyrosinase enabled the free cyanide to be eliminated under mild conditions and to provide conditions for the elimination of phenolic compounds. It is possible that this approach may also find applications in the bioremediation of other wastes or in biosensors.

The high efficiency of the crude tyrosinase suggests the utility of the further development of this catalyst, specifically its immobilization onto various supports, which would enable its continuous use or recycling.

*This work was supported by projects TA04021212 (Technology Agency of the Czech Republic) and LD12049 (Ministry of Education, Youth and Sports, programme COST CZ), Institute of Microbiology of the Academy of Sciences of the Czech Republic, v.v.i. (RVO61388971).*

#### Abbreviations

CHT = cyanide hydratase

CLEAs = cross-linked enzyme aggregates

PW = phenol water

IPTG = isopropyl  $\beta$ -D-1-thiogalactopyranoside

LB = Luria-Bertani medium (g/L tryptone 10, NaCl 10, yeast extract 5)

PVP = polyvinylpyrrolidone

TYR = commercial tyrosinase

TYR/AC = crude tyrosinase prepared by the extraction from fruiting bodies of *Agaricus bisporus*

#### Literature

1. Wada, S., Ichikawa, H., Tatsumi, K.: *Biotechnol. Bioeng.* **42**, 854 (1993).
2. Atlow, S. C., Bonadonna-Aparo, L., Klibanov, A. M.: *Biotechnol. Bioeng.* **26**, 599 (1984).
3. Ikehata, K., Nicell, J. A.: *Bioresource Technol.* **74**, 191 (2000).
4. Seo, S. Y., Sharma V. K., Sharma, N.: *J. Agric. Food Chem.* **51**, 2837 (2003).
5. Gasparetti, Ch., Nordlund, E., Jänis, J., Buchert, J., Kruus, K.: *Biochim. Biophys. Acta* **1824**, 598 (2012).
6. Rinágelová, A., Kaplan, O., Veselá, A. B., Chmátal, M., Křenková, A., Plíhal, O., Pasquarelli, F., Cantarella, M., Martínková, L.: *Proc. Biochem.* **49**, 445 (2014).
7. Fisher, F. B., Brown, J. S.: *Anal. Chem.* **24**, 1440 (1952).
8. Chmátal, M., Rinágelová, A., Veselá, A. B., Martínková, L.: *Sborník ICCT 2013*.
9. Pigatto, G., Lodi, A., Aliakbarian, B., Converti, A., Gonçalves da Silva, R. M., Palma, M. S. A.: *Bioresource Technol.* **143**, 678 (2013).
10. Romanovskaya, I. I., Shesterenko, Yu. A., Sevast'yanov, O. V.: *J. Water Chem. Technol.* **31**, 135 (2009).
11. Kampmann, M., Boll, S., Kossuch, J., Bielecki, J., Uhl, S., Kleiner, B., Wichmann, R.: *Water Res.* **57**, 295 (2014).
12. Shesterenko, Yu. A., Sevast'yanov, O. V., Romanovskaya, I. I.: *J. Water Chem. Technol.* **34**, 107 (2012).
13. Xu, D. Y., Chen, J. Y., Yang, Z.: *Biochem. Eng. J.* **63**, 88 (2012).

## DOUBLE REACTOR MEMBRANE HYBRID SYSTEM FOR PHENYLACETIC ACID PRODUCTION

**M. Mihal'**, I. Červeňanský, J. Markoš

*Institute of Chemical and Environmental Engineering, Faculty of Chemical and Food Technology, Slovak University of Technology, Radlinského 9, 812 37 Bratislava, Slovak Republic  
mario.mihal@stuba.sk, xcervenansky@stuba.sk, jozef.markos@stuba.sk*

### Abstract

Phenylacetic acid is the product of the 2-phenylethanol biotransformation by the strains of bacteria with incomplete oxidative metabolism such as *Gluconobacter oxydans*, which are able to oxidize primary alcohols to the corresponding carboxylic acids. 2-Phenylethanol can be easily produced by biotransformation from L-phenylalanine using ordinary yeasts such as *Saccharomyces cerevisiae*. Both phenylacetic acid and 2-phenylethanol are valuable components of flavors and their natural production is of great interest in the flavor industry. In an ordinary bioreactor produced 2-phenylethanol strongly inhibits the biomass growth and thus the biotransformation, which allows reaching the maximum 2-phenylethanol concentration of  $4 \text{ g L}^{-1}$  in the fermentation medium. To increase the production it is necessary to remove the product from the fermentation medium during the process. That can be easily made by applying continual membrane extraction using a capillary membrane module placed directly in the bioreactor. The organic solvent used as the extractant can be regenerated in a simple distillation unit. Another method for its regeneration is to reconnect the first and the second bioreactor via another capillary membrane module, where the extracted 2-phenylethanol can be continually transformed to phenylacetic acid. Such system represents the dual reactor membrane hybrid system.

In this work, phenylacetic acid was produced from L-phenylalanine in a dual reactor membrane hybrid system consisting of a 3 L stirred tank bioreactor for 2-phenylethanol production and of a 15 L internal loop airlift reactor for phenylacetic acid production. The bioreactors were connected with two immersed capillary membrane modules used for 2-phenylethanol transport between the bioreactors. In such a system, two biotransformation experiments with real 2-phenylethanol bioproduction from L-phenylalanine and its biotransformation to phenylacetic acid in non-growth conditions were carried out, one using the free cells of *Gluconobacter oxydans* and another one using the cells immobilized in lenticular LentiKats<sup>®</sup> particles.

### Introduction

Phenylacetic acid (PAA) can be produced by the biotransformation of 2-phenylethanol (PEA) with the strains of bacteria with incomplete oxidative metabolism such as *Gluconobacter oxydans* (Fig. 1) which are able to oxidize primary alcohols to the corresponding carboxylic acids<sup>1</sup>. Bioproduction of PEA is well known and it can be easily produced by the biotransformation from L-phenylalanine using ordinary yeasts such as *Saccharomyces cerevisiae* (Fig. 1)<sup>2</sup>. Both PAA and PEA are valuable components of flavors and their natural production is of great interest in the flavor industry. In an ordinary bioreactor produced PEA strongly inhibits the biomass growth and thus the biotransformation, which allows reaching the maximum PEA concentration of  $4 \text{ g L}^{-1}$  in the fermentation medium<sup>3</sup>.

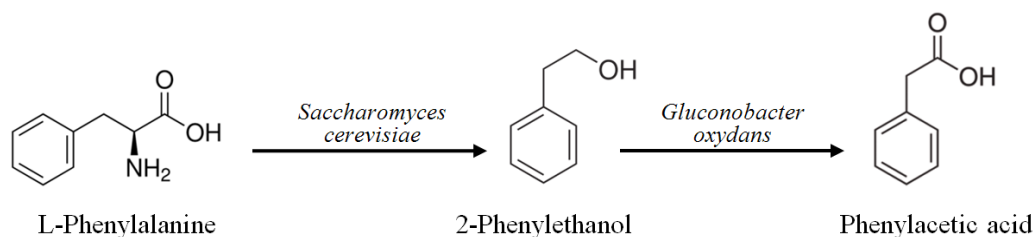


**Fig. 1.** Scheme of phenylacetic acid production from L-phenylalanine through the precursor 2-phenylethanol biocatalyzed by *Saccharomyces cerevisiae* and *Gluconobacter oxydans*.

To increase the PEA production it is necessary to remove the product from the fermentation medium during the process, which can be achieved by several ways<sup>4</sup>. A new suitable method for PEA removal is the application of continual membrane extraction using a capillary membrane module placed directly in the bioreactor<sup>5,6</sup>. The organic solvent used as the extractant can be regenerated in a simple distillation unit. Another method for the extractant regeneration is to reconnect the first and the second bioreactor via another capillary membrane

module, where the extracted PEA can be continually transformed to PAA. Such a system, a dual reactor membrane hybrid system, is studied in this work.

LentiKats<sup>®</sup> are lenticular particles based on polyvinyl alcohol used as a novel immobilization method for living cells and cross-linked enzymes<sup>7</sup> entrapment. These particles are non-toxic to biological materials, mechanically very stable, hardly biodegradable and their lenticular form is optimized for limitations of undesired diffusion effects. They can be used in different biotechnological application, e.g. pharmaceutical and food industry<sup>8</sup>, distilleries<sup>9</sup> or wastewater treatment<sup>10</sup>. Immobilization of microorganisms in such particles strongly enhances the stability of the enzymatic activities and simplifies the biocatalyst recovery.

In this work, phenylacetic acid was produced from L-phenylalanine in the dual reactor membrane hybrid system consisting of a 3 L stirred tank bioreactor for 2-phenylethanol production and of a 15 L internal loop airlift reactor for phenylacetic acid production. In the presented hybrid system, two biotransformation experiments with real PEA bioproduction from L-phenylalanine by *Saccharomyces cerevisiae* and its continual biotransformation to PAA were carried out, one using free cells of *Gluconobacter oxydans* and the other one using cells immobilized in the LentiKats<sup>®</sup> particles.

## Materials and methods

### Chemicals

2-Phenylethanol (99 %) and methyl benzoate (99 %) were purchased from Sigma–Aldrich (Steinheim, Germany). Acetophenone (98 %) was purchased from Merck (Hohenbrunn, Germany). Heptane (99 %) and glucose (monohydrate) were obtained from Mikrochem (Pezinok, Slovakia). Ethyl acetate was purchased from Lachema (Brno, Czech Republic). L-phenylalanine was obtained from Evonik (Slovenská Ľupča, Slovakia). Dipotassium phosphate, monopotassium phosphate and sodium hydroxide were purchased from Centralchem (Bratislava, Slovakia).

### Analytical methods

Concentrations of acetophenone, methyl benzoate, phenylacetic acid and 2-phenylethanol in the organic phase were measured by a gas chromatograph 6890N (Agilent Technologies, Santa Clara, USA) equipped with a column Agilent 19091N-113, flame ionization detector and an automatic sampler. For each analysis, acetophenone and methyl benzoate were used as internal standards added to the sample in form of an ethyl acetate solution. Each sample was analyzed twice using arithmetic means of the measured peak areas from the gas chromatograph.

Biomass concentration in the fermentation medium was analyzed spectrophotometrically at the wavelength of 600 nm using a spectrophotometer SPEKOL 11 (Carl Zeiss, Jena, Germany). Concentrations of L-phenylalanine, glucose and ethanol in the fermentation medium were analyzed by an analyzer Omnilab MINOR (Biorealis, Bratislava, Slovakia) using enzyme probes. Concentration of 2-phenylethanol in the fermentation medium was determined using the back extraction of 2-phenylethanol to heptane. Before the analysis, 1 ml of the sample was placed into a 10 ml test tube with an addition of 1 ml of heptane. The content of the test tube was then mixed for 5 min and then transferred to a centrifuge for 5 min at 5000 rpm. After the centrifugation, 200  $\mu$ L of the heptane phase were taken and analyzed using a gas chromatograph.

Phenylacetic acid concentration in the water phase was determined using the double back extraction of phenylacetic acid to ethyl acetate. Before the analysis, 1 ml of the sample was placed into a 10 ml test tube with an addition of inner standard, 10  $\mu$ L of sulfuric acid (50 % mass) and 1 ml of ethyl acetate. The content of the test tube was then mixed for 1 min and the organic phase was placed into another test tube. The process of extraction was repeated with another 1 ml of ethyl acetate and the extracts were mixed together. Then, 200  $\mu$ L of the extract were taken and analyzed using a gas chromatograph. In case of the analysis of phenylacetic acid in the fermentation medium containing free cells, the sample was centrifuged before the back extraction at the same conditions as formerly mentioned.

### Experimental equipment

The hybrid system (Fig. 2a) consisted of three main objects: a mechanically stirred tank bioreactor (STR), an internal loop airlift reactor (ALR) and a vessel with organic phase. Inside the bioreactors, the immersed capillary membrane

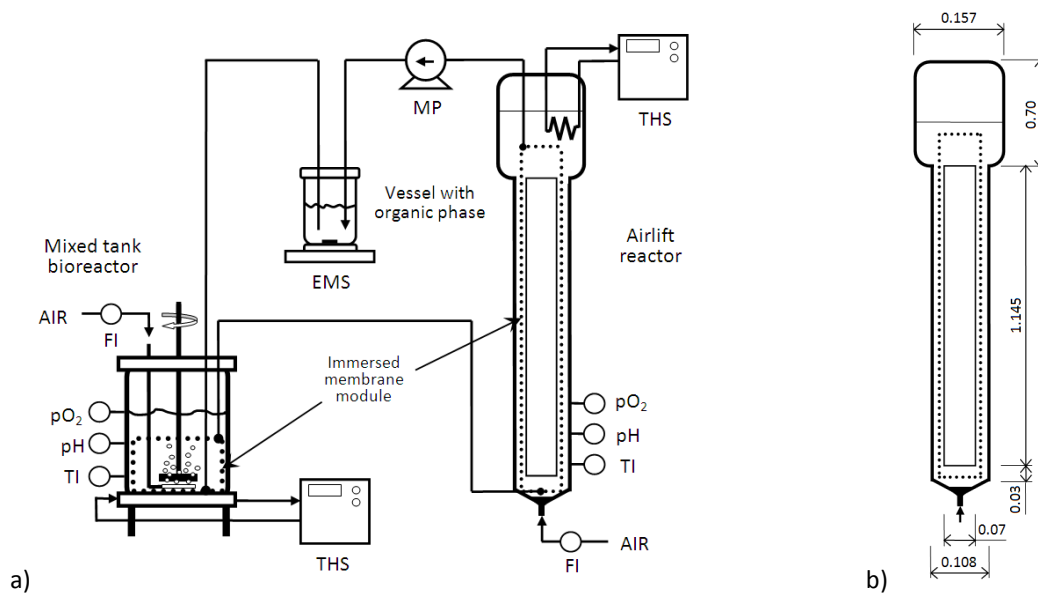


**Fig. 2.** Scheme of the dual hybrid bioreactor with immersed capillary membrane modules (a); dimensions of the airlift reactor in meters (b). (EMS – electromagnetic stirrer, FI – flow indicator, MP – membrane pump, pH – pH probe, pO<sub>2</sub> – oxygen probe, THS – thermostat, TI – temperature indicator).

modules were placed at the bottom of STR, in the downcomer and in the separator of ALR. The shell of STR was made of glass, the bottom and cover of stainless steel. Dimensions of the bioreactor were: outer height×width of 30×21 cm; inner height×width of 25×15 cm. Its working volume was in the range of 2.5-3.5 L. It was equipped with a Rushton turbine stirrer (6 blades, 6.7 cm in diameter) driven by an electric motor allowing fluent regulation of the stirrer speed from 200 to 1000 rpm. A circular sparger made of a stainless steel tube was installed below the stirrer. Dimensions of the ALR are shown in Fig. 2b. Its working volume was in the range of 10-15 L. Both bioreactors were equipped with a thermometer, pH and an oxygen probe. Flow rate of compressed air was regulated by a valve and measured by a rotameter. Temperature of the liquid in the STR was regulated using the double bottom of the bioreactor serving as a heat exchanger and connected to a thermostat. Temperature in the ALR was regulated using a stainless heating spiral also connected to the thermostat.

Membrane modules used for the membrane extraction were manually manufactured in our laboratory in three different dimensions (I, II, III) (Table I). For the construction of the membrane modules, hydrophobic capillary fibers Accurel® PP S6/2 (MEMBRANA GmbH, Wuppertal, Germany) were used. The fibers were made of polypropylene with the outer diameter of 2.7 mm and the wall thickness of 0.45 mm. Fibers were fixed at both terminals to two rings made of a polyethylene tube. Holes with the size of the outer fiber diameter were drilled in three circles into both rings and each fiber was crammed to these holes about 5 mm inwards without using any sealing material. The membrane module contained also an inlet and outlet of organic solvent created by a small polyethylene tube fixed and sealed with Teflon tape to each of the rings. The smallest membrane module I was placed at the bottom of the STR (Fig. 3a), membrane modules II and III were installed in the separator (Fig. 3b) or in the downcomer of the ALR (Fig. 3c), respectively.

**Table I.** Characteristics of the immersed capillary contactors installed in the hybrid system.

Membrane module	I	II	III
Dimensions of contactor, [mm]	150 × 94	142 × 195	104 × 1310
Outer/inner fitting tube diameter, [mm]	15/12	15/12	12/8
Outer/inner rings diameter, [mm]	150/124	140/115	104/80
Overall contact area, [m <sup>2</sup> ]*	0.135	0.457	1.84
Number of fibers	245	321	169
Effective fiber length, [mm]	65	168	1285

\* based on outer diameter

The inlet and outlet of the membrane modules installed in the STR and ALR were connected with flexible and chemical resistant tubes leading out from the bioreactors to a 1 L glass vessel with the organic phase. The vessel with the organic phase was continually mixed at 300 rpm using an electromagnetic stirrer. During the extraction, the organic solvent flowed from the reservoir vessel to the membrane module in the STR and subsequently to the membrane module in the ALR and back to the vessel. Pumping of the organic solvent was performed using a Teflon<sup>®</sup> membrane pump (Liquiport, KNF Flodos, Sursee, Switzerland) installed at the outlet from the membrane module installed in the ALR. The extraction capability of the simpler hybrid system consisted only of one bioreactor and the immersed extraction membrane modules for combinations of the STR - membrane module I and the ALR - membrane module III were tested and described in our previous papers<sup>5,11</sup>.

#### *Biotransformation experiments performed in hybrid system*

In the hybrid system, two biotransformation experiments, B1 and B2, were carried out. Experiment B1 was performed using immobilized biomass and membrane module II placed in the separator of the ALR. Experiment B2 was carried out with free biomass and membrane module III placed in the downcomer of the ALR. Experiments B1 and B2 were performed with real production of PEA in the STR by *Saccharomyces cerevisiae* and the PEA transport from the STR to the ALR with continual production of PAA in the ALR.

For both experiments, at the beginning of the biotransformation, the STR was filled with 2.5 L of the fermentation medium: a solution of distilled water with corn steep, essential micro and macro components, grow factors and glucose in the concentration of 5 g L<sup>-1</sup>. After the pH adjustment (to 5.5), tempering (27 °C) and aeration of the system (800 L h<sup>-1</sup>), 15 g of lyophilized baker's yeasts (*Saccharomyces cerevisiae*) were added to the fermentation medium and left to activate for half an hour. Then, 25 g of crystalline L-phenylalanine (Phe) were added to the fermentation medium and the biotransformation started (production of PEA in the STR). The STR was fed with a water solution of glucose (Glu) with the mass fraction of 50 % (feeding rate of 5 g of glucose per min) half an hour after the beginning of the biotransformation. L-Phenylalanine was fed several times in crystalline form to ensure the Phe concentration in the STR over 2 g L<sup>-1</sup>. Membrane extraction started 9 h after the start of the biotransformation with the average heptane flow rate of 0.1 L min<sup>-1</sup>. The reservoir for organic phase was filled with 1 L of clear heptane. The ALR was filled with the fermentation medium a short time before the extraction. As the fermentation medium, phosphate buffer, composed of a 0.1 M aqueous solution of potassium phosphate and a 0.1 M aqueous solution of potassium hydrogen phosphate mixed together in the ratio of cca 0.9:1 to get pH 6.8 of the final buffer solution, was used.

For experiment B1, the ALR contained 0.5 kg of wet particles with immobilized *Gluconobacter oxydans* (9.3 g of dry biomass) and 15 L of the total volume of fermentation medium. LentiKats<sup>®</sup> particles were prepared by the company LentiKat's a.s. (Stráž pod Ralskem, Czech Republic) from polyvinyl alcohol gel composed of 15 g of dry biomass, 100 g of polyvinyl alcohol and phosphate buffer on 1 L of gel, which is an equivalent of 800 g of wet particles (1 kg of wet particles contains 18.67 g of dry *Gluconobacter oxydans*). The prepared particles had lenticular shape with the diameter of 3-4 mm and the thickness of 200-400 µm. To ensure the proper function of membrane module II in the ALR, the space between the riser and the separator in the ALR was separated by a thin sieve, which restrained the LentiKats<sup>®</sup> particles in the space below the separator and prevented them to clog the space between the fibers of the membrane module. The sieve was freely permeable for the transport of air and liquid.

For experiment B2, at the beginning, the ALR contained 5.86 g of free cell mass of *Gluconobacter oxydans* (dry mass), increased by 2.9 g in 55 h of the experiment. In both experiments (B1, B2), aeration in the ALR was kept at 800 L h<sup>-1</sup>. Samples of the fermentation medium in the STR and ALR were taken every 3 h. At the same time, samples of the organic phase in the reservoir were also taken. The samples were analyzed for PEA, PAA, biomass, L-phenylalanine, glucose and ethanol concentration. During the biotransformation experiments in the hybrid system, the temperature of the fermentation medium in the ALR was kept at 27 °C and pH at 6.8 (with additions of 2 M NaOH).

#### **Results and discussions**

Biotransformation experiment B1 was carried out in the hybrid system with real production of PEA from L-phenylalanine (Phe) in an STR using growing *Saccharomyces cerevisiae*. The experiment lasted for 75 h. The concentration course of the individual compounds in the fermentation medium is shown in Fig. 3. Fig. 3a displays the concentration of PEA in the STR, in reservoir with heptane (RES) and in the ALR, and the concentration of PAA in the ALR. The concentration of PEA in the STR reached its maximum of 3.3 g L<sup>-1</sup> in 24 h and then it gradually decreased until the end of the experiment. High PEA concentration secured high driving force for the membrane

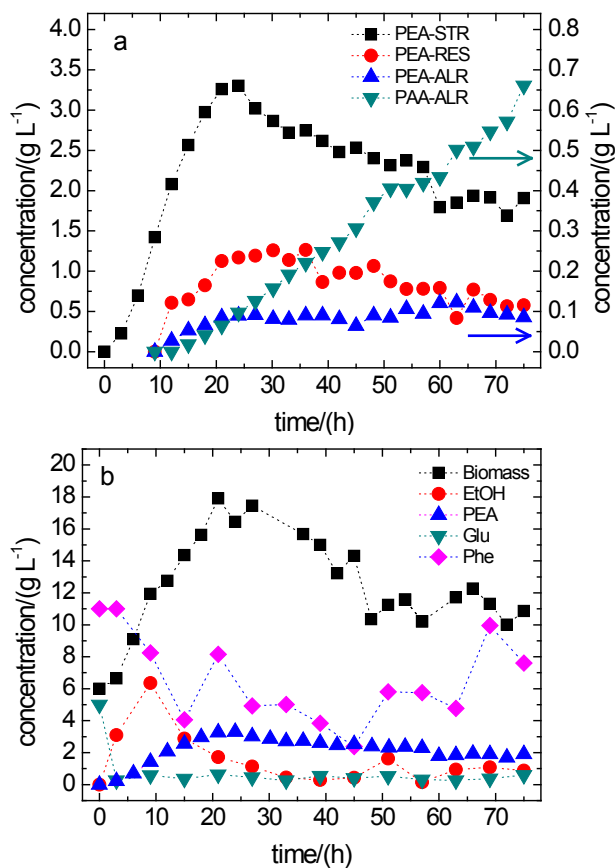


**Fig. 3.** Concentration profile of PEA in the STR, reservoir of the organic phase (RES), ALR and concentration profile of PAA in the ALR (a); concentration profile of PEA in the fermentation medium in the STR for biomass, EtOH, Phe, Glu and PEA (b) for biotransformation experiment B1 carried out in the double reactor membrane hybrid system using LentiKats<sup>®</sup> for PAA production.

Extraction, represented by the increasing PEA concentration in the reservoir and in the ALR. The increase of the PAA concentration in the ALR was quite constant and the PAA productivity reached  $15 \times 10^{-3} \text{ g h}^{-1}$  per 1 g of dry biomass. Relatively low PAA production was caused by the very low PEA concentration in the ALR due to the relatively slow PEA transport through the membrane system. Fig. 3b shows the concentration profile of the key components in the STR: biomass, PEA, L-Phenylalanine (Phe), glucose (Glu) and ethanol (EtOH). The concentration of biomass reached the maximum of  $18 \text{ g L}^{-1}$  in around 23 h, which copies the trend of the PEA concentration. From the time of 25 h to the end of the experiment, gradual decrease of the biomass concentration indicating the slowdown of the biomass growth due to the high PEA concentration and thus induced inhibition of the biomass growth. Thanks to the moderate rate of Glu feeding, the concentration of Glu was kept at a value close to zero, which helped to prevent the formation of EtOH.

In the biotransformation experiment B2, the contact area of the used membrane module III was four times higher than in experiment B1. This fact induced the increase of the PEA transport rate between the bioreactors of the hybrid system. The concentration profiles of PEA in the STR, reservoir with heptane (RES), and in the ALR and the

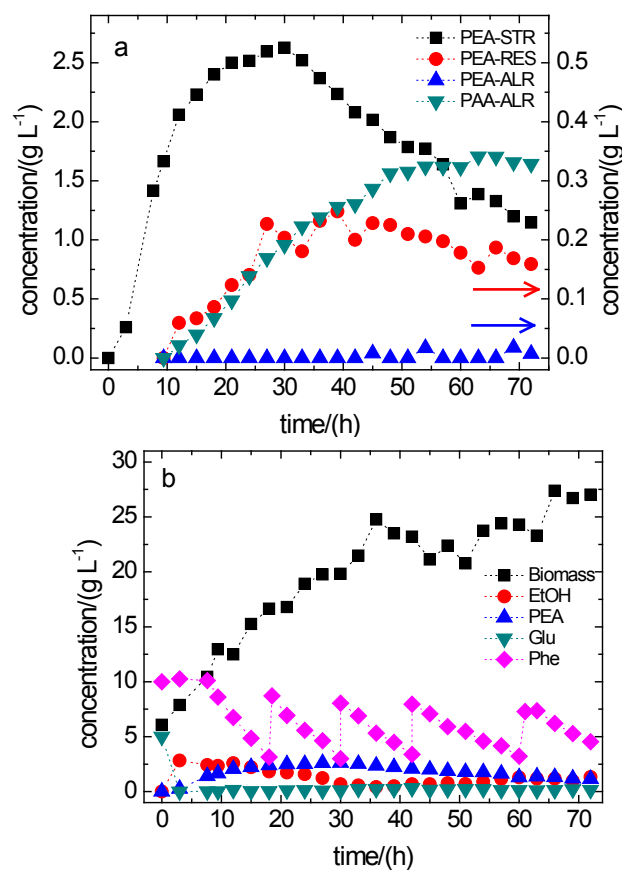


**Fig. 4.** Concentration profiles of PEA in the STR, reservoir of the organic phase (RES) and ALR, and of PAA in the ALR (a); PEA in the fermentation medium in the STR for biomass, EtOH, Phe, Glu and PEA (b) for biotransformation experiment B2 carried out in the double reactor membrane hybrid system using free cells for PAA production.

Concentration profiles of PAA in the ALR are displayed in Fig. 4a. High activity of free biomass in the ALR (free cells of *Gluconobacter oxydans* were approximately ten times more active than immobilized cells) caused the almost zero concentration of PEA in the ALR during all experiments. PEA concentration in the reservoir was stabilized at around 0.2 g L<sup>-1</sup> (average of 0.9 g L<sup>-1</sup> in experiment B1), which also indicates intensive PEA transport. Total concentration of produced PAA in the ALR reached 1.6 g L<sup>-1</sup>, which represents the PAA production of  $53 \times 10^{-3}$  g h<sup>-1</sup> per 1 g of dry biomass. Concentration profiles of the key components in the STR are shown in Fig. 4b. The concentration of biomass in the STR gradually increased to the maximum of 27 g L<sup>-1</sup>. The continual growth of the yeasts was ensured by the lower PEA concentration in the STR and thus by the lower inhibition of the biomass growth and the lower inhibition of the biotransformation in comparison with experiment B1.

### Conclusions

The proposed hybrid system for phenylacetic acid production consisted of two bioreactors: a stirred tank bioreactor and an airlift reactor; mutually connected by the immersed capillary membrane modules placed inside the bioreactors which allow continuous transport of 2-phenylethanol, the precursor of the production from the stirred tank reactor where it was produced by biotransformation from L-phenylalanine catalyzed by the baker's yeast *Saccharomyces cerevisiae* to an airlift reactor where it was consumed by biotransformation to phenylacetic acid catalyzed by *Gluconobacter oxydans*. *Gluconobacter oxydans* was used in two different forms: 1. immobilized in the LentiKats<sup>®</sup> particles; 2. as free biomass.

Entrapment of biomass in the LentiKats<sup>®</sup> particles provides a stable immobilized biocatalyst which can be easily used in the airlift reactor to ensure satisfactory productivity and easy operational features since no foam is formed, the biocatalyst can be recycled and the recovery of the product is simplified. Moreover, immobilized biomass is more resistant to mechanical and chemical stress, which can lead to its higher productivity and higher number of applied recycling cycles. On the other hand, free cells of biomass ensure much higher PAA

productivity but the stamina of the biomass is much lower with the rapid decrease of its activity from the maximum to almost zero. It is also quite complicated to recycle free biomass but for the real PAA production it is possible to use lower concentrations of free cells that must be more often refilled with fresh ones to secure stable PAA production.

The double reactor hybrid system is capable to continually produce phenylacetic acid from L-phenylalanine for 75 h and longer. Using the hybrid system, it was not necessary to process and purify 2-phenylethanol for its consequential use for phenylacetic acid production. Moreover, the back extraction of 2-phenylethanol to the second bioreactor serves as the regeneration of the extractant, substituting thus a regeneration unit.

#### **Acknowledgements:**

*This work was supported by the Slovak Research and Development Agency under the contract number APVV-0656-11.*

#### **Literature**

1. Švitel J., Šturdík E.: *Enzyme Microb. Tech.* 17, 546-550 (1995).
2. Wang C. T., Sun B. G., Cao Y. P., Wang J., Zhang H.: *Mod. Chem. Industry* 28, 38-43 (2008).
3. Stark D., Zala D., Münch T., Sonnleitner B., Marison I. W., von Stockar U.: *Enzyme Microb. Technol.* 32, 212-223 (2003).
4. Hua D., Xu P.: *Biotechnol. Adv.* 29, 654-660 (2011).
5. Mihaľ M., Goncalves R. F., Markoš J.: *Chem. Pap.* 68, 1656-1666 (2014).
6. Mihaľ M., Krištofiková Ľ., Markoš J.: *Chem. Eng. Process.* 72, 144-152 (2013).
7. Schlieker M., Vorlop K.-D.: *Immobilization of Enzymes and Cells, Methods in Biotechnology™* 22, 333-343 (2006).
8. Rebroš M., Rosenberg M., Mlichová Z., Krištofiková Ľ., Paluch M.: *Enzyme Microb. Technol.* 39, 800 - 804 (2006).
9. Rebroš M., Rosenberg M., Grosová Z., Krištofiková Ľ., Paluch M., Sipocz M.: *Appl. Biochem. Biotechnol.* 158, 561 - 570 (2009).
10. Trogl J., Bouskova A., Mrakota J., Pilarova V., Krudencova J., Mechurova J., Krizenecka S., Stloukal R.: *Desalination* 275, 82 - 86 (2011).
11. Mihaľ M., Gavin S. P., Vereš R., Markoš J.: *Chem. Pap.* 67, 1485-1494 (2013).

## IN VITRO ACTION OF BAICALEIN ON *CANDIDA ALBICANS*, *CANDIDA PARAPSILOSIS* AND *CANDIDA KRUSEI* GROWTH INHIBITION

**Kvasničková E.**, Masák J.

University of Chemistry and Technology Prague, Technická 5, 166 28, Prague 6, Czech Republic  
Eva.Kvasnickova@vscht.cz

### Introduction

Baicalein is 5,6,7-trihydroxyflavone (Figure 1), which belongs to the group of flavones. It is originally isolated from the roots of *Scutellaria baicalensis*<sup>1</sup>. This Chinese herb has been used for thousands years in traditional Chinese medicine for various purposes such as the treatment of fever, inflammatory diseases and allergies as documented in the Pharmacopoeia of the People's Republic of China<sup>2</sup>. *Scutellaria baicalensis* is a widespread herb, especially in Asia and is considered to be a cheap and unlimited source of new biomolecules. Its roots contain over than thirty different types of flavones with a variety of pharmacological properties<sup>1</sup>. The biological activities of extract from *Scutellaria baicalensis* include an antioxidant, anti-inflammatory, antibacterial, antiviral<sup>3</sup>, antifungal<sup>4</sup>, antiallergic, antihypertensive and a diuretic activity<sup>5</sup> and it may inhibit the function of lipoxygenase<sup>6</sup> and reverse transcriptase<sup>4</sup>. Purified baicalein due to its antibacterial and anti-inflammatory properties could be useful for the treatment of diseases such as bronchitis, urinary tract infections, hepatitis and inflammation of the oral cavity<sup>5</sup>. The mechanism of baicalein action is not completely understood. One of the proposed explanations is the induction of apoptosis or inhibition of quorum sensing system. Baicalein in combination with antibiotic treatment can reduce the excretion of drug out of the yeasts cells by efflux pump inhibition<sup>7</sup>.

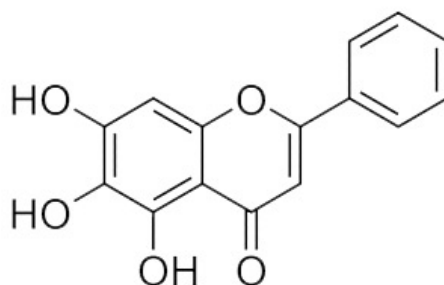


Figure 1 Baicalein chemical structure<sup>8</sup>

*Candida spp.* are the most common isolated yeasts from a variety of human infections. *Candida albicans* is often designated like the most isolated opportunistic pathogenic yeast, which may overgrow in the bloodstream, oral cavity or genital tract and subsequently causes fatal candidiasis in immunocompromised patients<sup>9,10</sup>. On the other hand, *Candida parapsilosis*, *Candida krusei*, *Candida tropicalis* and *Candida glabrata* have also attracted increasing attention in designing the treatment for infections, which are caused by these yeast strains<sup>9</sup>. The frequent use of antibiotics is the reason for easy emerging resistance what is the real problem in medicine today<sup>11</sup>.

The purpose of this study is to find new possibility for the treatment of *Candida* infections using the natural substance baicalein in combination with typically used antibiotic, because of its inefficiency in many cases can be fatal for many patients.

Key words: baicalein, antibiotic, *Candida*, antimicrobial activity, infections

### Materials and Methods

#### Fungal strains and cultivation conditions

*Candida parapsilosis* DBM 2165 and *Candida krusei* DBM 2163 and *Candida albicans* DBM 2164 were obtained from the collection of microorganisms from UCT, Prague. Stock cultures were stored at -70 °C and precultured, for 48 hours, aerobically at 30 °C before each experiment, in malt extract medium in the case of *C. parapsilosis* and *C. krusei* or yeast peptone dextrose medium (YPD) in the case of *C. albicans*. The experiments were also carried out in these growth media.

### Antifungal agents

Baicalein and amphotericin B were purchased from Sigma-Aldrich. Baicalein was dissolved in DMSO and amphotericin B was dissolved in appropriate cultivation medium. Each substance was stored, maximally for one week, at 4 °C until used. The final concentration of DMSO was until 1 % in all assays.

### Antifungal activity

The minimum inhibitory concentrations (MIC) of baicalein and amphotericin B for the *C. parapsilosis*, *C. krusei* and *C. albicans* were determined by microdilution method according to Sharma et al. (2010)<sup>12</sup>. The minimum inhibitory concentration was specified as the lowest concentration that did not exhibit growth (monitored by OD<sub>600nm</sub> determination) higher than 20 %. The cultivation was carried out in 100-well microtiter plates using Bioscreen C analyzer (Oy Growth Curves Ab Ltd., Finland). To each well 30 µl of standard cell suspensions of one of the microorganism (OD<sub>600nm</sub> = 0.1) were added. Drug-free and yeast-free controls were included. Plates were incubated for 24 h at 30 °C in the case of each yeast strain. Experiments were performed with five replicate wells for each experiment.

### Action of substances in combination

The combination testing of amphotericin B and baicalein was performed by the chequerboard method in microtiter plate according to Samadi et al. (2012)<sup>13</sup>. The influence of substances in combination was determined by monitoring microbial growth in 100-well microtiter plates using Bioscreen C analyzer (Oy Growth Curves Ab Ltd., Finland) influenced by the presence of both substances in sub-MIC concentration (10 % - 80 % MIC) in different ratios.

### Results and Discussion

The minimum inhibitory concentration of baicalein and amphotericin B was determined for suspended cells of *C. albicans*, *C. parapsilosis* and *C. krusei*. The MIC values that are shown in Table I were found to be very high for baicalein (up to 400 mg/l) in comparison to antibiotic amphotericin B MIC that are below 5 mg/l.

Table I Minimum inhibitory concentrations (MIC) of baicalein and amphotericin B for planktonic suspension cells

MIC [mg/l]			
	<i>C. parapsilosis</i>	<i>C. krusei</i>	<i>C. albicans</i>
baicalein	350	400	100
amphotericin B	1.5	2.5	4.5

Based on the determined MIC, the inhibitory influence of two substances combination in sub-MIC concentrations on the growth of each selected yeast strain was studied. The different combinations of concentration ratios were evaluated by monitoring the growth (in comparison with control – growth curve without antimicrobial presence). The lowest concentration combinations that lead to inhibition of the yeast growth were found out.

Figure 2 shows the combined action of baicalein and amphotericin B on the growth of *C. parapsilosis*. It was found that this yeast strain is sensitive to the presence of these two substances in combination – even the lowest studied ratio 10 % MIC of baicalein + 10 % MIC of amphotericin B (35 mg/l baicalein and 0.15 mg/l amphotericin B) leads to the growth inhibition. Baicalein and amphotericin B therefore can be concluded have a synergistic inhibitory effect on *C. parapsilosis*.

*C. krusei* did not display similar response to the combined presence of baicalein and amphotericin B as is shown

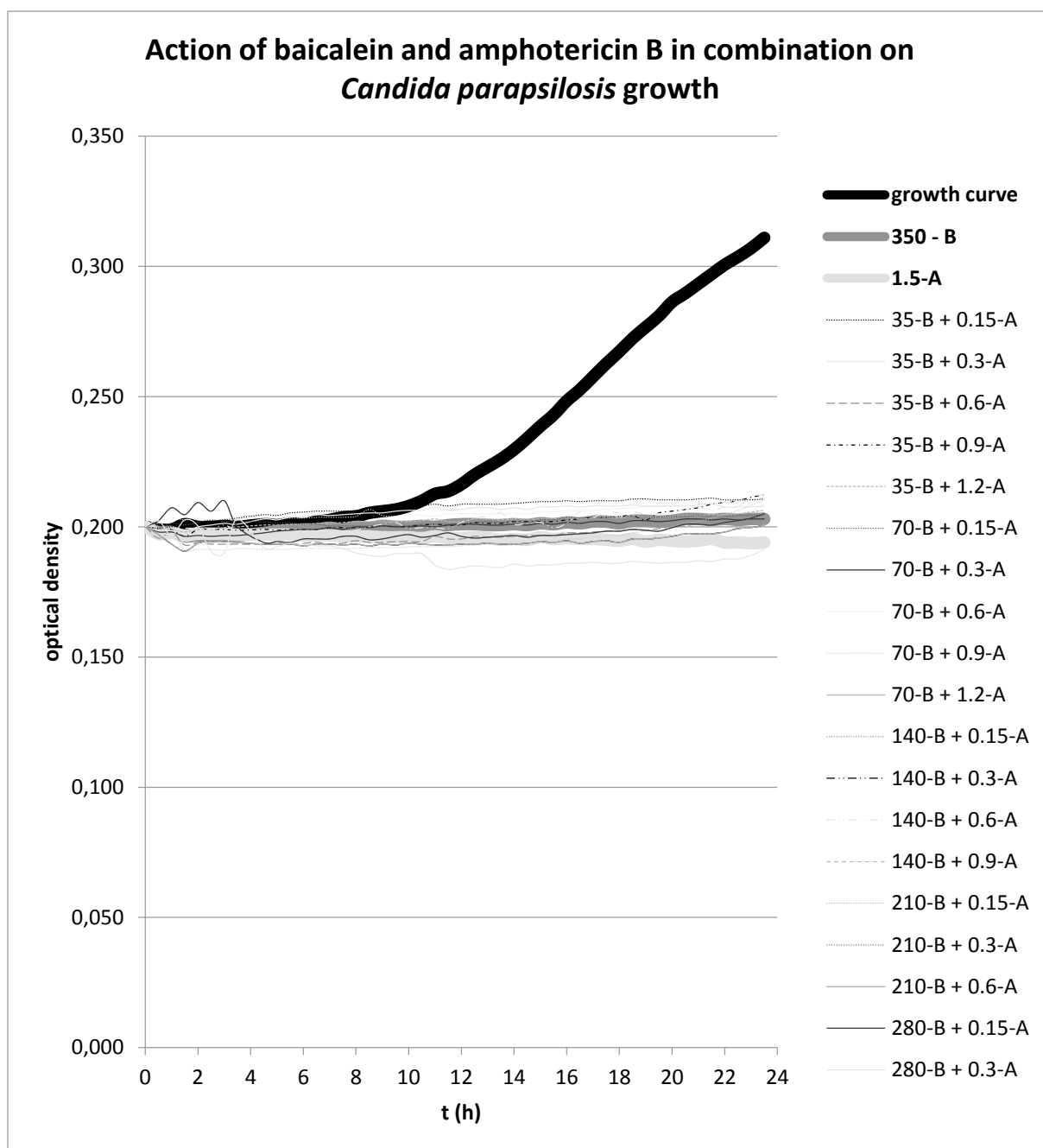


Figure 2 The influence of baicalein and amphotericin B combination on *C. parapsilosis* growth. The studied baicalein concentration (B) is stated in the legend as the first value; the actual concentration of amphotericin (A) is stated as second.

in Figure 3. The most of the observed concentration combinations lead to an increased growth in comparison with control cultivation. In some cases (combinations 10 % of baicalein MIC and 10, 20 a 40 % of amphotericin B MIC - 40 mg/l baicalein and 0.25, 0.5 a 1 mg/l amphotericin B, respectively) the growth was up to 30 % above the control as determined by optical density. However, the combination of baicalein and amphotericin B displays an antagonistic behavior toward *C. krusei*. Only the concentrations 320 mg/l (baicalein) and 0.5 mg/l (amphotericin B) lead to an inhibition of growth. These concentrations are very close to the MIC values and as such cannot be considered synergistic.

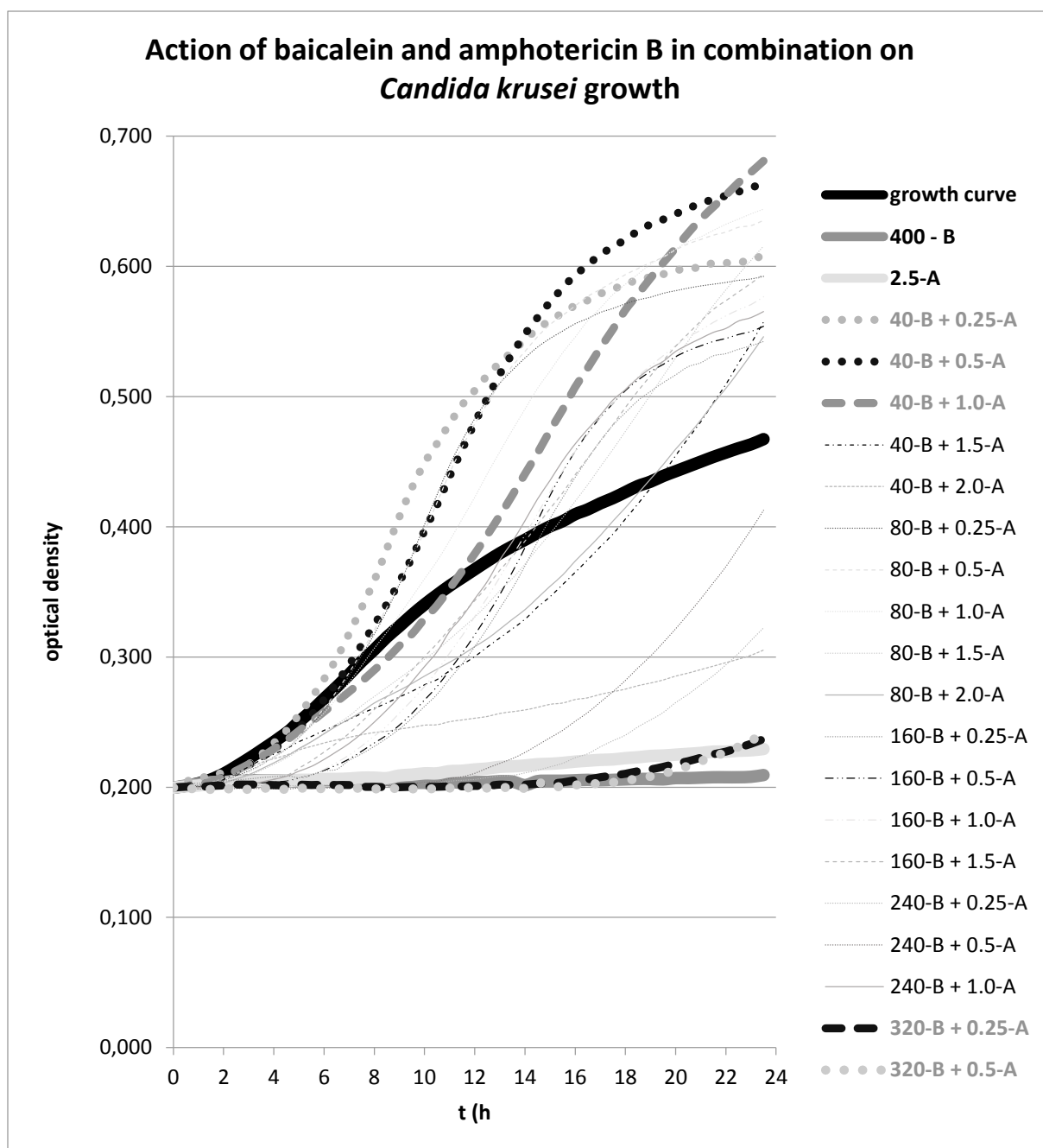


Figure 3 The influence of baicalein and amphotericin B combination on *C. krusei* growth. The studied baicalein concentration (B) is stated in the legend as the first value; the actual concentration of amphotericin (A) is stated as second.

The studied strain of *C. albicans* (Figure 4) showed similar behavior to *C. parapsilosis*. All studied concentration combinations lead to an inhibition of this yeast strain. The lowest effectual concentrations were therefore 10 % of MIC baicalein and 10 % of MIC amphotericin B (in this case 10 mg/l baicalein and 0.45 mg/l amphotericin B). Interesting effect of a low overall growth (less than 20 % of control without the substances) was observed in all studied combinations of 10% MIC amphotericin B with all baicalein concentrations, except the highest (80 % MIC, 80 mg/l). Although according to the MIC determination is as inhibitory considered growth less than 20 % of control cultivation, this effect of the low antibiotic concentration inhibition can be attributed to weakening synergistic effect and in long-term cultivation would be inadvisable for application (higher antibiotic concentration might be more appropriate).

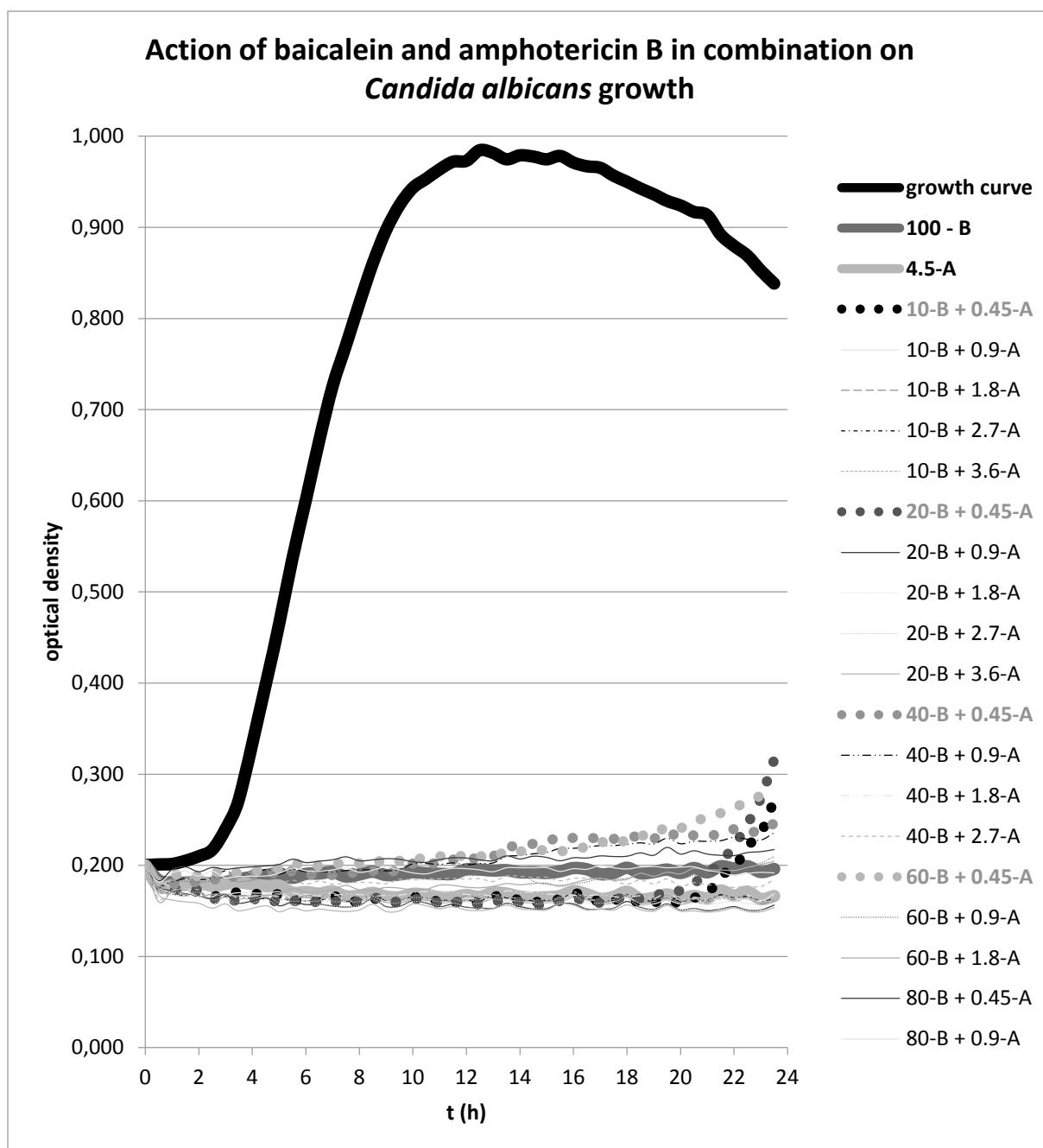


Figure 4 The influence of baicalein and amphotericin B combination on *C. albicans* growth. The studied baicalein concentration (B) is stated in the legend as the first value; the actual concentration of amphotericin (A) is stated as second.

#### Conclusion

In our study was confirmed, that even despite of the high minimum inhibitory concentration of baicalein for the suspension cells of each tested yeast strain, this natural substance is capable to support the growth inhibition of *C. parapsilosis* and *C. albicans* by polyene antibiotic amphotericin B. Baicalein in combination with amphotericin B inhibits the growth of *C. parapsilosis* and *C. albicans* even in 10 % from the value of MIC of both substances together. On the other hand, the synergistic effect of baicalein in combination with amphotericin B has not been demonstrated in the case of *C. krusei*, conversely the most of the tested combination ratios had antagonistic effect on its growth. In spite of it we consider these results very important and we already began to apply it for investigation of baicalein and amphotericin B effect in combination on the microbial adhesion inhibition and subsequent biofilm formation of these yeast strains.

## **Acknowledgment**

*Financial support from specific university research (MSMT No 20/2015) and by GACR grant 14-23597S, by the CR Ministry of Industry and Trade project no. FR-T11/456.*

## **Literature**

1. Kang K., Fong W. P., Tsang P. W., *Mycopathologia* 170, 391-396 (2010)
2. National Pharmacopoeia Committee, *Pharmacopoeia of the People's Republic of China*, Chemical Industry Press, Beijing 1, 26 (2005)
3. Duan C., Matsumura S., Kariya N., Nishimura M., Shimono T., *Pediatr. Dent. J.* 17, 58-64 (2007)
4. Cao Y., Dai B., Wang Y., Huang S., Xu Y., Cao Y., Gao P., Zhu Z., Jiang Y., *Int J Antimicrob. Agents* 32, 73-77 (2008)
5. Arweiler N. B., Pergola G., Kuenz J., Hellwig E., Sculean A., Auschill T. M., *Clin. Oral. Investig.* 15, 909-913 (2011)
6. Huang S., Cao Y. Y., Dai B. D., Sun X. R., Zhu Z. Y., Cyo Y. B., Wang Y., Gao P. H., Jiang Y. Y., *Biol Pharm Bull* 31, 2234-2236 (2008)
7. Serpa R., Franca E. J., Furlaneto-Maia L., Andrade C. G., Diniz A., Furlaneto M. C., *J. Med. Microbiol.* 61, 1704-1708 (2012)
8. Gong N., Wang X., Zhang B., Gao Z., Du G., Lv Y., *J. Pharm. Biomed. Anal.* 89, 106-110 (2014)
9. Kuhn D. M., George T., Chandra J., Mukherjee P. K., Ghannoum M. A., *Antimicrob. Agents Chemother.* 46, 1773-1780 (2002)
10. Chandra J., Kuhn D. M., Mukherjee P. K., Hoyer L. L., McCormick T., Ghannoum M. A., *J. Bacteriol.* 183, 5385-5394 (2001)
11. Asbeck E. C., Clemons K. V., Stevens D. A., *Crit. Rev. Microbiol.* 35, 283-309 (2009)
12. Sharma M., Manoharlal R., Negi A.S. & Prasad R., *Fems Yeast Res.* 10, 570-578 (2010)
13. Samadi N., Abadian N., Ahmadkhaniha R., Amini F., Dalili D., Rastkari N., *Folia Microbiol.* 57, 501-508 (2012)

## EXTRACTION OF CAROTENOIDS FROM SELECTED PLANTS

**Rousková M.**, Maléterová Y., Hanika J., Šolcová O.

*Institute of Chemical Process Fundamentals of the CAS, v. v. i., Rozvojová 2/135, 165 02 Prague 6 – Suchbát, www.icpf.cas.cz  
rousakova@icpf.cas.cz*

### Introduction

Carotenoids belong to the most widespread natural dyes, determining the colour of plants and animals. One of the main pigments responsible for the yellow colour of flowers is lutein. Lutein belongs to the dihydroxy-derivatives of carotenoids. It plays an important role in human nutrition due to its strong antioxidant effects<sup>1</sup> in neutralizing free radicals that cause degenerative changes in the retina<sup>2</sup>. It is used as an ingredient in feed for poultry; it is also applied as a colorant in a variety of foods. Lutein content was studied in carotenoid-rich flowers such as *Tagetes* and *Calendula*. The carotenoid content in blossoms of these flowers depends on the cultivar, planting conditions, growing season and vary with regions.

*Tagetes* is one of the richest natural sources of xanthophylls. They occur mainly in the form of esters of fatty acids - lauric, myristic, palmitic and stearic. The extract from the flowers is often added to the poultry feed to achieve intensive color of egg yolks. On the other hand, beneficial effects of lutein esters on human body are known. They are readily absorbed into the bloodstream and can reduce the growth of breast tumour cells, promote the formation of lymphocytes or suppress eye degeneration in an older age<sup>3</sup>. Their strong antioxidant effect, in general, appears to lead to the widespread use of marigold extracts as food supplements and/or functional foods<sup>4,5</sup>.

*Calendula* originates from southern Europe and the Orient. In ancient times it was used as a spice, sometimes replacing the scarce saffron. Yellow colour of petals, a mixture of carotenoids, is applied in the food industry to dye rice, butter, cheese and soups. Furthermore, the plant contains essential oils, sterols, triterpenoids faradiol, amyirin and lupeol, and polar flavonoids as isokvercitrin, rutin, narcissin etc. Significant components are also lipophilic substances, especially carotenoids and sterols<sup>6</sup>. All parts of the plant have a pungent smell which repels some insect species. Extracts of *Calendula* flowers are also effective agents against skin inflammations and swellings, accelerate wound healing.

A method for determining lutein and zeaxanthin isomers from marigold flower extract using hexane and ethyl ether, as an extracting solvent, has been reported by Hadden<sup>3</sup>. Numerous organic solvents<sup>7,8</sup> for extraction of carotenoids from vegetable and fruit samples, e.g. n-hexane, have been widely used.

### Materials and methods

Lutein was isolated from deep-frozen mixtures of 7 clones of *Tagetes* and *Calendula* (Institute of Botany of the CAS, v. v. i., Průhonice) and concentrated suspension of fresh brown-orange microalgae *Scenedesmus* sp. (Culture Collection of Autotrophic Organisms CCALA of the Institute of Botany of the CAS, v. v. i., Třeboň). The microalgal cells were cultivated in closed photobioreactor. To reduce water content in cultivated solution, filtration was deployed.

Dry matter in extracted biomass was determined before each extraction to assure the exact content of the dry biomass in the system (110 °C, to the constant weight).

Non-polar extraction agents - hexane and petroleum ether (p. a., Lach-Ner, CR) were applied. Ratio of sample weight/extraction agent 1/6 was used. Extraction of carotenoids was carried out directly from the frozen/fresh samples. Biomass was not dried in order to avoid undesirable losses of unstable substances.

Two procedures of lutein extraction were tested. The first procedure using Soxhlet apparatus was based on repetitive multistage extraction with fresh condensing solvent for 2 and 4 hours. This process is very efficient in terms of intensive contact of the solvent with the extracted material. Its disadvantage is the thermal stress of the sample and the resulting extract, because it operates at the boiling point of the solvent. The second procedure was single-stage extraction process in a stirred batch, at ambient temperature, protected from air and light, under inert atmosphere (nitrogen) for 2 and 4 hours. This procedure is suitable for the separation of thermally unstable materials susceptible to oxidation by atmospheric oxygen. The disadvantages include the necessary subsequent separation of the solid plant material from the extract, low efficiency limited by equilibrium and time consumption.

Individual phases (liquid organic extract and solid biomass or its water suspension) were separated from the obtained solutions by filtration. Part of the extract was then evaporated using the rotary evaporator under vacuum and thus extractable part (dry extract) was prepared.

Spectrophotometric analysis of lutein in liquid extracts and the dry extractable components from the tested plant and algal material was performed at the Department of Food Analysis and Nutrition of the University of Chemistry and Technology Prague. The lutein content in extracts from processed petals and microalgae was related to fresh/deep-frozen biomass.

### Results and discussion

The effect of experimental procedure, both in Soxhlet and batch arrangement, on extraction efficiency of lutein from *Tagetes* petals is compared in Table I. Extractables represent overall components which can be recovered from processed material to extract solution. Lutein content (the 3<sup>rd</sup> column of the Table I) in the extract is calculated to fresh material. Lutein concentration in dry extract after solvent removal from extract solution is stated in the 4<sup>th</sup> column of the Table I.

Table I  
Extract composition of *Tagetes* petals (dry mass 11.8 wt. %)

Processing	Extractables [wt. %]	Lutein content in extract [mg/kg]	Lutein content in dry extract [mg/kg]
Soxhlet, 2 hrs, hexane	10.5	193	361
Soxhlet, 2 hrs, petroleum ether	6.0	198	313
Soxhlet, 4 hrs, hexane	15.4	-	-
Stirred batch, 2 hrs, hexane, inert, lab. temp.	5.1	478	477
Stirred batch, 2 hrs, hexane, inert, lab. temp.	5.9	452	591

It is evident that Soxhlet extraction process strongly depends on time (in case of hexane application). Also, the amount of extractable components is lower in case of petroleum ether application in comparison with hexane. Therefore, subsequent test has been made using stirred batch extractor and hexane as a solvent. But, in this single-stage extraction the efficiency of the process is only 50 % in comparison to a Soxhlet one. On the other hand, lutein yield obtained at mild conditions exceeds Soxhlet arrangement.

If we compare literature data, for instance, the lutein content of *T. erecta* was reported<sup>9</sup> in the range of 0.216–0.976 g/kg based on the weight of fresh flowers, which equals 0.02–0.1 wt. %.

Similar extraction experiments were conducted under comparable conditions using *Calendula* petals. The results are given in Table II.

Table II  
Extract composition of *Calendula* petals (dry mass 13.6 wt. %)

Processing	Extractables [wt. %]	Lutein content in extract [mg/kg]	Lutein content in dry extract [mg/kg]
Soxhlet, 2 hrs, hexane	5.0	25	66
Soxhlet, 2 hrs, petroleum ether	7.6	26	142
Soxhlet, 4 hrs, hexane	6.6	-	-
Stirred batch, 2 hrs, hexane, inert, lab. temp.	3.7	80	99
Stirred batch, 2 hrs, hexane, inert, lab. temp.	4.6	108	153

The content of all extractables using hexane was in this case lower. It is interesting that by application of a Soxhlet apparatus and petroleum ether as an extraction agent concentration of extractables was higher than using hexane.

In comparison with *Tagetes*, *Calendula* provides yield approx. 50 % of extractables using a Soxhlet apparatus, and 75 % in stirred batch extractor arrangement under mild conditions (ambient temperature, under inert atmosphere and absence of light). Comparing *Calendula* results to data in Table I (*Tagetes*) lutein content achieved far lower concentration.

Table III brings similar data from experiments using fresh dense water suspension of brown-orange microalgae *Scenedesmus sp.* The tests were made using stirred batch extractor at ambient temperature under inert atmosphere and in the absence of light.

Table III

Extract composition of *Scenedesmus sp.* suspension (dry mass 21.3 wt. %)

Processing	Extractables [wt. %]	Lutein content in extract [mg/kg]	Lutein content in dry extract [mg/kg]
Stirred batch, 2 hrs, hexane, inert, lab. temp.	2.5	24	22
Stirred batch, 2 hrs, petroleum ether, inert, lab. temp.	2.1	15	18

Concentrated suspension of *Scenedesmus sp.* was processed gently to obtain an extract enriched in carotenoids. Only small amount of lutein (mg of lutein to kg of suspension) was isolated from studied samples. It is necessary to add, no direct comparison of lutein content in marigold flowers and microalgae has been reported in literature<sup>10</sup>.

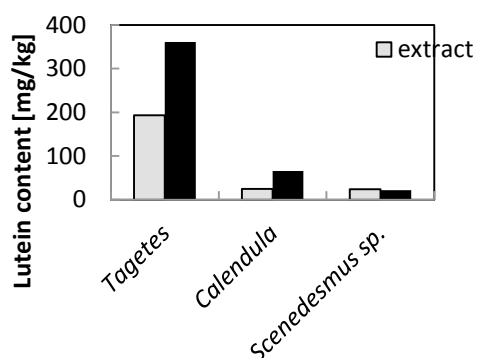


Figure 1. Comparison of lutein yield obtained from individual processed biomass (□ extract, ■ dry extract)

Summary comparison of different raw material extract efficiency is illustrated in Figure 1. Data are collected from batch experiments for 2 hours with hexane as a solvent under mild conditions.

### Conclusions

The great interest which lutein and all carotenoids have aroused during the last decades is conditioned not only by their interesting structure but by their biological and physiological importance. It is evident that their application in agriculture, food and pharmaceutical industry has a great potential for the future. Thus study of their isolation from natural resources is very important nowadays.

### Acknowledgment

The financial support of the Technology Agency of the Czech Republic, project "Biorefinery research centre of competence Bioraf" (TE01020080) is acknowledged.

**Keywords:** extraction, *Calendula*, *Tagetes*, *Scenedesmus*, carotenoids, lutein.

### Literature

- Guerin M., Huntley M. E., Olaizola M.: Trends Biotechnol. 21, 210 (2003).
- Perry A., Rasmussen H., Johnson, E. J.: J. Food Compos. Anal. 22, 9 (2009).
- Hadden W. L., Watkins R. H., Levy L. W., Regalado E., Rivadeneira D. M., van Breemen R. B., Schwartz S. J.: J. Agric. Food Chem. 47, 4189 (1999).
- Kumar R., Yu W., Jiang C., Shi C., Zhao Y.: J. Food Proc. Eng. 33, 1065 (2010).
- Khalil M., Raila J., Ali M., Islam K. M. S., Schenk R., Krause J. P., Schweigert F. J., Rawel H.: J. Funct. Foods 4, 602 (2012).
- Baumann D., Adler S., Grüner S., Otto F., Weinreich B., Hamburger M.: Phytochem. Anal. 15, 226 (2004).
- Gandul-Rojas B., Cepero M. R.-L., Mínguez-Mosquera M. I.: J. Agric. Food Chem. 47, 2207 (1999).
- Ferreira de França L., Reber G., Meireles M. A. A., Machado N. T., Brunner G.: J. Supercrit. Fluids 14, 247 (1999).
- Bosma T.L., Dole J. M., Maness N. O.: Crop Ecol. Manag. Qual. 43, 2118 (2003).
- Lin J.-H., Lee D.-J., Chang J.-S: Bioresource Technol. 184, 421 (2015).

## ANTIMICROBIAL ACTIVITY OF COBALT BIS(DICARBOLLIDE) AMINODERIVATIVES

**Kvasničková E.**<sup>1</sup>, Masák J.<sup>1</sup>, Šícha V.<sup>2</sup>

<sup>1</sup>University of Chemistry and Technology Prague, Technická 5, 166 28, Prague 6, Czech Republic

<sup>2</sup>Institute of Inorganic Chemistry AS CR, v.v.i., Husinec-Řež 1001, 250 68, Řež, Czech Republic  
Eva.Kvasnickova@vscht.cz

### Introduction

Microbial infections and more often emerging high antibacterial and antifungal resistance of microorganisms are the huge problems in human medicine today<sup>1,2</sup>. The most common isolated bacteria strains from nosocomial infections are coagulase-negative staphylococci, further *S. aureus*, *Staphylococcus epidermidis*, *Enterococcus faecalis*, *P. aeruginosa*, *E. coli*, *Klebsiella pneumoniae* and *Bacteroides species*. The representatives of yeasts are for example *Candida albicans*, *Candida parapsilosis*, *Candida krusei*, *Candida tropicalis*, *Candida glabrata* and *Trichosporon cutaneum* and also there may occur the molds, especially *Aspergillus fumigatus*<sup>3</sup>. It is extremely difficult to treat these infections with antibiotics and at present, surgical removal and the replacement of the infected tissue or medical device is the only possibility for patients in many cases<sup>4</sup>. Therefore, recently, scientists try to find new strategies, especially in using natural or unusual substances, which may help to solve these problems<sup>5,6,7</sup>. The examples of these agents are heteroboranes and their derivatives, 3D cluster inorganic compounds, which are basically composed of boron, hydrogen and other elements such as carbon, nitrogen, sulphur, etc<sup>8</sup>. Heterocarborane compounds and especially their derivatives are stable in air and in aqueous solutions, where they behave as hydrophobic substances (the surface of the molecules is formed by hydridic hydrogen atoms). The great advantage is that heteroboranes are usually noncytotoxic and it is possible to efficiently synthesize them<sup>9</sup>.

Heteroboranes involving the *o*-carborane cage are well described in the area of their application in boron neutron capture therapy (BNCT). In addition to this pharmacological improvement these substances dispose of many convenient properties useful in medicine such as inhibition of certain liver microsomal enzymes (*o*- and *m*-carboranes), neurotropic property (nitrogen-containing *o*-carborane derivatives) and the influence of as a chymotrypsin inhibition (carboranylalanine)<sup>10</sup>. Amine-carboxyborane derivatives have antitumor, cytotoxic, hypolipidemic and anti-osteoporotic activity<sup>11</sup>. The representatives of *o*-carboranes or cobalt bis(dicarbollides) are specific and potent inhibitors of HIV protease<sup>12</sup> and some of them are capable to inhibit carbonic anhydrase IX isoform, which is responsible for the spreading of cancerous proliferation in the human body<sup>13</sup>.

The bactericidal and fungicidal activity of 1-(aminoalkyl)-1,2-dicarba-*closo*-dodecaboranes and related compounds was described for the first time in 1970<sup>14</sup>. Further studies brought positive information about the antimicrobial activity of *o*-carboranes and *nido*-type dicarbollide anions against *Candida albicans*, *Aspergillus fumigatus* and *Trichophyton asteroides* and some representatives of gram-positive bacteria<sup>10</sup>. More information about these properties were recently published in article by Popova et al (2013)<sup>15</sup>, which was focused on the antimicrobial activity of cobalt bis(dicarbollides) derivatives. It was proved that these substances inhibit the microbial growth of *Candida* spp. and 16 other bacterial strains including *Staphylococcus aureus*, *Pseudomonas aeruginosa* and *Escherichia coli*<sup>15</sup>.

The group of heteroboranes include cobalt bis(dicarbollides) anion and its derivatives, which are substances with pharmaceutically usable properties. Our study was aimed at evaluating the effect of selected cobalt bis(dicarbollide) aminoderivatives on the microbial growth of several opportunistic pathogenic microorganisms, which are able to cause human infections.

Keywords: cobalt bis(dicarbollide), aminoderivatives, antimicrobial activity, *Staphylococcus aureus*, gram-negative bacteria, yeasts, MIC

### Materials and Methods

#### Microbial strains

The representative of yeasts, *Candida parapsilosis* (strain DBM 2165), and the representative of gram-positive bacteria, *Staphylococcus aureus* (strain DBM 3178), were obtained from Collection of Microorganisms of Institute of Biochemistry and Microbiology UCT Prague. The representative of gram-negative bacteria, *Pseudomonas aeruginosa* (strain B-59188), was obtained from microbial collection: ARS Culture collection, Bacterial Foodborne Pathogens and Mycology Research Unit, National Center for Agricultural Utilization Research, USA.

### Cultivation conditions

Stock cultures were stored at -70 °C and before each experiment precultured aerobically at 30 °C in the case of *C. parapsilosis* (in Malt Extract medium) and *P. aeruginosa* (in Luria Broth medium) and at 37 °C in the case of *S. aureus* (in Trypton Soya Broth medium), stirred at 100 rpm, harvested after 24 h, then centrifuged at 9000 g for 10 minutes and re-suspended in the same growth media. The experiments were also carried out in these growth media.

### Antimicrobial agents

The aminoderivatives of 3,3'-*commo*-Co<sup>III</sup>-bis-(1,2-*closo*-dicarbollide) sodium salt, [(1,2-*closo*-C<sub>2</sub>B<sub>10</sub>H<sub>10</sub>)-3,3'-Co<sup>III</sup>-*commo*-(1',2'-*closo*-C<sub>2</sub>B<sub>10</sub>H<sub>11</sub>)]<sup>-</sup> Na<sup>+</sup>, abbreviated as cobalt bis(dicarbollide), which structure is shown in Figure 1, were synthesized in the Institute of Inorganic Chemistry of Academy of Sciences of the Czech Republic, v.v.i. as described previously<sup>16</sup>. Cobalt bis(dicarbollide) and two representatives of its aminoderivatives were chosen for investigation of their antimicrobial activity. The parental anion is marked SK-1 (MW=346.738 g.mol<sup>-1</sup>), and the representatives of cobalt bis(dicarbollide) aminoderivatives are marked SK-2 [8-NH<sub>3</sub>-(1,2-*closo*-C<sub>2</sub>B<sub>10</sub>H<sub>10</sub>)-3,3'-Co<sup>III</sup>-*commo*-(1',2'-*closo*-C<sub>2</sub>B<sub>10</sub>H<sub>11</sub>)] (MW=339.771 g.mol<sup>-1</sup>) and SK-3 [8-BnzNH<sub>2</sub>-(1,2-*closo*-C<sub>2</sub>B<sub>10</sub>H<sub>10</sub>)-3,3'-Co<sup>III</sup>-*commo*-(1',2'-*closo*-C<sub>2</sub>B<sub>10</sub>H<sub>11</sub>)] (MW=429.894 g.mol<sup>-1</sup>). Each substance was dissolved in DMSO to a final concentration series from 0.1 mg/l to 90 mg/l. The concentration of DMSO was until 1 % in all assays.

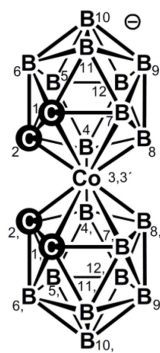


Fig. 1 Structural formula of parental cobalt bis(dicarbollide) anion, sodium salt [(1,2-*closo*-C<sub>2</sub>B<sub>10</sub>H<sub>10</sub>)-3,3'-Co<sup>III</sup>-*commo*-(1',2'-*closo*-C<sub>2</sub>B<sub>10</sub>H<sub>11</sub>)]<sup>-</sup> as SK-1

### Investigation of antimicrobial activity

The antimicrobial activity of SK-1, SK-2, SK-3 and an appropriate antibiotic for each microbial strain was determined by microdilution method according to Sharma et al. (2010)<sup>17</sup>. The cultivation was carried out in 100-well microtitre plates using Bioscreen C analyzer (Oy Growth Curves Ab Ltd., Finland). To each well 30 µl of standard cell suspensions of one of the microorganism (OD<sub>600nm</sub> = 0.1) were added. Drug-free and microorganism-free controls were included. Plates were incubated for 24 h at 30 °C in the case of *C. parapsilosis* and *P. aeruginosa* and at 37 °C in the case of *S. aureus*. Experiments were performed with five replicate wells for each experiment.

### Results and Discussion

The results of experiments are shown in Figures 1-10 as growth curves without any substances as control in comparison with the growth curves in the present of an appropriate concentration of SK-1, SK-2 or SK-3. The antibiotic amphotericin B inhibits the *C. parapsilosis* growth in concentration 1.5 mg/l, 2.5 mg/l of polymyxin B inhibits the *P. aeruginosa* growth and erythromycin inhibits *S. aureus* in concentration 1 mg/l (figures not shown).

In the Fig. 2 is depicted the effect of SK-1 on *C. parapsilosis*, in Fig. 3 on *P. aeruginosa* and in Fig. 4 on *S. aureus*. The cobalt bis(dicarbollide) is not able to inhibit the growth of *C. parapsilosis* in any tested concentration and in the case of *P. aeruginosa* this substance inhibits maximally 40 % of the growth after 24 hours of cultivation in the higher investigated concentration. On contrary, *S. aureus* is not able to grow even in the presence of 5 mg/l of SK-1.

Similar effect is confirmed in the determination of SK-2 antimicrobial activity (Figs. 4, 5, 6). The *C. parapsilosis* growth is promoted instead of inhibited by SK-2 in concentration 50 and 90 mg/l. This substance has no significant effect on inhibition of *P. aeruginosa* growth, but inhibits the growth of *S. aureus* in concentration 5 mg/l. Similar results were proven in the case of SK-3. These three representatives of heteroboranes affect

selectively the inhibition of gram-positive bacteria *S. aureus* in contrast to gram-negative bacteria *P. aeruginosa* or yeast *C. parapsilosis*.

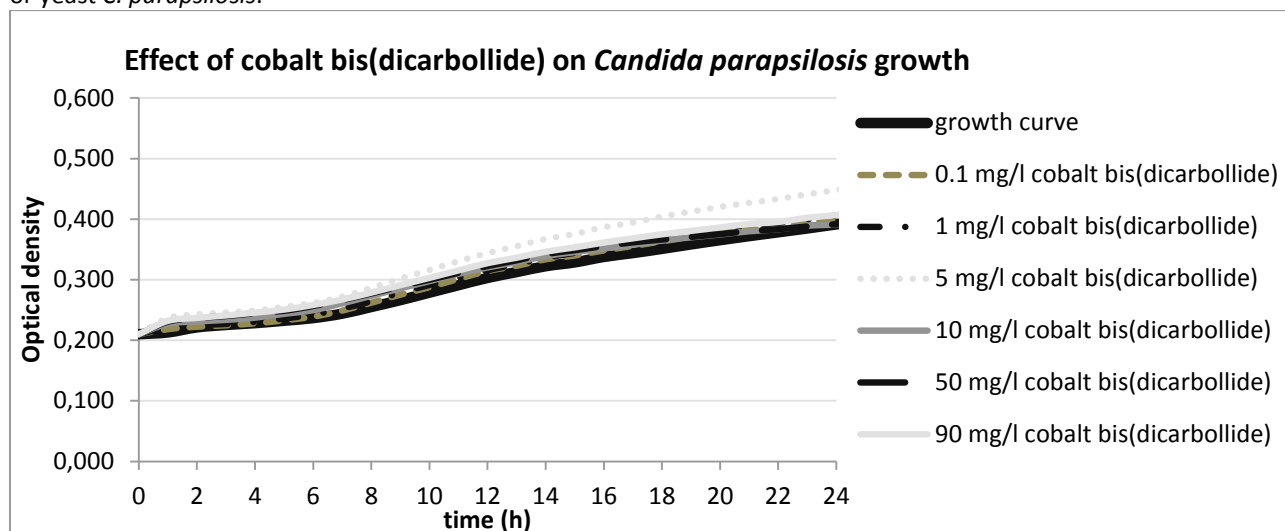


Figure 2. The effect of SK-1 on *C. parapsilosis* growth in the range of concentration from 0.1 to 90 mg/l

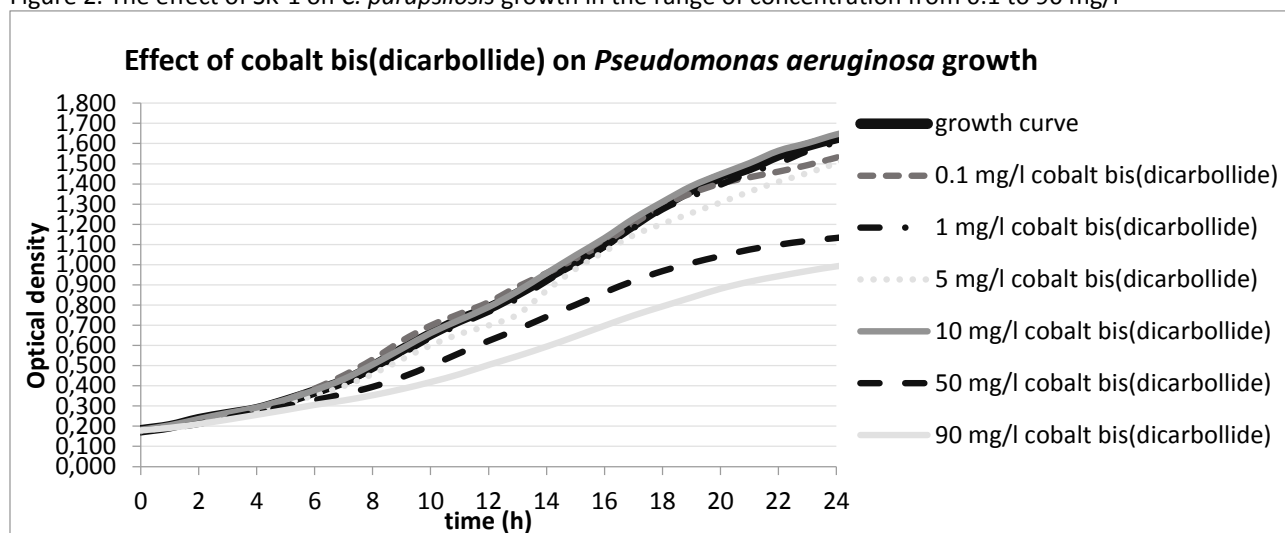


Figure 3. The effect of SK-1 on *P. aeruginosa* growth in the range of concentration from 0.1 to 90 mg/l

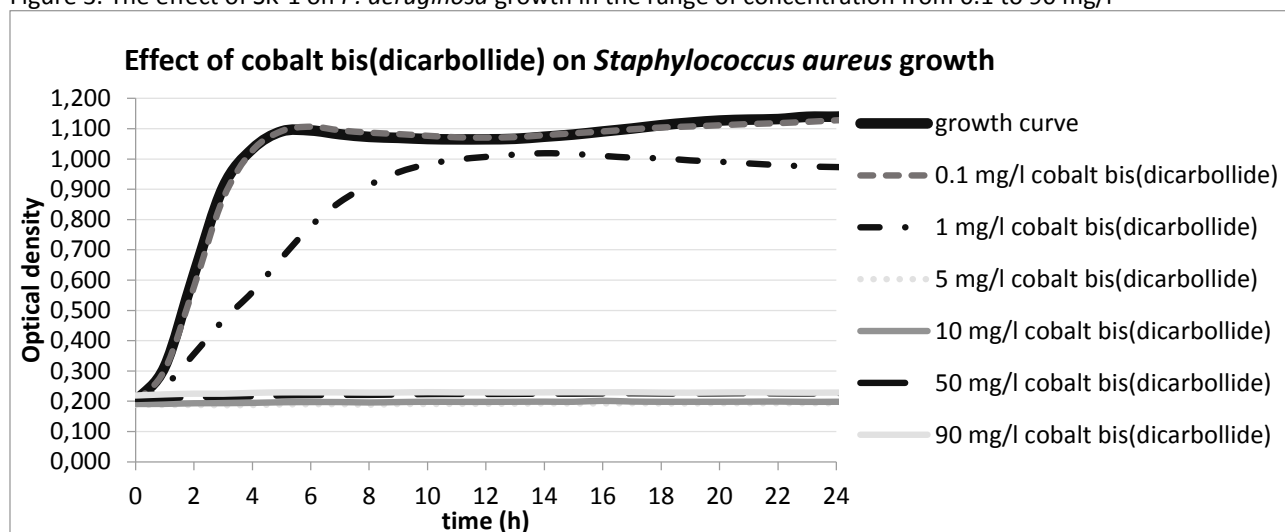


Figure 4. The effect of SK-1 on *S. aureus* growth in the range of concentration from 0.1 to 90 mg/l

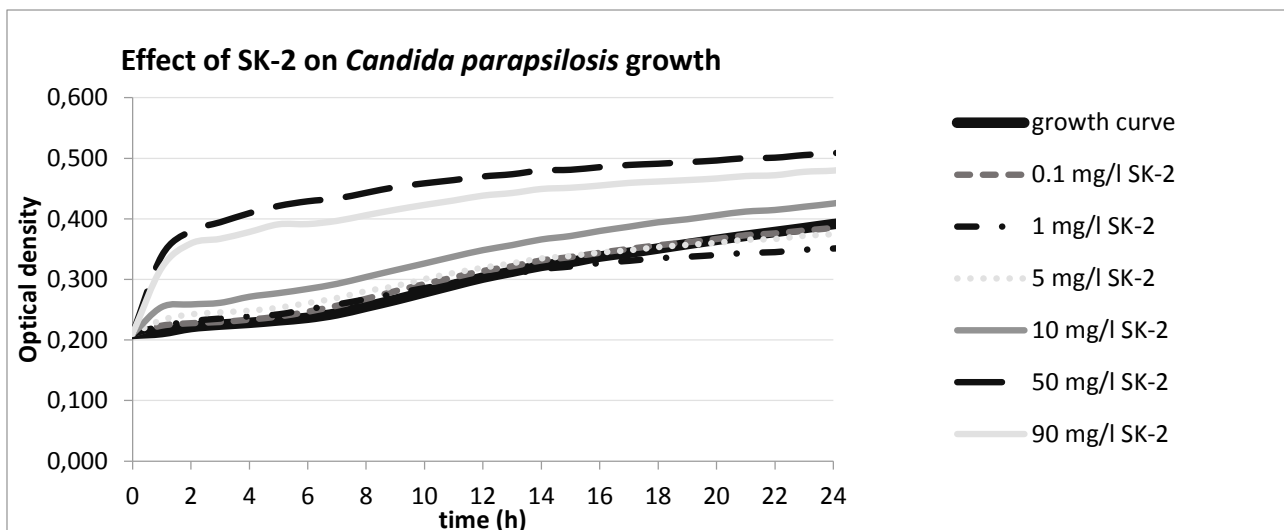


Figure 5. The effect of SK-2 on *C. parapsilosis* growth in the range of concentration from 0.1 to 90 mg/l

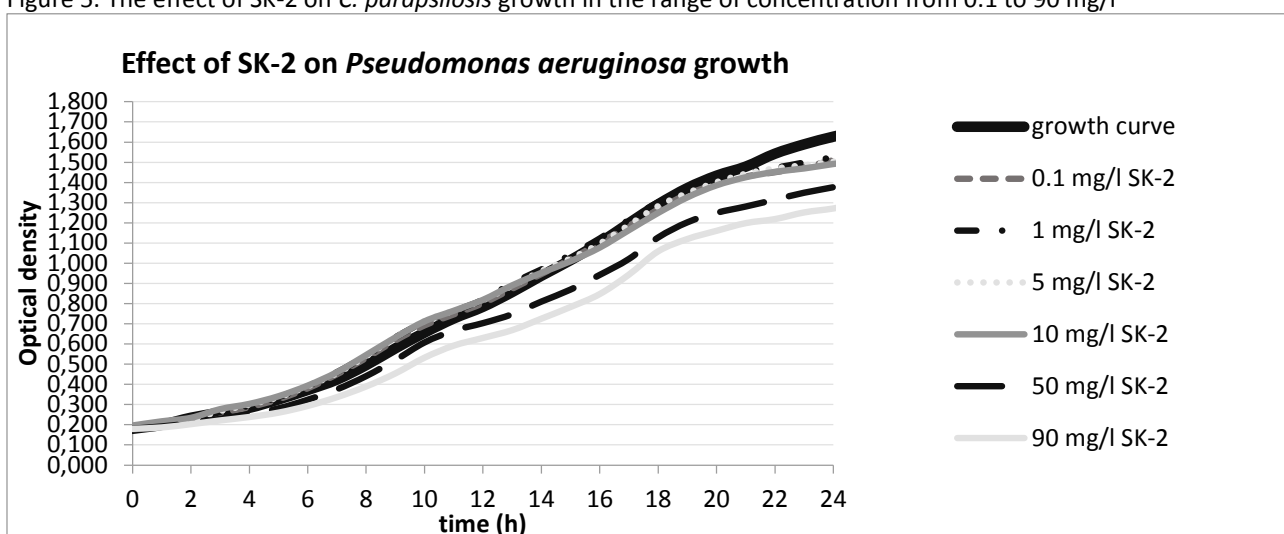


Figure 6. The effect of SK-2 on *P. aeruginosa* growth in the range of concentration from 0.1 to 90 mg/l

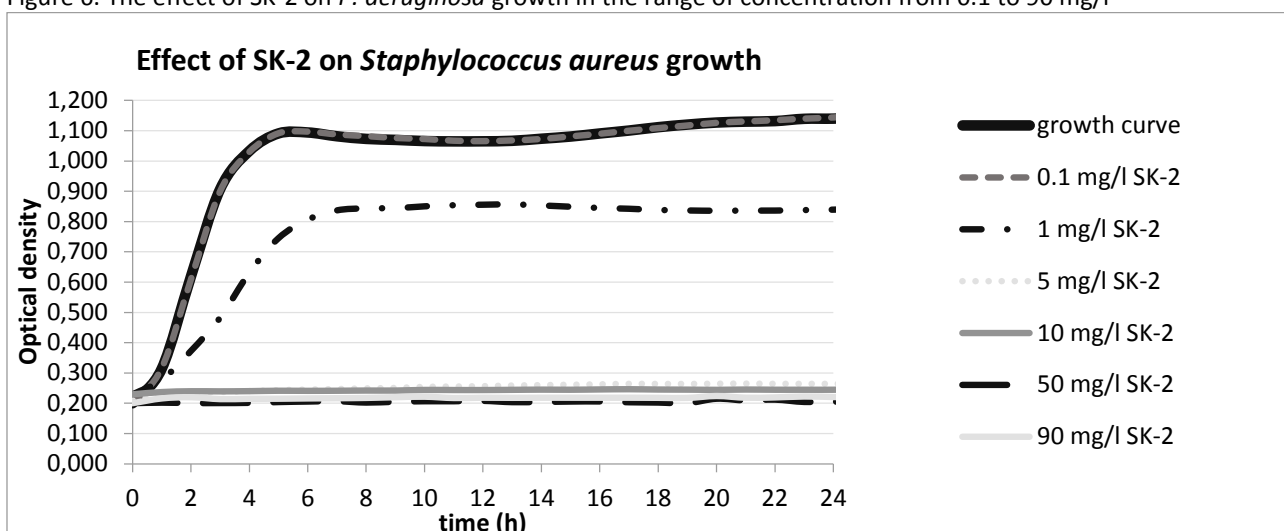


Figure 7. The effect of SK-2 on *S. aureus* growth in the range of concentration from 0.1 to 90 mg/l

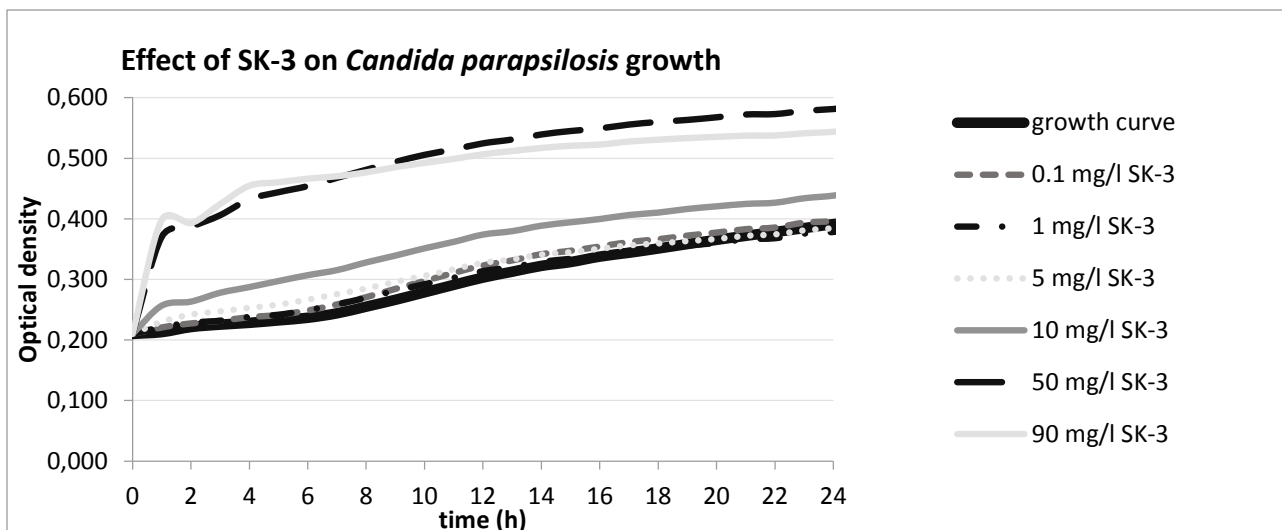


Figure 8. The effect of SK-1 on *C. parapsilosis* growth in the range of concentration from 0.1 to 90 mg/l

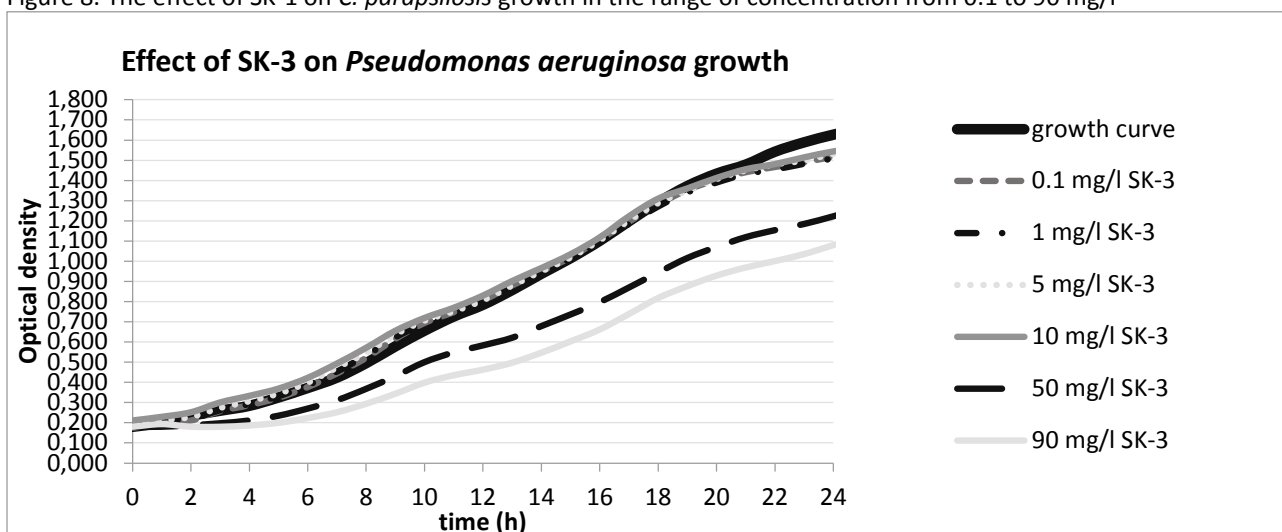


Figure 9. The effect of SK-3 on *P. aeruginosa* growth in the range of concentration from 0.1 to 90 mg/l

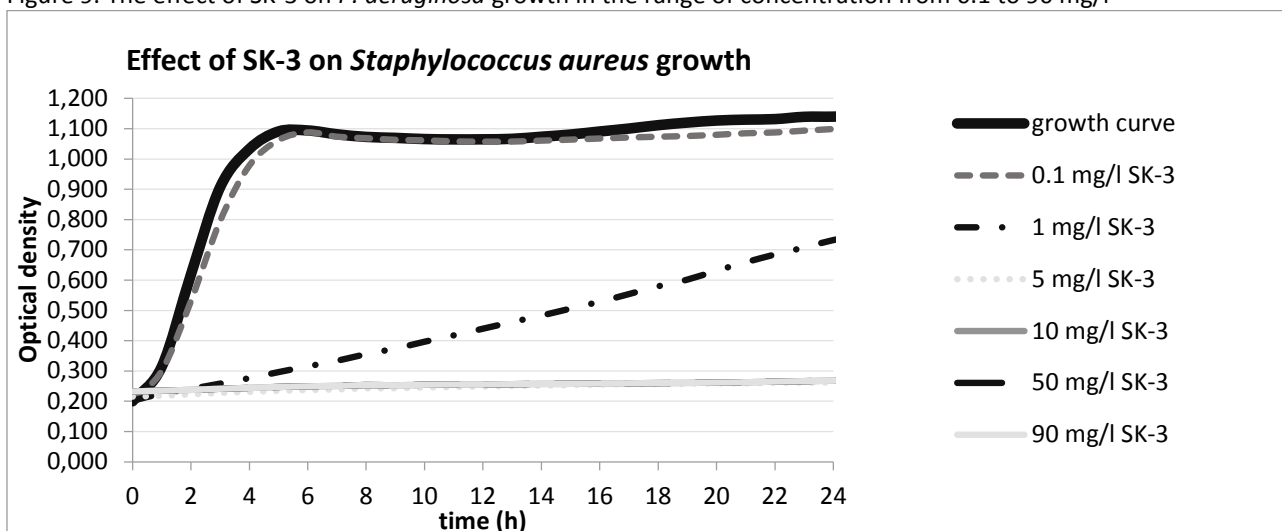


Figure 10. The effect of SK-3 on *S. aureus* growth in the range of concentration from 0.1 to 90 mg/l

### Conclusion

We carried out experiments focused on the determination of the antimicrobial activity of selected representatives of cobalt bis(dicarbollide) aminoderivates. It was proved, that studied yeast strain *C. parapsilosis* DBM 2165 is not sensitive to the cobalt bis(dicarbollide) or its aminoderivates. Gram-negative

bacteria *P. aeruginosa* B-59188 is weakly susceptible to cobalt bis(dicarbollide), but no significant inhibition of growth by cobalt bis(dicarbollide) aminoderivatives was observed. The highest effect on inhibition of microbial growth was confirmed in the case of gram-positive bacteria *S. aureus*. This observation demonstrates the real possibility of using these substances in the treatment of infection caused by gram-positive bacterial strains.

#### Acknowledgment

Financial support from specific university research (MSMT No 20/2015) and by GACR grant 14-23597S, by the CR Ministry of Industry and Trade project no. FR-TI1/456.

#### Literature

1. Watnick P., Kolter R., J. Bacteriol. 182, 2675-2679 (2000)
2. Stoodley P., Boyle J. D., Dioda I., Lappin-Scott H. M., in Biofilms: Community Interactions and Control: 3<sup>rd</sup> meeting of the Biofilm Club, 1-9 (1997)
3. Donlan R. M Clin. Infect. Dis. 33, 1387-1392 (2001)
4. Jefferson K. K., Fems Microbiol. Lett. 236, 163-173 (2004)
5. Řezanka T., Čejková A., Masák J., in Studies in Natural Products Chemistry 38 (Ed.: R. Atta ur), Elsevier, 269-298 (2012)
6. Abdel-Mawgoud AM, Lépine F, Déziel E.: Appl. Microbiol. Biotechnol. 86, 1323-1336 (2010)
7. Fulghesu L, Giallorenzo C; Savoia D.: J.Chemother. 19, 388-390 (2007)
8. Grimes R. N., in Carboranes, 2<sup>nd</sup> edition, Elsevier, p. 1139 (2011)
9. Matějčík P., Zedník J., Ušelová K., Pleštil J., Fanfrlík J., Nykänen A., Ruokolainen J., Hobza P., Procházka K., Macromolecules 42, 4829–4837 (2009)
10. Totani T., Aono K., Yamamoto K., Tawara K., J. Med. Chem. 24, 1492-1499 (1981)
11. Hall I. H., Chen S. Y., Rajendran K. G., Sood A., Spielvogel B. F., Shih J., Environ. Health Perspect. 102, 21-30 (1994)
12. Řezáčová P., Pokorná J., Brynda J., Kožíšek M., Cígler P., Lepšík M., Fanfrlík J., Řezáč J., Grantz Šašková K., Siegllová I., Plešek J., Šícha V., Grüner B., Oberwinkler H., Sedláček J., Kräusslich H.-G., Hobza P., Král V., Konvalinka J., J. Med. Chem. 52, 7132–7141 (2009)
13. Brynda J., Mader P., Šícha V., Fábry M., Poncová K., Bakardiev M., Grüner B., Cígler P., Řezáčová P., Angew. Chem., Int. Ed. 125, 14005-14008 (2013)
14. Nakagawa T., Watanabe H., Yoshizaki T., in Jpn. Tokkyo Koho, Vol. JP 45031940 Japan (1970)
15. Popova T., Zaulet A., Teixidor F., Alexandrova R., Viñas C., J. Organomet. Chem. 747, 229-234 (2013)
16. Šícha V., Plešek J., Kvíčalová M., Císařová I., Grüner B., Dalton Trans. 851-860 (2009)
17. Sharma M., Manoharlal R., Negi A.S. & Prasad R., Fems Yeast Res. 10, 570-578 (2010)

## MODELING OF WHITE WINE FERMENTATION – PARAMETER SENSITIVITY STUDY

**Báleš V.**, Baláž J., Timár P. Jr., Timár P.

*Department of Chemical and Biochemical Engineering, Institute of Chemical and Environmental Engineering, Faculty of Chemical and Food Technology, Radlinského 9, 812 37, Bratislava  
vladimir.bales@stuba.sk*

### Abstract

The efficient tank management of wine fermentation process in wineries is the key step in good wine production. We adapted a mathematical model of fermentation of grape musts based on kinetics of fermentation, kinetics of heat removal, production of CO<sub>2</sub> and ethanol. The model is very sensitive for kinetics of nitrogen consumption. The model should be validated for industrial winemaking conditions. We simulated several situations during fermentation. The ethanol, CO<sub>2</sub> and temperature profiles during the fermentation were calculated. Some cases of possible accident during the fermentation were simulated. We consider that this model can be used for most industrial fermentations of grape must.

### Introduction

Wine fermentation is a batch process, during which yeast consume sugar to produce approximately similar amount of alcohol and carbon dioxide gas. Due to that this conversion is exothermic, temperature inside the fermenter rise and must gets over heated without sufficient cooling. Maintaining ideal temperature plays great role of winemaking. Higher temperature tends to drive off volatile aromatic compounds, which are characteristic for wines and fermentations carrying out under higher temperature is also uncomfortable for the yeast. In order to achieve health and effective fermentation available nitrogen plays the great role to avoid either stuck or sluggish fermentation and excessive hydrogen sulfide production. But not only amount of the available nitrogen is important, but overall content of required nutrient is important as well.

### Model description

The used wine fermentation model includes mass and energy balances. The following assumptions are used in the model:

- The bubbles affects ideal stirring – the must is homogeneous during most of the fermentation.
- Fermentation tank is situated in a closed room and heat transfer between ambient (with a constant temperature during whole fermentation process and with no presence of air flux) and outside surface of the bioreactor involves a combination of both radiation and convection.
- The temperature of the outer surface is identical with must temperature (resistance to heat flow from the must to the wall is negligible and affect of conduction through the wall is also insignificant).
- Effect of total acidity on the fermentation process is negligible.
- Nitrogen is the limiting substrate.
- Although fructose is used concomitantly with glucose, yeasts prefer glucose over fructose (ratio of glucose/fructose is 1/1).
- Ethanol inhibits sugar consumption.
- CO<sub>2</sub> accumulation in gas phase is negligible.
- Biomass viability depends on a combined effect of ethanol and temperature.

Fermentation take place in an open fermenting vessel and taking into account previous assumptions fermentation is described by following main equations<sup>1</sup> (used parameters and constants are described in the appendix):

$$\frac{d(X_V \cdot H)}{dt} = (\mu - k_d) \cdot (X_V \cdot H) \quad (1)$$

$$\frac{d(N \cdot H)}{dt} = -\frac{\mu}{Y_{X/N}} \cdot (X_V \cdot H) \quad (2)$$

$$\frac{d(G \cdot H)}{dt} = -\left( \frac{\mu}{Y_{X/G}} + \frac{\beta_G}{Y_{E/G}} + m \cdot \frac{G}{G+F} \right) \cdot (X_V \cdot H) \quad (3)$$

$$\frac{d(F \cdot H)}{dt} = - \left( \frac{\mu}{Y_{X/F}} + \frac{\beta_F}{Y_{E/F}} + m \cdot \frac{F}{G+F} \right) \cdot (X_V \cdot H) \quad (4)$$

$$\frac{d(E \cdot H)}{dt} = (\beta_G + \beta_F) \cdot (X_V \cdot H) \quad (5)$$

$$F_{CO_2} = \left[ \left( \frac{\mu}{Y_{x/CO_2}} + \frac{\beta_G + \beta_F}{Y_{E/CO_2}} + m \right) \cdot X_V \cdot H \cdot A_F \right] - \left[ k_L a_{TF} \cdot H \cdot (c_{sat} - c_{CO_2L}) \cdot A_F \right] \quad (6)$$

$$A_F \frac{d(\rho \cdot H)}{dt} = -F_{CO_2} \quad (7)$$

$$\frac{d(\rho \cdot H \cdot T)}{dt} = (1 - x_{Q_{evaporation}}) \frac{\Delta H}{c_{p_m}} \cdot \frac{d(S \cdot H)}{dt} - \frac{A_{ef} \cdot U \cdot (T - T_{amb}) + Q_{cool}}{c_{p_m} A_F} \quad (8)$$

### Outcome of the simulation

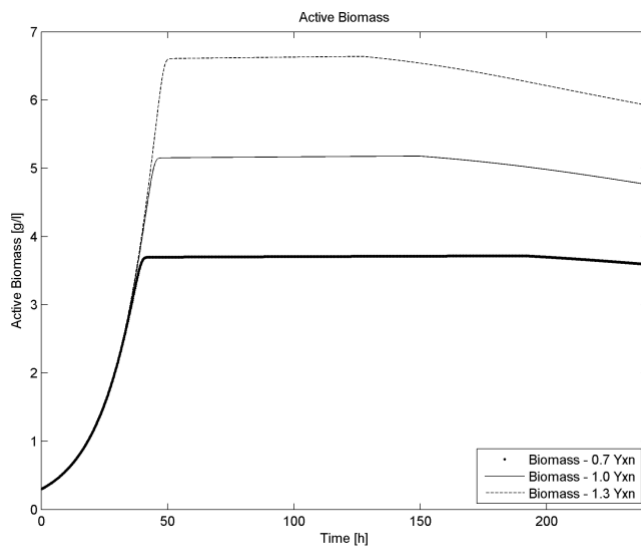


Figure 1. Concentration of active biomass during fermentation under different biomass/nitrogen yield coefficient

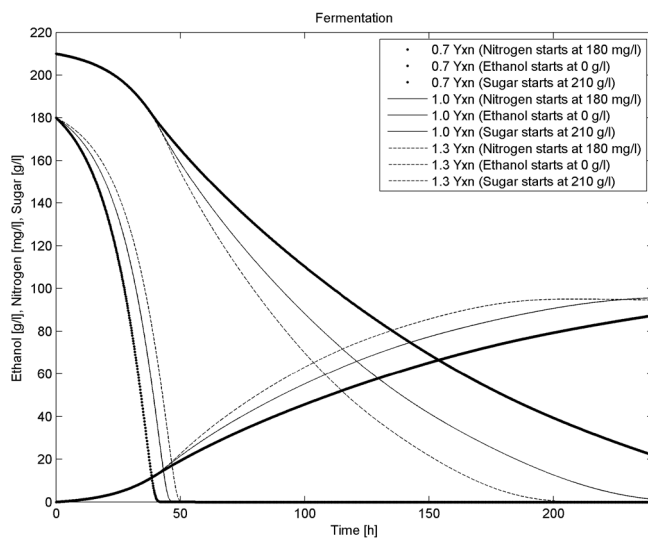


Figure 2. Concentrations of nitrogen, sugar and ethanol during fermentation under different biomass/nitrogen yield coefficients

Simulations were performed using 10 m<sup>3</sup> fermenter, which was filled up by must up to 88 % of his bulk. Ambient temperature was 15°C and desired temperature of the fermentation was maintaining at 16°C. Initial sugar and nitrogen concentrations are 210 g/l and 180 mg/l respectively. In figures 1 and 2 is shown sensitivity on biomass/nitrogen yield coefficient. It could be explained, that with increase value of initial nitrogen concentration, availability of other nutrients leads to growth limiting. In the Figure 1 and 2 we compared different biomass/nitrogen yield coefficients. Fermentation ends when residual sugar 5 g/l is reached. Fermentation carried out under origin yield coefficient (solid line) takes 225 hours with the maximum of the active biomass 6,6 g/l. In order to show sensitivity on biomass/nitrogen yield coefficient we reduced and upgrade our origin value in 30% and kept all other values constant. Reduced value (dotted line) caused longer fermentation (up to 303 hours) with the maximum concentration of active biomass 3,7 g/l. Upgraded value (dashed line) caused faster fermentation (only 180 hours) with the maximum of the active biomass 6,6 g/l. We simulate possible refrigeration failure (normal-origin biomass/nitrogen yield coefficient) and results are shown in figures 3 and 4. In the thime when maximum active biomass is observed (at 50th hour), refrigeration failure (on 24 hours) occurs. As is shown in figures below, temperature rose up to 19,9°C. To cool it back to the desired fermentation temperature in two hours, minimal refrigeration capacity 20,3 kW is needed.

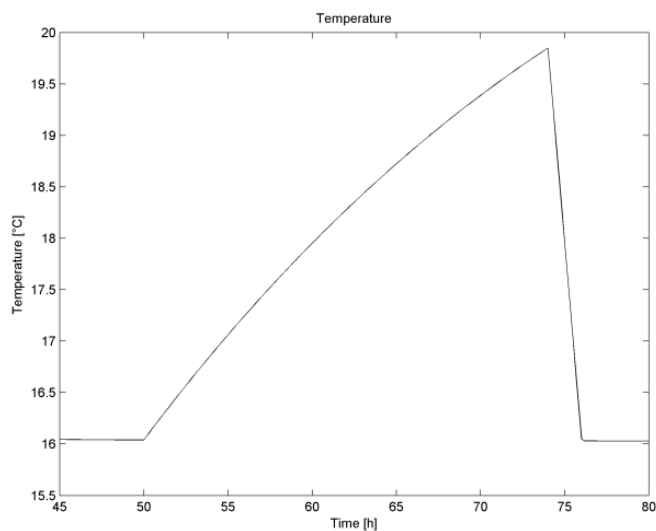


Figure 3. Temperature profile inside the fermenter when refrigeration failure occurs.

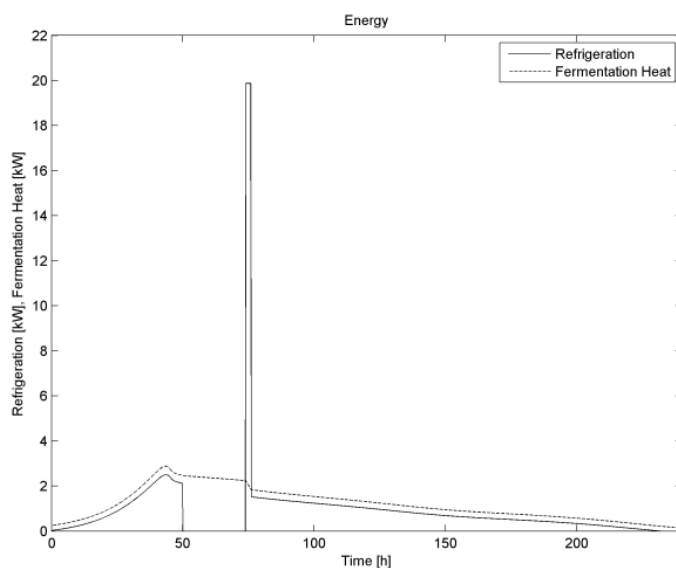


Figure 4. Refrigeration cooling and fermentation heat released during the fermentation

Within larger fermenters higher fermentation temperature can be expected. It is caused by ratio of surface area of the fermenter to the fermenting volume. Our results are shown in the Figure 5, where ratio diameter/height of the fermenter is the same, obtained from the real 10 m<sup>3</sup> fermenter. All other values are kept the same like in previous simulations with normal-origin biomass/nitrogen yield coefficient, which depends here on initial nitrogen concentration.

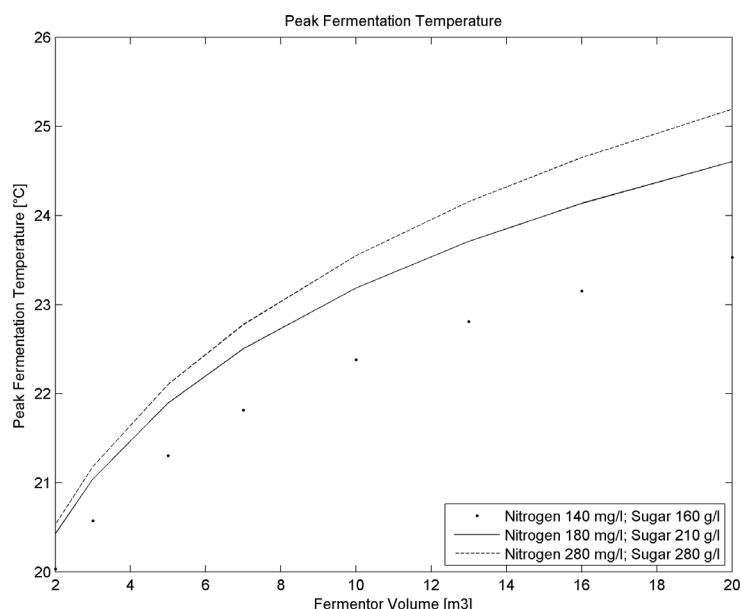


Figure 5. Fermentation without refrigeration cooling – temperature peak plotted over fermenter volume with the same ratio diameter/height.

### Conclusion

In this paper we described fermentation process within the fermenter from two points of view : material and energetic. Great impact of biomass/nitrogen yield coefficient was shown. Possible refrigeration failure on 24 hours was simulated and refrigeration capacity to cool it back in two hours was investigated. Last goal of this paper is the maximum temperature increase as a function of the vessel volume during the fermentation without refrigeration cooling.

### Appendix

Table 1 : Nomenclature used in the model with values of constants and dependence parameters used in the model.

Parameter/ Constant		Value/Equation/ Function of
$X_V$	biomass concentration, kg Bio/m <sup>3</sup>	eq. 1
$N$	nitrogen compounds concentration, kg N/m <sup>3</sup>	eq. 2
$G$	glucose concentration, kg G/m <sup>3</sup>	eq. 3
$F$	fructose concentration, kg F/m <sup>3</sup>	eq. 4
$S$	total sugar concentration, kg S/m <sup>3</sup>	F+G
$E$	ethanol concentration, kg E/m <sup>3</sup>	eq. 5
$H$	height of the must, m	-
$\mu$	specific growth rate, 1/s	$\mu(T, N,)$
$k_d$	specific death rate, 1/s	$k_d(E, T)$
$t$	time, s	-
$T$	must temperature, K	eq. 8

$T_{amb}$	ambient temperature, K	15 °C
$\rho$	must density, kg/m <sup>3</sup>	eq. 7
$c_{CO_2,L}$	dissolved CO <sub>2</sub> , kg CO <sub>2</sub> /m <sup>3</sup>	$c_{CO_2,L}(T)$
$c_{sat}$	saturation of dissolved CO <sub>2</sub> , kg CO <sub>2</sub> /m <sup>3</sup>	$c_{sat}(T)$
$k_L$	CO <sub>2</sub> mass transfer coefficient, kg CO <sub>2</sub> /(s m <sup>2</sup> kg CO <sub>2</sub> /m <sup>3</sup> )	$k_L a_{TF} = 0,07$ 1/h
$a_{TF}$	specific mass transfer area, m <sup>2</sup> /m <sup>3</sup>	$k_L a_{TF} = 0,07$ 1/h
$F_{CO_2}$	mass flow rate of liberated CO <sub>2</sub> , kg CO <sub>2</sub> /s	eq. 6
$A_F$	fermentation tank base area, m <sup>2</sup>	3,02 m <sup>2</sup>
$x_{Q_{evaporation}}$	term representing heat removal by evaporation	$x_{Q_{evaporation}}(T)$
$\Delta H$	specific metabolic heat, J/kg S	556,74 kJ/kg
$cp_m$	must specific heat, J/kg/K	$cp_m(S, E)$
$A_{ef}$	effective heat transfer area of the fermentation tank, m <sup>2</sup>	$A_{ef}(H)$
$U$	heat transfer coefficient between must and ambient, W/(m <sup>2</sup> K)	$U(T)$
$Q_{cool}$	refrigeration required to cool fermenter, W	-
$\beta_G$	specific production rate of ethanol, kg E/kg Bio/s	$\beta_G(G, E, T)$
$\beta_F$	specific production rate of ethanol, kg E/kg Bio/s	$\beta_F(G, F, E, T)$
$Y_{X/N}$	biomass/nitrogen yield coefficient, kg Bio/kg N	$Y_{X/N}(N_{initial})$
$Y_{X/G}$	biomass/glucose yield coefficient, kg Bio/kg G	1,60 kg Bio/kg F
$Y_{X/F}$	biomass/fructose yield coefficient, kg Bio/kg F	1,60 kg Bio/kg F
$Y_{E/G}$	ethanol/glucose yield coefficient, kg E/kg G	0,49 kg E/kg F
$Y_{E/F}$	ethanol/fructose yield coefficient, kg E/kg F	0,49 kg E/kg F
$Y_{X/CO_2}$	biomass/ CO <sub>2</sub> yield coefficient, kg Bio/kg CO <sub>2</sub>	12,72 kg Bio/kg CO <sub>2</sub>
$Y_{E/CO_2}$	ethanol/ CO <sub>2</sub> yield coefficient, kg E/kg CO <sub>2</sub>	1,05 kg E/kg CO <sub>2</sub>
$m$	maintenance coefficient, kg S/ kg Bio/s	$m(T)$

## Acknowledgement

*This article was created with the support of the Ministry of Education, Science, Research and Sport of the Slovak Republic within the Research and Development Operational Programme for the project "University Science Park of STU Bratislava", ITMS 26240220084, co-funded by the European Regional Development Fund.*

## Literature

1. Storm D. R., Winery Utilities: Planning, Design and Operation, Springer Science & Business Media, 2000.
2. Salmon J., "Effect of Sugar Transport Inactivation in *Saccharomyces cerevisiae* on Sluggish and Stuck Enological Fermentations," Applied and Environmental Microbiology, vol. 55, no. 4, pp. 953-958, 1989.
3. Neulicht R., „Emission Factor Documentation for AP-42,“ Midwest Research Institute, 1995.
4. Labovský J., Švandová Z., Markoš J., Jelemenský Ľ., Hodnotenie nebezpečenstva chemických procesov, Bratislava: Nakladateľstvo STU, 2014.
5. Jackson R. S., Wine Science: Principles and Applications, Elsevier, 2014.
6. Longauer J., Dojčanský J., Chemické inžinierstvo II, Bratislava: Malé centrum, 2000.
7. "Wines of Slovakia," Online.. Available: <http://www.winesofslovakia.com/>. Accessed 2015 April 2015..
8. Carroll J. J., Slupsky J. D., Mather A. E., "The solubility of Carbon Dioxide in Water at Low Pressure," J. Phys. Chem. Ref. Data, vol. 20, no. 6, pp. 1201-1209, 1991.
9. Coleman M. C., Fish R., Block D. E., „Temperature-Dependent Kinetic Model for Nitrogen-Limited Wine Fermentations,“ Applied and Environmental Microbiology, zv. 73, %1. vyd.18, pp. 5875-5884, 2007.

10. Smyth M., Russell J., Milanowski T., *Solar Energy in the Winemaking Industry*, Springer Science & Business Media, 2011.
11. Goelzer A., Charnomordic B., Colombié S., Fromion V., Sablayrolles J. M., „Simulation and optimization software for alcoholic fermentation in winemaking conditions,” *Food Control*, zv. 20, pp. 635-642, 2009.
12. Boulton R. B., Singleton V. L., Bisson L. F., Kunkee R. E., *Principles and Practices of Winemaking*, Gaithersburg, Maryland: Aspen Publishers, Inc., 1998.
13. Matošková D., Gálik J., “National Agricultural and Food Centre, Research Institute of Agricultural and Food Economics,” Online.. Available: [www.vuepp.sk/EP2014/4/tah4.php](http://www.vuepp.sk/EP2014/4/tah4.php). Accessed 18 April 2015..
14. Malherbe S., Fromion V., Hilbert N., Sablayrolles J. M., „Modeling the effects of assimilable nitrogen and temperature on fermentation kinetics in enological conditions,” *Biotechnology and bioengineering*, zv. 86, %1. vyd.3, pp. 261-272, 2004.
15. Zenteto M. I., Pérez-Correa J. R., Gelmi C. A., Agosin E., “Modeling temperature gradients in wine fermentation tanks,” *Journal of Food Engineering*, vol. 99, pp. 40-48, 2010.
16. Colombié S., Malherbe S., Sablayrolles J. M., „Modeling of heat transfer in tanks during wine-making fermentation,” *Food Control*, zv. 18, pp. 953-960, 2007.
17. El Haloui N., Picque D., Corrieu G., „Mesures physiques permettant le suivi biologique de la fermentation alcoolique en œnologie,” *Sciences des Aliments*, zv. 7, pp. 241-265, 1987.
18. Cramer A. C., Vlassides S., Block D. E., „Kinetic Model for Nitrogen-Limited Wine Fermentations,” *Biotechnology and Bioengineering*, zv. 77, %1. vyd.1, pp. 49-60, 2002.
19. Gupta V. K., Schmoll M., Maki M., Tuohy M., Mazutti M. A., *Applications of Microbial Engineering*, CRC Press, 2013.

## **PHARMACEUTICAL TECHNOLOGY**

### **OPTIMIZING FLOW AND SEGREGATION PROPERTIES OF LACTOSE/MICROCRYSTALLINE CELLULOSE MIXTURE FOR TABLET COMPRESSION**

**Zamostny P.**<sup>1</sup>, Kreibichova B.<sup>2</sup>, Hofmanova D.<sup>1</sup>, Kulaviak L.<sup>3</sup>, Zelenkova K.<sup>1</sup>, Ruzicka M.

<sup>1</sup>*University of Chemistry and Technology Prague, Faculty of Chemical Technology, Department of Organic Technology, Technická 5, 166 28, Praha 6, Czech Republic*

<sup>2</sup>*Zentiva k.s., U Kabelovny 130, 102 37, Prague, Czech Republic*

<sup>3</sup>*Institute of Chemical Process Fundamentals, Department of Multiphase Reactors, Czech Academy of Sciences, Rozvojova 135, 165 02, Prague, Czech Republic*  
*petr.zamostny@vscht.cz*

#### **Abstract**

The present study deals with optimizing the flow and segregation properties of levocetirizine hydrochloride formulation, where the delay between homogenization and tablet compression was found to affect the tablet content uniformity. In addition to API, the base formulation comprised spray dried lactose monohydrate, milled lactose monohydrate 200 mesh, Avicel PH 101 microcrystalline cellulose, and minor excipients. Several alternative mixtures were prepared using the same total composition, but different grades of lactose and microcrystalline cellulose. These mixtures were then tested for the segregation behavior in an in-house segregation device and the flow properties using the Freeman FT4 powder rheometer. The segregation tests showed the grade of lactose is essential for mixture in-flow segregation. While SD lactose mixtures increased the API content in a direction countercurrent to flow, the milled lactose mixtures segregated API concurrently. Mixtures using both lactose grades showed combined effect, resulting in the least segregation due to the two segregation processes competing with each other. However, the segregation was extremely sensitive to ageing of the mixture. It was also found that each type of lactose causes a different flow regime of the mixture in process vessels. In order to improve the content uniformity of the tablets, it was found the volumetric flow regime of transport to tablet press is required as well as the aggregate formation should be prevented.

#### **Introduction**

Lactose monohydrate/microcrystalline cellulose mixtures represent widely used formulation base for direct tablet compression. Both the lactose and celluloses are available in many grades, allowing for optimizing the flow and segregation properties of the formulation. The flow and segregation behavior may become even more complex, if other components of the mixture exhibit time-sensitive flow characteristics.

The present study deals with optimizing the flow and segregation properties of levocetirizine hydrochloride formulation based on lactose/microcrystalline cellulose mixture for direct tablet compression. During the process validation, an interesting behavior was observed. Namely, if there was a delay between the homogenization and the tablet compression, the duration of the delay affected the resulting tablet content uniformity. Since the mixture homogeneity was good and constant after the mixing step, the transport of the mixture to tablet press during the batch processing was suspected to be the critical step. The aim of this study was therefore to investigate mixture flow from the homogenization container to the tablet press inlet as well as the ability of the mixture to segregate during the gravitational flow. The study objective was to determine the sensitivity of the aspects above to the mixture composition, the component properties, and the time delay between unit operations.

#### **Experimental**

The experimental part of the study involved designing suitable model formulations, their preparation and subjecting the samples to segregation and flowability tests.

##### *Mixture composition and preparation*

The base formulation comprised levocetirizine hydrochloride (5 % w/w), Flowlac 100 spray dried lactose monohydrate (52.5 %), milled lactose monohydrate 200 mesh (15 %), Avicel PH 101 microcrystalline cellulose (MCC, 25 %), sodium starch glycolate (1 %), colloidal silicon dioxide (Aerosil 0.5 %) and magnesium stearate (1 %). Several alternative mixtures have been prepared with the same total composition, but using different proportions of different types of lactose and microcrystalline cellulose. The composition of prepared mixtures

is summarized in Table I. The preparation procedure involved introducing all ingredients except the magnesium stearate into the vessel of tote blender 0.8 l, through a 1 mm screen, blending for 20 minutes at 28 rpm, then adding magnesium stearate and additional blending for 5 minutes.

Table I  
Composition of model formulations involved in the case study

Component	API	Lactose 200 M	Lactose SD	MCC	Other
Sample ID	wt. %	wt. %	wt. %	wt. %	wt. %
SMix	5	15	52.5	25	2.5
SLacSD	5	-	67.5	25	2.5
SLac200	5	67.5	-	25	2.5

### Segregation tests

The segregation behavior of prepared mixtures was carried out in an in-house segregation device. The device consisted of two glass tubes (250 x 25 mm) equipped by a connector, enabling the powder to flow from one tube to another and taking samples during the process. The operation of the segregation device was as indicated in Fig. 1. The mixture to be tested was placed into the upper tube and the connector was opened, so as to allow the powder to flow gravitationally from the upper cell into the bottom cell. After the transfer was completed, the tubes switched their position and next cycle of the test was started. The test was finished after 30 cycles. The samples of the mixture were taken during cycles no 1, 5, 10, 15, and 30. The sampling cycles involved taking five samples per cycle during the powder flow from one tube to another. The position of the sample taken was recorded. The samples were then analyzed using HPLC, so as to determine API content.

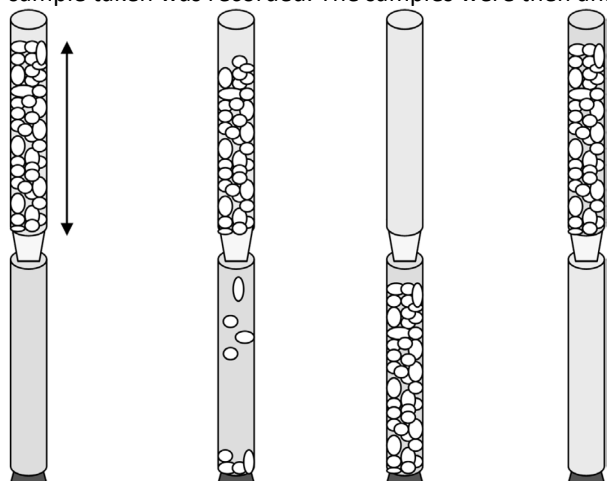


Figure 1. Scheme of segregation device operation (1. mixture is placed into the top cell; 2. mixture is flowed to the bottom cell, samples are taken during the process; 3. finished flow cycle; 4. the top and the bottom cells are swapped and next cycle begins)

### Flow properties

The powder rheometry was used to analyze powder flow characteristics of the sample mixtures using the Freeman FT4 powder rheometer. The test set included measuring the flow energy in both the forced flow and the unconfined flow regime. The stability of flow properties of the samples exposed to test conditions was also measured at the forced flow conditions. Shear tests were also performed in order to determine the internal friction and wall friction parameters. Wall friction experiments used the  $Ra \leq 0.05 \mu\text{m}$  stainless steel standard as an approximation of wall material of the process equipment.

### Results and Discussion

The primary focus was on API and major excipients used throughout this study. Since the use of minor excipients (sodium starch glycolate, Aerosil, and magnesium stearate) was unavoidable and their proportion in the mixture had not to be changed, their effect on the mixture behavior was not examined thoroughly. The assumption was that although their effect may be significant, it will not change significantly over the alternative formulations included in the comparison. The key components particles were examined for their morphology and particle size distribution using SEM (Fig. 2) and laser diffraction (Tab. II). The API particles are smallest of all key components by large margin and the Fig. 2 shows significant tendency of the material to aggregate. Lactose

200 M and MCC are of medium particle size, with the lactose having significant portion of fines. Particles of lactose SD are the largest, spherical, but formed as agglomerates of smaller crystals. Owing to these facts, the API will obviously form interactive mixtures at least partially with some of the excipients, which may affect the segregation behavior of the formulation.

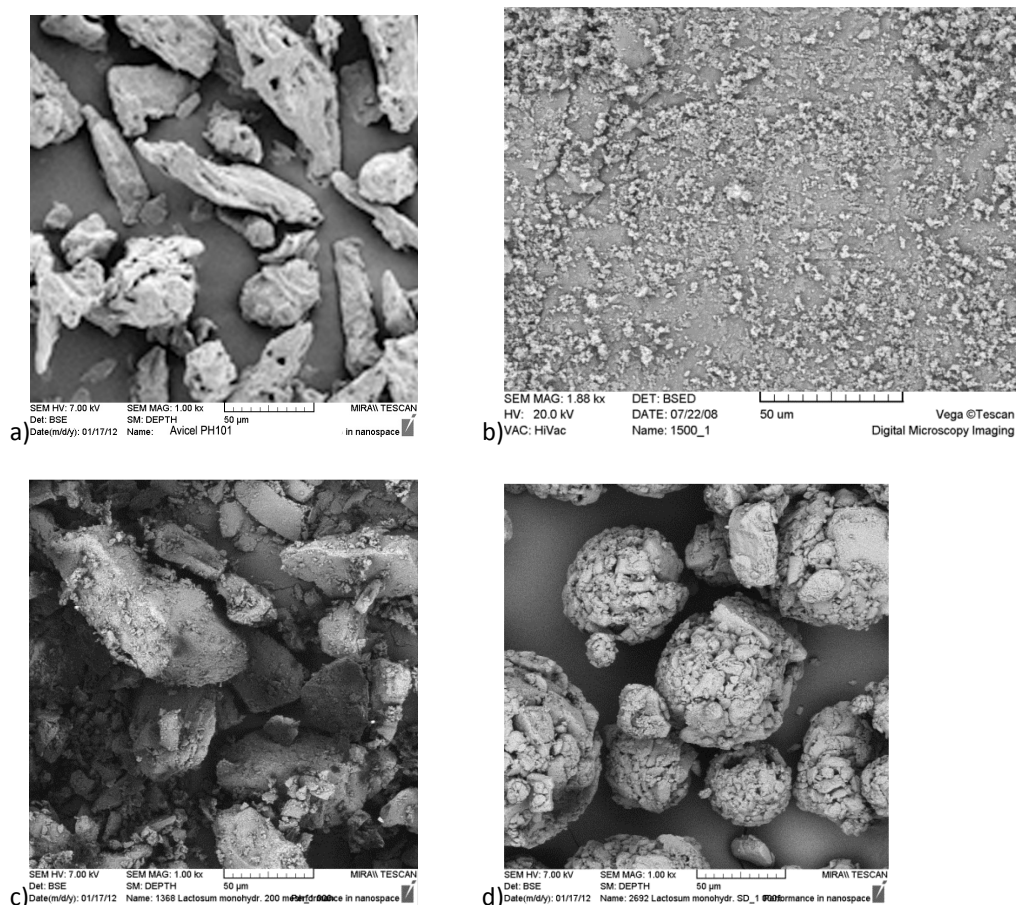


Figure 2. SEM images of a) MCC, b) levocetirizine hydrochloride, c) lactose monohydrate 200 mesh, d) lactose monohydrate SD

Table II

Particle size distribution of key components of model formulations (Malvern Mastersizer 2000)

	PSD, $\mu\text{m}$			
	API	Lactose 200 mesh	Lactose SD	MCC
d(0,1)	0,2	5	30	30
d(0,5)	5,7	30	120	50
d(0,9)	19,0	100	250	85

### Segregation tests

All prepared formulations were tested for their tendency to segregate. Powder mixtures may generally segregate by several mechanisms, but during the gravitational flow, the 'sifting' and 'fluidization' are the most important ones. The term sifting means percolation of finer particles through the voids between more coarse particles, leading to fines being accumulated downstream the powder flow direction. The fluidization may lead to finer particles being slowed down more than coarse ones due to the aerodynamic resistance, and hence they accumulate upstream the powder flow direction. Using the segregation device described above, the 30 cycles of the segregation test were carried out for each formulation. Illustrative results for SMix formulation are provided in Fig. (a-e). In each sampling cycle, five samples were taken along the segregation tube and the API content was determined using HPLC. Figure shows, that the concentration of API is not constant, but increases in the upwards direction of the segregation tube, after the first cycle. This trend becomes more pronounced in further sampling cycles. So as to obtain single-number overall measure of segregation the profiles are approximated by linear regression. The slopes of regression profiles (K) were plotted vs the

sampling cycle number and again processed by linear regression to provide segregation index KK. Although the linear approximation may not seem justified in some cases, it provides good overall trend indicator. The segregation index value is a good measure of the mixture tendency to segregate and positive or negative value may indicate the general direction of segregation trend.

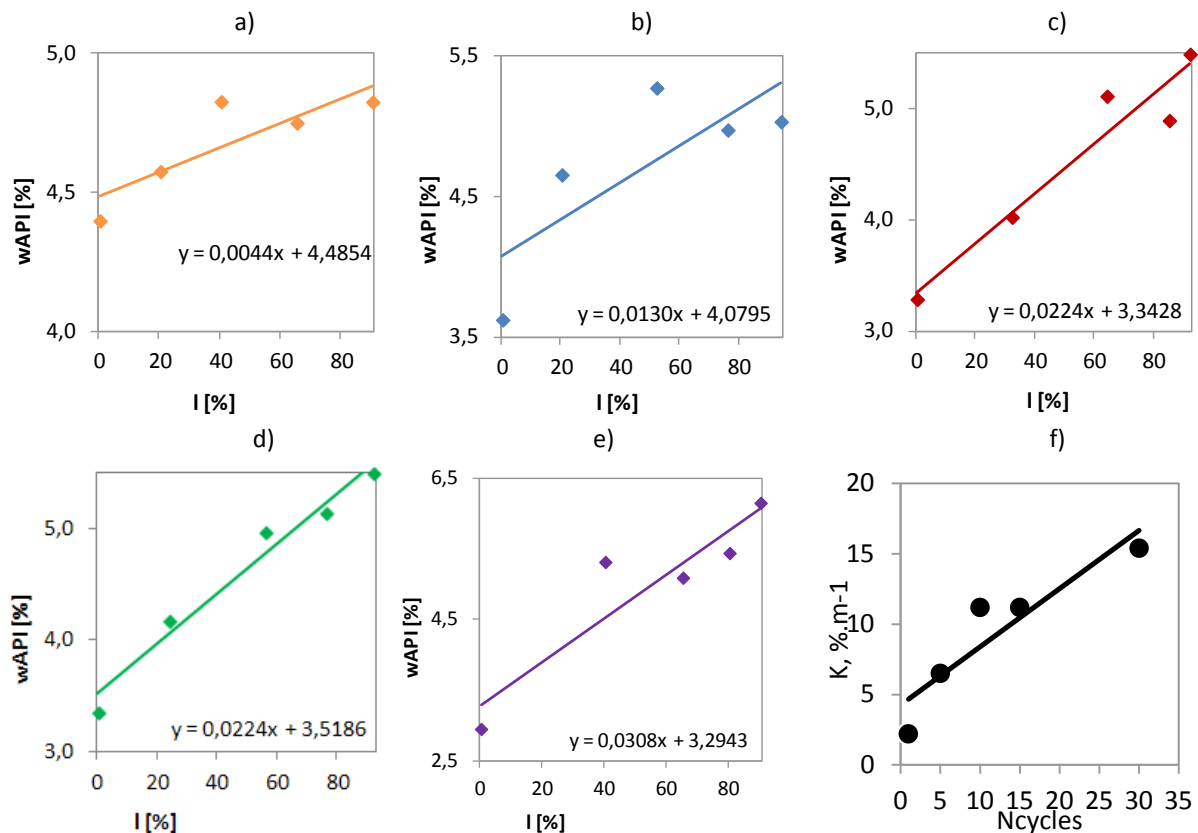


Figure 3. Illustration of primary data from segregation test obtained for SMix formulation after 1 (a), 5 (b), 10 (c), 15 (d) and 30 (e) test cycles. The tube length starts at 0 % at its bottom. The slopes K of profiles a-e are plotted vs the number of test cycles (f)

Table III  
Segregation indices of model formulation

KK, %·m <sup>-1</sup> ·{ncycles} <sup>-1</sup>			
SMix (I)	SMix (II)	SLac200	SLacSD
0.415	-0.400	-3.795	2.475

Results of the segregation tests are summarized in the Table III. Formulation SMix was prepared in two batches (I) and (II) which were both tested independently. The results revealed, there are multiple segregation mechanisms taking part in the overall segregation behavior. SLacSD mixture exhibits large positive segregation index. The positive value means the API tends to accumulate at the upper side of the segregation device tube, i.e. it accumulates upstream the flow direction. The API has the smallest particle size in the mixture; hence the segregation due to fluidization is the dominant mechanism in this case. Surprisingly, there is neither evidence of interactive mixture formation, nor any effect of it affecting the segregation, despite the SD lactose particle textured surface. Most likely, the surface area capacity of relatively big SD lactose particles is not large enough to bind significant portion of API. SLac200 mixture exhibits even larger, but negative segregation index, meaning the API accumulates downstream the powder flow during the segregation test. It may suggest there is sifting segregation acting in place, but it may hardly be the only process responsible for it. API-lactose aggregates are likely responsible for the part of the observed effect. The lactose 200 mesh is much more cohesive and the aggregates are able to develop, encapsulating the API. Those aggregates are bigger than any other primary particles present and they would segregate downstream by the fluidization mechanism. Both batches of SMix formulation exhibit low segregation index value due to balanced effects of two opposing segregation effects demonstrated above. However, there is quite substantial difference between the results of

the two batches, which means the balance is rather sensitive to batch-to-batch variability. Thus, the SMix formulation is resistant to segregation at its nominal quality, but problems may arise, if the mixture properties change during the manufacturing process. One of the important properties, that may be easily changed during the process or process delay are the flow properties and resulting flow regime of the mixture from the blender contained into the inlet of the tablet compression machine. Therefore, it was very important to examine the flow properties of the formulations.

#### Flow characteristics of the test formulations

Flow properties were measured at both forced flow conditions and the unconfined flow conditions. Stability test was performed at forced flow conditions at 100 mm/s tip speed of the blade (Fig 4a). The results indicate the mixtures containing SD Lactose may exhibit significant change of properties during the flowability tests. It also means the material property may change during time, if the material experience prolonged exposition to high-stress conditions. There is substantial difference between SMix I and II batches at the beginning, but the curves approaches each other. It indicates the SMix I probably suffered more mechanical damage during preparation and processing and thus it has the properties similar to those SMix II is getting to have after six repetitions of the stability test. It is not clear what the cause of this difference is, but the important conclusion is that the mixtures are rather unstable. The comparison of absolute values of total energies shows the SLac200 mixture possesses the smoothest particles and hence the lowest energy is required for flow at high-stress conditions. Such conditions are not much relevant to container-tablet press transport though and the situation in variable tip speed test was entirely different. The total energy consumption increases for SLac200 substantially as the tip slows down due to bigger and bigger “cake” of the powder is carried by the blade, suggesting the mixture is cohesive. This is important finding, as it supports assumption of aggregate formation in SLac200, which are supposed to be responsible for the negative segregation index observed. The cohesiveness of the SLac200 mixture is verified also by the higher value of specific energy for unconfined flow, compared to other formulations (Table IV).

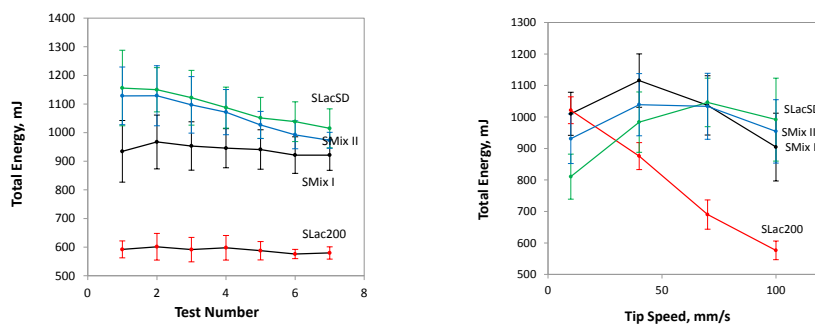


Figure 4. Stability test at 100 mm/s and flowability test at variable tip speed measured in FT4

Table IV

Powder properties for test formulations measured using FT4 powder rheometer

Formulation/Parameter	SMix	SLacSD	SLac200
Total energy at forced flow, mJ	954	971	588
Specific energy at unconfined flow, mJ/g	5.8	5.1	6.5
Wall-friction angle, $\delta^\circ$	8.0	7.0	7.2
Eff. Internal friction angle, $\phi_e^\circ$	30.1	30.5	37.1

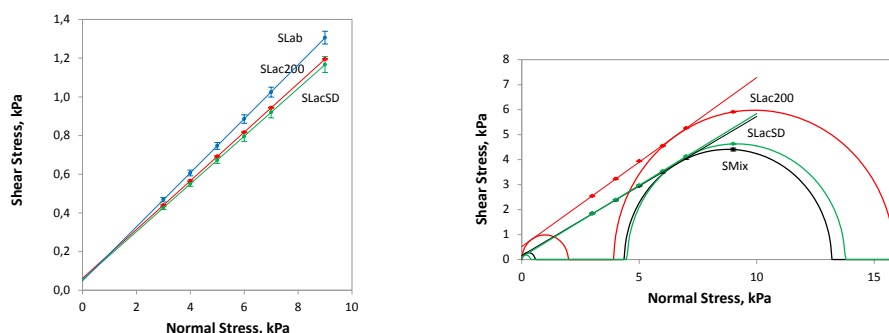


Figure 5. Wall friction test ( $R_a = 0.05 \mu\text{m}$ ) and shear test at 9 kPa pre-shear measured in FT4

Because of the substantial differences among the flow properties of the different mixtures, the flow regime of the mixture for tablet compression being discharged from the blender container to be brought into the tablet press, may be different. In pharma industry, the mass flow is generally preferred, as it is gentler to the particles due to low inter-particle shear, as well as it exhibits reduced relative movement of particles and hence less opportunity for the segregation to proceed. In order to find out, which flow regime is to be expected, the Jenike procedure was applied. The procedure requires three parameters of the flowing powder to be determined. First, the slope of the container wall was 45°. Second, the wall friction angle was determined by wall friction test using the polished steel wall sample ( $R_a = 0.05 \mu\text{m}$  roughness). The values are very similar for all three formulations (Fig. 5, Table IV). Third, the effective angle of internal friction was found being higher for SLac200 mixture, than for any other mixture.

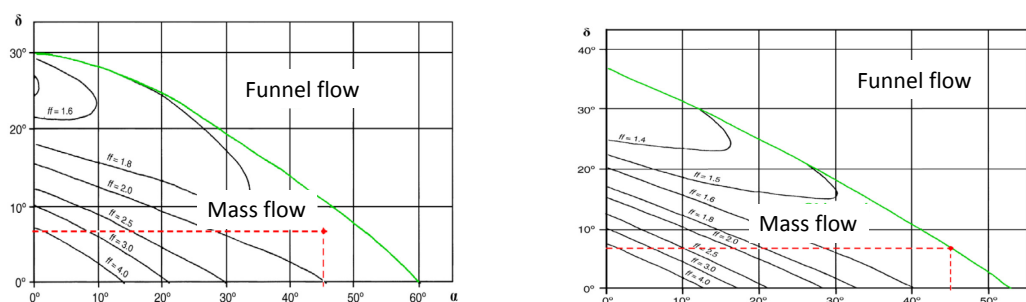


Figure 6. Flow regime prediction based on Jenike procedure for SLacSD (left,  $\phi_e = 30^\circ$ ) and SLac200 (right,  $\phi_e = 40^\circ$ ). Diagrams taken from<sup>3</sup>.

Fig. 6 shows the graphical representation of Jenike design procedure. While the SLacSD formulation is expected to flow safely in the mass flow regime, the SLac200 is expected to exhibit transient behavior, as the flow parameters are at the boundary between the mass-flow and funnel-flow regions. The same is true in limited extent for the SMix formulation. The formulation is expected to flow in a mass flow regime, but relatively slight change in properties or process parameters can shift the flow patterns into the funnel flow regime.

## Conclusions

The segregation tests showed the grade of lactose used is essential for mixture segregation during its flow. While SD lactose mixtures increased the API content in a direction countercurrent to flow, milled lactose mixtures promoted the API segregation concurrently to flow. Mixtures using both lactose grades showed combined effect, resulting in the least segregation due to the two segregation processes competing with each other. However, the segregation was extremely sensitive to ageing of the mixture due to formation of aggregates. The aggregates form and disintegrate during mechanical processing and cause non-uniformity of the tablet content. It was also found that each type of lactose used, causes a different flow regime of the mixture. In order to improve the content uniformity of the tablets, it is needed to ensure the volumetric flow regime in the hopper (by using specific type of lactose), or to ensure that tablets pressing follows the homogenization as soon as possible in order to minimize the time for aggregate formation. In order to improve the content uniformity of the tablets, it was found the volumetric flow regime of transport to tablet press is required as well as the aggregate formation should be prevented. This objective can be achieved by minimizing the delay between mixing and compression, but the more robust way would be e.g. dry-granulating the API premix.

## Acknowledgment

The financial support from specific university research (MSMT No 20/2015) and the financial support by the Czech Grant Agency "GACR" (Project No. 15-05534S, Panel P-108) is gratefully acknowledged.

## Literature

1. Majerová D., Bartáková M., Zámstný P.: Effect of particle size of calcium hydrogen phosphate dihydrate on flow properties and homogeneity of blends for direct tablet compression, - 21st International Congress of Chemical and Process Engineering CHISA 2014, Praha, 23-27.08.2014
2. Zámstný P., Patera J., Husková P.: Device to determine tendency of a mixture of particulate substances to segregation, Utility model CZ 22553, 10 Aug 2011.
3. Schulze D. Powders and Bulk Solids: Behavior, Characterization, Storage and Flow, Springer, 2007

## A STUDY OF DISSOLUTION AND STABILITY KINETICS OF SOLID DOSAGE FORM PREPARED BY HOT-MELT EXTRUSION

**Patera J.**<sup>1</sup>, Blažková K.<sup>1</sup>, Beneš M.<sup>2</sup>

<sup>1</sup>University of Chemistry and Technology, Technická 5, 166 28, Prague, Czech Republic

<sup>2</sup>Zentiva group, a.s., U Kabelovny 130, 102 37, Prague, Czech Republic

jan.patera@vscht.cz

### Abstract

The work is focused on the preparation of solid dispersion in order to prepare solid solution. Solid dispersions were prepared using hot-melt extrusion. Characterization of solid dispersions was performed by X-ray powder diffraction (XRPD) and differential scanning calorimetry (DSC). The stability of solid dispersions was also studied and was characterized by XRPD. The dissolution rate was studied by the flow-through cell apparatus (USP 4). It was prepared 5 mixtures of different composition API/ polymer. As a model drug Paracetamol and Phenylephrine hydrochloride or both of them in the mixture were chosen. Kollidon® VA64 was used as polymer.

The only composition resulting to solid solution by hot-melt extrusion technique was that with higher content of polymer (66,7 % polymer, 33,3 % API/ both APIs). From the dissolution experiments it was found that the initial dissolution rate is greatly affected by wetting the sample and the distribution of particle size in the sample. The modified stability study showed that the compositions containing 50 % of polymer and Paracetamol (or both of model drugs) are not stable and crystallization occurs, while the prepared mixture with Phenylephrine hydrochloride is stable.

### Introduction

Over 40% of active pharmaceutical ingredients (API) in development pipelines are poorly water-soluble drugs which limits formulation approaches, clinical application and marketability because of their low dissolution and bioavailability.<sup>1</sup> Even though the activity of modern drugs is usually very high, and thus only comparatively low plasma concentrations are needed to achieve the desired pharmacological effects<sup>2</sup>, low aqueous solubility now presents one of the most frequent and greatest challenges to formulation scientists in the pharmaceutical industry<sup>3</sup> where formulating solid dosage forms with specific dissolution profiles is of fundamental importance.<sup>4</sup> Various solubility enhancement strategies have been developed to address the low aqueous solubility challenges, including chemical modifications, such as pro-drugs and salt formation, or formulation methods, such as particle size reduction, co-crystal formation, inclusion complexes using cyclodextrins and lipid formulations, and solid form changes such as nanocrystals and amorphous dispersions of drugs and polymers.<sup>5</sup> Of these techniques, transformation of drugs from the crystalline to the amorphous state and furthermore to the molecular dispersion in a water soluble polymer matrix is a useful approach for overcoming the energy barrier in order to achieve an improved dissolution rate and to thereby improve bioavailability.<sup>5,6</sup>

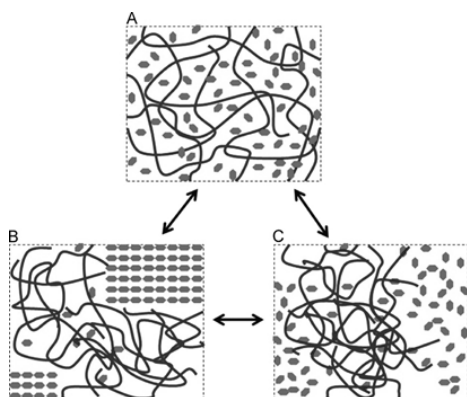


Figure 1. Structure of solid dispersions of API/polymer (A - ideal structure of solid dispersion, API is molecularly dispersed in polymer matrix; B – system consist parts of crystalline API; C – system consist parts of amorphous API)<sup>11</sup>

The term solid dispersions has been defined as a dispersion of one or more APIs in an inert carrier or matrix at the solid state<sup>1</sup> whereas solid solutions consist of just one phase, irrespective of the number of components. In the case of solid solutions, the drug's particle size has been reduced to its absolute minimum (molecular dimensions) and the dissolution rate is determined by the dissolution rate of the carrier.<sup>3</sup>

The mechanism of improvement in the dissolution characteristics of solid dispersions was at first attributed 100% to the reduction in particle size of the drug which is molecularly dispersed in the dissolution medium after the carrier has dissolved. A further reason for the improvement in the dissolution rate is that the drug has no crystal structure in the solid solution which eliminates the energy input normally required to break up the crystalline structure of the drug before it can dissolve.<sup>3</sup> It was also shown experimentally that solid solutions containing a high energy form of a drug can be used to provide metastable solutions of a drug which are significantly supersaturated with respect to the stable crystalline form.<sup>3,7,8</sup> The increased solution concentrations observed following the dissolution of amorphous solid dispersions have been attributed to the inhibition of API crystallization from the supersaturated solution by a polymer and to the increased equilibrium solubility of the API due to solution complexation with the polymer.<sup>9</sup> Although, the drug would precipitate due to supersaturation in the dissolution media, the size of the precipitated particles is still submicron (<1 $\mu$ m) and the dissolution rate of these particles is still higher than that of microparticles prepared by other techniques.<sup>1</sup> The precipitated drugs may also exist in an amorphous or a metastable polymorphic form with solubility higher than that of the most stable form, which only occurs in the presence of a polymer and which leads to faster dissolution.<sup>1,3,8</sup> Another mechanism described is the ability of polymer carriers to reduce the surface tension of aqueous fluids, thereby enhancing the dissolution rate by wetting.<sup>3,10</sup> Besides that, the effects of the polymer also include stabilization of the amorphous drug against crystallization during storage.<sup>11</sup>

In this work, the aim is to elucidate the relations among pilot scale methods and small laboratory techniques of producing solid dispersions, with a particular focus on their quality (Tg), in-vitro behaviour, and on the physical stability of the samples produced by different methods.

### Experimentals

Paracetamol and Phenylephrine hydrochloride were used as model substances. Kollidon® VA 64 was used as a polymer matrix. It was prepared five mixtures (Tab. 1), each raw material was weighed, sieved through a sieve of 0.8 mm mesh size and then homogenized in a Turbula T2F for 10 minutes at 30 rpm. For preparing solid dispersions the following techniques were used: free evaporation of the solvent from a solution, melting, spray drying and hot-melt extrusion.

Table I. Composition of prepared mixtures

Mixture	Composition (wt.%)		
	Paracetamol	Phenylephrine HCl	Kollidon® VA64
1	50,00	–	50,00
2	–	50,00	50,00
3	49,25	0,75	50,00
4	33,30	–	66,70
5	32,80	0,50	66,70

Hot-melt extrusion was performed on a Three Tec extruder. Prior to the start of extrusion gravimetric dosing devices were always calibrated. After that the individual process parameters were set – material feed, rotation of the screw and the temperature in each zone of the heating chamber (20 to 60 °C more than the Tg of the polymer). According to the resulting extrudate individual parameters were varied so as to obtain a glossy, clear extrudate (Fig. 2). The extrudates were milled and sieved through a sieve of mesh size 1.0 mm. Characterization of the prepared samples was performed by XRPD and DSC techniques.



Figure 2. Samples of obtained extrudates

#### USP 4 dissolution tests

Dissolution experiments were carried out on a Sotax Dissotest CE piston pump Sotax CY first cell was used for powder materials of 12 mm diameter in the open configuration. Dissolution medium was 0.1 M HCl at 37 °C. The flow of the dissolution medium was 25 ml / min. A total of 19 samples were collected, in 10 seconds interval, and then analysed on HPLC

#### Accelerated stability testing

Samples prepared using a hot-melt extrusion, spray-drying and melting were tested during accelerated tests of stability, which were divided into two parts (high temperature, high humidity). The samples were placed in open vials to the climate chamber and after 24 hours, they were analysed by XRPD.

#### Results and discussion

Within the samples prepared by melt extrusion preparation of a solid solution was achieved only for samples with higher polymer content, ie sample 4 and 5. Samples which contained polymer and Paracetamol in ratio 1:1 (sample 1 and 3) have been problematic in terms of stability of the solid phase, because, as one can see from the table e.g. in sample 1A was not detected in a XRPD crystalline phase, but records the DSC has already been. The difference was caused by the fact that the DSC record was taken after a longer interval than the XRPD, which were performed immediately after preparation. After two days of storing in dessicator in laboratory, paracetamol has to crystallize in these samples. Presence of crystalline paracetamol was observed od the DSC measurements where the melting point at ca 133°C occurred.

Table II. Basic characterisation of extrudates prepared by hot-melt extrusion

	DSC	XRPD
mixture 1	Tg=32°C; Tm=133°C	amorphous
mixture 2	Tg=24°C; Tg2=133°C	amorphous
mixture 3	Tg=30°C; Tm=129°C	crystalline (PAR)
mixture 4	Tg=45°C	amorphous
mixture 5	Tg=45°C	amorphous

From the dissolution of extrudates in the flow cell there were obtained primary data that show the dependence of concentration of the active substance over time. In order to compare different experiments dissolution rates ( $r$ ) were calculated (Eq. 1), where  $c$  is concentration of API,  $Q$  is the flow rate of the dissolution medium and  $V_c$  is the volume of the cell.

$$r(t) = \frac{c \cdot Q}{V_c} \quad (1)$$

It was proved, that paracetamol is rapidly soluble from solid dispersions than from the physical mixtures (Fig. 3). Initial rate of dissolution of paracetamol, was up to 4 times lower than for the extrudates with the same

content of API. When comparing the initial dissolution rate for both sets of samples with different content of API, it is seen that the samples containing larger amount of polymer (66.7% Kollidon VA64) have a lower initial dissolution rate than samples containing 50% polymer. Lower speed was caused by the formation of a gel-like layer on the particle surface and slower diffusion of API through that polymer layer.

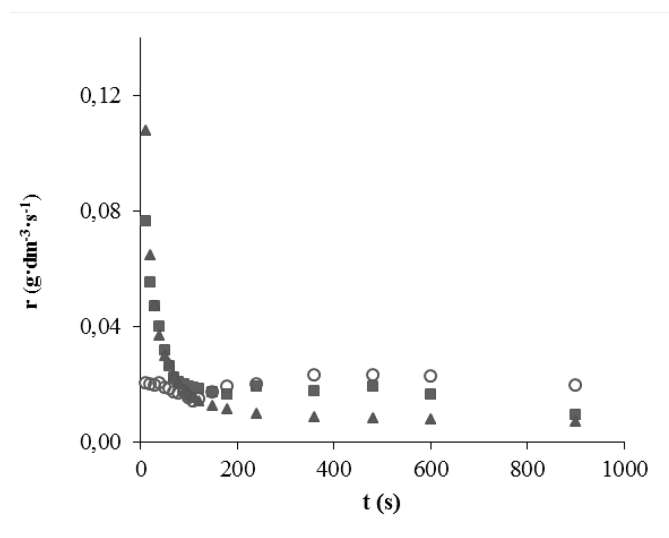


Figure 3. Dissolution profiles for paracetamol. (circles – physical mixture of 50%paracetamol and Kollidon VA64, squares – extrudates with 33.3% of paracetamol, triangles – extrudates with 50% of paracetamol)

Records of powder diffraction pattern of samples 1 and 4 prepared by melt extrusion of the extrudates shows instability with higher content API (Fig. 4). Both samples are amorphous prior to performing stability studies. After 1 day in a climate chamber under the conditions of stability studies (37°C, 80% RH) there is no evidence crystalline phase for sample 4. It is due to higher polymer content, because the sample 4 contained 33.3% of paracetamol and 66.7% polymer. API is in this case better dispersed and stabilised in the polymer matrix. While the sample 1, which contained 50% paracetamol and 50% polymer, shows the presence of the crystalline phase after 24 hrs. Kollidon absorbed water under conditions with high relative humidity and allow crystallization of from supersaturated solid dispersion.

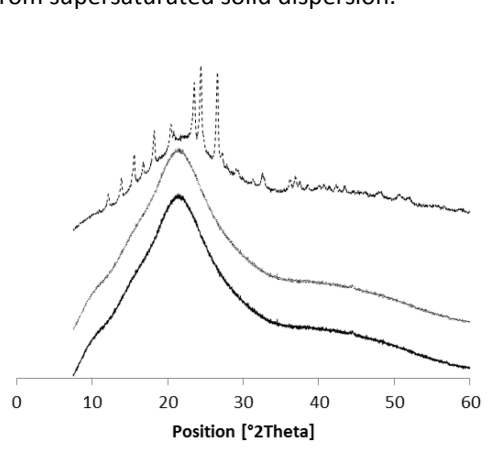


Figure 4. XRD measurement of samples during stability tests - 24 hrs, 37°C, 80% RH (full line – extrudates containing 50% of paracetamol before stability tests, dotted line – extrudates #4 with 33.3% of paracetamol after test, dashed line – extrudates #1 with 50% of paracetamol after test)

Samples containing phenylephrine hydrochloride were stable up to 50% of API in the extrudates. XRD measurements show only amorphous regions similar to sample 4 at Fig.4. All samples were instable in the term of physical stability. Prior to measurements in climate chamber they were milled and sieved. After 24 hrs in a climate chamber formation of a compact layer on the bottom of the vial took place for all the samples. This layer was at most samples tough but plastic. Only samples containing phenylephrine-HCl and Kollidon VA64 created very viscous material with glass temperature below ambient temperature and did not solidify.

## Conclusions

This work was focused on the preparation of solid dispersions by extrusion of the hot melt. The aim was to prepare a solid solution. As a model drug were used Paracetamol and phenylephrine hydrochloride, the starting polymer was Kollidon® VA64 (Copovidone). The stability and the rate of dissolution of prepared samples in the dissolution through the flow cell were studied. Preparation of the solid solution has been successful only with samples containing higher amounts of polymer i.e. 66.7%.

It was found that the initial dissolution rate decreases with increasing polymer content. Higher polymer content leads to the creation of a gel-like layer on the surface of the sample. The results of the modified stability studies showed that the samples containing only phenylephrine hydrochloride and the polymer are stable at the given conditions, while samples that contained only paracetamol and polymer are not stable unless they contain a larger amount of polymer. Thus, samples that contained 66.7% polymer were stable and crystallization did not occur. The same results were obtained for samples containing both the model drug and polymer.

## Literature

1. Okáčová L., Vetchý, D., Franc, A., Rabišková, M., Kratochvíl, B.: *Chem. Listy* 104, 21–26 (2010).
2. Okáčová L., Vetchý, D., Franc, A., Rabišková M.: *Chem. Listy* 105, 34–40 (2011).
3. Komárek P., Rabišková, M.: *Technologie léků*, 3rd ed., Galén: Praha 2006.
4. Swarbrick J.: *Encyclopedia of Pharmaceutical Technology*, 3rd ed., New York 2010.
5. Breitenbach J.: *European Journal of Pharmaceutics and Biopharmaceutics*, 54, 107–117, (2002).
6. Ghebre-Selassie I., Martin, Ch.: *Pharmaceutical Extrusion Technology*, CRC Press, 2003.
7. Repka M. A., Shah, S., Lu, J., et al. *Expert Opinion on Drug Delivery* 9 (1), 105–125 (2012).
8. Crowley M. M., Zhang, F., Repka, M. A., et al. *Drug Dev. Ind. Pharm.* 33, 909–926 (2007).
9. Aharoni S. M. *Polymers for Advanced Technologies* 9, 169–201 (1998).
10. Perissutti B., Newton J. M., Podczeczek F., Rubessa, F.: *Eur. J. Pharm. Biopharm.* 53 (1), 125–132 (2002).
11. Huang Y., Dai, W. G. *Acta Pharm. Sin. B* 4 (1), 18–25 (2014).

# EFFECT OF HYDROPHOBIC INCLUSIONS ON POLYMER SWELLING KINETICS STUDIED BY MAGNETIC RESONANCE IMAGING

**Gaidošová M.**<sup>1</sup>, Pěček D.<sup>2</sup>, Sarvašová N.<sup>1</sup>, Štěpánek F.<sup>1</sup>,

<sup>1</sup>*Department of Chemical Engineering, Institute of Chemical Technology, Prague, Technická 5, 166 28 Prague 6, Czech Republic*

<sup>2</sup>*Zentiva, k.s., U Kabelovny 130, Prague 10, Czech Republic*  
*Frantisek.Stepanek@vscht.cz*

## Abstract

Controlled delivery systems are widely used formulations in the pharmaceutical industry. Binding the active pharmaceutical ingredient (API) into the drug delivery system can solve some disadvantages of regular oral dosage forms. The simplest controlled delivery systems are polymeric matrices mixed with the API and excipients, further directly compressed into the tablet. Hydrophilic polymeric matrices create a gel layer after contact with a dissolution medium. This gel layer represents the regulation mechanism of the API liberation (by influencing the water penetration into the solid core of the tablet, its diffusion through the gel layer, the drug particle dissolution and the diffusion through the gel layer or the polymer chain disentanglement).

Despite the remarkable accomplishments in this field of study, there are still a lot of unknowns in the design of swellable drug delivery systems. It is complicated to produce the final formulation with desired dissolution profile of the API. It often requires the previous optimization of the matrix composition and of the production process. For that reason more studies and implementation of new technologies are required.

In our research, we implemented magnetic resonance imaging (MRI). It is a novel method in this field of research offering us the possibility to visualize the dissolution and swelling process in real time, non-destructively and in situ. The information obtained from image analysis, such as the kinetics of the gel layer creation could be the key for better understanding of the formulation-property relationships. The samples used in our study were binary mixtures of Hydroxypropyl Methylcellulose and carnauba wax (hydrophobic excipient). For MRI measurements a flow-through cell and a tablet holder were designed and manufactured by 3D printing. The experiments were performed under the specific conditions (phosphate buffer saline; pH 6, 37°C; flow rate of medium at 4 ml/min). To improve the visibility of the erosion front, contrast agent - composite magnetic nanoparticles SiO<sub>2</sub>/FeO<sub>x</sub> were used. For the better insight into the mechanisms of drug liberation, the dissolution studies of formulations with the addition of a highly soluble API (Levetiracetam) were conducted. The data obtained were used in mathematical calculations and interpreted.

## Introduction

Magnetic resonance imaging (MRI) is a technique widely used in medicine. By producing the cross-sectional images of organs and internal structures in the body it mainly serves as a diagnostic tool. The signal detected by MRI varies depending on the water content and local magnetic properties of a particular area of the body and thus different tissues or substances can be distinguished from one another. This mechanism of differentiating can also be utilized in the research of sustained release formulations based on swelling polymers<sup>1</sup>.

While water diffuses into the tablet, polymer swells and creates the gel layer. By this process, three areas with different content of water and local magnetic properties are created – solid core of the tablet (no water, fast relaxation – no signal on MRI), gel layer (dense layer of cross-linked hydrated polymer) and pure dissolution medium. Using MRI the erosion front and possibly also the swelling front of the studied dosage form can be determined.

The determination of swelling kinetics is important, because the created gel layer serves also as a regulation of the API liberation<sup>2</sup>. The drug release from swelling polymeric matrix tablets depends mainly on the properties of produced dosage form (i.e. physical structure of the tablet, drug particle size, state of the drug – amorphous/crystalline, drug distribution, surface properties)<sup>2, 3</sup> and on the technological parameters used during their production (i.e. compressing pressure)<sup>3</sup>. It is a very complex process and therefore the proper selection of the composition of tablet matrices is a crucial step for the resulting desired API liberation profile. As far as we are aware, there is no means that would notably simplify the selection of matrix components yet. And it is the accurate combination of matrix components that is supposed to lead to the desired dissolution profile of API.

Imaging methods as Attenuated total reflection with Fourier transform infrared spectroscopy imaging (ATR-FTIR imaging)<sup>4-7</sup>, X-ray microtomography (X-ray  $\mu$ CT)<sup>4, 6, 8</sup>, ultraviolet imaging (UV imaging)<sup>4, 9-11</sup> belong to the

methods most frequently used in this field of research. Comparing to these methods the significant advantage of MRI is the possibility of the real-time *in situ* visualization<sup>1, 4, 8</sup> of the real-sized dosage form in dissolution apparatus (USP4).

Therefore, in our study we focused on the MRI. *In vitro* monitoring of the dissolution of hydrophilic polymeric matrices utilizing MRI can contribute to understanding and to more proper engineering description of processes occurring during the dissolution experiments<sup>1</sup>. The aim of our study was to design the experiments in a flow-through apparatus for MRI measurements and to investigate the influence of hydrophobic inclusions in the hydrophilic matrix on the gel layer creation and API liberation.

## Materials and methods

### Chemicals

Hypromellose - HPMC (Methocel K100M, Dow Chemicals, USA) and carnauba wax - CW (Mach Chemicals s.r.o., Czech Republic) were used for the preparation of matrix tablets. As a model API, highly water soluble Levetiracetam (Zentiva k.s., Czech Republic) was used and as a 3-D print filament for the apparatus parts, acrylonitrile butadiene styrene (ABS) was used.

### Tablet preparation

The tablets were prepared by the direct compressing (excentric tablet press STYL'ONE, IMA s.p.a., Italy) of the previously homogenized mixture of API and excipients (homogenizer TURBULA type T2C, WaB Company, Switzerland – 10 min.). The composition of tablets used for the experiments is given in Table I. The produced tablets were round, biconvex, of diameter 10 mm and radius of biconvex surface of 13. All tablets were tested for average weight, mass variation and friability according to Ph.Eur. 8. The results were compliant with limits with regard to Ph. Eur. chapters.

Table I: Composition of tablets

The amount of substances in tablet (%)			The amount of substances in tablet (%)			
	HPMC K100M	CW		HPMC K100M	CW	LA
<b>CW90</b>	10	90	<b>CW80_LA</b>	10	80	10
<b>CW50</b>	50	50	<b>CW45_LA</b>	45	45	10
<b>CW10</b>	90	10	<b>CW10_LA</b>	80	10	10

### Apparatus for MRI measurements

For the tablet dissolution experiments in MRI, a tablet holder was designed using AutoCad 2014 and then printed utilizing the 3D printer MakerBot Replicator 2X. The tablet holder is shown in Figure 1. The tablet holder with an attached tablet was loaded into a plastic flow-through cell made by cutting the top of a 10 ml syringe, which was enclosed using a septum and connected to a recirculation pump by plastic tubing.

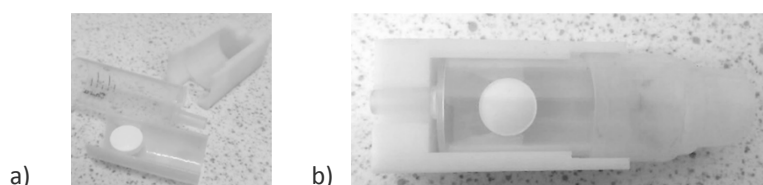


Figure 10: Custom designed flow-through cell and tablet holder – a) disassembled in parts; b) assembled together with a tablet inside

### MRI measurements conditions

Dissolution medium - phosphate buffer saline (PBS; pH 6.0; prepared according to Ph. Eur 8) was heated to 37±2°C by heating the environment of the experiment, the flow rate of the medium was 4 ml/min, and the time of the experiment was 6 h. One Tesla MRI desktop system Icon (Bruker Biospin GmbH, Germany) was used for measurements. Conditions of MRI measurements are shown in Table II.

**Table II** – parameters of the measurement

Protocol	MSME (multi-slice-multi-echo)
Echotime	18 ms
Repetition time	2000 ms
Number of averages	2
Bandwidth	2000 Hz
Matrix size	128x128 pixels
Field of view	1.8x1.8 cm
Number of axial slices	3
Slice thickness	1 mm

The images of each formulation were taken at certain time points (30 min; 1 h; 1.5 h; 2 h; 3 h; 4 h; 5 h; 6 h). Measurement of each formulation was repeated for three times and evaluation of the parameters for each image was also repeated for three different virtual slices. Composite  $\text{Fe}_3\text{O}_4/\text{SiO}_2$  nanoparticles were used as MRI contrast agent for the better visibility of the erosion front of the tablet.

#### Image processing

Image obtained using MRI and illustrative plot profile are shown in the Figure 2.

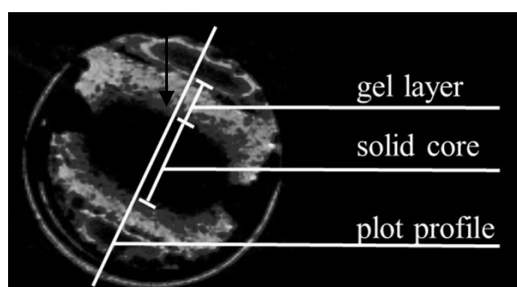


Figure 11: a) image of tablet CW50 in  $t = 300$  min with the

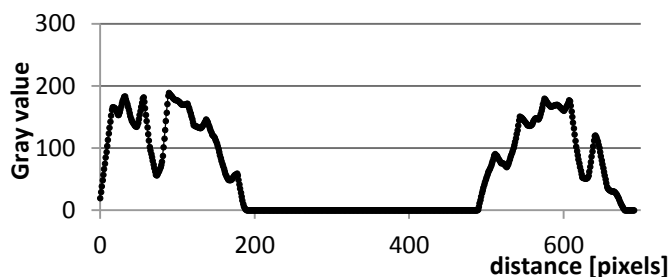


illustration of image processing b) given plot profile

All images were processed using ImageJ software. After the bilinear interpolation, contrast and brightness adjustments, the plot profile across the whole tablet was exported to MS Excel (Figure 2). From this plot, the points where solid core dissolves and gel layer erodes were determined. Finally, the distance between the layers in pixels was converted to mm. From the plot profile, for our purposes, we obtain the thickness of dry core of the tablet, the thickness of gel layer and the dimension of whole swollen tablet. The mean value and the standard deviation were calculated from these nine values and plotted as the function of time for each tablet formulation.

#### Dissolution tests

Dissolution tests were carried out in the same flow-through apparatus as imaging experiments. As a dissolution medium exactly the same PBS was used, only without the addition of contrast agent. Sampling times were chosen according to the MRI experiments. The medium was heated to  $37^\circ\text{C}$  and was recirculated through the cell with flowrate 4 ml/min. The volume of the stock medium was 250 ml. The concentration of dissolved LA was determined using UV-VIS spectrophotometer (Lightwave II UV/Visible Spectrophotometer) at wavelength 210 nm.

#### Results and discussion

Experimental setting for measurements inside the MRI was successfully developed. We were able to measure the kinetics of the gel layer creation and solid core reduction for the matrix tablets prepared from binary mixtures of HPMC and CW. Obtained results are shown in Figure 3.

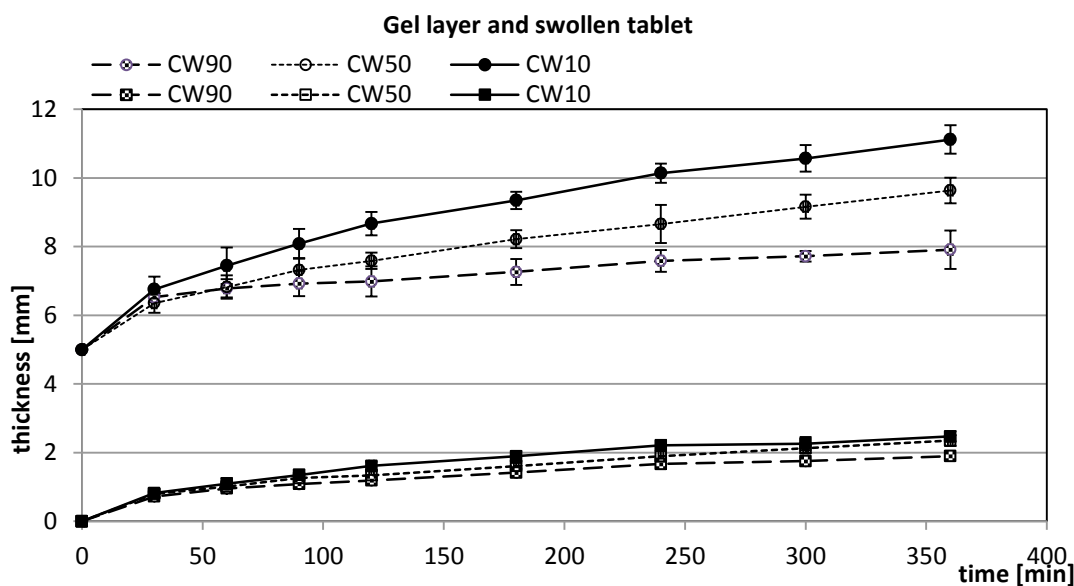


Figure 12: Dependence of the  $\varnothing$  size of the swollen tablet  $\square$  gel layer thickness on the time. Despite the small differences in the gel layer thickness with growing amount of hydrophobic inclusions, considering the standard deviation, the difference is negligible. These results are interesting in comparison with the evaluation of the total swelling of the tablet. The change with growing amount of CW in the formulation is apparent. Formulations with higher ratio of CW show the lower rate of gel layer creation. This can be caused by decreasing amount of gelling agent or by higher amount of hydrophobic inclusions. These inclusions can ease the access of water into the solid core by creating interstices in gel layer. Faster ingress of water into the solid core causes the faster dissolution, thus more rapid API liberation as can be seen in the Figure 4. But unexpected result is the increase of the size of the solid core above 100% with increasing amount of HPMC in matrix. We assume that the solid core is hydrated to a certain extent, but the amount of water in the matrix is too small to cause visible changes in images taken by magnetic resonance. This could be further investigated in our future studies using relaxometry studies and diffusion weight imaging.

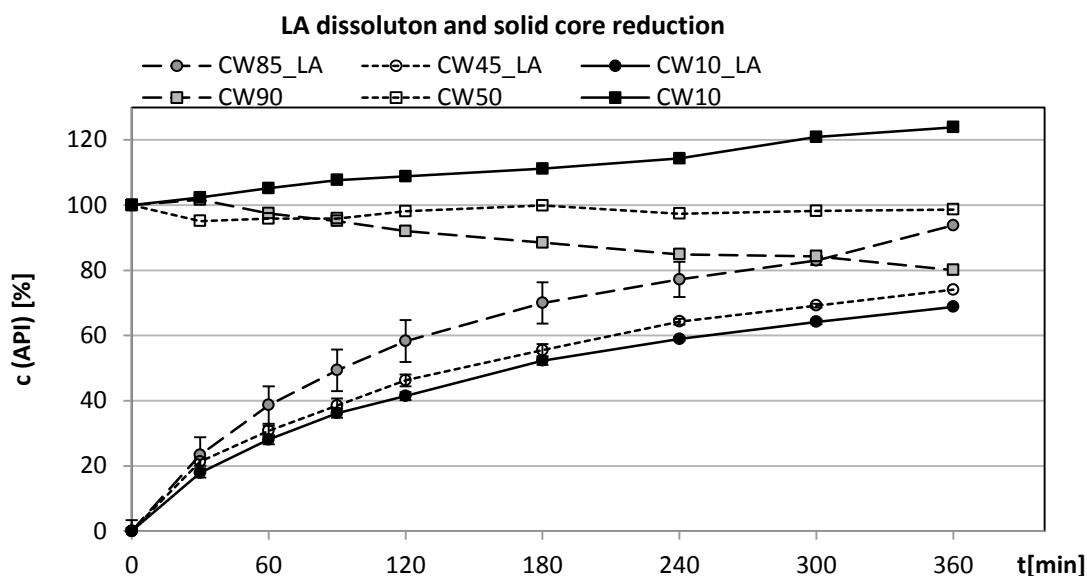


Figure 13: Dependence of the  $\varnothing$  dissolved API  $\square$  solid core thickness on the time

### Conclusions

To sum up, carnauba wax caused more rapid access of the water into the solid core of the tablet, thus more rapid API dissolution. That means the hydrophobic inclusions in hydrophilic swelling matrix do not slow down the process of API liberation but quite the opposite. Moreover, we discovered the limitation of the protocol we used - we were not able to determine the swelling front properly. Therefore, in future studies we will focus on further development of this method using relaxometry and diffusion weight imaging, which could lead to more

proper determination of the swelling front. Moreover, combining this method with the other imaging techniques and also with dissolution test may have an important impact on the knowledge in the studied field.

#### **Acknowledgements**

*M.G. would like to acknowledge financial support from the Specific University Research (project no. 20/2015).*

*F.S. would like to acknowledge support from the Grant Agency of the Czech Republic, grant no. 13-09914S.*

#### **Literature**

1. J. Kowalczyk and J. Tritt-Goc, *Eur. J. Pharm. Sci.* **42** (4), 354-364 (2011).
2. D. Nagendrakumar, G. Keshavshetti and A. Shardor, *Recent Res. Sci. Technol.* **5** (4) (2014).
3. K. Saeio, Y. Pongpaibul, H. Viernstein and S. Okonogi, *Sci. Pharm.* **75** (4), 147-163 (2007).
4. K. Huanbutta, K. Terada, P. Sriamornsak and J. Nunthanid, *Eur. J. Pharm. Biopharm.* **83** (3), 315-321 (2013).
5. S. G. Kazarian and K. A. Chan, *Macromolecules* **36** (26), 9866-9872 (2003).
6. P. Wray, K. L. Chan, J. Kimber and S. G. Kazarian, *J. Pharm. Sci.* **97** (10), 4269-4277 (2008).
7. S. G. Kazarian, K. W. T. Kong, M. Bajomo, J. Van der Weerd and K. L. A. Chan, *Food Bioprod. Process.* **83** (C2), 127-135 (2005).
8. P. R. Laity, M. D. Mantle, L. F. Gladden and R. E. Cameron, *Eur. J. Pharm. Biopharm.* **74** (1), 109-119 (2010).
9. J. Østergaard, E. Meng-Lund, S. W. Larsen, C. Larsen, K. Petersson, J. Lenke and H. Jensen, *Pharm Res* **27** (12), 2614-2623 (2010).
10. J. Østergaard, F. Ye, J. Rantanen, A. Yaghmur, S. W. Larsen, C. Larsen and H. Jensen, *J. Pharm. Sci.* **100** (8), 3405-3410 (2011).
11. J. Pajander, S. Baldursdottir, J. Rantanen and J. Østergaard, *Int. J. Pharm.* **427** (2), 345-353 (2012).

### **UNWELCOME RESULTS OF SAFETY ANALYSES**

**Ferjenčík M.**, Mašín J.

*Faculty of Chemical Technology, University of Pardubice, Studentská 95, 532 10 Pardubice, the Czech Republic  
milos.ferjencik@upce.cz*

#### **Introduction**

It happens that a safety analysis - it does not matter whether a prospective analysis focused on prediction of possible hazards and accident scenarios, or a retrospective analysis focused on learning from accidents and scenarios which already occurred – reveals weaknesses and suggests appropriate changes in safety management system, but the findings are ignored, although they do not show any error. There are articles discussing safety management failures, for instance the article<sup>1</sup>. These articles, however, also omit the following type of problem: “correct and appropriately feasible finding is ignored in the implementation of safety management program”.

Example from the article<sup>2</sup> could serve as an illustration of such a problem. When Norwegian researchers investigated relation between real risk level and its perception, they encountered professional group of fishermen, who use the small boats (smack/sjark) for fishing. Statistically recorded fatality of the fishermen during their work on smacks is very high. It is in contrast with the fact, that the fishermen usually underestimate the risk they are exposed to. The researchers stated in their oral presentation that they had proposed a few simple safety measures to the fishermen, which were able to decrease radically their risk. But the measures were mostly rejected or ignored.

A fisherman – as an owner and a crew of one-man smack - acts both as a manager of the system and an executive worker. It is not quite clear which role is to blame for the rejection and disregard. If it was an executive worker who refuses the recommendations, then the rejection could belong to one of categories described in the article<sup>1</sup>. However more probable is that a fisherman rejects the researchers' proposals in the role of manager i.e. someone who controls features and management of the particular system. In that case Norwegian researchers' findings would be in agreement with the scheme this article is intended to aim for: A researcher represents a consultant; a fisherman is in position of a client. A consultant, after research, presents his findings and recommendations how to enhance safety management to a client, but the client rejects them without an explanation. Results of safety analysis are unwelcome for him. Both sides suffer from this result – a client does not exploit the opportunity to improve safety, for which is he responsible, and consultant's work goes down the drain.

A few examples from chemical industry that correspond with this scheme are presented below. Our goal is to examine reasons, which caused that analysis results are unwelcome. We will take in consideration the reasons both on consultant's and client's side.

At first we gather examples. In accordance with the observation results, we will formulate hypotheses on reason of disregard. In the next section, we will compare these hypotheses with findings about reasons of communication denial. In the last section, we will summarize how the problem could be understood from the current safety management viewpoint.

#### **Observation results**

##### **Initial hypothesis**

Fishermen's reaction from example in the introduction actually is not that surprising. They did not ask for any safety analysis. They are not interested in unsolicited advices. We know this attitude from our personal lives. Why the aversion towards unsolicited advices could not play role also in relation of a client towards advices he receives from a consultant?

##### **Example 1: Risk analysis of a production plant**

Consultant prepared a risk analysis of a medium-sized production plant for safety report according to the law on severe accidents. Its results were summarized into a social risk curve. The curve's trend was quite satisfactory, however only when usual presumptions were fulfilled, especially that all safety management rules from local work procedures are always observed.

Consultant, aware of that some safety rules may represent a temptation for operators, constructed the alternative curve which described the situation when two of safety rules were not observed. The alternative curve trend was significantly less satisfactory. It was visible from the first sight.

The consultant proposed to the client, that he should take into account also this second social risk curve, and use it in safety training as a tool demonstrating the importance of the observation of safety rules.

Client, however, was not interested in this result. He only made sure, that the second less satisfactory curve would not be mentioned any way in the delivered documents.

This example appears to be in agreement with the initial hypothesis. It is similar to the situation when the researchers offer their help to the unprepared fishermen. The consultant offered unwanted result, unsolicited advice.

#### Example 2: Analysis of causes of ignition

Consultant's task was to provide client with an independent advice during the determination of possible sources of ignition in a chemical plant. Consultant's contributions to the work of investigation group were accepted as long as he took part in determining direct causes of the accident. A difficulty arose in the moment when the most probable direct causes has been determined, and the consultant consequently tried to identify underlying causes within the organization and management system, which contributed to the accident. Basically the consultant pointed out, that the management of change, which existed in the plant, was not introduced in the way that would prevent the accident.

Averse reaction of the client's management to this finding can hardly belong in unsolicited advices category, since the consultant was expressly asked for the accident causes. The reaction was rather a sign, that consultant's recommendation is not considered to be realistic, but in contradiction with the client's situation and capacity.

#### Revision of the hypothesis

Not only unsolicited advices should be avoided by a consultant. Also the recommendations which could give the impression, that they omit client's situation, responsibility and possibilities, should not be proposed. Consultant should not propose non-empathetic advice.

If we look back to preceding two examples, we see that in the both cases a client could get the impression, that he was given advices omitting his possibilities, lacking empathy.

#### Example 3: Analysis of causes of explosion

Similarly to the preceding Example 2, consultant's task was to help during the determination of possible causes of the accident in chemical plant. However in this case the accident was explosion. Analysis of its causes progressed slowly. Likewise in the Example 2, consultant's contributions to the work of investigation group were accepted, as long as direct accident causes were determined. In contrast with Example 2, the client was open even to findings aiming to reveal underlying causes in organization and management. The findings uncovered gradual loss of memory of designers' intentions during the life of organization, gaps in management of change and unwillingness to take into account external impulses focused on modernization of safety management. A change in the client's attitude arose, when the consultant tried to deduce recommendations from the underlying causes of the accident. The findings pointed to the deep gaps, and thus the necessity of large changes. Consultant tried to communicate this to the client briefly, but the brevity reduced recommendation to overall criticism of the local safety management system. In this moment, client started to show their disappointment, because in their opinion the recommendations did not reflect the reality, were non-empathetic.

#### Second revision of the hypothesis

The client's feeling that his consultant gives non-empathetic advice, and the growing rejection, may result not only from the recommendations which are not sufficiently realistic, but also from that they are too general, insufficiently detailed and specific. The consultant should ensure that his recommendations are adapted to local conditions and as specific as possible.

Insufficient specificity of advice probably did not play a role in the introductory example nor in Example 1. However, it could contribute to the rejection of the results in both the analyzes of accident causes i.e. in Examples 2 and 3.

#### Example 4: Hazard analysis of pilot plant

The task of the consultant in this case was to analyze the hazards in the upcoming pilot plant production process and make recommendations where the attention of care for safety should be focused. On the client side, the analysis was watched with interest and great expectations.

Analysis was routine and not particularly extensive. It did not point to any problem that the client was not aware of. The most significant recommendation that resulted from it can be summarized in the following sentence: "You really should not carry the acid upstairs in the bucket." The consultant, in order to avoid the error of too unspecific recommendation, specified the appropriate type of plastic canister which should be used for acid.

Despite the efforts of the consultant, the client's response to the results of the analysis combined disappointment and surprise. He was surprised that the analysis actually just named what he already knew and what he, in truth, does not want to change.

#### Third revision of the hypothesis

Let us repeat and complement previous formulations of the hypothesis. The consultant, who wants his reasonable and well-intentioned recommendations not to be rejected, should refrain from anything that could be perceived as unsolicited or non-empathetic advice. He should be empathetic to the situation of the client, giving realistic and specific recommendations. In addition, he should also timely cool excessive expectations on the client side. Finally, he should take into account the fact that the client does not want to change the status quo. Reluctance to change anything could play a role in all the above examples, including the example from Introduction.

#### View of popular psychology

The hypothesis from the preceding section provides opinion - based on certain selection of experience - on how a consultant should behave in relation to the client, in order to limit the chance that the results of the safety analyzes, although correct, are rejected. The hypothesis indicates that a consultant may face the difficult task of communication, resolution of which completely determines the fate of his analysis, and which yet is only partially under his control. The problem is thus shifted to the territory of psychology, where the authors of this paper do not feel at home.

The question of how it happens that the results of the safety analyzes become unwelcome, nevertheless, has such practical importance for authors that they do not want just to pass it into the care of professionals and lose it out of sight. Therefore, they are still trying to seek help in the field of the so-called popular psychology, even though they are aware that as laymen in this field they can easily fall into traps of various half-truths and myths<sup>3</sup>.

The authors propose to portray the problem of unwelcome results as a problem of partner communication, in which one party (the client) refuses to listen to what the other party (a consultant) says. This problem is - due to its general nature - widely discussed and commented on a large number of websites. The authors decided to use as a source text<sup>4</sup> that is dated, fairly comprehensive, and states the author (Susan Heitler). It is published on the Web site [www.psychologytoday.com](http://www.psychologytoday.com). The text lists the ten options that may cause the partner does not listen to partner.

Consider which of these options can contribute to the emergence of unwelcome results of the safety analyzes.

#### Option 1: confirmation bias and cognitive dissonance

According the text<sup>4</sup> both confirmation bias and cognitive dissonance may cause that the client will reject the dissonant data, that is, data that differ from what they previously have believed or that is spoken by someone toward whom they harbor negative feelings.

Hence, consultant's recommendations can be ignored because they are inconsistent with the client's beliefs, or because the client does not like the consultant.

#### Option 2: narcissism

Narcissistic listener is convinced that he knows best about everything, and that the opinions of others are not worth to listen to them.

The consultant's recommendations can be ignored because the client is narcissistic.

#### Option 3: anger

The consultant is ignored because the client is angry. Anger causes narcissistic reactions to the findings and recommendations of the consultant.

Option 4: distrust

Client considers the consultant to be more enemy than friend; therefore they reject the information that comes from the consultant.

Option 5: partner does not listen to me because of treating me the way I treat myself

According to the text<sup>4</sup> a partner may tend not to listen to us when feeling that we do not listen to ourselves.

Thus, the consultant can meet with rejection, if he recommends to the client something that he internally rejects.

Option 6: aggressive manner/ tone

Any hostile voice tones invite others to defend against instead of listening to what you are saying. If for instance, a consultant communicates its findings to the client with a tone of voice that shows annoyance, he might face rejection.

Option 7: communication exceeds the capacity of reception

If we speak too quiet or loud voice; too fast or too slowly; if we use the uptick voice at the end of sentences; if we string together too much data with excessive ands; all these possibilities impede partner's listening. The consultant must expect that if he commits these mistakes, the client will eventually ignore his advice.

Option 8: giving advice instead of information

People are much more inclined to listen to the findings and recommendations, which are communicated to them as information and give them space for independent decisions, than to direct advice. The consultant should take this fact into consideration when he formulates his findings.

Option 9: use of annoyingly repetitive words

These errors can cause the consultant will not be listened to.

Option 10: no listening as revenge

People sometimes do not listen to others, because they do not listen to them.

If the consultant rejects the findings and recommendations of the client, he has to count on the fact that his findings and recommendations will be rejected as well.

### **Comparison with examples**

All of these ten options would undoubtedly be involved in the development of unwelcome results of the safety analyzes. Unfortunately we do not have enough detailed information to give reasons for reliable confirmation or refusal. But the application of options 1, 8 and possibly 4 is conceivable, both in the initial example (Norwegian fishermen) and in the other four examples. In contrast, the application of options 6, 7 or 9 may be considered unlikely. Options 1-10 could provide a good starting guide for further data collection, if we wanted for any of the examples to determine precisely why the results became unwelcome.

Comparison with the third revision of the hypothesis

Options 1-10 are to some extent overlapping with the conditions that we mentioned in the third revision of hypothesis. So options 6 and 8 can be considered as confirmations of previous warning against unsolicited and non-empathetic advice. In addition, the recommendation to be empathetic promotes trust and assonance. We can say that options 1 and 4 are at least partially covered by the hypothesis. View of the role of client's expectations and reluctance to change the status quo, however, does not overlap with any of the options 1 to 10.

At the same time options 1-10 substantially broaden the range of conditions that may contribute to the rejection of the results.

What is outside the influence of consultant?

Most of the options can serve as hints of what the consultant should avoid, if he wants to make its results acceptable. Mostly it is within the power of a consultant to positively influence individual options, or at least realize their adverse effect. But if there are options 1-3 on the client side, then the consultant's potential to prevent their adverse effects is very limited.

Objections against the fourth revision of the hypothesis

Now, we could propose further revision of hypothesis about why the results of the safety analyzes can be rejected/ignored. The third revision should be extended to include the aforementioned ten options.

In accordance with the fourth revision of the hypothesis we could name recommendations for a consultant.

The consultant is recommended that:

(List of conditions should follow.)

The resulting list of recommendations already starts to be rather long, and begins strikingly remind list of rules of conduct in selected situations.

Consultant - recipient of our recommendations - can at this point say, "Yes, well, I can and I always try to speak intelligibly, inspire client's trust, not to create his anger, etc. but my main task is different. The main thing to do is, to find out what he should change in the interest of safety. Whether he accepts or not, it depends as much on him as on me. There are reasons for rejection, against which I cannot do anything. If for instance, distrustful narcissus sits on the other side of the table, then my findings have no chance."

### **A change of perspective – the role of client from current safety management viewpoint**

Until now we have concentrated on the problem of unwelcome results from the position of consultant. We asked what could cause rejection of the results, and what especially consultant can do to ensure that it does not happen. We have gathered the entire spectrum of possible causes and ideas about how a consultant should behave.

But now it is time to ask what the client should do for the successful exploitation of results.

Article<sup>5</sup> draws our attention in this direction. It states that process safety management is not, in fact, a technical issue but one of management and leadership. It asserts and shows, that keeping a plant safe is technically well within the capacity of any organization that deals with hazardous materials. But keeping a plant safe is managerially complex, demanding strong leadership and attention from senior site management.

Care for safety according to these views, which are presently representative, requires first and foremost a strong leadership of people on the client side. The key role of leaders, as article<sup>5</sup> states, is to develop and drive a culture for process safety within the organization. The term culture can be understood simply as "the way we do things around here".

Another article<sup>6</sup> confirms and describes in detail the irreplaceable role of leaders in safety. Leaders directly and indirectly influence systems and climate, and thereby hazards and exposure.

Article<sup>6</sup> also recapitulates the qualities that the people who will lead people should possess and the values that they should recognize. It lists five characteristics of the ideal person in the role of leader.

Of these, the most interesting for the conclusions of our considerations are agreeableness and openness to experience. Leader should be straightforward, trust others, and considerate others. He should have a sense of curiosity, an exploratory approach to challenges, and an imaginative mindset.

Let's go back to the problem of unwanted results. If a person with these behavioral characteristics would be present on the side of the client, then the situation is ready to receive any good results. Various barriers for adoption on the client side cannot arise and communication deficiencies on the part of the consultant cannot play a serious role.

### **Conclusions**

Your mission to analyze safety in an alien environment brings disappointment and bad news. It is relatively bearable if no one is waiting that you do something good. It is worse when you are expected to do a miracle. Moreover, finally you often say only something what all basically know but do not want to hear. Which is unwanted, banal, and can be regarded as arrogant. And besides, it sometimes also happens that the results, which you have struggled to come, are rejected without explanation.

A number of possible causes that may cause rejection of the results are identified in sections 2 and 3. Also a number of conditions that can be influenced by a consultant are recognized.

Yes, it is undoubtedly important and right that the consultant shall not only strive for good results, but he shall also submit them with a courtesy, understanding, trustworthy, etc.

Nevertheless the findings from section 4 add the alternative view which significantly lightens the burden carried by the consultant. This is not a consultant, but the client who bears the principal responsibility for how the results of analyzes are treated. If the results of safety analyzes are correct, then the way how they were

presented cannot be the main reason why they were ignored. The main reason is that a true leader is not listening to them on the client side.

Unwelcome results of the safety analyzes indicate a failure of leadership on the client side.

Unwelcome safety results are a symptom of a situation where care for the safety on the client side cannot rely on local leaders and leadership, and its only hope is in safety guerilla<sup>7</sup>.

This result is certainly true for all four of the examples from the chemical industry. With some caution (which originates from identifying the roles of managers and executives), it can also be applied to the introductory example of Norwegian fishermen.

#### Literature

1. Kelly B. D.: Why Process Safety Programs Sometimes Fail. *Process Safety Progress* 30, 307-309 (2011).
2. Bye R., Lamvik G. M.: Organizational culture and risk perception. In: *Advances in Safety and Reliability – Kolowrocki (ed.), proceedings of the European Safety and Reliability Conference ESREL 2005, Tri City (Gdynia-Sopot-Gdansk), Poland, 27-30 June 2005*. Taylor & Francis Group, London, 2005. ISBN 0 415 38340 4.
3. Lilienfeld S. O., Lynn S. J., Ruscio J., Beyerstein B. L.: *50 Great Myths of Popular Psychology: Shattering Widespread Misconceptions about Human Behavior*. Wiley-Blackwell, September 2009. (Český překlad pod názvem *50 největších mýtů populární psychologie* vydalo Universum v roce 2011.)
4. <https://www.psychologytoday.com/blog/resolution-not-conflict/201407/why-doesnt-shehe-listen-me-10-possibilities> [accessed 1 April 2015]
5. King C.: The Importance of Leadership and Management in Process Safety. *Process Safety Progress* 32, 179-184 (2013).
6. Killimett P.: Organizational Factors That Influence Safety. *Process Safety Progress* 25, 94-97 (2006).
7. Berger S.: The process safety guerrilla: Giving your company a future, even if it does not want one. *Process Safety Progress* 29, 186–191 (2010).

## ASPEN HYSYS MODELLING IN SAFETY ANALYSIS AUTOMATION

Janošovský J., Labovský J., Jelemenský Ľ.

*Institute of Chemical and Environmental Engineering, Slovak University of Technology, Bratislava, Slovakia  
ludovit.jelemensky@stuba.sk*

### Introduction

During the last decade chemical industry has undergone a considerable change. Economic pressure caused the requirement of higher yields and led to the modification of chemical processes towards extreme temperatures and pressures. The demand for detailed process hazard analysis is growing due to extreme conditions in which modern chemical productions are being operated. The necessity of appropriate process safety analysis is well recognized after occurrence of several tragic accidents that could have been avoided. There are several process hazard analysis methods including What-If, Checklist, Failure Modes and Effects Analysis (FMEA) and Hazard and Operability (HAZOP). HAZOP is one of the most used process hazard analysis technique. HAZOP study is a highly disciplined procedure based on combinations of guide words and process variables. When the guide word (more, less, none ...) is applied to a process variable, a deviation is generated. The objective of the HAZOP study is to monitor the causes, propagation and consequences of process variable deviations. Conventional final HAZOP report represents a list of all possible deviations, their causes and consequences, analysis of such consequences, existing level of protection and recommended actions<sup>1</sup>. HAZOP analysis was used and modified in many hazard identification procedures including determination of the required safety instrument level, blended hazard identification methodology and HAZOP analysis based on structural model<sup>2,3,4</sup>.

The disadvantages of a conventional HAZOP study are its time-consuming character and high cost. The lack of time and experiences of human expert team is often the major obstacle of a HAZOP execution in chemical industry. The most frequently proposed solution of these inconveniences is automation of HAZOP analysis. A literature review of the HAZOP-related research proved that nearly 40 % of published literature is focused on automating HAZOP (Figure 1)<sup>5</sup>. There are two preferred approaches in HAZOP automation: knowledge-based and model-based. The knowledge-based approach is based on systems using a knowledge base containing information about the failure mode, causes and consequences of various process units and/or pieces of equipment. Typical knowledge-based expert systems proposed particularly in the 20<sup>th</sup> century are HAZOExpert, TOPHAZOP and AHA<sup>6,7,8</sup>.

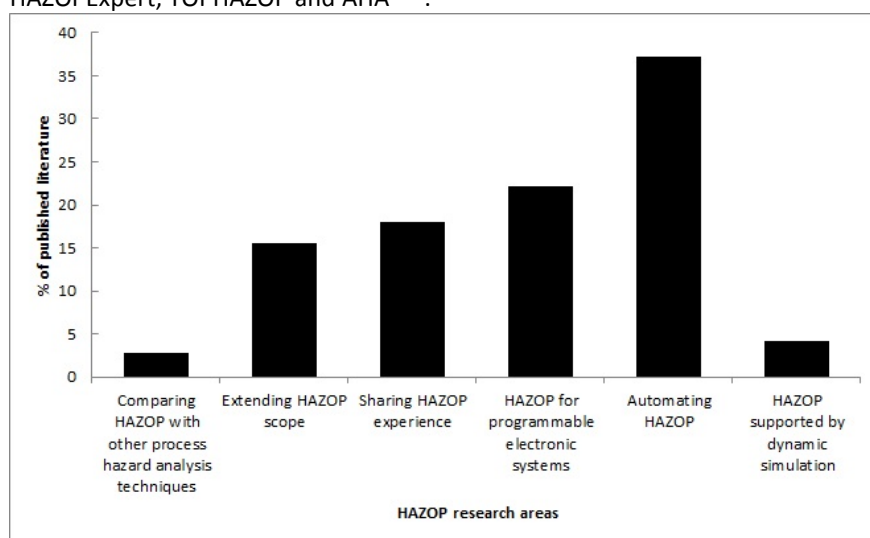


Figure 1. HAZOP-related publication review

The knowledge-based approach has one significant disadvantage: in the age of constant development of technology in chemical industry and pushing the limits of process variables to extreme values, it is questionable, if the identification of all possible hazardous events is sufficient using only large databases of experience. Together with development of computer technology in 21<sup>st</sup> century, these are the reasons, why the model-based approach has gained more importance. The main benefits of the use of mathematical modelling in hazard identification are presented in various case studies e.g. reactive distillation in MTBE production or fixed bed catalytic reactor with parallel reactions<sup>9</sup>. The model-based HAZOP study is based on the implementation of a detailed mathematical model of a chemical process. The conventional HAZOP study does

not consider the duration and value of deviations. These problems can be examined thanks to the model-based approach. Typical model-based expert systems are MATLAB<sup>®</sup> employment for educational purposes as well as using steady-state analysis and dynamic simulation for real process safety or using process simulation performed by the industrial simulation package Aspen Plus<sup>®</sup> version 2006.5 for continuous biodiesel production<sup>10,11,12</sup>.

The main objective of this paper is to summarize implementation issues of Aspen HYSYS modelling in automated process safety analysis and to present a simple automated HAZOP analysis tool. Aspen HYSYS was chosen because of its access to one of the most extensive property databases and the possibility of data transfer between external software and Aspen HYSYS v8.4 simulation environment. Ammonia synthesis was chosen as the case study because of its strong nonlinear behaviour which was confirmed by an incident in an industrial ammonia synthesis reactor<sup>13</sup>. In the first step, kinetics of reaction were taken from literature and implemented in Aspen HYSYS v8.4<sup>14</sup>. The next step was the generation of deviations and the analysis of the response of the examined system. This analysis was performed using Aspen HYSYS models and an external program written in the C# language. The external program was used to communicate with simulation environment of Aspen HYSYS v8.4. In the external program, process variable deviations were generated and simulation data were collected. The results of analysis are utilised in final study within the meaning of HAZOP methodology. The investigation of the chemical processes is strongly dependent on the selection of an appropriate mathematical model and parameters describing their physical properties, reaction kinetics etc.

### Case study

The proposed safety analysis automation is demonstrated on the case study of ammonia production. A mathematical model of presented production consists of one fixed-bed reactor, a simplified heat exchanger and refrigeration unit with vapour-liquid flash separator (Figure 2). The fixed-bed reactor system consists of three segments – beds in series with fresh feed quenching between each bed to achieve the optimal temperature profile in the reactor system. The main function of the heat exchanger is to preheat the feed with the outlet stream from the fixed-bed reactor. In the refrigeration system, the preheater outlet stream is cooled to the desired temperature. In the flash separator, the outlet stream from refrigeration system is separated to the liquid and gaseous phase.

Ammonia is produced according to the following reaction scheme:

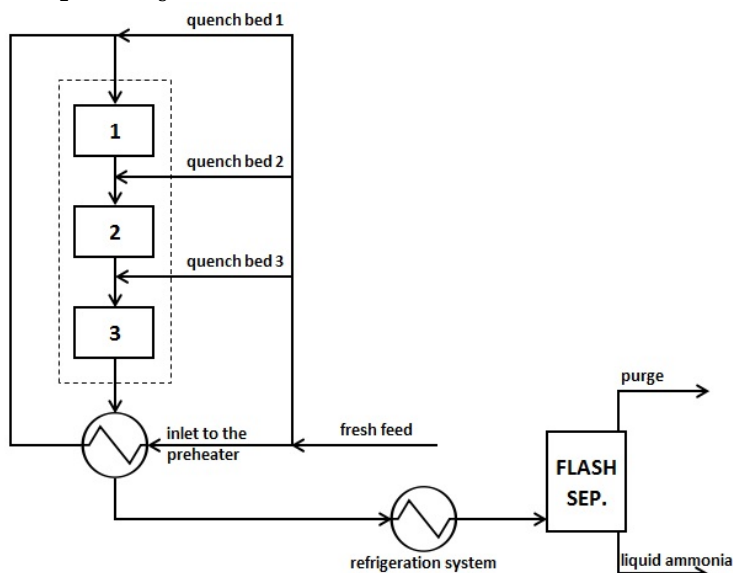
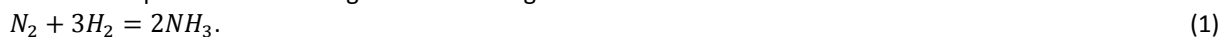


Figure 2. Schematic description of the ammonia synthesis unit

The mathematical model of the presented production was created in Aspen HYSYS v8.4 environment and is shown in Figure 3. An internal Aspen HYSYS v8.4 library was used to calculate the physicochemical properties of all pure components and the mixed physicochemical properties. The Peng-Robinson equation of state was selected as the property package. The plug flow reactor model was selected for mathematical modelling of individual segments of the fixed-bed reactor. A simple end point method was selected in the Aspen HYSYS Heat Exchanger Model. Overall heat transfer coefficient was calculated to achieve similar behaviour of the preheater as presented by Morud and Skogestad, where the heat exchanger provides a relationship in the form:

$$T_{inlet} = 0.629 \times T_{outlet} + 0.371 \times T_{feed}, \quad (2)$$

where  $T_{inlet}$  is the reactor inlet (preheater outlet) temperature,  $T_{outlet}$  the reactor outlet temperature and  $T_{feed}$  the temperature of the fresh feed<sup>13</sup>. The process variable values (Table I and Table II) were set to the design values that were adjusted to correlate with the work presented by Morud and Skogestad and with the current trends in ammonia production industrial units<sup>13</sup>.

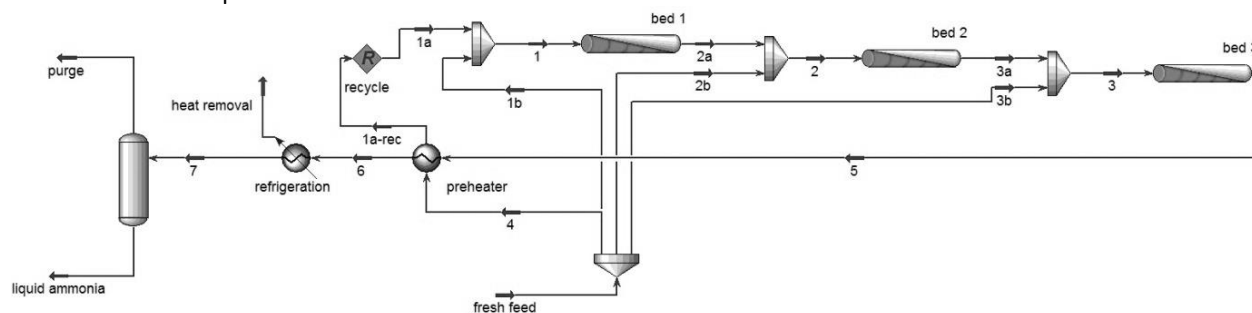


Figure 3. Ammonia synthesis unit in Aspen HYSYS v8.4

Table I

Design operation parameters

Stream	Mass flow [10 <sup>3</sup> kg/h]	Temperature [°C]	Pressure [MPa]	Mole fraction NH <sub>3</sub>	Mole fraction N <sub>2</sub>	Mole fraction H <sub>2</sub>
fresh feed	252	250	20	0.04	0.24	0.72
quench bed 1 (1b)	58	250	20	0.04	0.24	0.72
quench bed 2 (2b)	35	250	20	0.04	0.24	0.72
quench bed 3 (3b)	32	250	20	0.04	0.24	0.72
inlet to heat exchanger (4)	127	250	20	0.04	0.24	0.72
outlet bed 1 (2a)	185	520	20	0.14	0.22	0.64
outlet bed 2 (3a)	220	530	20	0.16	0.21	0.63
outlet bed 3 (5)	252	525	20	0.17	0.21	0.62
inlet refrigeration system (6)	252	436	20	0.17	0.21	0.62
purge	202	8	20	0.06	0.23	0.71
liquid ammonia	50	8	20	0.98	0.00	0.02

Table II

Design parameters of the individual beds

Bed No.	Length [m]	Diameter [m]	Total volume [m <sup>3</sup> ]
1	10.5	0.9	6.7
2	15.1	0.9	9.6
3	23.9	0.9	15.2

## Results and discussion

Conventional HAZOP study requires large-scale analysis of all possible process variable deviations. However, process parameters that are calculated during simulation are not accessible for changing from an external

environment. This fact complicates the manipulation with output streams. Therefore, only deviations of input parameters can be examined. The fresh feed stream was selected for process hazard analysis. The list of typical process variable deviations based on conventional combining guide words with selected feed parameters is presented in Table III. However, the consideration of the value of the deviation is allowed in a model-based HAZOP study by mathematical modelling. Detailed simulations of the presented system were carried out in order to perform the parametric sensitivity analysis of the reaction conditions and to evaluate the effect of selected deviations on the analysed reactor system.

Table III  
Process variable deviations generated by a conventional HAZOP study

Guide word	Process variable	Deviation	Deviation applied to the fresh feed stream
More	Temperature	Higher temperature	The fresh feed temperature higher than a design value
Less	Temperature	Lower temperature	The fresh feed temperature lower than a design value
More	Pressure	Higher pressure	The fresh feed pressure higher than a design value
Less	Pressure	Lower pressure	The fresh feed pressure lower than a design value

The first process variable selected for safety analysis was the fresh feed temperature. The effect of the fresh feed temperature change on the overall hydrogen conversion was monitored (Figure 4) and as shown, the steady state solution diagram exhibits two different steady states in the range approximately 220 – 270 °C. The design operating point (250 °C) is located in the region of multiplicity. From the design operation parameters (Table I) analysis, it is evident that the location of the design operating point is at the branch of the higher steady state conversions in this region.

When the HAZOP deviation “higher temperature” than a design value was applied to the process, the overall hydrogen conversion gradually decreased. However, when the HAZOP deviation “lower temperature” than a design value was applied to the process, two possible system responses were observed. When the feed temperature control failure caused decrease of the temperature by 10 %, to 225 °C, the overall hydrogen conversion gradually increased. When the feed temperature control failure caused decrease of the temperature by 20 %, to 200 °C, the reaction conditions changed significantly and the overall hydrogen conversion dramatically dropped. The reaction of ammonia synthesis was terminated. This phenomenon led to further investigation.

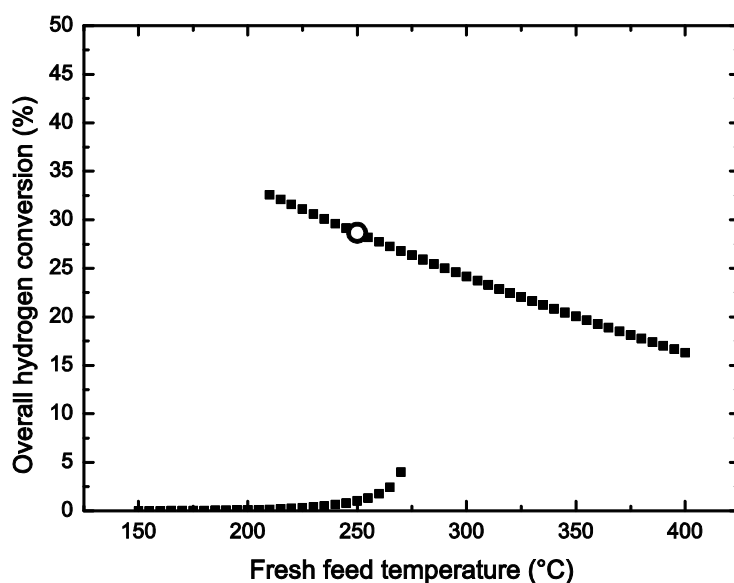
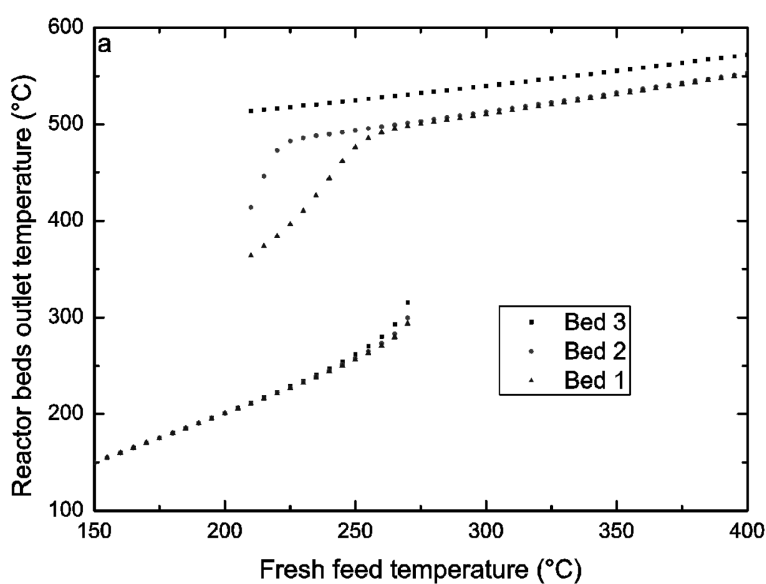


Figure 4 – Overall hydrogen conversion in the reactor system as a function of the fresh feed temperature (empty circle – design operating point)

Various operation process variables dependencies on the fresh feed temperature and pressure were monitored. Figure 5 presents the set of the steady states outlet temperatures of products, the molar fractions of ammonia from individual reactor beds and the required heat removal in the refrigeration unit for different fresh feed temperatures of the reactant mixture. Similar dependencies are depicted in Figure 6, where the set of the steady states outlet temperatures of products and the molar fractions of ammonia from individual reactor beds for different pressures of the reactant mixture is presented. It is evident, that the response of the process is dependent on the value of a deviation. When the fresh feed temperature was decreased to the value of 200 °C, the reaction conditions changed significantly. The temperature of the reactor outlet stream was decreased by approximately 70 % from the design intent (Figure 5a) and the analysis of the composition of the individual beds outlet streams confirmed the termination of the reaction (Figure 5b). The molar fraction of ammonia is approximately the same in the reactor beds outlet streams as in the fresh feed stream what means very low ammonia production in the reactor system. The required heat removal in the refrigeration unit is decreased from ca. 120 MW to ca. 60 MW (Figure 5c). When the pressure in the reactor system was decreased to the value of 12 MPa, the reactor outlet temperature was decreased by 50% from the design intent (Figure 6a) to the value practically identical with the fresh feed temperature. The termination of the ammonia production was confirmed by the analysis of the molar fraction of ammonia in the reactor beds outlet streams (Figure 6b). After correction of the process control failure and return of the operation process parameter to the desired operating point, the reaction conditions remained in the lower steady state. In this situation, the operation of the unit needs to be interrupted and the operating staff has to carry out a new reactor start-up procedure. The loss of operating time and money is unavoidable.



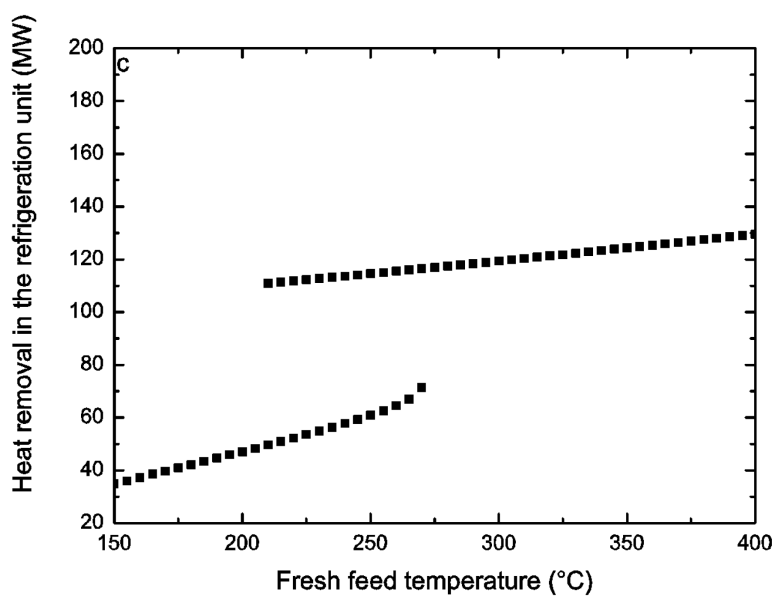
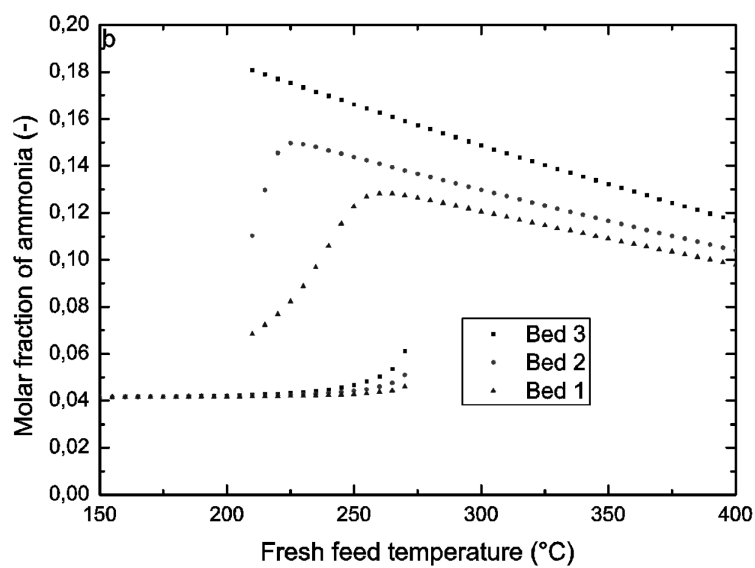


Figure 5 – Operation process variables dependence on the fresh feed temperature – reactor beds outlet temperature (a), molar fraction of ammonia in the beds outlet streams (b), required heat removal in the refrigeration system (c) (triangles – bed 1, circles – bed 2, squares – bed 3)

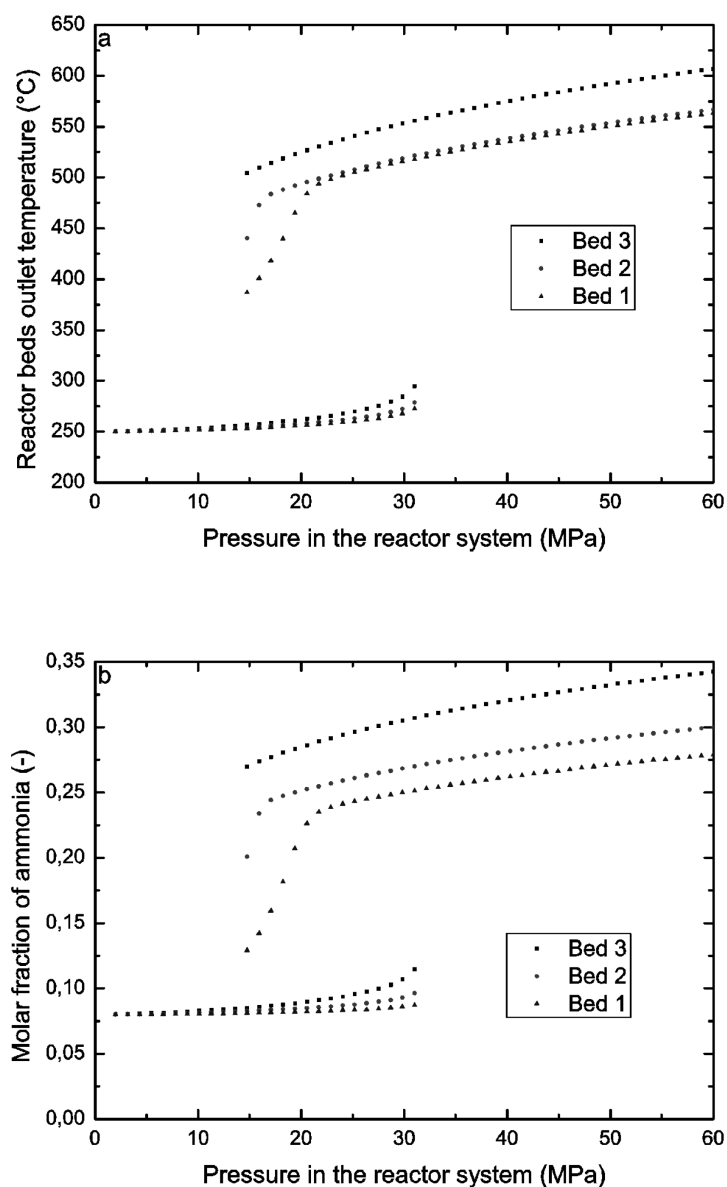


Figure 6 – Operation process variables dependence on the fresh feed pressure – reactor beds outlet temperature (a), molar fraction of ammonia in the beds outlet streams (b) (triangles – bed 1, circles – bed 2, squares – bed 3)

The process behaviour between the higher and lower solution branches is described by the unstable steady states. When the reaction system is forced by process variable deviation to change its steady state to an unstable one, the reaction conditions stabilize in a stable steady state located on the higher or lower solution branch depending on the value and duration of the deviation. The ammonia synthesis modelling in Aspen HYSYS v8.4 environment was unable to identify these unstable steady states<sup>15</sup>.

### Conclusions

A mathematical model suitable for the identification and accurate prediction of nonlinear behaviour of ammonia synthesis was proposed in this work. The case study was focused on the investigation of multiple steady states present in an ammonia synthesis fixed-bed reactor system. As presented, a reaction system can be operated in different regimes (temperature, conversion, pressure ...) under the same feed conditions. In the analysed reactor system, an approximately 20 % decrease of the fresh feed temperature or 40 % decrease of the pressure in the reactor system led to dramatic change of the reaction conditions. The reactor outlet temperature significantly dropped and a decrease of the reaction rate what resulted in very low ammonia production was observed. After returning the operation conditions to the desired operating point, the reaction

conditions remained in a stable steady state located on the lower solution branch. Therefore, a new reactor start-up is required. Knowledge of the multiple steady states phenomenon is crucial for stable and safe operation as well as for design phase of the ammonia synthesis unit.

Consequences revealed in this work are unlikely to be detected by a conventional HAZOP analysis and therefore, the performance of a model-based HAZOP study is necessary to avoid overlooking nonlinear character of process and its possible hazard consequences. Switching between different steady states can lead to an operational problem or a dangerous event. A failure of a single process variable (the fresh feed temperature and pressure control failures were presented) can cause operation regime change of the reaction conditions. The identification of unstable steady states as well as manipulation with some internal variables was not allowed by Aspen HYSYS v8.4 modelling. Therefore, a simulation tool optimised for safety engineering purposes has to be developed.

### Acknowledgments

*This work was supported by the Slovak Scientific Agency, Grant No. VEGA 1/0749/15 and by the OP Research and Development of the project University Science Park STU Bratislava, ITMS 26240220084, co-financed by the Fund of European Regional Development.*

### Literature

1. Kletz T. A.: *Reliab. Eng. Syst. Saf.* **55**, 263-266 (1997).
2. Dowell III A. M.: *ISA Trans.* **37**, 155 (1998).
3. Seligmann B. J., Németh E., Hangos K. M., Cameron I. T.: *J. Loss Prev. Process Ind.* **25**, 746 (2012).
4. Boonthum N., Mulalee U., Srinophakun T.: *Reliab. Eng. Syst. Saf.* **121**, 152 (2014).
5. Dunjó J., Fthenakis V., Vilchez J. A., Arnaldos J.: *J. Hazard. Mater.* **173**, 21 (2010).
6. Venkatasubramanian V., Vaidhyanathan R.: *AIChE J.* **40**, 496 (1994).
7. Khan F. I., Abbasi S. A.: *J. Loss Prev. Process Ind.* **10**, 333 (1997).
8. Kang B., Lee B., Kang K., Suh J., Yoon E.: *Expert Syst. Appl.* **16**, 183 (1999).
9. Labovský J., Švandová Z., Markoš J., Jelemenský Ľ.: *Chem. Eng. Sci.* **62**, 4915-4919 (2007).
10. Eizenberg S., Shacham M., Brauner N.: *J. Loss Prev. Process Ind.* **19**, 754 (2006).
11. Labovský J., Švandová Z., Markoš J., Jelemenský Ľ.: *J. Loss Prev. Process Ind.* **20**, 230 (2007).
12. Jeerawongsuntorn C., Sainyamsatit N., Srinophakun T.: *J. Loss Prev. Process Ind.* **24**, 412 (2011).
13. Morud J., Skogestad S.: *AIChE J.* **44**, 889 (1998).
14. Froment G. F., Bischoff K. B., in book: *Chemical Reactor Analysis and Design, 2<sup>nd</sup> edition*. p. 433. Wiley, New York 1990.
15. Labovská Z., Labovský J., Jelemenský Ľ., Dudáš J., Markoš J.: *J. Loss Prev. Process Ind.* **29**, 157-158 (2014).

## IDENTIFICATION OF HAZARDS ASSOCIATED WITH OPERATION OF INDUSTRIAL CEMENTATION FURNACE

**Mukhametzianova L.**, Kotek L.

*Fakulta strojního inženýrství, Vysoké učení technické v Brně, Technická 2896/2, 61669, Brno, y150051@stud.fme.vutbr.cz*

### Summary

In terms of safety, industrial cementation furnaces are a source of risk; they use dangerous substances (cementation liquids and gases, inert gases, fuel gases, combustible quenching oils) at high temperatures. Any failure or operator's error may cause damage to the health of employees, as well as more serious consequences - fire, explosion, asphyxiation. Therefore it is important to consider possible accident scenarios, determine their causes and consequences, to propose a sequence of actions in case of occurrence of hazardous event, and to recommend corrective measures - technical and organizational. This article discusses the possible hazards associated with the operation of cementation furnaces.

**Keywords:** risk analysis, hazard identification, cementation furnace

### Introduction

Automation of engineering processes exerts pressure on the use of new designs of electro-thermal equipment, such as industrial furnaces. To increase the surface hardness of the material and its internal toughness, a cementation process is used. During cementation, carbon is diffusively added into the steel surface by heating the material above the transformation temperature in a controlled carburizing atmosphere.

In terms of safety, cementation furnaces represent a source of risk for the operator<sup>1</sup>; they use hazardous substances (cementation liquids and gases, inert gases, fuel gases, combustible quenching oils) at high temperatures.

As a source of carbon in the furnace, it is possible to use a cementing powder or soluble hydrocarbons: propane, butane, acetylene. Since these gases are explosive, it is necessary to prevent their reaction with oxygen. For this purpose, inert gases, e.g. nitrogen, are used. Hazardous may not be only propane, which is used directly in the furnace, but also hydrogen, which is a result of chemical reaction during cementation. Hydrogen may form an explosive mixture with oxygen or air in a wide concentration range of (4-95% by volume of hydrogen in oxygen, and of 4-77% by volume of hydrogen in air)<sup>2</sup>.

Hardness of steel can also be increased by quenching. For this process, the following media can be used - water, oil, molten salt and metal baths or air. A disadvantage of using the oil is its combustibility. It is also necessary to mention that oil degradation causes a reduction in flash point, which can cause a fire. Therefore the early exchange of oil in the quenching bath is important. It is also necessary to mention the amount of oil in the tank, which is complemented manually by the operator. Due to the operator's error, the oil level may be higher; the oil may splash over the hot parts of the furnace and ignite. Therefore, in this case, a human error plays a considerable role. Any failure or operator's error may cause damage to the health of employees, as well as more serious consequences - fire, explosion, asphyxiation.

Quite often a fire of industrial furnaces occurs for various reasons, from technological defects of the furnace to organizational errors and operator's errors<sup>3,4,5</sup>. In terms of consequences, accidents represent considerable financial losses; in some cases there were also injuries of staff. Common causes of accidents are a failure to comply with safety principles, operator's error (failure to control the dosage of nitrogen), inadequate working conditions and organizational factors (the staff did not know about the existing hazards and were not trained).

Avoidance of hazardous events or reduction of the scope of their consequences can be achieved using a risk analysis: to consider potential accident scenarios, to determine their causes and consequences, to propose the sequence of steps in the event of occurrence of a hazardous event and to recommend corrective measures. The subject of this article will be a cementation furnace, where propane and methanol are used as a carbon source. Nitrogen is used as part of cementing atmosphere; the oil is used for quenching.

The cementation furnace, which is described in the article, consists of the following components:

- Casing;
- Pre-chamber, which contains a quenching bath;
- Steel refractory retort, where the process of cementation is carried out;
- Electric equipment of the furnace (cable, furnace cooling fan);
- Burner which burns the excess gas from the furnace;
- Media switchboard (propane, methanol, nitrogen, air).

## Methods

Hazard identification is an integral part of risk analysis and a basis for further identification of scenarios for potential accidents. For hazard identification, a systematic method HAZOP was used, where a team of experts, using combinations of keywords and individual parameters of the system, identifies potential scenarios, causes and consequences. Further, the team suggests the sequence of steps that need to be done in case of hazardous event and potential measures to avert such an event. A list of keywords, their importance and the example of their use for the cementation furnace is given in Table 1<sup>6,7</sup>.

Table I

Example of table for HAZOP method

Keyword	Logical meaning of word	Example of use
No	Negation of meaning of original function	No cooling
Higher	Quantitative increase	Higher flow
Lower	Quantitative decrease	Lower flow
And also, and as well	Qualitative increase	Penetration of water into reactor
Partial	Qualitative decrease	Partial flow
Reversion	Reversion of function	Reverse flow of medium
Other	Replacement	Presence of other substances

The HAZOP method was chosen due to its systematic approach and consistency. The example in the header of the table for HAZOP is given in Table 2<sup>7</sup>.

Table II

Header of table for implementation of HAZOP method

Keyword	Parameter	Deviation	Potential causes	Consequences	Safety functions	Actions, measures
---------	-----------	-----------	------------------	--------------	------------------	-------------------

## Results

Using keywords and parameters of each component of the furnace, deviations for each parameter were created. Table 3 shows an example of deviations for retort, pre-chamber and quenching bath.

Table III

Parameter deviations of cementation furnace components

Steel refractory retort	Pre-chamber	Quenching oil bath
<ul style="list-style-type: none"> <li>- lower temperature in retort;</li> <li>- higher temperature in retort;</li> <li>- absence of nitrogen in retort, and also of cementation atmosphere;</li> <li>- lower concentration of nitrogen in retort;</li> <li>- higher concentration of nitrogen in retort;</li> <li>- absence of cementation atmosphere in retort;</li> <li>- lower concentration of cementation atmosphere in retort;</li> <li>- higher concentration of cementation atmosphere in retort;</li> <li>- lower pressure in retort;</li> <li>- higher pressure in retort;</li> <li>- door of retort is closed, but should be open.</li> </ul>	<ul style="list-style-type: none"> <li>- higher temperature in pre-chamber;</li> <li>- higher concentration of cementation atmosphere in pre-chamber;</li> <li>- lower pressure in pre-chamber ;</li> <li>- higher pressure in pre-chamber ;</li> <li>- door of pre-chamber is closed but should be open.</li> </ul>	<ul style="list-style-type: none"> <li>- higher concentration of oxygen in oil vapours and also a source of initiation;</li> <li>- higher temperature of oil;</li> <li>- higher level of oil in the tank;</li> <li>- lower level of oil in the tank;</li> <li>- and also other substance in the oil bath (water);</li> <li>- and also degradation of oil.</li> </ul>

We also identified the causes of the respective deviation and consequences. During the analysis we identified the following causes and consequences of parameter deviations:

Consequences:

- explosion;
- burns of operator;
- scalds of operator;
- asphyxiation of operator;
- fire in pre-chamber;
- deteriorated quality of carburizing and quenching;
- destruction of equipment;
- production downtime, economic losses.

Causes:

- error of operator;
- manufacturing defect;
- failure of any component of facility (control system, sensor, valve, etc.);
- chemical reaction;
- external influences (cut of electric power supply).

Causes and consequences are shown in Table 4.

Table IV

Causes and consequences of parameter deviations of cementation furnace components

Consequences/causes	Error of operator	Manufacturing defect	Failure	Chemical reaction	External influences
Explosion	X	X	X	X	X
Burns of operator			X		
Scalds of operator	X				
Asphyxiation of operator		X	X		
Fire in pre-chamber	X			X	
Deteriorated quality of carburizing and quenching	X		X		
Destruction of equipment			X		
Production downtime, economic losses	X		X		X

An evaluation of the impact of the individual causes is shown in Figure 1. According to the Pareto principle, 80% of consequences are caused by 20% of causes. In the case of cementation furnace, the above consequences may be caused by: failure of any component of the facility, operator's error and manufacturing defect.

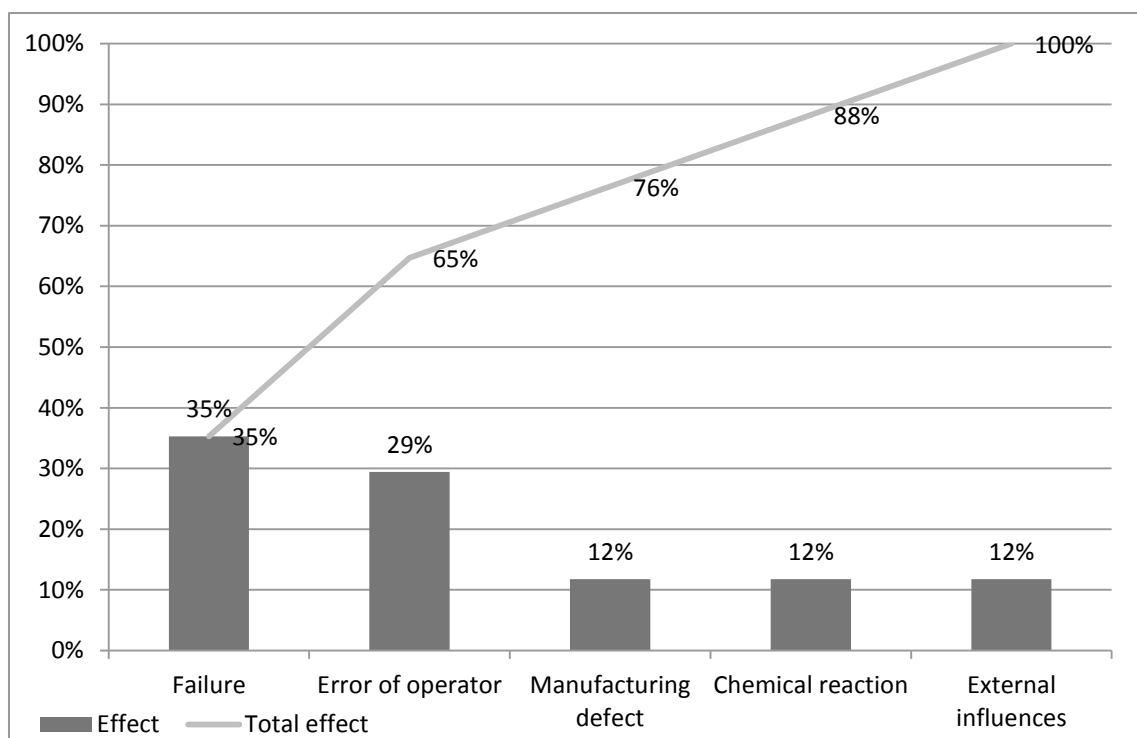


Figure 1. Evaluation of significance of the impact of individual causes

### Discussion

Explosions can be caused by production defect (leak), failure of device component (pressure relief valve, burner, control system, nitrogen valve), by operator's errors (failure to control the amount of nitrogen and propane for the burner), by a chemical reaction of propane and oxygen and also by external influences, such as cut of electric power supply.

Burns of operator can occur due to uncontrolled high temperature on the jacket surface, due to the failure of control system or temperature sensor. Scalds of operator may also occur in case of adding water into the oil bath instead of oil; water evaporates in large quantities. This is classified as the operator's error.

For safety reasons, the cementation furnace uses an inert gas - nitrogen, which in a certain quantity can cause asphyxiation. Leakage of nitrogen into the outer atmosphere may occur in case of failure of compactness of pre-chamber or retort, either due to a manufacturing defect or impairment of compactness arising during operation. The risk of operator's asphyxiation by inert gas is described in the article<sup>8</sup>.

A serious and fairly frequent scenario is a flare-up of quenching oil because of the presence of water in it. When a red-hot batch of 900°C is immersed into the quenching oil bath having a temperature of 120°C, water suddenly expands (up to 1700 times) and oxidizes the oil, thereby causing a formation of huge flame<sup>9</sup>. Therefore the water content in oil must be checked at every suspicion of its occurrence (foam on the bath surface, a larger amount of generated vapours, higher flames, etc.).

In addition to the threat to health and life of operator and staff present in the shop floor, any failure can also affect the quality of cementing or quenching of the material. Potential causes are as follows:

- operator's error (failure to control a sufficient amount of quenching oil, adding of water instead of oil into the tank, setting the cementation potential)
- failure of control system or the sensor (at a temperature lower than 750°C the gas entering the retort does not decompose into the required carbon and hydrogen necessary for cementation),
- a retort door got jammed ( a batch cannot pass to the pre-chamber for quenching)
- failure of oxygen probe which controls the composition of cementation atmosphere.

As it is known, the production downtime leads to economic losses; therefore it is important to ensure proper running of operation. The cementation furnace complies with the conditions necessary to initiate the cementation process; e.g. in case of malfunction of the burner, the furnace does not switch on, cementation cannot start at a temperature lower than 750°C, the control system does not allow the gases to enter. In a certain way, the operator can also contribute to malfunctioning of the burner if he/she fails to check the amount of propane in the tank or fails to open a ball valve.

Another consequence can be a destruction of equipment. For example, if the sensor sends a wrong signal about the temperature, an uncontrolled heating of furnace will consequently destruct the retort. If the temperature increases in the furnace electric-power area (e.g., due to a fan failure), a damage can occur to cables, dispenser, relay, etc.

### **Conclusion**

This article emphasizes the importance of risk analysis for cementation furnaces because of the existing hazards of fire, explosion, asphyxiation, and burns.

An important part of risk analysis is to identify hazards. For this purpose, various methods are used. The most commonly used method is a HAZOP method; using keywords enables us to find parameter deviations of the facility. This method was used to carry out the hazard identification of cementation furnace. Potential causes of accidents are as follows: operator's error, manufacturing defect, failure of any component of the facility, chemical reaction or external influences (cut of power supply, strike of lightning). During the analysis it was estimated that 35% of consequences is due to the failure of facility components, 29% - operator's error. Particularly important is the scenario of fire in the quenching bath due to the presence of water in the oil. A role of operator is particularly important here: if the oil is not checked for water content, the automatic control system is not able to identify it. To predict the operator's error is not easy. However, with technical and organizational measures it is possible to reduce the probability of errors. For example, the operator performing the task may be safeguarded by a control system or controlled by another person. A proper arrangement of the workplace also contributes to the reduction of human errors. The value of risk of accident or destruction of the equipment is dependent on the probability of failure (error) and the severity of consequences. The probability of failure of technical components is always lower than the probability of human failures, so the resulting value of risk caused by human error is higher.

To identify all potential hazards is an important step for further system analysis, proposal of procedure in case of hazardous event and preventive measures.

### **Acknowledgement**

*These results were obtained with the financial support of Brno University of Technology within the framework of the project FSI-S-14-2401 Green Production – Production machines and equipment.*

### **Literature**

1. Kotek L., Tabas M., Blecha P., Blecha R.: Risk and Hazard Analyses of the Industrial Furnaces. 11th Intl. Probabilistic Safety Assessment and Management Conference and the Annual European Safety and Reliability Conference 2012 (PSAM11 ESREL 2012). 2012.
2. Schroeder V., Holtappels T.: Explosion characteristics of hydrogen-air and hydrogen-oxygen mixture satelevated pressures. International Conference of Hydrogen Safety. 2005.
3. Fire caused due to contact with hot sludge during cleaning a quenching oil bath. In: Failure Knowledge Databaze. [cit. 2015-04-02]. [www.sozogaku.com/fkd/en/cfen/CC1000057.html](http://www.sozogaku.com/fkd/en/cfen/CC1000057.html)
4. Applying STAMP/STPA to Analyze the Causes of the Unexpected Fire Happening at the Heat Treatment Process. Univance. (2015).
5. Vishweshwaraiah Iron Steel Limited (VISL) fire disasters following ladle refining furnace accident, July 12, 1996. Burns. 36 (2010).
6. Kotek L., Tabas M.: HAZOP study with qualitative risk analysis for prioritization of corrective and preventive actions. Procedia Engineering. 2012. 42 (2012).
7. BS IEC 61882:2001. Hazard and operability studies (HAZOP studies). Application guide. British Standards Institution, 2001.
8. Kotek L., Mukhametzianova L., Blecha P., Holub M.: Low Concentration of Oxygen in External Environment - Modeling the Consequences of Accident. Chemical Engineering Transactions. 36 (2014).
9. WOTHERS, Peter. Modern Alchemy: Pouring Water on an Oil Fire. In: Ri Channel [online]. 2013.

## **AUTHORS AND CO-AUTHORS INDEX**

### **A**

Antoš P. 31

### **B**

Babka M. 286  
Balabánová J. 181  
Baláž J. 472  
Báleš V. 404, 410, 472  
Balgová V. 280, 286  
Bártová Š. 113, 341  
Bauerová D. 415  
Bělina P. 166, 201  
Bělohav Z. 156  
Beneš L. 395  
Beneš M. 484  
Bierská L. 172  
Bílková D. 45  
Blažek J. 126, 147  
Blažková K. 484  
Blažková Z. 345, 370  
Božek M. 258  
Brejcha J. 274  
Brozek V. 218  
Brummer V. 323  
Burkovičová A. 162

### **C**

Cais J. 235, 241, 253  
Cakl J. 345, 370  
Chmátal M. 444  
Chraska T. 218  
Ciahotný K. 71, 82  
Černý R. 15, 85, 91, 131, 137, 143  
Červeňanský I. 37, 450  
Červený L. 27, 45, 50  
Čmelík J. 31

### **D**

Danko M. 37, 41  
Dohnalová Ž. 162  
Dubovský M. 263  
Dudáš J. 37  
Ducháček V. 319

Duong V. M. 97, 382  
Dušek L. 349, 359, 365

### **F**

Ferjenčík M. 494  
Filipi M. 269, 314

### **G**

Gajdošová M. 489  
Gojny J. 308  
Gorodylova N. O. 210  
Graczová E. 117  
Grof A. 335  
Gruberová L. 150  
Grůza J. 275  
Gurung B. 296

### **H**

Hablovičová B. 188  
Hájek M. 308, 314  
Hájek P. 71  
Hájková K. 290  
Hájková T. 302  
Hamerníková J. 131, 137  
Hanika J. 435, 463  
Haninčík S. 263  
Hanus K. 404  
Hermann P. 166  
Herzigová L. 274  
Hidalgo J. M. 131  
Hnátková T. 353  
Hofmann J. 431  
Hofmanova D. 478  
Horová D. 31

### **J**

Janata M. 218, 230  
Janošovský J. 37, 41, 500  
Jecha D. 323  
Jelemenský L. 41, 500  
Jirátová K. 181  
Jirešová J. 431  
Jíša P. 131, 143

## K

Kadeřábková A.	319
Kalendová A.	302
Kaluža L.	181
Kaplan O.	444
Karaba A.	66
Karásková Nenadálová L.	107
Karolová L.	214
Kaštánek P.	435
Kittel H.	75
Klajmon M.	113
Klimtová M.	419
Kobetičová K.	428
Kočanová V.	359
Kočetková D.	126, 147
Kočí V.	107, 123, 389, 419, 428
Kolek J.	439
Kolena J.	10, 21, 55
Kořínková J.	415
Kotek L.	508
Koudelka L.	177
Koutník I.	424
Kovalčík T.	247
Krátká M.	27
Kratochvíl B.	150
Kratochvíla K.	275
Kreibichova B.	478
Krejzová E.	156
Krch J.	75
Křiška M.	353
Krupičková K.	50
Krupka J.	50, 60
Krýsa J.	172
Kříž J.	225
Kubatík F.T.	218, 225, 230
Kulaviak L.	478
Kůs P.	113, 341
Kušnierik O.	330
Kvasničková E.	457, 466

## L

Labovská Z.	37,41
Labovský J.	37, 41, 500
Lederer J.	66
Lestinsky P.	323

Losonszky G.	428
Luxová J.	193, 214

## M

Machač P.	71, 97, 123
Machalický O.	370, 415
Maléterová Y.	463
Marek I.	225
Markoš J.	450
Martínková L.	444
Masák J.	457, 466
Mastny L.	218
Mašín J.	494
Matějovský L.	147
Mierka O.	101
Mihaľ M.	450
Mikala O.	269, 308, 314
Milichovský M.	269, 308, 314
Morávek P.	10
Mošner P.	10, 177
Mukhametzianova L.	508
Mušálek R.	218, 230

## N

Němec J.	137
Novák P.	225, 247
Novotný L.	359

## O

Olšovský M.	258, 263
Opršal J.	395
Otmar J.	60

## P

Palarčík J.	345, 370
Palatý Z.	365
Palcheva R.	181
Pařízek O.	428
Patáková P.	439
Patera J.	484
Pawlesa J.	60
Pěček D.	489
Petrů J.	21
Pilař L.	123, 375
Pluhařová L.	201

Pospíšilová M.	31	Škopková T.	156
Potůček F.	290, 296	Šmejdomá V.	341
Prokešová A.	15, 85	Šolcová O.	435, 463
Purkarová E.	82	Špitová B.	424
<b>R</b>		Šťábová G.	10, 55
Račický A.	177	Štefanica J.	71, 123
Rinágelová A.	444	Štěpánek F.	489
Romero A. A.	131	Štěpánek K.	10
Rousková M.	463	Šulcová P.	162, 188, 193, 201, 210
Rozkošný M.	353	Šváb M.	82
Růžička M.	10, 478	Šveda H.	341
Ryšánek P.	31	Švrček J.	172, 258
Říhová Ambrožová J.	341	<b>T</b>	
Říhová M.	296	Těšitelová K.	210
<b>S</b>		Timár P.	404, 410, 472
Sadílek J.	280	Timár P., Jr.	404, 410, 472
Salvetr P.	225	Tlustý J.	75
Sarvašová N.	489	Tomášek J.	147
Seidl J.	431	Tomić A.	365
Seilerová L.	150	Trojan J.	214
Schöngut J.	10	Trojan M.	214
Skryja P.	323	Trousil V.	345, 370
Sleňhová E.	345, 370	Tukač V.	15, 85
Slezák M.	345	Tyuliev G.	181
Smolná K.	431	<b>U</b>	
Smutná J.	71, 123	Uotilla J.	335
Souček M.	172	<b>V</b>	
Soukupová L.	55	Váchová V.	126
Spojakina A.	181	Variny M.	101
Stáně R.	45	Věčeř M.	424
Staš M.	126	Veselá A.B.	444
Stehlík K.	113	Veselý M.	85
Steltenpohl P.	117	Veselý V.	375
Stopka J.	404, 410	Vilémová M.	230
Strouhal J.	201	Vlček M.	395
Sustek S.	206	Vlček Z.	375
Svoboda L.	166, 201, 206	Vojs M.	365
Svobodová J.	235, 241, 253	Vojtěch D.	247
Šerák J.	247	Vonková K.	113, 341
Šereš M.	353	Vráblík A.	85, 91, 131, 137
Šícha V.	466	Vrátničková Z.	286
Šimáček P.	126	Vrbková E.	50
Šimek M.	399	Vymazal J.	353
Šinkovská M.	193		

Vyňuchal J. 399  
Vyskočilová E. 27, 50

## **W**

Weidlich T. 395, 399  
Weiss V. 235, 241, 253  
Wertz F. 107

## **Y**

Yepez A. 131

## **Z**

Zakuciová K. 389  
Zámostný P. 21, 66, 478  
Zbuzek M. 15, 85, 137  
Zbuzková B. 147  
Zelenkova K. 478  
Zseliga Z. 375